



agriculture

Special Issue Reprint

Advances in Agricultural Engineering Technologies and Application

Volume II

Edited by
Muhammad Sultan, Redmond R. Shamshiri,
Md Shamim Ahamed and Muhammad Farooq

mdpi.com/journal/agriculture



**Advances in Agricultural Engineering
Technologies and Application—
Volume II**

Advances in Agricultural Engineering Technologies and Application— Volume II

Editors

Muhammad Sultan

Redmond R. Shamshiri

Md Shamim Ahamed

Muhammad Farooq



Basel • Beijing • Wuhan • Barcelona • Belgrade • Novi Sad • Cluj • Manchester

Editors

Muhammad Sultan
Bahauddin Zakariya
University
Multan, Pakistan

Redmond R. Shamshiri
Leibniz-Institut für
Agrartechnik und
Bioökonomie
Potsdam, Germany

Md Shamim Ahamed
University of California Davis
Davis, USA

Muhammad Farooq
University of Engineering
and Technology
Lahore, Pakistan

Editorial Office

MDPI
St. Alban-Anlage 66
4052 Basel, Switzerland

This is a reprint of articles from the Special Issue published online in the open access journal *Agriculture* (ISSN 2077-0472) (available at: https://www.mdpi.com/journal/agriculture/special-issues/aengineeringtechno_agriculture).

For citation purposes, cite each article independently as indicated on the article page online and as indicated below:

Lastname, A.A.; Lastname, B.B. Article Title. <i>Journal Name</i> Year , <i>Volume Number</i> , Page Range.
--

Volume II

ISBN 978-3-0365-9376-0 (Hbk)

ISBN 978-3-0365-9377-7 (PDF)

doi.org/10.3390/books978-3-0365-9377-7

Set

ISBN 978-3-0365-9372-2 (Hbk)

ISBN 978-3-0365-9372-2 (PDF)

Contents

About the Editors	vii
Preface	ix
Baidong Zhou, Yexin Li, Cong Zhang, Liewang Cao, Chengsong Li, Shouyong Xie and Qi Niu Potato Planter and Planting Technology: A Review of Recent Developments Reprinted from: <i>Agriculture</i> 2022 , <i>12</i> , 1600, doi:10.3390/agriculture12101600	1
Linrong Shi, Wuyun Zhao, Chengting Hua, Gang Rao, Junhai Guo and Zun Wang Study on the Intercropping Mechanism and Seeding Improvement of the Cavity Planter with Vertical Insertion Using DEM-MBD Coupling Method Reprinted from: <i>Agriculture</i> 2022 , <i>12</i> , 1567, doi:10.3390/agriculture12101567	29
Maham Navida, Muhammad Nadeem, Tahir Mahmood Qureshi, Rami Adel Pashameah, Faiqa Malik, Aqsa Iqbal, et al. The Synergistic Effects of Sonication and Microwave Processing on the Physicochemical Properties and Phytochemicals of Watermelon (<i>Citrullus lanatus</i>) Juice Reprinted from: <i>Agriculture</i> 2022 , <i>12</i> , 1434, doi:10.3390/agriculture12091434	51
Mingxiong Ou, Tianhang Hu, Mingshuo Hu, Shuai Yang, Weidong Jia, Ming Wang, et al. Experiment of Canopy Leaf Area Density Estimation Method Based on Ultrasonic Echo Signal Reprinted from: <i>Agriculture</i> 2022 , <i>12</i> , 1569, doi:10.3390/agriculture12101569	65
Xiaoxu Sun, Zhixiong Lu, Yue Song, Zhun Cheng, Chunxia Jiang, Jin Qian and Yang Lu Development Status and Research Progress of a Tractor Electro-Hydraulic Hitch System Reprinted from: <i>Agriculture</i> 2022 , <i>12</i> , 1547, doi:10.3390/agriculture12101547	79
Zihao Meng, Lixin Zhang, Huan Wang, Xiao Ma, He Li and Fanglei Zhu Research and Design of Precision Fertilizer Application Control System Based on PSO-BP-PID Algorithm Reprinted from: <i>Agriculture</i> 2022 , <i>12</i> , 1395, doi:10.3390/agriculture12091395	99
Xiuhua Song, Hong Li, Chao Chen, Huameng Xia, Zhiyang Zhang and Pan Tang Design and Experimental Testing of a Control System for a Solid-Fertilizer-Dissolving Device Based on Fuzzy PID Reprinted from: <i>Agriculture</i> 2022 , <i>12</i> , 1382, doi:10.3390/agriculture12091382	115
Se-Jun Park, In-Bok Lee, Sang-Yeon Lee, Jun-Gyu Kim, Young-Bae Choi, Cristina Decano-Valentin, et al. Numerical Analysis of Ventilation Efficiency of a Korean Venlo-Type Greenhouse with Continuous Roof Vents Reprinted from: <i>Agriculture</i> 2022 , <i>12</i> , 1349, doi:10.3390/agriculture12091349	131
Bowen Zheng, Zhenghe Song, Enrong Mao, Quan Zhou, Zhenhao Luo, Zhichao Deng, et al. An ANN-PSO-Based Method for Optimizing Agricultural Tractors in Field Operation for Emission Reduction Reprinted from: <i>Agriculture</i> 2022 , <i>12</i> , 1332, doi:10.3390/agriculture12091332	153
Yaoming Li, Yanbin Liu, Kuizhou Ji and Ruiheng Zhu A Fault Diagnosis Method for a Differential Inverse Gearbox of a Crawler Combine Harvester Based on Order Analysis Reprinted from: <i>Agriculture</i> 2022 , <i>12</i> , 1300, doi:10.3390/agriculture12091300	169

Wenqi Zhou, Chao Song, Xiaobo Sun, Ziming Liu, Xue Ni, Kangjia Shen, et al. Design of High-Efficiency Soil-Returning Liquid Fertilizer Deep-Application Furrow Openers for Improving Furrowing Performance in Cold Regions of Northeast China Reprinted from: <i>Agriculture</i> 2022 , <i>12</i> , 1286, doi:10.3390/agriculture12091286	183
Yaohua Hu, Huanbo Yang, Bingru Hou, Ziting Xi and Zidong Yang Influence of Spray Control Parameters on the Performance of an Air-Blast Sprayer Reprinted from: <i>Agriculture</i> 2022 , <i>12</i> , 1260, doi:10.3390/agriculture12081260	205
Dejiang Liu, Yan Gong, Xuejun Zhang, Qingxu Yu, Xiao Zhang, Xiao Chen and Yemeng Wang EDEM Simulation Study on the Performance of a Mechanized Ditching Device for Codonopsis Planting Reprinted from: <i>Agriculture</i> 2022 , <i>12</i> , 1238, doi:10.3390/agriculture12081238	219
Pavel Tikhonov, Konstantin Morenko, Arseniy Sychov, Vadim Bolshev, Alexander Sokolov and Alexander Smirnov LED Lighting Agrosystem with Parallel Power Supply from Photovoltaic Modules and a Power Grid Reprinted from: <i>Agriculture</i> 2022 , <i>12</i> , 1215, doi:10.3390/agriculture12081215	233
Bulent Tugrul, Elhoucine Elfatimi and Recep Eryigit Convolutional Neural Networks in Detection of Plant Leaf Diseases: A Review Reprinted from: <i>Agriculture</i> 2022 , <i>12</i> , 1192, doi:10.3390/agriculture12081192	245
Xinping Li, Wantong Zhang, Wenzhe Wang and Yu Huang Design and Test of Longitudinal Axial Flow Staggered Millet Flexible Threshing Device Reprinted from: <i>Agriculture</i> 2022 , <i>12</i> , 1179, doi:10.3390/agriculture12081179	267
Mei Jin, Min Zhang, Gang Wang, Suning Liang, Chongyou Wu and Ruiyin He Analysis and Simulation of Wheel-Track High Clearance Chassis of Rape Windrower Reprinted from: <i>Agriculture</i> 2022 , <i>12</i> , 1150, doi:10.3390/agriculture12081150	285
Meimei Wang, Qingting Liu, Yinggang Ou and Xiaoping Zou Numerical Simulation and Verification of Seed-Filling Performance of Single-Bud Billet Sugarcane Seed-Metering Device Based on EDEM Reprinted from: <i>Agriculture</i> 2022 , <i>12</i> , 983, doi:10.3390/agriculture12070983	305
Meimei Wang, Qingting Liu, Yinggang Ou and Xiaoping Zou Experimental Study of the Planting Uniformity of Sugarcane Single-Bud Billet Planters Reprinted from: <i>Agriculture</i> 2022 , <i>12</i> , 908, doi:10.3390/agriculture12070908	317
Tao Wang, Zhengdao Liu, Xiaoli Yan, Guopeng Mi, Suyuan Liu, Kezhou Chen, et al. Finite Element Model Construction and Cutting Parameter Calibration of Wild Chrysanthemum Stem Reprinted from: <i>Agriculture</i> 2022 , <i>12</i> , 894, doi:10.3390/agriculture12060894	333
Kezhou Chen, Xing Liu, Shiteng Jin, Longfei Li, Xin He, Tao Wang, et al. Design of and Experiments with an Automatic Cuttage Device for an Arch Shed Pillar with Force Feedback Reprinted from: <i>Agriculture</i> 2022 , <i>12</i> , 875, doi:10.3390/agriculture12060875	345
Hao Zhu, Xiaoning He, Shuqi Shang, Zhuang Zhao, Haiqing Wang, Ying Tan, et al. Evaluation of Soil-Cutting and Plant-Crushing Performance of Rotary Blades with Double-Eccentric Circular-Edge Curve for Harvesting <i>Cyperus esculentus</i> Reprinted from: <i>Agriculture</i> 2022 , <i>12</i> , 862, doi:10.3390/agriculture12060862	365

Dejiang Liu, Yan Gong, Xuejun Zhang, Xiao Chen, Guo Wang and Xiao Zhang Design and Experiment of Dry-Farming Cantaloupe Transplanter under Water Reprinted from: <i>Agriculture</i> 2022 , <i>12</i> , 796, doi:10.3390/agriculture12060796	387
Argelys Kessel-Domini, Daisy Pérez-Brito, Adolfo Guzmán-Antonio, Felipe A. Barredo-Pool, Javier O. Mijangos-Cortés, Lourdes Georgina Iglesias-Andreu, et al. Indirect Somatic Embryogenesis: An Efficient and Genetically Reliable Clonal Propagation System for <i>Ananas comosus</i> L. Merr. Hybrid “MD2” Reprinted from: <i>Agriculture</i> 2022 , <i>12</i> , 713, doi:10.3390/agriculture12050713	401
Syaifullah Muhammad, H. P. S. Abdul Khalil, Shazlina Abd Hamid, Yonss M. Albadn, A. B. Suriani, Suraiya Kamaruzzaman, et al. Insights into Agricultural-Waste-Based Nano-Activated Carbon Fabrication and Modifications for Wastewater Treatment Application Reprinted from: <i>Agriculture</i> 2022 , <i>12</i> , 1737, doi:10.3390/agriculture12101737	419
Ling Ren, Bindong Zhao, Weibin Cao, Wenbin Song and Ming Zhao Design of Stretchable Style Pick-Up Device for Tomato Seedling Transplanters Reprinted from: <i>Agriculture</i> 2022 , <i>12</i> , 707, doi:10.3390/agriculture12050707	439
Ahmad Mujtaba, Ghulam Nabi, Muhammad Masood, Mudassar Iqbal, Hafiz M. Asfahan, Muhammad Sultan, et al. Impact of Cropping Pattern and Climatic Parameters in Lower Chenab Canal System—Case Study from Punjab Pakistan Reprinted from: <i>Agriculture</i> 2022 , <i>12</i> , 708, doi:10.3390/agriculture12050708	453
Yiyuan Pang, Hong Li, Pan Tang and Chao Chen Synchronization Optimization of Pipe Diameter and Operation Frequency in a Pressurized Irrigation Network Based on the Genetic Algorithm Reprinted from: <i>Agriculture</i> 2022 , <i>12</i> , 673, doi:10.3390/agriculture12050673	473
Weixuan Jiao, Zhishuang Li, Li Cheng, Yuqi Wang and Bowen Zhang Study on the Hydraulic and Energy Loss Characteristics of the Agricultural Pumping Station Caused by Hydraulic Structures Reprinted from: <i>Agriculture</i> 2022 , <i>12</i> , 1770, doi:10.3390/agriculture12111770	489
Tao Zhang, Yaoming Li, Lizhang Xu, Yanbin Liu, Kuizhou Ji and Sheng Jiang Experimental Study on Fluidization Behaviors of Wet Rice Threshed Materials with Hot Airflow Reprinted from: <i>Agriculture</i> 2022 , <i>12</i> , 601, doi:10.3390/agriculture12050601	505

About the Editors

Muhammad Sultan

Dr. Muhammad Sultan is an Associate Professor of Agricultural Engineering at Bahauddin Zakariya University (Pakistan). He holds a B.Sc. and an M.Sc. in Agricultural Engineering from the University of Agriculture Faisalabad (Pakistan) and a Ph.D. in Energy and Environmental Engineering from Kyushu University (Japan). He also conducted postdoctoral research at Kyushu University (Japan) and Simon Fraser University (Canada). Dr. Sultan has been recognized as one of the World's Top 2% Scientists (2023) by Stanford University/Elsevier. He also ranked No. 1 as a Scientist in Agricultural Engineering (Pakistan) according to the AD Scientific Index. He has published more than 300 articles in international journals, conferences, books, and book chapters. He has been a reviewer for more than 100 renowned journals and holds editor roles for 15 SCI journals. His research focuses on developing energy-efficient temperature and humidity control systems for agricultural applications including greenhouse, fruit/vegetable storage, livestock, and poultry applications. His research involves adsorption heat pumps, desiccant air-conditioning, evaporative cooling, Maisotsenko cycle, adsorption desalination, energy recovery ventilator, atmospheric water harvesting, and wastewater treatment.

Redmond R. Shamshiri

Dr. Redmond R. Shamshiri is a senior scientist at the Leibniz-Institut für Agrartechnik und Bioökonomie working on agro-mechatronics projects. He holds a Ph.D. in Agricultural Automation with a focus on control systems and dynamics. His research fields include distributed collision avoidance for autonomous navigation of agricultural mobile robots, wireless sensors for digital farming applications, and optimization of controlled environment crop production systems. He is currently involved in the evaluation of 5G technology to reduce yield losses from potato fields.

Md Shamim Ahamed

Dr. Shamim Ahamed currently serves as an Assistant Professor in the Department of Biological and Agricultural Engineering at the University of California, Davis (UC Davis). He completed his bachelor's degree in Agricultural Engineering and master's degree in Farm Power and Machinery from Bangladesh Agricultural University (BAU) and his Ph.D. in Environmental Engineering from the University of Saskatchewan in Canada. Before joining UC Davis, he worked as a postdoctoral fellow at the City University of Hong Kong and Concordia University in Montreal. Dr. Ahamed is leading the Controlled Environment Engineering Lab at UC Davis and has been working in energy systems optimization and precision controls for controlled environment agriculture (CEA) systems (greenhouses, indoor vertical farming, and livestock barns) in 2013. His research mainly focuses on thermal environment modeling, energy-efficient controls, and HVAC systems designed for next-generation CEA. His research aims to integrate renewable energy into the operations of heating, ventilation, air conditioning, and dehumidification systems to achieve a net-zero energy status for CEA facilities. His research also spans automated fault detection and diagnosis of automatic and precision control of HVAC systems and other systems like nutrient management, CO₂ enrichment, and lighting.

Muhammad Farooq

Dr. Muhammad Farooq is an experienced professional with more than 15 years of blended experience with research, teaching, training, industry, and the management of projects around the world and has visited more than 25 countries for different activities related to his profession. Currently, he is working as an Associate Professor and Director Postgraduate Research and leading an international multidisciplinary research group focused on energy environment and sustainability research (EESR) at the department of Mechanical Engineering, University of Engineering and Technology Lahore Pakistan, with a team of 30+ researchers and international collaborators, while supervising a number of M.Sc. and PhD students. He is the author of 100+ leading international journal articles; has a cumulative impact factor of 500+; and advocates for worldwide net-zero and carbon-natural activities to achieve sustainable environments via application of the SDGs. His work has been cited 2000+ times according to Google Scholar. He is among the top 2% scientists according to the list issued by Stanford University, USA, and Elsevier/Scopus in October 2023. As an editor, he has handled more than 400 research articles of different journals and peer-reviewed international conferences. As a volunteer and recognized reviewer of leading international journals, he has reviewed more than 300 research papers and received recognition awards from top-notch journals of Elsevier, Springer, SAGE Publishing, MDPI, and the Taylor & Francis group.

Preface

Modernization in the agriculture sector is important to ensure food security and poverty alleviation, which are the primary themes of UN-SDGs. There are many challenges in developing advanced agricultural techniques, tools, and systems, by which sustainable agriculture and food security can be satisfied.

Worldwide, agricultural mechanization and modernization can be attained with advancements in agricultural engineering technologies and their associated applications. The concept is directly linked to the technological advancements in agricultural automation and robotics; precision agriculture; high-efficiency irrigation systems; farm energy systems; handling, storage, and processing of agricultural products; livestock and poultry sheds; farm water/wastewater management; biomass, biogas, and biochar; remote sensing and geographical studies; societal aspects in agriculture; and the associated bioenvironment.

Such advances in agricultural engineering technologies and applications are the need of the 21st century, particularly from the viewpoint of the agricultural food–energy–water security nexus. Therefore, this book provides a dedicated collection of original research and review studies in the abovementioned research areas.

Muhammad Sultan, Redmond R. Shamshiri, Md Shamim Ahamed, and Muhammad Farooq
Editors

Review

Potato Planter and Planting Technology: A Review of Recent Developments

Baidong Zhou, Yexin Li, Cong Zhang, Liewang Cao, Chengsong Li, Shouyong Xie and Qi Niu *

College of Engineering and Technology, Southwest University, Chongqing 400715, China

* Correspondence: niuqi2019@swu.edu.cn; Tel.: +86-152-0107-1052

Abstract: Potato is one of the most important food crops in the world, which is of great significance for sustainable agricultural development. Mechanized planting is the essential technical link in mechanized production, which has an essential component in the potato growing industry. The mechanization of potato planting technology is an effective method of increasing potato yields. A variety of potato planting technologies and machines have been developed around the world. This review presents the research progress and application status of potato planters and planting technology worldwide. It classifies the planting technology into four types: research of materials characteristics for potatoes, soil cultivation, seed potato separation, and zero-speed seeding. The most critical seed potato separation technology was divided into six types according to the structure of the seed metering device. Detailed features have been provided for some typical potato planters and soil cultivation machines. Finally, the developing trend of intelligent planting technology was analyzed, and some suggestions were proposed to promote the development of potato planters.

Keywords: potato planter; soil cultivation; mechanization; seed metering device; intelligent seeding

Citation: Zhou, B.; Li, Y.; Zhang, C.; Cao, L.; Li, C.; Xie, S.; Niu, Q. Potato Planter and Planting Technology: A Review of Recent Developments. *Agriculture* **2022**, *12*, 1600. <https://doi.org/10.3390/agriculture12101600>

Academic Editors: Muhammad Sultan, Redmond R. Shamshiri, Md Shamim Ahamed and Muhammad Farooq

Received: 1 September 2022

Accepted: 19 September 2022

Published: 2 October 2022

Publisher's Note: MDPI stays neutral with regard to jurisdictional claims in published maps and institutional affiliations.



Copyright: © 2022 by the authors. Licensee MDPI, Basel, Switzerland. This article is an open access article distributed under the terms and conditions of the Creative Commons Attribution (CC BY) license (<https://creativecommons.org/licenses/by/4.0/>).

1. Introduction

Potato (*Solanum tuberosum* L.), originated from the Andes of Peru in South America and was introduced into Europe through Spain, Asia, and other parts of the world through Europe [1]. At present, potatoes are grown and produced in more than 160 countries worldwide, the fourth-largest food in the world after wheat, rice, and corn [2].

Potato planting areas in China are widely distributed in 29 provinces. Differences in natural conditions, agronomic requirements, and cultivation conditions have led to significant differences in the degree of mechanization [3]. The largest potato-producing areas in the United States are distributed in the three northwest States, and the second-largest concentrated producing regions are distributed in the four northern states [4]. Relying on appropriate planting temperature, fertile soil, modern processing equipment, and professional experience inherited from generation to generation, the American potato industry has always been in a leading position worldwide. In Europe, the British potato granules distributed in the temperate and oceanic climate are advantageous to the potato from extreme temperatures, plenty of rainfall, and nutrient-rich soil ensure potato growth. Dutch dominance in kinds of potato production and production system to its highest level of potato production in the world. Potato production areas in Russia are mainly distributed in the northwest, which is a black soil area with fertile soil, which is conducive to potato growth [5]. Potato production in Japan is at a high level. It is in a leading position in Asia, with a yield per unit area similar to that in Europe and the United States. The main production areas are concentrated in Hokkaido, which belongs to a one-season potato cultivation area [6].

In recent years, the global potato planting area has declined, but the output is still increasing. With the continuous decline of the sown area and production in Europe, the United States and the continuous development in Asia and other regions, the global potato

production center has gradually shifted from developed to developing countries [7]. The major potato producers in the world are the USA, China, Germany, Russia, etc. Some countries' planting situation and yield data in recent years are shown in Tables 1 and 2.

Table 1. Harvested Area /production of potatoes in different countries. Date from reference [8]. Copyright 2022 FAO.

Year	China	U.S.A.	Britain	Germany	Russia	Category
2015	4788.1	426.7	129.0	236.7	2111.6	Harvested Area/ thousand ha
2016	4805.1	419.9	139.0	242.6	1425.6	
2017	4862.4	422.7	146.0	250.5	1335.6	
2018	4760.7	414.1	140.0	252.2	1313.5	
2019	4038.9	379.3	144.0	271.6	1238.6	
2020	4218.2	369.9	142.0	273.5	1178.1	
2015	82,893.2	20,012.7	5644.3	10,370.3	33,645.8	Production/ thousand tons
2016	84,986.5	20,426.4	5394.7	10,772.2	22,463.5	
2017	88,536.4	20,453.4	6218.0	11,720.4	21,707.6	
2018	90,321.4	20,607.3	5027.7	8921.0	22,395.0	
2019	75,657.9	19,251.3	5307.0	10,602.2	22,074.9	
2020	78,236.6	18,789.9	5520.0	11,715.1	19,607.4	

Table 2. Yield of potatoes in different countries. Date from reference [8]. Copyright 2022 FAO.

Year	China	U.S.A.	Britain	Germany	Russia	Category
2015	17.31	46.90	43.75	43.81	15.93	Yield/t/ha
2016	17.69	48.65	38.81	44.40	15.76	
2017	18.21	48.39	42.59	46.79	16.25	
2018	18.97	49.76	35.91	35.37	17.05	
2019	18.73	50.75	36.85	39.04	17.82	
2020	18.55	50.79	38.87	42.83	16.64	

Potato planting is the most important component of potato production. However, the cultivation modes and natural conditions are various due to the difference in the production of potatoes. In the complicated agronomic process, labor intensity also affects production efficiency [9]. Therefore, mechanized planting is crucial for improving production efficiency and reducing labor [10,11]. In plain areas, it is suitable for the operation of large and medium-sized sowing machinery [12] (as shown in Figure 1a), providing convenient conditions for the development of mechanization. Small potato planters have the characteristics of light weight, convenience, and simple structure, as shown in Figure 1b. These planters are mainly designed for hilly mountainous areas. However, this planter is rarely used nowadays because of its low working efficiency and needs manual assistance [13].



(a)



(b)

Figure 1. Different types of potato planters, they should be listed as: (a) large combined potato planter. Reprinted with permission from ref. [12]. Copyright 2021 Double L Industries; (b) small potato planter.

This paper introduces the potato planter and planting technology related content: “The key technology status of the mechanized planting” explores the existing key technology and categorized the applications into four types. “Machine of mechanized planting” elaborates on some typical commercial potato planters and soil cultivation machines. “Research of intelligent seeding technology” proposes a systematic analysis of future directions based on intelligent seeding technology. Finally, “Conclusions and recommendations” concludes the mechanized planting along with some current problems and makes some suggestions.

2. The Key Technology Status of the Mechanized Planting

In the process of mechanized potato planting, it is necessary to tillage machinery for soil preparation and then use the potato planter for mechanized seeding. According to the agronomic requirements, the potato planter needs one operation to complete the work requirements of ditching, spraying, seeding, fertilizing, and ridging. As the core part of potato planter [14], the performance of the seeding metering device will directly determine the operation quality and working effect of the planter [15,16]. The seeds in the seed hopper are generally arranged in disorder. It is necessary to pick up the potato seeds from the seed hopper through the seed metering device, separate them, and put them into the seed bed. The technical core of mechanized seeding is the orderly single granulation and the maintenance of a single granulation state, that is, the technology of seed tuber separation and whole row picking and stable seed guide [17]. In the process of potato plant design, it is often necessary to analyze the material characteristics of seed potatoes [18,19]. Therefore, according to the elements of the working process of mechanized planting, the critical technologies of mechanized planting can be divided into the research of material characteristics for potatoes, soil cultivation, the seed potato separation, and the seed guiding technology of the planter.

2.1. Research of the Material Characteristics of Seed Potatoes

The characteristics of potatoes are directly related to the design of critical components of the seed metering device, which affects the potato production level [20]. To design and optimize the device structure, the physical characteristics have been researched according to different types of potatoes. Generally, the physical attributes of seed potato can be divided into two aspects: essential physical characteristics and dynamic characteristics.

2.1.1. Division of Seed Potato types

In addition to differences in the planting areas, there are also differences in the types of seed tubers selected, which can be divided into the whole tuber, sliced tuber, and mini-tuber [21]. Figure 2 presents three kinds of seed tubers. At present, the most commonly used potato in China and India is the sliced potato, which has the advantages of being low cost and easy to obtain, but it needs to be graded, whole row cutting, spraying and lubricants, and other processes need to be carried, and it is easy to cause potato cross-infection in the treatment which will directly affect the yield. Whole potato seeding can avoid cross-infection caused by cutting, and causes minimal damage to seed potato and high germination rate, which is suitable for mechanized operation, but requires special cultivation [22]. Mini-tuber is a kind of potato produced by virus-free seeding, with a neat shape, uniform size, and excellent quality. It can be directly used for seeding, and the seedling emergence rate can reach 100% [23]. The main reason for the low yield of potato production in some regions is the small application area and low penetration rate of virus-free mini-tubers. In contrast, high-quality virus-free min-tubers are widely used in high-yield areas of developed countries.

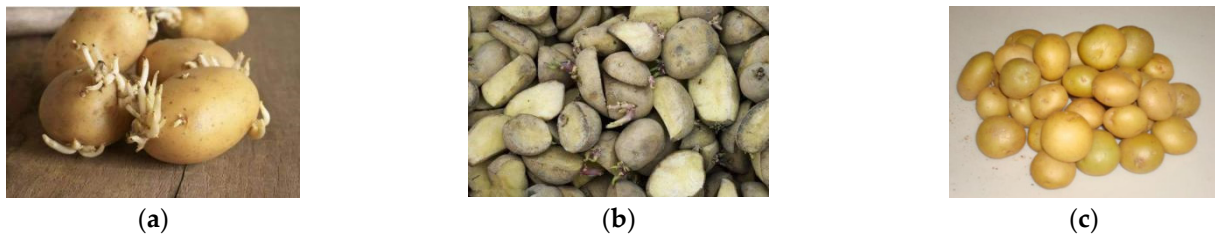


Figure 2. Types of potato: (a) whole tuber; (b) sliced tuber; (c) mini-tuber.

2.1.2. Research on the Basic Physical Characteristics of Seed Potatoes

The basic physical characteristics of potatoes mainly include triaxial size, shape, and density. It is an essential basis for designing the structure parameters of seed arrangement device and seed box.

In determining the essential physical characteristics of potatoes, vernier calipers are generally used to measure the overall dimension of potatoes, and the shape index (f) of seed tubers is obtained through the formula. Then the shape and size parameters of seeds are defined according to the shape index (f). Generally, the key structural parameters of the planter can be determined based on the shape and size parameters [24]. Seed potato moisture content is a crucial characteristic index of seed tuber and has a specific influence on the properties of other materials [25]. Seed potatoes with higher moisture content are easily damaged during the working process. The adhesion can easily affect seed picking performance—the general use of atmospheric constant temperature drying method or moisture meter measurement. To facilitate the theoretical modeling and virtual simulation of critical components, the volume density and monomer density of potatoes should be measured. When the seed potato moisture content is determined, volumetric density can be measured by mass volume ratio, and monomer density can be measured by suspension under liquid immersion [26].

2.1.3. Research of Dynamic Characteristics of Seed Potatoes

Potatoes can be classified as granular materials according to the classification of agricultural materials. The knowledge of the dynamic characteristic of granular material such as friction characteristics, compression characteristics, and flow characteristics between particle–particle or particle–surrounding can help improve the design and operation of the machine.

Before the simulation analysis, the physical model of the seed potato needs to be established. For the material with a tremendous difference in the shape of seed potato, the computerized tomographic (CT) technology [21], and image processing technology [27] were not suitable. DEM (Digital Elevation Model) is one of the advanced numerical methods used to study the dynamic characteristics of granular material, which is widely used in the study of the movement of agricultural granular materials. Since DEM discrete element simulation is based on the theoretic contact mechanical model, the simulation result is inconsistent with the actual one when the software is simulating the essential flow characteristics of the bulk materials. The pile angle can reflect the flow characteristics of the material [28,29]. Liu et al. used the method of combining test and simulation to calibrate the material parameters and established the test simulation model [30]. Seeds could be divided into class of spherical, small ellipsoid, and large ellipsoid according to shapes. The seed shape is shown in Figure 3, and the model is shown in Figure 4. The contracting parameters of the discrete particle were taken as the independent variables, the measurement results of the simulation model were taken as the evaluation, and then the relevant fitting equations were established and the corresponding results in the simulation model were obtained by changing the independent variables. Finally, the simulated contact parameters of the model were obtained by substituting the measured parameters in the actual test into the fitting equation. Due to the irregular shape of potato seeds, its dynamic characteristics in the seed metering device cannot be simulated by selecting a single spherical particle. The models of

large ellipsoidal particles, small ellipsoidal particles, and spherical-like mini-tuber seeds were established by generating particles from a template. The related motion process of the mini-tuber seed adopted a Hertz–Mindlin non-sliding contact mechanical model [30,31]. There are few relevant studies on sliced tuber. Whole potatoes were separated into two longitudinal pieces and the geometric model was established in Solidworks based on the mapping data and imported into EDEM [32].

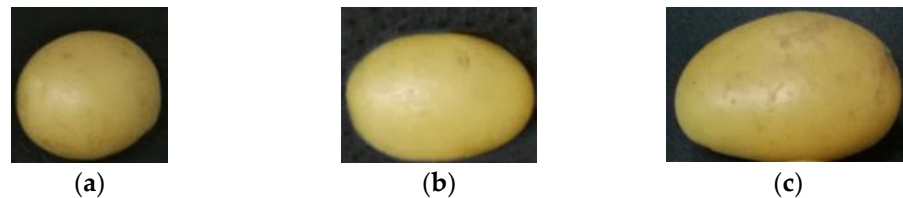


Figure 3. Classification of mini-tuber seeds: (a) class of spherical; (b) small ellipsoid; (c) large ellipsoid. Reprinted with permission from ref. [30]. Copyright 2018 China Agricultural University.

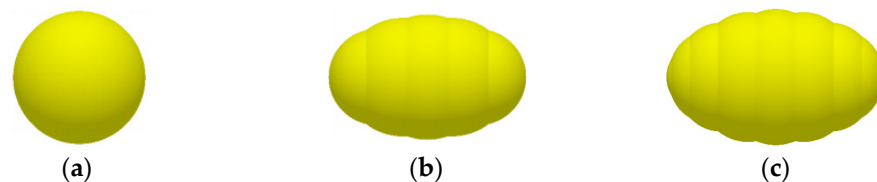


Figure 4. Discrete element model of mini-tuber seed: (a) class of spherical; (b) small ellipsoid; (c) large ellipsoid. Reprinted with permission from ref. [30]. Copyright 2018 China Agricultural University.

2.2. Soil Cultivation

In the process of mechanized potato planting, the quality of the seedbed has a direct impact on soil water storage capacity, adaptive, and potato yield. The high-quality seedbeds can effectively store water and conserve soil moisture, improve soil permeability, create suitable conditions for early sprout and seedling growth, and facilitate the standardization of field management later.

Potato ridging planting is an effective high-yield planting method. It is also one of the crucial steps of soil cultivation, Figure 5 shows potato ridging planting. Soil cultivation can provide appropriate conditions for ridging planting and improve the seeding quality [33].



Figure 5. Potato ridging planting.

In terms of the selection of the seedbed, a sufficient area convenient for the mechanization of the plot and for the standardization of the potato planting should be chosen. Different soil cultivation practices are usually used in different countries due to conditions. Sub-soiling and power harrow combined tillage is generally adopted in Europe. In contrast, multi-function large-combined tillage planters are mainly adopted in the USA. In addition, rotary tillage and subsoiling machines are the main methods used in Asia.

In the process of mechanized potato planting, a layer of plow bottom will be formed under the tillage layer because the seedbed soil has been compacted by the mechanical equipment plow for a long time. After the previous crop is harvested, the first treatment is sub-soiling, which can break the hard plow bottom. The depth of sub-soiling should be consistent, and the trench bottom should be flat. The coefficient of variation of sub-soiling depth should not exceed 15% [34]. It is usually carried out once every two to four years. Zhao et al. [35] conducted a comparative test on 300 mm sub-soiling, 250 mm sub-soiling, and 200 mm rotary tillage. It was found that the nitrogen, potassium, phosphorus, and other elements in the middle and lower layers of 300 mm sub-soiling were significantly higher than those of 200 mm traditional rotary tillage and 250 mm sub-soiling, which was conducive to the accumulation of nutrients in the lower layer. Similarly, the water content in the lower layer of 300 mm sub-soiling was also better than that of rotary tillage.

2.3. Potato Separation

Seed potato separation is one of the critical technologies of mechanized potato planting. It mainly refers to when seed potatoes stacked disorderly in the seed box are formed into a single seed potato through the function of the seed metering device. The technology of seed metering has been actively developed over the past several decades. In terms of the technology status of the seed metering device, the devices can be categorized into six types: cup-belt (chain) type, pneumatic-type, moving-belt-type, needle-type, and pickup-finger-type. Some typical seed metering devices are shown in Table 3.

Table 3. Some typical seed metering devices and their principles.

Type	Principle
Cup-belt (chain)-type seed metering device	The power of the seed belt (chain) is provided by the ground wheel or hydraulic motor, which drives the driving wheel to rotate through the transmission system. The seeds flow to the feeding area at the bottom of the seed box under gravity. In the forward motion of the seed belt/chain, the spoon mounted on the belt (chain) scoops up the seed potatoes in proper sequence. After the seeds shift to the seed clearing area, the excess materials are removed by the seed clearing device and returned to the seed box. When the cup reaches the highest point, the potato seeds fall on the back of the next cup. Potato seeds are carried by the cups to the seeding point, then dropped into the bottom of the seed furrow [36,37].
Pneumatic-type seed metering device	The seed-suction arm is driven to rotate by power. When the seed-suction arm is connected with the vacuum chamber, the seed-suction arm absorbs a single seed potato from the seed hopper by negative pressure, and stably carries the seed potato to rotate synchronously with the seed metering device. As the potatoes reach the release point, they fall into the seedbed by positive pressure and gravity [17,38,39].
Moving-belt-type seed metering device	When the seeds fall from the seed box to the conveyor belt, the transport speed of the two sides belt is opposite to that of the middle belt, where the middle belt is used to sort the seeds in a single row for seeding, and the two side belts are used to transport and collect the excess seeds to the seed collection port for preparation for subsequent seeding.
Needle-stabbed-type seed metering device	The needles are mounted on the circumference of the seeding rotary disk. Each needle stabs and obtains one seed in turns in the seed hopper. With the rotation of the seeding disk to the seed dropping area, the seed potatoes are separated from the needles under the function of scraping components and discharged into seed bed, completing a seeding process [40,41].
Pickup-finger seed metering device	The Pickup-fingers are mounted on the circumference of the seeding rotary disk. Under the elastic force, The pickup-finger is in a normally closed state. The finger arm touches the guide rail and opens in sequence when traveling to a feeding area, and each finger on the vertical disk picks up a seed and moves with it to the next area under rotation condition, the arm meets another set of guide rails, and opens in sequence again [42].
Vibration separation-type seed metering device	The conveyor belt is combined with the principle of forced vibration, and the potatoes are filled into the groove with manual assistance to achieve the function of separation and sorting. The grooves move with the movement of the conveyor belt, and at the release point the potatoes will fall into the seedbed to finish seeding.

Potato ridging planting is an effective high-yield planting method. It is also one of the crucial steps of soil cultivation. Soil cultivation can provide appropriate conditions for ridging planting and improve the seeding quality [33].

2.3.1. Cup-Belt (Chain)-Type Seed Metering Device

The cup-belt(chain) type is the most widely used seed arrangement method worldwide [19]. Compared with the cup-chain type, the cup-belt type (Figures 6–8) is more likely to slip in the process of movement, resulting in the heterogeneous spacing of seeds. Many researchers [37,43] have studied the dynamics characteristics of cup-belt potato planter and reformed its structure. In recent years, several attempts have been made to research the metering process through constructing mathematical model analysis. For example, to define the causation of the deviations in uniformity of placement of the potatoes, a theoretical model was established by Buitenwerf H. et al. [44]. Cai et al. [32] proposed a conical-shaped seed box to abate the missing rate caused by the arching problem for seed potatoes in the conventional potato planter. In order to minimize the reseeding rate and miss-seeding of potato planters, Wang et al. [45] designed a new type of cup-belt type device, which was composed of a motor vibration cleaning system conveyor belt with spoons, etc. Lü et al. [46] designed a cup-belt type device for potato planters and the structure of many vital components. Wollman A. E. et al. [47] added a missing seeding detection system and a reseeding mechanism to the potato planter.

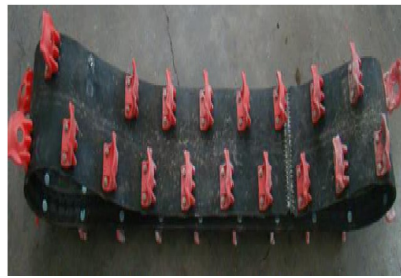


Figure 6. Seed metering belt. Reprinted with permission from ref. [48]. Copyright 2020 Chinese Heilongjiang Agricultural Commission.

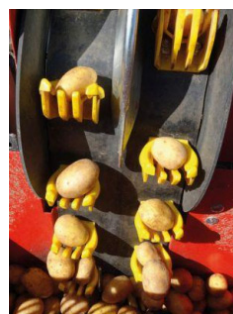


Figure 7. Cup-belt type. Reprinted with permission from ref. [49]. Copyright 2019 Miedema Industries.



Figure 8. Cup-chain type. Reprinted with permission from ref. [50]. Copyright 2021 Double L Industries.

2.3.2. Pneumatic-Type Seed Metering Device

The performance of a pneumatic seed metering device is greatly influenced by seed size, shape, the number of holes in the disk, and working pressure. There are several preponderances of these devices, such as low rate of seed damage, high seeding quality, and high planting speed. The negative pressure of seed suction will directly affect the seeding efficiency. Therefore, there are many technical difficulties in potato seeding. Currently, it is mainly used for sowing crops with low weight, such as maize [51], soybean, rapeseed [52,53], etc. According to the different ways of pneumatic seed separation, it can be divided into air suction type, air blowing type, air pressure type, and central gathering type [54]. Compared with other crops, potato seeds have the characteristics of large particle size and irregular shape, and the existing devices are limited to air suction type. Lü et al. [17,18] proposed a potato air-suction metering device (Figure 9) for the north of China.

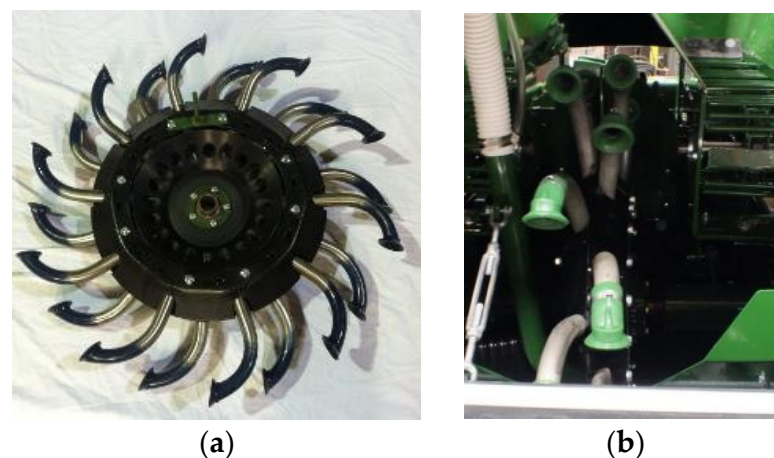


Figure 9. Pneumatic-type seed metering device. (a) The structure of a pneumatic-type seed metering device. Reprinted with permission from ref. [49]. Copyright 2019 Lockwood Industries. (b) Pneumatic-type seed metering device in Lockwood Air Cup Planter. Reprinted with permission from ref. [49]. Copyright 2019 Lockwood Industries.

McLeod C. D. et al. [10] researched and developed a pneumatic micro potato precision seeding device, which can absorb seeds under negative pressure, carry seeds, and row seeds under positive pressure, and a spray gun is set on the seeding device to remove excess seeds and reduce re-seeding. Yang, D. [51] designed a pneumatic horizontal disc potato seed metering device, which uses an intermittent feeding mechanism composed of a grooved wheel mechanism and a transmission chain to realize periodic quantitative seed delivery. Mao et al. [55] designed and optimized a tilting disk pneumatic precision seed metering device for virus-free mini-tuber as shown in Figure 10a. Compared with the traditional mechanical device, the pneumatic seed metering device reduces the mechanical damage and improves the quality of the seed potatoes. Due to the limitation of the working principle and configuration, the device will only miss seeding and will not re-seed. To solve the problem of limited seeding speed for the cup-belt-type seeding device and significant negative pressure required for the pneumatic seed metering device, a mechanical–pneumatic combined metering device for potato (Figure 10b) was designed [49]. The structural parameters and working regulation of the devices were investigated. Based on the theoretical analysis of the potato seed stress, the configuration and parameters of the critical components of the improved seed scoop (Figure 10c) were determined.

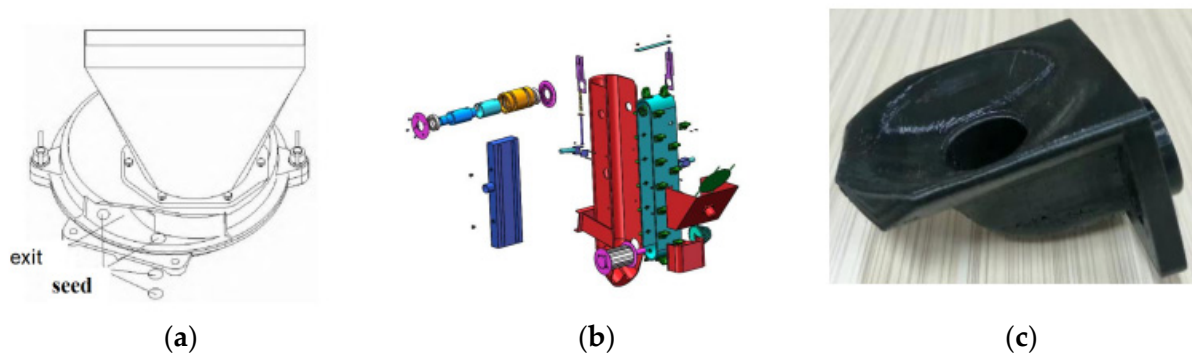


Figure 10. Improved pneumatic-type seed metering device. (a) Mao et al.'s research. Reprinted with permission from ref. [55]. Copyright 2013 Huazhong Agricultural University; (b) Liu et al.'s research. Reprinted with permission from ref. [49].; (c) Improved seed scoop. Reprinted with permission from ref. [49] Copyright 2019 Shandong Agricultural University.

2.3.3. Moving-Belt-Type Seed Metering Device

This device (Figure 11) has the advantages of simple structure and principle, small size, low rate of seed damage, and additional vital adaptability to diverse shapes of potato seeds. To reduce the damage rate of potato seeds in the process of mechanized planting, Meijer et al. [56] organized a moving-belt-type seed metering device and conducted experimental research on seeding performance. He et al. [57] created a new type of moving-belt-type belt mechanism and analyzed the overall structure and performance of each factor.

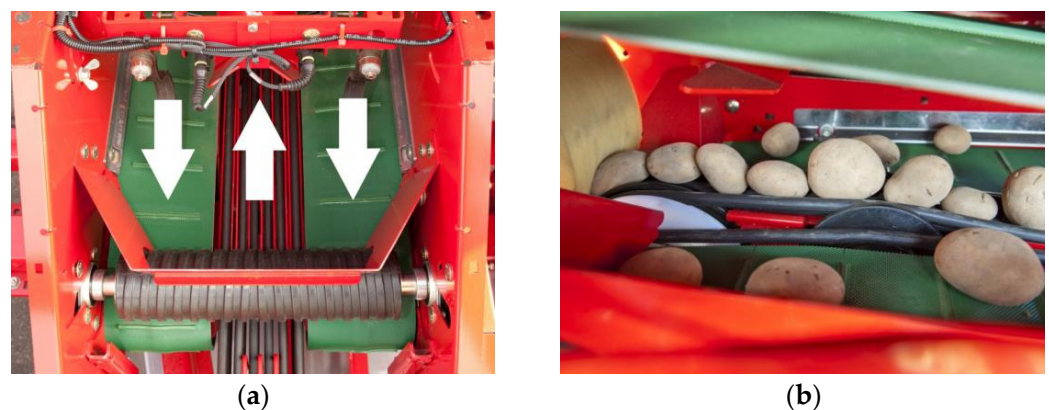


Figure 11. Moving-belt-type seed metering device. (a) The conveyor belt arrangement of the device. Reprinted with permission from ref. [58] Copyright 2022 Grimme Industries. (b) The working process of the device. Reprinted with permission from ref. [58] Copyright 2022 Grimme Industries.

2.3.4. Needle-Type Seed Metering Device

The needle-type uses the needle to pick seed tuber and throw seed, as shown in Figure 12. Although this device has good adaptability to the size and shape of seed tubers, it is easy to cause cross-infection due to the injury of seeds by needle-punched seed metering device and the emergence of virus-carrying seed tubers will cause infection. On the other hand, the impurities mixed in the soil, such as gravel and weeds, can deform the needle and cause damage [59]. Misener G.C. et al. [60] measured the seed piece distribution patterns completed by the cup and needle-type metering devices through numerous experiments. The consequences demonstrated that the needle metering device performed slightly more effectively than the cup type.



Figure 12. Needle-type seed metering device. Reprinted with permission from ref. [51] Copyright 2016 Lockwood Industries.

2.3.5. Pickup-Finger Seed Metering Device

This device is suitable for seeding whole or sliced tubers. The pickup-finger type (Figure 13) is greatly affected by the shape, size, and the seed extraction rate of the seed potato is different at different clamping positions, which requires high classification accuracy for the seed potato. Chen et al. [61] designed a novel device and carried out kinematics and dynamics analysis. Boydas M.G. et al. [62] explored the mechanism of influencing the seeding accuracy of the Pickup-finger device.



Figure 13. Pickup-finger type metering device. Reprinted with permission from ref. [48] Copyright 2016 Lockwood Industries.

2.3.6. Vibration Separation Seed Metering Device

Presently, the research on vibration seed metering devices at home and abroad mainly focuses on sowing crops with small particle sizes and regular shapes. Liu et al. [63] invented a planter for mini-tuber established on the principle of forced vibration, as shown in Figure 14. In this device, seeds were arranged and moved to the conveyor belt under the function of vibration plate, and single sequence of seeds was achieved under the restriction of device structure. Excess potatoes would be transported to the conveyor belt for sorting again under the action of vibration plate. The pressure belt was designed in the seed dropping channel for positioning, and the seed was sent to the seed dropping point under the cooperative effort of the conveyor belt and the pressure belt for final seeding.



Figure 14. Vibration-arranging-based planter. (a) The structure of vibration-arranging-based planter. Reprinted with permission from ref. [63]. Copyright 2019 China Agricultural University. (b) The working process of the vibration-arranging-based planter. Reprinted with permission from ref. [63]. Copyright 2019 China Agricultural University.

2.4. Zero-Speed Seeding

The seed guiding step is a connecting link between the preceding step of seed discharging from the seed metering device and the following step of dropping in the seedbed, which affects the orderly state of seeds in the planting process and determines the uniform distribution of subsequent seeds in the seedbed [64]. The seed potatoes will be offset or even jump on the ground, which will reduce the uniformity of plant spacing and sowing accuracy when the planting position is too high, or the horizontal velocity of seed potatoes is relatively high. Due to the large and irregular shape of seed potatoes, this negative effect is more serious. Therefore, reducing the height of seeding and the speed of seed tuber relative to the seedbed along the horizontal direction are essential ways to ensure the quality of seeding. Based on the type and technical features of seed metering device, zero-speed seeding technology of planter can be divided into low position seeding, seed guide tube seeding, and air blowing seeding.

2.4.1. Low Position Seeding

Low position seeding means that seed potatoes are transported to a lower position and dropped to the seedbed by carrying seed components through a seed metering device. This process directly drops to the seed bed without the guide components. Generally, the seeds in this method have a horizontal dividing speed relative to the backward device after the action of mechanical construction in the dropping process. The technology is now the most commonly used for potato planting model forms, including pneumatic-type device, moving-belt-type device, needle-type device, and the pickup-finger device using this method. By mechanical action, a kind of potato is made when leaving the metering device, which has a seeder with an initial velocity of movement in the opposite direction. Low-position direct seeding is low in height and does not require the installation of additional seed guide devices, but it is only suitable for low-speed seeding operations. It cannot meet the development trend of today's high-speed agriculture.

2.4.2. Seed Tube Seeding

The seed tube is adopted for maintaining seeds fallen from the seed metering device along its barrier to retain the uniformity of the seed quality. The seed tube can accelerate the speed in the opposite direction of movement of planter so that the seed can obtain the horizontal fractional rate in the opposite direction of the forward speed of the planter and then approach zero speed seeding [46]. Its structure and installation position on the seed tuber separation unit.

2.4.3. Air Blowing Seeding

The existing zero-speed seeding technology has many constraints, such as being unsuitable for high-speed operation and low seeding precision. In order to address these issues, a unique method of zero-speed seeding was presented by Lü et al. [65]. Positive pressure was used to make the seed accelerate in the opposite direction of seeding so that its velocity was zero relative to the seed bed. The precision of seeding was improved as well as the efficiency of seeding in this route.

3. Machine of Mechanized Planting

3.1. Soil Preparation Machine

The flipped plow is used for potato rotary tillage, which can complete the work of soil loosening, weeding, and so on. Both subsoiler and combined machines for subsoiling and soil preparation can realize all-directional sub-soiling.

Soil cultivators are a vital part of assuring potato planting. Effective soil cultivation maintains the quality of the soil and improves the retention of organic substances such as air and water. Some typical machines are shown in Table 4.

Table 4. Some typical soil preparation machines.




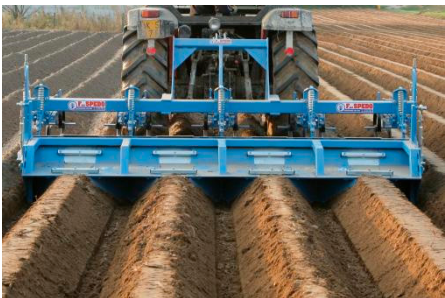

Model	Structure	Characteristic
Shandong Transce Agricultural Machinery 1SL-6A subsoiler [66]		Matched type, mounted; six seeding plough; minimum required power, 135 hp; pure weight, 1500 kg; The depth of the sub-soiling, 400–500 mm. The subsoiling shovel adopts a particular arc inverted ladder-type design. The operation does not disturb the soil and does not turn over the soil to achieve all-round Subsoiling.
Shandong Transce Agricultural Machinery 1LF-550 flipped plow [67]		Matched-type, mounted; six seeding plows; minimum required power, 65 hp; pure weight, 1300 kg; working width, 132/152/176/200 cm; the depth of tillage, 350–400 mm. The hydraulic piston rod drives the positive and negative plow on the plow frame to make vertical turnover movement and replace it alternately to the working position.
BOMET U473 Cultivators Dorado [68]		Matched-type, mounted; three rows; minimum required power, 38 hp; working depth, 13 cm; pure weight, 180 kg; working width, 210 cm; the depth of tillage, 130 mm. The essential equipment of the machine is two supporting wheels that set the machine’s working depth.
SPEDO VB4F/75 Bed Former [69]		Matched-type, mounted; four rows; minimum required power, 70 hp; pure weight, 720 kg; distance between rows, 80 cm; working width, 340 cm; working length, 200 cm. The flex springs, positioned on the front part of the bed former, move the land allowing the furrowing plow discs to form regular and uniform beds.

Table 4. Cont.

Model	Structure	Characteristic
GRIMME GF400 [70]		Matched-type, mounted; four rows; minimum required power, 134 hp; pure weight, 1800 kg; row width, 75–90 cm; working width, 3–3.6 m. The machine can also be used in combination with a potato planter, thus enabling soil cultivation and planting in a single pass. For soil cultivation and seeding of fine seeds in a single pass, the machine can be equipped with hydraulically driven ridge pressure rollers and a lifting frame for seeders.

3.2. Potato Planter

3.2.1. Cup-Belt (Chain) Type Potato Planter

Cup-belt (chain)-type potato planters rely on a simple structure, have a reliable performance, are easy to operate in all kinds of seeding machines, and have been widely used. With a combination of a simple structure, wide application, and innovative technology, many typical planters have been developed. Some common potato planters are shown in the Table 5.

Table 5. Introduction of Cup-belt (chain) type planters.




Country	Model	Structure	Characteristic
Germany	Grimme GL420 [71]		Matched-type, trailed; four seeding rows; minimum required power, 120 hp; distance between rows, 75–90 cm; seed box capacity, 2 t. Equipped with a hydraulic control system and electronic monitoring system, combination with a cultivator is possible for optimum soil preparation.
USA	Double L9560 [12]		Matched-type, trailed; six seeding rows; matched power, 168 hp; distance between rows, 71.12–101.6 cm; seed box capacity, 6.6 t. Optical seed sensors are used to monitor seed picking. The planter is equipped with optical sensors and GPS to ensure seeding accuracy.
Holland	Dewulf CP 42 [72]		Matched-type, trailed; four seeding rows; distance between rows, 75–90 cm; seed hopper capacity, 3.6 t. It is mechanically or hydraulically driven and equipped with a human–computer interaction system and electronic monitoring system.




Table 5. Cont.

Country	Model	Structure	Characteristic
China	Menoble 1240 [73]		Matched-type, mounted; four seeding rows; minimum required power, 100 hp; distance between rows, 80/90 cm; seed box capacity, 1.2 t. Seeding unit equipped with electronic vibration mechanism equipped with hydraulic control rowers.
Italy	Spedo SPA/A [74]		Matched-type, mounted; two seeding rows; distance between rows, 70–90 cm; required power, 50 hp; two seeding units; weight, 480 kg; seed box capacity, 500 kg; seeding velocity, 0.4–0.6 ha/h.
Poland	Bomet Sp. z o.o. Sp. K. [75]		Matched-type, mounted; matched power, 20 hp; single one seeding row; distance between rows, 290/320/350 mm; planting depth, 100–150 mm; pure weight, 130 kg. Changing the distance of seed potatoes in a row can be achieved by changing the diameter of the wheels.
India	SWAN AGRO NSE PPR-2 [76]		Matched-type, mounted; two seeding rows; distance between rows, 60–66 cm; required power, 40–60 hp; seed hopper capacity, 0.24 t; planting depth, 130–150 mm; working efficiency, 0.51 ha/h.

3.2.2. Pneumatic-Type Potato Planter

At present, there are few commercial potato planters using pneumatic seed potato separation and whole row picking technology. They include the PLMS series pneumatic drill produced by the French ERME company and the Lockwood600 series produced by the American Crary company (including 604, 606, 608 three models) air suction potato planter. Take the Lockwood 606p planter as an example. The planter can finalize ditching, sowing, fertilization, drip irrigation, soil covering, repression, and finalize operations simultaneously. Some typical potato planters are shown in the Table 6.

Table 6. Introduction of belt-type potato planters.

Country	Model	Structure	Characteristic
USA	Crary Lockwood 606 [77]		Matched-type, mounted; six seeding rows; minimum required power, 20 hp; distance between rows, 80–100 cm; weight of the machine, 5 t; Seed hopper capacity, 5.44 t; maximum planting speed, 4.5 mph. The planter is equipped with hydraulic drive device and GPS navigation system, which can ensure high working speed and sowing quality.
Germany	Grimme Pneumatic precision mini-tuber planter		Matched-type, mounted; double seeding rows; minimum required power, 120 hp; distance between rows, 80–100 cm, the machine itself is 1.5 T. maximum working speed, 8.2 km/h. It uses a vertical disc potato row, has strict requirements on the uniformity of the appearance and size of potatoes, and has a high rate of heavily missed seeding.
French	ERME PLMS planter [78]		Matched-type, mounted; four seeding rows; minimum distance between rows, 35 cm. Drive wheels adjustable in height.

3.2.3. Moving-Belt-Type Potato Planter

At present, the representative seeders using this technology include Grimme GB series belt seeders and Miedema Structural series produced by Dewulf. Some typical potato planters are shown in the Table 7.

Table 7. Introduction of moving-belt-type Planter.




Country	Model	Structure	Characteristic
Germany	Grimme GB 230 [58]		Matched-type, mounted; minimum required power, 120 hp; distance between rows, 70–90.4 cm; maximum working speed, 25 km/h; seed hopper capacity, 3 t. Seeding parameters and seeding quantity can be adjusted through the operator terminal.

Table 7. Cont.

Country	Model	Structure	Characteristic
Holland	Dewulf Miedema Structural 30 [79]		Matched-type, trailed; three seeding rows; minimum required power, 80 hp; distance between rows, 4–100 cm; seed box capacity, 3.5 t; maximum working speed, 11 km/h. The inclination of the seed box is adjusted by a hydraulic drive.
England	Standen Engineering ZENO 21 [80]		Matched-type, mounted; two seeding rows; matched power, 102 hp; distance between rows, 76–102 cm. Equipped with a hydraulic control system to control depth. The uniformity of sowing is ensured by monitoring the speed with sensors.

3.2.4. Needle-Stubbed Type Totato Planter

The research on the technology and equipment of needle-stabbed is mainly concentrated in the USA. A number of technological invention patents centering on the research and development of needle-stabbed were applied in the last century. Because this type of seeding device can easily cause bacterial infection, the application of this technology is less at present. The typical model is the Lockwood 6200 series planter [81] (Figure 15) and Harrison pick planter [82] (Figure 16).



Figure 15. Lockwood 6200 Needle-type potato planter. Reprinted with permission from ref. [48] Copyright 2018 Lockwood Industries.



Figure 16. Harriston Pick Planter. Reprinted with permission from ref. [48] Copyright 2019 Harriston Industries.

3.2.5. Pickup-Finger-Type Potato Planter

This type of planter has poor performance stability and operation quality. The curve of the finger clip guide rail of this structure is fixed, resulting in the fixed opening stroke of the finger clip. However, the overall dimensions of potatoes are different, so there is a high rate of reseeding and missed seeding, and it is impossible to operate at high speed. At present, this principle has been applied in the seed metering device with small particle size and regular shape for corn and soybean, while in the potato planter, only a few manufacturers, such as Lockwood and Harriston, have provided models that can be applied practically. The Lockwood 506 series potato planter is presented in Figure 17, the Harriston Clamp planter [83] is presented in Figure 18.



Figure 17. Lockwood 506 series potato planter. Reprinted with permission from ref. [48] Copyright 2018 Lockwood Industries.



Figure 18. Harriston Clamp planter. Reprinted with permission from ref. [83] Copyright 2019 Harriston Industries.

3.2.6. Vibration Separation-Type Potato Planter

Due to the limitation of manual capacity, the working speed of the planter using the vibration separation principle will not exceed 2 km/h. Figure 19 shows the Japanese JAGIRL vibrating separation row artificial cleaning (supplementary) seed potato planter, which is suitable for sowing in small plots.



Figure 19. JAGIRL man-aided potato planter (a) The structure of planter. Reprinted with permission from ref. [13] Copyright 2019 JAGIRL Industries (b) Manual assisted operation. Reprinted with permission from ref. [13] Copyright 2019 JAGIRL Industries.

At present, there are many types of potato planters for different regions; but the mechanization degree of small potatoes in hilly and mountainous areas is insufficient; which will be an important direction for future research and development. The types of planters in Asia are mainly traditional planters; while the development of planters in the United States and other regions is mainly focused on precision and high speed; and the application of many types of planters is also mature

4. Research on Intelligent Seeding Technology

The concept of the intelligent system of the planter was proposed as early as the 1940s, with research and development on intelligent control gradually conducted [84]. However, it was only until the recent four decades that intelligent seeding technology fully utilized the advances in sensor, artificial intelligence, and electrical driving technology [85,86]. Intelligent seeding technology requires the planter to meet the three conditions of precise seeding rate, spacing and seeding depth to sow the seed potato to the desired depth accurately.

4.1. Seeding Monitoring System and Seeding Compensation System

Miss seeding will reduce potato yields and soil efficiency, and the rate of missed seeding is reduced by improving the structure of the planter. However, the rate of missed seeding of the improved potato planter is still beyond 5% [87]. The simplest way to reduce this loss was manually assisted reseeding, but it required excellent labor intensity and reduced efficiency. Therefore, the current standard method is to use the monitoring system to monitor the miss seeding and add the compensation device [88].

The miss seeding rate of large potato planters is low, and the existing achievements mainly focus on essential information collection and alarm indication. For example, Grimme GB series planter, Dewulf CP series planter, and Double L series planter are equipped with photoelectric sensors [12] (Figure 20a) to monitor the process of seeding. The detection system generally uses the photoelectric sensor and distance sensor to monitor the seeding condition of the seeding unit. When the seeding is abnormal, the Single-Chip Microcomputer controls the alarm system to prompt the driver to eliminate the fault. When miss seeding is detected, the Single-Chip Microcomputer drives the compensation system to reduce the miss seeding and ensure the seeding quality. Advanced GPS technology has also been introduced into the Double L monitoring system.

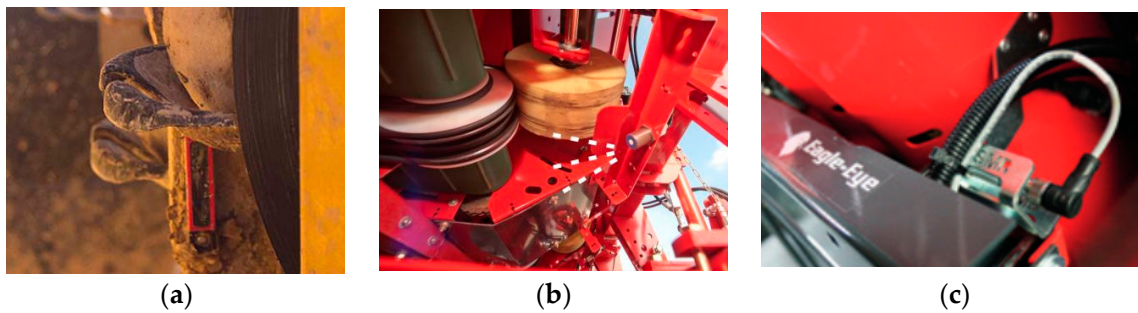


Figure 20. Seeding monitoring sensor: (a) Double L photo electric sensor. Reprinted with permission from ref. [12]. Copyright 2021 Double L Industries; (b) GB430 ultrasonic sensor Reprinted with permission from ref. [89] Copyright 2022 Grimme Industries; (c) Dewulf CP series Eagle-Eye. Reprinted with permission from ref. [72]. Copyright 2021 Dewulf Industries.

For the Grimme GB430 planter [89], the seeding distance is monitored by the ultrasonic sensor (Figure 20b), which counts the seeds as they fall into the seed bed and detect whether there is deviation at the same time. When a deviation occurs, it is fed back to the driver through the monitoring system and even adjusted [81].

For Dewulf CP series planter [72], the ‘Eagle-Eye’ (Figure 20c) registers each tuber. Two sensors for the issuing of the signal to the control terminal located in the cabin. The user can set a limit beforehand for the percentage of misses. When this threshold is exceeded, the system will issue both a visual as well as an audible signal. As a result, the user can check and modify the planting adjustments.

In addition to seeding monitoring, sensors are also used in other aspects of potato planters, such as the Dewulf Miedema series planter [79], a tipping automat sensor (Figure 21) that detects the number of potatoes in the seed box. Then the machine can ensure that the supply belts are supplied with a sufficient quantity of seed potatoes.



Figure 21. Tipping automat sensor. Reprinted with permission from ref. [80]. Copyright 2021 Dewulf Industries.

At present, the small and medium-sized potato seeder with a chain spoon seed metering device has a high rate of missed seeding, so the current related research focuses on intelligent and automatic monitoring system research. In order to ensure the anti-dust interference detection performance of the sensor, the detection sensor was installed in the upper section of the tube, and the seed cup was parallel to the horizontal plane. The transmitter and receiving end of the sensor should be installed on the same horizontal plane (as shown in Figure 22), and the center should be aligned. The sensor was installed on a row of tubes, and the installation spacing was determined according to the distance between cups.

Zhang et al. [91] proposed an electromechanical potato planter automatic compensation system composed of an infrared photoelectric sensor, Single-Chip Microcomputer, and stepper motor. Still, its missed seeding detection scheme was primitive and had low reliability. On this basis, a potato missed seeding compensation system based on an infrared miss-seeding detection and the AT90S2313 SCM was organized by Liu et al. [92]. Cao et al. [90] completed the hardware design of a miss-seeding early warning system,

including DC regulated power supply design, sensor module, MCU control module, alarm module, and display module. System software used C language to write the system monitoring program. A technique of monitoring potato missed seeding by infrared radiation was proposed by Sun and Wang et al. [93,94]. They also proposed a new architecture of two-point monitoring information statistics and ranking decisions, which makes the system response more advanced and overcomes the constraints of the first-generation detection technology on sensor installation positions. However, the system is still vulnerable to the threat of field dust, vibration, and other external factors, and its dependability still needs to be enhanced. To solve this problem, a new approach was proposed to construct a space capacitance sensor for the evaluation of seed-metering states and mass acquisition of seed potatoes by Zhu et al. [95]. Wang.G. et al. [96] proposed a kind of integrated seeding and compensating potato planter based on one-way clutch (Figure 23), a missed seeding and compensation system using an infrared radiation type missed seeding detection system to realize a one-way clutch and motor matching.

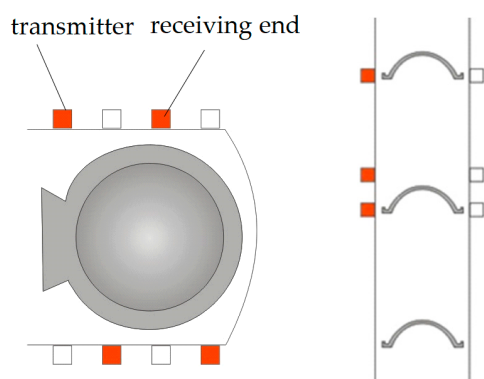


Figure 22. Monitoring location. Reprinted with permission from ref. [90]. Copyright 2013 Northwest A&F University.



Figure 23. Integrated seeding and compensating potato planter based on one-way clutch. Reprinted with permission from ref. [96]. Copyright 2019 Gansu Agricultural University.

Pneumatic type device also has the situation of missed seeding, the intelligent seed supply system of the air-suction potato planter (Figure 24) was designed by Lü et al. [18]. The controller collects information through the seed box weighing sensor and calculates and outputs the results to speed the stepping motor to control the seeding speed.

At present, the monitor and compensation control technology are mainly reflected in the material level detection device. The ultrasonic detection technology, infrared sensing technology, or image recognition technology is used to accurately and stably identify the number change of seed potato in the seed box, which can timely and stably drive the seed supply device for seed supply. Secondly, the structure principle of seed supply device is different, but its development trend is to provide stable seed precision and reduce the damage of seed potato.

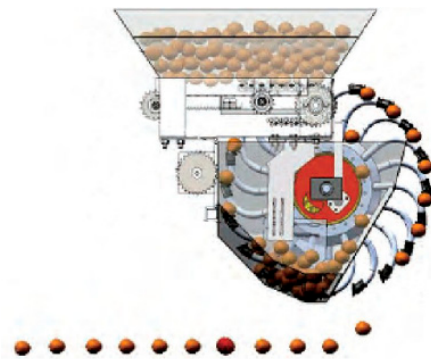
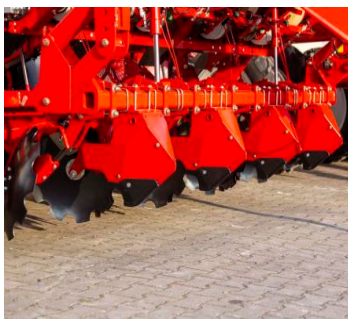


Figure 24. The intelligent seed supply system of the air-suction potato planter. Reprinted with permission from ref. [18] Copyright 2022 Northeast Agricultural University.

4.2. Seeding Depth Control

In the process of potato planting, due to the changes in the terrain in the field, the different properties of the soil, and the remaining stems and stubble on the ground, the sowing depth is difficult to be unified, resulting in the potato yield being affected.

The automatic hydraulic depth control is performed conveniently from the operator terminal in a large potato planter. Such as Grimme GB430 [89], trailed furrow openers are mechanically connected and guided in a parallelogram, as shown in Figure 25a. Moreover, change the number of feeler wheels used to pull furrow openers to suit different soil conditions. For lighter soils, the pulled furrow openers are individually guided in height by a feeler wheel, as shown in Figure 25b. For heavy soils, the pairwise mechanically connected, pulled furrow openers are guided in the depth by two large feeler wheels, as shown in Figure 25c.



(a)



(b)



(c)

Figure 25. Grimme GB 430 potato planter. (a) Trailed furrow openers of GB430. Reprinted with permission from ref. [89] Copyright 2022 Grimme Industries; (b) Structure for lighter soils. Reprinted with permission from ref. [89] Copyright 2022 Grimme Industries; (c) Structure for heavy soils. Reprinted with permission from ref. [89] Copyright 2022 Grimme Industries.

Dewulf Miedema CP 42 planters [72] (Figure 26) are equipped with an intelligent floating control system, which can monitor the depth of the seed trench timely and automatically adjusts the soil tillage depth through sensors during the seeding process so as to automatically maintain a certain tillage depth while ensuring sufficient seeding precision.

Grimme company mainly uses feeler wheels to pull the furrow openers to ensure the constant seeding depth. In the GL-34T potato planter [97] (Figure 27) suitable for large slopes, the lead screw with an adjustable depth limiting wheel is used to ensure the uniformity of seeding depth.



Figure 26. Dewulf Miedema CP 42 potato planter. Reprinted with permission from ref. [72]. Copyright 2021 Dewulf Industries.



Figure 27. Grimme GL-34T potato planter. Reprinted with permission from ref. [97]. Copyright 2018 Grimme Industries.

Zou et al. [98] designed a potato profiling ridging sowing device for potato seeding in dry land ridge cultivation, which can ensure a constant soil seeding depth through the soil covering profiling mechanism and limit sowing of the seedbed. Hu et al. [99] used a parallelogram ditcher to ensure the consistency of seeding depth in a 2CMW-4B micro potato planter, as shown in Figure 28.



Figure 28. Two views of the 2CMW-4B planter and the depth control device. (a) Operation process of the device; (b) Structure of ditching and seeding device. Reprinted with permission from ref. [99]. Copyright 2019 Shandong University of Technology.

4.3. Electrical Driving Technology and GPS

For large potato planters, automatic control or manual adjustment of seeding parameters by the driver is usually adopted, such as, Field-Ready Controller (Figure 29) was used

in the Double L9560 planter [12], the controller receives GPS, radar, and ground speed data from the tractor. The controller is usually used to control the hydraulic system to drive the seeding device. These parameters are mainly used to adjust the seeding spacing and fertilization amount, with control the number of seeds entering the seed metering device by monitoring and calculating the sowing conditions. The electrical driving system is performed conveniently from the HMI operator terminal, as shown in Figure 30.

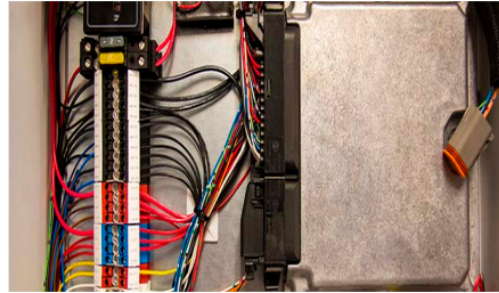


Figure 29. Field-Ready Controller. Reprinted with permission from ref. [12]. Copyright 2021 Double L Industries.



Figure 30. HMI operator terminal. Reprinted with permission from ref. [12]. Copyright 2021 Double L Industries.

For the Grimme GB430 potato planter [89], all planting components are jointly operated by a single hydraulic motor (Figure 31). The hydraulic drive can confirm the direct stepless adjustment of the seeding spacing to adapt to the transformations in the roadway consistency. Each belt planting element is driven by its hydraulic motor.



Figure 31. Hydraulic drive motor. Reprinted with permission from ref. [90] Copyright 2022 Grimme Industries.

Seed metering devices of potato planters are usually driven by a ground wheel and chain and sprocket system. This transmission scheme is easily affected by the slipping of the ground wheel and the vibration of the chain, so the uniformity of planting spacing cannot be guaranteed. Experiments have proved that the chain variation range of the slip rate of the ground wheel is as high as 20% [94].

In order to improve the seeding accuracy and ensure the seeding quality, some scholars proposed to use the motor to replace the ground wheel drive system. Wang et al. [94] used the hydraulic motor to drive the fine-tuning screw rotation to adjust the amplitude to achieve the step-less adjustment of the planting spacing. During the seeding operation, the hydraulic motor is driven by the hydraulic device of the tractor so as to drive the seed potato conveyor belt and seed potato cup. The device is equipped with two sensors. When one of them detects the seed potato bowl and the other does not detect the seed potato, that is, miss-seeding occurs, the main control module sends an adjustment command to the stepping motor to rotate the corresponding angle so as to adjust the vibration amplitude.

In order to improve the seeding accuracy of the potato planter, GPS technology is combined with the control system, as shown in Figure 32. By making use of GPS, the planter can map out the parcel. The machine will subsequently control that planting is performed accurately, allowing the driver to focus entirely on the planting process. For the farmer who places the very highest requirements on ease of use, efficiency, and precision, Dewulf has developed the GPS Planting-Comfort and GPS Planting-Control options. This easy-to-operate system automates many tasks.



Figure 32. Automatic Potato planter with GPS system. (a) Double L planter works under GPS navigation. Reprinted with permission from ref. [12]. Copyright 2021 Double L Industries. (b) Navigation test of planter.

5. Conclusions and Recommendations

Currently, potato is planted in a wide range of regions all over the world. The difference in environmental characteristics in each region leads to different planting modes and different agronomic requirements. Therefore, the development degree of planting mechanization is also different. In terms of the critical technologies of mechanized planting, the research on the characteristics of seed potatoes has made some achievements. Whereas various planters are marketed around the world, research is still ongoing. After years of development, some developed countries have used a large number of advanced technologies such as automatic control, hydraulic system for seed supply, seeding electronic monitoring, etc., with a high degree of intelligence and precision. However, the level of mechanization of potato planting in hilly mountain areas is relatively backward, and the yield of potatoes is not high. Accordingly, the following suggestions are put forward.

The breeding of seed potatoes plays a very important role in increasing potato yield. In order to improve potato yield, it is necessary to introduce new potato varieties with high yield, high resistance, and special purpose in some potato production areas, select high-quality varieties suitable for planting in various planting areas and promote characteristic potato varieties according to the conditions of potato planting areas. Secondly, it is necessary to increase the use of virus-free mini-tuber.

Accelerate the research and development of small and medium-sized machinery that can realize the whole process mechanization of potato, solve the sectional operation research, and support small machinery selection of mechanical seeding and mechanical harvesting, and accelerate the research and development process of miniature and medium-sized agricultural machinery and agronomic integration technology of potato. For hilly

and mountainous areas, strengthen the mechanization research and machinery selection under the conditions appropriate for viscous soil, and focus on the power chassis suitable for hilly and mountainous areas and small-scale tillage and land preparation machinery in Hilly and mountainous areas.

For the problems of poor seeding quality and stability of the current seed metering device, the mechanism of each type of seed metering device is further studied. At the same time, advanced technologies, new materials, and manufacturing procedure are continuously integrated into the manufacturing process of the seed metering device and the whole machine to improve the stability and reliability of the potato planter performance and develop new potato seed metering devices and seeding device.

In the future, the development of potato mechanized planting technology and equipment will focus on the precision, high-speed, intelligent large-scale potato planting equipment, and the synchronous research and development of economic, light, and simple potato mechanized planting technology and equipment in some particular areas will be the main development direction. Improving the automation and intelligence level of potato planters will be the focus of future research. In future studies, digital technology will become an essential part of improving work quality and efficiency.

Author Contributions: Conceptualization, B.Z., Y.L., C.Z. and Q.N.; validation, C.L. and L.C.; investigation, Y.L.; resources, S.X. and Q.N.; data curation, B.Z. and C.Z.; writing—original draft preparation, B.Z. All authors have read and agreed to the published version of the manuscript.

Funding: This work was supported by the Graduate Scientific Research Innovation Project of Chongqing, China (CYS22216), the Fundamental Research Funds for central Universities (SWU120004), Natural Science Foundation of Chongqing, China (cstc2021jcyj-msxmX1178) and the Science and Technology Plan Project of Sichuan, China (2021YFQ0070). The authors take full responsibility for the content of this paper.

Data Availability Statement: The study did not report any data.

Conflicts of Interest: The authors declare that they have no known competing financial interests or personal relationships that could have appeared to influence the work reported in this paper.

References

1. Brown, C.R. Origin and History of the Potato. *Am. Potato J.* **1993**, *70*, 363–373. [[CrossRef](#)]
2. Jiang, W.; Diao, P.; Zhang, H. Current Situation of Potato Production and Mechanized Harvest in China. *Agric. Equip. Veh. Eng.* **2021**, *59*, 18–22.
3. Zhang, S. Research on Potato Planting Regionalization in China. *Chin. Acad. Agric. Sci.* **2021**, *21*, 511–522.
4. Luo, Q.; Gao, M.; Zhang, S.; Lun, R. Comparative Analysis on Potato Industry between China and Other Countries. *Chin. J. Agric. Resour. Reg. Plan.* **2021**, *42*, 1–8.
5. Goffart, J.P. Potato Production in Northwestern Europe (Germany, France, the Netherlands, United Kingdom, Belgium): Characteristics, Issues, Challenges and Opportunities. *Potato Res.* **2022**, *65*, 503–547. [[CrossRef](#)] [[PubMed](#)]
6. Yu, T. The general state of the Potato industry in Japan. *Mod. Veg.* **2006**, *6*, 14–15.
7. Liu, Y.; Luo, Q.; Gao, J. Analysis on the development of potato production and trade in the world. *World Agric.* **2011**, *8*, 46–51.
8. Food and Agriculture Organization of the United Nations. FAO. [EB/OL]. 2022. Available online: <https://www.fao.org/faostat/zh/#home> (accessed on 1 July 2022).
9. Liu, W.; He, J.; Li, H.; Li, X.; Zheng, K.; Wei, Z. Calibration of simulation parameters for potato minituber based on EDEM. *Trans. Chin. Soc. Agric. Mach.* **2018**, *49*, 125–135.
10. McLeod, C.D.; Misener, G.C.; Tai, G.C.C.; Caissie, R. A precision seeding device for true potato seed. *Am. Potato J.* **1992**, *69*, 255–264. [[CrossRef](#)]
11. Raigond, B.; Verma, A.; Pathania, S.; Sridhar, J.; Kochhar, T.; Chakrabarti, S.K. Development of a reverse transcription loop-mediated isothermal amplification for detection of potato virus a in potato and in insect vector aphids. *Crop Prot.* **2020**, *137*, 105296. [[CrossRef](#)]
12. Double L9560 Planter. [EB/OL]. Available online: <https://www.doublelglobal.com/potato-planter.php#>. (accessed on 1 July 2022).
13. Li, Z.; Wen, X.; Lv, J.; Li, J.; Yi, S.; Qiao, D. Analysis and Prospect of Research Progress on Key Technologies and Equipments of Mechanization of Potato Planting. *Trans. Chin. Soc. Agric. Mach.* **2019**, *50*, 3.
14. Shi, S. Design and Experimental Research of the Pneumatic Maize Precision Seed-Metering Device with Combined Holes. Ph.D. Thesis, China Agricultural University, Beijing, China, 2015.

15. Boydas, M.G. Effect of cup size, seed characteristics and angular speed on the performance of an automatic potato planter under laboratory conditions. *J. Agric. Sci.* **2017**, *23*, 317–327. [[CrossRef](#)]
16. Yazgi, A.; Degirmencioglu, A. Optimisation of the seed spacing uniformity performance of a vacuum-type precision seeder using response surface methodology. *Biosyst. Eng.* **2007**, *97*, 347–356. [[CrossRef](#)]
17. Lv, J.; Yang, Y.; Li, Z.; Tian, E.; Shang, Q.; Wu, J. Design and experiment of an air-suction potato seed metering device. *Int. J. Agric. Biol. Eng.* **2016**, *9*, 33–42.
18. Lv, J.; Liu, Q.; Yang, D.; Su, W.; Li, Z.; Qi, Y. Design and Test of Intelligent Seed Supply System for Air Suction Potato Planter. *J. Agric. Mech. Res.* **2022**, *44*, 157–161.
19. Zhao, X. Design and Seed Metering Performance of Potato Seed Metering Device. Master's Thesis, Shihezi University, Xinjing, China, 2017.
20. Tai, W. Design and Experiment of Clamping Potato Precision Seed Metering Device. Master's Thesis, Northeast Agricultural University, Harbin, China, 2020.
21. Du, X.; Zeng, Y.; Gao, R.; Yan, J. 3-D Modelling of Irregular Shape Particles for Discrete Element Method Based on X-ray Tomography. *J. Shanghai Jiaotong Univ.* **2011**, *45*, 711–715.
22. Chen, E.; Shi, L.; Sun, X. Research Status and Development Trend of Potato Planters and Seed Platters. *For. Mach. Woodwork. Equip.* **2021**, *49*, 4–8.
23. Song, Y. Key Components Design of Potato Micro Seed Planter. *Agric. Eng.* **2018**, *8*, 98–100.
24. Niu, K.; Fang, X.; Liu, Y. Optimized design and performance evaluation of an electric cup-chain potato metering device. *Int. J. Agric. Biol. Eng.* **2017**, *10*, 36–43.
25. Zhang, Y. Design and Experimental of Air-Sucking Potato Miniature Planter. Master's Thesis, Kunming University of Science and Technology, Kunming, China, 2016.
26. Li, H.; Gao, F.; Li, Y.; Yan, J. Determination of Rice Grain Physical Properties. *J. Agric. Mech. Res.* **2014**, *36*, 23–27.
27. Yu, Y.; Zhou, H.; Fu, H.; Wu, X.; Yu, J. Modeling method of corn ears based on particles agglomerate. *Trans. Chin. Soc. Agric. Eng.* **2012**, *28*, 167–174.
28. Liu, C. Study and Application on Shape and Mechanical Rheological Properties of Potato. Master's Thesis, Northeast Agricultural University, Harbin, China, 2006.
29. Fu, H.; Wu, W.; Zhang, H.; Li, W. Feasibility Study on Measurement of Grain Moisture Content by Angle of Repose. *J. Agric. Mech. Res.* **2012**, *34*, 152–155+160.
30. González-Montellano, C.; Fuentes, J.M.; Ayuga-Téllez, E.; Ayuga, F. Determination of the mechanical properties of maize grains and olives required for use in DEM simulations. *J. Food Eng.* **2012**, *111*, 553–562. [[CrossRef](#)]
31. Wang, G. *Discrete Element Method and Its Practice on EDEM*; Northwestern Polytechnical University Press: Xi'an, China, 2010.
32. Cai, H.; Hu, B.; Chen, Y.; Luo, X.; Wang, J.; Mao, Z.; Yuan, C. Study of Patterns of Movement of Groups of Seed Potatoes in Conical Seed Box Based on the Dem-Model of the Process. *Processes* **2022**, *10*, 363. [[CrossRef](#)]
33. Chen, Y.; Tian, F.; Yan, Y.; Song, Z.; Li, F.; Chen, W. Development overview and analysis of tillage machinery abroad. *J. Chin. Agric. Mech.* **2018**, *39*, 7–11.
34. Wang, Y. Planting technology of potato mechanized ridge planting. *Farmers Consult.* **2022**, *2*, 87–89.
35. Zhao, L.; Liu, X.; Wang, J.; Zhuang, S. Effects of subsoiling on potato biomass and soil physicochemical properties. *Bull. Agric. Sci. Technol.* **2019**, *4*, 82–85.
36. Al-Gaadi, K.A. Performance evaluation of a cup-belt potato planter at different operation conditions and tuber shapes. *Am. -Eurasian J. Agric. Environ. Sci.* **2011**, *10*, 821–828.
37. Al-Gaadi, K.A.; Marey, S.A. Effect of forward speed and tuber characteristics on tuber spacing uniformity for a cup-belt potato planter. *Middle East J. Sci. Res.* **2011**, *8*, 753–758.
38. Wang, H.; Zhu, W.; Huang, Z.; Zhang, C.; Zhang, J. Research on the cone angle and clearance of main pump seal. *J. Mech. Sci. Technol.* **2015**, *29*, 2939–2947. [[CrossRef](#)]
39. Xing, H.; Wang, Z.; Luo, X.; Cao, X.; Liu, C.; Zang, Y. General structure design and field experiment of pneumatic rice direct-seeder. *Int. J. Agric. Biol. Eng.* **2017**, *10*, 31–42.
40. Ebrahim, I.A.; Amer, E.; Guidetti, R. A new small potato planter for Egyptian agriculture. *J. Agric. Eng.* **2011**, *42*, 7–13. [[CrossRef](#)]
41. Ilyes, S.; Popescu, S.; Voicu, E. Experimental device for the researches on the precision of the tubers planting distance within the row for different potato planters. *Res. People Actual Tasks Multidiscip. Sci.* **2011**, *2*, 153–158.
42. Kocher, M.F.; Coleman, J.M.; Smith, J.A.; Kachman, S.D. Corn seed spacing uniformity as affected by seed tube condition. *Appl. Eng. Agric.* **2011**, *27*, 177–183. [[CrossRef](#)]
43. Hamad, S.A.; Ismail, Z.E.; Hemeda, M.A. Development of a potato planter to plant tuber pieces with previously grown buds. *J. Agric. Sci. Mansoura Univ.* **1994**, *19*, 2321–2343.
44. Buitenwerf, H.; Hoogmoed, W.B.; Lerink, P.; Müller, J. Assessment of the Behaviour of Potatoes in a Cup-belt Planter. *Biosyst. Eng.* **2006**, *95*, 35–41. [[CrossRef](#)]
45. Wang, Z. Design and Experimental of Metering Device of Cup-Belt Type Potato Planter. Master's Thesis, Northeast Agricultural University, Harbin, China, 2015.
46. Lv, J.; Wang, Y.; Li, Z.; Dui, H.; Liu, Z.; Li, J.; Sun, H.; Peng, M. Performance analysis and experiment of cup-belt type potato seed-metering device with flow deflector. *Trans. Chin. Soc. Agric. Eng.* **2017**, *33*, 19–28.

47. Wollman, A.E.; Wollman, M.J. Potato Planters Improvement to Reduce Skips and Rolling. US20060283363A1, 12 December 2006.
48. Lü, J. *Mechanism and Parameter Optimization about Key Equipment of Pneumatic Potato Precision Planter*; Heilongjiang Bayi Agricultural University: Daqing, China, 2020.
49. Liu, W. *Design of Mechanical-Pneumatic Combined Metering Device for Potato*; Shandong Agricultural University: Taian, China, 2019.
50. Li, M. Design and Research on Pneumatic Metering Device with Cup Spoon Type for Potato. Master's Thesis, Huazhong Agricultural University, Wuhan, China, 2017.
51. Yang, D. Design on Research Pneumatic Metering Device with Horizontal Disc for Potato. Master's Thesis, Huazhong Agricultural University, Wuhan, China, 2016.
52. Li, Z.; Lei, X.; Cao, X. Design and experiment of pneumatic-typed precision centralized metering device for rapeseed. *Trans. Chin. Soc. Agric. Eng.* **2015**, *31*, 9–17.
53. Li, M.; Liao, X.; Liao, Y. Analysis on seeding process of pneumatic cylinder-type centralized rapeseed precision metering device. *Trans. Chin. Soc. Agric. Eng.* **2014**, *30*, 17–27.
54. Yang, L.; Yan, B.; Zhang, D. Research Progress on Precision Planting Technology of Maize. *Trans. Chin. Soc. Agric. Mach.* **2016**, *47*, 38–48.
55. Mao, Q. Design and Research on Key Components of the Planter for Virus-Free Mini-Potato Seeds. Master's Thesis, Huazhong Agricultural University, Wuhan, China, 2013.
56. Meijer, E.N.C.; Frederiks, J. Development of an automatic planter for presprouted seed. *Potato Res.* **1975**, *18*, 451–454. [[CrossRef](#)]
57. He, Y. Study on New Seed Arrangement Mechanism of Potato Planter. Master's Thesis, China Agricultural University, Beijing, China, 2006.
58. GRIMME GB230 Planter. [EB/OL]. Available online: <https://www.grimme.com/de/producttypes/legetechnik/gb-230> (accessed on 1 July 2022).
59. Gardner, J.S. New type potato planter invented. *Am. Potato J.* **1957**, *34*, 149–150. [[CrossRef](#)]
60. Misener, G.C. Relative Performance Of Cup and Pick Type Potato Planters. *Can. Agric. Eng.* **1979**, *21*, 131–134.
61. Chen, S. Study on the arrangement and supply device of potato planter. *Cereals Oils Process.* **1982**, *5*, 15–22.
62. Boydaş, M.G.; Uygan, F. Influence of seed physical properties and speed on the external mechanical damage index and in-row spacing uniformity in an automatic potato planter. *J. Agric. Sci.* **2012**, *18*, 126–136.
63. Liu, W.; He, J.; Li, H.; Li, X.; Lu, C.; Wei, Z.; Su, G.; Zhao, H.; Liu, P.; Wang, C. Seeding performance optimization on vibration-arranging type seeding device for potato micro-seed. *Trans. Chin. Soc. Agric. Eng.* **2019**, *35*, 1–11.
64. Liao, Y.; Li, C.; Liao, X.; Wang, L. Research Progress of Seed Guiding Technology and Device of Planter. *Trans. Chin. Soc. Agric. Eng.* **2020**, *51*, 12.
65. Lv, J.; Yang, Y.; Shang, Q.; Li, Z.; Li, J.; Liu, Z.; Wang, Y. Performance optimization test on air-suction potato seed metering device with positive pressure airflow and zero-speed seeding. *Trans. Chin. Soc. Agric. Eng.* **2016**, *32*, 40–48.
66. Transce Agricultural Machinery. 1SL-6A Subsoiler. [EB/OL]. Available online: http://www.xs-tc.com/gengzhengdijixie/xinghao-1SL-6A_65.html (accessed on 1 July 2022).
67. Transce Agricultural Machinery. 1LF-550 Flipped Plow. [EB/OL]. Available online: http://www.xs-tc.com/gengzhengdijixie/xinghao-1LF-550_1.html (accessed on 1 July 2022).
68. BOMET U473 Cultivators. [EB/OL]. Available online: <https://spedo.it/en/products/ridgers/bed-former/> (accessed on 1 July 2022).
69. Spedo VB4F/75 Bed Former. [EB/OL]. Available online: <https://spedo.it/en/products/ridgers/rotary-ridging-cultivator-with-bed-former/> (accessed on 1 July 2022).
70. GRIMME GF400 Planter. [EB/OL]. Available online: <https://www.grimme.com/de/producttypes/bodenbearbeitung/gf-400> (accessed on 1 July 2022).
71. Grimme GL420 Planter. [EB/OL]. Available online: <https://www.grimme.com/de/producttypes/legetechnik/gl-420> (accessed on 1 July 2022).
72. Dewulf CP42 Planter. [EB/OL]. Available online: <https://www.dewulfgroup.com/en/product/planting/planters/miedema-cup-planters/cp-42> (accessed on 1 July 2022).
73. Menoble 1240 Planter. [EB/OL]. Available online: <http://www.menoble.com> (accessed on 23 February 2022).
74. Spedo SPA/A Potato Planter. [EB/OL]. Available online: <https://spedo.it/en/products/potato-planter/automatic-potato-planter/> (accessed on 1 July 2022).
75. Bomet Sp. z o.o. Sp. K. Planter. [EB/OL]. Available online: <https://www.bomet.pl/One-row-potato-planter-Gemini.html> (accessed on 1 July 2022).
76. SWAN AGRO NSE PPR-2 Potato Planter. [EB/OL]. Available online: https://swanagro.in/index.php/product_detail?pdetid=29 (accessed on 1 July 2022).
77. Crary Lockwood 606 Planter. [EB/OL]. Available online: <http://www.lockwoodmfg.com/Lockwood-Potato-Equipment/Planters/AirCupSSeriesPlanter> (accessed on 1 July 2022).
78. ERME PLPS Planter. [EB/OL]. Available online: <http://www.erne-france.com/product/single-row-mechanical-garlic-onion-planter/3007/0> (accessed on 1 July 2022).
79. Dewulf Miedema Structural 30 Planter. [EB/OL]. Available online: <https://www.dewulfgroup.com/en/product/planting/planters/structural-belt-planters/structural-30> (accessed on 1 July 2022).

80. Standen Engineering ZENO 21 Planter. [EB/OL]. Available online: <https://standen.co.uk/products/planters/> (accessed on 1 July 2022).
81. Crary Lockwood Needle-Type Potato Planter. [EB/OL]. Available online: <http://www.lockwoodmfg.com/Lockwood-Potato-Equipment/Planters/PickPlanters#> (accessed on 1 July 2022).
82. Harriston Pick Planter. [EB/OL]. Available online: <https://www.harriston-mayo.com/harriston/pick-planter.php> (accessed on 1 July 2022).
83. Harriston Clamp Planter. [EB/OL]. Available online: <https://www.harriston-mayo.com/harriston/clamp-planter.php> (accessed on 1 July 2022).
84. Velandiaa, M.; Buschermohleb, M.; Larson, J.A.; Thompson, N.M.; Jernigan, B.M. The economics of automatic section control technology for planters: A case study of middle and west Tennessee farms. *Comput. Electron. Agric.* **2013**, *95*, 1–10. [CrossRef]
85. Okada, Y.; Ishikawa, K.; Nagata, M. Studies on the precision seeding-seed metering system using bowl type feeder. *J. Soc. Agric. Mach.* **1982**, *44*, 431–437.
86. Haase, W.C. Pioneer I—A Planter Computer system. *ASAE* **1986**, *36*, 135–145.
87. Sun, W.; Liu, X. Design of potato casingsoil planter in all-in-one machine combined with fertilizing, sowing, ridging, complete film mulching and planting line covering. *Trans. Chin. Soc. Agric. Eng.* **2017**, *33*, 14–22.
88. Liu, Q.; Wu, J.; Wang, D.; Sun, W.; Wang, G.; Shi, L. Current status and progress of the potato seeder. *Agric. Mech. Res.* **2013**, *6*, 238–241.
89. GRIMME GB430 Planter. [EB/OL]. Available online: <https://www.grimme.com/de/producttypes/legetechnik/gb-430> (accessed on 1 July 2022).
90. Cao, D. Study On Loss Sowing Monitoring and Early Waning System of Potato Precision Seeder. Master’s Thesis, Northwest A&F University, Xianyang, China, 2013.
91. Zhang, X. *Design of Automatic Monitoring and Compensation System for Potato Planter*; Gansu Agricultural University: Lanzhou, China, 2012; (In Chinese with English abstract).
92. Liu, Q.; Wu, J.; Wang, D. Design and test of a microcomputer-controlled loss sowing compensation system for 2CM-2 potato seeder. *Agric. Res. Arid. Areas* **2013**, *31*, 260–266, (In Chinese with English abstract).
93. Sun, W.; Wang, G.; Wu, J. Design and experiment on loss sowing testing and compensation system of spoon-chain potato metering device. *Trans. Chin. Soc. Agric. Eng.* **2016**, *32*, 8–15.
94. Wang, F.; Sun, C.; Shi, D.; Li, X.; Wei, C.; Su, G.; Wang, X. Development of the Intelligent Precision Planting System of the Potato. *J. Agric. Mech. Res.* **2017**, *39*, 107–111+117.
95. Zhu, L.; Wang, G.; Sun, W.; Zhang, H.; Liu, X.; Feng, B.; Wang, C.; Sun, L. Development of potato seed-metering state monitoring system based on space capacitance sensors. *Trans. Chin. Soc. Agric. Eng.* **2021**, *37*, 34–43.
96. Wang, G.; Sun, W.; Zhang, H.; Liu, X.; Zhu, L. Research on a kind of seeding-monitoring and compensating control system for potato planter without additional seed-metering channel. *Comput. Electr. Agric.* **2020**, *177*, 105681. [CrossRef]
97. Wang, X. Design and Experimental Research on Double-row Criss-cross Spoon-belt Potato Precision Seed Metering Device. Master’s Thesis, Northeast Agricultural University, Wuhan, China, 2016.
98. Zou, J. Study on the application of ridge planting contour seeder for potato and its seeding method. *Farm Mach.* **2018**, *10*, 79–81.
99. Hu, Z.; Yue, R.; Zhu, S. Design and Test of 2CMW-4B Mini-potato Planter. *J. Agric. Mech. Res.* **2019**, *41*, 60–64.

Article

Study on the Intercropping Mechanism and Seeding Improvement of the Cavity Planter with Vertical Insertion Using DEM-MBD Coupling Method

Linrong Shi ¹, Wuyun Zhao ^{1,*}, Chengting Hua ², Gang Rao ¹, Junhai Guo ¹ and Zun Wang ¹¹ College of Mechanical and Electrical Engineering, Gansu Agricultural University, Lanzhou 730070, China² Hangzhou Nichuang Technology Co., Ltd., Hangzhou 310000, China

* Correspondence: zhaowuy@gasau.edu.cn

Abstract: In the dry areas of Northwest China, cavity planters with vertical insertions are used for seeding on film. Due to the uncertain mechanism between cavity planters and maize seeds and soil, research on the cavity planter has been slow. Several theoretical and experimental methods have been developed to investigate the interaction between the cavity planter and maize seeds in soil. These methods enable exploration of the mechanism to reduce soil disturbance and improve seeding performance. However, these methods are unable to predict the dynamic force of tools and soil behavior because of non-linear soil properties. A simulation experiment was conducted using the DEM-MBD coupling method to explore soil disturbance caused by cavity seeders and the resistance to entry. Additionally, the effect of the maize shape and the cavity planter motion on the seed number qualification and the empty cavity rate was investigated. It was proposed that the inverted hook be used to prevent the movement of maize seeds up and down in cavity seeders, thereby improving seed filling performance. Simulations and experiments were conducted, and the results showed that the average empty cavity rate and the seed number qualification were 2.0% and 91.3%, respectively, which met the requirements of the maize sowing standards.

Keywords: maize; soil; cavity planter; interaction mechanism; DEM; verification

Citation: Shi, L.; Zhao, W.; Hua, C.; Rao, G.; Guo, J.; Wang, Z. Study on the Intercropping Mechanism and Seeding Improvement of the Cavity Planter with Vertical Insertion Using DEM-MBD Coupling Method.

Agriculture **2022**, *12*, 1567. <https://doi.org/10.3390/agriculture12101567>

Academic Editors: Muhammad Sultan, Redmond R. Shamshiri, Md Shamim Ahamed and Muhammad Farooq

Received: 27 August 2022

Accepted: 22 September 2022

Published: 28 September 2022

Publisher's Note: MDPI stays neutral with regard to jurisdictional claims in published maps and institutional affiliations.



Copyright: © 2022 by the authors. Licensee MDPI, Basel, Switzerland. This article is an open access article distributed under the terms and conditions of the Creative Commons Attribution (CC BY) license (<https://creativecommons.org/licenses/by/4.0/>).

1. Introduction

The main working process of the cavity planter with vertical insertion is to vertically insert the hole seeder into the soil and discharge the maize seeds into the hole. Therefore, the cavity planter mainly interacts with maize seeds and soil. The cavity planter's optimization is also based on them. Soil mechanics is a priority issue when designing and optimizing components to reduce resistance and consumption in agricultural tillage, precision seeding, and efficient harvesting [1]. As soil separation, mixing, cracking, and flow belong to the characteristics of a bulk particle, the discrete element method (DEM) is the best research choice. Initially, DEM was used for the movement analysis of rock slopes [2]. Subsequently, it has been widely developed in various fields, and DEM is mainly used in agricultural engineering to study the interaction between tools and soils. DEM has proved its reliability in predicting soil resistance by means of a deep pine shovel–soil interaction model [3,4]. The shape of the soil particles and the bond between the soil particles affect the resistance of the tool. Ono et al. [5] created six different shapes of soil particles with DEM and compared the working resistance of the bulldozers. The non-cohesive/cohesive particle model and Newtonian fluid/non-Newtonian fluid wet particle of soil cultivation model were analyzed by DEM [6]. Zhang et al. [7,8] added liquid bridge forces due to moisture to the particle contact model to simulate the cohesive interaction between soil particles using DEM. The slant-shank folding shovel's structure and parameters are optimized with the aid of DEM [9]. In addition, with DEM the maize models built by the spherical aggregation method are in good agreement with the experimental results in terms of bulk density,

repose angle, and flow motion [10,11]. In this regard, it is evident that DEM research on the interaction between tools and soil is on the rise.

Meanwhile, a cavity planter's performance is affected not only by the soil and maize, but also by the interaction between the non-circular gear drive forward speed compensation mechanism and the overall speed of the machine. In practice, the interaction between the cavity planter and the soil involves the compaction of the soil by the wheels, the support of the soil on the wheels and the sliding of the soil, the disturbance of the soil caused by the cavity planters, and also the circulation of the maize seeds and seed discharge. Thus, complex interactions are involved among them. It is challenging to clearly evaluate seed motion, soil and ground wheels, soil and cavity planters, seed circulation, and seed motion. It should be noted that the forward speed compensation mechanism on the cavity planter with vertical insertion is driven by a non-cylindrical gear, and that its contact motion is complex, and thus cannot be achieved by simple motion settings in EDEM, so it must be achieved using virtual prototyping software [12]. There are clear advantages to using the Korean FunctionBay software in the areas of large model calculations, sliding and collision contact, and the design and optimization of flexible bodies in motion [13].

As DEM and multibody dynamics (MBD) have developed, the coupled DEM-MBD numerical simulation technique has gained widespread use in industry [14]. Combining DEM with MBD is an excellent approach for understanding the interaction between maize seeds, soil, and forward speed compensation mechanisms. This paper focuses on the DEM-MBD coupled simulation and the self-developed 2BZ-2 cavity planter with vertical insertion. It examines the effect of various factors on soil disturbance and cavity planter performance to propose a plan and ideas for optimizing the direct hole sowing machine.

2. Materials and Methods

2.1. Virtual Prototype Establishment of the Cavity Planter with Vertical Insertion

The maize cavity planter with vertical insertion consists of a frame, engine, traction wheel, gearbox, differential, forward speed compensation mechanism, cavity seeder, outer grooved wheel seeder, guide wheel, guide frame, and handle, as demonstrated in Figure 1. The cavity seeder is the main part of the seeder, which participates in the interaction process between corn and seeder. A core component in the cavity seeder is the shaped groove, as shown in Figure 1c. The engine provides the power for the cavity seeding process, partly driving the traction wheel, and partly driving the forward speed compensation mechanism. The gearbox transmits the power input from the engine to the differential speed and forward speed compensation mechanism after speed regulation, shunting and reversing; the differential speed can achieve the steering of the traction wheel; the forward speed compensation mechanism is the core component of the direct maize cavity on film. The forward speed compensation mechanism is the core component of the maize cavity planter with vertical insertion, and is mainly responsible for "zero speed" processing of the traction speed of the whole machine during the seeding process, i.e., it generates movements that offset the horizontal speed of the whole machine so that the horizontal direction before and after insertion is approximately stationary with respect to the ground. The outer grooved wheel seeder provides an even seed supply to the seeder so that the seed in the seed tube of the seeder always maintains a seed volume conducive to seeding. The guide wheel and guide frame facilitate the adjustment of the seeder, and the handle facilitates manual operation. The angle between the crank rods of the two sets of forward speed compensation mechanisms is set at 180° , which improves the smoothness of the machine.

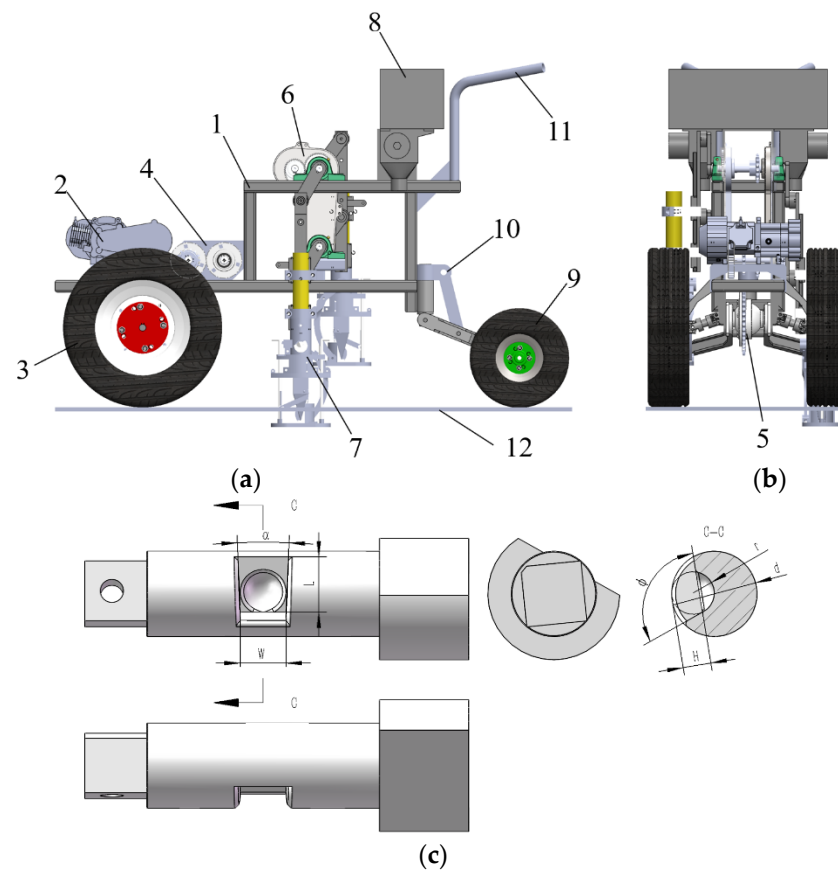


Figure 1. Structural components of the maize cavity planter with vertical insertion. (a) Main view. (b) Front view. (c) Structure schematic of shaped groove. (1) frame; (2) engine; (3) traction wheel; (4) gearbox; (5) differential; (6) forward speed compensation mechanism; (7) cavity seeder; (8) outer grooved wheel seed discharger; (9) guide wheel; (10) guide frame; (11) handle; (12) ground. Note, L is the length of shaped groove. W is its width. H is the height. α is opening angle of the groove. d is the diameter of seed taking wheel. r is the maximum diameter of the spherical hole. φ is the included angle of the inner groove line.

There is a non-circular gear that drives a complex drive system, which is assembled from virtual prototypes, to compensate for the forward speed of the cavity planter with vertical insertion. Virtual prototypes are constructed using constraints, motion, and drive information. In MBD simulation process, the parts that do not affect the simulation results can be omitted or simplified, thereby reducing the number of unnecessary constraints and parts. The specific operation is to export the 3D model x_t format, and import to Recurdyn V9R2 (FunctionBay Co., Seongnam, Korea), delete the redundant parts such as bolts and bearings, and delete the parts including bearings, mounting screws, pins, drive chains, gears, etc. Establish rotation, translation, and fixation constraints between components, and set related motion, add motion information based on rotation and translation subs. As shown in Figure 2b, the virtual prototype model consists of engine power output, speed change and reversing, ground drive system, transmission ratio conversion system, direct cavity seeder system, quantitative seed discharge system, and passive guide wheel system. Ground drive system includes differential mechanism. The cavity planter can turn flexibly on the ground. The traction wheel can be turned at different speeds by turning the handle.

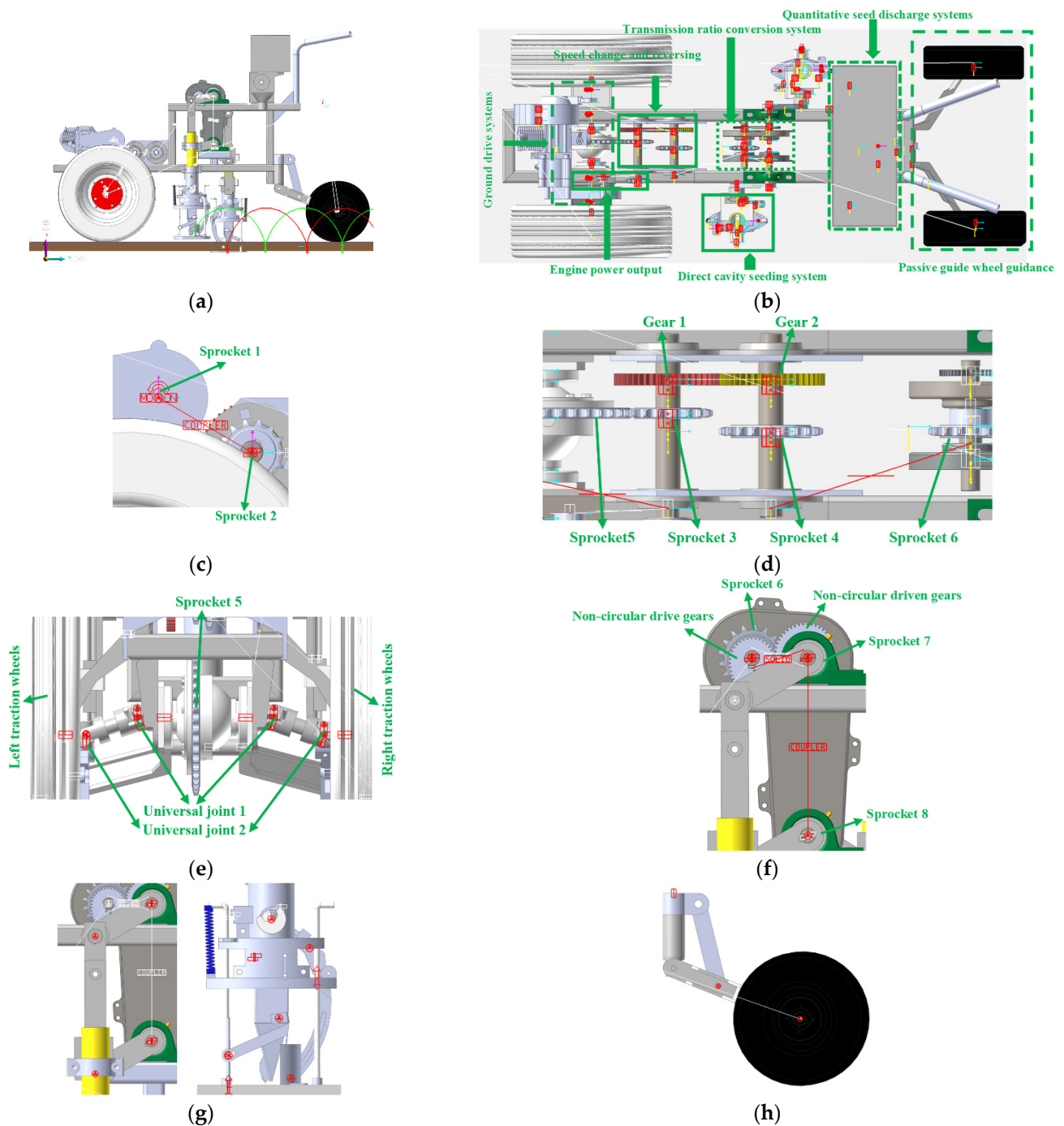


Figure 2. Constraint relationships of the cavity planter with vertical insertion. (a) Virtual prototype model. (b) Drive train division. (c) Engine power output. (d) Speed changing and reversing. (e) Ground drive system. (f) Transmission ratio conversion system. (g) Cavity seeding system. (h) Passive wheel guidance.

The working process is specifically that sprocket 1 is driven by engine power output to turn sprocket 2, and sprocket 2 is connected to sprocket 1 by a couple, and the transmission ratio is 1:1 in Figure 2c. The variable speed reversing power input shaft is hinged to the frame and is fixed to the power input sprocket. After speed changing and reversing, the power is distributed to the ground drive system and transmission ratio conversion system. Sprocket 3 in the speed changing and reversing is connected to sprocket 5 from the ground drive system, and the transmission ratio is 1:3.2, while gear 1 engages with the passive gear

2 that is hinged to the frame and fixedly connected to sprocket 4, as seen in Figure 2d. Then it is connected to sprocket 6 with chain. It drives the active non-circular gear to bring driven non-circular gears with variable ratios. It is fixedly connected to sprocket 7, then that drives sprocket 8 and the transmission ratio is 1:1, enabling cavity seeding with vertical insertion, as shown in Figure 2f. In another method, sprocket 5 that is mounted on the ground drive system drives universal joint 1 and universal joint 2 to make traction wheels rotate, as indicated. Other constraint relations are presented in Figure 2e,f for cavity seeding system and passive wheel guidance. The completed virtual prototype model is shown in Figure 2a.

2.2. Soil Modeling

Based on the soil type of China’s northwest dry zone, a simplified soil simulation model was developed to improve simulation efficiency. Specifically, soil model (length 3100 mm × width 1000 mm × height 320 mm) was created using SolidWorks 2018.sp5, saved as. x_t format and then imported into EDEM 2018 (Altair co., Richardson, TX, USA) through the geometry option [15–17]. Hysteretic Spring and Linear Cohesion were selected to simulate sandy loam, and the related simulation parameters are shown in Table 1. The Hertz–Mindlin model and Linear cohesion model were chosen to simulate sandy soils and the simulation parameters are seen in Table 2. The soil particles’ radius was set to 10 mm, and the variance of the radius was 0.05. The soil simulation parameters are shown in Table 3 at the same level. Therefore, the simplified model is indicated in Figure 3.

Table 1. Predicted simulation parameters of sandy loam.

Water Content %	Coefficient of Static Friction	Yield Strength/kPa	Rolling Friction Coefficient	Stiffness Factor	Damping Factor	Coefficient of Restitution	Cohesion Strength/kPa
1	0.06	10.38×10^6	0.01	0.73	0.95	0.6	7.04
6	0.05	9.55×10^6	0.01	0.73	0.95	0.6	6.13
12	0.05	8.89×10^6	0.01	0.73	0.95	0.6	6.14
18	0.03	8.78×10^6	0.01	0.73	0.95	0.6	3.64

Table 2. Predicted simulation parameters of sandy soil.

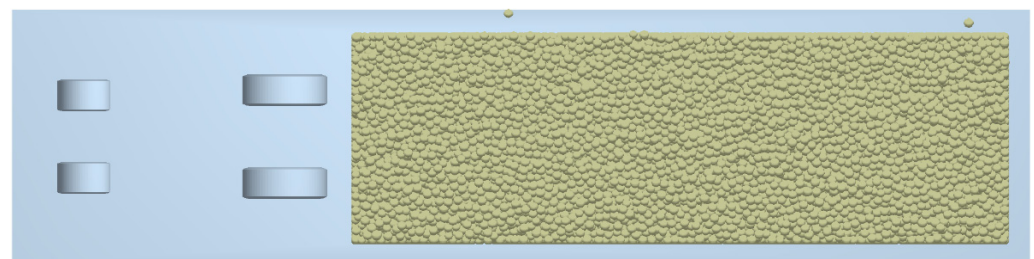
Water Content %	Coefficient of Static Friction	Rolling Friction Coefficient	Coefficient of Restitution	Cohesion Strength/kPa
1	0.1	0.72	0.6	11.04
6	0.07	0.68	0.6	8.09
12	0.02	0.66	0.6	3.26
18	0.02	0.59	0.6	3.14

Table 3. Simulation parameters.

Parameter	Value				Source
Water content of sandy soil/sandy loam/%	1	6	12	18	
Soil particle density of sandy soil/sandy loam/(kg/m ³)	1600/1200				Measurement
Poisson’s ratio of sandy soil/sandy loam	0.3/0.4				Literature [18,19]
Shear modulus of sandy soil/sandy loam/MPa	11.5/3.27				Calculation [18,19]
Steel density/(kg/m ³)	7850				Literature [20]
Steel Poisson’s ratio	0.3				Literature [20]
Steel shear modulus/MPa	7.9×10^4				Literature [20]

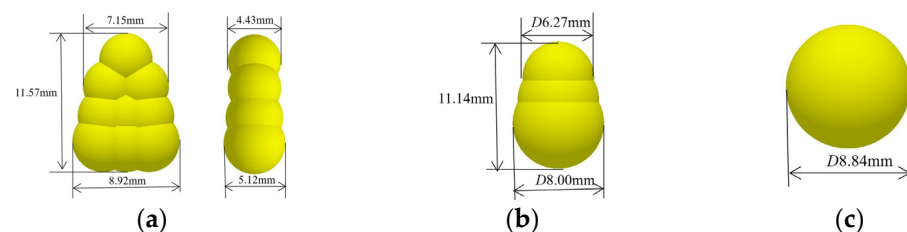
Table 3. *Cont.*

Parameter	Value	Source
Coefficient of static friction between soil and steel	0.5	Literature [20]
Coefficient of rolling friction between soil and steel	0.05	Literature [20]
Coefficient of restitution between soil and steel	0.6	Literature [20]
Rubber density/(kg/m ³)	940	Literature [16]
Rubber Poisson's ratio	0.47	Literature [16]
Shear modulus of rubber/MPa	2.9×10^3	Literature [16]
Coefficient of static friction between soil and rubber	0.57	Literature [16]
Coefficient of rolling friction between soil and rubber	0.31	Literature [16]
Coefficient of restitution between soil and rubber	0.6	Literature [16]

**Figure 3.** Soil simulation simplified model.

2.3. Maize Seed Modeling

Intercropping effects with maize also occur with the cavity seeder. The effect of maize shape on the seeding performance was investigated. Three typical shapes of maize models were used. Among them, the horse tooth seed consisted of nine unequal spherical particles, the spherical cone consisted of three unequal radius spherical particles, and the spherical particle consisted of one spherical particle, as presented in Figure 4.

**Figure 4.** The discrete element model of maize seeds. (a) Horse tooth. (b) Spherical cone. (c) Spherical.

Maize simulation parameters were set as: Poisson's maize model ratio was 0.4, the shear modulus was 1.37×10^8 Pa, and the density of maize grains was 1200 kg/m^3 . Interaction parameters between maize seeds included the coefficient of restitution, the coefficient of static friction, and the coefficient of rolling friction. The coefficient of restitution was set to 0.37, and the coefficient of static friction was set to 0.2. The coefficients of rolling friction of horse tooth, spherical cone, and spherical maize seeds were 0.013, 0.024, and 0.053, respectively. The coefficients between horse tooth and spherical cone, horse tooth and spherical, spherical cone and spherical maize models were 0.004, 0.003, 0.014, respectively. The coefficient of restitution between maize and steel was set to 0.37, the coefficient of static friction was set to 0.408, and the coefficient of rolling friction was 0.01 [21].

2.4. Coupling Modeling

During the coupling simulation of direct cavity sowing with soil and maize interactions, the parts of the virtual prototype that interact with the discrete element method soil and maize models need to be output in the form of walls. In the process of coupling simulation jointly with EDEM and RecurDyn, RecurDyn receives the external force from EDEM through the wall, and EDEM software receives the movement data from the contact geometry from RecurDyn through the wall. Based on the two-way DEM-MBD coupling method, maize seeds' complex motion and force process can be observed visually using discrete element software [22]. During the RecurDyn coupling setup, files were created and exported for the parts in contact with the particles, including two traction wheels, two guide wheels, two fixed and two movable cavity formers, and two support plates. The wall files were imported using the Import Geometry from RecurDyn function under the geometry's module in EDEM. The soil contact parts of the cavity planter include the traction wheel, the guide wheel, the fixed cavity seeder, the movable cavity seeder, and the support plate, with the traction wheel and guide wheel made of rubber and the fixed cavity seeder, movable cavity seeder, and support plate made of steel. The simulation model of the direct cavity seeder and soil interaction is shown in Figure 5.

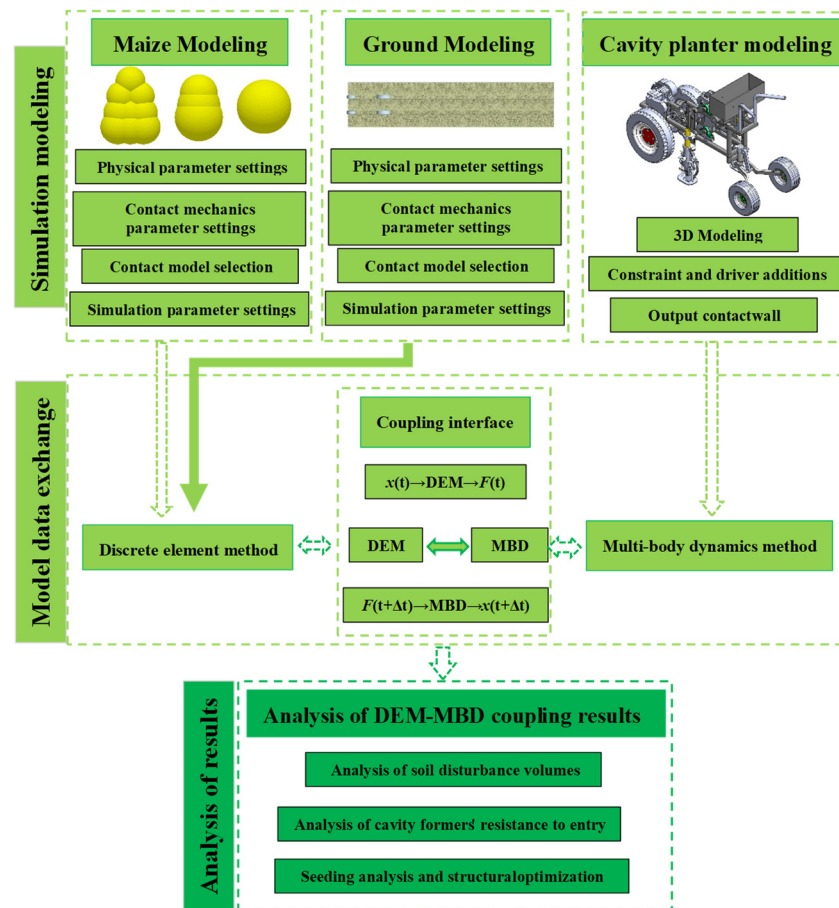


Figure 5. The flow on DEM-MBD coupling simulation.

3. Results

3.1. Coupling Process

It is necessary to conduct separate studies on the mechanism of intercropping between maize seeds, soil, and the cavity seeding considering the inconsistency of the particle contact models used for soils and maize seeds. Marker points were established at the two cavity seeder tips to track their motion trajectory. By measuring the course of the cavity seeder during travel, a transition section of 1200 mm was placed between the contact of the

cavity seeder and the soil model. The transition section allowed comparison of the effect of the ground wheel slip on the trajectory. Figure 5 illustrates the coupling process between the cavity seeder and soil in a simulation.

Figure 6 shows that the cavity seeder travels smoothly on the soil model, that the forward speed compensation mechanism is usually engaged, and that the seeder enters the soil at a suitable depth. From the trajectory, it is evident that the forward speed compensation mechanism has a good compensation effect in the transition section, and a weaker compensation effect in the coupling section. Research was conducted based on the interaction model to determine the influence of soil type and water content on soil disturbance and entry resistance. Several factors affect the impact of forward speed compensation, including soil conditions, traction wheels, and the input speed ratio of the forward speed compensation mechanism. During field operations, soil conditions and speed ratio can be selected at the right time.

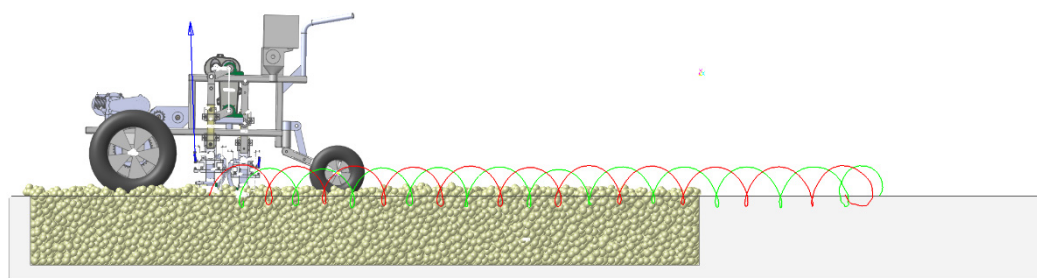


Figure 6. Simulation process of cavity seeding.

3.2. Effect of Soil Type on Soil Disturbance

There is a difference in compressibility between the sandy soils and sandy loams studied in this paper, but they both possess a certain degree of cohesion. For sandy soils, the Hertz-Mindlin (no slip) and Linear Cohesion models were selected, and for sandy loam soils, the Hysteretic Spring and Linear Cohesion models were selected. The cavity seeder slips and sags as it travels on the soil, which affects its forward speed compensation. Figure 7 provides a comparison of the forward speed of the cavity seeder for the two soil types at 1% water content.

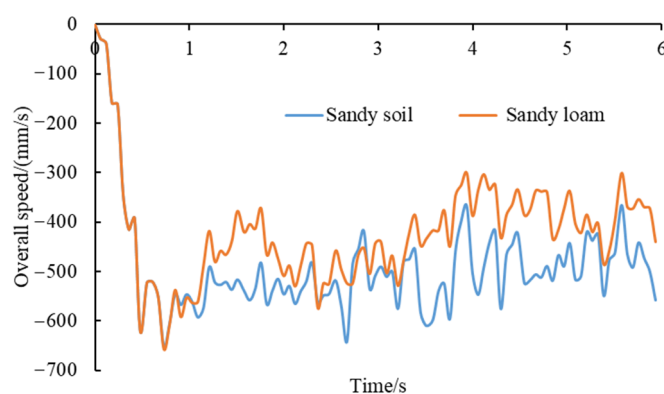


Figure 7. Overall speed of the cavity planter travelling on two different soils.

Figure 7 illustrates how soil type affects forward speed. In sandy loam, the average speed is -487.757 mm/s, and in sandy soil, the average speed is -420.035 mm/s. The cavity seeder produces less slip in sandy soil than in sandy loam because of the lower speed in sandy loam. It is necessary to compare the amount of soil drop between the two soil types since soil drop probably causes the seeder's speed to decrease, as shown in Figure 8.

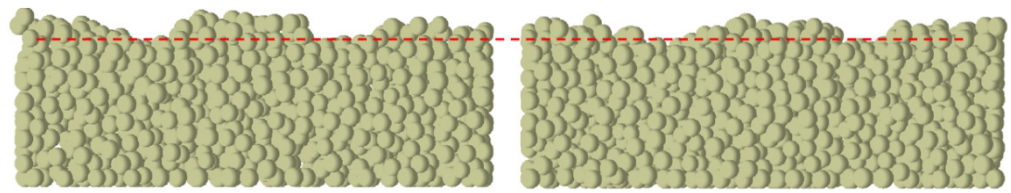


Figure 8. Amount of soil drop for two types of soil.

In both sandy soil and sandy loam models, the amount of soil drop is essentially similar, as seen in Figure 8. Accordingly, the cavity seeder slips on the soil model, and the amount of soil drop is not the primary cause.

3.3. Effect of Water Content on the Amount of Soil Disturbance

The influence of the two types of soils on the trajectory of the cavity seeder under different water content conditions was analyzed separately. The left and right cavity seeders were compared, as illustrated in Figure 9.

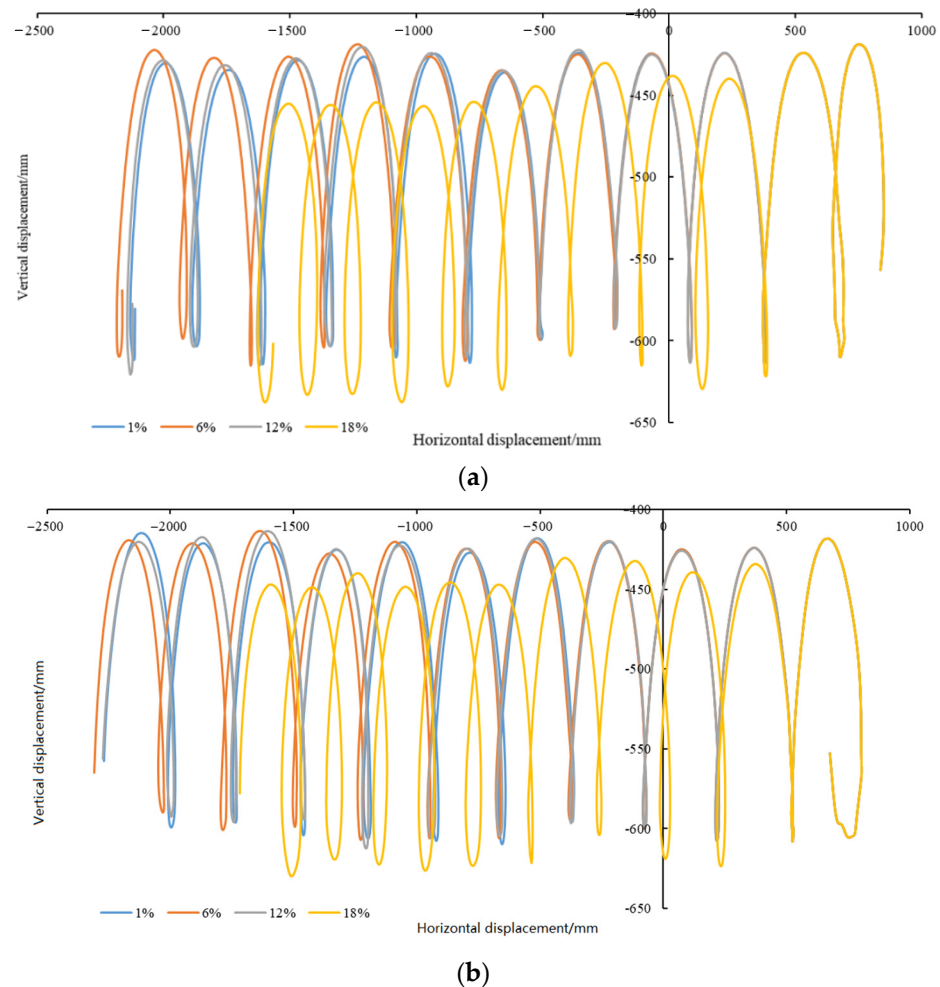


Figure 9. Trajectory of cavity seeder’s movement under sandy soil. (a) Right cavity seeder. (b) Left cavity seeder.

Figure 9 shows that sandy soil with varying water content affects the trajectory of the cavity seeder. The greatest distance was at 6%, the nearest at 18%, and the closest at 1% and 12%. According to the displacement in the vertical direction, there was a small amount of soil drop when the water content was between 1 and 12%. Comparatively, that was evident when the water content was 18%. Does the cavity seeder pattern in sandy loam

correspond to that in sandy soil? Figure 10 illustrates the trajectory of the cavity seeder under sandy loam.

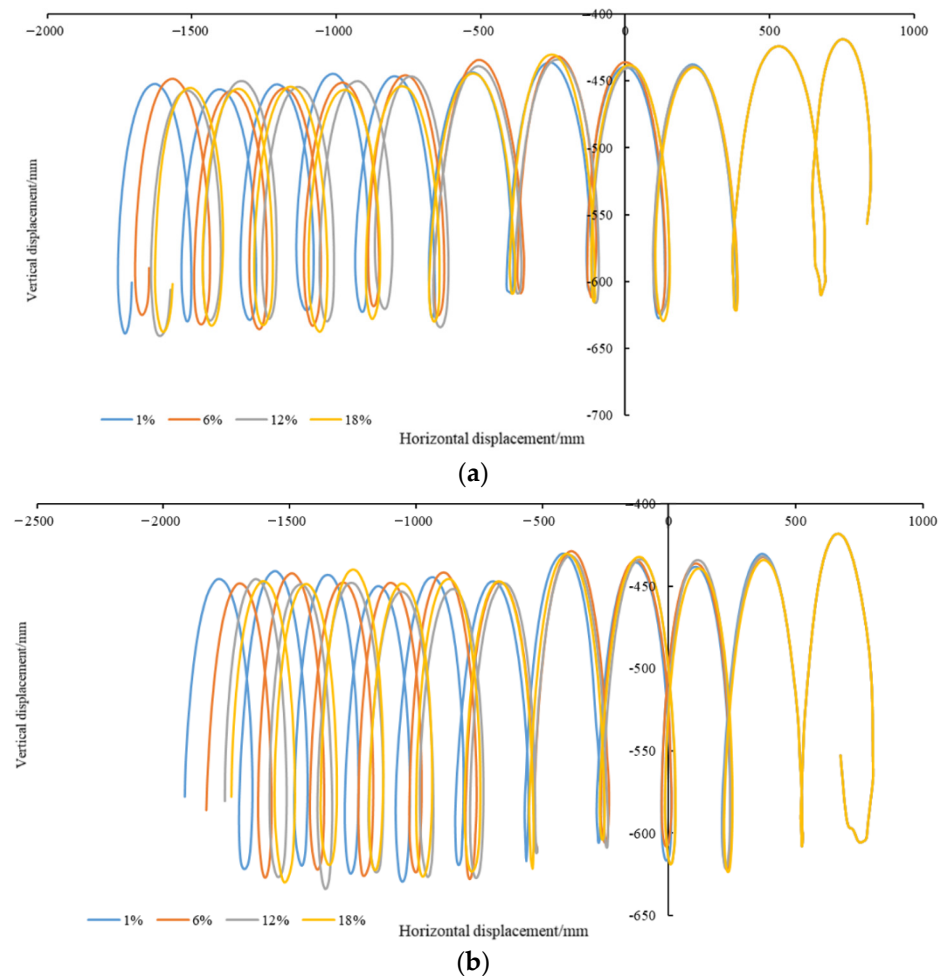


Figure 10. Trajectory of cavity seeders under sandy loam. (a) Right cavity seeder. (b) Left cavity seeder.

The trajectory of the cavity seeders was affected by sandy loam soil with different water contents, as shown in Figure 10a. The trajectory decreased from 1% to 18%, indicating that the slip rate of the cavity seeder increased as the water content increased. In terms of displacement in the vertical direction, the cavity seeder dropped more when the water content ranged from 6 to 18% as compared to 1%. Under all three conditions of water content, the amount of soil drop was equal. Figure 10b provides further evidence.

According to Figures 9 and 10, the slip rate of the cavity seeder traveling on sandy loam was significantly higher than that of sandy soil under the same water content conditions. Sandy loam soils performed 19% better than sandy soils when the water content was 1%. In sandy loam, the drop was 24% higher than in sandy soil when the water content was 6%. Sandy loam slips were 26% better than sandy soil when the water content was 12%. Sandy loam and sandy soil had similar slip amounts when the water content was 18%. It appears from the above results that the slip of sandy loam increases more rapidly with increasing water content than that of sandy soil. Nevertheless, both soil types were comparable when the water content was 18%. It seems that the input speed ratio between the traction wheel and the forward speed compensation mechanism needs to be adjusted for different types of soil to reduce soil disturbance. During cavity seeding, the soil water content should not exceed 18%. Next, we investigate the influence of the input speed ratio between the traction wheel and the forward speed compensation mechanism on soil disturbance.

3.4. Influence of the Rotation Speed Ratio on the Amount of Soil Disturbance

An investigation was conducted to determine the effect of traction wheel speed on soil disturbance. According to the theoretical analysis, an increase in the traction wheel speed will result in an increase in the forward speed of the cavity seeder. However, the forward speed compensation mechanism will remain unchanged. Five speed ratios are listed in Table 4. As a result, the cavity seeder will move backward relative to the ground. Cavity seeders move slowly relative to the ground when the speed of the traction wheels decreases. Large displacements forward and backwards can disrupt the soil disturbance and change the seed germination environment in the cavity hole. Figure 11 illustrates the trajectory of cavity seeding under different transmission ratio conditions.

Table 4. Rotation speed ratio.

Parameters	Value				
Rotation speed of forward speed compensation mechanism/(rad/s)	11.50	11.50	11.50	11.50	11.50
Rotation speed of traction wheel/(rad/s)	4.44	3.72	3.2	2.81	2.51
Ratio	2.59	3.09	3.59	4.09	4.59

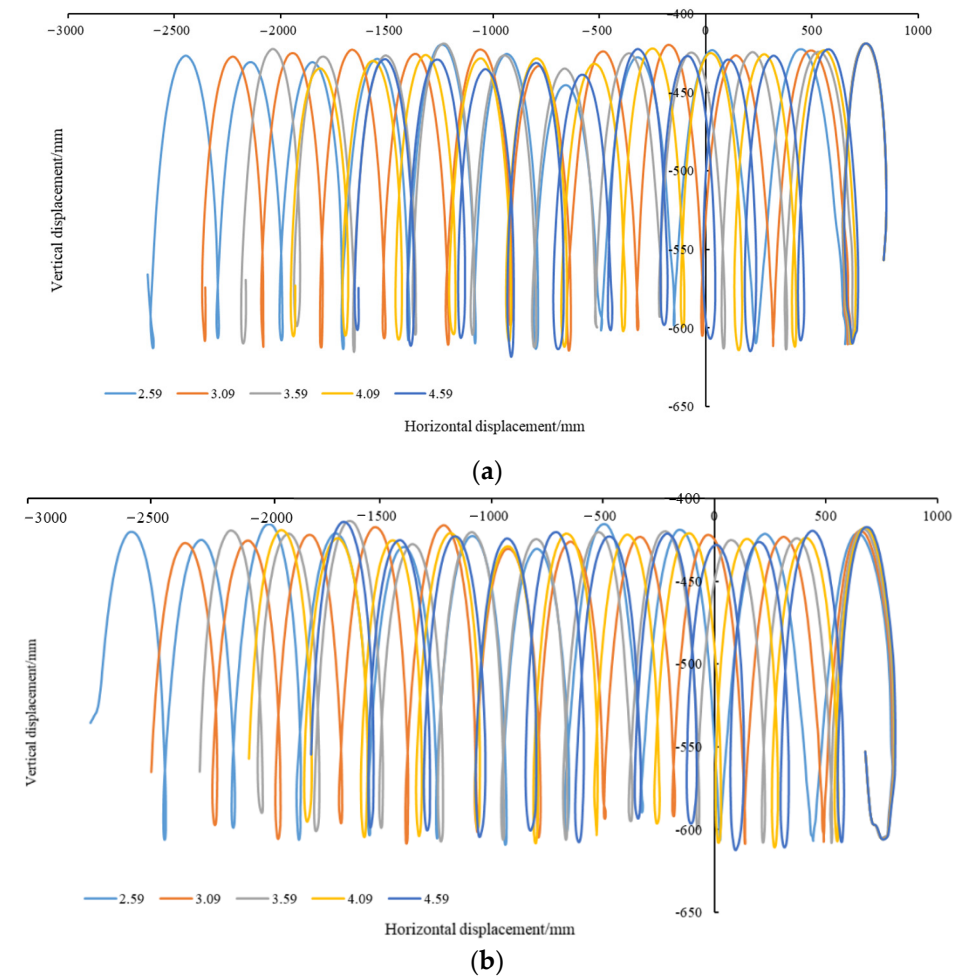


Figure 11. Trajectory of cavity seeders under different rotation speed ratios. (a) Right cavity seeder. (b) Left cavity seeder.

According to Figure 11, as the speed of the traction wheel decreases, the trajectory of the cavity seeder gradually moves backward. In the forwarding speed compensation mechanism, the horizontal speed cannot be compensated, so the intersection of trajectory shifts upward, and the theoretical seeding depth increases. As the ratio decreases, the traction wheel speed increases, and the motion trajectory gradually advances. There is no doubt that the cavity seeder will cause soil disturbance due to the different types of soil. Due to the deeper soil disturbance caused by the cavity seeder, the seed growth layer will be destroyed. Furthermore, the cavity seeder can loosen the soil above the seed and allow air to enter the seed bed. As a result, it is recommended to moderately disturb the soil above the intersection of trajectory to enlarge the hole seeder and increase air circulation.

3.5. Effect of Water Content on the Resistance to Soil Entry

The resistance of the cavity seeder to soil affects the power input of the cavity seeder and the smoothness of the machine [23]. It is necessary to examine the effect of two soil types with four water contents on the resistance of the cavity seeder. The purpose of this is to provide some support for the cavity seeder. Figure 12 illustrates the resistance of the cavity seeder.

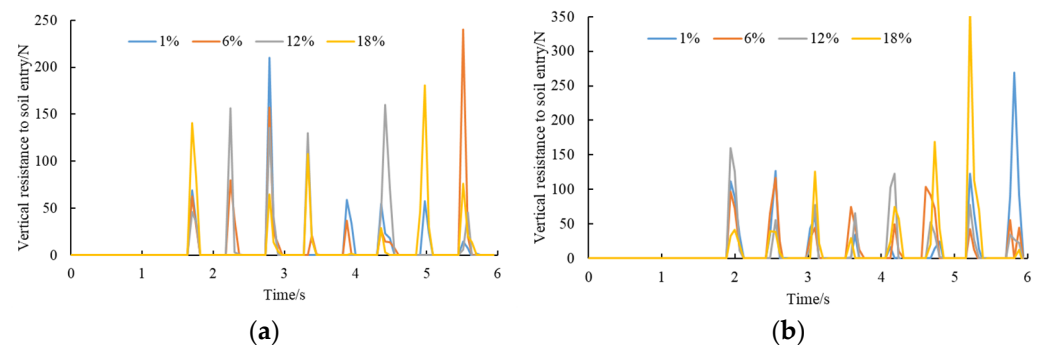


Figure 12. Entry resistance of the cavity seeder in sandy soil. (a) Left cavity seeder. (b) Right cavity seeder.

As shown in Figure 12a, the water content of sandy soil also affects the entry resistance of cavity seeders. The maximum resistance for the four water contents can be compared based on their average values. As a result, the average value was 57.99 N at 1%, 78.09 N at 6%, 84.29 N at 12%, and 78.03 N at 18%. It was found that when the water content was 1–12%, the entry resistance increased on the left side and decreased when the water content was 18%. According to Figure 12b, the average value was 88.55 N at 1%, 72.97 N at 6%, 76.39 N at 12%, and 106.90 N at 18%. It is evident that the entry resistance increased when the water content ranged from 6 to 18%. Figure 13 illustrates the resistance to cavity penetration in sandy loam soils.

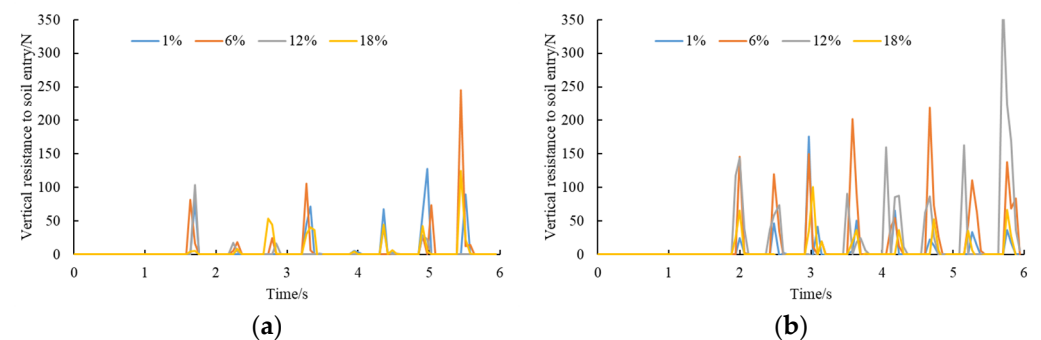


Figure 13. Entry resistance of the cavity seeder in sandy loam. (a) Left cavity seeder. (b) Right cavity seeder.

According to Figure 13a, the water content of sandy loam soils also influences entry resistance. For each of the four water content conditions, the average value of the maximum penetration resistance of sandy loam soil can be compared. According to the results, the average value was 55 N at 1%, 78.42 N at 6%, 29.35 N at 12%, and 40.52 N at 18%. There was an increase in entry resistance when the water content was between 1 and 6%. In contrast, there was a decrease in entry resistance when the water content was between 6 and 12%. Figure 13b shows average values of 56.83 N at 1%, 142.35 N at 6%, 127.78 N at 12%, and 49.18 N at 18%. The entry resistance increased when the water content was between 1 and 6%. In the range of 6–18% water content, the entry resistance decreased. As the moisture content of the sandy loam soil increased, the resistance first increased and then decreased. Compared to sandy soil, sandy loam has a significantly higher cavity resistance.

During the insertion of the cavity seeder into the soil, the duckbill is subjected to resistance from the soil. At the same time, the duckbill is also strongly stressed against the soil. A cloud plot of the change in stress between the duckbill and the soil from the start insertion to near the bottom of the cavity is observed in a sandy loam soil with a moisture content of 6%.

From Figure 14a, the fixed duckbill stress remains blue, but the stress is changing, transitioning from 1.11×10^5 Pa to 1.35×10^5 Pa. From Figure 14b, the axial stress of the duckbill on the soil appears red, with the soil stress at 1.39×10^5 Pa when the duckbill first enters the soil, gradually decreasing to 7.96×10^4 Pa before increasing in small floats to 9.10×10^4 Pa.

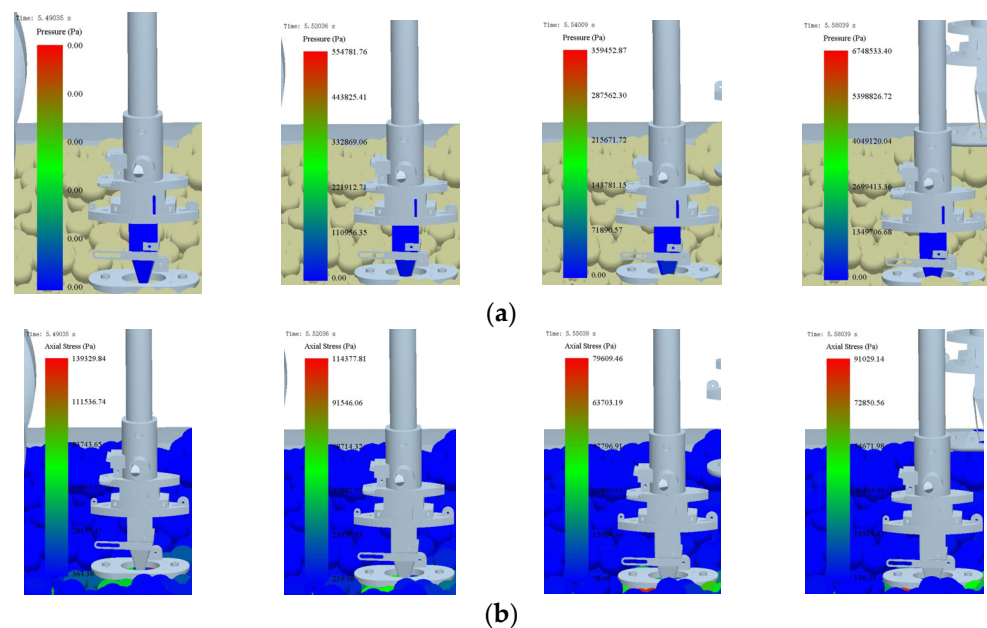


Figure 14. Entry soil stress change in the cavity seeder in sandy loam. (a) Duckbill stress. (b) Soil stress.

3.6. Effect of Maize Type on Seeding Performance

In addition to seeding performance, seeding discharge is affected by the movement of the direct hole sowing process. Among these, maize seed filling nest performance is the most significant [24,25]. The key to improving seeding quality is to improve seed filling performance [26]. There are several factors that influence the seed filling process, such as the maize shape, the shape of the hole, the rotation speed of the wheel that picks up seeds, and the motion of the cavity seeder. In particular, the maize shape and the movement of the cavity seeder have a greater influence on seed filling. As a first step, we examine the effect of seed shape on seeding performance. Figure 15 shows the trajectory of 50 maize seeds during seeding.

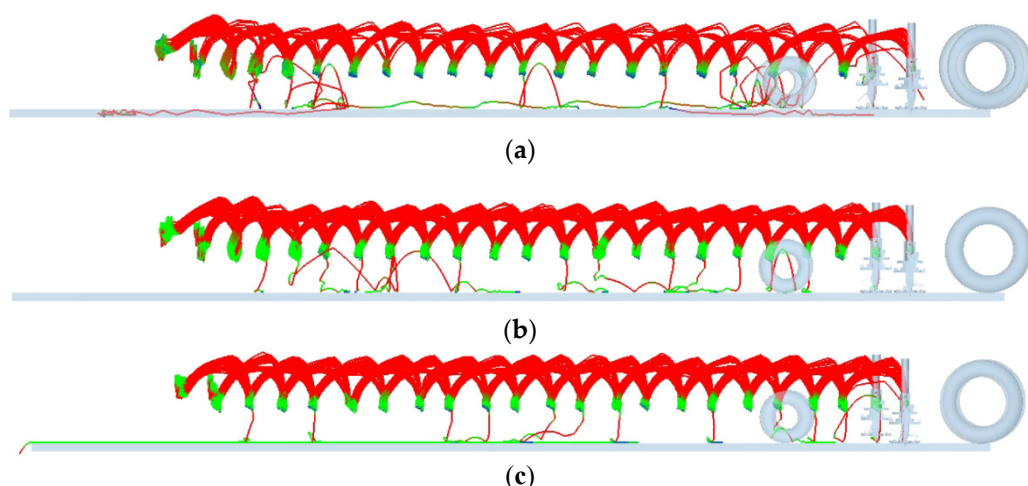


Figure 15. Effect of the maize shape on seeding performance. (a) Horse tooth. (b) Spherical cone. (c) Spherical. Note: the color of the maize seeds represents the movement speed, with red representing high speed, blue representing low speed, and green representing medium speed.

Figure 15 shows that the cavity seeder performed 22 seeding operations during the seeding process, excluding two seeding operations before the cavity seeder was stabilized. A total of 20 holes were seeded. As can be seen in Figure 15a, when sowing horse tooth shape maize, the number of qualified seeds was ten times for one seed and two times for two seeds. As a result, only 50% of seeds qualified for seeding. From Figure 15b, when seeding spherical cone shape maize, the number of seeds was 15 for one seed, and two for two seeds. Thus, 75% of seeds qualified for seeding. Figure 15c illustrates that when seeding spherical maize, 13 seeds qualified for one seed and zero for two seeds. The result was a seeding qualification rate of 65%. Figure 15 shows that the maize seed moves violently in the seed tube during filling, resulting in difficulty filling the seed. As a result, conventional hole seeders are of low quality. Additionally, the horse tooth shape maize seeds are not as well circulated as spherical cone and spherical seeds, resulting in poor seeding performance. It is necessary to mix the spherical seed with good fluidity into the horse tooth and spherical cone seed population with poor fluidity to improve the seed filling performance. Furthermore, it was found that the movement of the cavity seeder significantly affected seed filling. It is essential to improve and optimize the structure of the cavity seeder to avoid maize seeds accelerating in an upward and downward movement. Next, the motion of the horse tooth maize seeds are examined again in the cavity seeder.

3.7. Effect of Maize Seeds' Movement in Cavity Seeder on Seed Filling Performance

In response to the self-weight and forward speed compensation mechanism, the seed in the seed tube moves, as shown in Figure 16. Seeds remain in contact with the seed tube for too long during the filling process, resulting in a delay in the seed filling process. The maize has only 0.07 s to fill the shaped space during a cycle of 1.50 s to 1.57 s. Figure 16 illustrates the movement of horse tooth maize seeds inside a traditional structural seed tube.

From Figure 16, the maize seeds were primarily in contact with the inner wall of the seed tube during the entire process of filling the shaped slot. Even though the direction of movement of the maize seeds gradually changed from the vertical inner wall of the seed tube to the lower right side of the seed tube, the contact height between the maize and the inner wall was large, which did not facilitate seed filling. It was decided to add the inverted hook to the seed tube to separate the seed population while the seed above could slide into the inverted hook, as seen in Figure 17. A cavity seeder with the inverted hook was simulated by conducting a seed discharge simulation under the same condition. In addition, we observed the seed transport within the seed tube during 1.50–1.57 s. Figure 18 illustrates the movement of maize in the seed tube after the inverted hook was added.

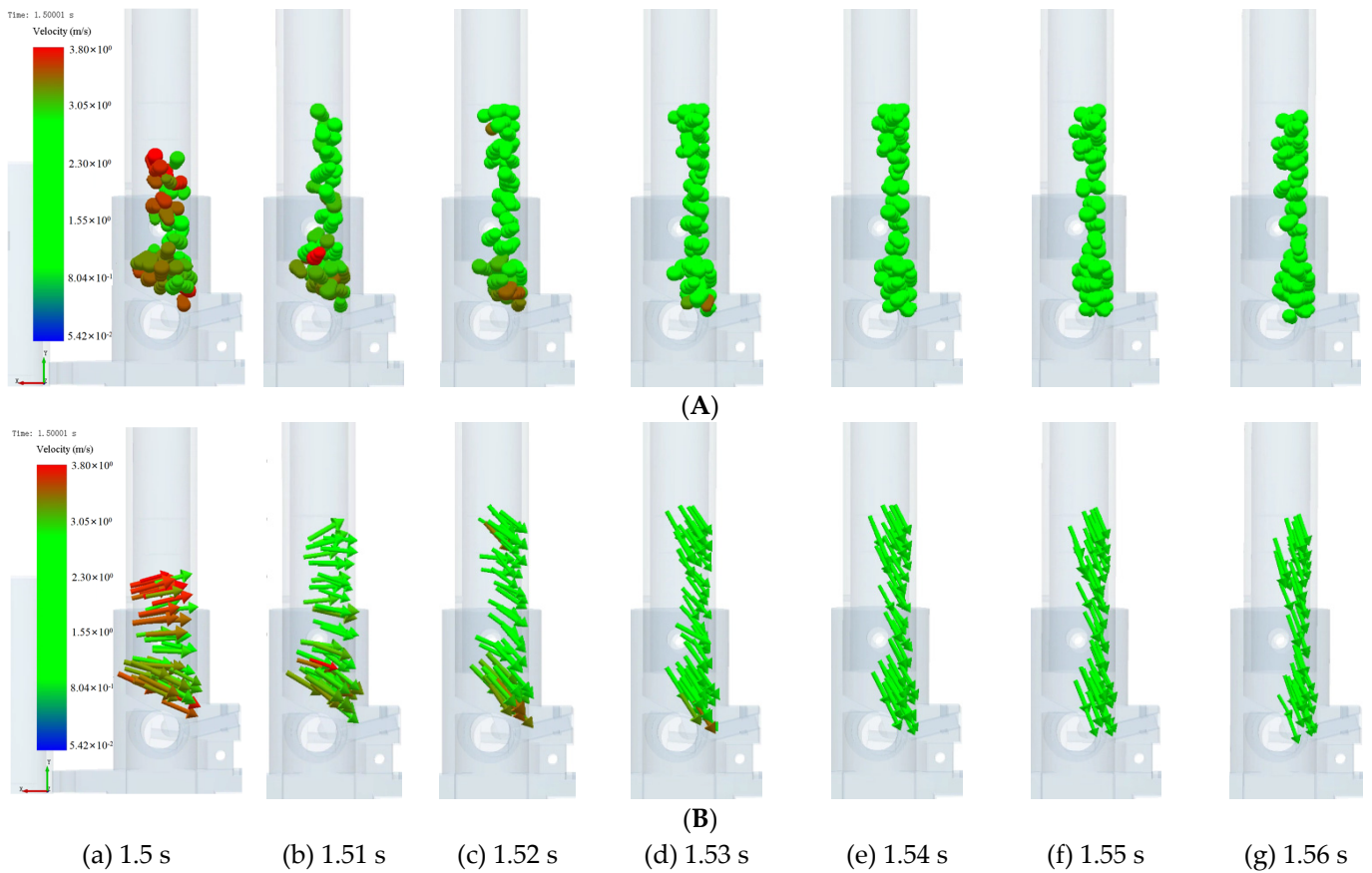


Figure 16. Movement process of horse tooth maize in traditional structural seed tube. (A) Default display. (B) Vector display.

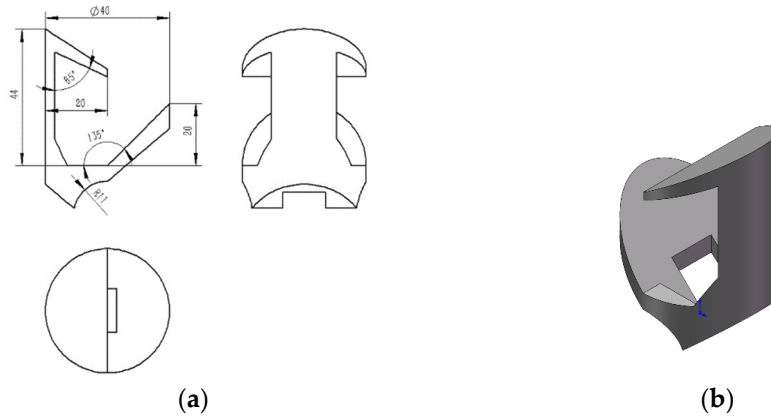


Figure 17. Shape and size of the inverted hook. (a) Two-dimensional view. (b) Three-dimensional view.

In Figure 18, we can see that the maize group was divided into upper and lower parts. Inverted hooks prevented maize seeds from flowing upward and backward. While seeds closer to the seed picking wheel did not move upwards, maize above could slide into the inverted curve. Nevertheless, the inverted hook did not effectively channel the slow-moving maize into the shaped groove of the seed picking wheel. Additionally, the left side structure of the inverted hook failed to function. A redesigned inverted hook for guiding seeds is illustrated in Figure 19, and the movement of the maize during seed filling in the seed tube with the inverted hook added for guiding seeds is illustrated in Figure 20.

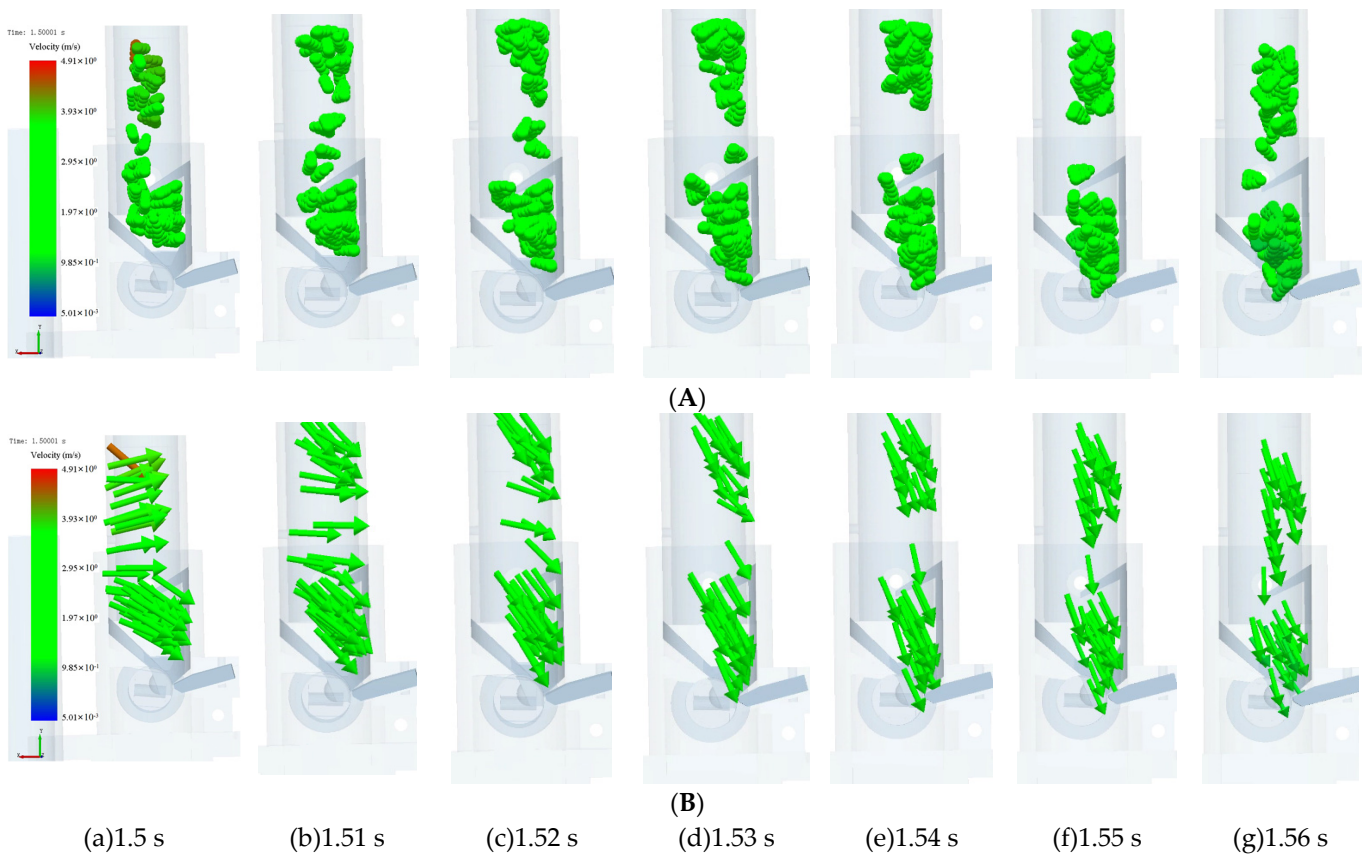


Figure 18. Movement process of maize in the seed tube with the added inverted hook. (A) Default display. (B) Vector display.

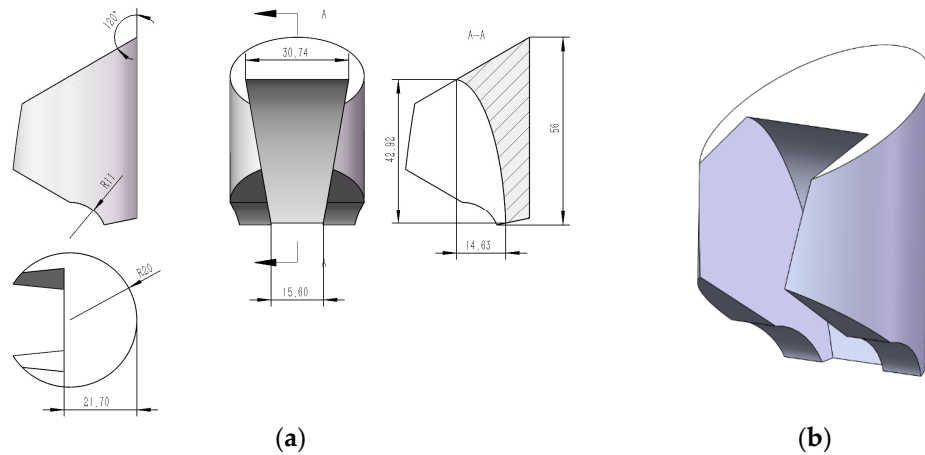


Figure 19. Shape and size of the inverted hook for guiding seeds. (a) Two-dimensional view. (b) Three-dimensional view.

A barbed hook is used to separate the maize in the seed tube into upper and lower populations. This is shown in Figure 20. The maize model above the inverted hook moved at a faster speed and had an uneven distribution. The maize below, on the other hand, moved uniformly and moved downward under the influence of the seed guide curve. Additionally, the guiding seed's cross-section was funnel-shaped, which enhanced the seed's filling speed. A few maize seeds can fit into the shaped groove of the seed picking wheel.

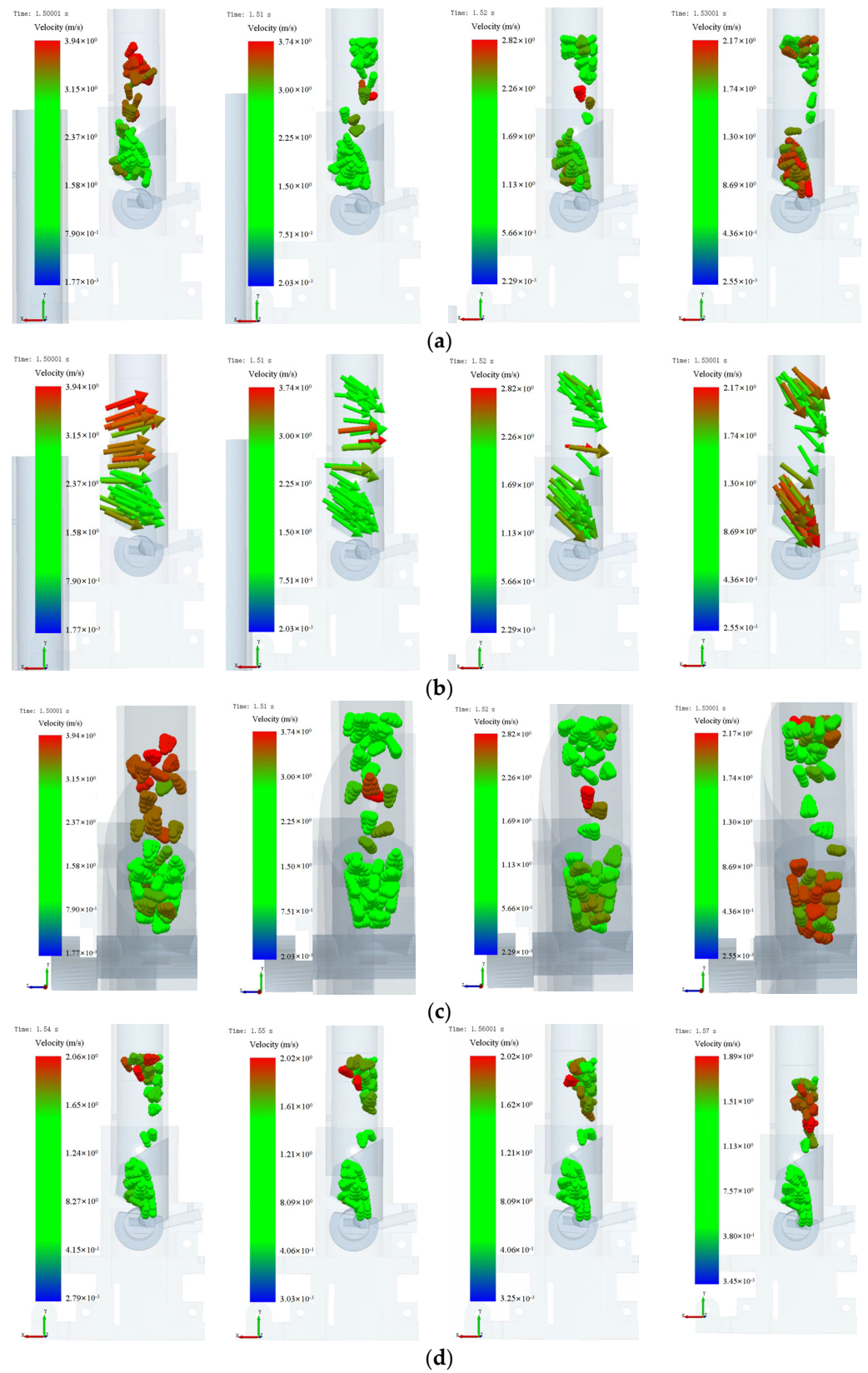


Figure 20. Cont.

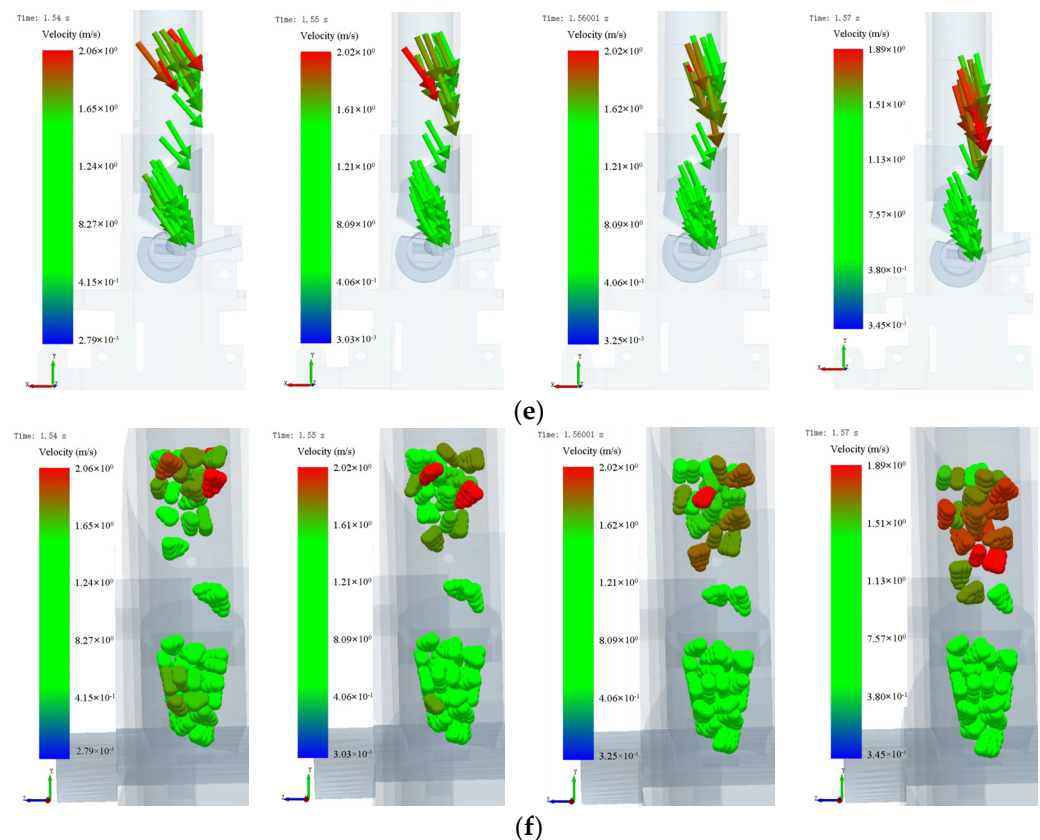


Figure 20. Movement process of maize in the seed tube with inverted hook added for guiding seed. (a) Default display of left view. (b) Vector display of left view. (c) Default display of front view. (d) Default display of left view. (e) Vector display of left view. (f) Default display of front view.

3.8. Simulation and Experimental Verification

From the above mechanism of interaction between maize seeds and cavity seeders, the effect of the seeder's movement on seed filling has been determined. It is necessary to verify the seeding performance under certain conditions of the shaped groove structure size in the next step. The diameter of the seed taking wheel was 22 mm, the included angle of the inner groove line was 110° , the width of the shaped groove was 11.79 mm, the height was 7.23 mm, the length was 14.67 mm, the opening angle was 15° , and the maximum diameter of the spherical hole was 5.5 mm. The shaped groove was made of high-precision 3D printing. The maize trajectory line during seeding is seen in Figure 21.

Based on simulation experiments, the single grain rate was 75%, the reseeding rate was 25%, and the missed seed rate was 0%. Additionally, a field trial was conducted at Taohe Tractor Factory, Lintao County, Gansu Province, China, on 11 March 2021. The experiment field was oriented east–west with pre-rotational plowing and leveling. It was a sandy loam soil. The soil water content ranged from 11.7% to 13.6%, and the average soil firmness measured with a TJSD-B firmness instrument at 45 mm depth was 137 kg/cm^2 (Beijing Jingcheng Huatai Instrument Co., Ltd., Beijing, China). The maize material was Longdan No. 339. The mass of one thousand grains was 371 g, and the average size of the seeds was 14.2 mm by 10.8 mm by 7.3 mm. We used a self-propelled cavity planter of type 2BZ-2 with vertical insertion at a forward speed of 0.5 m/s. The prototype is illustrated in Figure 22.

Before optimization, the best seeding result of the cavity planter was a seed number qualification of 75% and the empty cavity rate was 15%. After optimization, the results of the experiment indicated that the average seed number qualification and the empty cavity rate were 2% and 91.30%, respectively. Thus, the seed number qualification increased by 17.85%, and the empty cavity rate decreased by 86.67%. Meanwhile, it was found that the drive of the cavity planter operated smoothly during the experiment. Additionally,

the forward speed compensation mechanism compensated for the forward speed of the machine without jamming or slipping. Experimental results were in accordance with the design and agronomic requirements [27].

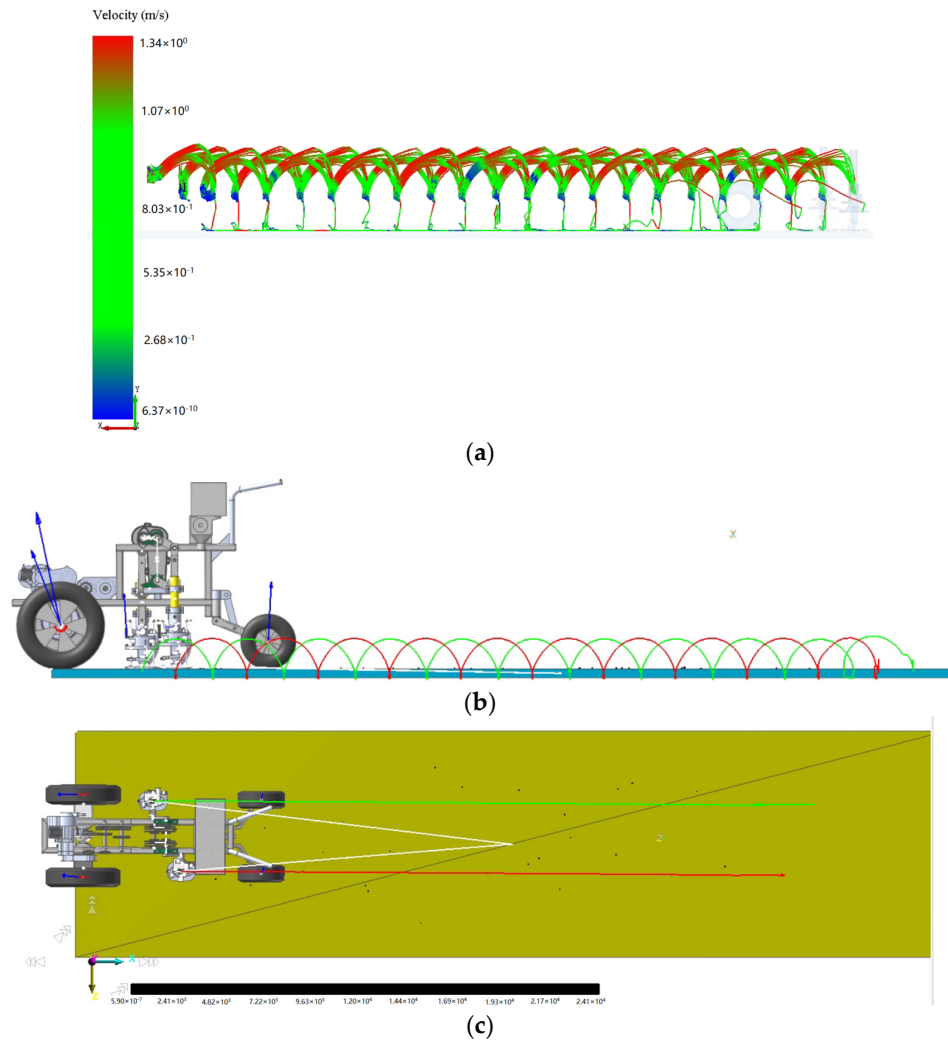


Figure 21. Simulation seeding performance of the cavity planter with vertical insertion. (a) Seed movement trajectory. (b) Trajectory of the cavity seeder (main view). (c) Trajectory of the cavity planter (top view).



Figure 22. 2BZ-2 type cavity planter with vertical insertion.

4. Conclusions

A simulation experiment was conducted using the DEM-MBD coupling method to study the soil disturbance by the cavity planter and the entry resistance. Additionally, the effect of maize shape and the cavity seeder motion on the seed number qualification and the empty cavity rate were studied in detail.

- (1) The results of the simulation show that soil type and water content influence the trajectory of the cavity seeder. The slip rate of the cavity planter on sandy loam is significantly higher than that of sandy soils at the same water content. As the speed of the traction wheel decreases, the trajectory of the cavity planter gradually moves backward. As the ratio decreases, the traction wheel speed increases, and the motion trajectory gradually advances. The cavity planter causes soil disturbance due to the different types of soil. It is recommended to moderately disturb the soil above the intersection of trajectory to enlarge the hole seeder and increase air circulation.
- (2) During the cavity seeding machine's operation, the resistance of the cavity planter basically increased with the rise in the water content of sandy soil and sandy loam. It was found that the entry resistance of sandy loam is significantly higher than that of sandy soil.
- (3) As the contact height between maize and the inner wall was large, this did not facilitate seed filling. After two improvements to the inverted hook structure in the seed tube, the maize model above the inverted hook moved at a faster speed and had an uneven distribution. The inverted hook for guiding seeds enhanced the seed filling. Finally, the seeds' seeding performance was verified under certain conditions of the shaped groove structure size with an angle of the inner groove line of 110° , the width of the shaped groove of 11.79 mm, the height of 7.23 mm, the length of 14.67 mm, the opening angle of 15° , and the maximum diameter of the spherical hole of 5.5 mm. The results showed that the empty cavity rate was 25%, and the seed number qualification was 75%, while the average empty cavity rate and the seed number qualification were 2.0% and 91.3%, respectively. The improved structure meets design and agronomic requirements.

Author Contributions: Conceptualization, W.Z.; methodology, L.S.; Recurdyn software, C.H.; formal analysis, G.R.; investigation, Z.W. and J.G. All authors have read and agreed to the published version of the manuscript.

Funding: This research was funded by the Excellent Ph.D. Dissertation of Gansu Agricultural University: YB2020003; The National Natural Science Foundation of China grant number: 52065004, 52165028.

Institutional Review Board Statement: Not applicable.

Informed Consent Statement: Not applicable.

Conflicts of Interest: The authors declare no conflict of interest.

References

1. Zhao, C.G. Current status of soil mechanics and discussion of some problems in its numerical analysis methods. *Geotechnical* **2006**, *27*, 1361–1364.
2. Cundall, P.A. A Computer Model for Simulating Progressive Large Scale Movement sin Blocky Rock Systems. *Proc. Int. Symp. Rock Fract.* **1971**, *1*, 8–11.
3. Fielke, J.M.; Ucgul, M.; Saunders, C. Discrete element modeling of soil-implement interaction considering soil plasticity, cohesion and adhesion. In *Proceedings of the 2013 ASABE Annual International Meeting, Kansas City, MO, USA, 21–24 July 2013*; American Society of Agricultural and Biological Engineers: St. Joseph, MI, USA, 2013.
4. Zhang, Z.G.; Xue, H.T.; Wang, Y.C.; Xie, K.T.; Deng, Y.X. Design and Experiment of Panax notoginseng Bionic Excavating Shovel Based on EDEM. *Trans. Chin. Soc. Agric. Mech.* **2022**, *53*, 100–111.
5. Ono, I.; Nakashima, H.; Shimizu, H.; Miyasaka, J.; Ohdoi, K. Investigation of elemental shape for 3D DEM modeling of interaction between soil and a narrow cutting tool. *J. Terramech.* **2013**, *50*, 265–276. [[CrossRef](#)]
6. Xu, Y.; Li, H.Y.; Huang, W.B. Three-dimensional discrete element modeling and simulation scheme planning for tillage soil mechanics. *Trans. Chin. Soc. Agric. Eng.* **2003**, *19*, 34–38.

7. Zhang, R.; Li, J.Q. Simulation on mechanical behavior of cohesive soil by distinct element method. *J. Terramech.* **2006**, *43*, 303–316. [[CrossRef](#)]
8. Zhang, R.; Li, J.Q.; Zhou, C.H.; Xu, S.C. Discrete element simulation of the effect of dozer surface morphology on soil dynamic behavior. *Trans. Chin. Soc. Agric. Eng.* **2007**, *23*, 13–19.
9. Zhang, X.R.; Zeng, W.Q.; Liu, J.X.; Wu, P.; Dong, X.H.; Hu, H.N. Design and Experiment of Lateritic Soil Inclined Handle Folding Wing Subsoiling Shovel Based on Discrete Element Method. *Trans. Chin. Soc. Agric. Mech.* **2022**, *53*, 40–49.
10. Markauskas, D.; Ramirez-Gomez, A.; Kacianauskas, R.; Zdancevicius, E. Maize grain shape approaches for DEM modeling. *Comput. Electron. Agric.* **2015**, *118*, 247–258. [[CrossRef](#)]
11. Chen, Z.R.; Yu, J.Q.; Xue, D.M.; Wang, Y.; Zhang, Q.; Ren, L.Q. An approach to and validation of maize-seed-assembly modeling based on the discrete element method. *Powder Technol.* **2018**, *328*, 167–183. [[CrossRef](#)]
12. Zhao, Y.C.; Teng, H.L.; Dong, W.T.; Zhao, X.L.; Jia, S.H.; Li, M.; Yuan, C. Application of ADAMS in the simulation design of agricultural machinery. *Agric. Net. Inform.* **2013**, 41–44. [[CrossRef](#)]
13. Zhang, C.Q. Application of virtual prototype technology on agricultural machinery design. *Agric. Equip. Tech.* **2021**, *47*, 48–49.
14. Hu, J.P.; Pan, J.; Chen, F.; Yue, R.C.; Yao, M.J.; Li, J. Simulation Optimization and Experiment of Finger-clamping Seedling Picking Claw Based on EDEM-RecurDyn. *Trans. Chin. Soc. Agric. Mech.* **2022**, *53*, 75–85, 301.
15. Zeng, Z.W.; Ma, X.; Cao, X.L.; Li, Z.H.; Wang, X.C. Current status and the prospect of application of discrete element method in agricultural engineering research. *Trans. Chin. Soc. Agric. Mech.* **2021**, *52*, 1–20.
16. Ji, L.L.; Xie, H.X.; Yang, H.G.; Wei, H.; Yan, J.C.; Shen, O. Simulation analysis of dry soil clearing device for potato based on EDEM_Recurdyn coupling. *Chin. J. Agric. Chem.* **2021**, *42*, 109–115.
17. Wang, X.L.; Hu, H.; Wang, Q.J.; Li, H.W.; He, J.; Chen, W.Z. Discrete element-based calibration method for soil model parameters. *Trans. Chin. Soc. Agric. Mech.* **2017**, *48*, 78–85.
18. Zhang, X.C.; Li, H.W.; Du, R.C.; Ma, S.C.; He, J.; Wang, Q.J.; Chen, W.Z.; Zheng, Z.Q.; Zhang, Z.Q. Influence of key structural parameters of sliding trencher on soil characteristics of seed beds. *Chin. Agric. Dig. Eng.* **2017**, *29*, 7–15, 32.
19. Shi, L.R.; Zhao, W.Y.; Sun, W. Discrete element-based particle contact model and parameter calibration for agricultural soils in dry areas of Northwest China. *Trans. Chin. Soc. Agric. Eng.* **2017**, *33*, 181–187.
20. Das, B.M. *Advanced Soil Mechanics*; Taylor & Francis: New York, NY, USA, 1997; pp. 14–20.
21. Li, X.F.; Liu, F.; Zhao, M.Q.; Zhang, T.; Li, F.L.; Zhang, Y. Determination of contact parameters between maize seed and seed row. *Agric. Mech. Res.* **2018**, *40*, 149–153.
22. Jia, G.X. *Design and Experiment of Chain Spoon Type Ginseng Precision Seeder*; Kunming University of Science and Technology: Kunming, China, 2021.
23. Zhang, R.; Han, T.L.; Ji, Q.L.; He, Y.; Li, J.Q. Research on the calibration method of sand and soil parameters in discrete element simulation. *Trans. Chin. Soc. Agric. Mech.* **2017**, *48*, 49–56.
24. Liu, J.; Cui, T.; Zhang, D.X.; Yang, L.; Gao, N.N.; Wang, B. Effect of seed grading treatment of maize on the sowing effect of pneumatic precision seeder. *Trans. Chin. Soc. Agric. Eng.* **2010**, *26*, 109–113.
25. Li, Y.F.; Yi, S.J.; Sun, Z.J.; Chen, T.; Ma, C.C.; Dong, J. Research on the seed filling performance of nest-groove type cereal hole sowing and seeding device. *Trans. Chin. Soc. Agric. Mech.* **2021**, *43*, 57–63.
26. Lai, Q.H.; Jia, G.X.; Su, W.; Hong, F.W.; Zhao, J.W. Design and experiment of convex packet shaped hole nest-groove wheel type ginseng precision seed row. *Trans. Chin. Soc. Agric. Mech.* **2020**, *51*, 60–71.
27. Wang, Y.X.; Liang, Z.J.; Zhang, D.X.; Cui, T.; Shi, S.; Li, K.H.; Yang, L. Calibration of interspecific contact parameters for discrete element-based maize seed particle model. *Trans. Chin. Soc. Agric. Eng.* **2016**, *32*, 36–42.

Article

The Synergistic Effects of Sonication and Microwave Processing on the Physicochemical Properties and Phytochemicals of Watermelon (*Citrullus lanatus*) Juice

Maham Navida¹, Muhammad Nadeem^{1,*}, Tahir Mahmood Qureshi², Rami Adel Pashameah³, Faiqa Malik¹, Aqsa Iqbal¹, Muhammad Sultan^{4,*}, Hala M. Abo-Dief⁵ and Abdullah K. Alanazi⁶

¹ Institute of Food Science and Nutrition, University of Sargodha, Sargodha 40100, Pakistan

² Department of Food Sciences, Cholistan University of Veterinary & Animal Sciences, Bahawalpur 63100, Pakistan

³ Department of Chemistry, Faculty of Applied Science, Umm Al-Qura University, Makkah 24230, Saudi Arabia

⁴ Department of Agricultural Engineering, Bahauddin Zakariya University, Multan 60800, Pakistan

⁵ Department of Science and Technology, University College-Ranyah, Taif University, Taif 21944, Saudi Arabia

⁶ Department of Chemistry, College of Science, Taif University, Taif 21944, Saudi Arabia

* Correspondence: nadeem.abdul@uos.edu.pk (M.N.); muhammadsultan@bzu.edu.pk (M.S.)

Abstract: In recent years, consumers have increasingly demanded nutritious, healthy, and fresh-like food products with high organoleptic quality. Watermelon is rich in water, which is 92% mandatory for body functioning, and contains several vitamins, amino acids, antioxidants, carotenoids, and lycopenes with various health benefits. The present study examines the combined effect of ultrasound (US) and microwave (MW) on the physico-chemical and phytochemicals of watermelon juice during storage (up to 120 days). Sonication was employed for different time intervals, particularly from 2 to 8 min at 20 kHz frequency and 525 W power, while microwave was applied at two different time intervals (1 min 50 s and 2 min) at 1000 W power and a frequency of 2450 MHz. The product was stored at 4 °C up to 120 days for further examination. Our results revealed that treatment T₅ (10 min ultrasound & 1 min 50 s microwave) manifested the maximum cloud value (3.00), acidity (0.15%), vitamin C content (202.67 mg/100 mL), phenolics (852.57 mgGAE/100 mL), flavonoids (1970.9 µg CE/100 mL), and total antioxidant activity (8650.3 µg equivalent of ascorbic acid/mL of juice). Sonication in combination with microwave proved to be an efficient technique for increasing the antioxidant potential of watermelon juice. Thus, US and MW treatments may be incorporated for enhancing the phytochemical release and shelf life of watermelon juice.

Keywords: watermelon; sonication; microwave; synergistic effects; quality characteristics

Citation: Navida, M.; Nadeem, M.; Qureshi, T.M.; Pashameah, R.A.; Malik, F.; Iqbal, A.; Sultan, M.; Abo-Dief, H.M.; Alanazi, A.K. The Synergistic Effects of Sonication and Microwave Processing on the Physicochemical Properties and Phytochemicals of Watermelon (*Citrullus lanatus*) Juice. *Agriculture* **2022**, *12*, 1434. <https://doi.org/10.3390/agriculture12091434>

Academic Editor: Sara Lombardo

Received: 1 August 2022

Accepted: 7 September 2022

Published: 9 September 2022

Publisher's Note: MDPI stays neutral with regard to jurisdictional claims in published maps and institutional affiliations.



Copyright: © 2022 by the authors. Licensee MDPI, Basel, Switzerland. This article is an open access article distributed under the terms and conditions of the Creative Commons Attribution (CC BY) license (<https://creativecommons.org/licenses/by/4.0/>).

1. Introduction

Fruits and vegetables are rich in antioxidants, minerals, and fiber and, due to their bioactive chemicals, contribute to disease protection [1]. Watermelon (*Citrulluslanatus*) belongs to the family Cucurbitaceae, has a connotation with cucumber, pumpkin, and gourds, and is therefore botanically considered as fruit. It is believed that watermelon was first cultivated in Egypt around 5000 years ago [2]. The consumption per capita of watermelon in Asia is practically three times that of the rest of the world [3,4]. This fruit contains on average 92% water [5–7] and, in desert regions, is treasured as a substitute source of water. It is also known as a fruit loaded with nutrients [3] but low in calories and devoid of cholesterol. It is a rich source of vitamin A, vitamin C, vitamin B (especially B1 and B6), amino acids, carotenoids, lycopenes, and minerals like magnesium and potassium [8,9]. Watermelon also contains phenolic compounds in abundance.

Nowadays people are demanding healthy and nutritious food [10]. Despite this, watermelon is sometimes a neglected fruit in agriculture-based developing countries. As a

result, most watermelon is wasted during the months of surplus production, particularly June and July. The food industry in various developing countries has not yet become involved in processing watermelon juice for marketing. Watermelons appear on the market for a very short span during the summer season and are usually used during hot days to quench thirst. In recent years, watermelon juice has gained widespread popularity due to its sensory, physical, and nutritional benefits [11]. As the temperature ($>30\text{ }^{\circ}\text{C}$) remains high in Punjab for nearly 8 months, it would be fitting for watermelon juice to be available for most of the time throughout the year.

Thermal processing of watermelon juice should not be carried out simply to avoid nutritional losses and changes in taste. Equally important is the fact that HMF is undesirable in food since it is harmful to human health, and its presence and concentration are also significant quality criteria for food processing [12,13]. Although thermal processing ensures safe food with longer stability, it leads to the loss of heat-sensitive nutrients. Similarly, chemical preservatives extend the shelf life of food but can contribute to a variety of health concerns in humans, including neurological dysfunction, asthma, hyperactivity, hypersensitivity, dermatitis, allergies, and gastrointestinal and respiratory difficulties [14].

Novel processing techniques, particularly ultrasound, ozone, high-pressure processing, and irradiations, are currently popular because they deliver food with improved functionalities, high quality, and a “fresh-like” physical appearance [15–17]. Such kinds of processed juice can be packed and then marketed. On the other hand, nonthermal technologies may result in incomplete inactivation of the indigenous enzymes of different foods and a further reduction in the microbial load with improved qualitative parameters [18,19]. The combined use of nonthermal processing techniques for fruits and vegetable juices has been shown to improve the abovementioned quality, safety, and shelf stability.

Less processing time, a lower energy requirement, and a higher output are among the benefits of ultrasound [20]. Moreover, sonication also results in a significant increase in vitamin C, phenolic compounds, total antioxidant capacity, and 2,2-diphenyl-1-picrylhydrazyl (DPPH) free radical scavenging activity, and a reduction in the microbial population [18,21]. Microwaves are described as electromagnetic waves with frequencies and wavelength ranging from 300 MHz to 300 GHz and 1 mm to 1 m, respectively [22]. Microwaving boosts the quality and safety of foods by inactivating microorganisms and enzymes in a short period of time, thereby preserving the foods’ nutritional value—e.g., the retention of vitamins—to a greater extent. The effect of microwave heating on the bioactive components and chemical contents (volatile organic compounds and fatty acids) of an orange juice–milk beverage was investigated. The microwave-treated orange juice–milk beverage demonstrated a lower browning index and greater amounts of ascorbic acid, carotenoids, total phenolics, and antioxidants, according to the study’s findings [23].

In our review of the literature, we found no indication that ultrasonic or microwave treatment of watermelon juice was conducted. Additionally, to avoid post-harvest losses and ensure year-round availability, watermelon juice was preserved using nonthermal processing technologies such as sonication and microwave. These techniques also serve as an alternative to chemical preservatives by mitigating their adverse effects. The application of novel technologies resulted in healthy juice with a long shelf life. Hence, based on the above-mentioned benefits of using novel processing techniques, this study aimed at evaluating the synergistic effects of microwave and ultrasonication treatments on the physicochemical characteristics, phytochemicals, and shelf stability of watermelon juice stored at a refrigerated temperature.

2. Materials and Methods

2.1. Collection of Raw Materials

Thirty fully ripened high-quality sugar baby watermelons were randomly obtained from the local fruit-and-vegetable market. Other raw materials such as glass bottles and potassium-meta bisulphite (KMS) were also procured from the market. To eliminate dirt and dust, the fruits were sorted and cleaned.

2.2. Chemicals and Reagents

All the chemicals used in the study were of analytical grade, were purchased from Sigma Aldrich (Seelze, Germany), and were available in the local market.

2.3. Preparation of the Watermelon Juice

The peel, seeds, matured portions, and stem of the watermelon were removed. The peeled watermelons were put into an electric blender (MJ-M176P, Panasonic Manufacturing, Berhad, Malaysia) to extract the juice, then the juice was further strained through a double layer of muslin cloth to remove the fiber content and seeds. The juice was then poured into sterilized glass bottles and capped tightly as per reported method [10]. The juice was stored at a refrigerated temperature (4 °C) for further analysis.

2.4. Ultrasound Treatment

The prepared juice was subjected to US treatment using an ultrasound processor type UP400S (Hielscher Ultrasonics GmbH Hielscher, Oderstr. 53. D-14513 Teltow, Germany) with a probe of 0.5 inch and a power output of 400 W (see treatment plan in Table 1). Sonication for a working juice sample (200 mL confined in a 500 mL beaker) was performed at 20 kHz frequency, 525 W power, and 70% amplitude level by keeping the sample probe at 25 mm [18,21,24]. The juice samples were given sonication treatment for 2, 4, 6, 8, and 10 min. Using an HI 9063 thermocouple (Hanna Instruments Ltd., Leighton Buzzard, UK), the ultrasonic intensity was measured to be 2 W/cm². By allowing cold water to flow through a jacketed vessel, a constant temperature of 20 °C was maintained, and all the procedures were carried out in the dark to prevent light from interfering with the samples. The ultrasonic parameters were established by revising prior studies and conducting preliminary experiments [25,26]. The US treatment was performed three times to make triplicate samples for each treatment.

Table 1. Treatment plan for the watermelon juice.

Treatment	Use of Preservative, Ultrasonication and Microwave	Frequency	Power (W)	Amplitude (%)
T ₀₋	-	-	-	-
T ₀₊	0.1% KMS	-	-	-
T ₁	2 min Ultrasound & 1 min 50 s Microwave	Ultrasonication 20 kHz Microwave 2450 MHz	Ultrasonication: 525 W Microwave: 1000 W	70%
T ₂	4 min Ultrasound & 1 min 50 s Microwave	Ultrasonication: 20 kHz Microwave: 2450 MHz	Ultrasonication: 525 W Microwave: 1000 W	70%
T ₃	6 min Ultrasound & 1 min 50 s Microwave	Ultrasonication: 20 kHz Microwave: 2450 MHz	Ultrasonication: 525 W Microwave: 1000 W	70%
T ₄	8 min Ultrasound & 1 min 50 s Microwave	Ultrasonication: 20 kHz Microwave: 2450 MHz	Ultrasonication: 525 W Microwave: 1000 W	70%
T ₅	10 min Ultrasound & 1 min 50 s Microwave	Ultrasonication: 20 kHz Microwave: 2450 MHz	Ultrasonication: 525 W Microwave: 1000 W	70%

2.5. Microwave Treatment

After sonication, the juice was treated with a domestic microwave processor (Model No: DW-131A, Dawlance, Lahore, Pakistan) operating at 1000 W power and a frequency of 2450 MHz at two different time intervals (1 min 50 s and 2 min) (see the treatment plan in Table 1). In sterile beakers, samples of watermelon juice (200 mL) were microwaved (500 mL). Immediately after pasteurization, the product was transferred and packaged in pre-sterilized 250 mL plastic bottles that were immersed in ice-cold water to prevent shrinking of the bottles and to rapidly cool the product, as the temperature after 1 min and 50 s of pasteurization is 90 ± 2 °C. The juice was stored at 4 ± 2 °C [18,27,28].

2.6. Chemical Preservation

To compare the juice with the control and other treatments, KMS was introduced in treatment T₀₊ [29]. The treatment plan is described in Table 1.

2.7. Storage

The sonicated and microwaved juice was stored at a refrigerated temperature (4 °C) in pre-sterilized glass bottles for further analysis.

2.8. Physicochemical Analysis

The total soluble solids (TSS measured in °B) were determined using a digital refractometer (Model HI-96801 Hanna, Germany), and the pH of the watermelon juice was observed using a pH meter (Lutron PH-209B, Lutron Electronic Co., Ltd., Tokyo, Japan) by following the method 981.12 of AOAC [17,19]. The acidity of the samples was evaluated using the standard titration technique through the method 942.15 of AOAC [30].

2.9. Determination of Vitamin C (Ascorbic Acid)

The dye (2, 6-dichlorophenol-indophenol (C₁₂H₆Cl₂NNaO₂·2H₂O)) titration reduction method 967.21 was used for the determination of ascorbic acid content [30]. The acquired results are expressed as milligrams of ascorbic acid per 100 mL of the sample, and the calculation was performed as described below:

$$\text{Ascorbic acid mg/100 mL} = \frac{(\text{titer} \times \text{dye factor} \times \text{concentration} \times 100)}{(\text{extract aliquot used for estimation} \times \text{volume of sample use for estimation})}$$

2.10. Determination of Cloud Value

The cloud value of the samples was evaluated through the procedure reported by Versteeg et al. [31]. Centrifugation of all the samples was carried out at 5000 rpm for 20 min, and later absorbance was taken on a spectrophotometer (HettichRotofix32 A, Tuttlingen, Germany) at a wavelength of 660 nm.

2.11. Determination of Total Flavonoids

The total flavonoids (TF) of the watermelon juice were determined according to Saeeduddin et al. [32]. 1.5 mL aliquot of diluted watermelon juice was added into a 75 µL of sodium nitrite (5%) solution. After vortexing for 1 min, 150 µL of an aluminum chloride (10%) solution was added. Then after adding 0.5 mL of 1 M NaOH, absorbance was measured at 510 nm using a spectrophotometer (Halo DB-20, UV-VIS double beam, Diepoldsau, Switzerland). The results were calculated in µg of catechin equivalent (CE) per 100 mL of juice.

2.12. Determination of Total Phenolic Contents

The total phenolics were determined by using the Folin–Ciocalteu reagent method with some modifications [28]. 1 mL aliquot of diluted watermelon juice was mixed with 1 mL of the Folin–Ciocalteu reagent (10%). After vortexed, 2 mL of sodium carbonate (20%) solution was added into the mixture. After incubation for 60 min at 30 °C in the dark,

the absorbance was measured at 760 nm using a spectrophotometer (Halo DB-20, UV-VIS double beam). The results were calculated in mg gallic acid equivalent (GAE) per 100 mL of juice.

2.13. Determination of Total Antioxidant Activity

The total antioxidant activity of the watermelon juice was determined using the method described by Prieto et al. [33]. 1 mL of diluted watermelon juice was mixed with 4 mL of reagent (0.6 M sulphuric acid, 28 M sodium phosphate, and 4 M ammonium molybdate) solution. After incubating the mixture (95 min at 90 °C), the absorbance was measured at 695 nm using a spectrophotometer. The results were calculated in µg equivalent of ascorbic acid per 100 mL of juice.

2.14. Determination of Viscosity

The viscosity of the juice samples was monitored according to the method described by Nindo et al. [34] by using a rotatory viscometer (Rheomat RM 100, Lamy Rheology, Champagne-au-Mont-d'Or, France) equipped with a precision cylindrical spindle (R-2) rotating adapter. The viscosity of the juices at various dilutions was measured using a concentric cylinder geometry (stator inner radius 15 mm, rotor outer radius 14 mm, cylinder immersed height 42 mm, and gap 5920 µm). Approximately 19 mL of juice was added to the rheometer cup. The RM100 features a Peltier plate for precise temperature regulation within the gap.

2.15. Statistical Analysis

Statistical analysis was performed through Minitab statistical software version 16 (Minitab Inc., State College, PA, USA), using the two-way ANOVA and Tukey's tests for pairwise comparison in analysis of variance at the level of $p < 0.05$ by Steel et al. [35]

3. Results and Discussion

3.1. Total Soluble Solids of Watermelon Juice

Variations in the TSS of the watermelon juice (Table 2) indicated highly significant differences among treatments during storage conditions. The mean values of the TSS of the watermelon juice during storage indicated that the TSS of all the treated samples increased significantly during the storage period up to 120 days. The observed increase in the TSS throughout storage was from 7.87 to 12.50 °B. The highest TSS value was found in T₁ and T₂ (10.03 °B and 10.00 °B), while the lowest value was observed in T₀₋ (7.87 °B) at the start of the study. The TSS of treatment T₀₊ (chemically preserved juice) increased up to 90 days and then decreased. Treatment T1 and T3 also showed an increasing trend in TSS during storage. This increase in TSS during storage might be attributed to polysaccharide breakdown into monosaccharides and oligosaccharides. In a study of carrot and grapes juice blend reported by Nadeem et al. [18], a significant ($p < 0.05$) increment (from 12.5 to 13.02 °B) in the TSS was also observed due to sonication. Similarly, in another study, it was also reported that the TSS of thermo-sonicated pear juice increased with the increase in the storage period [32]. The same findings were also reported by Walkling-Ribeiro et al. [36]. They claimed that different processing methods increased the amount of TSS in various fruit juices.

Table 2. pH, acidity, total soluble solids (TSS measured in °B), cloud value, and vitamin C (mg/100 mL of juice) of the watermelon juice during storage.

Treatments	Days	pH	Acidity	TSS	Cloud Value	Vitamin C
T ₀₋	0	5.90 ± 0.02 ^b	0.06 ± 0.04 ^o	7.87 ± 0.11 ^j	1.10 ± 0.01 ^{i-k}	175.0 ± 21.20 ^{a-c}
	30	4.45 ± 0.05 ^{kl}	0.13 ± 0.04 ^{g-l}	7.87 ± 0.32 ^j	1.14 ± 0.04 ^{i-k}	100.0 ± 10.10 ^{f-l}
	60	4.55 ± 0.01 ^{jk}	0.16 ± 0.04 ^{c-f}	8.73 ± 0.15 ^{f-j}	1.22 ± 0.02 ^{h-j}	119.00 ± 2.09 ^{d-i}
	90	4.29 ± 0.005 ^{l-n}	0.19 ± 0.04 ^{ab}	9.97 ± 0.05 ^{b-d}	1.20 ± 0.01 ^{h-j}	50.67 ± 7.36 ^l
	120	3.95 ± 0.02 ^p	0.19 ± 0.01 ^a	7.90 ± 0.10 ^j	0.76 ± 0.06 ^k	51.67 ± 6.01 ^l
T ₀₊	0	6.27 ± 0.27 ^a	0.08 ± 0.04 ^{no}	8.07 ± 0.15 ^{ij}	1.19 ± 0.02 ^{ij}	163.33 ± 20.21 ^{a-d}
	30	5.81 ± 0.02 ^{bc}	0.14 ± 0.01 ^{e-i}	8.47 ± 0.31 ^{h-j}	1.17 ± 0.05 ^{i-k}	124.67 ± 13.47 ^{c-i}
	60	5.29 ± 0.01 ^{de}	0.11 ± 0.08 ^{lm}	9.07 ± 0.05 ^{d-i}	1.42 ± 0.02 ^{g-i}	113.33 ± 23.09 ^{d-j}
	90	5.71 ± 0.03 ^{bc}	0.15 ± 0.08 ^{h-m}	10.03 ± 0.05 ^{b-d}	1.28 ± 0.05 ^{hi}	49.67 ± 8.58 ^l
	120	4.09 ± 0.03 ^{n-p}	0.17 ± 0.04 ^{g-l}	8.03 ± 0.05 ^{ij}	0.85 ± 0.07 ^{jk}	54.00 ± 4.17 ^{kl}
T ₁	0	5.81 ± 0.04 ^{bc}	0.12 ± 0.07 ^{g-l}	10.03 ± 0.06 ^{b-d}	2.63 ± 0.04 ^{ab}	157.00 ± 17.53 ^{a-e}
	30	5.21 ± 0.01 ^{ef}	0.15 ± 0.01 ^{d-g}	9.47 ± 0.46 ^{b-h}	1.87 ± 0.13 ^{ef}	128.00 ± 11.68 ^{c-h}
	60	5.02 ± 0.03 ^{f-h}	0.12 ± 0.07 ^{g-l}	9.60 ± 0.10 ^{b-f}	1.36 ± 0.03 ^{g-i}	111.33 ± 9.62 ^{d-j}
	90	5.07 ± 0.04 ^{fg}	0.16 ± 0.01 ^{c-f}	8.85 ± 0.25 ^{e-j}	1.33 ± 0.18 ^{hi}	74.00 ± 3.89 ^{i-l}
	120	5.05 ± 0.03 ^d	0.16 ± 0.07 ^{c-f}	12.50 ± 0.72 ^a	1.13 ± 0.01 ^{i-k}	78.67 ± 8.77 ^{h-l}
T ₂	0	6.12 ± 0.02 ^a	0.11 ± 0.07 ^{k-m}	10.00 ± 0.10 ^{b-d}	2.45 ± 0.01 ^{bc}	182.67 ± 47.15 ^{ab}
	30	5.31 ± 0.01 ^{de}	0.12 ± 0.07 ^{k-m}	10.23 ± 0.42 ^{bc}	2.64 ± 0.36 ^{ab}	157.00 ± 17.54 ^{a-e}
	60	4.82 ± 0.02 ^{hi}	0.09 ± 0.03 ^{mn}	9.60 ± 0.20 ^{b-f}	1.48 ± 0.19 ^{g-i}	98.33 ± 19.51 ^{f-l}
	90	4.73 ± 0.06 ^{ij}	0.14 ± 0.01 ^{f-j}	9.80 ± 0.10 ^{b-e}	1.45 ± 0.25 ^{g-i}	93.67 ± 6.25 ^{f-l}
	120	4.12 ± 0.03 ^{n-p}	0.16 ± 0.01 ^{c-f}	9.77 ± 0.94 ^{b-f}	1.59 ± 0.01 ^{f-h}	64.00 ± 5.84 ^{j-l}
T ₃	0	5.68 ± 0.01 ^c	0.12 ± 0.07 ^{i-m}	8.80 ± 0.34 ^{e-j}	3.00 ± 0.01 ^a	157.00 ± 17.53 ^{a-e}
	30	5.70 ± 0.20 ^{bc}	0.10 ± 0.07 ^{lm}	8.80 ± 0.62 ^{e-j}	2.90 ± 0.10 ^a	157.00 ± 17.54 ^{a-e}
	60	4.59 ± 0.01 ^{jk}	0.10 ± 0.07 ^{lm}	8.55 ± 0.15 ^{g-j}	1.39 ± 1.51 ^{g-i}	107.33 ± 16.84 ^{e-k}
	90	4.33 ± 0.04 ^{k-m}	0.16 ± 0.02 ^{c-f}	9.05 ± 0.05 ^{d-i}	1.37 ± 0.09 ^{g-i}	88.67 ± 11.14 ^{g-l}
	120	4.23 ± 0.02 ^{m-o}	0.17 ± 0.07 ^{b-e}	10.43 ± 0.30 ^b	1.37 ± 0.01 ^{hi}	78.00 ± 9.63 ^{h-l}
T ₄	0	5.69 ± 0.01 ^{bc}	0.14 ± 0.07 ^{f-k}	9.53 ± 0.40 ^{b-g}	2.27 ± 0.01 ^{b-d}	144.00 ± 29.36 ^{b-f}
	30	5.89 ± 0.03 ^{bc}	0.11 ± 0.04 ^{j-m}	9.63 ± 0.55 ^{b-f}	1.95 ± 0.05 ^{d-f}	140.00 ± 14.10 ^{b-g}
	60	4.72 ± 0.01 ^{ij}	0.11 ± 0.03 ^{j-m}	9.75 ± 0.05 ^{b-f}	2.09 ± 0.04 ^{c-e}	119.00 ± 20.09 ^{d-i}
	90	4.39 ± 0.01 ^{k-m}	0.17 ± 0.01 ^{b-d}	9.25 ± 0.05 ^{c-h}	1.97 ± 0.18 ^{d-f}	113.33 ± 23.09 ^{d-j}
	120	4.07 ± 0.02 ^{op}	0.18 ± 0.01 ^{a-c}	9.23 ± 0.25 ^{c-h}	1.72 ± 0.02 ^{e-g}	82.67 ± 4.86 ^{h-l}
T ₅	0	5.86 ± 0.04 ^{bc}	0.15 ± 0.01 ^{d-h}	9.56 ± 0.11 ^{b-g}	3.05 ± 0.01 ^a	202.67 ± 29.27 ^a
	30	4.40 ± 0.27 ^{k-m}	0.08 ± 0.04 ^{no}	9.60 ± 0.36 ^{b-f}	3.00 ± 0.01 ^a	157.00 ± 17.54 ^{a-e}
	60	4.12 ± 0.07 ^{n-p}	0.17 ± 0.07 ^{b-e}	8.80 ± 0.20 ^{e-j}	2.97 ± 0.01 ^a	140.00 ± 15.21 ^{b-g}
	90	4.04 ± 0.05 ^{op}	0.18 ± 0.02 ^{a-c}	8.15 ± 0.05 ^{ij}	1.94 ± 0.06 ^{d-f}	111.33 ± 9.62 ^{d-j}
	120	4.02 ± 0.04 ^{g-i}	0.19 ± 0.07 ^{ab}	8.73 ± 0.25 ^{f-j}	2.05 ± 0.01 ^{de}	93.67 ± 6.25 ^{f-l}

T₀₋ = control (watermelon juice with no preservative or treatment); T₀₊ = control (watermelon juice preserved with KMS); T₁ = 2 min ultrasound & 2 min microwave; T₂ = 4 min ultrasound & 1 min 50 s microwave; T₃ = 6 min ultrasound & 1 min 50 s microwave; T₄ = 8 min ultrasound & 1 min 50 s microwave; T₅ = 10 min ultrasound & 1 min 50 s. Values exhibiting similar alphabets (superscripts) are statistically non-significant.

3.2. Titratable Acidity of Watermelon Juice

The mean acidity values during storage of all the treated samples increased significantly from 0 to 120 days (Table 2). The highest acidity values were observed in T₅ (0.15%) and T₄ (0.14%), while T₀₋ (0.06%) showed the lowest value without storage. The maximum acidity value was obtained at 120 days in T₀₋ and in T₅ and the minimum value (0.16%) after 120 days in treatment T₁ and T₂, respectively. The overall increase in acidity was observed in T₀₋ from 0.06–0.19% in 120 days. With the increase in ultrasonication time, the acidity values increased, because ultrasound induction generates heat. The results were inconsistent with the findings of Nadeem et al. [18], who reported an increasing trend in the acidity of phalsa juice treated through the sonication technique. Malik et al. [28] reported an increase in the acidity of microwave-treated lemon cordial after storage and

hypothesized that the increase in acidity is due to increased production of organic acids during anaerobic fermentation. Another study stated that the acidity of pineapple juice increased during storage, which could be attributed to fermentation and spoilage leading to conversion of sugars into acids, carbon dioxide, or alcohol [37].

3.3. pH of Watermelon Juice

The mean pH values of the watermelon juice indicated that the pH of all the treated samples dropped significantly during storage from 0 to 120 days. The drop in pH is linked with the rise in acidity, which could assist in the shelf-life extension of watermelon juice [21]. The highest pH values were found in T₂ (6.12), followed by T₀₋ (5.90), and the least value was detected in T₀₋ (5.68) at start of the storage period. The maximum and minimum pH values were obtained at 0 day (6.12) and 120 days (3.95), respectively, as shown in Table 2. It has been reported that the overall reduction in pH was from 5.68 to 3.95 in the microwave-treated lemon cordial [28]. They asserted that the acidic compounds, such as lactic acid and acetic acid, accumulated because of microbial activity during the natural fermentation process, which was the primary reason for the decrease in pH values. Due to conceivable biochemical reactions, ethanol is made during storage, and this is the principal reason for pH degeneration. In liquids, the application of high-power sonication creates free radicals such as H⁺ and OH⁻. These radicals are formed by the decomposition of water inside the cavities [38]. The results concerning the increase in pH are consistent with the previous results of ultrasonicated carrot blends [39,40].

3.4. Cloud Value of Watermelon Juice

Cloud value plays an important role in developing the color and flavor of fruit juices. The cloud stability of fruit juices is a pictorial quality parameter for consumers [41]. The mean cloud value of all the treated samples varied significantly during storage from 0 to 120 days, as shown in Table 2. The highest cloud value was detected in T₃ and T₅ (3.00), and the lowest was detected in T₀₋ (1.10), and T₀₊ (1.19). The maximum (3.00) and minimum mean cloud values (0.76) were obtained at 0 day and 120 days, respectively. Cloud values considerably increased ($p < 0.05$) in grapefruit juice due to sonication treatments. The increased cloud value may be due to the high-pressure gradient formed by cavitation during sonication treatment, which results in the colloidal dissolution, dispersion, and degradation of larger molecules to smaller ones, thus making the juice properly homogenized and more consistent [42].

3.5. Vitamin C Content (Ascorbic Acid) of Watermelon Juice

The mean values of the vitamin C content of the watermelon juice indicated that vitamin C, of all treated samples, increased significantly (Table 2). The highest vitamin C value was found in T₅ (202.67 mg/100 mL of juice) and the least in T₄ (140.00 mg/100 mL of juice). During storage, an overall decrease in vitamin C content was observed. The maximum decrease was observed in T₀₋ (175.00 to 51.67 mg/100 mL). Ascorbic acid is a form of vitamin C [43]. In grapefruit juice, sonication treatment resulted in a significant increase ($p < 0.05$) in ascorbic acid content. Samples that were sonicated for 90 and 60 min showed higher values of ascorbic acid as compared to the control sample and to a sample sonicated for 30 min. Sonication is directly responsible for the rise in ascorbic acid in grapefruit juice; it depletes the dissolved oxygen in the juice through cavitation without the addition of heat [42]. In comparison to the control, samples treated with sonication and microwave retained more ascorbic acid. The retention of ascorbic acid during sonication treatment is most likely due to the removal of the dissolved oxygen required for ascorbic acid content breakdown during storage [43].

3.6. Total Phenolic Content of the Watermelon Juice

The mean values of the TP of the watermelon juice indicated that the phenolic content of all the treated samples decreased significantly during storage from 0 to 120 days (Figure 1). The highest TP value was found in T₅ (852.57 mg of GAE/100 mL of juice), and

the lowest value in T_{0-} (143.10 mg of GAE/100 mL of juice) followed by T_{0+} (158.60 mg of GAE/100 mL of juice), correspondingly. The plant's secondary metabolites, such as phenolic compounds, are responsible for color and flavor improvement in fruit juices. Higher concentration of phenolics could be attributed to the inactivation of polyphenol oxidase enzymes, which employ these chemicals as a substrate and cause their breakdown during storage. The effect of sonication on the phenolic contents of apple juice was studied by Abid et al. [41]. Fruit juice samples were sonicated for 30, 60, and 90 min in a bath-type sonicator. The TP contents increased as the sonication time was extended but decreased as the storage period progressed. The impact of sonication on the phenolic content of carrot juice was studied by Jabbar et al. [24]. The carrot juice was given sonication and heat treatment at various temperatures. The phenolic content of the carrot juice samples was found to be considerably higher in the sonicated samples than in the control samples.

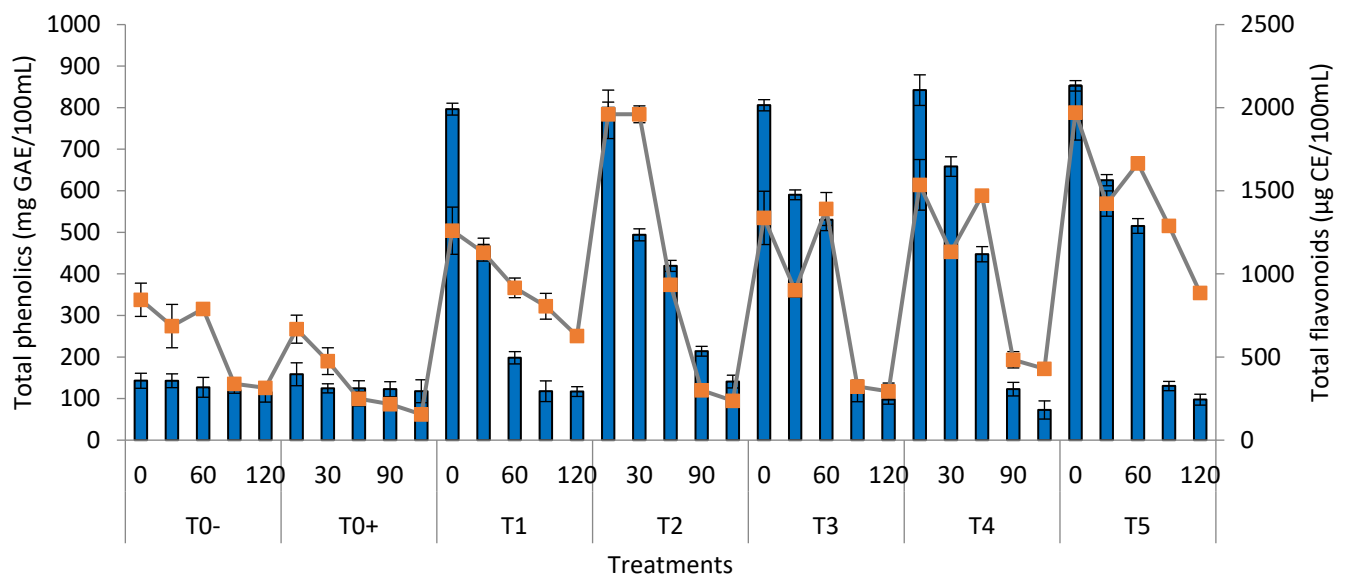


Figure 1. Phytochemicals (total phenolics and flavonoids) of watermelon juice (T_{0-} = control (watermelon juice with no preservative and treatment); T_{0+} = control (watermelon juice preserved with KMS); T_1 = 2 min ultrasound & 2 min microwave; T_2 = 4 min ultrasound & 1 min 50 s microwave; T_3 = 6 min ultrasound & 1 min 50 s microwave; T_4 = 8 min ultrasound & 1 min 50 s microwave; T_5 = 10 min ultrasound & 1 min 50 s) during storage.

3.7. Total Flavonoid Contents of the Watermelon Juice

The mean values of the TF of the watermelon juice indicated that the flavonoid content of all treated samples decreased significantly during storage from 0 to 120 days (Figure 1). The overall decline in the TF content during storage was reported to be from 1960.2 to 236.3 $\mu\text{g CE}/100\text{ mL}$ of juice. The highest TF value was found in T_5 (1970.9 $\mu\text{g CE}/100\text{ mL}$ of juice), followed by T_2 (1960.2 $\mu\text{g CE}/100\text{ mL}$ of juice) and T_{0+} (1668.4 $\mu\text{g CE}/100\text{ mL}$ of juice), whereas the lowest value was found in T_{0-} (1260.3 $\mu\text{g CE}/100\text{ mL}$ of juice). A higher concentration of flavonoids could be attributed to the inactivation of PPO enzymes, which employ these chemicals as a substrate and cause their breakdown during storage. The effect of sonication on the flavonoid concentration of apple juice was studied by Abid et al. [41]. They sonicated the apple juice samples for 30, 60, and 90 min. It was observed that as the sonication period was extended, the TF content increased. When compared to non-sonicated juice samples, the TF concentration increased from 486 $\mu\text{g GAE}/\text{g}$ to 600 $\mu\text{g GAE}/\text{g}$. Malik et al. [28] asserted that the TF content of the microwave-treated lemon cordial decreased during storage and that the increased production of free radicals was responsible for the decrease in flavonoid content. The effect of thermo-sonication on the phytochemical characteristics of carrot juice was studied by Jabbar et al. [24]. In comparison to the control, the juice was treated to ultrasonic processing for 30 and 60 min at 20 °C. The total flavonoid

content increased when the temperature increased from 30 to 60 °C. The flavonoid content of the juice samples increased from 344.76 ± 0.05 (catechin equivalent lg/g) to 544.56 ± 0.07 (catechin equivalent lg/g).

3.8. Total Antioxidant Activity of the Watermelon Juice

The mean values of the total antioxidant activity (TAC) of the watermelon juice indicated that antioxidants of all the treated samples varied significantly during storage from 0 to 120 days (Figure 2). The overall reduction in total antioxidants in the watermelon juice during storage was from 6139.2 to 229.5 μg , the equivalent of ascorbic acid/mL of juice in the control treatment. The highest TAC value was found in T_5 (8650.3) and T_4 (7106.3 μg equivalent of ascorbic acid/mL of juice), and the least value in T_{0-} (6139.2 μg equivalent of ascorbic acid/mL of juice). Depreciation was observed in 120 days of storage. The increased TAC in the treated juice may be attributed to the fact that a combined ultrasound and microwave treatment inhibits the enzymes responsible for triggering oxidation. In the study by Abid et al. [41], the apple juice samples were sonicated at different temperatures, such as 30, 60, and 90 min. During storage, the TAC of the sonicated juice samples decreased. Antioxidant activity increased from 324.57 mg ascorbic acid/g to 363.05 mg ascorbic acid/g in the sonicated samples. The increase in the polyphenolic and ascorbic content of the apple juice was responsible for the increase in the TAC. Because of the enhanced availability and extraction of these phytochemical components due to the creation of cavities during sonication, there will be more polyphenolic compounds if there is an increase in antioxidant chemicals [41]. According to Saeeduddin et al. [32], when pear juice is exposed to ultrasound at 25 °C, its antioxidant capacity increases significantly. The amount of total phenolics and ascorbic acid in the sample determines the antioxidant activity. Ultrasound pasteurization is particularly successful at 65 °C, and it retains more antioxidant components than doestradiational pasteurization.

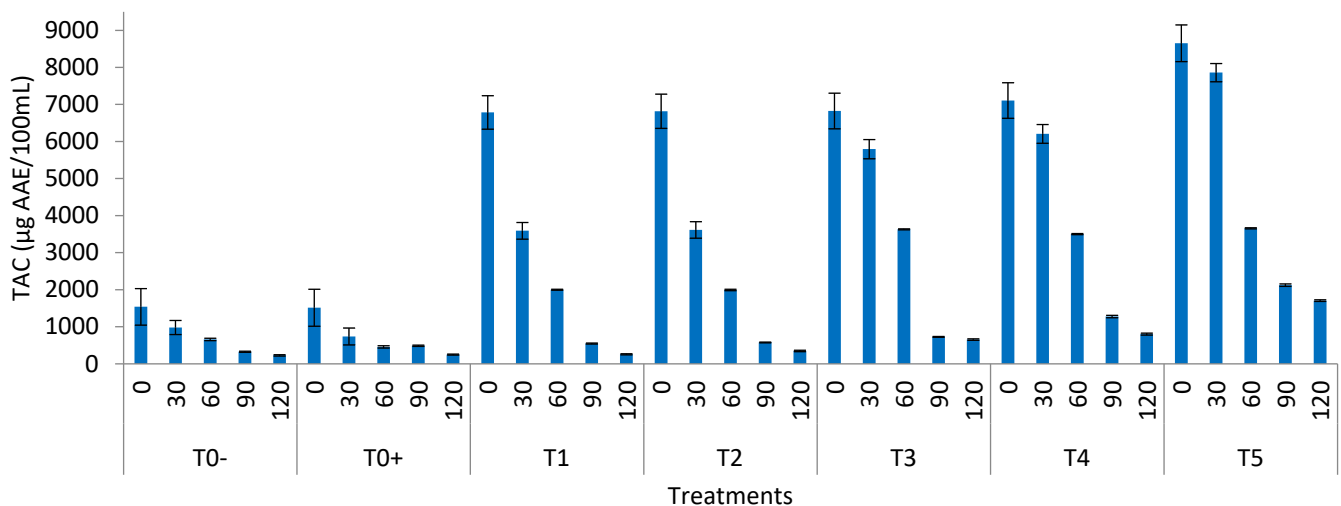


Figure 2. Total antioxidant capacity (TAC) of the watermelon juice (T_{0-} = control (watermelon juice with no preservative and treatment); T_{0+} = control (watermelon juice preserved with KMS); T_1 = 2 min ultrasound & 2 min microwave; T_2 = 4 min ultrasound & 1 min 50 s microwave; T_3 = 6 min ultrasound & 1 min 50 s microwave; T_4 = 8 min ultrasound & 1 min 50 s microwave; T_5 = 10 min ultrasound & 1 min 50 s) during storage.

3.9. Viscosity of the Watermelon Juice

The viscosity of all the treated samples decreased significantly with the time passage from 0 to 120 days of storage. The maximum viscosity values were observed in T_5 (44.19 mPa·s) and the minimum value in T_{0-} (21.21 mPa·s). Within the storage mean, the greatest value of viscosity was obtained at 0 day (44.19), and the least value at 120 days (16.82 mPa·s) (Figure 3). The viscosity of processed as well as untreated watermelon juice

decreased during the storage period. The considerable increase in viscosity in the treated samples may be ascribed to the decrease in the particle size or to the inactivation of the PME. Thermally and nonthermally treated juices keep the highest values because of the inactivation of enzymes [44]. The sonication treatments may promote the extraction of the bound forms of the macromolecules, which increases their concentration in the aqueous system, making the juice more viscous [41].

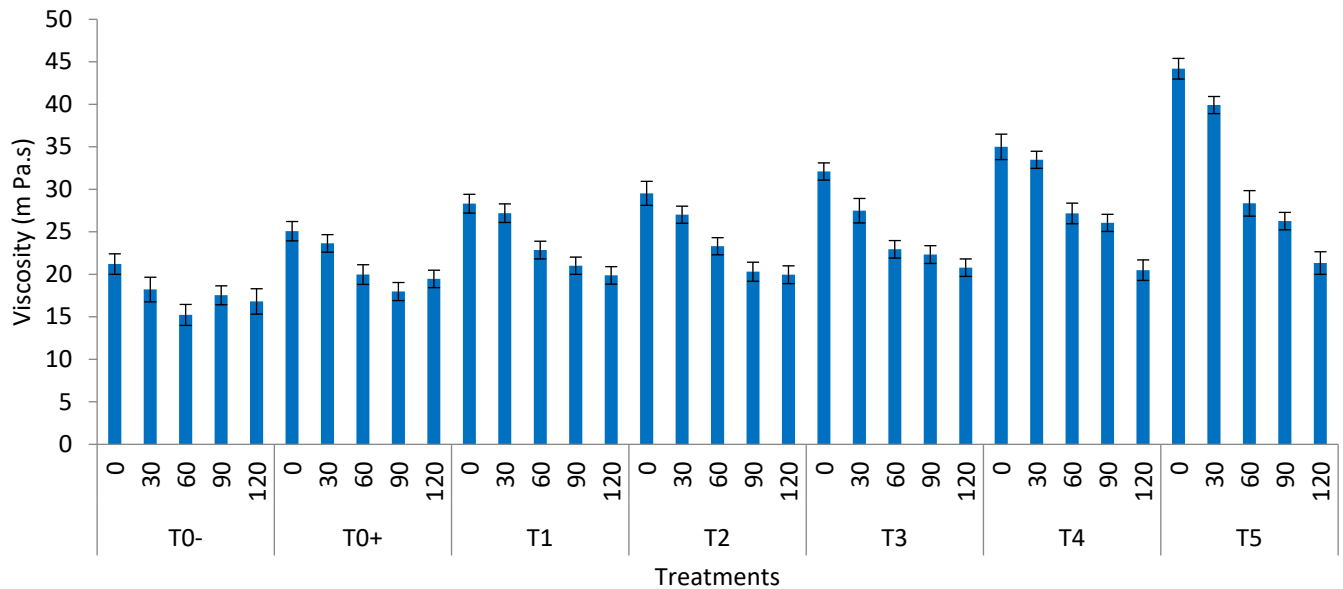


Figure 3. Viscosity of the watermelon juice (T_{0-} = control (watermelon juice with no preservative or treatment); T_{0+} = control (watermelon juice preserved with KMS); T_1 = 2 min ultrasound & 2 min microwave; T_2 = 4 min ultrasound & 1 min 50 s microwave; T_3 = 6 min ultrasound & 1 min 50 s microwave; T_4 = 8 min ultrasound & 1 min 50 s microwave; T_5 = 10 min ultrasound & 1 min 50 s) during storage.

4. Conclusions

This study was conducted to evaluate the impact of ultrasonication and microwave treatment on the physico-chemical parameters of watermelon juice during 120 days of storage. The synergistic impact of ultrasound and of microwave on the watermelon juice progressively enhanced the TSS, cloud value, acidity, ascorbic acid, TP, TF, and TAC. Treatment T_5 sonicated and microwaved for 10 min and 1 min and 50 s, respectively, showed maximum values for acidity (0.15%), cloud value (3.00), vitamin C content (202.67 mg/100 mL), TP (852.57 mgGAE/100 mL), TF (1970.9 μ g CE/100 mL), and TAC (8650.3 μ g equivalent of ascorbic acid/mL of juice). Moreover, the mentioned treatment also exhibited greater cloud stability and enhanced antioxidant potential. This study suggests that sonication coupled with microwave must be implemented commercially to process commercially unavailable watermelon juice, as these “green” techniques are the best alternates to chemical preservatives and conventional pasteurization practices. Additionally, combined ultrasound and microwave therapy has been demonstrated to be beneficial to the health of the individual, hence exerting a positive impact on consumer satisfaction and bioactive characteristics. New research is required to build models, such as surface response methods, for optimizing process factors during combined ultrasound–microwave procedures. In order to improve the quality of watermelon juice, it is advised that a combination of nonthermal food processing techniques be utilized to examine their synergistic influence on quality characteristics.

Author Contributions: Conceptualization, M.N. (Maham Navida), M.N. (Muhammad Nadeem), and T.M.Q.; Data curation, M.N. (Maham Navida), F.M., A.I. and M.S.; Formal analysis, M.N. (Maham Navida) and M.N. (Muhammad Nadeem); Funding acquisition, M.N. (Muhammad Nadeem), R.A.P., H.M.A.-D. and A.K.A.; Investigation, M.N. (Maham Navida), M.N. (Muhammad Nadeem), R.A.P., F.M., H.M.A.-D. and A.K.A.; Methodology, M.N. (Maham Navida), M.N. (Muhammad Nadeem), and T.M.Q.; Project administration, M.N. (Muhammad Nadeem); Resources, M.N. (Muhammad Nadeem) and M.S.; Software, M.N. (Maham Navida) and M.N. (Muhammad Nadeem); Supervision, M.N. (Muhammad Nadeem); Validation, M.N. (Maham Navida) and M.N. (Muhammad Nadeem); Visualization, R.A.P., M.S., H.M.A.-D. and A.K.A.; Writing—original draft, M.N. (Maham Navida), M.N. (Muhammad Nadeem), T.M.Q., F.M. and A.I.; Writing—review & editing, R.A.P., F.M., A.I., M.S., H.M.A.-D. and A.K.A. All authors have read and agreed to the published version of the manuscript.

Funding: The authors would like to thank the Deanship of Scientific Research at Umm Al-Qura University for supporting this study by Grant Code: (22UQU4320141DSR36).

Institutional Review Board Statement: Not applicable.

Informed Consent Statement: Not applicable.

Data Availability Statement: The data are contained within the article.

Acknowledgments: The authors would like to thank the Deanship of Scientific Research at Umm Al-Qura University for supporting this study by Grant Code: (22UQU4320141DSR36). The authors are thankful to the University of Sargodha for its financial support of this study.

Conflicts of Interest: The authors declare no conflict of interest.

Abbreviations

DPPH	2,2-diphenyl-1-picrylhydrazyl
KMS	Potassium-meta bisulphite
TSS	Total soluble solids
TF	Total flavonoid
TP	Total phenolic
TAC	Total antioxidant activity

References

1. Yikmuş, S. Sensory, Physicochemical, Microbiological and Bioactive Properties of Red Watermelon Juice and Yellow Watermelon Juice after Ultrasound Treatment. *J. Food Meas. Charact.* **2020**, *14*, 1417–1426. [[CrossRef](#)]
2. Manivannan, A.; Lee, E.-S.; Han, K.; Lee, H.-E.; Kim, D.-S. Versatile Nutraceutical Potentials of Watermelon—A Modest Fruit Loaded with Pharmaceutically Valuable Phytochemicals. *Molecules* **2020**, *25*, 5258. [[CrossRef](#)] [[PubMed](#)]
3. Gebhardt, S.; Lemar, L.; Haytowitz, D.; Pehrsson, P.; Nickle, M.; Showell, B.; Thomas, R.; Exler, J.; Holden, J. *USDA National Nutrient Database for Standard Reference, Release 21*; United States Department of Agriculture: Washington, DC, USA, 2008.
4. Li, X.; Yue, X.; Huang, Q.; Zhang, B. Effects of Wet-Media Milling on Multi-Scale Structures and in Vitro Digestion of Tapioca Starch and the Structure-Digestion Relationship. *Carbohydr. Polym.* **2022**, *284*, 119176. [[CrossRef](#)] [[PubMed](#)]
5. Ali, E.S.; Asfahan, H.M.; Sultan, M.; Askalany, A.A. A Novel Ejectors Integration with Two-Stages Adsorption Desalination: Away to Scavenge the Ambient Energy. *Sustain. Energy Technol. Assess.* **2021**, *48*, 101658. [[CrossRef](#)]
6. Imran, M.A.; Xu, J.; Sultan, M.; Shamshiri, R.R.; Ahmed, N.; Javed, Q.; Asfahan, H.M.; Latif, Y.; Usman, M.; Ahmad, R. Free Discharge of Subsurface Drainage Effluent: An Alternate Design of the Surface Drain System in Pakistan. *Sustainability* **2021**, *13*, 4080. [[CrossRef](#)]
7. Munyasya, A.N.; Koskei, K.; Zhou, R.; Liu, S.-T.; Indoshi, S.N.; Wang, W.; Zhang, X.-C.; Cheruiyot, W.K.; Mburu, D.M.; Nyende, A.B. Integrated On-Site & off-Site Rainwater-Harvesting System Boosts Rainfed Maize Production for Better Adaptation to Climate Change. *Agric. Water Manag.* **2022**, *269*, 107672.
8. Jiang, G.; Ameer, K.; Kim, H.; Lee, E.-J.; Ramachandriah, K.; Hong, G.-P. Strategies for Sustainable Substitution of Livestock Meat. *Foods* **2020**, *9*, 1227. [[CrossRef](#)]
9. Bruton, B.D.; Fish, W.W.; Roberts, W.; Popham, T.W. The Influence of Rootstock Selection on Fruit Quality Attributes of Watermelon. *Open Food Sci. J.* **2009**, *3*, 5–34. [[CrossRef](#)]
10. Rawson, A.; Tiwari, B.K.; Patras, A.; Brunton, N.; Brennan, C.; Cullen, P.J.; O'Donnell, C. Effect of Thermosonication on Bioactive Compounds in Watermelon Juice. *Food Res. Int.* **2011**, *44*, 1168–1173. [[CrossRef](#)]
11. Shahzad, T.; Ahmad, I.; Choudhry, S.; Saeed, M.K.; Khan, M.N. DPPH Free Radical Scavenging Activity of Tomato, Cherry Tomato and Watermelon: Lycopene Extraction, Purification and Quantification. *IJPPS* **2014**, *6*, 223–228.

12. Li, Z.; Yuan, Y.; Yao, Y.; Wei, X.; Yue, T.; Meng, J. Formation of 5-Hydroxymethylfurfural in Industrial-Scale Apple Juice Concentrate Processing. *Food Control* **2019**, *102*, 56–68. [[CrossRef](#)]
13. Liu, Y.; He, C.; Song, H. Comparison of Fresh Watermelon Juice Aroma Characteristics of Five Varieties Based on Gas Chromatography-Olfactometry-Mass Spectrometry. *Food Res. Int.* **2018**, *107*, 119–129. [[CrossRef](#)] [[PubMed](#)]
14. Gomez-Mejia, L.R.; Cruz, C.; Berrone, P.; De Castro, J. The Bind That Ties: Socioemotional Wealth Preservation in Family Firms. *Acad. Manag. Ann.* **2011**, *5*, 653–707. [[CrossRef](#)]
15. Ameer, K.; Shahbaz, H.M.; Kwon, J.-H. Green Extraction Methods for Polyphenols from Plant Matrices and Their Byproducts: A Review. *Compr. Rev. Food Sci. Food Saf.* **2017**, *16*, 295–315. [[CrossRef](#)] [[PubMed](#)]
16. Munir, M.; Nadeem, M.; Qureshi, T.M.; Gamlath, C.J.; Martin, G.J.O.; Hemar, Y.; Ashokkumar, M. Effect of Sonication, Microwaves and High-Pressure Processing on ACE-Inhibitory Activity and Antioxidant Potential of Cheddar Cheese during Ripening. *Ultrason. Sonochem.* **2020**, *67*, 105140. [[CrossRef](#)]
17. Zhao, Z.-Y.; Wang, P.-Y.; Xiong, X.-B.; Wang, Y.-B.; Zhou, R.; Tao, H.-Y.; Grace, U.A.; Wang, N.; Xiong, Y.-C. Environmental Risk of Multi-Year Polythene Film Mulching and Its Green Solution in Arid Irrigation Region. *J. Hazard. Mater.* **2022**, *435*, 128981. [[CrossRef](#)]
18. Nadeem, M.; Ghaffar, A.; Hashim, M.M.; Murtaza, M.A.; Ranjha, M.M.A.N.; Mehmood, A.; Riaz, M.N. Sonication and Microwave Processing of Phalsa Drink: A Synergistic Approach. *Int. J. Fruit Sci.* **2021**, *21*, 993–1007. [[CrossRef](#)]
19. Lee, H.-G.; Jo, Y.; Ameer, K.; Kwon, J.-H. Optimization of Green Extraction Methods for Cinnamic Acid and Cinnamaldehyde from Cinnamon (*Cinnamomum Cassia*) by Response Surface Methodology. *Food Sci. Biotechnol.* **2018**, *27*, 1607–1617. [[CrossRef](#)]
20. Zenker, M.; Heinz, V.; Knorr, D. Application of Ultrasound-Assisted Thermal Processing for Preservation and Quality Retention of Liquid Foods. *J. Food Prot.* **2003**, *66*, 1642–1649. [[CrossRef](#)]
21. Qureshi, T.M.; Nadeem, M.; Maken, F.; Tayyaba, A.; Majeed, H.; Munir, M. Influence of Ultrasound on the Functional Characteristics of Indigenous Varieties of Mango (*Mangifera Indica* L.). *Ultrason. Sonochem.* **2020**, *64*, 104987. [[CrossRef](#)]
22. Ameer, K.; Bae, S.-W.; Jo, Y.; Lee, H.-G.; Ameer, A.; Kwon, J.-H. Optimization of Microwave-Assisted Extraction of Total Extract, Stevioside and Rebaudioside-A from *Stevia Rebaudiana* (Bertoni) Leaves, Using Response Surface Methodology (RSM) and Artificial Neural Network (ANN) Modelling. *Food Chem.* **2017**, *229*, 198–207. [[CrossRef](#)] [[PubMed](#)]
23. Martins, C.C.P.; Cavalcanti, R.N.; Cardozo, F.T.S.; Couto, S.M.; Esmerino, A.; Guimarães, J.T.; Balthazar, C.F.; Rocha, R.S.; Pimentel, T.C.; Freitas, M.Q.; et al. Effects of Microwave Heating on the Chemical Composition and Bioactivity of Orange Juice-Milk Beverages. *Food Chem.* **2021**, *345*, 128746. [[CrossRef](#)] [[PubMed](#)]
24. Jabbar, S.; Abid, M.; Hu, B.; Wu, T.; Hashim, M.M.; Lei, S.; Zhu, X.; Zeng, X. Quality of Carrot Juice as Influenced by Blanching and Sonication Treatments. *LWT-Food Sci. Technol.* **2014**, *55*, 16–21. [[CrossRef](#)]
25. Nadeem, M.; Tehreem, S.; Mudassar Ali Nawaz Ranjha, M.; Ahmad, A.; Din, A.; Mueen Ud Din, G.; Javeria, S.; Nadeem Riaz, M.; Siddeeq, A.; Ali Nawaz Ranjha, M.; et al. Probing of Ultrasonic Assisted Pasteurization (UAP) Effects on Physicochemical Profile and Storage Stability of Jambul (*Syzygiumcumini* L.) Squash. *Int. J. Food Prop.* **2022**, *25*, 661–672. [[CrossRef](#)]
26. Nadeem, M.; Modassar, M.; Ranjha, A.N.; Ameer, K.; Ainee, A.; Yasmin, Z.; Javaria, S.; Teferra, T.F. Effect of Sonication on the Functional Properties of Different Citrus Fruit Juices. *Int. J. Fruit Sci.* **2022**, *22*, 568–580. [[CrossRef](#)]
27. Saikia, S.; Mahnot, N.K.; Mahanta, C.L. A Comparative Study on the Effect of Conventional Thermal Pasteurisation, Microwave and Ultrasound Treatments on the Antioxidant Activity of Five Fruit Juices. *Food Sci. Technol. Int.* **2015**, *22*, 288–301. [[CrossRef](#)]
28. Malik, F.; Nadeem, M.; Ainee, A.; Kanwal, R.; Sultan, M.; Iqbal, A.; Mahmoud, S.F.; Alshehry, G.A.; Al-Jumayi, H.A.; Algarni, E.H. Quality Evaluation of Lemon Cordial Stored at Different Times with Microwave Heating (Pasteurization). *Sustainability* **2022**, *14*, 1953. [[CrossRef](#)]
29. Sasikumar, R. Preparation of Therapeutic RTS Beverage from Aloe Vera Gel and Aonla Fruit Juice and Evaluation of Storage Stability. *Asian J. Dairy Food Res.* **2015**, *34*, 151–155. [[CrossRef](#)]
30. AOAC. *Official Methods of Analysis*, 18th ed.; The Association of Official Analytical Chemists: Gaithersburg, MD, USA, 2016.
31. Versteeg, C.; Rombouts, F.M.; Spaansen, C.H.; Pilnik, W. Thermostability and orange juice cloud destabilizing properties of multiple pectinesterases from orange. *J. Food Sci.* **1980**, *45*, 969–971. [[CrossRef](#)]
32. Saeeduddin, M.; Abid, M.; Jabbar, S.; Wu, T.; Hashim, M.M.; Awad, F.N.; Hu, B.; Lei, S.; Zeng, X. Quality Assessment of Pear Juice under Ultrasound and Commercial Pasteurization Processing Conditions. *LWT-Food Sci. Technol.* **2015**, *64*, 452–458. [[CrossRef](#)]
33. Prieto, P.; Pineda, M.; Aguilar, M. Spectrophotometric Quantitation of Antioxidant Capacity through the Formation of a Phosphomolybdenum Complex: Specific Application to the Determination of Vitamin E. *Anal. Biochem.* **1999**, *269*, 337–341. [[CrossRef](#)]
34. Nindo, C.I.; Tang, J.; Powers, J.R.; Singh, P. Viscosity of Blueberry and Raspberry Juices for Processing Applications. *J. Food Eng.* **2005**, *69*, 343–350. [[CrossRef](#)]
35. Steel, R.G.D.; Torrie, J.H.; Dicky, D.A. *Principles and Procedures of Statistics: A Biometrical Approaches*, 3rd ed.; McGraw Hill Book Co., Inc.: Singapore, MI, USA, 1997; pp. 204–227.
36. Walkling-Ribeiro, M.; Noci, F.; Riener, J.; Cronin, D.A.; Lyng, J.G.; Morgan, D.J. The Impact of Thermosonication and Pulsed Electric Fields on *Staphylococcus Aureus* Inactivation and Selected Quality Parameters in Orange Juice. *Food Bioprocess Technol.* **2008**, *2*, 422. [[CrossRef](#)]
37. Jan, A.; Masih, E.D. Development and Quality Evaluation of Pineapple Juice Blend with Carrot and Orange Juice. *Int. J. Sci. Res. Publ.* **2012**, *2*, 1–8.

38. Bhardwaj, R.L.; Pandey, S. Juice Blends—A Way of Utilization of Under-Utilized Fruits, Vegetables, and Spices: A Review. *Crit. Rev. Food Sci. Nutr.* **2011**, *51*, 563–570. [[CrossRef](#)]
39. Cansino, N.C.; Carrera, G.P.; Rojas, Q.Z.; Olivares, L.D.; García, E.A.; Moreno, E.R. Ultrasound Processing on Green Cactus Pear (*Opuntia Ficus Indica*) Juice: Physical, Microbiological and Antioxidant Properties. *J. Food Process. Technol.* **2013**, *4*, 1000267. [[CrossRef](#)]
40. Jingfei, G.; Vasantha, H.P.; Nutritional, R. Physicochemical and Microbial Quality of Ultrasound-Treated Apple-Carrot Juice Blends. *Food Nutr. Sci.* **2012**, *3*, 212–218.
41. Abid, M.; Jabbar, S.; Wu, T.; Hashim, M.M.; Hu, B.; Lei, S.; Zeng, X. Sonication Enhances Polyphenolic Compounds, Sugars, Carotenoids and Mineral Elements of Apple Juice. *Ultrason. Sonochem.* **2014**, *21*, 93–97. [[CrossRef](#)]
42. Aadil, R.M.; Zeng, X.-A.; Han, Z.; Sun, D.-W. Effects of Ultrasound Treatments on Quality of Grapefruit Juice. *Food Chem.* **2013**, *141*, 3201–3206. [[CrossRef](#)]
43. Oms-Oliu, G.; Odriozola-Serrano, I.; Soliva-Fortuny, R.; Martín-Belloso, O. Effects of High-Intensity Pulsed Electric Field Processing Conditions on Lycopene, Vitamin C and Antioxidant Capacity of Watermelon Juice. *Food Chem.* **2009**, *115*, 1312–1319. [[CrossRef](#)]
44. Aguiló-Aguayo, I.; Soliva-Fortuny, R.; Martín-Belloso, O. Color and Viscosity of Watermelon Juice Treated by High-Intensity Pulsed Electric Fields or Heat. *Innov. Food Sci. Emerg. Technol.* **2010**, *11*, 299–305. [[CrossRef](#)]

Article

Experiment of Canopy Leaf Area Density Estimation Method Based on Ultrasonic Echo Signal

Mingxiong Ou ^{1,2,*}, Tianhang Hu ^{1,†}, Mingshuo Hu ^{1,†}, Shuai Yang ¹, Weidong Jia ^{1,2}, Ming Wang ^{1,2}, Li Jiang ^{1,2}, Xiaowen Wang ^{1,2} and Xiang Dong ³

¹ School of Agricultural Engineering, Jiangsu University, Zhenjiang 212013, China

² High-Tech Key Laboratory of Agricultural Equipment and Intelligence of Jiangsu Province, Jiangsu University, Zhenjiang 212013, China

³ State Key Laboratory of Soil-Plant-Machinery System Technology, Chinese Academy of Agricultural Mechanization Sciences, Beijing 100083, China

* Correspondence: myomx@ujs.edu.cn

† These authors contributed equally to this work.

Abstract: Variable-rate spray systems with canopy leaf area density information detection are an important approach to reducing pesticide usage in orchard management. In order to estimate the canopy leaf area density using ultrasonic sensors, this article proposed three parameter model equations based on ultrasonic echo peaks for canopy leaf area density estimation and verified the accuracy of the three parameter model equations using laboratory-simulated canopy and outdoor tree experiments. The orthogonal regression statistics results from the laboratory-simulated canopy experiment indicated that parameter V_c is more suitable for canopy leaf area density estimation compared to parameter V_a and V_b when the density ranges from 0.54 to 5.4 m^2m^{-3} . The model equation from parameter V_c has minor systematic errors, and the predicted and observed values of parameter V_c have good agreement with the experimental conditions. The laboratory-simulated canopy and outdoor tree canopy leaf area density verification experiments of parameter V_c were carried out, and the results indicated that the absolute value of the mean relative error is 5.37% in the laboratory-simulated canopy and 2.84% in outdoor tree experiments. The maximum absolute value of the relative error is 8.61% in the laboratory-simulated canopy and 14.71% in the outdoor tree experiments, and the minimum absolute value of the relative error is 3.21% in the laboratory-simulated canopy and 0.56% in the outdoor tree experiments. The laboratory-simulated canopy leaf area density verification results showed that the mean relative errors under canopy leaf area density 0.98 and 4.92 m^2m^{-3} conditions are 6.29% and 5.82%, respectively, which is larger than the mean relative error under 2.95 m^2m^{-3} ; nevertheless, these results proved that this model equation is applicable for canopy information detection and advanced pesticide application development in future.

Keywords: ultrasonic sensor; canopy leaf area density; ultrasonic echo signal; verification experiment

Citation: Ou, M.; Hu, T.; Hu, M.; Yang, S.; Jia, W.; Wang, M.; Jiang, L.; Wang, X.; Dong, X. Experiment of Canopy Leaf Area Density Estimation Method Based on Ultrasonic Echo Signal. *Agriculture* **2022**, *12*, 1569. <https://doi.org/10.3390/agriculture12101569>

Academic Editor: Michele Pisante

Received: 25 July 2022

Accepted: 21 September 2022

Published: 28 September 2022

Publisher's Note: MDPI stays neutral with regard to jurisdictional claims in published maps and institutional affiliations.



Copyright: © 2022 by the authors. Licensee MDPI, Basel, Switzerland. This article is an open access article distributed under the terms and conditions of the Creative Commons Attribution (CC BY) license (<https://creativecommons.org/licenses/by/4.0/>).

1. Introduction

Pesticide application is one of the most important factors in agricultural production processes to ensure the quality and yield of agricultural production. The excessive use of pesticides in pest control increases pesticide resistance, environmental contaminants, and labor hazards [1,2]. Precision pesticide application technology based on plant sensing is one of the effective ways to reduce pesticide dosage and cost, especially in orchard management; the tree-canopy sensing technique and variable-rate spray systems can significantly reduce pesticide dosage and off-target drifts [3–5]. Variable-rate spray systems based on canopy information detection usually have an automatic adjustment function for the pesticide rate. Variable-rate spray systems developed for pesticide sprayers can adjust the pesticide flow rate in real-time according to the canopy geometric dimension, canopy leaf area density, or

spray distance, which is obtained from sensors in real-time; therefore, the pesticide droplet deposition is mainly affected by the tree canopy and sensor detection method [6,7].

Previously, researchers have analyzed the tree-canopy-volume detection methods in forests using images from remote sensing technology, but due to the limitation of image resolution and quality, remote sensing technology is not available in single-tree-canopy-volume detection and cannot accurately detect tree-canopy information in real-time [8,9]. With the development of sensor technology for pesticide applications, sensors such as infrared, laser, machine vision, and ultrasonic are widely used in tree-canopy information detection. In pesticide application practices, infrared sensors could be easily disturbed by external light intensity and canopy color depth, and the detailed size of the target canopy cannot be detected [10,11]. Light Detection and Ranging (LIDAR) systems were used to detect the 3-D structure and canopy density of the trees in the orchard and vineyard, and the results indicated good correlations between the manual and sensor measuring results. As a non-destructive method in canopy detection, LIDAR measuring technology showed potential for pesticide applications; nevertheless, the expensive process unit and 3-D points cloud real-time algorithm still needs to be improved for LIDAR system applications [12,13]. Asaei et al. [14] developed a site-specific orchard sprayer with a machine vision sensor that could detect the spacing of the trees along the orchard rows, and the orchard sprayer avoided pesticide waste compared to a conventional continuous sprayer, which sprays pesticide in the spacing between the trees. The field tests indicated that the site-specific orchard sprayer resulted in 54% less pesticide use compared with conventional sprayers; nevertheless, the vision sensor system requires further research for more orchard models, and it is also easily affected by light conditions. Ultrasonic sensors are a widely used technology in industry, they are less affected by light and weather conditions, which is suitable in many application areas, and they are also more suitable for tree-canopy detection than other sensors under outdoor conditions. Former research showed that ultrasonic sensors could not only be used to measure distance but also detect the tree-canopy information in agriculture applications; considering its low cost and high-reliability characteristics, ultrasonic sensors have a good potential for application [15–18]. Palleja et al. [19,20] proposed a real-time estimation method of canopy density by using ultrasonic sensors; the experiments in greenhouse and orchards indicated that the ultrasonic signal is highly correlated with the canopy density, and the maximum relative error was about 14.1% under vineyards condition. The system could also be used in apple or vineyard tree monitoring during the whole-life growing season; nevertheless, the accuracy of the real-time detection method still needs improvement. Gil et al. [21] developed a variable-rate multi-nozzle air blast sprayer with ultrasonic sensors; the spray rate was modified according to the crop width, which was detected by the ultrasonic sensor in an undirected way, and the experimental results indicated that the sprayer saved 58% of the pesticide compared to the normal continuous sprayer, and there were no significant differences between the sprayers. Zhai et al. [22] established the canopy model equations of a planar orchard target that could be used to calculate the canopy density in real-time, and this study proposed a time-domain energy analysis method for canopy density detection through ultrasonic echo signal. There was good applicability between the model and planar orchard target when under four layers of leaves; nevertheless, the maximum relative error of the model equations from the experimental data was about 29.92%, which requires improvement for future applications. In order to reduce the relative error of the canopy model from the planar orchard target, Nan et al. [23] designed a cylindrical simulated canopy and established a new model equation for the canopy leaf area density calculation. This model equation considered the mean value of the ultrasonic echo signal for the canopy leaf area density calculation, and the laboratory test results showed that the relative error between the observed and predicted echo signal ranged from 1.02 to 16.8%, and the outdoor test showed that the relative error between the observed and predicted canopy leaf area density ranged from 0.23 to 35.5%. Ou et al. [24] proposed a new algorithm for measuring tree-canopy thickness based on ultrasonic echo signal and verified that the method is

effective under laboratory and outdoor conditions. The results indicated that the ultrasonic sensor had a high measurement accuracy for canopy-thickness detection. The maximum relative errors in the laboratory and outdoor test results were 8.8% and 19.4%, respectively; the thickness calculation algorithm also provided a new perspective on ultrasonic echo signal analysis in the tree canopy, this study demonstrated that the ultrasonic echo signal is affected by the canopy thickness and leaves on the ultrasonic waves propagation path.

Previous studies indicated that ultrasonic sensors have good robustness and potential for agriculture applications, and the canopy information, such as the leaf area density and thickness, could be calculated and predicted by the ultrasonic echo signal, which could be very useful for pesticide application in orchard management. Nevertheless, the relative error of the leaf area density equations in these articles is still too large and unstable, which could affect the pesticide droplet deposition and uniformity. The objectives of this article are to establish and analyze the mathematical model equations between the canopy leaf area density and the ultrasonic echo signal and to verify the accuracy and applicability of mathematical model equations through laboratory-simulated canopy experiments and outdoor tree canopy experiments. The simulated leaves used in this paper are beneficial to the repeatability and controllability of the changes in the modeling parameters; the different characteristics of plant species and leaves will have some effect on the accuracy of mathematical modeling. The ultrasonic echo signal intensity is basically affected by the size of the obstacle in the ultrasonic wave's propagation path, so this study used simulated leaves, which have similar sizes to the *Osmanthus* tree used in the verification experiment. The mathematical model equation established by the method proposed in this paper could be used in the real-time detection of canopy leaf area density with minor errors, which could also provide an effective and reliable real-time canopy leaf area density estimation solution for variable-rate sprayer system development.

2. Materials and Methods

2.1. Laboratory-Simulated Canopy Experimental Setup

To measure the canopy leaf area density with an ultrasonic sensor, a laboratory-simulated canopy experiment system was built, as shown in Figure 1. The system was composed of a simulated canopy, a computer, a 12V DC power unit (6-QW, Camel Group Co., Ltd., Xiangyang, China), a USB data acquisition card (USB3200, Beijing ART Technology Development Co., Ltd., Beijing, China), an ultrasonic sensor (MB7092-101, MaxBotix, Inc., Brainerd, MN, USA), and a microprocessor control board (STM32F4 development board, Guangzhou Xingyi Electronic Technology Co., Ltd., Guangzhou, China).

The simulated canopy had a similar leaf distribution and leaf area density to the tree target; it was designed for the laboratory-simulated canopy experiment. The ultrasonic sensor refresh rate was 10 Hz, and it had one pin for the analog voltage envelope output with the acoustic waveform. The maximum measurement range was 7.65 m, and the diffusion angle of the ultrasonic sensor was about 14° [24]. The USB data acquisition card was used to convert the analog voltage envelope output into a digital signal, which had a 12-bit ADC conversion chip to achieve a maximum conversion rate of up to 500 KHz in data receiving and transferring, and the conversion rate used in this system was 125 KHz. An operating software installed in the computer was used to save the digital signal information from the USB data acquisition, the start and stop of the data acquisition task could be manually controlled in the experiment process, and the digital signal sampling frequency and the sampling times could be set through the operating software according to the experimental requirements. The microprocessor control board was supplied by a 12V DC power unit and offered stable voltage input for the ultrasonic sensor, which means that the system is available in the laboratory and outdoor conditions.

The simulated canopy was composed of a steel profile frame, simulated leaves, and nylon wires, the diameter of the nylon wire was 0.468 mm, and it was less than the wavelength of the ultrasonic sensor, so it barely affects the ultrasonic propagation, which is also adopted in reference [24]. The size of the steel profile frame (length × width × height)

was 200 cm × 90 cm × 110 cm, and due to the steel profile frame boundary, the size of the simulated canopy was about 140 cm × 75 cm × 80 cm, and the simulated leaf used in the experiments was heart-shaped, and the average area was about 44 cm². The simulated canopy had 2, 3, 4, or 5 planar leaf layers in the experiments, each layer had many simulated leaves, which were fixed on the nylon wires, and the nylon wires were arranged up and down in the steel profile frame. The nylon wires are moveable in the simulated canopy, which is convenient for adjusting the simulated canopy thickness and leaf area density, similar to the experimental setup used in reference [21]. The leaves on the nylon wires are basically evenly arranged along the wires according to the number of leaves. The temperatures ranged from 20 to 25 °C, and the humidity ranged from 38 to 50%.

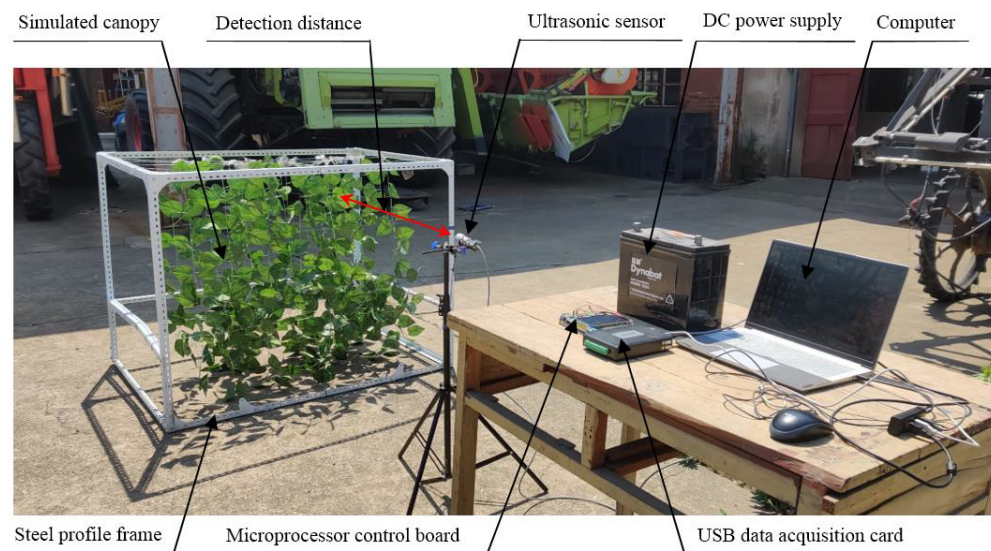


Figure 1. Simulated canopy leaf area density detection system.

2.2. Canopy Leaf Area Density Estimation Equations

The pesticide application with canopy leaf-area-density detection is an effective way for pesticide rate control and reduction. Canopy leaf-area density ρ_s refers to the sparseness of leaves in the tree canopy, which is an important parameter in describing canopy characteristics and pesticide application target volume assessments. The canopy leaf area density ρ_s can be expressed as follow:

$$\rho_s = \frac{S}{V} = \frac{\sum_{i=1}^n A_i}{V} \quad (1)$$

In Equation (1), ρ_s (m²m⁻³) is the canopy leaf area density, n is the total number of leaves in the canopy space, S (m²) is the total area of leaves in the canopy space, V (m³) is the space volume of the canopy space, i is the number of the leaf, A_i (m²) is the area of the leaf.

Ou et al. [24] found out that the ultrasonic echo signal is mostly affected by the detection distance, canopy density, and geometric dimension, and the ultrasonic echo signal contains multiple echo peaks, which are directly related to the leaves in the ultrasonic waves propagation path, and this study indicated that there are multiple reflections happening when the ultrasonic waves pass the tree canopy. Zhai et al. [22] proposed a time-domain energy analysis method that considered the whole range of ultrasonic echo signals in the canopy leaf area density estimation, and there is a correlation between the echo energy and canopy leaf area density; nevertheless, there is also a relative error in the verification results. Based on the former studies and data results, considering the ultrasonic waves propagation process and characteristics in the tree canopy, in order to predict the canopy leaf area density with higher accuracy, this article proposed three parameters (V_a , V_b

and V_c), which are calculated by the ultrasonic echo peaks to estimate the canopy leaf area density. Parameters V_a , V_b , and V_c have different expression equations, as shown in Equations (2)–(4). $V_1, V_2, V_3 \dots, V_n$ are the value of peaks in the ultrasonic echo signal, as shown in Figure 2, and the parameters were processed using the MATLAB 2015b software (Math Works, Natick, MA, USA).

$$V_a = \max(V_1, V_2, \dots, V_n). \quad (2)$$

$$V_b = \max(V_1, V_2, \dots, V_n) \times n \quad (3)$$

$$V_c = \frac{V_1 + V_2 + V_3 \dots V_n}{n} \quad (4)$$

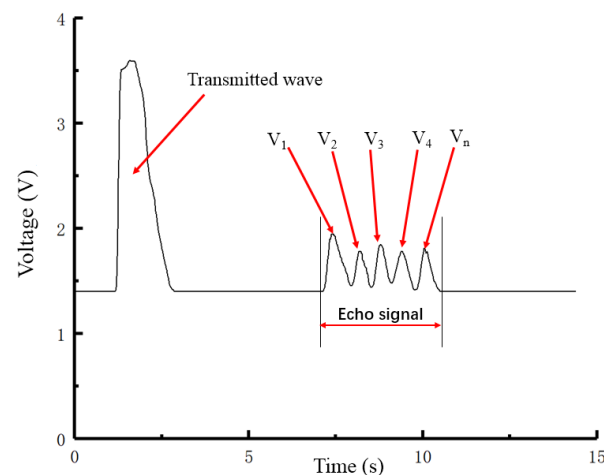


Figure 2. Schematic of ultrasonic return wave.

In Equations (2)–(4), V_a , V_b and V_c (Voltage) are the proposed parameters for canopy leaf-density estimation, $V_1, V_2, V_3 \dots, V_n$ (Voltage) are the peaks values in the ultrasonic echo signal, and n is number of the peaks in the ultrasonic echo signal.

2.3. Experiment to Establish Canopy Leaf Area Density Model

2.3.1. Orthogonal Regression Experiment Design

Based on the former studies used in canopy information estimation, this article used the orthogonal regression central composite experiment setup in the experiment design, which selects the representative experimental points in the multi-factor and multi-level experimental conditions. Through the analysis of orthogonal experimental results, the relationship between the factors and variables based on the experimental results can be concluded, which reduces the work and cost of the experiments compared to full-scale experiments, it also improves the work efficiency, and saves time [22]. In order to conclude the canopy leaf area density model, the experimental factors were canopy leaf area density and the detection distance. The detection distance is the distance between the ultrasonic sensor and the target canopy along the ultrasonic wave direction, as shown in Figure 1, parameters V_a , V_b and V_c are the experimental result values.

According to the normal orchard plant mode and pesticide application requirements, the detection distance in this experiment ranged from 0.5 to 1.5 m, and the canopy leaf area density ranged from 0.54 to 5.4 m^2m^{-3} . The total number of experiments N in this experiment consisted of three parts: the number of orthogonal experiments m_c , the number of zero-level repeated experiments m_0 , and the number of axial experiments m_r , where p is the number of experimental factors.

$$m_c = 2^p \quad (5)$$

$$m_r = 2p \quad (6)$$

$$N = m_c + m_r + m_0 \tag{7}$$

In this experiment, the number of experimental factors p is 2, and the number of zero-level repeated experiments m_0 is 3. According to Equation (7), the total number of experiments is 11. Another important parameter, γ , in the experiment is the star arm parameter, $\gamma = 1.13$ obtained by Equation (8).

$$\gamma = \sqrt{-2^{p-1} + (2^p + 2p + m_0)^{\frac{1}{2}} \times 2^{\frac{p}{2}-1}} \tag{8}$$

In this experiment, the detection distance (m) and canopy leaf area density (m^2m^{-3}) were selected as the experimental factors, which were denoted as x_1 and x_2 . The factor levels coding were as shown in Table 1, and the experimental scheme was designed according to this table, as shown in Table 2. The normative variables of the regression equation were z_1 and z_2 .

Table 1. Factor levels coding.

Code	Factors	
	x_1	x_2
−r	0.5	0.54
−1	0.55	0.79
0	0.9	2.95
1	1.25	5.09
r	1.3	5.4

Table 2. Binary quadratic regression orthogonal combination design coding.

Number	Z_1	Z_2	x_1 (m)	x_2 (m^2m^{-3})
1	0	0	0.9	2.95
2	−r	0	0.5	2.95
3	0	r	0.9	5.4
4	1	1	1.25	5.09
5	1	−1	1.25	0.79
6	0	0	0.9	2.95
7	0	−r	0.9	0.54
8	0	0	0.9	2.95
9	r	0	1.3	2.95
10	−1	−1	0.55	0.79
11	−1	1	0.55	5.09

2.3.2. Detection Points Arrangement

The ultrasonic sensor aimed at the simulated canopy direction was installed in front of the simulated canopy, as shown in Figure 1, and the detection point was the position where the ultrasonic wave passes through the simulated canopy. There were 9 detection points arranged in front of the simulated canopy, as shown in Figure 3, and in order to avoid the influence of the steel profile frame boundary during the ultrasonic detection, the left and right edge detection points were 70 cm away from the frame boundary horizontally, and the upper and lower edge points were 30 cm away from the frame boundary vertically. The horizontal spacing between the detection points was 30 cm, and the vertical spacing between the detection points was 20 cm, at each of the 9 detection points, the values of parameters V_a , V_b and V_c were obtained by three replicated measurements, and the average values were used as the experimental results. During the experiment period, the environmental temperatures ranged from 20 to 25 °C, and the relative humidity ranged from 40 to 51%.

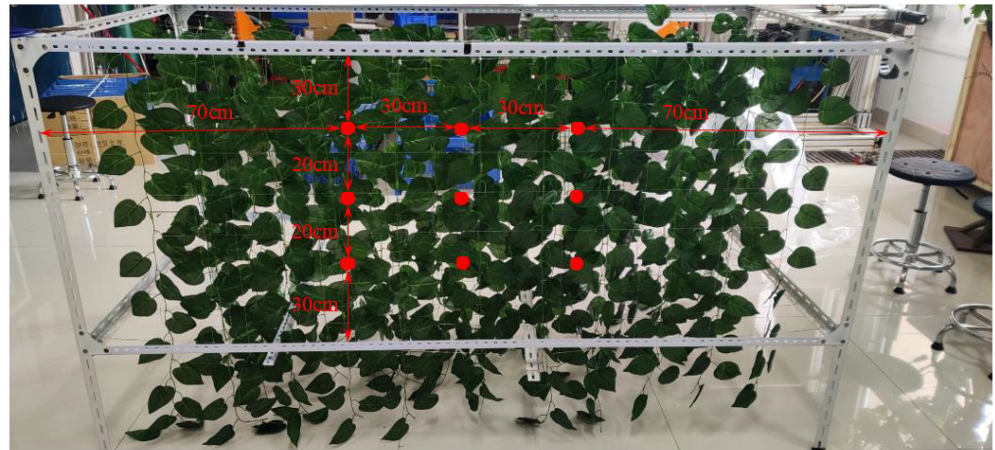


Figure 3. Detection points in front of Simulated canopy.

2.4. Laboratory-Simulated Canopy Verification

To verify the accuracy and applicability of the canopy leaf area density model equation under laboratory-simulated canopy conditions, this article designed nine verification conditions with different distances and canopy leaf area densities, which were different to the conditions in Table 2. The verification experiments were also carried out with the laboratory-simulated canopy experimental system stated in Section 2.1.

The canopy leaf area density of the nine verification conditions were 0.98, 2.95, 4.92 m^2m^{-3} , respectively, and the detection distances were 0.8, 1.0, 1.2 m, respectively. The detection points were selected as described in Section 2.3.2, and each point was also measured three times.

2.5. Outdoor Tree Canopy Verification

To verify the accuracy and applicability of the canopy leaf area density model equation under outdoor tree canopy conditions, three *Osmanthus* trees were selected as the experimental objects in place ($32^\circ 12' 22''$ N, $119^\circ 31' 14''$ E) on April 2022, as shown in Figure 4. The environmental temperature ranged from 10 to 20 $^\circ\text{C}$, and the relative humidity ranged from 45 to 57%. There were 15 detection points that were arranged in front of the canopies randomly. The calculation formula of canopy leaf area density in experiments is expressed in Equation (10) according to former studies and ultrasonic wave propagation law in reference [24].

$$V_t = \pi r^2 D \quad (9)$$

$$\rho_s = \frac{\bar{S} \times N_i}{V_t} \quad (10)$$

where, V_t is the volume within the effective detection range (m^3); r is the lower radius of the effective area (m); D is the ultrasonic penetration of canopy distance along the detection direction (m); ρ_s is the canopy leaf area density by manual measurement (m^2m^{-3}); \bar{S} is the average leaf area (m^2); and N_i is the total number of leaves in the effective volume. According to the definitions, there were 30 leaves collected from the upper, middle, and lower locations of the tree canopy, respectively. Commercial image analysis code IPP (Image Pro Plus, Meyer instruments, Inc., Houston, TX, USA) was used to measure the leaf area after leaf scanning. The average leaf area \bar{S} was about $1.55 \times 10^{-3} \text{m}^2$, and the canopy leaf area density of the selected detection points ranged from 1.80 to 5.88 m^2m^{-3} .



Figure 4. Osmanthus trees for outdoor verification.

3. Results

3.1. Mathematical Model Analysis

The laboratory-simulated canopy experimental results based on the parameters V_a , V_b , and V_c are shown in Table 3, these results could be used to analyze the relationships between the canopy leaf area density, detection distance, and the parameters.

Table 3. Laboratory-simulated canopy experimental results.

X_1 (m)	X_2 (m^2m^{-3})	V_a (v)	V_b (v)	V_c (v)
0.90	2.95	1.95	4.51	1.83
0.50	2.95	2.14	5.41	1.96
0.90	5.40	1.94	5.05	1.81
1.25	5.09	1.90	4.11	1.79
1.25	0.79	1.70	2.47	1.65
0.90	2.95	1.94	4.53	1.84
0.90	0.54	1.59	1.97	1.57
0.90	2.95	1.96	4.52	1.82
1.30	2.95	1.86	3.74	1.76
0.55	0.79	1.82	3.62	1.71
0.55	5.09	2.11	5.25	1.92

The regression statistics of canopy leaf area density models based on the three parameters are shown in Table 4. All the coefficient R^2 of the models are larger than 0.90, which means the experimental and predicted values of the three parameters are in good agreement. The p -values are all smaller than 0.05, which means the three canopy leaf area models are significant; meanwhile, only the Lack of Fit p -value of V_c is bigger than 0.05, which means that the canopy leaf area model based on parameter V_c is more suitable for estimating the canopy leaf area density.

Table 4. Analysis of model results.

	V_a (v)	V_b (v)	V_c (v)
p value	0.0005	0.0023	0.0003
R^2	0.97	0.95	0.93
Lack of Fit p value	0.0461	0.0005	0.0722

The analysis of variance of the canopy leaf density model based on V_c is shown in Table 5, the F value of the model is 29.80, and the p -value is 0.0010, which indicate that the mathematical model of the canopy leaf-area density is very significant. The F value of the lack of fit is 13.01, and the p -value is 0.0722, which indicate that the lack of fit of the

canopy density model is not significant. The p -value of $X_1 \times X_2$ is 0.2745, which indicates that $X_1 \times X_2$ is not significant in the mathematical model equation and could be ignored in the model equation.

Table 5. Analysis of variance of the mathematical model based on V_c .

Source	Sum of Squares	df	Mean Square	F Value	p Value
Model	0.12	4	0.024	29.80	0.0010
X_1	0.026	1	0.026	32.24	0.0024
X_2	0.060	1	0.06	73.26	0.0004
$X_1 \times X_2$	1.235×10^{-3}	1	1.235×10^{-3}	1.50	0.2745
X_1^2	4.085×10^{-3}	1	4.085×10^{-3}	4.98	0.0461
X_2^2	0.032	1	0.032	39.33	0.0015
Residual	5.340×10^{-3}	6	8.210×10^{-4}		
Lack of Fit	5.140×10^{-3}	4	1.300×10^{-3}	13.01	0.0722
Pure Error	2.000×10^{-4}	2	1.000×10^{-4}		
Cor Total	0.13	10			

After removing $X_1 \times X_2$ from the mathematical model equation, the new analysis of variance of the canopy leaf-density model based on V_c is shown in Table 6, the F value of the model is 34.01, and the p -value is 0.0003, which indicate that the mathematical model of canopy leaf area density is very significant. The F value of the lack of fit is 12.85, and the p -value is 0.0735, which indicate that the lack of fit of the canopy density model is not significant, and the mathematical model could be used in canopy leaf area density prediction. Based on the above analysis, the model equation is expressed with Equation (11).

$$y = 1.9 - 0.688x_1 + 0.169x_2 + 0.281x_1^2 - 0.021x_2^2 \tag{11}$$

where, y is the value of predicted parameter V_c (V), x_1 is the detection distance (m), and x_2 is the canopy leaf area density (m^2m^{-3}).

Table 6. Analysis of variance of the regression equation.

Source	Sum of Squares	df	Mean Square	F Value	p Value
Model	0.12	4	0.030	34.01	0.0003
X_1	0.026	1	0.026	29.77	0.0016
X_2	0.060	1	0.060	67.57	0.0002
X_1^2	4.085×10^{-3}	1	4.085×10^{-3}	4.59	0.0449
X_2^2	0.032	1	0.032	36.28	0.0009
Residual	5.340×10^{-3}	6	8.900×10^{-4}		
Lack of Fit	5.140×10^{-3}	4	1.285×10^{-3}	12.85	0.0735
Pure Error	2.000×10^{-4}	2	1.000×10^{-4}		
Cor Total	0.13	10			

The scatter plot of the observed versus the predicted parameter V_c from the laboratory-simulated canopy experimental result is shown in Figure 5, which reflects the fitting degree of the mathematical model equation to the experimental data, and the value of predicted parameter V_c was calculated with Equation (11). There is a smaller systematic estimation error between the observed and the predicted parameter V_c , compare with the mean echo voltage parameter used by Nan et al. [23], and there is no systematic underestimation situation in the results shown in Figure 5. Meanwhile, this result showed a stronger linear ($R^2 = 0.96$) than the results in reference [23] ($R^2 = 0.944$), the agreement between the predicted and the observed V_c showed potential for parameter and canopy leaf-area density prediction.

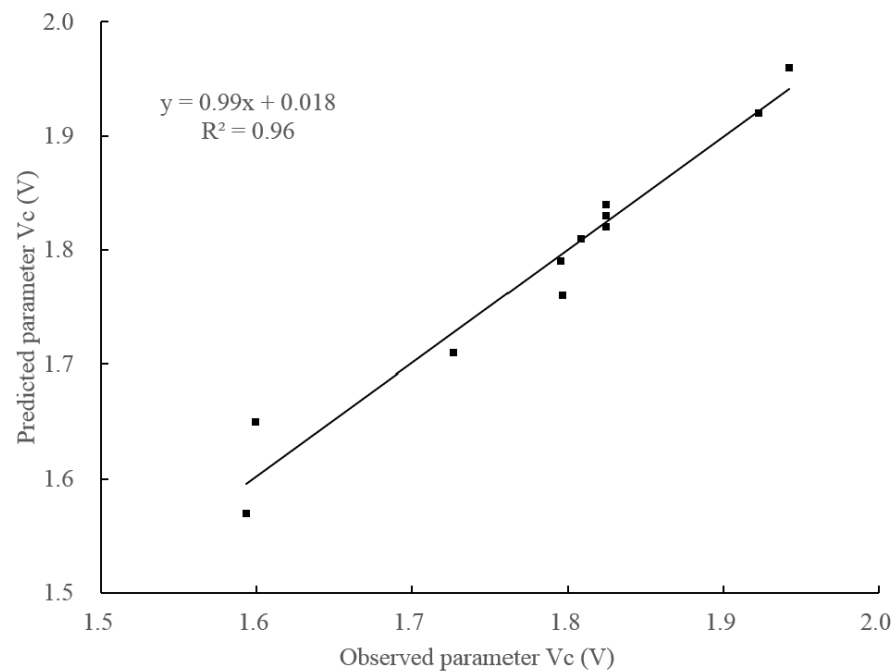


Figure 5. Scatter plot of observed vs. predicted parameter V_c .

3.2. Laboratory-Simulated Canopy Verification Results

The laboratory-simulated canopy verification experiment was carried out, and the results are listed in Table 7. There were nine conditions under three different detection distance and canopy leaf area density, the detection distance range from 0.8 to 1.2 m, the canopy leaf area density ranged from 0.98 to 4.92 m^2m^{-3} , these experimental conditions are consistent with the real situation of some orchard pesticide applications. The relative error between the observed and predicted V_c is listed in Table 7, and the observed V_c values were calculated from the experimental results according to Equation (4), and the predicted V_c values were calculated according to Equation (11). The maximum absolute value of the relative error is 8.61%, the minimum absolute value of relative error is 3.21%, and the absolute value of the mean relative error is 5.37%. The mean relative errors under the detection distance 0.8, 1.0 and 1.2 m conditions are 4.47%, 4.15%, and 2.49%, respectively, and the mean relative errors under canopy leaf-area density 0.98, 2.95, and 4.92 m^2m^{-3} conditions are 6.29%, -0.99% , and 5.82%, respectively.

Table 7. Laboratory-simulated canopy verification experiment results.

Detection Distance (m)	Canopy Leaf Area Density (m^2m^{-3})	Predicted V_c (V)	Observed V_c (V)	Relative Error
0.8	0.98	1.67	1.60	4.37%
1.0	0.98	1.64	1.51	8.61%
1.2	0.98	1.62	1.53	5.88%
0.8	2.95	1.85	1.77	4.52%
1.0	2.95	1.81	1.87	-3.21%
1.2	2.95	1.79	1.87	-4.28%
0.8	4.92	1.85	1.77	4.52%
1.0	4.92	1.82	1.70	7.06%
1.2	4.92	1.80	1.70	5.88%

Zhai et al. [22] established the model equation for canopy-density estimation through similar laboratory-simulated canopy experiments, and the results showed that the maximum and minimum absolute value of relative error are 29.92% and 1.23%, respectively, and the absolute value of the mean relative error was 13.4%. Compared to the results

from reference [22], the maximum absolute value, mean value, and value variable based on parameter V_c are much smaller. These results indicated that the equation based on parameter V_c has better applicability and accuracy in laboratory-simulated canopy leaf-area density detection.

3.3. Outdoor Tree Canopy Verification Results

The outdoor tree canopy verification experiment was carried out, and the results are listed in Table 8. There were 15 detection points results with different detection distances and canopy leaf-area densities, and the detection distances were calculated by the time difference between the transmitted wave and peak value V_1 , according to the ultrasonic distance measurement principle, and considering the real situation of some orchard pesticide applications. The canopy leaf-area density ranges from 1.80 to 5.88 m^2m^{-3} . The maximum absolute value of the relative error is 14.71%, the minimum absolute value of relative error is 0.56%, and the absolute value of mean relative error is 2.84%.

Table 8. Outdoor tree canopies verification experiment results.

Detection Point	Detection Distance (m)	Canopy Leaf Area Density (m^2m^{-3})	Predicted V_c (V)	Observed V_c (V)	Relative Error
1	1.05	2.11	1.75	1.73	1.36
2	0.88	2.05	1.77	1.76	0.73
3	0.90	2.63	1.81	1.65	9.32
4	1.06	3.27	1.82	1.83	-0.79
5	1.04	1.80	1.72	2.02	-14.71
6	1.02	5.60	1.78	1.84	-3.27
7	1.11	4.71	1.81	1.91	-5.25
8	1.11	5.28	1.79	1.82	-1.91
9	1.10	5.88	1.75	1.76	-0.56
10	1.11	5.41	1.78	1.92	-7.03
11	1.02	4.82	1.82	1.93	-6.04
12	1.04	5.38	1.79	1.82	-1.46
13	1.08	4.71	1.82	1.99	-8.56
14	1.07	4.82	1.81	1.86	-2.36
15	1.11	5.40	1.78	1.82	-2.06

Nan et al. [23] conducted similar outdoor tree-canopy detection experiments with different model equations, and the results showed that the maximum and minimum absolute value of relative error are 35.5% and 0.23%, respectively, and the absolute value of mean relative error is 15.7%. Compared with the results from reference [23], the maximum absolute value, mean value, and value variable based on parameter V_c are much smaller. The outdoor tree canopy verification experiments also proved that the equation based on parameter V_c has better applicability and accuracy in tree canopy leaf-area density detection.

As shown in Table 8, these results verified the accuracy and applicability of the model equation based on parameter V_c , and indicated that the model equation has good potential in canopy leaf-area density prediction and detection for pesticide application in orchards.

4. Discussion

Previous researchers studied and verified the quantitative relationship between the canopy characteristics and the ultrasonic echo signals, compared with the previous method of canopy leaf area-density detection in reference [19,22,23], this article studied new parameters for the detection and prediction of canopy leaf-area density based on the peaks value of an ultrasonic echo signal. Some previous articles demonstrated that the ultrasonic echo signal was affected by the detection distance and canopy leaf-area density, the peaks in the echo signal were affected and caused by the canopy targets, such as leaves and branches, and the ultrasonic multiple reflection phenomenon was confirmed and studied before. In order to study the detail of the echo signal, Ou et al. [24] proposed a new theory

about canopy thickness detection and verified the canopy-thickness calculation formula; the results proved that the peaks in the echo signal were caused by the ultrasonic multiple reflection phenomenon on the ultrasonic waves propagation path, the peaks indicated that the leaves, branches, or other objects when the ultrasonic sensor was used in canopy detection, this ultrasonic multiple reflection phenomenon provided the theoretical basis for the canopy information detection with ultrasonic sensor.

Previous researchers used average or time-domain parameters of the ultrasonic echo signal in the canopy leaf-area density estimation equations; nevertheless, they require the identification of the echo signal boundary and to process more voltage data out of the echo signal. Considering the theory basis of echo signal in canopy detection, this article proposed parameter V_a , V_b and V_c , which are directly calculated by ultrasonic echo peaks for canopy leaf-area density estimation. Compared with the parameters calculated with a whole ultrasonic echo signal, parameters V_a , V_b , and V_c require fewer signal data and could be suitable in real-time detection. The orthogonal regression analysis of the parameters based on laboratory-simulated canopy experiments showed that the model equation based on parameter V_c is significantly more suitable for canopy leaf-area density estimation, and the interaction factor of the detection distance and the canopy leaf-area density has no significant influence on the parameter V_c prediction. The scatter plot of the observed versus predicted parameter V_c from the laboratory-simulated canopy experiment proved that the predicted and the observed parameter V_c were in good agreement within the experimental conditions.

The laboratory-simulated canopy leaf area density verification results showed that Equation (11) could be used to predict parameter V_c within a good accuracy, the absolute value of the mean relative error is 5.37%, and the maximum absolute value of the relative error is 8.61%. The mean relative errors under the canopy leaf-area density of 0.98 and 4.92 m^2m^{-3} conditions are 6.29% and 5.82%, respectively, which are larger than the mean relative error under 2.95 m^2m^{-3} , this is a result of the ultrasonic wave penetration effect, and the leaves on the ultrasonic waves propagation path have major and complex influences on parameter prediction. When the canopy leaf area density is lower, the ultrasonic wave will pass through the canopy, and when the canopy leaf area density is higher, the penetration distance of the ultrasonic wave is smaller than the canopy thickness, and the ultrasonic echo signal in lower or higher canopy leaf-area density has different reflection characteristics, and the penetration distance changes are mainly affected by the canopy leaf area density.

The outdoor tree canopy leaf area density verification results showed that the absolute value of mean relative error is 2.84%, which is lower than the laboratory-simulated canopy verification result. The maximum absolute value of relative error is 14.71%, which is larger than the laboratory-simulated canopy verification result, which could result from the branches in the tree canopy, which were different from the laboratory-simulated canopy conditions. The branches in the tree canopy will also cause some echo peaks in the ultrasonic echo signal. Even though the ultrasonic echo signal intensity is basically affected by the size of the obstacle in the ultrasonic wave's propagation path, the shape difference between the leaves in the laboratory and field experiments could also cause some additional data errors. For specific target crop detection, the shape characteristics of the leaves could be considered in the model-building experiments. For agriculture pesticide application, these errors are acceptable to some extent, and these results showed good applicability in canopy leaf-area density detection for *Osmanthus* trees.

Compared with the previous verification results from reference [22,23], the maximum absolute value, mean value, and value variable based on parameter V_c are much smaller than the previous results in reference [22,23]. These results indicated that the equation based on parameter V_c has better applicability and accuracy in canopy leaf-area density detection.

This article analyzed and established the mathematical model equations for canopy leaf-area density detection with an ultrasonic sensor and studied the relative errors under laboratory-simulated canopy and outdoor trees conditions, and the results showed that the model equations based on parameter V_c have a good accuracy and applicability for

real-time canopy leaf-area density estimation in the pesticide application field. For the next development plan, the variable-rate spray system based on the canopy leaf area density detection using ultrasonic sensors is available, and in order to achieve higher accuracy, the leaf area and branch factors should also be considered and studied in future experiments.

5. Conclusions

This article proposed and analyzed three new parameter model equations for canopy leaf-area density estimation, the orthogonal regression experiment based on laboratory-simulated canopy indicated that the model equation based on parameter V_c is suitable for parameter and canopy leaf area density predictions.

The laboratory-simulated canopy and outdoor tree canopy leaf area density verification experiments were carried out within the designed conditions, and these results indicated that the absolute value of the mean relative error is 5.37% in the laboratory-simulated canopy experiment and 2.84% in the outdoor tree experiment, and the maximum absolute value of the relative error is 8.61% in the laboratory-simulated canopy experiment and 14.71% in the outdoor tree experiment, these results proved the applicability of this model equation for pesticide application detection.

The laboratory-simulated canopy verification experiment showed that the relative errors were affected by leaf area density, and the relative errors became larger under higher and lower density conditions; nevertheless the relative error values are acceptable in practice. When using the model building method proposed in this article, it is recommended to consider the characteristics of the target plant species and the leaves, which will improve the accuracy of the model building.

According to the studies above, the model equation based on parameter V_c showed better potential and accuracy for canopy leaf-area density estimation than previous model equations. The previous study demonstrated that the peak values in an ultrasonic echo signal could be used in canopy thickness estimation within an acceptable accuracy [24]. These studies revealed the ultrasonic wave multiple reflection phenomenon and law in canopy detection and proved that the echo peaks are mostly caused by the leaves and branches in the canopy.

This study established and proved the mathematical models of canopy leaf-area density detection using an ultrasonic sensor and expanded the capability and function of ultrasonic sensors in agriculture pesticide applications. For future research, considering both the canopy thickness and leaf-area density information could be calculated from ultrasonic echo peaks with good accuracy, combining ultrasonic detection and variable-rate spray systems in advanced orchard sprayer development will be one of the most effective ways to reduce chemical usage in orchard management.

Author Contributions: Conceptualization, M.O. and W.J.; methodology, M.O., T.H., M.H., S.Y., M.W., L.J. and X.W.; validation, M.O. and X.D.; formal analysis, T.H., M.H. and S.Y.; data curation, T.H., M.H. and S.Y.; writing—original draft preparation, T.H., M.H. and S.Y.; writing—review and editing, M.O., T.H., M.H. and S.Y.; supervision, M.O. and W.J.; funding acquisition, M.O. and W.J. All authors have read and agreed to the published version of the manuscript.

Funding: This work was funded by the Project of Faculty of Agricultural Equipment of Jiangsu University (grant number NZXB20200204, NZXB20210101), the Jiangsu Agriculture Science and Technology Innovation Fund (JASTIF) (CX(20)3065).

Institutional Review Board Statement: Not applicable.

Informed Consent Statement: Not applicable.

Data Availability Statement: The data are available within the article.

Acknowledgments: The authors thank Faculty of Agricultural Equipment of Jiangsu University and the High-tech Key Laboratory of Agricultural Equipment and Intelligence of Jiangsu Province for the facilities and support.

Conflicts of Interest: The authors declare no conflict of interest.

References

- Appah, S.; Jia, W.; Ou, M.; Wang, P.; Asante, E.A. Analysis of Potential Impaction and Phytotoxicity of Surfactant-Plant Surface Interaction in Pesticide Application. *Crop Prot.* **2020**, *127*, 104961. [[CrossRef](#)]
- Lu, X.; Garcia-Ruiz, F.; Fabregas, F.X. Pesticide dose based on canopy characteristics in apple trees: Reducing environmental risk by reducing the amount of pesticide while maintaining pest and disease control efficacy. *Sci. Total Environ.* **2022**, *826*, 154204. [[CrossRef](#)]
- Abbas, I.; Liu, J.; Faheem, M.; Noor, R.S.; Shaikh, S.A.; Solangi, K.A.; Raza, S.M. Different Sensor Based Intelligent Spraying Systems in Agriculture. *Sens. Actuators Phys.* **2020**, *316*, 112265. [[CrossRef](#)]
- Nan, Y.; Zhang, H.; Xu, Y.; Jiao, X.; Zheng, J.; Liu, D. Research progress on profiling target spray and its control technology in agriculture and forestry. *World For. Res.* **2018**, *31*, 54–58.
- Salcedo, R.; Zhu, H.; Jeon, H.; Ozkan, E.; Wei, Z.; Gil, E. Characterisation of activation pressure, flowrate and spray angle for hollow-cone nozzles controlled by pulse width modulation. *Biosyst. Eng.* **2022**, *218*, 139–152. [[CrossRef](#)]
- Jeon, H.Y.; Zhu, H. Development of a Variable-Rate Sprayer for Nursery Liner Applications. *Trans. ASABE* **2012**, *55*, 303–312. [[CrossRef](#)]
- Dou, H.; Zhang, C.; Li, L.; Hao, G.; Ding, B.; Gong, W.; Huang, P. Application of Variable Spray Technology in Agriculture. *IOP Conf. Ser. Earth Environ. Sci.* **2018**, *186*, 012007. [[CrossRef](#)]
- Mäkelä, H.; Pekkarinen, A. Estimation of Forest Stand Volumes by Landsat TM Imagery and Stand-Level Field-Inventory Data. *For. Ecol. Manag.* **2004**, *196*, 245–255. [[CrossRef](#)]
- Carreiras, J.M.B.; Pereira, J.M.C.; Pereira, J.S. Estimation of Tree Canopy Cover in Evergreen Oak Woodlands Using Remote Sensing. *For. Ecol. Manag.* **2006**, *223*, 45–53. [[CrossRef](#)]
- Solanelles, F.; Escolà, A.; Planas, S.; Rosell, J.R.; Camp, F.; Gràcia, F. An Electronic Control System for Pesticide Application Proportional to the Canopy Width of Tree Crops. *Biosyst. Eng.* **2006**, *95*, 473–481. [[CrossRef](#)]
- Giles, D.K.; Klassen, P.; Niederholzer, F.J.A.; Downey, D. “Smart” Sprayer Technology Provides Environmental and Economic Benefits in California Orchards. *Calif. Agric.* **2011**, *65*, 85–89. [[CrossRef](#)]
- Rosell Polo, J.R.; Sanz, R.; Llorens, J.; Arnó, J.; Escolà, A.; Ribes-Dasi, M.; Masip, J.; Camp, F.; Gràcia, F.; Solanelles, F.; et al. A Tractor-Mounted Scanning LIDAR for the Non-Destructive Measurement of Vegetative Volume and Surface Area of Tree-Row Plantations: A Comparison with Conventional Destructive Measurements. *Biosyst. Eng.* **2009**, *102*, 128–134. [[CrossRef](#)]
- Rosell, J.R.; Llorens, J.; Sanz, R.; Arnó, J.; Ribes-Dasi, M.; Masip, J.; Escolà, A.; Camp, F.; Solanelles, F.; Gràcia, F.; et al. Obtaining the Three-Dimensional Structure of Tree Orchards from Remote 2D Terrestrial LIDAR Scanning. *Agric. For. Meteorol.* **2009**, *149*, 1505–1515. [[CrossRef](#)]
- Asaei, H.; Jafari, A.; Loghavi, M. Site-Specific Orchard Sprayer Equipped with Machine Vision for Chemical Usage Management. *Comput. Electron. Agric.* **2019**, *162*, 431–439. [[CrossRef](#)]
- Llorens, J.; Gil, E.; Llop, J.; Escolà, A. Ultrasonic and LIDAR Sensors for Electronic Canopy Characterization in Vineyards: Advances to Improve Pesticide Application Methods. *Sensors* **2011**, *11*, 2177–2194. [[CrossRef](#)]
- Jeon, H.Y.; Zhu, H.; Derksen, R.C.; Ozkan, H.E.; Krause, C.R.; Fox, R.D. Performance Evaluation of a Newly Developed Variable-Rate Sprayer for Nursery Liner Applications. *Trans. ASABE* **2011**, *54*, 1997–2007. [[CrossRef](#)]
- Tewari, V.K.; Chandel, A.K.; Nare, B.; Kumar, S. Sonar Sensing Predicated Automatic Spraying Technology for Orchards. *Curr. Sci.* **2018**, *115*, 1115–1123. [[CrossRef](#)]
- Tumbo, S.D.; Salyani, M.; Whitney, J.D.; Wheaton, T.A.; Miller, W.M. Investigation of laser and ultrasonic ranging sensors for measurements of citrus canopy volume. *Appl. Eng. Agric.* **2002**, *18*, 367–372. [[CrossRef](#)]
- Palleja, T.; Landers, A.J. Real Time Canopy Density Estimation Using Ultrasonic Envelope Signals in the Orchard and Vineyard. *Comput. Electron. Agric.* **2015**, *115*, 108–117. [[CrossRef](#)]
- Palleja, T.; Landers, A.J. Real Time Canopy Density Validation Using Ultrasonic Envelope Signals and Point Quadrat Analysis. *Comput. Electron. Agric.* **2017**, *134*, 43–50. [[CrossRef](#)]
- Gil, E.; Escolà, A.; Rosell, J.R.; Planas, S.; Val, L. Variable Rate Application of Plant Protection Products in Vineyard Using Ultrasonic Sensors. *Crop Prot.* **2007**, *26*, 1287–1297. [[CrossRef](#)]
- Li, H.; Zhai, C.; Weckler, P.; Wang, N.; Yang, S.; Zhang, B. A Canopy Density Model for Planar Orchard Target Detection Based on Ultrasonic Sensors. *Sensors* **2017**, *17*, 31. [[CrossRef](#)] [[PubMed](#)]
- Nan, Y.; Zhang, H.; Zheng, J.; Bian, L.; Li, Y.; Yang, Y.; Zhang, M.; Ge, Y. Estimating Leaf Area Density of Osmanthus Trees Using Ultrasonic Sensing. *Biosyst. Eng.* **2019**, *186*, 60–70. [[CrossRef](#)]
- Zhou, H.; Jia, W.; Li, Y.; Ou, M. Method for Estimating Canopy Thickness Using Ultrasonic Sensor Technology. *Agriculture* **2021**, *11*, 1011. [[CrossRef](#)]

Review

Development Status and Research Progress of a Tractor Electro-Hydraulic Hitch System

Xiaoxu Sun ¹, Zhixiong Lu ^{1,*}, Yue Song ¹, Zhun Cheng ², Chunxia Jiang ³, Jin Qian ¹ and Yang Lu ¹¹ College of Engineering, Nanjing Agricultural University, Nanjing 210031, China² Department of Vehicle Engineering, Nanjing Forestry University, Nanjing 210037, China³ College of Mechanical Engineering, Anhui Science and Technology University, Chuzhou 233100, China

* Correspondence: luzx@njau.edu.cn; Tel.: +86-13951715780

Abstract: A tractor electro-hydraulic hitch system is considered one of the most important systems that play a strategic role in the power transmission and operation depth control of a tractor's field operation. Its performance directly affects the operation quality of the whole work unit of the tractor. Furthermore, a tractor electro-hydraulic hitch system has gained the interest of many in the agricultural machinery sector because of its stable performance, high production efficiency, good operation quality and its low energy consumption. To fully benefit from the potential of the tractor electro-hydraulic hitch system, it is significant to understand and address the problems and challenges associated with it. This study, therefore, aims to contribute to the development of the tractor electro-hydraulic hitch system by investigating the research methods, technical characteristics and emerging trends in three key aspects that include the tillage depth adjustment method, the tillage depth control algorithm and the core components of the electro-hydraulic hitch system. The characteristics and applicable conditions of the different tillage depth adjustment methods of the electro-hydraulic hitch system were summarized. The realization methods and the control characteristics of the different algorithms were elaborated and discussed for both the PID control algorithm and the intelligent control algorithm. The working characteristics of the core components of the electro-hydraulic hitch system were analyzed based on the hydraulic control valves and sensing elements. The results have shown that the multi-parameter tillage depth adjustment method met the operation quality standard while taking the engine load stability and traction efficiency into account, and it has a greater research significance and value. The working quality can be improved effectively by introducing the intelligent algorithm. In addition, the study of smart valves with built-in sensing elements and how to improve the anti-interference ability of sensing elements, are the aspects that requires further consideration. Aiming to improve the working quality and reduce energy consumption, further research into the tractor electro-hydraulic hitch system is necessary. The results of this comprehensive review provide a reference for the intelligent operation of tractors under the precision agriculture.

Citation: Sun, X.; Lu, Z.; Song, Y.; Cheng, Z.; Jiang, C.; Qian, J.; Lu, Y. Development Status and Research Progress of a Tractor Electro-Hydraulic Hitch System. *Agriculture* **2022**, *12*, 1547. <https://doi.org/10.3390/agriculture12101547>

Academic Editors: Muhammad Sultan, Redmond R. Shamshiri, Md Shamim Ahamed, Muhammad Farooq and Jiyu Li

Received: 31 August 2022

Accepted: 21 September 2022

Published: 25 September 2022

Publisher's Note: MDPI stays neutral with regard to jurisdictional claims in published maps and institutional affiliations.



Copyright: © 2022 by the authors. Licensee MDPI, Basel, Switzerland. This article is an open access article distributed under the terms and conditions of the Creative Commons Attribution (CC BY) license (<https://creativecommons.org/licenses/by/4.0/>).

Keywords: tractor; electro-hydraulic hitch system; tillage depth adjustment; tillage depth control algorithm; key components

1. Introduction

Precision agriculture is a modern agricultural management concept developed in the 1990s, based on a series of high-tech technologies, such as modern information technology, biotechnology and engineering equipment technology. It has great advantages in improving the agricultural output, making efficient use of agricultural resources, promoting agricultural sustainable development and protecting the ecological environment [1,2]. Among these, engineering equipment technology plays an important role as the premise and basis for realizing the whole system of precision agriculture [3,4]. A tractor hitch system is the core component to complete the connection between the tractor and the agricultural machinery. On the one hand, it transmits the power of the tractors, and on

the other hand, it performs the lifting and attitude control of the agricultural machinery. The tractor completes different field operations and uses different machinery to complete different field operations through the use of the hitch system. The plough unit, combined with the suspension plough, is a typical example. With the development of electromechanical integration technology, electro-hydraulic proportional control technology, sensing technology, CAN bus technology and microcomputer technology, these technologies are gradually being applied to the tractor hydraulic hitch system, which promotes the transformation of the traditional mechanical hydraulic hitch system into a more intelligent system. However, due to the complexity of the field environment and the diversity of operation types, the tractor causes large disturbances and has a strong nonlinearity in its working process [5,6]. Therefore, there are still many problems in introducing intelligent technology into agricultural production [7,8].

As an indispensable operation in agricultural production, tillage is one of the main reasons for energy consumption [9–11]. Plowing takes up more traction energy than the other operations involved in tilling [12]. Compared with the traditional mechanical hydraulic hitch system, the tractor electro-hydraulic hitch system has more working adjustment modes, which can reduce the energy consumption of the tractor ploughing unit in operation, reduce the use of fuel and improve the operation efficiency [13–15]. In addition, due to the use of the automatic control method of the working depth, combined with the high precision sensor unit, the CAN bus technology and other information technologies eliminate the use of suspension operating handles on the original tractor and these are removed. Therefore, it greatly reduces the labor intensity of drivers, improves the level of intelligence and the automation of tractors, and makes tractors more suitable for the development requirements of fine agriculture, in the future [16,17].

Operation quality is an important index to evaluate the control performance of a tractor electro-hydraulic hitch system. At present, the method of improving the control performance of a tractor electro-hydraulic hitch system by optimizing the control method, has been widely criticized. Based on the analysis of the development status and research progress of the tractor electro-hydraulic hitch system in the world, this study aims to contribute to the development of the tractor electro-hydraulic hitch system by investigating the research methods, technical characteristics and emerging trends in three key aspects, including the tillage depth adjustment method, the tillage depth control algorithm and the core components of the electro-hydraulic hitch system. Different adjustment methods can meet the complex constraints of the working terrain and soil conditions in different regions. Using modern control theory and technology to control the operation depth, is conducive to improving the response performance of the control system. In addition, the continuous development of modern sensor detection technology and valve control technology are important means to accomplish the real-time feedback and precise control. The integration of the abovementioned technologies contributes greatly to the improvement of the operation quality and the reduction of energy consumption.

The goal of this study was to comprehensively review the existing literature related to the tractor electro-hydraulic hitch system and its key technologies. This article was based on the following aspects and organized as follows. Section 2 states the research status of the tractor electro-hydraulic hitch system at home and abroad, commenting on different types of tractor electro-hydraulic hitch systems. Then, Sections 3 and 4 discuss the development status of the different tillage depth adjustment methods and the tillage depth control algorithms. Section 5 provides a review of the key components of the tractor electro-hydraulic hitch system. Finally, in Section 6, the future development trends are given for the tractor electro-hydraulic hitch system.

2. Development Status of the Tractor Electro-Hydraulic Hitch System

In the early days, tractors completed operations through agricultural tools with traction units. Prior to 1933, the Irish scholar Harry Ferguson invented the three-point hitch device that has been widely recognized all over the world. The system is still being used and has

become the standard in the industry [18]. The traditional mechanical hydraulic hitch system is a mechanical-hydraulic integrated product which makes full use of the characteristics and advantages of the hydraulic transmission. The driver adjusts the position of the distributor by operating the handle to control the direction and flow of the hydraulic oil to adjust the lifting and lowering of the agricultural machinery. It has the advantages of low design and manufacturing costs [19,20]. The structure principle is shown in Figure 1.

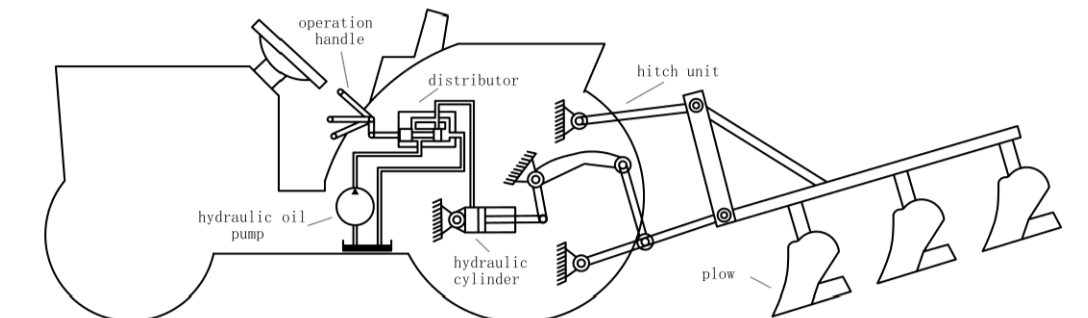


Figure 1. The structure principle of the traditional mechanical hydraulic hitch system.

However, due to the complex structure of the system, it is not only difficult to assemble, but also difficult to maintain once damage occurs. Furthermore, because of the deformation of the mechanical mechanism and the hysteresis of the elastic element itself, it is unable to ensure a good quality of operation, and does not adapt to the developing trend of precision agriculture. With the development and maturity of electronic technology and microcomputer technology, scholars in China and abroad began to study the tractor based on the integrative technology of mechanics-electrics-hydraulics. The traditional mechanical hydraulic hitch system is gradually being replaced by the modern electro-hydraulic hitch system. Figure 2 shows the structural principle of the modern electro-hydraulic hitch system.

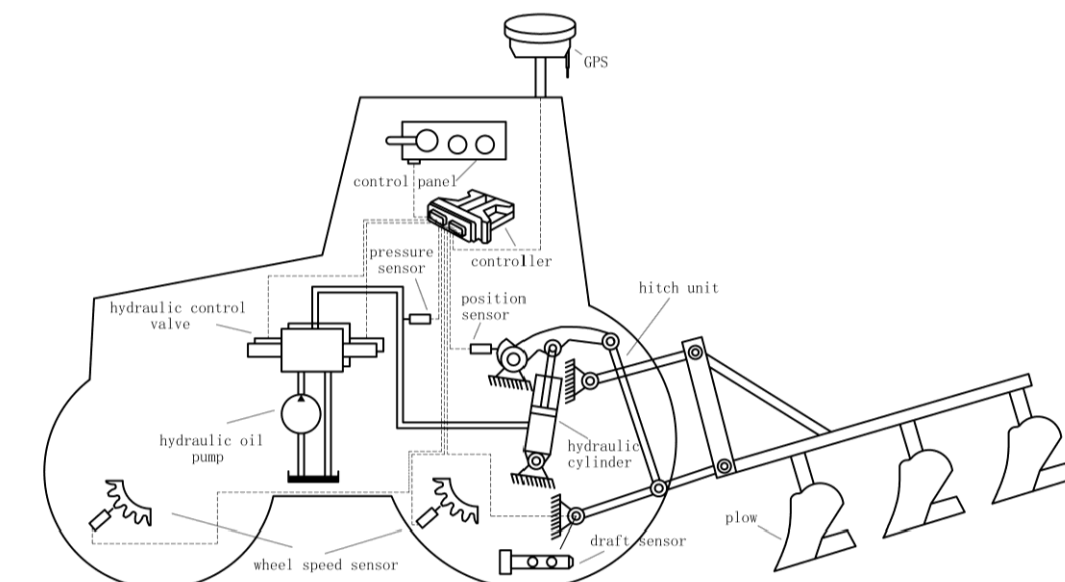


Figure 2. The structure principle of the modern electro-hydraulic hitch system.

2.1. Basic Types of Hitch Systems

The tractor hitch system is mainly composed of an oil pump, a distributor (hydraulic control valve) and a hydraulic cylinder. According to the installation positions of the three

main hydraulic components, they are divided into three types: split type, integral type and semi-split type [21]. Table 1 shows the comparison of the different hitch systems

Table 1. Comparison of different hitch systems.

Type	Layout Characteristics	Advantages	Disadvantages	Application of the Tractor
Split	Pumps, distributors (hydraulic control valves) and cylinders are installed at different locations	Flexible layout, Easier maintenance, Easy to be standardized	Complex connection pipeline, Easy to leak	Dongfanghong-75 (YTO, Luoyang, China) TN-55 (TT, Tianjin, China) M1304-R (LOVOL, Weifang, China)
Semi-split	Distributor (hydraulic control valve) and cylinder installed together, pump arranged separately	Compact structure	Inconvenient to fault check	TM130 (New Holland, WI, USA) 800 (CF, Changzhou, China)
Integral	Oil pump, distributor (hydraulic control valve) and oil cylinder are installed together	Compact structure, good sealing	Complex structure, big volume, Difficult to standardize	T8000 (New Holland, WI, USA) 35 (FS, Shanghai, China)

2.2. Development Status of the Electro-Hydraulic Hitch System in Foreign Countries

Foreign scholars began to study the electro-hydraulic hitch system in the 1970s. In 1978, Germany's Mercedes Benz first applied the electro-hydraulic hitch system to its agricultural tractor, marking the successful application of the electro-hydraulic control technology in the field of agriculture [22]. Subsequently, the Toshiba Corporation of Japan developed an IC electro-hydraulic hitch control system with the position regulation function. This system can not only adjust the depth of the rotary tillage operation, but also automatically adjusts the posture of the agricultural machinery in order to reduce the influence of the left and right tilts of the agricultural tools on the quality of its operation [23]. In 1986, Bosch developed the CAN bus technology and for the first time it was applied to the tractor control system by Scarlett in the early 1990s, which effectively improved the quality of the tillage depth and reduced the operating intensity of the tractor drivers [24,25]. Major foreign universities have also conducted in-depth research into the electro-hydraulic hitch system, they have designed electro-hydraulic hitch systems to meet different needs, and have verified the feasibility of their design scheme through experiments. For instance, Kyoto University in Japan, the University of the Witwatersrand in South Africa and The Technical University of Braunschweig in Germany [26–28].

The tractor electro-hydraulic hitch systems designed in foreign countries after years of development, have formed a more mature product. Major companies such as Bosch–Rexroth [29], Walvoil [30] and Danfoss [31] have launched similar electro-hydraulic hitch systems. At present, the leading position in the foreign market is the tractor electro-hydraulic hitch control system (EHC) introduced by Bosch–Rexroth. This system is mainly composed of a controller, operating panel, hydraulic pump, hydraulic cylinder and a solenoid valve. With a wheel speed sensor, force sensor, displacement sensor, pressure sensor, radar and other sensors. Each electronic control unit on the tractor transmits data through the CAN bus, which makes the tractor have a high operation efficiency and good operation coordination ability. This system meets various functions such as force control, position control, pressure control, slip rate control and force-position integrated control. Drivers only need to select the appropriate working mode through the operating panel according to the actual operating requirements. Experiments show that compared with the existing mechanical hydraulic control system, the slip rate achieved using the EHC system is reduced by 7–30%, the energy consumption of the whole machine is reduced by 2–3% and the work efficiency is improved by 3.4–3.8% [18]. Therefore, at present, most tractors in western countries have applied the system from companies such as John Deere, DEUTZ, New Holland, etc.

2.3. Development Status of the Electro-Hydraulic Hitch System in China

Due to the late start of the tractor industry in China, the tractor hitch technology is relatively backward. In the 1980s, foreign famous brands of tractors, such as John Deere, Fiat and so on, were introduced in China. The tractor hitch technology in China has since improved. Following the 1990s, with the rapid development of electronic technology, many universities in China began to study the electro-hydraulic hitch system of tractors.

Zhan et al. [32] used a single chip microcomputer for the control of the tractor hitch system. Taking the tractor ploughing unit as the research object, the mathematical model of each part was established, and the simulation operation was completed. In this study, several problems regarding the digital simulation of the tractor electro-hydraulic hitch system through the use of a microcomputer were discussed. Fang et al. [33] changed the valve core of the Jangsu-50 tractor (YTO, Luoyang, China) distributor into an electromagnetic drive and established a closed-loop feedback control system by installing angle sensors. The accuracy of the control system was proved using the comparison test with the traditional mechanical feedback system.

In the 21st century, more new technologies, such as electronic technology and computer control technology, have been applied to the tractor electro-hydraulic suspension system. China has achieved fruitful results in the study of the tractor electro-hydraulic suspension control system. Xie et al. [34] reformed the traditional mechanical hydraulic hitch system, replaced the distributor with electro-hydraulic proportional valve and achieved the digital control through a single chip microcomputer. The good performance of the improved suspension system was verified through an experiment. Later, Xie et al. [35] also carried out the research on the application of the CAN bus in the electro-hydraulic hitch system. At the same time, large tractor enterprises in China also carried out a series of studies for the tractor hitch system. For example, YTO, Lovol and Dongfeng et al. have launched intelligent tractor products with a variety of working modes. The technical characteristics of the hydraulic suspension type of some tractors are shown in Table 2.

Table 2. Types and Technical Characteristics of Hydraulic Suspension Systems in China.

Model	Company	Type	Adjustment Mode	Maximum Lifting Force (kN)
M604-E	LOVOL	semi-split	Position, Draft, Mixed draft-position adjustment	≥ 10.1
LF1504	YTO	semi-split	Position, Draft, Height, Mixed draft-position adjustment	≥ 28
M2204-R	LOVOL	split	Position, Height, adjustment	≥ 39
CFK1804	Changfa	split	Position, Draft, Height, Mixed draft-position adjustment	≥ 42

3. Research Progress into the Tillage Depth Adjustment Methods

Due to the complexity and diversity of the tractor field working environment, it is often necessary to adjust the tillage depth repeatedly to obtain a stable and uniform tillage depth. Therefore, the development of the tillage depth adjustment method is a necessary means to obtain an accurate and efficient adjustment. In the early stage, the mechanical hydraulic hitch system was generally adjusted manually by adjusting the operating handle, which was not only inefficient but also poor in quality. With the development of the electro-hydraulic hitch system, the tillage depth adjustment method has gradually changed from the manual adjustment to the automatic adjustment. Currently, there are three major ways to adjust a tractor's tillage depth: by a single parameter adjustment, mixed draft-position adjustment and mixed draft-position-slip adjustment.

3.1. Method of the Single Parameter Adjustment

The single parameter adjustment method adjusts the position of the three-point hitch device with a single parameter as the main control index, so as to obtain the desired effect. This way can be well targeted for different terrain characteristics. At present, there are two kinds of single parameter adjustment methods: the position adjustment and the draft adjustment.

According to the position regulation principle of the tractor electro-hydraulic hitch system, Chen et al. [36] designed the position regulation controller based on a microcontroller and a displacement sensor and verified it on the simulation test bench. The experimental results showed that the system had an anti-disturbance ability and could achieve automatic control. However, this study only carried out the position adjustment control in the simulation state, and the control effect needs further experimental verification [36]. Based on the CAN bus technology, Zhang et al. [37] proposed an adjustment scheme with the PLC as the core, according to the technical requirements of the system. In order to verify the feasibility of the scheme, the lifting and lowering experiments were carried out by using Simulink. However, the simulation test condition in this study were too ideal to consider the interference problem in the actual operation process. In addition, Lee et al. [38,39] and Xia et al. [40], based on the displacement sensor feedback of the tillage depth for the position adjustment, also increased the inclination sensor to measure the attitude of the farm tool. In the study by Xia et al. [40], the test results showed that the maximum coefficient of variation of the tillage depth under each working condition was 4.28%. This method had a good correction effect on the tillage depth error caused by uneven road surfaces.

Hao et al. [41] built a tractor electro-hydraulic hitch system model based on AMESIM and ADAMS. The force regulation simulation was carried out under soil disturbance conditions. The simulation results showed that the adjustment error of the hitch system is within 1.7%. It provided a reference for the construction of the joint simulation platform. However, the accuracy of the simulation model still lacks verification. Chen et al. [42], Wang et al. [43] and Xu et al. [44] analyzed the advantages and disadvantages of the original mechanical hydraulic hitch system with the draft adjustment method, proposed the draft adjustment scheme of the electro-hydraulic hitch system based on a single chip microcomputer, and built the indoor bench to test and verify the feasibility of the scheme. However, due to the limited conditions, there was a certain deviation between the simulated loading and the actual working conditions of the loading system, which needs to be further improved, according to the field test. Zhang et al. [45] studied the prediction of the tillage resistance in the process of the draft adjustment. Aiming at the problem of a low prediction accuracy of the tillage resistance in the process of the draft adjustment, the nonlinear modeling method based on ANFIS was used to construct the prediction model of the tillage resistance in the process of operation, and the adaptive adjustment was realized. The accuracy of the method was verified by field experiments.

3.2. Method of the Mixed Draft-Position Adjustment

The mixed draft-position adjustment is a comprehensive adjustment method that combines the uniformity of the tillage depth of position adjustment and the stability of the engine traction load with the draft adjustment. At present, the mixed draft-position adjustment method generally adopts two forms, the switching method and the weighted coefficient method. The former allows to switch between the position adjustment and the draft adjustment, according to soil changes, and the latter adds the two adjustment methods according to a certain weight.

Shang et al. [46] applied the switching method and the weighted coefficient method to the comprehensive adjustment of the force and position. Through a simulation verification, it was concluded that the weighted coefficient method had more long-term research and application value. Zhao et al. [47], Xu et al. [48] and Guo et al. [49] studied the weight coefficient of the mixed draft-position adjustment method, but they were limited to the comparative analysis of the artificially set weight coefficient.

Li [50] proposed a mixed draft-position adjustment scheme with variable weights (Figure 3). In the adjustment process, the weight of the initial draft adjustment was preset by the driver, and then the weight was corrected according to the actual operation situation. In the areas with uniform soil change, the weight of the draft adjustment is reduced to ensure the tillage quality of tractors. Conversely, the weight is increased to ensure that the tractor

can pass in the areas with large soil changes. The effectiveness of the scheme was verified by simulation and experiment. However, since the initial weight and weight adjustment of the scheme still need to be set manually by the driver, the adjustment efficiency is not high.

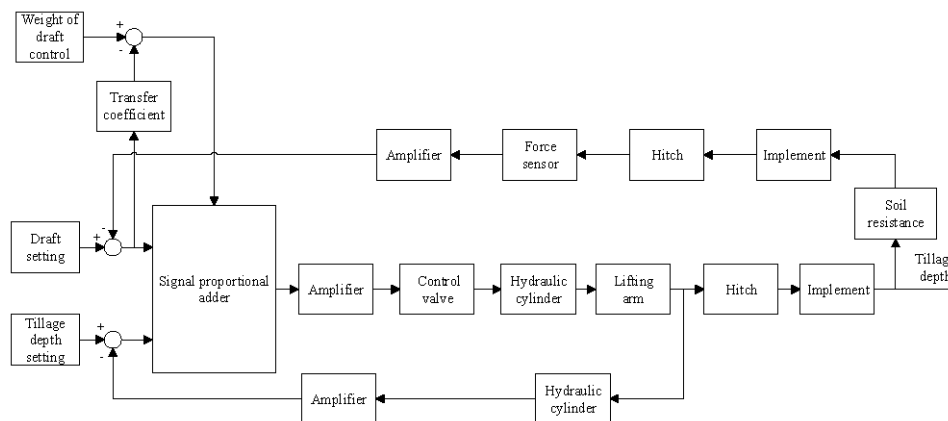


Figure 3. Mixed draft–position adjustment scheme with variable weights.

Based on the consideration of the influence of the soil specific resistance on the weight coefficient, Wang et al. [51] established the relationship model between the weight coefficient and the soil specific resistance. Then, a variable weight mixed draft-position adjustment method based on the soil specific resistance was designed. According to the simulation data and a large number of field operations, the approximate relationship between the weight coefficient and the soil specific resistance was obtained. This method can automatically adjust the weight coefficient according to the soil specific resistance, which improves the operation effect of the tractors in areas with large changes in soil specific resistance.

3.3. Method of the Mixed Draft-Position-Slip Adjustment

The three-parameter comprehensive adjustment of the draft-position-slip is a kind of adjustment method that introduces the sliding rate on the basis of the mixed draft-position adjustment. On the one hand, this method can obtain a stable power output on the basis of ensuring the tillage depth uniformity; on the other hand, because of the high traction efficiency of the tractor, it can obtain a good fuel economy [52]. At present, there are two forms of the method of the mixed draft-position-slip adjustment, the weighted coefficient method and the logic threshold method.

Gao [53] designed a three-parameter comprehensive adjustment scheme based on the weight coefficient method. The adjustment logic is shown in the Figure 4. In his research, the output of the draft-position adjustment and the slip adjustment were weighted according to a certain proportion to form a total output. Adjusting the weight of the two ratios can change the ratio of resistance, position and slip in the adjustment process. The proportion of the draft, the position and the slip involved in the adjustment process can be changed by adjusting the weight of the two proportions. The principle of this method is simple, but the weights of the two proportions are subjectively set by the driver, and the adjustment has a certain randomness.

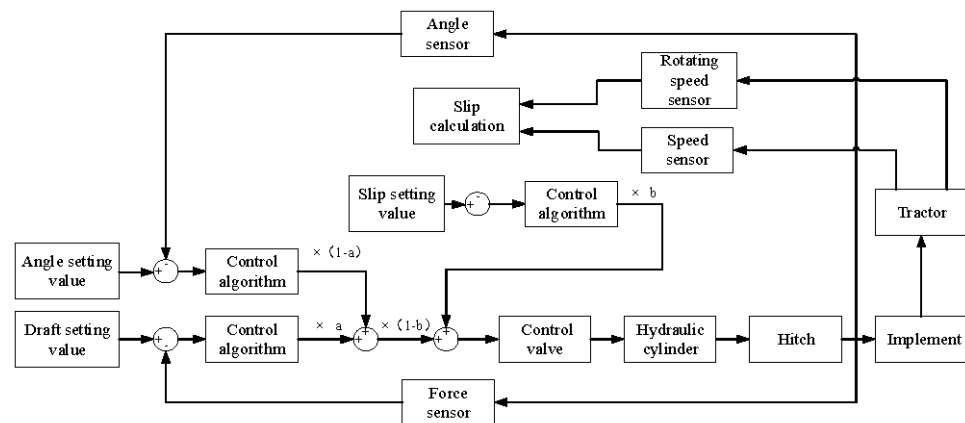


Figure 4. Three-parameter comprehensive adjustment scheme based on the weight coefficient. a. Weight of position adjustment; b. Weight of slip adjustment.

Ma et al. [52], Mu et al. [54] and Bai et al. [55], designed a three-parameter comprehensive adjustment scheme based on the logic threshold method. The adjustment logic is shown in the Figure 5. The principle of this scheme is that in the tillage process, the system will calculate the slip rate in real time, and when the slip rate is within the set threshold range, the system enters the mixed draft-position adjustment; When the slip ratio exceeds the set threshold range, the system enters the slip adjustment until the slip ratio is adjusted to the optimal range and then enters the mixed draft-position adjustment again, so the different adjustment modes are switched in this cycle. The results showed that this scheme not only ensured the traction efficiency of the tractor, but also obtained good uniformity of the tillage depth [52]. However, in the actual operation process, it is difficult to achieve a real-time accurate measurement of the slip rate due to the complex force of the tire and the sensitive change of the slip rate.

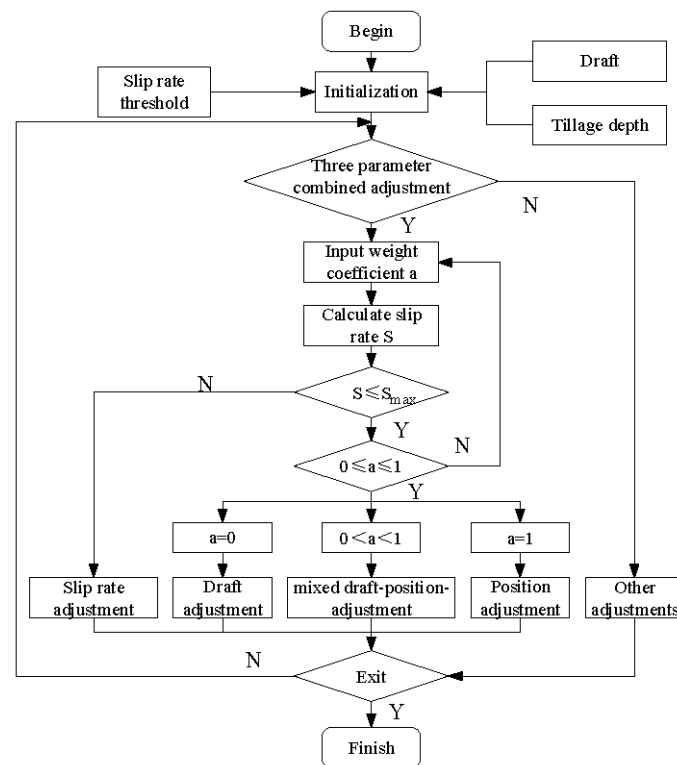


Figure 5. Three-parameter comprehensive adjustment scheme based on the logic threshold.

In summary, the method of the single parameter adjustment is simple and convenient, but it is difficult to ensure the quality of the operation for the complex and changeable field working conditions. For example, in the uneven terrain area, the position adjustment does not have a profiling function; the draft adjustment causes a poor stability of the tillage depth in areas with large soil changes. Compared with the method of the single parameter adjustment, the method of the mixed draft-position adjustment can adapt to a variety of working environments and improve the working quality. Among them, the weighted coefficient method has more long-term research and practical value. However, there are still some problems, on the one hand, the weighting coefficient is affected by human factors, on the other hand, the adhesion conditions in the process of the tractor operation are not considered. In addition, although the method of the mixed draft-position-slip adjustment combines the advantages of the different methods, due to the difficulty in the real-time measurement and the calculation of the slip rate of the driving wheel in complex working environments, and whether the method of the mixed draft-position-slip adjustment can achieve seamless coupling, remains to be verified. This method needs further research [56]. Different adjustment methods have their own advantages and scopes for use, but they also have their own shortcomings. In order to understand the characteristics of the different adjustment methods more intuitively, the comparison table of the different adjustment methods is shown in Table 3.

Table 3. Comparison of the different tillage depth adjustment methods.

Item	Position Adjustment	Draft Adjustment	Draft-Position Mixed Control	Draft-Position-Slip Mixed Control
Engine load stability	Bad	Best	Good	Best
Traction efficiency	Bad	Good	Good	Best
Operation quality on different soils	Good	Bad	Good	Best
Operation quality on rough surface	Bad	Good	Good	Best
Application	Shallow tillage	Deep tillage	All operation	All operation

4. Research Progress of the Tillage Depth Control Algorithm

In order to improve the stability and accuracy of the tillage depth control of the tractor electro-hydraulic hitch system, researchers also tried to start from the control algorithm and achieved certain results. The current research is mainly divided into the classical control algorithm represented by the PID control and the intelligent control algorithms.

4.1. PID Control Algorithm of the Tillage Depth

The PID control is one of the earliest developed control algorithms. It is widely used in the industrial controls because of its simple structure and strong adaptability [57]. The key to the creation of the PID control algorithm lies in the establishment of the mathematical model of the control system and the tuning of the PID parameters.

The essence of the tractor electro-hydraulic hitch control system is to control the spool displacement of the hydraulic valve so as to achieve the lifting and lowering of the agricultural tools. So, the mathematical model of the hydraulic system can be used to analyze the characteristics of the PID controller. Relevant scholars established the general transfer function of the tractor electro-hydraulic hitch system, as shown in Equations (1) and (2) [34,58–60].

$$\frac{Y(s)}{X(s)} = \frac{K_q / A}{\frac{MV_f}{4\beta_e A^2} S^3 + \left[\frac{MK_{ce}}{A^2} + \frac{B_p V_f}{4\beta_e A^2} \right] S^2 + \left[1 + \frac{B_p K_{ce}}{A^2} + \frac{K_f}{4\beta_e A^2} \right] S + \frac{K_L K_{ce}}{A^2}} \tag{1}$$

$$\frac{Y(s)}{F_L(s)} = \frac{-K_{ce} \left[1 + \frac{V_f}{4\beta_e K_{ce}} S \right]}{\frac{MV_f}{4\beta_e A^2} S^3 + \left[\frac{MK_{ce}}{A^2} + \frac{B_p V_f}{4\beta_e A^2} \right] S^2 + \left[1 + \frac{B_p K_{ce}}{A^2} + \frac{K_f}{4\beta_e A^2} \right] S + \frac{K_L K_{ce}}{A^2}} \tag{2}$$

Among it: Y is the displacement of the hydraulic cylinder, m; X is the displacement of the spool, m; F_L is the external load; K_q is the valve flow co-efficient; A is the area of the hydraulic cylinder, m^2 ; M is the inertia mass, kg; V_t is the fluid volume, m^3 ; K_{ce} is the total leakage co-efficient; β_e is the bulk modulus of the oil, Pa; B_p is the viscous co-efficient of the fluid, N·s/m.

Zhang [37] took the hydraulic hitch system of a DF354 tractor (DFAM, Changzhou, China) as the research object and established the mathematical model. Then, the step response characteristics were simulated and analyzed (1) without the use of a PID control, (2) with a proportional controller, (3) with a proportional-integral controller and (4) with a PID controller. Finally, the response rise time of the system was 0.0298 s, and the adjustment time to reach the set value was 0.179 s. This study provides a theoretical basis for the design of the actual system. However, the system only performs a simulation verification under the position adjustment, thus lacking any field test verification and the interference problem in the actual operation process was not considered.

Li et al. [61] and Li et al. [57] took the tillage depth control system of the rotary cultivator as the research object, and the simulation model of the electro-hydraulic hitch system was built using the SIMHYDRAULIC module in MATLAB. Aimed at solving the problem concerning the system's overshoots and oscillation, an integral separation PID control system was proposed and simulated. The simulation results showed that the amount of time to achieve the stability using the integral separation PID control algorithm, was 3.6 s less than that without the PID control. Zhou et al. [62] introduced a neural network algorithm to design the variable-gain single-neuron PID controller for the conventional PID controller that has no self-learning and adaptive abilities. In the face of the strong time-varying field conditions, the PID parameters can be adjusted according to the environmental changes. The robustness and adaptability of the tillage depth control system were greatly enhanced.

4.2. Intelligent Control Algorithm of the Tillage Depth

Zadeh first proposed the concept of the membership function in his 'fuzzy sets' and created the fuzzy set theory in 1965 [63]. The British scholar Ebrahim Mamdani applied the fuzzy set theory to the steam engine control, and built one of the first fuzzy control systems to control a steam engine together with a boiler, in 1974 [64]. It was a modern intelligent control algorithm with artificial thinking based on the fuzzy mathematics language. Pang [65] first introduced the fuzzy control into the tractor electro-hydraulic hitch control system. The integrated control simulation model, based on the engine load rate, driving wheel slip rate and operating resistance was established and the discontinuous variables and continuous variables of the fuzzy control algorithms were designed, respectively. It was verified by comparison that the automatic control was more accurate than the manual experience control.

In order to improve the accuracy of the tillage depth of the control system, Lu et al. [66] designed a tractor tillage depth fuzzy controller and developed a fuzzy control rule table of the electronically controlled hydraulic hitch system. Figure 6 shows the fuzzy control principle diagram of the tillage depth. The bench verification results showed that the response time of the tillage depth to the specified target was less than 1.7 s, and the maximum error of the tillage depth was ± 1 cm. This method reduces the influence of surface roughness disturbance and the parameter variation on the control effect. The feasibility of applying the fuzzy controller to the tractor electro-hydraulic hitch system was verified.

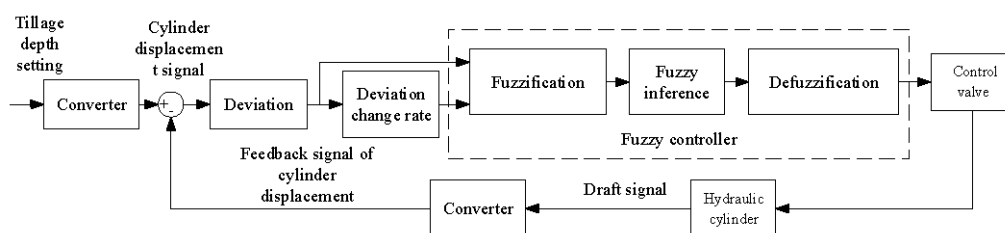


Figure 6. Principle diagram of fuzzy control algorithm.

Serhat et al. [67] took the slip rate of the driving wheel as the system input, and designed a tractor slip rate controller based on the fuzzy control. Then, the adjustment of the tillage depth was determined based on the fuzzy rules, and the effectiveness of the control system was verified by field experiments. Han et al. [68] proposed a draft-position mixed control strategy for the electro-hydraulic hitch system and designed a fuzzy controller based on a Jinma 1204 tractor (Yueda, Yancheng, China). The experimental results showed that the ploughing depth error was less than ± 2 cm, but the system response time was 4.8 s. However, the designed controller's processing speed needs to be further improved. Tan et al. [69] and Gao et al. [70] compared the PID controller and the fuzzy controller. In the study by Tan [69], the PID control was more accurate than the fuzzy control, but the system was always within regulation and unstable. The fuzzy control did not adjust when the deviation was small, which was beneficial to the system energy saving. However, this conclusion lacks the verification of field experiments. Using a Dongfanghong-1604 tractor (YTO, Luoyang, China), an experiment verification was carried out by Gao et al. [70]. The results showed that the tillage depth error was controlled within 2 cm. Compared with the PID control, the fuzzy control had a shorter response time and a smaller response curve amplitude. However, they only studied the position control, and did not consider the influence of the road roughness and soil specific resistance.

Shafaei et al. [71] developed a tractor fuzzy draft-position control system and wrote a set of instructions containing four fuzzy rules. In order to verify the characteristics of the control system, the field experiments were designed at three tillage depth levels (10, 20, 30 cm), three forward speeds (2, 4, 6 km/h) and with three plow types (plow plate, disc plow, chisel plow) and compared their results with the original MF399 tractor control system. The test results showed that the application of the fuzzy control increases both the tractor traction efficiency and the overall energy efficiency by up to 20% and 73%, respectively, the tillage depth error, the driving wheel slip rate, and the fuel consumption were decreased by 53%, 34% and 34%, respectively. In addition, the study showed that the tillage depth and plow type have no effect on the control performance, and the forward speed had an effect on the control performance of the system ($p \leq 0.01$). Therefore, in future studies of the electro-hydraulic hitch system, the working speed of the tractor needs to be considered.

In order to combine the advantages of the different algorithms, Li et al. [72] introduced the fuzzy control theory into the PID control and designed a fuzzy PID adaptive controller. As shown in Figure 7, the principle was to calculate the PID parameters by fuzzy inference, and then output the control signal by the PID. The simulation and experimental verifications were carried out under the position control and the draft control. The simulation results showed that the transition time of the fuzzy PID adaptive control was reduced by 15.5 s compared with the conventional PID under the position control, and the system had no overshoot. Under the draft control, the transition time of the fuzzy PID adaptive control was reduced by 2.8 s compared with the conventional PID, and the system changed smoothly without oscillation. The experimental results showed that the fuzzy PID adaptive control effect was basically consistent with the simulation in the position control, but it was worth noting that the overshoot of the system reached 25% in the position control mode.

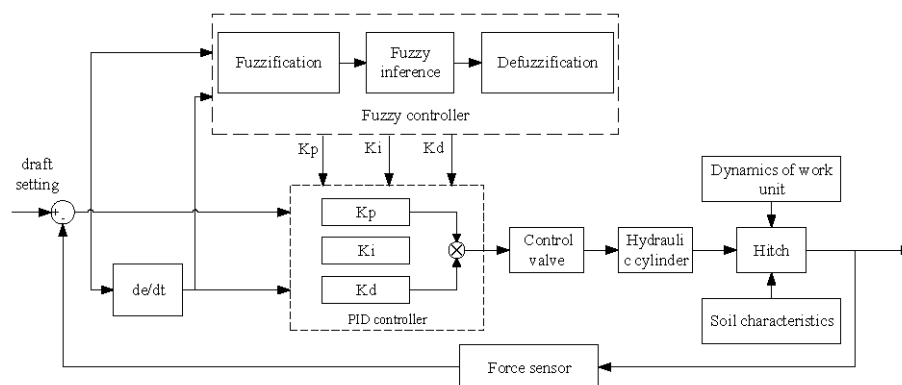


Figure 7. Principle Diagram of the Fuzzy–PID Control Algorithm.

Wang et al. [73] introduced the variable universe fuzzy PID control in the tillage depth control. The simulation platform of the draft-position mixed control was established based on MATLAB and the system characteristics when using a PID controller, a fuzzy PID controller and a variable universe fuzzy PID controller were simulated and compared. The results showed that the PID control results have 19.2% overshoot and the system response time was 1 s. The fuzzy PID control results had no overshoot, and the response time was reduced by 0.1 s compared with the PID control. There was no overshoot in the variable universe fuzzy PID control, and the response time was reduced by 0.44 s compared with the fuzzy PID control. This study provided a method for the selection of the initial domain in the fuzzy control. However, due to the constraints of the conditions, the experiments were carried out only under one single soil specific resistance, and there was a lack of verification of the simulation results.

In addition to the above algorithm, Zhang et al. [74] introduced a more advanced sliding mode variable structure controller algorithm. The dynamic model of the tractor ploughing unit was established, and a comprehensive control strategy of the slip rate, based on the tractor traction characteristics, was proposed. The comparison with the fuzzy PID control showed that the average absolute deviation of the tractor slip rate, the variation of the tillage depth adjustment and the variation of the draft adjustment were reduced by 27%, 27% and 42% when using the sliding mode variable structure controller algorithm. The control performance and superiority of this way were verified. There was a concern in this study. The derivation of this method involved many physical quantities, and most of them were difficult to obtain directly through measurement. However, it should be worth noting that this study was an exploration of the application of future intelligent algorithms in electro-hydraulic hitch systems.

In summary, with the continuous development and maturity of the advanced control theory, in the study of the tractor tillage depth control algorithm, researchers have not only been limited to the simple PID control, but also transformed it into a control mode combining multiple control algorithms. With the introduction of intelligent algorithms, the response characteristics and control accuracy of the tillage depth control system are greatly improved.

5. Research Progress of Key Components of the Electro-Hydraulic Hitch System

Compared with the traditional mechanical hydraulic hitch system, in order to obtain a good working quality and to reduce energy consumption, the electro-hydraulic hitch system not only adopts advanced control methods, but also constantly updates and develops the composition hardware. Among them, the control valves and sensing elements, as the core components, have attracted wide attention from scholars in China and abroad.

5.1. Hydraulic Control Valve

The hydraulic control valve is the core component of the tractor electro-hydraulic hitch system. The early commonly used control valve is the mechanical control valve,

generally of the slide rod type, through which the operation handle drives the slide rod movement, so as to realize the oil circuit connection and closure. With the development of the electro-hydraulic proportional control technology, the electro-hydraulic proportional valve is gradually used in the tractor electro-hydraulic hitch system. A large number of research results on the design of hydraulic control valve of tractor electro-hydraulic hitch system have been accumulated by relevant scholars. A comparison of several typical schemes is shown in Table 4.

Table 4. Comparison of the hydraulic control valves with different principles.

Scheme	Structure	Control Mode	Features
1 [75]	Rotary type	Motor control	Proportional valve, Single-acting
2 [41,76,77]	plate design	Direct electromagnetic actuation	Proportional valve, Single-acting, With load sensitive
3 [78]	threaded cartridge	Pilot control	Proportional valve, Single-acting, With load sensitive, With position feedback

The scheme 1 consists of a three-position four-way directional valve and a safety valve. The working oil port is connected with the hydraulic cylinder. The pressure relief valve is used to control the maximum working pressure of the whole system and improve the safety of the system. Three four-way directional valve to change the flow direction of oil, and the lifting and lowering of the agricultural machinery are controlled by the motion of the oil cylinder. The structure and principle of scheme 1 is simple, but the tractor electro-hydraulic hitch system using this scheme needs a separate oil supply, which cannot carry out the simultaneous operations of the multiple actuators. The scheme 2 chooses to realize the lifting and lowering of the agricultural machinery through two valves separately, and adds a pressure compensator and shuttle valve to the system. Pressure compensator is used to maintain the stability of the pressure difference in the process of operation, so that the flow of the control valve is only related to the opening of the valve port. Therefore, the operation depth of tractor electro-hydraulic hitch system can be controlled by controlling the displacement of spool. The shuttle valve can be matched with a load sensitive pump to achieve the function of the load sensitive. On the one hand, the flow can be adjusted on demand through the system pressure change fed back by the shuttle valve, so that the energy loss of the whole system is reduced. On the other hand, the load independent flow distribution can be realized, which can work with other actuators and does not require a separate oil supply. The scheme 3 is a hydraulic control valve based on pilot control, which can meet the demand of large flow control. At the same time, this scheme is equipped with a spool displacement sensor in addition to the load sensing function. The spool stroke is fed back to the control unit through the displacement sensor, and the control unit controls the spool position through the current of the pilot valve, which improves the control accuracy of the entire control valve.

Scholars have also invested a lot of theoretical research on hydraulic control valves. Li et al. [79] designed the proportional lift valve of the electro-hydraulic hitch system of the high-power tractor, and the flow characteristics of four different types of regulator orifices were analyzed. The results showed that the valve core with the half-round regulator orifice had a shorter travel and better low-flow rate characteristics. Zhao et al. [80] took the multi-way reversing valve as the research object. Then, the state equation of the multi-way reversing valve was established based on the theoretical analysis and the performance of the multi-way reversing valve was verified by building a hydraulic system test platform, based on closed-center load sensing. Based on the state space method of the modern control theory, Hua et al. [81] established the nonlinear mathematical model of the proportional lift valve. The performance was verified by simulation and bench tests, which provided a reference for the theoretical research method of the control valve of the electro-hydraulic hitch system.

5.2. Sensor

The sensor is an essential detecting element for the tractor electro-hydraulic hitch system. As the key component of the control system, the sensors provide feedback signals for the control system, so as to realize the closed-loop control of the tillage depth. Therefore, the type and performance of the sensors directly affect the performance of the control system. For the different control modes, the types of sensors selected are also different. At present, there are two kinds of sensors most widely used in the tractor electro-hydraulic hitch system: the displacement sensor and the draft sensor. Figure 8 shows the schematic illustration of the installation of the sensors.

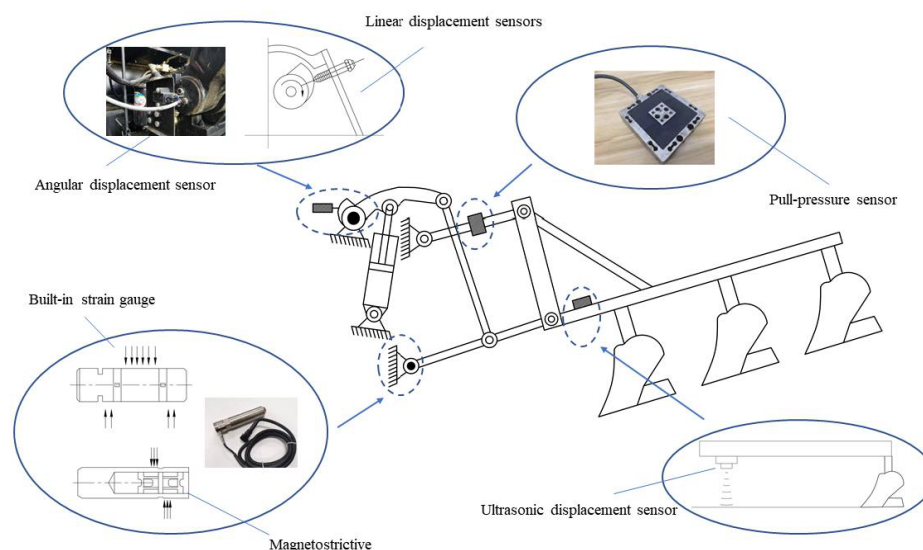


Figure 8. Schematic illustration of the installation of the sensors.

5.2.1. Displacement Sensors

The displacement sensors are mainly used to feedback the tillage depth in real time in the process of controlling the operation depth by the electro-hydraulic hitch system. Currently, there are mainly two different types according to the measurement method: contact and non-contact.

Adamchuk et al. [82] and Li et al. [83] used a non-contact ultrasonic displacement sensor to feedback the tillage depth. The sensor mainly uses the uniform transmission of sound waves to obtain the measured distance by calculating the time interval and sound velocity between the sound waves emitted and received. The study by Li [83], compared the resistance displacement sensor with the accuracy of the ultrasonic displacement sensor, which was higher than that of resistance displacement sensor.

A swinging arm type of frame height sensor was designed to measure the distance variation between the soil surface by Mouazen et al. [84]. The sensor was mainly composed of a metal wheel and a linear variable displacement sensor connected with the metal wheel shaft. An analytical–statistical hybrid model was developed based on the kinematics analysis and the tests were performed on four surfaces: asphalt road; rough dirt track; and agricultural silty clay loam soil (bare soil and soil with stubble present). The results showed that compared with the ultrasonic sensor, the sensor can reduce the influence of plant residues and stubble on the measurement results. However, due to the existence of a certain weight of the metal wheel, there would be subsidence in the wet and soft ground, which affects the accuracy of the measurement results.

MacQueene et al. [85] used inductive linear displacement sensors to obtain the tillage depth. The inductive linear displacement sensor is an electromagnetic inductive displacement measuring element, its principle mainly uses the self-inductance or mutual inductance of the coil inside the sensor to convert the displacement signal of the measured object into an electrical signal for the output [86]. In this study, a cam disc was installed on the lifting

arm to convert the rotation angle signal into a linear displacement signal, and then the inductive displacement sensor was used to measure the stroke of the cam. According to the kinematic relationship between the rods of the three-point suspension device, the rotation angle of the lifting arm was converted into the height of the farm tool. The principle of this method is simple, but the installation position of the cam and the adjustment convenience of the linear displacement sensor should be considered in the use process. Cai et al. [87] replaced the linear displacement sensor with the angular displacement sensor based on similar principles to measure the angle of the lifting arm directly. Due to its simple installation and accurate measurement, it is widely used in current research.

5.2.2. Draft Sensors

The draft sensors are designed to measure the draft exerted by farm implements on the tractor drawbar. According to the different measurement positions, these are grouped into two major categories: the drawbar dynamometers and the three-point hitch dynamometers [88].

Zhang et al. [89] and Bentaher et al. [90] used the upper link with a pull-pressure sensor and an angle sensor to replace the original upper link of the tractor and to it connect with agricultural machinery. Then, the horizontal and vertical drafts can be obtained by the force and angle of the upper link. Kumar et al. [91] and Roul et al. [92] installed an annular sensor based on the principle of strain gauge and a rotary potentiometer to achieve the draft measurements. However, the above studies need to reform the upper link, so it has not been widely applied. Bhondave et al. [93] directly used the sense implement load via the top link of the three-point linkages by the axial pin draft sensor. This method is more convenient because it does not need to modify the structure of the upper link. However, it should be worth noted that Gao et al. [94] studied the characteristics and the quality of the draft signals in two sensing methods of the upper links and lower links under different tillage conditions. The dynamic model of the three-point hitch mechanism was analyzed, and the results showed that the absolute error of the lower link measurement was smaller than that of the upper link measurement. Therefore, the lower links measurement method should be used to improve the measurement accuracy.

A draft sensing pin was used to attach the lower links to the implement by Singh et al. [95] The principle of the sensor is to use the deformation of the resistance strain gauge inside the sensor to generate the differential pressure signal, so as to convert the force signal of the measured object into an electrical signal for the output. Li et al. [96] proposed a special sensor to achieve the draft measurements for the electro-hydraulic hitch system of the high horsepower tractor. The sensor was based on the magneto-strictive effect. When the sensing element is subjected to force, the internal permeability changes to produce voltage. Compared with the strain gauge sensor, the sensor has a good anti-interference ability. However, the sensors can only withstand the shear force in one direction. Therefore, the accuracy of the measurement results may be affected by the direction offset when the three-point hitch mechanism moves. Based on Li's study, Li [97] designed a new kind of structure which changed the excitation magnetic core from columnar to cruciform. For the design, the mechanical dimensions were changed from 2D to 3D which can be more adaptable for a bad working environment.

Kheiralla et al. [98] and Al-Jalil et al. [99] designed a three-point hitch dynamometer with a similar structure. The force sensor consists of three sliding arms, which can adjust the position by sliding. There is an inverted U-shaped cantilever beam at the end of each sliding arm, and the two strain gauges are installed on each cantilever to form a Wheatstone bridge. The dynamometer was used to connect the tractor to farm implements, so as to measure the horizontal and vertical drafts of the farm implements.

In the existing electro-hydraulic hitch control system, the angular displacement sensor and shaft pin force sensor are widely used because of their low cost, simple working principle and convenient installation. However, there are still some problems. The accuracy and stability of the force sensor will be affected by the harsh working conditions in the field,

the vibration of the farm implements, the weight of the hitch system and the asymmetry of the force. In addition, the angular displacement sensor converts the angle of the lifting arm into the tillage depth, but there are still many connecting links of the three-point hitch system between the lifting arm and the farm implements. The driver may adjust the length of the connecting links in the actual operation process, so that the geometric parameters of the three-point hitch system are changed, resulting in inaccurate results of the tillage depth. Therefore, more exploration is needed to find more suitable methods.

6. Conclusions and Prospects

The tractor electro-hydraulic suspension system can reduce labor intensity and improve comfort. The tractor can work in the best conditions by automatically adjusting the tillage depth of the machine of the tractor electro-hydraulic hitch system according to the different land conditions. A large number of studies have been carried out to improve the working quality of the tractor electro-hydraulic suspension system and reduce energy consumption. A systematic literature review discussing the prevailing state of the tractor electro-hydraulic hitch system in the agriculture sector was presented in this study from three aspects: the tillage depth adjustment method, the tillage depth control algorithm and the key components of the tractor electro-hydraulic hitch system. Conclusions were drawn as follows:

- (1) The single-parameter adjustment method does not conform with the high-standard tillage quality requirements of modern precision agriculture. The coupling mechanism between the different adjustment parameters should be paid attention to in further research.
- (2) The integration of intelligent control algorithms can effectively improve the quality of work, but the impact of the different soil environments on the control system is not clear, and more field experiment tests will be required.
- (3) In terms of hardware, it is necessary to put forward higher design requirements for the key components of the electro-hydraulic hitch system. It is necessary to develop more intelligent control valves and strong anti-interference ability sensing elements.

Therefore, aiming at the key technology of the tractor electro-hydraulic hitch system, the following subsections briefly highlight future emerging trends of the tractor electro-hydraulic hitch system.

6.1. Tillage Depth Adjustment Methods

At present, the tillage depth adjustment methods of the tractor electro-hydraulic hitch system are mainly based on the position adjustment, draft adjustment and mixed draft-position adjustment. There are relatively few studies on slipping, and they are mainly concentrated in single soil conditions and in a single ploughing mode. In the future, the comprehensive adjustment method based on slipping should be explored, so as to improve the applicability under the different operating modes and operating environments.

In addition, in the current multi-parameter adjustment method, the slip rate is more frequently used as a threshold to achieve switch control. Therefore, carrying out research on the coupling mechanism between the multi-parameters based on position, force and slip rate to achieve seamless switching between multi-parameters is also an aspect that most of the current research needs to further consider.

6.2. Tillage Depth Control Algorithm

With the continuous development and maturity of the advanced control theory, in order to realize the optimal tillage depth control of the tractor electro-hydraulic hitch system, more advanced intelligent algorithms should be explored in combination with the characteristics of the tractor electro-hydraulic hitch system. Intelligent algorithms such as the neural network, sliding mode variable structure control can adapt well to the nonlinear tillage depth control system, so as to improve the robustness and accuracy of the control system.

In addition, in the study of the tractor tillage depth control algorithm, researchers have not only been limited to a single algorithmic control, but they also transformed a control mode into combining multiple control algorithms to adapt well to the different control needs.

6.3. Key Components of the Electro-Hydraulic Hitch System

While the tillage depth adjustment method and the tillage depth control algorithm are continuously studied, in order to achieve the required control effect, higher design requirements should be put forward for the key components of the electro-hydraulic hitch system. The intellectualization and digitization of the hydraulic control valves are the trend of future development. Through the built-in sensing elements and the application of the electro-hydraulic digital control, the hydraulic system and control technology can be better combined to improve the control performance of the hydraulic control valves.

For the sensing element, further exploration of new functional materials, such as magnetorheological fluid, magnetostriction material, piezoelectric material, etc., in order to achieve new characteristics and improve the reliability of the sensing element, so as to adapt well to the harsh working conditions, is necessary. In addition, with the development of high-tech, such as autonomous driving and positioning navigation, the research on the multi-sensor fusion technology should be committed and combine with intelligent control algorithms to achieve precision operations.

Author Contributions: Conceptualization, X.S. and Z.L.; writing—original draft preparation, X.S.; writing—review and editing, X.S., Y.S., C.J., Z.C. and J.Q.; English language and style, Y.L. and C.J. All authors have read and agreed to the published version of the manuscript.

Funding: This research was funded by the National Key Research and Development Plan of China (Grant No. 2016YFD0701103) and Postgraduate Research and Practice Innovation Program of Jiangsu Province, China (Grant No. KYCX22_0716).

Institutional Review Board Statement: Not applicable.

Informed Consent Statement: Not applicable.

Data Availability Statement: Not applicable.

Acknowledgments: The authors would like to thank all teachers and students for their invaluable support.

Conflicts of Interest: The authors declare no conflict of interest.

References

1. Kiroopoulos, K.; Bibi, S.; Vakouftsi, F.; Pantzios, V. Precision agriculture investment return calculation tool. In Proceedings of the 17th International Conference on Distributed Computing in Sensor Systems (DCOSS), Pafos, Cyprus, 14–16 July 2021; IEEE: Electr Network, 2021; pp. 267–271.
2. Gyarmati, G.; Mizik, T. *The Present and Future of the Precision Agriculture, 2–4 June 2020*; IEEE: Budapest, Hungary, 2020; pp 593–596.
3. Yang, X.; Shu, L.; Chen, J.N.; Ferrag, M.A.; Wu, J.; Nurellari, E.; Huang, K. A Survey on Smart Agriculture: Development Modes, Technologies, and Security and Privacy Challenges. *IEEE-CAA J. Autom. Sin.* **2021**, *8*, 273–302. [[CrossRef](#)]
4. Bolfe, E.L.; Jorge, L.A.d.C.; Sanches, I.D.A.; Junior, A.L.; Costa, C.C.d.; Victoria, D.d.C.; Inamasu, R.Y.; Greog, C.R.; Ferreira, V.R.; Ramirez, A.R. Precision and digital agriculture: Adoption of technologies and perception of brazilian farmers. *Agriculture* **2020**, *10*, 653. [[CrossRef](#)]
5. Anche, G.M.; Devika, K.B.; Subramanian, S.C. Robust Pitching Disturbance Force Attenuation for Tractor Considering Functional Constraints. *IEEE Access* **2020**, *8*, 86419–86432. [[CrossRef](#)]
6. Shen, W.; Wang, J.H.; Huang, H.L.; He, J.Y. Fuzzy sliding mode control with state estimation for velocity control system of hydraulic cylinder using a new hydraulic transformer. *Eur. J. Control* **2019**, *48*, 104–114. [[CrossRef](#)]
7. Sunusi, I.I.; Zhou, J.; Wang, Z.Z.; Sun, C.Y.; Ibrahim, I.E.; Opiyo, S.; Korohou, T.; Soomro, S.A.; Sale, N.A.; Olanrewaju, T.O. Intelligent tractors: Review of online traction control process. *Comput. Electron. Agric.* **2020**, *170*, 105176. [[CrossRef](#)]
8. Aravind, K.R.; Raja, P.; Manuel, P.R. Task-based agricultural mobile robots in arable farming: A review. *Span. J. Agric. Res.* **2017**, *15*, e02R01. [[CrossRef](#)]
9. Mamkagh, A.M. Effect of soil moisture, tillage speed, depth, ballast weight and, used implement on wheel slippage of the tractor: A review. *Asian J. Adv. Agric. Res.* **2019**, *9*, 1–7. [[CrossRef](#)]

10. Mamkagh, A.M. Effect of tillage speed, depth, ballast weight and tire inflation pressure on the fuel consumption of the agricultural tractor: A review. *J. Eng. Res. Rep.* **2018**, *3*, 1–7. [[CrossRef](#)]
11. Benkovic, R.; Sumanovac, L.; Jug, D.; Jug, I.; Japundzic-Palenkic, B.; Miroslavljivic, K.; Popijac, M.; Benkovic-Lacic, T. Influence of Aggregated Tillage Implements on Fuel Consumption and Wheel Slippage. *Teh. Vjesn. Tech. Gaz.* **2021**, *28*, 956–962.
12. Mamkagh, A.M. Review of fuel consumption, draft force and ground speed measurements of the agricultural tractor during tillage operations. *Asian J. Adv. Res. Rep.* **2019**, *3*, 1–9. [[CrossRef](#)]
13. Singha, P.S.; Kumar, A.; Sarkar, S.; Baishya, S.; Kumar, P. Development of Electro-Hydraulic Hitch Control System through Lower Link Draft Sensing of a Tractor. *J. Sci. Ind. Res.* **2022**, *81*, 384–392.
14. Xu, J.K.; Li, R.C.; Li, Y.C.; Zhang, Y.S.; Sun, H.L.; Ding, X.K.; Ma, Y. Research on Variable-Universe Fuzzy Control Technology of an Electro-Hydraulic Hitch System. *Processes* **2021**, *9*, 1920. [[CrossRef](#)]
15. Wang, L.; Wang, Y.; Dai, D.; Wang, X.; Wang, S.M. Review of electro-hydraulic hitch system control method of automated tractors. *Int. J. Agric. Biol. Eng.* **2021**, *14*, 1–11. [[CrossRef](#)]
16. Xiong, L.; Sun, S.L.; Xiao, M.T. Agricultural machinery automation and intelligent research and application. *IOP Conf. Ser. Mater. Sci. Eng.* **2018**, *452*, 042077. [[CrossRef](#)]
17. Choudhary, R.; Rajarathnam, M.; Alekya, M.; Prithiv, H.K.; Selva, K.S. Agriculture automation system. *J. Phys. Conf. Ser.* **2020**, *1706*, 012089. [[CrossRef](#)]
18. Kovacev, I.; Kosutic, S.; Jecic, V.; Copec, K.; Pliestic, S. Impact of electronic-hydraulic hitch control on rational exploitation of tractor in ploughing. *Strojarsstvo* **2008**, *50*, 287–294.
19. Du, Q.L.; Chen, X.H. Design on control system for electro-hydraulic hitch equipment of tractor. *Adv. Mater. Res.* **2014**, *945–949*, 1513–1516. [[CrossRef](#)]
20. Olson, D.J.; Cornell, C.R. Simulation of an electrohydraulic hitch control system on an agricultural tractor. *SAE Trans.* **1987**, *96*, 1253–1258. [[CrossRef](#)]
21. Li, W.Z.; Xu, Q.C. *Automobile and Tractor*; China Agricultural Press: Beijing, China, 2008; pp. 149–150.
22. Hobbs, J.; Hesse, H. Electronic/hydraulic hitch control for agricultural tractors. *SAE Trans.* **1980**, *89*, 3211–3219. [[CrossRef](#)]
23. Xu, T.W. Research and Development of Electronically Controlled Hydraulic System for Medium and Small Tractor Suspension. Master's Thesis, Qingdao Agricultural University, Qingdao, China, 2016.
24. Han, C.H.; Gao, X.H. CAN bus technology and its application. *Manuf. Autom.* **2010**, *32*, 146–149.
25. Scarlett, J.A. Integration of tractor engine, transmission and implement depth controls (Part2, Control Systems). *J. Agric. Eng. Res.* **1993**, *54*, 89–112. [[CrossRef](#)]
26. Dwyer, M. The effect of draught control response on the performance of agricultural tractors. *J. Agric. Eng. Res.* **1969**, *14*, 295–312. [[CrossRef](#)]
27. Jerzy, Z.; Zbigniew, Z. A functional model of a tractor working with mounted tools. *J. Inn. Mong. Polytech. Univ.* **2003**, *22*, 93–100.
28. Kannakara, S.; Kushwaha, R.L.; Lague, C. Numerical modeling of soil stress and pressure distribution on a flat tillage tool using computational fluid dynamics. *Biosyst. Eng.* **2007**, *97*, 407–414.
29. Bosch Rexroth Electronic-Hydraulic Hitch Control. Available online: https://dc-boschrexroth-cn.resource.bosch.com/media/cn/product/product_groups_1/mobile/mobile_systems/ehc_user_menu.png (accessed on 20 August 2022).
30. Walvoil Hitch Control System. Available online: https://www.walvoil.com/allegati/catalogo/D1WWCB06_ENG.png (accessed on 20 August 2022).
31. System Description-Hitch Control. Available online: <https://assets.danfoss.com/documents/150036/AB152886482484en-000204.png> (accessed on 20 August 2022).
32. Zhan, K.; Zhang, L.Y.; Qin, W.Q. The simulation study of tractor-hanging farm implements tillage unit on microcomputer. *J. Jilin Univ. Eng. Technol. Ed.* **1990**, *04*, 81–88.
33. Fang, C.L.; Wu, J.H. Theoretical and experimental study on electrohydraulic control of tractor suspension system. *Trans. Chin. Soc. Agric. Mach.* **1994**, *03*, 6–11.
34. Xie, B. Study on Electrohydraulic Control Technology of Suspension System of Tractor Farm Tool Simulation Operation Unit. Master's Thesis, China Agricultural University, Beijing, China, 2000.
35. Xie, B.; Mao, E.R.; Tan, Y. Development of tractor electrohydraulic suspension system controller based on CAN bus. *Mach. Tool Hydraul.* **2006**, *08*, 185–187.
36. Chen, M.J.; Lu, Z.X.; Yuan, Y.Y.; Wang, Q.M. Design of the position-adjust controller for electro-hydraulic hitch system of tractor. *Mach. Electron.* **2008**, *11*, 19–22.
37. Zhan, C. Research on the Tractor Electric-Hydraulic Hitch Congtrol System Based on CAN Bus. Master's Thesis, Nanjing Agricultural University, Nanjing, China, 2008.
38. Lee, J.; Yamazaki, M.; Oida, A.; Nakashima, H.; Shimizu, H. Electro-hydraulic tillage depth control system for rotary implements mounted on agricultural tractor design and response experiments of control system. *J. Terramech.* **1998**, *35*, 229–238. [[CrossRef](#)]
39. Lee, J.; Yamazaki, M.; Oida, A.; Nakashima, H.; Shimizu, H. Field performance of proposed foresight tillage depth control system for rotary implements mounted on an agricultural tractor. *J. Terramech.* **2000**, *37*, 99–111. [[CrossRef](#)]
40. Xia, J.F.; Li, D.; Liu, G.Y.; Cheng, J.; Zhen, K.; Luo, C.M. Design and test of an electro-hydraulic monitoring device for hitch tillage depth based on measurement of tractor pitch angle. *Trans. Chin. Soc. Agric. Mach.* **2021**, *52*, 386–395.

41. Hao, X.Y.; Wang, Y.L.; Xu, T.W.; Li, Z.M.; Zhang, J.; Geng, C. Modeling and simulation of tractor electronically controlled hydraulic suspension system based on AMESim. *J. Qingdao Univ. Eng. Technol. Ed.* **2018**, *33*, 125–129.
42. Cheng, M.J. Research on Resistance-adjustment for Tractor Electro-hydraulic Hitch System Based on the Fuzzy Algorithm. Master's Thesis, Nanjing Agricultural University, Nanjing, China, 2009.
43. Wang, Q.M. The Research and Design of Electronic Hydraulic Control Technology of Hitch Control Unit for the Tractor. Master's Thesis, Nanjing Agricultural University, Nanjing, China, 2008.
44. Xu, H.; Lu, Z.X.; Song, Y.D. Force-position Adjustment Design of Tractor Hitch System Based on DSP. *Appl. Mech. Mater.* **2014**, *462–463*, 483–486. [[CrossRef](#)]
45. Zhang, B.; Zhou, J. Research on prediction of traction resistance of tractor farming based on fuzzy neural network. *J. Gansu Agric. Univ.* **2020**, *55*, 213–220+228.
46. Shang, G.G.; Peng, H.J.; Xia, Y. Study on auto-control method and simulation for tractor depth fuzzy control. *Res. Agric. Mod.* **2014**, *35*, 825–829.
47. Zhao, J.J.; Zhu, Z.X.; Song, Z.H.; Zhou, R.J.; Wang, R.P.; Mao, E.R. Design of electro-hydraulic suspension proportional controller for heavy tractor. *Trans. Chin. Soc. Agric. Mach.* **2014**, *45* (Suppl. S1), 10–16.
48. Xu, H.; Lu, Z.X.; Song, Y.D. Study on force-position regulation of tractor electro-hydraulic hitch system. *Acta. Agric. Zhejiangensis* **2013**, *25*, 879–883.
49. Guo, B. Research on Force-position Combined Control for Tractor Electronically Controlled Hydraulic Hitch System. Master's Thesis, Nanjing Agricultural University, Nanjing, China, 2013.
50. Li, M.S. Research on the Dynamic Performance of Electro-hydraulic Hitch System in Big-Power Tractor. Ph.D. Thesis, China Agricultural University, Beijing, China, 2013.
51. Wang, S.Y.; Liu, Z.; Li, R.C.; Xu, J.K.; Liu, Y.J. Variable weight force-position mixed control of high-power tractor based on soil specific resistance. *Trans. Chin. Soc. Agric. Mach.* **2018**, *49*, 351–357.
52. Ma, Y. Research on Tillage Depth Control Technology of Heavy Tractor Based on Variable Universe Fuzzy PID. Master's Thesis, Shandong University of Science and Technology, Qingdao, China, 2019.
53. Gao, L.L. Study of Electronic Control Technology for Tractor's Hydraulic Hitch System. Master's Thesis, Jiangsu University, Jiangsu, China, 2014.
54. Mu, C.P. Research on Control Technology of Tillage Depth of Electro-Hydraulic Suspension System of Large Tractor. Master's Thesis, Shandong University of Science and Technology, Qingdao, China, 2020.
55. Bai, X.F.; Lu, Z.X.; Chang, J.X.; Li, H.; Zhou, W.W. Fuzzy control algorithm simulation of automatic control of tilling depth for tractor based on slip rate. *Trans. Chin. Soc. Agric. Mach.* **2012**, *43* (Suppl. S1), 6–10.
56. Yu, F.; Lin, Y. *Vehicle System Dynamics*; China Machine Press: Beijing, China, 2016; pp. 42–46.
57. Li, C.J. Research on electro-hydraulic tillage depth control system based on PID control. Master's Thesis, Southwest University, Chongqing, China, 2017.
58. Shen, Z.F. Modeling and Simulation Analysis of Electronically Controlled Hydraulic Suspension System of Tractor. Master's Thesis, Jiangsu University, Zhenjiang, China, 2010.
59. Wang, Z.Y. Dynamic Characteristics Analysis of Tractor Electronically Controlled Hydraulic Suspension System. Master's Thesis, Jiangsu University, Zhenjiang, China, 2012.
60. Zhu, S.H.; Zhang, C. Study on PID control simulation of tractor electro-hydraulic hitch system. *Mach. Des. Manuf. Eng.* **2008**, *21*, 49–53.
61. Li, D.; Ye, J.; Li, M.S.; Li, C.J.; Xu, H.G. Research on tillage depth regulation system based on integral-separated PID control. *J. Southwest-China Norm. Univ. Nat. Sci. Ed.* **2018**, *43*, 121–127.
62. Zhou, M.K.; Xia, J.F. Development of a depth control system based on variable-gain single-neuron PID for rotary burying of stubbles. *Agriculture* **2022**, *12*, 30. [[CrossRef](#)]
63. Zadeh, L.A. Fuzzy sets. *Inf. Control* **1965**, *8*, 338–353. [[CrossRef](#)]
64. Xie, L.Y. Research on Plowing Depth Automatic Control for High-Power Tractor Electro-Hydraulic Hitch System. Master's Thesis, Jiangsu University, Zhenjiang, China, 2016.
65. Pang, C.L.; Zong, B.H.; Er, Z.M. Fuzzy integrated control model and simulation test of tractor working unit. *Trans. CSAE* **2003**, *4*, 111–113.
66. Lu, Z.X.; Guo, B.; Gao, Q. Fuzzy automatic control method and experimental study of tractor tillage depth. *Trans. CSAE* **2013**, *29*, 23–29.
67. Soyulu, S.; Arman, K. Fuzzy logic based automatic slip control system for agricultural tractors. *J. Terramech.* **2021**, *95*, 25–32. [[CrossRef](#)]
68. Han, J.Y.; Xia, C.G.; Shang, G.G.; Gao, X. In-field experiment of electro-hydraulic tillage depth draft-position mixed control on tractor. *IOP Conf. Ser. Mater. Sci. Eng.* **2017**, *274*, 012028. [[CrossRef](#)]
69. Tan, Y. Study on Performance of Hydraulic Suspension and Loading System of Tractor. Master's Thesis, China Agricultural University, Beijing, China, 2004.
70. Gao, X.; Sun, C.W.; Shi, J.Z.; Wang, Q. Research of fuzzy control method for electronic hydraulic hitch of tractor. *Tractor Farm Transp.* **2008**, *35*, 12–14.

71. Shafaei, S.M.; Loghavi, M.; Kamgar, S. A practical effort to equip tractor-implement with fuzzy depth and draft control system. *Eng. Agri. Environ. Food*. **2019**, *12*, 191–203. [[CrossRef](#)]
72. Li, M.S.; Zhao, J.J.; Zhu, Z.X.; Xie, B.; Chi, R.J.; Mao, E.R. Fuzzy PID adaptive control method for tractor electro-hydraulic suspension system. *Trans. Chin. Soc. Agric. Mach.* **2013**, *44* (Suppl. S2), 295–300.
73. Wang, P.Y. Study on the Technology of Adjusting the Plough Depth of Modern Agricultural Tractor Based on Variable Universe Fuzzy Control. Master's Thesis, Shandong Agricultural University, Qingdao, China, 2020.
74. Zhang, S.; Wu, Z.B.; Chen, J.; Li, Z.; Zhu, Z.X.; Song, Z.H.; Mao, E.R. Control method of driving wheel slip rate of high-power tractor for ploughing operation. *Trans. CSAE* **2020**, *36*, 47–55.
75. Moradinejad, N. Electronic hitch control valve for Massey Ferguson 285 tractor. *AMA-Agr. Mech. Asia Af.* **2018**, *49*, 50–56.
76. Zhang, S. Study on slip rate control of heavy tractor for ploughing based on sliding mode variable structure control. Ph.D. Thesis, China Agricultural University, Beijing, China, 2018.
77. Liu, C.Q.; Hua, B.; Du, Y.F.; Li, Z.; Zhu, Z.X.; Mao, E.R. Dynamic pressure feedback correction method for tractor electro hydraulic hitch. *Trans. Chin. Soc. Agric. Mach.* **2020**, *51* (Suppl. S1), 1–9.
78. Zhao, H.P.; Zhou, J.J.; Bao, Q.Q.; Ma, H.C. Characteristic analysis of intelligent reversing valve based on high-speed on-off valve. *Acta Armamentarii*. **2022**. [[CrossRef](#)]
79. Li, M.S.; Zhu, Z.X.; Mao, E.R.; Song, Z.H.; Xie, B.; Li, C.L. Design of proportional raise valve in electro-hydraulic lifting mechanism of big-power tractor. *Trans. Chin. Soc. Agric. Mach.* **2012**, *43*, 31–35+89.
80. Zhao, J.J.; Zhu, Z.X.; Song, Z.H.; Mao, E.R.; Liu, S.R.; Liu, D.L. Simulation and test of multi-way directional valve for heavy tractor electro-hydraulic hoist. *Trans. Chin. Soc. Agric. Mach.* **2014**, *45* (Suppl. S1), 1–9.
81. Hua, B.; Zhao, J.J.; Liu, C.Q.; Du, Y.F.; Mao, E.R.; Song, Z.H. Performance simulation and test of plug-in proportional raising valve of electro-hydraulic hitch for heavy tractor. *Trans. CSAE* **2019**, *35*, 109–117.
82. Adamchuk, V.I.; Hummel, J.W.; Morgan, M.T.; Upadhyaya, S.K. On-the-go soil sensors for precision agriculture. *Comput. Electron. Agric.* **2004**, *44*, 71–91. [[CrossRef](#)]
83. Li, Z.X. Research and design of operating depth measurement apparatus for farm implement. *Trans. Chin. Soc. Agric. Mach.* **2000**, *31*, 88–91.
84. Mouazen, A.M.; Anthonis, J.; Saeys, W.; Ramon, H. An automatic depth control system for online measurement of spatial variation in soil compaction, Part 1: Sensor design for measurement of frame height variation from soil surface. *Biosyst. Eng.* **2004**, *89*, 139–150. [[CrossRef](#)]
85. MacQueene, J.; Schwarz, P.; Nielsen, B. Development of the electronic draft control system for the ford New Holland 8210 tractor. *SAE Trans.* **1990**, *99*, 327–339.
86. Chen, G.; Zhang, B.; Liu, P.; Ding, H. An adaptive analog circuit for LVDT's nanometer measurement without losing sensitivity and range. *IEEE Sens. J.* **2015**, *15*, 2248–2254. [[CrossRef](#)]
87. Cai, L.F. Research on the Plowing Depth Automatic Control of Tractor Hydraulic System Based on Electronic Control. Master's Thesis, Jilin University, Changchun, China, 2016.
88. Chethan, C.R.; Tewari, V.K.; Nare, B.; Kumar, S.P. Transducers for measurement of draft and torque of tractor-implement system—A review. *Agric. Mech. Asia Afr. Lat. Am.* **2018**, *49*, 81–87.
89. Zhang, L.Y.; Zheng, X.; Qin, C.M.; He, X.C. Performance test and analysis of super-deep plow. *J. Gansu Agric. Univ.* **2016**, *51*, 156–160.
90. Bentaher, H.; Hamza, E.; Kantchev, G.; Maalej, A.; Arnold, W. Three-point hitch-mechanism instrumentation for tillage power optimization. *Biosyst. Eng.* **2008**, *100*, 24–30. [[CrossRef](#)]
91. Kumar, A.A.; Tewari, V.K.; Nare, B. Embedded digital draft force and wheel slip indicator for tillage research. *Comput. Electron. Agric.* **2016**, *127*, 38–49. [[CrossRef](#)]
92. Raul, A.K.; Raheman, H.; Pansare, M.S.; Machavaram, R. Predicting the draught requirement of tillage implements in sandy clay loam soil using an artificial neural network. *Biosyst. Eng.* **2009**, *104*, 476–485. [[CrossRef](#)]
93. Bhondave, B.; Ganesan, T.; Varma, N.; Renu, R.; Sabarinath, N. Design and development of electro hydraulics hitch control for agricultural tractor. *SAE Int. J. Commer. Veh.* **2017**, *10*, 405–410. [[CrossRef](#)]
94. Gao, X.; Wang, Z.Y.; Pan, D.Y. Resistance regulation characteristic analysis of tractor rear hitch mounted hanging plough in multi-operative modes. *J. Anhui Agric. Sci.* **2012**, *40*, 14132–14135.
95. Singh, C.D.; Singh, R.C. Computerized instrumentation system for monitoring the tractor performance in the field. *J. Terramech.* **2011**, *48*, 333–338. [[CrossRef](#)]
96. Li, M.S.; Chi, R.J.; Mao, E.R.; Zhang, J.Y.; Liu, Y. Design of draft sensor in big-power tractor raiser based on magnetostriction. *Trans. Chin. Soc. Agric. Mach.* **2013**, *44*, 8–12+32.
97. Li, R.C.; Guo, K.; Yang, J.R.; Xu, J.K.; Chi, Y.R. Magnetic circuit design and simulation of draft sensor in electro-hydraulic lifting mechanism of high-power tractor. *Trans. Chin. Soc. Agric. Mach.* **2017**, *48*, 358–367.
98. Kheiralla, A.F.; Yahya, A.; Bardae, M.Z.; Ishak, W. Design and development of a three-point auto hitch dynamometer for an agricultural tractor. *ASEAN J. Sci. Technol. Dev.* **2003**, *20*, 271–288. [[CrossRef](#)]
99. Al-Jalil, H.F.; Khadair, A.; Mukahal, W. Design and performance of an adjustable three-point hitch dynamometer. *Soil Tillage Res.* **2001**, *62*, 153–156. [[CrossRef](#)]

Article

Research and Design of Precision Fertilizer Application Control System Based on PSO-BP-PID Algorithm

Zihao Meng, Lixin Zhang *, Huan Wang, Xiao Ma, He Li and Fenglei Zhu

Department School of Mechanical and Electrical Engineering, Shihezi University, Shihezi 832003, China

* Correspondence: zhlx2001329@163.com

Abstract: China has had the highest fertilizer use rate in the world for years, but today a large number of farmlands still use traditional manual fertilizer application methods, which rely entirely on personal experience and not only cause the waste of fertilizer and water resources but also make the local ecological environment polluted. This paper researches and designs a BP neural network PID controller based on PSO optimization to address the above problems. The PSO algorithm is used to optimize the initial weights of the BP neural network, and then optimize the control parameters of the PID to achieve accurate control of the liquid fertilizer flow. A precision fertilizer control system based on the STM32 microcontroller was also developed, and the performance of this controller was verified in tests. The results showed that compared with the conventional PID controller and BP neural network-based PID controller, this controller had good control accuracy and robustness, the average maximum overshoot was 6.35%, and the average regulation time was 41.17 s; when the fertilizer application flow rate was 0.6 m³/h, the shortest adjustment time is 30.85 s, which achieves the effect of precise fertilizer application.

Citation: Meng, Z.; Zhang, L.; Wang, H.; Ma, X.; Li, H.; Zhu, F. Research and Design of Precision Fertilizer Application Control System Based on PSO-BP-PID Algorithm. *Agriculture* **2022**, *12*, 1395. <https://doi.org/10.3390/agriculture12091395>

Academic Editors: Muhammad Sultan, Redmond R. Shamshiri, Md Shamim Ahamed and Muhammad Farooq

Received: 13 August 2022

Accepted: 2 September 2022

Published: 5 September 2022

Publisher's Note: MDPI stays neutral with regard to jurisdictional claims in published maps and institutional affiliations.



Copyright: © 2022 by the authors. Licensee MDPI, Basel, Switzerland. This article is an open access article distributed under the terms and conditions of the Creative Commons Attribution (CC BY) license (<https://creativecommons.org/licenses/by/4.0/>).

Keywords: precision fertilizer application; BP neural network; PSO optimization algorithm; PID control

1. Introduction

China has a serious shortage of water resources, and agricultural irrigation water is generally wasted and underutilized. Some remote areas still use the traditional manual fertilization method, which relies solely on personal experience and is a huge waste of fertilizer and may even cause harm to the land. Water-fertilizer integration technology is a highly efficient, water- and fertilizer-saving agricultural technology recognized worldwide today, which can mix liquid fertilizer with irrigation water and deliver it evenly, regularly, and quantitatively to the crop root zone through drip irrigation pipelines, which not only greatly reduces water pollution caused by excessive fertilizer application, but also has many advantages such as improving soil environment and crop quality [1,2].

However, the process of regulating water and fertilizer flow in precision agriculture has volume delays in the transmission pipeline, which leads to time-varying, hysteresis, and non-linear characteristics of the system, so quick and effective regulation of water and fertilizer flow during fertilizer application is a hot issue in water and fertilizer integration technology today. Xiuyun Xue et al. [3] designed a variable-speed liquid fertilizer applicator based on ZigBee technology for deep fertilization. The liquid flow information was collected through a flow meter, and the frequency of the inverter was dynamically adjusted using an incremental PID control algorithm to accurately achieve the set liquid fertilizer flow rate, and field trials were conducted. The results showed that the fertilizer application accuracy could reach 99.52%, and the maximum flow output difference was within 0.2 L/min for fertilizer application depth variation. Yingzi Zhang et al. [4] designed a slave computer control system for applying variable-speed liquid fertilizer, using SMC as the core processor and an electronically controlled pressure regulator as the actuating component,

and obtained the characteristic equations of the system using classical control theory and verified the performance of the slave computer by bench testing. The results showed that the fertilizer application error was less than 0.9 and the fertilizer application accuracy was greater than 97%. Zhiyun Zou et al. [5] proposed a new nonlinear Hammerstein MAC algorithm and compared it with linear MAC and PID controllers in simulations. The simulation results showed that the nonlinear Hammerstein MAC algorithm still had good stability and robustness even in the case of large modeling errors. Zhounian Lai et al. [6] used a fuzzy adaptive controller to approximate the system parameters to achieve control in a delay-free model while introducing an extended Smith predictor variable to compensate for the time delay of the system. The effectiveness of the control strategy was verified experimentally, and the results showed that the controller had good control performance.

The emergence of many emerging algorithms and theories also brings more effective solutions for precision fertilization. Yuhong Dong et al. [7] proposed a wavelet-BP neural network-based method for accurate fertilization of maize, which effectively extracted information about soil nutrients, fertilization, and yield from the original signal by wavelet transform, and combined wavelet analysis with an optimized BP neural network to achieve better accuracy of fertilization prediction. Guozeng Feng et al. [8] proposed a BP neural network-based valve-opening prediction model and tested the prediction of the model under different conditions. The results showed that the approximation capability of the neural network model can be used to directly output the position of the demand valve at the VAV terminal, reducing the convergence time and stabilization time. Isabel S. Jesus et al. [9] used Smith-fuzzy fractional order control to solve the time lag of the system. The fuzzy controller was embedded in the Smith predictor structure and its parameters were tuned by a genetic algorithm to evaluate the performance of the algorithm with two different approximation models. The algorithm showed excellent control in nonlinear, time-lagged systems compared to traditional integer-order control schemes. Jinbin Bai et al. [10] proposed a variable-speed fertilizer-application-control system for liquid fertilizer based on the beetle tentacle search algorithm, optimized three parameters of PID using the search algorithm, analyzed the response time and overshoot of the system by software simulation, and experimentally verified the control effect of the control system. The results showed that the actual response time of the variable-speed fertilizer-application-control system based on the beetle tentacle search algorithm could reach 2 s, and the average relative error could reach 1.27%. Qiang Fu et al. [11] used a fuzzy clustering algorithm with Particle Swarm Optimization (PSO) to delineate soil nutrient management areas and analyzed actual sample soil nutrient data from each management area using one-way ANOVA. The delineation results showed that the fuzzy clustering algorithm of PSO optimization had good performance in delineating the management areas and provided a basis for variable fertilization techniques.

In this paper, a BP neural network PID control algorithm based on PSO optimization is designed, which can make fast and effective regulation of fertilizer flow and reduce the influence of time lag and nonlinearity in the flow regulation process.

Section 1 of this paper introduces the current research status of water-fertilizer integration technology; Section 2 introduces the working principle of precision fertilizer application control system and establishes the mathematical model of the system; Section 3 derives the principles of PID algorithm, BP neural network algorithm, and Particle Swarm Optimization algorithm and analyzes their advantages and disadvantages; Section 3 establishes simulation models for each of the above three algorithms using Matlab software and analyzes the simulation results; Section 3 carries out experimental verification of the dynamic performance of the controller; and Section 4 summarizes the conclusions obtained.

2. Materials and Methods

2.1. Precision Fertilization Control System Structure Composition

Figure 1 shows the structure of the precision fertilization control system. The system consists of a reservoir, fertilizer tank, filter, solenoid valve, flow sensor, pressure gauge, hose pump, and other devices, which can be opened and closed by the corresponding

solenoid valve to achieve irrigation, or irrigation and fertilization at the same time. Among them, pressure gauges were installed at each end of the filter of the fertilizer tank, and the clogging of the filter is judged by the before and after values of the pressure gauges to regularly clean and replace the filter to prevent solid deposits in the fertilizer from clogging the pipe. The irrigation main was equipped with a pressure regulator to ensure stable pressure in the pipeline during irrigation; one-way valves were installed in the irrigation mains and fertilizer mix output pipes to prevent backflow of irrigation water and fertilizer mix and two flow meters were installed in front of the main valve to monitor the supplied irrigation water flow and the fertilizer application flow. When solenoid valves 13, 14, 16, and 19 are opened, independent irrigation can be performed, and when solenoid valves 13, 14, 16, 17, and 18 are opened, irrigation and fertilization can be performed simultaneously. The hose pump was chosen as the conveying device of the fertilizer application system. The three-phase asynchronous motor was connected with the pump body of the hose pump, and the material to be conveyed is surrounded by the hose without contact with other parts. When the rotor rotates, the hose is compressed and rebounded as the position of the roller changes, causing the pump to produce suction and pressure out effects to achieve the purpose of fertilizer delivery. The system precisely regulates the fertilizer application flow rate at the hose pump outlet by changing the frequency of the inverter connected to the hose pump.

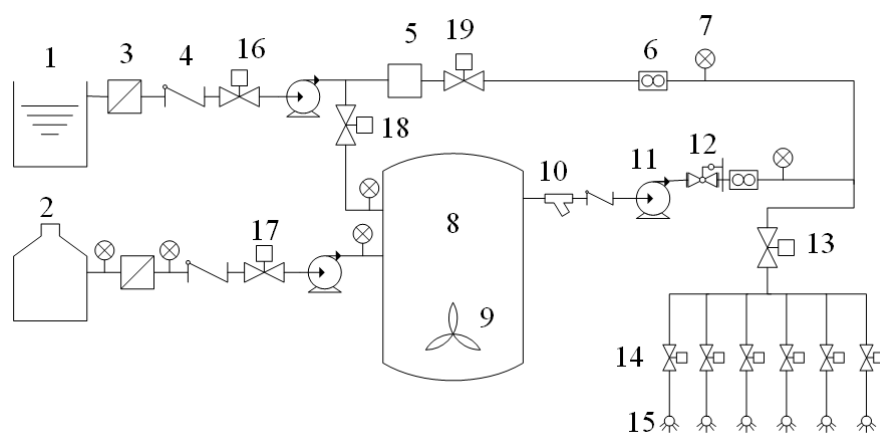


Figure 1. Structure diagram of precision fertilization control system: 1. Reservoir; 2. Fertilizer tank; 3. Filter; 4. One-way valve; 5. Pressure regulator; 6. Flow sensor; 7. Pressure gauge; 8. Mixing tank; 9. Agitator pump; 10. Y-filter; 11. Hose pump; 12. Pressure holding valve; 13. Master valve; 14. Branch valve; 15. Drip irrigation belt; 16–19. Solenoid valve.

The STM32F103ZET6 microcontroller was selected as the control element, and the BP neural network PID control algorithm based on PSO optimization was written into the microcontroller, with the set fertilizer flow rate as the desired value and the actual flow rate collected by the flow sensor as the feedback value, and the corresponding control quantity was calculated to control the motor speed in the hose pump [12] to finally realize the accurate control of the fertilizer flow rate.

When irrigation and fertilizer application are carried out, the set fertilizer flow rate will be input into the system, the solenoid valve at the reservoir and fertilizer storage tank will be opened at the same time, and the hose pump will pump water and fertilizer into the mixing tank respectively according to the proportion, and in the process of fertilizer mixing, the agitation pump will be used to mix the fertilizer and water evenly, when the flow sensor monitors the deviation of the fertilizer flow rate from the set value, the system will automatically adjust the hose pump flow rate at the outlet of the mixing tank to maintain a stable state.

Since the object of this paper is the fertilization control system, it is necessary to obtain the mathematical model of this system, and according to the fertilization characteristics

and the complexity of the system, the first-order inertia plus delay link transfer function was chosen to describe the mathematical model of the fertilization control system [13].

$$G(s) = \frac{Ke^{-\tau s}}{Ts+1} \tag{1}$$

The expected value of fertilizer application flow rate was used as the input of the open-loop system with a sampling interval of 1 s to obtain the data on flow rate variation. The first-order approximation method was used to fit the data in Matlab software, the gain coefficient K of the system was obtained as 1, the delay time τ as 11 s, and the time constant T as 3.63. The mathematical model of the fertilization control system was obtained above.

2.2. BP Neural Network PID Controller Design Based on Particle Swarm Optimization

2.2.1. Conventional PID Controller Design

The conventional PID controller consists of three units: proportional, integral, and differential, which have the advantages of simple and reliable operation, high robustness, and can solve most practical applications in the industry [14]. The structure of the PID controller in this paper is shown in Figure 2.

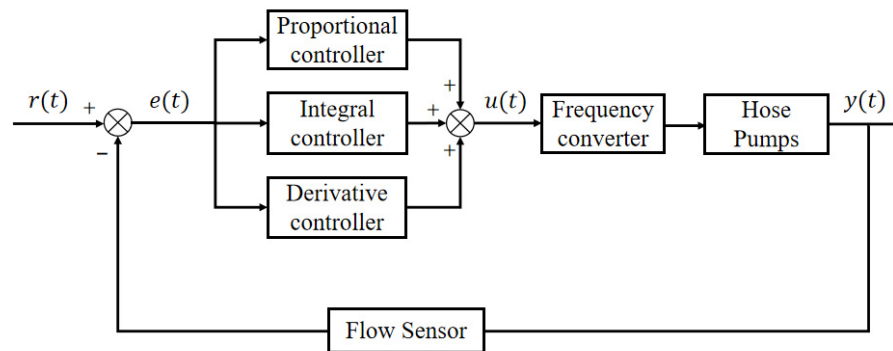


Figure 2. Conventional PID controller structure.

In the controller, the set value $r(t)$ is compared with the measured value $y(t)$ to obtain the deviation $e(t) = r(t) - y(t)$. The control law gives the control quantity $u(t)$ according to the deviation $e(t)$, and the control quantity $u(t)$ is applied to the controlled object as a way to correct and regulate the response of the control system. The control quantity $u(t)$ is specifically expressed as:

$$u(t) = K_p[e(t) + \frac{1}{T_i} \int_0^t e(\tau) d\tau + T_d \frac{de(t)}{dt}] \tag{2}$$

where K_p is the scaling factor.

T_i is the integration time constant and T_d is the differential time constant.

The above equation describes a continuous PID control algorithm, but in a real control system, the deviation value $e(t)$ needs to be obtained by sampling, so Equation (2) needs to be discretized. Assuming that the sampling period is T and a total of k samples are taken, the integral part of the control algorithm can be represented by Equation (3) and the differential part can be represented by Equation (4).

$$\int_0^t e(t) dt \approx T \sum_{j=0}^k e(j) \tag{3}$$

$$\frac{de(t)}{dt} \approx \frac{e(kT) - e[(k-1)T]}{T} = \frac{e_k - e_{k-1}}{T} \tag{4}$$

Bringing Equations (3) and (4) into Equation (2), the PID control algorithm expression is obtained.

$$u(k) = K_p e_k + K_i \sum_{j=0}^k e_j + K_d (e_k - e_{k-1}) \tag{5}$$

where K_p is the proportionality factor, K_i is the integration factor and K_d is the differentiation factor; $K_i = K_p \frac{T}{T_i}$, $K_d = K_p \frac{T_d}{T}$.

In this paper, the incremental PID control algorithm is used to operate on the variation of the control quantity $\Delta u(k)$, which can be obtained recursively according to Equation (5):

$$u(k-1) = K_p e_{k-1} + K_i \sum_{j=0}^{k-1} e_j + K_d (e_{k-1} - e_{k-2}) \tag{6}$$

Equation (6) is subtracted from Equation (5) to obtain:

$$\Delta u(k) = K_p (e_k - e_{k-1}) + K_i e_k + K_d (e_k - 2e_{k-1} + e_{k-2}) \tag{7}$$

Thus, the control quantity $u(k)$ can be expressed as:

$$u(k) = u(k-1) + \Delta u(k) \tag{8}$$

The parameter tuning of the PID controller is the core content of control system design, which determines the proportionality coefficient, integration time, and differentiation time of the PID controller according to the characteristics of the controlled process. At present, the main methods are the Cohen–Coon method, critical proportionality method, decay curve method, and other rectification methods. The common point of these methods is that the controller parameters are adjusted by test and then according to the engineering experience formula, which is simple and easy to master.

The Cohen–Coon method is used to initially rectify the three parameters K_p , T_i , and T_d . The Cohen–Coon method is mainly used to obtain the optimal PID parameter rectification value by configuring the dominant pole of the system so that the transition curve of the object decays at a decay rate of 4:1 [15]. The rectification equation is shown in Equation (9).

$$\begin{cases} K_p = \frac{T}{K\tau} \left(\frac{4}{3} + \frac{\tau}{4T} \right) \\ T_i = \tau \left(\frac{32 + \frac{6\tau}{T}}{13 + \frac{8\tau}{T}} \right) \\ T_d = \tau \left(\frac{4}{11 + \frac{2\tau}{T}} \right) \end{cases} \tag{9}$$

The mathematical model of the control object is shown in Equation (1), and the corresponding parameters are brought into Equation (1) to obtain $K_p = 0.69$, $K_i = 0.05$, and $K_d = 1.78$.

Although PID control can solve most engineering problems, it also has shortcomings, for example, the control parameters of conventional PID cannot follow changes dynamically, so it is difficult to obtain better control results when it is applied to complex systems [16].

2.2.2. BP Neural Network-Based PID Controller Design

The BP neural network-based PID controller can dynamically adjust the parameters of the PID through the autonomous learning capability of the neural network, thus replacing the human empirical values and making the parameters achieve the best control according to the changes in the environment [17,18].

According to the characteristics of cooperation and constraints of three parameters K_p , K_i , and K_d of PID control, the mapping ability of the BP neural network to nonlinear functions is used to obtain the optimal solution for the nonlinear combination of the three parameters. The structure of the BP neural network-based PID controller is shown in Figure 3.

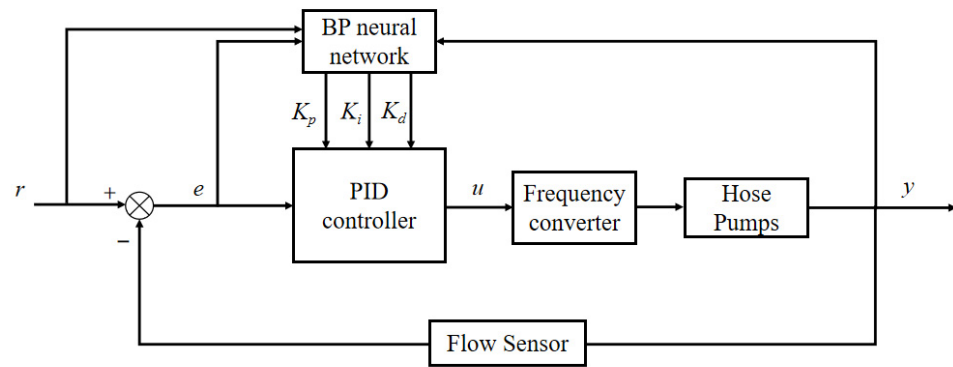


Figure 3. Structure of the BP neural network-based PID controller.

The structure is divided into two parts. Bulleted lists look like this:

1. Conventional PID controller generates control quantities through K_p, K_i, K_d output from BP neural network to realize feedback control of controlled objects.
2. The BP neural network provides optimal parameters for the PID controller based on the system operating state and the learning algorithm.

The network structure is shown in Figure 4.

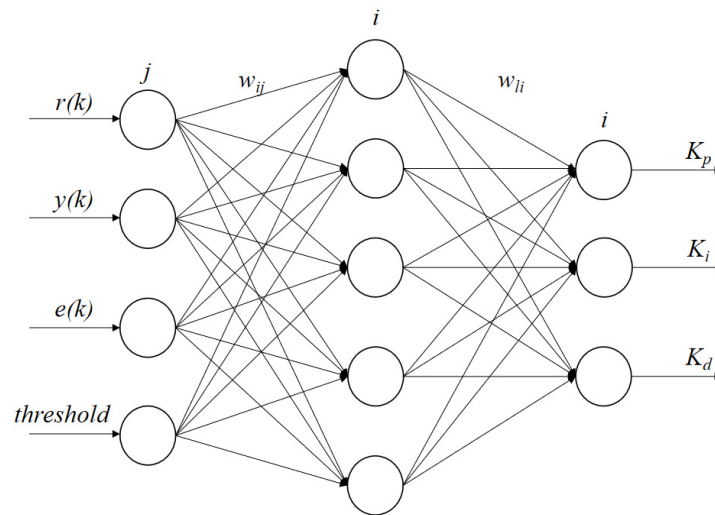


Figure 4. BP neural network structure.

The input of neurons in the input layer of the neural network is the output:

$$O_j^{(1)} = x(j) \quad (j = 1, 2, \dots, M) \tag{10}$$

where M is the number of input layer variables of the neural network, which can be adjusted according to the complexity of the controlled object, and the input layer variables in this paper are expected value, actual value, error, and network threshold.

The input and output of the implicit layer neurons are:

$$net_i^{(2)} = \sum_{j=0}^M w_{ij}^{(2)} O_j^{(1)} \tag{11}$$

$$O_i^{(2)}(k) = f\left(net_i^{(2)}(k)\right) \quad (i = 1, 2, \dots, Q) \tag{12}$$

where Q is the number of neurons in the hidden layer, which is set to 5 in order to simplify the complexity of the system and accelerate the learning speed. $w_{ij}^{(2)}$ denotes the weight between the i th neuron in the hidden layer and the j th neuron in the input layer, and the continuous function can be approximated with arbitrary accuracy in the neural network

using the Sigmoid function, so the transformation function of the hidden layer is chosen as the positive and negative symmetric Sigmoid function, as in Equation (13).

$$f(x) = \frac{e^x - e^{-x}}{e^x + e^{-x}} \tag{13}$$

The output layer neuron inputs and outputs are:

$$net_l^{(3)}(k) = \sum_{i=0}^Q w_{li}^{(3)} O_i^{(2)}(k) \tag{14}$$

$$O_l^{(3)}(k) = g\left(net_l^{(3)}(k)\right) \quad (l = 1, 2, 3) \tag{15}$$

where $w_{li}^{(3)}$ denotes the weight between the l th neuron of the output layer and the i th neuron of the input layer, and the three outputs of the output layer correspond to the three adjustable parameters K_p , K_i , and K_d of the PID controller, respectively. Since K_p , K_i , and K_d cannot be negative, the transformation function of the output layer neurons is taken as a non-negative Sigmoid function, as in Equation (16).

$$g(x) = \frac{e^x}{e^x + e^{-x}} \tag{16}$$

To ensure the real-time performance of the system, the online learning method is used, and the quadratic of the error is used as the performance indicator, so the performance indicator function is chosen as:

$$E(k) = \frac{1}{2} [r(k) - y(k)]^2 \tag{17}$$

The gradient descent method is used to adjust the weights of each layer of the BP neural network in the direction of the negative gradient of E [19]. To improve the convergence speed, the inertia term with α as the inertia factor is added.

$$\Delta w_{li}^{(3)}(k) = -\eta \frac{\partial E(k)}{\partial w_{li}^{(3)}} + \alpha \Delta w_{li}^{(3)}(k - 1) \tag{18}$$

where η is the learning rate and α is the inertia factor, according to the chain rule we get:

$$\frac{\partial E(k)}{\partial w_{li}^{(3)}} = \frac{\partial E(k)}{\partial y(k)} \times \frac{\partial y(k)}{\partial \Delta u(k)} \times \frac{\partial \Delta u(k)}{\partial O_l^{(3)}(k)} \times \frac{\partial O_l^{(3)}(k)}{\partial net_l^{(3)}(k)} \times \frac{\partial net_l^{(3)}(k)}{\partial w_{li}^{(3)}(k)} \tag{19}$$

After simplification and approximation, the final amount of regulation between the weight of the l th neuron in the output layer and the i th neuron in the hidden layer after learning is obtained as:

$$\frac{\partial E(k)}{\partial w_{li}^{(3)}} = \frac{\partial E(k)}{\partial y(k)} * \frac{\partial y(k)}{\partial \Delta u(k)} * \frac{\partial \Delta u(k)}{\partial O_l^{(3)}(k)} * \frac{\partial O_l^{(3)}(k)}{\partial net_l^{(3)}(k)} * \frac{\partial net_l^{(3)}(k)}{\partial w_{li}^{(3)}(k)} \tag{20}$$

$$\Delta w_{li}^{(3)}(k) = \alpha \Delta w_{li}^{(3)}(k - 1) + \eta \delta_l^{(3)} O_i^{(2)}(k) \tag{21}$$

$$\delta_l^{(3)} = e(k) \operatorname{sgn}\left(\frac{\partial y(k)}{\partial \Delta u(k)}\right) \frac{\partial \Delta u(k)}{\partial O_l^{(3)}(k)} g'\left(net_l^{(3)}(k)\right) \quad (l = 1, 2, 3) \tag{22}$$

Similarly, the amount of weight regulation between the i th neuron in the hidden layer and the j th neuron in the input layer can be obtained as:

$$\Delta w_{ij}^{(2)}(k) = \alpha \Delta w_{ij}^{(2)}(k - 1) + \eta \delta_i^{(2)} O_j^{(1)}(k) \tag{23}$$

$$\delta_i^{(2)} = f'\left(net_i^{(2)}(k)\right) \sum_{l=1}^3 \delta_l^{(3)} w_{li}^{(3)}(k) \quad (i = 1, 2, \dots, Q) \tag{24}$$

In summary, Equations (20) and (22) are the calculation equations for the regulation amount of the weight coefficients of each layer of the network. The BP neural network algorithm flow is shown in Figure 5.

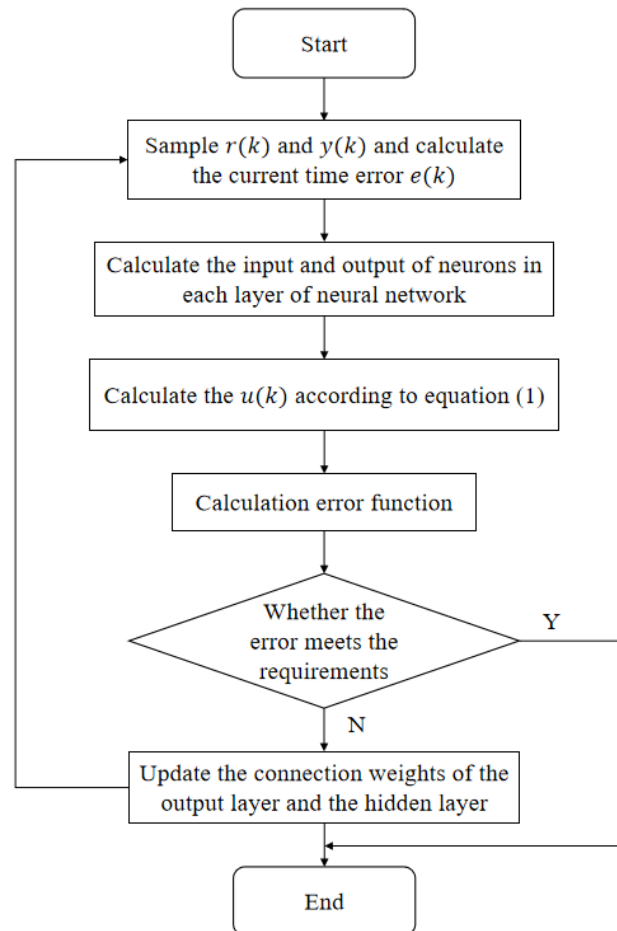


Figure 5. BP neural network algorithm process.

The inclusion of the BP neural network algorithm in the PID controller enables the dynamic regulation of the PID parameters, but due to the gradient descent method, the BP neural network converges more slowly and is prone to local minima when trained in places where the error curve is flat [20]. Therefore, this paper makes use of the global optimum and fast convergence of the Particle Swarm algorithm to improve the BP neural network and optimize the initial weights of the BP neural network, to overcome the defects that the neural network is prone to fall into local minima and slow convergence speed.

2.2.3. BP Neural Network PID Controller Design Based on PSO Optimization

The Particle Swarm Optimization (PSO) algorithm, first proposed by Eberhart and Kennedy in 1995, is an intelligent algorithm designed by simulating the predatory behavior of a flock of birds. Its basic core is to use the sharing of information by individuals in the group to continuously update their position and velocity information, thus making the motion of the whole group produce an evolutionary process from disorder to order in the problem-solving space, and finally obtaining the optimal solution of the problem [21,22].

The structure of the BP neural network PID controller based on PSO optimization is shown in Figure 6.

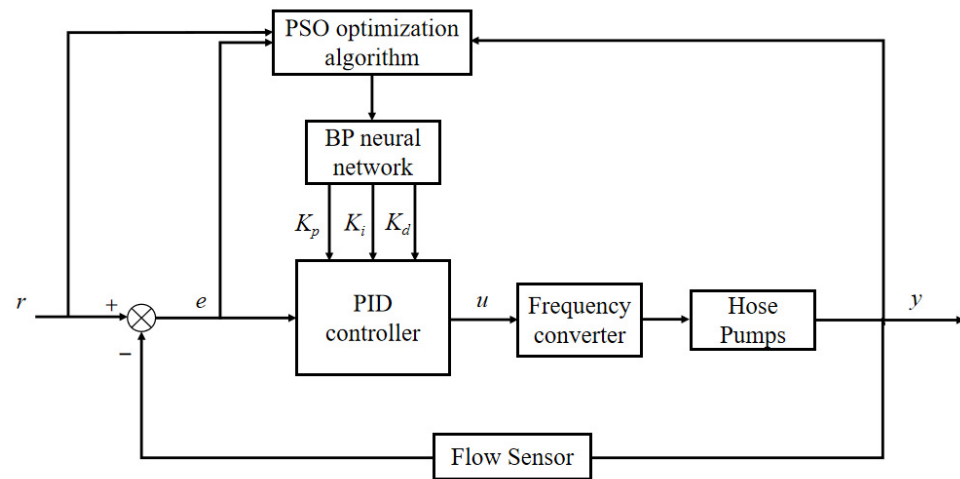


Figure 6. Structure of BP neural network PID controller based on PSO optimization.

The PSO algorithm is described in detail as follows:

In the PSO algorithm, each particle possesses two attributes: velocity V and position X . V represents the speed of particle movement, and X determines the direction of particle search. Assume that in a D -dimensional search space, a population $X = (X_1, X_2, \dots, X_n)$ is composed of n particles, and the position and velocity of the i th particle are denoted as follows:

$$X_i = (x_{i1}, x_{i2}, \dots, x_{iD}) \quad (i = 1, 2, \dots, n) \tag{25}$$

$$V_i = (v_{i1}, v_{i2}, \dots, v_{iD}) \quad (i = 1, 2, \dots, n) \tag{26}$$

where X_i represents not only the particle position, but also a potential solution to the problem, i.e., the initial weights of a set of BP neural networks. The fitness value corresponding to each particle position can be calculated by substituting X_i into the fitness function.

The current individual optimal solution P_{best} of the particle, and the current global optimal solution g_{best} of the whole particle population will be used as the basis for updating V and X in the optimization search process.

$$P_{best} = (P_{i1}, P_{i2}, \dots, P_{iD}) \quad (i = 1, 2, \dots, n) \tag{27}$$

$$g_{best} = (g_1, g_2, \dots, g_D) \tag{28}$$

V and X of the particle are updated by Equations (28) and (29), respectively.

$$v_{id}^{k+1} = w_k v_{id}^k + c_1 r_1 (P_{id}^k - x_{id}^k) + c_2 r_2 (g_d^k - x_{id}^k) \tag{29}$$

$$x_{id}^{k+1} = x_{id}^k + v_{id}^{k+1} \tag{30}$$

where $d = 1, 2, \dots, D; i = 1, 2, \dots, n; k$ is the number of current iterations; w_k is the inertia weight; c_1, c_2 are learning factors, generally take $c_1 = c_2 = 2$; r_1, r_2 are generally taken as random numbers in the range of $[0, 1]$.

The inertia weight w_k decreases as the number of iterations increases.

$$w_k = w_s - (k - 1) \frac{(w_s - w_e)}{T_{max}} \tag{31}$$

where w_s and w_e are the upper and lower bounds of inertia weights in the range of $[0.4, 0.9]$, respectively, and T_{max} is the maximum number of iterations.

In this paper, Equation (17) is used as the fitness function of the PSO algorithm, and since the optimization object is the weight of the BP neural network and the neural network structure is $4 - 5 - 3$, the dimension D is set to $4 \times 5 + 3 \times 5 = 35$, the maximum number of iterations is set to 50, the particle swarm size is taken as 20, and the initial weights of

20 groups of BP neural network are generated randomly. To prevent the particles from searching blindly, the position X and velocity V are limited to a certain range. The PSO optimization algorithm flow is shown in Figure 7.

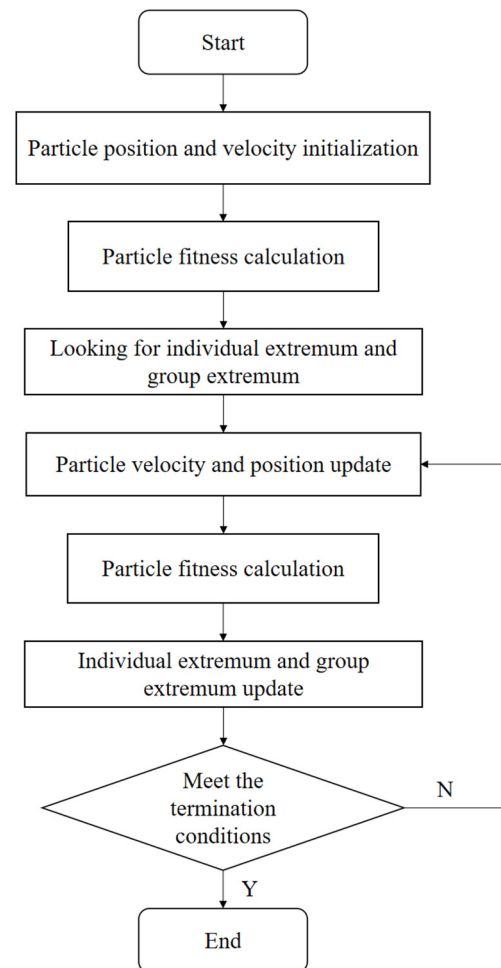


Figure 7. PSO optimization algorithm process.

3. Results

3.1. Analysis of Simulation Results

Matlab software was used for simulation, and three different control methods were used in the simulation experiments, namely: conventional PID control, BP neural network-based PID control (BP-PID control), and PSO optimization-based BP neural network PID control (PSO-BP-PID control). The unit step was used as input signal, respectively, and the simulation time was 100 s. The simulation results are as follows:

Figure 8 shows the iterative process of the PSO algorithm under unit step response, and the optimal individual adaptation value was obtained after 50 iterations. Figure 9 shows the comparison of the control effects of the three controllers under the unit step response.

The dynamic performance index was used to evaluate the control effect of the controller, where the rise time indicates the time when the system is excited by the step signal and reaches the steady-state value for the first time; the peak time indicates the time when the system is excited by the step response and reaches the peak; the regulation time indicates the time required for the system to reach stability, i.e., to enter the error tolerance range; the maximum overshoot reflects the controller control process stability. The dynamic performance of the three controllers is shown in Table 1.

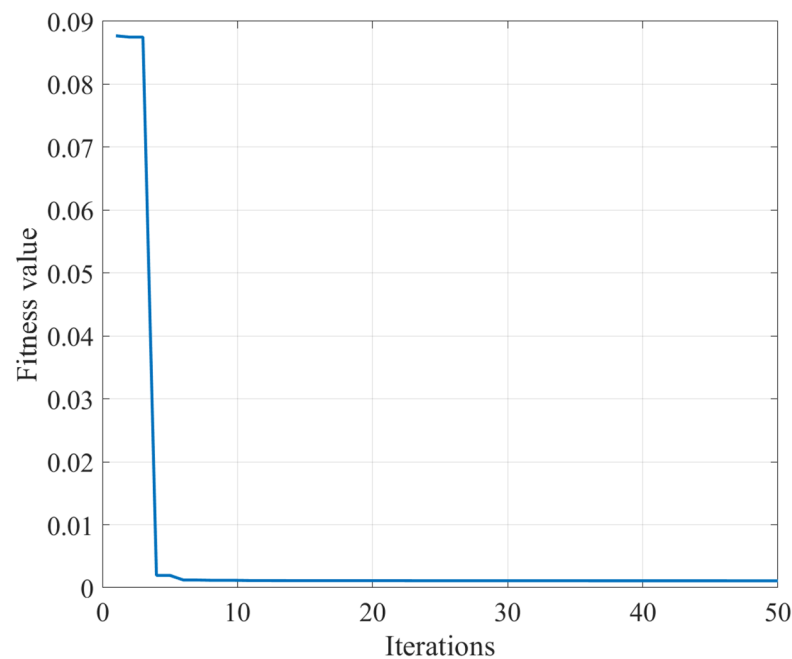


Figure 8. Iterative process of PSO algorithm under unit step response.

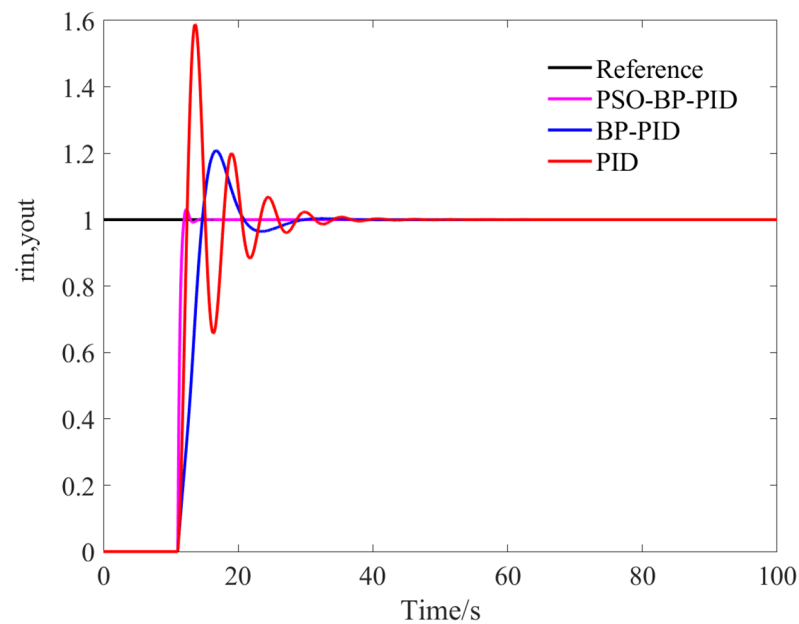


Figure 9. Comparison of the control effect of three controllers under unit step response.

Table 1. Dynamic performance of the three controllers.

Controller Type	Rise Time(s)	Peak Time (s)	Regulation Time (s)	Maximum Overshoot
PID	12.41	13.62	25.07	58.53%
BP-PID	14.69	16.73	19.68	20.74%
PSO-BP-PID	11.97	12.31	11.77	3.19%

From Figure 9 and Table 1, it can be seen that the conventional PID controller produced larger oscillation and overshoot, with 58.23% overshoot and longer regulation time although the rise time was shorter; compared with the conventional PID controller, the BP-PID

controller had a longer rise time and peak time but the overall response was relatively stable and the overshoot was reduced to 20.74%; the PSO-BP-PID controller compared with the other two controllers, the dynamic performance has been significantly improved, not only were the rise time and regulation time shortened to 11.97 s and 11.77 s, respectively, but also the overshoot amount was 3.19%, and the response was more rapid and smooth.

3.2. Precision Fertilizer Control System Flow Regulation Test

3.2.1. Testing Device and System Design

To verify the practical performance of the PSO-BP-PID algorithm, a corresponding flow rate regulation test platform was built for this paper. Using the STM32F103ZET6 microcontroller as the control element, the signal from the flow sensor received at the I/O port was calculated inside the microcontroller and converted into a variable voltage signal to adjust the output frequency of the inverter and finally changed the fertilizer flow rate at the outlet of the mixing tank. The maximum conveying flow of the hose pump is 1 m³/h, rated power is 1.5 kW, and rated voltage is 380 V. The frequency converter is rated at 2.2 kW, with an output frequency between 0 and 400 Hz and a rated voltage of 380 V. The flow sensor was selected from the stainless-steel electromagnetic flowmeter of Meacon China, model LDG-MIK, with an accuracy of 0.5%. The volume of liquid in the mixing tank was kept at 50 L during operation. The flow rate regulation test platform is shown in Figure 10.



Figure 10. Flow regulation test platform.

The USB-1252A data collector from Smacq was used to collect the data needed in the test. The collector has an advanced measurement and control system with 16 analog input channels, 12-bit vertical resolution, and up to 500 kSa/s analog acquisition capability. The schematic diagram of the data acquisition and control system is shown in Figure 11.

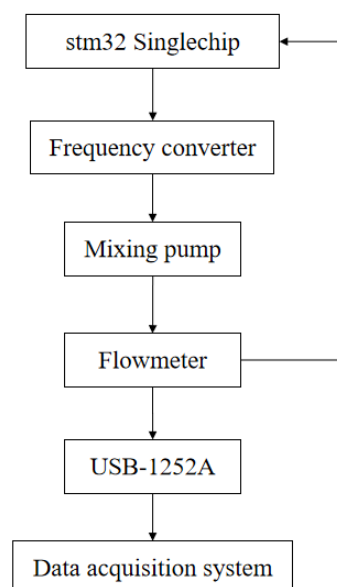


Figure 11. Schematic diagram of data acquisition and control system.

3.2.2. Analysis of Test Results

The fertilized crop in this paper is cotton, and since the fertilizer flow rate is determined by the fertilizer demand of the crop, the fertilizer demand of cotton is different in different growing periods. The flow rate of the hose pump at the outlet of the mixing tank was set to $0.4 \text{ m}^3/\text{h}$, $0.6 \text{ m}^3/\text{h}$, and $0.8 \text{ m}^3/\text{h}$ in turn, and the performance of the three controllers was tested. The test results are shown in Figures 12–14, and the performance indexes of the three controllers are shown in Tables 2–4.

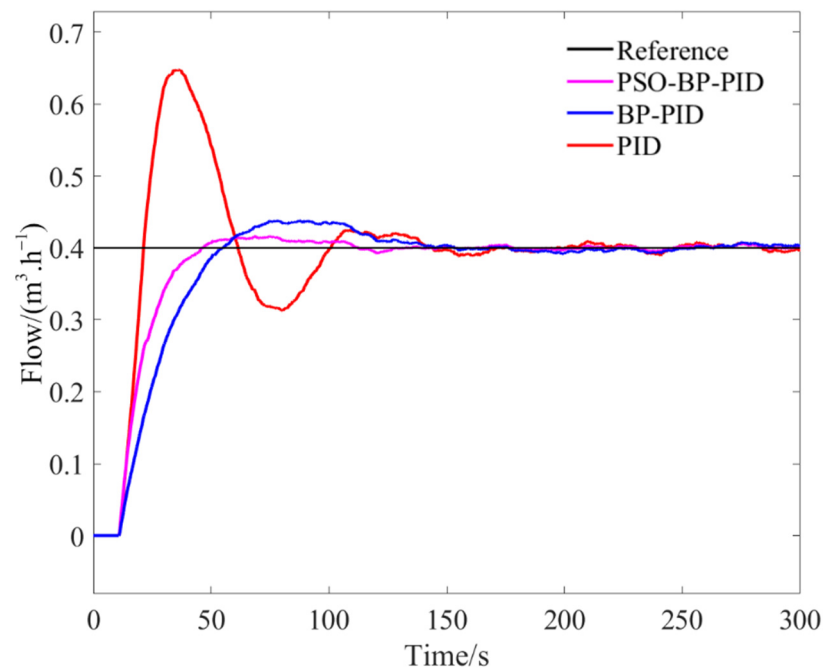


Figure 12. Regulation curves of three controllers at fertilizer application flow rate of $0.4 \text{ m}^3/\text{h}$.

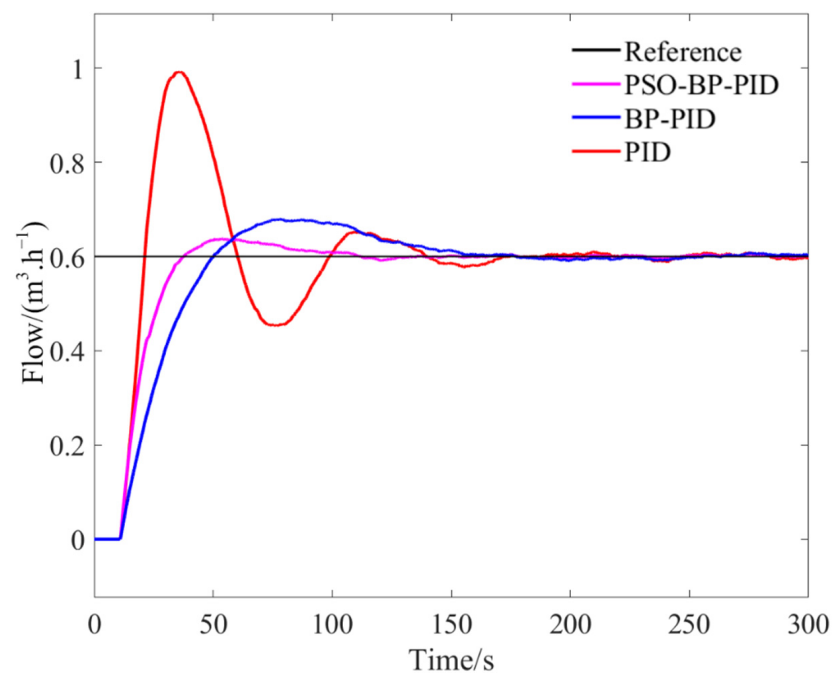


Figure 13. Regulation curves of the three controllers at a fertilizer application flow rate of $0.6 \text{ m}^3/\text{h}$.

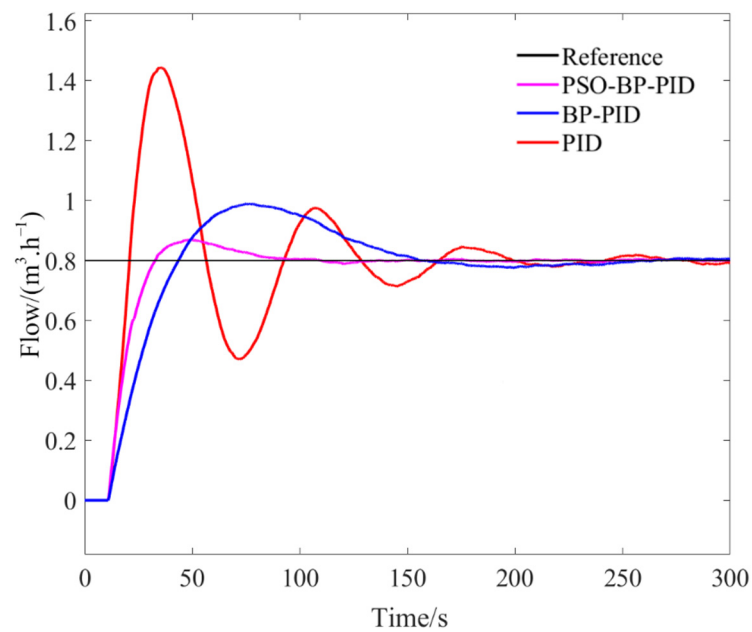


Figure 14. Regulation curves of the three controllers at a fertilizer application flow rate of $0.8 \text{ m}^3/\text{h}$.

Table 2. Comparison of the dynamic performance of three controllers at fertilizer application flow rate of $0.4 \text{ m}^3/\text{h}$.

Controller Type	Rise Time (s)	Peak Time (s)	Regulation Time (s)	Maximum Overshoot	Root Mean Square Error
PID	21.33	34.97	90.51	61.95%	0.058
BP-PID	54.88	87.47	43.10	9.55%	0.015
PSO-BP-PID	46.27	68.37	31.36	4.08%	0.004

Table 3. Comparison of the dynamic performance of three controllers at fertilizer application flow rate of $0.6 \text{ m}^3/\text{h}$.

Controller Type	Rise Time (s)	Peak Time (s)	Regulation Time (s)	Maximum Overshoot	Root Mean Square Error
PID	21.22	36.05	115.86	65.27%	0.084
BP-PID	50.13	77.97	112.52	13.15%	0.028
PSO-BP-PID	37.53	53.36	30.85	6.23%	0.014

Table 4. Comparison of the dynamic performance of three controllers at fertilizer application flow rate of $0.8 \text{ m}^3/\text{h}$.

Controller Type	Rise Time (s)	Peak Time (s)	Regulation Time (s)	Maximum Overshoot	Root Mean Square Error
PID	20.80	34.97	155.83	80%	0.125
BP-PID	43.50	74.94	131.46	23.75%	0.070
PSO-BP-PID	32.76	48.64	61.30	8.75%	0.027

The results in Tables 2–4 showed that the performance of the three controllers also changed with the increase in fertilizer flow rate. The conventional PID controller had the fastest rise time at all three fertilizer flow rates, but the overshoot was large and the flow rate had large fluctuations and could not reach the desired value quickly; the BP-PID controller had significantly less overshoot compared with the conventional PID controller, but the response speed was slower; the PSO-BP-PID controller had the minimum overshoot

and root-mean-square error at all three fertilizer flow rates, and could balance the response speed and stability of the control process at higher flow rates with good robustness to meet the control requirements in practical applications.

In recent years, the need to improve water use efficiency in irrigated agriculture has attracted a great deal of attention from researchers. The PSO-BP-PID controller developed in this paper uses a closed-loop intelligent irrigation feedback control strategy to greatly improve the efficiency of irrigation water use in the field and provide ideas for future water sustainability.

4. Conclusions

In this paper, the precision fertilizer control system was studied, its mathematical model was fitted, and the transfer function of the system was obtained. Based on the BP neural network PID adaptive control, a PSO optimization algorithm was added to optimize the initial weights of the neural network, and a BP neural network PID controller based on PSO optimization was designed, and the dynamic performance of the three controllers, PID, BP-PID, and PSO-BP-PID, were compared and analyzed.

The test results showed that the PSO-BP-PID controller was significantly better than the other two controllers in terms of control accuracy and adjustment time. At the fertilizer application flow rate of 0.4 m³/h, 0.6 m³/h, and 0.8 m³/h, respectively, the set value was reached quickly with an average maximum overshoot of 6.35% and an average adjustment time of 41.17 s. Among them, the shortest adjustment time was 30.85 s when the fertilizer application flow rate was at 0.6 m³/h. This indicates that the controller has the best control of irrigation fertilization at this flow rate.

The BP neural network PID control algorithm based on PSO optimization can adjust the PID parameters online according to changes of the environment, which improves the decision making of the controller. The algorithm reasonably determines the initial weights of the BP neural network; it solves the problems that the BP neural network easily falls into local minima and converges slowly; and not only approximates the control target faster, but also has a shorter response time; thus providing a feasible method for the control of nonlinear time-lag systems.

Author Contributions: Conceptualization, Z.M. and L.Z.; software design, Z.M.; software validation, H.W., X.M. and H.L.; resources, Z.M.; data curation, Z.M.; writing—original draft, Z.M.; writing—review and editing, H.W. and X.M.; project administration, H.L. and F.Z.; funding acquisition, X.M. All authors have read and agreed to the published version of the manuscript.

Funding: This research was funded by National Natural Science Foundation of China, grant number 52065055.

Institutional Review Board Statement: Not applicable.

Data Availability Statement: All relevant data presented in the article are stored according to institutional requirements and, as such, are not available on-line. However, all data used in this Manuscript can be made available upon request to the authors.

Conflicts of Interest: The authors declare no conflict of interest.

References

1. Silber, A.; Xu, G.; Levkovitch, I.; Soriano, S.; Bilu, A.; Wallach, R. High fertigation frequency: The effects on uptake of nutrients, water and plant growth. *Plant Soil* **2003**, *253*, 467–477. [[CrossRef](#)]
2. Wang, H.; Li, J.; Cheng, M.; Zhang, F.; Wang, X.; Fan, J.; Wu, L.; Fang, D.; Zou, H.; Xiang, Y. Optimal drip fertigation management improves yield, quality, water and nitrogen use efficiency of greenhouse cucumber. *Sci. Hortic.* **2019**, *243*, 357–366. [[CrossRef](#)]
3. Xiuyun, X.; Xufeng, X.; Zelong, Z.; Bin, Z.; Shuran, S.; Zhen, L.; Tiansheng, H.; Huixian, H. Variable Rate Liquid Fertilizer Applicator for Deep-fertilization in Precision Farming Based on ZigBee Technology. *IFAC-PapersOnLine* **2019**, *52*, 43–50. [[CrossRef](#)]
4. Ying-Zi, Z.; Hai-Tao, C.; Shou-Yin, H.; Wen-Yi, J.; Bin-Lin, O.; Guo-Qiang, D.; Ji-Cheng, Z. Design and Experiment of Slave Computer Control System for Applying Variable-rate Liquid Fertilizer. *J. Northeast Agric. Univ.* **2015**, *22*, 73–79. [[CrossRef](#)]
5. Zou, Z.; Yu, M.; Wang, Z.; Liu, X.; Guo, Y.; Zhang, F.; Guo, N. Nonlinear Model Algorithmic Control of a pH Neutralization Process. *Chin. J. Chem. Eng.* **2013**, *21*, 395–400. [[CrossRef](#)]

6. Lai, Z.; Wu, P.; Wu, D. Application of fuzzy adaptive control to a MIMO nonlinear time-delay pump-valve system. *ISA Trans.* **2015**, *57*, 254–261. [[CrossRef](#)]
7. Dong, Y.; Fu, Z.; Peng, Y.; Zheng, Y.; Yan, H.; Li, X. Precision fertilization method of field crops based on the Wavelet-BP neural network in China. *J. Clean. Prod.* **2020**, *246*, 118735. [[CrossRef](#)]
8. Feng, G.; Lei, S.; Gu, X.; Guo, Y.; Wang, J. Predictive control model for variable air volume terminal valve opening based on backpropagation neural network. *Build. Environ.* **2021**, *188*, 107485. [[CrossRef](#)]
9. Jesus, I.S.; Barbosa, R.S. Smith-fuzzy fractional control of systems with time delay. *AEU Int. J. Electron. Commun.* **2017**, *78*, 54–63. [[CrossRef](#)]
10. Bai, J.; Tian, M.; Li, J. Control System of Liquid Fertilizer Variable-Rate Fertilization Based on Beetle Antennae Search Algorithm. *Processes* **2022**, *10*, 357. [[CrossRef](#)]
11. Fu, Q.; Wang, Z.; Jiang, Q. Delineating soil nutrient management zones based on fuzzy clustering optimized by PSO. *Math. Comput. Model.* **2010**, *51*, 1299–1305. [[CrossRef](#)]
12. Navarro, J.L.; Diez, J.L.; Valera, A.; Valles, M. Remote Fuzzy Control of a DC Motor. *IFAC Proc. Vol.* **2008**, *41*, 13652–13658. [[CrossRef](#)]
13. Estofanero, L.; Edwin, R.; Claudio, G. Predictive Controller Applied to a pH Neutralization Process. *IFAC-PapersOnLine* **2019**, *52*, 202–206. [[CrossRef](#)]
14. Zhao, C.; Guo, L. Towards a theoretical foundation of PID control for uncertain nonlinear systems. *Automatica* **2022**, *142*, 110360. [[CrossRef](#)]
15. Joseph, S.B.; Dada, E.G.; Abidemi, A.; Oyewola, D.O.; Khammas, B.M. Metaheuristic algorithms for PID controller parameters tuning: Review, approaches and open problems. *Heliyon* **2022**, *8*, e09399. [[CrossRef](#)]
16. Chang, W.-D.; Shih, S.-P. PID controller design of nonlinear systems using an improved particle swarm optimization approach. *Commun. Nonlinear Sci. Numer. Simul.* **2010**, *15*, 3632–3639. [[CrossRef](#)]
17. Tang, G.; Lei, J.; Du, H.; Yao, B.; Zhu, W.; Hu, X. Proportional-integral-derivative controller optimization by particle swarm optimization and back propagation neural network for a parallel stabilized platform in marine operations. *J. Ocean Eng. Sci.* **2022**. [[CrossRef](#)]
18. Li, H.; Zhen-Yu, Z. The application of immune genetic algorithm in main steam temperature of PID control of BP network. *Phys. Procedia* **2012**, *24*, 80–86. [[CrossRef](#)]
19. Huang, G.; Yuan, X.; Shi, K.; Wu, X. A BP-PID controller-based multi-model control system for lateral stability of distributed drive electric vehicle. *J. Frankl. Inst.* **2019**, *356*, 7290–7311. [[CrossRef](#)]
20. Huang, J.; He, L. Application of Improved PSO—BP Neural Network in Customer Churn Warning. *Procedia Comput. Sci.* **2018**, *131*, 1238–1246. [[CrossRef](#)]
21. Ren, C.; An, N.; Wang, J.; Li, L.; Hu, B.; Shang, D. Optimal parameters selection for BP neural network based on particle swarm optimization: A case study of wind speed forecasting. *Knowl. Based Syst.* **2014**, *56*, 226–239. [[CrossRef](#)]
22. Zhang, J.-R.; Zhang, J.; Lok, T.-M.; Lyu, M.R. A hybrid particle swarm optimization–back-propagation algorithm for feedforward neural network training. *Appl. Math. Comput.* **2007**, *185*, 1026–1037. [[CrossRef](#)]

Article

Design and Experimental Testing of a Control System for a Solid-Fertilizer-Dissolving Device Based on Fuzzy PID

Xiuhua Song, Hong Li ^{*}, Chao Chen, Huameng Xia, Zhiyang Zhang and Pan Tang

Research Center of Fluid Machinery and Technology, Jiangsu University, Zhenjiang 212013, China

^{*} Correspondence: hli@ujs.edu.cn; Tel.: +86-139-5289-1655

Abstract: To overcome the problem of poor uniformity of solid-fertilizer-dissolving devices due to lag of fertilizer dissolution, a closed-loop control system based on fuzzy proportional-integral-derivative (PID) was designed and tested. A fertilizer concentration regulation model was then established according to the results. In this system, the control core was an STM32 used to feed back the fertilization concentration by detecting the electrical conductivity. For real-time adjustment of the fertilizer flow rate and water flow rate, a fuzzy PID control algorithm was utilized to compare the detected concentrations with the set concentrations. The linear relationships between quantities such as the fertilizer rate and PWM frequency, water flow rate and PWM duty ratio of the direct-current pump, and fertilizer concentration and electrical conductivity were all established to calibrate the system. The influence of the fertilizer flow rate and water flow rate on fertilizer concentration was determined by the control variable test method. The results showed a positive linear relationship between fertilizer concentration and fertilizer flow rate, while a reverse linear relationship was established between fertilizer concentration and water flow rate. After the introduction of the control system into the self-developed solid-fertilizer-dissolving device, the fertilizer concentration fluctuated near the set concentration in a range of no more than 1 g/L. After the disturbance of the fertilization device, the control system fine-tuned the device with a steady-state error of about 0.55 g/L after the system reached stability. The control system designed in this study was shown to run normally with good stability, speed, and accuracy, and with improved fertilization uniformity of the solid-fertilizer-dissolving device. This study lays the foundation for further study of fertilization control systems. It also provides a reference for the development of precise and intelligent fertigation.

Citation: Song, X.; Li, H.; Chen, C.; Xia, H.; Zhang, Z.; Tang, P. Design and Experimental Testing of a Control System for a Solid-Fertilizer-Dissolving Device Based on Fuzzy PID. *Agriculture* **2022**, *12*, 1382. <https://doi.org/10.3390/agriculture12091382>

Academic Editors: Muhammad Sultan, Redmond R. Shamshiri, Shamim Ahamed and Muhammad Farooq

Received: 14 August 2022

Accepted: 1 September 2022

Published: 3 September 2022

Publisher's Note: MDPI stays neutral with regard to jurisdictional claims in published maps and institutional affiliations.



Copyright: © 2022 by the authors. Licensee MDPI, Basel, Switzerland. This article is an open access article distributed under the terms and conditions of the Creative Commons Attribution (CC BY) license (<https://creativecommons.org/licenses/by/4.0/>).

Keywords: fertilization uniformity; closed-loop control; single-chip microcomputer; fuzzy PID; solid-fertilizer-dissolving device

1. Introduction

Fertigation is a planting technology combining irrigation with fertilization to achieve precise irrigation and uniform fertilization according to the soil conditions, water requirements, fertilizer requirements, and nutrient contents of different crops [1–3]. The fertigation technology can greatly improve the conservation of water and fertilizer, as well as enhancing the quality and yield of crops [4,5]. With the continuous development of modern agriculture, fertigation is developing towards low energy consumption and intelligence [6].

In recent years, various fertigation equipment and control systems have been developed based on many technologies [7]. For instance, Leedy et al. [8] designed a fertilizer distribution device for a sprinkler irrigation system to achieve fertigation. However, their system required prior mixing of water and fertilizer in the device. Zhang et al. [9] designed a control system to detect the temperature, humidity, illumination, and substrate moisture content of crops in a greenhouse with real-time feedback. Using multi-information data fusion modeling, the authors then designed a device that could dynamically control irrigation and fertilization and achieve accurate control of the ratio of liquid fertilizer and water. Yang et al. [10] proposed a fertilization device combining allocation algorithm estimation

and a precision fertilization control model to ensure an optimal control process. Anthony et al. [11] designed a liquid fertilizer fully mixed with water injected into the pipeline of the spraying system to achieve uniform distribution of the fertilizer in water flow.

In terms of fertigation control systems, Wang et al. [12] adopted a segmented control strategy to solve problems, such as lag and instability of EC values in the detection of water and fertilizer mixtures during vegetable production to effectively overcome overshoot. Bi et al. [13] integrated fuzzy PID based on grey prediction to control the fertigation process and achieve precision irrigation of water and fertilizer. Wang et al. [14] developed a remote automatic irrigation control system for strawberries based on PLC and configuration software. Zhang et al. [15] proposed an adaptive nonlinear model identification control algorithm for the integrated irrigation of water, fertilizer, and medicine in a greenhouse. Peng et al. [16] designed an intelligent fertigation system using the Internet of Things, big data, and other technologies to combine expert experience and agricultural technology for providing the optimal irrigation scheme according to the collected information and experience. Sun et al. [17] designed an integrated control system for water and fertilizer based on neural network prediction and fuzzy control.

The traditional water and fertilizer control system is often suitable for small lags. However, the stability of the control system greatly affects control systems with severe lags [18]. PID control has defects that are greatly influenced by the external environment, and the parameter settings are often complex. However, the operation of proportional-integral-derivative (PID) control is simple and widely used [19,20]. Fuzzy control does not require the establishment of mathematical models, but needs control rules to be set according to control experience. However, since no integral part exists, the steady-state error is often difficult to eliminate [21,22]. Therefore, PID control and fuzzy control can be combined to obtain an accurate water and fertilizer control system [23].

Current research dealing with fertigation control systems and equipment uses liquid fertilizer or dissolves the solid fertilizer ahead of the application. In the present work, a control system for the dissolution of solid fertilizer was designed using a fuzzy PID algorithm to solve the lag of solid fertilizer dissolution. The control system was applied to the self-developed solid-fertilizer-dissolving device to adjust the working parameters in real time according to the set concentration. The results showed that the fertilizer concentration could be stabilized around the set value, solving the problem of poor fertilizer uniformity caused by the lag of solid fertilizer dissolution.

2. Design of the Solid-Fertilizer-Dissolving Control System

2.1. Structure and Working Principle of the Solid-Fertilizer-Dissolving Device

The structure of the dissolving device is shown in Figure 1. The system mainly consists of the fertilizer-adding part, mixing part, and control part. The fertilizer-adding part is mainly composed of a hopper, screw rod, and stepping motor, allowing the addition of solid fertilizer according to the set rate. The mixing part consists of a direct-current motor, a mixer, a filter, a mixing barrel, and a direct-current pump, all used to fully mix the water and solid fertilizer. The filter is installed in the stirring drum and used to screen the water-insoluble impurities in the solid fertilizer. The control part consists of a flow sensor, EC sensor, and circuit board installed in the control cabinet. Meanwhile, the circuit board in the control cabinet is used to control the stepping motor, direct-current motor, and direct-current pump, as well as to process the signals collected by the flow sensor and the conductivity sensor. Additionally, the water inlet pipe extends to the outer wall of the filter through the mixing barrel. In this way, the water inlet pipe impacts the solid fertilizer accumulated at the bottom to accelerate the dissolution of the fertilizer. On the other hand, the fertilizer solution outlet pipe also extends to the outer wall of the filter through the mixing barrel. The EC sensor is installed on the fertilizer solution outlet pipe to measure the fertilizer solution's concentration at the device outlet. Finally, a sewage outlet pipe is used to discharge excess residual fertilizer solution.

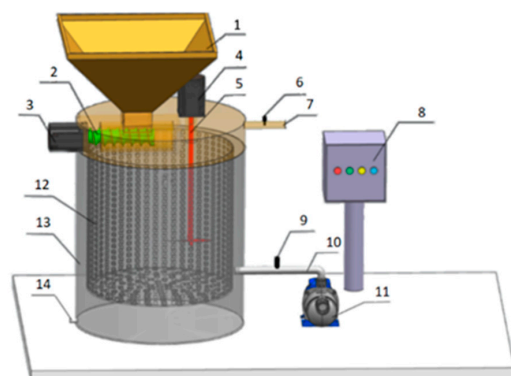


Figure 1. Schematic diagram of the solid-fertilizer-dissolving and -applying device: (1) hopper; (2) screw rod; (3) stepping motor; (4) direct-current motor; (5) mixer; (6) EC sensor; (7) fertilizer solution outlet pipe; (8) control cabinet; (9) flow sensor; (10) water inlet pipe; (11) direct-current pump; (12) filter; (13) mixing barrel; (14) sewage outlet pipe.

2.2. Design of the Control System

2.2.1. Design of the Hardware System

The main controller of the solid fertilizer dissolution control system was an STM32, used for processing and sending signals [24]. The hardware design of the control system included three parts: (i) fertilizer flow rate control, (ii) water flow rate control, and (iii) fertilizer solution concentration detection. The fertilizer flow rate control was achieved by changing the speed of the stepping motor. In other words, faster speeds of the stepping motor would yield faster fertilizer flow rates. The stepping motor turned the electric pulse signal into angular displacement through the driver. Therefore, a PWM wave with a duty ratio of 50% and adjustable frequency was set as a pulse signal input to the front end of the stepping motor's drive circuit, and the output of multiple pulse numbers was determined through interrupt counting. In addition, a timer function was used to stop and start the stepping motor.

The adjustment of the water flow rate was achieved by changing the motor speed of the direct-current pump. To solve the problem of insufficient driving ability of the single-chip microcomputer's output signal, a full-bridge driving circuit was employed to control the speed of the direct-current motor, which then controlled the direct-current water pump [25]. The flow of the direct-current water pump was regulated by a PWM wave with different duty cycles given by the single-chip microcomputer. After completing the water supply, the timer was turned off to stop the operation of the direct-current water pump. An input-level sensor was also used in this design for real-time monitoring of the height of the fertilizer solution present in the bucket [26]. When the liquid level in the fertilizer barrel exceeded the preset dangerous liquid level, the power supply of the device was cut off automatically to prevent the fertilizer from overflowing. This design indirectly detects the concentration of the fertilizer solution by estimating the EC value of the fertilizer solution exported by the device. The EC value of the fertilizer solution was measured by the conductance electrode. The detection circuit was mainly composed of an RC oscillator, Schmidt trigger, and binary divider.

2.2.2. System Software Design

In the second part, reserved for adding the fertilizer, a stepping motor was used to adjust the amount of fertilizer in real time to achieve precise fertilizer allocation. The stepping motor drive flowchart is provided in Figure 2.

The stepping motor drive functioned as a timer. Firstly, the timer was initialized, and the count started after assigning the initial value. The output pulse wave drove the motor to rotate, and the encoder fed back the motor speed. The control system then fine-tuned the stepping motor according to the relationship between the stepping motor speed and amount of added fertilizer to control the fertilizer flow rate. At relatively fast speeds of the

stepping motor, the pulse frequency was reduced; otherwise, it increased. After complete addition of the fertilizer, the timer was turned off, and the stepping motor stopped running.

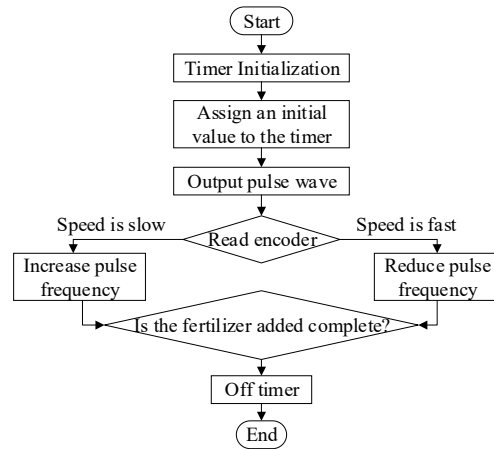


Figure 2. Stepping motor drive control process flowchart.

The direct-current water pump in the water supply section was adjusted by PWM and enabled the signal given by the single-chip microcomputer. The current signal was generated upon water flowing through the flow sensor, while the voltage signal was obtained through the I/U conversion circuit. The single-chip microcomputer was used to measure the average voltage after sampling several times, followed by converting the water flow rate according to the relationship between voltage and flow rate. This would adjust the PWM duty cycle, thereby controlling the water flow rate.

To produce signal acquisition conductance electrodes through the design of a signal conditioning circuit and a stable output voltage signal, the ADC was sampled many times by the single-chip microcomputer to calculate the average voltage. To reduce the error, the EC value of the fertilizer solution was calculated according to the numerical relationship between the voltage and the electrode range. Finally, the fertilizer solution concentration was converted according to the functional relationship between the fertilizer solution concentration and the electrical conductivity calibrated experimentally. The program flowchart of fertilizer solution concentration detection is depicted in Figure 3.

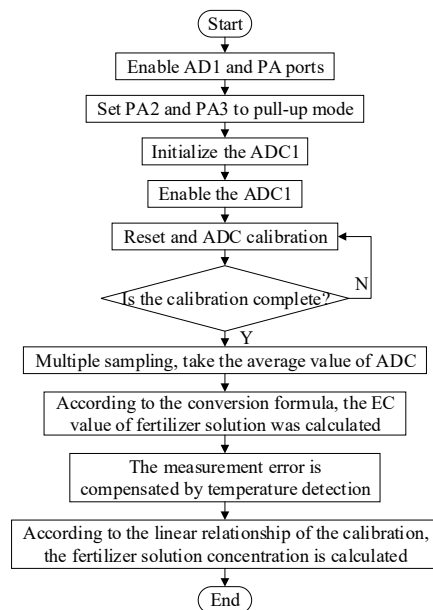


Figure 3. Flowchart of fertilizer concentration detection.

2.2.3. Design of the Closed-Loop Feedback System Based on Fuzzy PID

Since the dissolution and application of water and fertilizer occurred in real time, great uncertainty should be expected. To obtain better control of the water and fertilizer dissolution, a simplified dynamic model of dissolution was thus established to analyze the changing characteristics of the dissolution process by ignoring other interfering factors and assuming mixed fertilizer barrels with an unchanged liquid level. Moreover, the liquid fertilizer product remained the same, and the input of the whole fertilizer mixing process for solid fertilizer and water supply after the solid fertilizer and water were mixed adequately yielded a uniform fertilizer solution concentration. The latter was used as the output for the solution of mixed fertilizer. The dynamic model of the composting process established in this paper is illustrated in Figure 4.

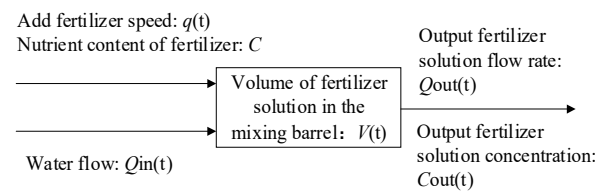


Figure 4. Dynamic model of the composting process.

According to the principle of fertilizer balance, Equation (1) can be obtained when the system reaches dynamic equilibrium. This can be accomplished by following the conservation of fertilizer quantity. Furthermore, Equation (2) can be obtained by following the conservation of fertilizer solution volume in the fertilizer mixing barrel.

$$\frac{d[V(t)C_{out}(t + \tau)]}{dt} = Cq(t) - Q_{out}(t)C_{out}(t + \tau) \tag{1}$$

$$\frac{dV(t)}{dt} = Q_{in}(t) + q(t) - Q_{out}(t) \tag{2}$$

Equation (3) consists of the following hypothetical condition:

$$Q_{in}(t) + q(t) = Q_{out}(t) \tag{3}$$

After substituting Equations (2) and (3) into Equation (1), the dynamic expression of the fertilizer mixing process can be obtained:

$$V(t)\frac{dC_{out}(t + \tau)}{dt} + Q_{out}(t)C_{out}(t + \tau) = Cq(t) \tag{4}$$

where $Q_{in}(t)$ is the water flow rate (m^3/h), $Q(t)$ represents the fertilizer addition rate (kg/min), C is the nutrient content of the fertilizer, $Q_{out}(t)$ denotes the flow rate of the output fertilizer solution (m^3/h), $C_{out}(t)$ is the concentration of the output fertilizer solution (g/L), and $V(t)$ refers to the volume of the fertilizer solution in the fertilizer mixing barrel (L).

Equation (4) is a simplified dynamic model of solid fertilizer dissolution and the application process integrating water and fertilizer. Based on this model, PID control and fuzzy control were further adopted in this study to set the control parameters of both fertilizer flow rate and water flow rate in the software program, so as to accurately adjust the fertilizer concentration at the outlet of the mixing equipment. Fuzzy control includes three processes: (i) fuzzy, (ii) fuzzy control rules, and (iii) defuzzification [27]. Such a design achieves several features: The first consists of fertilizer solution concentration values as input variables in the system. The second concerns the preliminary test data as the fuzzy rules to detect the fertilizer solution concentration as the feedback variable system. The third deals with input variables after variable feedback by defuzzification to adjust the fertilizer solution concentration until meeting the preset fertilizer solution density. According to the deviation $e(t)$ between the given value $r(t)$ of the system and the output

response $c(t)$, the PID controller uses the PID algorithm to calculate the control quantity and adjust the concentration of the fertilizer solution. The control law can be expressed as follows:

$$U(t) = K_p \left\{ e(t) + \frac{1}{T_i} \int_0^t e(t)dt + T_d \frac{de(t)}{dt} \right\} \tag{5}$$

among the following quantities:

$$e(t) = r(t) - c(t) \tag{6}$$

where K_p is the proportional gain, T_i represents the integral time constant, T_d is the differential time constant, $e(t)$ refers to the control deviation (g/L), $r(t)$ is the set fertilizer solution concentration (g/L), and $c(t)$ denotes the actual fertilizer solution concentration (g/L).

In the actual control process, sampling the concentration of the fertilizer solution at different times was necessary to calculate the deviation in the concentration of the fertilizer solution, as well as to calculate the control quantity to necessary achieve good control of the system. Therefore, the above continuous formulae required discretization. The discretized PID consisted of two forms: (i) position, and (ii) incremental [28].

- Position PID control algorithm

At extremely small sampling periods, multiple sampling time points kT were set to replace the continuous time t . The sum of the deviation of all time points was replaced by integration, and the deviation increment of adjacent time points was replaced by differentiation. The results can be obtained using Equations (7) and (8):

$$\int_0^t e(t)dt = \sum_{i=0}^k Te(i) \tag{7}$$

$$\frac{de(t)}{dt} = \frac{e(k) - e(k-1)}{T} \tag{8}$$

where T is the sampling period and k represents the sampling serial number.

Substituting Equations (7) and (8) into Equation (5) yields the position PID control algorithm formula:

$$U(k) = K_p \left\{ e(k) + \frac{T}{T_i} \sum_{i=0}^k e(i) + \frac{T_d}{T} [e(k) - e(k-1)] \right\} \tag{9}$$

- Incremental PID control algorithm

The incremental PID only outputs the incremental $\Delta U(k)$ of the control quantity. The output expression of $(k - 1)$ times can be obtained from Equation (9):

$$U(k-1) = K_p \left\{ e(k-1) + \frac{T}{T_i} \sum_{i=0}^k e(i) + \frac{T_d}{T} [e(k-1) - e(k-2)] \right\} \tag{10}$$

The incremental PID control algorithm formula can be obtained by subtracting Equations (9) and (10):

$$\Delta U(k) = K_p [e(k) - e(k-1)] + K_i e(k) + K_d [e(k) - 2e(k-1) + e(k-2)] \tag{11}$$

where K_p is the proportional gain, K_i represents the integral coefficient, and K_d is the differential coefficient.

According to Equation (11), only $e(k)$, $e(k - 1)$, and $e(k - 2)$ would affect the output of delta $\Delta U(k)$ to reduce the influence of calculation error on the output control quantity. The control quantity $U(k)$ in the position algorithm corresponds to the state of the controlled object. Upon disturbance of the control quantity and distortion of the signal, the controlled object produces a large error. Therefore, the incremental PID control algorithm was adopted in this paper. Fat-soluble solid fertilizer equipment, through the sensor detection and feedback of fertilizer solution concentration information, was used to determine the current

time from the combination of fertilizer solution density deviation e and error change ec as inputs. This was set according to the fuzzy controller to meet the requirements of different PID parameter self-tuning times, real-time adjustment of the fertilizer flow rate, and real-time control of the water flow rate. The actual fertilizer solution concentration was then adjusted close to the preset value. The block diagram of the fuzzy PID control system is shown in Figure 5.

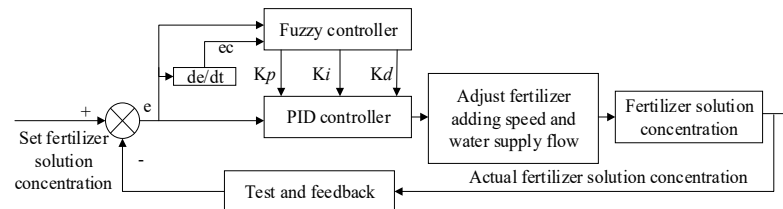


Figure 5. Fuzzy PID control system program diagram.

3. Test Scheme and Methods

The control system studied in this paper was designed to adjust the stepping motor speed by changing the PWM frequency. By varying the duty ratio of the PWM wave to adjust the water flow rate, the fertilizer solution concentration was determined by measuring the electrical conductivity. To precisely control and detect the solid fertilizer dissolution and application device using the control system, calibration of the relationships between the above parameters through experiments was necessary to establish the relationship of the control program. Furthermore, a dissolution and application device equipped with the control system was taken as the research object to analyze the control performance of the system. As shown in Figure 6b, a device performance test rig was built. A schematic diagram of the device performance test is shown in Figure 6a.

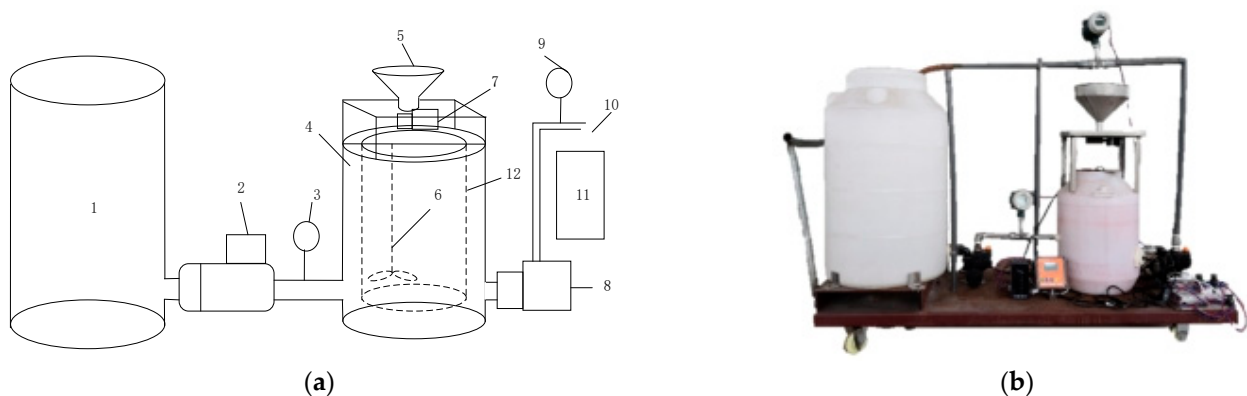


Figure 6. (a) Schematic diagram of the performance test of the dissolving device: (1) source of water; (2) water pump; (3) flowmeter; (4) mixed fertilizer bucket; (5) fertilizer inlet; (6) stirrer; (7) stepping motor; (8) water pump; (9) flowmeter; (10) fertilizer solution export; (11) control panel; (12) filter. (b) Performance test bench of the solution applicator equipped with the control system.

The experiments were carried out in the Sprinkler Irrigation Laboratory of the Fluid Mechanical Engineering Technology Research Center of Jiangsu University. To facilitate the observation, both the outlet pump and the inlet pump used direct-current water pumping. The white plastic bucket on the left-hand side stored the water for supply. The solid fertilizer was then added to the funnel of fertilizer inlet, followed by installing the sensors and control components, as well as other equipment. Next, the device was checked to ensure that it was in good condition, and then tested to confirm the relevant operation state.

3.1. Calibration Testing of the Fertilizer Addition Rate

In a previous study [29], the following formula was proposed to calculate the fertilizer rate:

$$q = 0.304\pi\rho^{1.036}(D^2 - d^2)^{0.932}n^{0.948}L^{0.964} \times 10^{-9} \tag{12}$$

where q is the fertilizer flow rate (kg/min), ρ represents the fertilizer bulk density (kg/m³), n is the motor speed (r/min), D is the outer diameter of the screw (mm), d is the internal meridian of the screw (mm), and L denotes the screw pitch (mm).

In Figure 6b, the outer diameter, inner diameter, and pitch of the screw in the test bed are set to 25 mm, 12 mm, and 18 mm, respectively. As a result, the fertilizer flow rate in the testing bed can be calculated as follows:

$$q = 4.43 \times 10^{-6}\rho^{1.036}n^{0.948} \tag{13}$$

For the same fertilizer, the fertilizer flow rate was only related to the speed of the stepping motor, which can be adjusted through frequency. Therefore, calibration tests were carried out on the relationship between the speed of the stepping motor and the frequency. Here, the single-chip microcomputer sent PWM waves with frequencies of 120, 180, 240, 300, 360, 420, 480, 540, and 600 Hz. The number of turns driven by the motor to rotate the screw within 2 min was tested.

3.2. Calibration Testing of the Water Flow Rate

The water source bucket was filled with water. Moreover, the direct-current pump's control duty ratio was adjusted to 15%, 20%, 25%, 50%, 75%, and 100%. The time taken for the water in the water source bucket to be pumped out was tested under different duty ratios. Finally, the time was converted into water flow rate and analyzed as a function of the duty ratio.

3.3. Calibration Testing of the Relationship between the Concentration and Conductivity of the Fertilizer Solution

In this experiment, two different kinds of fertilizer were tested to calibrate the test of the fertilizer solution concentration: the first consisted of potassium chloride (total nutrient: K₂O ≥ 60%; average particle size: 0.60 cm), and the second was a compound fertilizer (N-P₂O₅-K₂O: 17-5-7, total nutrient ≥ 24%, average particle size: 0.45 cm). Their saturated solubility at 20 °C was 0.230 and 0.922 g/cm³, respectively. Briefly, 1 L of water was put into the bucket, and 10 g of each fertilizer was poured in sequence and left to dissolve in the water. After even mixing, the EC value of the fertilizer solution was recorded after each dissolution. According to the scattered points of the recorded test data, the relationship between the concentration of fertilizer solution and the EC value was fitted through regression.

3.4. Effects of the Fertilizer Flow Rate and Water Flow Rate on the Fertilizer Solution Concentration

The changes in the fertilizer solution concentration under different fertilizer flow rates and water flow rates were investigated. Additionally, the variations in the fertilizer solution concentration after adding the control system were compared. According to Equation (13), stepping motor speeds of 60, 30, and 15 r/min led to corresponding fertilizer addition rates of 0.26, 0.13, and 0.07 kg/min, respectively. The respective water flow rates were 1.5, 1.0, and 0.5 m³/h. The fertilizer flow rate and water flow rate were tested in pairs, and the results are listed in Table 1.

Table 1. Combined experiments of different fertilizer flow rates and water flow rates.

Pattern	A	B	C	D	E	F	G	H	I
Water flow rate/m ³ h ⁻¹	1.5	1.5	1.5	1.0	1.0	1.0	0.5	0.5	0.5
Fertilizer flow rate/kg min ⁻¹	0.26	0.13	0.07	0.26	0.13	0.07	0.26	0.13	0.07

The mean deviation was used to measure the dispersion degree of a set of data, but the stability of the fertilizer solution's concentration required evaluation in this study [30]. Hence, Equation (14) was developed in this paper to calculate the fertilization uniformity coefficient of this system:

$$D_S^* = \left(1 - \frac{A.D.}{\bar{C}}\right) \times 100\% \quad (14)$$

where D_S^* is the uniformity coefficient of fertilization (%), $A.D.$ represents the average deviation of the concentration data (g/L), and \bar{C} is the arithmetic mean value of the data (g/L).

To determine the long-term working state of the device, the dissolution and application time of each combination test was extended to 110 min. The fertilizer was then continuously added for the first 90 min and stopped for the last 20 min. After obtaining a stable test bed, the control variable test method was used for testing, and data under combined tests were obtained.

3.5. Control System Performance Testing

In practical applications, the fertilizer would take some time to dissolve completely. Thus, the control system developed in this study fine-tuned the fertilizer flow rate and water flow rate through fuzzy PID control to yield a stable concentration of fertilizer solution in the fertilizer application device. For this reason, the control performance of the control system was tested on the test platform (Figure 6b). Potassium chloride was employed as the test fertilizer; the initial water flow rate was set to 2 m³/h, and the fertilizer flow rate was 0.5 kg/min. The concentrations of the fertilizer solution were fixed at 2, 4, 6, 8, and 10 g/L. The electrical conductivity in the mixing barrel of the device equipped with a control system was converted into concentration. After completion of the setting, the test stand was started, and fertilizer was supplemented to the hopper at all times. The data were measured every 1 min from the start of the process, and the experiment lasted 90 min. The change in the fertilizer solution's concentration in the mixed fertilizer barrel over time was plotted for analysis. The control system was evaluated in terms of three performance indicators (i.e., stability, rapidity, and accuracy) to analyze its performance. The three indicators of the control system were represented by specific parameters: Stability consisted of the time taken by the control system to return to the set value after adjusting the concentration of the fertilizer solution when interference was recorded as the adjustment time. Rapidity represented the time required for the fertilizer solution's concentration to reach the set value from the beginning, denoted as the response time. Accuracy was the absolute value of the difference between the output value and the set value when the concentration of the fertilizer solution became stable, denoted as the steady-state error (Equation (6)).

4. Results and Analysis

4.1. Relationship between Fertilizer Flow Rate and PWM Wave Frequency

The relationship between speed and PWM wave frequency after testing is shown in Figure 7. An obvious linear relationship between motor speed and PWM wave frequency was observed. After fitting, the relationship between motor speed and PWM wave frequency can be expressed by Equation (15):

$$n = f/4 \quad (15)$$

where n is the stepping motor speed (r/min) and f represents the pulse frequency (Hz).

Substituting Equation (15) into Equation (13) yields the relationship between fertilizer flow rate and frequency:

$$q = 1.19 \times 10^{-6} \rho^{1.036} f^{0.948} \quad (16)$$

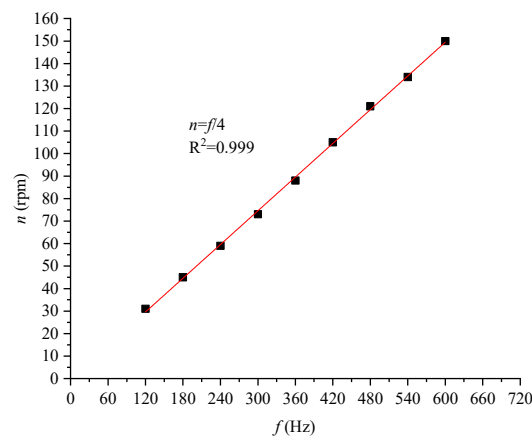


Figure 7. The relationship between the fertilizer flow rate and the frequency of PWM waves.

4.2. Relationship between Water Flow Rate and PWM Duty Cycle

The relationship between water flow rate and PWM wave duty cycle after testing is shown in Figure 8. After fitting, the relationship between the flow rate and PWM duty cycle can be expressed as follows:

$$q = 0.014DC - 0.05 \tag{17}$$

where q is the water flow rate (m^3/h) and DC refers to the duty ratio.

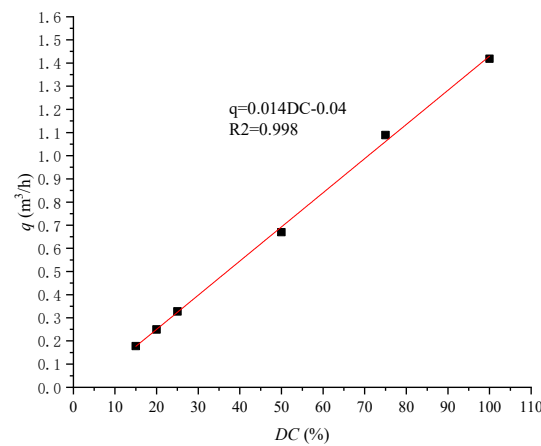


Figure 8. The relationship between the water flow rate and PWM duty ratio.

The experimental results showed a linear relationship between the water flow rate and PWM duty cycle.

4.3. Relationship between the Concentration of Fertilizer Solution and Electrical Conductivity

The experimental relationship between the concentrations of the potash fertilizer and compound fertilizer solution and the EC values is illustrated in Table 2. After fitting, an obvious linear relationship between the concentration of the fertilizer solution and the EC value was observed [31]. The relationship between the concentration of the fertilizer solution and the conductivity of the two fertilizers can be further obtained by Equations (18) and (19):

$$C_K = 0.48EC - 2.5 \tag{18}$$

$$C_F = 0.92EC - 0.92 \tag{19}$$

where C_K represents the concentration of the potash fertilizer solution (g/L), C_F is the concentration of the compound fertilizer solution (g/L), and EC is the conductivity value of the fertilizer solutions (mS/cm).

Table 2. Test data sheet of the relationship between the concentration of fertilizer and the conductivity.

Fertilizer Solution Concentration (g/L)	0	10	20	30	40	50	60	70	80	90	100
EC of K_2O (mS/cm)	0.6	34.42	46.67	68.27	90.12	111.3	131.02	151.18	171.7	189.49	207.2
EC of $N-P_2O_5-K_2O$ (mS/cm)	0.58	14.14	25.13	35.34	43.1	62.83	59.1	68.06	77.61	95.78	115.89

After fitting, the correlation coefficients of the potash fertilizer solution concentration, compound fertilizer solution concentration, and EC value were estimated to be 0.999, 0.96, and 0.97, respectively. The linear relationship between the concentration of the potash fertilizer solution and the EC value was the best. Therefore, the potash fertilizer was used as the test fertilizer in subsequent experiments to improve the control accuracy of the fertilizer solution concentration. The control system of the designed fertilizer solution concentration detection process only required conversion of the EC value of the fertilizer solution to yield the concentration of the fertilizer solution.

4.4. Influence of the Control System on Fertilizer Solution Concentration

The variation curves of fertilizer concentration over time, with or without a control system, in different modes, are depicted in Figures 9 and 10. In different modes and after some time, the concentration of the solution reached a stable value. When the concentration of the fertilizer solution changed greatly, the control system adjusted to ensure the stability of the concentration of the fertilizer solution. Comparing Figures 9 and 10, it can be seen that the uniformity and stability of the fertilizer solution’s concentration were significantly improved using the control system.

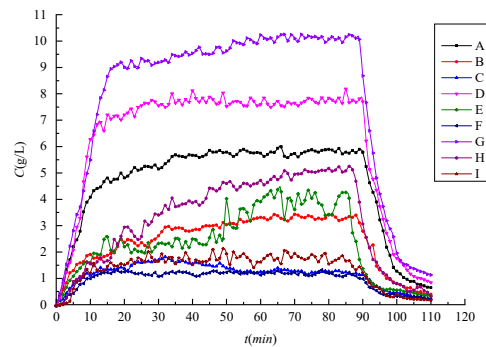


Figure 9. Diagram showing changes over time without a control system.

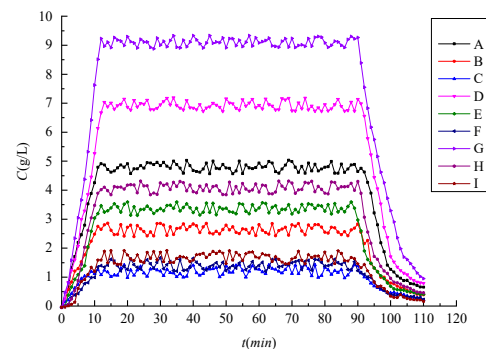


Figure 10. Diagram showing changes over time with a control system.

Based on Equation (14), the fertilization performance parameters of the dissolution and application device were obtained when the control system was adjusted (Table 3). According to the uniformity coefficient of fertilization, the stability of the fertilizer solution's concentration was significantly improved when the fertilizer was regulated by the control system. The uniformity coefficient of fertilization in each mode reached more than 65%, with an average of 69.16% and a maximum of 74.58%. Using the control variable method, A-B-C, D-E-F, and G-H-I were divided into three groups. When the water flow rate was constant, the concentration of the fertilizer solution increased with the fertilizer flow rate until reaching a stable value, with an approximately positive linear relationship. A-D-G, B-E-H, and C-F-I were divided into three groups. When the rate of fertilizer addition was constant, the change trend of the fertilizer solution's concentration was similar, while the stable value appeared different. The fertilizer solution concentration increased as a function of the decrease in the water flow rate until reaching a stable value, with a negative linear relationship.

Table 3. Fertilizer performance parameters of the solution application device under different fertilizer flow rates and water flow rates.

Different Patterns	A	B	C	D	E	F	G	H	I
Fertilizer solution concentration at stabilization/(g/L)	4.78	2.64	1.21	6.89	3.36	1.41	9.08	4.07	1.68
The average concentration of the fertilizer solution/(g/L)	4.01	2.21	1.03	5.70	2.71	1.17	7.53	3.30	1.37
Coefficient of evenness of fertilization/(%)	71.10	71.36	74.58	68.66	65.13	69.18	69.72	65.71	66.96

4.5. Control System Performance

After setting the target fertilizer concentration at the outlet of the fertilizer mixing barrel, the actual fertilizer concentration was measured, and the change curve of fertilizer concentration was obtained. In Figure 11, A, B, C, D, and E represent the fertilizer solution concentration change curves with the set values of 2, 4, 6, 8, and 10 g/L, respectively. It can be seen that the export of fertilizer solution concentration reached a set value after a certain time to prevent any further rise in the fertilizer solution concentration, which would yield excessive overshoot. Thus, the software program limited the range within ± 1 g/L, so that the fertilizer solution concentration under the adjustment of the control system slowly became close to the set value. Over time, the concentration of the fertilizer solution fluctuated less from the the set concentration.

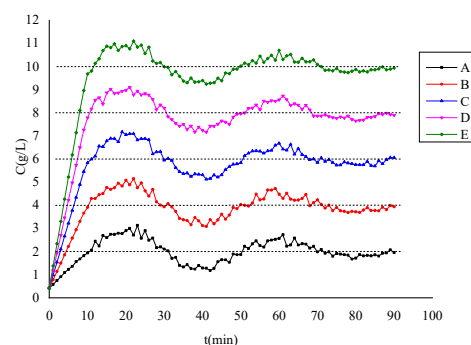


Figure 11. Variations of fertilizer concentration at different set values.

The related performance indices of the control system are shown in Table 4. The concentration of the fertilizer solution changed stably after controlling the solution application device with the automatic control system and fuzzy PID control algorithm. After setting the target concentration of the fertilizer solution, the control system quickly responded to the target value, with a response time of about 10 min. After reaching the target value, the

fluctuation range of the fertilizer solution's concentration did not exceed 1 g/L, leading to a time of about 10 min from the addition of the fertilizer to its complete dissolution. After interference, the system was fine-tuned. The adjustment time from the beginning to the dissolution and stabilization of the fertilizer solution was 20 min, with a steady-state error of about 0.55 g/L. After about 1.5 h, the concentration of the fertilizer solution became consistent with the set value. Overall, the design of the control system showed good stability, speed, and accuracy.

Table 4. Performance indices of the mixed application control system.

Different Patterns	A	B	C	D	E
The set value/(g·L ⁻¹)	2	4	6	8	10
Average fertilizer solution concentration/(g·L ⁻¹)	1.92	3.82	5.72	7.63	9.52
Stability: adjust the time/min	20.16	20.23	20.31	20.46	20.57
Speed: the response time/min	10.63	10.71	10.89	10.91	10.98
Accuracy: the steady-state error/(g·L ⁻¹)	0.55	0.53	0.57	0.54	0.56

5. Discussion

In order to solve the problem of poor fertilization uniformity caused by the decomposition hysteresis of solid fertilizer, a system combining fuzzy PID control with a fertilization device was proposed, and achieved continuous and stable output of the fertilizer solution, which was verified by tests to have good fertilization uniformity. This paper explores the relationship between fertilizer flow rate and pulse-width-modulated wave frequency. The results were consistent with those of Mirzakhani et al. [32], who used a PWM valve to change the speed of a hydraulic motor and then adjust the feeding amount. The relationship between the concentration of fertilizer solution and the electrical conductivity was also investigated. Saiful et al. [33] tested the relationship between the volume of liquid fertilizer and the EC value, and obtained the same linear fitting relationship as in this study. The control system was evaluated in terms of stability, speed, and accuracy, and its superiority was verified. This study lays the foundation for further study of fertilization control systems. It provides a reference for the development of precise and intelligent fertigation. In future research, it will be possible to develop more intelligent and widely applicable systems. For example, the control system of the Internet of Things could be applied in fertigation, enabling greater efficiency.

6. Conclusions

In this study, a solid fertilizer dissolution and application control system based on a fuzzy PID algorithm was designed and tested as a self-developed fertigation device. The control system consisted of the control of fertilizer flow rate and water flow rate, and the detection of fertilizer concentration. The precise adjustments of fertilizer flow rate and water flow rate were achieved. The fertilizer flow rate and water flow rate were changed in real time to ensure the uniform and adjustable concentration of the fertilizer solution at the outlet of the mixing equipment.

The relationship between fertilizer flow rate and PWM wave frequency, water flow rate, and PWM wave duty ratio, as well as the relationship between the concentration of the fertilizer solution and the electrical conductivity of two common solid fertilizers, was determined to provide theoretical guidance for the improvement of the control system program.

Using the control system, the uniformity of fertilization reached more than 65%, with a maximum of 74.58%. The dissolving device with the control system quickly responded to the target value, and the fertilizer concentration fluctuated within the range of the set value (at most ± 1 g/L). The response time from the beginning of the system to the complete dissolution of fertilizer was about 10 min, and the adjustment time from the fine-tuning of the system to the stabilization was around 20 min. The steady-state error was estimated to be about 0.55 g/L, showing good stability, speed, and accuracy. After verifying the

regulation using the control system, the device had better fertilization uniformity, solving the problem of solid fertilizer dissolution hysteresis.

Author Contributions: Conceptualization, X.S. and H.L.; methodology, X.S., C.C., H.X. and Z.Z.; validation, X.S.; formal analysis, X.S., C.C. and P.T.; investigation, X.S., C.C. and P.T.; data curation, X.S.; writing—original draft preparation, X.S.; writing—review and editing, P.T. and C.C.; visualization, X.S.; supervision, P.T. and C.C.; project administration, H.L. All authors have read and agreed to the published version of the manuscript.

Funding: This work was supported by the National Natural Science Foundation of China (grant number 51939005); the Key Research and Development Program of Jiangsu Province (grant number BE2021340, BE2021379); and Demonstration and Promotion Project of Modern Agricultural Machinery, Equipment, and Technology of Jiangsu Province (NJ2021-24).

Institutional Review Board Statement: Not applicable.

Informed Consent Statement: Not applicable.

Data Availability Statement: Not applicable.

Conflicts of Interest: The authors declare no conflict of interest.

References

1. Tang, P.; Li, H.; Issaka, Z.; Chen, C. Effect of manifold layout and fertilizer solution concentration on fertilization and flushing times and uniformity of drip irrigation systems. *Agric. Water Manag.* **2018**, *200*, 71–79. [[CrossRef](#)]
2. Sharmasarkar, F.C.; Sharmasarkar, S.; Miller, S.D.; Vance, G.F.; Zhang, R. Assessment of drip and flood irrigation on water and fertilizer use efficiencies for sugarbeets. *Agric. Water Manag.* **2001**, *46*, 241–251. [[CrossRef](#)]
3. Wu, H.; Yue, Q.; Guo, P.; Xu, X.; Huang, X. Improving the AquaCrop model to achieve direct simulation of evapotranspiration under nitrogen stress and joint simulation-optimization of irrigation and fertilizer schedules. *Agric. Water Manag.* **2022**, *266*, 107599. [[CrossRef](#)]
4. Jovarauskas, D.; Steponavičius, D.; Kemzūraitė, A.; Zinkevičius, R.; Venslauskas, K. Comparative analysis of the environmental impact of conventional and precision spring wheat fertilization under various meteorological conditions. *J. Environ. Manag.* **2021**, *296*, 113150. [[CrossRef](#)]
5. Kumar, M.; Kumar, R. Hydraulics of water and nutrient application through drip irrigation-A review. *J. Soil Water Conserv.* **2018**, *17*, 65. [[CrossRef](#)]
6. Silva, S.; Duarte, D.; Valente, A.; Soares, S.; Soares, J.; Pinto, F.C. Augmented Intelligent Distributed Sensing System Model for Precision Agriculture. In Proceedings of the 2021 Telecoms Conference (ConfTELE), Leiria, Portugal, 11–12 February 2021.
7. Nesthad, N.; Kurien, E.K.; Varughese, A.; Mathew, E.K. Evaluation of different fertigation equipments and the hydraulic performance of the drip fertigation system. *J. Agric. Sci.* **2013**, *1*, 12–17.
8. Leedy, C.T.; Leedy, M.L. Fertilizer Mixing Device for Sprinkler Systems. U.S. Patent US20020145057A1, 10 October 2002.
9. Zhang, X.; Mao, H.; Gao, H.; Zuo, Z.; Zhang, Y. Multi-Scale Habitat Information-Based Method and Device for Detecting and Controlling Water and Fertilizer for Crops in Seedling Stage. U.S. Patent US20210289692A1, 23 September 2021.
10. Yang, L.; Wu, G.; Wu, Z.; Li, T.; Mao, C. Fertilization Precision Control Method for Water and Fertilizer Integrated Equipment and Control System Thereof. U.S. Patent US10918014B2, 17 January 2019.
11. Anthony, B.C.; Johnson, D.N.; Igancio, C. A Device for Injecting and Mixing Liquid Fertilizer with Water Flow in a Sprinkler System Pipeline. WO WO2007021512A2, 22 February 2007.
12. Wang, H.; Fu, Q.; Meng, F.; Mei, S.; Wang, J.; Li, L. Optimal design and experiment of fertilizer EC regulation based on subsection control algorithm of fuzzy and PI. *Trans. Chin. Soc. Agric. Eng.* **2016**, *32*, 110–116.
13. Bi, P.; Zheng, J. Study on Application of Grey Prediction Fuzzy PID Control in Water and Fertilizer Precision Irrigation. In Proceedings of the IEEE International Conference on Computer & Information Technology, Xi'an, China, 11–13 September 2014; pp. 789–791.
14. Wang, J.; Wang, S.; Chen, J.; Liu, H.; Xu, D. Research on Automatic Irrigation Algorithm of Strawberry Greenhouse Based on PLC. In Proceedings of the International Conference on Computer and Computing Technologies in Agriculture, Beijing, China, 18–20 September 2013.
15. Zhang, J.; Zhang, W.; Zhang, F.; Zhang, J.; Zhang, J. Research of adaptive nonlinear model by integrated irrigation of water and soils in greenhouse for environment and ecological balance. *IOP Conf. Ser. Earth Environ. Sci.* **2021**, *804*, 042087. [[CrossRef](#)]
16. Zhang, P.; Zhang, Q.; Liu, F.; Li, J.; Cao, N.; Song, C. The Construction of the Integration of Water and Fertilizer Smart Water Saving Irrigation System Based on Big Data. In Proceedings of the 2017 IEEE International Conference on Computational Science and Engineering (CSE) and IEEE International Conference on Embedded and Ubiquitous Computing (EUC), Guangzhou, China, 21–24 July 2017.

17. Sun, F.; Ma, W.; Li, H.; Wang, S. Research on Water-Fertilizer Integrated Technology Based On Neural Network Prediction and Fuzzy Control. *IOP Conf. Ser. Earth Environ. Sci.* **2018**, *170*, 032168. [[CrossRef](#)]
18. Aguilar, J.V.; Langarita, P.; Rodellar, J.; Linares, L.; Horvath, K. Predictive control of irrigation canals—Robust design and real-time implementation. *Water Resour. Manag.* **2016**, *30*, 3829–3843. [[CrossRef](#)]
19. Lacasta, A.; Morales-Hernández, M.; Brufau, P.; García-Navarro, P. Simulation of PID Control Applied to Irrigation Channels. *Procedia Eng.* **2014**, *70*, 978–987. [[CrossRef](#)]
20. Fernández-Ramos, J.; Narvarte, L.; López-Soria, R.; Almeida, R.H.; Carrêlo, I.B. An assessment of the proportional-integral control tuning rules applied to Photovoltaic Irrigation Systems based on Standard Frequency Converters. *Sol. Energy* **2019**, *191*, 468–480. [[CrossRef](#)]
21. Jaiswal, S.; Ballal, M.S. Fuzzy inference based irrigation controller for agricultural demand side management. *Comput. Electron. Agric.* **2020**, *175*, 105537. [[CrossRef](#)]
22. Benyezza, H.; Bouhedda, M.; Rebouh, S. Zoning irrigation smart system based on fuzzy control technology and IoT for water and energy saving. *J. Clean. Prod.* **2021**, *302*, 127001. [[CrossRef](#)]
23. Shan, Y.; Zhang, L.; Ma, X.; Hu, X.; Hu, Z.; Li, H.; Du, C.; Meng, Z. Application of the Modified Fuzzy-PID-Smith Predictive Compensation Algorithm in a pH-Controlled Liquid Fertilizer System. *Processes* **2021**, *9*, 1506. [[CrossRef](#)]
24. Qu, X.; Liu, S.; Fu, S.; He, H.; Hu, Y.; Xiao, L. Design and Implementation of Wireless Environment Monitoring System Based on STM32. *Sci. Program.* **2021**, *2021*, 6070664.
25. Abebe, R.; Vakil, G.; Lo Calzo, G.; Cox, T.; Lambert, S.; Johnson, M.; Gerada, C.; Mecrow, B. Integrated motor drives: State of the art and future trends. *IET Electr. Power Appl.* **2016**, *10*, 757–771. [[CrossRef](#)]
26. Alonso-Hernández, O.; Ramos-Fernández, J.C.; Márquez-Vera, M.A.; López-Morales, V.; Ruiz-Vanoye, J.A.; Suárez-Cansino, J.; Trejo-Macotela, F.R. Fuzzy infrared sensor for liquid level measurement: A multi-model approach. *Flow Meas. Instrum.* **2020**, *72*, 101696. [[CrossRef](#)]
27. Magzoub, M.A.; Alquthami, T. Optimal Design of Automatic Generation Control Based on Simulated Annealing in Interconnected Two-Area Power System Using Hybrid PID—Fuzzy Control. *Energies* **2022**, *15*, 1540. [[CrossRef](#)]
28. Carlucho, I.; De Paula, M.; Villar, S.A.; Acosta, G.G. Incremental Q-learning strategy for adaptive PID control of mobile robots. *Expert Syst. Appl.* **2017**, *80*, 183–199. [[CrossRef](#)]
29. Zhang, Z.; Chen, C.; Li, H.; Xia, H. Design, Development, and Performance Evaluation of a Fertigation Device for Distributing Solid Fertilizer. *Water* **2020**, *12*, 2621. [[CrossRef](#)]
30. McGaghie, W.C.; Crandall, S. Data analysis and statistics. *Acad. Med.* **2001**, *76*, 936–938. [[CrossRef](#)]
31. Saoudi, O.; Ghaouar, N.; Othman, T. Conductivity measurements of laccase for various concentrations, pH and ionic liquid solutions. *Fluid Phase Equilibria* **2017**, *433*, 184–192. [[CrossRef](#)]
32. Mirzakhani-fachi, H.; Singh, M.; Bector, V.; Gupta, O.P.; Singh, R. Design and Development of a Variable Rate Applicator for Real-Time Application of Fertilizer. *Sustainability* **2021**, *13*, 8694. [[CrossRef](#)]
33. Joseph, C.; Thirunavuakarasu, I.; Bhaskar, A.; Penujuru, A. Automated fertigation system for efficient utilization of fertilizer and water. In Proceedings of the 2017 9th International Conference on Information Technology and Electrical Engineering (ICITEE), Phuket, Thailand, 12–13 October 2017.

Article

Numerical Analysis of Ventilation Efficiency of a Korean Venlo-Type Greenhouse with Continuous Roof Vents

Se-Jun Park ¹, In-Bok Lee ^{2,3,*}, Sang-Yeon Lee ¹, Jun-Gyu Kim ¹, Young-Bae Choi ¹, Cristina Decano-Valentin ^{1,4}, Jeong-Hwa Cho ¹, Hyo-Hyeog Jeong ¹ and Uk-Hyeon Yeo ⁵

¹ Department of Rural Systems Engineering, Research Institute for Agriculture and Life Sciences, College of Agriculture and Life Sciences, Seoul National University, 1, Gwanakno, Gwanak-gu, Seoul 08826, Korea

² Department of Rural Systems Engineering, Research Institute for Agriculture and Life Sciences, Global Smart Farm Convergence Major, College of Agriculture and Life Sciences, Seoul National University, 1, Gwanakno, Gwanak-gu, Seoul 08826, Korea

³ Research Institute of Green Eco Engineering, Institute of Green Bio Science and Technology, Seoul National University, 1477, Pyeongchang-daero, Daehwa-myeon, Pyeongchang-gun 25354, Korea

⁴ Department of Agricultural and Biosystems Engineering, College of Engineering, Mariano Marcos State University, Batac 2906, Philippines

⁵ Agriculture, Animal & Aquaculture Intelligence Research Center, Electronics and Telecommunications Research Institute, 218 Gajeong-ro, Yuseong-gu, Daejeon 34129, Korea

* Correspondence: iblee@snu.ac.kr; Tel.: +82-2-880-4586; Fax: +82-2-873-2087

Citation: Park, S.-J.; Lee, I.-B.; Lee, S.-Y.; Kim, J.-G.; Choi, Y.-B.; Decano-Valentin, C.; Cho, J.-H.; Jeong, H.-H.; Yeo, U.-H. Numerical Analysis of Ventilation Efficiency of a Korean Venlo-Type Greenhouse with Continuous Roof Vents. *Agriculture* **2022**, *12*, 1349. <https://doi.org/10.3390/agriculture12091349>

Academic Editors: Muhammad Sultan, Redmond R. Shamshiri, Md Shamim Ahamed and Muhammad Farooq

Received: 30 June 2022

Accepted: 19 August 2022

Published: 31 August 2022

Publisher's Note: MDPI stays neutral with regard to jurisdictional claims in published maps and institutional affiliations.



Copyright: © 2022 by the authors. Licensee MDPI, Basel, Switzerland. This article is an open access article distributed under the terms and conditions of the Creative Commons Attribution (CC BY) license (<https://creativecommons.org/licenses/by/4.0/>).

Abstract: A Venlo-type greenhouse with a continuous roof vent (CR-Venlo greenhouse) was proposed by the Ministry of Agriculture, Food and Rural Affairs, South Korea (2019) for natural ventilation even during summers. It is ventilated through the buoyancy effect of the heated air using the high eave elevation. However, the CR-Venlo greenhouse was not distributed domestically, and its ventilation efficiency was not quantitatively evaluated. We aimed to analyze the natural ventilation efficiency of the greenhouse according to the eave height, using computational-fluid-dynamics. The simulation model was analyzed for hot summer conditions. The target greenhouse is ventilated only through the roof vent with all roof windows open; therefore, the air introduced through the roof window is easily exhausted. To evaluate the efficiency of ventilation, the external air entering through the roof window was calculated and evaluated. The amount of incoming air varied greatly with the location of the span and average temperature of the greenhouse; The temperature of the crop zone decreased lognormally with increasing height of the eave. Moreover, the ventilation efficiency of CR-Venlo greenhouse could be increased by improving the ventilation structure such as a shape, position or combination of roof window.

Keywords: computational fluid dynamics (CFD); eave height; natural ventilation; venlo greenhouse

1. Introduction

Crop production through facility cultivation has developed continuously over the past several years by ensuring stable productivity and high-quality crops throughout the year. Recent data from the Ministry of Agriculture, Food and Rural Affairs, South Korea (MAFRA) indicated that the scale of production has been steadily increasing from the 1970s to the present; the area of domestic vegetable cultivation and total production were 54,443 ha and 2,441,000 tons in 2019, respectively [1]. Meanwhile, the domestic agricultural population is steadily aging and declining, whereas the demand for agricultural products has been growing. In addition, there is an increase in automation and the number of large-scale greenhouses. The development of ICT technology and the expansion of investments in smart farms are accelerating the enlargement of greenhouses. In particular, the area of multi-span greenhouses in Korea increased from 5227 ha in 2012 to 7088 ha in 2019 [1]. A large greenhouse enables easy automation and improved productivity. It has the advantage of

relatively low heating cost in winter but, inevitably, the disadvantage of having a large cooling demand in high-temperature environments in summer.

Therefore, a Venlo-type greenhouse with a continuous roof vent (CR-Venlo greenhouse) has been developed by the MAFRA in 2019 to reduce high-temperature stress to crops even in high-temperature environments in summer. The CR-Venlo greenhouse has a structure similar to that of the conventional Venlo-type greenhouse (C-Venlo greenhouse). Ventilation occurs due to the buoyancy effect of heated air inside the greenhouse in summer due to the high eave height. Most of the roof area of the CR-Venlo greenhouse is designed with roof vents; therefore, there is the possibility of wind ventilation using a large roof vent. In particular, the temperature inside the greenhouse decreases as the elevation of the eave increases [1]; therefore, the temperature difference between the inside and outside of the greenhouse decreases. In this study, we evaluated a single-span greenhouse and designed the opening angle of the roof window to be significantly large. In a single-span greenhouse, the natural ventilation effect is greater than that in a multi-span greenhouse. When the opening angle of the roof window is considerably large, the inflow of external air into the greenhouse is smooth. Furthermore, in a single-span greenhouse, the influence of side window ventilation is great. However, in a multi-span greenhouse, the ventilation effect by the side windows decreases rapidly as the number of the multi-span increases. Therefore, the ventilation through the roof window is highly important for the stagnant area of the multi-span greenhouse. The roof vent window should be designed based on the quantitative analysis of natural ventilation. The CR-Venlo greenhouse has a high ventilation efficiency due to the structural characteristics of the ventilation window; however, its ventilation efficiency has not yet been quantitatively evaluated [2].

Changes in the thermal environment inside the greenhouse according to ventilation design have been well studied [3–18]. Most studies analyze the horizontal temperature distribution at a specific height, such as the height of a crop. Only a few studies have been reported on the vertical temperature distribution inside the greenhouse for large, high-altitude greenhouses. In a greenhouse with a high eave height, there is more space for the heated air to rise from the bottom via buoyancy in summer; this results in a vertical temperature deviation. In particular, the temperature at the height of the crop zone could be lowered. It is necessary to quantitatively analyze the vertical temperature distribution inside the greenhouse due to the buoyancy effect and to analyze the reduction in temperature in the crop zone in summers, in the high-elevation greenhouse.

Therefore, in this study, the ventilation efficiency and temperature distribution in a CR-Venlo greenhouse during summer were evaluated according to the eave height. A computational fluid dynamics (CFD) program (FLUENT19.0, ANSYS, New York, NY, USA) was used to analyze various environmental conditions, such as the external wind speed. The internal air flow and ventilation efficiency of the CR-Venlo greenhouse were evaluated according to the external wind speed and eave height of the CR-Venlo greenhouse. This was followed by the evaluation of the ventilation effectiveness of a greenhouse with a high lateral elevation. The CR-Venlo greenhouse has a roof vent with both windward and leeward side openings; therefore, air flowing through the windward-side opening easily flows out through the opposite leeward-side opening. Therefore, two efficiencies were evaluated; one for air inflow through the roof vent and the other for air incoming into the greenhouse. Furthermore, the average temperature of the entire greenhouse and at the height of the crop zone was evaluated at varying external wind speeds and heights of the greenhouse. Finally, improved models with higher ventilation efficiencies than those in the CR-Venlo greenhouse are suggested based on ventilation efficiencies under the same environmental conditions for the CR-Venlo and C-Venlo greenhouses.

2. Materials and Methods

Figure 1 displays the research flow chart for this study. A CFD simulation model was designed to evaluate the ventilation efficiency of a CR-Venlo greenhouse. The standardized design of the CR-Venlo greenhouse was disseminated only recently; therefore, there are no

actual constructions. Lee et al. [14] evaluated the ventilation rate of the high-eave height 1-2W type 3-span Korean greenhouse in summer [14]. The CFD model information, such as crop module, turbulence model, and external area information, from this report was used in this study because both studies focus on the ventilation rate in greenhouses with high eave height in summer. However, previous study focused on the 1-2W and 3-span greenhouse, which is the most commonly used model in South Korea. Therefore, it was necessary to verify whether the information from the CFD simulation model [14] could be applied to other types of greenhouses; field experiments and verification of the simulation model were performed. The CFD model of the CR-Venlo greenhouse was designed, and the ventilation efficiency according to the eave height of the greenhouse was analyzed. First, the amount of air inflow and outflow through the roof vent were calculated according to the external wind speed and the eave height of the greenhouse were calculated. Next, the thermal environment of the CR-Venlo greenhouse was evaluated by calculating the average temperature of the entire greenhouse and the height of the crop zone. To address the limitations of the ventilation structure that uses only the roof vent of the CR-Venlo greenhouse, the possibility of improving ventilation efficiency by modulating the opening and closing of the roof vent and auxiliary facilities was evaluated.

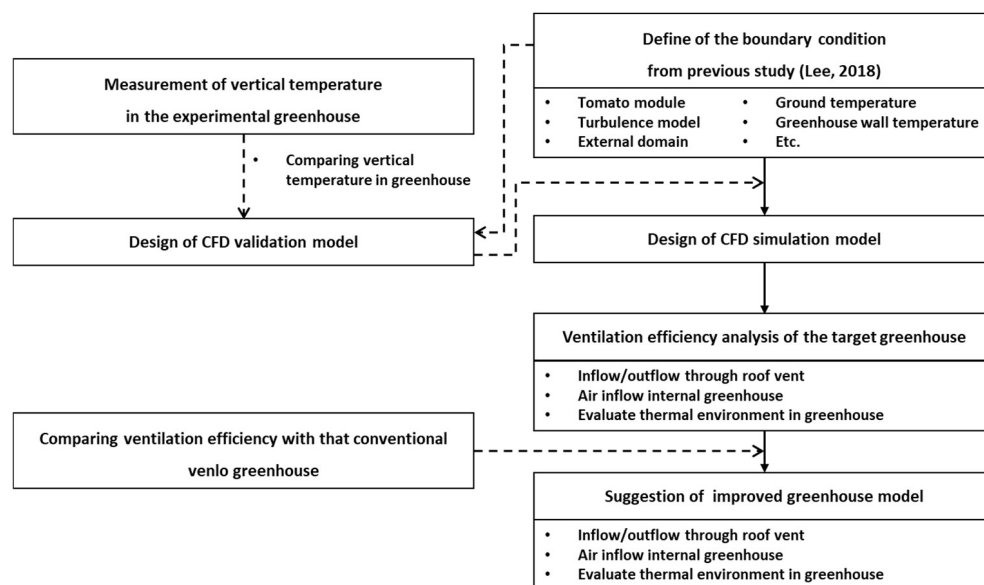


Figure 1. Flow chart of the experimental procedure.

2.1. Target Greenhouse

The CR-Venlo greenhouse, the target facility of this study, is an even-span greenhouse with a high eave height. It is like a C-Venlo greenhouse, but it has a large roof area with continuous roof windows (Figure 2). In this greenhouse, both the windward and leeward windows are open. It allows a lot of air to flow in and out through a large-area roof window and has excellent heat buffering capacity because of its large volume and ventilation rate due to a large-area roof window. Therefore, this type of greenhouse is beneficial in the cultivation of paprika and tomatoes in all seasons. A standard design of a CR-Venlo greenhouse has been developed; however, it has not yet been distributed to actual farms because of the lack of quantitative-analysis data on its ventilation efficiency. The CR-Venlo greenhouse in this study was designed based on the specifications presented in 19-Yeondong-3 (MAFRA, 2019) of the internal type of standard design drawing. The greenhouse length is 40.0 m; it is a 15-span greenhouse with a width of 8.0 m. The eave height is 7.0 m, and the ridge height is 1.1 m higher than the eave height. The covering of the greenhouse is 15.0 mm polyolefin film. The ceiling, side, front, and back of the greenhouse are all covered with film, and the floor is concrete. The roof vent of the CR-Venlo greenhouse is 1.0 m in width and 36.0 m in length. It has a large area of 39.4%

compared to approximately 14.7% of the total ceiling area of a C-Venlo greenhouse of the same volume. Ventilation is conducted by opening all roof windows by up to 45 degrees; a separate ventilation system was not considered, including side windows. In addition, a separate cooling system was not considered because the system was expected to have excellent thermal buffering capacity due to the high structural feature of the side elevation.

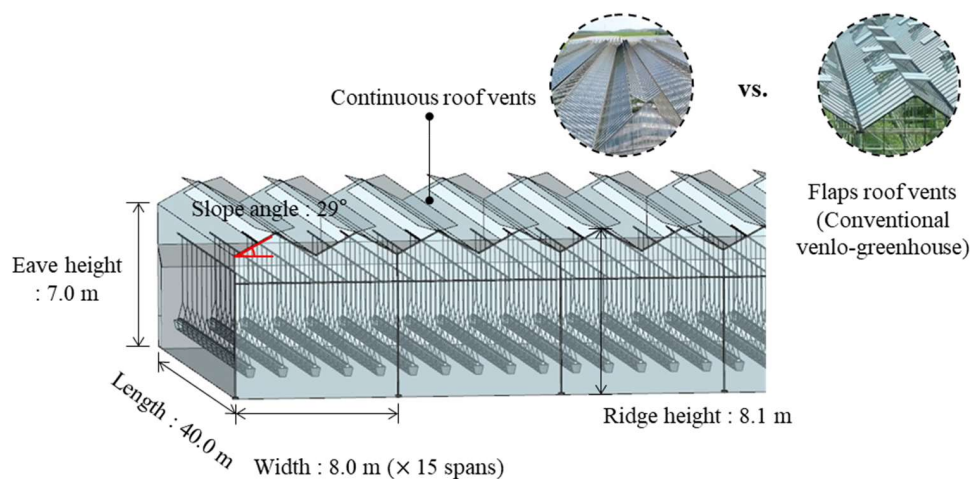


Figure 2. Schematic of a Korean Venlo-type greenhouse with continuous roof vents (MAFRA, 2019).

Tomatoes (*Solanum lycopersicum*), typically grown in domestic horticultural facilities, were chosen for cultivation in the target greenhouse. Tomato is conducive to continuous cropping through a hydroponics that reduces labor [19]. Five beds per span were arranged at 1.6 m intervals with two rows per bed (Figure 3). The beds were placed at 0.7 m from the ground; the width and height of the bed were 0.3 m and 0.15 m, respectively. A seedling cube with a width of 0.3 m and a height of 0.15 m was placed on the bed. The shape of the tomato crop was established as a cuboid with a width of 0.5 m and a height of 2.0 m.

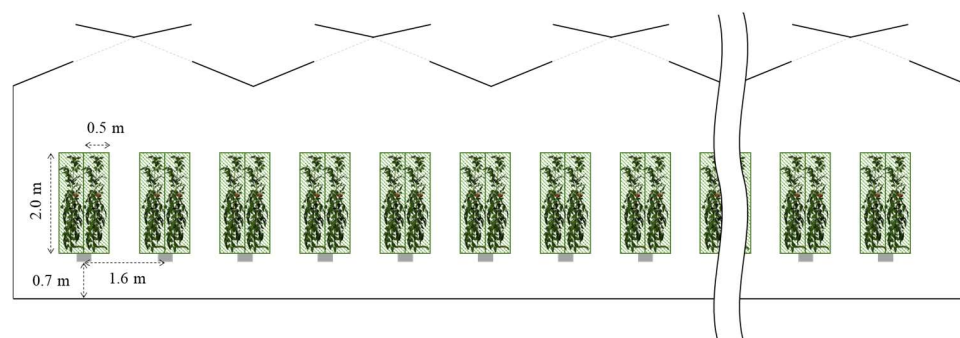


Figure 3. Schematic diagram of tomato arrangement in CFD simulation model.

2.2. Computational Fluid Dynamics (CFD)

Computational Fluid Dynamics (CFD) is a numerical analysis tool that can analyze fluid flow, heat transfer, and chemical action through computer simulation for a system containing a fluid. CFD uses the Navier-stokes equation, a nonlinear differential equation, as the governing equation. It is a tool for simulating numerical analysis using the finite difference method. It is actively used in various fields, including machinery, aviation, chemical engineering, manufacturing, civil engineering and construction, and environmental studies. It is applied in the agricultural field to evaluate livestock facilities and greenhouse environment [20–24].

In this study, a three-dimensional grid was designed using a commercial program for CFD (ver. 18.2, ANSYS Inc, Canonsburg, PA, USA) to analyze the ventilation efficiency of the CR-Venlo greenhouse. The calculation was performed by setting boundary conditions

for the target domain. Fluent is a program that numerically analyzes the flow of fluid in an analysis space designed as a two- or three-dimensional grid, based on the law of conservation of mass, energy, and momentum. The equations used in the calculation are as follows:

$$\frac{\partial \rho}{\partial t} + \nabla \cdot (\rho \vec{v}) = S_m \quad (1)$$

$$\frac{\partial}{\partial t} (\rho \vec{v}) + \nabla \cdot (\rho \vec{v} \vec{v}) = -\nabla P + \nabla \vec{\tau} + \rho \vec{g} + \vec{F} \quad (2)$$

$$\frac{\partial}{\partial t} (\rho E) + \nabla \cdot (\vec{v} (\rho E + P)) = \nabla \cdot (k_{eff} \nabla T - \sum h \vec{J}_i + (\vec{\tau}_{eff} \vec{v})) + S_h \quad (3)$$

where ρ is the density of the fluid ($\text{kg}\cdot\text{m}^{-3}$), \vec{v} is the flow velocity of the fluid ($\text{m}\cdot\text{s}^{-1}$), P is the static pressure (Pa), $\vec{\tau}$ is the stress tensor (Pa), and \vec{g} is the acceleration due to gravity ($\text{m}\cdot\text{s}^{-2}$), \vec{F} is the external force ($\text{N}\cdot\text{m}^{-3}$), S_m is the source term of the mass ($\text{kg}\cdot\text{m}^{-3}$), k_{eff} is the effective conductivity ($\text{kg}\cdot\text{m}^{-2}\cdot\text{s}^{-1}$), T is the temperature (K), E is the specific enthalpy indicating the enthalpy per unit mass ($\text{J}\cdot\text{kg}^{-1}$), t is the time (s), \vec{J}_i is the diffusion flux of type i ($\text{kg}\cdot\text{m}^{-1}\cdot\text{s}^{-1}$), and S_h is the total enthalpy ($\text{kg}\cdot\text{m}^{-1}\cdot\text{s}^{-3}$).

2.3. Experimental Procedure

2.3.1. Field Experiment and Modelling for Validation of the CFD Simulation Model

A field experiment was conducted to verify the simulation model for a wide-span type greenhouse using roof vents similar to those in the structure of the CR-Venlo greenhouse (Figure 4). The target greenhouse is a 5-span wide type greenhouse located in Moga-myeon, Icheon-si, Gyeonggi-do ($37^{\circ}18'N$, $127^{\circ}48'E$). The dimension of the 1-span of target greenhouse was a width of 9 m, a length of 30.0 m, an eave height of 3.5 m, and a ridge height of 5.5 m. The tomato (*Solanum lycopersicum*) was grown hydroponically inside the target greenhouse. The planting density was approximately $3 \text{ plants}\cdot\text{m}^{-2}$, and the plants were cultivated in the one-stem attraction method. Tomatoes were approximately 60 days old during the experiment. The cultivation environment was controlled by ventilation using roof vents based on the values obtained using the central temperature sensor. The temperature was maintained at $24\text{--}26^{\circ}\text{C}$, which is the optimal growing temperature for tomatoes. The field experiment was conducted on 8 July 2020, and the vertical temperature distribution was measured for six points (0.8–4.8 m) at 0.8 m height intervals regarding the central location of the greenhouse. The internal air temperature was measured at 1 s intervals using a Type-T thermocouple; the measured data was processed to obtain a 10 s average value.

The CFD model for validation was designed for the greenhouse on which the field experiments were performed. The model information, including the turbulence model and grid size, was like that of the CFD model of the CR-Venlo greenhouse. External weather data, such as wind direction, wind speed, and air temperature, were obtained from the Ochang Meteorological Observatory, the closest meteorological station. The external weather data of the period in which the vertical wind ($\pm 15^{\circ}$) blows against the sidewall of the greenhouse, and the average values of the wind speed and air temperature were used. Tomatoes in the mature stage exchange sensible and latent heat and act as resistance to airflow. Therefore, the CFD model was designed based on the values of a previous study for a mature tomato plant [25] (Table 1).



Figure 4. Experimental greenhouse located in Moga-myeon, Icheon-si, Gyeonggi-do Province (37° 18'N, 127° 48'E) and field experiment (a) External view of the experimental greenhouse, (b) Sensor installation for measuring vertical air temperature, (c) Internal view of the experimental greenhouse and (d) Sensor installation to avoid direct radiation.

Table 1. Values of the boundary condition of the CFD simulation model for validation.

Boundary Condition		Input Values	Reference
Outside air temperature (°C)		27.4	
Wind speed ($\text{m} \cdot \text{s}^{-1}$)		1.40	Field experiment and Ochang weather station (Average value during field experiment period)
Wind direction (°)		90	
Greenhouse wall	Temperature (°C)	27.4	
	Thickness (m)	0.0001	
Latent energy sources ($\text{W} \cdot \text{m}^{-3}$)		−30.0	Lee [25]
Tomato	Viscous resistance (m^{-2})	2.53	
	Inertial resistance (m^{-1})	1.92	
Turbulence model		Realizable $k-\epsilon$	

2.3.2. Design of External Domain and Wind Environment of the CFD Simulation Model

The external wind environment is an important factor in calculating the natural ventilation rate. The wind speed and the turbulence distribution by height vary depending on the stability of the atmosphere. Therefore, to apply these conditions to the CFD model,

the average profiles of wind-speed, turbulence-energy, and turbulence-dissipation-rate were calculated through the conditional equations reported earlier; a user-defined function was created as a code and was reflected in the model [26,27]. The flow velocity profile and turbulence profile applied to CFD in the external wind environment are as follows:

$$u(z) = \frac{u_{ABL}^*}{k} \ln\left(\frac{z+z_0}{z_0}\right), \quad (4)$$

$$\varepsilon(z) = \frac{u_{ABL}^{*3}}{k(z+z_0)}, \quad (5)$$

$$\omega(z) = \frac{\varepsilon}{C_\mu k}, \quad (6)$$

where u is the wind speed at height z ($\text{m}\cdot\text{s}^{-1}$), u_{ABL}^* is the friction velocity ($\text{m}\cdot\text{s}^{-1}$), k is the Kármán constant (dimensionless), z_0 is the roughness length (m), ε is the turbulent energy dissipation ($\text{m}^2\cdot\text{s}^{-3}$), ω is the specific dissipation rate (s^{-1}), and C_μ is the empirical constant (dimensionless).

Until recently, there was no detailed standard for designing the external domain of a 3D computational fluid dynamics model; approximate values had been suggested through empirical or experimental verification [28–30]. Kim et al. [31] proposed the minimum length of the outer region where the atmospheric boundary layer reaches the center based on the height of the target building, to prevent the internal boundary layer from continuously growing [31]. The size of the entire computational domain can be determined by the height of the study object. If there is an object larger than the study object, it should also be considered. The vortex formed at the highest point dissipates at the farthest point within the analysis domain.

Therefore, in this study, the external area for natural ventilation was designed based on the results of previous research [31]; the length of the upstream section on the windward side was set at $3H$. The side and upper surfaces of the analysis area were designed to be $5H$ each in a range where the vortex formed from the greenhouse does not affect them. The length of the downstream section was designed to be $15H$ considering the convergence and economic feasibility. The size of mesh inside the greenhouse was 0.3 to 0.5 m, and the total number of meshes was approximately 8.1 million (Figure 5).

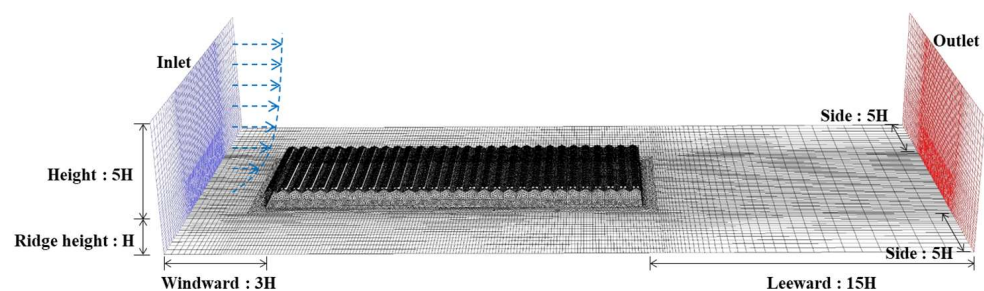


Figure 5. Design of the CFD simulation model domain.

2.3.3. Boundary Conditions of the CFD Simulation Model

The 3D simulation model of the CR-Venlo greenhouse was designed referring to the 19-Yeondong-3 model of the standard design [1] and was designed for five eave heights to analyze the ventilation efficiency at different eave heights of the greenhouse. The simulation target period was established for the hot summer season, the temperature of the outside air was set to $35\text{ }^\circ\text{C}$, which corresponds to 1% of the TAC (Technical Advisory Committee) temperature of the summer weather data (1990–2020) for the last 30 years in Daegu. The turbulence model, the size of grid, and boundary conditions such as internal ground temperature, sensible heat, and latent heat of tomato were designed referring to the modeling conditions of a previous study [25] (Table 2).

Table 2. Boundary condition values of the CFD simulation model for case study.

Boundary Condition		Input Values	Reference
Outside air temperature (°C)		35.0	Weather station data (1990-2020) and
Greenhouse wall	Temperature (°C)	35.0	
	Thickness (m)	0.0001	MAFRA (2019)
Ground temperature inside the greenhouse (°C)		45.0	
Ground temperature outside the greenhouse (°C)		44.16	
Tomato	Latent energy sources ($W \cdot m^{-3}$)	-30.0	Lee [25]
	Viscous resistance (m^{-2})	2.53	
	Inertial resistance (m^{-1})	1.92	
Turbulence model		Realizable k- ϵ	

2.3.4. Analytical Conditions for Evaluation of Ventilation Efficiency

When the external wind speed is over $2.0 \text{ m} \cdot \text{s}^{-1}$, wind-driven ventilation is dominant; when the external wind speed is less than $0.5 \text{ m} \cdot \text{s}^{-1}$, gravity with buoyancy driven ventilation is dominant [4,32]. Depending on the wind speed, there are variations in the main factors that affect the ventilation efficiency of natural ventilation. The wind speed at which wind-driven ventilation and buoyancy-driven ventilation are predominant differ with the number and size of the peristaltic ventilation of the greenhouse. Therefore, in this study, the external wind speed conditions at the height of the greenhouse eave were established at 0.5 , 1.5 , and $3.0 \text{ m} \cdot \text{s}^{-1}$ to include both conditions where buoyancy-driven ventilation and wind-driven ventilation are dominant for the CR-Venlo greenhouse. Wind direction conditions were subjected to a 90° wind perpendicular to the length of the greenhouse. To analyze the changes in the ventilation rate with the height of the CR-Venlo greenhouse, 15 case simulation models were analyzed for different measured heights of the greenhouse (5, 6, 7, 8, and 9 m) (Table 3).

Table 3. Analysis cases for the evaluation of ventilation efficiency using the CFD simulation model.

Analysis Cases	Conditions
Wind direction (°)	90
Wind speed ($\text{m} \cdot \text{s}^{-1}$)	0.5, 1.5, 3.0 (at the roof height of the greenhouse model)
Rigid height of the greenhouse	5, 6, 7, 8, 9
Total	15 cases

The CR-Venlo greenhouse is expected to have high ventilation because of the large area of the roof vent window. However, the inflow air immediately flows out because the windward and leeward roof windows facing each other are open. Therefore, in wind-driven ventilation conditions in which air inflow and outflow through the roof window are actively performed, ventilation efficiency could be reduced. To overcome the limitations of the ventilation structure, an improvement is proposed by analyzing the opening and closing of each roof window in the CR-Venlo greenhouse and the natural ventilation efficiency, based on the installation of auxiliary facilities under wind-driven ventilation conditions ($3 \text{ m} \cdot \text{s}^{-1}$) (Figure 6 and Table 4). To strengthen the main airflow according to the location of each span, Case 1–3 models were proposed in which the roof windows in the windward and leeward direction were all opened according to the location of the 15 span greenhouses. In addition, the airflow toward the bottom of the greenhouse was strengthened by installing a virtual windbreak at the mid-point of the roof window or by increasing the roof opening angle.



Figure 6. Schematic depicting the improved model ventilation structure of the CR-venlo greenhouse with continuous roof vents: (a) Case 0: CR-venlo greenhouse, (b) Case 1: Opening of windward roof vents at 1–5 span and leeward roof vents at 11–15 span, (c) Case 2: Opening of windward roof vents at 1–7.5 span and leeward roof vents at 7.5–15 span, (d) Case 4: Opening of all windward roof vents, (e) Case 4: Windbreak installation in the center of all roof vents, (f) Case 5: Increasing the opening angle of roof vents.

Table 4. Specifications of the modified CFD simulation model to improve ventilation rate.

Model	Installation of Wind Break in the Roof	Opening Condition of Roof Vents	Opening Angle of Roof Vents (°)
Case 0	X	All spans: Open on both windward and leeward sides	45
Case 1	X	1–5 spans: Open on the windward side 6–10 spans: Open on both windward and leeward sides 11–15 spans: Open on leeward side	45
Case 2	X	1–7.5 spans: Open on windward side 7.5–15 spans: Open on leeward side	45
Case 3	X	All spans: Open on leeward side	45
Case 4	O	All spans: Open on both windward and leeward sides	45
Case 5	X	All spans: Open on both windward and leeward sides	75

2.3.5. Evaluation of Ventilation Efficiency and Thermal Environment

A large amount of fresh outside air should flow into the greenhouse, and the heated air inside the greenhouse should be smoothly discharged to the outside. The CR-Venlo greenhouse does not have a side window and can only be ventilated through the roof window; the inlet and outlet have the same structure. In addition, the distance between the roof windows is considerably short, and all the facing roof windows are open. The air introduced through the roof window can immediately flow out through the facing roof

window. Therefore, it is necessary to evaluate whether fresh air is introduced into the greenhouse through the roof window and whether it replaces the air inside the greenhouse.

In this study, the ventilation efficiency through the roof window of the CR-venlo greenhouse was evaluated by calculating the air inflow and outflow through the roof vent of each span (Figure 7a). Based on the roof window surface of the greenhouse, the inside direction was designated as '+' and the outside direction as '-'. Air inflow through the greenhouse roof window (Air_{inflow}) was calculated as the mass flow rate in the positive direction $((1+2)/2)$ and air outflow through the greenhouse roof window ($Air_{outflow}$) was calculated as the mass flow rate in the negative direction $((3+4)/2)$. The air introduced through the roof window that flows into the interior space of the greenhouse was assessed by defining a virtual reference plane parallel to the floor of the greenhouse in the area near the roof of the greenhouse and by calculating the mass flow rate (5) of the air that flows into the interior of the greenhouse (Figure 7b). Figure 8 indicates the position of each span where the ventilation efficiency was calculated.

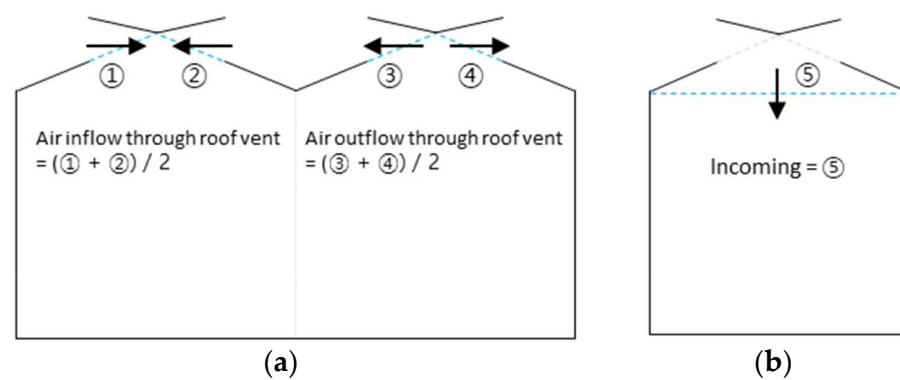


Figure 7. Schematic diagram of the evaluation of air inflow/outflow through the roof vent and the incoming air inflow. (a) Evaluation of air inflow/outflow through the roof vent, (b) Evaluation of incoming air inflow.

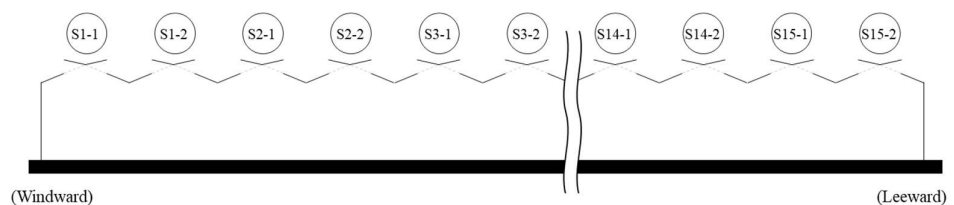


Figure 8. Region definitions for Korean Venlo-type greenhouses with continuous roof vents used to evaluate ventilation efficiency.

The design of the CR-Venlo greenhouse is expected to decrease the temperature of the lower part of the greenhouse by allowing hot air to rise to the upper part of the greenhouse during summer due to the high elevation of the structure. Therefore, the reduction in air temperature at different heights of the greenhouse was analyzed. The average air temperature at different heights of the greenhouse, was also calculated, and the average air temperature at the height of the tomato crop zone (0.7–2.7 m), which directly affects the growth of the crops.

3. Results

3.1. Validation of the CFD Simulation Model

To verify the CFD simulation model, the changes in the vertical temperature inside the greenhouse with changes in the external weather conditions were measured for a wide-span greenhouse (Figure 9). In the case of the field experiment, the wind direction, wind speed, and the external temperature continuously changed. The CFD model in this

study analyzed the ventilation rate of the greenhouse for each wind direction and wind speed condition; therefore, the analysis was performed assuming a steady-state. The data measured at constant wind direction and blowing time among the experimental field data were used for validation. The wind direction ($246^\circ \pm 15^\circ$) that is perpendicular to the sidewall of the greenhouse, which can effectively influence the change in temperature inside the greenhouse due to the inflow of external air, the blows, and the data for the time (PM 12:20) of high external air was used. The external wind speed was $1.4 \text{ m}\cdot\text{s}^{-1}$.

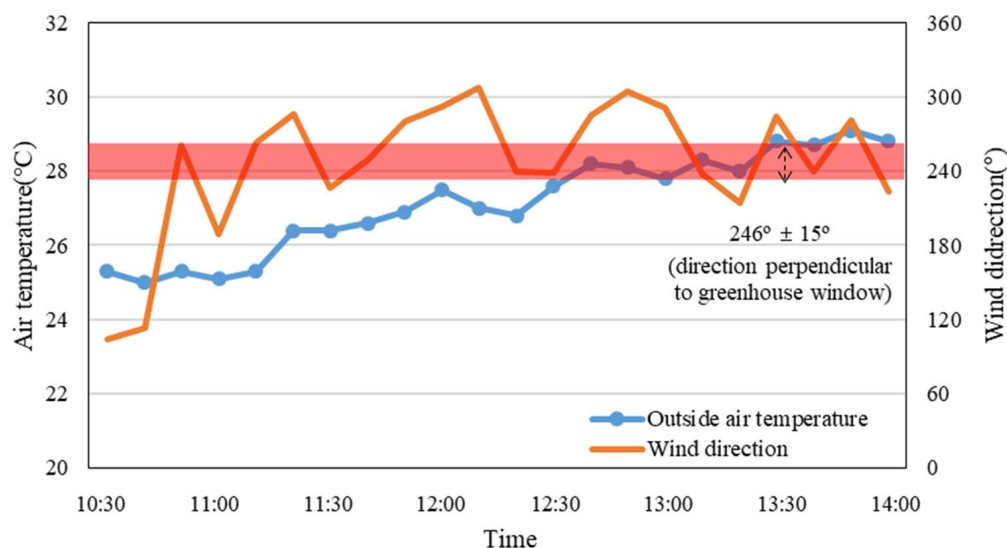


Figure 9. The outside air temperature and wind direction in the experimental greenhouse located in Moga-myeon, Icheon-si, Gyeonggi-do Province ($37^\circ 18'N$, $127^\circ 48'E$) during the experimental period (July 2020).

The data measured through the field experiment change in real time despite using 10 s average data measured for 1 min for a relatively constant time under a specific wind direction and speed; therefore, the changes in the internal vertical temperature profile with the measurement time were evaluated (Figure 10). The temperature profile exhibited a tendency to change the temperature at the top height. It was influenced by wind conditions changing in real-time. According to the wind conditions, the influence of outside air entering the greenhouse through the roof window was variable. In the CFD verification model, the simulation was performed assuming a steady state; therefore, the location where the outside air is introduced through the roof vent and the location where the air inside the greenhouse flows out are divided according to the span location of the greenhouse. A constant vertical temperature profile was calculated according to the span position of the greenhouse. In the central position of the greenhouse, which is the verification position, the internal temperature exhibited a tendency to increase as the height of the greenhouse increased.

In field experiments and simulation results for comparative verification, because field experiments were conducted at the central location of the greenhouse, the simulation calculation results of the same location were used. The CFD verification model was validated; therefore, it exhibited a similar trend to the field test result and the shape of the vertical temperature profile at the central location of the greenhouse (RMSE: $0.3 \sim 1.1 \text{ }^\circ\text{C}$; R^2 : $0.88\sim 0.99$); it predicted the vertical temperature inside the greenhouse by roof-window ventilation.

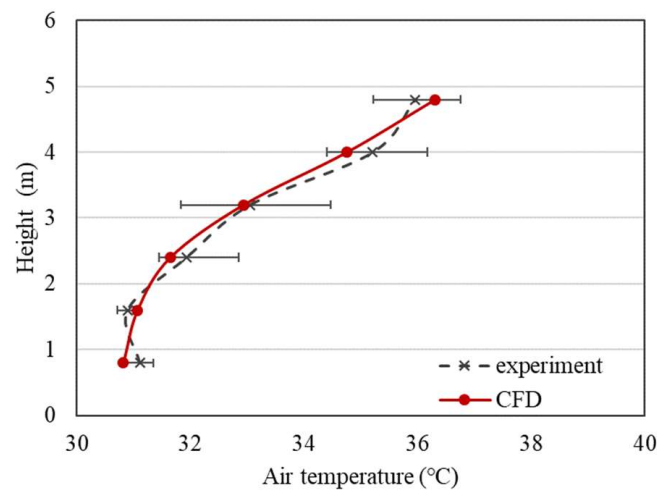


Figure 10. Validation of the CFD simulation model for the vertical temperature in the greenhouse. (The error bar of the field experiment in the unsteady state means the range of the maximum and minimum values).

3.2. Evaluation of Air Inflow and Outflow Rate through Roof Vent According to Wind Speed

3.2.1. Analysis of Airflow Pattern According to Wind Speed

A single or multi-span greenhouse where the number of spans is not large is greatly affected by wind ventilation when the external wind speed is $2.0 \text{ m}\cdot\text{s}^{-1}$ or higher, whereas large-scale greenhouses with many spans are relatively less affected by wind ventilation [8]. The target is a large greenhouse with a high side elevation and 15 spans; therefore, the conditions that predominantly affect ventilation according to the wind speed would be different. In case of simulation calculations for a low wind speed ($0.5 \text{ m}\cdot\text{s}^{-1}$), the flow inside the greenhouse is formed according to the external air inflow and an upward airflow from the floor is formed due to buoyancy. (Figure 11). Therefore, gravity with buoyancy driven ventilation is dominant. With simulation results for high wind speed (1.5 and $3.0 \text{ m}\cdot\text{s}^{-1}$) there is no upward airflow due to buoyancy on the windward side. The flow of air introduced from the roof window reached the bottom of the crop and greenhouse, and the internal airflow was majorly formed.

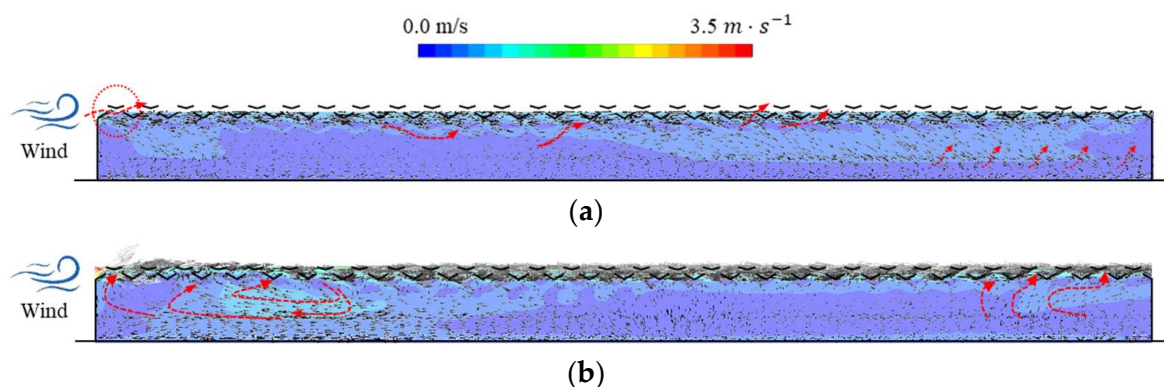


Figure 11. CFD computed airflow distribution at the center of the cross section of the greenhouse according to the external wind speed (the external wind direction was fixed perpendicular to the side window). (a) Airflow distribution in the eave height 7m and external wind speed $0.5 \text{ m}\cdot\text{s}^{-1}$ (Center cross section of the greenhouse). (b) Airflow distribution in the eave height 7 m and external wind speed $3.0 \text{ m}\cdot\text{s}^{-1}$ (Center cross section of the greenhouse).

Here, wind ventilation dominates, and below $0.5 \text{ m}\cdot\text{s}^{-1}$, gravity with buoyancy driven ventilation dominates; as the number of spans increases, the effect of gravity with buoyancy driven ventilation increases. In the greenhouse case of the inside on the downwind side, the

influence of the air flowing in from the outside was relatively reduced; therefore, an updraft was formed because of buoyancy. The ventilation efficiency of the Korean-style interlocking greenhouse was evaluated according to the wind-environment conditions because the main mechanisms affecting greenhouse ventilation varied with the wind speed conditions.

3.2.2. Estimation of Inflow/Outflow Rate at Roof Vent

The inflow/outflow rate through the roof vents of the CR-Venlo greenhouse according to the external wind speed was quantified (Figure 12). The calculation of the airflow rate passing through the roof vents of the CR-Venlo greenhouse under low wind speed ($0.5 \text{ m}\cdot\text{s}^{-1}$) conditions for each span revealed that the highest air inflow ($\text{Air}_{\text{inflow}}$) was in the first span on the windward side with $14.99 \text{ kg}\cdot\text{s}^{-1}$, and the air inflow gradually decreased toward the leeward side. The air outflow ($\text{Air}_{\text{outflow}}$) through the greenhouse roof vent in each span was greater on the windward side and decreased toward the leeward side. Under low ($0.5 \text{ m}\cdot\text{s}^{-1}$) and high wind speed ($3.0 \text{ m}\cdot\text{s}^{-1}$) conditions, the coefficient of variation (CV) for the air outflow through the greenhouse roof vents was 28.4% and 32.5%, respectively. Therefore, under low wind-speed conditions, the overall air outflow is uniform for all spans, and indirectly indicates that the airflow inside the greenhouse is predominantly influenced by gravity with buoyancy driven ventilation.

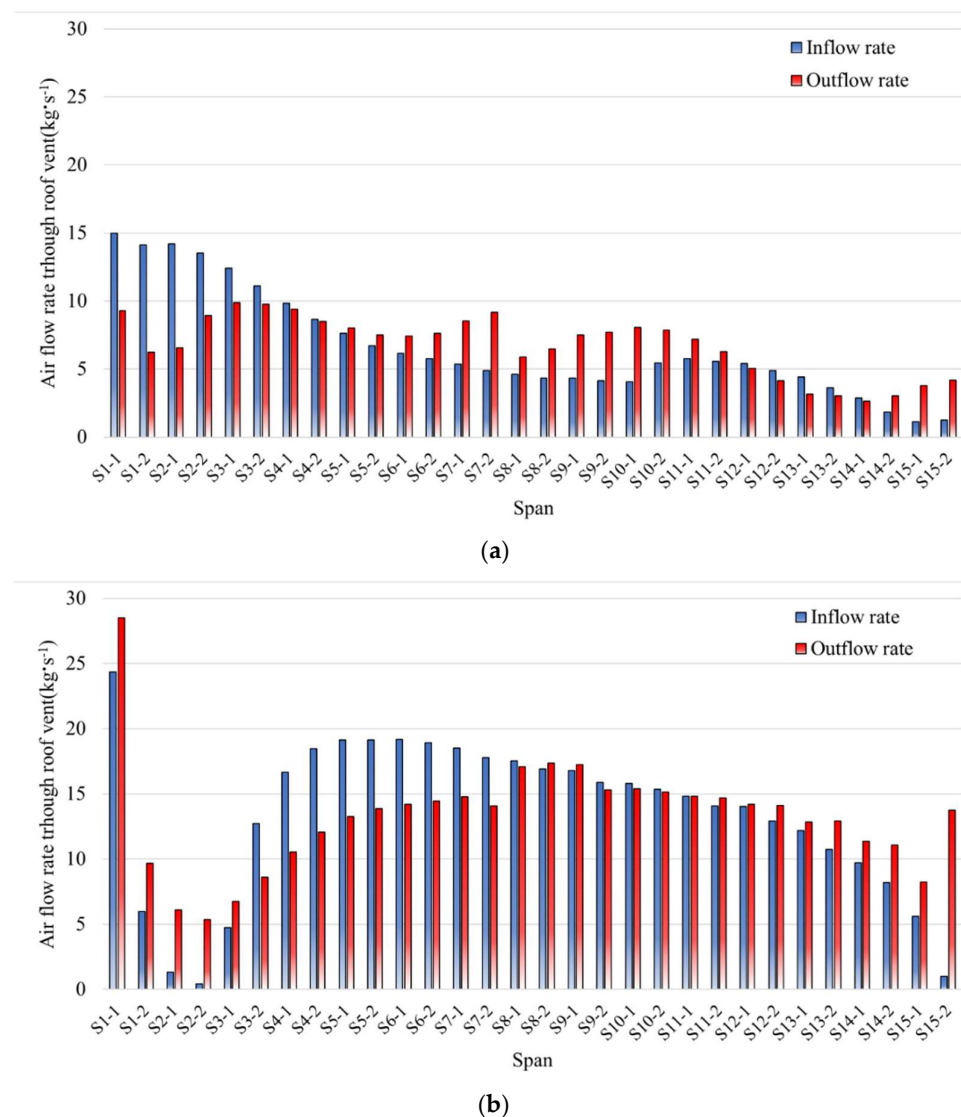


Figure 12. Air inflow and outflow through roof vent with 7 m eave height according to wind speed. (a) External wind speed $0.5 \text{ m}\cdot\text{s}^{-1}$, (b) External wind speed $3.0 \text{ m}\cdot\text{s}^{-1}$.

The calculation of the flow rate for air passing through the greenhouse roof vents at high wind speed for each span revealed that the first span on the windward side had the highest air inflow ($\text{Air}_{\text{inflow}}$) with $24.35 \text{ kg}\cdot\text{s}^{-1}$, and the air outflow ($\text{Air}_{\text{outflow}}$) was also high with $28.53 \text{ kg}\cdot\text{s}^{-1}$. Except for the first span, little air flowed through the roof vents in spans on the windward side, and after the span in the center of the greenhouse, air inflow rate through the roof vents increased to approximately 80% of that of the first span. This was because most of the air flowed in through the first span on the windward side, and the airflow separation was largely generated by the greenhouse structure at first span. The inflow through the roof vents gradually decreased toward the spans on the leeward side, and the air outflow rate was greater than that of the inflow. In particular, the volume of outflow from the last span on the leeward side was four times that of the inflow, indicating that the outflow of internal air was dominant at the leeward side.

3.2.3. Estimation of Incoming Flow Rate

The volume of inflow and outflow through the roof vent indicates the ventilation efficiency of the CR-Venlo greenhouse roof vent; however, it does not guarantee to increase the ventilation rate at the height of the crop zone in the CR-Venlo greenhouse. Because all facing roof vents on the same span are open and the distance between roof vents is considerably short; most air escapes through the roof vent on the opposite side in the case of ventilation under high external wind speed (Figure 13). Therefore, quantitative evaluation of air inflow through the roof vent is necessary to determine if air actually flows into the greenhouse. To quantitatively compare this, a CFD model for the general Venlo greenhouse, which has the same shape as the CR-Venlo greenhouse but with a different roof vent, was created. Ventilation efficiency was compared, and the volume replacement rate per minute was calculated (Table 5). The volume replacement rate per minute in the CR-Venlo greenhouse under low wind-speed conditions ($0.5 \text{ m}\cdot\text{s}^{-1}$) was $0.17 \text{ AER min}^{-1}$, which was higher than that in the European-style Venlo greenhouse ($0.10 \text{ AER min}^{-1}$). The volume replacement rate per minute of the CR-Venlo greenhouse under high wind-speed conditions ($3.0 \text{ m}\cdot\text{s}^{-1}$) was $0.28 \text{ AER min}^{-1}$, which was lower than that in the European-style Venlo greenhouse ($0.49 \text{ AER min}^{-1}$). The CR-Venlo greenhouse has a structure similar to that of the European-style Venlo greenhouse, but the CR-Venlo greenhouse has a relatively large area of roof window. It means that the large roof window area of the CR-Venlo greenhouse helps gravity with buoyancy driven ventilation very efficiently under low wind speed conditions. In high wind speed conditions, where the influence of wind-driven is ventilation high, ventilation through the wide roof window area was not effective. This result contradicts the results obtained when much of the external air flows through the roof window of the CR-Venlo greenhouse, indicating that the influx of external air through the roof window was ineffective.

The ventilation efficiency was evaluated considering the characteristics of a CR-Venlo greenhouse vent; the total inflow of external air through the roof vent and actual air inflow ($\text{Air}_{\text{incoming}}$) into the greenhouse was assessed.

Table 5. CFD computed ventilation rates based on the MFR method of the CR-Venlo greenhouse and C-Venlo greenhouse.

External Wind Speed ($\text{m}\cdot\text{s}^{-1}$)	Air Exchange Rate Per Minute (AER min^{-1})	
	Venlo-Type Greenhouse with Continuous Roof Vent Open	Conventional Venlo-Type Greenhouse
0.5	0.17	0.10
3.0	0.28	0.49

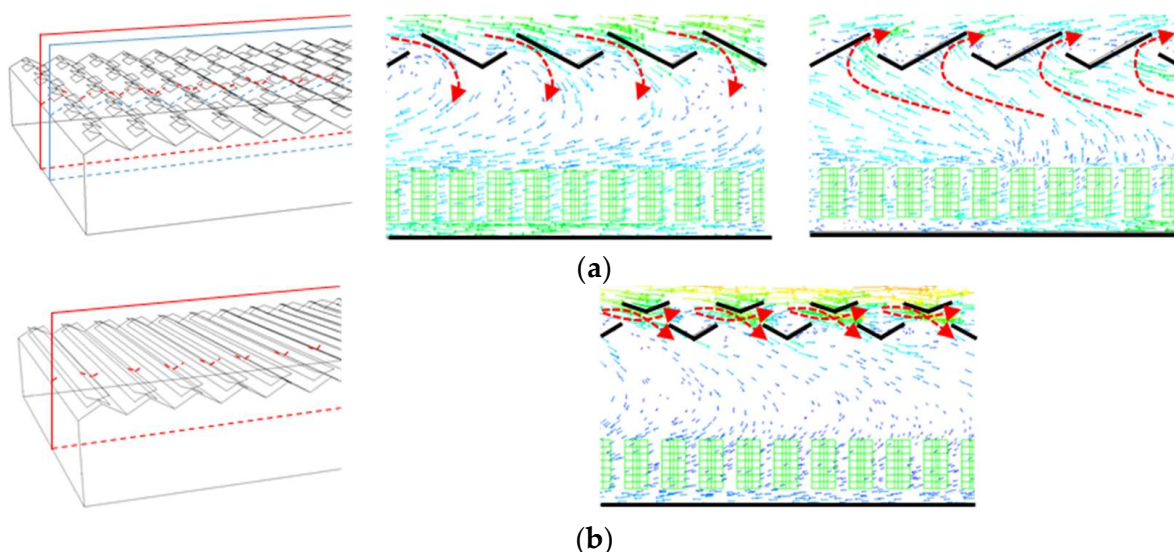


Figure 13. Airflow in middle span of the greenhouse with a ridge height of 7 m under the external wind speed of $3 \text{ m}\cdot\text{s}^{-1}$. (a) Airflow pattern of Dutch Venlo-type greenhouse through the roof vents, (b) Air flow pattern of Korean Venlo-type greenhouse through the roof vents.

The top graph in Figure 14a depicts the air inflow ($\text{Air}_{\text{inflow}}$) through the roof vent at various heights of the greenhouse at an external wind speed of $0.5 \text{ m}\cdot\text{s}^{-1}$, and the bottom graph indicates the air inflow ($\text{Air}_{\text{incoming}}$) through the roof window. On the top graph, the efficiency of inflow of external air in each span in the greenhouse can be evaluated, and on the bottom graph, the efficiency of the air flow out of the greenhouse can be evaluated. The mass inflow rate ($\text{Air}_{\text{inflow}}$) was higher in the span on the windward side, where the inflow of external air begins. It gradually decreased toward the spans on the leeward side. Air flowing into the greenhouse ($\text{Air}_{\text{incoming}}$) was higher in the span on the windward side and gradually decreased toward the spans on the leeward side. The air inflow in each span changed gradually and the airflow separation in the first span in the greenhouse was not severe. This could be attributed to the dominant gravity with buoyancy driven ventilation because the external wind speed was relatively low. The air flow into the greenhouse, compared to the mass inflow rate through the roof vent in the greenhouse, presented at 30.3–61.4% in most spans, except for the span on the windward side (81.0~100%).

Figure 14c depicts the air inflow ($\text{Air}_{\text{inflow}}$) through the roof vent at different heights of the greenhouse under an external wind speed of $3 \text{ m}\cdot\text{s}^{-1}$, as well as the air flow into the greenhouse ($\text{Air}_{\text{incoming}}$). With the first and second spans on the windward side, which had high levels of mass inflow rate, most air did not flow into the greenhouse. The ratio of air that actually flowed into the greenhouse was less than 2%, with most air (98%) flowing out of the greenhouse. Furthermore, most of the spans, except for the first and second spans on the windward side and the last span on the leeward side, exhibited an air inflow efficiency of 12.55–34.41%. Therefore, although the mass replacement rate was high due to the opening of all facing roof vents, the actual air inflow efficiency was not.

When the height of the greenhouse increased, the ratio of air that flowed into the greenhouse improved by a maximum of 4.59% in the span at the center of the greenhouse. This indicates that airflow separation that occurs on the sidewall on the windward side was greater, and consequently, the air inflow efficiency in the span in the center of the greenhouse increased. However, in most greenhouse spans, the improvement of air inflow efficiency with the height of the greenhouse was minimal, ranging from 0.16 to 3.50%. Therefore, improvements are necessary to allow a lot of air to enter the greenhouse through the roof vent.

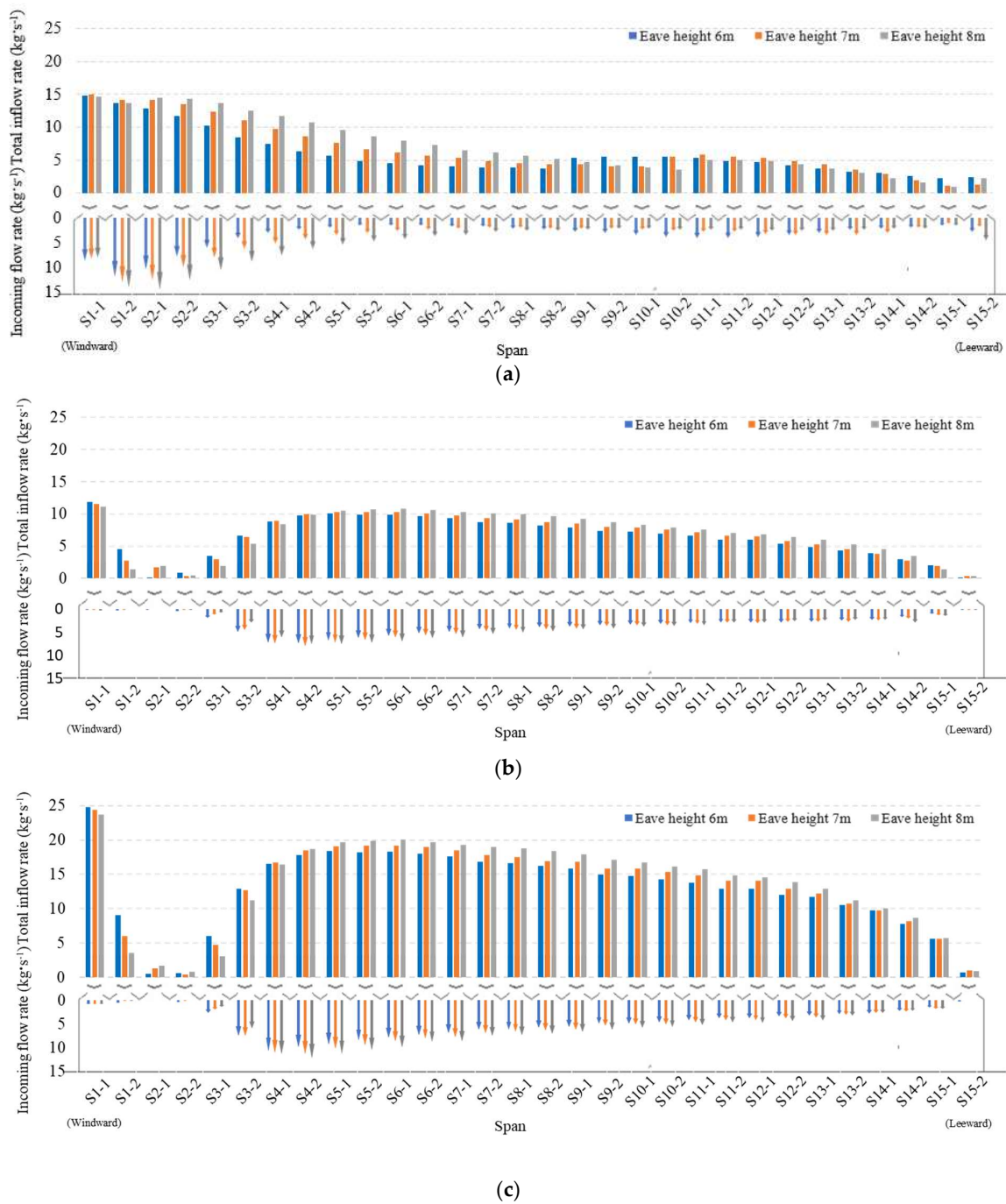


Figure 14. Total inflow rate and incoming flow rate according to the eave height and external wind speed. (a) External wind speed $0.5 \text{ m} \cdot \text{s}^{-1}$, (b) External wind speed $1.5 \text{ m} \cdot \text{s}^{-1}$, (c) External wind speed $3.0 \text{ m} \cdot \text{s}^{-1}$.

3.3. Evaluation of the Thermal Environment of the Greenhouse According to the Height of the Eave

The thermal environment analysis of the CR-Venlo greenhouse revealed that, except for the first span, the temperature increased as the internal height of the greenhouse increased in the spans on the windward side (Figure 15). The amount of air entering the roof vent is small; however, the amount of internal air flowing out was dominant in these spans. For the central span, the temperature increased with increasing internal height of the greenhouse; however, the temperature decreased after a certain height. The inflow of air separated from the sidewall on the windward side through the roof vent after the central span possibly lowers the temperature at the top of the greenhouse. With the leeward side span, the higher

the location inside the greenhouse, the higher the temperature. The dominant amount of external air inflow in the central span of the greenhouse moving toward the spans on the leeward side and flowing out through the roof vents have caused this.

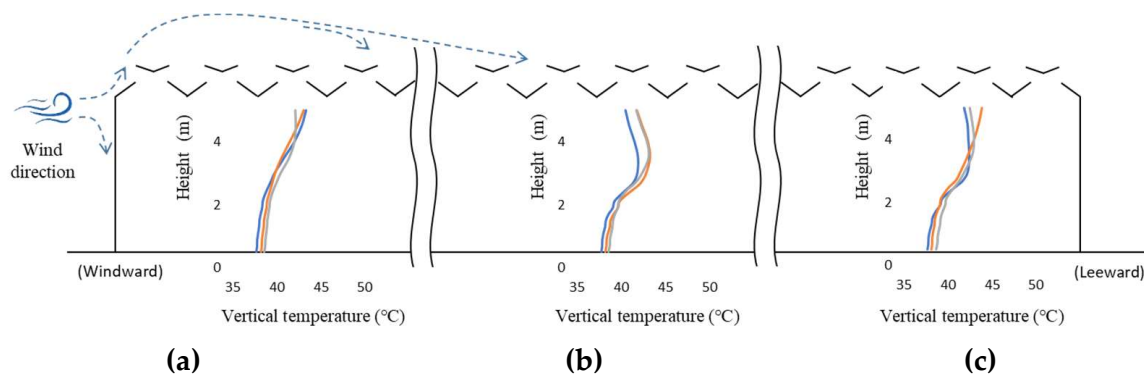


Figure 15. Vertical temperature profile of greenhouse according to the external wind speed (— $0.5 \text{ m}\cdot\text{s}^{-1}$ — $1.5 \text{ m}\cdot\text{s}^{-1}$ — $3.0 \text{ m}\cdot\text{s}^{-1}$). (a) 1~5 span, (b) 6~10 span, (c) 11~15 span.

Analysis of average greenhouse temperature and crop zone temperature at different heights of the CR-Venlo greenhouse revealed that the higher the height of the greenhouse, the lower was the average greenhouse temperature and crop zone temperature, under all wind conditions (Figure 16). This could be attributed to the increased volume of the greenhouse, combined with the increase in the greenhouse height. This causes hot air to move to the upper part of the greenhouse, resulting in the rapid removal of heat. These results are in line with those in earlier reports [1]. However, when the external wind speed was $1.5 \text{ m}\cdot\text{s}^{-1}$, the amount of temperature decrease with increasing greenhouse height was reduced. The temperature of the crop zone decreased by $0.6 \text{ }^\circ\text{C}$ when the greenhouse height was 6 m compared to that at 5 m; it decreased by $0.1 \text{ }^\circ\text{C}$ when the height was 9 m compared to that at 8 m. This may be due to the low efficiency of the flow of external air into the greenhouse because in the ventilation structure of the CR-Venlo greenhouse, all facing roof vents are open. When the height of the greenhouse increases, the heated air on the floor of the greenhouse should move up and escape to the outside through the roof vent; the efficiency of hot air removal is influenced by the low efficiency of ventilation through the roof vent. Consequently, the overall temperature of the internal greenhouse and the crop zone decreased slightly with increasing height of the CR-Venlo greenhouse.

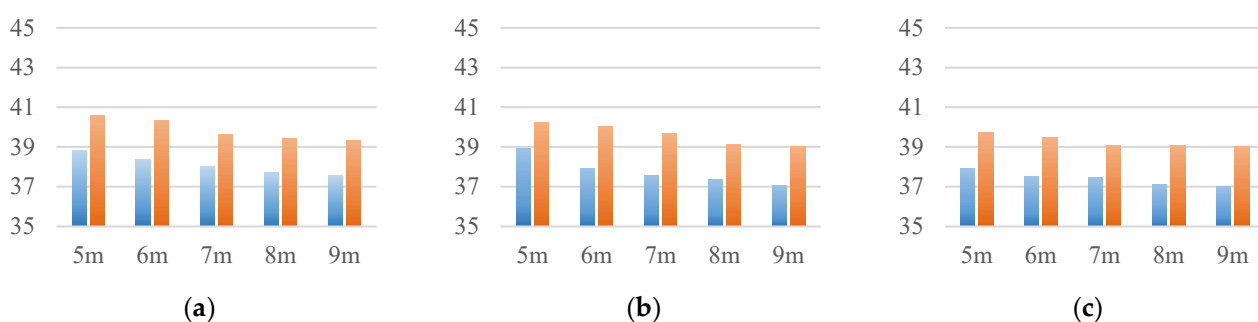


Figure 16. Average temperature in the whole greenhouse and crop zone according to the eave height of greenhouse (X-axis: eave height of greenhouse; Y-axis: Air temperature ($^\circ\text{C}$); ■ Air temperature of the crop zone, ■ Average air temperature of the greenhouse). (a) External wind speed $0.5 \text{ m}\cdot\text{s}^{-1}$, (b) External wind speed $1.5 \text{ m}\cdot\text{s}^{-1}$, (c) External wind speed $3.0 \text{ m}\cdot\text{s}^{-1}$.

3.4. Evaluation of the Ventilation Efficiency of the Improved Korean Venlo-Type Greenhouse with Continuous Roof Vents

The height difference between the upper and lower parts of the CR-Venlo greenhouse is sufficient due to the high eaves, and the buoyancy effect in hot summer is expected

to be particularly large due to the temperature differences between the upper and lower parts of the greenhouse. However, because the inflow and outflow of air occur through the same roof vent, they move against each other, resulting in the decreased efficiency of the greenhouse's inflow of external air and outflow of internal air.

In the CR-Venlo greenhouse, most of the inflow air from the roof vent on the windward side escapes through the opposite roof vent on the leeward side; therefore, the actual ventilation efficiency inside the greenhouse is considerably low. This phenomenon intensifies with an increase in airflow speed and is especially noticeable when ventilation based on external wind conditions is the dominant factor. Consequently, for wind ventilation, we designed and analyzed an improvement plan that involves changing the method of opening and closing the roof vents or opening the roof vent at a high angle, as well as installing a virtual windbreak to induce air inflow into the greenhouse.

In the models for Cases 1 and 2, which improved the operation of the opening and closing of the roof vents, the air inflow ($Air_{incoming}$) increased by 43% and 68%, respectively, compared to that in the existing model. In Case 3, the air inflow decreased by 35.6%. In Cases 1 and 2, the air inflow ($Air_{incoming}$) in the first span on the windward side increased markedly; a lot of air entered to the greenhouse in the central span where the separated air on the sidewall on the windward side entered the greenhouse. In Case 3, air inflow slightly increased in the leeward side span compared to that in the existing model; however, the air inflow ($Air_{incoming}$) decreased in most other spans.

The roof vent on the windward side was closed, and only the roof vent on the leeward side was open in Case 3; therefore, the air separated from the roof vent on the windward side entered through the roof vent on the leeward side. This model had significantly little air inflow ($Air_{incoming}$) in the span on the windward side, the central span, and the spans on the leeward side. In Case 3, the air separated at the roof vent on the windward side did not efficiently enter through the roof vent on the leeward side due to the short distance between the roof vents (Figure 17).

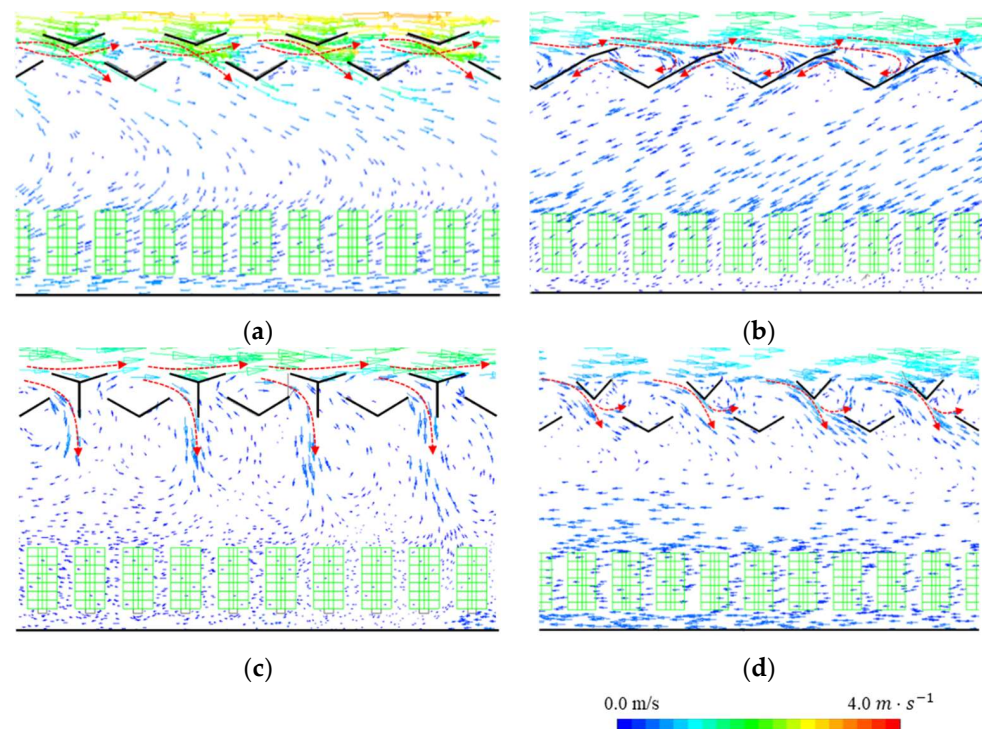


Figure 17. Airflow field from the roof windows of improved models: (a) Case 0: Korean multi-span greenhouse, (b) Case 3: Opening of all windward roof vents, (c) Case 4: Windbreak installation in the center of all roof vents, (d) Case 5: Increasing opening angle of roof vents.

In Case 4, where a virtual wall was installed on the roof vent of the CR-Venlo greenhouse, the amount of air inflow ($Air_{in\text{coming}}$) increased by approximately 43% compared to that in the existing model. Air inflow ($Air_{in\text{coming}}$) in the first span on the windward side increased markedly ($0.89 \text{ kg}\cdot\text{s}^{-1} \rightarrow 20.87 \text{ kg}\cdot\text{s}^{-1}$). In Case 5, the amount of air inflow ($Air_{in\text{coming}}$) increased by approximately 95.9% compared to that in the existing model. Air inflow ($Air_{in\text{flow}}$) in the first span on the windward side increased markedly; the improvement was the greatest in the spans after the central span. The flow of air was induced toward the floor of the greenhouse due to the windbreak and the roof vent with a high opening angle (Figure 18). The structure directs the external air entering the greenhouse through the roof vent to the inside of the greenhouse. Therefore, a structure that effectively directs the external air entering through the roof vent to the inside of the greenhouse is important; in particular, the high opening angle of the roof vent is effective.

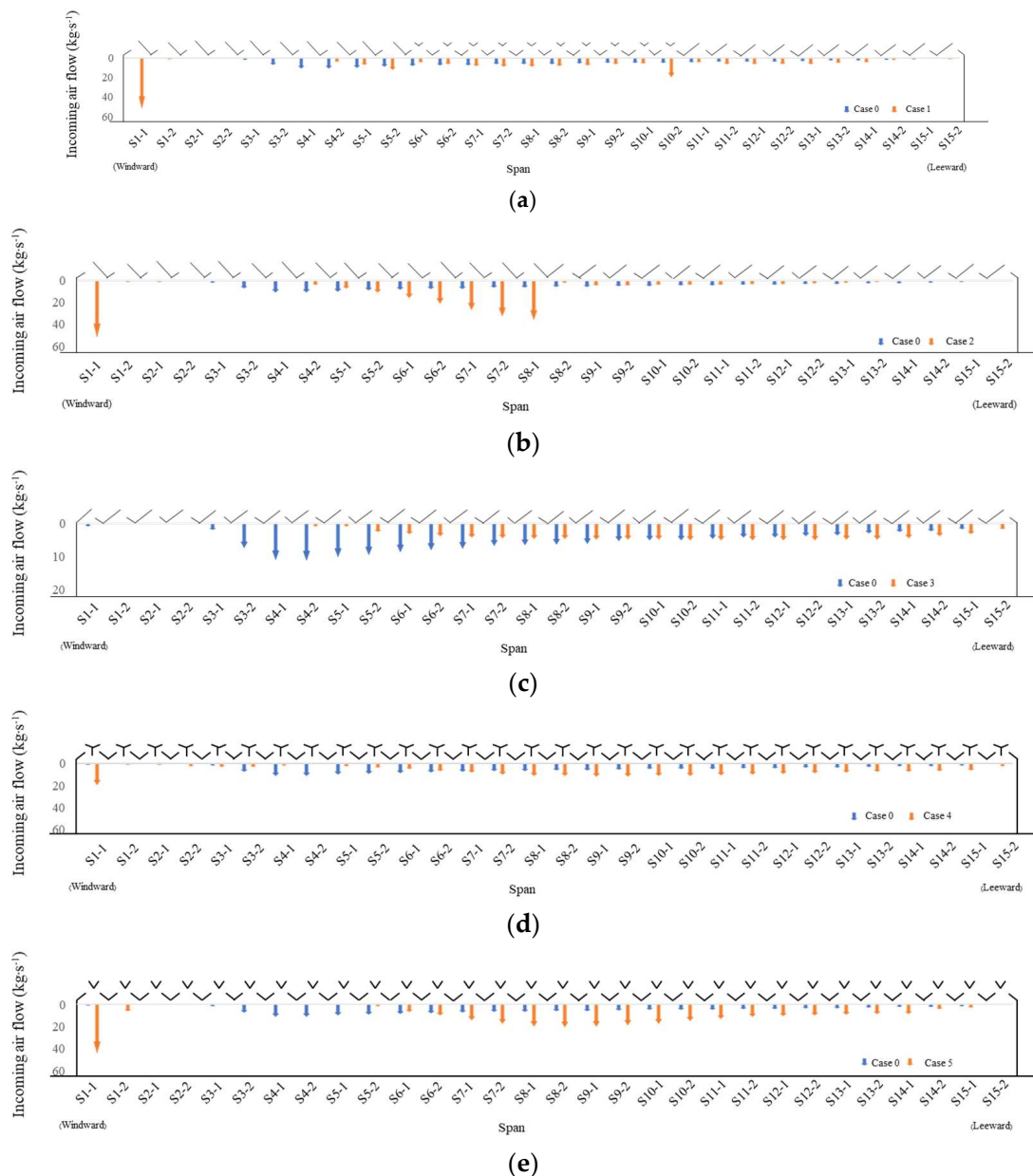


Figure 18. The incoming flow rate of the improved Korean Venlo-type greenhouse with continuous roof vents at an external wind speed of $3.0 \text{ m}\cdot\text{s}^{-1}$. (a) Case 1, (b) Case 2, (c) Case 3, (d) Case 4, (e) Case 5.

Accordingly, the CR-Venlo greenhouse can replace a lot of air due to its large roof vent area; however, the considerably short distance between the roof vents and the open roof vents can cause a low ventilation rate; most of the air that enters through the roof vent escapes through the roof vent on the opposite side. The improvement plans in this study indicate that ventilation efficiency must be improved by managing the opening and closing of roof vents and installing walls.

4. Conclusions

This study evaluated the ventilation efficiency of a CR-Venlo greenhouse using CFD. Depending on wind speed, gravity with buoyancy driven ventilation and wind-driven ventilation were the dominant factors considering the air flow pattern in greenhouse and inflow/outflow rate. For an external wind speed of $0.5 \text{ m}\cdot\text{s}^{-1}$, gravity with buoyancy driven ventilation was the dominant factor, whereas the dominant factor was wind-driven ventilation, when the external wind speed was relatively fast at 1.5 and $3.0 \text{ m}\cdot\text{s}^{-1}$. In particular, when external wind ventilation was dominant, the air inflow ($\text{Air}_{\text{inflow}}$) through the roof vent was high, but the actual airflow rate into the greenhouse ($\text{Air}_{\text{incoming}}$) was significantly low, less than 30% in most cases.

The average greenhouse temperature and the average crop-zone temperature at varying heights of the CR-Venlo greenhouse revealed that, at a higher greenhouse height, the average temperatures of the greenhouse and crop zone decreased lognormally; this is consistent with the results of an earlier report [3]. Considering the exponential decrease in temperature with the increase in the height of the greenhouse, a height of 6 m or 7 m is efficient. However, the cost of greenhouse construction and maintenance should be considered.

In a CR-Venlo greenhouse, a lot of air flows in and out through the roof vent due to its wide structure; however, the amount of air entering the greenhouse was considerably low. Consequently, this study attempted to improve ventilation efficiency by managing the opening and closing of the greenhouse roof vent according to airflow. Based on the opening and closing of the roof vent, the air inflow rate ($\text{Air}_{\text{incoming}}$) inside the greenhouse either increased by 43 to 95.9% or decreased by 35.6%. Therefore, improving the ventilation rate for the CR-Venlo greenhouse requires a thorough evaluation of various conditions of the wind environment, conditions of opening and closing of the vent, and improvement plans for the roof vent. It may be that a controller may adjust vent opening according to wind speed and direction and thus improve ventilation efficiency.

Author Contributions: Conceptualization, S.-J.P. and I.-B.L.; methodology, S.-J.P.; S.-Y.L.; validation, S.-J.P. and H.-H.J.; investigation, S.-J.P., J.-G.K.; writing—original draft preparation, S.-J.P. and I.-B.L.; writing—review and editing, S.-J.P., C.D.-V., J.-H.C. and U.-H.Y.; visualization, Y.-B.C.; All authors have read and agreed to the published version of the manuscript.

Funding: This work was supported by the Korea Institute of Energy Technology Evaluation and Planning (KETEP) and the Ministry of Trade, Industry & Energy (MOTIE) of the Republic of Korea (No. 20212020800050).

Institutional Review Board Statement: Not applicable.

Informed Consent Statement: Not applicable.

Data Availability Statement: Not applicable.

Conflicts of Interest: The authors declare no conflict of interest.

References

1. Ministry of Agriculture Food and Rural Affairs. 2020. Available online: <https://www.mafra.go.kr> (accessed on 10 June 2022).
2. Flores-Velazquez, J.; Montero, J.I.; Baeza, E.J.; Lopez, J.C. Mechanical and natural ventilation systems in a greenhouse designed using computational fluid dynamics. *Int. J. Agric. Biol. Eng.* **2014**, *7*, 1.

3. Fatnassi, H.; Boulard, T.; Benamara, H.; Roy, J.C.; Suay, R.; Poncet, C. Increasing the height and multiplying the number of spans of greenhouse: How far can we go? In Proceedings of the International Symposium on New Technologies and Management for Greenhouses, Evora, Portugal, 19–23 July 2015; pp. 19–23.
4. Boulard, T.; Meneses, J.F.; Mermier, M.; Papadakis, G. The mechanisms involved in the natural ventilation of greenhouses. *Agric. Forest Meteorol.* **1996**, *79*, 61–77. [[CrossRef](#)]
5. Okushima, L.; Sase, S.; Lee, I.-B.; Bailey, B.J. Thermal environment and stress of workers in naturally ventilated greenhouses under mild climate. *Acta Hortic.* **2001**, *559*, 793–798. [[CrossRef](#)]
6. Bartzanas, T.; Boulard, T.; Kittas, C. Effect of vent arrangement on windward ventilation of a tunnel greenhouse. *Biosyst. Eng.* **2004**, *88*, 479–490. [[CrossRef](#)]
7. Kacira, M.; Sase, S.; Okushima, L. Effects of side vents and span numbers on wind-induced natural ventilation of a gothic multi-span greenhouse. *Jpn. Agric. Res. Q.* **2004**, *38*, 227–233. [[CrossRef](#)]
8. Baeza, E.J.; Pérez-Parra, J.J.; Montero, J.I.; Bailey, B.J.L.; Gázquez, J.C. Analysis of the role of sidewall vents on buoyancy-driven natural ventilation in parral-type greenhouses with and without insect screens using computational fluid dynamics. *Biosyst. Eng.* **2009**, *104*, 86–96. [[CrossRef](#)]
9. Fidaros, D.K.; Baxevanou, C.A.; Bartzanas, T.; Kittas, C. Numerical simulation of thermal behavior of a ventilated arc greenhouse during a solar day. *Renew. Energy* **2010**, *35*, 1380–1386. [[CrossRef](#)]
10. Ishii, M.; Okushima, L.; Moriyama, H.; Sase, S.; Fukuchi, N.; Both, A.J. Experimental study of natural ventilation in an open-roof greenhouse during the summer. In *ISHS Acta Horticulturae 1107: XXIX International Horticultural Congress on Horticulture: Sustaining Lives, Livelihoods and Landscapes (IHC2014): International Symposium on Innovation and New Technologies in Protected Cropping*; ISNS: Leuven, Belgium, 2014; pp. 67–74.
11. Ha, J. Evaluation of Natural Ventilation Efficiency of Protected Cultivation System in Reclaimed Land Using Aerodynamic Simulation. Master's Thesis, Seoul National University, Seoul, Korea, 2015.
12. Benni, S.; Tassinari, P.; Bonora, F.; Barbaresi, A.; Torreggiani, D. Efficacy of greenhouse natural ventilation: Environmental monitoring and cfd simulations of a study case. *Energy Build.* **2016**, *125*, 276–286. [[CrossRef](#)]
13. Boulard, T.; Roy, J.; Pouillard, J.; Fatnassi, H.; Grisey, A. Modelling of micrometeorology, canopy transpiration and photosynthesis in a closed greenhouse using computational fluid dynamics. *Biosyst. Eng.* **2017**, *158*, 110–133. [[CrossRef](#)]
14. Lee, S.Y.; Lee, I.B.; Kim, R.W. Evaluation of wind-driven natural ventilation of single-span greenhouses built on reclaimed coastal land. *Biosyst. Eng.* **2018**, *171*, 120–142. [[CrossRef](#)]
15. Zhao, Y.; Teitel, M.; Barak, M. Vertical temperature and humidity gradients in a naturally ventilated greenhouse. *J. Agric. Eng. Res.* **2001**, *78*, 431–436. [[CrossRef](#)]
16. Jung, D.H.; Kim, H.J.; Kim, J.Y.; Lee, T.S.; Park, S.H. Model predictive control via output feedback neural network for improved multi-window greenhouse ventilation control. *Sensors* **2020**, *20*, 1756. [[CrossRef](#)]
17. Chauhan, K.K.; Lunagaria, M.M. Interpolation of Microclimatic Parameters over Capsicum under Open Ventilated Greenhouse. *Int. J. Econ. Plants* **2022**, *9*, 95–100. [[CrossRef](#)]
18. Yeo, U.H.; Lee, S.Y.; Park, S.J.; Kim, J.G.; Choi, Y.B.; Kim, R.W.; Lee, I.B. Rooftop Greenhouse:(1) Design and Validation of a BES Model for a Plastic-Covered Greenhouse Considering the Tomato Crop Model and Natural Ventilation Characteristics. *Agriculture* **2022**, *12*, 903. [[CrossRef](#)]
19. Chung, S.J.; Seo, B.S.; Kang, J.K.; Kim, H.G. Development of hydroponic technique of fruit vegetables using perlite and mixtures with perlite as a substrate: 1. Effects of containers and substrates on the growth and fruit quality of hydroponically grown cucumber. *J. Bio-Environ. Control.* **1995**, *4*, 159–166.
20. Kim, R.W.; Lee, I.B.; Yeo, U.H.; Lee, S.Y. Evaluation of various national greenhouse design standards for wind loading. *Biosyst. Eng.* **2019**, *188*, 136–154. [[CrossRef](#)]
21. Norton, T.; Grant, J.; Fallon, R.; Sun, D.-W. Improving the representation of thermal boundary conditions of livestock during CFD modelling of the indoor environment. *Comput. Electron.* **2010**, *73*, 17–36. [[CrossRef](#)]
22. Seo, I.-H.; Lee, I.-B.; Moon, O.-K.; Hong, S.-W.; Hwang, H.-S.; Bitog, J.P.; Kwon, K.; Ye, Z.; Lee, J. Modelling of internal environmental conditions in a full-scale commercial pig house containing animals. *Biosyst. Eng.* **2012**, *111*, 91–106. [[CrossRef](#)]
23. Wu, W.; Zhai, J.; Zhang, G.; Nielsen, P.V. Evaluation of methods for determining air exchange rate in a naturally ventilated dairy cattle building with large openings using computational fluid dynamics (CFD). *Atmos. Environ.* **2012**, *63*, 179–188. [[CrossRef](#)]
24. Yeo, U.H.; Lee, I.B.; Kim, R.W.; Lee, S.Y.; Kim, J.G. Computational fluid dynamics evaluation of pig house ventilation systems for improving the internal rearing environment. *Biosyst. Eng.* **2019**, *186*, 259–278. [[CrossRef](#)]
25. Lee, M.H. Analysis of Aerodynamic Improvements about Major Environmental Problems in Highrise Multi-Span Greenhouse. Master's Thesis, Seoul National University, Seoul, Korea, 2019.
26. Richards, P. *Computational Modelling of Wind Flow Around Low-Rise Buildings Using PHOENICS*; AFRC Institute of Engineering Research: Silsoe, UK, 1989.
27. Bartzanas, T.; Kittas, C.; Sapounas, A.; Nikita-Martzopoulou, C. Analysis of airflow through experimental rural buildings: Sensitivity to turbulence models. *Biosyst. Eng.* **2007**, *97*, 229–239. [[CrossRef](#)]
28. Bournet, P.E.; Ould Khaoua, S.A.; Boulard, T. Numerical prediction of the effect of vent arrangements on the ventilation and energy transfer in a multi-span glasshouse using a bi-band radiation model. *Biosyst. Eng.* **2007**, *98*, 224–234. [[CrossRef](#)]

29. Bournet, P.-E.; Boulard, T. Effect of ventilator configuration on the distributed climate of greenhouses: A review of experimental and CFD studies. *Comput. Electron. Agric.* **2010**, *74*, 195–217. [[CrossRef](#)]
30. Tominaga, Y.; Mochida, A.; Murakami, S.; Sawaki, S. Comparison of various revised Ke 3 models and les applied to flow around a high-rise building model with 1:1:2 shape placed within the surface boundary layer. *J. Wind Eng. Ind. Aerodyn.* **2008**, *96*, 389–411. [[CrossRef](#)]
31. Kim, R.W.; Lee, I.B.; Kwon, K.S. Evaluation of wind pressure acting on multi-span greenhouses using CFD technique, part 1: Development of the CFD model. *Biosyst. Eng.* **2017**, *164*, 235–256. [[CrossRef](#)]
32. Papadakis, G.; Mermier, M.; Meneses, J.F.; Boulard, T. Measurement and analysis of air exchange rates in a greenhouse with continuous roof and side openings. *J. Agric. Eng. Res.* **1996**, *63*, 219–227. [[CrossRef](#)]

Article

An ANN-PSO-Based Method for Optimizing Agricultural Tractors in Field Operation for Emission Reduction

Bowen Zheng^{1,2}, Zhenghe Song^{1,2,*}, Enrong Mao^{1,2}, Quan Zhou^{1,2}, Zhenhao Luo^{1,2}, Zhichao Deng^{1,2}, Xuedong Shao^{1,2} and Yuxi Liu^{1,2}

¹ College of Engineering, China Agricultural University, Beijing 100083, China

² Beijing Key Laboratory of Modern Agricultural Equipment Optimization Design, China Agricultural University, Beijing 100083, China

* Correspondence: songzhenghe@cau.edu.cn; Tel.: +86-010-6373-6730

Abstract: Aiming at the serious problem of agricultural tractor emission pollution, especially the limitation of nitrogen dioxide (NO_x) and soot emissions, we took an agricultural diesel engine as the research object, and a diesel engine combustion chamber model was established for both simulated calculations and experimental verification analysis. The in-cylinder pressure and heat release obtained from the combustion chamber model simulation calculations were within 6% error of the experimental data. The overall trend of change was basically consistent. The established model can simulate the working conditions of the experimental engine relatively well. An artificial neural network (ANN) was also established as an agent model based on the indentation rate, tab depth, and combustion chamber depth as the input, and NO_x and soot as the output. The decision coefficients of the ANN model were $R^2 = 0.95$ and 0.93 , with corresponding Mean Relative Error (MRE) values of 10.13 and 8.18%, respectively, which are within the generally required interval, indicating that the obtained ANN model has good adaptability and accuracy. On the basis of the general particle swarm optimization (PSO) algorithm, an improved PSO algorithm was proposed, in which the inertia factor is continuously adjusted with the help of the skip line function in the optimization process so that the inertia factor adapts to different rates and adjusts the magnitude of the corresponding values in different periods. The improved PSO algorithm was used to optimize the optimal input parameter matching of the agent model to form a new combustion chamber structure, which was imported into CONVERGE CFD software for emission simulation and comparison with the emissions of the original combustion chamber. It was found that the NO_x reduction was about $1.21 \text{ g} \cdot (\text{kW} \cdot \text{h})^{-1}$, and the soot reduction was about $0.06 \text{ g} \cdot (\text{kW} \cdot \text{h})^{-1}$ with the new combustion chamber structure. The ANN + PSO optimization method proved to be effective in reducing the NO_x and soot emissions of diesel engine pollutants, and it may also provide a reference and ideas for the design and development of relevant agricultural engine combustion chamber systems.

Citation: Zheng, B.; Song, Z.; Mao, E.; Zhou, Q.; Luo, Z.; Deng, Z.; Shao, X.; Liu, Y. An ANN-PSO-Based Method for Optimizing Agricultural Tractors in Field Operation for Emission Reduction. *Agriculture* **2022**, *12*, 1332. <https://doi.org/10.3390/agriculture12091332>

Academic Editors: Muhammad Sultan, Redmond R. Shamshiri, Md Shamim Ahamed and Muhammad Farooq

Received: 11 July 2022

Accepted: 14 August 2022

Published: 29 August 2022

Publisher's Note: MDPI stays neutral with regard to jurisdictional claims in published maps and institutional affiliations.



Copyright: © 2022 by the authors. Licensee MDPI, Basel, Switzerland. This article is an open access article distributed under the terms and conditions of the Creative Commons Attribution (CC BY) license (<https://creativecommons.org/licenses/by/4.0/>).

Keywords: tractor; diesel engine; emission; artificial neural network; improved particle swarm algorithm

1. Introduction

With increasing levels of agricultural mechanization operations in China, the overall quantity of agricultural machinery has also been increasing. By the beginning of 2022, the total power consumption of agricultural machinery in China was 107,768.02 million kilowatts, the total number of medium and large tractors was 477,737, and the number of small tractors was 17,275,995 [1]. The vast majority of these tractors source their power from diesel engines. Compared to gasoline engines, diesel soot (soot), and nitrogen oxide, (NO_x) emissions from diesel engines are significantly increased, which is a serious hazard in respect of human health and the environment [2]. In China, in order to solve this problem, the Ministry of Environmental Protection introduced emission regulations for non-road mobile machinery (the “National IV” emission standards) on 1 December 2022, but the

current emission levels of agricultural machinery in most regions are still dominated by the National II and National III emission standards. In the face of increasingly stringent emission regulations and serious energy and environmental issues, reducing the emission of pollutants from agricultural machinery is of great significance to the stable development of China's economy and society and to environmental protection [3,4].

There are three mainstream methods used to reduce pollutants in diesel engines: Pre-treatment technology (oil technology), in-cylinder technology (in-engine purification technology), and post-treatment technology (off-engine exhaust after-treatment technology) [5]. Internal optimization, such as combustion chamber system optimization, can effectively improve the combustion efficiency of the engine and reduce pollutant emissions [6]. As the main container for fuel mist formation and combustion, the combustion chamber plays a key role in mixture formation and combustion. Different combustion chamber structure designs can change the oil–gas mixture state in the cylinder and affect the fluid motion state and combustion process in the cylinder [7]. An appropriate combustion chamber design can enhance the interaction between vortex and turbulence in the cylinder, accelerate the formation of the oil–gas mixture, and distribute it well in the cylinder, thus improving the combustion efficiency of the whole engine and effectively reducing the generation of harmful emission gases. In this regard, a significant amount of research has been conducted in China and abroad. The team of Su Wanhua of Tianjin University designed a BUMP-type combustion chamber based on the phenomenon of convex ring stripping wall jets [8–10], where a finite flow edge is set on the inner wall of the combustion chamber so that a secondary jet is formed in the combustion chamber after the oil beam touches the wall, which accelerates the mixture formation rate and improves the overall combustion efficiency while reducing soot and NO_x emissions. Rakopoulos et al. [11] investigated the effect of combustion chamber structure on diesel engine performance and emissions based on a high-speed direct injection diesel engine and found that combustion chamber structure, fuel injection, and airflow motion are the key factors affecting diesel engine performance and emissions. Li et al. [12] investigated the effect of different combustion chamber crater depths on diesel engine performance and emissions, and the results showed that indented combustion chambers exhibit better oil–gas mixing and open combustion chambers exhibit better combustion performance at low-speed operating conditions. Abdul et al. [13] investigated the effect of the swirl ratio on engine performance and emissions under different combustion chambers and showed that a lower indentation rate leads to an increase in NO_x emissions and a decrease in soot emissions. Jafarmadar et al. [14] investigated the effect of the piston combustion chamber structure on the swirl number and uniformity index and found that a larger crater diameter generally has a higher swirl number and causes lower soot emissions, while a smaller crater depth results in a stronger squeeze flow and output power. Shahanwaz et al. [15] studied the effects of different combustion chamber sizes and injection cone angles on engine emissions and found that an annular combustion chamber structure with different injection cone angle couplings can enable oil and gas to mix more fully and reduce carbon soot emission. At present, scholars at both domestic and international levels mainly focus on two methods for combustion chamber design and optimization. One involves designing and optimizing the traditional combustion chamber shape, and the other involves developing new combustion chambers based on new concepts. However, the common purposes of both are to improve the quality of the oil–gas mixture in the combustion chamber, improve the combustion process, and reduce pollutant emissions. The main research approaches include empirical formulations [16], numerical simulations [17], and complete engine experiments [18,19]. However, most of the methods have long working cycles, high costs, and high accuracy requirements in respect of the experimental models. In recent years, the rise in popular computer technologies, such as machine learning, has provided a new research idea for the rapid prediction of combustion chamber emissions and the mining of new methods and new information [20].

Based on the above, in this study, we first established a diesel engine combustion chamber model based on a YTO Company (China, Luoyang) agricultural tractor diesel

engine for simulation, and the simulation model was then tested to enable validation and analysis. The in-cylinder pressure and heat release values obtained from the simulation of the combustion chamber model were within 6% error of the test data. The overall trend of change was basically consistent. The simulation model can simulate the working conditions of the test engine relatively well. Next, an artificial neural network was established as an agent model based on the indentation rate, tab depth, and combustion chamber depth as the input, and NOx and diesel soot emitted from the engine as the output. Subsequently, based on the general particle swarm optimization (PSO) algorithm, an improved PSO algorithm was proposed, which continuously adjusts the inertia factor with the help of a skip line function during the optimization process, so that the inertia factor adapts to different rates and adjusts the magnitude of the corresponding values in different periods, thus facilitating the PSO in switching gradually from local optimization seeking to global optimization seeking. The improved PSO algorithm was used to optimize the optimal input parameter matching of the proxy model, and the new combustion chamber structure was formed and imported into CONVERGE CFD (Convergent Science Company, Madison, WI, USA) software for comparison with the original combustion chamber. It was found that the new combustion chamber structure can effectively reduce diesel engine emission soot and NOx, which provides suggestions and references for the development of relevant engine combustion chamber systems.

2. Materials and Methods

2.1. Theoretical Modeling Basis

In this study, a typical fluid dynamics approach was used as the theoretical basis for the gas flow model in the engine cylinder, and the laws of conservation of mass, conservation of momentum, and conservation of energy were chosen as the theoretical basis for calculation. The mass conservation equation is as follows:

$$\frac{\partial \rho}{\partial t} + \frac{\partial(\rho u_x)}{\partial x} + \frac{\partial(\rho u_y)}{\partial y} + \frac{\partial(\rho u_z)}{\partial z} = 0 \tag{1}$$

In Equation (1), ρ denotes density in kg/m³ and t denotes time in seconds; u_x, u_y, u_z are the components of the velocity vector u in the $x, y,$ and z directions in units of m/s. The mass conservation equation reflects the relationship between fluid motion and mass and follows the law of mass conservation. That is, the increase in mass within the control system is equal to the difference between the mass flowing into the control system and the mass flowing out of the control system.

The conservation of momentum equation is as follows:

$$\begin{cases} \frac{\partial(\rho u_x)}{\partial t} + \text{div}(\rho u_x u) = -\frac{\partial p}{\partial x} + \frac{\partial \tau_{xx}}{\partial x} + \frac{\partial \tau_{xy}}{\partial y} + \frac{\partial \tau_{xz}}{\partial z} + F_x \\ \frac{\partial(\rho u_y)}{\partial t} + \text{div}(\rho u_y u) = -\frac{\partial p}{\partial y} + \frac{\partial \tau_{yx}}{\partial x} + \frac{\partial \tau_{yy}}{\partial y} + \frac{\partial \tau_{yz}}{\partial z} + F_y \\ \frac{\partial(\rho u_z)}{\partial t} + \text{div}(\rho u_z u) = -\frac{\partial p}{\partial z} + \frac{\partial \tau_{zx}}{\partial x} + \frac{\partial \tau_{zy}}{\partial y} + \frac{\partial \tau_{zz}}{\partial z} + F_z \end{cases} \tag{2}$$

In Equation (2), p is the surface force acting on the fluid micro-element in the cylinder in N; $\tau_{xx}, \tau_{xy}, \tau_{xz}$ denote the components of viscous stress in the $x, y,$ and z directions in Pa; F_x, F_y, F_z denote the volume force acting on the micro-element in the $x, y,$ and z directions in N. The momentum conservation equation is the embodiment of Newton’s second law in fluid mechanics, which means that the increased momentum in the control body is equal to the difference between the inflowing momentum and the impulse produced by the surface and volume forces. div denotes the divergence, and the divergence equation is shown in Equation (3):

$$\text{div}(\rho u) = \frac{\partial(\rho u_x)}{\partial x} + \frac{\partial(\rho u_y)}{\partial y} + \frac{\partial(\rho u_z)}{\partial z} \tag{3}$$

The momentum conservation equation is the embodiment of Newton’s second law in fluid mechanics, i.e., the increased momentum in the control body is equal to the difference between the inflowing momentum and the impulse produced by the surface and volume forces. div denotes the scatter, and the scatter equation is shown in Equation (3).

The conservation of energy equation is as follows:

$$\frac{\partial(\rho T)}{\partial t} + \frac{\partial(\rho u_x T)}{\partial x} + \frac{\partial(\rho u_y T)}{\partial y} + \frac{\partial(\rho u_z T)}{\partial z} = \frac{\partial}{\partial z} \left[\frac{h}{C_p} \frac{\partial y}{\partial x} \right] + \frac{\partial}{\partial z} \left[\frac{h}{C_p} \frac{\partial y}{\partial y} \right] + \frac{\partial}{\partial z} \left[\frac{h}{C_p} \frac{\partial y}{\partial z} \right] + S_T \tag{4}$$

In Equation (4), C_p denotes the constant pressure-specific heat capacity in $\text{J}/(\text{kg}\cdot\text{K})$, T denotes the temperature in K , h denotes the fluid heat transfer coefficient, and S_T denotes the viscous consumption term in J . That is, when the fluid is subject to viscous friction in the flow process, the mechanical energy of the fluid is converted into thermal energy. The conservation of energy equation is the application of the law of conservation of energy in fluid mechanics, that is, the total energy of the fluid is equal to the sum of kinetic energy and internal energy.

The turbulence model was selected as the $\text{RNG}_{\kappa-\varepsilon}$ model in CONVERGE CFD because it has good stability and convergence and can better reflect the effects of rotation, shock, and stratification within the flow field. The turbulent kinetic energy equation is as follows:

$$\frac{1}{\sqrt{g}} \frac{\partial(\sqrt{g}\rho k)}{\partial t} + \frac{\partial}{\partial x_j} \left(\rho \bar{u}_j k - \frac{\mu_{eff}}{\sigma_k} \frac{\partial k}{\partial x_j} \right) = \mu_t(P + P_B) - \rho\varepsilon - \frac{2}{3} \left(\mu_t \frac{\partial u_i}{\partial x_i} + \rho k \right) \frac{\partial u_i}{\partial x_i} \tag{5}$$

The turbulent dissipation rate equation is as follows:

$$\begin{aligned} & \frac{1}{\sqrt{g}} \frac{\partial(\sqrt{g}\rho\varepsilon)}{\partial t} + \frac{\partial}{\partial x_j} \left(\rho \bar{u}_j \varepsilon - \frac{\mu_{eff}}{\sigma_k} \frac{\partial \varepsilon}{\partial x_j} \right) \\ = & c_{\varepsilon 1} \frac{\varepsilon}{k} \left[\mu_t P - \frac{2}{3} \left(\mu_t \frac{\partial u_i}{\partial x_i} + \rho k \right) \frac{\partial u_i}{\partial x_i} \right] + c_{\varepsilon 3} \frac{\varepsilon}{k} \mu_t P_B - c_{\varepsilon 2} \frac{\varepsilon^2}{k} + c_{\varepsilon 4} \rho \varepsilon \frac{\partial u_i}{\partial x_i} - \frac{\rho \varepsilon^2 c_{\mu} \eta^3 (1-\eta/\eta_0)}{k (1+\beta\eta^3)} \end{aligned} \tag{6}$$

$$\eta \equiv S \frac{k}{\varepsilon}, S \equiv (2S_{ij}S_{ij})^{\frac{1}{2}}, S_{ij} = \frac{1}{2} \left(\frac{\partial u_i}{\partial x_i} + \frac{\partial u_i}{\partial x_j} \right), P \equiv 2S_{ij} \frac{\partial u_i}{\partial x_i}, P_B \equiv -\frac{g}{\sigma_{h,t}} \frac{1}{\rho} \frac{\partial \rho}{\partial x_i}$$

where k is the turbulent kinetic energy in J , \sqrt{g} is the distance tensor determinant, x_j is the coordinate ($j = 1,2,3$), and u_j is the velocity component in m/s in the x , y , and z directions. η is the ratio of average flow to turbulent time scale, u_i is the velocity component in the direction of coordinate axis x_i in m/s . $c_{\varepsilon 1}$, $c_{\varepsilon 2}$, $c_{\varepsilon 3}$, $c_{\varepsilon 4}$, σ_k , $\sigma_{h,t}$, c_{μ} , and η_0 are empirical constants.

2.2. Building Geometric Models and Validation

A three-dimensional model was designed based on a YTO Company agricultural tractor diesel engine combustion chamber. This engine is a four-stroke supercharged intercooled diesel engine and is mainly used in agricultural machinery field operation conditions. According to the engine parameters provided by YTO, the three-dimensional model was drawn and imported into CONVERGE CFD software. The calibrated power condition was selected, and the flow medium was air. The testing location was the Luoyang Xiyuan Vehicle and Power Inspection Institute. The main technical parameters of the diesel engine are shown in Table 1. The engine model used in the study includes intake and exhaust pipes, intake and exhaust valves, cylinders, and a combustion chamber in-cylinder geometry model, as shown in Figure 1. In CONVERGE 3.0 software, a combination of adaptive encryption and fixed encryption was used to dynamically generate a hexahedral mesh, and the base mesh size of the model was determined to be $8 \text{ mm} \times 8 \text{ mm} \times 8 \text{ mm}$, with dynamic adaptive encryption according to the temperature and velocity gradient, and the highest encryption level being 3. The smaller base mesh size and higher encryption level allow the model calculation results to be more convergent. The initial conditions used in the calculation are shown in Table 2.

Table 1. Main technical parameters of diesel engine.

Parameters	Value
Cylinder bore × stroke	105 mm × 125 mm
Total capacity	4.33 L
Rated power	73.5 KW
Rated speed	2200 rpm
Maximum torque	400 N·m
Maximum torque speed	1400–1600 rpm
Compression ratio	17.5
Combustion geometry	ω -type



Figure 1. Engine geometry model and grid structure.

Table 2. Calculation model initial conditions.

Condition	Area	Temperature/K	Pressure/MPa
Initial conditions	Air intake tract	309	1.83
	Exhaust tract	800	1.21
	Combustion chamber	533	1.56
Boundary conditions	Air inlet	309	1.83
	Exhaust port	800	1.20
	Combustion chamber wall surface	433	—
	Cylinder head bottom surface	525	—
	Piston top surface	553	—

In order to verify the reliability of the model and calculation method, the in-cylinder combustion process was simulated under the working conditions of the agricultural engine with a speed of 2000 rpm/min and a torque of 305 N-m. Figure 2 shows the comparison of the simulated calculation results for in-cylinder pressure and heat release with the test data. The peak phase of in-cylinder pressure and heat release obtained from the simulation is basically the same as that of the test data, and the error did not exceed 6%. The overall trend of change is basically consistent, and the simulation model can simulate the test engine conditions relatively well.

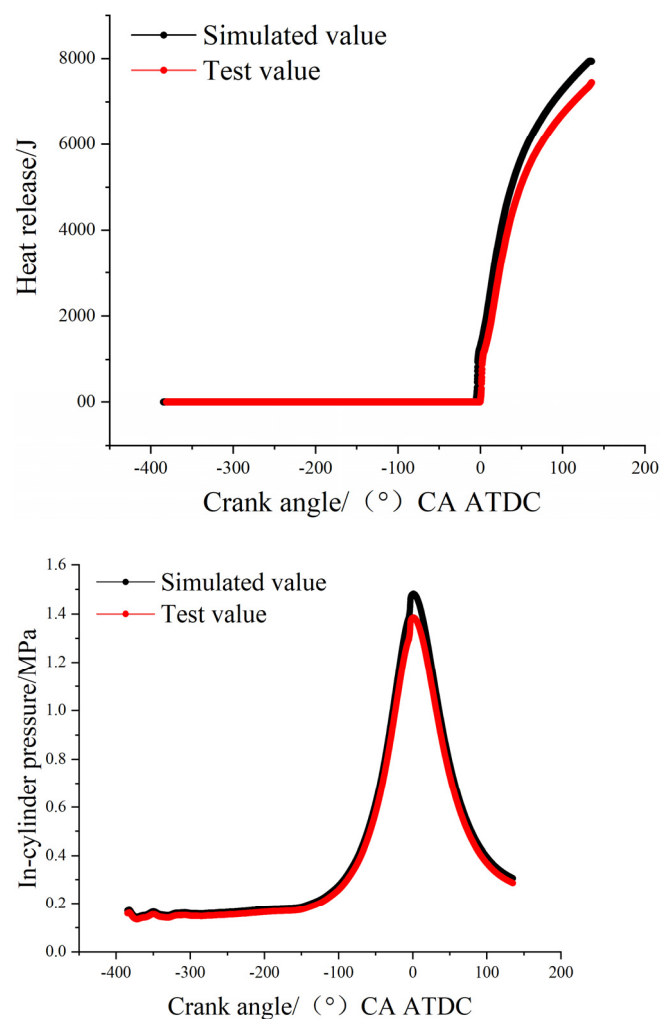


Figure 2. Comparison of numerical and experimental pressure and heat release in the cylinder.

2.3. Combustion Chamber Structure and Parameters

The geometric shape characteristics of the engine combustion chamber are defined as shown in Figure 3. The parameters indentation rate δ and diameter-depth ratio γ are introduced and calculated as:

$$\delta = \frac{d_m - d_k}{d_m} \times 100\% \quad (7)$$

$$\gamma = \frac{d_m}{H} \quad (8)$$

where d_m is the maximum diameter of the combustion chamber in mm, d_k is the indentation diameter of the combustion chamber in mm, H is the depth of the combustion chamber in mm, and h is the depth of the tab in mm.

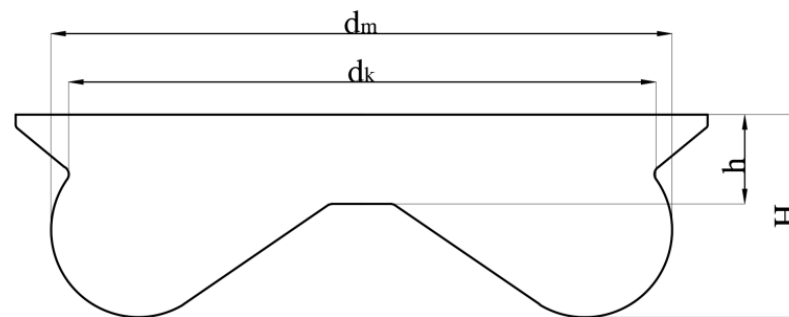


Figure 3. Structural diagram of combustion chamber.

The combustion chamber indentation rate has an important influence on the airflow movement at the end of the compression process in the cylinder and also increases the heat load inside the piston. The indentation diameter d_k reflects the volume of the combustion chamber, which in turn affects the formation and combustion of the oil and gas mixture. As the diameter of the indentation increases, the oil-gas mixture and combustion rate in the combustion process will increase, and the combustion temperature inside the cylinder will increase, so there will be more areas in the cylinder in which to meet the high temperature and sufficient oxygen conditions required for NO_x generation, and NO_x will increase. However, as the temperature increases, it will accelerate some of the soot oxidation, thus reducing the production of soot. If the diameter of the indentation is too large, the combustion temperature decreases, and NO_x generation decreases while soot generation increases. The change in the indentation depth h affects the partition ratio of oil and gas spray after hitting the wall in the cylinder, which has an impact on the combustion process and combustion temperature and ultimately, on the emission generation. The design of the combustion chamber depth H affects the height of the piston in the cylinder. If the piston height is too large, the exhaust gas cannot easily be discharged from the exhaust port, increasing the heat load in the combustion chamber, and leading to a series of problems such as reduced piston life. Therefore, it can be seen that the combustion chamber indentation rate, tab depth, and combustion chamber depth have an important impact on the design of the combustion chamber system and are also important factors for the optimization of agricultural diesel engine emissions. The airflow motion inside the combustion chamber is mainly turbulent motion, which is a highly nonlinear type of fluid motion. The traditional multi-objective optimization method for a diesel combustion chamber cannot easily ensure a good optimization effect when the multi-objective problem presents complex features such as nonlinearity and high dimensionality. Therefore, in this study, the ANN-PSO approach was used to optimize the diesel engine combustion chamber dimensions with the lowest NO_x and soot emissions as the optimization objective and then reduce the engine emissions.

2.4. Construction of Artificial Neural Network (ANN) Model and Validation

In this study, the indentation rate, tab depth, and combustion chamber depth of the combustion chamber were used as inputs, and the nitrogen oxide (NOx) and diesel soot (diesel soot) emitted from the engine were used as outputs to build an artificial neural network as an agent model. The structure of the model is shown in Figure 4, and consists of an input layer, hidden layer, and output layer. Based on the premise of not changing the overall structure of the original 3D model, 200 sets of random data were collected for building the artificial neural network model by using CONVERGE CFD software to randomly generate and collect sample points for three input quantities: Indentation rate, tab depth, and combustion chamber depth. Approximately 75% of the data were used to train the model, and 25% were used to test the model. The logistic sigmoid activation function with distinguishable, continuous, and nonlinear advantages was chosen to formulate the model [21,22]. In addition, gradient descent with momentum weights and a bias learning function (LEARNINGDM) was used to minimize the error [23].

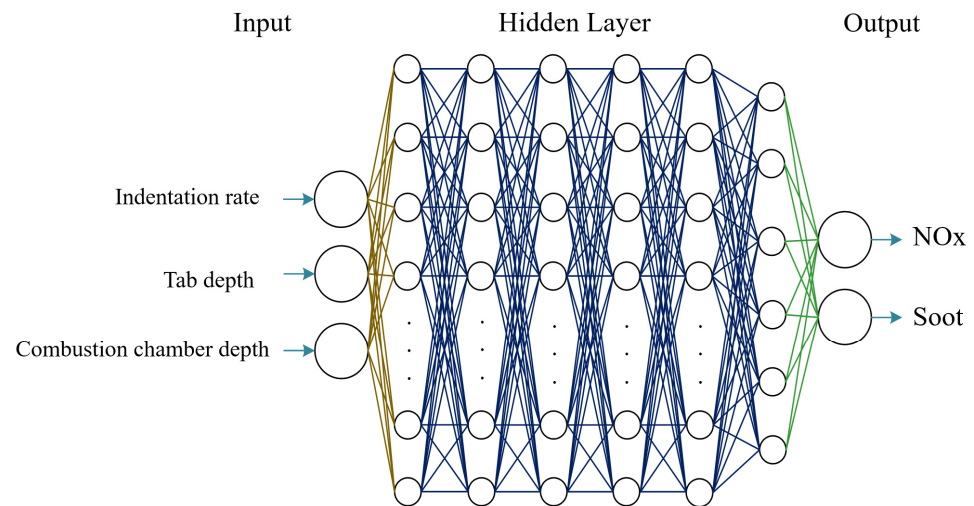


Figure 4. ANN structure diagram.

In order to ensure the adaptability and accuracy of an established ANN model, the model is generally tested for significance, and the coefficient of determination (R^2) and MRE are often used to verify the accuracy of the model. Usually, the R^2 value is required to be between 0.9 and 1. The calculation formulas are shown in Equations (9) and (10):

$$R^2 = \frac{S_{SR}}{S_{ST}} = \frac{S_{SR} - S_{SE}}{S_{ST}} = 1 - \frac{\sum_{i=1}^n (t_i - o_i)^2}{\sum_{i=1}^n (o_i)^2} \quad (9)$$

$$\text{MRE}(\%) = \frac{1}{n} \sum_i^n \left| 100 \frac{t_i - o_i}{t_i} \right| \quad (10)$$

where S_{ST} is the total sum of squares, S_{SR} is the regression sum of squares, S_{SE} is the residual sum of squares, n is the number of points in the information set, o denotes the test data, and t denotes the actual data. Combined with the typical agricultural engine operating conditions, the accuracy of the established ANN model was verified and the R^2 values were calculated under a speed of 2200 rpm/min, as shown in Figure 5, and the R^2 values were 0.95 and 0.93, MRE values were 10.13% and 8.18%, respectively, which are within the generally required interval.

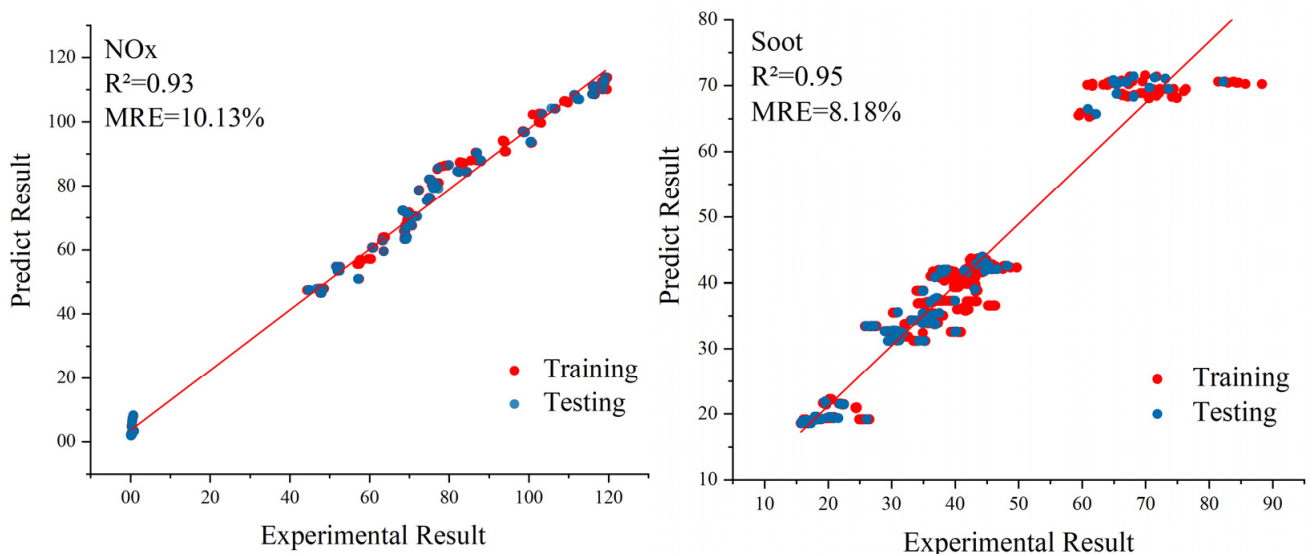


Figure 5. ANN results diagrams.

2.5. Improved Particle Swarm Algorithm (PSO) Application

Particle swarm optimization was jointly proposed by Kennedy and Eberhart in 1995. The particle swarm algorithm is an evolutionary algorithm inspired by the foraging behavior of bird groups in nature and has been widely used in various complex experimental tests and practical engineering applications in view of its simple implementation, efficient searching, and fast convergence. Ven den Bergh [24] analyzed and proved the stability and convergence of the PSO algorithm from a theoretical perspective. In 2002, Cello and Lechuga [25] formally published the results of the multi-objective particle swarm optimization algorithm. The particle swarm algorithm for solving multi-objective optimization problems is called the multi-objective particle swarm optimization (MOPSO) algorithm. With the PSO algorithm, the individual position or food of the flock is treated as the solution to the optimization problem, and the information interaction between the individuals in the flock and the optimal individual, and between the individuals, is used to guide the individuals in the whole flock to converge toward the optimal individual of the flock while retaining their own diversity information, and gradually find the optimal solution through continuous updating. Individuals in the flock are abstracted as “particles”, ignoring their mass and volume, and the topological structure determines that the particles are influenced by the combined information of their own and group states in each iteration, i.e., the update mechanism of particles is obtained by the organic combination of population history optimal particles and individual history optimal particles. The particle update mechanism is obtained through the organic combination of population history optimal particles and individual history optimal particles, as shown in Figure 6. The current velocity $v_j(t)$ of particle J , its own optimal position $pb_j(t)$, and the global optimal position $gb_j(t)$ determine the velocity $v_j(t+1)$ at the next moment, after which the particle moves from the original position $p_j(t)$ to the new position $p_j(t+1)$ with the updated velocity $v_j(t+1)$. As the number of iterations increases, the particle reaches the entire global optimal position by continuously updating the speed and position, thus completing the search for the optimal solution in space.

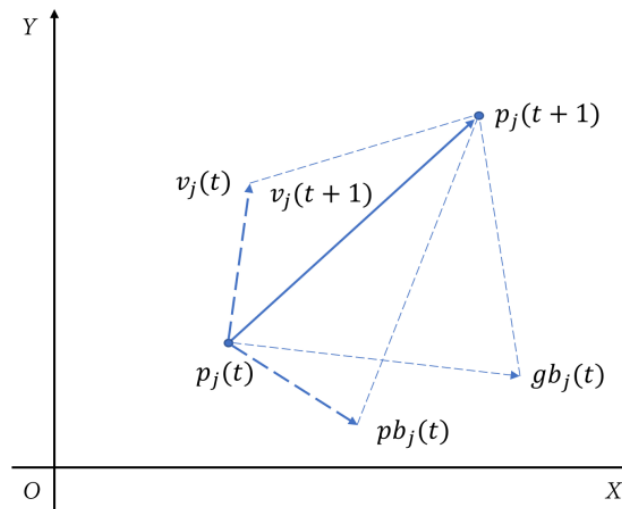


Figure 6. Schematic diagram of the general particle swarm algorithm.

The selection of the objective function mainly considers the emission performance of the combustion chamber, where a better emission performance is defined in the PSO algorithm as the emission of less NOx and soot. According to the analysis of previous tests, different indentation ratios, tab depths, and combustion chamber depth dimensions will affect the emissions of NOx and soot. Therefore, the objective function is shown in Equation (11):

$$\min f(a, b, c) = \delta_1 NOx + \delta_2 Soot \tag{11}$$

where a , b , and c denote the indentation rate, tab depth, and combustion chamber depth, respectively, NOx and soot are NOx emissions and soot emissions, respectively, and δ_1 and δ_2 are their corresponding constant coefficients. Each particle in the PSO algorithm has two attributes, velocity and position, and the velocity and position are iterated several times in the optimization process, whose iterative formula is shown in Equation (12):

$$\begin{aligned} v_i^{j+1} &= wv_i + c_1r_1(pbest_i^j - p_i^j) + c_2r_2(gbest_i^j - g_i^j) \\ p_i^{j+1} &= p_i^j + v_i^{j+1} \end{aligned} \tag{12}$$

where w is the inertia factor, whose value is non-negative and represents the degree of influence of the last velocity of the particle on the current particle. According to experience, w is generally taken as 0.9. c_1 and c_2 are learning factors, usually taken as $c_1 = c_2 = 2$; r_1 and r_2 are random values whose values range from 0 to 1. In the general PSO algorithm, the inertia factor is a constant because the inertia factor plays different roles in different stages of optimization, which is to say, at the beginning of optimization, a larger inertia factor can enhance the global search ability, but at the end of optimization, a smaller inertia factor can enhance the local search ability. In general, PSO algorithms are influenced by the “optimal” particles, and sometimes the population will converge too fast and lead to “premature maturity”, and the particles will fall into the local optimum. Therefore, a larger value of the inertia factor at the beginning of optimization and a smaller value at the end of optimization can significantly improve the solving ability of PSO, and it has been found that the rate of change of the inertia factor will also greatly affect the global optimal finding ability of PSO. Based on the improved PSO algorithm proposed by Feng et al. [26], the inertia factor is continuously adjusted during the optimization process with the help of the skip line function so that the inertia factor takes a larger value and changes slowly at the beginning of the iteration, and takes a smaller value and changes quickly at the end of the iteration, which facilitates the gradual switch from local to global optimization in respect

of PSO. The skip line function is shown in Equation (13). The second-order derivative of Equation (13) is solved to obtain Equation (14).

$$y = \frac{8a^3}{x^2 + 4a^2} \tag{13}$$

$$y'' = \frac{-16a^3(4a^2 - 3x^2)}{(4a^2 + x^2)^3} \tag{14}$$

From Equation (14), it can be derived that the coordinates of the inflection point of the skip line function are $(\pm \frac{2\sqrt{3}}{3}a, \frac{3}{2}a)$. The function has the following characteristics: Its function value at the point $(0, 2a)$ is larger, and the rate of change of the curve is a minimum, while at the inflection point, the function value is smaller, and the rate of change of the curve is a maximum. Based on these characteristics, the adjustment strategy of the inertia factor is designed as follows:

$$\begin{aligned} w(i) &= w_{min} + (w_{max} - w_{min}) \left\{ \frac{2}{a} \left[\frac{8a^3}{(\frac{\eta_i}{\eta_{max}} \frac{2\sqrt{3}}{3}a) + 4a^2} \right] - 3 \right\} \\ &= w_{min} + (w_{max} - w_{min}) \left(\frac{12}{h(i)^2 + 3} - 3 \right) \end{aligned} \tag{15}$$

where w_{min} and w_{max} are the maximum and minimum values of the inertia factor, η_i and η_{max} denote the current iteration number and the maximum iteration number. Finally, after calculating 200 sets of data iteratively, the parameters of the combustion chamber optimization model were obtained as in Table 3.

Table 3. Comparison of combustion chamber parameters before and after optimization.

Combustion Parameters	Original Value	ANN + PSO Optimization Value
Indentation rate	0.924	0.82
Tab depth	7.9	8.1
Combustion chamber depth	17.8	18.56

3. Discussion and Results

In this study, the results of the standard PSO algorithm optimization and the improved PSO algorithm optimization were compared, as shown in Figure 7. The improved PSO algorithm has two main improvements compared with the general PSO algorithm. On the one hand, it can enable the particles to jump out of the local optimum to reach the global optimum during the optimization search process, and on the other hand, it further reduces the objective function value under the premise of satisfying the constraints. Thus, the optimal combination of indentation rate, tab depth, and combustion chamber depth is obtained.

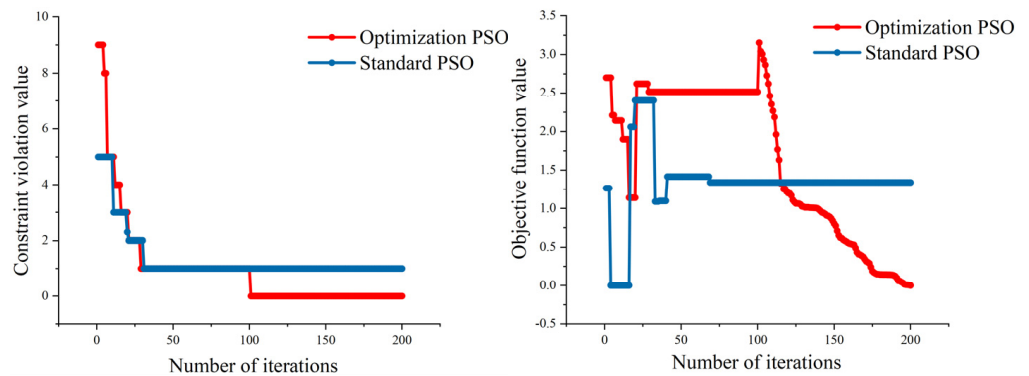


Figure 7. Comparison charts showing combustion chamber parameter optimization iterations.

The combustion emission process was re-run by redesigning the combustion chamber imported into CONVERGE CFD software. The emissions of the engine are shown in Table 4 and Figure 8, with reductions of approximately $1.21 \text{ g}\cdot(\text{kW}\cdot\text{h})^{-1}$ for NO_x and $0.06 \text{ g}\cdot(\text{kW}\cdot\text{h})^{-1}$ for soot. The indentation rate was reduced from 0.924 to 0.82, indicating that the NO_x emission level increased, and the soot emission level decreased as the diameter of the shrinkage became larger. This is due to the increase in the oil–gas mixture and the combustion level in the cylinder after the indentation diameter became larger, and the increase in temperature during the whole combustion process promoting the NO_x generation efficiency and suppressing the soot generation. The tab depth increased from 7.9 to 8.1 mm, which affected the in-cylinder temperature and which, in turn, affected the in-cylinder NO_x and soot generation rates. The combustion chamber depth increased from 17.8 to 18.56 mm, and the NO_x emission level decreased with the increase in the combustion chamber depth, while the soot exhibited an opposite pattern of changes. The trend in the parameters optimized by the improved PSO algorithm is consistent with the results of the conventional experimental verification. The ANN + PSO method shortens the experimental period and saves experimental costs compared with the conventional method.

Table 4. Comparison of combustion chamber emissions before and after optimization.

Emission/ $\text{g}\cdot(\text{kW}\cdot\text{h})^{-1}$	NO_x	Soot
Non-road National III Emission Limits	4.00	0.20
Non-road National IV Emission Limits	2.00	0.025
Original Engine Emission Value	3.45	0.20
Optimized Engine Emission Value	2.24	0.14

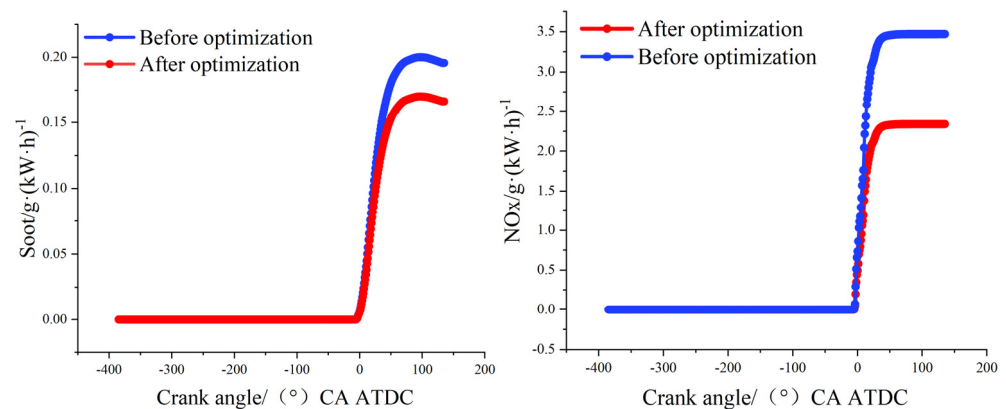


Figure 8. Comparison of combustion chamber emission generation.

Furthermore, by comparing with the existing studies in the literature, we found that ANN + PSO is feasible [27]. It can be found that most of the studies take the engine body as the object of study and use different parameters as inputs, such as different ratios of biodiesel mixed with diesel, different injection pressure and engine load, etc. Then the performance and emission of the engine are taken as the output, and an ANN model or other models such as support vector machine (SVM), K-nearest neighbors (k-NN) are established, and predictions are made based on the established models [28]. Some studies use standard PSO algorithms and other algorithms combined together to find the optimal input parameter ratios and obtain the optimized performance and emission data [27]. Some studies compared the prediction results after using different models cross-sectionally, such as comparing ANN, SVM, k-NN, etc. [29]. In this study, the same cross-sectional comparison method was used to build ANN model, SVR model and k-NN model using the same data collected, and the R^2 and MRE of ANN model, SVR model and k-NN model were compared as shown in Table 5. It was found that the accuracy of all three models met the requirements, but the accuracy of ANN model was higher compared with other

models. In this study, to address the current situation that the emission level of domestic agricultural machinery engines is still at a low level, an engine combustion chamber system is used as the research object to investigate the effect of changing the size of combustion chamber parameters on the engine emission by changing the size of the internal parameters of the combustion chamber system, and an improved particle swarm algorithm based on the standard PSO algorithm is used to optimize the established combustion chamber proxy model. An improved particle swarm algorithm based on the standard PSO algorithm is used to optimize the established combustion chamber proxy model and find the optimal size of the engine combustion chamber with the lowest emission as the optimization objective. In addition, by comparing the existing studies, the fitting accuracy of the ANN model used and established in this study meets the basic conditions of the proxy model, and the relevant accuracy parameters R^2 and MRE meet the requirements, which ensures the accuracy of the model, and the ANN model, as a proxy model in the intermediate process, only needs the accuracy of the established model to meet the requirements. Compared with other literature, the improved particle swarm algorithm used in this study can solve the problem that the particles are easy to fall into the local optimum in the process of finding the optimum and can find the optimum value in the global search, which can further reduce the cost of the objective function value while satisfying the constraints, so as to obtain the best combination of parameters of indentation rate, tab depth, and combustion chamber depth with the lowest emission as the optimization goal.

Table 5. Comparison of fitting accuracy of different models.

Model Name	Emission	R^2	MRE
ANN	NOx	0.937	10.13%
	Soot	0.955	8.18%
SVM	NOx	0.902	15.67%
	Soot	0.911	20.45%
k-NN	NOx	0.915	16.21%
	Soot	0.902	25.21%

Table 6 lists some of the literature reviews using the ANN + PSO approach for the relevant emission optimization.

Table 6. Comparison of prediction capability of different techniques and the developed PSO-ANN.

Reference	NOx	Soot
Roy et al. [30] ANFIS	0.08054	N/A
Roy et al. [30] ANN	0.1224	N/A
Norhayati et al. [31]	N/A	N/A
Sakthivel et al. [32]	9.9636	3.1611
Rai et al. [33]	N/A	0.3057
Kokkulunk et al. [34]	7.5102	2.1451
Ozener et al. [35]	0.0852	N/A
Isin et al. [36]	N/A	N/A
Nishant et al. [37] ANFIS	0.7708	N/A
Nishant et al. [37] GA-ANFIS	0.6354	N/A
Nishant et al. [37] PSO-ANFIS	0.4893	N/A

4. Conclusions

In this study, a diesel engine combustion chamber model was established based on a YTO Group agricultural diesel engine for simulation modeling and calculation, followed by an experimental verification analysis of the simulation model. The results show the following:

- (1) The in-cylinder pressure and heat release obtained from the combustion chamber model simulations were within 6% error of the test data. The overall trend of change was basically consistent. The simulation model can simulate the working conditions of the test engine relatively well.
- (2) An artificial neural network was established as an agent model with the indentation rate, tab depth, and combustion chamber depth as inputs and NO_x and soot emitted from the engine as outputs. The R² values were 0.95 and 0.93. The MRE values were 10.13% and 8.18%, respectively, which indicates that the obtained ANN model has good adaptability and accuracy.
- (3) On the basis of the general particle swarm (PSO) algorithm, an improved PSO algorithm was proposed in which the inertia factor is continuously adjusted with the help of the skip tongue function in the optimization process so that the inertia factor adapts to different rates in different periods and adjusts the size of the corresponding value. On the one hand, it is beneficial for PSO to gradually switch from local to global optimization. On the other hand, this can further reduce the value of the objective function needed to reach the optimum under the condition of satisfying the constraints. The improved PSO algorithm was used to optimize the agent model and obtain the optimal combination of input parameters (i.e., an optimized combustion chamber structure with indentation rate, tab depth, and combustion chamber depth of 0.82, 8.1, and 18.56 mm, respectively). The model was then imported into CONVERGE CFD software for combustion emission calculation to obtain the emission generation compared with the original combustion chamber. It was found that the optimized combustion chamber reduced NO_x by about 1.21 g·(kW·h)⁻¹ and soot by about 0.06 g·(kW·h)⁻¹, which values are close to the National IV emission standards.

For future applications of tractor emission reduction in agriculture, we will focus on the optimization of tractors with different horsepower in different field operating environments and working conditions. We will also increase the complexity of the artificial neural networks used in order to perform larger-scale model building and optimization.

Author Contributions: Conceptualization, B.Z.; methodology, B.Z.; software, B.Z.; validation, B.Z., Z.D.; formal analysis, Z.L.; investigation, X.S., Z.L., Y.L.; writing—original draft preparation, B.Z.; writing—review and editing, Z.S., Q.Z., E.M.; funding acquisition, Z.S.. All authors have read and agreed to the published version of the manuscript.

Funding: This research was funded by the National Key Research and Development Plan of China (2017YFD0700301).

Institutional Review Board Statement: Not applicable.

Informed Consent Statement: Not applicable.

Data Availability Statement: Not applicable.

Conflicts of Interest: The authors declare no conflict of interest.

References

1. National Bureau of Statistics. *China Statistical Yearbook*; China Statistics Press: Beijing, China, 2021.
2. Bai, H.; Meng, L.; He, C. Study on technical routes to achieve standards of emission stage III for non-road diesel engine. *J. Chin. Agric. Mech.* **2015**, *36*, 193–196.
3. Xie, B.; Wu, Z.; Mao, E. Development and Prospect of Key Technologies on Agricultural Tractor. *Trans. Chin. Soc. Agric. Mach.* **2018**, *49*, 1–17.
4. Guo, J. *Bowl Geometry Optimization of a Heavy-Duty Diesel Engine in High Density-Low Temperature Combustion*; Tianjin University: Tianjin, China, 2020. [[CrossRef](#)]
5. Tan, P.; Wang, D.; Lou, D.; Hu, Z. Progress of control technologies on exhaust emissions for agricultural machinery. *Trans. Chin. Soc. Agric. Mach.* **2018**, *34*, 1–14.
6. Geng, Y. Tail Gas Pollution from the Vehicles and Its Control Technology. *Environ. Sci. Surv.* **2010**, *29*, 62–69. [[CrossRef](#)]
7. Wang, G.; Yu, W.; Li, X.; Su, Y.; Yang, R.; Wu, W. Experimental and numerical study on the influence of intake swirl on fuel spray and in-cylinder combustion characteristics on large bore diesel engine. *Fuel* **2019**, *237*, 209–221. [[CrossRef](#)]

8. Pei, Y.; Su, W.; Lin, T. The BUMP Combustion Chamber Presented Based on the Concept of Lean Diffusion Combustion in a D.I. Diesel Engine with Common Rail Fuel Injector. *Trans. CSICE* **2002**, *20*, 381–386. [[CrossRef](#)]
9. Su, W.; Lin, T.; Pei, Y. A Compound Technology for HCCI Combustion in a DI Diesel Engine Based on the Multi-Pulse Injection and the BUMP Combustion Chamber. In Proceedings of the SAE 2003 World Congress & Exhibition, Detroit, Michigan, 3–6 March 2003.
10. Zhao, C.; Su, W.; Wang y Yu, J.; Lin, T. A Study on the Mechanism of New Conceptual Mixture Formation of Lean Diffusion Combustion in the Bump Combustion Chamber of a Diesel Engine. *J. Combust. Sci. Technol.* **2004**, 327–335.
11. Rakopoulos, C.D.; Kosmadakis, G.M.; Pariotis, E.G. Investigation of piston bowl geometry and speed effects in a motored HSDI diesel engine using a CFD against a quasi-dimensional model. *Energy Convers. Manag.* **2010**, *51*, 470–484. [[CrossRef](#)]
12. Li, J.; Yang, W.M.; An, H.; Maghbouli, A.; Chou, S.K. Effects of piston bowl geometry on combustion and emission characteristics of biodiesel fueled diesel engines. *Fuel* **2014**, *120*, 66–73. [[CrossRef](#)]
13. Gafoor, C.A.; Gupta, R. Numerical investigation of piston bowl geometry and swirl ratio on emission from diesel engines. *Energy Convers. Manag.* **2015**, *101*, 541–551. [[CrossRef](#)]
14. Jafarmadar, S.; Taghavifar, H.; Taghavifar, H.; Navid, A. Numerical assessment of flow dynamics for various DI diesel engine designs considering swirl number and uniformity index. *Energy Convers. Manag.* **2016**, *110*, 347–355. [[CrossRef](#)]
15. Khan, S.; Panua, R.; Bose, P.K. Combined effects of piston bowl geometry and spray pattern on mixing, combustion and emissions of a diesel engine: A numerical approach. *Fuel* **2018**, *225*, 203–217. [[CrossRef](#)]
16. Lei, J.; Yu, Y.; Xin, Q.; Shen, L.; Song, G.; Chen, L. Investigation and application of systematic design method for combustion chamber of diesel engine. *Trans. Chin. Soc. Agric. Mach.* **2020**, *36*, 36–46.
17. Zhu, J.; Huang, C.; Yao, M.F. Numerical Simulation on the Effect of Combustion Chamber Geometry on Diesel Engine Combustion Process. *Chin. Intern. Combust. Engine Eng.* **2007**, *28*, 14–18.
18. Li, S.; Ge, M.; Shen, L.; Luo, F. Influence of Combustion Chamber Structure on Diesel Engine Emission Based on Simulation and Experiment. *Veh. Engine* **2013**, 22–26. (In Chinese)
19. Zhao, C.; Sun, Y.; Wang, Y.; Zhang, Z.; Zhu, Y. Numerical Simulations of Piston Bowl Geometry on Marine Diesel Engines. *China Mech. Eng.* **2017**, *28*, 2176–2182.
20. Wang, Z.; Chen, S.; Fan, W. Effect of neural network width on combustor emission prediction. *Acta Aeronaut. Astronaut. Sin.* 1–12. Available online: <http://kns.cnki.net/kcms/detail/11.1929.V.20220119.1003.016.html> (accessed on 12 July 2022).
21. Javed, S.; Murthy, Y.S.; Baig, R.U.; Rao, D.P. Development of ANN model for prediction of performance and emission characteristics of hydrogen dual fueled diesel engine with Jatropa Methyl Ester biodiesel blends. *J. Nat. Gas Sci. Eng.* **2015**, *26*, 549–557. [[CrossRef](#)]
22. Bhowmik, S.; Paul, A.; Panua, R.; Ghosh, S.K.; Debroy, D. Performance-Exhaust Emission Prediction of Diesosenol Fueled Diesel Engine: An ANN Coupled MORSM Based Optimization. *Energy* **2018**, *153*, 212–222. [[CrossRef](#)]
23. Aydogan, H. Prediction of diesel engine performance, emissions and cylinder pressure obtained using Bioethanol-biodiesel-diesel fuel blends through an artificial neural network. *J. Energy S. Afr.* **2015**, *26*, 74–83. [[CrossRef](#)]
24. Van, D. Analysis of the Particle Swarm Optimization Algorithm. Ph.D. Dissertation, University of Pretoria, Pretoria, South Africa, 2002.
25. Coello, C.; Lechuga, M.S. MOPSO: A proposal for multiple objective particle swarm optimization. In Proceedings of the 2002 Congress on Evolutionary Computation (CEC'02), Honolulu, HI, USA, 12–17 May 2002.
26. Feng, J.; Wang, Y.; Wang, Q.; Biao, X. Fast reflector self-anti-disturbance control based on improved particle swarm algorithm. *Syst. Eng. Electron.* **2021**, 3675–3682.
27. Dhahad, H.A.; Hasan, A.M.; Chaichan, M.T.; Kazem, H.A. Prognostic of diesel engine emissions and performance based on an intelligent technique for nanoparticle additives. *Energy* **2022**, *238*, 121855. [[CrossRef](#)]
28. Ağbulut, Ü.; Ayyıldız, M.; Sarıdemir, S. Prediction of performance, combustion and emission characteristics for a CI engine at varying injection pressures. *Energy* **2020**, *197*, 117257. [[CrossRef](#)]
29. Ağbulut, Ü.; Gürel, A.E.; Sarıdemir, S. Experimental investigation and prediction of performance and emission responses of a CI engine fuelled with different metal-oxide based nanoparticles–diesel blends using different machine learning algorithms. *Energy* **2021**, *215*, 119076. [[CrossRef](#)]
30. Roy, S.; Das, A.K.; Bhadouria, V.S.; Mallik, S.R.; Banerjee, R.; Bose, P.K. Adaptive-neuro fuzzy inference system (ANFIS) based prediction of performance and emission parameters of a CRDI assisted diesel engine under CNG dual-fuel operation. *J. Nat. Gas Sci. Eng.* **2015**, *27*, 274–283. [[CrossRef](#)]
31. Norhayati, I.; Rashid, M. Adaptive neuro-fuzzy prediction of carbon monoxide emission from a clinical waste incineration plant. *Neural Comput. Appl.* **2018**, *30*, 3049–3061. [[CrossRef](#)]
32. Sakthivel, G.; Snehikumar, B.; Ilangkumaran, M. Application of fuzzy logic in internal combustion engines to predict the engine performance. *Int. J. Ambient. Energy* **2016**, *37*, 273–283. [[CrossRef](#)]
33. Rai, A.; Kumar, N.S.; Rao, B.R.S. Fuzzy logic based prediction of performance and emission parameters of a LPG-diesel dual fuel engine. *Procedia Eng.* **2012**, *38*, 280–292. [[CrossRef](#)]
34. Kökkülünk, G.; Akdoğan, E.; Ayhan, V. Prediction of emissions and exhaust temperature for direct injection diesel engine with emulsified fuel using ANN. *Turk. J. Electr. Eng. Comput. Sci.* **2013**, *21*, 2141–2152. [[CrossRef](#)]

35. Özener, O.; Yüksek, L.; Özkan, M. Artificial neural network approach to predicting engine-out emissions and performance parameters of a turbo charged diesel engine. *Therm. Sci.* **2013**, *17*, 153–166. [[CrossRef](#)]
36. Isin, O.; Uzunsoy, E. Predicting the exhaust emissions of a spark ignition engine using adaptive neuro-fuzzy inference system. *Arab. J. Sci. Eng.* **2013**, *38*, 3485–3493. [[CrossRef](#)]
37. Singh, N.K.; Singh, Y.; Sharma, A.; Kumar, S. Diesel engine performance and emission analysis running on jojoba biodiesel using intelligent hybrid prediction techniques. *Fuel* **2020**, *279*, 118571. [[CrossRef](#)]

Article

A Fault Diagnosis Method for a Differential Inverse Gearbox of a Crawler Combine Harvester Based on Order Analysis

Yaoming Li *, Yanbin Liu, Kuizhou Ji and Ruiheng Zhu

Key Laboratory of Modern Agricultural Equipment and Technology, Ministry of Education, Jiangsu University, Zhenjiang 212013, China

* Correspondence: ymli@ujs.edu.cn

Abstract: The single HST (Hydro Static Transmission) mechanical differential transmission gearbox of crawler combine harvester is subjected to the impact of alternating loads in the field operation, resulting in its fatigue failure. The traditional durability fatigue test can improve the fault-free working time of machinery, but it is not suitable for agricultural machinery with time-varying load frequency bandwidth and stress amplitude. Therefore, in this paper, a fault diagnosis method based on order analysis was proposed considering the comprehensive influence of load amplitude and frequency on the fatigue life of gearbox. The location and the corresponding type of fault were found by comparing the spectral line peak changed before and after. Then, the test verification was carried out on the gearbox assembly fatigue test bench according to the compiled load spectrum. The results show that the analysis results of the fault diagnosis method based on order analysis were consistent with the unpacking inspection, which had reference significance for the research on the fault diagnosis method of the crawler combined harvester gearbox.

Keywords: combine harvester; differential inverse gearbox; order analysis; fault diagnosis method; fatigue test

Citation: Li, Y.; Liu, Y.; Ji, K.; Zhu, R. A Fault Diagnosis Method for a Differential Inverse Gearbox of a Crawler Combine Harvester Based on Order Analysis. *Agriculture* **2022**, *12*, 1300. <https://doi.org/10.3390/agriculture12091300>

Academic Editors: Muhammad Sultan, Redmond R. Shamshiri, Md Shamim Ahamed and Muhammad Farooq

Received: 27 July 2022

Accepted: 22 August 2022

Published: 25 August 2022

Publisher's Note: MDPI stays neutral with regard to jurisdictional claims in published maps and institutional affiliations.



Copyright: © 2022 by the authors. Licensee MDPI, Basel, Switzerland. This article is an open access article distributed under the terms and conditions of the Creative Commons Attribution (CC BY) license (<https://creativecommons.org/licenses/by/4.0/>).

1. Introduction

The single HST (hydro static transmission) mechanical differential inverse gearbox is one of the important parts of the transmission system of a crawler combine harvester; it can realize radius steering, unilateral braking steering and differential steering. Due to the harsh working environment of combine harvester, the gearbox bears complex alternating loads for a long time in the working process [1]. Therefore, the gearbox is prone to fatigue failure, which seriously affects the fault-free working time of the machinery [2–4]. To improve the service life of the gearbox, the tester generally judge faults in the gearbox through traditional durability fatigue tests based on its abnormal running conditions [5]. However, this method cannot determine the initial location and type of early faults when various faults occur in the gearbox. Therefore, gearbox fault diagnosis is a very important topic in the field of machinery diagnostics.

The fault vibration signal in the early stage of gearbox is weak and difficult to be detected under the interference of noise or other signals. However, when the external driving speed and load change, the early fault information hidden during the stable working condition may be highlighted [6]. In this case, the frequency components of vibration signals under non-stationary conditions are complex, and the characteristic parameters of fault signals are time-varying. The natural frequency and damping ratio of the impact response components representing local faults will fluctuate under the influence of variable loads, and the impact response interval is no longer periodic. Traditional spectrum analysis technology is prone to 'frequency ambiguity' phenomenon, resulting in missed diagnosis and misjudgment [7].

Therefore, many fault diagnosis methods for non-stationary vibration signals have been proposed, for instance, time-frequency analysis and order analysis [8]. Order analysis

is one of the effective methods for the non-stationary signal analysis of rotating machinery, and its main idea is to map time-varying frequency components into constant frequency components [9]. In recent years, the fault diagnosis technology of gearboxes based on order analysis has been receiving increasing attention. Wan et al. [10] proposed a time-domain synchronous averaging method based on order analysis for the offline detection of an automobile gearbox. By intercepting several signal segments equal to the specified periodic signal and averaging them, the periodic signal can be separated from the random signal, which was helpful for the rapid fault diagnosis of the downline. Feng et al. [9] studied the fault diagnosis of a planetary gearbox under non-stationary conditions based on the combined envelope and frequency order spectrum analysis of iterative generalized demodulation. Through the comparative analysis of planetary gearbox simulation and engineering tests, the authors verified that the proposed method could effectively extract distributed and local gear faults under non-stationary conditions. He et al. [11] proposed a novel order tracking method to analyze the fault diagnosis of wind turbine gearbox based on discrete spectrum correction technique. The effectiveness and robustness of the proposed method were verified through simulations and actual tests. However, the order analysis method has not been reported in the field of fault diagnosis of single HST (hydro static transmission) mechanical differential inverse gearbox for crawler combine harvester.

Therefore, in this paper, a gearbox fault diagnosis method for crawler combine harvester based on order analysis was proposed. The detailed objectives were: (1) to simulate the main working conditions of differential inverse gearbox in the room, its fatigue test bench was built; (2) to establish the order calculation model of differential reverse gearbox to obtain the main meshing order of gears and the first harmonic of key bearing order in common working gear; (3) to carry out the experimental verification on the gearbox assembly fatigue test bench according to the compiled load spectrum.

2. Materials and Methods

2.1. Structure and Working Principle of Differential Inverse Gearbox

The structure of the mechanical differential inverse gearbox is shown in Figure 1 [12,13]. When the harvester moved forward, the engine transmitted its driving force to the HST via belts and pulleys. Then, when the tooth was embedded in the structure on the left and right sides, the power was transmitted to the output half shaft on both sides through the first stage gear transmission (1, 2), the second stage gear transmission (3, 4, 5, 6), the third stage gear transmission (7, 9), the fourth stage gear transmission (10, 12) and the fifth stage gear transmission (12, 13). This caused the drive wheels on both sides of the chassis to output equivalent rotational speed in the same direction. When the harvester turned left, the left tooth embedded structure was separated, and the power output on the right was normal. The walking chassis realized unilateral braking steering by locking the unilateral brake gear to the clutch driven gear (10), and the steering radius was about half of the track center distance. When the central gear ring of the clutch driving gear (8) was locked by the differential steering brake gear (11), the power on the right side was transferred to the left side through the planetary gear meshing transmission to reverse the differential steering.

2.2. Fault Diagnosis Method Based on Order Analysis

2.2.1. Principle

Mechanical vibration is a powerful signal for directly reflecting the operation status of the equipment. The vibration of the gearbox during normal operation mainly comes from the meshing transmission of the gear. According to the difference of medium, it can be divided into air acoustic vibration and structural acoustic vibration. The structural acoustic vibration will be transmitted to the box along the shaft, bearing and other parts, which will be collected by the sensor. It can be seen in Figure 2, the signal acquisition system included pulse collector, vibration sensor (including signal amplifier and extension cable), signal acquisition and processing unit, and PC. In addition, PC had built-in special signal analysis and processing software. The vibration sensor was installed at the lifting

of the loading and unloading hook in the right box of the gearbox, and its center line was perpendicular to the axis of the transmission shaft of the gearbox. If the direction of the transmission axis was Z, the actual vibration measurement was X and Y axis directions.

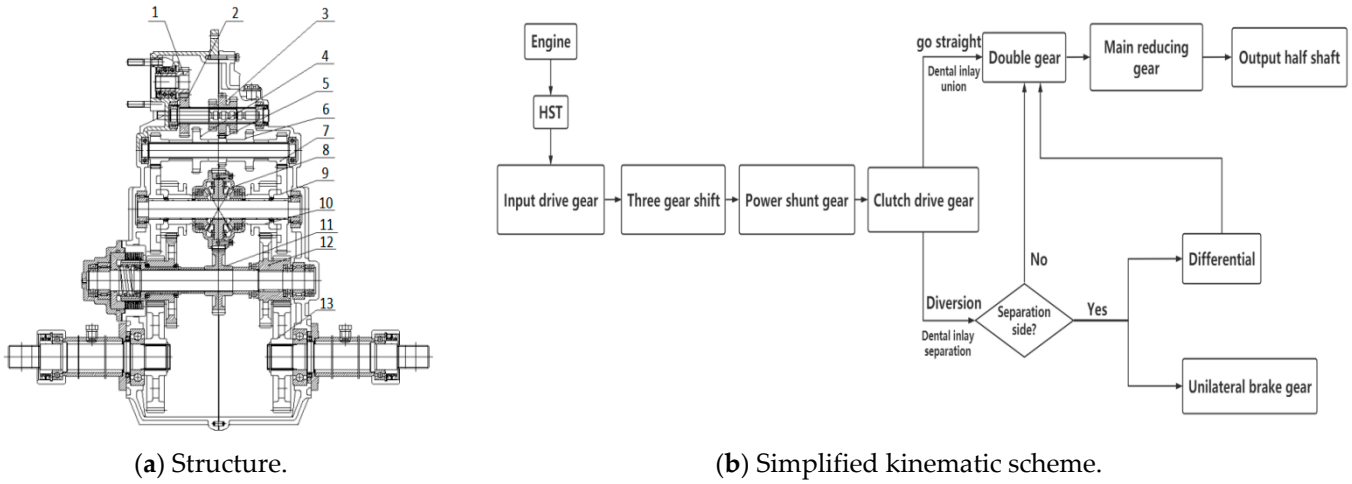


Figure 1. Diagram of differential inverse gearbox: 1—Input driving gear; 2—Input driven gear; 3—Shift transmission gear (first gear, third gear, second gear from left to right); 4—First driven gear; 5—Third driven gear; 6—Second driven gear; 7—Power shunt gear; 8—Clutch driving gear; 9—Clutch driven gear; 10—Clutch driven gear; 11—Differential steering brake gear; 12—Double gear; 13—Main reducing gear.



Figure 2. Signal acquisition system.

The fault diagnosis method based on order analysis first converts a non-stationary vibration signal in the time domain into a stationary vibration signal in the angle domain. Then, the order spectrum, which clearly reflects each characteristic order, is obtained by fast Fourier transform (FFT). By comparing the peak changes in the spectral lines before and after looking up the order calculation table, the fault location and the corresponding fault type can be found. In this paper, the computational order analysis method (COT) based on spline interpolation was used to realize the equal angle sampling of vibration signals. The specific troubleshooting process is shown in Figure 3.

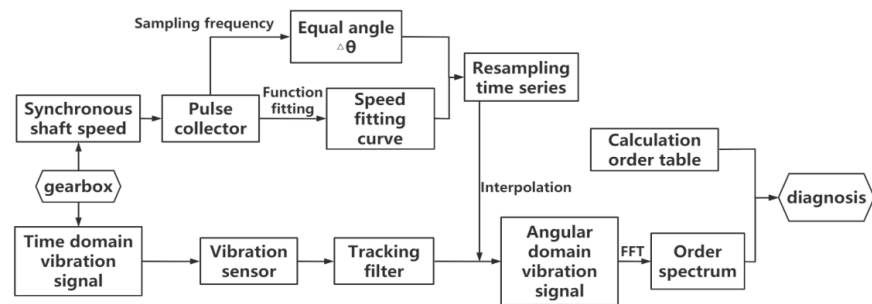


Figure 3. Fault diagnosis flow chart.

2.2.2. Order Calculation of Differential Inverse Gearbox

The relationship between frequency and order in rotating machinery structure is shown in Equation (1):

$$O = \frac{f}{f_1} \tag{1}$$

where O is the order, f is the frequency, and f_1 is the synchronous frequency.

In addition to rotating shafts, gears, and other structural components, there were a wide variety of bearings that support rotation in the gearbox. The rolling bearing was mainly composed of outer ring, inner ring, rolling body, and cage. The corresponding calculation methods are shown in Equations (2)–(5), respectively:

$$O_{oo} = |(C_o - O_o) \times n_b| \tag{2}$$

$$O_{oi} = |(C_o - O_i) \times n_b| \tag{3}$$

$$O_b = \left(\frac{d_{pc}}{d_b}\right) \times \left(1 - \left(\frac{d_b}{d_{pc} \times \beta}\right)^2\right) \times (|O_i - O_o|) \tag{4}$$

$$C_o = \frac{O_i}{2} \times \left(\frac{1 - (\cos b \times R_b)}{R_i + R_b}\right) + \frac{O_o}{2} \times \left(\frac{1 - (\cos b \times R_b)}{R_i + R_b}\right) \tag{5}$$

where O_{oo} is the outer ring order; O_{oi} is the inner ring order; O_b is the rolling body order; C_o is the cage order; O_i is the inner ring rotation order; O_o is the outer ring rotation order; b is the radian pressure angle; R_b is the rolling body radius; R_i is the inner ring radius; n_b is the number of rolling bodies; d_{pc} is the bearing pitch diameter; d_b is the roller diameter; β is the contact angle, $\beta = \cos \alpha \times 3.14/\pi$; α is the pressure angle.

Because the torque speed sensor was installed on the output shaft at both ends of the differential steering gearbox, the output speed was taken as the synchronization object in the order calculation. The input data of differential inverse gearbox, the order calculation model of differential inverse gearbox and its main order are shown in Tables 1 and 2 and Figure 4, respectively. The first harmonic of key bearing order under medium speed gear is shown in Table 3.

Table 1. Input data of differential inverse gearbox.

Gear	Speed (R/min)	Torque (N.m)	Transmission Ratio	Power (kW)
First	2787	167	30.966	48.74
Second	2798	195	21.5	57.14
Third	2865	242	14.955	72.62

Table 2. Main order of differential steering gearbox in each gear.

Item	First Harmonic	Second Harmonic	Third Harmonic
First gear meshing	282.733	565.467	848.2
First gear input shaft	18.859	37.698	56.547
First gear output shaft	11.781	23.561	35.342
Second gear meshing	235.611	471.222	706.833
Second gear input shaft	13.089	26.179	39.269
Second gear output shaft	11.781	23.561	35.342
Third gear meshing	200.269	400.539	600.808
Third gear input gear	9.103	18.206	27.309
Third gear Output gear	11.781	23.561	35.342

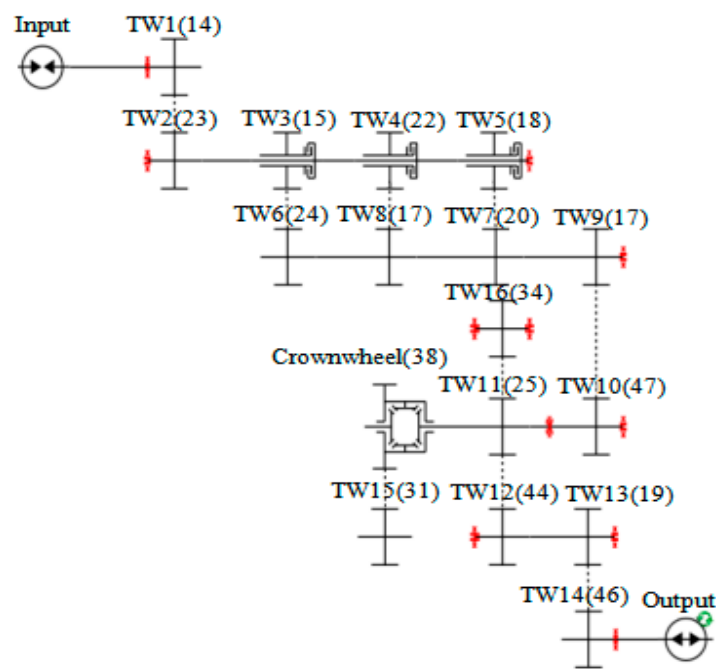


Figure 4. Order calculation model. The red dots are bearings.

Table 3. Main order of differential steering gearbox in each gear.

Model	Retainer	Inner Race	Outer Race	Rolling Element
6007RZ	9.3220	255.8257	195.7623	79.4098
NJ205E	5.3520	123.7995	85.6323	34.7195
6205E	4.8168	111.4199	77.0691	31.2476
NJ306E	1.6912	35.9776	23.6772	9.8933
51208	1.2105	18.1579	18.1579	6.5066
NJ2207E	1.0031	21.2697	15.0461	6.8562
6310	0.4118	8.8235	6.1765	2.7451

2.3. Durability Test

2.3.1. Gearbox Assembly Fatigue Test Bench

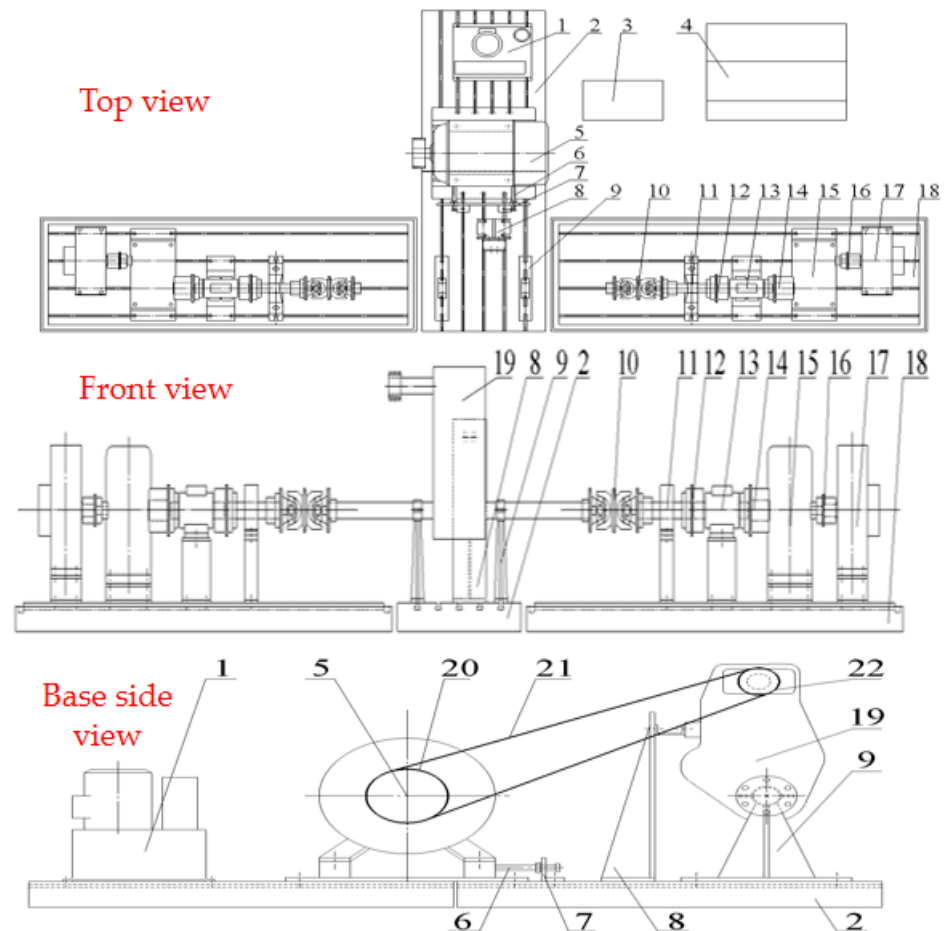
As shown in Figure 5, the durability fatigue test-bed for the gearbox assembly was composed of a main power cabinet, central control cabinet, driving device, loading device, small hydraulic station, torque speed sensor, sliding bearing seat, universal coupling, base and cushion, etc. When working, the main power supply cabinet started the drive motor, and the power was transferred to the input of the differential inverse gearbox through a five-slot B belt to drive the box to run. The tester could complete the test load spectrum loading, hydraulic steering control, and key test parameter monitoring on the central control cabinet.

The program control interface of the loading device is shown in Figure 6, which was compiled using the virtual instrument software Labview. The load was mainly composed of constant torque, alternating torque and noise. The alternating torque included sine wave, triangular wave, serration wave, square wave. At the same time, it had the functions of setting the test running time and real-time acquisition and displaying and storing test parameters such as torque and rotational speed.

2.3.2. Test Design

According to the actual field working conditions and gear frequency of the combine harvester, the fatigue test scheme was mainly divided into the following working conditions: small load forward (first gear, second gear, third gear), full load forward (first gear, second gear, third gear), unilateral brake left turn (first gear), unilateral brake right turn (first

gear), differential left turn (first gear, second gear), differential right turn (first gear, second gear). The second gear was the common working gear of the differential inverse gearbox. Therefore, the running time ratio of the first gear, the second gear and the third gear was 1:2:1. Consult the relevant data [14], the time proportions of the operating conditions for small load forward, full load forward and left turn are 0.08, 0.75 and 0.08, respectively. The experiment is conducted for 12 h a day, and the specific shift schedule is shown in Table 4.



(a)



(b)

Figure 5. Gearbox assembly test bench structural schematic diagram (a) and physical diagram (b). 1. hydraulic station, 2. longitudinal installation base, 3. main power cabinet, 4. central control cabinet, 5. drive motor, 6. positioning bolt, 7. positioning support, 8. gearbox installation support, 9. gearbox fixed support, 10. universal coupling, 11. sliding bearing, 12. double coupling A, 13. torque speed sensor, 14. coupling B, 15. reduction box, 16. coupling C, 17. magnetic powder brake 18. transverse mounting support, 19. gearbox under test, 20. large pulley 21. five-slot B belt, 22. small pulley.

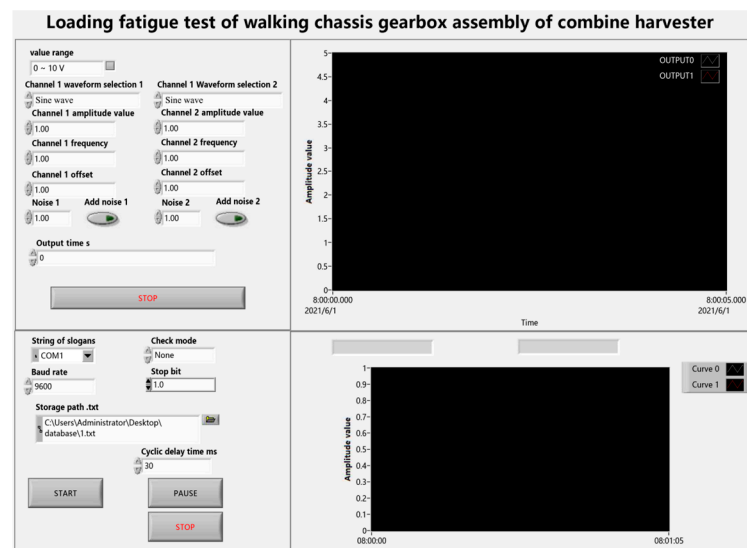


Figure 6. Program control interface.

Table 4. Schedule of shifts.

Shift	Gear	Time
First shift	First gear	8:00–9:00
	Second gear	9:00–11:00
	Third gear	11:00–12:00
Second shift	First gear	13:00–14:00
	Second gear	14:00–16:00
	Third gear	16:00–17:00
Third shift	First gear	18:00–19:00
	Second gear	19:00–21:00
	Third gear	21:00–22:00

The load spectrum data needed for the test were mainly from the research results [15–17]. According to the basic performance parameters of the combine harvester equipped with the differential steering gearbox, the whole machine weight was 3.64 t, the forward speed was 0–1.5 m/s, and the crop feed rate was 5 kg/s. The specific load values are shown in Tables 5 and 6.

Table 5. Proportion of working time under different working condition.

Gear	Left Half Shaft		Right Half Shaft	
	Small Load/kW	Full Load/kW	Small Load/kW	Full Load/kW
First gear	0.97	1.47	1.14	1.95
Second gear	2.35	6.62	2.76	8.34
Third gear	3.61	10.22	4.85	14.61

Table 6. Peak power of two steering modes in first gear and second gear.

Gear	Unilateral Brake Steering		Differential Steering	
	Left/kW	Right/kW	Left/kW	Right/kW
First gear	8.05	9.39	6.12	6.12
Second gear	9.68	11.27	10.98	10.98

To decrease the test cost, the relevant theory of accelerated fatigue test was used to strengthen the load data to get the load spectrum. The theoretical basis of accelerated fatigue test came from Miner’s linear cumulative damage theory. Under the action of cyclic load,

the fatigue damage of mechanical structure can be linearly accumulated, and the stresses were independent and irrelevant. Fatigue failure will occur when the cumulative damage reached a certain value. Common accelerated fatigue test methods included increasing test loading frequency, linear enhanced load spectrum method, nonlinear enhanced load spectrum method. The linear enhanced load spectrum method was to multiply the load amplitudes under different frequencies in the original load spectrum by an enhancement coefficient, while the frequency ratio corresponding to each load remains unchanged. The acceleration effect of the linear enhanced load spectrum on the fatigue test was remarkable. When the strengthening coefficient was small (close to 1), the enhanced load spectrum and the original load spectrum can well meet the similar load conditions of the Miner principle to ensure that the fatigue test results were consistent with the actual fatigue damage. Therefore, in this experiment, the load spectrum was enhanced by increasing the test loading frequency and linear strengthening load spectrum. The strengthened load data is shown in Table 7.

Table 7. Peak power of two steering modes in first gear and second gear: the forward working condition is uniformly used to carry a larger load of the right walking half shaft; the steering condition is unilateral braking steering in (), and the rest is differential steering; the time column takes the first shift time as an example, which is divided according to the running time of each gear.

Working Condition		Original Power/kW	Strengthening Power/kW	Strengthening Coefficient	Time/min
First gear	Small load	2.28	3.19	1.4	5
	Full load	3.9	4.68	1.2	50
	Left turn	6.12 (8.05)	8.57 (11.27)	1.4	5
	Right turn	6.12 (9.39)	8.57 (13.15)	1.4	5
Second gear	Small load	5.52	7.73	1.4	10
	Full load	16.68	20.02	1.2	100
	Left turn	10.98	15.37	1.4	10
	Right turn	10.98	15.37	1.4	10
Third gear	Small load	9.7	13.58	1.4	5
	Full load	29.22	35.06	1.2	50

According to the relevant data [18], the load change frequency of combine harvester under field conditions was generally within 2 Hz. Considering the limitation of response time of magnetic powder brake, the frequency range of alternating torque that can be set in the program control interface was 0–2 Hz, the fluctuation amplitude of alternating torque was 0–20% of constant torque, and the wave momentum range was 20 Nm. After completing the setting of the above parameters and running time, the automatic control of the loading device can be realized. The specific torque loading form is shown in Table 8.

Table 8. Torque loading form.

Working Condition	Constant Torque/Nm	Alternating Torque		Wave Momentum/Nm	
		Amplitude/Nm	Frequency/Hz		
First gear	Small load	140	30	2	20
	Full load	210	40	2	20
	Left turn	540 (990)	110 (200)	2	20
	Right turn	540 (1150)	110 (250)	2	20
Second gear	Small load	240	50	2	20
	Full load	610	120	2	20
	Left turn	470	90	2	20
	Right turn	470	90	2	20
Third gear	Small load	300	60	2	20
	Full load	780	150	2	20

3. Results and Discussion

The start time of the test is 26 June 2021, and the whole test process was monitored by the fault diagnosis system. After a total of about 50 h of running time, the trend index curve suddenly rose and exceeded the alarm limit, and the alarm signal was issued at 15:45 on 4 July. The gearbox was in the small load of third gear condition.

3.1. Overall overview of trend curve

To clearly analyze the fault type and evolution process in the differential steering gearbox during the fatigue test, the global overview diagram of the trend index of each working condition was observed through the signal analysis and processing software of the fault diagnosis system, as shown in Figures 7–9. The trend index is the set of vibration energy amplitudes corresponding to all order points, and each trend index point is obtained by superposition and summation of change spectral lines. The calculation equation is shown in Equation (6). The limit value of the trend index depends on the comprehensive fatigue performance of the gearbox, which was determined as 3000 g through a large number of tests.

$$TI = \sum_{i=1}^n |X_i - Y_i| \tag{6}$$

where TI is the trend index, g ; X_i is the actual energy amplitude corresponding to each sampling order, g ; and Y_i is the upper and lower tolerance band limit obtained in the learning phase, g .

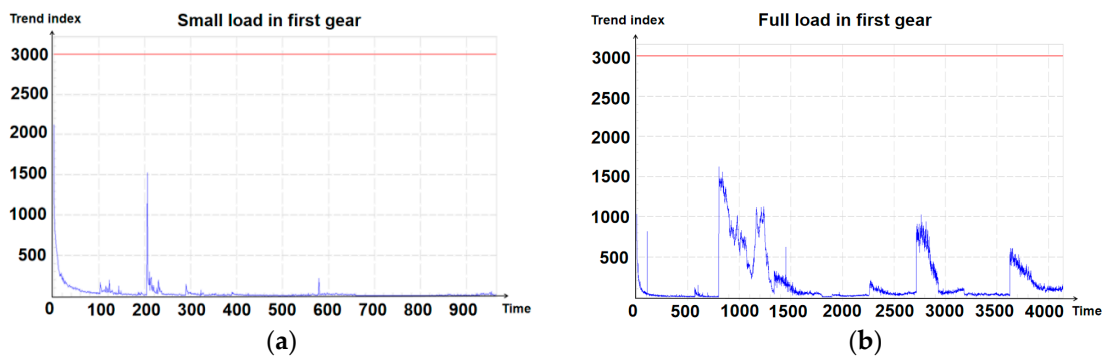


Figure 7. Small load (a) and full load (b) in first gear.

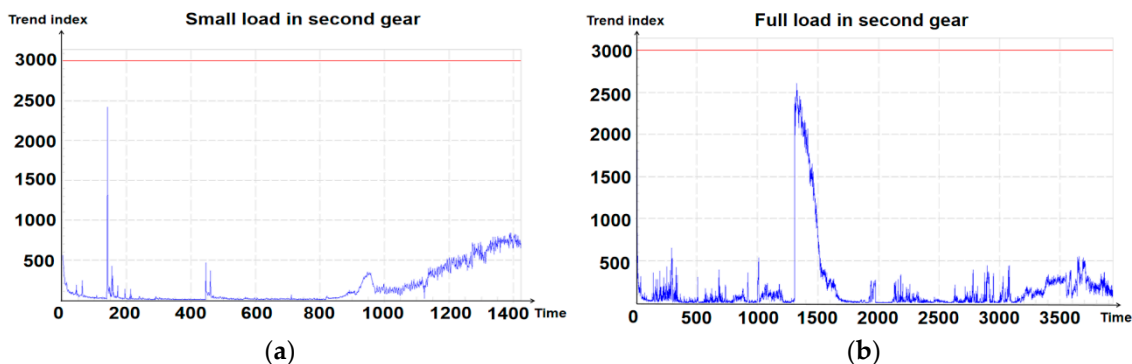


Figure 8. Small load (a) and full load (b) in second gear.

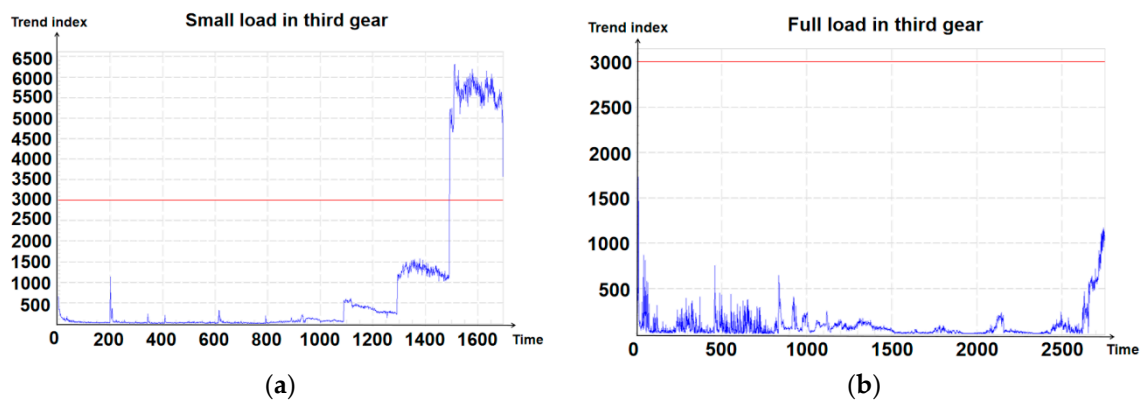


Figure 9. Small load (a) and full load (b) in third gear.

Seeing Figures 7–9, the trend index curve of the fault diagnosis system exceeded the alarm limit under small load of third gear conditions, and the curve increased suddenly in many places at the same time. The trend curve increased obviously in the second gear low load condition, the second gear full load condition and the third gear full load condition. The sudden rise and slow decline of the trend index curve for a full load may be related to the change of oil temperature in the gearbox. By analyzing the boundary conditions of the six data cards, the test conditions such as torque and rotational speed were stable and all within the learning range. Therefore, the increase of the trend index curve was not caused by the test conditions, which indicated that the internal mechanical structure of the gearbox had changed.

Because the first gear trend curve was basically stable and the monitoring stage was greatly affected by the oil temperature, the fault analysis was only carried out for the second and third gear working conditions.

3.2. Third Gear Fault Analysis

Seeing Figure 10, according to the order calculation table of the differential steering gearbox, the order 200.25 in the figure was the meshing order of the third-gear master–slave gear, the meshing order of the power shunt gear and the tooth-embedded driving gear. The 167.5 order and 232.75 order in the diagram were the side frequencies of the meshing order, and the side frequency interval was 32.5, which was close to the third harmonic (35.342) of the shaft where the third-gear driven gear and power shunt gear were located. Therefore, the fault may occur on these two gears. Simultaneously, the order of the side frequency band was less, the distribution was more concentrated and the amplitude was higher, which was the typical characteristic of distributed fault pitting fatigue failure.

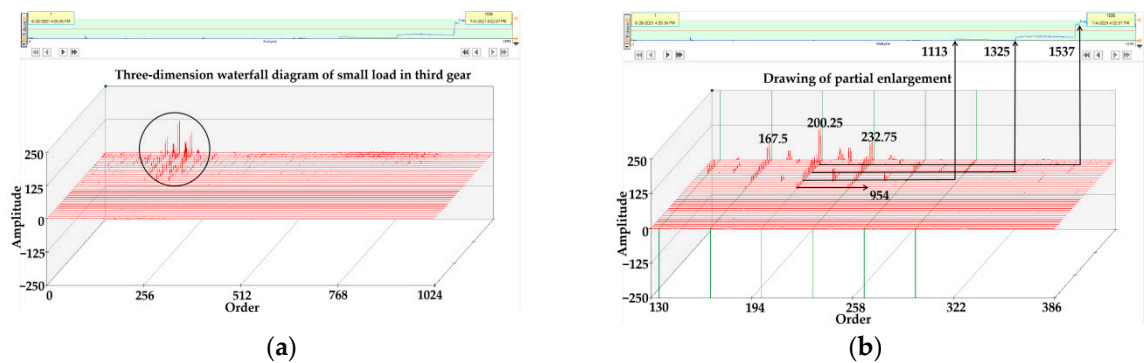


Figure 10. Three-dimension waterfall diagram (a) and drawing of partial enlargement (b) of difference spectrum of small load in third gear.

It can be also seen from the Figure 10 that the fault first occurred in the 954th analysis, and the vibration amplitudes of the meshing order and side frequency began to increase at the 1113th and the 1325th analysis, respectively. This indicated that the fault was gradually intensifying. At the 1537th analysis, the energy amplitude reached the alarm limit and the shutdown was triggered, indicating that the fault had deteriorated to a certain extent. At the 135th analysis, there was a side frequency with an interval of 18.75 around the main meshing order, which was basically consistent with the second harmonic (18.2063) of the shaft frequency of the third-gear drive gear. According to the characteristics of less and concentrated side frequency, it was judged that the pitting corrosion phenomenon also occurred in the third-gear drive gear at this time. After unpacking, the damage of the gear inside the gearbox was consistent with the fault analysis results, as shown in Figure 11.

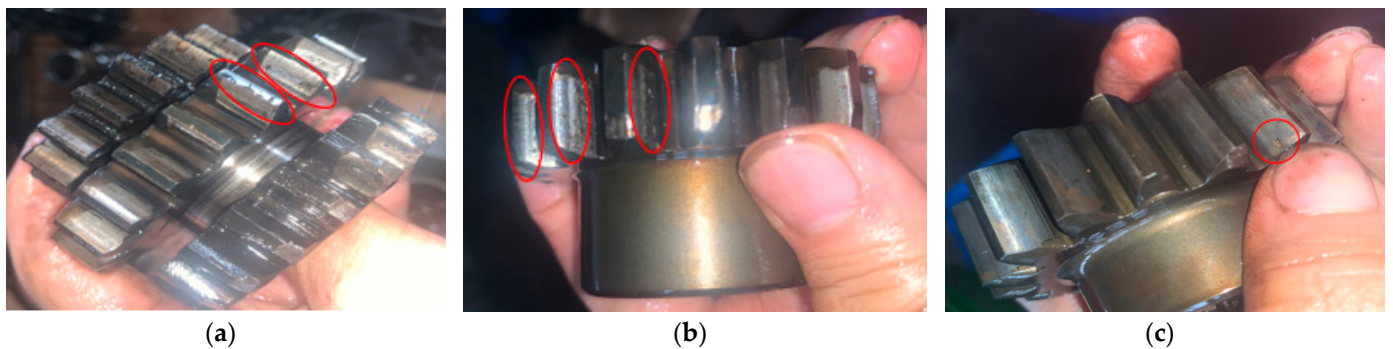


Figure 11. Damage of third-gear drive gear (a), third-gear driven gear (b) and power shunt gear (c) inside the gearbox.

Seeing Figure 12, in the 2717th analysis of the trend index curve under the third gear full load condition, the energy of the high-frequency part increased significantly, which may be attributed to metal friction in the gearbox body. This was completely consistent with the time of partial increase of high frequency energy during the 135th analysis under low load conditions, which began during the third-gear test from 21:00 to 22:00 in the evening of 3 July 2021. According to the unpacking results, high frequency metal frictions were occurred on the side of the power shunt gear, the outer ring of the NJ205E cylindrical roller bearing and the wall of the housing hole of the box bearing, as shown in Figure 13.

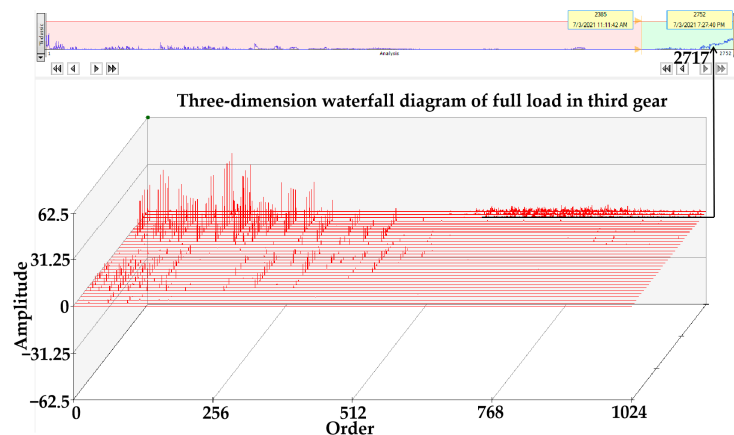


Figure 12. Three-dimension waterfall diagram of full load in third gear.

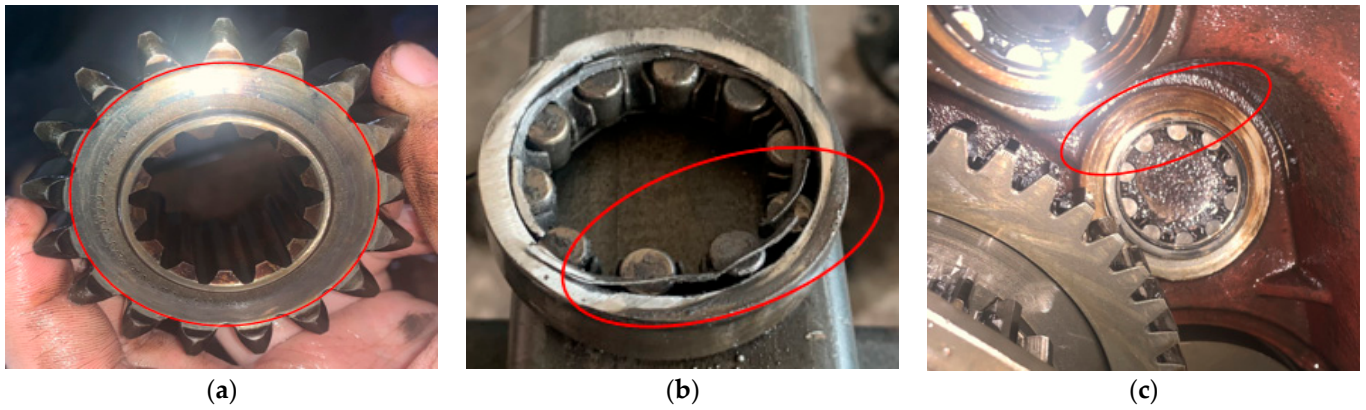


Figure 13. Internal damages of power shunt gear side (a), NJ205E cylinder roller bearing (b) and bearing hole wall (c).

3.3. Second Gear Fault Analysis

As shown in Figure 14, with the small increase in the energy of the low-frequency part in varying degrees, the trend index curve indicating the change of mechanical vibration characteristics in the gearbox began to rise slowly. This indicated that there was some kind of fault in the internal mechanical structure of the gearbox. A side frequency band with an interval of 45 appeared around the 235th order, which was exactly the same as the fourth harmonic of the shaft frequency of the second driven gear. According to the characteristic that the band order of this side was small and concentrated, it was judged that the pitting distributed fault may occur in the second driven gear. This fault can also be observed in the 3D waterfall diagram of the second gear full load, as shown in Figure 15, and the fault occurred at the same time. The gear damage after unpacking can be seen in Figure 16. This was basically consistent with the results of fault analysis.

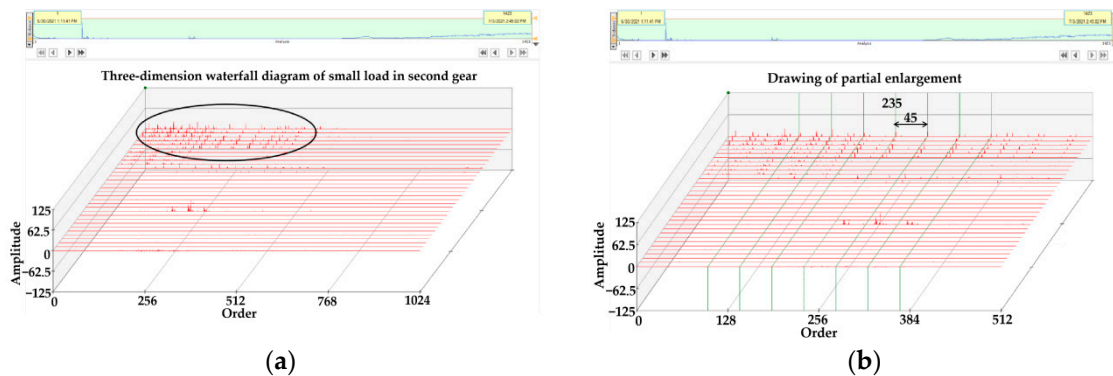


Figure 14. Three-dimension waterfall diagram (a) and drawing of partial enlargement (b) of difference spectrum of small load in second gear.

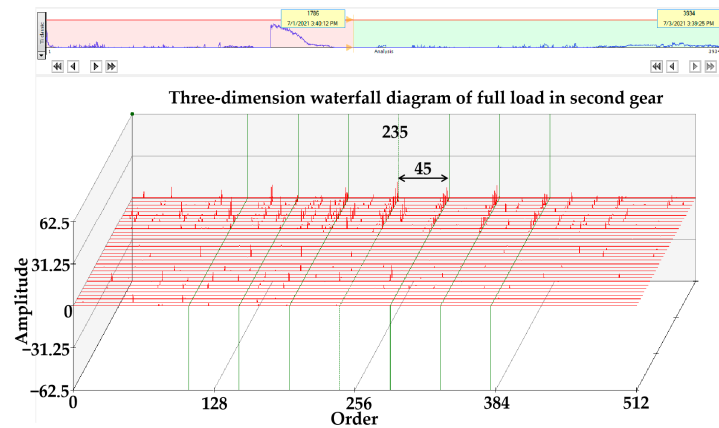


Figure 15. Three-dimensional waterfall diagram of full load in second gear.

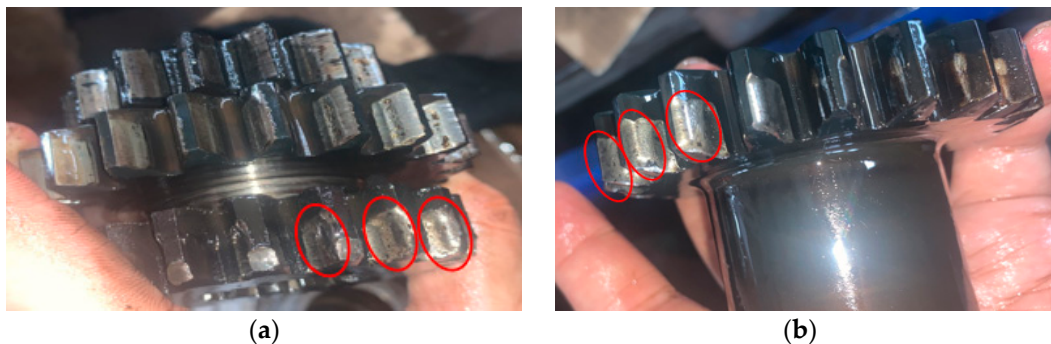


Figure 16. Damage of second drive gear (a) and second driven gear (b) inside the gearbox.

4. Conclusions

A fault diagnosis method for a differential inverse gearbox of a crawler combine harvester based on order analysis was studied in this paper. The main conclusions were as follows:

- The edge frequencies with an interval of 45 with few edge band orders and relatively concentrated distribution appeared around meshing order 235 of the second-gear master–slave gear, and the edge frequency with an interval of 32.5 and 18.5 with few edge band orders and relatively concentrated distribution appeared around the meshing order 200.25 of third-gear master–slave gear, power shunt gear and clutch driving gear. This indicated that pitting distributed faults occurred in the second-gear driven gear, third-gear master–slave gear and power shunt gear. This was consistent with unpacking and inspection.
- This method can send out the test stop signal according to the vibration energy level of the test object and can reflect the possible early fault type and location to the test personnel through the order spectrum generated under each gear without unpacking the gearbox. This had reference significance for research on the fault diagnosis method of a crawler combined harvester gearbox.

Author Contributions: Data curation, Y.L. (Yanbin Liu) and R.Z.; Funding acquisition, Y.L. (Yaoming Li); Investigation, R.Z.; Methodology, Y.L. (Yanbin Liu) and R.Z.; Project administration, Y.L. (Yaoming Li); Supervision, K.J.; Validation, R.Z.; Writing—Original draft, Y.L. (Yanbin Liu); Writing—Review & editing, K.J. All authors have read and agreed to the published version of the manuscript.

Funding: The work was supported by Jiangsu Province’s major scientific and technological achievements Transformation project (BA2020054), Major scientific and technological innovation project in Shandong Province (2019jzzy010729).

Institutional Review Board Statement: Not applicable.

Informed Consent Statement: Not applicable.

Data Availability Statement: Not applicable.

Conflicts of Interest: The authors declare no conflict of interest.

References

1. Li, Y.; Tian, J.; Zhao, Z.; Xu, L. Fatigue analysis of gears in combine harvester chassis gearbox. *Trans. Chin. Soc. Agric. Eng.* **2011**, *27*, 106–110.
2. Li, B.; Tang, B.; Deng, L.; Wei, J. Joint attention feature transfer network for gearbox fault diagnosis with imbalanced data. *Mech. Syst. Signal Process.* **2022**, *176*, 109146. [[CrossRef](#)]
3. Su, Y.; Meng, L.; Kong, X.; Xu, T.; Lan, X.; Li, Y. Small sample fault diagnosis method for wind turbine gearbox based on optimized generative adversarial networks. *Eng. Fail. Anal.* **2022**, *140*, 106573. [[CrossRef](#)]
4. Ha, J.M.; Youn, B.D. Fault diagnosis of a planetary gearbox by D norm-based time synchronous averaging (DTSA) with roughly estimated phase information under an encoder-less operating condition. *J. Sound Vib.* **2022**, *520*, 116545. [[CrossRef](#)]
5. Yuan, X.; Cai, L. Variable amplitude Fourier series with its application in gearbox diagnosis-Part II: Experiment and application. *Mech. Syst. Signal Process.* **2005**, *19*, 1067–1081. [[CrossRef](#)]
6. Li, B. *Research on the Generalized Demodulation Time-Frequency Analysis Method and Application to Gear Fault Diagnosis*; Hunan University: Changsha, China, 2010.
7. Feng, Z.; Chen, X.; Wang, T. Time-varying demodulation analysis for rolling bearing fault diagnosis under variable speed conditions. *J. Sound Vib.* **2017**, *400*, 71–85. [[CrossRef](#)]
8. Lin, J.; Zhao, M. Dynamic signal analysis for speed-varying machinery: A review. *Sci. Sin.* **2015**, *45*, 669–686.
9. Feng, Z.; Chen, X.; Liang, M. Joint envelope and frequency order spectrum analysis based on iterative generalized demodulation for planetary gearbox fault diagnosis under nonstationary conditions. *Mech. Syst. Signal Process.* **2016**, *76–77*, 242–264. [[CrossRef](#)]
10. Wan, D.; Sun, D.; Zhao, Y. Synchronous revolution order analysis application in fault diagnosis of auto gearbox. *Comput. Meas. Control* **2006**, *3*, 299–300.
11. He, G.; Ding, K.; Li, W.; Jiao, X. A novel order tracking method for wind turbine planetary gearbox vibration analysis based on discrete spectrum correction technique. *Renew. Energy* **2016**, *87*, 364–375. [[CrossRef](#)]
12. Chen, J. *Dynamic Analysis and Experimental Study for the Differential Steering System of the Tracked Combine Harvester*; Jiangsu University: Zhenjiang, China, 2016.
13. Huang, J. *Design and Experimental Study on Differential Inverse Gearbox of Tracked Rice Field Combine Harvester*; Jiangsu University: Zhenjiang, China, 2018.
14. Ye, X.; Li, Y.; Xu, L.; Pang, J.; Ma, Z. Fatigue analysis half axle of combine harvester. *J. Agric. Mech. Res.* **2014**, *36*, 32–35.
15. Li, Y.; Ye, X.; Xu, L.; Pang, J.; Ma, Z. Construction and performance experiment of load test system for half axle of combine harvester. *Trans. Chin. Soc. Agric. Eng.* **2013**, *29*, 35–41.
16. Li, Y.; Chen, J.; Liang, Z.; Ma, X.; Jiang, X. Design and experiment of differential steering mechanism for track combine harvester. *Trans. Chin. Soc. Agric. Mach.* **2016**, *47*, 127–134.
17. Ji, X.; Li, Y.; Xu, L.; Pang, J.; Ye, X. The design and experiment of load measurement system for combine harvester. *J. Agric. Mech. Res.* **2013**, *35*, 131–134.
18. Ye, X. *Load Testing and Reliability Analysis of Combine Harvester Halt Axle*; Jiangsu University: Zhenjiang, China, 2013.

Article

Design of High-Efficiency Soil-Returning Liquid Fertilizer Deep-Application Furrow Openers for Improving Furrowing Performance in Cold Regions of Northeast China

Wenqi Zhou ¹, Chao Song ¹, Xiaobo Sun ¹, Ziming Liu ¹, Xue Ni ¹, Kangjia Shen ¹, Yi Jia Wang ^{2,*} and Liqun Tian ³

¹ College of Engineering, Northeast Agricultural University, Harbin 150030, China

² Department of Industrial and Manufacturing Systems Engineering, The University of Hong Kong LG-108, Composite Building, Pokfulam Road, Hong Kong SAR 999077, China

³ Key Laboratory of Crop Harvesting Equipment Technology of Zhejiang Province, Jinhua Polytechnic, Jinhua 321007, China

* Correspondence: yijiaow@connect.hku.hk; Tel.: +86-166-2097-4902

Citation: Zhou, W.; Song, C.; Sun, X.; Liu, Z.; Ni, X.; Shen, K.; Wang, Y.J.; Tian, L. Design of High-Efficiency Soil-Returning Liquid Fertilizer Deep-Application Furrow Openers for Improving Furrowing Performance in Cold Regions of Northeast China. *Agriculture* **2022**, *12*, 1286. <https://doi.org/10.3390/agriculture12091286>

Academic Editors: Muhammad Sultan, Redmond R. Shamshiri, Md Shamim Ahamed and Muhammad Farooq

Received: 21 July 2022

Accepted: 18 August 2022

Published: 23 August 2022

Publisher's Note: MDPI stays neutral with regard to jurisdictional claims in published maps and institutional affiliations.



Copyright: © 2022 by the authors. Licensee MDPI, Basel, Switzerland. This article is an open access article distributed under the terms and conditions of the Creative Commons Attribution (CC BY) license (<https://creativecommons.org/licenses/by/4.0/>).

Abstract: Liquid-fertilizer deep-application techniques are techniques for applying fertilizers to the root system of crops, which can effectively improve the utilization rate of fertilizers and reduce application amounts. Due to the soil viscosity of soils in the cold region of Northeast China, the soil return rate of furrow openers for liquid-fertilizer deep applications is low, which can easily cause excessive volatilizations of liquid fertilizers. Therefore, aiming at the operational requirements of low soil disturbance for liquid-fertilizer furrowing and deep applications, an efficient soil-returning liquid-fertilizer deep-application furrow opener was innovatively designed based on soil characteristics during the inter-cultivation period in the cold region of Northeast China. The discrete element method (DEM) was used to analyze the operating performance of the high-efficiency soil-returning liquid-fertilizer deep-application furrow openers, which is determined by key operating parameters including width and slip cutting angle. The DEM Virtual Simulation Experiment results show that the optimal combination is the width of 37.52 mm and a slip cutting angle of 43.27°, and the test results show that the optimal performance of the high-efficiency soil-returning liquid-fertilizer deep-application furrow opener is that the soil disturbance rate is 51.81%, and the soil-returning depth is 52.1 mm. This paper clarifies the relationship between the width and the slip cutting angle in furrowing resistance and soil disturbance and the mechanism by which the width and slip cutting angle affect soil disturbance. Above all, this study provides a theoretical and practical reference for the design of liquid-fertilizer deep-application furrow openers.

Keywords: highly efficient soil return; liquid fertilizer deep application technique; DEM; soil bin test

1. Introduction

The soil type in the cold region of Northeast China is a very rare cold black soil with a very slow formation rate, which is a very valuable resource [1–3]. Since the beginning of the second “green revolution” in the world, the application of chemical fertilizers has surged in most countries in the world, and the crop quality and per capita output of grain have significantly improved [4,5]. At the same time, the long-term large-scale application of chemical fertilizers has also introduced many problems, such as the decline of black soil fertility, the destruction of soil aggregate structure, and the excessive pollution of farmland environment [6–9]. Therefore, curbing the excessive use of chemical fertilizers can effectively protect valuable black soil resources in this region [6,10,11].

In recent years, liquid fertilizers have been widely used due to its advantages in convenient production, possessing a flexible ratio, low environmental pollution and high crop-absorption rates, which can effectively curb the excessive application of chemical

fertilizers [10,11]. In agricultural production, the methods of furrowing and the deep application of liquid fertilizers effectively improved fertilizer utilization rates [12,13]. However, the commonly used furrow opener for deep applications of liquid fertilizers is prone to causing large soil disturbances, resulting in high volatilization rates of liquid fertilizers and affecting crop growth and the promotion of liquid-fertilizer deep-application techniques [13–15]. Obviously, in order to successfully promote the application of liquid-fertilizer deep-applications technique, a liquid-fertilizer deep-application furrow opener that can realize highly efficient soil returns during operation is needed, which will greatly improve the promotion of liquid-fertilizer deep-application techniques in this region.

Many scholars have studied and analyzed the interaction between furrow openers and soil. Godwin and Spoor [16,17] analyzed soil disturbances caused by furrow openers by using the soil bin test, and they concluded that soil disturbances as two approximate geometric contours comprising a wedge and a crescent. These studies treat the soil as a whole and analyze soil disturbances through the damage introduced by furrow openers to whole soil without considering the interaction between soil particles; thus, the construction of the analysis model in the above studies is not sufficient. Solhjou et al. [18] conducted an experimental study on soil disturbance caused by narrow point openers and quantified the furrow contour by using cubic PVC missing agents embedded in the soil. The results showed that the chamfer of the furrow opener significantly reduced soil disturbances. Rodhe and Etana [19] developed V-shaped discs, which reduced the loss rate of liquid fertilizers compared with band spreading, but furrowing resistance was too large, which led to a wide shape and a superficial depth and caused an excessive volatilization of the liquid fertilizer. The above studies show that the innovative design of the furrow opener's geometry can achieve low soil-disturbance rates and reduce the rate of liquid fertilizer volatilization. Therefore, the structural innovative design of the liquid-fertilizer deep-application furrow opener can significantly improve its operation performance. Shuhong et al. [20] designed a new opener to reduce the working resistance of the furrow opener by conducting a bionic study of the sailfish head curve and concluded that the working resistance, the width of soil disturbance and the depth of soil return increased with the increase in furrow-opening depth at a water content of $12\% \pm 1\%$. At the furrow opening depth of 60 mm, the working resistance increased with the increase in water content. However, the effects on soil disturbance width and soil-return depth were not obvious.

Many scholars evaluated the performance of new openers by computer simulation tests. Computer-aided design and simulation tests can reduce the number of test steps, save test costs and reduce the resources required for the design and manufacture of openers [21]. Ever since the discrete element method (DEM) has been proposed, the use of discrete element methods to construct coupled opener–soil interaction models has been proven by many scholars to be effective, and it is an efficient method for studying granular media with dynamics and optimal design [22,23].

In this study, a DEM virtual-simulation model of black soil in the cold region of Northeast China was constructed by sampling and measuring the relevant parameters of the black soil widely distributed in the cold region of Northeast China, and an optimal test has been carried out for the key structural parameters of liquid-fertilizer deep-application furrow openers. Moreover, a high-efficiency soil-returning liquid-fertilizer deep-application furrow opener with excellent operating performances was designed. The accuracy of the DEM virtual simulation test model is verified by the soil bin test. This study can provide research ideas and design methods for the design of liquid-fertilizer deep-application furrow openers. At the same time, it can facilitate the promotion of liquid-fertilizer deep-application techniques in the cold regions of Northeast China, reduce the amount of chemical fertilizer application in local areas, and protect precious black soil resources.

2. Materials and Methods

2.1. DEM Virtual Simulation Test

2.1.1. Measurement of Physical Parameters of Black Soil

As one of the three major corn-producing areas in China, the black soil in the main corn-producing area of Northeast China was selected for sampling and determination, and the soil was sampled at a test plot ($126^{\circ}58'31''$ N, $45^{\circ}32'29''$ E) in Acheng District, Harbin, Heilongjiang province, China, on 25 June 2021. The bulk density of black soil was measured using the cutting ring method. Measuring equipment comprised an aluminum cutting ring (100 cm^3) and an electronic balance (accuracy 0.01 g, Changzhou Lucky Electronic Equipment Co., Ltd., Changzhou, China), as shown in Figure 1a. The moisture content of the black soil was measured by the oven drying method [24], and measuring equipment included an electric constant-temperature drying box (Model GZ008, Dongguan Bai hui Electronic Co., Ltd., Dongguan, China), as shown in Figure 1b. The soil shear modulus and Poisson's ratio were measured using a strain-controlled soil direct-shear apparatus (Model ZJ, Changzhou Lingkun Automation technique Co., Ltd., Changzhou, China), as shown in Figure 1c.

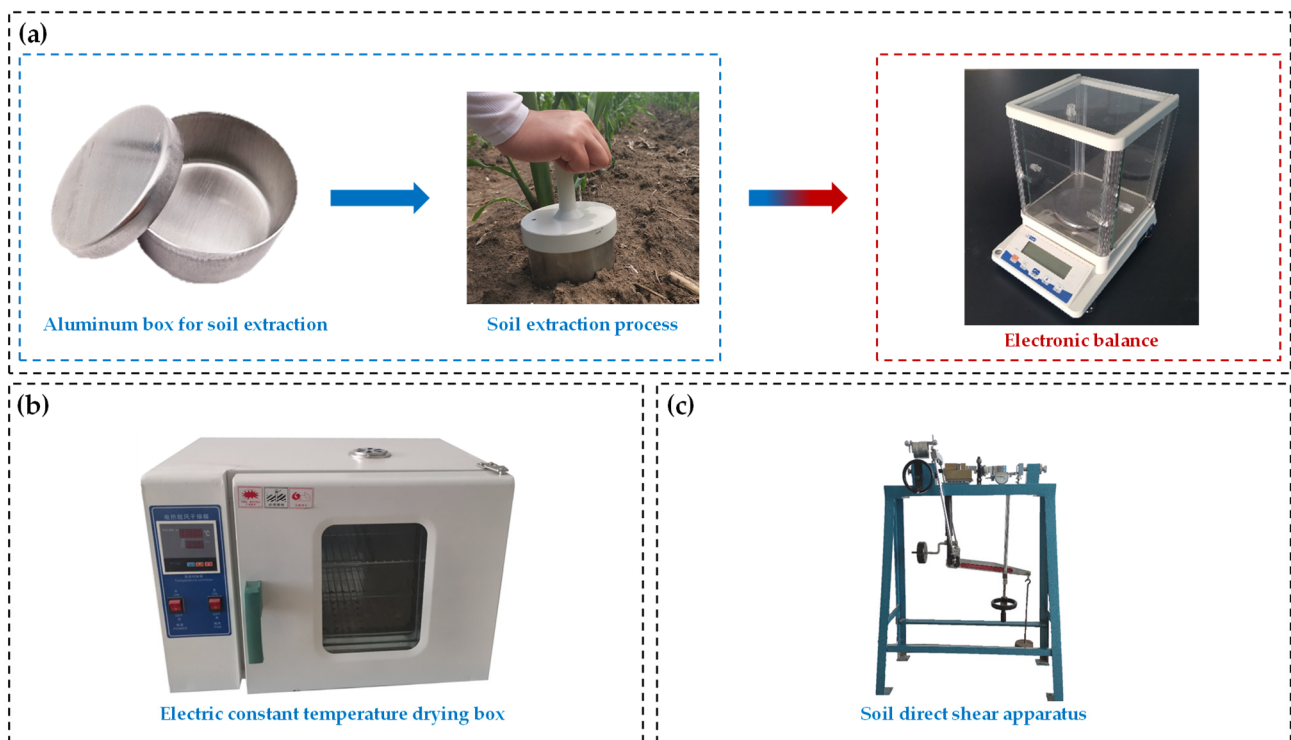


Figure 1. Measurement process and equipment for measuring black soil physical parameters. (a) Measurement process and equipment for measuring black soil bulk density parameters. (b) Measurement process and equipment for measuring black soil moisture content. (c) Measurement process and equipment for measuring black soil shear modulus and Poisson's ratio parameters.

2.1.2. Measurement of Black Soil Contact Parameters

In this study, the sliding and rolling friction coefficients of soil and 65 Mn material were measured by using a slope test, as shown in Figure 2a. The collision recovery coefficient between the soil and 65 Mn material was measured by a collision test. The measuring equipment included a high-speed camera (PCO.DIMAX CS4 model, Kelheim, Bagolia, Germany). After the collision between spherical soil and a 65 Mn steel plate, the ratio of the normal rebound velocity to the normal forward velocity before the collision was used to determine the collision's recovery coefficient, as shown in Figure 2b.

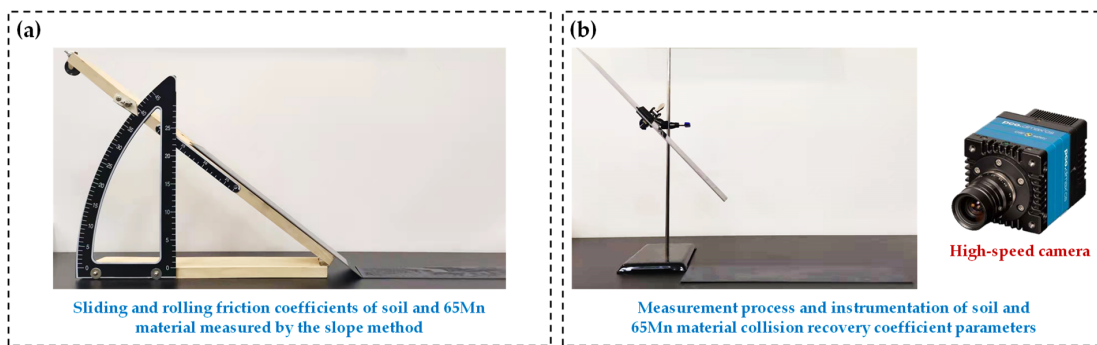


Figure 2. Measurement process and equipment for measuring contact parameters of black soil and 65 Mn. (a) Measurement process and equipment for measuring rolling friction coefficient of black soil and 65 Mn material. (b) Measurement process and equipment for measuring collision recovery coefficient of black soil and 65 Mn material.

2.1.3. Setting and Calibration of DEM Virtual Simulation Parameters

The soil in the cold region of Northeast China comprises black soil with high moisture content; thus, the contact model should fully consider the effect of inter-particle cohesion force on particle movements [25,26]. The Hertz-Mindlin with the JKR Cohesion contact model in EDEM is a cohesion contact model. Based on the Hertz contact theory and JKR theory, it considers the influence of the inter-particle cohesion force on particle movement, and it is suitable for simulating material bonding and agglomeration between particles due to electrostatic, moisture and other reasons, such as crops and soil. When using Hertz-Mindlin with the JKR Cohesion contact model to simulate black soil, the contact model parameter (that is, the surface energy density) needs to be determined. This parameter cannot be obtained directly and is determined by the stacking angle test.

Select a hopper with an inlet diameter of 300 mm, outlet diameter of 50 mm and height of 270 mm; adjust the position of the hopper to a distance of 250 mm between the bottom of the outlet and the plate; close the outlet; fill the hopper with soil and then open the outlet. After the soil on the plate is stable, shoot it in a perpendicular manner to the horizontal plane and the marked stacking angle.

Using EDEM 2020 to carry out the soil stacking angle simulation test, the contact model parameters were corrected and calibrated with the real soil stacking angle as the target. The stacking angle method is used to measure the surface energy density in order to reduce the error between the simulation results and the actual test results.

After correcting the surface energy density several times, when the surface energy density of the contact model was finally determined to be 5.5 J m^{-2} , the real stacking angle of soil and the simulated stacking angle are basically the same, which are 23.27° and 24.09° respectively. The measurement process and results are shown in Figure 3.

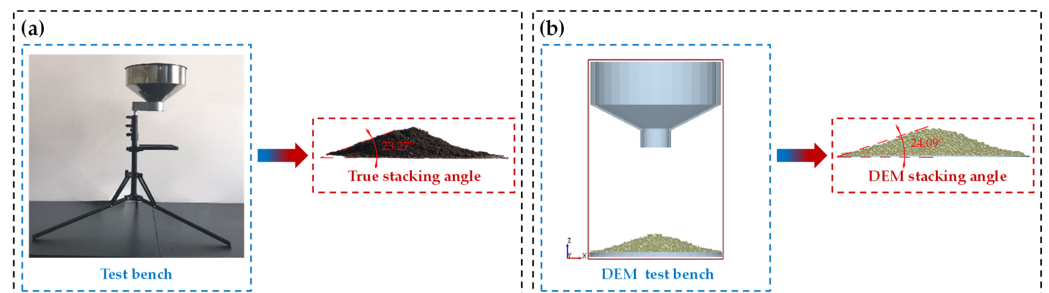


Figure 3. Measurement process and equipment of black soil stacking angle parameters. (a) Measurement process and equipment of real black soil stacking angle parameters. (b) Measurement process and equipment of black soil stacking angle parameters in DEM virtual simulation tests.

2.1.4. DEM Virtual Simulation Soil Bin Construction

In order to efficiently carry out the DEM virtual simulation test, a single spherical particle is selected as the virtual soil particle model [27]. In order to render the virtual soil as close as possible to actual soil conditions in the field, the EDEM virtual soil parameters were set according to physical and mechanical property parameters, contact model parameters and material contact parameters of the soil measured in the previous stage, and a virtual soil model was constructed. The virtual soil parameters are shown in Table 1.

Table 1. Parameters of DEM virtual simulation test model.

Parameters	Values
Soil particle size (mm)	2~3
Soil density ($\text{g}\cdot\text{cm}^{-3}$)	1.516
Soil Poisson's ratio	0.39
Soil shear modulus (MPa)	1.00
Coefficient of static friction between soil particles	0.53
Coefficient of dynamic friction between soil particles	0.78
Recovery coefficient between soil particles	0.23
surface energy density ($\text{J}\cdot\text{m}^{-2}$)	5.50
Soil–65 Mn static friction coefficient	0.47
Soil–65 Mn rolling friction coefficient	0.11
Soil–65 Mn collision recovery coefficient	0.09

2.1.5. DEM Virtual Simulation Model Construction

In order to clearly and intuitively observe the operation process of the furrow opener, a soil model was constructed with a thickness of 20 mm, and the soil at a depth of 0–100 mm was used as the operation layer. The soil particles were randomly generated in this depth and settled naturally, with 120,000 particles in each layer. The soil at a depth of 100–140 mm was used as a buffer layer, which was used to isolate the operation layer and the boundary of the soil bin so as to avoid the excessive extrusion of the soil by the boundary of the soil bin during the simulation, which will affect simulation results. The preparation area and the data collection area are set along the operation direction of the furrow opener of the virtual soil bin. The length of the preparation area is 100 mm, which is the buffer area for the furrow opener to enter the soil for stable operations. The length of the data collection area is 1400 mm, which is the stable operation area of the furrow opener for data collection.

To sum up, the overall size of virtual soil is determined to be 1500 mm \times 600 mm \times 140 mm, as shown in Figure 4a. The Creo 6.0 software was used to construct a model for the high-efficiency deep-application furrow opener. The interaction between the furrow opener and soil can be divided into five processes: cutting, lifting and crushing, pushing, guiding and shaping. In order to realize the above processes, the sliding–cutting edge and curved surface structure are designed with symmetrical layouts. Based on the sliding and cutting principle, the head of the furrow opener is designed as the sliding–cutting edge to achieve the cutting of soil. The surface structure was designed based on the structural characteristics of wedge-surface crushing and the extruding soil, including disturbed soil surfaces, extruded soil surfaces, guide inclined surfaces and shaping surfaces. The disturbed soil surface improves the soil crushing ability of the high-efficiency soil-returning liquid-fertilizer furrow opener. The wedge structure is helpful for breaking the upper soil layer and for promoting soil flow from the surface of the furrow opener to the tail of the furrow opener. The extruded soil surface squeezes and cuts the soil, which is beneficial for forming smooth fertilizer furrows quickly and efficiently. The inclined surface guides the falling soil to fall behind the fertilizer spray needle in order to realize the falling soil and overlaying fertilizer. The shaping surface extrudes the soil sideways in order to shape the fertilizer's furrow. The fertilizer spray needle is embedded in the tail of the high-efficiency soil-returning liquid-fertilizer furrow opener as a fertilizer-spraying execution component, as shown in Figure 4b. After all models are constructed, the high-efficiency soil-returning

liquid-fertilizer furrow opener is imported into the EDEM 2020 software (Altair Engineering, Inc., Troy, MI, USA) for DEM simulation tests, and the post-processing module is used to obtain test results, as shown in Figure 4c.

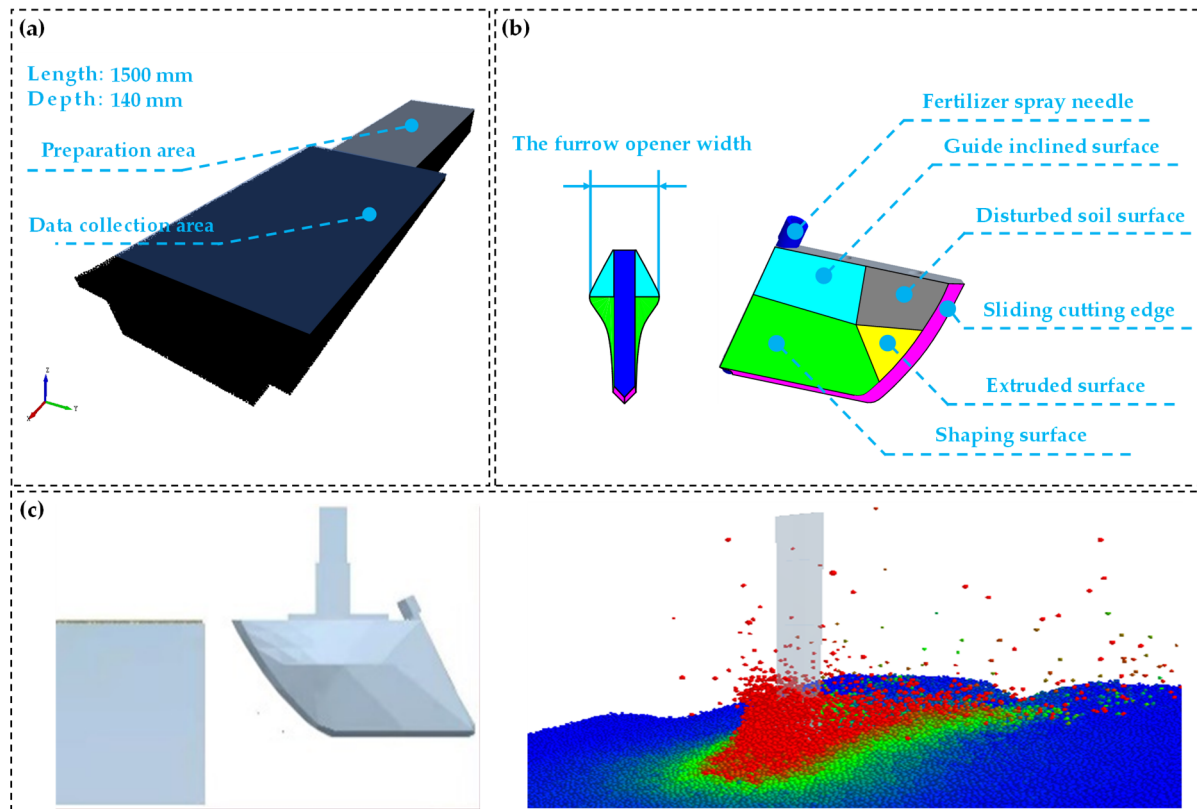


Figure 4. Construction and simulation process of the DEM virtual simulation model. (a) Construction of the DEM virtual simulation soil bin model. (b) Construction of the 3D model of high-efficiency soil-returning liquid-fertilizer deep-application furrow openers. (c) High-efficiency soil-returning liquid-fertilizer deep-application furrow opener and DEM virtual simulation test processes.

The operating performance of the furrow opener is related to the slip cutting angle θ_2 and width l . In this study, 2 factors and 5 levels were used to conduct the DEM simulation test. The minimum selection of the opener width l 20 mm is based on the current size of the fertilizer spray needle mostly in the range of 10 to 20 mm to ensure a certain structural strength relative to the fertilizer spray needle in order to allow space for installation; the initial selection of the opener width l was 20 mm as the minimum value for testing. Widths of 20, 26, 40, 54 and 60 mm were selected. Slip cutting angles of 25, 31, 45, 59 and 65° were selected. Under the conditions of an operating depth of 80 mm and a forward speed of 1.0 ms⁻¹, simulation results were used to analyze the significance and influence law of the factors affecting the test indicators, and the optimal structural parameter combination was finally obtained.

The soil disturbance rate and soil-return depth were selected as the test indicators, and the soil disturbance rate and soil-return depth quantified the soil disturbance behavior and soil return performance of the furrow opener, respectively, as shown in Figure 5.

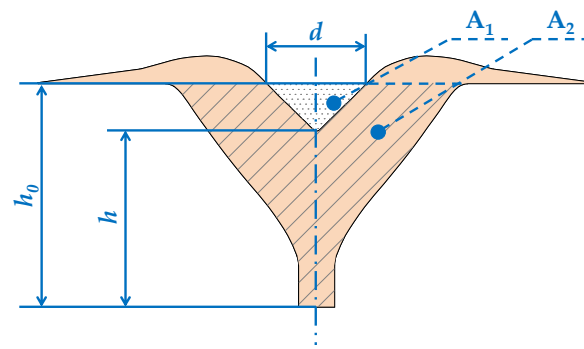


Figure 5. Schematic diagram of furrow contour section parameters.

- Soil disturbance rate ρ

The soil disturbance rate ρ is an important indicator of the soil disturbance behavior of the furrow opener. The larger the disturbance rate is, the more disturbed soil is during the operation. Disturbance rate ρ refers to the ratio of the disturbed soil area in the furrow contour multiplied by the width and depth of the gully, as shown in Figure 5; the soil disturbance rate is calculated according to Equation (1).

$$\rho = (A_1 + A_2)/dh \times 100\% \quad (1)$$

- Soil-return depth h

Soil-return depth is an important indicator of the soil return performance of the furrow opener. The higher the soil-return depth h , the more superior the soil return performance of the furrow opener.

2.2. Soil Bin Verification and Performance Test

In order to verify the accuracy of the DEM virtual simulation parameter setting and the rationality of the structure optimization of the high-efficiency soil-returning liquid-fertilizer deep-application furrow opener, this study was conducted in May 2021 in the Agricultural Tools and Soil Bin Laboratory of Northeast Agricultural University (126°43'25" N, 45°44'27" E). Taking the operating speed of the high-efficiency soil-returning liquid fertilizer deep application furrow opener as the experimental factor, it was set to six levels of 0.2, 0.4, 0.6, 0.8, 1.0 and 1.2 m s⁻¹ to verify the accuracy of the DEM virtual simulation model. The performance test of the furrow opener was carried out to examine the influence of the operating speed of the furrow opener on its soil disturbance behavior and soil return performance.

Before the test, the organisms, weeds and large clods in the soil were removed by a round-hole sieve. According to the actual situation in the field, the soil was sprayed with water, the soil's moisture content was adjusted, and a ridge platform was built. The soil conditions and parameter indicators are shown in Figure 6a. The test was carried out under the condition of an 80 mm operating depth and 1 m s⁻¹ operating speed. The test equipment comprised a soil bin trolley, a high-speed camera, a frequency conversion cabinet (model F1000-G055T3C, Yantai Ougri Transmission Electric Co., Ltd., Yantai, China) and a three-phase asynchronous motor (model Y2-10L2-4, Shanghai Yongce Machinery Equipment Co., Ltd., Shanghai, China), as shown in Figure 6b. The high-speed camera system captures the soil disturbance behavior of the furrow opener and records it by using supporting software. After the furrow opener operation, outer-layer gullies were delineated, and the gullies were delineated a second time after loose soil was removed with a brush. The results of the two depictions were combined as the extraction results of furrow contour parameters under this operating conditions, and relevant parameters were obtained. The test process is shown in Figure 6c.

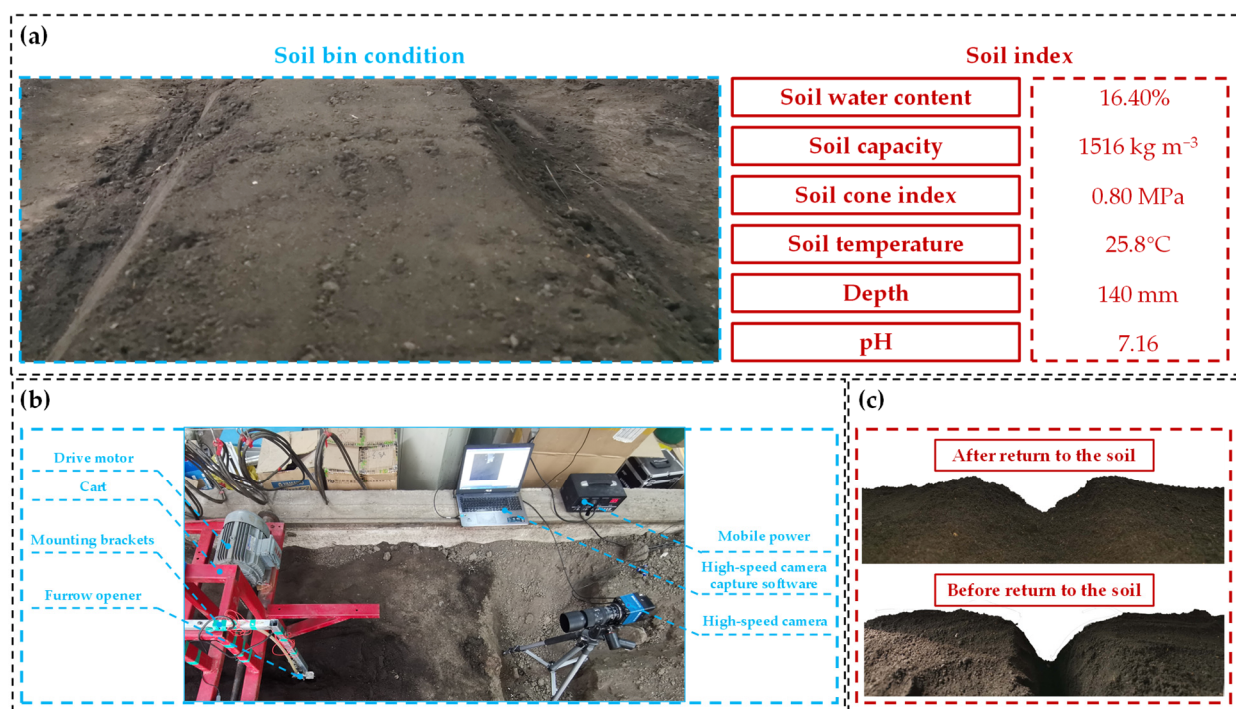


Figure 6. Soil bin test process and equipment. (a) Soil conditions and indicators of the indoor soil bin test. (b) Relevant equipment related to the indoor soil bin test. (c) The extraction process and results of soil furrow contour parameters.

3. Results

As shown in Figure 7a,b, when the slip cutting angle is fixed and the slip cutting angle is less than 59°, the soil disturbance rate increases with the increase in the furrow opener’s width. When the slip cutting angle is less than 59°, the soil disturbance rate first decreases and then increases with the increase in the furrow opener’s width. As the width of the furrow opener increases, the soil-return depth first increases and then decreases. As shown in Figure 7c,d, when the width of the furrow opener is fixed, the soil disturbance rate first decreases and then increases, and the soil-return depth first increases and then decreases. Equations (2) and (3) are obtained using Design-Expert 8.0.6 software. The factors of width x_1 and the slip cutting angle x_2 have significant effects on soil disturbance rate ρ and soil-return depth h , and the p values of the out-of-fit test item of the two regression models are all greater than 0.1; the regression model is shown in Table 2.

Table 2. Optimization model of test data.

Resources	Regression Model on Slip Cut Angle				Regression Model on Width			
	Sum of Squares	df	F-Value	p-Value	Sum of Squares	df	F-Value	p-Value
Model	259.19	5	33.50	<0.0001	213.26	5	24.88	<0.0001
x_1	126.53	1	81.77	<0.0001	16.99	1	9.91	0.0104
x_2	25.30	1	16.35	0.0023	10.50	1	6.13	0.0328
x_1x_2	12.96	1	8.38	0.0160	4.62	1	2.70	0.1316
x_1^2	64.52	1	41.70	<0.0001	54.34	1	31.69	0.0002
x_2^2	29.88	1	19.31	0.0013	126.80	1	73.96	<0.0001
Residual	15.47	10			17.15	10		
Lack of fit	11.30	3	6.31	0.0211	1.88	3	0.29	0.8337
Pure error	4.18	7			15.27	7		
Cor total	274.67	15			230.41	15		

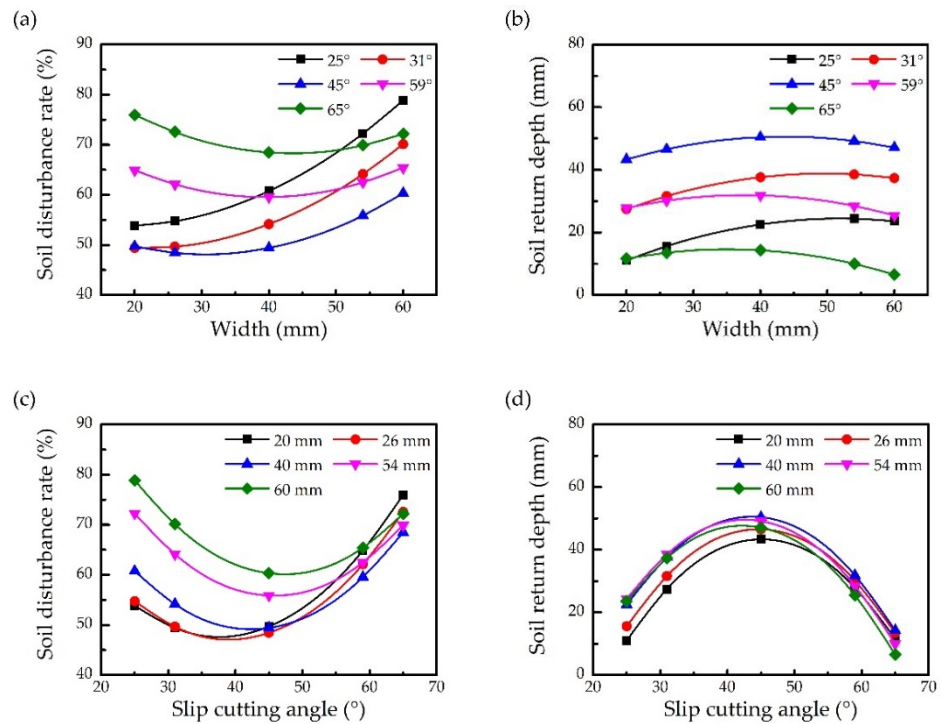


Figure 7. DEM virtual simulation test results. (a) The effect of the furrow opener’s width on soil disturbance rate. (b) The effect of the furrow opener’s width on soil-return depth. (c) The effect of slip cutting angle on soil disturbance rate. (d) The effect of the slip cutting angle on the soil-return depth.

The above test results show that both regression models can solve the optimal solution of the parameters. Using the Design-Expert software, the minimum soil disturbance rate and maximum soil-return depth were taken as solving conditions to obtain the optimal solution parameter combination: the slip cutting angle is 43.27°, the width is 37.52 mm, the soil disturbance rate is 50.23%, and the soil-return depth is 50.9 mm. According to the optimization results, the virtual simulation verification shows that the soil disturbance rate is 51.81%, and the soil-return depth is 52.1 mm, which is basically consistent with the optimization results.

$$\rho = 97.079 - 0.0448x_1 - 2.507x_2 - 0.018x_1x_2 + 0.014x_1^2 + 0.038x_2^2 \quad (2)$$

$$h = -146.683 + 1.629x_1 + 7.434x_2 - 0.011x_1x_2 - 0.013x_1^2 - 0.08x_2^2 \quad (3)$$

3.1. Soil Bin Verification Test Results

In order to verify the accuracy of the parameter setting of the DEM virtual simulation model and the rationality of the structure optimization of the high-efficiency soil-returning liquid-fertilizer deep-application furrow opener, the soil bin verification test was carried out at a depth of 80 mm and an operating speed of 1.0 m s⁻¹, and the test was repeated for three groups. Take the average value as the test result, and extract the furrow contour after the operation of the high-efficiency soil-returning liquid-fertilizer furrow opener. The obtained soil disturbance rate and soil-return depth parameter results are compared, as shown in Table 3.

The soil disturbance rates in the virtual simulation and soil bin verification tests are 52.81% and 50.37%, respectively. The soil-return depths are 50.8 and 52.7 mm. The relative errors are 5.45%, 4.68%, 3.61% and 4.84%. The results of the DEM virtual simulation and the soil bin verification test are consistent.

Table 3. Comparison of DEM virtual simulation test and soil bin test results.

Test Form	No.	Soil Disturbance (%)	Soil-Return Depth (mm)
DEM virtual simulation test	1	52.81	50.8
Soil bin test results	1	50.11	52.7
	2	51.07	53.3
	3	49.92	52.2
	Average value	50.37	52.7

Soil disturbance behavior in the operation of high-efficiency soil-returning liquid-fertilizer furrow opener is captured by a high-speed camera, and a group of high-speed camera photos was randomly selected for qualitative comparison and analysis with the DEM virtual simulation test, as shown in Figure 8. Figure 8a shows the soil disturbance behavior of the high-efficiency soil-returning liquid-fertilizer deep-application furrow opener in the DEM virtual simulation test, in which the color of soil particles changes from red to blue as the speed decreases. The results show that when the furrow opener is working, the soil on both sides of the disturbed soil surface behaves in a lateral throwing manner, and the soil in the forward direction exhibits lifting and throwing relative to the negative direction.

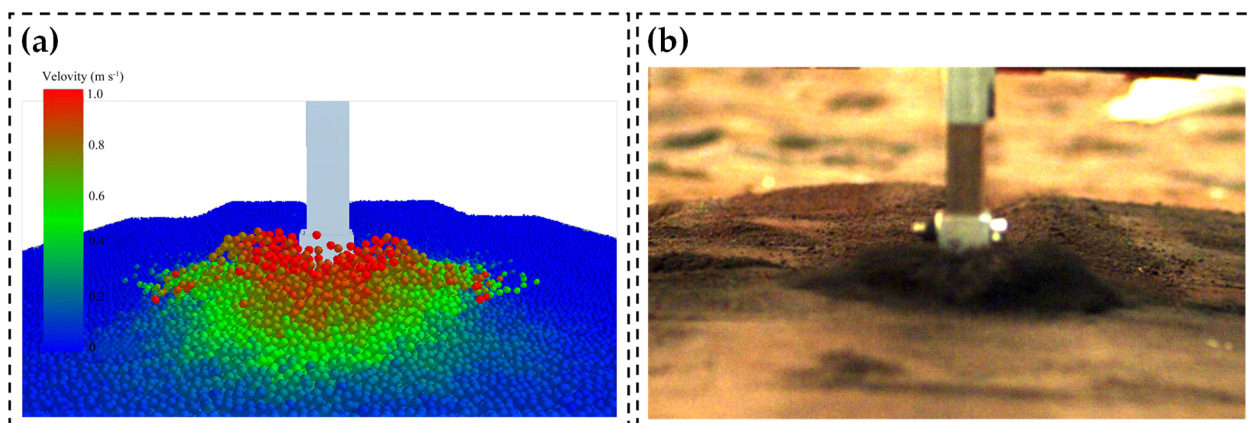


Figure 8. Comparison of results between DEM virtual simulation test and soil bin test. (a) Comparison of furrow contour. (b) Comparison of soil disturbance rate.

Figure 8b shows the soil disturbance behavior of the high-efficiency soil-returning liquid-fertilizer deep-application furrow opener in the soil bin verification test. The dark area is the area with high soil-particle velocity, and the bright area is the area with low soil-particle velocity. The color on both sides of the disturbed soil surface in the figure is extremely dark, and it gradually becomes brighter from the inside to the outside, indicating that the soil in this area exhibits lateral throwing movements. The soil in the direction of operation changes from dark to bright from the bottom to the top and from the front to the back, indicating that the soil is lifted and broken by disturbances and flows in the opposite direction of the operation along the furrow opener's surface.

3.2. Soil Bin Verification Test Results

Taking the operating speed as the test factor, the soil bin performance test was carried out to examine the influence of the operating speed of the furrow opener on its soil disturbance behavior and soil return performance. The soil disturbance behavior of the furrow opener during operations and the soil disturbance rate and soil return performance after operation were qualitatively analyzed at different operating speeds. The test results are shown in Figure 9a,b.

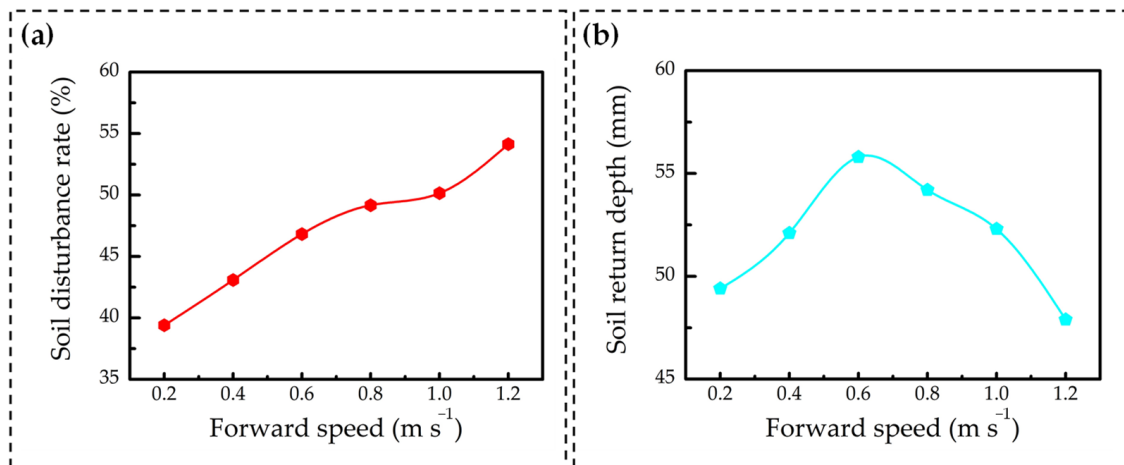


Figure 9. Soil bin performance test results. (a) Effect of working speed on soil-disturbance rate. (b) Effect of working speed on soil-return depth.

The soil-return depth first increases and then decreases with the increase in working speed. When the working speed is in the range of 0.4–1.0 m s⁻¹, the soil’s return depth is relatively high, and the maximum and minimum soil-return depths reach 55.8 and 52.1 mm, respectively. In the range of 0.2~0.4 m s⁻¹, the soil’s return depth is low.

4. Discussion

4.1. Analysis of Soil-Returning Behavior of High-Efficiency Soil-Returning Liquid Fertilizer Deep Application Furrow Opener

The furrow opener disturbs the soil during operation; it is completely buried in the soil, which produces disturbance behaviors for the soil, including lifting and breaking, lateral throwing and squeezing of the soil [28]. The squeezing of the soil affects the width below the furrowing contour, while lifting and breaking and lateral throwing determine the lateral throwing width and soil backfill rate. The behavior of soil disturbance is analyzed when the furrow opener is completely buried in the soil, as shown in Figure 10a. CDE and C₁D₁E₁ are the cross-sections of the furrow and ridge formed by the lateral throwing of soil, GG₁H₁H is the upwardly lifted and broken soil, and EE₁I is the cross-section of the fertilizer furrow. During the furrow opener’s operation, the fertilizer furrow is divided into upper and lower fertilizer furrows, which are the EE₁F₁F and F₁FI areas, respectively. The soil in the EE₁F₁F area is lifted and laterally thrown to form the upper fertilizer furrow, and the soil in the F₁FI area is extruded to form the lower fertilizer furrow. In this process, the soil volume is conserved; thus, the cross-sectional area of soil is conserved [29], and the cross-sectional area of soil after disturbance should satisfy the following:

$$S_{EE_1F_1F} = S_{CDE} + S_{C_1D_1E_1} + S_{GC_1H_1H} \tag{4}$$

where S_{EE₁F₁F} is the cross-sectional area of soil in the backfill area, mm². S_{KDE} and S_{K₁D₁E₁} are the cross-sectional areas of the falling soil after being laterally thrown, mm².

The soil disturbance behavior of the furrow opener is inevitable. The fallback soil is mainly observed in EE₁F₁F, DKE and D₁K₁E₁ regions [8], and the filled area is mainly the F₁F₁ region of the lower fertilizer furrow. When the soil’s return depth *h* is higher than the depth *h*₁ of the lower fertilizer furrow (that is, *h* > *h*₁) the furrow opener realizes the soil’s return function.

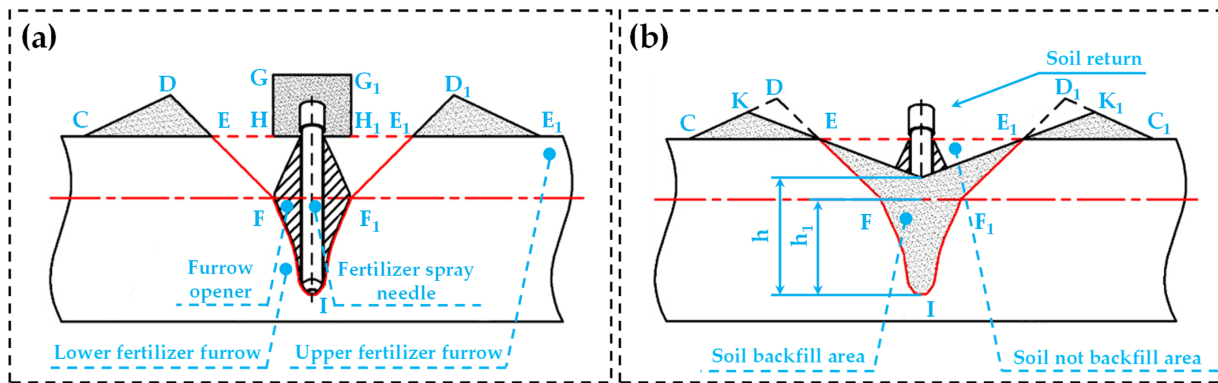


Figure 10. Schematic diagram of soil-returning behavior of high-efficiency soil-returning liquid-fertilizer deep-application furrow opener. (a) Schematic diagram of soil disturbance behaviors. (b) Schematic diagram of the soil-return principle.

4.2. Disturbed Surface Analysis

The main function of the disturbed soil surface is to break the soil and promote the falling back of soil into the furrow. The disturbed soil surface of the furrow opener with the wedge-shaped surface structure [30] is shown in Figure 11, and the LL₁ spacing is width l . The dynamic analysis of a single soil particle on the disturbed soil is describes as follows:

$$\begin{cases} F_{Ny} + f_{yz} \sin \frac{\beta}{2} - f_{xy}' = ma_y \\ F_{Nz} - mg - f_{yz} \cos \frac{\beta}{2} = ma_z \\ \Sigma F = (F_{Nz}^2 + F_{Ny}^2 + F_{Nz}^2)^{\frac{1}{2}} \\ f_{xy}' = \tan \varphi \sin \frac{\alpha}{2} (F_{Nz}^2 + F_{Ny}^2)^{\frac{1}{2}} \end{cases} \quad (5)$$

where ΣF is the resultant force of soil particles on the disturbed soil surface, N . F_{Ny} is the component force of the resultant force on the soil particle in the y direction, N . F_{Nz} is the component force of the resultant force on the soil particle in the x direction, N . f_{yz} is the friction force of soil particles in the yOz plane, N . a_y is the acceleration of soil particles in the y direction on the disturbed soil' surface, $m s^{-2}$. a_z is the acceleration of soil particles in the z direction on the disturbed soil surface, $m s^{-2}$.

Arrange Equation (5) to obtain the following.

$$\begin{cases} a_y = \Sigma F (\cot \frac{\alpha}{2} - \tan \varphi) \left(1 + \cot^2 \frac{\beta}{2} + \tan^2 \frac{\alpha}{2}\right)^{-\frac{1}{2}} m^{-1} \\ a_z = \Sigma F \left(\tan \frac{\beta}{2} - \tan \varphi\right) \left(1 + \cot^2 \frac{\beta}{2} + \tan^2 \frac{\alpha}{2}\right)^{-\frac{1}{2}} m^{-1} \end{cases} \quad (6)$$

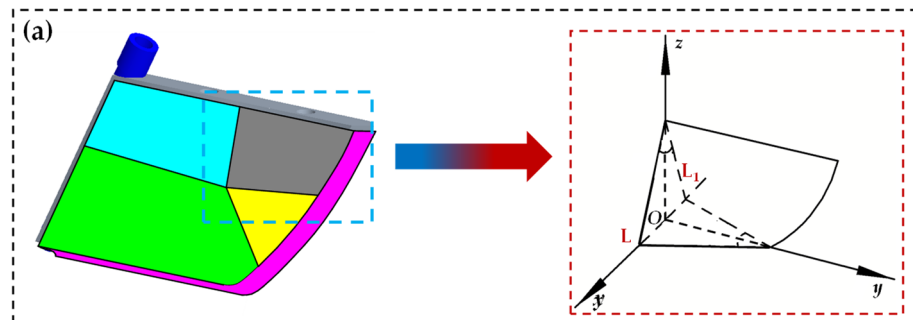


Figure 11. Cont.

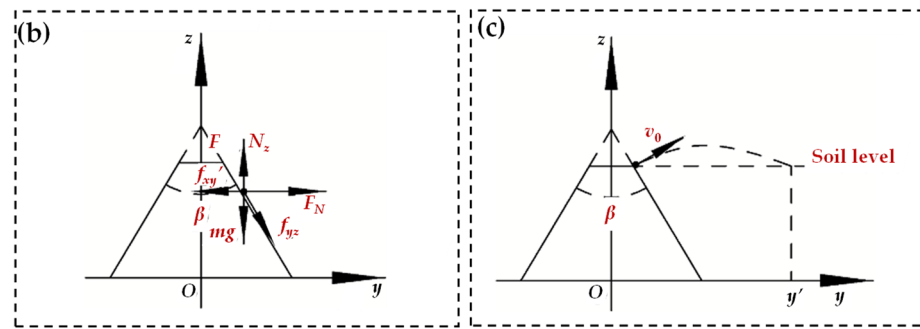


Figure 11. Schematic diagram of disturbed soil surface structure and kinematic analysis of soil particles. (a) Schematic diagram of disturbed soil surface structure. (b) Force analysis of soil particles. (c) Analysis of oblique throwing motion of soil particles.

It can be seen from Equation (6) that acceleration a_y in the y direction and acceleration a_z in the z direction are related to angle α and angle β , and angle α and angle β are related to width l . When the width increases, angle α and angle β increase, the acceleration a_y in the y direction decreases, the acceleration a_z in the z direction increases, the lateral extrusion force of the disturbed soil surface on the soil decreases, and the breaking force on the upper soil layer increases, which is conducive to breaking the soil.

The kinematic analysis of soil particles on the disturbed soil surface is carried out, as shown in Figure 11b. Soil particles on the disturbed soil surface can be approximately regarded as oblique throwing motions [31]. v_0 is the initial velocity of oblique throwing motion and y' is the horizontal displacement of oblique throwing motion. The oblique throwing equation of soil particles is shown in Equation (7).

$$y' = v_0^2 \sin \frac{\beta}{2} g^{-1} \tag{7}$$

The larger the width l , the larger the angle β , and the better the effect of disturbed soil surface on soil loosening and breaking, but the lateral throwing displacement y' of soil particles increases accordingly, which is difficult for the thrown soil to fall back. When $\alpha = \beta = 90^\circ$, $a_y = a_z$ and $F_{Ny} = F_{Nz}$, the extruding and breaking effects of disturbed soil surface are consistent. When the width continues to increase, as width l increases, the amount of externally thrown soil and externally throwing horizontal displacement continues to increase, which is likely to cause a decrease in the amount of returned soil. At the same time, the soil disturbance behaviors on the disturbed soil's surface mainly include breaking and lateral throwing, and with the increase in the furrow's width and the amount of lateral throwing soil, the cross-sectional area of the furrow contour increases. According to the soil disturbance rate equation, the cross-sectional area of the furrow contour increases and the soil disturbance rate increases.

4.3. Guide Inclined Surface Analysis

The guide inclined surface is used to guide the loose and broken soil to fall back into the fertilizer furrow. The soil flows to the tail of the furrow opener along the guided inclined surface and finally falls into the fertilizer spray needle to achieve falling soil and burial of the fertilizer. The structure of the guided inclined surface is shown in Figure 12.

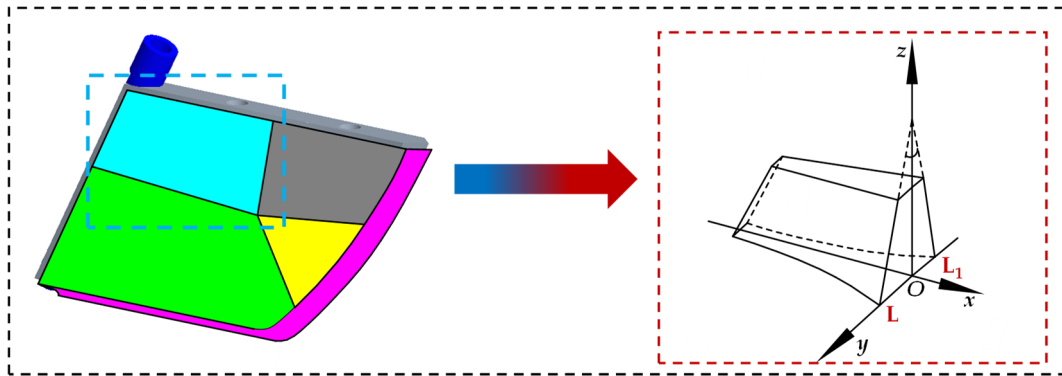


Figure 12. Schematic diagram of guide inclined surface structure.

4.4. Analysis of Extruded Soil Surface

The extruded soil surface is mainly used to push the soil during the operation of the furrow opener to form a fertilizer furrow. The structure of the extruded soil surface is shown in Figure 13.

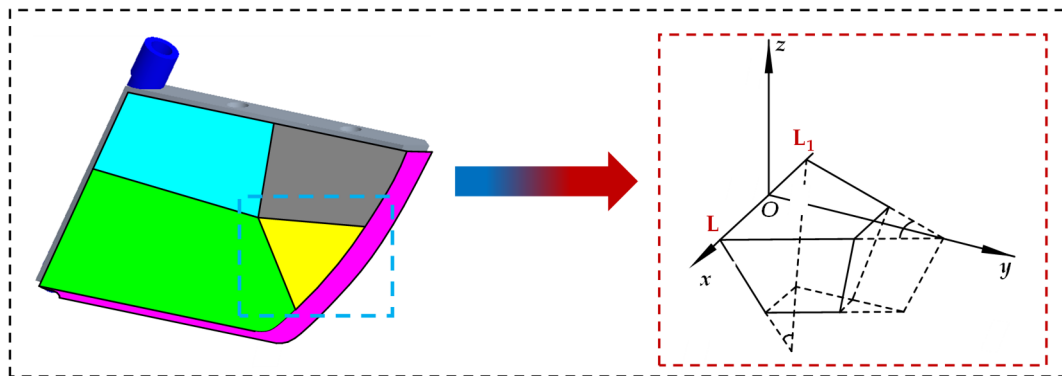


Figure 13. Schematic diagram of the extruded soil surface structure.

4.5. Analysis of Shaping Surface

The shaping surface extrudes the soil so as to achieve the purpose of shaping the fertilizer furrow and the furrow wall. The structure diagram of the shaping surface is shown in Figure 14a. The dynamics and force analysis of a single soil particle on the shaping surface are shown in Figure 14b,c.

The dynamic equations of a single soil-particle column along x , y and z directions on the shaping surface are described as follows:

$$\begin{cases} F_{Nx} + f_{xy} \cos \frac{\gamma}{2} = ma_x \\ F_{Ny} + f_{yz}' - f_{xy}' = ma_y \\ F_{Nz} + f_{yz} \sin \frac{\gamma}{2} + mg = ma_z \\ \Sigma F = (F_{Nx}^2 + F_{Ny}^2 + F_{Nz}^2)^{\frac{1}{2}} \\ f_{xy}' = \tan \varphi \sin \delta (F_{Nx}^2 + F_{Ny}^2)^{\frac{1}{2}} \\ f_{yz}' = \tan \varphi \sin \frac{\gamma}{2} (F_{Ny}^2 + F_{Nz}^2)^{\frac{1}{2}} \end{cases} \quad (8)$$

where ΣF is the resultant force on the shaping surface of soil particles, N . f_{xy}' is the component force of f_{xy} in the y direction, N . f_{yz}' is the component force of f_{yz} in the y direction, N . δ is the angle between the shaping surface and the x -axis, ($^\circ$).

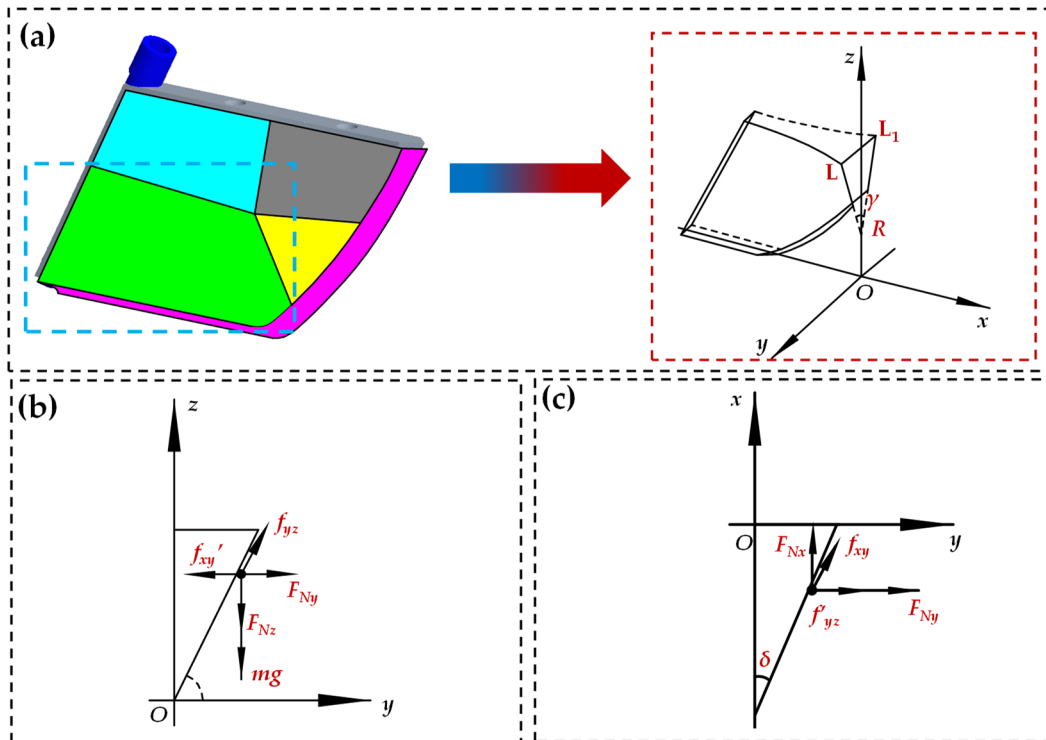


Figure 14. Schematic diagram of the guide inclined surface structure. Schematic diagram of the shaping surface structure and soil particle kinematics analyses. (a) Schematic diagram of the disturbed soil surface structure. (b) Force analysis on the yOz plane. (c) Force analysis on the xOy plane.

Sort Equation (8).

$$\begin{cases} a_x = F_{Nx}(\tan \delta + \tan \varphi)(1 + \cot^2 \frac{\gamma}{2} + \tan^2 \delta)^{-\frac{1}{2}} m^{-1} \\ a_y = F_{Ny}[1 + \tan \varphi(\cot \frac{\gamma}{2} - \tan \delta)](1 + \cot^2 \frac{\gamma}{2} + \tan^2 \delta)^{-\frac{1}{2}} m^{-1} \\ a_z = F_{Nz}(\cot \frac{\gamma}{2} - \tan \varphi)(1 + \cot^2 \frac{\gamma}{2} + \tan^2 \delta)^{-\frac{1}{2}} m^{-1} + g \end{cases} \quad (9)$$

It can be seen from Equation (9) that pressures F_{Ny} and F_{Nz} in the horizontal and vertical directions of the soil on the shaping surface play a major role in shaping the furrow wall, and they are only related to angles γ and δ , which are determined by the width; thus, the operating performance of the shaping surface is related to the width. When the width increases, a_y and a_z increase. The horizontal and vertical pressures F_{Ny} and F_{Nz} of the shaping surface on soil increase, and the downward extruding ability of the shaping surface on soil increases. However, with the increase in width, the extrusion of the furrow opener’s shaping surface on the soil is intensified, resulting in a furrow shape that is too wide and the soil is unable to bury the fertilizer well.

4.6. Analysis of Sliding–Cutting Edge

The high-efficiency soil-returning liquid fertilizer furrow opener cuts the soil by the sliding–cutting edge. During the sliding and cutting process, the soil is extruded by the sliding–cutting edge until the soil stress reaches the failure limit and shear fracture occurs [32]. The dynamics analysis of soil particle M on the xOz plane is carried out, as shown in Figure 15.

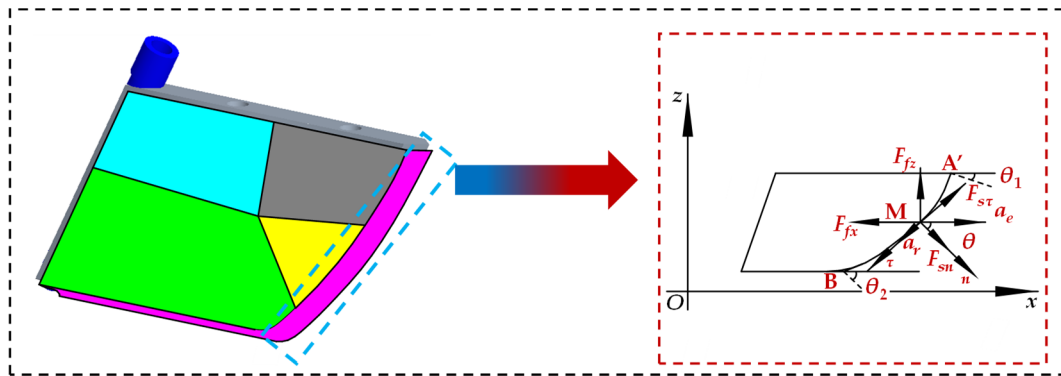


Figure 15. Dynamics analysis of soil particles at the sliding-cutting edge.

In Figure 15, the particle’s dynamics equations of particle M along the τ direction (tangential direction) and the n direction (normal direction) are as follows:

$$\begin{cases} F_{Ns} - F_{fx} \cos \theta - F_{fz} \sin \theta = ma_e \cos \theta \\ F_{s\tau} - F_{fx} \sin \theta - F_{fz} \cos \theta = m(a_e \sin \theta - a_r) \\ F_{s\tau} = F_{sn} \tan \varphi \end{cases} \quad (10)$$

where m is the mass of the soil particle M, kg. θ is the slip cutting angle, $^\circ$. φ is the soil friction angle, $^\circ$. a_r is the relative acceleration of the soil particle M, m/s^2 . a_e is the involved acceleration of the soil particle M, m/s^2 . F_{sn} is the positive pressure on the soil particle M, N. $F_{s\tau}$ is the tangential force on the soil particle M, N. F_{fx} is the component force along the x -axis of the resistance given to the soil particle M by the surrounding soil on the xOy plane, N. F_{fz} is the component force along the y -axis, N, of the resistance given by the soil particle M by the surrounding soil in the xOy plane.

Simplify Equation (10) to obtain the following.

$$F_{sn}(\tan \theta - \tan \varphi) - F_{fz} \sin^{-2} \theta = ma_r \quad (11)$$

From Equation (11), it can be seen that when the slip cutting angle is greater than the soil’s friction angle (that is, $\theta > \varphi$), the relative acceleration of the particle is $a_r > 0$, and the sliding-cutting edge produces sliding-cutting actions on the soil [32]; the larger the slip cutting angle, the stronger the sliding-cutting action of the sliding-cutting edge on the soil [33]. For the convenience of analysis, θ_1 on the sliding-cutting edge in Figure 16 is defined as the initial slip cutting angle, and θ_2 is the terminational slip cutting angle. There is always $\theta_1 < \theta < \theta_2$ on the sliding-cutting edge. When the initial slip cutting angle θ_1 is determined, the larger the terminational slip cutting angle θ_2 , the larger slip cutting angle θ anywhere on the sliding-cutting edge, and the larger the terminational slip cutting angle θ_2 , the stronger the sliding-cutting action of the sliding-cutting edge on the soil [34]. The shape of the sliding-cutting edge is a parabola AB, as shown in Figure 17.

The equation of the sliding-cutting curve AB is defined as follows.

$$z = ax^2 \quad (12)$$

The equation of the sliding-cutting curve AB is defined as follows.

$$\begin{cases} z'_A = \tan\left(\frac{\pi}{2} - \theta_1\right) = 2ax_1 \\ z'_B = \tan\left(\frac{\pi}{2} - \theta_2\right) = 2ax_2 \end{cases} \quad (13)$$

The equation of the parabola AB is defined as follows.

$$z = (\cot \theta_1 - \cot \theta_2)x^2 z_{AB}^{-1} \quad (14)$$

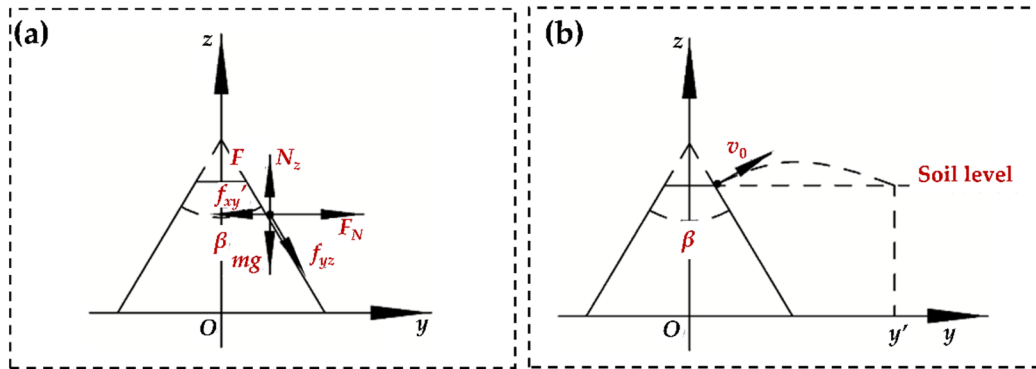


Figure 16. Sliding-cutting curve and soil particle motion analysis. (a) Sliding-cutting curve. (b) Distance of soil particles moving along the sliding-cutting edge.

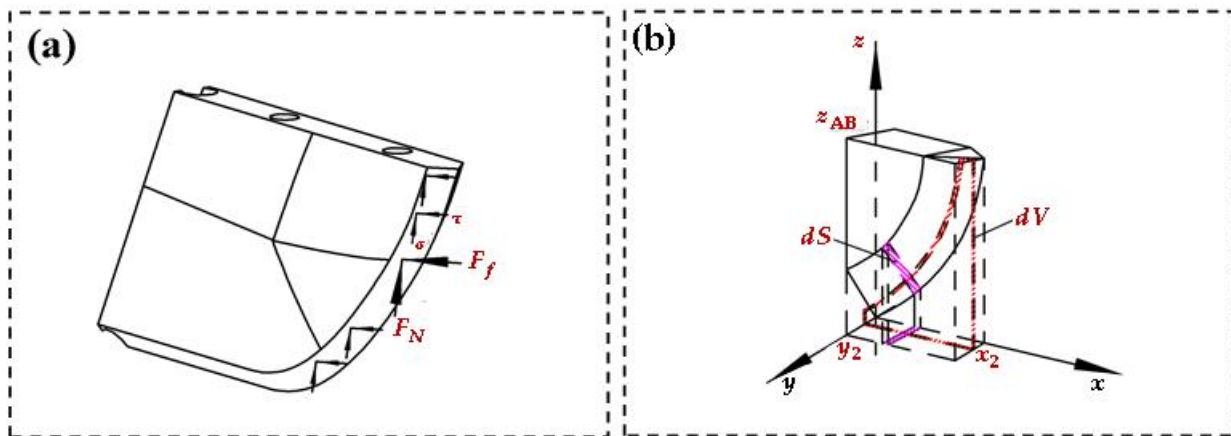


Figure 17. Analysis of the interaction between the sliding-cutting force and soil. (a) The force of the sliding-cutting edge. (b) The interaction analysis between the sliding-cutting edge and the soil.

It can be seen from Equation (14) that the shape of the sliding-cutting curve is jointly determined by the initial slip cutting angle θ_1 , the terminational slip cutting angle θ_2 and the furrow opener height z_{AB} . The kinematics analysis of soil particles at different terminational slip cutting angles is carried out, as shown in Figure 17b. The black-line terminational slip cutting angle is θ_2 , which is smaller than the red-line terminational slip cutting angle θ_2' . Set the furrow opener operating at speed v and calculate the movement path of soil particles on the furrow opener after it advances at a certain distance.

$$S_{\theta_2} = \int_{x_2}^{x_4} \left[\left(\frac{\cot \theta_1 - \cot \theta_2}{2} \right)^{\frac{1}{2}} z_{AB}^{-\frac{1}{2}} \right] x dx \tag{15}$$

$$S_{\theta_2'} = \int_{x_3}^{x_4} \left[\left(\frac{\cot \theta_1 - \cot \theta_2'}{2} \right)^{\frac{1}{2}} z_{AB}^{-\frac{1}{2}} \right] x dx \tag{16}$$

Simplify the above equation as follows.

$$S_{\theta_2} = \frac{2}{3} \left(1 + \frac{\cot \theta_1 - \cot \theta_2}{z_{AB}} \right) \left(x_4^{\frac{3}{2}} - x_2^{\frac{3}{2}} \right) \tag{17}$$

$$S_{\theta_2'} = \frac{2}{3} \left(1 + \frac{\cot \theta_1 - \cot \theta_2'}{z_{AB}} \right) \left(x_4^{\frac{3}{2}} - x_3^{\frac{3}{2}} \right) \tag{18}$$

From Equations (17) and (18), the sliding distance s of soil particles along the sliding-cutting edge is determined by the terminational slip cutting angle θ_2 . When the furrow

opener operates at speed v and travels through a certain operating stroke, if the slip cutting angle θ_2 is larger, the soil particles will slide rapidly along the sliding-cutting edge [34], and the soil will quickly move along the sliding-cutting edge to the part with larger slip cutting angle.

During the operation of the furrow opener, the soil on which the sliding-cutting edge acts is a deformed body, and the stress situation is relatively complex; thus, a material mechanics method is used for analysis, as shown in Figure 17.

Since the sliding-cutting edge is a symmetrical structure, only one side of the sliding-cutting edge is needed for mechanical analysis. When the sliding-cutting edge interacts with the soil, the extrusion force of the soil on the sliding-cutting edge comes from normal stress, and the resistance of the furrow opener comes from the shear stress, as shown in Figure 17a. According to the mechanics of materials, the integral of the stress on the contact area between the sliding-cutting edge and the soil is the force on the sliding-cutting edge, as shown in Equation (19):

$$\begin{cases} F_N = \iint \sigma dS \\ F_f = \iint \tau dS \end{cases} \quad (19)$$

where S is the contact area between the sliding-cutting edge and soil, mm^2 .

The contact surface between the sliding-cutting edge and the soil is a curved surface, and directly calculating the contact area is difficult. Therefore, the contact area and the extruded soil volume between the sliding-cutting edge and the soil are calculated by integration, as shown in Figure 17b, and the calculation of the contact area is shown in Equation (20).

$$\begin{aligned} S &= \int_0^{y_1} \left\{ \int_0^{x_1} \frac{1}{\cos \theta_2} \left[1 + \left(\frac{\cot \theta_1 - \cot \theta_2}{2z_{AB}} x \right)^2 dx \right]^{\frac{1}{2}} dy \right. \\ &= \frac{1}{\cot^2 \theta_1 + \cot^2 \theta_2 - 2 \cot^2 \theta_1 \sin \theta_2} \left\{ \begin{aligned} &\frac{x_1}{2} \left(1 + \frac{\cot \theta_1 - \cot \theta_2}{4z_{AB}^2} x_1^2 \right) \\ &+ \ln \left[x + \left(1 + \frac{\cot \theta_1 - \cot \theta_2}{4z_{AB}^2} x_1^2 \right) \right] \end{aligned} \right\} \end{aligned} \quad (20)$$

S is the contact area between the sliding-cutting edge and the soil. It can be seen that the larger the terminational slip cutting angle θ_2 , the larger the contact area between the sliding-cutting edge and the soil, and the greater the extrusion force of the sliding-cutting edge on the soil and, thus, the greater the resistance from the soil, which indicates that the terminational slip cutting angle is the main factor affecting the extruding effect of the sliding-cutting edge on the soil. In order to quantify the degree of soil extrusion by the sliding-cutting edge, an integral equation is used to calculate the amount of soil extrusion.

$$V = \int_0^{y_1} \left[\int_0^{x_1} \frac{\cot \theta_1 - \cot \theta_2}{z_{AB}} x^2 dx \right] dy = \frac{\cot \theta_1 - \cot \theta_2}{3z_{AB}} x_1^3 y_1 \quad (21)$$

According to Equation (21), it can be seen that as the terminational slip cutting angle θ_2 increases, the amount of soil extruded by the sliding-cutting edge increases. To sum up, the terminational slip cutting angle θ_2 is an important factor affecting the operating performance of the sliding-cutting edge. The increase in the terminational slip cutting angle θ_2 increases the cutting ability of the sliding-cutting edge on soil, but at the same time, it will increase the resistance of the furrow opener and cause the soil to rapidly flow to the sliding-cutting edge with a larger slip cutting angle, resulting in soil accumulation. At this time, the sliding-cutting edge severely extrudes the soil, and then the soil is compressed and bonded. the amount of broken soil is reduced, and the soil's return performance worsens. According to the research of Zhao et al. [35], when the value of the terminational slip cutting angle θ_2 is between 35° and 55° , improving the soil's breaking performance of the sliding-cutting edge and improving the soil's return performance of the furrow opener are beneficial. When increasing the terminational slip cutting angle, the sliding-cutting effect of the sliding-cutting edge on the soil is enhanced, the soil has better fluidity on the surface of

the sliding–cutting edge, the degree of soil extrusion is lighter, and the cross-sectional area of the furrow contour is small. According to the soil disturbance rate equation, the soil’s disturbance rate does not change significantly. When the terminational slip cutting angle is too large, the sliding–cutting edge mainly pushes the soil; a large amount of soil flows rapidly to the part with a larger slip cutting angle, and soil accumulation occurs at the terminational slip cutting angle. The soil is extruded during the operation of the furrow opener, which results in soil compression. The amount of broken soil decreases, the cross-sectional area of the furrow contour increases, and the soil disturbance rate increases rapidly.

4.7. Analysis of Furrow Contour Parameter Results in Soil Bin Verification Test

The test results of the virtual simulation and the soil bin verification tests are basically the same, but the maximum lateral throwing soil width and furrow width in the soil bin verification test are slightly smaller than those of the virtual simulation, and the soil-return depth is slightly higher than that of the virtual simulation. The reason is that the volume and mass of soil particles in the virtual simulation is larger than that of actual soil particles, which affects the particle’s movement behavior during virtual simulation operation, resulting in parameter differences [36–38].

4.8. Analysis of High-Speed Camera Results of Soil Bin Verification Test

Based on the qualitative comparison and analysis of the soil disturbance behavior of the two, it can be seen that, under the same conditions, the particle’s velocity area formed during the operation of high-efficiency soil-returning liquid-fertilizer furrow opener is basically the same, and the soil disturbance behavior and soil movement state of the furrow opener are basically the same. The parameter settings in the EDEM virtual simulation are more accurate [39].

4.9. Analysis of Soil Bin Performance Test Results

When the operating speed is low, the soil is compressed and bonded by the extruding action of the furrow opener, and the amount of broken soil is small, and the depth of soil return is low. When the speed is too high, the soil’s return depth decreases sharply. The reason is that the high operating speed accelerates the soil disturbance behavior of the furrow opener and increases the amount of soil thrown out, leading to a difficulty in the soil’s ability to fall back, and the soil’s return depth decreases.

5. Conclusions

We found that the key parameters of the high-efficiency soil-returning liquid-fertilizer deep-application furrow opener with low disturbance and high soil return include the width and slip cutting angle, which have significant impacts on the soil’s return rate and soil-return depth. The parameter combination suitable for the cold region of Northeast China is a slip cutting angle of 43.27° and a width of 37.52 mm.

Under the optimal combination of structural parameters, the soil disturbance rate of the high-efficiency soil-return liquid-fertilizer opener is 50.23% and the soil-return depth is 50.9 mm. According to the virtual simulation verification of the optimized results, the soil disturbance rate is 51.81% and the soil-return depth is 52.6 mm, which is basically consistent with the optimized results.

The interaction process of the sliding–cutting edge soil, wedge surface soil and the mechanical and kinematic models of the furrow opener constructed by us can provide a theoretical basis for the design of future furrow openers. The qualitative and quantitative analyses of soil disturbance behaviors and soil-return performance of the high-efficiency return liquid-fertilizer opener at different forward speeds (0.2, 0.4, 0.6, 0.8, 1.0 and 1.2 m s^{-1}) of the opener were conducted. The qualitative analysis showed that the soil disturbance behavior of the opener gradually intensified with the increase in forward speed, and the soil’s return performance was first enhanced and then weakened with the increase in forward speed, and the appropriate soil disturbance behavior can, to a certain extent,

promote the soil's return performance of the high-efficiency soil return liquid-fertilizer opener. The quantitative analysis showed that the soil disturbance rate ρ was moderate in the speed range of 0.4–1.0 m s⁻¹, and the minimum and maximum values of soil-return depth h reached 52.1 mm and 55.8 mm, respectively, which both met the design requirements of the high-efficiency soil-return liquid-fertilizer opener.

We only conducted experiments and studies on soil conditions in the cold region of Northeast China, and further studies on soil applicability in other regions are needed.

Author Contributions: Conceptualization, W.Z.; software, C.S. and X.S.; validation, Z.L.; formal analysis, X.N. and K.S.; resources, Y.J.W.; data curation, L.T.; writing—original draft preparation, W.Z.; writing—review and editing, Y.J.W.; supervision, Y.J.W.; project administration, Y.J.W.; funding acquisition, Y.J.W. All authors have read and agreed to the published version of the manuscript.

Funding: This research was financially supported by the Natural Science Foundation of China (Grant No. 51905086), China Postdoctoral Science Foundation Funded Project (Grant No. 2019M66124), Heilongjiang Postdoctoral Science Foundation Specially Funded Project (Grant No. LBH-Z19044), and Heilongjiang Province General Undergraduate Higher Education Institution Young Innovative Talents Training Program (UNPYSCT-2020100).

Institutional Review Board Statement: Not applicable.

Data Availability Statement: Not applicable.

Acknowledgments: The authors would like to thank their schools and colleges, as well as the funding providers of the project. All support and assistance are sincerely appreciated.

Conflicts of Interest: The authors declare no conflict of interest.

Nomenclature

L	The opener width (mm)
θ	The slip cutting angle (°)
θ_1	The initial slip cutting angle (°)
θ_2	The larger the terminational slip cutting angle θ_2 (°)
φ	The soil friction angle (°)
ρ	The soil disturbance rate (%)
h	The higher the soil-return depth (mm)

References

- Sun, B.; Jia, S.; Zhang, S.; McLaughlin, N.B.; Zhang, X.; Liang, A.; Chen, X.; Wei, S.; Liu, S. Tillage, seasonal and depths effects on soil microbial properties in black soil of Northeast China. *Soil Tillage Res.* **2016**, *155*, 421–428. [[CrossRef](#)]
- Zhang, S.; Chen, X.; Jia, S.; Liang, A.; Zhang, X.; Yang, X.; Wei, S.; Sun, B.; Huang, D.; Zhou, G. The potential mechanism of long-term conservation tillage effects on maize yield in the black soil of Northeast China. *Soil Tillage Res.* **2015**, *154*, 84–90. [[CrossRef](#)]
- Qu, Y.; Pan, C.; Guo, H. Factors Affecting the Promotion of Conservation Tillage in Black Soil—The Case of Northeast China. *Sustainability* **2021**, *13*, 9563. [[CrossRef](#)]
- Liu, Q.; Wu, K.; Song, W.; Zhong, N.; Wu, Y.; Fu, X. Improving crop nitrogen use efficiency toward sustainable green revolution. *Annu. Rev. Plant Biol.* **2022**, *73*, 523–551. [[CrossRef](#)] [[PubMed](#)]
- Pimentel, D. Green revolution agriculture and chemical hazards. *Sci. Total Environ.* **1996**, *188*, S86–S98. [[CrossRef](#)]
- Han, T.; Jinwu, W.; Changsu, X.U.; Wenqi, Z.; Jinfeng, W.; Xiu, W. Research progress analysis on key technology of chemical fertilizer reduction and efficiency increase. *Nongye Jixie Xuebao/Trans. Chin. Soc. Agric. Mach.* **2019**, *50*, 1–19.
- Shi, C.L.; Li, Y.; Zhu, J.F. Rural labor transfer, excessive fertilizer use and agricultural non-point source pollution. *J. China Agric. Univ.* **2016**, *21*, 169–180.
- Zhu, L.Z.; Qiu, J.; Fang, X. Soil conservation measures and enlightenment in foreign countries. *Soil Fertil. Ences China* **2015**, *2*, 1–4.
- Chen, Y.; Zhang, Q.; Petkau, D.S. Evaluation of different techniques for liquid manure application on grassland. *Appl. Eng. Agric.* **2001**, *17*, 489. [[CrossRef](#)]
- Swanepoel, P.A.; Labuschagne, J. Canola is injured by in-row nitrogen placement associated with disc openers, but not by tine openers. *Crop Sci.* **2020**, *60*, 466–474. [[CrossRef](#)]
- Xie, J.S.; Yang, Y.S.; Chen, G.S.; Zhu, J.M.; Zeng, H.D.; Yang, Z.J. Effects of vegetation restoration on water stability and organic carbon distribution in aggregates of degraded red soil in subtropics of China. *Acta Ecol. Sin.* **2008**, *28*, 702–709.

12. Zhang, L.; He, Y.; Yang, H.; Tang, Z.; Zheng, X.; Meng, X. Analysis of the relationship between the development of liquid fertilizer machinery and modern agriculture. *J. Chin. Agric. Mech.* **2021**, *42*, 34–40.
13. Wenqi, Z.; Hong, X.; Ziming, L.I.U.; Jinwu, W.; Huinan, H.; Aoxue, W. Design and Test of SYJ-3 Deep Application-type Inclined Liquid Fertilizer Hole Applicator. *Nongye Jixie Xuebao/Trans. Chin. Soc. Agric. Mach.* **2020**, *51*, 78–86.
14. Wang, J.; Wen, N.; Liu, Z.; Zhou, W.; Tang, H.; Wang, Q.; Wang, J. Coupled Bionic Design of Liquid Fertilizer Deep Application Type Opener Based on Sturgeon Streamline to Enhance Opening Performance in Cold Soils of Northeast China. *Agriculture* **2022**, *12*, 615. [[CrossRef](#)]
15. Wang, J.; Pan, Z.; Zhou, W.; Wang, J.; He, J.; Lang, C. Design and test of SYJ-2 type liquid variable fertilizer. *Trans. Chin. Soc. Agric. Mach.* **2015**, *46*, 53–58.
16. Godwin, R.J.; Spoor, G. Soil failure with narrow tines. *J. Agric. Eng. Res.* **1977**, *22*, 213–228. [[CrossRef](#)]
17. Godwin, R.J. A review of the effect of implement geometry on soil failure and implement forces. *Soil Tillage Res.* **2007**, *97*, 331–340. [[CrossRef](#)]
18. Solhjou, A.; Desbiolles, J.M.; Fielke, J.M. Soil translocation by narrow openers with various blade face geometries. *Biosyst. Eng.* **2013**, *114*, 259–266. [[CrossRef](#)]
19. Rodhe, L.; Etana, A. Performance of slurry injectors compared with band spreading on three Swedish soils with ley. *Biosyst. Eng.* **2005**, *92*, 107–118. [[CrossRef](#)]
20. Shuhong, Z.; Hongjun, L.; Hewen, T. Design and performance experiment of opener based on bionic sailfish head curve. *Trans. Chin. Soc. Agric. Eng.* **2017**, *33*, 32–39.
21. Beyaz, A.; Gerdan, D. Computer-aided Stress Analysis of a Model of Tractor Mounted Auger Drill. *Agric. Sci. Dig.-A Res. J.* **2019**, *39*, 90–95. [[CrossRef](#)]
22. Bravo, E.L.; Tijkskens, E.; Suárez, M.H.; Cueto, O.G.; Ramon, H. Prediction model for non-inversion soil tillage implemented on discrete element method. *Comput. Electron. Agric.* **2014**, *106*, 120–127. [[CrossRef](#)]
23. Mak, J.; Chen, Y.; Sadek, M.A. Determining parameters of a discrete element model for soil–tool interaction. *Soil Tillage Res.* **2012**, *118*, 117–122. [[CrossRef](#)]
24. Topp, G.C.; Parkin, G.W.; Ferré, T.P.A.; Carter, M.R.; Gregorich, E.G. Soil water content. In *Soil Sampling and Methods of Analysis*; Canadian Society of Soil Science: Pinawa, MB, Canada, 2008; pp. 939–962.
25. Li, J.; Tong, J.; Hu, B.; Wang, H.B.; Mao, C.Y.; Ma, Y. Calibration of parameters of interaction between clayey black soil with different moisture content and soil-engaging component in northeast China. *Trans. CSAE* **2019**, *35*, 130–140.
26. Tian, X.; Cong, X.; Qi, J.; Guo, H.; Li, M.; Fan, X. Parameter Calibration of Discrete Element Model for Corn Straw-Soil Mixture in Black Soil Areas. *Trans. Chin. Soc. Agric. Mach.* **2021**, *52*, 100–108+242.
27. Zhao, J.; Wang, X.; Zhuang, J.; Liu, H.; Wang, Y.; Yu, Y. Coupled Bionic Design Based on Primnoa Mouthpart to Improve the Performance of a Straw Returning Machine. *Agriculture* **2021**, *11*, 775. [[CrossRef](#)]
28. Liu, H.; Han, J.; Chen, J.; Lv, J.; Zhao, S. Performance simulation and experiment on rigid press wheel for hilly area. *Nongye Jixie Xuebao/Trans. Chin. Soc. Agric. Mach.* **2018**, *49*, 114–122.
29. Shuhong, Z.; Hewen, T.; Jiayi, W. Design and experiment of multifunctional integrated seeding opener. *Trans. Chin. Soc. Agric. Eng. (Trans. CSAE)* **2018**, *34*, 58–67.
30. Xiaodong, Y. The Theory Analysis of Furrower Soil Backfilling. *Agric. Sci. Technol. Equip.* **2014**, *11*, 37–39. [[CrossRef](#)]
31. Jun, S. Simulation Study and Analysis of Materials Conveying Process by the Belt Conveyor Based on EDEM. *Mech. Res. Appl.* **2019**, *32*, 59–61. [[CrossRef](#)]
32. Jia, H.; Zheng, J.; Yuan, H.; Guo, M.; Wang, W.; Jiang, X. Design and experiment of profiling sliding-knife opener. *Trans. Chin. Soc. Agric. Eng.* **2017**, *33*, 16–24.
33. Barr, J.B.; Ucgul, M.; Desbiolles, J.M.A.; Fielke, J.M. Simulating the effect of rake angle on narrow opener performance with the discrete element method. *Biosyst. Eng.* **2018**, *171*, 1–15. [[CrossRef](#)]
34. Jian, Z.; Honglei, J.; Yunhai, M. Design and experiment of sliding-knife-type disc opener. *Trans. Chin. Soc. Agric. Mach.* **2013**, *44*, 83–88.
35. Zhao, S.; Liu, H.; Zhang, X.; Yang, Y.; Lü, B.; Tan, H. Design and optimization experiment of working performance of sliding push opener. *Trans. Chin. Soc. Agric. Eng.* **2016**, *32*, 26–34.
36. Aikins, K.A.; Ucgul, M.; Barr, J.B.; Jensen, T.A.; Antille, D.L.; Desbiolles, J.M.A. Determination of discrete element model parameters for a cohesive soil and validation through narrow point opener performance analysis. *Soil Tillage Res.* **2021**, *213*, 105123. [[CrossRef](#)]
37. Wang, Y.; Xue, W.; Ma, Y.; Tong, J.; Liu, X.; Sun, J. DEM and soil bin study on a biomimetic disc furrow opener. *Comput. Electron. Agric.* **2019**, *156*, 209–216. [[CrossRef](#)]
38. Bai, H.; Li, S.; Wang, D.; Fang, X.; Niu, K.; Zhou, L.; Xiong, S.; Fan, C. Design and EDEM simulation of fertilizer stratification and deep application device. In *Proceedings of the ASABE Annual International Meeting, American Society of Agricultural and Biological Engineers, Boston, MA USA, 7–10 July 2019*; p. 1.
39. Barr, J.; Desbiolles, J.; Ucgul, M.; Fielke, J.M. Bentleg furrow opener performance analysis using the discrete element method. *Biosyst. Eng.* **2020**, *189*, 99–115. [[CrossRef](#)]

Article

Influence of Spray Control Parameters on the Performance of an Air-Blast Sprayer

Yaohua Hu ¹, Huanbo Yang ², Bingru Hou ², Ziting Xi ² and Zidong Yang ^{1,*}¹ College of Optical, Mechanical and Electrical Engineering, Zhejiang A&F University, Hangzhou 311300, China² College of Mechanical and Electronic Engineering, Northwest A&F University, Xianyang 712100, China

* Correspondence: 20150032@zafu.edu.cn

Abstract: Orchard plant protection machinery in China still has a low application efficiency. Air-blast sprayers represent the primary development direction of pesticide applications in orchards. The spray control parameters have to be matched to the tree canopy status to achieve precise results. In this study, a vertical patternator was used to determine the accuracy of spraying fruit trees. The influences of three control parameters (blower speed, spray angle, and spray distance) on the spray performance of the air-blast sprayer were analyzed, and the volume of the spray was measured in collection plates at different heights. The quantitative relationship between the overall collection volume and the critical height collection volume was obtained for different parameter values, and the combined effects of any two control parameters on the collection performance and the position of the optimum collection area were obtained. The regression model describing the relationship between the collection volume in the critical height range and the three factors was established, and the main effects of the control parameters were determined. The results showed that if one parameter remained constant, the correlation between the other two parameters was non-significant. The collection volume in the critical height range increased initially and then decreased as the spray distance increased. The maximum collection volume was obtained at a spray distance of 1.762 m. The regression model can be used to obtain the optimum values of the parameters.

Citation: Hu, Y.; Yang, H.; Hou, B.; Xi, Z.; Yang, Z. Influence of Spray Control Parameters on the Performance of an Air-Blast Sprayer. *Agriculture* **2022**, *12*, 1260. <https://doi.org/10.3390/agriculture12081260>

Academic Editors: Muhammad Sultan, Redmond R. Shamshiri, Md Shamim Ahamed and Muhammad Farooq

Received: 12 July 2022

Accepted: 12 August 2022

Published: 19 August 2022

Publisher's Note: MDPI stays neutral with regard to jurisdictional claims in published maps and institutional affiliations.



Copyright: © 2022 by the authors. Licensee MDPI, Basel, Switzerland. This article is an open access article distributed under the terms and conditions of the Creative Commons Attribution (CC BY) license (<https://creativecommons.org/licenses/by/4.0/>).

Keywords: air-blast sprayer; precision spraying; spray control parameter; three-factor regression analysis

1. Introduction

The development of orchards in China ranks first in the world in terms of area and yield, but economic losses caused by diseases and insect pests are substantial. The effective control of diseases and insect pests in orchards can recover nearly 10% of economic losses [1–3]. At present, the control of diseases and insect pests has primarily relied on chemical pesticides, which are sprayed 8–15 times annually during the growth cycle of apple trees. The workload accounts for about 30% of the total workload of fruit tree management [4–6]. However, most orchard spraying operations use backpack sprayers and frame-mounted sprayers with low spraying efficiency [7–9]. In addition, spraying causes environmental pollution and affects the quality and competitiveness of Chinese agricultural products [10–12]. Air-blast sprayers have a strong flow generated by a blower to penetrate the dense fruit tree canopy; this ensures that the pesticide can reach most parts of the leaves, and the utilization rate of the pesticide is 30–40% [13–16].

The existing orchard spraying equipment does not meet the requirement of accurate detection and spraying on demand, which is a common problem in the world at present [17]. In order to achieve the effect of pest control, excessive spraying is mostly used in actual operation, which leads to a large number of chemical pesticide residues, seriously polluting the ecological environment and threatening the safe production of fruits [18]. Therefore, it will be helpful for the development of orchard spraying machinery to study the intelligent control technology of spraying amount, in order to realize the target variable spraying and

the control method of wind variable to realize the on-demand air supply. The existing spraying control technologies mainly include: the total dosage control pipeline method, and the independent dosage control nozzle method. The total dosage control pipeline method can use the flow sensor to monitor the spraying quantity in real time, and use the electric regulating valve to change the spraying pressure of the pipeline according to the spraying demand, so as to control the spraying quantity. The existing control methods mainly include hysteresis switch control [19], classical PID control [20,21], fuzzy control [22–24] and artificial neural network [25]. In the independent control spray nozzle method, spray nozzles with different flow rates are arranged at different heights to realize different spray amounts. In order to control the nozzle flow, a proportional valve can be added in the front section of the nozzle, and the nozzle flow can be regulated by adjusting the opening of the proportional valve in real time [26–33].

Air-blast sprayers have the advantages of good spray performance, low cost, high efficiency, and low labor intensity; therefore, they are the primary development direction of pesticide applications in orchards [34–39]. In recent years, many researchers worldwide have focused on optimizing the spraying parameters according to the crop canopy status to increase the pesticide utilization rate of air-blast sprayers and improve the precision of spraying technology. In Refs. [39–41], different blower speeds were tested to investigate the influence of the airflow on the collection volume. Farooq & Landers [42] analyzed the wind field of an air-blast sprayer and adjusted the spray distance to achieve the desired effect. He et al. [43] determined the effect of wind speed on the collection volume of the pesticide. The results showed that the penetration and collection volume in the canopy were positively correlated with the wind speed. Lü et al. [44] tested different levels of spray pressure, blower outlet wind speed, driving speed, and sampling height to determine the influence of the parameters of the air-blast sprayer on the collection volume and pesticide distribution. Reichard et al. [45] presented the air velocity distribution of an air-driven orchard sprayer at different driving speeds in the open field and in the peach orchard. With the change of driving speed, the airflow velocity distribution had no significant change, but the tree structure and natural wind speed had a certain influence on the auxiliary airflow velocity. As the distance between the monitoring point and the nozzle outlet increased, the airflow speed decreased rapidly, and the decreasing rate depended on the airflow rate. By establishing a mathematical model, Fox [46,47] calculated the energy of airflow velocity at different positions in the air jet field and estimated the power requirements for designing an axial-flow air-fed sprayer. At the same time, they also simulated the deflection of the auxiliary airflow under the influence of the natural wind speed and the speed of the sprayer, pointing out that the narrower the width of the airflow outlet, the more significant the deflection of the airflow path. Fox and Svebsson [48–50] showed that the combination of two fans with transverse airflow formed a constant airflow organization to improve airflow penetration in low apple trees.

In these studies, the effects of various control parameters on the amount of pesticide at different heights of the canopy were not investigated. In addition, no regression models have been developed to describe the relationship between manually controlled parameters and the spray height.

The blower speed, spray angle, and the distance from the sprayer to the canopy have to be matched to the tree canopy conditions to reduce spray drift. Therefore, the objectives of this study are (1) to analyze the influence of single control parameters on the collection volume of pesticide at different heights; (2) to determine the influence of any two control parameters on the collection volume; (3) to assess the influence of three control parameters on the collection volume at the critical height and establish a regression model; (4) to provide a strategy for precise spray control based on the optimization of the control parameters.

2. Materials and Methods

2.1. Materials and Equipment

The experiment was performed on 20 May 2021 outside of the Agricultural Machinery Laboratory of the College of Mechanical and Electronic Engineering at Northwest A & F University. The daily ambient temperature was 27 ± 1 °C, and the relative humidity was 73%; the influence of wind was negligible.

The equipment used in the experiment included a vertical patternator with a guide rail (Salvarani BVBA, AAMS Company, Maldegem, Belgium); a lead-acid battery (NP-12-24, Ruiwu Electric, Shanghai, China); a tape measure (A5, Aicevoos, Wuhan, China); and an air-blast sprayer (self-developed).

There were 20 collection plates in the vertical patternator, numbered 1–20, as shown in Figure 1. The 20 collection plates were positioned into two columns (left and right), with odd-numbered plates on the left and even-numbered plates on the right. The height range of plate 1 was 225–425 mm, and that of plate 2 was 450–650 mm. Each board was 200 mm tall, and the distance between the boards was 225 mm. The height parameters of the collecting plate of the vertical distributor are shown in Table 1.

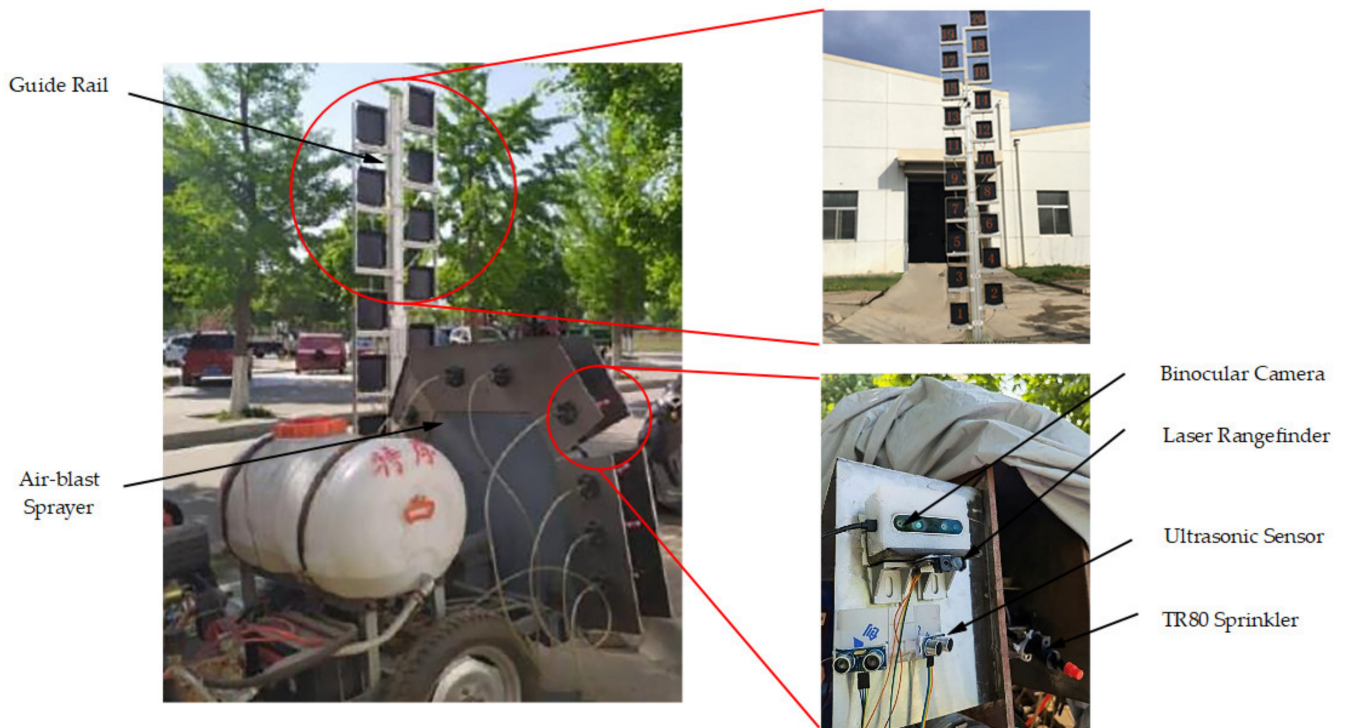


Figure 1. Experimental equipment and experimental ground.

Table 1. The height parameters of collecting plate of vertical distributor.

Number	Height Range (mm)	Number	Height Range (mm)	Number	Height Range (mm)	Number	Height Range (mm)
1	225–425	6	1350–1550	11	2475–2675	16	3600–3800
2	450–650	7	1575–1775	12	2700–2900	17	3825–4025
3	675–875	8	1800–2000	13	2825–3025	18	4050–4250
4	900–1100	9	2025–2225	14	3150–3350	19	4275–4475
5	1125–1325	10	2250–2450	15	3375–3575	20	4500–4700

The vertical patternator was powered by matching lead-acid batteries and achieved a constant speed of 1 m/s on the guide rail; the length of the guide rail was 6 m. A liquid pump was used in the experiment. The sprayer used in the experiment was a self-developed

sprayer (2.75 m × 1.15 m × 1.16 m) with 5 sprinklers (TR80, Lechler, Metzingen, Germany) on one side. The parameters of the sprinkler and liquid pump are shown in Table 2. The spray head was installed on a rotating plate, and the angle of the spray head changed as the plate rotated. An axial-flow fan (SFG4-4, Shanghai Zaize Electric Machinery Factory, Shanghai, China) with 3000 r/min maximum speed was used. The axis of the blower was parallel to the face of plates, and the distance from the ground to the axis was 780 mm.

Table 2. The parameters of main experimental equipment.

Project	Sprinkler	Liquid Pump	Axial-Flow Fan
Diameter (mm)	57	130	415
Length (mm)	155	290	331
Working flow (m ³ /h)	0.04–0.96	2400	5870
Working pressure (bar)	0.25	1.70	1.49
Range (m)	2.50–10.70	—	—
Angle adjustment	0–180°	—	—
Power (W)	—	400	550
Voltage (V)	—	220	220

2.2. Experimental Methods

The influence of the spray control parameters on the collection volume was analyzed. The blower speed (N), the spray angle (W), and the spray distance (L) were the control parameters. In this research, it was 0° when the sprinkler was horizontal to the ground, and the counterclockwise direction was the positive direction of the sprinkler movement. The spray angle was controlled by changing the angle of the rotating plate using a stepper motor, the blower speed was controlled by a hydrostatic device (a speed of 2000 r/min), and the spray distance between the axis of the blower and the axis of the vertical patternator was controlled by moving the blower; the distance was measured with a tape. The control parameters were selected based on previous investigations, a literature review, and the requirements of practical applications. The plates were rotated by controlling the variables and using bilateral spraying of the air-blast sprayer. All the experiments were conducted five times, and the average was obtained. The experimental data of this research would be imported into Origin 2018 for a data analysis and graph drawing.

3. Results and Discussion

3.1. Single-Factor Analysis of Spray Control Parameters for All Collection Plates

Figure 2 shows the relationship between the blower speed and the collection volume for constant values of the spray angle (45°) and the spray distance (1.0 m). Figure 3 shows the relationship between the spray angle and the collection volume for constant values of the spray distance (1.5 m) and blower speed (2400 r/min). Figure 4 shows the relationship between the spray distance and the collection volume for constant values of the spray angle (45°) and blower speed (2400 r/min).

The middle of the tree crown is the crucial target area for spraying; therefore, the collection volumes obtained at heights of 1.35–1.55 m are of primary importance.

As shown in Figure 2, as the blower speed increased from 2000 r/min to 2800 r/min, the collection volume at high heights increased gradually, whereas that at low heights decreased. The total collection volume increased from 532 mL to 627 mL, and that at the height of 1.35–1.55 m decreased from 123 mL to 72 mL.

Figure 3 shows that, as the spray angle increased from 45° to 85°, the collection volume of the lower and middle heights decreased and that of the high heights increased; the total collection volume increased from 592 mL to 653 mL and that at the height of 1.35–1.55 m decreased from 151 mL to 73 mL.

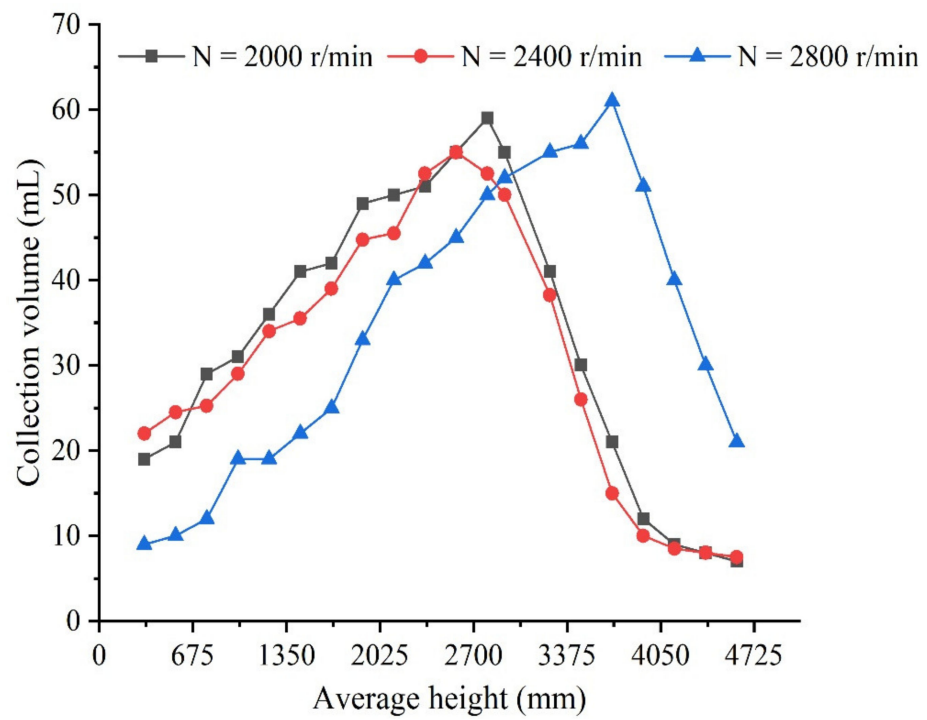


Figure 2. Influence of blower speed on the collection volume ($W = 45^\circ$, $L = 1.0$ m).

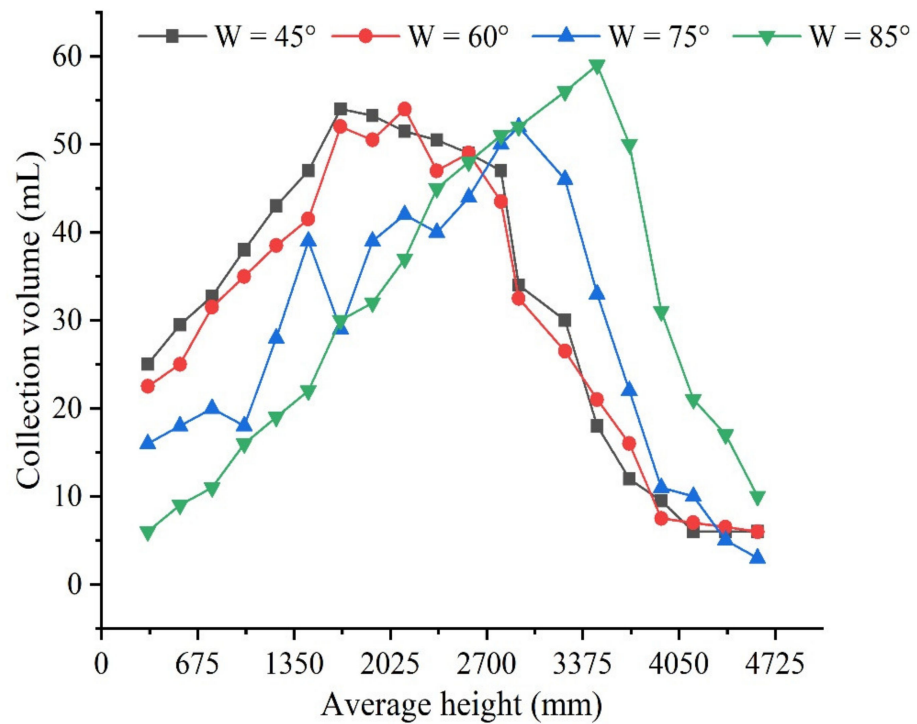


Figure 3. Influence of spray angle on the collection volume ($N = 2400$ r/min, $L = 1.5$ m).

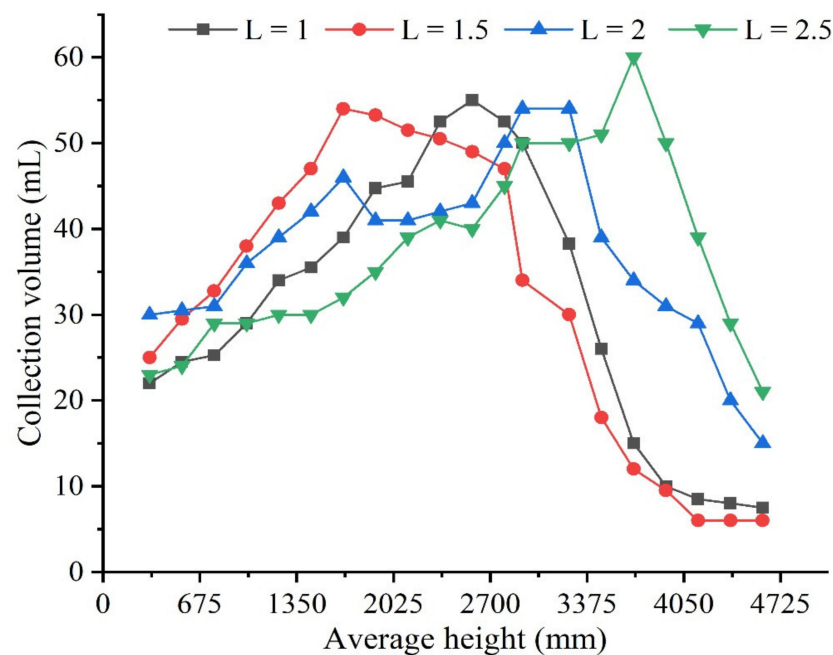


Figure 4. Influence of spray distance on the collection volume ($W = 45^\circ$, $N = 2400$ r/min).

As shown in Figure 4, as the spray distance increased from 1.0 m to 2.5 m, the collection volume of the middle heights increased; the collection volume of the high and lower heights decreased and reached the peak value at a spray distance between 1.5 m and 2.0 m. Then, as the distance increased further, the collection volume of the low heights increased, and that of the high and middle heights decreased. The total collection volume increased from 584 mL to 576 mL, and that at the height of 1.35–1.55 m decreased from 110 mL to 76 mL.

In summary, it is concluded that when the other two factors remain unchanged, the increase in the blower speed and spray angle results in an increase in the collection volume, but the collection volume differs for different heights. When the blower speed increased, the collection volume was larger at high heights and lower at the middle and lower heights. With an increase in the spray angle, the collection volume was larger in the upper plates and lower in the middle and lower plates.

Due to the parabolic trajectory of the droplets, the spray distance affects the collection volume; at a relatively short spray distance, an increase in the spray distance increases the collection volume at higher and middle heights. However, when the spray distance is relatively large, the collection volume is larger at high heights and lower at low heights.

3.2. Two-Factor Analysis of the Spray Control Parameters

The average height range of 0.325–3.25 m was selected for the two-factor analysis because it provided a good representation of the changes in the collection volume, as shown in Figures 2 and 3.

In this experiment, the spray distance was 1.0 m, and the spray angles were 60° and 75° . As shown in Figure 5a,b, when the spray angle and blower speed both increased, the peak of the curve moved to the right. When the blower speed increased and the spray angle decreased, the peak moved to the right, the peak value was higher, and the curve was more even.

In practical applications, when the blower speed and spray angle both increase, the collection volume is higher in the upper part of the tree crown, but the overall collection volume does not change. When the spray angle increased and the blower speed decreased in the experiment, the optimum spray area moved to the higher height, but the collection volume was low; in the other plates, the collection volume was higher and exhibited fewer fluctuations.

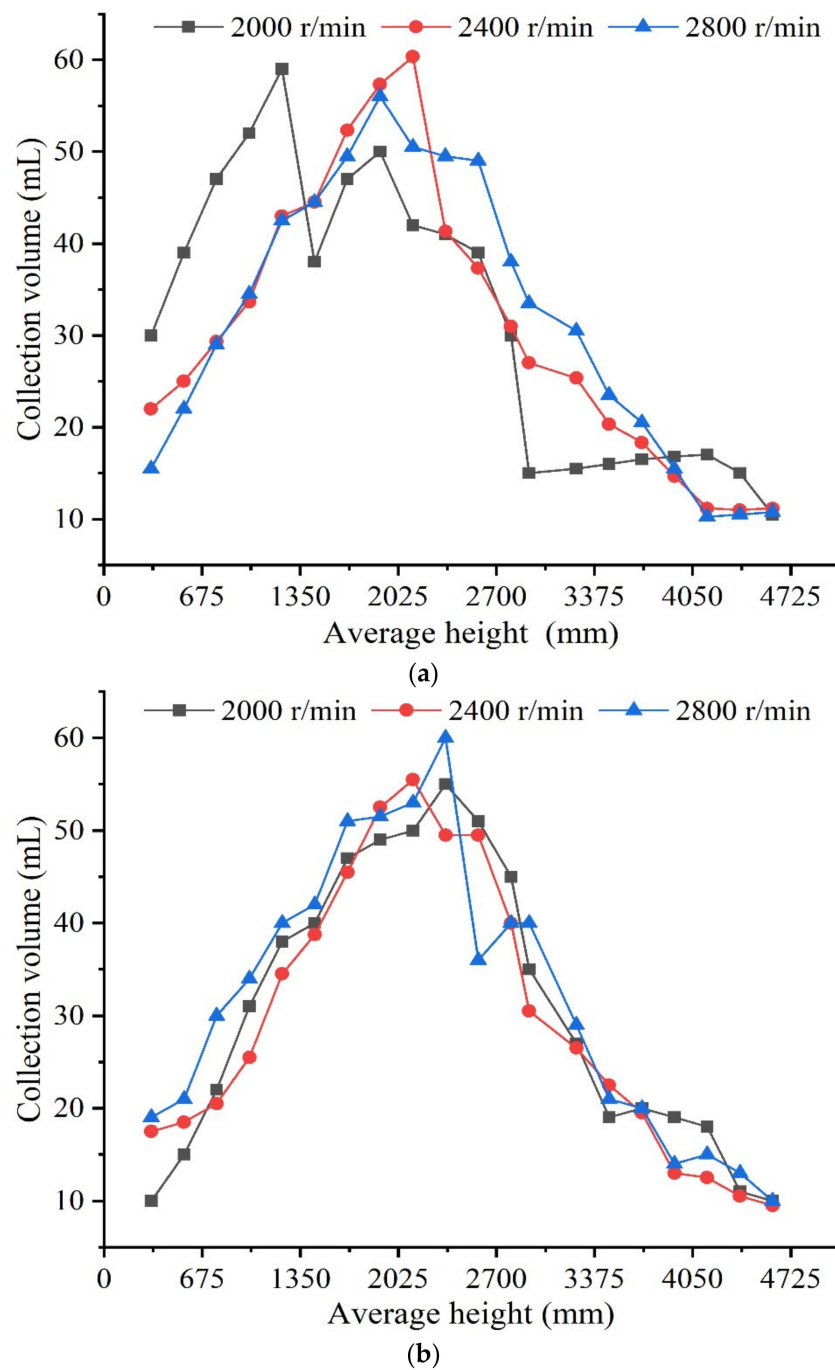


Figure 5. Influence of the blower speed on the collection volume at different spray angles ($L = 1.0$ m). (a) Influence of the blower speed on the collection volume ($W = 60^\circ$). (b) Influence of the blower speed on the collection volume ($W = 75^\circ$).

Figure 6 shows the influence of the spray distance on the collection volume at different blower speeds (2400 r/min and 2800 r/min) for a spray angle of 60° . The results shown in Figure 6a,b indicate that at a constant spray angle, when the blower speed and the spray distance increased, the peak of the curves moved to the right and increased slightly. The rate of increase was unchanged, and the rate of increase became higher while the collection volume of the lower collection plate decreased.

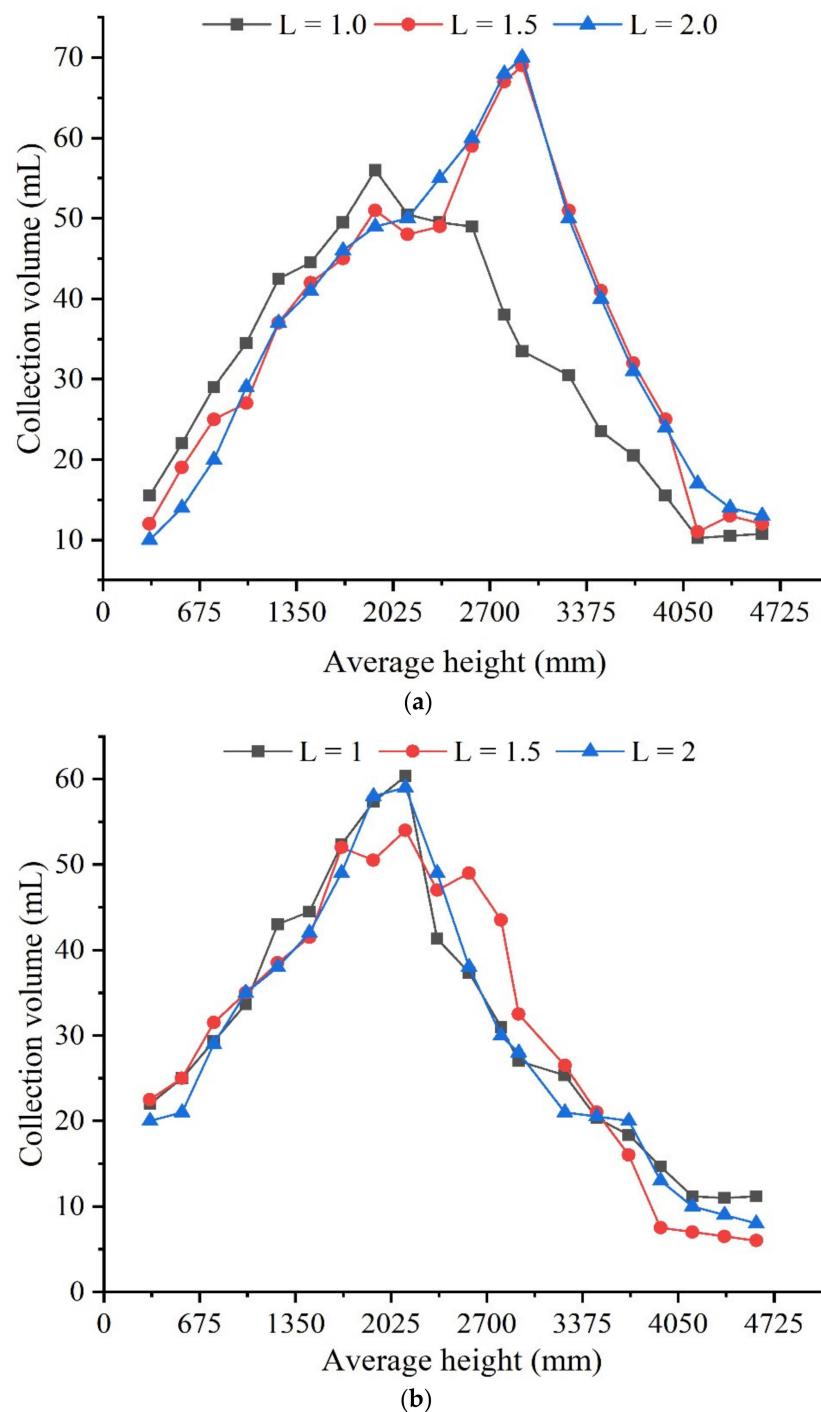


Figure 6. Influence of the spray distance on the collection volume at different blower speeds ($W = 60^\circ$). (a) Influence of the spray distance on the collection volume ($N = 2800$ r/min). (b) Influence of the spray distance on the collection volume ($N = 2400$ r/min).

When the blower speed increased, the spray distance decreased, and the peak of the curve moved to the right and increased slightly; the increase range decreased first and then increased with the decrease in the spray distance. In practical applications, when the blower speed and spray distance both increase, the collection volume increases, and the optimum spray move upward in the tree crown. In the experiment, the collection volume was slightly higher in the optimum collection area. It did not change, whereas the collection volume decreased in the lower part of the tree crown, and the variability of the

collection volume increased as the blower speed increased. At a small spray distance, the optimum collection area occurred at a greater height, and the collection volume was slightly higher; the range of improvement increased first and then decreased with the increase in the spray distance.

Figure 7 shows the influence of the spray angle on the collection volume at different spray distances (1.0 m and 2.0 m) and a blower speed of 2400 r/min. Figure 7a,b show that as the spray angle and spray distance increased, the maximum spray volume remained unchanged, and the peak decreased slightly. The collection volume of the lower collection plates first decreased and then increased. As the spray angle increased, the spray distance decreased, the peaks increased slightly, and the increase range first decreased and then increased with a decrease in the spray distance.

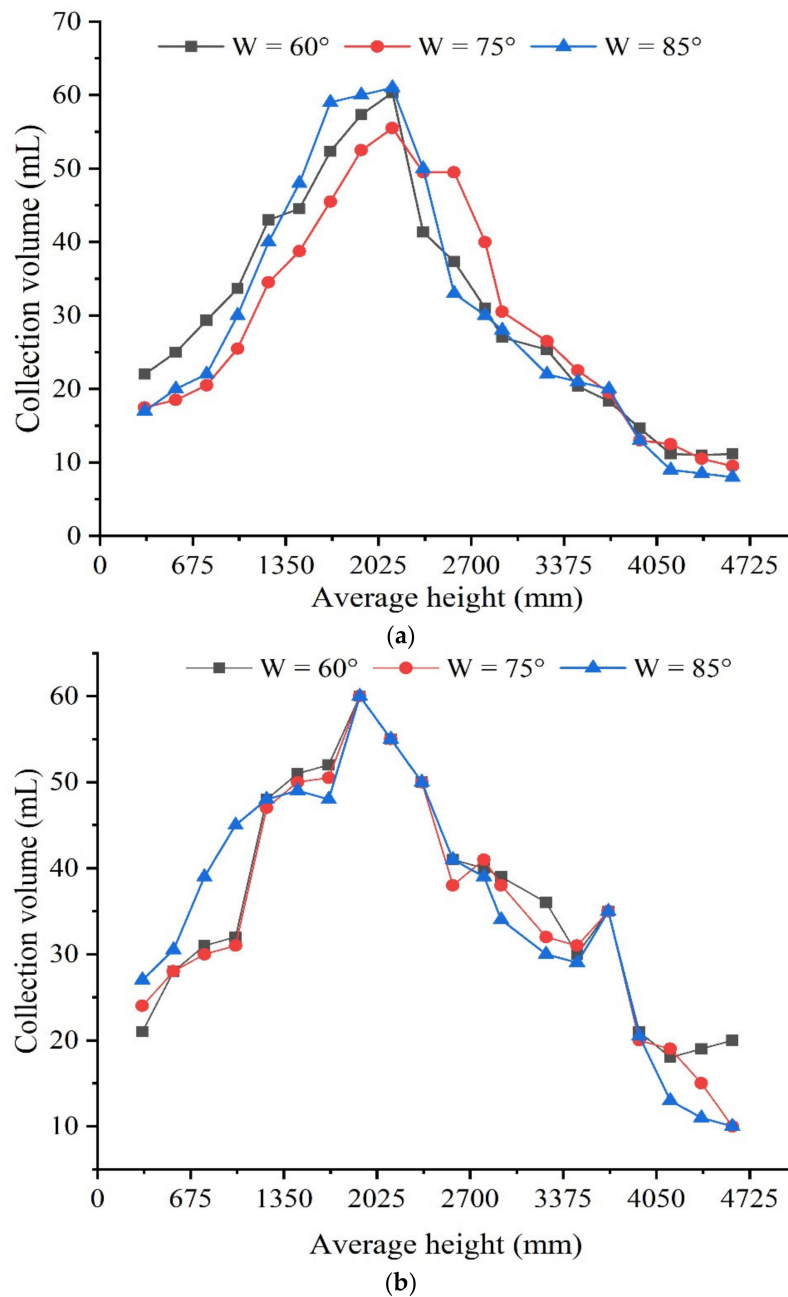


Figure 7. Influence of the spray angle on the collection volume at different spray distances (N = 2400 r/min). (a) Influence of the spray angle on the collection volume (L = 1.0 m). (b) Influence of the spray angle on the collection volume (L = 2.0 m).

In practical applications, this would mean that when the spray angle and spray distance increased, the collection volume and the optimum spray area would not change. In the experiment, the collection volume of the optimum collection area decreased, and the collection volume of the lower part of the tree canopy first decreased and then increased with an increase in the values of both parameters. As the spray angle increased, the spray distance decreased, and the collection volume decreased. The optimum collection area did not change, and the collection volume of the optimum collection area increased with the range of improvement, increasing first and then decreasing with an increase in the spray distance.

In summary, it can be concluded that when one of the parameters remained unchanged, the influence of the other two parameters was relatively small. An increase in the blower speed and spray angle were, respectively, the primary and secondary reasons for the upward movement of the optimum collection area. As the blower speed and spray angle increased, the collection efficiency of the optimum collection area remained unchanged; as the blower speed increased, and the spray distance decreased, the collection volume of the optimum collection area decreased. The spray distance had little effect on the position of the optimum collection, and the collection volume of the optimum collection area first increased and then decreased with the increase in the spray distance. The collection volume was higher at lower heights and lower at higher heights.

3.3. Three-Factor Analysis of the Control Parameters of the Key Collection Plates

The literature [10–12] indicates that the crown height of apple trees in the young fruit stage is about 2.5–3.5 m; the middle part of the crown is the spray target area. The results of the two-factor analysis showed that the collection volume was stable in the range of 1.35–1.55 m. Therefore, the collection volume in this range was selected as the dependent variable, and the spray angle, spray distance, and blower speed were used as the independent variables in the regression.

Figure 8 shows the influence of the three control parameters blower speed, spray angle, and the spray distance on the collection volume. The results show that due to the parabolic trajectory of the droplets, the increase in the spray angle and the spray distance will cause the collection volume in the range of 1.35–1.55 m to decrease, and the increase in the blower speed will increase the collection in the range of 1.35–1.55 m to some extent.

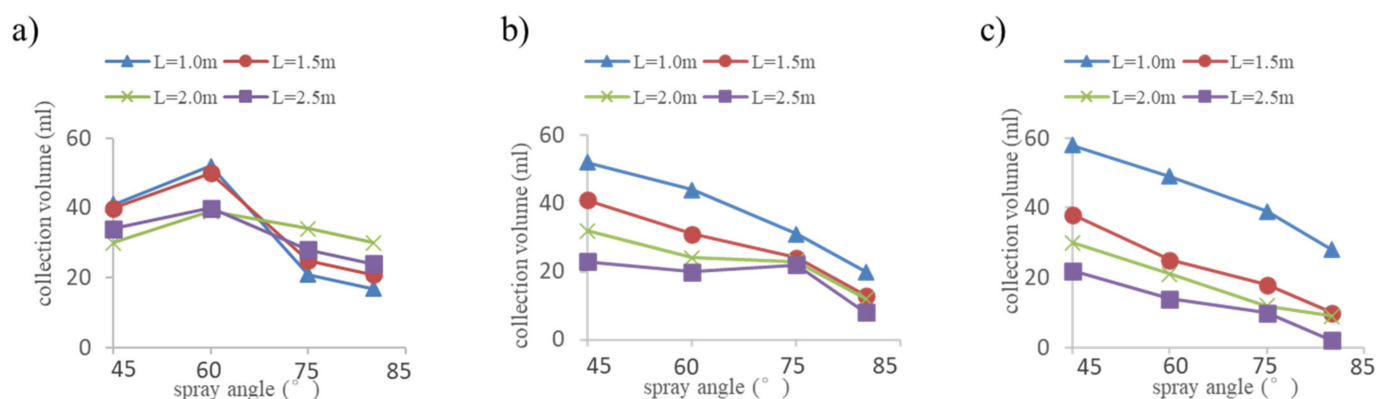


Figure 8. Influence of the three control parameters on the collection volume. (a) Influence of the spray angle and spray distance on the collection volume ($N = 2000$ r/min). (b) Influence of the spray angle and spray distance on the collection volume ($N = 2400$ r/min). (c) Influence of the spray angle and spray distance on the collection volume ($N = 2800$ r/min).

The inter-subject effect test results of the model are shown in Table 3. The dependent variable was the collection volume, and the independent variables were the blower speed, spray angle, spray distance, and position of collection plates. From Table 3, it can be concluded that the SIG of spray angle and spray distance is less than 0.0001, so it has a

significant impact on the spray effect, and the SIG of the fan speed is less than 0.005, so it has a significant impact on the spray effect to a certain extent.

Table 3. Inter-subject effect test.

Data Source	Sum of Squares	DF	Mean Square	F	SIG	Non-Central Parameter
Calibration model	59,803.112	18	3130.032	85.239	0.0000	1782.298
Intercept	208,942.321	1	208,942.321	620.019	0.0000	6201.230
Spray distance	12,230.031	2	6108.120	178.040	0.0000	317.271
Spray angle	72.132	2	26.200	1.324	0.0001	3.042
Blower speed	13.024	3	6.171	0.314	0.0054	0.431
Collection plate position	43,831.211	9	3103.121	98.141	0.0000	1235.020

Abbreviation: DF: degrees of freedom; SIG: significance.

A regression analysis on three control parameters was made, and the *p*-values of the spray distance, spray angle, and blower speed were less than 0.05, indicating that these parameters had significant effects on the collection volume. The regression equation in the height range of 1.35–1.55 m is:

$$Y = 123.3499 - 0.5242X_1 + 5.5833X_2^2 - 30.4583X_2 - 0.0110X_3 \tag{1}$$

where *Y* is the collection volume at heights of 1.35–1.55 m; *X*₁, *X*₂, and *X*₃ are, respectively, the values of the spray angle (°), the spray distance (m), and the blower speed (r/min).

The coefficient of determination *R*² of the regression equation was 0.80, the corrected *R*² was 0.82, and the standard error was 7.62, indicating a good fit.

The partial derivatives of the three factors were obtained:

$$\frac{\partial Y}{\partial X_1} = -0.5242 \tag{2}$$

$$\frac{\partial Y}{\partial X_2} = 11.1666X_2 - 30.4583 \tag{3}$$

$$\frac{\partial Y}{\partial X_3} = -0.0110 \tag{4}$$

The analysis of the three factors in the crown height range of 1.35–1.55 m shows that an increase in the spray angle and blower speed results in a decrease in the collection volume due to the parabolic trajectory of the droplets. The effect of the spray angle on the collection volume is the most obvious.

In addition, the proposed regression model can be modified using data from field experiments because differences exist in the canopy density and surface characteristics between the vertical patternator and real trees.

4. Conclusions

In this study, the influences of different control parameters on the spray performance of an air-blast sprayer were determined. A regression equation was established to describe the relationship between the collection volume at the critical height range and the spray angle, blower speed, and spray distance. The influences of the three spray parameters on the collection volume at different heights were analyzed:

- (1) Under the experimental conditions, an increase in the spray angle and blower speed increased the overall spray volume and decreased the spray volume at the critical height.
- (2) The influence of any single parameter on the other parameters was relatively small. The increase in the blower speed and spray angle were the primary and secondary reasons for an increase in the height of the optimum collection area.

- (3) The spray distance affected the collection volume due to the parabolic trajectory of the droplets. The collection volume in the critical height range first increased and then decreased as the spray distance increased, and the largest collection volume was obtained at a distance of 1.762 m.
- (4) A quadratic regression model was established to predict the collection volume at the critical height of the tree crown based on the spray distance, spray angle, and blower speed. When one parameter is given, the other two parameters can be adjusted to achieve the desired spray effect.

Author Contributions: Conceptualization, Y.H. and Z.Y.; methodology, Y.H. and H.Y.; software, B.H.; validation, Z.Y.; formal analysis, Z.X.; investigation, H.Y.; resources, Z.Y.; data curation, Y.H.; writing—original draft preparation, Y.H.; writing—review and editing, Z.Y.; project administration, Y.H.; funding acquisition, Z.Y. All authors have read and agreed to the published version of the manuscript.

Funding: This research was funded by the Talent start-up Project of Zhejiang A&F University Scientific Research Development Foundation No. 2021LFR066 and the National Key R & D Program of China (2016YFD0200700).

Institutional Review Board Statement: Not applicable.

Data Availability Statement: Not applicable.

Conflicts of Interest: The authors declare that they have no conflict of interest regarding this research.

References

1. Zhou, L.F.; Xue, X.Y.; Zhou, L.X.; Zhang, L.; Ding, S.M.; Chang, C.; Zhang, X.J.; Chen, C. Research situation and progress analysis on orchard variable rate spraying technology. *Trans. Chin. Soc. Agric. Eng.* **2017**, *33*, 80–92.
2. Shen, C.J.; Jia, S.X.; Tang, Z.H.; Zhou, Y.; Meng, X.J.; Yuan, L.Q. Research Actuality and Application Prospects of Pesticide. *Electrost. Spray. J. Agric. Mech. Res.* **2010**, *32*, 10–13.
3. Liu, H.; Feng, X.; Liu, J.; Li, J. Design and experiment of Orchard Air-blast Sprayer. *J. Anhui Agric. Sci.* **2011**, *39*, 20911–20913.
4. Zhang, H.F.; Xu, L.Y. Summary of research status on orchard sprayer. *J. Chin. Agric.* **2014**, *35*, 112–118.
5. Li, J.; Xu, J.T.; Yang, Z.; Niu, M.; Xue, K.; Mo, M. Design and experiment on real-time mixing system for air-assisted sprayer. *Trans. Chin. Soc. Agric. Eng.* **2016**, *32*, 62–69.
6. Gil, E.; Arnó, J.; Llorens, J. Advanced technologies for the improvement of spray application techniques in Spanish viticulture: An overview. *Sensors* **2014**, *14*, 691–708. [\[CrossRef\]](#)
7. Li, H.; Zhai, C.; Zhang, B.; Yang, S. Status analysis of orchard spray target detection technology. *J. Agric. Mech. Res.* **2016**, *38*, 1–5.
8. Ding, T.H.; Cao, S.M.; Xue, X.Y.; Ding, S. Current situation and development trend of air-assistend orchard sprayer. *J. Chin. Agric. Mech.* **2016**, *37*, 221–226.
9. Yuan, Q.; Hu, L.; Luo, X.; Zhang, M.; Zhou, H.; Zhao, R. Design and Experiment of Online Mixing Spraying System. *Trans. Chin. Soc. Agric. Mach.* **2016**, *47*, 176–181.
10. Qi, L.; Fu, Z. The droplet distribution on apple trees atomized by an air-assisted sprayer. *Trans. CSAE* **1998**, *03*, 140–144.
11. Mac, N.A.Z.; Teske, M.E.; Barry, J.W. A technique to characterize spray deposition orchard and tree canopies. *Trans. ASAE* **1997**, *40*, 1529–1536.
12. Cross, J.V.; Walklate, P.J.; Murray, R.A. Spray deposits and losses in different sized apple trees from an axial fan orchard sprayer: 2. Effects of spray quality. *Crop Prot.* **2001**, *20*, 333–343. [\[CrossRef\]](#)
13. Doruchowski, G.; Holownicki, R. Environmentally friendly spray techniques for tree crops. *Crop Prot.* **2000**, *19*, 617–622. [\[CrossRef\]](#)
14. Pezzi, F.; Rondelli, V. The performance of an air-assisted sprayer operating in vineyard. *J. Agric. Eng. Res.* **2000**, *76*, 331–340. [\[CrossRef\]](#)
15. Li, J.; Zhao, C.Q.; Li, S.J.; Chen, H.; Ding, S.F. Study on droplet deposition characteristics of orchard air blast sprayer based on CFD. *J. Huazhong Agric. Univ.* **2019**, *06*, 171–177.
16. Qiu, B.; Yan, R.; Ma, J.; Guan, X.; Ou, M. Research Progress Analysis of Variable Rate Sprayer Technology. *Trans. Chin. Soc. Agric. Mach.* **2015**, *46*, 59–72.
17. Zhai, C.; Sha, X.U.; Long, J.; Hanzhe, L.I.; Zhang, B.; Zhu, R. Optimization design of orchard air-assisted sprayer and mathematical model for spray height control. *J. Northwest A F Univ. (Nat. Sci. Ed.)* **2018**, *46*, 148–154.
18. Solanelles, F.; Escolà, A.; Planas, S.; Rosell-Polo, J.R.; Camp, F.; Gràcia, F. An electronic control system for pesticide application proportional to the canopy width of tree crops. *Biosyst. Eng.* **2006**, *95*, 473–481. [\[CrossRef\]](#)
19. Wang, L.; Zhang, S.; Ma, C.; Xu, Y.; Qi, J.; Wang, W. Design of variable spraying system based on ARM. *Trans. Chin. Soc. Agric. Eng. (Trans. CSAE)* **2010**, *26*, 113–118, (In Chinese with English abstract).

20. Gonzalez, R.; Pawlowski, A.; Rodriguez, C.; Guzman, J.L.; Sánchez-Hermosilla, J. Design and implementation of an automatic pressure-control system for a mobile sprayer for greenhouse applications. *Span. J. Agric. Res.* **2012**, *10*, 939–949. [[CrossRef](#)]
21. Huang, S.; Zhu, R.; Wang, Y.; Liu, W. Design and algorithm of constant pressure and variable flow control system of variable pesticide application machine. *J. Agric. Mech. Res.* **2011**, *2*, 19–22, (In Chinese with English abstract).
22. Berk, P.; Stajanko, D.; Lakota, M.; Belsak, A. Real time fuzzy logic system for continuous control solenoid valve in the process of applying the plant protection product. *J. Agric. Eng.* **2015**, *15*, 1–9.
23. Liu, Z.; Hong, T.; Zhang, W.; Fan, Z. Fuzzy control implementing and testing on electromechanical flow valve. *Trans. Chin. Soc. Agric. Eng. (Trans. CSAE)* **2010**, *26* (Suppl. S1), 22–26, (In Chinese with English abstract).
24. Song, L.; Dong, Z.; Xiang, L.; Xing, S. Variable universe adaptive fuzzy PID control of spray flow valve. *Trans. Chin. Soc. Agric. Eng. (Trans. CSAE)* **2010**, *26*, 114–118, (In Chinese with English abstract).
25. Chen, S.; Yin, D.; Wei, X.; Pei, W. Design and simulation of variable weed spraying controller based on adaptive neural fuzzy inference system. *J. Drain. Irrig. Mach. Eng.* **2011**, *29*, 272–276, (In Chinese with English abstract).
26. Na, G.; Jingtao, H. Design and experiment of variable rate spaying system on Smith-Fuzzy PID control. *Trans. Chin. Soc. Agric. Eng. (Trans. CSAE)* **2014**, *30*, 56–64, (In Chinese with English abstract).
27. Wei, D.; Xiongkui, H.; Weimin, D. Droplet size and spray pattern characteristics of PWM-based continuous variable spray. *Int. J. Agric. Biol. Eng.* **2009**, *2*, 8–18.
28. Huanyu, J.; Mingchuan, Z.; Junhua, T.; Yan, L. PWM variable spray control based on Kalman filter. *Trans. Chin. Soc. Agric. Mach.* **2014**, *5*, 60–65, (In Chinese with English abstract).
29. Zhai, C.Y.; Wang, X.; Liu, D.Y.; Ma, W.; Mao, Y.J. Nozzle flow model of highpressure variable-rate spraying based on PWM technology. *Adv. Mater. Res.* **2012**, *422*, 208–217. [[CrossRef](#)]
30. Li, L.; He, X.; Song, J.; Zhong, C. Spray characteristics on pulse-width modulation variable application based on high frequency electromagnetic valve. *Trans. Chin. Soc. Agric. Eng. (Trans. CSAE)* **2016**, *32*, 97–103, (In Chinese with English abstract).
31. Huanyu, J.; Lijun, Z.; Guangyuan, L.; Weinan, S.H.I. Experiment on dynamic spray deposition uniformity for PWM variable spray of single nozzle. *Trans. Chin. Soc. Agric. Mach.* **2017**, *48*, 41–46, (In Chinese with English abstract).
32. Liu, H.; Zhu, H.; Shen, Y.; Chen, Y.; Ozkan, H.E. Development of digital flow control system for copy multi-channel variable-rate sprayers. *Trans. ASABE* **2014**, *57*, 273–281.
33. Xu, Y.; Bao, J.; Fu, D.; Zhu, C. Design and experiment of variable spraying system based on multiple combined nozzles. *Trans. Chin. Soc. Agric. Eng. (Trans. CSAE)* **2016**, *32*, 47–54, (In Chinese with English abstract).
34. Dekeyser, D.; Duga, A.T.; Verboven, P.; Endalew, A.M.; Hendrickx, N.; Nuytens, D. Assessment of orchard sprayers using laboratory experiments and computational fluid dynamics modelling. *Biosyst. Eng.* **2013**, *114*, 157–169. [[CrossRef](#)]
35. Shen, Y.; Zhu, H. Embedded computer-controlled premixing inline injection system for air-assisted variable-rate sprayers. *Trans. ASABE* **2015**, *58*, 39–46.
36. Zhang, W.; Liu, Z. Experiment on variable rate spray with real-time mixing pesticide of 3WY-A3 sprayer. *Trans. Chin. Soc. Agric. Eng. (Trans. CSAE)* **2011**, *27*, 130–133, (In Chinese with English abstract).
37. Hu, K.; Zhou, Z.; Qi, L.; Wang, X.; Ji, R. Spraying performance of the direct injection variable-rate sprayer. *Trans. Chin. Soc. Agric. Mach.* **2010**, *41*, 70–74, 102, (In Chinese with English abstract).
38. Yang, Z.; Niu, M.; Li, J.; Xu, X.; Xu, J.; Chen, Z. Design and experiment of an electrostatic sprayer with on-line mixing system for orchard. *Trans. Chin. Soc. Agric. Eng. (Trans. CSAE)* **2015**, *31*, 60–67, (In Chinese with English abstract).
39. Cai, X.; Walgenbach, M.; Doerpmund, M.; Lammers, P.S.; Sun, Y. Direct nozzle injection sprayer based on electromagnetic-force valve. *Trans. Chin. Soc. Agric. Mach.* **2013**, *44*, 69–72, (In Chinese with English abstract).
40. Jens, K.W.; Tanja, P.; Katrin, A. Assessment of Different Parameters Influencing the Quality of Spray Distribution on Orchard Sprayers. *Gesunde Pflanz.* **2019**, *71*, S9–S15.
41. Qiu, W.; Gu, J.; Ding, W.; Sun, C.; Li, Y.; Zhao, S. The droplet deposition distribution in fruit canopy using air-assisted sprayer. *J. Yangzhou Univ. (Agric. Life Sci. Ed.)* **2015**, *36*, 68–72.
42. Farooq, M.; Landers, A.J. Interactive Effects of Air, Liquid and Canopies on Spray Patterns of Axial-flow Sprayer. In Proceedings of the Annual Meeting of the ASAE, “Dynamic Partnerships for an Environmentally Safe and Healthy World”, Ottawa, ON, Canada, 1–4 August 2004.
43. He, X.K.; Zeng, A.; He, J. Effect of Wind Velocity from Orchard Sprayer on Droplet Deposit and Distribution. *Trans. Chin. Soc. Agric. Eng.* **2002**, *4*, 75–77.
44. Lü, X.L.; Fu, X.; Wu, P.; Ding, S.; Zhou, L.; Yan, H. Influence of Spray Operating Parameters on Droplet Deposition. *Trans. Chin. Soc. Agric. Mach.* **2011**, *42*, 70–75.
45. Reichard, D.L.; Zhu, H.; Downer, R.A.; Fox, R.D.; Brazee, R.D.; Ozkan, H.E.; Hall, F.R. A laboratory system to evaluate effects of shear on spray drift retardants. *Trans. ASAE* **1996**, *39*, 1993–1999. [[CrossRef](#)]
46. Fox, R.D.; Brazee, R.D.; Reichard, D.L.; Hall, F.R. Power in an Air Sprayer Jet. *Trans. ASAE Am. Soc. Agric. Eng.* **1982**, *25*, 1181–1184. [[CrossRef](#)]
47. Fox, R.D.; Brazee, R.D.; Svensson, S.A.; Reichard, D.L. Air Jet Velocities from a Cross-flow Fan Sprayer. *Trans. ASAE* **1992**, *35*, 1381–1384. [[CrossRef](#)]
48. Pergher, G.; Gubiani, R.; Tonetto, G. Foliar deposition and pesticide losses from three air-assisted sprayers in a hedgerow vineyard. *Crop Prot.* **1997**, *16*, 25–33. [[CrossRef](#)]

49. Svensson, S.A.; Brazee, R.D.; Fox, R.D.; Williams, K.A. Air jet velocities in and beyond apple trees from a two-fan cross-flow sprayer. *Trans. ASAE* **2003**, *46*, 611–621. [[CrossRef](#)]
50. Svensson, S.A.; Fox, R.D.; Hansson, P.A. Forces on apple trees sprayed with a cross-flow fan air jet. *Trans. ASAE* **2002**, *45*, 889–895. [[CrossRef](#)]

Article

EDEM Simulation Study on the Performance of a Mechanized Ditching Device for Codonopsis Planting

Dejiang Liu ^{1,2}, Yan Gong ^{1,*}, Xuejun Zhang ², Qingxu Yu ¹, Xiao Zhang ¹, Xiao Chen ¹ and Yemeng Wang ¹

¹ Nanjing Institute of Agricultural Mechanization, Ministry of Agriculture and Rural Affairs, Nanjing 210014, China

² College of Mechanical and Electrical Engineering, Xinjiang Agricultural University, Urumqi 830052, China

* Correspondence: gongyan@caas.cn

Abstract: Codonopsis pilosula is cultivated mainly in sandy soils, especially in the Dingxi area of the Gansu province, northwest China. They are mainly planted in hilly areas, where large machines cannot reach easily. Codonopsis pilosula transplanting has been adopted with a conventional flat planting way, film mulching and seedling outcrops. While its planting requires opening a shallow ditch, short operation cycle, considerable labor intensity and is in large demand, a simulation analysis was performed according to specific tillage resistance, helpful in the optimization design in later stages and the improvement of a domestic ditching plow's performance. This paper studies the simulation performance of an adjustable trench plough and analyzes the orthogonal test and Design-Expert response surface of the data. EDEM simulation software was used to analyze the traction resistance of the furrow ditching mechanism in the ditching process. The results show that the traction resistance increased from 1751.31 N to 2197.31 N as the simulation working speed increased from 0.9 m/s to 1.5 m/s, 1.25 times higher than the former. It indicates that speed had significant effects on traction resistance. With the increase in working speed, the furrow traction resistance and specific consumed power were increased considerably. Using the stability coefficient of the ditching depth and consistency coefficient of ditching bottom width as test indices, speed and angle of furrowing as impact factors, Box–Behnken orthogonal experiment design method, and establishing test indices and test factors, the regression model between the analysis of the influence of the test index, comprehensive agronomic requirements and MATLAB factor optimization of the experiment, the optimized operation parameter combination was obtained: the forward speed was 0.9 m/s, the angle of ditching was 35° and the stability coefficient of the ditching depth and consistency coefficient of ditch bottom width were 97.57% and 98.03%, respectively. The data after the simulation comparison test can provide a design reference for the domestic small trench operation.

Citation: Liu, D.; Gong, Y.; Zhang, X.; Yu, Q.; Zhang, X.; Chen, X.; Wang, Y. EDEM Simulation Study on the Performance of a Mechanized Ditching Device for Codonopsis Planting. *Agriculture* **2022**, *12*, 1238. <https://doi.org/10.3390/agriculture12081238>

Academic Editors: Muhammad Sultan, Redmond R. Shamshiri, Md Shamim Ahamed and Muhammad Farooq

Received: 24 June 2022

Accepted: 13 August 2022

Published: 17 August 2022

Publisher's Note: MDPI stays neutral with regard to jurisdictional claims in published maps and institutional affiliations.



Copyright: © 2022 by the authors. Licensee MDPI, Basel, Switzerland. This article is an open access article distributed under the terms and conditions of the Creative Commons Attribution (CC BY) license (<https://creativecommons.org/licenses/by/4.0/>).

Keywords: Codonopsis planting; ditching device; working parameters; EDEM simulation; orthogonal test; data analysis and discussion

1. Introduction

Traditional Chinese medicine is one of the characteristic industries in the Gansu province, China. Since national industrial policy transferred to characteristic industries, the areas of traditional Chinese medicine are gradually increasing year by year in the Gansu province. The planting for Chinese medicine is an effective way for vast rural areas and farmers to avoid poverty and increase their wealth. The traditional Chinese medicine cultivation area has a large scale and high visibility. In the Gansu province, Radix Codonopsis accounts for 60% of the whole country. Codonopsis pilosula is a traditional Chinese medicine, also known as “tiaodang”, belonging to herbs of the Platycodon family. It has a soft and solid texture, slightly fissured section and yellow and white skin. It enhances the body's stress ability functions, immune functions, delaying senescence, and has anti-ulcer, anti-tumor, anti-bacterial, etc., properties. The shape of Codonopsis pilosula

is oval, and its long and short axis is about 1.2 mm and 0.68 mm, respectively. *Codonopsis pilosula* planting can be achieved through sowing or seedling transplanting. The sowing process has a long growing cycle (3–5 years), for which is difficult to achieve scale benefits. The seedling transplanting method is usually adopted with the film mulching model and seedling outcrops. In this method, *Codonopsis pilosula* seedlings are inside the soil, but outside the film. It ensures a smooth emergence and prevents the occurrence of burning seedlings. It prevents drought and waterlogging, and also provides convenience for mechanical harvest, enhancing the commodity rate, and achieving production goal and thus increased income. For *Codonopsis*-membrane-covered outcrop cultivation, a ditch is needed first (the ditch type should be an inclined ditch), and then *codonopsis* is planted obliquely, then covered with the soil film, and finally leveled, which is the entire process to complete the planting of *Codonopsis*. Based on the cultivation agronomy of *codonopsis pilosula* with the film-covered outcrop, there is no mechanical operation in the ditching cultivation process to match it, and the traditional manual operation is adopted, which has high labor intensity and low production efficiency, seriously restricting the development of the traditional Chinese medicinal materials industry in Gansu [1–3].

Northwest China has a vast area, dry climate and large spatial difference of soil. When the ditching device is in direct contact with the soil, it is subject to the random resistance and friction of the soil and the vibration generated by the machine, which can easily cause the deformation of the ditching plow structure and affect the ditching accuracy. At present, domestic and international scholars have carried out relevant research on the force analysis of ditching devices in soil, analyzing soil movement characteristics, the influence law of ditching power consumption, etc. [4–6]. Wang Shaowei et al. designed the ditching components of the Mountain Orchard ditching machine, optimized the structure parameters of the ditching blade by simulation tests [7] and analyzed the influence of operation parameters on ditching power consumption. Zhang Yongliang et al. applied the theory of throwing soil to analyze the process of throwing soil, finding the trajectory equation of the thrown soil particles, and establishing a mechanics model of soil discrete element contact studying its throwing performance with the method of experimental verification [8]. Kang Jianming et al. established a finite element model for a soil ditching cutter head by using the smoothed particle hydrodynamics method and obtained the variation law of power consumption of the slotting cutter head in the soil cutting process through simulation analysis [9]. Barr et al. studied the effects of different openers on soil disturbance and soil pressure at different speeds through the orthogonal test and reduced soil disturbance by increasing the ditching operation speed [10].

In view of the above problems, based on plough-type opener trenching as the research object, through EDEM simulation and orthogonal experiment analysis, the analysis of different furrow forms of change and the influence of structure parameters on traction resistance are investigated, seeking to arrive at the soil components combined furrowing device for low consumption, as well as the theory of drag reduction design in order to obtain a better drag reduction characteristic form of furrowing. It provides a design reference for domestic small ditching operation.

2. Materials and Methods

2.1. The Dimensions of the Entire Structure and the Working Principle of Double-Side-Flip Plough Ditching Device

2.1.1. Dimensions of the Entire Structure

Based on the planting agronomic requirements of *codonopsis pilosula*'s oblique ditching, a double-sided inverted ditching plough that can open oblique ditches was designed. The size diagram is shown in Figure 1. The length of the plough wall is 35 cm, the ground clearance is 37 cm, the section of the plough column is a square with a width of 6 cm, the total length of the plough blade and the plough bracket is 34 cm, the width of the plough bracket is 18 cm, and the length from plough tip to the end of the plough bracket is 36 cm. The adjustable double-sided inverted ditching plough can complete ditching, soil covering,

ploughing and other operations. The ploughshare can be turned around. The direction and angle of soil turning can be adjusted [11,12].

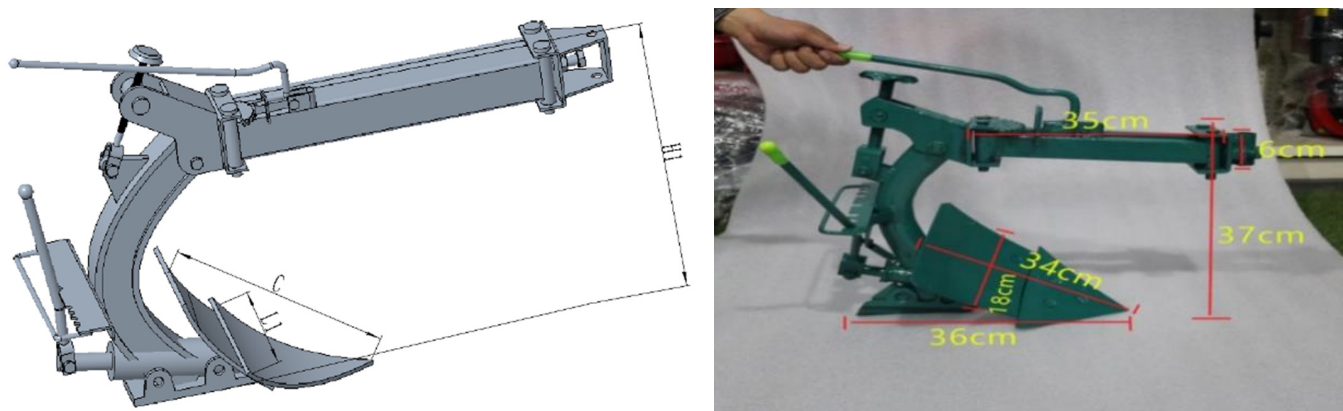


Figure 1. Overall dimension drawing of the double-sided turning plough ditching device.

2.1.2. Working Principle of Double-Side-Flip Plough Ditching Device

The power part equipped with the micro-tiller during the operation is shown in Figure 6. The double-side-flip plough ditching device is mainly composed of the main frame, plough blade, plough wall, tillage depth's adjusting rod and angle's adjusting rod, etc. The plough blade is installed at the bottom of plough. It cuts the soil laterally and keeps the same level at the bottom of trench. To dig an oblique flat trench horizontally, An adjustable rod is used to adjust the soil-insert depth. Once the planting ditch is finished, the seedlings are covered, and then another furrow is ditched. Using another furrow's soil to cover the prior furrow's seedlings, the process continues until we finish all ditching and soil covering. The ploughshare can be turned around towards the left or right direction. The structure is simple, compact and flexible, and is suitable for small plot operation.

2.2. Planting Agronomic Requirements

During the survey, we found that, in actual production, *Codonopsis pilosula* are transplanted obliquely, as is shown in diagram 1. For this, an oblique furrow was dug, achieving a bottom depth at 10–15 cm. The seedlings were placed on one of the sloping surfaces evenly (angle of sloping surface is 10–40°). The distance between each seedling was 5–8 cm, and the top of seedling was 3–4 cm above the ground. We filled the soil after the seedlings were placed, leveling afterwards. The row spacing was 30 cm.

As shown in Figure 2b, the overall furrow was dug firstly, and the average depth was 8–10 cm. Then, the seedlings were put horizontally, as shown in Figure 2c. The distance between seedlings was 10–12 cm. The mulching film was covered along the red line. The edge of plastic film was 2–3 cm from the tip of seedling, which shows the tip outside the film. In the end, we covered the soil, as shown in Figure 2d. The depth of soil covering was 3–5 cm. The width and thickness were 900 mm and 0.012 mm, respectively, for each ridge.

2.3. Design Analysis of Key Mechanisms

2.3.1. Design of Double-Flip Plough Ditching Device with a Tilting-Plough Blade

In the tilting plough of the double-flip plough ditching device, the soil was spilled on the side of the plough body, which was convenient for ground grading lately and offset the lateral force of the plough body. Firstly, the curved wire was drawn, as shown in Figure 3a. The curved wire refers to the curve where the plough surface intersects with the vertical plane. In order to improve the soil flip effect, the plane of the curved wire is at the end of share blade, as shown in Figure 2b. The plough body surface was controlled by a straight element line, and the angle between the straight element line and the trench wall is the angle between the straight element line, which changes along the height of the plough body.

In the ploughshare part, it changes in a straight line and, in the plough wall part, it changes in a broken line, as shown in Figure 3c.

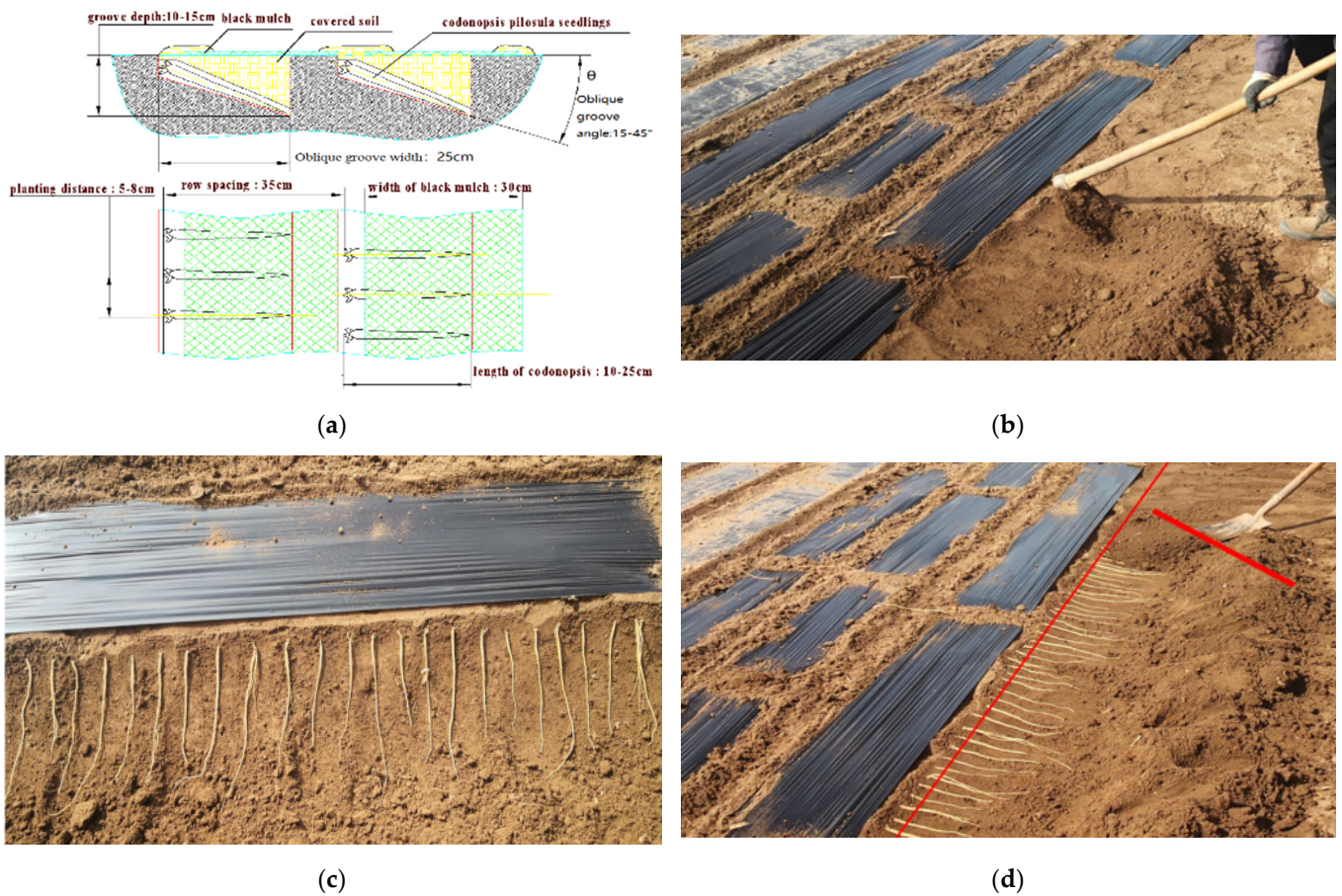


Figure 2. Codonopsis planting agronomic. (a) Codonopsis pilosula's planting agronomy. (b) Ditching. (c) Codonopsis transplanting seedlings. (d) Soil and film covering.

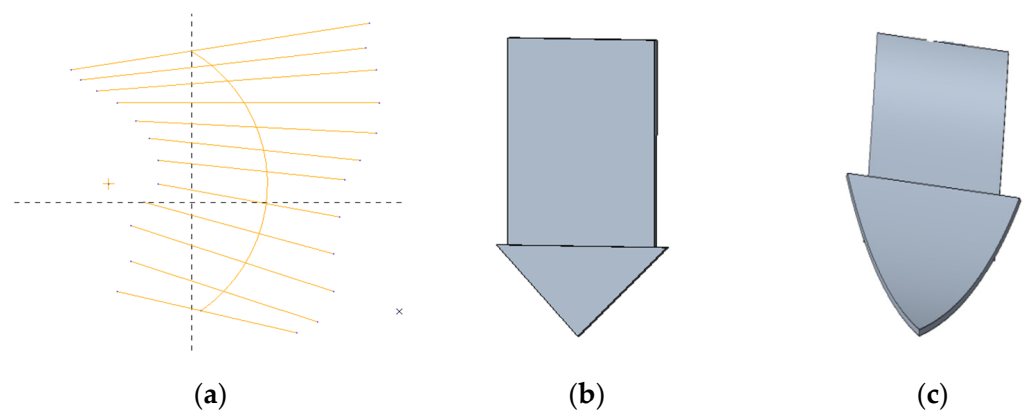


Figure 3. Codonopsis pilosula planting agronomy. (a) The plough plots the curve. (b) Straight plough. (c) The bent plough blade.

2.3.2. Plough Body Parameter Design

The adjustable ditching plough belongs to plough-type ditching device, with a simple structure, reliable work, strong ability of breaking soil into the soil, the heavy soil, wasteland and weeds of the plot have a strong adaptability, the ploughing angle and pushing angle of the plow body according to the structural parameters of the share plow design, the main design of the width of the plough body and the height of the plough body.

In the actual working process, the installation position of the ditching plough is directly in front of the intermediate gearbox, so the space is limited. The width of the plough body C should be larger than the width of the bottom of the intermediate gearbox box (300 mm). At the same time, considering that the plough body will tear the soil, the actual width of the plough is slightly larger than the width of the working groove surface L_1 . That is, $L_1 < C \leq 350$ mm, the width C of the plough body should meet L_1 .

The height of soil sliding along the plough is approximately equal to the depth of the working ditching h . In order to avoid soil sliding over the top of the plough, the soil should still be inside the plough after reaching the surface, and the height H_1 designed for the plough should meet the following requirements [9,10]:

$$H_1 \geq h = \frac{L_1 - A}{2} \tan\theta$$

In the formula, θ is the ridge body accumulation Angle ($^\circ$) after ridge initiation, which was annotated in Figure 2a; H_1 is the design height of plough body (mm); L_1 is the width of the working groove surface (mm); h is the working ditching depth (mm); A is the width of the trench bottom (mm), which is 150 mm. Since the height of the plough from the ground can also be adjusted through the height adjustment holes on the screw and the support rod, after comprehensive consideration, the height H_1 of the plough was determined to be 370 mm. See Figure 1 for letter labeling in the formula. The main technical parameters of the machines and tools are shown in Table 1.

Table 1. The main technical parameters of the machines.

Project	Technical Parameters
Hang way	Tractor traction type
Supporting power (Metric horsepower)	≥ 30
Machine weight (kg)	60
Outline dimensions (mm) Length \times width \times height	450 \times 300 \times 390
Ground speed (m/s)	0.9–1.5
Trenching depth (mm)	80–100
The stability coefficient of ditching depth (%)	$\geq 90\%$
Consistency coefficient of ditching bottom width (%)	$\geq 85\%$
Efficiency of operations (ha/h)	≥ 0.5
Leakage rate (%)	≤ 4

2.4. Discrete Element Simulation Analysis

The EDEM discrete element soil simulation model was established and verified by the soil through test results. EDEM simulation was carried out on the plough surface parameters and operating speeds, and the change rule of the plough traction resistance under different operating speeds and the change in the plough parameter element line angle were obtained.

2.4.1. Establishment of Mechanical Models

Discrete element contact mechanical models can be divided into soft sphere model, as shown in Figure 4a, and hard sphere model, as shown in Figure 4b. Due to the relatively low movement speed of soil particles and plough body and the fixed adhesion between soil particles, HertzMindlin soft ball model was adopted in this paper [13,14]. The model mainly includes physical property parameters (tangential elastic coefficient k_T , normal elastic coefficient k_N , tangential damping coefficient C_t and normal damping coefficient C_n) and geometric parameters, normal overlap δ_n and tangential overlap δ_T .

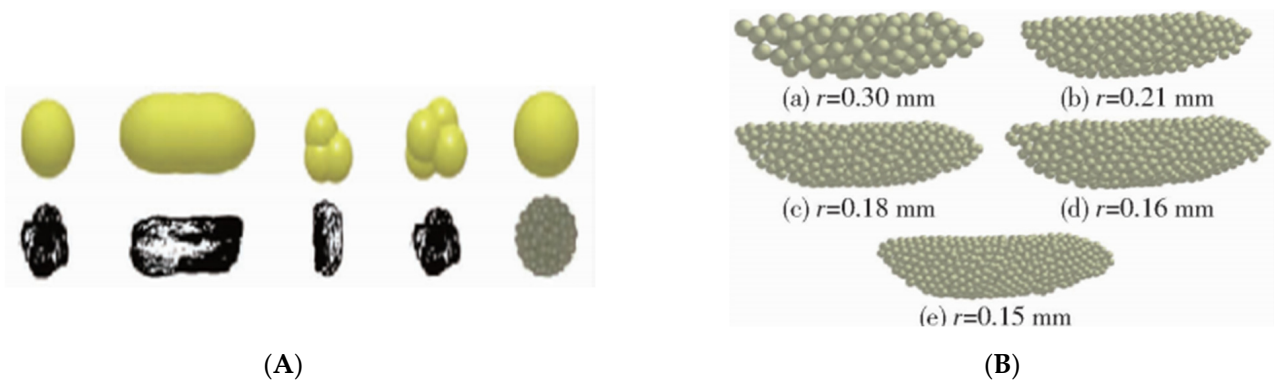


Figure 4. Discrete element contact mechanical models. (A) Soft sphere model. (B) Hard sphere model.

2.4.2. Parameter Calibration

In the simulation model, tangential elastic coefficient k_T and normal elastic coefficient k_N were calculated according to elastic modulus E and shear modulus G [9]. Tangential damping coefficient C_t and normal damping coefficient C_n were calculated according to the corresponding normal and tangential elastic coefficients, material density ρ and recovery coefficient e [13]. Tangential contact force F_t was calculated according to the Mindlin theory [14], and normal contact force F_n was calculated according to the Hertz theory. According to the Hertz contact theory [14–16], particles are regarded as isotropic materials in the process of particle collision, and the relationship between shear modulus G and elastic modulus E is:

$$G_j = \frac{E_j}{2(1+\nu_j)}$$

$(j = 1, 2)$

where,

- G_j —shear modulus of particle, Pa;
- ν_j —Poisson’s ratio of particle, %;
- E_j —elastic modulus of particle, Pa.

2.4.3. Calibration Model

In Figure 5a, which shows that the soil is composed of solid particles, the joint strength between the soil particles is far less than the strength of the soil itself, so under the action of external forces between the soil particles, mutual dislocation occurs, causing one part of the soil relative to another part of the slide. The resistance of the soil to this slide is called the shear resistance of the soil. In Figure 5b, which shows when the soil accumulation, the slope of the pile (i.e., the angle between the pile and the ground) is called accumulation angle.

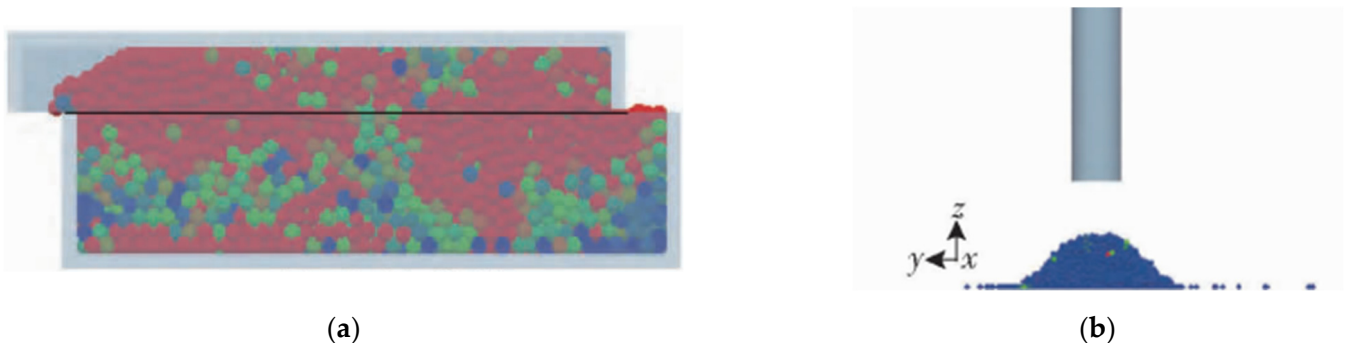


Figure 5. Calibration model. (a) Soil self-shear model (time 1.5 s). (b) Soil particle calibration accumulation angle (time 3.5 s).

According to the relationship between shear modulus G , elastic modulus E and Poisson's ratio ν , the third parameter can be determined by providing two of them. The soil particle radius is 5.5 mm, the static friction coefficient is 0.45, and the rolling friction coefficient is 0.21 [17]. In this paper, EDEM software was used to conduct simulation test research. The calibration model of soil parameters is shown in Figure 5: Figure 5a is the discrete element shear model of soil, Figure 5b is the soil accumulation angle model and the simulation parameters are shown in Table 2.

Table 2. The calibration model of the soil parameters.

Parameter Attribute	Parameter	Value of Number
Soil particle properties	Density ρ /(kg/m ³)	2500
	Shear modulus G /Pa	2.2×10^7
	Poisson's ratio ν	0.45
	Soil particle radius r /mm	5.5
Material properties of the plough body	Density ρ' /(kg/m ³)	7.8×10^3
	Shear modulus G' /Pa	7.0×10^{10}
	Poisson's ratio ν'	0.35
Interaction between plough and soil	Quiet friction factor of soil particles and particles μ_1	0.45
	Dynamic friction factor between soil particles and particles μ_2	0.21
	Soil particle and particle collision recovery factor R_1	0.11
	Quiet friction factor between the soil particles and the plough μ_3	0.3
	Dynamic friction factor between soil particles and plough μ_4	0.26
	Impact recovery factor between the soil particles and the plough R_2	0.2
Other parameters	Acceleration of gravity g /m·s ⁻²	9.8
	Deep ploughing of the plough h /mm	80–100
	Width of the plough L /mm	260
	Number of soil particles N /number	450,000

2.4.4. Establishment of Discrete Element Model for the Trenching Operation of the Trenching Plough

In order to improve the simulation accuracy of the discrete element, the adjustable ditching plow was imported into the EDEM simulation software. Based on the theory of soil stratification analysis, according to the overall size and operation parameters of the ditching device, a soil trough with a length of 4000 mm, a width of 900 mm and a soil layer thickness of 600 mm was established in EDEM software according to the simulation parameters in the table above, as shown in Figure 6. The thickness and section shape of the soil trough are consistent with the field situation. The soil thickness of plough layer is 200 mm, the soil thickness of plough bottom is 180 mm, and the soil thickness of bottom layer is 220 mm. The radius of soil particle unit in each layer is 5.5 mm.

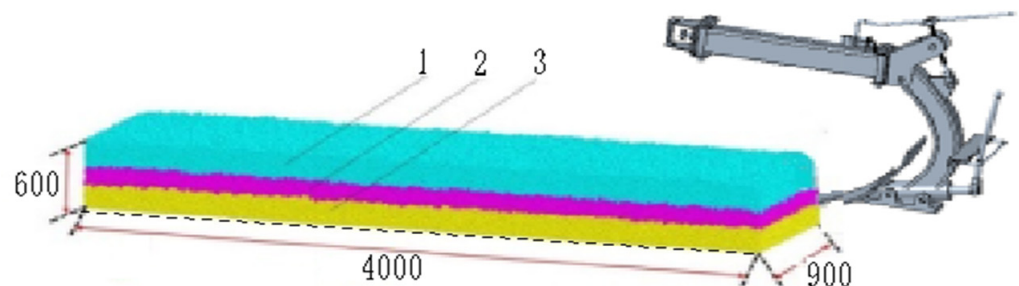


Figure 6. Simulation of the soil groove and ditching device geometric model. 1. Plough layer soil; 2. Plow sole; 3. Subsoil.

The following parameters are set in the Creator module of EDEM software. The forward speed of ditching was 0.9 m/s and 1.5 m/s, respectively, and the direction was

along the forward direction of ditching device. The angle between the ditching plough and the ground plane was set at 25° and 45° . The following parameters were set in the EDEM Simulator module: the time step was 2.1×10^{-4} s, the action time was 4.5 s, the data storage interval was 0.06 s, and the grid cell size was 2.5 times the minimum radius of the soil particles. After all parameters were set, the ditching simulation was carried out in EDEM, and the operation status of the ditching device is shown in Figure 7.

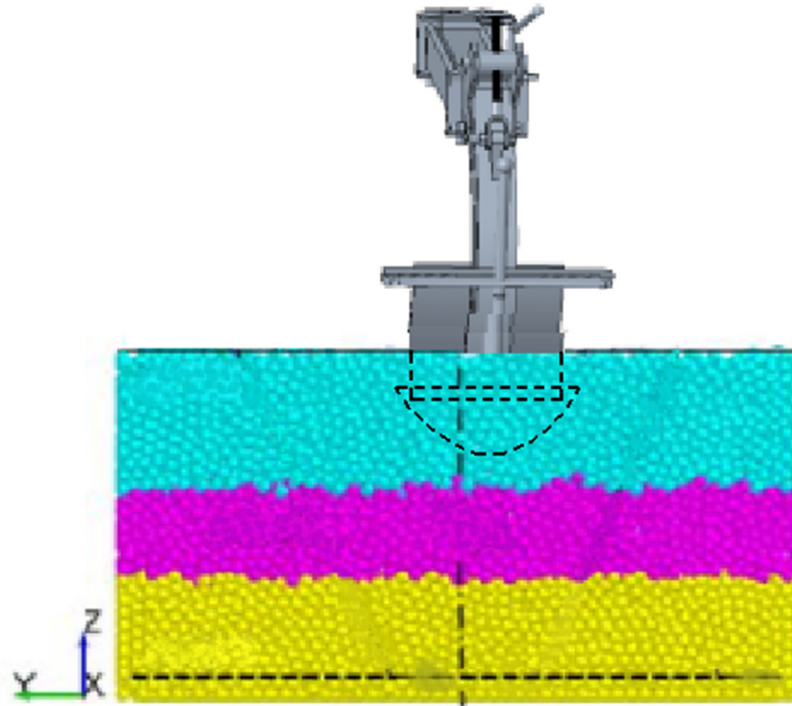


Figure 7. Ditching operation simulation diagram.

3. Results

3.1. Single Factor Analysis of Simulation Data

In order to study the influence of the change in the operating parameters of the adjustable tilting plough on the traction resistance and the evaluation index of ditching operation, the forward speed V and the angle θ between the ditching plough and the ground plane were taken as experimental factors. In the single factor analysis, the angle between the ditching plough and the ground plane was 25° , and the forward speed (0.9 m/s and 1.5 m/s) was changed. The influence of velocity change on traction resistance change was analyzed, as shown in Figure 8a,b.

According to the results of simulation, the plough body stress was introduced into the soil bin data, the data to map Figure 8a,b in 15 cm deep tillage, furrow plough Angle 25° , under different working speeds of traction resistance with the displacement variation, graph data for furrow plough and furrowing opener to open the soil to complete through the data between the data collection phases. As can be seen from the figure, the traction resistance of the trenching plough increases rapidly when it enters the soil, and then fluctuates back and forth within a certain range. The relationship between traction resistance and displacement is similar at different forward speeds. As the simulation speed increases from 0.9 m/s to 1.5 m/s, the traction resistance increases from 1751.31 N to 2197.31 N, which is 1.98 times that of the former, and the increase trend gradually increases. It shows that the speed has a significant influence on the traction resistance. With the increase in working speed, the traction resistance of the plough body and the corresponding power consumption increase significantly. In order to reduce power dissipation in actual production and cultivation, it is necessary to advance at a low speed. According to the analysis data in this paper, the best forward matching speed will be further studied in orthogonal experiments.

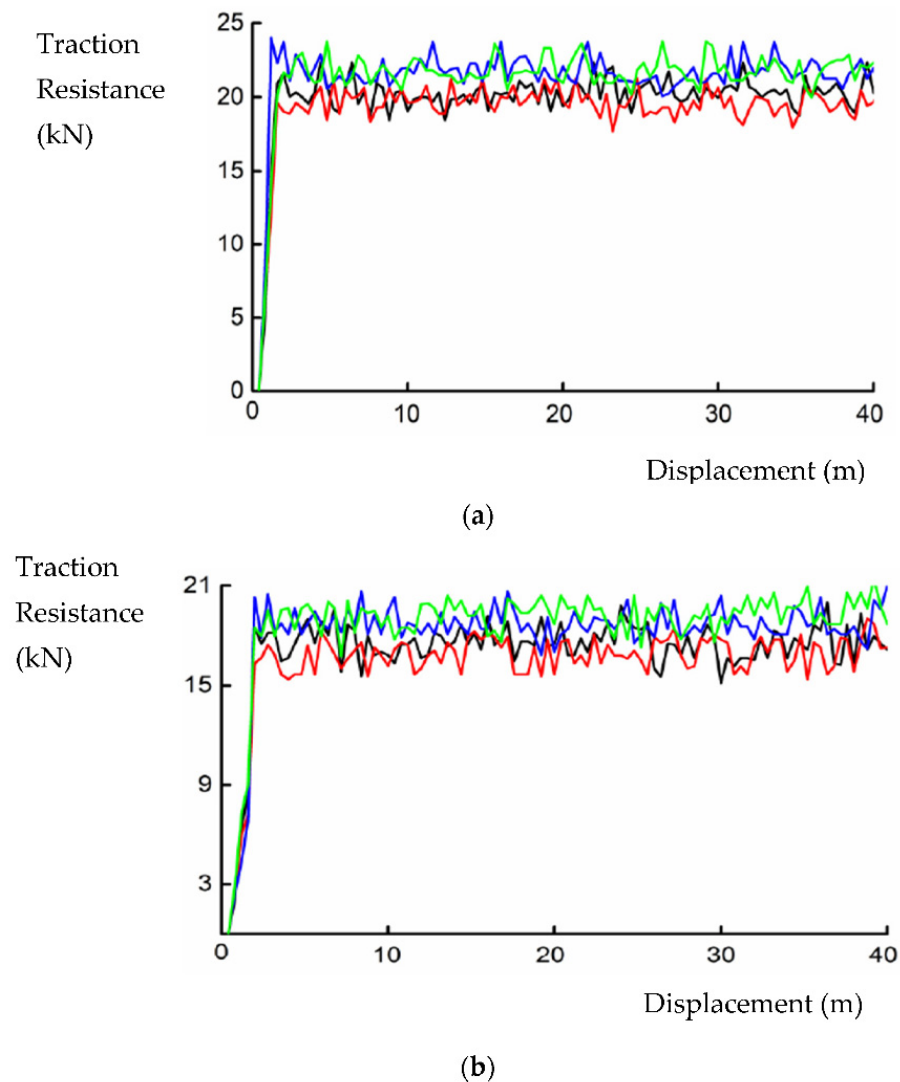


Figure 8. Traction resistance–displacement diagram of deep loose shovel at 15 cm tillage depth (the angle $\theta = 25^\circ$ between the ditching plough and the ground plane). (a) Forward speed (0.9 m/s). (b) Forward speed (1.5 m/s).

3.2. Orthogonal Test

3.2.1. Test Design

In order to explore the interaction and influence law of the forward speed V and the angle θ between the ditching plough and ground plane on the stability coefficient of ditching depth and consistency coefficient of ditching bottom width, the Box–Behnken experimental design method was used to carry out the simulation test of the adjustable ditching operation parameters of *Codonopsis pilotica*, so as to study the optimal operation parameter combination of the ditching device. According to the test design, the forward speed and the angle between the ditching plough and the ground were set as independent variables X_1 and X_2 , and the stability coefficient of ditching depth and the consistency coefficient of ditching bottom width were set as evaluation indexes Y_1 and Y_2 . After the trench device is operated under certain working parameters, the degree to which the trench depth remains stable is expressed by the stability coefficient of ditching depth Y_1 . After the trench device is operated under certain working parameters, the degree of consistency of the trench bottom width is expressed by the consistency coefficient of the trench bottom width Y_2 . Additionally, the test factors and coding level of 2 factors 2 were specified, as shown in Table 3. The test results are shown in Table 4.

Table 3. Response surface test factor and levels.

Level	Forward Speed $X_1/(m \cdot s^{-1})$	Angle between the Ditching Plough and the Ground $X_2(^{\circ})$
−1 low level	0.9	15
0 middle level	1.2	30
1 high level	1.5	45

Table 4. Quadratic regression experimental design and response value.

Test Number	Forward Speed	Angle	Stability Coefficient of Ditching Depth $y_1/(%)$	Consistency Coefficient of Ditching bottom Width $y_2/(%)$
1	0	1	94.02	95.08
2	0	−1	94.36	93.19
3	1	0	96.52	96.26
4	1	−1	94.96	94.87
5	0	0	95.65	96.22
6	−1	1	97.02	95.75
7	0	1	93.95	94.46
8	0	0	98.01	95.22
9	0	−1	94.85	93.55
10	1	1	98.01	94.96
11	−1	0	93.44	95.21
12	−1	−1	96.69	96.36
13	−1	0	97.76	96.56
14	0	0	95.88	95.74

3.2.2. Establishment of the Regression Model and Analysis of Variance

Design-expert statistical analysis software was used to perform multi-distance regression fitting analysis on the test data in the above table, and the quadratic regression models of the coded values of the stability coefficient of the ditching depth and the consistency coefficient of the ditching bottom width were obtained, as shown in Equations (1) and (2).

$$y_1 = 96.03 - 1.35x_1 - 0.24x_2 + 0.95x_1x_2 + 1.02x_1^2 - 0.016x_2^2 \quad (1)$$

$$y_2 = 97.63 - 0.79x_1 + 0.29x_2 + 0.53x_1x_2 - 1.52x_1^2 - 0.02x_2^2 \quad (2)$$

Thus, a response surface regression model was established for the stability of the trenching depth and the consistency coefficient of trenching width of the forward speed, and the angle between the trenching plough and the ground; the variance analysis was conducted for the regression model. The results are shown in Table 5.

As can be seen from Table 5, the significant p -value of the retrospective model of the ditching depth stability and ditching bottom width consistency is less than 0.05, indicating that the regression model is significant. The p -values of the misfitting terms were all greater than 0.05, indicating that there was no misfitting factor, indicating that the regression equation had a high fitting degree. The R^2 coefficients of the model determination were 0.8736 and 0.9751, respectively, indicating that the model could describe the experimental results well.

Table 5. Variance analysis of the regression model.

Evaluation Indices	Source of Variance	Quadratic Sum	Degrees of Freedom	Mean Square	<i>p</i>	Significance
Stability coefficient of the ditching depth y_1 (%)	model	8.42	5	4.21	0.0172	*
	X_1	0.21	1	0.41	0.6121	
	X_2	0.32	1	0.52	0.6014	
	X_1X_2	4.19	1	6.67	0.0331	*
	X_1^2	0.44	1	0.72	0.3927	
	X_2^2	3.26	1	5.68	0.0124	*
	Residual	3.71	5	-	-	
	Loss of quasi item	3.02	3	5.02	0.0702	
	Pure error summation	0.69	2	-	-	
		12.13	10	-	-	
Consistency coefficient of the ditching bottom width y_2 %	model	16.48	5	8.52	0.0039	**
	X_1	4.55	1	16.43	0.0074	**
	X_2	0.26	1	0.74	0.5703	
	X_1X_2	1.44	1	4.61	0.2109	
	X_1^2	1.27	1	5.02	0.0922	
	X_2^2	8.96	1	30.63	0.0027	**
	Residual	2.67	5	-	-	
	Loss of quasi item	0.91	3	0.86	0.6134	
	Pure error summation	1.76	2	-	-	
		19.15	10	-	-	

Note: * Means significant influence, $p < 0.05$; ** means very significant, $p > 0.01$.

3.2.3. Analysis of the Effects of Interaction

According to the regression equation analysis, using the response surface, we investigated the influence of various parameters on the evaluation index, studying speed v , namely, the furrowing plough blade with ground plane angle θ . Two factor interactions are split groove depth stability and the influence of the groove width uniformity; the corresponding surface interaction diagram should be drawn as shown in Figure 9a,b, as shown in the analysis of interaction effects, in order to obtain the optimal parameter combination.

Figure 9a shows the speed and angle of furrowing. The mutual influence of the split groove depth stability coefficient can be seen from the figure; the trenching depth with the increase in the furrowing angle stability declines slowly after the first increases the change trends, and the current speed is at a low level, furrowing angle split groove depth stability coefficient is significant. In addition, the curve changes sharply, indicating that the forward speed varies within the range of 0.9–1.1 m·s⁻¹. Appropriately reducing the opening angle can significantly improve the stability of the opening depth. As can be seen from Figure 9a, when the opening angle is constant, the stability of the trenching depth decreases gradually with the increase in the forward speed.

Figure 9b is the speed and angle of the furrowing. The mutual of groove width uniformity coefficient of interaction can be seen in the figure. The current into the speed is constant, as is the groove width uniformity coefficient, which increases the furrowing angle after the first increase with a slowly decreasing trend. When the open groove angle must have a groove width uniformity coefficient, it decreases with the increase in speed; when the trenching angle is at a low level, the forward speed has a significant impact on the consistency of the trench bottom width, which is shown in the figure as the steep curve changes, indicating that when the trenching Angle is suitable for 25–35°, appropriately reducing the forward speed can significantly improve the consistency of the trench bottom width.

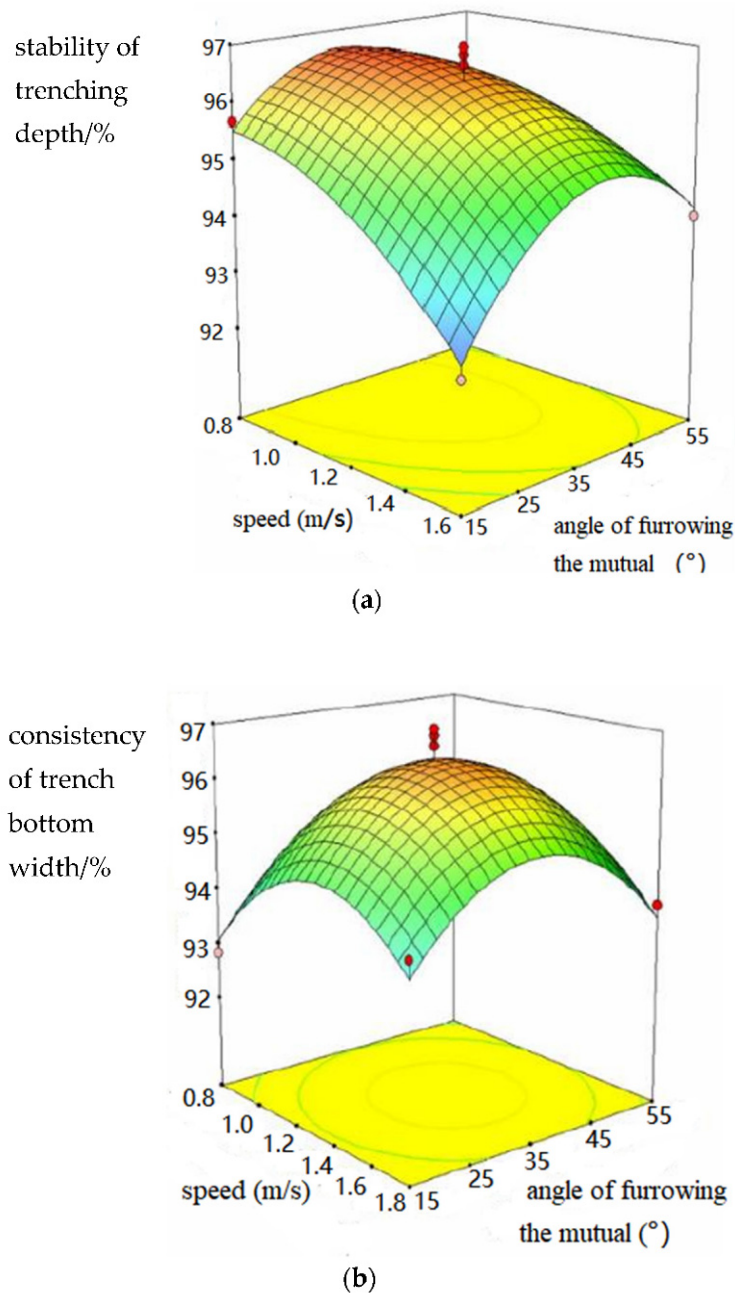


Figure 9. Response surface diagram of the interaction. (a) Influence of the interaction of trenching depths on the stability. (b) Effect of the interaction of trench bottom width on consistency.

3.2.4. Optimization of the Parametric Model

According to the agronomic requirements of the ditching operation of *Codonopsis pilosula* and the actual situation of the entire machine operation, it is required to ensure the stability of the ditching depth and the consistency of the ditch bottom width at the same time to achieve the best results. Because the influence of various factors on its target value was not consistent, a multi-objective optimization solution was needed. Taking the stability of the ditching depth and the consistency of the ditching bottom width as the objective function, the two experimental factors of the forward speed and ditching angle of the ditching device were optimized. The mathematical model is as shown in Equation (1) $\{x_1 \in [0.9, 1.5]\}$ and Equation (2) $\{x_2 \in [15, 45]\}$ in Section 3.2.2.

The influence of the two factors on the stability of the ditching depth and consistency of ditch bottom width was comprehensively considered and optimized and solved

by MATLAB. Finally, the optimal operation parameter combination was obtained: the forward speed was 0.9 m/s, the angle of ditching was 35° and the stability coefficient of the ditching depth and consistency coefficient of ditch bottom width were 97.57% and 98.03%, respectively.

4. Discussion

The harvest object of *Codonopsis pilosula* is the stem. *Codonopsis codonopsis* is a deep-rooted plant, suitable for viscous soil. Water-logged soil is not beneficial for it. *Codonopsis pilosula* is mainly implemented with oblique transplanting. To plant it, an oblique ditch must be dug, and the seedlings must be inserted evenly on the sloping surface. Then, cover the seedlings with soil and level it. The main planting area for *codonopsis pilotica* is the Weiyuan county in the Gansu province, northwest China. The place is called “the home of *Codonopsis pilotica* in China”. At present, there is no sufficient research on the mechanized ditching technology of *Codonopsis pilosula*, and there is no research on the ditch planting of *Codonopsis pilosula* in related fields.

In this paper, the key factors affecting the quality of the ditching operation (the stability coefficient of the ditching depth and the consistency coefficient of the trench bottom’s width) were analyzed by statistical methods combining EDEM simulation analysis and experiment, single factor test analysis and orthogonal test analysis. The discrete element calibration of the soil particles was completed with EDEM software. The regression model between the test indexes and test factors was established by Design Expert analysis software. We analyzed each factor’s influence on the test indices and optimized each experimental factor comprehensively. Finally, we obtained the optimal parameter combination, which provides a technical basis for the mechanization of *Codonopsis pilosula*’s ditching operation.

5. Conclusions

- (1) An EDEM discrete element simulation model was established in this paper. The simulation results show that the traction resistance of the plough body was affected by the operating speed. The traction resistance increased linearly in low-speed stage and exponentially in the high-speed stage along with an increase in the operating speed. As the simulation speed increased from 0.9 m/s to 1.5 m/s, the traction resistance increased from 1751.31 N to 2197.31 N, which was 1.25 times than before. The increase trend gradually increased. It showed that speed had a significant influence on the traction resistance. With the increase in working speed, the traction resistance of the plough body and the corresponding power consumption increased significantly.
- (2) Using the stability coefficient of the ditching depth and the consistency coefficient of the trench bottom width as test indices, the speed and the angle of ditching were considered as impact factor. We used a Box–Behnken orthogonal experimental design method to establish a regression model between the test indices and factors, then analyzing the influence of each test index. Combining agronomic requirements and MATLAB’s optimal test factors, an optimized operational parameter combination was obtained. The forward speed was 0.9 m/s, the angle of ditching was 35°, and the stability coefficient of ditching depth and consistency coefficient of trench bottom’s width were 97.57% and 98.03%, respectively.
- (3) The field experiment showed that the evaluation indices of the performance of the adjustable ditching device’s performance were in line with the national standards and *codonopsis pilosula*’s planting agronomic requirements. The stability coefficients of the ditch depth and the compartment surface reached 94.67% and 97.53%, respectively, better than the industrial standards.
- (4) The paper showed that the adjustable small ditching plough has the characteristics of flexible performance, small power, energy saving, simple operation and convenient operation. The product’s application and promotion are relatively speedy.

Author Contributions: Conceptualization, D.L. and Y.G.; methodology, X.C. and X.Z. (Xiao Zhang); software, Q.Y.; validation, D.L., X.C. and Y.W.; formal analysis, Y.G.; investigation, D.L.; data curation, Q.Y.; writing—original draft preparation, D.L.; writing—review and editing, D.L.; supervision, X.Z. (Xuejun Zhang) and Y.G. All authors have read and agreed to the published version of the manuscript.

Funding: This research was supported by the Central Public-interest Scientific Institution Basal Research Fund, grant number S202101-02; the China Agriculture Research System, grant number CARS-25.

Institutional Review Board Statement: Not applicable.

Data Availability Statement: The data presented in this study are available on-demand from the first author at (liudejiang@caas.cn).

Conflicts of Interest: The authors declare that they have no competing interest.

References

1. Gan, L.; Sun, D.; Cheng, H. Design of 1FFSL-5 type shallow-deep flip plow. *J. Agric. Mech. Res.* **2018**, *41*, 136–138.
2. Kumar, G.V.P.; Raheman, H. Automatic feeding mechanism of a vegetable transplanter. *Int. J. Agric. Biol. Eng.* **2012**, *5*, 20–27.
3. Chen, Y. 2018 development report on mechanized production of vegetables in China. *J. Chin. Agric. Mech.* **2019**, *40*, 1–6.
4. Liu, D.; Xie, F.; Ye, Q.; Ren, S.; Li, X.; Liu, M. Analysis and experiment on influencing factors on power of ditching parts for 1K-50 orchard ditching. *Trans. CSAE* **2019**, 19–28.
5. Hasimu, A.; Chen, Y. Soil disturbance and draft force of selected seed openers. *Soil Tillage Res.* **2014**, *140*, 48–54. [[CrossRef](#)]
6. Jia, H.; Meng, F.; Liu, L.; Shi, S.; Zhao, J.; Zhuang, J. Biomimetic design and experiment of coeshare furrow opener. *Trans. Chin. Soc. Agric. Mach.* **2020**, *51*, 44–49.
7. Wang, S.; Li, S.; Zhang, Y.; Zhang, C.; Chen, H.; Meng, L. Design and optimization of inclined helical ditching component for mountain orchard ditcher. *Trans. CSAE* **2019**, *34*, 11–22.
8. Zhang, Y. Simulation and Experimental Study on Soil Throwing Performance of Reverse Rotary Tillage Fertilizing Seeder Based on Discrete Element Method. Master's Thesis, Jiangsu University, Zhenjiang, China, 2012.
9. Kang, J.; Li, S.; Yang, X.; Liu, L.; Li, C. Experimental verification and simulation analysis on power consumption of disc type ditcher. *Trans. CSAE* **2016**, *32*, 8–15.
10. Barr, J.B.; Desbiolles-Jack, M.A.; Fielke, J.M. Minimizing soil disturbance and reaction forces for high speed sowing using bentleg furrow openers. *Biosyst. Eng.* **2016**, *151*, 53–64. [[CrossRef](#)]
11. Zhao, X.; Guo, H.; Zhang, J.; Yang, W.; Han, J. The status quo and development trend of dryland transplanter in Xinjiang. *Xinjiang Rural. Mech.* **2014**, *4*, 25–29.
12. Zhang, H.; Su, D.; Liu, W.; Qiu, L. Development of Multi-directional Hydraulic Trenching Plow. *Agric. Mech. Res.* **2012**, *8*, 49–52.
13. Liu, W.; Su, D.; Zhang, L. Development of Adjustable Small Ditching Plough. *Jiaozuo Univ. Acta Geogr. Sin.* **2011**, *3*, 103–105.
14. Ding, Q.; Ge, S.; Ren, J. Characteristics of subsoiler traction and soil disturbance in paddy soil. *Nongye Jixie Xuebao* **2017**, *48*, 47–56,63.
15. Liu, X.; Zhang, Q.; Liu, L. Optimization of soil contact surface of ship ditching device based on differential geometry and EDEM. *Trans. Chin. Soc. Agric. Mach.* **2019**, *50*, 59–69.
16. Zeng, Z.; Ma, X.; Cao, X. Current situation and prospect of discrete element Method in agricultural engineering research. *Trans. Chin. Soc. Agric. Mach.* **2021**, *52*, 1–20.
17. Liu, X. Design and Working Mechanism of Ditching Tillage Preparation Components of Rapeseed Direct-Seeding Machine. Master's Thesis, Huazhong Agricultural University, Wuhan, China, 2018.

Article

LED Lighting Agrosystem with Parallel Power Supply from Photovoltaic Modules and a Power Grid

Pavel Tikhonov ^{1,*}, Konstantin Morenko ¹, Arseniy Sychov ¹, Vadim Bolshev ^{2,*}, Alexander Sokolov ³ and Alexander Smirnov ³

¹ Laboratory of Unconventional Energy, Federal Scientific Agroengineering Center VIM, 109428 Moscow, Russia

² Laboratory of Power Supply and Heat Supply, Federal Scientific Agroengineering Center VIM, 109428 Moscow, Russia

³ Laboratory of Lighting Engineering, Federal Scientific Agroengineering Center VIM, 109428 Moscow, Russia

* Correspondence: ptikhonov@inbox.ru (P.T.); vadimbolshev@gmail.com (V.B.)

Abstract: The paper considers the operation of an LED lighting system with a parallel power supply from photovoltaic modules and a power grid. Such systems are supposed to be widely applicable in premises with limited natural lighting, particularly agrosystems where artificial light of a certain spectrum is specifically required to ensure efficient plant growth. The paper presents the scheme of the developed LED lighting system, as well as an assembled prototype containing a single 36-watt lamp. The data of the experimental study are provided on the developed LED lighting system using the developed monitoring system. The experimental study demonstrates an efficient power take-off and the reliability of the proposed scheme to competently select the characteristics and circuit solutions for the converter of voltage from the PV module. The proposed LED system allows simplification of the PV system by eliminating circuits with an inverter and storage devices, hence significantly reducing the cost of the photovoltaic systems. Likewise, such a simplicity has a positive effect on PV system reliability, which benefits the cost as well.

Keywords: photovoltaic module; LED lighting system; power grid; step-up converter; efficient power take-off; monitoring system

Citation: Tikhonov, P.; Morenko, K.; Sychov, A.; Bolshev, V.; Sokolov, A.; Smirnov, A. LED Lighting Agrosystem with Parallel Power Supply from Photovoltaic Modules and a Power Grid. *Agriculture* **2022**, *12*, 1215. <https://doi.org/10.3390/agriculture12081215>

Academic Editors: Muhammad Sultan, Redmond R. Shamshiri, Md Shamim Ahamed and Muhammad Farooq

Received: 12 July 2022

Accepted: 11 August 2022

Published: 12 August 2022

Publisher's Note: MDPI stays neutral with regard to jurisdictional claims in published maps and institutional affiliations.



Copyright: © 2022 by the authors. Licensee MDPI, Basel, Switzerland. This article is an open access article distributed under the terms and conditions of the Creative Commons Attribution (CC BY) license (<https://creativecommons.org/licenses/by/4.0/>).

1. Introduction

Much attention is paid to the use of renewable energy sources all over the world [1–3]. Energy production in this industry is growing by tens of GW per year [1,2]. Solar radiation is one of the most promising types of alternative energy resources. The greatest role in this is played by photovoltaic conversion. Photovoltaic modules (PVM) are already able to compete economically with installations using fossil fuels [1]. The scope of use of photovoltaic converters continues to grow.

At the same time, there are still a number of problems that prevent the mass use of photovoltaic plants. One of them is the matching of networks according to the type of current and voltage level, which requires the conversion of electrical energy and converters (including for systems based on “smart grid”). These converters and devices are technically complex and require high maintenance costs [4–6].

One of the main constraining economic factors is a significant capital intensity. Its main reason is the inconstancy of the energy supply [7,8]. During periods when there is no flow of renewable energy, it is necessary to guarantee electricity supply, which is more often realized with the use of storage devices than with power from another source. Electrochemical batteries are often used in low-power systems. To date, the cost of energy storage in such batteries is so high [9,10] that it is economically advisable to use them only under strict conditions for the autonomy of the system or the guarantee of power supply.

The predominance of alternating current networks is also one of the problems hindering the development of photovoltaic systems, as the photovoltaic modules generate direct current, which requires further conversion to alternating current to transmit electricity to the consumer, and if, in the 20th century, it was mainly AC consumers, today, with the growth and development of semiconductor devices, all the internal circuits of many modern household appliances, office equipment, and other electrical equipment actually work from DC [11–13]. Complex electronic control circuits most often cause this. These devices are powered by AC power and use rectifiers to power all internal circuits.

Such devices can be switched to DC operation without significant changes, for example, devices with collector motors and resistive heating elements. Technically, these devices are capable of operating directly from the DC network, but this possibility is not claimed by the manufacturers, and most importantly, from a technical point of view, this will not require significant complications and increases in the cost of devices. Changing this situation requires the significant collaboration of scientists, engineers, and manufacturers.

The method for the wide introduction of direct current networks is promising, with the help of which consumers will be able to use electricity from photovoltaic modules without additional transformations and losses [14,15]. On the one hand, the development of DC networks contributes to the development of renewable energy, and on the other hand, the development of renewable energy will also impact the expansion of DC networks use.

Taking into account that noted above, it is obvious that the development of DC networks [16–20] and mixed networks [21–23] is the important component of the widespread introduction of PVM. At the same time, there should be a proliferation of consumer equipment that can work from DC networks. This will lead to the simplification of systems in the future and reduce the need for accumulation.

For experimental verification of the proposed solutions, a lighting system based on LED lamps with a parallel power supply from photovoltaic converters and a general-purpose power grid was developed [15].

2. Materials and Methods

One of the universal schemes is shown in Figure 1 [15]. On its basis, a photovoltaic LED lighting system was developed and manufactured.

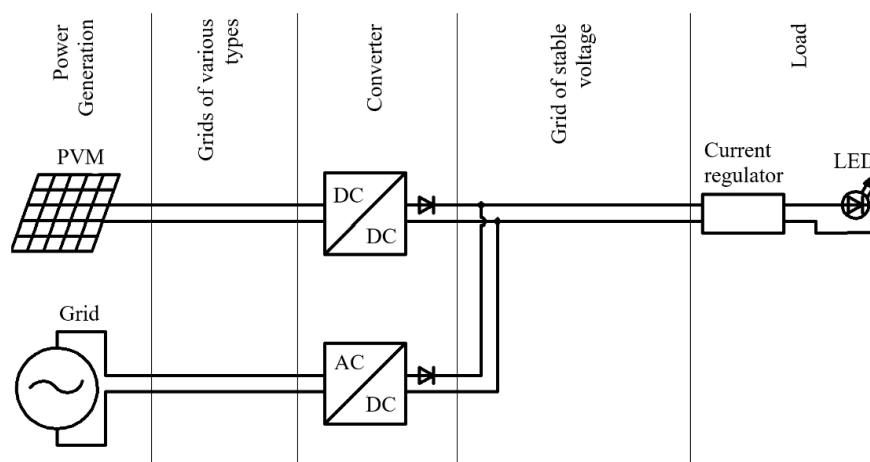


Figure 1. General electrical diagram of a lighting system with a combined power supply and the use of a step-up converter.

When the incoming solar radiation flux is sufficient to power the light sources, the power comes from the PVM. When the incoming solar radiation and the production of PVM decrease, the lack of energy is compensated by using a mains power supply (AC/DC) connected to an electrical grid.

The circuit uses step-up and step-down converters with voltage and current stabilization. This allows us to match devices with different levels of voltage and current, which significantly expands the possibilities for using different generators and loads.

The voltage stabilizer at the output of the PVM operates in a wide range of input voltage. Its task is to increase the power take-off from the PVM in comparison with the direct connection of the PVM to the grid at an equal voltage. The current stabilizer at the input of the lamp provides the current operation mode of the LEDs. Diodes protect against power flows between generators at voltage deviations in various operating modes.

An electrical circuit with additional sensors was developed for conducting experimental studies (Figure 2). This scheme uses a parallel connection of LED lines.

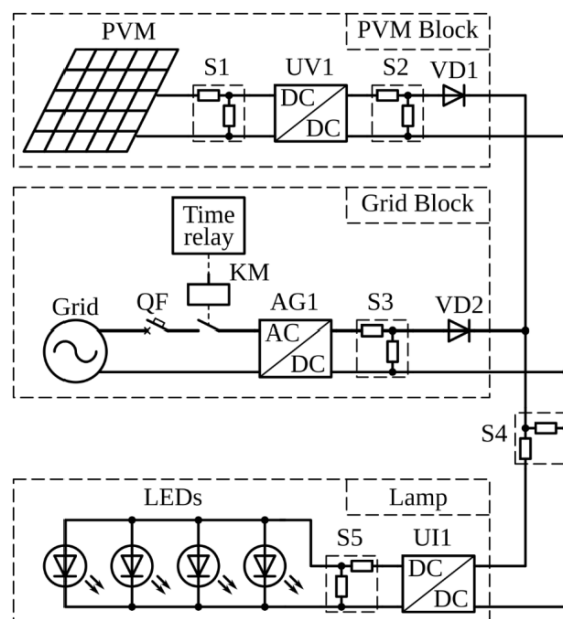


Figure 2. Electrical schematic diagram of a lighting system with a parallel power supply from photovoltaic modules and the power grid: (UV1) step-up converter QSKJ QS-1224CCBD; (AG1) power supply unit XD-DC 2425; (UI1) current stabilizer (step-down converter) QSKJ QS-2405CCBD; (S1 . . . S5) current and voltage sensors INA226; (VD1 . . . VD2) Schottky diodes 90SQ045; (QF) circuit breaker; (KM) contactor.

The operating voltage of individual LED lines is about 35 V and is only slightly lower than the maximum voltage of most step-up converters (36 . . . 40 V). For the development and wide distribution of such systems, it is desirable to use a higher voltage. This will reduce losses. It is planned to increase the voltage to the voltage of four lines connected in series (140 V). It is possible to use any other voltage level corresponding to the micro-networks in which the system will function [24–26].

Table 1 shows the list of equipment of the experimental system.

Table 1. Main characteristics of equipment for a lighting system with parallel power supply from photovoltaic modules and the power grid.

N	Equipment	Voltage, V (Input/Output)	Current, A	Power, W
1	Step-up converter QSKJ QS-1224CCBD	10–35/12–35	10	100
2	Current stabilizer (step-down converter) QSKJ QS-2405CCBD	7–40/1.2–35	8	200
3	Power supply unit XD-DC 2425	~230/35	7	-
4	LED line LEDPREMIUM	28–35 B	0.3	10
5	Schottky diodes 90SQ045	45 B	9	-

The study of the operating modes of the LED lighting system requires the use of a device for monitoring parameters. Such a device was developed on the basis of the Arduino Mega (Figure 3). It allows us to obtain information about the currents and voltages in the LED lighting system and the incoming flow of solar energy. The SD card stores collected data.

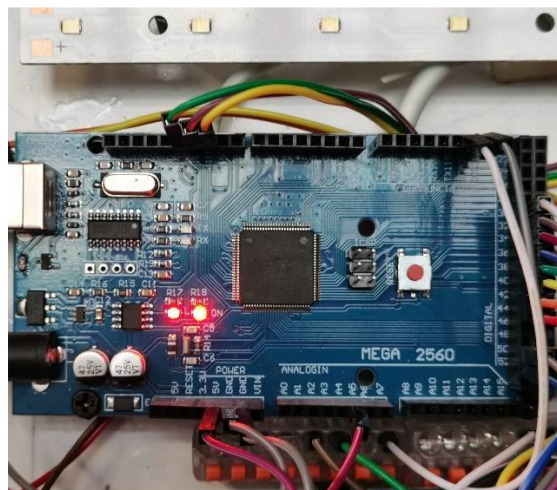


Figure 3. The main board of the autonomous parameter monitoring system.

The autonomous parameter monitoring system includes:

- PCB with a microcontroller;
- Digital seven-segment indicator for visual continuous monitoring of the system operation parameters;
- Membrane keyboard for switching modes and displayed information;
- Real-time clock for logging the time;
- Memory card module for interaction of the microcontroller with the SD card;
- Current and voltage sensors INA226 for converting electrical parameters of the system into data;
- Backup power source based on a lithium-ion battery for uninterrupted operation of the system when the network and/or PVM are disconnected.
- The system logs data with an interval of one second.

Current sensors and voltage sensors measure the operating modes of the circuit (Figure 2). Each element of the INA226 is a current sensor and a voltage sensor [27] (Table 2). In the diagram, they are presented as separate elements in the block. Sensors 1 and 2 measure the parameters before and after the PVM converter, sensor 3—after the AC-DC power supply, sensors 4 and 5—before and after the LED load current stabilizer.

Table 2. Main metrological characteristics of the devices used.

Device	Measured Value	Range	Accuracy
Multimeter UT61E	Voltage DC	0 ... 220 mV 0 ... 220 V	±(0.1% + 5) ±(0.1% + 2)
INA226	Voltage	0 ... 36 V	±0.1%
Pyranometer GSM/O-U10	Solar radiation intensity	0 ... 1300 W/m ²	±10%
Arduino	Voltage	0 ... 5 V	±2 LSB (±0.01 V)

As the INA226 uses an external shunt to measure current, after its installation, calibration was performed using a UNI-T model UT61E multimeter [28].

The FuehlerSysteme eNET International pyranometer GSM/O-U10 model is used to measure the incoming flow of solar radiation [29]. The analog output of the pyranometer is connected to the ADC of the monitoring device.

The metrological characteristics of the devices used are given in Table 2.

3. Results

The developed modular LED lighting system with the parallel power supply from the PVM and the power grid has passed a number of field studies on the territory of the Federal Scientific Agroengineering Center VIM, Moscow, Russia (Figure 4). For the experiments, a minimum module was implemented, consisting of one standard lamp with a power of 36 W and a PVM with a power of 20 W. In general, when choosing the power of the PVM for such a system, it is necessary that the output power of the PVM completely covers the load power at maximum output. This will ensure high values of the PVM efficiency. At the same time, the capacity of the PVM should be selected by taking into account the technical characteristics and climatic operating conditions of the system [30].

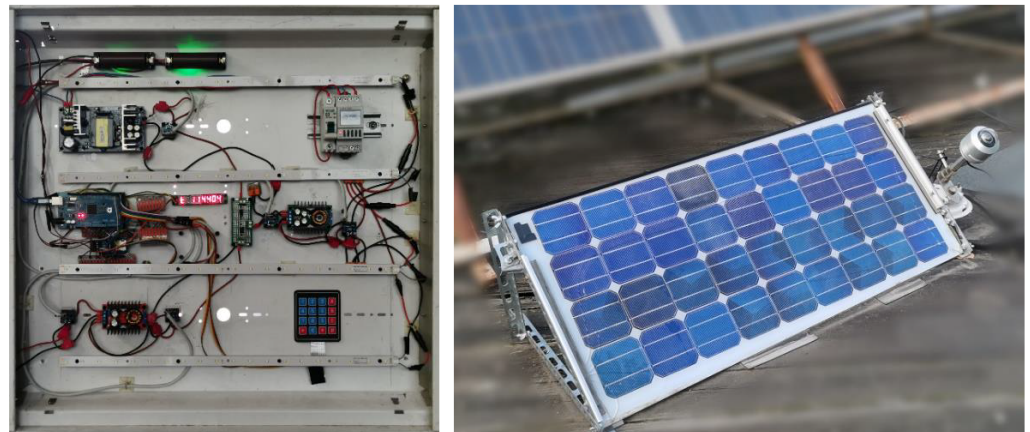


Figure 4. Elements of the developed system.

It is also important to correctly select the load for developed systems. Buildings with rooms where artificial lighting is necessary during the working day seem to be the most optimal. As an example, they can be warehouse complexes for agricultural holdings, poultry farms, livestock buildings, mushroom farms, shopping centers, and underground passages. Recently, urban plant factories have also been gaining popularity, where cultivation is carried out indoors under artificial irradiation. In such factories, the use of LEDs in irradiation installations is a nonalternative option, as it is necessary to achieve high energy efficiency due to the precise selection of radiation spectral composition for the grown crop [31].

The system has shown its efficiency according to the schedule from 10 to 18 h on working days for one month. Operation data of the system during the period of experimental studies are presented in Figures 5–7. The module was directed to the south and installed at an angle of 45° to the horizon. The orientation of the module did not change during the entire study period. The pyranometer during the experiment was located at the same angle and azimuth as the photovoltaic module involved in the research, namely, the tilt for solar irradiance measurement was 45 directed to the south, and the latitude of measurement location was 55.7249 N.

For a clear demonstration of the system's operation at different intensities of incoming solar irradiation (SI), the article presents the system's performance indicators on one of the days with variable clouds (Figure 5). According to these data, it is possible to evaluate the operation of the system both in clear weather and in cloudy conditions.

As noted above, the power flow from the PVM and from the power grid is regulated by the voltage level at these sources. The operating voltages on the system elements on one of the days of field studies are shown in Figure 6.

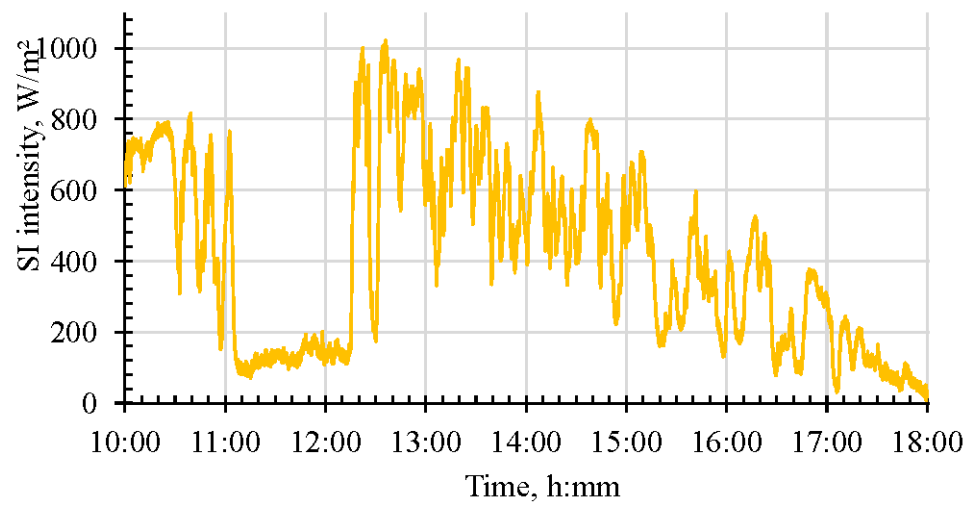


Figure 5. Solar radiation intensity.

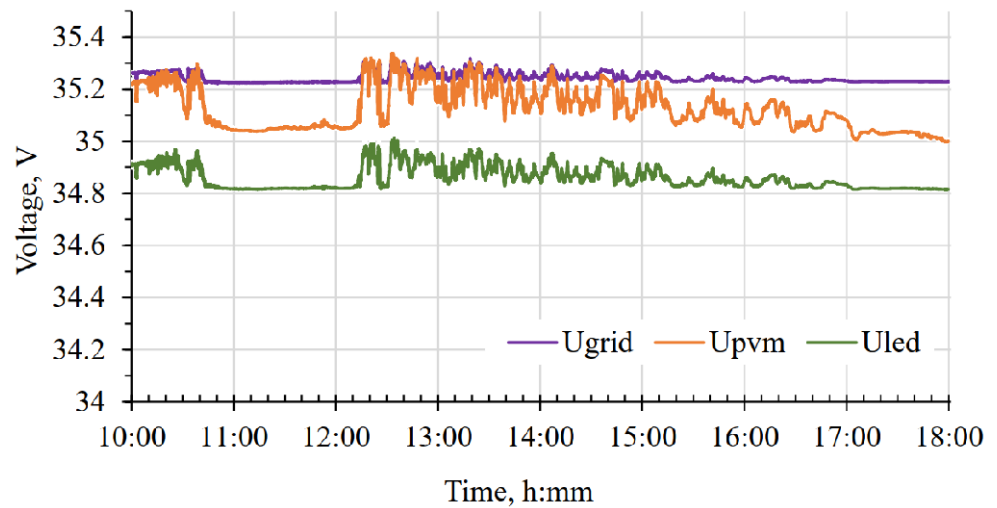


Figure 6. Voltages on the elements of LED lighting system: (U_{PVM}) voltage at the output of the PVM converter; (U_{grid}) voltage at the output of the grid converter; (U_{LED}) voltage at the input of the LED current supply.

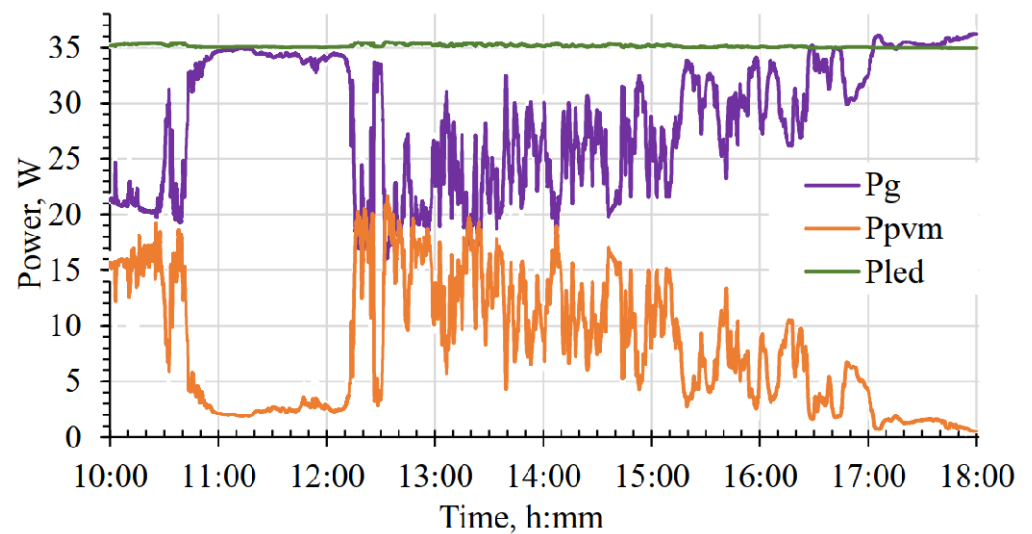


Figure 7. Power indicators of the lighting system elements: (P_{LED}) LED power; (P_{PVM}) power at the output of the PVM converter; (P_G) power at the output of the network converter.

The figure shows how the voltages change with fluctuations in the power generation of a photovoltaic module. Despite the decrease in the voltage at the output of the PVM converter below the voltage at the output of the grid converter under the conditions of a SI intensity decrease, the power from the PVM continues to flow to the LEDs, which is shown in the graph in Figure 7. This is explained by the fact that, depending on the flowing current, the voltage drop on the Schottky diodes VD1 and VD2 changes.

At the same voltage after the diodes, different voltages are set before the diodes. The difference depends on the current ratio of the power coming from the network and from the PVM to the lamp. In addition, the oscillatory processes are observed, in which the values of the voltages before and after the PVM converter fluctuate significantly without correlation with changes in the intensity of the incoming SI. It is assumed that it is possible to avoid the oscillatory processes or reduce their magnitude by selecting the smoothing capacitors.

Let us take a closer look at the system power indicators (Figure 7). In any time interval, including at a low level of SI arrival, all the energy generated by the PVM is consumed on the LEDs (not counting conversion losses), and its lack is compensated by network energy through the power supply unit. At the same time, exactly the amount of energy that is necessary to compensate for the missing power for the operation of the lighting system in the nominal mode is consumed from the power grid. The power received by the LED strip is 36 W and is kept relatively unchanged.

In cloudy conditions, the arrival of SI decreases and the efficiency of the boost converter, which takes power from the PVM, decreases (Figures 5 and 8).

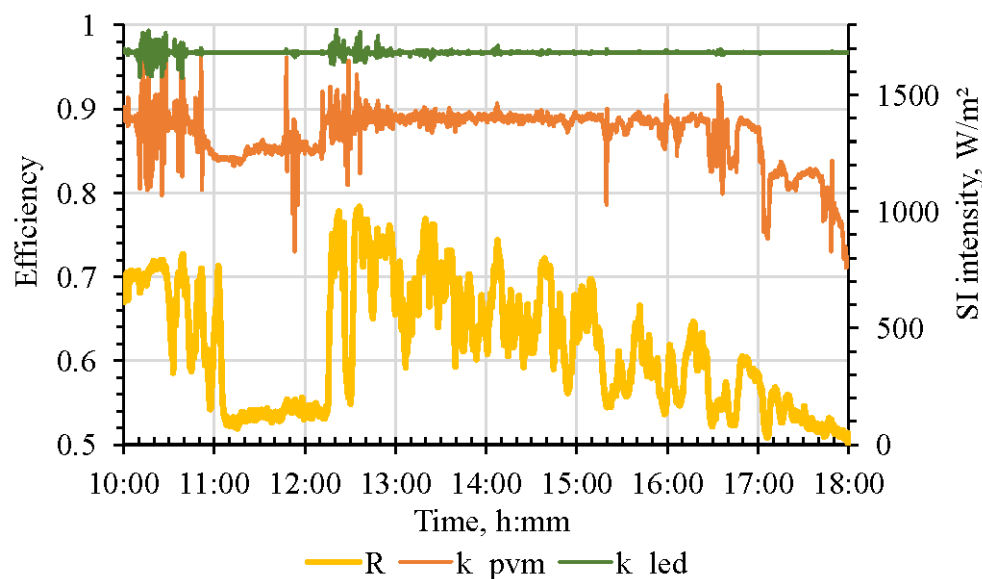


Figure 8. Efficiency of the converters: (R) SI intensity; (k_{PVM}) efficiency of the PVM step-up converter; (k_{LED}) efficiency of the current stabilizer of LED lamp.

Based on the data obtained, it can also be concluded that the step-up converter works together with the PVM with high efficiency at a solar radiation intensity above 100 W/m^2 . With sufficient solar radiation, the conversion efficiency reaches about 89%, and only when the SI intensity is below 50 W/m^2 , the conversion efficiency is less than 75%, while the power generated by the PVM is less than 10% of its rated power (Figures 5, 7 and 8).

In view of the above-mentioned features, the question remains whether an improvement of the converter at the PVM output is required to increase the efficiency of its operation at low solar radiation intensity. Such an improvement will not be justified, as the converted electric power during such periods is significantly lower in comparison with the nominal operating mode (Figures 7 and 8). At the same time, in the nominal operating mode, on the

contrary, a schematic revision of the converting device is necessary to increase its efficiency (above 89%).

During a number of experiments, the volt-ampere characteristics (VACs) of a photovoltaic module were taken at different SI (Figure 9). The characteristics were measured using the load block of resistors and UT61E multimeters.

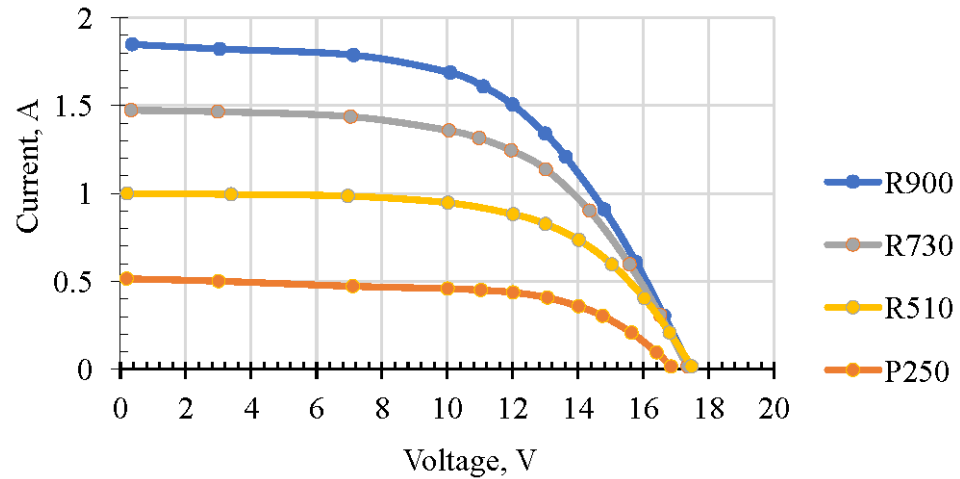


Figure 9. VAC of a PVM at different solar radiation intensities: (R900) at an average intensity of 900 W/m²; (R730) at 730 W/m²; (R510) at 510 W/m²; (R250) at 250 W/m².

The obtained VACs were converted into the volt-watt characteristics (VWCs) of the photovoltaic module, shown in Figure 10.

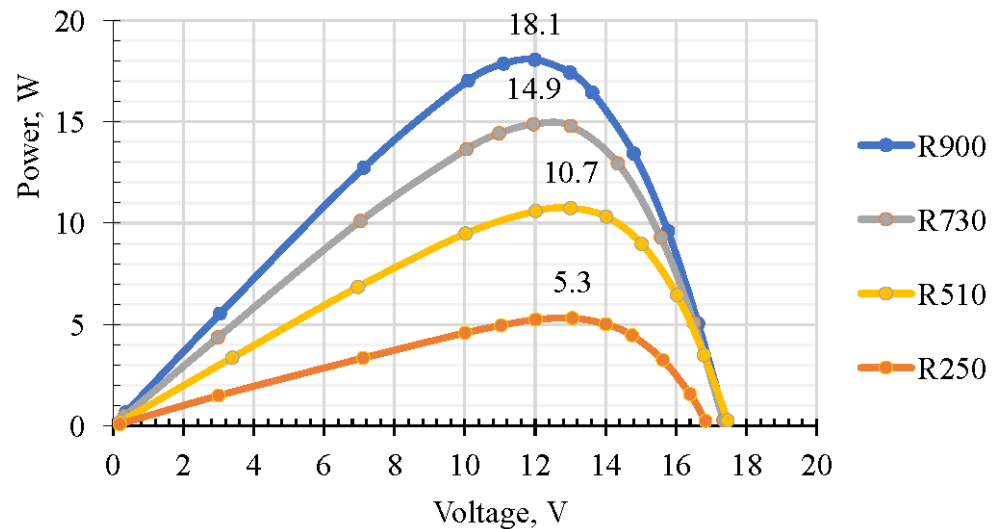


Figure 10. VWC of the photovoltaic module at different solar radiation intensities: (R900) at an average intensity of 900 W/m²; (R730) at 730 W/m²; (R510) at 510 W/m²; (R250) at 250 W/m².

As can be seen from the figure, the maximum power of the module was about 18 W at an SI intensity of 900 W/m². Immediately after taking the characteristics, the module was connected directly to the lighting system according to the scheme shown in Figure 2. At the same time, with the use of the monitoring system, its operating parameters were recorded for 30 s. The data of these measurements are shown in Figure 11. The power taken from the PVM was determined by calculation using the current and voltage sensor S1 (see Figure 2).

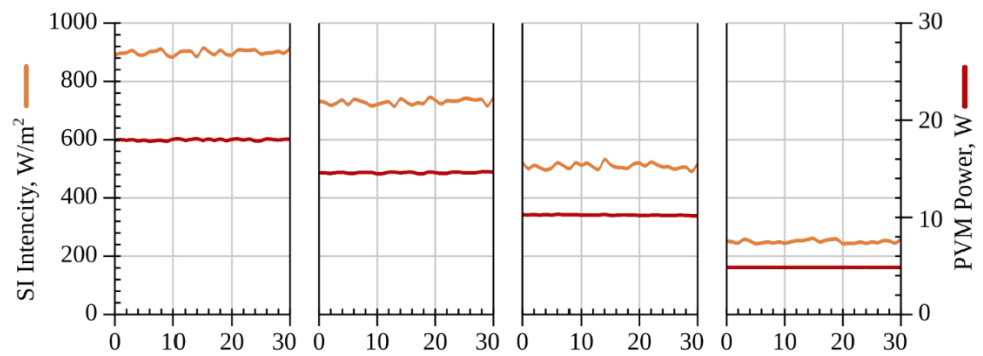


Figure 11. Indicators of the SI intensity and the power consumed from the PVM to the lighting system.

After analyzing the experimental data, several facts can be noted. Comparing the data of the maximum power on the VWC of the PVM (Figure 10) with the experimental data (Figure 11), it can be noted that the module in the system operates in a mode close to the maximum power mode (Figure 12). In absolute values, the decrease in the power taken from the PVM in comparison with the power of the VWC is insignificant. The dotted line corresponds to the ideal (reference) version of the operation of the PVM and the system, when the power take-off from the PVM always goes at the point of its maximum power. The red line is drawn along the points corresponding to the data shown in Figure 11 and characterizes the actual operation of the UV1 converter (Figure 2).

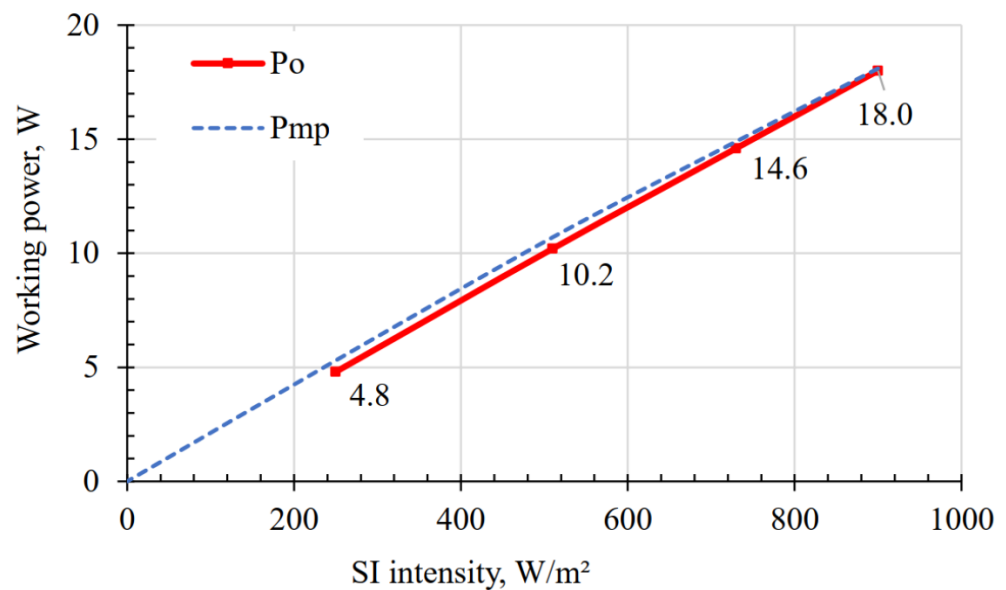


Figure 12. Indicators of the power taken from the PVM in operation, relative to its power by VWC at different solar radiation intensities: (P_o) indicators of the power of PVM in operation; (P_{mp}) power of PVM at the points of maximum power.

For the points shown in Figure 12, power deviations from ideal operating modes were calculated. Figure 13 shows these values. The decrease in the power take-off efficiency from the PVM is nonlinear in nature and depends on the SI intensity. The maximum deviations of the real power of the PVM, from the power that could potentially be taken-off in accordance with the VWC, are observed during a strong decrease in the intensity of solar irradiation and a reduction in energy production. It is obvious that at low powers, energy from the PVM is taking-off less efficiently.

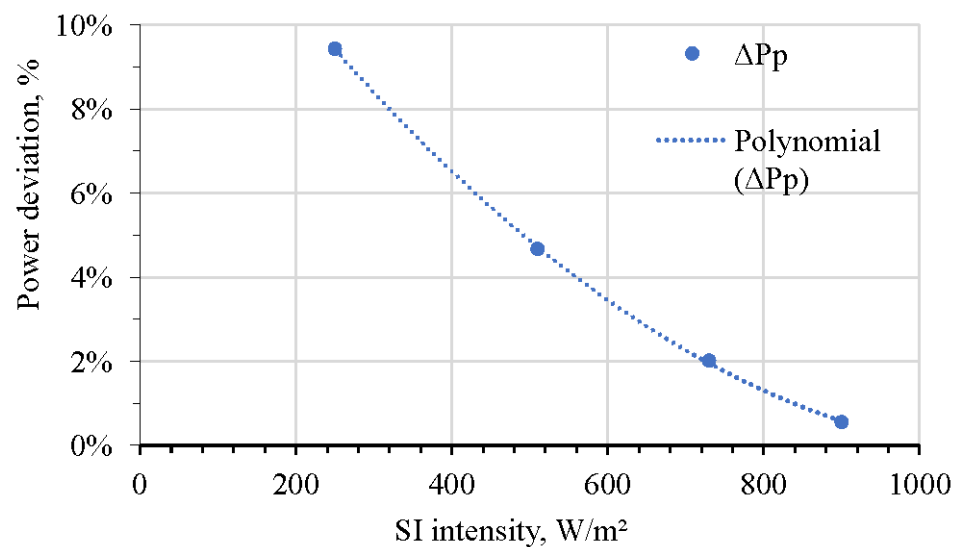


Figure 13. Reducing the power take-off of the PVM from the maximum possible according to VWC, depending on the SI intensity: (ΔP_p) indicators of deviation in the generated power from the point of maximum power of PVM; (Polynomial ΔP_p) interpolation curve characterizing the dependence of the ΔP_p .

The obtained data show that under conditions of high SI intensity and with the correct selection of circuit solutions of the UV1 converter, it is possible to take power close to the maximum power point, using inexpensive converters without the function of searching for the maximum power point. Nevertheless, with a decrease in the SI intensity, the efficiency of the converter decreases, while both the power take-off efficiency (Figure 13) and the conversion efficiency in the UV1 converter itself decrease (Figure 7). A significant decrease in the efficiency of the UV1 converter is observed at a low intensity of solar radiation, at which the output is minimal. The question of the expediency of increasing the efficiency of the converter in such modes requires additional study.

4. Conclusions

When looking for ways to reduce the cost of the photovoltaic systems, a simple lighting system was developed that implements the concept of direct connection of DC consumers to DC power supply networks from the PVM using an AC grid. The AC grid in this system made it possible to get rid of circuits with an inverter and storage devices and significantly simplify the system itself. This has a positive effect on reliability and cost. The proposed scheme made it possible to create a lighting system with a parallel power supply and self-regulation of energy flows. At the same time, there is no need to monitor the process, provide various kinds of switching in the circuit, or store energy in supercapacitors or batteries, as with traditional circuits.

A number of experimental studies have allowed us to evaluate the operation of the system in practice and to identify the influence of some factors on the operation of the system as a whole. The LED lighting system showed its efficiency and, most importantly, the efficiency of direct connection of photovoltaic modules to a DC load without additional converters. It is also worth noting the stable and trouble-free operation that the system demonstrated during a month of operation.

The experiments allowed us to evaluate the efficiency of the system. The converter provided highly efficient power take-off from the PVM in modes close to the maximum-power modes without using special logic and maximum power point tracking (MPPT) algorithms. Such an efficient operation was facilitated by the correct choice of the power of the module and the converter for it. In this regard, it can be argued that a conventional converter in parallel mode with a properly selected circuit and parameters can provide highly efficient operation of the system without using more expensive MPPT devices.

Despite the significant decline in PVM prices over the past decades, photovoltaic technologies need developments to increase the efficiency and reduce the cost of systems based on them. In this regard, the developed technology of direct use of solar energy for powering DC consumers with parallel operation from the grid allows us to take a step toward reducing the cost of generated energy and improving the reliability of the power supply. This takes us one step closer to the widespread use of solar energy with the use of photovoltaic converters.

Therefore, the developed technology for the direct use of solar energy to power DC consumers with parallel operation from photovoltaic modules and the AC network makes it possible to realize the advantages of various technologies through the use of a hybrid network. It should be noted that any other DC load can be used instead of the LED load. Hybrid networks are becoming a necessary element on the way to increasing efficiency and reducing the cost of products at various agricultural facilities, the power supply of which is partially carried out from PV modules.

5. Patents

Tikhonov P.V., Kharchenko V.V., Makarov A.E., Sychev A.O., Komisarov N.S. Method and system for supplying DC consumers with an electricity source based on renewable energy resources. RF Patent No. 2759009, filed 8 December 2020, and issued 8 November 2021.

Author Contributions: Conceptualization, P.T.; Methodology, P.T. and K.M.; Software, K.M. and A.S. (Arseniy Sychov); Validation, V.B. and A.S. (Alexander Sokolov); Formal analysis, P.T., V.B. and A.S. (Alexander Smirnov); Investigation, P.T., K.M. and A.S. (Arseniy Sychov); Resources, P.T. and V.B.; Data curation, K.M., A.S. (Arseniy Sychov) and V.B.; Writing—original draft preparation, P.T. and A.S. (Arseniy Sychov); Writing—review and editing, K.M. and V.B.; Visualization, K.M., V.B. and A.S. (Alexander Smirnov); Supervision, A.S. (Alexander Sokolov) and V.B.; Project administration, P.T.; Funding acquisition, P.T., K.M., A.S. (Arseniy Sychov), V.B., A.S. (Alexander Sokolov) and A.S. (Alexander Smirnov). All authors have read and agreed to the published version of the manuscript.

Funding: This research received no external funding.

Institutional Review Board Statement: Not available.

Data Availability Statement: Not applicable.

Conflicts of Interest: The authors declare no conflict of interest.

Abbreviations

AC	Alternating current
DC	Direct current
GW	Gigawatt
LED	Light-emitting diode
MPPT	Maximum power point tracking
PVM	Photovoltaic modules
SI	Solar irradiation
VAC	Volt-ampere characteristics
VWC	Volt-watt characteristics

References

1. *Global Market Outlook for Solar Power 2021–2025/Michael Schmela, Walburga Hemetsberger, Gianni Chianetta*; SolarPower Europe: Belgium, Brussels, 2021; p. 136. ISBN 9789464073492. Available online: <https://www.solarpowereurope.org> (accessed on 25 May 2022).
2. *Renewables 2021 Global Status Report/Lisa Mastny, Leah Brumer–France, Paris: REN21. 2021, p. 371. Available online: https://www.ren21.net/wp-content/uploads/2019/05/GSR2021_Full_Report.png (accessed on 27 May 2022).*
3. *PHOTOVOLTAICS REPORT/Bruno Burger, Lorenz Friedrich, Christoph Kost, and Others. Fraunhofer Institute for Solar Energy Systems ISE. 2021, p. 51. Available online: <https://www.ise.fraunhofer.de> (accessed on 23 May 2022).*
4. Chakraborty, A. Advancements in power electronics and drives in interface with growing renewable energy resources. *Renew. Sustain. Energy Rev.* **2011**, *15*, 1816–1827. [[CrossRef](#)]

5. Fang, X.; Misra, S.; Xue, G.; Yang, D. Smart Grid—The New and Improved Power Grid: A Survey. *IEEE Commun. Surv. Tutor.* **2011**, *14*, 944–980. [CrossRef]
6. Hirsch, A.; Parag, Y.; Guerrero, J. Microgrids: A review of technologies, key drivers, and outstanding issues. *Renew. Sustain. Energy Rev.* **2018**, *90*, 402–411. [CrossRef]
7. Gür, T.M. Review of electrical energy storage technologies, materials and systems: Challenges and prospects for large-scale grid storage. *Energy Environ. Sci.* **2018**, *11*, 2696–2767. [CrossRef]
8. Dunn, B.; Kamath, H.; Tarascon, J.-M. Electrical Energy Storage for the Grid: A Battery of Choices. *Science* **2011**, *334*, 928–935. [CrossRef] [PubMed]
9. Yin, W.-W.; Fu, Z.-W. The Potential of Na–Air Batteries. *ChemCatChem* **2016**, *9*, 1545–1553. [CrossRef]
10. Faisal, M.; Hannan, M.A.; Ker, P.J.; Hussain, A.; Mansor, M.B.; Blaabjerg, F. Review of Energy Storage System Technologies in Microgrid Applications: Issues and Challenges. *IEEE Access* **2018**, *6*, 35143–35164. [CrossRef]
11. Opiyo, N.N. A comparison of DC- versus AC-based minigrids for cost-effective electrification of rural developing communities. *Energy Rep.* **2019**, *5*, 398–408. [CrossRef]
12. Justo, J.J.; Mwasilu, F.; Lee, J.; Jung, J.-W. AC-microgrids versus DC-microgrids with distributed energy resources: A review. *Renew. Sustain. Energy Rev.* **2013**, *24*, 387–405. [CrossRef]
13. Planas, E.; Andreu, J.; Garate, J.I.; de Alegria, I.M.; Ibarra, E. AC and DC technology in microgrids: A review. *Renew. Sustain. Energy Rev.* **2015**, *43*, 726–749. [CrossRef]
14. Tikhonov, P.V.; Mayorov, V.A.; Morenko, K.S. Energy-Saving Systems Using Photovoltaic Modules. In *Handbook of Research on Smart Computing for Renewable Energy and Agro-Engineering*; Kharchenko, V., Vasant, P., Eds.; IGI Global: Hershey, PA, USA, 2020; pp. 464–485. [CrossRef]
15. Tikhonov, P.V. The Energy-Saving System of LED Lighting with Parallel Power Supply by Photovoltaic Modules and Power Supply Network. *Light Eng.* **2020**, *28*, 36–40. [CrossRef]
16. Noroozian, R.; Abedi, M.; Gharehpetian, G.; Hosseini, S. Combined operation of DC isolated distribution and PV systems for supplying unbalanced AC loads. *Renew. Energy* **2009**, *34*, 899–908. [CrossRef]
17. Kwasinski, A. Quantitative Evaluation of DC Microgrids Availability: Effects of System Architecture and Converter Topology Design Choices. *IEEE Trans. Power Electron.* **2010**, *26*, 835–851. [CrossRef]
18. Wang, B.; Sechilariu, M.; Locment, F. Intelligent DC Microgrid with Smart Grid Communications: Control Strategy Consideration and Design. *IEEE Trans. Smart Grid* **2012**, *3*, 2148–2156. [CrossRef]
19. Dragičević, T.; Lu, X.; Vasquez, J.C.; Guerrero, J.M. DC Microgrids—Part I: A Review of Control Strategies and Stabilization Techniques. *IEEE Trans. Power Electron.* **2016**, *31*, 4876–4891. [CrossRef]
20. Dragicevic, T.; Lu, X.; Vasquez, J.C.; Guerrero, J.M. DC microgrids—Part II: A review of power architectures, applications, and standardization issues. *IEEE Trans. Power Electron.* **2015**, *31*, 3528–3549. [CrossRef]
21. Nejabatkhah, F.; Li, Y.W. Overview of Power Management Strategies of Hybrid AC/DC Microgrid. *IEEE Trans. Power Electron.* **2015**, *30*, 7072–7089. [CrossRef]
22. Murari, K.; Padhy, N.P. Framework for Assessing the Economic Impacts of AC-DC Distribution Network on the Consumers. In Proceedings of the IEEE 59th International Scientific Conference on Power and Electrical Engineering of Riga-Technical-University–2018, Riga, Latvia, 12–13 November 2018.
23. Ahrabi, R.R.; Li, Y.W.; Nejabatkhah, F. Hybrid AC/DC Network with Parallel LCC-VSC Interlinking Converters. *IEEE Trans. Power Syst.* **2020**, *36*, 722–731. [CrossRef]
24. Sannino, A.; Postiglione, G.; Bollen, M. Feasibility of a DC network for commercial facilities. *IEEE Trans. Ind. Appl.* **2003**, *39*, 1499–1507. [CrossRef]
25. Zheng, Y.; Wang, X. Research on DC Micro-grid system of photovoltaic power generation. *IOP Conf. Ser. Earth Environ. Sci.* **2018**, *108*, 052041. [CrossRef]
26. Gago-Calderón, A.; Orejón-Sánchez, R.D.; Hermoso-Orzáez, M.J. DC Network Indoor and Outdoor LED Lighting. In *Light Emitting Diode*; Sastra University: Tamil Nadu, India, 2018; pp. 2–22. [CrossRef]
27. INA226 Datasheet—Texas Instruments. Available online: <https://www.ti.com/lit/ds/symlink/ina226.png> (accessed on 27 May 2022).
28. UT61E Modern Digital Multimeter English Manual; Uni-Trend Technology (China) Co., Ltd.: Dongguan, China. Available online: <https://www.uni-trend.com/uploadfile/cloud/English%20manual/General%20Meters/UT61%20English%20Manual.png> (accessed on 25 May 2022).
29. Pyranometer GSM/O-U10.FuehlerSysteme eNET International. Available online: https://fuehler-systeme.ru/images/files/188/GSM_O_%D0%9E%D0%BF%D0%B8%D1%81%D0%B0%D0%BD%D0%B8%D0%B5.png (accessed on 23 May 2022).
30. Komissarov, N.S. LED Lighting System with Parallel Power Supply from Photovoltaic Modules and AC Power. Master’s Thesis, Federal Scientific Agroengineering Center VIM, Moscow, Russia, 2021; 81p. (In Russian)
31. Mironyuk, S.S.; Smirnov, A.; Sokolov, A.; Proshkin, Y. Optimization of spectral composition and energy economy effectiveness of phyto-irradiators with use of digital technologies. In *Handbook of Research on Energy-Saving Technologies for Environmentally-Friendly Agricultural Development*; IGI-Global: Hershey, PA, USA, 2020; pp. 191–212.

Review

Convolutional Neural Networks in Detection of Plant Leaf Diseases: A Review

Bulent Tugrul, Elhoucine Elfatimi and Recep Eryigit *

Department of Computer Engineering, Ankara University, Ankara 06830, Türkiye

* Correspondence: reryigit@eng.ankara.edu.tr; Tel.: +90-312-203-3300

Abstract: Rapid improvements in deep learning (DL) techniques have made it possible to detect and recognize objects from images. DL approaches have recently entered various agricultural and farming applications after being successfully employed in various fields. Automatic identification of plant diseases can help farmers manage their crops more effectively, resulting in higher yields. Detecting plant disease in crops using images is an intrinsically difficult task. In addition to their detection, individual species identification is necessary for applying tailored control methods. A survey of research initiatives that use convolutional neural networks (CNN), a type of DL, to address various plant disease detection concerns was undertaken in the current publication. In this work, we have reviewed 100 of the most relevant CNN articles on detecting various plant leaf diseases over the last five years. In addition, we identified and summarized several problems and solutions corresponding to the CNN used in plant leaf disease detection. Moreover, Deep convolutional neural networks (DCNN) trained on image data were the most effective method for detecting early disease detection. We expressed the benefits and drawbacks of utilizing CNN in agriculture, and we discussed the direction of future developments in plant disease detection.

Keywords: machine learning; deep learning; plant leaf diseases

Citation: Tugrul, B.; Elhoucine, E.; Eryigit, R. Convolutional Neural Networks in Detection of Plant Leaf Diseases: A Review. *Agriculture* **2022**, *12*, 1192. <https://doi.org/10.3390/agriculture12081192>

Academic Editors: Muhammad Sultan, Redmond R. Shamshiri, Md Shamim Ahamed and Muhammad Farooq

Received: 7 July 2022

Accepted: 8 August 2022

Published: 10 August 2022

Publisher's Note: MDPI stays neutral with regard to jurisdictional claims in published maps and institutional affiliations.



Copyright: © 2022 by the authors. Licensee MDPI, Basel, Switzerland. This article is an open access article distributed under the terms and conditions of the Creative Commons Attribution (CC BY) license (<https://creativecommons.org/licenses/by/4.0/>).

1. Introduction

Plant diseases are one of the most critical elements impacting food production. They are responsible for a significant drop in the economic productivity of crops, as well as being an obstruction to this activity in some cases. According to [1], disease management and control procedures must be carried out effectively to reduce output losses and ensure agricultural sustainability, underlining the importance of continual crop monitoring paired with prompt and accurate disease detection. In addition, as the world's population continues to rise, a significant increase in food production is required (FAO) [2]. This must be combined with the preservation of natural ecosystems through the use of environmentally-friendly farming methods. Food must keep a high nutritious value while still being secure worldwide [3]. This can be accomplished by using new scientific methodologies for leaf disease diagnosis and crop management, as well as applying these new technologies to large-scale ecosystem monitoring.

The main point for researchers is correctly identifying diseases affecting crops [4]. According to Miller et al. [5], manual practices in conventional farming operations cannot cover large areas of crops and provide early background information for decision-making processes. As a result, researchers have never stopped looking for ways to develop automated practical solutions and effective methods for detecting plant diseases. DL-based models, in particular, have found many applications in plant disease detection. They have overcome the problems associated with traditional classification methods and represent cutting-edge technology in this field. DL [6] is an advanced technique that has shown great promise and success in various fields where it has been used [7]. It is, however, a group of machine learning methods that attempt to model at a high level of data abstraction through articulating structures of various transformations.

The current review aims to describe the state-of-the-art identification and examination of plant disease detection problems using a specific class of DL called CNN, which extends classic Artificial Neural Networks (ANN) by adding more “depth” to the network, as well as the various convolutions that allow the data to be successfully applied in various problems related to images [8]. Therefore, the inquiry of this survey discusses significant contributions concerning CNN and various innovations which aimed to improve the performance of CNN and thus correctly identify diseases.

The motivation for conducting this survey comes from the fact that CNN has recently been primarily used in agriculture, with CNN’s growing popularity and success in solving many problems related to agriculture, and the fact that multiple research efforts using CNN to discuss various agricultural problems exist today. As a result of its success, CNN is perhaps the most popular and commonly used approach in agricultural research today.

Regarding image analysis, the current survey focuses on a particular subset of DL models and techniques since there are very few of this type of survey in the agricultural field, especially about CNN utilization. Thus it would be beneficial to present and analyze relevant work to help the authors conduct a more comprehensive review. A discussion about innovative and high-potential techniques for solving numerous difficulties in agriculture-related to image and DL will be presented. In addition to reviewing recent research in this area, significant practical features of CNN based on images are presented to explain the technique’s advantages and disadvantages further.

The rest of the paper is structured as follows: Section 2 provides related work. Section 3 describes the methodologies used in this study. Section 4 presents CNN. Section 5 discusses the applications of CNN in agriculture, Section 6 provides the main problems and solutions associated with the CNN used in plant disease detection, Section 7 presents the discussion and Section 8 concludes the paper.

2. Related Work

Many studies have been conducted to find an ideal solution to the problem of crop disease detection by creating techniques that can assist in identifying crops in an agricultural environment. This section will provide the most recently reviewed studies on CNN’s applicability in the broad field of agriculture; this section includes papers from peer-reviewed articles that use CNN methods and plant datasets.

Abade et al. [9] reviewed CNN algorithms for the detection of plant diseases. The authors studied 121 papers that were published between 2010 and 2019. PlantVillage was selected as the most widely used dataset, while TensorFlow was identified as the most frequently used framework in this review. Dhaka et al. [10] outlined the basic methods of CNN models used to identify plant diseases using leaf images. They also compared CNN models, pre-processing approaches, and frameworks. The study also looks at the datasets and performance measures used to assess model efficiency. Moreover, Nagaraju et al. [11] also provided a review to find the best datasets, pre-processing approaches, and DL techniques for various plants. They reviewed and analyzed 84 papers on DL’s applicability in plant disease diagnosis. They observed that so many DL methods are limited in their ability to analyze original images and that effective model performance necessitates using a suitable pre-processing technique.

Kamilaris et al. [12] found that DL approaches were used to solve various agricultural challenges. According to the study, DL methods performed better than standard image processing techniques. Fernandez-Quintanilla et al. [13] evaluated weed-monitoring technologies in crops. They focused on weed monitoring devices in agricultural fields that were both remote sensed and ground-based. Weed monitoring is critical for weed control, according to them. They predicted that data acquired by various sensors would be saved in a public cloud and used in appropriate contexts at the optimal time. Lu et al. [14] introduced a review for plant disease classification using a CNN. They evaluated the significant problems and solutions of CNN used for plant disease classification and DL criteria in

plant disease classification. They discovered that additional research with more complex datasets was required to obtain a more satisfactory result.

Golhani et al. [15] presented a review paper on hyperspectral data for plant leaf disease identification, highlighting existing problems and potential prospects. They also presented NN approaches for SDI development in a short time. They discovered that, as long as SDIs remain relevant for proper crop protection, they must be tested on various hyperspectral sensors at the plant leaf scale. Bangari et al. [16] presented a review on disease detection using CNN, focusing on potato leaf disease. They reviewed several papers and concluded that convolutional neural networks work better at detecting the disease. They also identified that CNN contributed significantly to the maximum possible accuracy for disease identification.

3. Methodology

In this work, we discussed the most recent research papers on applying DL in the agricultural field. Moreover, this work was accomplished through two essential stages: the first is the collection of 100 previous research works that discuss DL in its relationship to the agricultural field, and the second is a thorough examination and analysis of the collected work.

In the first stage, we looked for papers and articles published within the last five years using scientific databases such as Science Direct and Elsevier and web-based scientific indexing services. In addition, we conducted our searches for relevant papers using several keywords, the most prominent of which were agriculture, CNN and DL. Papers mentioning CNN but not applying it to the agricultural domain were thus removed. In the second stage, the papers chosen in the first stage were analyzed one by one, taking into account the following research questions:

- The approach used.
- The problem presented.
- The datasets used.
- The performance achieved.
- Limitations of the study, if any.
- Have the authors compared their CNN-based approach with other technologies, and what is the difference in performance?

Examining how CNN performs is an essential aspect of this study. As a result, we reviewed and analyzed several relevant studies. We also compared CNN to other current technologies and summarized the most important advantages and disadvantages that affect CNN's performance. It should be noted that the current paper focuses on comparing techniques used for the same data and on the same scale. We also investigated and discussed the most significant problems and limitations identified by previous research.

4. Convolutional Neural Networks (CNN)

ANNs consist of three different layers: input, one or more hidden, and output layers. Neurons placed in hidden layers have an associated weight and a bias value. These values are multiplied by the input values and sent to an activation function. If the output value is greater than the specified threshold, that node carries the output value to the next layer of the network. Otherwise, no data is transmitted. The process of spreading data in the network from one layer to the successive layer is called a feed-forward network. The ultimate objective is to minimize the cost function for any input when tuning the model weights and bias. The process is depicted in Figure 1. CNNs, a form of multi-layer neural networks, are designed to extract dependencies in a grid-structured input such as images and text. The convolution operation applied in many intermediate layers is the most crucial property of CNNs. Similarly, a convolution operation is a dot-product of a set of grid-structured weights and another set of similarly structured inputs.

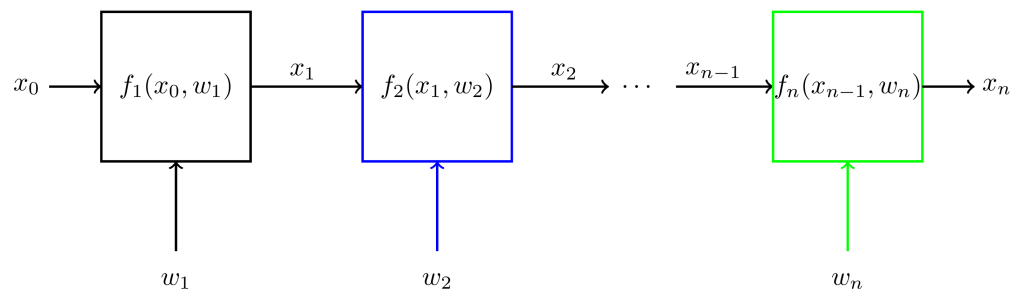


Figure 1. The Computational Architecture of ANNs.

The term CNN refers to a type of ANN widely used in image recognition and processing. Since the introduction of LeNet-5 in 1998, various innovations in CNN architectures have been presented [17]. In addition, before developing DL for computer vision, learning relied on extracting interesting variables called features. However, these methods require a significant amount of experience in image processing. CNN introduced by [18] have revolutionized image processing and removed manual feature extraction. CNNs operate directly on matrices or even tensors in the case of RGB color three-channel images.

CNNs are now widely used for image classification, image segmentation, face recognition and object recognition. They have been successfully applied by many organizations in various domains such as health, web, mail services, etc. CNN can receive any data input, including images, video, sound, speech, and natural language [19,20]. However, CNN is simply a stack of several layers (see Figure 2), pooling and fully connected layers, beginning with a convolution layer and progressing through the following layers: pooling, Relu correction, and ending with a fully-connected layer [21]. As a result, each image received as input will be filtered, reduced, and corrected several times, to finally form a vector. The strength of the CNN is found in the convolution layer. The CNN will learn the most valuable filters for the task (such as detection). Another benefit is that several convolution layers can be considered: the output of one convolution becomes the input of the next one, and the pooling layer is another component of a CNN. It performs downsampling, which significantly reduces computational weight, memory usage, and the number of parameters. On the other hand, in fully Connected Layers, as the name implies, each layer has a complete connection with the layer that comes before it. We can use a “sigmoid” or “softmax” function with the last fully connected layer for class predictions.

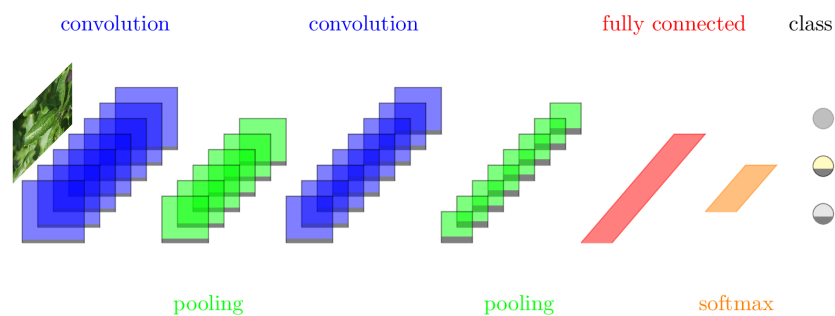


Figure 2. A common CNN architecture.

As a result, the convolutional layers extract features from the input images, which are then reduced in dimensionality by the pooling layers. Typically, the fully connected layers use the high-level features learned to classify input images into predefined classes at the final layer [22]. Moreover, the classification layer can extract features for classification and detection tasks [23]. Figure 2 provides an overview of the architecture of a typical CNN.

4.1. Comparison of Popular CNN Frameworks

CNN frameworks play an important role in projects that use the CNN architecture. Therefore, we now have many frameworks available that allow us to develop tools that can offer a higher level of expertise while simplifying complicated programming difficulties, with each framework created differently for different purposes. Therefore, numerous tools and platforms are available to researchers for conducting DL experimental studies [24]; the most famous of them is resumed in Table 1.

Table 1. Comparison of CNN frameworks.

Framework	Programming Language	Operating System Compatibility	Open Source	Interface
Keras [25]	Python	Windows, Linux, macOS	Yes	Yes
Caffe [26]	C++	Windows, Linux, macOS	Yes	Python C++, MATLAB
Torch [27]	C, Lua	Windows, Linux, macOS	Yes	C, C++
TensorFlow [28]	Python, C++, CUDA	Windows, Linux, macOS	Yes	Java, Python, JavaScript
Theano [29]	Python	Cross-platform	Yes	Python
Matlab Toolbox [30]	MATLAB, C, C++, Java	Windows, Linux, macOS	No	MATLAB
deeplearning4j [31]	Python, Java	Windows, Linux, macOS	Yes	Python Java, Clojure

Developments in DL provide various tools and platforms to implement CNN in different applications, including the fields of agriculture. Therefore, so many applications and studies in agriculture have used the framework described above, each one employed depending on the author's study conditions, data type, size and complexity of the project. The following sections will provide a detailed description of CNN applications in agricultural fields.

4.2. Pre-Trained Network

A pre-trained model has already been trained to solve a similar problem. Using a pre-trained model with transfer learning instead of creating a model from scratch to solve a similar problem is usually much quicker and more straightforward than training a network from scratch. Naik et al. [32] classified five diseases of the chili with 12 different deep learning models (AlexNet, DarkNet53, DenseNet201, EfficientNetb0, InceptionV3, MobileNetV2, NasNetLarge, ResNet101, ShuffleNet, SqueezeNet, VGG19, and XceptionNet). The VGG19 model produced the best accuracy value of 83.54% without data augmentation. On the other hand, DarkNet53 gave the best result with data augmentation. They reached the best accuracy values of 98.63% and 99.12% with Squeeze-and-Excitation-based Convolutional Neural Networks (SECNN) without and with augmentation, respectively. The study examined tomato maturity levels with three different CNN models (VGG, Inception and ResNet). The best accuracy value was calculated for VGG19 at 97.37% for batch size 32 and epoch 50.

Partel et al. [33] studied the performance of the YOLO-v3 [34], Faster R-CNN [35], ResNet-50, ResNet-101, and Darknet-53 [36] models to create an intelligent sprayer for real-time plant leaf control. The recall value, precision, and ResNet-50 model performed better than others. Bin-guitcha-Fare and Sharma [37], on the other hand, used the ResNet-101 model. They proved that the input image's size might impact the performance of the ResNet-101. Sahu et al. [38] presented a method for classifying Bean Crop Diseases. The proposed method found that fine-tuning pre-trained networks performed significantly better than training from scratch. The fine-tuning of hyperparameters raises GoogleNet's accuracy

from 90.1% to 95.31% and VGG16's accuracy from 89.6% to 93.75%. The effect of transfer learning is later clarified in this study by the network's ability to reuse and transmit features from one specific problem to another.

Mukti et al. [39] presented a method for identifying plant diseases using a transfer learning model based on ResNet50. There are 87,867 images in their dataset. A total of 80% of the dataset was used for training and 20% for validation. Their highest accuracy performance was 99.80%. According to Arya et al. [40], CNN can perform well in detecting various plant diseases. They introduced a method based on a pre-trained model to compare different CNN architectures (i.e., AlexNet, shallow CNN) to identify diseases in potato and mango leaves. The approach was considered more effective using AlexNet (up to 98.33%) than using a shallow CNN, which obtained only 90.85% accuracy.

4.3. Training from Scratch

Milioto et al. [41] developed a CNN model for discriminating blobs-wise. They suggested a system that coupled vegetation detection with high-quality plant classification into important crops and weeds in the field. To train the model, they used multi-spectral data. Furthermore, they tested this system on images taken from various sugar beet fields, analyzing different combinations of convolutional layers and fully connected layers to find an efficient and problem-free model. Finally, they achieved a superior result by combining three convolutional layers with two fully linked layers. They addressed that this strategy had no geometric priors, such as planting crops in rows.

Lu et al. [42] reported a novel rice disease detection approach based on DCNN. They trained the suggested model from scratch to identify ten common rice diseases using a dataset of 500 images of infected and healthy rice leaves, all of which were taken from a rice field. The suggested CNN-based model achieves an accuracy of 95.48% using a 10-fold cross-validation technique. The accuracy of this model is substantially higher than that of a traditional machine learning model. Zhang et al. [43] proposed a method for detecting Broad-leaf weeds using a CNN model with three fully connected classification layers and six convolutional layers. They also compared CNN to SVM and reported that the model succeeded in identifying weeds with an accuracy of 96.88%, while SVM could only achieve 89.4%. As a result, they showed that the CNN model outperformed the SVM model in detecting broad-leaf weeds in pastures. Liang et al. [44] also demonstrated that the CNN model performs better than both the LBP and HoG approaches in classification. They developed a low-cost weed identification system using a CNN architecture that includes three pooling, three convolutional, four Dropout layers, and a fully connected layer.

Dyrmann et al. [45] demonstrate a method for detecting plant species in color pictures using a convolutional neural network. The network was created from the ground up and tested on 10,413 images featuring 22 early-stage crop species. Dyrmann et al. created a new system based on their needs, utilizing a combination of convolutional layers, max-pooling layers, fully connected layers, activation functions, batch normalization, and residual layers. The network was then capable of classifying 22 species with an accuracy of 86.2%. Chen et al. [46] suggested a method for detecting tea plant diseases from leaf images based on DCNN. They built and trained the model from scratch. Furthermore, to extract the properties of tea plant diseases from images, they employed a CNNs model called LeafNet that was constructed with several feature extractors. They also employed SVM and MLP classifiers to classify diseases using DSIFT (dense scale-invariant feature transform). The three disease identification classifiers had various performance results, with an average accuracy of 90.16% for LeafNet, 60.62% for the SVM algorithm, and 70.77% for the MLP algorithm.

Nkemelu et al. [47] presented a study for plant seedling classification. They compared the CNN's performance to that of the K-Nearest Neighbor (KNN) algorithm, which scored 56.84%, and SVM, which scored 61.47%, and they proved that CNN was better at distinguishing crop plants diseases. Furthermore, to reach 92.6%, they used three fully connected layers and six convolutional layers in the CNN architecture. They also tested CNN's accuracy using

both the original and pre-processed pictures. In another study, Pearlstein et al. [48] presented a study for plant disease detection. They utilized synthetic image data to evaluate and train the CNN model on real data. They constructed a CNN model using two fully connected layers and five convolutional layers. The results demonstrated that CNN could accurately distinguish crop plants from natural images, even when many occlusions were present.

5. Applications of CNN in Agriculture

DL techniques, especially CNN, have made substantial advances in image analysis. Numerous studies for the automatic identification of plant disease have been implemented. This implementation and interest, in particular, could open the way for developing automatic imaging techniques for plant disease diagnosis and classification, plant recognition, fruit counting, and weed detection. Such technologies could assist farmers in adopting more farming techniques, good agricultural practices, and improving food security.

The researcher has presented several plant leaf disease detection methods based on CNNs in the last five years. Remarkably, almost all of the publications were released and published after 2016, demonstrating how new and modern this method is in agriculture. Figure 3 depicts the number of research articles published on the automatic detection of plant leaf diseases using CNN from 2013 to 2022. The graph demonstrates that automatic disease detection research peaked in 2016, which confirmed the field's newness and freshness. Data were collected by performing a keyword search on journal articles published in ScienceDirect, Springer, MDPI and Google Scholar databases between 2013 and 2022.

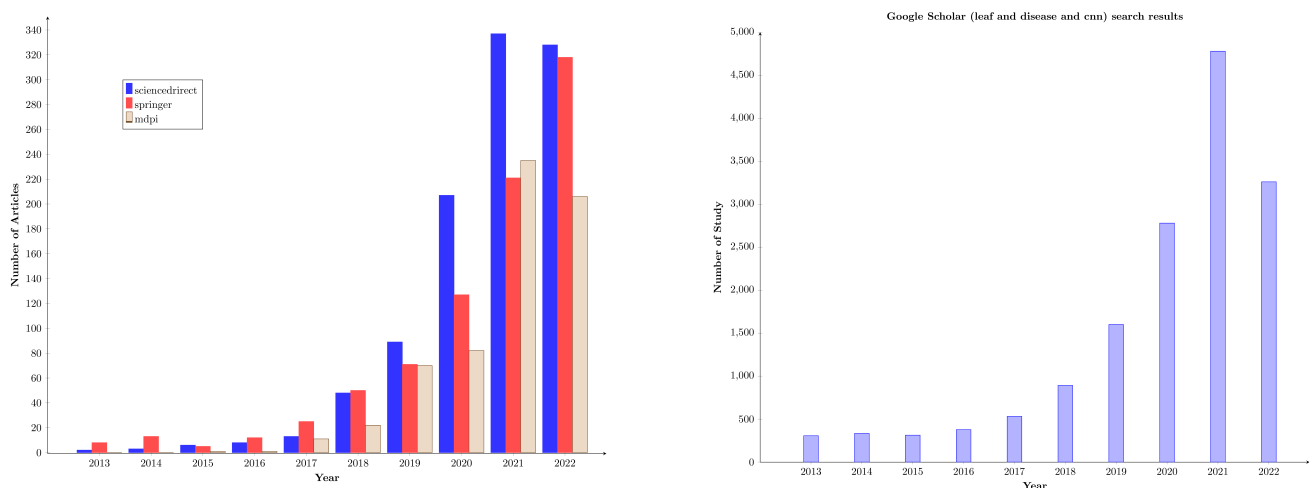


Figure 3. Number of articles published for the detection of plant leaf diseases using CNN from 2013 to 2022.

All of these studies are concerned with identifying and classifying plant diseases on images. This article reviewed both pre-trained and custom CNN-based models developed by the authors. CNN models given different names by the authors were taken as CNN. However, a comparison of various studies reveals that, rather than constructing a new CNN model from scratch, most researchers use transfer learning to meet their needs and complete their tasks quickly and easily. The CNN model then is used to perform different tasks for various research in transfer learning. Jiang et al. [49] employed VGG16 to diagnose diseases in rice and wheat plants. As a consequence of the experimental comparisons with other state-of-the-art, the overall accuracy on rice and wheat plants was 97.22% and 98.75%, respectively.

Sravan et al. [50] presented the fine-tuning of hyperparameters of current ResNet-50 for disease identification and classification. They reached a higher accuracy of 99.26% on the Plant Village dataset, which contained 20,639 images. Shin et al. [51] presented a method for detecting disease on strawberry leaves. They compared six CNN models for detecting disease on strawberry leaves using various criteria such as speed, accuracy, videlicet, and hardware requirements. ResNet-50 had the highest classification accuracy of

98.11%, SqueezeNet-MOD2 required the least amount of memory, and AlexNet had the fastest processing time. Mohanty et al. [4] worked on multiple crops to identify 26 diseases using PlantVillage, GoogLeNet, and AlexNet. The result recorded an accuracy of 99.35%. Ferentinos et al. [27] also worked on various crops for plant disease identification and diagnosis, and they had a reasonable success rate with Alex-NetOWTB and VGG.

Brahimi et al. [52] conducted a study in which they used AlexNet and GoogLeNet to classify nine tomato leaf diseases, with an accuracy rate of 99.18%. Darwish et al. [53] proposed a method for detecting three maize diseases; in this study, they used VGG16 and 19 and reported a 98.2% average accuracy. Similarly, the authors presented similar studies to identify and recognize diseases in maize using CNN architecture [54,55]. Furthermore, there are other plants in which the authors used CNN architectures. For instance, they used CNN to detect apple disease [56,57]. In [31], they presented a study to detect Black Sigatoka and Black speckled disease in banana plants. The authors used Inception-v3 and 2756 images to detect cassava diseases. Yuwana et al. proposed a study to detect Tea diseases [58], using 5632 images of tea, MCT, AlexNet, and GoogLeNet. Only two segmentation methods were used in the proposed study, each with a kernel size of five and a rotation of 40. Kawasaki et al. [59] proposed a method for detecting cucumber diseases such as melon yellow spot virus and zucchini yellow mosaic virus using CNN.

There are also several studies to detect olive plant disease, such as [60], where Cruz et al. use PlantVillage to detect symptoms of Olive Quick Decline Syndrome. However, their study task may be challenging for large numbers of samples or quarantine pests with restricted modifications. In [61,62], the authors have presented a method to distinguish Fusarium wilt disease in the radish plant. They achieved 93.3% and 90% accuracy, respectively. Another study using CNN to identify ten different diseases of the rice plant may be found in [63]. Table 2 summarizes and clarifies all relevant information to assist readers in selecting one or more criteria and comparing various DL models.

Table 2. Comparison of CNN models in the detection of plant leaf diseases.

	Ref. #	Species	Data Source	Model	Accuracy	Year
1	[59]	cucumber	self	CNN	94.90	2015
2	[64]	rice	self	CNN	95.48	2015
3	[4]	multiple	PlantVillage	GoogLeNet	99.35	2016
4	[57]	apple	PlantVillage	AlexNet	97.30	2016
5	[65]	wheat	self	VGG-FCN-VD16	97.95	2017
6	[42]	rice	self	DCNN	95.48	2017
7	[52]	tomato	self	GoogLeNet	99.18	2017
8	[56]	apple	PlantVillage	AlexNet	97.62	2017
9	[31]	banana	PlantVillage	LeNet	99.00	2017
10	[66]	cassava	self	Inception-v3	93.00	2017
11	[67]	apple	PlantVillage	VGG16	90.40	2017
12	[60]	olive	PlantVillage	LeNet	99.00	2017
13	[68]	potato	PlantVillage	VGG	96.00	2017
14	[61]	radish	self	VGG-A	93.30	2017
15	[62]	radish	self	GoogLeNet	90.00	2017
16	[69]	tomato	PlantVillage	AlexNet	95.60	2017
17	[27]	multiple	PlantVillage	VGG	99.53	2018
18	[70]	mango	self	CNN	96.67	2018
19	[71]	tomato	PlantVillage	AlexNet	97.49	2018
20	[72]	banana	self	CNN	93.60	2018
21	[73]	wheat	self	ResNet-50	96.00	2019
22	[39]	multiple	PlantVillage	ResNet50	99.80	2019
23	[46]	tea	self	LeafNet	90.16	2019
24	[63]	rice	self	Lenet5	95.83	2019
25	[55]	maize	PlantVillage	CNN	92.85	2019
26	[74]	guava	self	DCNN	98.74	2019
27	[75]	mango	self	MCNN	97.13	2019

Table 2. Cont.

	Ref. #	Species	Data Source	Model	Accuracy	Year
28	[76]	multiple	PlantVillage	CNN	96.46	2019
29	[77]	multiple	PlantVillage	ResNet-50	95.61	2020
30	[53]	maize	Kaggle	VGG16	98.20	2020
31	[78]	multiple	PlantVillage	DCNN	88.46	2020
32	[79]	tomato	self	VGG16	91.90	2020
33	[80]	soybean	self	CNN	98.14	2020
34	[81]	grape	self	DICNN	97.22	2020
35	[82]	plum	self	Inception-v3	92.00	2020
36	[83]	eggplant	self	VGG16	99.40	2020
37	[84]	pepper	self	ResNet50	88.38	2020
38	[85]	cucumber	self	Efficient-B5-SwinT	99.25	2021
39	[38]	bean	Kaggle	GoogleNet	93.75	2021
40	[86]	apple	kaggle	VGG19	87.70	2021
41	[87]	tomato	PlantVillage	AlexNet	99.86	2021
42	[88]	multiple	Kaggle	CNN	100.00	2021
43	[89]	multiple	PlantVillage	EfficientNetB0	99.56	2021
44	[90]	peach	self	CNN	98.75	2021
45	[91]	multiple	PlantVillage	EfficientNet	98.42	2021
46	[92]	tomato	self	Inception v3	99.60	2021
47	[32]	chili	self	SECNN	99.12	2022
48	[32]	chili	plantvillage	SECNN	99.28	2022
49	[32]	apple	plantvillage	SECNN	99.78	2022
50	[32]	maize	plantvillage	SECNN	97.94	2022
51	[32]	pepper	plantvillage	SECNN	99.19	2022
52	[32]	potato	plantvillage	SECNN	100.00	2022
53	[32]	tomato	plantvillage	SECNN	97.90	2022
54	[93]	soybean	self	R-CNN	83.84	2022
55	[94]	multiple	self	DADCNN-5	99.93	2022
56	[95]	grape	self	InceptionV1	96.13	2022
57	[96]	grape	PlantVillage	GoogleNet	94.05	2022
58	[97]	maize	PlantVillage	GhostNet	92.90	2022
59	[97]	maize	PlantVillage	LDSNet	95.40	2022
60	[98]	apple	kaggle	Resnet	95.80	2022
61	[99]	multiple	kaggle	Resnet	99.89	2022
62	[100]	multiple	PlantVillage	EfcientNet-B3	98.91	2022
63	[101]	cassava	kaggle	CNN	87.00	2022
64	[102]	apple	self	ConvVIT	96.85	2022
65	[103]	multiple	kaggle	EfficientNet	99.70	2022
66	[104]	wheat	PlantVillage	Inception-v3	92.53	2022
67	[105]	cotton	self	CNN	98.53	2022
68	[106]	cassava	self	ResNet-50	89.70	2022
69	[107]	multiple	Plantvillage	CNN	98.61	2022
70	[107]	multiple	MepcoTropicLeaf	CNN	90.02	2022
71	[108]	multiple	self	AlexNet	86.85	2022
72	[109]	mango	self	MobilenetV2	99.43	2022
73	[110]	pepper	PlantVillage	CNN	95.80	2022
74	[110]	potato	PlantVillage	CNN	94.10	2022
75	[110]	tomato	PlantVillage	CNN	92.60	2022
76	[111]	grape	PlantVillage	CNN	98.40	2022
77	[112]	maize	Kaggle	InceptionV3	99.66	2022
78	[113]	multiple	self	CNN	96.88	2022
79	[114]	multiple	PlantVillage	CNN	99.86	2022
80	[115]	maize	PlantVillage	AlexNet	99.16	2022
81	[116]	multiple	Kaggle	CNN	99.00	2022
82	[117]	multiple	PlantVillage	CNN	98.41	2022
83	[118]	multiple	PlantVillage	DCNN	99.79	2022
84	[119]	wheat	PlantVillage	ResNet152	95.00	2022
85	[120]	rice	self	VGG16	92.24	2022

Table 2. Cont.

	Ref. #	Species	Data Source	Model	Accuracy	Year
86	[121]	potato	PlantVillage	MobileNet V2	97.73	2022
87	[122]	cucumber	PlantVillage	DCCNN	98.23	2022
88	[122]	popato	PlantVillage	DCCNN	99.83	2022
89	[122]	grape	PlantVillage	DCCNN	99.78	2022
90	[122]	apple	PlantVillage	DCCNN	99.78	2022
91	[122]	maize	PlantVillage	DCCNN	98.85	2022
92	[123]	grape	PlantVillage	VGG16	98.40	2022
93	[123]	tomato	PlantVillage	VGG16	95.71	2022
94	[124]	multiple	PlantVillage	VGG-ICNN	99.16	2022
95	[124]	apple	PlantVillage	VGG-ICNN	94.24	2022
96	[124]	maize	PlantVillage	VGG-ICNN	91.36	2022
97	[124]	rice	PlantVillage	VGG-ICNN	96.67	2022
98	[125]	grape	PlantVillage	CNN	99.34	2022
99	[126]	multiple	PlantVillage	MobileNet	98.34	2022
100	[127]	bean	Kaggle	MobileNet	97.00	2022

Most researchers apply similar CNN architectures, as indicated in Table 2, and achieve similar experiment results. As a result, new requirements and experiments with more datasets and new architectures should be performed; otherwise, much work will be duplicated.

A comparison of CNN architectures reveals that the choice of appropriate CNN models is impacted by experimental settings, dataset, and data size. Figure 4 compares several architectures based on plant type and accuracy trained by various authors.

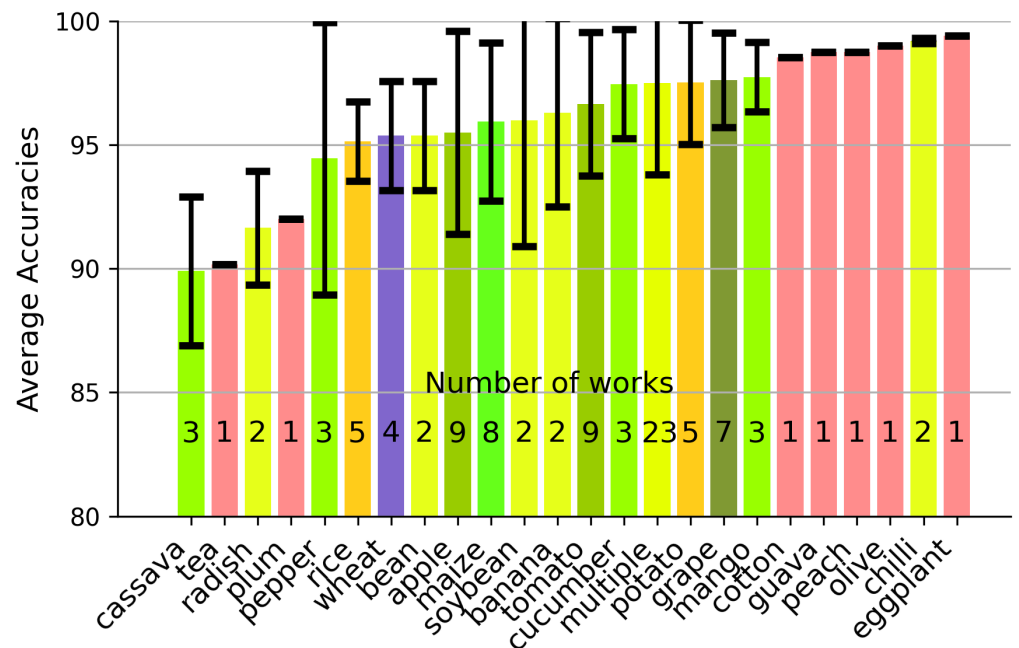


Figure 4. Comparison of CNN architectures in terms of plant types and accuracy.

When comparing the performance of these studies, it was noticed that CNN performed very well. The results appeared to be close because the methods used were applied using somewhat similar architectures.

Analysis and Data Extraction

In this section, we give discrete data derived from 100 studies to assist researchers in generating responses to their queries and to provide insight into the application of CNN in the agriculture field, including the datasets, plants, and model architectures used. In the paper collection phase, we choose 100 studies concerning CNN to conduct the data

extraction technique, then excluded 25 similar papers. After reviewing the rest of the papers, we summarized 100 studies that met the criteria for our review objectives. Figure 5 depicts the percentage distribution and the number of crops most frequently used in 100 reviewed studies that applied CNN to detect diseases. It is obvious that the majority of authors used multiple crops (more than one type of crop) in their studies with a percentage of 19.2%, and thus make use of datasets with different plant phenotypes. We also observed that maize (11.5%) is the second most commonly used crop in the 100 summarized studies, while the least used were cassava, blueberry, strawberry, olive, and soybean at only 1.9%.

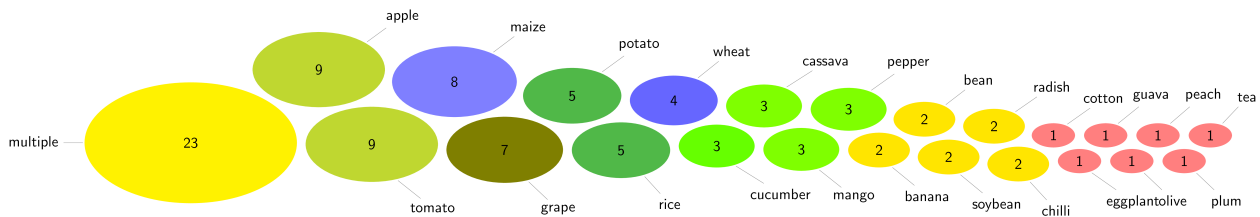


Figure 5. Number of plants used in 100 summarized studies that applied CNN to detect diseases.

Figure 6 illustrates the distribution and number of studies categorized by the algorithm used in the approach development process. Among the 100 summarized studies, the newly developed architecture was the most widely used architecture in plant diseases using CNN. A total of 10 studies, representing 22.2% of the summarized studies, used new architecture. While we observed that Alexnet is the second most commonly used CNN algorithm. In addition, we presented in Figure 7 the accuracy characteristics of 7 CNN architectures used in 100 reviewed studies to detect plant leaf diseases. It could be seen that almost all models converged by the 100th epoch of training reported accuracies of more than 99%. Models such as AlexNet and VGG yielded the highest accuracy when compared to the other models such as ResNet and MobileNet.

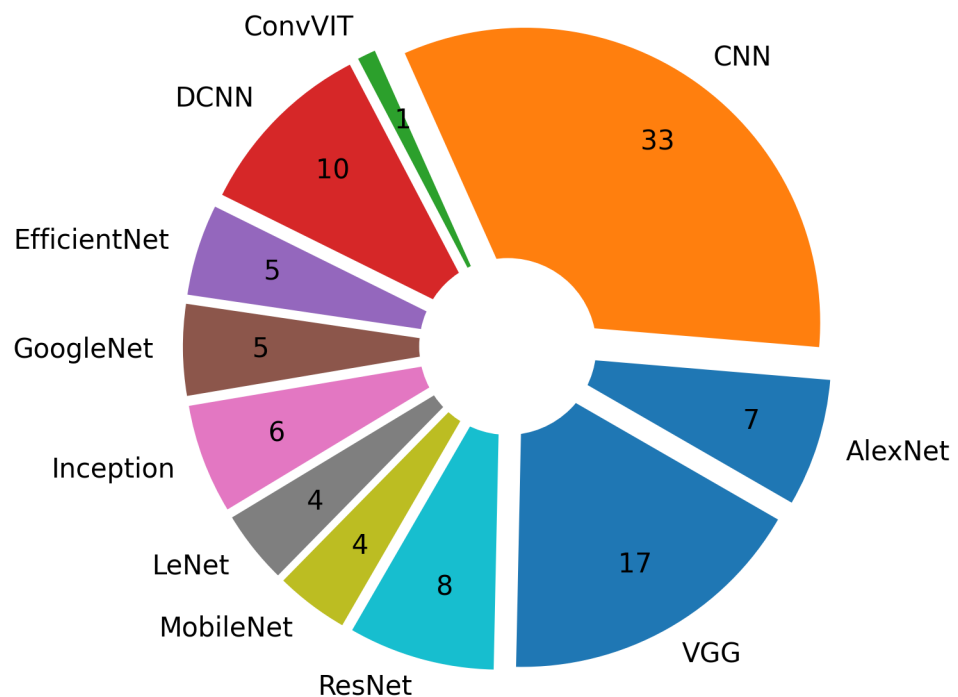


Figure 6. Distribution of the widely applied CNN algorithm in 100 reviewed studies.

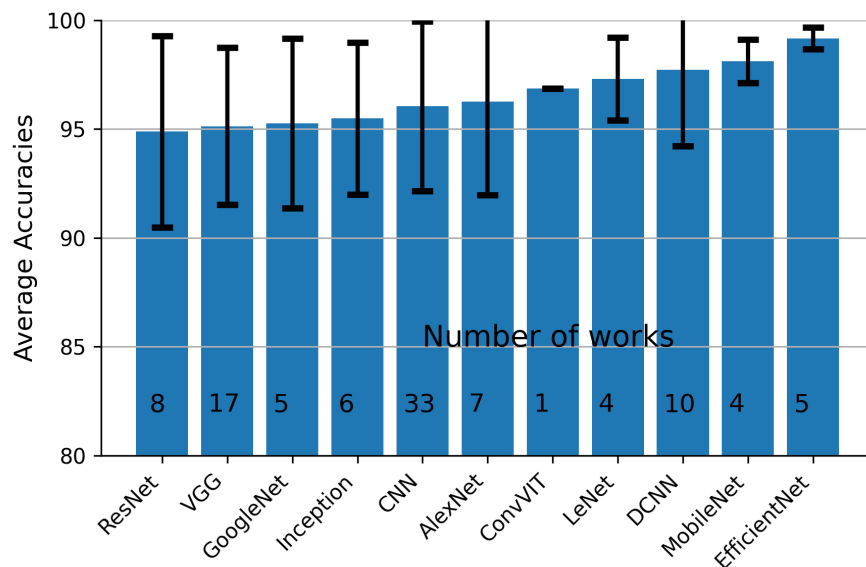


Figure 7. Accuracy characteristics of CNN architectures used in 100 reviewed studies.

The diversity of the data used is also a critical factor for the performance of the CNN to detect disease in the plant. Therefore, with respect to the characteristics of the datasets most frequently used in the studies examined, we generated a distribution of studies by dataset by previously correlating the data for each dataset used in the summarized studies (see Figure 8a).

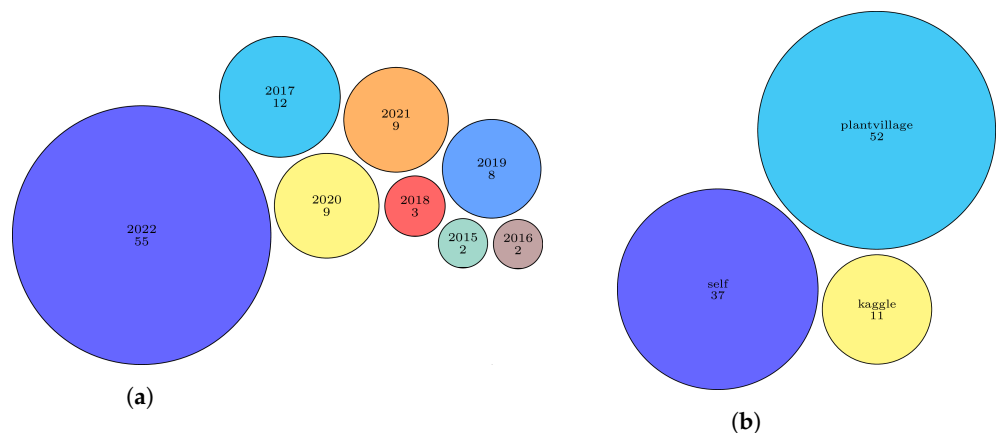


Figure 8. Distribution of the year and dataset used in 100 reviewed studies.

6. CNN’s Agriculture Applications: Major Problems and Solutions

This section may be divided into subheadings. It should provide a concise and precise description of the experimental results, their interpretation, and the experimental conclusions that can be drawn.

6.1. Limited Plant Leaf Datasets

In the last five years, CNN has become increasingly used to detect plant leaf disease. However, CNN faces numerous hurdles. Therefore, in this section, we explained and summarized the problems and solutions encountered in developing CNN-based plant disease detection.

Datasets are critical for CNN models. As a result, the main challenge to using CNN for plant disease detection and classification is the requirement for large datasets. Thus, insufficient dataset size significantly impacts the practical implementation, which means that the results will be inaccurate no matter how efficient the model is. However, there are few publicly released datasets for agricultural researchers to work with, and in many

cases, researchers must create their datasets of images from scratch. Furthermore, external environmental factors such as climate can readily affect data collection, making it time-consuming, and several days of work may be required. Moreover, to solve the problem of an insufficient and limited dataset, we provide the following solutions:

1. **Data augmentation techniques:** Data augmentation techniques increase the diversity of the data during training by artificially generating additional samples from the real dataset. Furthermore, image augmentation is a technique that creates new data from existing data to help train a deep neural network model. The most recent augmentation techniques. Fast Auto Augment [128], AugMix [129], Rand Augment [130], and population-based augmentation [131]. Liu et al. [56] used data augmentation techniques to increase the dataset size from 1053 to 13,689 images. Sladojevic et al. [132] used data augmentation to increase from 4483 to 33,469 images using perspective transformation and rotation methods. With the expansion of the dataset, the accuracy improved as well. In another study, Barbedo [133] used resizing and image segmentation methods to increase the size of the dataset from 1567 images to 46,409 images. The accuracy improved by 10.83% over the no expanded dataset.
2. **Transfer learning:** Transfer learning is a machine learning technique in which we reuse a previously trained model as the base for a new model on a new task. As a result of the new datasets, it will just retrain a few layers of pertained networks which helps to reduce the amount of data required [133]. Chen et al. [46] introduced the INC-VGGN DL architectural features to detect plant diseases, which used transfer learning by changing the pre-trained VGGNet. On the public dataset Plant Village, the suggested model obtained an accuracy of 91.83%, while on their dataset, it obtained an accuracy of 92.00%. Coulibaly et al. suggested a method for detecting mildew diseases in pearl millet using transfer learning. This method was developed using the VGG16 CNN model, which was pre-trained on the public dataset. The study provided a satisfactory result, with a 94.5% recall rate and a 95.00% accuracy rate [134].
3. **Citizen science:** In 1995, the concept of citizen science was proposed. Nonprofessional participants collect data as part of a scientific study in this technique. Farmers submit the collected images to a server for plant disease and pest classification, after which the images are correctly labeled and analyzed by an expert [133].
4. **Data sharing:** Data sharing is another way of increasing datasets. Several studies are now being conducted worldwide on accurate disease detection. The dataset will become more accurate if the different datasets are shared. This situation will encourage more significant and satisfying study results. PlantVillage [4] and Kaggle [53] are the most commonly employed public datasets in the literature on DL methods for plant disease classification and detection. Table 3 describes these datasets as the most widely applied public datasets.

Table 3. A glimpse of available plant datasets from Kaggle.

Dataset	Number of Classes	Number of Images Not Augmented	Source
PlantVillage	39	61,486	Kaggle
Kaggle (plant pathology)	12	18,632	Kaggle
Kaggle (cassava)	5	15,000	Kaggle
Kaggle (rice)	4	1200	Kaggle

6.2. Image Background

From the section above, we found that almost all of the datasets used in training a CNN model for different studies used large datasets of images. However, one of the problems researchers face is the effect of image background on detection. Most of the time, this effect

is unclear by the overlapping of many factors. The most remarkable is the interaction of plants with each other and the organization process. When images are collected in real-time conditions with a crowded background, some of the background features are similar to the area of interest; thus, a leaf segmentation technique is required in these conditions. Otherwise, the model will learn background features throughout training, leading to inaccurate classification results. On the other hand, some researchers are interested in organizing the image collection. In this case, the background is usually preserved because it creates relatively homogeneous backgrounds. It does not affect detection and may even improve detection accuracy.

Mohanty et al. [4] conducted a study in which they employed three different versions of the PlantVillage dataset to identify plant diseases and examine the influence of image background on identification outcomes, namely gray-scaled, color, and segmentation. The researchers concluded that the CNN model's performance with colored images was better than the model's performance with segmented images. As a result, we believe that the problem of image background can be solved in two ways: (i) Organize the image collection to obtain a homogeneous background. (ii) By utilizing image segmentation.

6.3. Variability in Symptoms

Symptoms are the impact and changes in the appearance of the plant. It may provide a significant change in appearance, color, or functionality. Therefore, the symptoms of plant diseases are the interaction of diseases, environment, and plants [135]. In general, there is much overlap between the symptoms of the diseases. Many factors in nature, such as humidity, temperature, sunlight, wind, and others, might affect disease symptoms. The interplay of diseases, plants, and the environment can affect various symptom changes, making it difficult to take and report on data.

The main challenge in plant disease identification is that numerous diseases may be identified and combined on the same plant leaves. Therefore, the symptoms may rapidly change, making it challenging to recognize disease types [135], and also, similar symptoms usually develop between many different diseases, further complicating disease identification [136]. Solving this type of problem is to continue increasing the database's diversity in real applications [137]. Researchers are increasingly employing this strategy to improve data diversity successfully. Furthermore, this method is seen to be more realistic because it allows researchers to collect all of the variations and information on the disease in a timely and efficient manner.

7. Discussion

In this work, we analyzed research on the application of CNN in agriculture, especially on the application of CNN methods in the detection of plant leaf diseases. In addition to leaf disease, this study also focused on CNN architectures, CNN frameworks, datasets applied, dataset size, CNN Pros and Cons, and experimental results of various models used to detect plant leaf diseases. Moreover, in this study, the review is based on research completed in the last five years, and as a result, there has been an increase in research on using CNN techniques for plant leaf disease detection.

Furthermore, the current analysis has revealed that CNN performs well in detecting plant leaf disease. Most studies found that the results were almost identical because the architecture used appeared to be similar. Consequently, new requirements and experiments with larger datasets and new architectures are required; otherwise, much work will be duplicated.

According to the literature, CNN, with various models, has become necessary in agriculture. These models are resilient under challenging conditions such as images with a complex background, non-uniform size, symptom variability, and insufficient datasets. Thus, creating a large dataset from various locations and under different conditions is necessary. On the other hand, most of the datasets mentioned in the summarized studies have a class imbalance, which could lead to model overfitting. The problem must be addressed

in future research; this can be accomplished by employing correct data redistribution techniques or class balancing classifiers [138].

Through the evaluation and analysis we have conducted on the reviewed studies, traditional algorithms are dominant in almost all of the studies summarized. The most prominent of these algorithms are AlexNet [139], GoogLeNet [8], ResNet [140], VGG [141], LeNet [142]. They frequently achieve good results and high performance, which explains the importance of their widespread use in various studies. Moreover, one of the reasons for its widespread use is the employment of transfer learning methods and fine-tuning to improve the accuracy of their results. However, many researchers still choose to use their ways to detect plant diseases; for instance, we found that 22.2% of the studies employed innovative architectures, while the remainder used traditional approaches. This is due to several factors, the most important of which are the nature of the research, the data available, and the work's goals. Nevertheless, the assessed studies do not include the possibility of recommending algorithms with substantial documentation, application examples, and usability, which can assist readers and provide inspiration for future initiative approaches.

After reviewing several studies, it became evident that maize, potato, apple, rice, cucumbers, wheat, potatoes, radish, and bananas are the most widely used and studied plants. We also observed that some researchers focus on one crop's disease, while others choose to study diseases in multiple crops as data that can include more than one plant. In the reviewed studies, we found that 19.2% of the comprehensive research used multiple crops, including different plants. The second percentage and area of interest were applying CNN to determine Maize disease. Moreover, when analyzing the results that study the types of plant diseases, we conclude the relationship between diseases and the factors causing them, as it is noted that the majority of diseases are identified and classified by fungi, and this can be explained by the fact that this pathogen causes a large proportion of plant diseases; we found that diseases caused by viruses and bacteria follow a consistent quantitative approach that is determined by the crops present in the datasets. Plant disease identification is critical, especially when employing CNN approaches. However, there are several challenges, the most significant of which are disease overlap, the presence of many disease Symptoms in a single image, and a lack of sufficient and organized data; all these challenges should be considered and worked on in the future.

8. Conclusions and Future Directions

CNN methods are widely used in the detection of plant diseases. It has solved the problems of traditional object detection and classification methods. In this study, we presented a detailed review of CNN-based research on plant leaf disease detection in crops over the last five years. A total of 100 publications were reviewed based on detection methods and model performance evaluation, comparison of popular CNN frameworks, detailed description of CNN applications in agricultural fields, dataset preparation, the problem and solution related to plant leaf disease detection, and publicly released datasets in the relevant field. We addressed highly related research articles to present a comparative analysis of various CNN models.

Most studies used CNN approaches, and they note that pre-training models compared with training from scratch models on plant leaf datasets can quickly improve performance accuracy, especially if there is a sufficient dataset for each class to train the models. Moreover, we found that most CNN approaches have many problems and challenges, one of which is the lack of dataset, a severe challenge that researchers face while doing their work. However, an essential future impact would be to develop highly efficient detection approaches employing large datasets with different plant leaf diseases. This would also address the class imbalance by requiring large generalized datasets.

Author Contributions: Conceptualization, E.E. and B.T.; methodology, E.E. and R.E.; formal analysis, E.E. and R.E.; writing—original draft preparation, E.E., B.T. and R.E.; writing—review and editing, E.E., B.T. and R.E.; supervision, B.T. and R.E. All authors have read and agreed to the published version of the manuscript.

Funding: This research received no external funding.

Institutional Review Board Statement: Not applicable.

Informed Consent Statement: Not applicable.

Data Availability Statement: Not applicable.

Conflicts of Interest: The authors declare no conflict of interest.

Abbreviations

The following abbreviations are used in this manuscript:

DL	Deep Learning
CNN	Convolutional Neural Networks
DCNN	Deep Convolutional Neural Networks
FOA	The Food and Agriculture Organization

References

- Altieri, M.A. *Agroecology: The Science of Sustainable Agriculture*; CRC Press: Boca Raton, FL, USA, 2018.
- Gebbers, R.; Adamchuk, V.I. Precision agriculture and food security. *Science* **2010**, *327*, 828–831. [[CrossRef](#)] [[PubMed](#)]
- Carvalho, F.P. Agriculture, pesticides, food security and food safety. *Environ. Sci. Policy* **2006**, *9*, 685–692. [[CrossRef](#)]
- Mohanty, S.P.; Hughes, D.P.; Salathé, M. Using deep learning for image-based plant disease detection. *Front. Plant Sci.* **2016**, *7*, 1419. [[CrossRef](#)] [[PubMed](#)]
- Miller, S.A.; Beed, F.D.; Harmon, C.L. Plant disease diagnostic capabilities and networks. *Annu. Rev. Phytopathol.* **2009**, *47*, 15–38. [[CrossRef](#)]
- LeCun, Y.; Bengio, Y.; Hinton, G. Deep learning. *Nature* **2015**, *521*, 436–444. [[CrossRef](#)]
- Najafabadi, M.M.; Villanustre, F.; Khoshgoftaar, T.M.; Seliya, N.; Wald, R.; Muharemagic, E. Deep learning applications and challenges in big data analytics. *J. Big Data* **2015**, *2*, 1–21. [[CrossRef](#)]
- Szegedy, C.; Liu, W.; Jia, Y.; Sermanet, P.; Reed, S.; Anguelov, D.; Erhan, D.; Vanhoucke, V.; Rabinovich, A. Going deeper with convolutions. In Proceedings of the IEEE Conference on Computer Vision and Pattern Recognition, Boston, MA, USA, 7–12 June 2015; pp. 1–9.
- Abade, A.; Ferreira, P.A.; de Barros Vidal, F. Plant diseases recognition on images using convolutional neural networks: A systematic review. *Comput. Electron. Agric.* **2021**, *185*, 106125. [[CrossRef](#)]
- Dhaka, V.S.; Meena, S.V.; Rani, G.; Sinwar, D.; Ijaz, M.F.; Woźniak, M. A survey of deep convolutional neural networks applied for prediction of plant leaf diseases. *Sensors* **2021**, *21*, 4749. [[CrossRef](#)]
- Nagaraju, M.; Chawla, P. Systematic review of deep learning techniques in plant disease detection. *Int. J. Syst. Assur. Eng. Manag.* **2020**, *11*, 547–560. [[CrossRef](#)]
- Kamilaris, A.; Prenafeta-Boldú, F.X. Deep learning in agriculture: A survey. *Comput. Electron. Agric.* **2018**, *147*, 70–90. [[CrossRef](#)]
- Fernández-Quintanilla, C.; Peña, J.; Andújar, D.; Dorado, J.; Ribeiro, A.; López-Granados, F. Is the current state of the art of weed monitoring suitable for site-specific weed management in arable crops? *Weed Res.* **2018**, *58*, 259–272. [[CrossRef](#)]
- Lu, J.; Tan, L.; Jiang, H. Review on convolutional neural network (CNN) applied to plant leaf disease classification. *Agriculture* **2021**, *11*, 707. [[CrossRef](#)]
- Golhani, K.; Balasundram, S.K.; Vadmalai, G.; Pradhan, B. A review of neural networks in plant disease detection using hyperspectral data. *Inf. Process. Agric.* **2018**, *5*, 354–371. [[CrossRef](#)]
- Bangari, S.; Rachana, P.; Gupta, N.; Sudi, P.S.; Baniya, K.K. A Survey on Disease Detection of a potato Leaf Using CNN. In Proceedings of the 2nd IEEE International Conference on Artificial Intelligence and Smart Energy (ICAIS), Coimbatore, India, 23–25 February 2022; pp. 144–149.
- LeCun, Y.; Bottou, L.; Bengio, Y.; Haffner, P. Gradient-based learning applied to document recognition. *Proc. IEEE* **1998**, *86*, 2278–2324. [[CrossRef](#)]
- Le Cun, Y.; Jackel, L.D.; Boser, B.; Denker, J.S.; Graf, H.P.; Guyon, I.; Henderson, D.; Howard, R.E.; Hubbard, W. Handwritten digit recognition: Applications of neural network chips and automatic learning. *IEEE Commun. Mag.* **1989**, *27*, 41–46. [[CrossRef](#)]
- Abdel-Hamid, O.; Mohamed, A.R.; Jiang, H.; Deng, L.; Penn, G.; Yu, D. Convolutional neural networks for speech recognition. *IEEE/ACM Trans. Audio Speech Lang. Process.* **2014**, *22*, 1533–1545. [[CrossRef](#)]
- Kamilaris, A.; Prenafeta-Boldú, F.X. Disaster monitoring using unmanned aerial vehicles and deep learning. *arXiv* **2018**, arXiv:1807.11805.
- Canziani, A.; Paszke, A.; Currucciello, E. An analysis of deep neural network models for practical applications. *arXiv* **2016**, arXiv:1605.07678.
- Schmidhuber, J. Deep learning in neural networks: An overview. *Neural Netw.* **2015**, *61*, 85–117. [[CrossRef](#)]

23. Alom, M.Z.; Taha, T.M.; Yakopcic, C.; Westberg, S.; Sidike, P.; Nasrin, M.S.; Hasan, M.; Van Essen, B.C.; Awwal, A.A.; Asari, V.K. A state-of-the-art survey on deep learning theory and architectures. *Electronics* **2019**, *8*, 292. [[CrossRef](#)]
24. Bahrapour, S.; Ramakrishnan, N.; Schott, L.; Shah, M. Comparative study of deep learning software frameworks. *arXiv* **2015**, arXiv:1511.06435.
25. Chollet, F. Xception: Deep learning with depthwise separable convolutions. In Proceedings of the IEEE Conference on Computer Vision and Pattern Recognition, Honolulu, HI, USA, 21–26 July 2017; pp. 1251–1258.
26. Jia, Y.; Shelhamer, E.; Donahue, J.; Karayev, S.; Long, J.; Girshick, R.; Guadarrama, S.; Darrell, T. Caffe: Convolutional architecture for fast feature embedding. In Proceedings of the 22nd ACM International Conference on Multimedia, Orlando, FL, USA, 3–7 November 2014; pp. 675–678.
27. Ferentinos, K.P. Deep learning models for plant disease detection and diagnosis. *Comput. Electron. Agric.* **2018**, *145*, 311–318. [[CrossRef](#)]
28. Abadi, M.; Barham, P.; Chen, J.; Chen, Z.; Davis, A.; Dean, J.; Devin, M.; Ghemawat, S.; Irving, G.; Isard, M.; et al. {TensorFlow}: a system for {Large-Scale} machine learning. In Proceedings of the 12th USENIX Symposium on Operating Systems Design and Implementation (OSDI 16), Savannah, GA, USA, 2–4 November 2016; pp. 265–283.
29. Bastien, F.; Lamblin, P.; Pascanu, R.; Bergstra, J.; Goodfellow, I.; Bergeron, A.; Bouchard, N.; Warde-Farley, D.; Bengio, Y. Theano: new features and speed improvements. *arXiv* **2012**, arXiv:1211.5590.
30. Kim, P. *Matlab Deep Learning: With Machine Learning, Neural Networks and Artificial Intelligence*; Apress: New York, NY, USA, 2017; p. 130.
31. Amara, J.; Bouaziz, B.; Algergawy, A. A deep learning-based approach for banana leaf diseases classification. In Proceedings of the Datenbanksysteme für Business, Technologie und Web (BTW 2017)—Workshopband, Stuttgart, Germany, 6–10 March 2017.
32. Naik, B.N.; Ramanathan, M.; Palanisamy, P. Detection and classification of chilli leaf disease using a squeeze-and-excitation-based CNN model. *Ecol. Inform.* **2022**, *69*, 101663. [[CrossRef](#)]
33. Partel, V.; Kim, J.; Costa, L.; Pardalos, P.M.; Ampatzidis, Y. Smart Sprayer for Precision Weed Control Using Artificial Intelligence: Comparison of Deep Learning Frameworks. In Proceedings of the International Symposium on Artificial Intelligence and Mathematics, ISAIM 2020, Fort Lauderdale, FL, USA, 6–8 January 2020.
34. Redmon, J.; Farhadi, A. Yolov3: An incremental improvement. *arXiv* **2018**, arXiv:1804.02767.
35. Ren, S.; He, K.; Girshick, R.; Sun, J. Faster r-cnn: Towards real-time object detection with region proposal networks. In Proceedings of the Advances in Neural Information Processing Systems 28 (NIPS 2015), Montreal, QC, Canada, 7–12 December 2016.
36. Redmon, J. Darknet: Open Source Neural Networks in C. 2013–2016. Available online: <http://pjreddie.com/darknet/> (accessed on 13 June 2022).
37. Binguitcha-Fare, A.A.; Sharma, P. Crops and weeds classification using convolutional neural networks via optimization of transfer learning parameters. *Int. J. Eng. Adv. Technol. (IJEAT)* **2019**, *8*, 2249–8958.
38. Sahu, P.; Chug, A.; Singh, A.P.; Singh, D.; Singh, R.P. Deep Learning Models for Beans Crop Diseases: Classification and Visualization Techniques. *Int. J. Mod. Agric.* **2021**, *10*, 796–812.
39. Mukti, I.Z.; Biswas, D. Transfer learning based plant diseases detection using ResNet50. In Proceedings of the 4th IEEE International Conference on Electrical Information and Communication Technology (EICT), Khulna, Bangladesh, 20–22 December 2019; pp. 1–6.
40. Arya, S.; Singh, R. A Comparative Study of CNN and AlexNet for Detection of Disease in Potato and Mango leaf. In Proceedings of the IEEE International Conference on Issues and Challenges in Intelligent Computing Techniques (ICICT), Ghaziabad, India, 27–28 September 2019; Volume 1, pp. 1–6.
41. Milioto, A.; Lottes, P.; Stachniss, C. Real-Time Blob-Wise Sugar Beets VS Weeds Classification for Monitoring Fields Using Convolutional Neural Networks. *ISPRS Ann. Photogramm. Remote Sens. Spat. Inf. Sci.* **2017**, *4*, 41–48. [[CrossRef](#)]
42. Lu, Y.; Yi, S.; Zeng, N.; Liu, Y.; Zhang, Y. Identification of rice diseases using deep convolutional neural networks. *Neurocomputing* **2017**, *267*, 378–384. [[CrossRef](#)]
43. Zhang, W.; Hansen, M.F.; Volonakis, T.N.; Smith, M.; Smith, L.; Wilson, J.; Ralston, G.; Broadbent, L.; Wright, G. Broad-leaf weed detection in pasture. In Proceedings of the 3rd IEEE International Conference on Image, Vision and Computing (ICIVC), Chongqing, China, 27–29 June 2018; pp. 101–105.
44. Liang, W.C.; Yang, Y.J.; Chao, C.M. Low-cost weed identification system using drones. In Proceedings of the 7th IEEE International Symposium on Computing and Networking Workshops (CANDARW), Nagasaki, Japan, 26–29 November 2019; pp. 260–263.
45. Dyrmann, M.; Karstoft, H.; Midtby, H.S. Plant species classification using deep convolutional neural network. *Biosyst. Eng.* **2016**, *151*, 72–80. [[CrossRef](#)]
46. Chen, J.; Liu, Q.; Gao, L. Visual tea leaf disease recognition using a convolutional neural network model. *Symmetry* **2019**, *11*, 343. [[CrossRef](#)]
47. Nkemelu, D.K.; Omeiza, D.; Lubalo, N. Deep convolutional neural network for plant seedlings classification. *arXiv* **2018**, arXiv:1811.08404.
48. Pearlstein, L.; Kim, M.; Seto, W. Convolutional neural network application to plant detection, based on synthetic imagery. In Proceedings of the 2016 IEEE Applied Imagery Pattern Recognition Workshop (AIPR), Washington, DC, USA, 18–20 October 2016; pp. 1–4.

49. Jiang, Z.; Dong, Z.; Jiang, W.; Yang, Y. Recognition of rice leaf diseases and wheat leaf diseases based on multi-task deep transfer learning. *Comput. Electron. Agric.* **2021**, *186*, 106184. [[CrossRef](#)]
50. Sravan, V.; Swaraj, K.; Meenakshi, K.; Kora, P. A deep learning based crop disease classification using transfer learning. *Mater. Today Proc.* **2021**, *Epub ahead of printing*. [[CrossRef](#)]
51. Shin, J.; Chang, Y.K.; Heung, B.; Nguyen-Quang, T.; Price, G.W.; Al-Mallahi, A. A deep learning approach for RGB image-based powdery mildew disease detection on strawberry leaves. *Comput. Electron. Agric.* **2021**, *183*, 106042. [[CrossRef](#)]
52. Brahimi, M.; Boukhalfa, K.; Moussaoui, A. Deep learning for tomato diseases: classification and symptoms visualization. *Appl. Artif. Intell.* **2017**, *31*, 299–315. [[CrossRef](#)]
53. Darwish, A.; Ezzat, D.; Hassanien, A.E. An optimized model based on convolutional neural networks and orthogonal learning particle swarm optimization algorithm for plant diseases diagnosis. *Swarm Evol. Comput.* **2020**, *52*, 100616. [[CrossRef](#)]
54. DeChant, C.; Wiesner-Hanks, T.; Chen, S.; Stewart, E.L.; Yosinski, J.; Gore, M.A.; Nelson, R.J.; Lipson, H. Automated identification of northern leaf blight-infected maize plants from field imagery using deep learning. *Phytopathology* **2017**, *107*, 1426–1432. [[CrossRef](#)]
55. Sibiya, M.; Sumbwanyambe, M. A computational procedure for the recognition and classification of maize leaf diseases out of healthy leaves using convolutional neural networks. *AgriEngineering* **2019**, *1*, 119–131. [[CrossRef](#)]
56. Liu, B.; Zhang, Y.; He, D.; Li, Y. Identification of apple leaf diseases based on deep convolutional neural networks. *Symmetry* **2017**, *10*, 11. [[CrossRef](#)]
57. Nachtigall, L.G.; Araujo, R.M.; Nachtigall, G.R. Classification of apple tree disorders using convolutional neural networks. In Proceedings of the 28th IEEE International Conference on Tools with Artificial Intelligence (ICTAI), San Jose, CA, USA, 6–8 November 2016; pp. 472–476.
58. Yuwana, R.S.; Suryawati, E.; Zilvan, V.; Ramdan, A.; Pardede, H.F.; Fauziah, F. Multi-condition training on deep convolutional neural networks for robust plant diseases detection. In Proceedings of the 2019 IEEE International Conference on Computer, Control, Informatics and Its Applications (IC3INA), Tangerang, Indonesia, 23–24 October 2019; pp. 30–35.
59. Kawasaki, Y.; Uga, H.; Kagiwada, S.; Iyatomi, H. Basic study of automated diagnosis of viral plant diseases using convolutional neural networks. In *Proceedings of the International Symposium on Visual Computing*; Springer: Berlin/Heidelberg, Germany, 2015; pp. 638–645.
60. Cruz, A.C.; Luvisi, A.; De Bellis, L.; Ampatzidis, Y. X-FIDO: An effective application for detecting olive quick decline syndrome with deep learning and data fusion. *Front. Plant Sci.* **2017**, *8*, 1741. [[CrossRef](#)] [[PubMed](#)]
61. Ha, J.G.; Moon, H.; Kwak, J.T.; Hassan, S.I.; Dang, M.; Lee, O.N.; Park, H.Y. Deep convolutional neural network for classifying Fusarium wilt of radish from unmanned aerial vehicles. *J. Appl. Remote Sens.* **2017**, *11*, 042621. [[CrossRef](#)]
62. Dang, L.M.; Syed, I.H.; Suhyeon, I. Drone agriculture imagery system for radish wilt. *J. Appl. Remote Sens.* **2017**, *11*, 16006.
63. Liang, W.j.; Zhang, H.; Zhang, G.F.; Cao, H.x. Rice blast disease recognition using a deep convolutional neural network. *Sci. Rep.* **2019**, *9*, 1–10. [[CrossRef](#)] [[PubMed](#)]
64. Ioffe, S.; Szegedy, C. Batch normalization: Accelerating deep network training by reducing internal covariate shift. In Proceedings of the International Conference on Machine Learning, PMLR, Lille, France, 7–9 July 2015; pp. 448–456.
65. Lu, J.; Hu, J.; Zhao, G.; Mei, F.; Zhang, C. An In-field Automatic Wheat Disease Diagnosis System. *Comput. Electron. Agric.* **2017**, *142*, 369–379. [[CrossRef](#)]
66. Ramcharan, A.; Baranowski, K.; McCloskey, P.; Ahmed, B.; Legg, J.; Hughes, D.P. Deep learning for image-based cassava disease detection. *Front. Plant Sci.* **2017**, *8*, 1852. [[CrossRef](#)]
67. Wang, G.; Sun, Y.; Wang, J. Automatic image-based plant disease severity estimation using deep learning. *Comput. Intell. Neurosci.* **2017**, *2017*, 2917536. [[CrossRef](#)]
68. Oppenheim, D.; Shani, G. Potato disease classification using convolution neural networks. *Adv. Anim. Biosci.* **2017**, *8*, 244–249. [[CrossRef](#)]
69. Durmus, H.; Günes, E.O.; Kirci, M. Disease detection on the leaves of the tomato plants by using deep learning. In Proceedings of the 6th International Conference on Agro-Geoinformatics, Fairfax, VA, USA, 7–10 August 2017; pp. 1–5.
70. Arivazhagan, S.; Ligi, S.V. Mango leaf diseases identification using convolutional neural network. *Int. J. Pure Appl. Math.* **2018**, *120*, 11067–11079.
71. Rangarajan, A.K.; Purushothaman, R.; Ramesh, A. Tomato crop disease classification using pre-trained deep learning algorithm. *Procedia Comput. Sci.* **2018**, *133*, 1040–1047. [[CrossRef](#)]
72. Nandhini, M.; Kala, K.U.; Thangadarshini, M.; Verma, S.M. Deep Learning model of sequential image classifier for crop disease detection in plantain tree cultivation. *Comput. Electron. Agric.* **2022**, *197*, 106915. [[CrossRef](#)]
73. Picón, A.; Alvarez-Gila, A.; Seitz, M.; Ortiz-Barredo, A.; Echazarra, J.; Johannes, A. Deep convolutional neural networks for mobile capture device-based crop disease classification in the wild. *Comput. Electron. Agric.* **2019**, *161*, 280–290. [[CrossRef](#)]
74. Howlader, M.R.; Habiba, U.; Faisal, R.H.; Rahman, M.M. Automatic Recognition of Guava Leaf Diseases using Deep Convolution Neural Network. In Proceedings of the 2019 International Conference on Electrical, Computer and Communication Engineering (ECCE), Cox's Bazar, Bangladesh, 7–9 February 2019; pp. 1–5.
75. Singh, U.P.; Chouhan, S.S.; Jain, S.; Jain, S. Multilayer Convolution Neural Network for the Classification of Mango Leaves Infected by Anthracnose Disease. *IEEE Access* **2019**, *7*, 43721–43729. [[CrossRef](#)]

76. GeethaRamani, R.; ArunPandian, J. Identification of plant leaf diseases using a nine-layer deep convolutional neural network. *Comput. Electr. Eng.* **2019**, *76*, 323–338.
77. Fang, T.; Chen, P.; Zhang, J.; Wang, B. Crop leaf disease grade identification based on an improved convolutional neural network. *J. Electron. Imaging* **2020**, *29*, 013004. [[CrossRef](#)]
78. Mishra, S.; Sachan, R.; Rajpal, D. Deep convolutional neural network based detection system for real-time corn plant disease recognition. *Procedia Comput. Sci.* **2020**, *167*, 2003–2010. [[CrossRef](#)]
79. Mkonyi, L.; Rubanga, D.; Richard, M.; Zekeya, N.; Sawahiko, S.; Maiseli, B.; Machuve, D. Early identification of Tuta absoluta in tomato plants using deep learning. *Sci. Afr.* **2020**, *10*, e00590. [[CrossRef](#)]
80. Karlekar, A.; Seal, A. SoyNet: Soybean leaf diseases classification. *Comput. Electron. Agric.* **2020**, *172*, 105342. [[CrossRef](#)]
81. Liu, B.; Ding, Z.; Tian, L.; He, D.; Li, S.; Wang, H. Grape Leaf Disease Identification Using Improved Deep Convolutional Neural Networks. *Front. Plant Sci.* **2020**, *11*, 1082. [[CrossRef](#)]
82. Ahmad, J.; Jan, B.; Farman, H.; Ahmad, W.; Ullah, A. Disease Detection in Plum Using Convolutional Neural Network under True Field Conditions. *Sensors* **2020**, *20*, 5569. [[CrossRef](#)]
83. Rangarajan, A.K.; Purushothaman, R. Disease Classification in Eggplant Using Pre-trained VGG16 and MSVM. *Sci. Rep.* **2020**, *10*, 2322. [[CrossRef](#)] [[PubMed](#)]
84. Yin, H.; Gu, Y.H.; Park, C.J.; Park, J.H.; Yoo, S.J. Transfer Learning-Based Search Model for Hot Pepper Diseases and Pests. *Agriculture* **2020**, *10*, 439. [[CrossRef](#)]
85. Wang, F.; Rao, Y.L.; Luo, Q.; Jin, X.; Jiang, Z.H.; Zhang, W.; Li, S. Practical cucumber leaf disease recognition using improved Swin Transformer and small sample size. *Comput. Electron. Agric.* **2022**, *199*, 107163. [[CrossRef](#)]
86. Subetha, T.; Khilar, R.; Christo, M.S. A comparative analysis on plant pathology classification using deep learning architecture—Resnet and VGG19. *Mater. Today Proc.* **2021**, Epub ahead of printing. [[CrossRef](#)]
87. Indu, V.T.; Priyadharsini, S.S. Crossover-based wind-driven optimized convolutional neural network model for tomato leaf disease classification. *J. Plant Dis. Prot.* **2021**, *129*, 559–578. [[CrossRef](#)]
88. Vallabhajosyula, S.; Sistla, V.; Kolli, V.K.K. Transfer learning-based deep ensemble neural network for plant leaf disease detection. *J. Plant Dis. Prot.* **2021**, *129*, 545–558. [[CrossRef](#)]
89. Hassan, S.M.; Maji, A.K.; Jasinski, M.F.; Leonowicz, Z.; Jasińska, E. Identification of Plant-Leaf Diseases Using CNN and Transfer-Learning Approach. *Electronics* **2021**, *10*, 1388. [[CrossRef](#)]
90. Yadav, S.; Sengar, N.; Singh, A.; Singh, A.; Dutta, M.K. Identification of disease using deep learning and evaluation of bacteriosis in peach leaf. *Ecol. Inform.* **2021**, *61*, 101247. [[CrossRef](#)]
91. Atila, Ü.; Uçar, M.; Akyol, K.; Uçar, E. Plant leaf disease classification using EfficientNet deep learning model. *Ecol. Inform.* **2021**, *61*, 101182. [[CrossRef](#)]
92. Ahmad, I.; Hamid, M.; Yousof, S.; Shah, S.T.; Ahmad, M.O. Optimizing Pretrained Convolutional Neural Networks for Tomato Leaf Disease Detection. *Complexity* **2020**, *2020*, 8812019:1–8812019:6. [[CrossRef](#)]
93. Zhang, K.; Wu, Q.; Chen, Y. Detecting soybean leaf disease from synthetic image using multi-feature fusion faster R-CNN. *Comput. Electron. Agric.* **2021**, *183*, 106064. [[CrossRef](#)]
94. Pandey, A.; Jain, K. A robust deep attention dense convolutional neural network for plant leaf disease identification and classification from smart phone captured real world images. *Ecol. Inform.* **2022**, *70*, 101725. [[CrossRef](#)]
95. Jin, H.; Li, Y.; Qi, J.; Feng, J.; Tian, D.; Mu, W. GrapeGAN: Unsupervised image enhancement for improved grape leaf disease recognition. *Comput. Electron. Agric.* **2022**, *198*, 107055. [[CrossRef](#)]
96. Javidan, S.M.; Banakar, A.; Vakilian, K.A.; Ampatzidis, Y. Diagnosis of Grape Leaf Diseases Using Automatic K-Means Clustering and Machine Learning. *SSRN Electron. J.* **2022**, *3*, 100081. [[CrossRef](#)]
97. Zeng, W.; Li, H.; Hu, G.; Liang, D. Lightweight dense-scale network (LDSNet) for corn leaf disease identification. *Comput. Electron. Agric.* **2022**, *197*, 106943. [[CrossRef](#)]
98. Yu, H.; Cheng, X.; Chen, C.; Heidari, A.A.; Liu, J.; Cai, Z.; Chen, H. Apple leaf disease recognition method with improved residual network. *Multimed. Tools Appl.* **2022**, *81*, 7759–7782. [[CrossRef](#)]
99. Wei, K.; Chen, B.; Zhang, J.; Fan, S.; Wu, K.; Liu, G.; Chen, D. Explainable Deep Learning Study for Leaf Disease Classification. *Agronomy* **2022**, *12*, 1035. [[CrossRef](#)]
100. Hanh, B.T.; Manh, H.V.; Nguyen, N.V. Enhancing the performance of transferred efficientnet models in leaf image-based plant disease classification. *J. Plant Dis. Prot.* **2022**, *129*, 623–634. [[CrossRef](#)]
101. Ravi, V.; Acharya, V.; Pham, T.D. Attention deep learning-based large-scale learning classifier for Cassava leaf disease classification. *Expert Syst.* **2022**, *39*, e12862. [[CrossRef](#)]
102. Li, X.; Li, S. Transformer Help CNN See Better: A Lightweight Hybrid Apple Disease Identification Model Based on Transformers. *Agriculture* **2022**, *12*, 884. [[CrossRef](#)]
103. Sun, X.; Li, G.; Qu, P.; Xie, X.; Pan, X.; Zhang, W. Research on plant disease identification based on CNN. *Cogn. Robot.* **2022**, *2*, 155–163. [[CrossRef](#)]
104. Jiang, J.; Liu, H.; Zhao, C.; He, C.; Ma, J.; Cheng, T.; Zhu, Y.; Cao, W.; Yao, X. Evaluation of Diverse Convolutional Neural Networks and Training Strategies for Wheat Leaf Disease Identification with Field-Acquired Photographs. *Remote Sens.* **2022**, *14*, 3446. [[CrossRef](#)]

105. Memon, M.S.; Kumar, P.; Iqbal, R. Meta Deep Learn Leaf Disease Identification Model for Cotton Crop. *Computers* **2022**, *11*, 102. [[CrossRef](#)]
106. Chen, Y.; Xu, K.; Zhou, P.; Ban, X.; He, D. Improved cross entropy loss for noisy labels in vision leaf disease classification. *IET Image Process.* **2022**, *16*, 1511–1519. [[CrossRef](#)]
107. Russel, N.S.; Selvaraj, A. Leaf species and disease classification using multiscale parallel deep CNN architecture. *Neural Comput. Appl.* **2022**. [[CrossRef](#)]
108. Gaikwad, S.S.; Rumma, S.S.; Hangarge, M. Fungi affected fruit leaf disease classification using deep CNN architecture. *Int. J. Inf. Technol.* **2022**. [[CrossRef](#)]
109. Prabu, M.; Chelliah, B.J. Mango leaf disease identification and classification using a CNN architecture optimized by crossover-based levy flight distribution algorithm. *Neural Comput. Appl.* **2022**, *34*, 7311–7324. [[CrossRef](#)]
110. Kurmi, Y.; Saxena, P.; Kirar, B.S.; Gangwar, S.; Chaurasia, V.; Goel, A. Deep CNN model for crops' diseases detection using leaf images. *Multidimens. Syst. Signal Process.* **2022**, *33*, 981–1000. [[CrossRef](#)]
111. Nagi, R.; Tripathy, S.S. Deep convolutional neural network based disease identification in grapevine leaf images. *Multimed. Tools Appl.* **2022**, *81*, 24995–25006. [[CrossRef](#)]
112. Subramanian, M.; Shanmugavadivel, K.; Nandhini, P.S. On fine-tuning deep learning models using transfer learning and hyper-parameters optimization for disease identification in maize leaves. *Neural Comput. Appl.* **2022**, *34*, 13951–13968. [[CrossRef](#)]
113. Gajjar, R.; Gajjar, N.P.; Thakor, V.J.; Patel, N.P.; Ruparelia, S. Real-time detection and identification of plant leaf diseases using convolutional neural networks on an embedded platform. *Vis. Comput.* **2022**, *38*, 2923–2938. [[CrossRef](#)]
114. Xu, Y.; Kong, S.; Gao, Z.; Chen, Q.; Jiao, Y.B.; Li, C. HLNet Model and Application in Crop Leaf Diseases Identification. *Sustainability* **2022**, *14*, 8915. [[CrossRef](#)]
115. Singh, R.K.; Tiwari, A.; Gupta, R.K. Deep transfer modeling for classification of Maize Plant Leaf Disease. *Multimed. Tools Appl.* **2022**, *81*, 6051–6067. [[CrossRef](#)]
116. Ruth, J.A.; Uma, R.; Meenakshi, A.; Ramkumar, P. Meta-Heuristic Based Deep Learning Model for Leaf Diseases Detection. *Neural Process. Lett.* **2022**. [[CrossRef](#)]
117. Pandian, J.A.; Kanchanadevi, K.; Kumar, V.D.; Jasińska, E.; Goño, R.; Leonowicz, Z.; Jasinski, M.L. A Five Convolutional Layer Deep Convolutional Neural Network for Plant Leaf Disease Detection. *Electronics* **2022**, *11*, 1266. [[CrossRef](#)]
118. Pandian, J.A.; Kumar, V.D.; Geman, O.; Hnatiuc, M.; Arif, M.; Kanchanadevi, K. Plant Disease Detection Using Deep Convolutional Neural Network. *Appl. Sci.* **2022**, *12*, 6982. [[CrossRef](#)]
119. Borhani, Y.; Khoramdel, J.; Najafi, E. A deep learning based approach for automated plant disease classification using vision transformer. *Sci. Rep.* **2022**, *12*, 11554. [[CrossRef](#)] [[PubMed](#)]
120. Yakkundimath, R.; Saunshi, G.; Anami, B.S.; Palaiah, S. Classification of Rice Diseases using Convolutional Neural Network Models. *J. Inst. Eng. Ser. B* **2022**, *103*, 1047–1059. [[CrossRef](#)]
121. Chen, W.; Chen, J.; Zeb, A.; Yang, S.; Zhang, D. Mobile convolution neural network for the recognition of potato leaf disease images. *Multimed. Tools Appl.* **2022**, *81*, 20797–20816. [[CrossRef](#)]
122. Yogeswararao, G.; Naresh, V.; Malmathanraj, R.; Palanisamy, P. An efficient densely connected convolutional neural network for identification of plant diseases. *Multimed. Tools Appl.* **2022**. [[CrossRef](#)]
123. Paymode, A.S.; Malode, V.B. Transfer learning for multi-crop leaf disease image classification using convolutional neural networks VGG. *Artif. Intell. Agric.* **2022**, *6*, 23–33. [[CrossRef](#)]
124. Thakur, P.S.; Sheorey, T.; Ojha, A. VGG-ICNN: A Lightweight CNN model for crop disease identification. *Multimed. Tools Appl.* **2022**. [[CrossRef](#)]
125. Math, R.M.; Dharwadkar, D.N.V. Early detection and identification of grape diseases using convolutional neural networks. *J. Plant Dis. Prot.* **2022**, *129*, 521–532. [[CrossRef](#)]
126. Kamal, K.; Yin, Z.; Wu, M.; Wu, Z. Depthwise separable convolution architectures for plant disease classification. *Comput. Electron. Agric.* **2019**, *165*, 104948.
127. Elfatimi, E.; Eryigit, R.; Elfatimi, L. Beans Leaf Diseases Classification Using MobileNet Models. *IEEE Access* **2022**, *10*, 9471–9482. [[CrossRef](#)]
128. Lim, S.; Kim, I.; Kim, T.; Kim, C.; Kim, S. Fast autoaugment. *Adv. Neural Inf. Process. Syst.* **2019**, *32*, 6665–6675.
129. Hendrycks, D.; Mu, N.; Cubuk, E.D.; Zoph, B.; Gilmer, J.; Lakshminarayanan, B. Augmix: A simple data processing method to improve robustness and uncertainty. *arXiv* **2019**, arXiv:1912.02781.
130. Cubuk, E.D.; Zoph, B.; Shlens, J.; Le, Q.V. Randaugment: Practical automated data augmentation with a reduced search space. In Proceedings of the IEEE/CVF Conference on Computer Vision and Pattern Recognition Workshops, Seattle, WA, USA, 14–19 June 2020; pp. 702–703.
131. Ho, D.; Liang, E.; Chen, X.; Stoica, I.; Abbeel, P. Population based augmentation: Efficient learning of augmentation policy schedules. In Proceedings of the International Conference on Machine Learning, PMLR, Long Beach, CA, USA, 9–15 June 2019; pp. 2731–2741.
132. Sladojevic, S.; Arsenovic, M.; Anderla, A.; Culibrk, D.; Stefanovic, D. Deep neural networks based recognition of plant diseases by leaf image classification. *Comput. Intell. Neurosci.* **2016**, *2016*, 3289801. [[CrossRef](#)]
133. Barbedo, J.G.A. Plant disease identification from individual lesions and spots using deep learning. *Biosyst. Eng.* **2019**, *180*, 96–107. [[CrossRef](#)]

134. Coulibaly, S.; Kamsu-Foguem, B.; Kamissoko, D.; Traore, D. Deep neural networks with transfer learning in millet crop images. *Comput. Ind.* **2019**, *108*, 115–120. [[CrossRef](#)]
135. Barbedo, J.G.A. A review on the main challenges in automatic plant disease identification based on visible range images. *Biosyst. Eng.* **2016**, *144*, 52–60. [[CrossRef](#)]
136. Zhang, H.; Tang, Z.; Xie, Y.; Gao, X.; Chen, Q. A watershed segmentation algorithm based on an optimal marker for bubble size measurement. *Measurement* **2019**, *138*, 182–193. [[CrossRef](#)]
137. Barbedo, J.G. Factors influencing the use of deep learning for plant disease recognition. *Biosyst. Eng.* **2018**, *172*, 84–91. [[CrossRef](#)]
138. Taherkhani, A.; Cosma, G.; McGinnity, T.M. AdaBoost-CNN: An adaptive boosting algorithm for convolutional neural networks to classify multi-class imbalanced datasets using transfer learning. *Neurocomputing* **2020**, *404*, 351–366. [[CrossRef](#)]
139. Krizhevsky, A.; Sutskever, I.; Hinton, G.E. Imagenet classification with deep convolutional neural networks. In Proceedings of the 26th Annual Conference on Neural Information Processing Systems 25, Lake Tahoe, NV, USA, 3–6 December 2012.
140. He, K.; Zhang, X.; Ren, S.; Sun, J. Deep residual learning for image recognition. In Proceedings of the IEEE Conference on Computer Vision and Pattern Recognition, Las Vegas, NV, USA, 27–30 June 2016; pp. 770–778.
141. Simonyan, K.; Zisserman, A. Very deep convolutional networks for large-scale image recognition. *arXiv* **2014**, arXiv:1409.1556.
142. LeCun, Y.; Boser, B.; Denker, J.S.; Henderson, D.; Howard, R.E.; Hubbard, W.; Jackel, L.D. Backpropagation applied to handwritten zip code recognition. *Neural Comput.* **1989**, *1*, 541–551. [[CrossRef](#)]

Article

Design and Test of Longitudinal Axial Flow Staggered Millet Flexible Threshing Device

Xinping Li *, Wantong Zhang, Wenzhe Wang and Yu Huang

College of Agricultural Equipment Engineering, Henan University of Science and Technology, Luoyang 471000, China

* Correspondence: 9903239@haust.edu.cn

Abstract: In order to solve the problems of high millet agglomerates rate, high damage rate, and high undelivered net loss rate in the process of mechanized harvesting of millet, a longitudinal axial flow-staggered flexible threshing device for millet was designed on the basis of the existing threshing device. The “staggered teeth” threshing drum and the micro rotating circular tube concave screen work together to realize the flexible and low damage threshing of millet. The pre experiment was carried out first, and the factors that have a great impact on the millet agglomerates rate, the undelivered net loss rate, and the damage rate were found to be the feeding amount, the rotating speed of the drum, and the threshing clearance. In order to further explore the influence of the interaction between the factors on the millet agglomerates rate, the undelivered net loss rate, and the damage rate, the regression orthogonal rotation combination test was carried out, and after the test, the optimal parameter combination of feeding amount, drum speed, and threshing clearance was determined. The results showed that when the feeding amount was 1.3 kg/s, the rotating speed of the drum was 762 r/min⁻¹ and the concave clearance was 15 mm, the millet agglomerates rate was 2.92%, the high undelivered net loss rate was 1.58%, and the damage rate was 0.37%.

Citation: Li, X.; Zhang, W.; Wang, W.; Huang, Y. Design and Test of Longitudinal Axial Flow Staggered Millet Flexible Threshing Device. *Agriculture* **2022**, *12*, 1179. <https://doi.org/10.3390/agriculture12081179>

Academic Editors:

Muhammad Sultan, Redmond R. Shamshiri, Md Shamim Ahamed and Muhammad Farooq

Received: 12 July 2022

Accepted: 5 August 2022

Published: 8 August 2022

Publisher's Note: MDPI stays neutral with regard to jurisdictional claims in published maps and institutional affiliations.



Copyright: © 2022 by the authors. Licensee MDPI, Basel, Switzerland. This article is an open access article distributed under the terms and conditions of the Creative Commons Attribution (CC BY) license (<https://creativecommons.org/licenses/by/4.0/>).

Keywords: longitudinal axial flow; flexible; millet threshing device; staggered threshing element; micro rotary tubular concave screen

1. Introduction

Millet is an important cereal crop in China, and its production and consumption scale ranks first in the world. According to the statistics of the national millet and sorghum industrial technology system, in 2020, China's millet planting area was about 1.5 million hm², with a total output of about 10 million tons. Moreover, millet is also an important cash crop in China. The output of millet in China accounts for about 80% of the world's output. The raw grain of millet is mainly exported to Japan, South Korea, and other countries [1–5]. The mechanized harvest of millet is an important link to realize the mechanization of the whole process of millet production. It can reduce grain loss, reduce labor intensity, and improve production efficiency.

The threshing device is the core component of grain harvesters, which determines the quality of grain harvest. Longitudinal axial flow threshing devices have the advantages of long threshing time, soft threshing, low damage rate, and high threshing efficiency [6–9]. The threshing elements of traditional grain combine harvesters are rigid. The grain code can easily fall off during threshing, so the millet agglomerates rate and damage rate are both high. Therefore, it is urgent to design a new type of millet threshing device with low millet agglomerates rate, low damage rate, and low undelivered net loss rate.

Millet cultivation in foreign developed countries is lower, and it is mostly used as feed [10–12], so the research that can be used as a reference is limited. Arnold [13] divided the traditional threshing into impact threshing, rubbing threshing, and combing threshing through many experiments, and pointed out that impact threshing is the main threshing

form causing grain damage. According to this conclusion, the threshing device designed in this study will reduce the impact on millet. Powar [14] found that the main cause of millet grain damage is mechanical impact, but did not put forward an effective method to solve this problem. Gummert [15] conducted the threshing performance test of the axial-flow threshing device and found that appropriately increasing the rotating speed of the threshing drum within a certain range can significantly improve the threshing efficiency of threshing device, but there is a lack of research on the impact of increasing the rotating speed of threshing drum on various indexes of threshing quality.

The research and development of domestic millet combine harvesters is still in its infancy. With the national attention to the realization of mechanized grain harvest, the research of scientific researchers has also made some progress. Xu [16] theoretically analyzed the axial threshing and separation system and established a mathematical model to provide a design basis for the structural design of the longitudinal axial flow drum. Wu [17] conducted a flexible beating test on Millet ears, which proved that the flexible threshing method can be applied to millet threshing. First, the suitable parameters of grain separation in high-speed photography were established, and then the appropriate parameters of grain separation in high-speed photography were established. Zhang [18] developed an axial-flow threshing and separation test-bed for millet with rod teeth, but the rod teeth had a great impact on the ear of millet, which could easily increase the grain damage rate and millet agglomerates rate, and the overall threshing effect was poor. Zong [19] found that the combination effect of impact and rubbing was better by comparing the effects of three different threshing methods on the threshing effect of rape, which proved the feasibility of integrating multiple threshing methods for optimizing the threshing effect.

At present, there is little research on flexible threshing elements at home and abroad. Most of the threshing elements of the threshing drum on the combine harvester are mainly rigid elements such as corrugated rods and rod teeth [20–25], but this is not suitable for threshing millet. The traditional threshing device such as bar threshing devices can not meet the requirements of millet threshing because of its high millet agglomerates rate, high damage rate, and high undelivered net loss rate. The purpose of this study was to reduce the millet agglomerates rate to less than 3.5%, the undelivered net loss rate to less than 3%, and the damage rate to less than 0.5%. In order to achieve this goal, the plan of this study was to design the threshing device according to the existing foundation. Then the mathematical model was established by using Hertz collision theory and D'Alembert principle to carry out kinematic analysis. Finally, according to the experimental data, we analyzed the influencing factors and established a mathematical model for parameter optimization. The type of threshing element in this design was a "staggered type", which has a better fit with the ear of millet and is conducive to millet threshing. The material of the threshing element is rubber, which has a flexible impact on millet. The combination of the "staggered teeth" threshing element and the micro rotating circular tube concave screen can effectively solve the problems of high millet agglomerates rate, high damage rate, and high undelivered net loss rate in the threshing process of millet.

2. Materials and Methods

2.1. Complete Machine Structure

Based on the existing design methods of threshing devices, this study used Hertz contact theory and D'Alembert's principle to design the threshing device. The structure of the longitudinal axial flow staggered millet flexible threshing device is shown in Figure 1. It is mainly composed of a feeding inlet, "staggered" threshing drum, top cover, micro rotating circular tubular concave screen, frequency conversion motor, receiving box, and frame. Among them, the "staggered" threshing drum is mainly composed of a conical spiral feeding part and "staggered" flexible threshing part. The conical spiral feeding part is mainly used to transport compressed grain logistics. The "staggered" threshing element material is rubber, and its section shape is gear like. It is arranged on the whole threshing drum in such a way that two adjacent threshing units are staggered by one tooth in turn, so

it is called a “staggered tooth” threshing drum. The threshing unit on the “tooth stagger” threshing drum can be well matched with the ear, and has good milling and threshing performance for the millet. A deflector is installed on the inner surface of the drum top cover, which is conducive to the axial transportation of millet materials. The micro rotating circular tube concave screen is mainly composed of a circular tube screening unit that can rotate around its own fixed axis and a micro support device. The rotary tubular screening unit and the “staggered” threshing unit cooperate to form the principle of grinding and threshing. The micro motion support device can perform reciprocating micro motion along the horizontal direction. Compared with the traditional fixed concave screen, the vibration formed in the threshing process makes the grain layer fluffy, which is more conducive to the separation of millet and reduce the entrainment loss. A receiving box is placed at the lower part of the device to collect the effluent, which is convenient for testing and analysis.

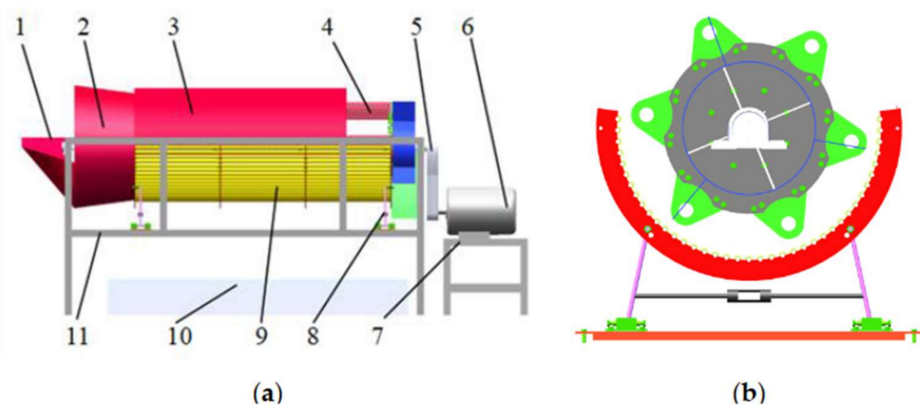


Figure 1. Structural diagram of longitudinal axial flow staggered millet threshing device: 1. feed inlet; 2. conical spiral feed housing; 3. top cover; 4. staggered threshing drum; 5. drive belt; 6. variable frequency motor; 7. motor support; 8. concave screen micro motion support device; 9. rotary tubular concave screen; 10. receiving box; 11. frame. (a) Assembled frame; (b) schematic diagram of combination of “staggered teeth” threshing drum and micro rotating circular tubular concave screen.

2.2. Working Principle

During operation, the millet plant is fed evenly and continuously by the conveyor belt at the feeding inlet. The shaft of the threshing drum is driven by the motor to rotate. The conical spiral feeding head at the front end of the “staggered” threshing drum gradually transports and compresses the loose grain plants and forcibly pushes them to the threshing chamber. Under the combined action of the continuous feeding of materials in the threshing chamber and the deflector on the inner surface of the top cover, the grain moves spirally along the axial direction of the drum. At the same time, the material layer is squeezed in the threshing chamber, and the threshing process is completed under the joint action of the “staggered tooth” threshing unit of the threshing drum and the rotary tubular screening unit on the concave screen. The adjacent rotary tubular screening unit of the concave screen can rotate around its own fixed axis under the action of grain logistics. The friction generated by rotation is conducive to the separation of millet agglomerates and grain on the ear, which can further increase the depurification rate and reduce the millet agglomerates rate. The concave screen is added with a micro motion support device. During threshing, the concave screen is subjected to the continuous reaction force exerted by the millet plant, and then the concave screen performs reciprocating micro motion in the horizontal direction. The micro motion will weaken the impact force accompanying the threshing process, increase the fluffy degree of the grain layer, further increase the separation rate of the grain passing through the concave screen, and then the grain falls into the aggregate box. The threshed millet stalks and miscellaneous residues are discharged out of the machine through the straw discharge board.

2.3. Key Component Design

2.3.1. The Design of Threshing Drum

The structure of the threshing drum is shown in Figure 2.

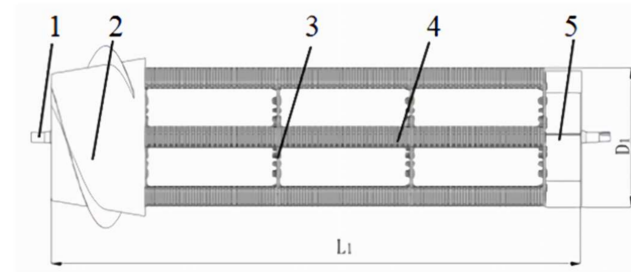


Figure 2. Structure diagram of threshing drum: 1. Main shaft; 2. conical spiral feed head; 3. spoke; 4. staggered threshing element; 5. grass discharge plate.

In order to balance the threshing effect and working load of the threshing device [26], the length of the drum is designed according to Formula (1).

$$L_1 \geq \frac{q_1}{q_0} \quad (1)$$

In the formula, L_1 is total length of threshing drum, m; q_1 is the feeding amount of the threshing device, kg/s; q_0 is the feeding amount per unit length of the threshing element, 0.8~0.9 kg/(s·m).

When calculating the length of the threshing drum, the feeding amount must be determined first. According to the research of Zhalnin [27], the density of grain in the threshing gap is jointly affected by the feeding amount and the length of the threshing drum. This also affects the damage rate of millet. Therefore, the feeding amount should take a reasonable value. The feeding amount of the threshing device is 1.5 kg/s, which can be obtained from Formula (1), and the value range of the total length of the threshing drum is 1.67~1.875 m. Comprehensively, the length of the threshing drum in this design was 1.8 m.

In order to solve the winding problem of millet plants on the threshing drum, the circumference of the threshing drum must be greater than the length of millet plants. Through the calculation of the length of millet plants in this test, it can be seen that the length of millet plants is between 1000 and 1100 mm. It is found that the calculation formula of the roller diameter [28] is

$$D_1 \geq \frac{1.5L_2}{\pi} \quad (2)$$

In the formula, D_1 is total length of threshing drum, m; L_2 is the feeding amount of the threshing device, kg/s.

According to Formula (2), the diameter of the drum is 477~525 mm. Comprehensively, the diameter of threshing drum in this design is 500 mm.

2.3.2. The Design of Conical Spiral Feeding Head

The function of the conical spiral feeding head is to compress the grain plants and push them into the threshing chamber so that the grains can spiral around the threshing drum under the action of the deflector.

The conical spiral feeding head will produce high centrifugal force and friction in the process of rotary feeding. The conical spiral feeding head rotates at an angular speed of. The speed analysis of grain at any point e of the conical spiral feeding head is shown in Figure 3.

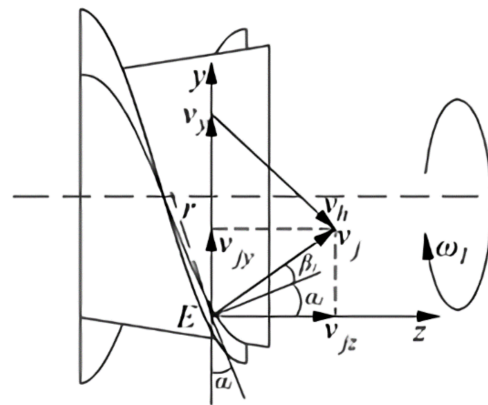


Figure 3. Grain speed analysis diagram of the feeding head.

The Figure 3 shows v_y is the centripetal speed of grain on the conical spiral feeding head, and the direction is pointing to the rotation center along point E; v_h is the sliding speed of grain on the conical spiral feeding head, and the direction is the tangent direction parallel to the spiral line at point E; v_j is the absolute speed of grain on the conical spiral feeding head, and the direction is the deflection angle along the horizontal direction $\alpha_1 + \beta_1$ of point E, where α_1 is the spiral angle of the conical spiral feeding head and β_1 is the friction angle of grain on the conical spiral feeding head, which is measured to be 19° ; v_{jz} is the partial speed of the absolute speed of grain on the conical spiral feeding head on the shaft, and the direction is parallel to the z shaft; v_{jy} is the absolute speed of grain on the conical spiral feeding head and the partial speed on the y shaft, and the direction is parallel to the y shaft. It can be obtained from the speed analysis diagram in Figure 3.

$$\begin{cases} v_y = \omega_1 r \\ \mu_1 = \tan \beta_1 \\ \frac{v_y}{v_j} = \frac{\sin(90^\circ + \beta_1)}{\sin(\alpha_1)} \\ \frac{v_h}{v_y} = \frac{\sin(90^\circ - \alpha_1 - \beta_1)}{\sin(90^\circ + \beta_1)} \\ v_{jz} = v_j \cos(\alpha_1 + \beta_1) \\ S = 2\pi r \tan \alpha_1 \\ \omega_1 = \frac{\pi n_1}{30} \end{cases} \quad (3)$$

In the formula, μ_1 is the dynamic friction coefficient between grain and conical spiral feeding head; r is the radius of the gyration of grain at point e; S is the pitch length of the conical spiral feeding head, mm; n_1 is the rotating speed of the conical spiral feeding head, $r \cdot \text{min}^{-1}$.

From Formula (3)

$$v_{jz} = \frac{n_1 S}{60} \cos^2 \alpha_1 (1 - \mu_1 \tan \alpha_1) \quad (4)$$

According to Formula (4), if we want to move the grain along the axial direction, $v_{jz} > 0$, we need to meet $1 - \mu_1 \tan \alpha_1 > 0$, that is, $\tan \alpha_1 < \cot \beta_1$; therefore, $\alpha_1 < 90^\circ - \beta_1$, $\alpha_1 < 71^\circ$, select the helix angle $\alpha_1 = 30^\circ$.

2.3.3. The Design of “Staggered Teeth” Threshing Element

The “staggered teeth” threshing element designed in this study and its assembly relationship on the drum are shown in Figure 4. The utility model comprises a “staggered” rubber roller, a spoke, an arc-shaped fixing plate, and a bolt group.

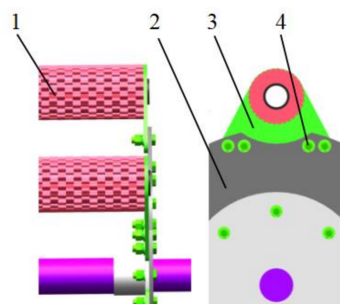


Figure 4. Installation diagram of “staggered teeth” threshing element: 1. “Staggered” rubber roller; 2. spoke; 3. arc fixed plate; 4. bolt group.

The arrangement of threshing elements is “staggered type”, which has the following advantages. First, the contact mode between threshing element and millet during threshing is surface contact. Compared with the line contact of traditional threshing element, the contact area is larger and the shear force on the ear is smaller [29]. The millet agglomerates is less likely to break from the spike stalk, so the millet agglomerates rate is also smaller. Second, this arrangement will cause grooves on the outer surface of the threshing elements. During threshing, there will be a pressure difference between the ears inside and outside the groove, which is conducive to the separation of grains and grain yards, and can optimize the threshing effect. Third, the concave convex arc caused by this arrangement can increase the friction force on the millet, which is conducive to improving the threshing rate of the millet and reducing the undelivered net loss rate.

2.3.4. Structural Design of Micro Motion Rotary Tubular Concave Screen

The grid bar of the traditional grid concave screen is a cuboid [30]. During threshing, the shear force of the edge of the cuboid on the ear will cause the grain yard to break from the ear handle. It is also easy to cause damage to the grain of millet, so the traditional grid concave screen has a high grain stacking rate and damage rate. In view of the above problems, this paper designed a micro rotating circular tube concave screen, and its structure is shown in Figure 5. The micro rotary tube concave screen is composed of a hollow tube rotary screening unit and a concave screen support device.

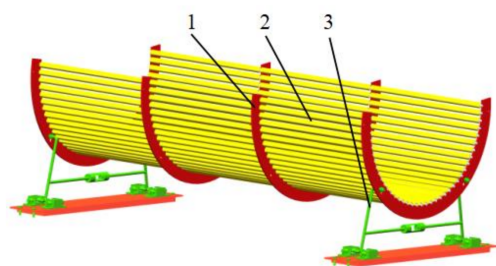


Figure 5. Structural diagram of micro rotating circular tubular concave screen: 1. side arc plate; 2. hollow circular tube rotary screening unit; 3. concave screen support device.

The calculation formula for the diameter of the micro rotating circular tubular concave screen [31] is

$$D_2 = D_1 + 2\delta \tag{5}$$

In the formula, δ is clearance between micro rotating circular tubular concave screen and drum, mm.

The clearance between the micro rotating circular tubular concave screen and the drum is 10 mm, and the diameter of the micro rotating circular tubular concave screen is 510 mm.

The structure of the hollow circular tube rotary screening unit is shown in Figure 6. The material of the hollow round pipe is polyurethane, which has high strength, tear resistance, wear resistance, and other characteristics [32]. The hollow tube is installed on the outermost layer of the rotary screening unit, and the ball support ring is located between the hollow tube and the support shaft. The hollow tube rotary screening unit has the following advantages: first, the hollow tube can rotate around its own axis, so the rolling effect is better when it is matched with the roller. Second, the sieve hole formed between the hollow round tubes is a long hole, which is conducive to the millet grains falling off the grain yard and directly falling into the receiving box, increasing the separation rate of the millet. Third, compared with the cuboid grid, the material of the hollow tube is flexible and has a larger contact area with the ear of grain. Therefore, the impact force and shear force of the hollow tube on the ear are smaller, which reduces the damage rate of the millet. Fourth, compared with the traditional grid concave, when the concave screen has the same size and the same number of rotations, the number of collisions between the hollow tube and the hollow tube screening unit is lower, so the grain damage rate is reduced.

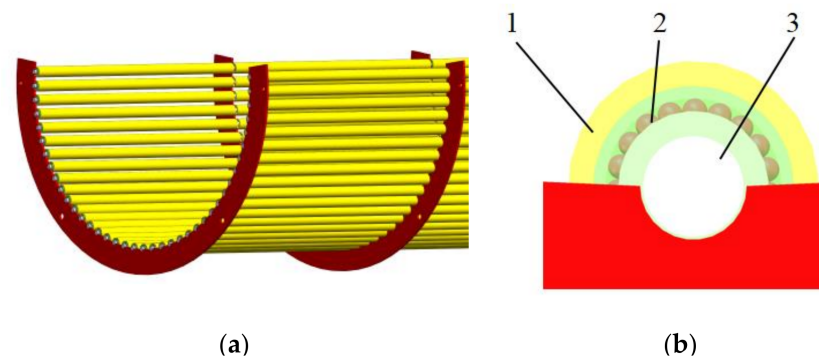


Figure 6. Schematic diagram of micro rotating circular tube concave screen: 1. side arc plate; 2. hollow circular tube rotary screening unit; 3. concave screen support device. Structure diagram of hollow circular tube rotary screening unit: (a) the overall structure diagram; (b) the side view.

The structure of concave screen support device is shown in Figure 7. Driven by the grain logistics, the horizontal displacement wheel drives the concave screen to move slightly left and right. The limit displacement is controlled by the micro adjustment bolt. The isosceles connecting rod ensures the stability of the support device. The threshing clearance range is 5~20 mm, which is adjusted by the opening and closing angle of the isosceles connecting rod.

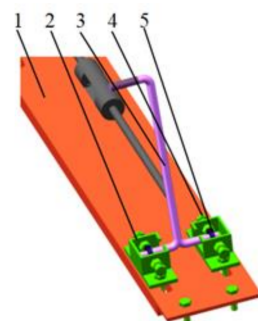


Figure 7. Structural diagram of concave screen support device: 1. plane fixing plate; 2. concave screen support base; 3. isosceles connecting rod; 4. micro adjustment bolt; 5. horizontal displacement roller.

2.3.5. Dynamic Analysis of Millet on the Side of Top Cover

The dynamic model of the material on the top cover side is established by applying the Hertz contact theory and D'Alembert's principle, and the force analysis of the material moving to the top cover side at any position D is carried out, as shown in Figure 8.

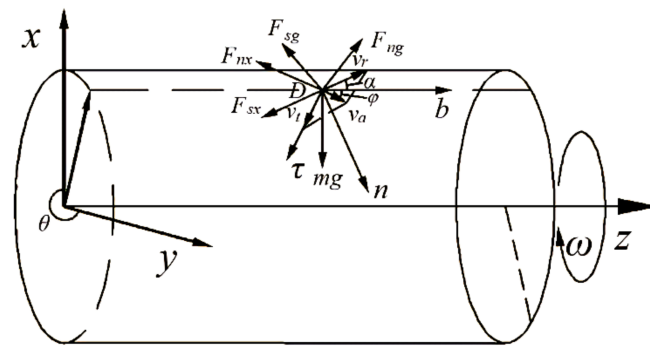


Figure 8. Schematic diagram of stress on the side of the top cover.

In the figure, F_{sg} is the friction force between the cover plate and the material, and F_{sx} is the friction force between the rubber threshing element and the material. Let the relative angular displacement between the material and the drum be θ , and the axial displacement be z , $\theta \in [\pi, 2\pi]$, θ and z , which are all functions of time t . Then there is

$$\begin{cases} mR(\ddot{\theta})^2 = f_1 F_{nx} \sin \alpha \sin \phi - mg \sin \theta - F_{nx} \cos \phi \\ mR\ddot{\theta} = F_{nx} \sin \phi - f_3 F_{ng} \sin \phi + f_1 F_{nx} \sin \alpha \cos \phi - F_{ng} \cos \phi + mg \cos \theta \\ m\ddot{z} = F_{ng} \sin \phi - f_3 F_{ng} \cos \phi - f_1 F_{nx} \cos \alpha \end{cases} \quad (6)$$

In the formula, f_3 is the dynamic friction coefficient between the material and concave plate; ϕ is the helix angle of the material relative to the cover plate, $^\circ$.

From the above theoretical model, it can be concluded that the effect of the threshing element and concave plate on material in axial flow threshing space is not only related to the gravity of material, the friction characteristics between threshing element, top cover, and concave screen and material, the structural parameters of threshing element, but also related to the movement of the material in the threshing space.

3. Results

3.1. Test Materials and Equipment

The millet variety used in this experiment was Yugu 23, and its morphological structure is shown in Figure 9.

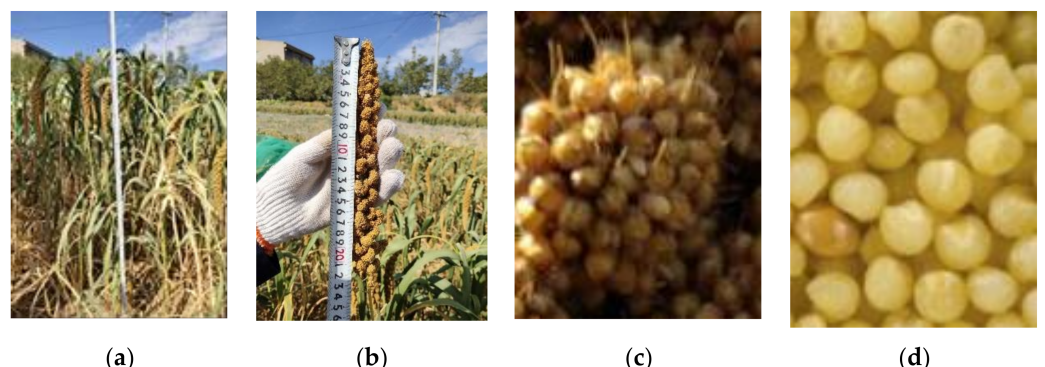


Figure 9. Yugu 23 millet: (a) the figure shows the millet plant; (b) the figure shows the millet ear head; (c) the figure shows the millet agglomerates; (d) the figure shows the millet grain.

The basic parameters of millet are shown in Table 1.

Table 1. Basic parameters of the experimental millet.

Parameter	Numerical Value
Average plant length/mm	1089
Average length of spike head of millet/mm	185
Number of grain yards on the head of millet spike/piece	90~110
Average diameter of millet agglomerates/mm	8.4
Average grain diameter/mm	1.48
Plant moisture content/%	26.8~28.7
Grain moisture content/%	14.9~17.4
Mass of 1000 grains/g	2.98

The real object of the longitudinal axial flow staggered millet flexible threshing device test-bed is shown in Figure 10.

**Figure 10.** Physical drawing of the millet flexible threshing device test bench.

3.2. Test Purpose

Through the single factor experiment on the threshing device, it was determined that the key influencing factors on the millet agglomerates rate, damage rate, and non threshing undelivered net loss rate were: feeding amount, drum speed, and threshing clearance. The optimal level of each factor was determined, in which the optimal level range of feeding amount is 0.8~1.8 kg/s, the optimal level of drum speed is 650~950 r·min⁻¹, and the optimal level of threshing clearance is 8~16 mm. In order to further explore the joint influence law of the main threshing parameters on threshing effect, an orthogonal regression rotation combination design experiment was adopted to achieve the purpose.

3.3. Test Method

Before the test, calculate and weigh the grain amount of a single test according to the feeding amount, and then lay the millet plants evenly parallel to the feeding and conveying direction. The conveyor belt shall reserve a 3 m long acceleration area. Adjust the rotating speed of threshing drum to meet the test requirements. After its operation is stable, start the conveyor belt to complete the process of conveying, feeding, threshing separation, and receiving.

A regression orthogonal rotation combination experimental design was adopted [33,34]. Taking the feeding amount A, drum speed B, and threshing clearance C as test factors and millet agglomerates rate y_1 , undelivered net loss rate y_2 , and damage rate y_3 as evaluation indexes, 23 groups of tests were completed. The test was carried out in accordance with the national standard GB/T 5982-2017 thresher test method. Each test was repeated three times, and the test results were taken as the average value. The better range of each factor level is determined according to the single factor test, and the factor level coding table is shown in Table 2.

Table 2. Coad of factor level.

Code	Factor		
	A/(kg·s ⁻¹)	B/(r·min ⁻¹)	C/(mm)
1.682	1.8	950	20
1	1.6	890	17.5
0	1.3	800	14
−1	1	710	10.5
−1.682	0.8	650	8

Referring to the national standard GB/T 5982-2017 test method for the thresher, the calculation formulas of millet agglomerates rate y_1 , undrained undelivered net loss rate y_2 , and damage rate y_3 .

$$y_1 = \frac{m_1}{m} \times 100\% \quad (7)$$

$$y_2 = \frac{m_2}{m} \times 100\% \quad (8)$$

$$y_3 = \frac{m_3}{m_0} \times 100\% \quad (9)$$

In the formula, m_1 is the grain weight of millet agglomerates in the mixture of stripped products, g; m_2 is the loss of grain quality without threshing, grain remaining on the ear discharged from the grass outlet, g; m_3 is the mass of damaged grain in the sample, g; m is the total grain mass, g; m_0 is the total mass of grain sampled, g.

3.4. Analysis of Test Results

The test scheme and its results are shown in Table 3. Among them, x_1 , x_2 , and x_3 correspond to the coding values of A, B, and C respectively.

Table 3. Test scheme and results.

Serial Number	A	B	C	$y_1/\%$	$y_2/\%$	$y_3/\%$
1	−1	−1	−1	5.65	1.8	0.62
2	1	−1	−1	5.1	0.71	0.32
3	−1	1	−1	5.98	1.42	0.9
4	1	1	−1	6.02	1.75	1.31
5	−1	−1	1	1.05	0.82	0.20
6	1	−1	1	2.533	1.8	0.42
7	−1	1	1	7.02	1.55	0.63
8	1	1	1	4.6	1.65	1.05
9	−1.682	0	0	6.1	0.46	1.52
10	1.682	0	0	2.51	0.75	1.91
11	0	−1.682	0	2.40	1.75	0.35
12	0	1.682	0	7.6	1.52	1.04
13	0	0	−1.682	5.5	1.54	0.55
14	0	0	1.682	5.5	1.54	0.10
15	0	0	0	3.02	1.54	0.49
16	0	0	0	3.49	1.61	0.48
17	0	0	0	3.2	1.42	0.48
18	0	0	0	4.4	1.48	0.31
19	0	0	0	4.85	1.58	0.39
20	0	0	0	3.12	0.51	1.42
21	0	0	0	3.58	1.49	0.58
22	0	0	0	2.95	1.51	0.63
23	0	0	0	3.3	1.57	0.53

The software design expert 10.0.7 was applied to carry out multiple regression analysis on the test data. The quadratic model of millet agglomerates rate y_1 , undelivered net loss rate y_2 , and damage rate y_3 was significant ($p < 0.0001$). The regression coefficient was F-tested under the confidence of 0.05. The simplified regression equation obtained after excluding the insignificant items as follows:

$$y_1 = 3.54 - 0.698x_1 + 1.171x_2 - 0.590x_3 + 0.593x_2x_3 + 0.566x_2^2 + 0.474x_3^2 \tag{10}$$

$$y_2 = 1.51 + 0.085x_1 - 0.084x_2 + 0.043x_3 + 0.045x_1x_2 - 0.068x_1x_3 + 0.077x_1^2 + 0.048x_2^2 + 0.041x_3^2 \tag{11}$$

$$y_3 = 0.48 + 0.11x_1 + 0.23x_2 - 0.106x_3 + 0.081x_1x_2 + 0.074x_1^2 + 0.106x_2^2 \tag{12}$$

3.4.1. Analysis of Variance of Regression Model

The analysis of variance of Formulas (10)–(12) was carried out, and the analysis results are shown in Table 4. It can be seen from the table that the model mismatches of the three indicators y_1 , y_2 , and y_3 were $p > 0.05$, indicating that the model fitting effect of the three indicators is good. The regression equation of indicator is $p < 0.0003$, and the regression equation of indicators and is $p < 0.0001$, indicating that the regression equation was extremely significant.

Table 4. Analysis of variance.

Index	Source of Variation	SS	df	MS	F	p
y_1	Regression	44.06	9	4.9	8.8	0.0003
	Surplus	7.23	13	0.56		
	Misfit	3.8	5	0.76	1.78	0.2242
	Error	3.43	8	0.43		
	Total	51.29	22			
y_2	Regression	0.44	9	0.049	12.31	<0.0001
	Surplus	0.051	13	0.0039		
	Misfit	0.014	5	0.0029	0.63	0.6861
	Error	0.037	8	0.0046		
	Total	0.49	22			
y_3	Regression	1.36	9	0.15	12.03	<0.0001
	Surplus	0.16	13	0.013		
	Misfit	0.092	5	0.018	2.04	0.1762
	Error	0.072	8	0.0090		
	Total	1.53	22			

The test results of partial regression coefficient of regression equation show that the primary and secondary relationships of various factors on millet agglomerates rate y_1 and damage rate y_3 were drum speed, feeding amount, and threshing clearance. The primary and secondary relationships of each factor on the non threshing undelivered net loss rate y_2 were feeding amount, drum speed, and threshing clearance.

3.4.2. Analysis of the Influence of Various Factors on the Millet Agglomerates Rate

The relationship surface between each factor and millet agglomerates rate y_1 is shown in Figure 11. As can be seen from Figure 11a, the drum speed increased from 710 r·min⁻¹ to 890 r·min⁻¹, and the millet agglomerates rate showed a gradual increasing trend. With the increase of the rotating speed of the drum, the speed and acceleration of the millet plant in the threshing and separation space became larger, the resultant force of the millet agglomerates on the ear became larger, the millet agglomerates and the ear handle were easier to break, and the broken millet agglomerates were easier to pass through the concave screen and fall into the aggregate box, resulting in the increase of the millet agglomerates rate. The drum speed remained unchanged at a certain level, the feeding amount increased from 1 kg/s to 1.6 kg/s, and the millet agglomerates rate decreased gradually. With the increase of feeding amount, more grains entered the separation space per unit time,

resulting in the increase of grain logistics density, the proportion of ear millet agglomerates subjected to friction from each other in the threshing process increased, and the resultant force was gentler, which reduces the possibility of millet agglomerates breaking from ear head. At the same time, with the increase of grain logistics density, the broken millet agglomerates do not easily pass through the concave screen, and continue to be threshed by grinding in the threshing separation space, which is further conducive to the reduction of millet agglomerates rate.

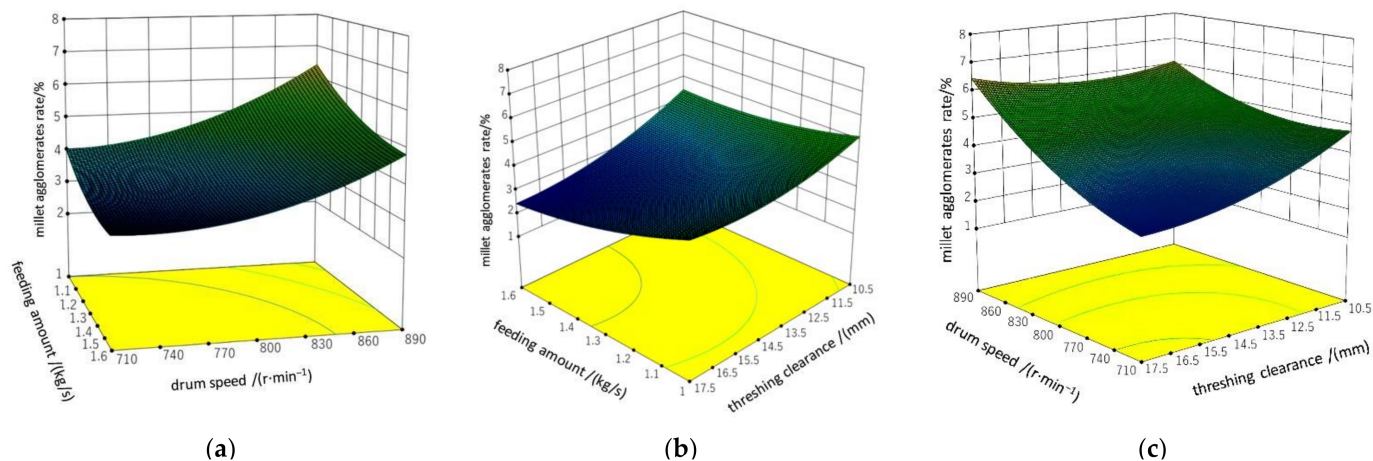


Figure 11. Influence of drum speed, feeding amount, and threshing clearance on millet agglomerates rate. (a) the picture shows the influence of drum speed and feeding amount on millet agglomerates rate; (b) the picture shows the effect of threshing clearance and feeding amount on millet agglomerates rate; (c) the picture shows the effect of threshing clearance and drum speed on millet agglomerates rate.

As can be seen from Figure 11b, as the threshing gap increased from 10.5 mm to 17.5 mm, the millet agglomerates rate gradually decreased. With the increase of threshing clearance, the grinding and rubbing effect of grain in the threshing space decreased, the rubbing force of millet agglomerates of ear decreased, and the possibility of millet agglomerates and ear fracture decreased. At the same time, with the increase of threshing clearance, the movement space of grain in the threshing space increased, and the millet agglomerates weight was lighter, which is easier to be in the upper layer of the threshing space, which can further reduce the millet agglomerates rate.

As can be seen from Figure 11c, when the threshing clearance is fixed to a certain level, the millet agglomerates rate also decreased gradually with the decrease of drum speed, indicating that there is a positive correlation between drum speed and millet agglomerates rate.

3.4.3. Analysis on the Influence of Various Factors on Undelivered Net Loss Rate

The relationship surface between each factor and undelivered net loss rate is shown in Figure 12. As can be seen from Figure 12a, when the drum speed increases from 710 r/min⁻¹ to 890 r/min⁻¹, the undelivered net loss rate of non-stripping tended to decrease gradually. With the increase of drum speed, the intensity and frequency of grinding and rubbing of grains in the threshing space gradually increased, and the threshing effect on grains was further enhanced. Millet grains more easily fall off from the ear, which is conducive to reducing the undelivered net loss rate of millet. When the rotating speed of the fixed drum reached a certain level, the feeding amount increased from 1 kg/s to 1.6 kg/s, and the undelivered net loss rate gradually increased. With the increase of the feeding amount, the grain logistics density in the threshing space increased, the threshing element did not thresh the grain completely, and the rubbing force on the ears between the grain layers decreased, resulting in the increase of the undelivered net loss rate.

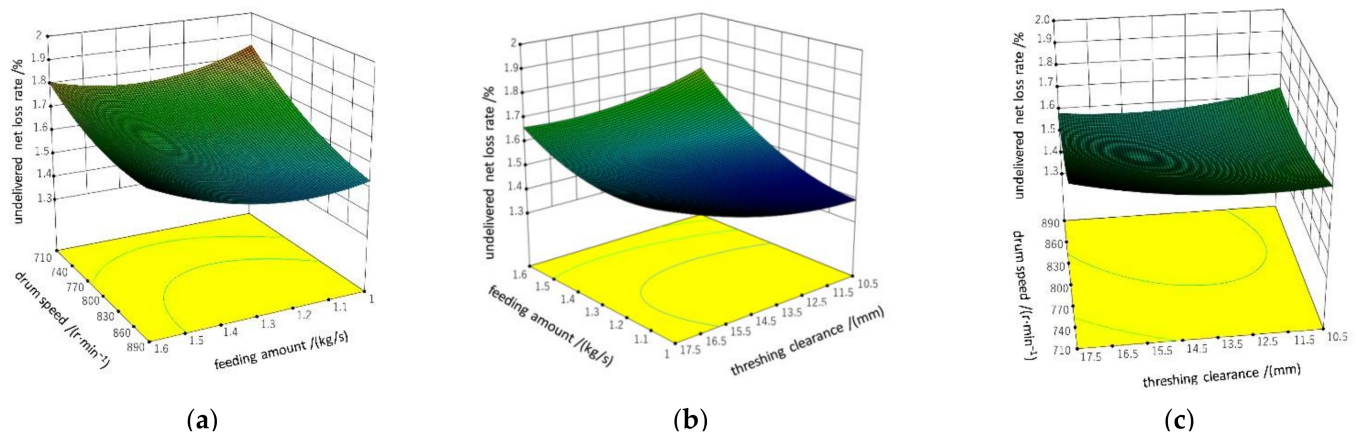


Figure 12. Influence of drum speed, feeding amount, and threshing clearance on undelivered net loss rate. (a) the picture shows the influence of drum speed and feeding amount on undelivered net loss rate; (b) the picture shows the effect of threshing clearance and feeding amount on undelivered net loss rate; (c) the picture shows the effect of threshing clearance and drum speed on undelivered net loss rate.

As can be seen from Figure 12b, as the threshing gap increased from 10.5 mm to 17.5 mm, the undelivered net loss rate of non threshing decreased gradually. This is related to the structure of the concave screen designed in this paper. The threshing gap increased, the resultant force of the contact between the millet ear in the threshing unit and the screening unit decreased in the axial direction, the acceleration of the grain logistics in the axial direction decreased, the time of the grain logistics in the threshing space became longer, and the threshing was more sufficient, which is conducive to the reduction of the undelivered net loss rate of non threshing.

It can be seen from Figure 12c that when the threshing clearance was fixed to a certain level, the non threshing loss decreased first and then increased with the increase of drum speed, indicating that there was a negative correlation between drum speed and undelivered net loss rate.

3.4.4. Analysis of Influence of Various Factors on Damage Rate

The relationship surface between each factor and damage rate y_3 is shown in Figure 13. As can be seen from Figure 13a, the damage rate increased significantly as the drum speed increased from 710 r/min^{-1} to 890 r/min^{-1} . With the increase of the rotating speed of the drum, the intensity and frequency of the impact and grinding of the threshing element on the grain flow located in the threshing separation space increase, resulting in the increase of the damage rate of millet grains. When the rotating speed of the drum was fixed to a certain level, the feeding amount increased from 1 kg/s to 1.6 kg/s, and the damage rate increased slowly, but the increase was small. With the increase of feeding amount, the grain logistics density increased, which leads to the increase of the resultant force of rolling and rubbing of the ear being direct contact with the threshing element, and the enhancement of rolling and rubbing effect leads to the increase of the damage rate.

As can be seen from Figure 13b, as the threshing clearance increased from 10.5 mm to 17.5 mm, the damage rate gradually decreased. The reason is that with the increase of threshing clearance, the grinding and rubbing effect of grains located in the threshing space decreased, and the millet ears had a larger buffer space when impacted by the roller, resulting in a smaller damage rate.

It can be seen from Figure 13c that when the fixed threshing gap was at a certain level, the drum speed increased and the damage rate increased, indicating that the drum speed was positively correlated with the damage rate.

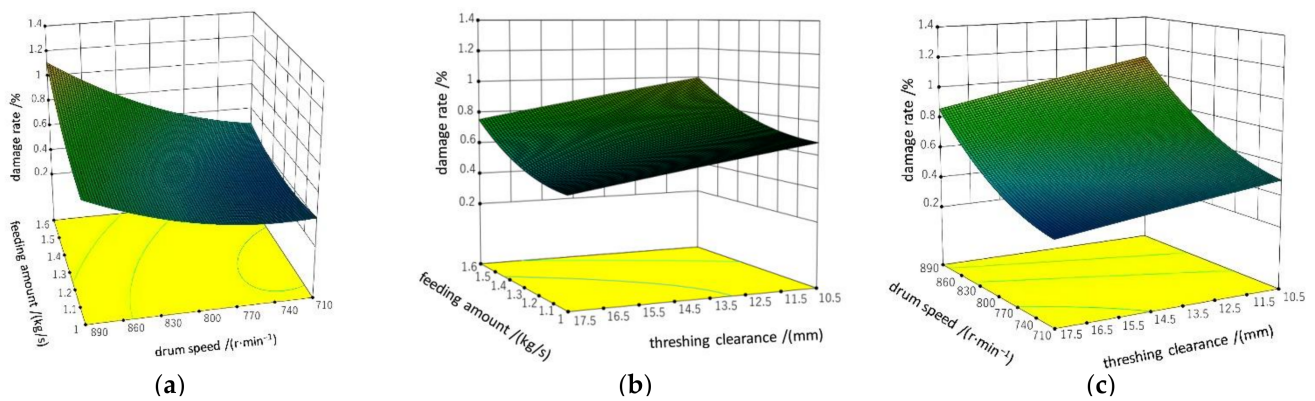


Figure 13. Influence of drum speed, feeding amount, and threshing clearance on damage rate. (a) the picture shows the influence of drum speed and feeding amount on damage rate; (b) the picture shows the effect of threshing clearance and feeding amount on damage rate; (c) the picture shows the effect of threshing clearance and drum speed on damage rate.

3.4.5. Parameter Optimization Analysis of Threshing Device

Learn the theory of multivariate statistical analysis and establish a mathematical model to optimize and analyze the millet agglomerates rate, undelivered net loss rate and damage rate.

(1) Objective function

Using the mathematical model established in Formulas (10)–(12), the millet agglomerates rate, undelivered net loss rate and damage rate are minimized under constraints, and the objective functions $\min y_1$, $\min y_2$, and $\min y_3$ are established.

(2) Constraints

Indexes y_1 , y_2 , and y_3 shall be greater than 0 while obtaining the minimum value respectively. The coding value of each factor must be within the range selected by the test, and the established constraints are

$$\begin{cases} y_j \geq 0, & (j = 1, 2, 3) \\ -1.682 \leq x_i \leq 1.682, & (i = 1, 2, 3) \end{cases} \quad (13)$$

The regression mathematical model was established according to Formula (13) and optimized by using design expert 10.0.7 software. The weights of millet agglomerates rate y_1 , undelivered net loss rate y_2 , and damage rate y_3 were 0.4, 0.3, and 0.3 respectively. The optimum parameter combination was optimized and determined as follows: the feeding amount was 1.3 kg/s, the rotating speed of the drum was 762 r/min⁻¹, and the concave clearance was 15 mm. At this time, the millet agglomerates rate of millet was 2.92%, the undelivered net loss rate of undrained grain was 1.58% and the damage rate was 0.37%.

3.5. Verification Test

The optimal parameter combination of software optimization did not appear in the test, so it is necessary to carry out verification test. The results are shown in Table 5. The verification test results are close to the software optimization results. Within the allowable error range, it is considered that the test results are consistent with the software prediction results.

Table 5. Verification test results.

Test Serial Number	Index		
	$y_1/\%$	$y_2/\%$	$y_3/\%$
Estimate	2.92	1.58	0.37
Test 1	2.89	1.57	0.39
Test 2	2.91	1.59	0.41
Test 3	2.93	1.61	0.36

4. Conclusions

- (1) Aiming at the existing problems of millet threshing, a longitudinal axial flow staggered flexible threshing device for millet was designed. Compared with traditional threshing devices such as peg-tooth axial flow threshing and separating unit, bar threshing device, and 5GJT-400 millet thresher, it has the following advantages: the threshing element material of the drum adopts wear-resistant rubber, and the threshing process is gentler. The concave screen is a micro rotating circular tube concave screen. The concave screen screening unit can rotate, and the concave screen support device can micro move. The whole system uses the grinding principle to thresh. The device can meet the requirements of low millet agglomerates rate, low undelivered net loss rate, and low damage rate.
- (2) The key structural parameters of the threshing drum and flexible micro motion concave were designed and analyzed, and the dynamic analysis of grain located on the side of top cover at any time was carried out by using the principle of d'Alembert. The results showed that the effect of the threshing element of the drum and screening unit of the concave screen on grain and the gravity of grain, the friction characteristics between grains, the structural parameters of the threshing element and screening unit, and the motion track of grain in the separation space acceleration are related.
- (3) Through the analysis of the test results, it was found that the primary and secondary relationships of each factor on the millet agglomerates rate and damage rate were drum speed, feeding amount, and threshing clearance. The primary and secondary relationships of the influence of various factors on the undelivered net loss rate of non-threshing were feeding amount, drum speed, and threshing clearance.
- (4) For millet plants with grain moisture content in the range of 14.9~17.4%, the optimal parameter combination of longitudinal axial flow staggered millet flexible threshing device is as follows: feeding amount of 1.3 kg/s, drum speed of 762 r/min⁻¹ and concave clearance of 15 mm. At this time, the millet agglomerates rate of millet was 2.92%, the undelivered net loss rate of non-threshing was 1.58%, and the damage rate was 0.37%.

Author Contributions: Conceptualization, X.L.; methodology, W.Z.; software, W.W.; validation, X.L., W.W. and Y.H.; investigation, Y.H.; data curation, W.Z.; writing—Original draft preparation, W.Z.; writing—Review and editing, X.L.; visualization, X.L.; supervision, X.L. All authors have read and agreed to the published version of the manuscript.

Funding: This research was funded by National Key Research and Development Plan Key Projects, grant number 2016YFD0701802.

Institutional Review Board Statement: Not applicable.

Informed Consent Statement: Not applicable.

Data Availability Statement: The data presented in this study are available on request from the corresponding author.

Conflicts of Interest: The authors declare no conflict of interest.

References

- Jia, G.Q.; Diao, X.M. Current Status and Perspectives of Innovation Studies Related to Foxtail Millet Seed Industry in China. *Sci. Agric. Sin.* **2022**, *55*, 653–665.
- Li, S.G.; Liu, F.; Liu, M.; Cheng, R.H.; Xia, E.J.; Diao, X.M. Current Status and Future Prospective of Foxtail Millet Production and Seed Industry in China. *Sci. Agric. Sin.* **2021**, *54*, 459–470.
- Li, S.G.; Liu, F.; Liu, M.; Zhao, Y.; Wang, H.J. Current situation, development trend and Countermeasures of millet industry in China. *Agric. Mod. Res.* **2014**, *35*, 531–535.
- Li, Y.H.; Guo, E.H.; Fan, H.P.; Wang, L.X.; Zhang, A.Y.; Liu, X.; Cheng, L.P. Discussion on the development of millet industry. *Mod. Agric. Sci. Technol.* **2019**, *22*, 28–29.
- Jia, G.; Liu, X.; Schnable, J.C.; Niu, Z.; Wang, C.; Li, Y.; Wang, S.; Wang, S.; Liu, J.; Guo, E. Microsatellite Variations of Elite Setaria Varieties Released during Last Six Decades in China. *PLoS ONE* **2015**, *10*, e0125688. [[CrossRef](#)]
- Tang, X.H.; Jin, C.Q.; Zhang, G.T.; Guo, Z.; Zhao, N.; Xu, B. Research status of threshing and separation device of combine harvester in China. *Res. Agric. Mech.* **2022**, *44*, 1–9. [[CrossRef](#)]
- Yang, L.Q.; Wang, W.Z.; Zhang, H.M.; Li, L.H.; Wang, M.M.; Hou, M.T. Improved design and bench test of tangential transverse axial flow corn threshing system. *Trans. Chin. Soc. Agric. Eng.* **2018**, *34*, 35–43.
- Tang, Z.; He, J.Z.; Zhou, Y.P.; Liu, J.B. Threshing parameter test and analysis of multi drum threshing and separation device. *Res. Agric. Mech.* **2017**, *37*, 153–157.
- Miu, P.I.; Kutzbach, H.-D. Modeling and simulation of grain threshing and separation in axial threshing units: Part II. Application to tangential feeding. *Comput. Electron. Agric.* **2008**, *60*, 105–109. [[CrossRef](#)]
- Gao, Y.E. Brief introduction of grain combine production abroad. *Grain Oil Process. Food Mach.* **1987**, *5*, 18–20.
- Lu, W.T.; Wang, R.X.; Deng, Z.G. Research status and Prospect of threshing technology for combined harvest of coarse grains. *China J. Agric. Chem.* **2017**, *38*, 11–16. [[CrossRef](#)]
- Wu, H.Y.; Liu, H.X.; Yang, Z.J.; Li, X.H.; Jiao, H.; Wang, C.J.; Zhang, G.J. Analysis on the current situation and development trend of millet production mechanization. *Agric. Technol. Equip.* **2012**, *12*, 14–17.
- Arnold, R.E. Experiments with rasp bar threshing drum. *J. Agric. Eng. Res.* **1964**, *9*, 99–131.
- Powar, R.; Aware, V.; Shahare, P. Optimizing operational parameters of finger millet threshing drum using RSM. *J. Food Sci. Technol.* **2019**, *56*, 3481–3491. [[CrossRef](#)] [[PubMed](#)]
- Gummert, M.; Kutzbach, H.D.; Muhlbauer, W.; Wacker, P.; Quick, G.R. Performance evaluation of an IRRI axial-flow paddy thresher. *Agric. Mech. Asia Afr. Latin Am.* **1992**, *23*, 47–54.
- Xu, D.X. Preliminary analysis of longitudinal axial flow drum. *J. Luoyang Inst. Agric. Mach.* **1980**, *1*, 115–131.
- Wu, X.F. *Analysis and Experimental Study on Relevant Mechanical Characteristics of New Millet Thresher*; Shanxi Agricultural University: Taigu, China, 2005.
- Zhang, D.M.; Yi, S.J.; Tao, G.X.; Mao, X. Development of millet axial threshing and separation test bench. *Res. Agric. Mech.* **2019**, *41*, 62–67.
- Zong, W.Y.; Liao, Q.X.; Chen, L.; Li, H.T.; Huang, P. The effect of different threshing methods on rapeseed pod at the end of ripening stage. *Trans. Chin. Soc. Agric. Eng.* **2012**, *28*, 29–34.
- Sun, C.L.; Zuo, J.W.; Lu, F.Y.; Geng, L.X. Design and test of combined axial flow drum for oat threshing. *Res. Agric. Mech.* **2021**, *43*, 135–141.
- Lu, W.T. Experimental study on performance of millet threshing system. *Agric. Mach.* **2020**, *6*, 100–103.
- Tang, Z.; Li, Y.; Xu, L.; Li, H.; Pang, J. Experiment and evaluating indicators of wheat threshing and separating on test-bed of longitudinal axial-threshing unit. *Trans. Chin. Soc. Agric. Eng.* **2012**, *28*, 14–19.
- Wang, J.; Li, Z.; Hussain, S.; Lu, Q.; Song, H.; Zheng, D. Design and threshing outputs study of internal and external rotary roller buckwheat thresher. *INMATEH-Agric. Eng.* **2020**, *60*, 173–182. [[CrossRef](#)]
- Lachuga, Y.F.; Bur'yanov, A.; Pakhomov, V.; Chervyakov, I. Adaptation of Threshing Devices to Physical and Mechanical Characteristics of Harvested Crops. *Russ. Agric. Sci.* **2020**, *46*, 198–201. [[CrossRef](#)]
- Samuel, A.A.; Alice, K.A.; Seckley, E.M.; Adetunla, A.O. Development of a Threshing Device for Pearl Millet. *Curr. J. Appl. Sci. Technol.* **2019**, *33*, 1–12. [[CrossRef](#)]
- Fan, C.L.; Cui, T.; Zhang, D.X.; Ynag, L.; Qu, Z.; Li, Y.H. Design and test of low damage combined corn threshing and separation device. *Trans. Chin. Soc. Agric. Mach.* **2019**, *50*, 113–123.
- Zhalnin, E.V.; Chaplygin, M.E. Dynamics of Fractional Composition of Grain-and-Straw Mass Being Threshed in the Threshing Mechanism of a Combine Harvester. *Eng. Technol. Syst.* **2022**, *32*, 249–262. [[CrossRef](#)]
- Li, Y.M. *Design and Analysis of Grain Combine*, 1st ed.; China Machine Press: Beijing, China, 2014; pp. 34–40.
- Wang, Z.B.; Wang, Z.W.; Zhang, Y.P.; Yan, W.X.; Chi, Y.J.; Liu, C.Q. Design and test of longitudinal axial flow flexible hammer claw corn threshing device. *Trans. Chin. Soc. Agric. Mach.* **2020**, *51*, 109–117.
- Chen, M.Z.; Xu, G.F.; Wang, C.X.; Diao, P.S.; Zhang, Y.P.; Niu, G.D. Design and test of longitudinal axial flow roller combined corn flexible threshing and separation device. *Trans. Chin. Soc. Agric. Mach.* **2020**, *51*, 123–131.
- Wang, X.W. *Study on Threshing Separation System with Adjustable Threshing Clearance*; Hunan Agricultural University: Changsha, China, 2019.

32. Wang, D.R. Development and application progress of polyurethane elastomer. *China Rubber Plast. Technol. Equip.* **2021**, *47*, 24–28. [[CrossRef](#)]
33. Ren, L.Q. *Experimental Design and Optimization*, 2nd ed.; Science Press: Beijing, China, 2009; pp. 7–35.
34. Singh, K.; Pardeshi, I.; Kumar, M.; Srinivas, K.; Srivastva, A. Optimisation of machine parameters of a pedal-operated paddy thresher using RSM. *Biosyst. Eng.* **2008**, *100*, 591–600. [[CrossRef](#)]

Article

Analysis and Simulation of Wheel-Track High Clearance Chassis of Rape Windrower

Mei Jin ^{1,2}, Min Zhang ², Gang Wang ², Suning Liang ², Chongyou Wu ² and Ruiyin He ^{1,*}¹ College of Engineering, Nanjing Agricultural University, Nanjing 210031, China; jinmei@caas.cn² Nanjing Institute of Agricultural Mechanization, Ministry of Agriculture and Rural Affairs, Nanjing 210014, China; zhangmin01@caas.cn (M.Z.); wanggang32@caas.cn (G.W.); liangsuning@caas.cn (S.L.); wuchongyou@caas.cn (C.W.)

* Correspondence: ryhe@njau.edu.cn

Abstract: The middle and lower reaches of the Yangtze River are the main production area of rapeseed. Small windrowers with two tracks are adopted in this area, which have lower efficiency. With the advancement of large-scale rape planting, medium and large windrowers are urgently needed; however, most medium and large windrowers are wheeled machines which have poor adaptability to sticky soil in rice–rape rotation areas. Therefore, a wheel-track high clearance chassis for rape windrower was developed. Theoretical analysis and simulation of the main performance of this chassis were investigated. Mathematical models of the relationship between the chassis eccentricity and running resistance, uphill and downhill angle and the height of obstacle were established. Then, three-dimensional modeling and dynamic simulations of a wheel-track high clearance chassis of a rape windrower in wet clay soil were carried out based on Pro/E and RecurDyn software. The simulation results indicated that when the chassis ran on flat hard road at the same speed, eccentricity had little effect on average walking speed; the coefficient variation of speed decreased with the increase of eccentricity, while the driving torque and its coefficient variation decreased first and then increased. The minimum driving torque and the coefficient variations were obtained when the eccentricities were 1484 mm and 1584 mm. Field experiments were carried out on two kinds of ground. The results showed that on flat hard road, the speed of the wheel-track high clearance rape windrower was 0–20.22 km/h, the minimum turning radius was 5.965 m; on rice stubble field with 38.7% water content, the working speed was 0–9.12 km/h, the minimum turning radius was 6.498 m, and the climbing angle was over 20°. All parameters of the wheel-track high clearance chassis met the design specifications, and the working efficiency increased over 100% compared with the existing two-tracked rape windrower. A new kind of rape windrower for the middle and lower reaches of the Yangtze River was provided.

Citation: Jin, M.; Zhang, M.; Wang, G.; Liang, S.; Wu, C.; He, R. Analysis and Simulation of Wheel-Track High Clearance Chassis of Rape Windrower. *Agriculture* **2022**, *12*, 1150. <https://doi.org/10.3390/agriculture12081150>

Academic Editors:
Muhammad Sultan, Redmond
R. Shamshiri, Md Shamim Ahamed
and Muhammad Farooq

Received: 4 July 2022

Accepted: 29 July 2022

Published: 3 August 2022

Publisher's Note: MDPI stays neutral with regard to jurisdictional claims in published maps and institutional affiliations.



Copyright: © 2022 by the authors. Licensee MDPI, Basel, Switzerland. This article is an open access article distributed under the terms and conditions of the Creative Commons Attribution (CC BY) license (<https://creativecommons.org/licenses/by/4.0/>).

Keywords: wheel-track high clearance chassis; walking performance; climbing angle; simulation; rape windrower

1. Introduction

The existing chassis of rape windrowers is divided into two types: two tracked chassis and four wheeled high clearance chassis. A two tracked chassis has strong adaptability to soil, which is mainly applicable to rape windrower in the middle and lower reaches of the Yangtze River. A four wheeled high clearance chassis is mainly used for rape windrower of dry-land cultivation in northern China [1,2]. With the gradual advancement of land transfer, rape planting areas in rice–oil rotation regions of the Yangtze River Basin have been expanding, so medium and large-sized harvesting equipment is urgently needed. Most of the large-sized rape windrowers have wheeled chassis, which are not suitable for sticky and heavy soil with high moisture content. They sink and slip easily and cannot work well [3–5]. In this paper, a wheel-track high clearance chassis is proposed. Triangular

tracks and rubber tires are combined to make full use of the high passing of the track and the flexibility of the wheel.

In China, research on wheel-track structure has mainly focused on mobile robots. Conversion mechanisms of different walking forms such as wheel, track and leg have been designed, motion equations in various states have been constructed, and various virtual prototypes have been established. The step walking performance, stability and power consumption of each walking mechanism under different working environments have been analyzed [6–11]. All these studies investigated the machines used in workshops or setting hard roads.

In recent years, in order to increase the walking performance and adaptability of agricultural machinery equipment, research on agricultural machinery chassis under various working environments has been carried out. These chassis were used for sugarcane harvesting, orchard plant protection and harvesting, forest land slope operation, coal mine underwater operation and so on. A triangle tracked chassis for a sugarcane harvester was designed by Bai Yuanqiang. The adaptability of a triangle track and flat track combination to slope ground was better than that of a traditional track sugarcane harvester [12]. A four triangular tracked camellia fruit picking machine with good adaptability to southern gentle slope land was developed by Cai Gangchu [13]. A two triangle tracked orchard chassis was designed by Wang Feng and the performance met the actual requirements of orchard work [14]. A wheel-track high clearance chassis of a paddy field sprayer was designed by Zeng Shan, and the theoretical analysis of steering performance was carried out. The force analysis of trapezoidal support under load was carried out to optimize the walking device. The minimum turning radius of this machine was 3380 mm [15]. A multifunctional power chassis for orchard was designed by Hao Chaohui. The turning performance, stability performance and ridge crossing performance of the chassis were analyzed theoretically. The minimum turning radius was 2000 mm and the maximum climbing angle was 24° [16]. The performance analysis of the tracked tractor climbing obstacle was carried out by Pan Guanting. The relationship between the obstacle height, slope angle and the centroid position of the tractor was obtained by simulation, and the obstacle heights under different speeds and ramp angles were also obtained [17].

Several kinds of chassis, such as four triangular tracked flat tracked chassis or two-wheeled two-tracked type chassis, are widely used for large tractors, harvesters and seeders, which provide greater ground contact and effectively reduce grounding pressure and soil damage. The John Deere 9620RX four triangular tracked tractor, C100 two-wheeled two-tracked harvester, CASE 6088 two triangular tracked two wheeled harvester and CLAAS LEXION770 two flat tracked two wheeled harvester have advantages.

It follows that research on wheeled and tracked chassis in China or abroad are mainly applied to special function robots and some farm machinery for woodland, orchards or large farms in dry land areas. However, this kind of chassis is seldom used for high clearance machines.

In this paper, a detailed analysis of the walking performance and stability performance of a high clearance chassis for rape windrower was carried out, which provided a basis for the development of large-scale rape windrowers in the Yangtze River Basin.

2. Performance and Simulation Analysis of Chassis

2.1. Structure and Working Principle of a Wheel-Track High Clearance Chassis for Rape Windrower

The structure of a wheel-track high clearance chassis for rape windrower is shown in Figure 1. It mainly includes two parts: swath header and wheel-track high clearance chassis. The front walking mechanisms are two triangle tracks, which are the driving parts; the back walking mechanisms of the chassis are two rubber tires which are follower wheels. The chassis is also composed of the engine, the pump motor power system, the chassis frame, the header suspension frame, and the fuel tank.

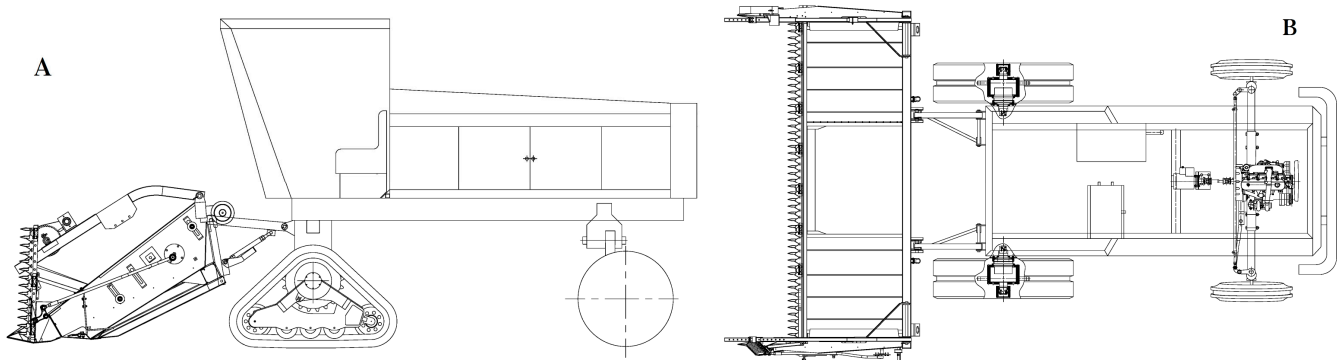


Figure 1. Structural diagram of a wheel-track high clearance rape windrower. (A) Main view; (B) Vertical view (removal of cab and frame top cover).

Triangular tracks are driven by a hydraulic system to pull the machine forward and backward. The steering mechanism is driven by a hydraulic system with a selector valve, which is controlled by the steering wheel in the cab. The rubber tires are deflected by the steering mechanism to steer the machine. When the machine works, the cutter cuts the crops down, which are then moved to the middle gap by the conveyor belt on both sides of the header. Therefore, the chassis not only needs the functions of walking, climbing and crossing the terrain, but also needs enough space to let the plants that have been cut lay smoothly under the chassis. The specific structural parameters and technical indicators are shown in Table 1.

Table 1. Main technical parameters of the wheel-track high clearance chassis.

Parameters/Units	Numerical Value (Manner)
Power/kW	68
Driving mode	Two-track drive
Steering mode	Rear-wheel steering
Walking mechanism	Wheel-track combination
Minimum ground clearance/mm	970
Front track gauge/mm	2090
Rear wheel gauge/mm	2646
Wheelbase	2950
Uphill and downhill angle/°	20
Walking speed/km/h	≥20

2.2. Analysis of Driving Resistance

2.2.1. Analysis of Wheel and Track Load

The force diagram of the chassis frame and swath header (located in the harvesting state) on the horizontal ground is shown in Figure 2. O_1 and O_2 are, respectively, the force points of the frame on the triangular track and wheel, O_3 is the center of gravity of the header, and O_4 is the center of gravity of the chassis. Two equations are used to explain the balance at steady state, as below.

$$\begin{cases} F_t + F_w = G_3 + G_4 \\ G_3 l_1 + F_w L = G_4 e \end{cases} \quad (1)$$

After calculating:

$$\begin{cases} F_w = \frac{G_4 e - G_3 l_1}{L} \\ F_t = \frac{(G_3 + G_4)L - G_4 e + G_3 l_1}{L} \end{cases} \quad (2)$$

where l_1 is the horizontal distance between the gravity center of the swath header and the action point of the track on the frame, 1880 mm; L is wheelbase, 2950 mm; e is the

eccentricity of the chassis frame (chassis frame: swath header, tires and tracks are not included), which is the horizontal distance between the gravity center of the chassis frame and the center point of the track, mm; all the eccentricities mentioned below are equivalent to e ; G_3 is the weight of header and G_4 is the weight of chassis frame, which may be taken as 10,000 N and 20,000 N, respectively. F_w , F_t are the forces applied by the wheel and the track, respectively, to the frame, N.

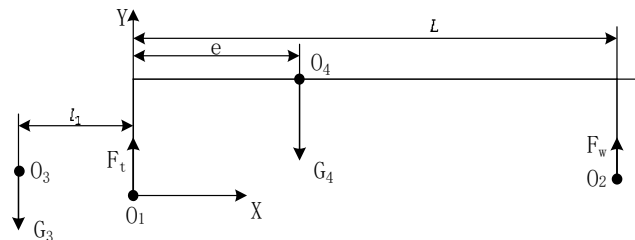


Figure 2. Force analysis of rape windrower on flat road.

2.2.2. Analysis of Driving Resistance

When the track is running, the soil is compacted and the compaction resistance is produced on the track, which is related to the force bearing point from the chassis frame and the geometric center of the track [18–21]. The motor output shaft is connected to the triangular track’s driving wheel to transmit torque and force. The projection of the drive wheel center on the ground coincides with the projection of the track geometric center on the ground. The schematic diagram of the interaction force between a single triangular track and the ground is shown in Figure 3.

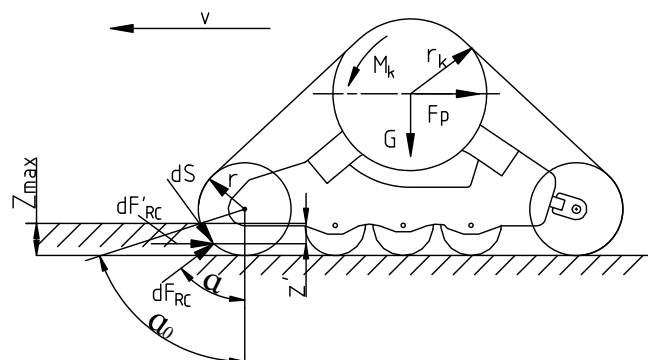


Figure 3. Interaction between track guide wheel and soil.

The differential formula of soil deformation resistance to the front guiding wheel pressed into the internal arc area of soil can be established from Figure 3 [20]:

$$dF_{RC} = p'bdS \tag{3}$$

where dF_{RC} is the deformation resistance of soil caused by ground extrusion of tack microelement connection, kN; p' is per unit area ground pressure of track, kPa; b is the width of track; dS is microelement arc length in extruded soil in the front of guide wheel, m.

It can be seen from Figure 3:

$$dS = r d\alpha \tag{4}$$

where r is radius of guiding wheel, m. $d\alpha$ is the microelement angle between the radius of any part of the guiding wheel and the radius perpendicular to the ground, rad.

Track subsidence depth of any part in the calculation range:

$$Z' = r \cos\alpha - r \cos\alpha_0 = r(\cos\alpha - \cos\alpha_0) \tag{5}$$

where Z' is the rack subsidence depth, m. a_0 is the angle between the radius of the guiding wheel contacted with the ground and the radius perpendicular to the extruded ground, rad. α is the angle between the radius of any point and the radius perpendicular to the extruded ground.

The relationship between ground pressure p' and subsidence depth for any part of the track is as follows:

$$p' = \left(\frac{K_c}{b} + K_\varphi \right) (Z')^n \tag{6}$$

where K_c is the deformation modulus determined by viscous composition of soil, kN/m^{n+1} . K_φ is the deformation modulus determined by frictional elements of soil, kN/m^{n+2} . n is soil deformation index. b is the width of track.

Insert Equation (5) into Equation (6):

$$p' = \left(\frac{K_c}{b} + K_\varphi \right) r^n (\cos\alpha - \cos\alpha_0)^n \tag{7}$$

It can be seen from Figure 3 that the horizontal resistance differential equation of soil deformation is:

$$dF'_{RC} = dF_{RC} \sin\alpha = p' b \sin\alpha dS \tag{8}$$

Insert Equations (4) and (7) into Equation (8):

$$dF'_{RC} = b \left(\frac{K_c}{b} + K_\varphi \right) r^{n+1} (\cos\alpha - \cos\alpha_0)^n \sin\alpha d\alpha \tag{9}$$

The horizontal deformation resistance is obtained by integrating Equation (9):

$$F'_{RC} = \int_0^{\alpha_0} dF'_{RC} = \frac{b}{n+1} \left(\frac{K_c}{b} + K_\varphi \right) r^{n+1} (1 - \cos\alpha_0)^{n+1} \tag{10}$$

It can be seen from the geometrical relationship of Figure 3:

$$\cos\alpha_0 = \frac{r - Z_{max}}{r} \tag{11}$$

where Z_{max} is the maximum subsidence depth, m.

Insert Equation (11) into Equation (10):

$$F'_{RC} = \frac{b}{n+1} \left(\frac{K_c}{b} + K_\varphi \right) Z_{max}^{n+1} \tag{12}$$

According to Equations (6) and (12), the horizontal deformation resistance of one of the tracks is:

$$F'_{RC} = \frac{b}{n+1} P_{max} Z_{max} \tag{13}$$

where P_{max} is the maximum ground pressure, kPa.

The machine has two tracks, and the gravity center of the track coincides with the geometric center in the horizontal direction. Track ground contact pressure is assumed to be uniform, and the average contact pressure can be calculated according to the following equation.

$$P_a = \frac{G}{2bL_a} \tag{14}$$

where G is the combined forces of gravity and vertical load on two tracks, kN.

The average subsidence depth is as follows:

$$Z_a = \left[\frac{G}{2bL_a \left(\frac{K_c}{b} + K_\varphi \right)} \right]^{\frac{1}{n}} \quad (15)$$

where Z_a is the average subsidence depth.

Insert Equations (14) and (15) into Equation (13), and the soil resistance of a single track is:

$$F'_{RC} = \frac{b}{n+1} P_a Z_a \quad (16)$$

Therefore, the total soil resistance of the two tracks is:

$$F'_{RC} = \frac{2b}{(n+1) \left(\frac{K_c}{b} + K_\varphi \right)^{\frac{1}{n}}} \left(\frac{G}{2bL_a} \right)^{\frac{n+1}{n}} \quad (17)$$

It can be seen that increasing the track length is more effective than widening the track to reduce the compaction resistance under the same ground pressure.

In addition to the resistance of soil deformation, the internal friction also generates resistance during the driving process, which is proportional to the vertical force on the track as Equation (18).

$$F_{RF} = f_0 G \quad (18)$$

where F_{RF} is the friction resistance of the track, N; f_0 is internal friction resistance coefficient of track (generally, $f_0 = 0.07$).

Therefore, the total resistance of the track when it walks is:

$$F_R = F'_{RC} + f_0 G = \frac{2b}{(n+1) \left(\frac{K_c}{b} + K_\varphi \right)^{\frac{1}{n}}} \left(\frac{G}{2bL_a} \right)^{\frac{n+1}{n}} + f_0 G \quad (19)$$

where $G = F_t + G_t$ the total weight of two tracks $G_t = 8800$ N, F_t can be found from Equation (2), soil deformation modulus $K = \frac{K_c}{b} + K_\varphi$. Test value of viscous soil is selected as 90 kN/m^{n+2} , soil deformation index $n = 0.5$ [20].

2.3. Performance Analysis of Uphill and Downhill

The longitudinal stability is an important indicator of the high clearance machine, and it also reflects the uphill and downhill performance of the machine. For climbing performance, in addition to considering the traction performance of the machine, safety is more important. It should meet the following two points, i.e., that the machine can go up or down the slope safely. Firstly, the whole machine does not flip, and the contact force between the front track and the ground should be greater than 0 when it is uphill, and the contact force between the rear wheel and the ground should be greater than 0 when it is downhill. Secondly, the triangular track does not turn 360° around driving shaft. Because the front track is only connected with the frame through the central axis O_1 of the driving wheel, the triangular track can rotate 360° around O_1 . In order to ensure that the track does not flip entirely, it is necessary to ensure that the intersection of the extension line of force sustained by the track at O_1 and the slope should be in the contact surface of the track and slope [22].

When the machine goes up or down the slope, the header would rise to the highest position, and the gravity center of the header rises too. The stress diagram is shown in Figure 4.

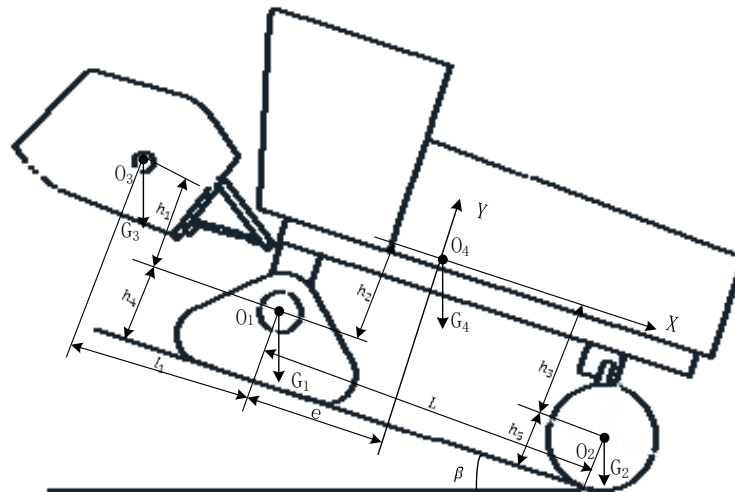


Figure 4. Schematic of the rape windrower when climbing up.

2.3.1. The Whole Machine Stability Analysis of Uphill and Downhill

When the machine is in the critical condition of uphill, the force between the front track and ground is 0. The tire is regarded as a rigid body, and the moment-equilibrium equation is:

$$G_3 \sin \beta(h_1 + h_4) + G_1 \sin \beta h_4 + G_4 \sin \beta(h_2 + h_4) + G_2 \sin \beta h_5 = G_3 \cos \beta(l_1 + L) + G_1 \cos \beta L + G_4 \cos \beta(L - e) \quad (20)$$

So:

$$\tan \beta = \frac{G_3(l_1 + L) + G_1 L + G_4(L - e)}{G_3(h_1 + h_4) + G_1 h_4 + G_4(h_2 + h_4) + G_2 h_5} \quad (21)$$

where G_1 , G_2 are weights of track and wheel, 8800 N and 1200 N, l_1 is distance along X axis between gravity center of header and the force bearing point of track, 1957 mm; L is wheelbase, 2950 mm; h_1 is the distance along Y axis between gravity center of header and triangle track rotation center of 808 mm (header is in lifting position); h_2 is the distance along Y axis between gravity center of chassis frame and triangle track rotation center, 873 mm; h_4 is the distance along Y axis between triangle track rotation center and ground. h_5 is the distance along Y axis between the tire center and the ground, 497.5 mm.

Putting the known values in Equation (21), the maximum angle of the slope that the machine can climb is:

$$\beta_{up} = \tan^{-1} \frac{13403 - 2e}{5050.34} \quad (22)$$

The calculation of downhill critical angle is similar to that of uphill. If the whole machine is unstable when going downhill, the chassis frame and header would flip around the drive shaft of the track. When the contact force between the rear wheel and ground is 0, the torque balance equation of the critical state is:

$$G_3 \sin \beta h_1 + G_3 \cos \beta l_1 + G_4 \sin \beta h_2 + G_2 \sin \beta(h_4 - h_5) = G_4 \cos \beta e + G_2 \cos \beta L \quad (23)$$

We can get:

$$\tan \beta = \frac{G_4 e + G_2 L - G_3 l_1}{G_3 h_1 + G_4 h_2 + G_2(h_4 - h_5)} \quad (24)$$

The known parameters are substituted into Equation (24):

$$\beta_d = \tan^{-1} \frac{2e - 1603}{2569.66} \quad (25)$$

2.3.2. The Track Stability Analysis of Uphill and Downhill

The contact area and contact force between the track and ground change a lot when the machine is on the slope compared with that on the flat ground. In order to ensure that the track does not flip, the force at point O_1 needs to be determined first. From the above analysis, it can be seen that the rear wheel is a slave wheel without driving force, and the walking resistance is much smaller than that of the track. The ground support reaction force of the wheel is much larger than the frictional resistance, so the support reaction force of the wheel on the frame is simplified to the force perpendicular to the slope. The stress analysis of the frame is shown in Figure 5.

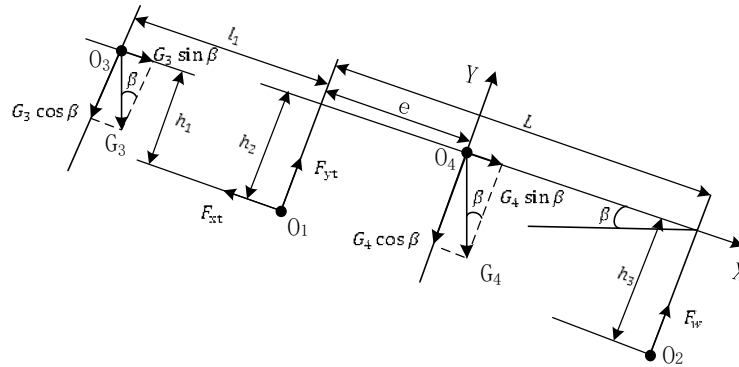


Figure 5. Force schematic of the rape windrower when climbing up.

The moment balance equations are as below:

$$\begin{cases} G_3 \sin \beta + G_4 \sin \beta - F_{xt} = 0 \\ F_{yt} + F_w - G_3 \cos \beta - G_4 \cos \beta = 0 \\ G_3 \sin \beta h_1 + G_4 \sin \beta h_2 + G_4 \cos \beta e - G_3 \cos \beta l_1 - F_w L = 0 \end{cases} \quad (26)$$

where F_{xt} , F_{yt} are forces of track on frame in X and Y direction, N. F_w is the force of rear wheel on frame, N; h_3 is the distance along Y axis between force bearing point of the wheel and the centroid of chassis, mm.

After calculation, F_{xt} and F_{yt} can be expressed as below:

$$F_{xt} = G_3 \sin \beta + G_4 \sin \beta \quad (27)$$

$$F_{yt} = \frac{G_3 \cos \beta (L - l_1) + G_4 \cos \beta (L - e) - G_3 \sin \beta h_1 - G_4 \sin \beta h_2}{L} \quad (28)$$

The force sustained by the track from the chassis frame and its own gravity is shown in Figure 6. The triangular track is subjected to the ground force, the frame reaction force F'_{xt} , F'_{yt} and its own gravity G_t . The track is arranged symmetrically on the left and right sides, and the distance from the center of the driving axle to the center of its gravity point O_5 is h'_2 . When the triangular track reaches the critical flipping position, it contacts the ground only at point Q. Therefore, the requirement that the triangular track does not flip itself is:

$$(F'_{yt} + G_t \cos \beta) l'_1 > F'_{xt} h'_1 + G_t \sin \beta (h'_1 - h'_2) \quad (29)$$

where F'_{xt} and F'_{yt} have equal values but opposite directions with F_{xt} and F_{yt} , l'_1 is the distance from the track driving center to the only contact point of track and ground along X axis, 550 mm; h'_1 is the distance from track driving center to the ground along Y axis, 633 mm; h'_2 is the distance from track driving center to the gravity center along Y axis, 238 mm.

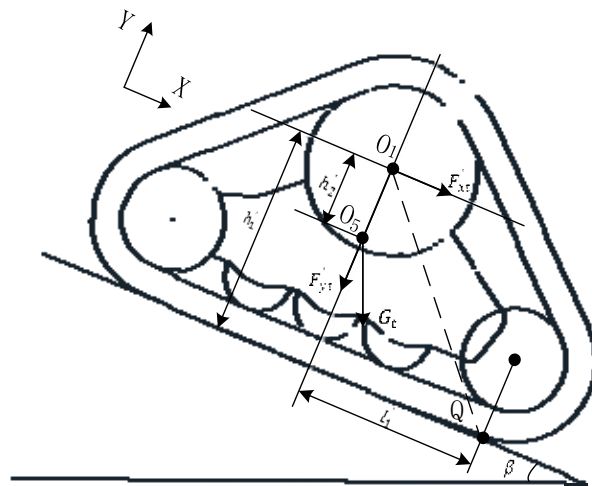


Figure 6. Partial force schematic of the triangular track when climbing up.

According to Equations (27)–(29), an inequality can be derived as below:

$$\tan \beta < \frac{G_3 L l'_1 + G_4 L l'_1 + G_3 l_1 l'_1 + G_t L l'_1 - G_4 l'_1 e}{G_3 h_1 l'_1 + G_4 h_2 l'_1 + (G_3 + G_4) L h'_1 + G_t L (h'_1 - h'_2)} \quad (30)$$

The known parameters are substituted into the above equation:

$$\tan \beta < \frac{13403 - 2e}{14604} \quad (31)$$

When the machine is uphill, the maximum angle that the triangle track can work normally is as below:

$$\beta_{sup} = \tan^{-1} \frac{13403 - 2e}{14604} \quad (32)$$

The analysis method of downhill is similar to that of uphill. The force schematics of the rape windrower going downhill are shown in Figure 7, and the equation is established as follows:

$$\begin{cases} G_3 \sin \beta + G_4 \sin \beta - F_{xt} = 0 \\ F_{yt} + F_w - G_3 \cos \beta - G_4 \cos \beta = 0 \\ G_3 \sin \beta h_1 + G_3 \cos \beta l_1 + G_4 \sin \beta h_2 - G_4 \cos \beta e + F_w L = 0 \end{cases} \quad (33)$$

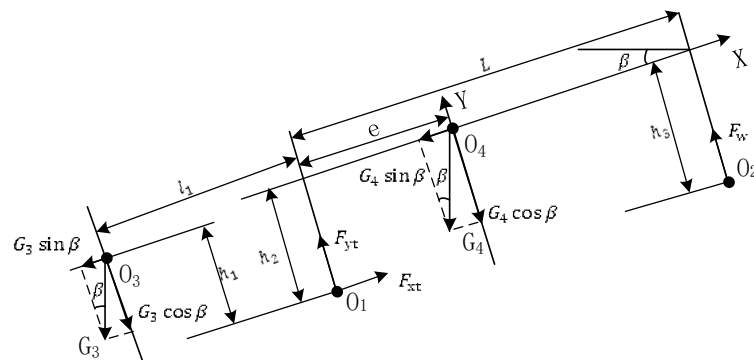


Figure 7. Force schematics of the rape windrower when driving down the slope.

Results obtained by calculation as follows:

$$F_{xt} = G_3 \sin \beta + G_4 \sin \beta \quad (34)$$

$$F_{yt} = \frac{G_3 \cos \beta(L + l_1) + G_4 \cos \beta(L - e) + G_3 \sin \beta h_1 + G_4 \sin \beta h_2}{L} \tag{35}$$

The requirement that triangle track does not flip 360° when it is downhill is the same as uphill:

$$(F'_{yt} + G_t \cos \beta)l'_1 > F'_{xt}h'_1 + G_t \sin \beta(h'_1 - h'_2) \tag{36}$$

So, the critical angle is:

$$\tan \beta < \frac{G_3(L + l_1)l'_1 + G_4(L - e)l'_1 + G_t l'_1 L}{G_3 L h'_1 + G_4 L h'_1 + G L (h'_1 - h'_2) - G_3 h_1 l'_1 - G_4 h_2 l'_1} \tag{37}$$

The known parameters are substituted by values, then Equation (37) can be simplified to the following:

$$\tan \beta < \frac{13403 - 2e}{9496} \tag{38}$$

When the machine is downhill, the maximum angle where the triangle track does not flip 360° is:

$$\beta_{sd} = \tan^{-1} \frac{13403 - 2e}{9496} \tag{39}$$

From Equations (22), (25), (32) and (39), the relationship between the critical angle of the uphill and downhill slope of the machine and the eccentricity of the chassis is shown in Figure 8. The critical angle of uphill and downhill decreases with the increase of chassis frame eccentricity; the critical angle of the triangular track downhill decreases and that of uphill increases. In Figure 8, the vertical coordinate of point A is 20°, which is the minimum angle of uphill and downhill that the machine should satisfy, and the corresponding horizontal coordinate is 1269 mm, which is the minimum eccentricity for the chassis. With the increase of eccentricity, the limit angle of uphill and downhill of the whole machine gradually increases, and the angle of uphill gradually decreases after reaching point B. The eccentricity of the horizontal coordinate corresponding to point B is 1684.3 mm, and the vertical coordinate is 34.5°, which is the maximum angle uphill and downhill of the whole machine.

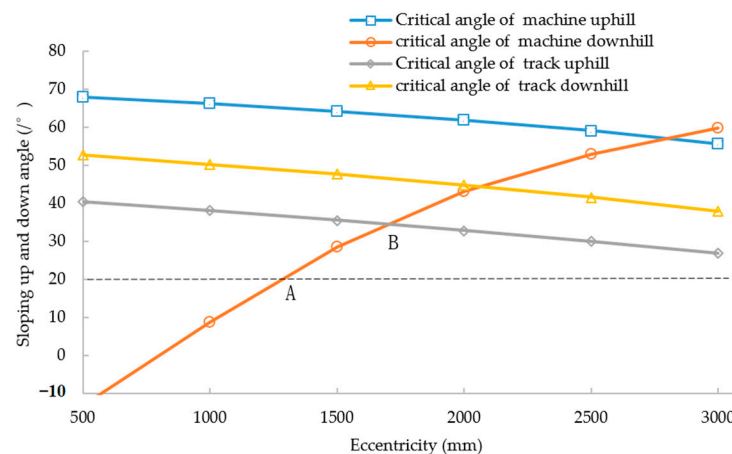


Figure 8. The maximum angle uphill and downhill.

2.4. Performance Analysis of Ridge Crossing

There are great differences between a wheel-track chassis, a four-wheel chassis and a double-track chassis. The schematic of a triangle track crossing ridge is shown in Figure 9. It mainly experiences the following four stages when crossing the ridge [23].

In the first stage, the track contacts the steps, and the triangular track rotates clockwise around the center of the rotation axis; the whole machine also rotates clockwise besides moving forward. If one track and one tire are selected as the research objects, in this

process, the contact between the machine and ground changes from one point (contact point between wheel and ground) and one face (face and face contact between the track and ground) to two lines and one point, namely lines A and B in Figure 9 and the contact point between wheel and ground.

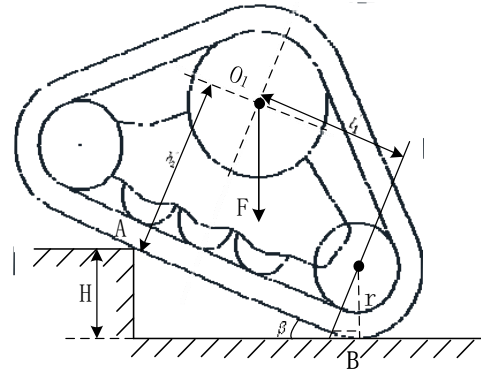


Figure 9. Schematic of triangular track crossing the ridge.

The second stage is the obstacle crossing process where the machinery continues to move forward. The rotation angle of the triangular track increases until the counterclockwise torque is generated around O_1 by the force exerted on the triangular track at point A, then the contact force at point B gradually decreases to 0. In this process, the relationship between the machine and ground changes from a three-point contact to two-point contact.

The third stage is the completion stage of track obstacle crossing. In this process, the track gradually ascends and rotates counterclockwise around point O_1 until it fully contacts the ridge. The relationship between machine and ground changes from two-point contact to point-surface contact.

The fourth stage is the completion stage of the whole machine obstacle crossing. As the machine continues to move forward, the wheels make contact with the ridge and cross to complete the whole process of an over-obstacle.

It is necessary to ensure that the triangular track does not flip itself when the machine crosses the ridge completely, and the height of the obstacle is less than the radius of the rear wheel. Therefore, the following conditions should be satisfied between the ridge height and the triangular track parameters:

$$\begin{cases} H = (l'_1 - h'_2 \tan \beta) \sin \beta + (r' - r' \cos \beta) \\ H < h_5 \end{cases} \quad (40)$$

In the formula, H is the height of an obstacle that the machine can cross, mm; r' is the distance from the center of guiding wheel to ground, 245 mm; β is the angle between the track and ground.

According to Equation (32), we can see the angle range at which the track does not flip 360° when uphill. According to Equation (40), the maximum height of the obstacle can be obtained. It is also known that the maximum height of the obstacle which the machine can cross is related to the mechanism parameters and eccentricity of the chassis. When the chassis structure parameters are determined, the relationship between the maximum obstacle height and eccentricity is as follows:

$$\begin{cases} \tan \beta = \frac{13403 - 2e}{14604} \\ H_{max} = (550 - 238 \tan \beta) \sqrt{\frac{\tan^2 \beta}{1 + \tan^2 \beta}} + 245 \left(1 - \sqrt{\frac{1}{1 + \tan^2 \beta}} \right) \end{cases} \quad (41)$$

When the eccentricity increases, the critical angle of flipping 360° of the triangle track decreases, and the obstacle height decreases.

2.5. Analysis of Turning Performance

When the machine turns, it should avoid additional resistance with the ground and require the wheel (track) to roll purely without sliding, so the turning movement process conforms to Ackermann steering geometry and the axes of all wheels intersect at the center of rotation [24]. When the machine turns, rear wheels are active steering, one of them is deflected by index cylinder, and the other one is deflected by four-bar linkage, while the front tracks steer by differential. Taking the right turning as an example, the turning plane is shown in Figure 10.

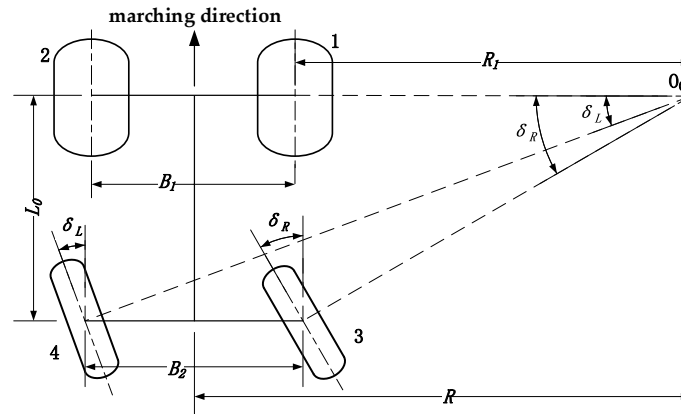


Figure 10. Diagram of turning.

According to the geometric relationship:

$$\begin{cases} L = \left(R - \frac{B_1}{2} \right) \tan \delta_R \\ L = \left(R + \frac{B_2}{2} \right) \tan \delta_L \end{cases} \quad (42)$$

where R is turn radius, distance from turning center point to chassis center line, m; B_1 is the distance of two tracks, m; B_2 is the distance of two rear wheels, m; δ_L is the left back steer angle, rad; δ_R is the right back steer angle, rad.

In order to satisfy the above equations, the turn angles δ_L and δ_R of the outer and inner wheels should meet the following requirements:

$$\delta_R = \cot^{-1} \left(\cot \delta_L - \frac{B_2}{L} \right) \quad (43)$$

When steering, any point of the machine rotates around point O_0 , and if the windrower steering angular velocity is named ω , the speed of the two tracks and two wheels are as follows:

$$\begin{cases} v_1 = \omega \left(R - \frac{B_1}{2} \right) \\ v_2 = \omega \left(R + \frac{B_1}{2} \right) \\ v_3 = \omega \left(\frac{R - \frac{B_2}{2}}{\cos \delta_R} \right) \\ v_4 = \omega \left(\frac{R + \frac{B_2}{2}}{\cos \delta_L} \right) \end{cases} \quad (44)$$

where v_1, v_2, v_3, v_4 are speeds of wheels and tracks, B_1 is the distance of two tracks.

Therefore, the speed relationship of the left and right tracks is:

$$\frac{v_1}{v_2} = \frac{R_1}{R_1 + B_1} \quad (45)$$

The geometric relationship in Figure 10 shows:

$$R_1 = L \cot \delta_R + \frac{B_2 - B_1}{2} \quad (46)$$

Put Equation (46) into Equation (45), and the speed ratio of two tracks can be obtained as:

$$\frac{v_1}{v_2} = \frac{2L \cot \delta_R + B_2 - B_1}{2L \cot \delta_R + B_2 + B_1} \quad (47)$$

The theoretical turn radius is:

$$R = L \cot \delta_R + \frac{B_2}{2} \quad (48)$$

Equation (48) shows that the theoretical turn radius is related to the steering angle and the center distance between two rear wheels. The larger the turn angle is, the smaller the turning radius becomes. Putting known values $L = 2950$ mm, $\delta_R = 35^\circ$, $B_2 = 2646$ mm into Equation (48), the minimum turn radius 5537.28 mm can be gained.

2.6. Kinematics Simulation and Analysis

2.6.1. Creation of Simulation Model

A three-dimensional solid model is created based on Pro/E software, and the model is exported in Parasolid (*.x-t) format. Then, the model is imported into software RecurDyn, maintaining the assembly relationship and simplifying the solid model [25–29]. As the model is simplified, the weight of the machine is quite different from the actual weight, so it is reset according to the actual weight of the machine [30].

The front triangle track is built in Track (LM) module of RecurDyn, the wheel model is built in Tire module, and the constraints and traction between components are built [31,32]. The track system is connected with the frame by rotating join. The track drives the movement of each link through the rotation of the driving wheel to pull the machine forward. The modeling is shown in Figure 11. The driving function of two tracks is: step (time, 0, 0, 1.5, −3.32), which means that the speed of the driving wheel increases from 0 to 3.32 rad/s in the period of 0~1.5 s.

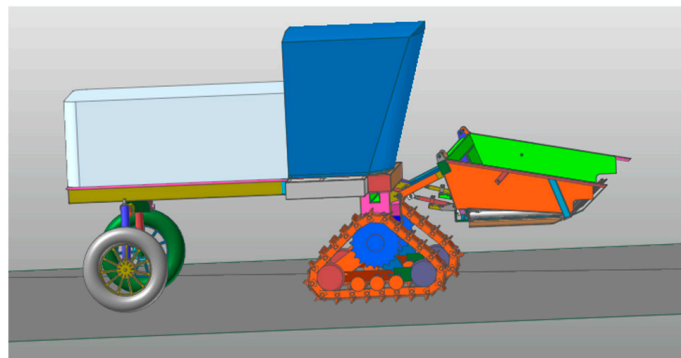


Figure 11. Three-dimensional model of a rape windrower.

2.6.2. Simulation Analysis of Walking on Flat Ground

Clay soil model is selected as track contact soil. With the increase of eccentricity, the ability of crossing ridge is reduced. Therefore, the eccentricity is set based on the points A and B in Figure 8. Simulations are operated at 100 mm increments from 1184 mm to 1784 mm. A single factor simulation test is carried out with test indexes of walking speed and driving torque. The simulation time is set as 15 s and the number of steps is set as 100. The simulation results of the walking speed and the driving torque of a single track when the chassis eccentricity is 1184 mm, 1484 mm and 1784 mm are shown in Figures 12 and 13.

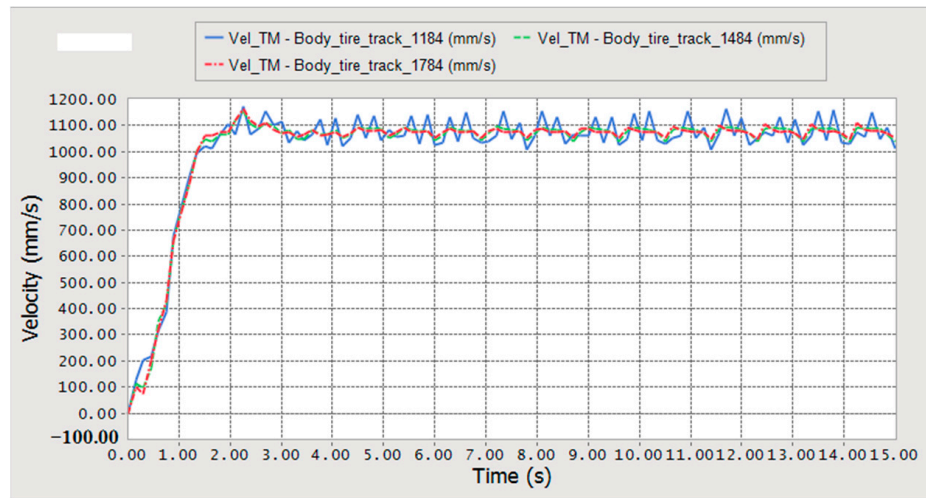


Figure 12. Walking speed with different eccentricities.

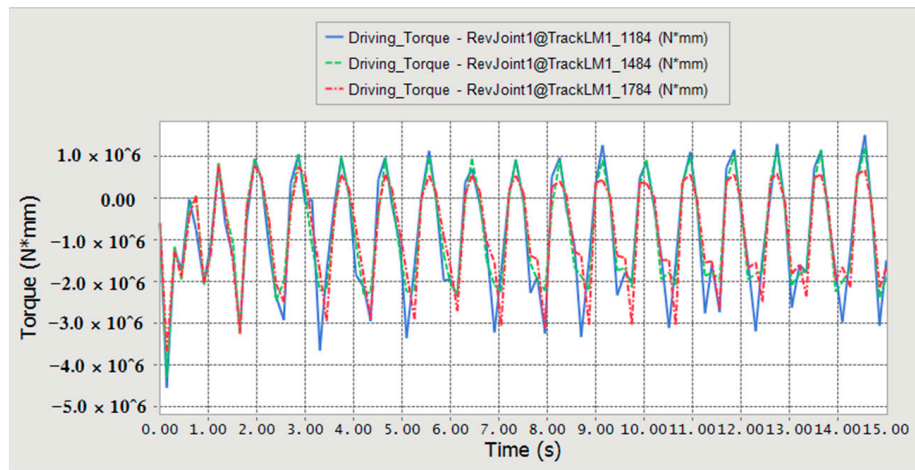


Figure 13. Driving torque with different eccentricities.

In Figures 12 and 13, the blue curves are velocity–time curve and torque–time curve at eccentricity of 1184 mm, the green curves are velocity–time curve and torque–time curve at eccentricity of 1484 mm, and the red curves are velocity–time curve and torque–time curve at eccentricity of 1784 mm. It can be seen that with the increase of eccentricity, the smoother the velocity and torque become.

When the system is stable, the average speed and average driving torque of the simulation during 3~14 s are selected. The average speed is calculated as follows:

$$\bar{v} = \frac{1}{n} \sum_{i=1}^n v_i \tag{49}$$

where \bar{v} is the average speed, mm/s; v_i is instantaneous speed of each sampling point, mm/s; n is the number of sampling points.

The relationship between eccentricity and average speed and average driving torque is shown in Figure 14.

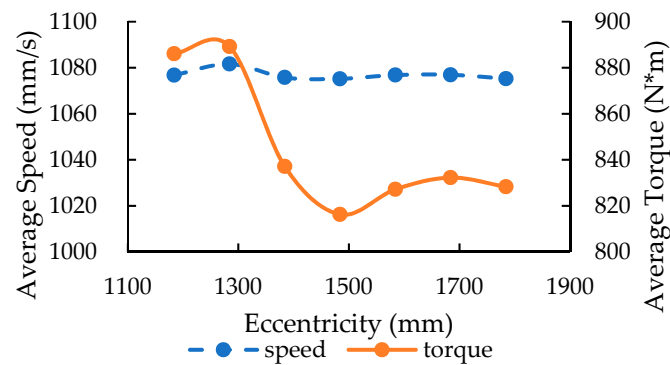


Figure 14. Relationship between speed, torque and eccentricity.

With the increase of eccentricity, the average speed of the machine changes very little. When the eccentricity is 1284 mm, the maximum speed is 1081.6 mm/s. The average driving torque decreases first and then increases slowly with the increase of eccentricity. When the eccentricity is 1484 mm, the minimum driving torque of a single track is 816.26 N·m. Inserting this value of eccentricity into Equations (2) and (19), the theoretical driving resistance of the track is 5789 N. As the diameter of the driving wheel is 577 mm, the theoretical driving torque of a single track is 835.1 N·m. The internal friction of the machine is not considered in the simulation, so the value of simulation is smaller than that of the theoretical calculation, which verifies the correctness of the theoretical calculation.

Average speed and torque reflect the performance of the machine in a period of time. Regular vibration occurs when the track links make contact with the ground, so the instantaneous speed and torque have large differences, and coefficient variation (CV) can be used to judge the instantaneous stability which is calculated in Formulas (50) and (51).

$$S = \sqrt{\frac{1}{n-1} \sum_{i=1}^n (v_i - \bar{v})^2} \tag{50}$$

where S is speed standard deviation.

$$C_V = \frac{S}{\bar{v}} \times 100\% \tag{51}$$

where C_V is coefficient variation of speed.

The calculation method of torque coefficient variation is the same as that of the speed coefficient variation.

The relationship between the coefficient variation of speed and torque and eccentricity is shown in Figure 15. The coefficient variation of speed decreases with the increase of eccentricity, and the stability becomes better and better. When the eccentricity is less than 1384 mm, the coefficient variation of speed varies significantly with the eccentricity. When the eccentricity is over 1384 mm, the change is slow and tends to be stable. The coefficient variation of driving torque decreases first and then increases with the increase of eccentricity. When the eccentricity is 1584 mm, the smallest coefficient variation is obtained, so the stability is the best.

The mechanical analysis shows that the eccentricity has a great influence on the driving resistance, stability, climbing performance and obstacle crossing ability of the machine. The simulation analysis of the machine walking in sticky soil shows that the eccentricity has little influence on the average walking speed, but has great influence on the speed stability, average driving torque and driving torque stability. When the values of eccentricity are 1484 mm and 1584 mm, the value of minimum driving torque is 816.26 N·m and its coefficient variation is 140.99%.

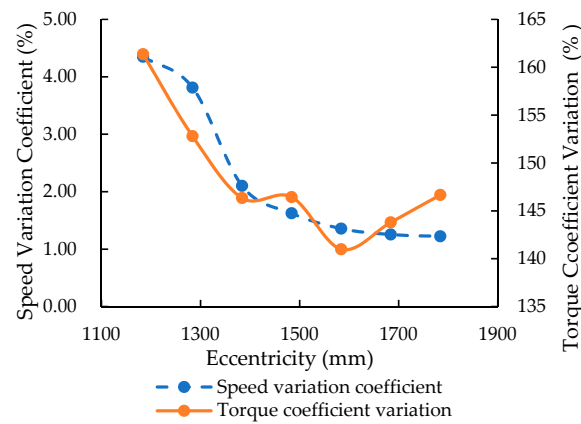


Figure 15. Relationship between speed variation coefficient, torque variation coefficient and eccentricity.

According to the analysis of Section 2.3.2, when the uphill and downhill angle of the machine meets the design requirement of 20° , the eccentricity should be greater than 1269 mm. The maximum uphill and downhill angle can be obtained when the eccentricity is 1684.3 mm. In summary, taking driving torque as the main reference, and considering other indicators, the eccentricity is selected as 1500 mm. Therefore, the working parts can be arranged according to this eccentricity.

2.6.3. Simulation of Uphill and Downhill

The simulation of uphill and downhill is carried out with the eccentricity of 1500 mm, as in Figures 16 and 17. The normal uphill and downhill states are shown in Figures 16A and 17A. The instability state of uphill and downhill is shown in Figures 16B and 17B. When the machine is uphill, the triangle track is unstable first, and the track flips around the driving axle. When the machine is downhill, the chassis frame flips around the driving axle first, which is consistent with the theoretical calculation results and verifies the correctness of the theoretical calculation.

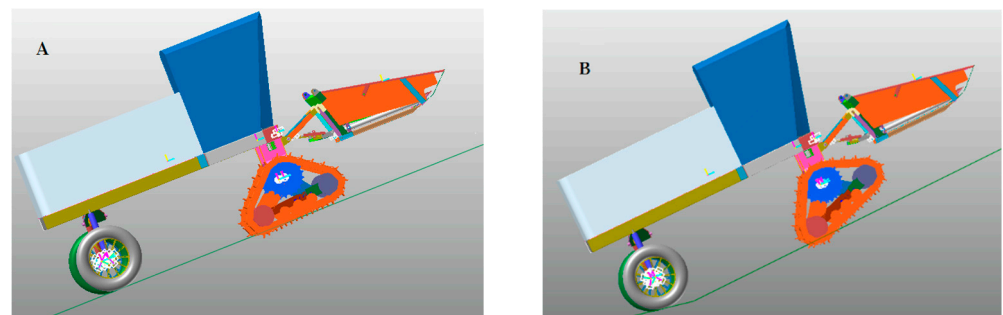


Figure 16. Uphill simulation. (A) Stable uphill state; (B) Unstable uphill state.

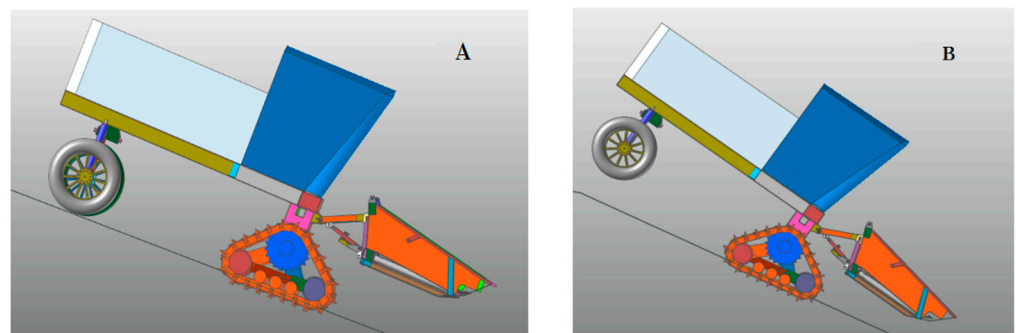


Figure 17. Downhill simulation. (A) Stable downhill state; (B) Unstable downhill state.

The simulation shows that the maximum climbing angle of the machine is 28° , which is about 8.5° smaller than the theoretical calculation value. When the track is uphill, the combined force direction of the track deviates greatly from the track center line, which leads to the uneven distribution of the pressure between the track and the ground. The pressure on the latter part of the track is significantly higher than that on the front part. Therefore, the subsidence depth is not uniform, as shown in Figure 16B. The flipping of the track is not only affected by the slope angle, but also by the different subsidence depths of the track; at the same time, the vibration in the movement process also affects the stability, so the simulation angle is smaller than the theoretical calculation value.

The maximum downhill angle of the simulation is 26° , which is about 2.5° smaller than the theoretical calculation value. It can be seen from Figure 17B that even if the whole machine flips, the subsidence depth of the whole track does not change much, so the triangle track is relatively stable. The deviation between the simulation value and theoretical value is mainly affected by vibration factors in movement.

3. Test Results and Discussion

3.1. Walking Performance

In order to test the walking performance of the wheel-track high clearance chassis of this rape windrower, experiments were carried out on hard flat road and rice stubble field, as shown in Figures 18 and 19. The rice stubble field was located in Comprehensive Demonstration Base of Rice and Wheat Science and Technology in Taizhou, Jiangsu, China. It was a rice stubble field after full straw returning. Soil physical parameters were as follows: moisture content was 38.7%, average soil hardness at 15 cm depth was 1233.4 kPa, average soil hardness at 30 cm depth was 1654.8 kPa, and the stubble height of rice was less than 10 cm.



Figure 18. Running on the flat hard ground.



Figure 19. Running on rice stubble field.

First, the driver increased the speed to the top value of the corresponding gear position in the preparatory area. Then, the machine passed through the 20 m test area at a uniform speed, and the passing time was recorded. This process was repeated three times. The three 20 m passing times on hard flat ground of walking gear were 3.61 s, 3.48 s and 3.59 s; the average speed was 20.22 km/h. The three 20 m passing times of working gear on rice stubble field were 7.71 s, 7.56 s and 8.40 s and the average speed was 9.12 km/h, which satisfied the design index.

3.2. Climbing Test

The climbing performance test was carried out on the ground shown in Figure 20. Two steel plate tracks with a length of 6 m and a width of 0.8 m and four supporting legs were used to build the ramp. The large slope angle adjustment was realized by changing the supporting legs at different heights. The slope fine-tuning was implemented by changing the installation position of legs. In order to avoid danger, a limit block was installed on the side of the triangular track to prevent security accidents caused by automatic flipping of the track during climbing.



Figure 20. Climbing test.

In the experiment, the machine could climb up the 20° slope with a slow speed, and the design performance of the machine was satisfied.

3.3. Turning Radius Test

Turning tests were conducted on the flat hard road and rice stubble field respectively. According to the minimum turning radius measurement method of GB/T3871.5-93 *Test methods for agricultural wheeled and tracklaying tractors*, the machine was driven at a low and uniform speed; at the same time, the steering wheel was respectively turned to the left or right limit positions. The machine drove out of the experiment block after it finished a whole circle path. Then, the turning radius of the inner track of the machine was measured. The experiments on two fields were both conducted three times; the results are shown in Table 2.

Table 2. Turning radius of inner track.

Serial Number		1/mm	2/mm	3/mm	Average Value/mm
Flat and hard road	Left-turn	4950	4880	4890	4906.7
	Right-turn	4960	4900	4900	4920
Rice stubble field	Left-turn	5450	5440	5440	5443.3
	Right-turn	5460	5450	5450	5453.3

The minimum turning radius of the machine was $R_{min} = R_a + 0.5B_1$, where R_a is the radius of inner track, mm; B_1 is the track gauge, 2090 mm.

Therefore, the minimum turning radius of the machine on flat hard road was 5.965 m, and the minimum turning radius on rice stubble field was 6.498 m.

In the theoretical calculation, it is assumed that the four wheels (tracks) are pure rolling without transverse or longitudinal slip. However, in fact, when the machine turns, the direction is controlled by the rear wheel, the front tracks were in a passive differential steering motion, and the slip phenomenon is inevitable. Therefore, the experimental radius is greater than the theoretical one. When the ground condition becomes worse, the resistance becomes larger, thus the effect of differential steering is poor, and a larger turning radius is acquired when running on rice stubble field than on flat hard ground.

4. Conclusions

- (1) The mechanism and working principle of the wheel-track high clearance chassis of rape windrower were introduced, and the models of mathematical relations between the walking performance, stability performance and the eccentricity of the chassis frame were built.
- (2) Three-dimensional model and dynamic simulations of a wheel-track high clearance rape windrower were conducted using Pro/E and RecurDyn software. When the machine was driven at the same speed, the walking speed changed little with the increase of eccentricity, and the coefficient variation of speed decreased gradually. The average driving torque and the coefficient variation decreased first and then increased. Minimum driving torque and the coefficient variation were obtained when the eccentricities were 1484 mm and 1584 mm. The chassis frame eccentricity was defined as 1500 mm, according to the theoretical calculation and simulation analysis. The maximum angle of uphill and downhill was 28° and the maximum height of the crossing ridge was 266.15 mm.
- (3) The performance experiments of wheel-track high clearance rape windrower in flat hard ground and rice stubble field were carried out. The test showed that the speed running on flat hard road was 0~20.22 km/h and the minimum turning radius was 5.965 m; the working speed in rice stubble field was 0~9.12 km/h and the minimum turning radius was 6.498 m. The machine could steadily climb the slope of 20°.
- (4) A new kind of wheel-track high clearance chassis was developed, which could hang on the swath header over than 3.5 m wide. All parameters of the chassis met the design requirements, and the work efficiency increased over 100% compared with the existing two-tracked rape windrower. This provided another kind of equipment for rapeseed harvesting in the Yangtze River Basin.

Author Contributions: Conceptualization, M.J. and M.Z.; methodology, C.W. and R.H.; software, G.W.; validation, S.L.; formal analysis, M.J.; investigation, M.J., M.Z. and S.L.; resources, C.W.; data curation, M.J.; writing—original draft preparation, M.J.; writing—review and editing, M.J.; visualization, R.H.; supervision, R.H.; project administration, M.Z.; funding acquisition, S.L. All authors have read and agreed to the published version of the manuscript.

Funding: This research was funded by Key Research Program & Technology Innovation Program of Chinese Academy of Agricultural Sciences (CAAS-ZDRW202105), and China Agriculture Research System of MOF and MARA (CARS-12).

Data Availability Statement: Data are available.

Acknowledgments: The authors thank the editor and anonymous reviewers for providing helpful suggestions for improving the quality of this manuscript.

Conflicts of Interest: The authors declare no conflict of interest.

References

1. Shi, Z.; Wu, M.; Yang, W. Research status and development measures of rape segment harvester in China. *Agric. Eng.* **2015**, *5*, 1–4.
2. Li, P. Experimental Study and Working Mechanism of Key Parts for Rape Windrower for 4SY 1.8. Ph.D. Thesis, Huazhong agricultural university, Wuhan, China, 2014.

3. Jin, C.; Yang, T.; Liu, G. Design and Test of Posture Controlled Chassis for Caterpillar Combine. *Trans. Chin. Soc. Agric. Mach.* **2020**, *51*, 393–402.
4. Hu, K.; Zhang, W.; Li, K. Multi-body dynamics modeling and experiment of triangular tracked chassis with high ground clearance. *Trans. Chin. Soc. Agric. Mach.* **2021**, *52*, 386–394.
5. Zhou, J.; Cheng, X.; Li, H. Research and development on the wheel electric rape harvester. *J. Agric. Mech. Res.* **2012**, *34*, 80–85.
6. Zhu, Y.; Fei, Y.; Xu, H. Analysis for obstacle negotiation of a wheel-track-leg hybrid mobile robot machine design and research. *Mach. Des. Res.* **2017**, *33*, 28–32.
7. Shuai, L.; Su, H.; Zhen, L. Study on steering movement of track-wheel mobile robot. *J. Harbin Eng. Univ.* **2017**, *38*, 1630–1634.
8. Zhang, S.; Yao, J.; Xu, Y. Design and analysis of moving mechanism of shape reconfigurable mobile robot. *Trans. Chin. Soc. Agric. Mach.* **2019**, *50*, 418–426.
9. Guo, T. Power consumption of tracked and wheeled small mobile robots on deformable terrains—model and experimental validation. *Mech. Mach. Theory* **2019**, *133*, 347–364. [[CrossRef](#)]
10. Jun, L.; Andrew, A.G. Development of a terrain adaptive tracked vehicle and its derivative-dual mode vehicle. In Proceedings of the 1st WRC Symposium on Advanced Robotics and Automation, Beijing, China, 16 August 2018.
11. Zang, L.; Yang, S.; Wu, C. Design and kinematics analysis of coordinated variable wheel-track walking mechanism. *Int. J. Adv. Robot. Syst.* **2020**, *17*, 1–12. [[CrossRef](#)]
12. Bai, Y. Design and Test on Delta Tracks Chassis of Chopper Sugarcane Harvester. Master's Thesis, South China Agricultural University, Guangzhou, China, 2014.
13. Cai, G. The Design and Mechanical Analysis of Oil Camellia Fruit Picking Machine's Rubber Track System Chassis. Ph.D. Thesis, Central South University of Forestry and Technology, Changsha, China, 2014.
14. Wang, F. Study on Slope Passability of the Orchard Power Chassis in Hilly Area. Master's Thesis, Southwest University, Chongqing, China, 2020.
15. Zeng, S.; Liu, J.; Luo, X. Design and experiment of wheel-track compound power chassis for high clearance sprayer in paddy field. *J. South China Agric. Univ.* **2019**, *40*, 14–22.
16. Hao, Z.; Yang, X.; Liu, L. Design and experiment of multifunctional dynamic chassis for orchard. *Trans. Chin. Soc. Agric. Mach.* **2018**, *49*, 66–73+92.
17. Pan, G.; Yang, F.; Sun, J. Analysis and test of obstacle negotiation performance of small hillside crawler tractor during climbing process. *Trans. Chin. Soc. Agric. Mach.* **2020**, *51*, 374–383.
18. Feng, Y. *Tank and Armored Vehicle Design*; Chemical Industry Press: Beijing, China, 2015; pp. 31–72.
19. Ge, J.; Zhang, D.; Wang, X.; Cao, C.; Fang, L.; Duan, L. Tractive performances of single grouser shoe affected by different soils with varied moisture contents. *Adv. Mech. Eng.* **2019**, *11*, 1–11. [[CrossRef](#)]
20. Yao, H.; Chen, B. *Engineering Machinery Chassis Theory*; China Communications Press: Beijing, China, 2001; pp. 15–70.
21. Deng, Z.; Ding, L.; Gao, H. Influence of soil properties on lunar rover's wheel-oil interaction mechanics. *J. Harbin Inst. Technol.* **2010**, *42*, 1724–1729.
22. Zhao, J.; Wang, F.; Yu, B. Research on All-terrain profiling crawler power chassis. *Trans. Chin. Soc. Agric. Mach.* **2014**, *45*, 20–24.
23. Zhu, Y.; Sang, Y.; Hu, M. Design and stability analysis of sprayer with adjustable height gap. *J. Agric. Mech. Res.* **2020**, *42*, 68–73.
24. Xu, C.; Chen, Y.; Li, R. Design and research on Highland gap self-propelled lance spray. *J. Chin. Agric. Mech.* **2016**, *37*, 51–54.
25. Wang, H.; Wang, Q.; Rui, Q. Analyzing and testing verification the performance about high-speed tracked vehicles in steering process. *J. Mech. Eng.* **2014**, *50*, 162–172. [[CrossRef](#)]
26. Jiao, X.; Zhang, J.; Peng, B. *Recurdyn Multibody Systems Optimization Simulation Technology*; Tsinghua University Press: Beijing, China, 2010; pp. 62–101.
27. Liu, Y.; Zhang, T.; Xie, N. Multi-body dynamic modeling and verification of small agricultural crawler chassis. *Trans. Chin. Soc. Agric. Eng.* **2019**, *3*, 39–46.
28. Chen, J.; Huang, R.; Mo, R. Analysis and simulation of obstacle crossing performance of tracked chassis of small hedge trimmer based on RecurDyn. *J. Chin. Agric. Mech.* **2020**, *41*, 89–98.
29. Ma, P.; Liu, Y.; Shi, C. Dynamics analysis and simulation of variant wheel-track wheel based on RecurDyn. *J. Mil. Transp. Univ.* **2017**, *19*, 35–39.
30. Jiang, Q.; Ni, W.; Zhang, X.; Chen, P.; Yang, Y. Evaluation of tractor driving comfort according to the steering angle and speed using a virtual prototype. *Proc. Inst. Mech. Eng. Part D J. Automob. Eng.* **2021**, *235*, 50–61. [[CrossRef](#)]
31. Zhao, J.; Wang, W.; Sun, Z. Improvement and verification of pressure-sinkage model in homogeneous soil. *Trans. Chin. Soc. Agric. Eng.* **2016**, *32*, 60–66.
32. Yao, Y. Research on the trafficability of low-seed tracked vehicle based on track-soil coupling system. Ph.D. Thesis, Jilin University, Changchun, China, 2016.

Article

Numerical Simulation and Verification of Seed-Filling Performance of Single-Bud Billet Sugarcane Seed-Metering Device Based on EDEM

Meimei Wang ¹, Qingting Liu ^{2,*}, Yinggang Ou ² and Xiaoping Zou ²

¹ School of Mechanical Engineering, Anyang Institute of Technology, Anyang 455000, China; 20160297@ayit.edu.cn

² Key Laboratory of Key Technology on Agricultural Machine and Equipment, Ministry of Education, South China Agricultural University, Guangzhou 510642, China; ouying@scau.edu.cn (Y.O.); 13416229168@126.com (X.Z.)

* Correspondence: qingting@scau.edu.cn

Abstract: The seed filling of a seed-metering device is a critical process in sugarcane cultivation operations. To analyze the contact between billets, the related mechanical components, and the law of billets movement in the seed-metering device, a simulation of the seed-filling process based on EDEM was proposed, and a geometric model of the seed-metering device, a particle model, and a contact model were established by EDEM software. The physical experimental results and simulation results of the angle of repose were compared. The experimental results showed that the relative error of the angle of repose experiment was 6.67%, which verified the effectiveness of the material parameters of single-bud billet; the linear correlation coefficient of the seed-filling experiment was 0.762 for S_q and 0.869 for S_e , which demonstrated the validity of using EDEM software to simulate the seed-filling process. Finally, the velocity and force of the particles in the seed-filling process were analyzed in EDEM. The analysis results indicated that there are two circulation circles in the seed box, and the larger the circulation circle, the easier the billets enter the rake bar. The EDEM simulation provides a basis for optimizing the structure and parameters of the sugarcane billet planter in future work.

Keywords: numerical simulation; seed-filling; single-bud billet; seed-metering; EDEM

Citation: Wang, M.; Liu, Q.; Ou, Y.; Zou, X. Numerical Simulation and Verification of Seed-Filling Performance of Single-Bud Billet Sugarcane Seed-Metering Device Based on EDEM. *Agriculture* **2022**, *12*, 983. <https://doi.org/10.3390/agriculture12070983>

Academic Editors: Muhammad Sultan, Redmond R. Shamshiri, Md Shamim Ahamed and Muhammad Farooq

Received: 2 June 2022

Accepted: 29 June 2022

Published: 7 July 2022

Publisher's Note: MDPI stays neutral with regard to jurisdictional claims in published maps and institutional affiliations.



Copyright: © 2022 by the authors. Licensee MDPI, Basel, Switzerland. This article is an open access article distributed under the terms and conditions of the Creative Commons Attribution (CC BY) license (<https://creativecommons.org/licenses/by/4.0/>).

1. Introduction

Sugarcane planting is one of the most labor-intensive and time-intensive procedures in sugarcane production. Traditional planting method of whole-stalk planters and real-time cutting planters requires great human force and large number of seed stalks. Therefore, billet planter is increasingly popular in sugarcane cultivation because of its high efficiency and low labor intensity. [1]. The single-bud billet planter discharges single-bud billets from a seed box using rake bars [2]. Seed-filling is critical in the entire seed metering process, whereas the seed-filling uniformity has a direct impact on the seed metering quality of the planter. The seed-filling process is as follows: the billets in the seed box fill the rake bar when the rake bar chain moves, and then the billets move toward the seeding channel inlet because of the gravity, the rake bar driving force, and the billet interaction. The mechanical structure parameters, physical and mechanical properties of billets, and their mutual movement all affect the seed-filling process. The interaction force between billets and the mechanical structure, billet displacement, and velocity are important for designing and optimizing sugarcane billet planter machinery components. The discrete element method (DEM) proposed by P.A. Cundall [3] has become a general method for analyzing the contact between particles and the related mechanical components [4], and the law of seed movement in measurements [5].

Most of the traditional agricultural machinery research methods are based on theoretical analysis and experimental research [6], but the traditional test method is time-consuming, laborious, and subject to seasonal constraints. With the rapid development of computer technology, DEM and its numerical simulation software, EDEM, have been extensively used in the field of agricultural engineering [7,8].

The EDEM simulation software is often adopted to analyze the velocity, force, and other important information about seeds in the working process. Sun et al. [9] obtained the maximum discharging velocity and force of the particles at different helix angles in the drilling process. Yudao et al. [10] used EDEM to simulate the working process of a cottonseed-metering device at various speeds and tilt angles. The trajectories of individual seeds in the seed-metering device were obtained, and the stress variation trend in the grain group was determined as a function of time. Based on the EDEM theory, Miao et al. [11] studied the vibration and seed population distribution of *Pinus sylvestris* var. *Mongolica*. Ghodki et al. [12] simulated the motion of black pepper seeds in a cryo-grinding system in all directions and studied their flow characteristics. Horabik et al. [13] investigated the variation trends of stress radial distribution during seed movement by simulating the distribution of stress components within the bulk of pea seeds in a shallow model silo.

Meanwhile, a plethora of studies conducted EDEM simulation tests to optimize machinery structures. Li et al. [14] simulated the sowing process, established the regression equation for sowing depth, and determined the structural size of the telescopic pipe. Lu et al. [15] studied the movement principles of rice seeds on the vibration plate and optimized the parameters of a vibratory even-seeding device for hybrid rice by using the Hertz-Mindlin non-sliding contact model to simulate the working process of a V-T type vibrating plate. Xu et al. [6] used EDEM to simulate the crushing process of cucumber straw and investigate the optimal crushing process parameters to improve the crushing efficiency and reduce power consumption. He et al. [16] designed a centralized fertilizer ejecting device and analyzed the fertilizer ejecting performance using EDEM to optimize the structural parameters of the fertilizer ejecting wheel. Liu et al. [17] established the simulation model of the fertilizer shunt plate and an evaluation model of the fertilization effect to optimize the structural parameters of the fertilizer shunt plate through EDEM simulation. Liu et al. [18] used EDEM to simulate the nest hole wheel with three different hole structures and then conducted experiments to validate the simulation results.

Based on the previous research on the seed-filling uniformity of sugarcane single-bud billet planter and the physical and mechanical properties of single-bud billets, this study established the particle model of a single-bud billet, the geometric model of a sugarcane seed-metering device, the contact model between the billet and the boundary, and the contact model between billets. With EDEM, the seed-filling process of single-bud billets in the seed-metering device was simulated, and the angle of repose physical experimental result and simulation result were compared to validate the input parameters. Meanwhile, the seed-filling physical experimental result and the simulation result were compared to validate the feasibility of the simulation experiment using EDEM. Finally, the interaction between the billet and rake bar and the movement law of billets in the seed box were investigated in the EDEM software, providing a theoretical basis for future digital planter design.

2. Materials and Methods

2.1. Particle Model of Single-Bud BILLET

The particle model of a single-bud billet in the building module of the EDEM particle model was established as follows. First, the particle model of a single-bud billet is approximated to a cylindrical shape, and the material particle is assembled by three filling spheres according to the radius and length of the billet, as shown in Figure 1. Then, the radius and position coordinates of the filling spheres are calculated based on the billet size. Finally, the particle models of the same shapes with different sizes are randomly generated within a diameter range of 25–30 mm based on the size distribution of single-bud billets.

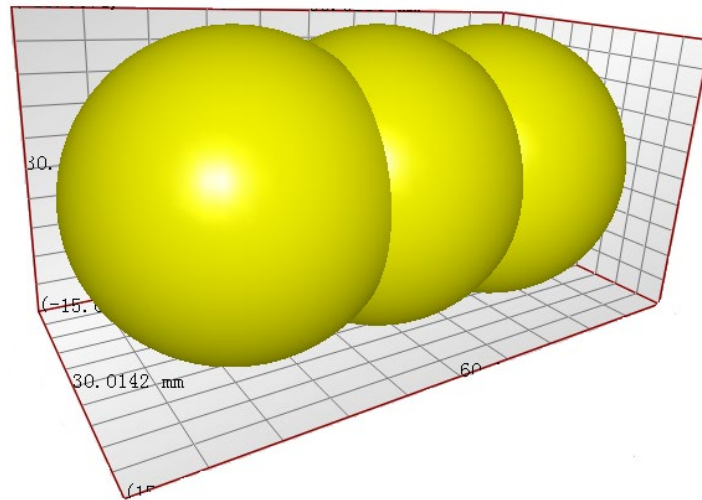


Figure 1. Model diagram of single-bud billet.

The particles were dynamically generated under a normal distribution in the particle plant at a rate of 60 particles per second, with 800 particles for the simulation experiments of the angle of repose and 200 particles for the seed-filling simulation experiment, and the same number of billets was used in physical experiments. It took 4 s for the 200 particles produced to drop completely, and then the rake bar began to move at a uniform linear speed of 0.848 m/s. The total simulation time was 57.6 s. The time step was set to 20% of the Rayleigh time step to ensure the simulation accuracy, and the simulation grid was set to two times of the particle radius to reduce the calculation time.

2.2. Geometric Model of Single-Bud Billet Seed-Metering Device

The three-dimensional model of the single-bud billet seed-metering device was created using the ProE software and then imported into the EDEM software, as shown in Figure 2. Because only the seed-filling process was studied in the simulation experiments, the geometric model was simplified to include only the seed box, rake bar chain, and rake bar in the simulation environment, thus reducing the calculation amount in the simulation process. The rake bar chain in the seed box drives the rake bar to expel the single-bud billet from the billet population in the seed box. The material of seed-metering device is steel.

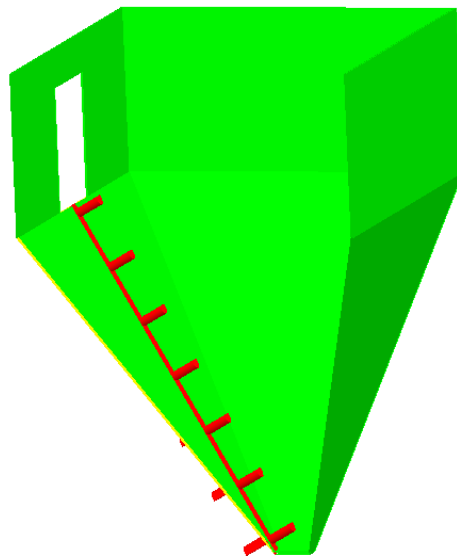


Figure 2. Model diagram of seed-metering device.

The linear speed of the rake bar moving in a straight line along the seed box can be calculated with the rotational speed n and radius R of the driving wheel of the rake bar chain. The calculation formula is as follows:

$$V = 2\pi \cdot R \cdot n \quad (1)$$

In the simulation and physical experiment of the seed-filling process, the rotational speed of the driving wheel of the rake bar chain was set to 90 rpm, and the corresponding linear speed of the rake bar is 0.848 m/s.

2.3. Contact Model and Parameters Setting

In EDEM, the Hertz-Mindlin (no-slip) contact model was adopted for particle-particle and particle-boundary (including the rake bar and seed box) to achieve accurate and efficient seed-filling simulation results, and there is no binding effect between billet particles.

The parameter setting of the global variable significantly affects the simulation accuracy of EDEM preprocessing [9]. According to Liu et al. [19], the sugarcane billet particles were set with a Poisson's ratio of 0.344 and a shear modulus of 1.08×10^7 Pa. All the steel geometries in the model were set with a Poisson's ratio of 0.3, a shear modulus of 7.9×10^{10} Pa, and a density of 7850 kg/m^3 [20]. The setting of other physical and contact mechanical property parameters is shown in Table 1. The average values of these parameters were selected based on the test measurement results of the previous study [21].

Table 1. The setting of the material physical and contact mechanical property parameters.

Materials	Parameter	Value
Billet	Poisson's ratio	0.344
	Shear modulus (Pa)	1.08×10^7
	Density (kg/m ³)	244.67
Steel	Poisson's ratio	0.3
	Shear modulus (Pa)	7.9×10^{10}
	Density (kg/m ³)	7850
Billet–billet	Coefficient of restitution	0.668
	Static friction coefficient	0.352
	Rolling friction coefficient	0.026
Billet–steel	Coefficient of restitution	0.572
	Static friction coefficient	0.377
	Rolling friction coefficient	0.039

2.4. Angle of Repose Experiment

The angle of repose is the maximum angle between the surface of the bulk material pile naturally formed on the plane and the horizontal plane [22]. It reflects the macroscopic flow characteristics of the particulate system and is strongly related to inter-particle friction properties [23,24].

The hollow cylinder method was used to determine the static angle of repose of a cohesionless material [25]. The method is convenient and simple, and it has been widely used [26–29]. The variety of sugarcane billet used in this paper was Tai Tang F66. The selected billets were poured into the bottomless stainless-steel cylinder with a diameter of 40 cm and a length of 120 cm on the horizontal plane, and the billet surface was kept flat. Then, the cylinder was lifted to a certain distance at a speed of 33 mm/s, and the billets in the cylinder would completely overflow under gravity until a static condition was reached. The angle of repose was calculated by measuring the radius and height of the pile. In the experiment, each group of tests was repeated three times.

The simulation test procedure was similar to the physical test procedure. The factory was located at the top of the cylinder, and the generated particles fell under gravity. The

cylinder was raised at a speed of 33 mm/s, and then the billet particles began to flow, forming a static billet pile. The angle measurement tool “protractor” and the slicing tool in the EDEM software were used to measure the angle of repose, and the slice orientation was set in the X-direction with a slice depth of 50 mm and close to the center, as shown in Figure 3.

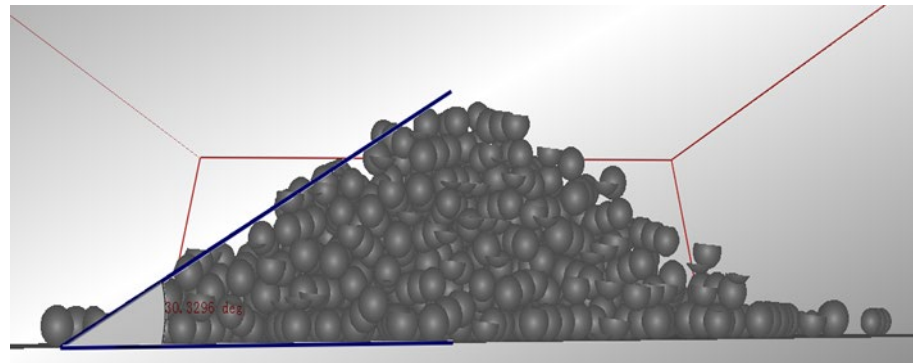


Figure 3. Generation of single-bud billets model’s pile for simulation.

2.5. Seed-Filling Experiment

Figure 4 shows the physical seed-filling experiment setup for seed-metering device. The details of seed-metering device design in the reference [2]. During the experiments, a hydraulic motor drove the rake bar chain using the driving wheels, and the billets were driven by the rake bar to move along the wall of the seed box. The sugarcane billets filled the rake bar and moved toward the inlet of the seeding channel. The lateral plate of the seed box was removed to better observe the seed-filling process. A hall sensor was used to measure the rotational speed of the rake bar chain wheel. Meanwhile, a hydraulic cylinder was adopted to adjust the angle of the rake bar chain, and a digital camcorder was used to record the seed-filling process. The ratio between the number of rake bars with 1–2 billets and the total number of rake bars is called the qualification filling rate S_q . The ratio between the number of rake bars with no billets and the total number of rake bars is called the miss out filling rate S_e . In this study, the two indexes were used to evaluate the seed-filling uniformity. According to previous work [2], the rotation speed of the rake bar chain wheel was set to 90 rpm, the number of billets was set to 200, and the angle of the rake bar chain was set to four levels (97° , 107° , 117° , and 127°) with each treatment being repeated three times.



Figure 4. The physical seed-filling experiment setup.

The simulation experiment was conducted as follows: First, the 3D model of the single-bud billet seed-metering device was imported into the EDEM software. The material was configured using the parameters listed in Table 1, and the movement parameters are introduced in Section 2.2. After 200 billet particles were generated, the rake bar chain began to move, and the total simulation time was 53.6 s. The simulation experiment was repeated three times for each rake bar chain angle.

3. Results and Discussion

3.1. Analysis of the Angle of Repose Results

Under the condition of a bottomless stainless-steel cylinder, the angles of repose of the physical experiment are 27.57°, 28.63°, and 29.41°, with an average of 28.54°. Meanwhile, the simulation angles of repose are 30.85°, 30.36°, and 30.33°, with an average of 30.51°. Compared to the physical angle of repose of single-bud billet, the relative error of the simulation experiment is 6.67%, which is within a reasonable range. It verifies the feasibility of the material parameter setting of the single-bud billet. A parameter calibration study can be conducted in the future to improve the accuracy of the simulation results. These parameters were used in the seed-filling simulation and compared to the physical results to further validate the feasibility of the EDEM simulation experiments.

3.2. Analysis of the Seed-Filling Experiment Results

As illustrated in Figure 5, the qualification filling rate S_q and the miss out filling rate S_e under different angles of the rake bar chain in the physical and simulation experiments have the same variation trend. With the increase in the angle of the rake bar chain, the S_q increases first from 43.52% to 76.4% and then decreases to 71.96% in the physical experiments, whereas it increases first from 67.92% to 89.84% and then decreases to 80.46% in the simulation experiments. The variation trend of S_e is the opposite to that of S_q . Because there were only 200 billets in the seed box, the S_q in both physical and simulation experiments is low. The increase in billets improves the S_q , which has been demonstrated in the previous study [2], but it also increases the simulation time. The S_q in the simulation experiments is generally higher than that in the physical experiments, which may be related to the individual difference in the billets of the physical experiments. The parameters are also variable, and the vibration of the rake bar chain and seed box may affect the physical experimental results. According to the linear regression analysis of the simulation and physical experimental results, the linear correlation coefficient was 0.762 for S_q and 0.869 for S_e . The simulation result is consistent with the physical experiment result, demonstrating the validity of using the EDEM software to simulate the seed-filling of billets. The single-bud billet seed-metering device has been applied in HN 2CZD-2 single-bud sugarcane planter. The planter did a good job in the farm of Guangdong Guangken Agricultural Machinery Service Co., Ltd., Guangzhou, China.

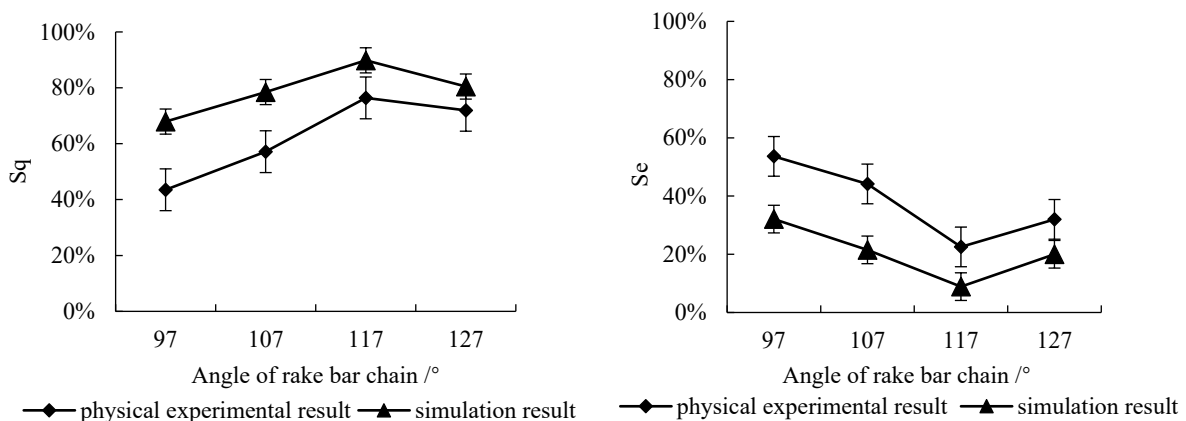


Figure 5. The relationship between the angle of the rake bar chain and the qualification filling rate S_q and the miss out filling rate S_e .

3.3. Motion of Single-Bud Billet in Seed-Metering Device Analysis

Figure 6 shows the motion of the single-bud billet in the rake bar of the seed-metering device. According to physical experimental results, the rake bar chain speed was set to 90 rpm, the billet number was set to 200, and the initial velocity of the billet in the seed box was set to 0 m/s. When the rake bar chain began to move, the billets were lifted into the rake bar, moved to the highest point in the seeding channel, and finally thrown out. Figure 5 shows a cross-sectional view of the middle of the seed box to illustrate the movement of billets in the rake bar and seed box. In this figure, the particle velocity is represented by red, green, and blue from high to low. The particle velocity in the seed-metering device varies with color. Under the action of the rake bar, the billets in the rake bar moved at a relatively high speed. The surrounding billets followed the movement trend of the rake bar due to the friction among the billets and moved lower, whereas other billets that were not affected by the movement remained stationary.

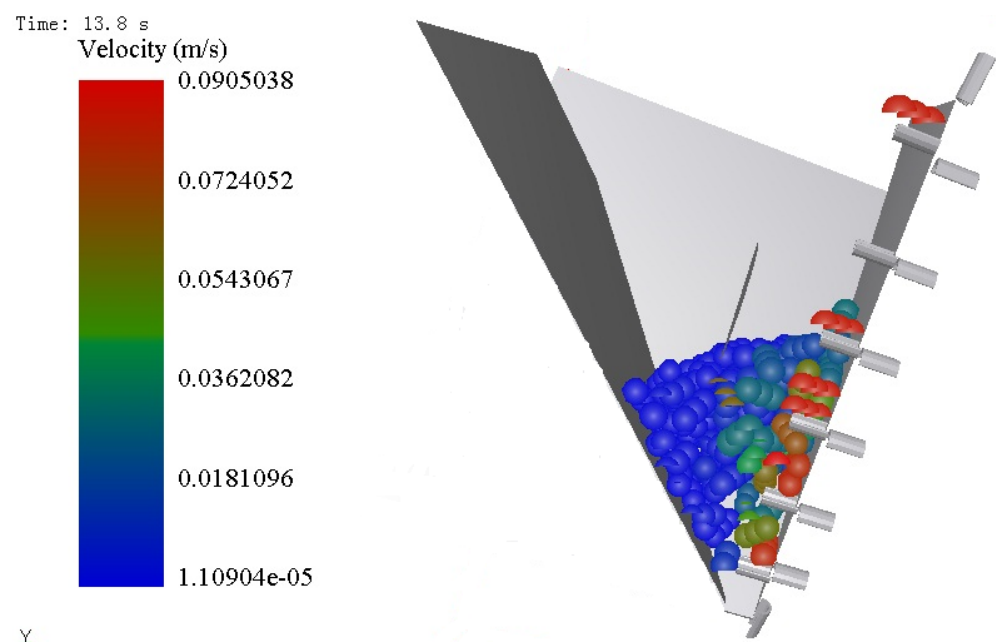


Figure 6. Motion simulation results.

To clearly illustrate the movement trajectory of billets, the seed box was sliced from the middle with a slice depth of 100 mm, and the movement of each billet is shown as a stream type in Figure 7. As shown in Figure 7a, the billets close to the rake bar moved upward with the rake bar, whereas those not filling the rake bar moved to both sides when the rake bar left the billet population. Other billets gradually moved along the inclined plane of the seed box towards the rake bar chain, forming two small circulation circles on both sides of the rake bar chain. An obvious circulation circle can be observed on the side view of the seed box (Figure 7b). When the rake bar left the billet population, the billets moved counterclockwise to return around the rake bar chain. It can be inferred that the more inclined the rake bar, the larger the circle, and the greater the probability of billets entering the rake bar. However, the high probability of multiple billets entering one rake bar will affect the seed-filling uniformity, which explains why there is an optimal value of the rake bar angle. In both physical and simulation experiments, the optimal angle of the rake bar was 117° .

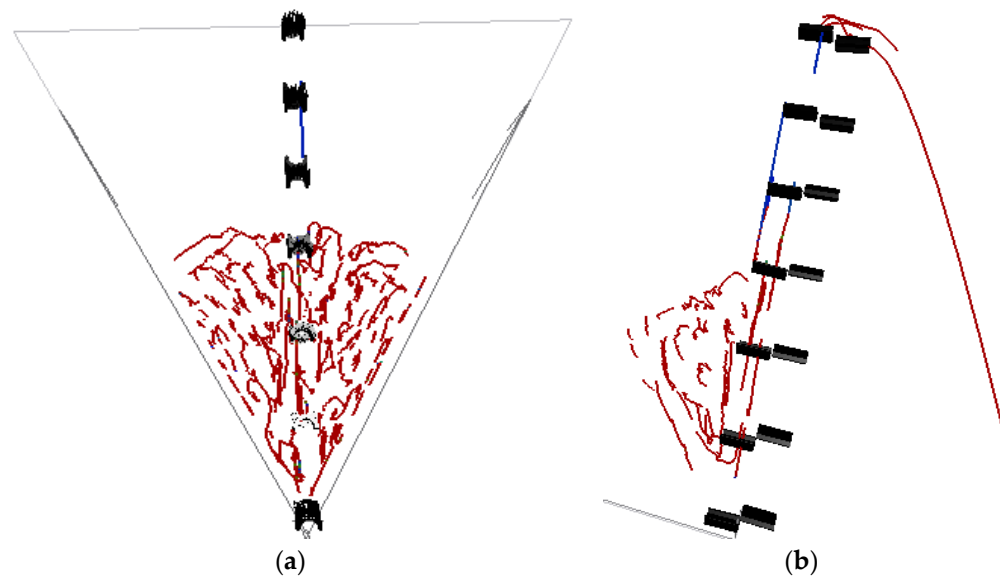


Figure 7. The simulated motion of billets in the seed-filling process. (a) Front view of the seed box; (b) side view of the seed box.

As shown in Figure 8, the single particle trajectory in the EDEM simulation was extracted by selecting the moving particle in the seed box. The trajectories of three billets that failed to enter the rake bar are shown in Figure 8a. Due to population friction, the three billets in the upper population gradually moved down close to the rake bar and then began to move upward following the rake bar. More specifically, billet 1 was far from the rake bar and quickly stopped moving; billet 2 did not enter the rake bar and remained in the upper population when the rake bar left the population; billet 3 entered the rake bar but quickly dropped back into the population.

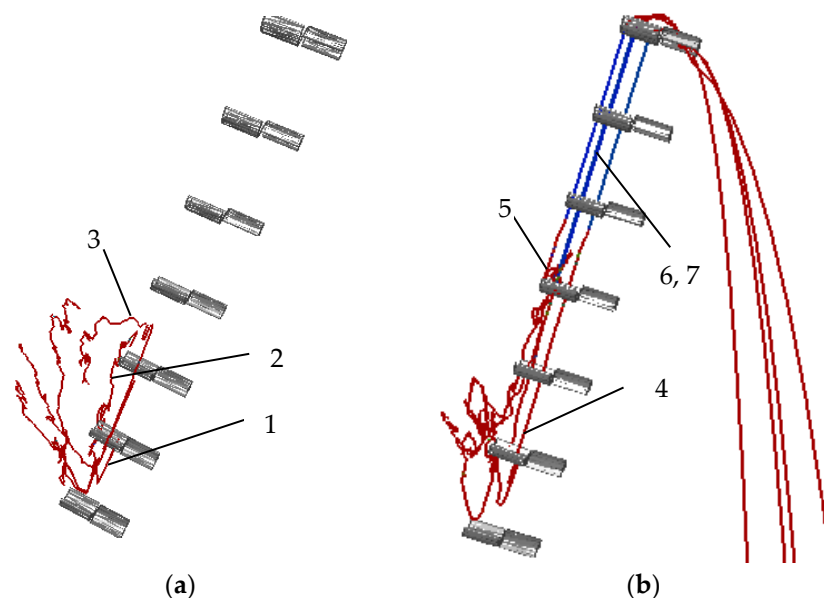


Figure 8. The trajectory of the selected billets in the seed-filling process. (a) The trajectory of the billet that did not enter the rake bar; 1: billet 1; 2: billet 2; 3: billet 3; (b) the side view of the trajectory of the billet that entered the rake bar; 5: billet 5; 6: billet 6; 7: billet 7.

Figure 8b shows the trajectory of four billets that successfully entered the rake bar. Billet 4 entered the rake bar while it was still inside the population; billet 5 entered the rake bar before it left the population; billets 6 and 7 entered the same rake bar at the same time,

and their trajectories intersected until they fell. The color of the trajectory indicates the magnitude of acceleration, with the brown line indicating a greater acceleration magnitude than the blue line. When the four billets moved at a uniform speed with the rake bar, the acceleration was zero, and the trajectory was colored in blue. The comparison of Figures 6 and 7 indicate that the trajectory of the billets entering or exiting the rake bar is included in the circulation. The larger the circulation circle, the easier it is for billets to enter the rake bar. Therefore, the seed-metering device can be improved to bring more billets close to the rake bar while covering the rake bar more to expand the circulation circle.

The velocity and total force of a random particle at a certain time can also be obtained in EDEM. Figure 9 shows the motion parameters of billet 3 in Figure 7a. After 4 s of particle generation, the rake bar began to move. Meanwhile, billet 3 moved downward at a slow speed due to population friction. The billet encountered the rake bar at the time of 30 s but did not enter it. The total force and velocity fluctuated several times due to the action of other rake bars.

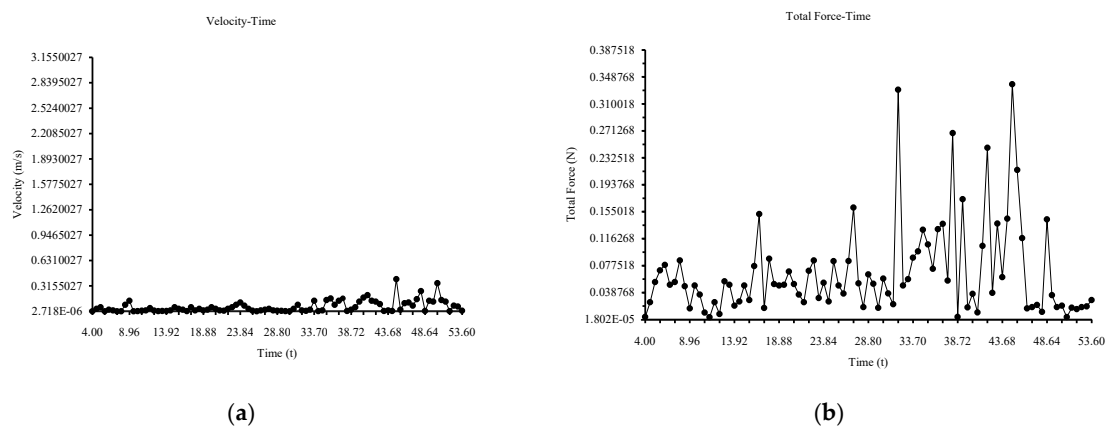


Figure 9. The motion of billet 3 with time (a) the velocity of billet 3; (b) the total force of billet 3.

Figure 10 shows the motion parameters of billet 4 in Figure 8b. Billet 4 was generated in the lower part of the population and subjected to the population friction from 4 s to 9 s, but the velocity was low, and the total force fluctuated slightly. The total force changed dramatically as billet 4 entered the rake bar at 9 s and followed the rake bar through the population at a uniform speed. Then, billet 4 and the rake bar left the population at 14 s. The velocity was constant, and the force was zero. At 19 s, billet 4 reached the highest point and began to fall, and its velocity rose rapidly until landing. By comparing Figures 8 and 9, the billets that did not successfully enter the rake bar were affected more by forces, and whether this will cause damage to the billets needs further investigation.

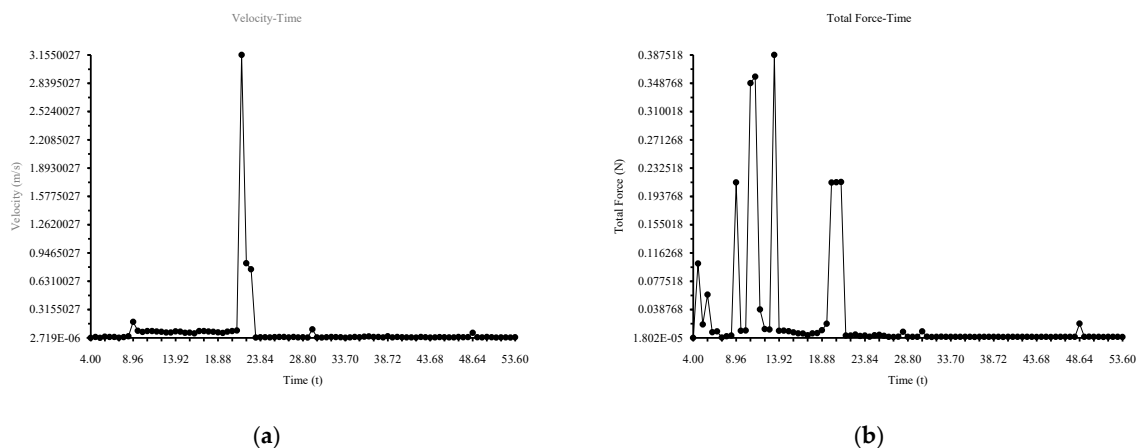


Figure 10. The motion of billet 4 with time (a) the velocity of billet 4; (b) the total force of billet 4.

4. Conclusions

In this paper, the seed-filling process of single-bud billets in the seed-metering device was simulated in EDEM. The single-bud billet particle model was established based on three filling spheres, the contact model was the Hertz-Mindlin (no slip), and there was no binding effect between billet particles. The physical and simulation experiments of the billet angle of repose were conducted, and the relative error of the physical and simulation results was 6.67%, indicating that the material parameters of single-bud billet are effective. Meanwhile, the seed-filling physical and simulation experiments were carried out, and the results showed that the linear correlation coefficient between the physical and simulation results was 0.762 for S_q and 0.869 for S_e , which demonstrates the validity of using the EDEM software to simulate the seed-filling process of billets. Moreover, the motion information of the seed-filling process was analyzed in EDEM. The analysis results show that the seed box has two small circulation circles on both sides of the rake bar chain, and the larger the circulation circle, the easier it is for billets to enter the rake bar. Additionally, the seed-metering device can be improved to bring more billets close to the rake bar while covering the rake bar more to expand the circulation circle. The analysis of the total force simulation of billets in EDEM reveals that the billets that did not successfully enter the rake bar were affected more by forces; the damage to billets during the seed-filling process needs to be investigated in the future. This EDEM simulation method provides a basis for optimizing the structures and parameters of the sugarcane billet planter in future work.

Author Contributions: Conceptualization, Q.L. and Y.O.; methodology, M.W., X.Z. and Q.L.; data analysis, M.W.; writing—original draft preparation, M.W.; funding acquisition, Q.L. All authors have read and agreed to the published version of the manuscript.

Funding: This research was funded by National Key R&D Program of China (2020YFD1000600) and Guangdong Provincial Team of Technical System Innovation for Sugarcane Sisal Industry (2019KJ104-11).

Institutional Review Board Statement: Not applicable.

Informed Consent Statement: Not applicable.

Data Availability Statement: The data presented in this study are available on demand from the first author at (wmmscau@163.com).

Conflicts of Interest: The authors declare no conflict of interest.

References

1. Saengprachatanarug, K.; Wongpichet, S.; Ueno, M.; Taira, E. Comparative discharge and precision index of a sugar cane billet planter. *Appl. Eng. Agric.* **2016**, *32*, 561–567. [[CrossRef](#)]
2. Wang, M.; Liu, Q.; Ou, Y.; Zou, X. Experimental Study of the Seed-Filling Uniformity of Sugarcane Single-Bud Billet Planter. *Sugar Tech.* **2021**, *23*, 827–837. [[CrossRef](#)]
3. Cundall, P.A.; Strack, O.D. A discrete numerical model for granular assemblies. *Geotechnique* **1979**, *29*, 47–65. [[CrossRef](#)]
4. Zhou, L.; Yu, J.; Wang, Y.; Yan, D.; Yu, Y. A study on the modelling method of maize-seed particles based on the discrete element method. *Powder Technol.* **2020**, *374*, 353–376. [[CrossRef](#)]
5. Owen, P.J.; Cleary, P.W. Prediction of screw conveyor performance using the Discrete Element Method (DEM). *Powder Technol.* **2009**, *193*, 274–288. [[CrossRef](#)]
6. Xu, Y.; Zhang, X.; Wu, S.; Chen, C.; Wang, J.; Yuan, S.; Chen, B.; Li, P.; Xu, R. Numerical simulation of particle motion at cucumber straw grinding process based on EDEM. *Int. J. Agric. Biol. Eng.* **2020**, *13*, 227–235. [[CrossRef](#)]
7. Shi, L.; Zhao, W.; Sun, B.; Sun, W. Determination of the coefficient of rolling friction of irregularly shaped maize particles by using discrete element method. *Int. J. Agric. Biol. Eng.* **2020**, *13*, 15–25. [[CrossRef](#)]
8. Wang, Y.; Liang, Z.; Zhang, D.; Cui, T.; Shi, S.; Li, K.; Yang, L. Calibration method of contact characteristic parameters for corn seeds based on EDEM. *Trans. Chin. Soc. Agric. Eng.* **2016**, *32*, 36–42.
9. Sun, J.; Chen, H.; Duan, J.; Liu, Z.; Zhu, Q. Mechanical properties of the grooved-wheel drilling particles under multivariate interaction influenced based on 3D printing and EDEM simulation. *Comput. Electron. Agric.* **2020**, *172*, 105329. [[CrossRef](#)]
10. Yudao, L.I.; Shulun, X.I.N.G.; Shasha, L.I.; Liu, L.; Zhang, X.; Zhanhua, S.O.N.G.; Fade, L.I. Seeding performance simulations and experiments for a spoon-wheel type precision cottonseed-metering device based on EDEM. *Mech. Eng. Sci.* **2020**, *2*, 1–8. [[CrossRef](#)]

11. Miao, Z.; Li, Z.; Xu, K.; Wu, L.; Su, N.; Song, G.; Liu, Y. The Numerical Simulation Analysis of *Pinus sylvestris* var. *Mongolica* seeds Vibration Situation Based on EDEM. *Iop Conf. Ser. Earth Environ. Sci.* **2019**, *252*, 052111. [[CrossRef](#)]
12. Ghodki, B.M.; Goswami, T.K. DEM simulation of flow of black pepper seeds in cryogenic grinding system. *J. Food Eng.* **2017**, *196*, 36–51. [[CrossRef](#)]
13. Horabik, J.; Parafiniuk, P.; Molenda, M. Stress profile in bulk of seeds in a shallow model silo as influenced by mobilisation of particle-particle and particle-wall friction: Experiments and DEM simulations. *Powder Technol.* **2018**, *327*, 320–334. [[CrossRef](#)]
14. Li, H.; Zeng, S.; Luo, X.; Fang, L.; Liang, Z.; Yang, W. Design, DEM simulation, and field experiments of a novel precision seeder for dry direct-seeded rice with film mulching. *Agriculture* **2021**, *11*, 378. [[CrossRef](#)]
15. Lu, F.; Ma, X.; Qi, L.; Tan, S.; Tan, Y.; Jiang, L.; Sun, G. Parameter optimization and experiment of vibration seed-uniforming device for hybrid rice based on discrete element method. *Trans. Chin. Soc. Agric. Eng.* **2016**, *32*, 17–25.
16. He, Y.; Li, C.; Zhao, X.; Gao, Y.; Li, S.; Wang, X. Simulation analysis of the fertilizer ejecting device of corn fertilizer applicator based on EDEM. *J. Phys. Conf. Ser.* **2020**, *1633*, 012061. [[CrossRef](#)]
17. Liu, J.S.; Gao, C.Q.; Nie, Y.J.; Yang, B.; Ge, R.Y.; Xu, Z.H. Numerical simulation of Fertilizer Shunt-Plate with uniformity based on EDEM software. *Comput. Electron. Agric.* **2020**, *178*, 105737. [[CrossRef](#)]
18. Liu, T.; He, R.; Lu, J.; Zou, Y.; Zhao, M. Simulation and verification on seeding performance of nest hole wheel seed-metering device based on EDEM. *J. South China Agric. Univ.* **2016**, *37*, 126–132.
19. Liu, Q.T.; Ou, Y.G.; Qing, S.L.; Chen, H.B. Failure tests of sugarcane stalks under torsion, compression and tension load. *Trans. CSAE* **2006**, *6*, 201–204.
20. Fengwei, G.; Youqun, Z.; Feng, W.; Zhichao, H.; Lili, S. Simulation analysis and experimental validation of conveying device in uniform rushed straw throwing and seed-sowing Machines using CFD-DEM coupled approach. *Comput. Electron. Agric.* **2022**, *193*, 106720. [[CrossRef](#)]
21. Wang, M.; Liu, Q.; Ou, Y.; Zou, X. Determination of physical and mechanical properties of sugarcane single-bud billet. *arXiv* **2022**, arXiv:2203.16916. Available online: <https://arxiv.org/abs/2203.16916> (accessed on 31 March 2022).
22. Chen, S.; Cao, S.; Gao, K.; Cao, W.; Cui, S.; Ma, J. Research on Wheat Modeling Method Based on EDEM. In Proceedings of the Journal of Physics. Conference Series (Online), Wetherby, UK, 6 February 2021; Volume 1798, p. 012048. [[CrossRef](#)]
23. Guo, Z.; Chen, X.; Liu, H.; Guo, Q.; Guo, X.; Lu, H. Theoretical and experimental investigation on angle of repose of biomass-coal blends. *Fuel* **2014**, *15*, 131–139. [[CrossRef](#)]
24. Matuttis, H.G.; Luding, S.; Herrmann, H.J. Discrete element simulations of dense packings and heaps made of spherical and non-spherical particles. *Powder Technol.* **2000**, *109*, 278–292. [[CrossRef](#)]
25. Al-Hashemi, H.M.; Al-Amoudi, O.S. A review on the angle of repose of granular materials. *Powder Technol.* **2018**, *1*, 397–417. [[CrossRef](#)]
26. Tan, Y.; Yu, Y.; Fottner, J.; Kessler, S. Automated measurement of the numerical angle of repose (aMAoR) of biomass particles in EDEM with a novel algorithm. *Powder Technol.* **2021**, *388*, 462–473. [[CrossRef](#)]
27. Zhou, L.; Yu, J.; Liang, L.; Wang, Y.; Yu, Y.; Yan, D.; Sun, K.; Liang, P. DEM Parameter Calibration of Maize Seeds and the Effect of Rolling Friction. *Processes* **2021**, *9*, 914. [[CrossRef](#)]
28. Wenzheng, L.; Jin, H.; Hongwen, L.; Xueqiang, L.I.; Kan, Z.H.; Zhongcai, W.E. Calibration of simulation parameters for potato minituber based on EDEM. *Trans. Chin. Soc. Agric. Mach.* **2018**, *49*, 125–135.
29. Du, Y.; Cui, T.; Zhang, D.; Wei, Y.; Yang, R.; Wu, H. Establishment and Parameter Calibration of Broad Bean Seeds Simulation Particles in EDEM. In *2019 ASABE Annual International Meeting*; American Society of Agricultural and Biological Engineers: St. Joseph, MI, USA, 2019; Volume 1. [[CrossRef](#)]

Article

Experimental Study of the Planting Uniformity of Sugarcane Single-Bud Billet Planters

Meimei Wang¹, Qingting Liu^{2,*}, Yinggang Ou² and Xiaoping Zou²

¹ Department of Mechanical Engineering, Anyang Institute of Technology, Anyang 455000, China; wmmsscau@163.com

² College of Engineering, South China Agricultural University, Wushan Road, Tianhe District, Guangzhou 510642, China; ouying@scau.edu.cn (Y.O.); 13416229168@126.com (X.Z.)

* Correspondence: qingting@scau.edu.cn

Abstract: Planting uniformity is a key evaluation index for planters. This paper investigated the effect of rotational speed, the angle of the rake bar chain, and the number of billets on the planting uniformity of a seed-metering device in the laboratory. The experimental results showed that the optimal planting uniformity can be achieved under a rake bar chain angle of 117° , a number of billets of 500, and a rotational speed of the rake bar chain of 70 rpm. Under this condition, the quality index Z_q was 97.22% and the multiple index Z_m was 0%, while the miss index Z_e was 2.78%. Based on the above parameters, a single-bud planter was improved with three rake bar chains per seed box. Field experiments with different operation parameters (rotational speed, forward speed) were conducted. Results indicated that when the rotational speed was 40 rpm and the forward speed was 2.26 km/h, the planting uniformity was the best and the quality index Z_q was 93.38%. The research results provide a basis for the application of single-bud billet planters in the field.

Keywords: single-bud; billet planter; planting uniformity

Citation: Wang, M.; Liu, Q.; Ou, Y.; Zou, X. Experimental Study of the Planting Uniformity of Sugarcane Single-Bud Billet Planters. *Agriculture* **2022**, *12*, 908. <https://doi.org/10.3390/agriculture12070908>

Academic Editors: Muhammad Sultan, Redmond R. Shamshiri, Md Shamim Ahamed and Muhammad Farooq

Received: 18 May 2022
Accepted: 18 June 2022
Published: 22 June 2022

Publisher's Note: MDPI stays neutral with regard to jurisdictional claims in published maps and institutional affiliations.



Copyright: © 2022 by the authors. Licensee MDPI, Basel, Switzerland. This article is an open access article distributed under the terms and conditions of the Creative Commons Attribution (CC BY) license (<https://creativecommons.org/licenses/by/4.0/>).

1. Introduction

Planting is an important procedure in the production of sugarcane, but it is highly labor-intensive and time-intensive [1]. The sugarcane industry has been moving towards mechanized field planting to address the problems of labor shortage and high production costs [2]. Rípoli et al. [3] analyzed the cost-effectiveness of five different sugarcane planters by comparing them with the semi-mechanized system under the same field conditions and found that the mechanized system was significantly cheaper than the semi-mechanized planter. Moreover, the automatic planter has a lower operating cost than the semi-automatic one. It greatly saves manpower in the operation process, and the mechanized planter can work for long periods during the day and nighttime shifts [4]. At present, the main types of sugarcane planting machines are whole-stalk planters, real-time cutting planters, and pre-cutting planters.

However, the traditional planting method with whole-stalk planters and real-time cutting planters requires great human force and needs to store a lot of cane seeds in the planter. The large mass of planting material makes it difficult to transport, handle, and store the cane seed [5–7].

In comparison, billet planting is more cost-effective than whole-stalk planting. The fully automatic billet planter can solve the problems of labor shortage and planting delay [8]. Additionally, the billet planter has a high field capacity and efficiency [6]. At present, the billet planter usually adopts 2–3-bud billets and distributes them over the ground surface [9]. However, single-bud billets are less bulky, easy to transport, more economical, and can improve the quality of seed [10]. According to Gujja et al. [11], shoots of the same age contribute to the uniformity in growth and sugar accumulation in the canes, as well as a better germination percentage. Sugarcane planting by bud chip has been proven to have a

higher production efficiency and a lower cost of planting material, achieving a cane yield of 106.8 t/ha, 13.86% higher than that of the conventional cane crop planting method [12].

Therefore, the sugarcane single-bud billet planter is the development trend of sugarcane planters in the future and has a good prospect. We designed a seed-metering device with a rake bar chain for a sugarcane single-bud billet planter and tested the seed-filling uniformity of the seed-metering device [13]. In sugarcane production, productivity depends on locating the billets in the furrow with uniform distribution [14]. The rate of billet dropping by the metering device is a key factor to evaluating the economic efficiency of any planter machine [15]. The major problem of the billet planter is its low consistency of discharging rates, which, in turn, results in lower sugarcane yields [6].

A plethora of research on the uniformity of sugarcane billet planters has been conducted. Razavi et al. [16] studied the effect of forwarding speed and angle of the chain conveyor on planting uniformity in a sugarcane billet planter. Taghinezhad et al. [17] investigated the effect of the angle and speed of sugarcane billet planters on discharging and precision indexes. Saengprachatanarug et al. [18] improved the discharge consistency of the sugarcane billet planter by changing the inclination of the container. Saengprachatanarug et al. [6] developed a metering device for sugarcane billet planters by modifying the arrangement of the cleats conveyor. Then, the discharge index and consistency of the developed and original metering devices were evaluated and compared. Moslem et al. [9] designed a single-cupboard metering device that could plant billets with a length of 50 cm. On a laboratory test rig, the effects of planting speed, cane variety, and angle-of-chain structure on the uniformity of the planted billets were evaluated.

Based on the results of our previous experiments, the single-bud billet seed-metering device with a rake bar chain has good seed-filling uniformity [13]. However, considering the effects of forwarding speed, seeding flap, and complex field environments, the planting uniformity is different from the seed-filling uniformity. To study the planting uniformity of the seed metering, experiments with different structural parameters were conducted in the laboratory. According to the experimental results, a new single-bud billet planter with the optimum combination of structural parameters was designed and fabricated, and the optimal operation parameters were studied by field experiments. The research of this paper are valuable for improvements in the redesigning of sugarcane single-bud billet planters.

2. Materials and Methods

2.1. Billet Preparation

Single-bud billets are prepared by the billet-cutting machine shown in Figure 1 for both laboratory and field experiments. The billet-cutting machine consists of a JB04-1 electric punch machine with a nominal pressure of 10 kN, a slider stroke of 40 mm, a maximum closed height of 150 mm, a table size of 270 × 270 mm, and a motor power of 0.37 kW. Two cutters are fixed to the slider with inner hexagon bolts. To ensure the length of the billet, the distance between the two cutters is 60 mm. The fixing plate 40 mm above the table can hold the billet while the cutter cuts through the billet. The footswitch of the machine is turned on after the sugarcane is put on the table, and the cutter cuts the sugarcane down. The billet cutting machine is equipped with a protective cover for safety (not shown in Figure 1).

2.2. Laboratory Experiment

The seed-metering device we designed [13] was mounted on a trolley system in the soil bin laboratory (Figure 2). The driving wheel of the rake bar chain and the oil cylinder for adjusting the angle of the seed-metering device were driven by the hydraulic station on the trolley. During the experiment, the trolley could move forward along the track on both sides of the soil bin, and the driving wheel drove the rake bar to transport billets to the seeding channel and drop them into the pre-dug furrow. In this process, the distribution of billets in the furrow was evaluated.

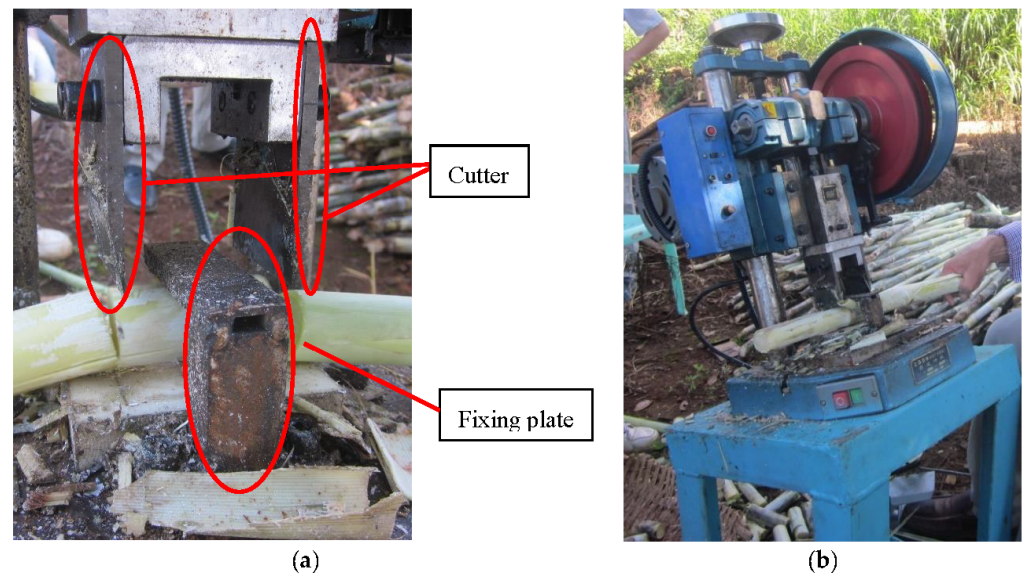


Figure 1. Preparation of sugarcane billets: (a) billet-cutting machine; (b) cutter and fixing plate.



Figure 2. Laboratory experimental set-up.

2.2.1. Experimental Evaluation of the Planting Uniformity

Numerous studies have been conducted to evaluate the uniformity of sugarcane planting. For example, Taghinezhad et al. [14] exploited the middle band of billets to calculate the spacing between billets. The distribution of plant spacing was quantified by the multiple index, miss index, and the quality-of-feed index following the single-seed method [19]. Moslem et al. [9] considered an overlap of 12.5 cm as a normal pattern of planting; values higher and lower than 12.5 cm would result in over overlapping and under overlapping, respectively. Kumar et al. [20] used the length of 10 setts and actual length covered by 10 setts to calculate the overlap and the gap when the sugarcane planter was run in the field with a length of 12 m. In the trial of Johnson et al. [21], the number of billets planted was 109,000 per hectare, and the results showed that the effect of the position of the billets within the planting furrow on sugar yield was not economically significant. Silva et al. [22] suggested that a good stand of buds per meter should be provided since the quality of planting is the most important factor for good yield.

The single-bud billet is shorter than the multiple-bud billet and larger than the grain seed. After comprehensive consideration, the number of billets per unit length was taken as the evaluation standard. The unit length was 1 m in lab experiments and 0.5 m in field experiments in this study. Meanwhile, quality index Z_q , multiple index Z_m , miss index Z_e ,

and coefficient of variation (CV) were adopted to evaluate the planting uniformity. The theoretical number of billets per unit length can be calculated according to the rotational speed and forward speed of the driving wheel of the rake bar chain. The calculation formulas of the evaluation indexes are as follows:

$$Z_q = \frac{n_1}{N} \times 100\%. \quad (1)$$

$$Z_m = \frac{n_2}{N} \times 100\% \quad (2)$$

$$Z_e = \frac{n_3}{N} \times 100\%. \quad (3)$$

$$CV = \frac{\delta}{\bar{X}} \times 100\%. \quad (4)$$

where n_1 is the number of units in which the number of billets is more than 0.5 times and less than 1.5 times the theoretical number of billets; n_2 is the number of units where the number of billets is more than 1.5 times the theoretical number of billets; n_3 is the number of units where the number of billets is less than 0.5 times the theoretical number of billets; N is the total number of units; δ is the standard deviation of the number of billets per unit; and \bar{X} is the average number of billets in all units.

2.2.2. Experimental Method

Based on the results of previous experiments [13], the factors of the seed-filling uniformity of the seed-metering device were the rotational speed of the rake bar chain (A), the angle of the rake bar chain (B), and the number of billets (C). For comparison, the same factors were used in this study. A furrow with a depth of 0.2 m and a length of 11 m was opened in the soil bin beforehand. The seeding port of the seed-metering device was directly above the furrow, and there was a small gap between the seeding flap and the furrow. The trolley system discharged billets into the furrow at a constant forward speed during the experiment (Figure 3).



Figure 3. Laboratory experiment on planting uniformity.

A single-factor experiment was conducted to study the influence of each factor on the planting uniformity, and then the effective level range of each factor was selected for the orthogonal experiment. Based on this, the influence of various factors on planting uniformity was analyzed, and the optimal combination of factors was obtained. Each treatment was repeated three times.

2.2.3. Experiment Design

As for the single-factor experiment for factor A, the value of factor B was set to 117° and the value of factor C was set to 500. The value of factor A had nine levels, including 50 rpm, 60 rpm, 70 rpm, 80 rpm, 90 rpm, 100 rpm, 110 rpm, 120 rpm, and 130 rpm.

As for the single-factor experiment for factor B, the value of factor A was set to 90 rpm and the value of factor C was set to 500. The value of factor B had four levels, including 97° , 107° , 117° , and 127° .

As for the single-factor experiment for factor C, the value of factor B was set to 117° and the value of factor A was set to 90 rpm. The value of factor C had ten levels from 100 to 1000, with an interval of 100.

According to the results of the single-factor experiments, the levels of the factors in the orthogonal experiment are listed in Table 1. The orthogonal experiment table $L_{27}(3^{13})$ was selected to arrange the experiment.

Table 1. Factors and levels of the orthogonal experiment.

Level	Factor		
	Rotational Speed of Rake Bar Chain A/rpm	Angle of Rake Bar Chain B/ $^\circ$	Number of Billets C
1	70	107	200
2	90	117	500
3	110	127	800

2.3. Field Experiments

According to the influence of the above factors on the planting uniformity, the single-bud billet planter was designed with the angle of the rake bar chain set to 117° , and an adjustment plate was installed in the seed box to ensure that there were 500–800 billets in the effective working area of the rake bar chain. To further improve the qualified rate of filling, the planter adopted three rake bar chains in each seed box to increase the rate of seed filling. Considering that the high rotational speed of the rake bar chain may cause damage to the billets, the use of three bar chains per seed box could adapt to the fast-speed operation at a lower rotational speed. Meanwhile, a parabolic guide plate was designed at the seeding port to make the billets fall into the furrow more smoothly. The single-bud planter was equipped with two seed boxes, two openers, two fertilizing devices, two sett-covering devices, two film-covering devices, and other devices. The whole plant system was composed of a JOHN DEERE 1204 tractor (120 kW) and an HN 2CZD-2 single-bud sugarcane planter (Figure 4). Field experiments were carried out in the farm of Guangdong Guangken Agricultural Machinery Service Co., Ltd., in the city of Zhanjiang, Guangdong Province, China. The test field was latosol, deep-soil-layer, sticky heavy texture, poor fertility, acidic soil.

2.3.1. Field Evaluation of the Planting Uniformity

According to the sugarcane planting requirements and the characteristics of single-bud billets, the number of billets in a unit length of 0.5 m was counted as shown in Figure 5. The indexes used to evaluate the field planting uniformity were the same as those used in the laboratory, i.e., the quality index Z_q , multiple index Z_m , and miss index Z_e .



Figure 4. HN 2CZD-2 single-bud sugarcane planter.



Figure 5. Statistics of billet quantity.

2.3.2. Experimental Method

According to the theoretical number of billets at each chain rotational speed, the matching forward speed was determined for the field planting uniformity experiment. Due to the planting requirements of 12 effective buds per meter in the furrow [23] and the stable operating speed range of the tractor in the field, three levels of the rotational speed of the rake bar chain, (30 rpm, 40 rpm, and 50 rpm), and two levels of forwarding speed, 2km/h and 3km/h, were selected to study their effects on field planting uniformity. The planter worked 50 m per treatment.

2.4. Statistical Analysis

In the laboratory experiments, the factors and levels in single-factor tests were selected based on the results of previous experiments [13]. The effective ranges were selected to provide optimal parameters for the orthogonal tests. Each test was repeated three times.

IBM SPSS Statistics 27.0 software was used to analyze the variance of the test data. Full-factor tests of rotational speed and forward speed in field experiments were conducted; the planter worked 50 m per treatment. The test indexes were computed using Microsoft Excel (2016).

3. Results and Discussion

3.1. Analysis of Laboratory Experiment Results

3.1.1. The Effect of the Rotational Speed of the Rake bar Chain on Planting Uniformity

According to a univariate analysis of variance, at the 95% confidence interval, the rotational speed had a significant effect on the quality index Z_q ($F = 2.508, p = 0.048 < 0.05$) and miss index Z_e ($F = 2.508, p = 0.048 < 0.05$). In the previous experiment [13], rotational speed had no significant effect on the uniformity of seed filling, indicating that the forward speed may promote the influence of the rotational speed on the planting uniformity. Reference [23] also mentioned the influence of forward speed on planting. The specific trends can be seen in Figure 6: when the rotational speed increased from 50 rpm to 130 rpm, the value of the quality index Z_q changed little and remained above 80%; the value of the multiple index Z_m was always zero; the value of the miss index Z_e first decreased with the increase in rotational speed, and then was almost zero when the rotational speed was between 100 rpm and 120 rpm. Yazgi et al. [24] also found that the qualification rate of the seeding unit increased first and then decreased with the increasing sprocket speed. The value of the miss index Z_e then increased slightly when the rotational speed reached 130 rpm. That indicated that increasing the rotational speed could increase the probability of acquiring billets in the rake bar and thus improve the planting uniformity, but when the rotational speed is too high, the probability decreases, and the bud may be damaged. Therefore, the rotational speed should be as low as possible when meeting planting requirements.

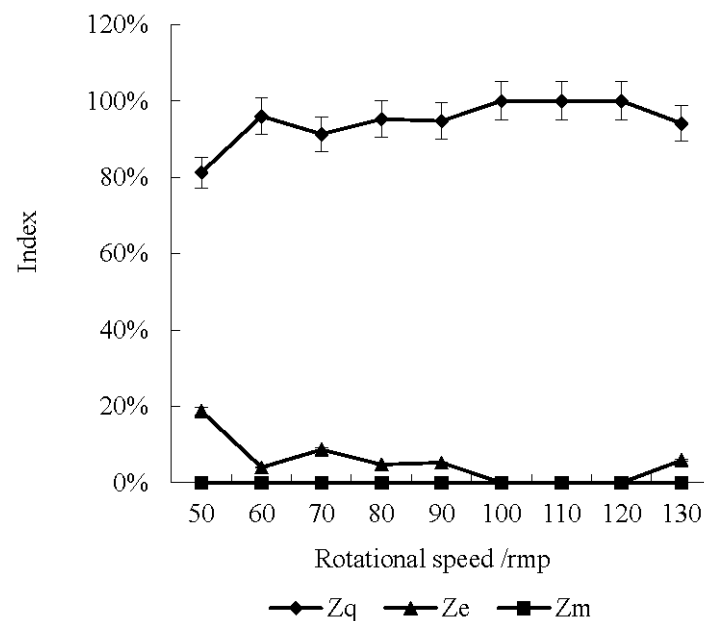


Figure 6. The effect of the rotational speed of the rake bar chain on planting uniformity.

The statistical results of the test samples are listed in Table 2, where “Min” and “Max” indicate the minimum and the maximum number of billets per meter. As shown in Table 2, the coefficient of variation (CV) of planting uniformity decreased with the increase in the rotational speed; the lower the coefficient of variation, the better the planting uniformity. When the rotational speed was 100 rpm, the value of CV was at the minimum of 13.25%, and then increased slightly as the rotational speed increased.

Table 2. Statistical data of the single-factor experiment on the rotational speed of the rake bar chain.

Rotational Speed /Rpm	Sample Number	δ	CV	Min	Max
50	32	2.614	32.43%	1.00	14.00
60	25	2.330	20.22%	6.00	15.00
70	23	2.651	20.60%	8.00	18.00
80	21	2.804	19.31%	10.00	20.00
90	19	3.142	19.32%	11.00	21.00
100	15	2.658	13.25%	16.00	27.00
110	16	3.633	17.77%	16.00	28.00
120	14	3.342	14.31%	18.00	28.00
130	17	4.535	19.52%	14.00	33.00

3.1.2. The Effect of Angle of Rake Bar Chain on Planting Uniformity

According to the univariate analysis of variance, at the 95% confidence interval, the angle of the rake bar chain had a significant effect on the quality index Z_q ($F = 20.477$, $p = 0.001 < 0.05$), the multiple index Z_m ($F = 50.281$, $p = 0.001 < 0.05$), and the miss index Z_e ($F = 49.629$, $p = 0.001 < 0.05$), which is consistent with the results of the previous seed-filling uniformity experiment [13], and the other sugarcane billet planter had the same trend [9]. As shown in Figure 7, with the increase in the angle of the rake bar chain, the quality index Z_q first increased and then decreased. When the angle was 117° , the quality index Z_q reached the maximum of 89.47%. When the angle continued to increase to 127° , the quality index Z_q decreased and the multiple index Z_m increased significantly to 53.85%, while the miss index Z_e decreased to zero. It is evident that the increase in angle makes more billets enter the working area of rake bar chain, which was beneficial to improve the planting uniformity. However, if the angle was too inclined, too many billets would be taken out, resulting in the increase in the multiple index Z_m ; as such, the optimal angle was 117° .

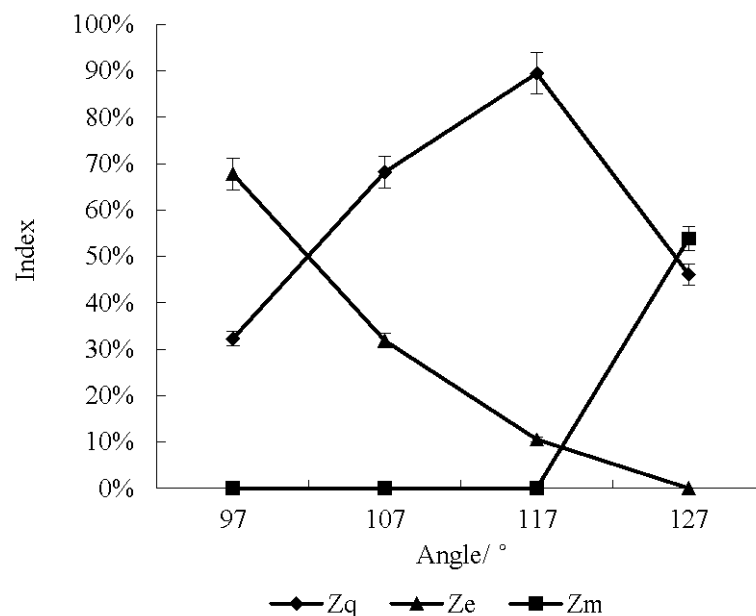


Figure 7. The effect of the angle of the rake bar chain on planting uniformity.

As listed in Table 3, the coefficient of variation (CV) of the planting uniformity decreased gradually with the increase in angle. CV reached the minimum value of 17.2% when the angle was 127° . Considering the quality index, 117° was still the optimal option.

Table 3. Statistical data of the single-factor experiment on the angle of the rake bar chain.

Angle ρ	Sample Number	δ	CV	Min	Max
97	31	2.693	28.59%	5	14
107	22	3.554	26.15%	7	20
117	19	4.221	25.62%	7	25
127	13	5.464	17.20%	22	38

3.1.3. The Effect of the Number of Billets on Planting Uniformity

According to the univariate analysis of variance, at the 95% confidence interval, the rotational speed had a significant effect on the quality index Z_q ($F = 13.274, p = 0 < 0.05$) and miss index Z_e ($F = 3.059, p = 0.015 < 0.05$), which is consistent with the results of the previous seed-filling uniformity experiment [13]. As illustrated by Figure 8, as the number of billets increased, the quality index Z_q increased, and the multiple index Z_m was generally low, while the miss index Z_e gradually decreased. In the literature [18], it was also found that the discharge index was high at the beginning of the test, while the container bin was fully loaded. When the number of billets was 900, the quality index Z_q reached the maximum of 100%. However, when the number continued to increase to 1000, the quality index Z_q decreased. Meanwhile, Table 4 reveals the CV was only 16.96% when the number was 900. It can be inferred that, in addition to increasing the angle, increasing the number of billets could also increase the qualified rate, but a number too high could also lead to an increase in the multiple index Z_m . Therefore, the quantity should be kept within the appropriate range (200–900) from Figure 8.

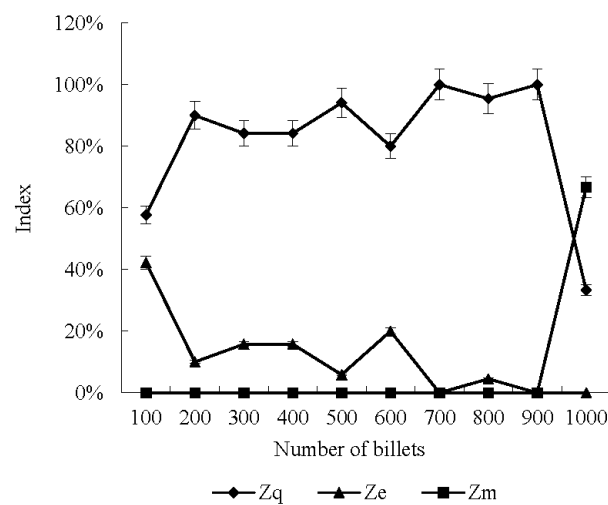


Figure 8. The effect of the angle of the rake bar chain on planting uniformity.

Table 4. Statistical data of the single-factor experiment on the number of billets.

Number of Billets	Sample Number	δ	CV	Min	Max
100	26	4.308	39.86%	1.00	19.00
200	20	2.458	17.07%	10.00	19.00
300	19	4.045	25.53%	10.00	23.00
400	19	4.525	28.56%	7.00	24.00
500	17	4.106	22.96%	7.00	24.00
600	20	4.256	28.95%	8.00	25.00
700	19	2.594	15.45%	12.00	21.00
800	22	5.402	27.96%	11.00	30.00
900	16	4.335	16.96%	18.00	33.00
1000	12	7.292	21.09%	21.00	45.00

3.1.4. Analysis of Orthogonal Test Results

The results are given in Table 5, and were averaged three times.

Table 5. Arrangements and results of the orthogonal experiment.

No	A	B	A×B	A×B	C	A×C	A×C	B×C	B×C	Z _q	Z _m	Z _e
	1	2	3	4	5	6	7	8	11			
1	1	1	1	1	1	1	1	1	1	25.00%	75.00%	0.00%
2	1	1	1	1	2	2	2	2	2	4.17%	95.83%	0.00%
3	1	1	1	1	3	3	3	3	3	4.00%	96.00%	0.00%
4	1	2	2	2	1	1	1	2	3	37.93%	62.07%	0.00%
5	1	2	2	2	2	2	2	3	1	8.33%	91.67%	0.00%
6	1	2	2	2	3	3	3	1	2	0.00%	94.44%	5.56%
7	1	3	3	3	1	1	1	3	2	12.50%	87.50%	0.00%
8	1	3	3	3	2	2	2	1	3	0.00%	93.33%	6.67%
9	1	3	3	3	3	3	3	2	1	0.00%	7.14%	92.86%
10	2	1	2	3	1	2	3	1	1	31.82%	68.18%	0.00%
11	2	1	2	3	2	3	1	2	2	9.09%	90.91%	0.00%
12	2	1	2	3	3	1	2	3	3	10.53%	89.47%	0.00%
13	2	2	3	1	1	2	3	2	3	25.00%	75.00%	0.00%
14	2	2	3	1	2	3	1	3	1	0.00%	100.00%	0.00%
15	2	2	3	1	3	1	2	1	2	0.00%	81.82%	18.18%
16	2	3	1	2	1	2	3	3	2	15.00%	85.00%	0.00%
17	2	3	1	2	2	3	1	1	3	0.00%	93.33%	6.67%
18	2	3	1	2	3	1	2	2	1	0.00%	13.33%	86.67%
19	3	1	3	2	1	3	2	1	1	84.62%	15.38%	0.00%
20	3	1	3	2	2	1	3	2	2	40.54%	59.46%	0.00%
21	3	1	3	2	3	2	1	3	3	0.00%	100.00%	0.00%
22	3	2	1	3	1	3	2	2	3	0.00%	100.00%	0.00%
23	3	2	1	3	2	1	3	3	1	0.00%	100.00%	0.00%
24	3	2	1	3	3	2	1	1	2	0.00%	100.00%	0.00%
25	3	3	2	1	1	3	2	3	2	0.00%	100.00%	0.00%
26	3	3	2	1	2	1	3	1	3	0.00%	71.43%	28.57%
27	3	3	2	1	3	2	1	2	1	0.00%	0.00%	100.00%

General linear models variance analysis was conducted on the orthogonal test results, and the results are listed in Table 6. Factor A had no significant effect on the quality index Z_q ($p = 0.642 > 0.05$), multiple index Z_m ($p = 0.556 > 0.05$), or miss index Z_e ($p = 0.83 > 0.05$), which is consistent with the single-factor test results in 3.1.1.

Table 6. Variance analysis of the orthogonal experiment results.

Source	Z _q		Z _m		Z _e	
	Sig	Eta ²	Sig	Eta ²	Sig	Eta ²
A	0.642	0.105	0.556	0.136	0.83	0.046
B	0.013 *	0.661	0.000 **	0.972	0.046 *	0.536
C	0.03 *	0.583	0.000 **	0.967	0.02 *	0.625
B×C	0.001 **	0.885	0.000 **	0.978	0.465	0.331
A×C	0.742	0.198	0.566	0.282	0.938	0.086
A×B	0.169	0.515	0.124	0.557	0.161	0.522

** means a significant effect within a 99% confidence interval; * means a significant effect within a 95% confidence interval. Eta2 is the contribution rate of the factors to the test indicators.

Factors B and C had significant effects on the quality index Z_q (for B, $p = 0.013 < 0.05$; for C, $p = 0.003 < 0.05$), multiple index Z_m (for B, $p = 0 < 0.05$; for C, $p = 0 < 0.05$), and miss index Z_e (for B, $p = 0.046 < 0.05$; for C, $p = 0.02 < 0.05$); their interaction had significant effects on the quality index Z_q ($p = 0.001 < 0.05$) and multiple index Z_m ($p = 0 < 0.05$), while the other interactions had no significant effects on the three indexes.

According to the value of η^2 in Table 6 and Figure 9, the greater the value of η^2 , the greater influence of the factor. The order of factors affecting the quality index Z_q and multiple index Z_m was $B \times C > B > C > A$, and the order of factors affecting the miss index Z_e was $C > B > B \times C > A$.

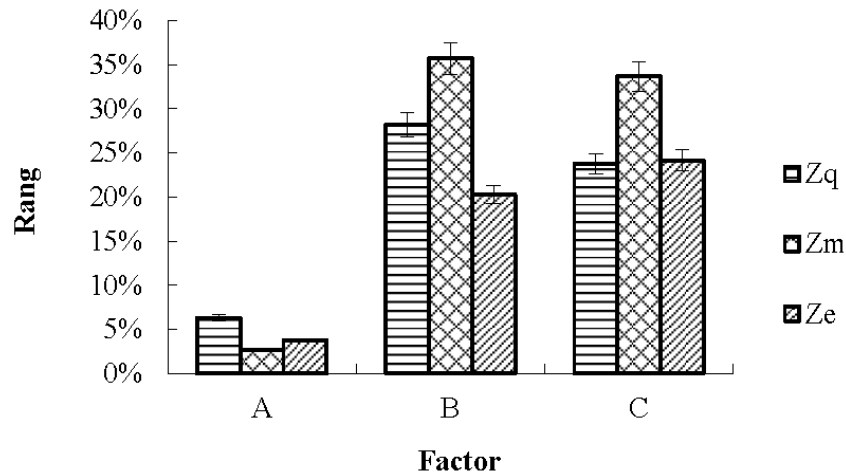


Figure 9. Range diagram.

Among the test indexes, the quality index Z_q can best reflect the planting uniformity. Meanwhile, a comprehensive analysis was conducted by referring to the multiple index Z_m and miss index Z_e , respectively. If the interaction has a significant influence on the test index, the interaction should be given priority. The orthogonal experiment results were extracted and sorted into Figure 10 and Table 7 to illustrate more clearly the optimal level of each factor and the interaction between B and C. It can be concluded that:

1. According to Figure 10, the quality index Z_q was highest at the first level of factor A and the second levels of factor B and C, respectively. Considering the interaction of B2C2, the quality index Z_q was the highest in Table 7, so the optimal combination for Z_q is A1B2C2;
2. The multiple index Z_m reached the minimum at the first levels of factor A, B, and C, respectively, in Figure 10. Z_m reached the minimum under multiple combinations of factor B and factor C, including B2C2 in Table 7;
3. The miss index Z_e reached the minimum at the first level of factor A and the third levels of B and C, respectively, in Figure 10. Considering the interaction of B and C, Z_e reached the minimum under multiple combinations of factor B and factor C and was only 2.78% under B2C2;
4. According to the three indexes, the optimal combination was A1B2C2. Under this combination, the quality index Z_q was 97.22% and the multiple index Z_m was 0%, while the miss index Z_e was 2.78%.

Table 7. The interaction of factor B and C.

Factor	Z_q			Z_m			Z_e		
	C1	C2	C3	C1	C2	C3	C1	C2	C3
B1	52.85%	82.07%	95.16%	0.00%	0.00%	0.00%	47.15%	17.93%	4.84%
B2	79.02%	97.22%	92.09%	0.00%	0.00%	7.91%	20.98%	2.78%	0.00%
B3	90.83%	86.03%	6.82%	0.00%	13.97%	93.18%	9.17%	0.00%	0.00%

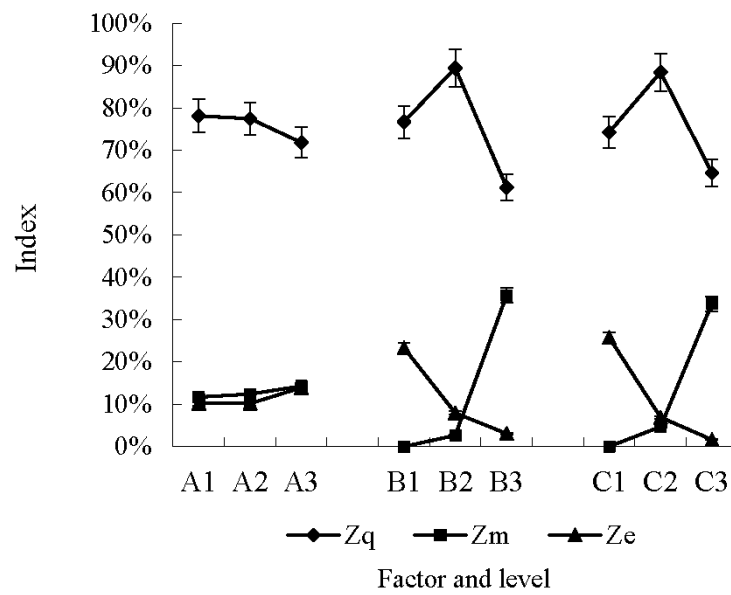


Figure 10. Affecting trends of different factors.

3.2. Analysis of Field Experiment Results

The planting effect of the sugarcane planter with single-bud billets in the field is shown in Figure 11a. As detailed in Figure 11b, the number of billets in a furrow was measured in units of 0.5 m, and a total of 427 units were counted.



Figure 11. Field planting experiment: (a) planting effect; (b) field measurement.

The results of the field planting experiments are listed in Table 8. When the rotational speed was 50 rpm, the increase in the forward speed had little effect on the quality index Z_q , and the multiple index Z_m increased slightly.

Table 8. Results of the field experiment on planting uniformity.

Rotational Speed (rpm)	Forward Speed (km/h)	Z_q	Z_e	Z_m
50	1.61	87.50%	10.58%	1.92%
50	2.23	87.64%	10.11%	2.25%
40	2.26	93.38%	4.41%	2.21%
30	2.25	71.72%	10.10%	18.18%

However, there are great differences in planting uniformity with different rotational speeds under the same forward speed. As indicated in Figure 12, the quality index Z_q is the highest (93.38%) while the miss index Z_e and the multiple index Z_m are the lowest (4.41%, 2.21%) when the rotational speed is 40 rpm. Therefore, the field planting uniformity was the best when the rotational speed of 40 rpm was matched with the forward speed of 2.2 km/h; there were 3 to 8 sugarcane billets per 0.5 m in the furrow. Under the high quality, the forward speed is better than the sugarcane-cum-potato planter (0.5m/s) [25].

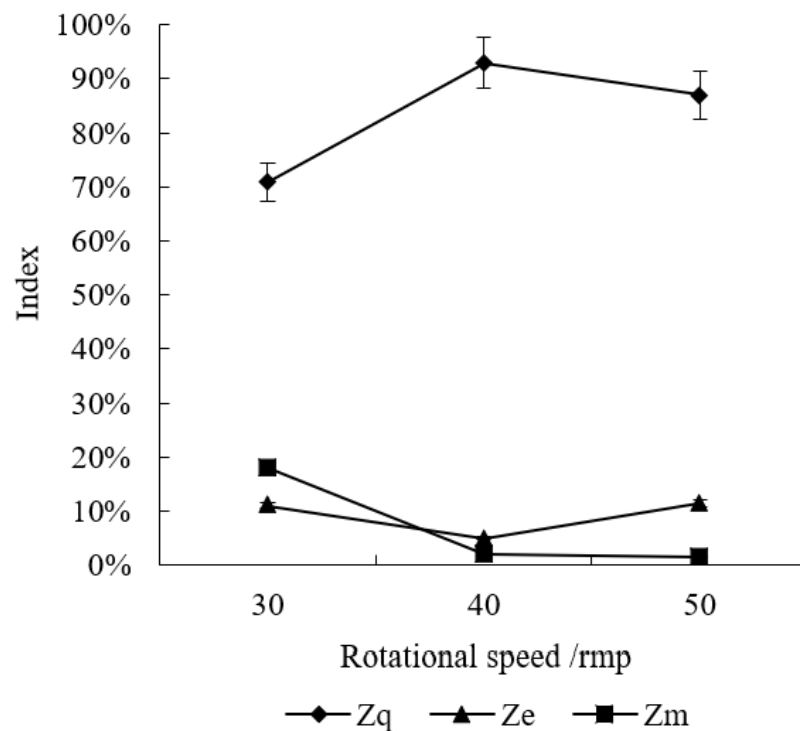


Figure 12. The effect of the rotational speed of the rake bar chain on field planting uniformity.

4. Conclusions

According to the single-factor and orthogonal experimental results in the laboratory, the rotational speed of the rake bar chain had no significant effect on the planting uniformity, while the angle of the rake bar chain, the number of billets, and their interaction had significant effects on the planting uniformity. Meanwhile, the quality index Z_q was the highest when the angle of the rake bar chain was 117° and the number of billets was 500, but it changed little and was high when the number of billets was between 500–800. The orthogonal experiment showed that optimal planting uniformity can be achieved under a rotation speed of 70 rpm, an angle of the rake bar chain of 117° , and a number of billets of 500. Under this condition, the quality index Z_q was 97.22% and the multiple index Z_m was 0.00%, while the miss index Z_e was 2.78%. Therefore, the single-bud planter was designed with an angle of the rake bar chain of 117° , and an adjustment plate was installed in the seed box to ensure that there were 500–800 billets in the effective working area of the rake bar chain. Three rake bar chains were adopted per seed box in the planter to increase the rate of seed filling.

Field experiments showed that when the rotation speed was 40 rpm and the forward speed was 2.26 km/h, the planting uniformity was the best and the quality index Z_q was 93.38%. There were 3 to 8 sugarcane billets per 0.5 m in the furrow. Due to the limited forward speed of the tractors in field operations, the range of forwarding speed was small in the field experiment. Future work will investigate the planting uniformity under different forward speeds and matching rotational speeds. High rotational speeds can also lead to the bud damage. Therefore, the rotational speed should be as low as possible when meeting

planting requirements. In addition, bud damage should be further studied in the future. These works provide great reference value for the future design, improvement, and field operation application of sugarcane single-bud billet planters.

Author Contributions: Conceptualization, Q.L. and Y.O.; methodology, M.W., X.Z., and Q.L.; data analysis, M.W.; writing—original draft preparation, M.W.; funding acquisition, Q.L. All authors have read and agreed to the published version of the manuscript.

Funding: This research was funded by National Key R&D Program of China (2020YFD1000600) and Guangdong Provincial Team of Technical System Innovation for Sugarcane Sisal Industry (2019KJ104-11).

Institutional Review Board Statement: Not applicable.

Informed Consent Statement: Not applicable.

Data Availability Statement: The data presented in this study are available on demand from the first author at (wmmscau@163.com).

Conflicts of Interest: The authors declare no conflict of interest.

References

- Singh, A.K.; Singh, P.R. Development of a Tractor Operated Sugarcane Cutter Planter for Mechanisation of Sugarcane Planting in Deep Furrows. *Sugar Tech* **2016**, *19*, 1–8. [CrossRef]
- Cebim, G.J. Plantio mecânico de cana-de-açúcar (*Saccharum* spp.): Desempenho operacional e econômico. *Stab* **2008**, *31*, 40–47.
- Rípoli, M.L.; Rípoli, T.C.; Casagrandi, D.V.; Ide, B.Y. Evaluation of five sugar cane planters. *Eng. Agriculture Jaboticabal* **2010**, *30*, 1110–1122. [CrossRef]
- Khedkar, M.B.; Kamble, A.K. Evaluation of mechanized planting of sugarcane. *Int. J. Agric. Eng.* **2008**, *1*, 136–139.
- Deshbhandari, A.; Adesh, K.S.; Karthik, K.S.; Dileep, S.L. Design and Fabrication of Sugarcane Node Cutter Machine. Ph.D. Thesis, CMR Institute of Technology, Bangalore, India, 2021.
- Saengprachatanarug, K.; Chaloeonthoi, C.; Kamwilaisak, K.; Kasemsiri, P.; Chaun-Udom, S.; Taira, E. Effect of metering device arrangement to discharge consistency of sugarcane billet planter. *Eng. Agric. Environ. Food* **2018**, *11*, 139–144. [CrossRef]
- Jain, R.; Solomon, S.; Shrivastava, A.K.; Chandra, A. Sugarcane bud chips: A promising seed material. *Sugar Tech* **2010**, *12*, 67–69. [CrossRef]
- Salassi, M.E.; Breaux, J.B.; Hoy, J.W. Estimated cost differences between whole-stalk and billet sugarcane planting methods in Louisiana. *J. Am. Soc. Sugar Cane Technol.* **2004**, *24*, 250–257.
- Moslem, N.; Jalil, R.; Ali, K. Fabrication and evaluation of a metering device for a sugarcane billet planter. *Yüzüncü Yıl Üniversitesi Tarım Bilimleri Derg.* **2015**, *25*, 1–12.
- Galal, M.O.A. A new technique for planting sugarcane in Egypt. *Inst. Integr. Omics Appl. Biotechnol. J.* **2016**, *7*, 15–21.
- Gujja, B.; Loganandhan, N.; Goud, V.V.; Agarwal, M.; Dalai, S. Sustainable Sugarcane Initiative (SSI) Improving Sugarcane Cultivation. *ICRISAT Prasesh India* **2009**, 1–36. Available online: <http://www.agritech.tnau.ac.in/pdf/English%20SSI.png> (accessed on 18 March 2022).
- Patnaik, J.R.; Singh, S.N.; Sarangi, D.; Nayak, P.K. Assessing potentiality of bud chip technology on sugarcane productivity, profitability and sustainability in real farming situations under south east Coastal Plain Zone of Odisha India. *Sugar Tech* **2017**, *19*, 373–377. [CrossRef]
- Wang, M.; Liu, Q.; Ou, Y.; Zou, X. Experimental Study of the Seed-Filling Uniformity of Sugarcane Single-Bud Billet Planter. *Sugar Tech* **2021**, *23*, 827–837. [CrossRef]
- Taghinezhad, J.; Alimardani, R.; Jafary, A. Design and evaluation of three metering devices for planting of sugarcane billets. *J. Agric. Sci.* **2014**, *20*, 164–174.
- Robotham, B.G.; Chappell, W.J. High quality planting billets-whole-stalk planter billets compared to billets from modified and unmodified harvesters. In Proceedings of the 2002 Conference of the Australian Society of Sugar Cane Technologists held at Cairns, Queensland, Australia, 29 April–2 May 2002; pp. 199–206.
- Razavi, J.; Namjoo, M. Determination of forward speed effect on planting uniformity in a sugarcane billet planter. In Proceedings of the XVIIth World Congress of the International Commission of Agricultural and Biosystems Engineering (CIGR), Quebec City, QC, Canada, 13–17 June 2010. Paper No. CSBE001142.
- Taghinezhad, J.; Alimardani, R.; Jafari, A. Optimization cane traction output from hopper in full-automatic sugarcane planters by using response surface modeling and analytical hierarchy process. *Agric. Eng. Int. CIGR J.* **2013**, *15*, 138–147.
- Saengprachatanarug, K.; Wongpichet, S.; Ueno, M.; Taira, E. Comparative discharge and precision index of a sugar cane billet planter. *Appl. Eng. Agric.* **2016**, *32*, 561–567.
- Kachman, S.D.; Smith, J.A. Alternative measures of accuracy in plant spacing for planters using single seed metering. *Trans. ASAE* **1995**, *38*, 379–387. [CrossRef]

20. Kumar, M.; Dogra, B.; Sanghera, G.S.; Manes, G.S. Modification and evaluation of commercially available sugarcane trench planter for its application under Punjab conditions. *Sugar Tech* **2019**, *21*, 586–595. [[CrossRef](#)]
21. Johnson, R.M.; Viator, R.P.; Richard, E.P., Jr. Effects of billet planting rate and position on sugarcane yields in Louisiana. *J. Am. Soc. Sugar Cane Technol.* **2011**, *31*, 79–90.
22. Silva, M.D.A.; Carlin, S.D.; Perecin, D. Fatores que afetam a brotação inicial da cana-de-açúcar. *Revista Ceres* **2004**, *51*, 457–466.
23. Compagnon, A.M.; da Silva, R.P.; Furlani, C.E.A.; Cavichioli, F.A.; Arriel, F.H. Operational uniformity for a sugarcane planter. *Afr. J. Agric. Res.* **2017**, *12*, 953–962.
24. Yazgi, A.; Degirmencioglu, A. Measurement of seed spacing uniformity performance of a precision metering unit as function of the number of holes on vacuum plate. *Measurement* **2014**, *56*, 128–135. [[CrossRef](#)]
25. Gupta, R.; Singh, P.R.; Singh, A.K. Development of sugarcane-cum-potato planter for mechanisation of simultaneous planting of sugarcane and potato. *Sugar Tech* **2017**, *19*, 517–525. [[CrossRef](#)]

Article

Finite Element Model Construction and Cutting Parameter Calibration of Wild Chrysanthemum Stem

Tao Wang, Zhengdao Liu *, Xiaoli Yan, Guopeng Mi, Suyuan Liu, Kezhou Chen, Shilin Zhang, Xun Wang, Shuo Zhang and Xiaopeng Wu

College of Mechanical and Electronic Engineering, Northwest A&F University, Xianyang 712100, China; wangtao666@nwafu.edu.cn (T.W.); yxl9212@nwsuaf.edu.cn (X.Y.); miguopeng@nwafu.edu.cn (G.M.); liusuyuan@nwafu.edu.cn (S.L.); ckz@nwafu.edu.cn (K.C.); shilinzhang@nwafu.edu.cn (S.Z.); lwxn@nwafu.edu.cn (X.W.); zhangshuo914@nwafu.edu.cn (S.Z.); 2021055938@nwafu.edu.cn (X.W.)

* Correspondence: liuzd@nwafu.edu.cn

Abstract: Due to a lack of an accurate model in finite element simulation of mechanized harvesting of wild chrysanthemum, the stem of wild chrysanthemum in the harvesting period is taken as the research object. ANSYS Workbench 19.0 software and LS-DYNA software (LS-PrePOST-4.3-X64) are used to calibrate the finite element simulation model of wild chrysanthemum stem cutting. The stem diameter distribution at the cutting height of the chrysanthemum is obtained. The maximum shear forces at different diameters (7 mm, 8 mm, 9 mm, 10 mm, and 11 mm) within the cutting range are determined as 120.0 N, 159.2 N, 213.8 N, 300.0 N, and 378.2 N, respectively, by using a biomechanical testing machine and a custom-made shear blade. The Plastic_Kinematic failure model is used to simulate the cutting process by the finite element method. The Plackett–Burman test is employed to screen out the test factors that significantly affect the results, namely, the yield stress, failure strain, and strain rate parameter C. The regression model between the shear force and significant parameters is obtained by central composite design experiments. To obtain the model parameters, the measured values are substituted into the regression equation as the simulation target values. In other words, the yield stress is 17.96 MPa, the strain rate parameter C is 87.27, and the failure strain is 0.0387. The maximum shear force simulation test is carried out with the determined parameters. The results showed that the maximum error between the simulated and the actual value of the maximum shear force of wild chrysanthemum stems with different diameters is 7.8%. This indicates that the calibrated parameters of the relevant stem failure model can be used in the finite element method simulation and provide a basis for subsequent simulations.

Keywords: *Chrysanthemum indicum* L.; maximum shear force; finite element; calibration

Citation: Wang, T.; Liu, Z.; Yan, X.; Mi, G.; Liu, S.; Chen, K.; Zhang, S.; Wang, X.; Zhang, S.; Wu, X. Finite Element Model Construction and Cutting Parameter Calibration of Wild Chrysanthemum Stem.

Agriculture **2022**, *12*, 894. <https://doi.org/10.3390/agriculture12060894>

Academic Editors: Muhammad Sultan, Redmond R. Shamshiri, Md Shamim Ahamed and Muhammad Farooq

Received: 1 June 2022

Accepted: 19 June 2022

Published: 20 June 2022

Publisher's Note: MDPI stays neutral with regard to jurisdictional claims in published maps and institutional affiliations.



Copyright: © 2022 by the authors. Licensee MDPI, Basel, Switzerland. This article is an open access article distributed under the terms and conditions of the Creative Commons Attribution (CC BY) license (<https://creativecommons.org/licenses/by/4.0/>).

1. Introduction

Wild chrysanthemum is a common Chinese herbal medicine characterized by antibacterial and inflammatory effects that can be used to treat diseases such as influenza, cerebrospinal meningitis, and snake bite [1,2]. Its stem characteristics are characterized by a high degree of lignification and hardness. Most of the wild chrysanthemum harvest is artificial. Approximately 15–20 people are required per day per acre to harvest wild chrysanthemum, but the harvest cost is relatively high and rises every year. The mechanized harvest of wild chrysanthemum is in its initial stage. The main attempt is to harvest in sections. The existing windrowers (such as the rape windrower) are used for harvesting, but the efficiency is not high. About a third of the thick stems are difficult to cut. The finite element simulation method has been used in mechanical optimization in recent years [3]. The finite element method has the outstanding advantages of high efficiency, low costs, and shortening the research and the development cycles [4].

A series of finite element simulation cutting studies were carried out to explore the cutting performance of crops in agriculture. In the 1970s, Tay first used the finite

element method to calculate orthogonal cutting tools [5]. In 2004, Yen et al. [6] analyzed the relationship between the cutting-edge shape and the cutting force during cutting via the finite element method. Meng et al. [7] used large CAE software ANSYS/LS-DYNA to perform dynamic simulation on small mulberry tree cutting circular saw blades. The results showed that, under the optimal parameter matching, the cutting section of the mulberry branch performed well, and the working efficiency was relatively high. Souza et al. [8] used finite element software to explore the influence of the harvester speed on the harvesting process in mechanized coffee harvesting. Yang et al. [9] established a sugarcane cutting system model based on the FEM (finite element method) and SPH (smoothed particle hydrodynamics) coupling algorithm. Moreover, the authors verified the rationality of the model with physical tests. The finite element simulation method was used to study the force on the sugarcane root, which is of great significance for reducing the cutting resistance. Fielke [10] predicted the influence of cutting edges with different geometric shapes on tillage force via FEM. Ibrahim et al. [11] studied the influence of the cutting depth, cutting speed, and cutting angle on the tillage force of a template plow used in North Africa. The results showed that vertical force decreased linearly with an increase in the cutting angle. When the working depth was 150 mm, the speed was 1 m/s, the lifting angle was 20°, the cutting angle was 30° to 45°, and the energy consumption was minimized. In China, the use of finite element cutting started relatively late. Zhang et al. [12] used ANSYS/LS-DYNA software to establish the geometric and material models of the cutting device in sugarcane cutting machinery. Two unknown tensors of sugarcane were experimentally and numerically determined, namely, the radial elastic modulus of sugarcane $E_x = E_y = 1934$ MPa and the radial Poisson's ratio of sugarcane $U_{xz} = U_{yz} = 0.314$. Guo et al. [13] obtained stress and energy changes in cutting tomato vine straw using LS-DYNA software. Xi et al. [14] conducted a display dynamics analysis on the process of cutting the stem with a rotor milling cutter. The results showed that the power consumption of the cutting stem was minimized when the rotor milling cutter speed was 1400 r/min, the blade thickness was 7 mm, and the blade angle was 25°. Huang et al. [15] used finite element technology to investigate the effect of the cutter angle and cutting speed on the cutting force and improve the performance of the sugarcane cutter. The results showed that the cutting force was minimized when the cutter angle was 0° and the cutter speed was 0.5–0.9 m/s.

Few simulation studies currently exist on the cutting of wild chrysanthemum stem. Furthermore, the simulation process lacks more accurate wild chrysanthemum stem material model parameters. Based on the maximum shear force, physical tests were employed to determine different diameters of wild chrysanthemum flower stalks. On this basis, the Plackett–Burman test and a central composite design experiment were carried out by using finite element simulation to calibrate the stem material parameters. Different diameters of wild chrysanthemum stem test values were compared with the simulation results to validate the accuracy of the calibration parameters. The proposed model will provide a reference for selecting finite element cutting material parameters of wild chrysanthemum stem.

2. Materials and Methods

2.1. Materials

Wild chrysanthemum stems from the biennial wild chrysanthemum cultivation base in Qianxian county, Shaanxi (jointly cultivated by China Resources Sanjiu Medical & Pharmaceutical Co., Ltd. (Shenzhen, China), and Shaanxi Quintuonong Agricultural Technology Development Co., Ltd. (Xi'an, China)) were selected for the experiment. As shown in Figure 1, the row spacing was 60 cm and the plant spacing was 50 cm. The average moisture content was 48.98%. The test materials were randomly selected on 6 November 2021. Fresh plants with good growth and no disease and insect pests were selected, and mechanical damage to the stem was avoided as best as possible. The chrysanthemum stems were cut horizontally with respect to the ground.



Figure 1. Wild chrysanthemum stem planting diagram.

2.2. *Wild Chrysanthemum Stem Diameter Distribution*

Fifty wild chrysanthemum stems were randomly selected, and the diameter of each wild chrysanthemum stem at a height of 20 cm was measured with an electronic vernier caliper (Mitutoyo Co., Ltd., Kanagawa, Japan) with a precision of 0.01 mm (according to the wild chrysanthemum base measurement, the stubble height of wild chrysanthemum stem was roughly 20 cm). The stem of each wild chrysanthemum was measured three times and averaged. The fitting curve of the normal distribution of the obtained size is shown in Figure 2. The diameter of wild chrysanthemum stems mostly varied between 7 mm and 11 mm at the stubble height.

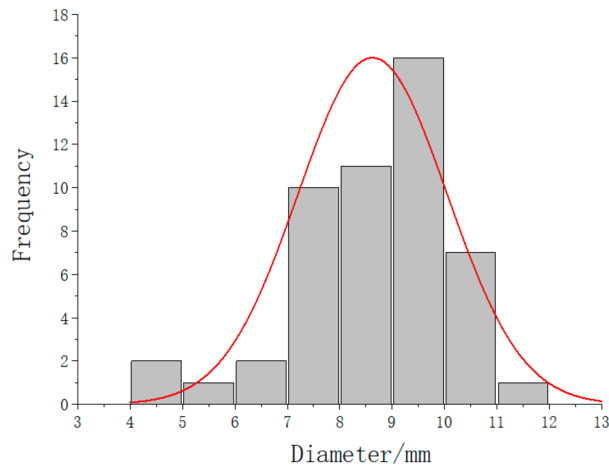


Figure 2. Normal distribution of wild chrysanthemum stem diameter.

2.3. Shear Tests

The test samples were collected from the same base mentioned above. Wild chrysanthemum stems of 7–11 mm were divided into five grades to determine the cutting effect of wild chrysanthemum stems with different diameters. Six groups of experiments were conducted for each grade of stems, and a total of 30 wild chrysanthemum stem samples were made. A total of 25 mm lengths were taken upward and downward by taking the position of the stem at 20 cm as the midpoint, and the final length of each sample was 50 mm.

The main instrument used in this test is the experimental biomechanics machine (DDL10) with a custom-made blade, as shown in Figure 3. The blade is made of steel, and its size is shown in Table 1. The material parameters are shown in Table 2. The shear process that utilizes a biomechanical testing machine is shown in Figure 4. The distance between the two supports is 20 mm, the cutting speed is 100 mm/min, and the starting preload is less than 5 N.

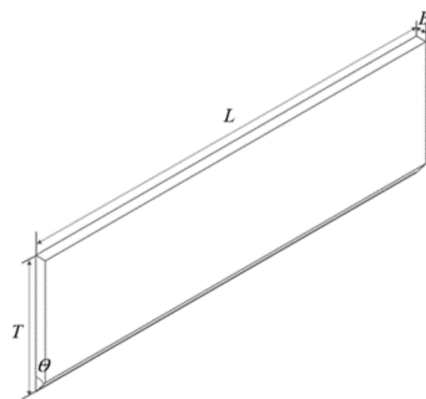


Figure 3. Custom-made cutting blade, where L is the length, T is width, B is the thickness, and θ is the edge angle.

Table 1. Custom-made blade size.

Physical Characteristics	Units	Size
L	mm	90
T	mm	28
B	mm	2.3
θ	$^{\circ}$	37.5

Table 2. Custom-made blade materials [16].

Parameters	Units	Numerical Value
Density	kg/m ³	7800
Elasticity modulus	GPa	207
Poisson's ratio	1	0.3

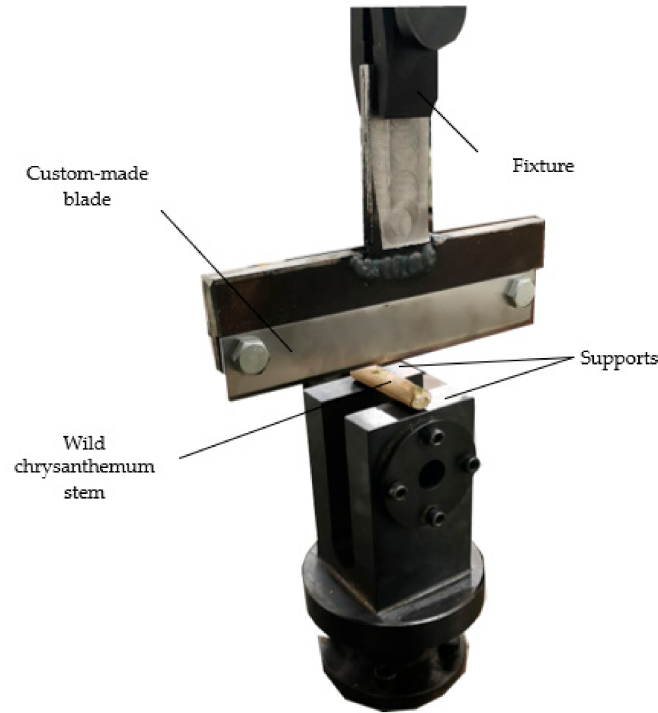


Figure 4. Shear test site.

2.4. Finite Element Model

According to the material and structural characteristics of wild chrysanthemum stem, the cuticle and lumen of the stem are defined as anisotropic, non-uniform, and non-linear viscoelastic materials, as shown in Figure 5. Compared with the cuticle, the lumen part of stem had a minor effect on cutting. The stem was regarded as a hollow cylinder, and its material model was defined as an isotropic elastic–plastic material model to facilitate modeling. After measurement, the average ratio of the inner to the outer diameter of the wild chrysanthemum stem was 0.41.



Figure 5. Structure of wild chrysanthemum stem.

2.4.1. Selection of Stem Material Model in the LS-DYNA Software

LS-DYNA software is a display solution software that can solve the dynamic problem of highly nonlinear structure and effectively perform finite element analysis of the cutting process. In essence, the numerical analysis of the stem cutting process is the failure of the unit material defined after large deformation, or stress overload of the stem unit, i.e., stem cutting can be visually represented. The wild chrysanthemum stem was regarded as a whole, and its material model was defined as Plastic_Kinematic, i.e., an isotropic elastoplastic material model. The equivalent fracture strain defined by the model can be expressed as [16,17]:

$$\sigma_y = \left| 1 + \left(\frac{\dot{\epsilon}_1}{C} \right)^P \right| (\sigma_o + \beta E_p \epsilon_p^f),$$

where $\dot{\epsilon}_1$ is the strain rate, C and P are strain rate parameters, E_p is the plastic hardening modulus, and ϵ_p^f is the effective plastic strain.

2.4.2. Modeling in Ansys Workbench and LS-DYNA Software

SOLIDWORKS 2018 software was used to establish a 3D model of a wild chrysanthemum cutting with a diameter of 8 mm. Then, the model was imported into the Explicit Dynamic (LS-DYNA Export) module in Ansys Workbench 19.0. The stem, the blade, and the supports were divided into grids. The grid size of the stem was set as 1 mm, and the final number of grids was 7624. The overall model is shown in Figure 6.

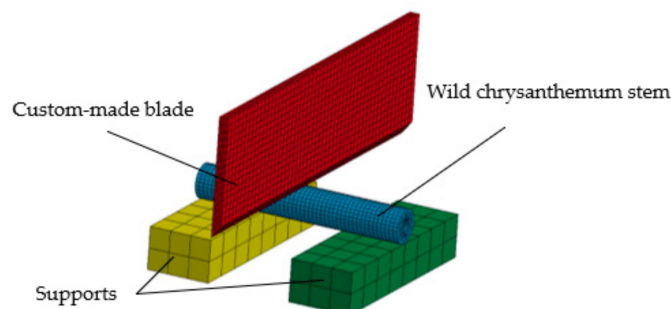


Figure 6. Finite element cutting model.

The following constraints were added to the model. The displacement of the blade model was constrained in the X- and Y-directions, whereas the rotation was constrained in the X-, Y-, and Z-directions. Displacement and rotation of the support base model were constrained in the X-, Y-, and Z-directions, but the stem model was not constrained. The blade speed loading direction was defined as the Z-direction, the constant loading speed was 100 mm/min, and the simulation time was set to 0.5 s. Other parameters were set in LS-DYNA post-processing software LS-PrePOST-4.3-X64. The material parameters were set as shown in Table 3, and the contact parameters [13,16] were set as shown in Table 4.

Table 3. Material parameters.

Part	Materials	Parameters
Blade and base	MAT_RIGID	See Table 2
Stem	MAT_Plastic_Kinematic	Screening by test

Table 4. Contact parameters.

Contact Position	Contact Type	Friction Coefficient
Blade and stem	ERODING_SURFACE_TO_SURFACE	Static friction coefficient 0.15, dynamic friction coefficient 0.1
Stem and base	AUTOMATIC_SURFACE_TO_SURFACE	

The stem and blade models should not come in contact when defining the contact mode. However, the distance between them should be as close as possible to reduce the calculation free time before shearing. Simulation fracture is shown in Figure 7.

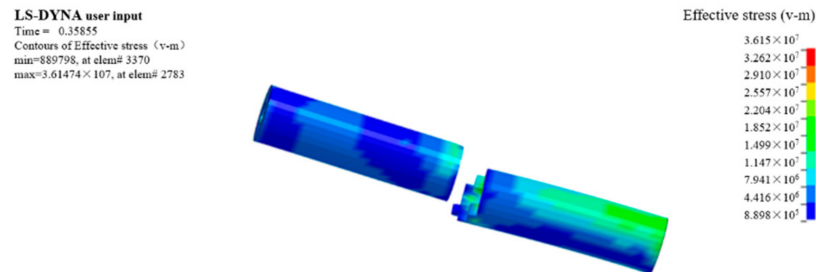


Figure 7. Simulated fracture diagram.

2.5. Parameter Calibration Experimental Design

2.5.1. Plackett–Burman Experimental Design

The Plackett–Burman experiment was designed using Design-Expert (version 11.0.4.x64) software to screen the parameters that significantly affect the maximum shear force. The Plackett–Burman test was carried out on the density, elastic modulus, Poisson’s ratio, yield stress, shear modulus, hardening parameter, strain rate parameter C, strain rate parameter P, and failure strain as experimental factors. The research on mechanical and physical characteristics of wild chrysanthemum stem is not perfect, especially regarding the parameters of the finite element model. In this paper, parameter values of various stems in the literature were employed to determine the value or range of each parameter in the test [16]. Test parameters are shown in Table 5.

Table 5. Plackett–Burman test parameters.

Symbol	Parameters	Low Level	High Level
X1	Density (kg/m ³)	1000	1200
X2	Elastic modulus (Mpa)	800	1200
X3	Poisson’s ratio	0.2	0.4
X4	Yield stress (Mpa)	10	20
X5	Shear modulus (Mpa)	0.4	0.6
X6	Hardening parameter	0	0.1
X7	Strain rate (C)	80	100
X8	Strain rate (P)	4	12
X9	Failure strain	0.01	0.05

2.5.2. Central Composite Experimental Design

The central composite design experiments were carried out for the selected significance parameters. The middle value of the high and low level of non-significant factors was selected. The stem model of wild chrysanthemum was established to carry out simulation analysis of the maximum shear force, thus obtaining the regression model between the maximum shear force and significance parameters. The shear force value of the chrysanthemum stem was substituted into the regression equation as the simulation target to obtain the simulation model parameters.

3. Results and Discussion

3.1. Plackett–Burman Test

The test design and results are shown in Table 6. Design-Expert software was used for significance analysis and variance analysis of the data, and the results are shown in Table 7.

Table 6. Design scheme and results of the Plackett–Burman test.

No.	X1	X2	X3	X4	X5	X6	X7	X8	X9	Maximum Shear Force/N
1	1000	800	0.4	10	0.6	0.1	80	12	0.05	90.3
2	1200	1200	0.4	10	0.4	0	100	4	0.05	100
3	1000	800	0.2	10	0.4	0	80	4	0.01	44.6
4	1000	1200	0.2	20	0.6	0	100	12	0.05	180.3
5	1200	800	0.4	20	0.4	0.1	100	12	0.01	123.9
6	1200	1200	0.2	10	0.4	0.1	80	12	0.05	81.6
7	1200	1200	0.2	20	0.6	0.1	80	4	0.01	101.4
8	1000	1200	0.4	20	0.4	0	80	12	0.01	105.8
9	1000	1200	0.4	10	0.6	0.1	100	4	0.01	43
10	1200	800	0.2	10	0.6	0	100	12	0.01	58.7
11	1200	800	0.4	20	0.6	0	80	4	0.05	182
12	1000	800	0.2	20	0.4	0.1	100	4	0.05	201.3

Table 7. Significance analysis of Plackett–Burman test parameters.

Parameters	Effect	Contribution/%	Sum of Squares	F-Value	p-Value
X1	−2.95	0.08	26.11	0.6131	0.5156
X2	−14.78	2.09	655.64	15.40	0.0592
X3	−3.82	0.14	43.70	1.03	0.4177
X4	79.42	60.19	18,921.02	444.32	0.0022 **
X5	−0.25	0.001	0.1875	0.0044	0.9531
X6	−4.98	0.24	74.50	1.75	0.3169
X7	16.92	2.73	858.52	20.16	0.0462 *
X8	−5.28	0.27	83.74	1.97	0.2959
X9	59.68	34	10,686.30	250.95	0.0040 **

Note: ** represents extremely significant effect ($p < 0.01$), * represents significant effect ($p < 0.05$).

According to Table 7, X₄ and X₉ extremely significantly affected the maximum shear force of the stem ($p < 0.01$). X₇ significantly affected the maximum shear force of the stem ($p < 0.05$), whereas the remaining parameters did not significantly affect the maximum shear force ($p > 0.05$). Therefore, yield stress (X₄), failure strain (X₉), and strain rate parameter C (X₇) were selected as three key factors for the response surface optimization and design.

3.2. Central Composite Design Experiment

In the central composite test, all non-significant test parameters were adopted with high and low intermediate values, and the remaining significant factors were selected according to the test. The test factor coding is shown in Table 8, and the central composite experiment design and the simulation results are shown in Table 9. Multiple regression fitting was conducted on the data in Table 9, thus obtaining the wild chrysanthemum flower regression equation of the maximum shear force:

$$Y = 120.42 + 31.82X_4 + 11.20X_9 + 4.22X_7 - 4.75X_4X_9 - 3.25X_4X_7 - 1.75X_9X_7 + 1.29X_4^2 - 0.8292X_9^2 - 2.88X_7^2. \quad (1)$$

Table 8. Central composite design factor coding.

Factor Level	X ₄	X ₉	X ₇
1.682	20.00	0.05	100.00
1	17.98	0.04	95.95
0	15.00	0.03	90.00
−1	12.02	0.02	84.05
−1.682	10.00	0.01	80.00

Table 9. Test results and scheme of central composite design experiment.

No.	X ₄	X ₉	X ₇	Maximum Shear Force/N
1	14.995	0.03	90	122
2	12.02	0.02	95.95	84
3	14.995	0.03	90	112
4	12.02	0.04	95.95	107
5	17.98	0.02	84.05	151
6	14.995	0.0468179	90	140
7	9.99167	0.03	90	76
8	19.9983	0.03	90	175
9	17.98	0.04	84.05	162
10	12.02	0.02	84.05	64
11	14.995	0.03	90	123
12	14.995	0.03	90	124
13	12.02	0.04	84.05	102
14	14.995	0.03	90	121
15	14.995	0.03	79.9933	120
16	14.995	0.03	100.007	140
17	17.98	0.02	95.95	150
18	17.98	0.04	95.95	162
19	14.995	0.03	90	120
20	14.995	0.0131821	90	99

According to variance analysis (Table 10), the overall model fitting degree was extremely significant ($p < 0.0001$). X₄, X₉, and X₇ extremely significantly affected the maximum shear force, whereas X₄, X₉, and X₇² significantly affected the maximum shear force. X₄, X₇, X₉X₇, X₄², and X₉² had no significant effect on the maximum shear force, indicating that the influence of the test factors on the overall response value had a higher-power relationship. The p -value of the lack of fit was 0.3189, indicating that no other major factors affected this index. The determination coefficient R² was equal to 0.99, indicating that the regression model agreed with the actual results and may be used to predict the maximum shear force of the stem.

Table 10. ANOVA of central composite design experiment.

Source	Sum of Squares	df	Mean Square	F-Value	p -Value
Model	16,225.35	9	1802.82	75.48	<0.0001 **
X ₄	13,823.69	1	13,823.69	578.77	<0.0001 **
X ₉	1713.04	1	1713.04	71.72	<0.0001 **
X ₇	243.24	1	243.24	10.18	0.0096 **
X ₄ X ₉	180.50	1	180.50	7.56	0.0205 *
X ₄ X ₇	84.50	1	84.50	3.54	0.0894
X ₉ X ₇	24.50	1	24.50	1.03	0.3350
X ₄ ²	24.07	1	24.07	1.01	0.3392
X ₉ ²	9.91	1	9.91	0.4148	0.5340
X ₇ ²	119.79	1	119.79	5.02	0.0490 *
Residual	238.85	10	23.88		
Lack of fit	145.51	5	29.10	1.56	0.3189
Pure error	93.33	5	18.67		
Core total	16,464.20	19			

Note: ** represents extremely significant effect ($p < 0.01$), * represents significant effect ($p < 0.05$).

The maximum shear force of experimentally measured wild chrysanthemum stem with a diameter of 8 mm was taken as the target value in the optimization module of the

Design-Expert software. The optimization was carried out to seek the optimal solution for the regression model. The objectives and constraints equations can be expressed as:

$$\begin{cases} Y(X_4, X_9, X_7) = 159.2 \\ \text{s.t.} \begin{cases} 10 \leq X_4 \leq 20 \\ 0.01 \leq X_9 \leq 0.05 \\ 80 \leq X_7 \leq 100. \end{cases} \end{cases} \quad (2)$$

The calibration parameter results are shown in Table 11.

Table 11. Parameter calibration values.

Parameter	Numerical Calibration
Yield stress	17.96
Failure strain	0.0387
Strain rate parameter C	87.27

3.3. Validation Tests

In order to ensure the feasibility, accuracy, and universal applicability of the calibrated model parameters, stem cutting models with diameters of 7 mm, 9 mm, 10 mm, and 11 mm were established for verification. The models were set according to the calibrated parameters (Table 12), whereas the remaining setting conditions remained unchanged. The finite element model was established and the actual test results were compared.

Table 12. Finite element simulation parameters of wild chrysanthemum stem.

Parameters	Value
X ₁	1100
X ₂	1000
X ₃	0.3
X ₄	17.96
X ₅	0.5
X ₆	0.05
X ₇	87.27
X ₈	8
X ₉	0.0387

The maximum shear force of wild chrysanthemum stem measured by physical tests and the one obtained by the simulation are shown in Table 13.

Table 13. Comparison of the maximum shear force of wild chrysanthemum stem.

Stem Diameter/mm	Maximum Shear Force Measured/N	Maximum Shear Force Simulation Value/N	Error/%
7	120	129.4	−7.8
8	159.2	169	−6
9	213.8	201.4	5.8
10	300	281	6.3
11	378.2	350	−7.5

The maximum shear force error between the simulation and the actual test was less than 7.8%. Moreover, the maximum shear force had a good linear relationship with the stem diameter, indicating that the parameter calibration method was correct and the established finite element model was accurate.

The influence of physical parameters on the maximum shear force was not completely consistent for different crop stems. The yield stress significantly affected the maximum

shear force of the wild chrysanthemum stem, which is consistent with Jiang's [16] research on the rape stem. The remaining two significant factors were different, which might have been caused by the complex internal structure of different stems. Zheng et al. [18] constructed a finite element model of cotton rod and calibrated the cutting parameters. Contrary to the method proposed in this paper, the author regarded the cotton stalk as an anisotropic material. Through a series of physical tests, the author measured nine parameters that could represent the mechanical properties of an anisotropic material and complete the calibration. In this paper, the stem of wild chrysanthemum was regarded as an isotropic material. Plackett–Burman tests and a central composite design experiment were used to calibrate the stem parameters, and the physical cutting test was used to verify the calibration accuracy. Liao et al. [19,20] used discrete elements to calibrate stem parameters for the rape stalk shredding problem and obtained significant factors for the angle of repose. The difference occurred due to various types of problems and measurement indexes.

4. Conclusions

(1) According to the preliminary investigation, the cutting height of wild chrysanthemum stem was approximately equal to 20 cm. The diameter of the cutting height of the wild chrysanthemum stem was experimentally measured, and the diameter of the stem was mostly distributed between 7 mm and 11 mm within the cutting range.

(2) Through the Plackett–Burman test, the yield stress, failure strain, and strain rate parameter C , all of which significantly affected the results, were selected. The central composite design experiment was carried out by the finite element method to investigate the effects of yield stress, failure strain, and strain rate parameter C on the maximum shear force of the stem. Moreover, the regression model between the shear force and significance parameters was obtained. The measured values were substituted into the regression equation as simulation target values to obtain the following simulation model parameters: yield stress 17.96 Mpa, failure strain 0.0387, and strain rate parameter C 87.27.

(3) The calibration parameters were used to establish simulation models of stem cutting with different diameters. The highest error between the simulation and actual tests was 7.8%. In addition, the maximum shear force had a good linear relationship with stem diameter, indicating that the calibration parameters were accurate and reliable and that the established finite element model was correct and feasible.

In this paper, the physical shear test was used as a comparison to calibrate the failure model parameters of the stem of wild chrysanthemum, which filled the blank of finite element cutting model parameters of wild chrysanthemum stem.

Author Contributions: Conceptualization, T.W.; methodology, G.M.; software, S.L.; validation, S.Z. (Shilin Zhang); formal analysis, X.W. (Xun Wang); investigation, K.C.; resources, S.Z. (Shuo Zhang) and X.W. (Xiaopeng Wu); data curation, T.W.; writing—original draft preparation, T.W.; writing—review and editing, Z.L.; visualization, T.W.; supervision, X.Y.; project administration, Z.L.; funding acquisition, Z.L. All authors have read and agreed to the published version of the manuscript.

Funding: This research was funded by the National Natural Science Foundation of China youth Science Foundation project (No. 32101629), the Key Research and Development Program of Shaanxi Province, China (No. 2022NY-227), and the China Postdoctoral Science Foundation project (No. 2021M692657).

Institutional Review Board Statement: Not applicable.

Informed Consent Statement: Not applicable

Data Availability Statement: Not applicable.

Conflicts of Interest: The authors declare no conflict of interest.

References

- Li, G.; Chen, Y.; Wang, P.; Guan, R.; Ye, Y.; Zhao, J.; You, A.; Bi, Y. Protection of terpenes and flavonoids from *Chrysanthemi Indici* Flos on immunological liver injury. *Chin. Tradit. Herb. Drugs* **2013**, *44*, 3510–3514.
- Jiang, Z.; Li, X.; Luo, B. Anti-inflammatory and Analgesic Effects of Essential Oil from *Chrysanthemi Indici* Flos. *Chin. J. Exp. Tradit. Med. Formulae* **2015**, *21*, 124–127.
- Peng, W. The application of virtual reality technology in mechanical engineering. *Sci. Technol. Innov. Her.* **2015**, *12*, 39.
- Wu, Y.; Xie, W. Analysis of the development status and application direction of virtual design. Analysis of the development status and application direction of virtual design. *Pop. Sci. Technol.* **2010**, *12*, 18–19.
- Tay, A.O.; Stevenson, M.G.; De Vahl Davis, G.; Oxley, P.L.B. A numerical method for calculating temperature distributions in machining, from force and shear angle measurements. *Int. J. Mach. Tool Des. Res.* **1976**, *16*, 335–349. [[CrossRef](#)]
- Yen, Y.; Jain, A.; Altan, T. A finite element analysis of orthogonal machining using different tool edge geometries. *J. Mater. Processing Technol.* **2004**, *146*, 72–78. [[CrossRef](#)]
- Meng, Y.; Wei, J.; Wei, J.; Chen, H.; Cui, Y. An ANSYS/LS-DYNA simulation and experimental study of circular saw blade cutting system of mulberry cutting machine. *Comput. Electron. Agric.* **2019**, *157*, 38–48. [[CrossRef](#)]
- Souza, V.H.S.; Dias, G.L.; Santos, A.A.R.; Costa, A.L.G.; Santos, F.L.; Magalhães, R.R. Evaluation of the interaction between a harvester rod and a coffee branch based on finite element analysis. *Comput. Electron. Agric.* **2018**, *150*, 476–483. [[CrossRef](#)]
- Yang, W.; Zhao, W.; Liu, Y.; Chen, Y.; Yang, J. Simulation of forces acting on the cutter blade surfaces and root system of sugarcane using FEM and SPH coupled method. *Comput. Electron. Agric.* **2021**, *180*, 105893. [[CrossRef](#)]
- Fielke, J.M. Finite Element Modelling of the Interaction of the Cutting Edge of Tillage Implements with Soil. *J. Agric. Eng. Res.* **1999**, *74*, 91–101. [[CrossRef](#)]
- Ibrahmi, A.; Bentaher, H.; Hbaieb, M.; Maalej, A.; Mouazen, A.M. Study the effect of tool geometry and operational conditions on mouldboard plough forces and energy requirement: Part 1. Finite element simulation. *Comput. Electron. Agric.* **2015**, *117*, 258–267. [[CrossRef](#)]
- Zhang, Z.; Liang, S.; Lv, H.; Dai, X. Finite Element Analysis for Flexspline of Veer Machine in the Agricultural Manipulator by Using Harmonic Gearing. *J. Agric. Mech. Res.* **2010**, *32*, 64–67, 77.
- Guo, Q.; Zhang, X.; Xu, Y.; Li, P.; Chen, C. Mechanism and simulation analysis of efficient cutting for tomato straw. *J. Agric. Mech. Res.* **2017**, *39*, 11–24.
- Diao, P.; Yuan, C.; Zhang, D.; Lu, L.; Li, P. Experiment of the Rotor Cutter Chop Stalk on ANSYS/LS-DYNA. *J. Agric. Mech. Res.* **2011**, *33*, 57, 116–119.
- Huang, H.; Wang, Y.; Tang, Y.; Zhao, F.; Kong, X. Finite element simulation of sugarcane cutting. *Trans. Chin. Soc. Agric. Eng.* **2011**, *27*, 161–166.
- Jiang, Y. Design and Test of Key Equipments for Fodder Rapeseed Harvester. Ph.D. Thesis, Huazhong Agricultural University, Wuhan, China, 2019.
- Liu, P.; Shi, K.; Huang, H. 3D-numerical Simulation Acceleration of Projectile Penetrating Steel Target. *J. Detect. Control* **2006**, *28*, 25–28.
- Zheng, C.; Zhao, J.; Zhang, J.; Zhang, R.; Li, F. Construction of Finite Element Model of Cotton Pole and Calibration of Cutting Parameters. *J. Agric. Mech. Res.* **2021**, *43*, 198–203.
- Liao, Y.; Wang, Z.; Liao, Q.; Wan, X.; Zhou, Y.; Liang, F. Calibration of Discrete Element Model Parameters of Forage Rape Stalk at Early Pod Stage. *Trans. Chin. Soc. Agric. Mach.* **2020**, *51*, 236–243.
- Liao, Y.; Liao, Q.; Zhou, Y.; Wang, Z.; Jiang, Y.; Liang, F. Parameters Calibration of Discrete Element Model of Fodder Rape Crop Harvest in Bolting Stage. *Trans. Chin. Soc. Agric. Mach.* **2020**, *51*, 73–82.

Article

Design of and Experiments with an Automatic Cuttage Device for an Arch Shed Pillar with Force Feedback

Kezhou Chen, Xing Liu, Shiteng Jin, Longfei Li, Xin He, Tao Wang, Guopeng Mi, Yinggang Shi and Wei Li *

College of Mechanical and Electronic Engineering, Northwest A&F University, Xianyang 712100, China; ckz@nwafu.edu.cn (K.C.); njhlxhn@nwsuaf.edu.cn (X.L.); jin2020010193@nwafu.edu.cn (S.J.); llf@nwafu.edu.cn (L.L.); xnhexin@nwafu.edu.cn (X.H.); wangtao666@nwafu.edu.cn (T.W.); miguopeng@nwafu.edu.cn (G.M.); syg9696@nwsuaf.edu.cn (Y.S.)

* Correspondence: liweizibo@nwsuaf.edu.cn; Tel.: +86-139-0925-8177

Abstract: In order to realize the automatic cutting of arch shed pillars, an automatic cuttage device for an arch shed pillar with force feedback was designed in this study. First, the wind resistance of the arch shed was simulated and analyzed using ANSYS, and the cuttage depth of the arch shed pillar was determined. According to the environment for the cuttage operation of the arch shed pillar and the agronomic requirements, such as the arch shed span, arch shed height, and cuttage depth, the function, structure, and basic design parameters of the arch shed automatic cuttage device were determined. Then, to reduce the damage rate of the pillar and achieve equal-depth cuttage, a force feedback system for the actuator of the cuttage device was constructed to estimate the cuttage resistance and depth in real time. To reduce the impact of the starting and stopping of each motor in the actuator, trajectory planning of the execution end in the pillar transfer stage was performed in the Cartesian coordinate system. The motion law of portal trajectory based on the L ame curve was analyzed, and MATLAB simulations were used to solve the relevant motion parameters. In addition, the modality of key components of the cuttage device was simulated and analyzed by using the SOLIDWORKS simulation plug-in. Finally, the experimental prototype was constructed according to the simulation results. The simulation and field cuttage experiments showed that the cuttage device produced equal-depth cuttage for the arch shed pillar, where the depth of the arch shed pillar was 10 cm, the average cuttage time of a single pillar was 6.2 s, and the error of the cuttage depth was ± 0.5 cm in wet soil. The operation of the device was stable, as evidenced by the smooth and mutation-free operation trajectory and speed curve of the execution end. The results of the modal experiment suggest that resonance would not occur during the operation for resonance frequencies between 303 Hz and 565 Hz. This arch shed pillar automatic cuttage device has an optimal operation performance and meets the agronomic requirements of arch shed pillar cuttage.

Citation: Chen, K.; Liu, X.; Jin, S.; Li, L.; He, X.; Wang, T.; Mi, G.; Shi, Y.; Li, W. Design of and Experiments with an Automatic Cuttage Device for an Arch Shed Pillar with Force Feedback. *Agriculture* **2022**, *12*, 875. <https://doi.org/10.3390/agriculture12060875>

Academic Editors:

Muhammad Sultan, Redmond R. Shamshiri, Md Shamim Ahamed and Muhammad Farooq

Received: 12 May 2022

Accepted: 15 June 2022

Published: 17 June 2022

Publisher's Note: MDPI stays neutral with regard to jurisdictional claims in published maps and institutional affiliations.



Copyright:   2022 by the authors. Licensee MDPI, Basel, Switzerland. This article is an open access article distributed under the terms and conditions of the Creative Commons Attribution (CC BY) license (<https://creativecommons.org/licenses/by/4.0/>).

Keywords: arch shed; automatic cuttage; force feedback; simulation design; trajectory planning

1. Introduction

Mulching film cultivation technology in arch sheds can preserve heat, moisture, and soil, improving the survival rate and shortening the planting cycle of crops [1–3]. At present, the embedded depth of an arch shed pillar depends on the experience of farmers, which can lead to poor wind resistance of the arch shed and is not conducive to the automatic construction of arch sheds. Many literature studies exist on automatic cuttage devices for arch sheds, such as the arch shed cuttage and filming machine developed by Fujiki Agricultural Machinery Manufacturing Institute (Higashiosaka, Japan), the arch shed frame construction machine developed by French CM-REGERO Industries (La Chapelle-Basse-Mer, France) and RABAUD (La Chapelle-Basse-Mer, France), the arch shed cuttage machine developed by Dubios Agrinovation Inc. (Saint-R emi, Canada), the arch shed cuttage machine jointly developed by Mark William, Tunnelmatic Inc. (RABAUD La

Chapelle-Basse-Mer, France), and LesAgrisudvende Inc. (Libourne, France), and the arch shed automatic cuttage device developed by Liu et al. [4,5]. In China, the planting area that utilizes arch shed film mulching cultivation technology reaches 13,000 square kilometers every year [6,7], which requires many automatic cuttage machines. However, the sizes of the currently studied arch shed cuttage machines and cuttage devices are large, which is insufficient to meet the requirements of the small-scale operating environment of the Chinese farmland. These devices require auxiliary manual operation with less automation. The pillar can also be easily broken during cuttage in a hard-soil environment. In order to solve these problems, we aimed to develop an automatic cuttage device for arch shed pillars with a pillar protection function that is suitable for small field operations.

According to previous studies, the small arch sheds used for seedling cultivation in Shaanxi and Gansu have a span of 60 cm and a height of more than 35 cm (Figure 1). The most commonly used arch shed pillar has a span of 60 cm, a height of 50 cm, and a diameter of 1 cm, with a spacing of 1 m between adjacent pillars. To ensure wind resistance of the arch shed, “equal-depth cuttage” should be adopted for the pillar. At the same time, it is necessary to avoid film rupturing caused by pillar damage, which can lead to a decline in the heat preservation performance of arch sheds [8,9]. During the automated cuttage operation of the arch shed, it is important to first achieve automatic cuttage with a lower damage rate, and then ensure the consistency of the highest point of the 1 cm arch shed after the cuttage at the same time—namely, equal-depth pillar cuttage.

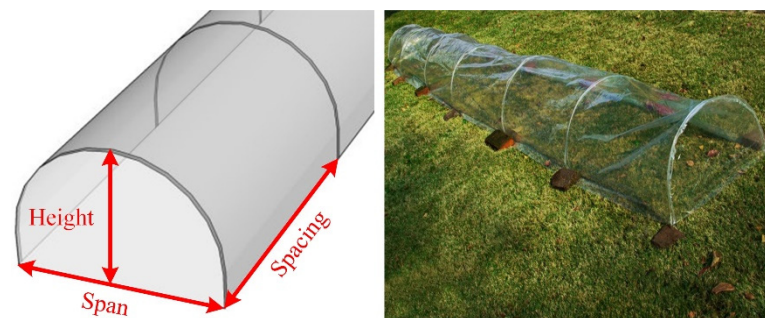


Figure 1. Plastic-film-covered cultivation in an arch shed.

According to the operation environment and the experience of farmers, the basic requirements for the automatic cuttage of arch sheds are as follows:

- (1) The cuttage span of the arch shed pillar should be 60 cm with less than 1 cm of error;
- (2) The height of the arch shed pillar after cuttage should be 40 cm with less than 1 cm of error;
- (3) The diameter of the arch shed pillar that can be cut should be 1 cm;
- (4) The cuttage depth should be equal at the ends of the arch shed pillar;
- (5) The damage rate of the arch shed pillar should remain below 5%;
- (6) The cuttage device should operate smoothly, have optimal stability, and have a long service life.

According to agronomic requirements and to the operation environment of arch shed pillars, the process of the automatic cuttage of arch shed pillars was constructed, as shown in Figure 2. In this process, the cuttage device installed on the chassis moved forward along a straight line, stopped after reaching the cuttage position, and performed a pillar cuttage.

In the automatic arch shed pillar cuttage process, the span and height can be determined through the mechanical design of the cuttage device, and the diameter of the arch shed pillar can be customized in advance. However, several problems still need to be addressed:

- (1) Suitable pillar cuttage depth;
- (2) A quick and convenient method for determining the ideal cuttage depth at both ends of the pillar;

- (3) Ensuring that the damage rate of the pillar is controlled below 5%;
- (4) Ensuring the optimal operation and stability of the device.

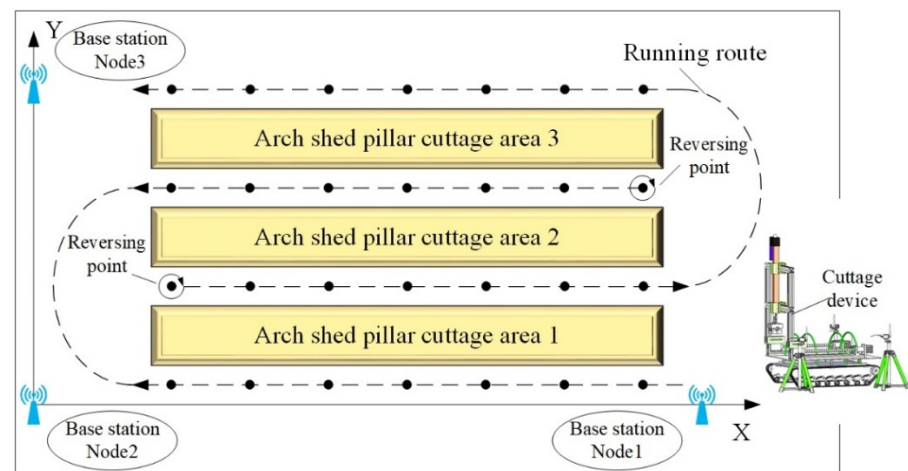


Figure 2. Automatic cutting process of arch shed pillars.

Wind resistance is an important index for evaluating the firmness of a small arch shed [10]. The pillar cuttage depth determines the wind resistance of the arch shed. The analyses of wind resistance for greenhouses have mostly focused on the environment of the greenhouse [11–13]. A small arch shed covered with a flexible plastic film is strongly sensitive to wind load. The wind resistance of an arch shed is related to the spacing, span, and embedded depth of the arch shed pillar [14]. However, the current embedded depth of arch shed pillars is essentially determined based on experience, which is not supported by the theoretical data.

According to the agronomic requirements for the cuttage of arch shed pillars in a greenhouse, soft soil with a rotary tillage depth of about 25 cm is suitable during cuttage, while the embedded depth of the arch shed pillars should be greater than 5 cm. The stability of an arch shed increases with an increase in cuttage depth. However, since the size of an arch shed pillar is fixed, increasing the cuttage depth inevitably reduces the height of the arch shed and weakens the preservation of heat and moisture. The mechanical characteristics of the pillar at different cuttage depths and under different levels of wind force can be determined using a statistical analysis of the wind force during the spring in Shaanxi, China. In other words, a reasonable pillar cuttage depth that meets the wind resistance of the arch shed can be deduced by analyzing the wind resistance of the arch shed pillar at different cuttage depths.

To achieve equal-depth cuttage of the arch shed pillar, it is necessary to design a detection mechanism for a stable cuttage depth to monitor the embedded depth of the arch shed pillar in real time. However, this task is currently difficult to implement. Mossadeghi-Björklund et al. [15] reported a positive correlation between soil penetration resistance and penetration depth. Based on this principle, monitoring of the cuttage resistance can be used to detect the cuttage depth.

Therefore, the development of real-time monitoring for cuttage resistance has become the focus and difficulty of research. Many relevant studies have been conducted in different research fields, including industries and services concerning torque detection. According to the law that the resistance moment of a joint will increase rapidly and the current of a joint motor will jump when the manipulator is collapsed, Spong et al. [16] constructed a flexible joint that could estimate the impact moment value of the manipulator joint by using the current jumping value of the joint motor. Chen et al. [17] proposed a general sensorless collision-detection algorithm for robot actuator faults. Shi et al. [18] designed a flexible picking manipulator with an obstacle-avoidance function that could detect the collision resistance of the manipulator during fruit and vegetable picking. For the monitoring of

cuttage depth, a cuttage depth feedback mechanism based on “current–force–depth” was constructed in this study, and a cuttage resistance feedback device based on an electric push rod was built. A cuttage-resistance feedback algorithm was designed that could be used to explore the relationship between the current jumping value and the cuttage resistance. Moreover, the resistance of the electric push rod was obtained by detecting the motor current, and the cuttage depth of the pillar was indirectly obtained according to the relationship between the resistance and cuttage depth.

Excessive impact force leads to the damage of the pillar cuttage. Impact force is a result of hard obstacles under the soil layer that are encountered during the pillar cuttage. The hard obstacles under the soil layer are uncontrollable factors, which can be avoided by the sensing ability of the force through the execution end based on the detection of cuttage resistance using the “current–force–depth” feedback system.

In the process of transporting the pillar for cuttage, the curves of the operation trajectory, speed, and acceleration at the execution end are not smooth, which makes the cuttage device subject to impact force. Therefore, a trajectory curve was planned to ensure smooth curves of the operation trajectory, speed, and acceleration. Meanwhile, the vibration characteristics of the cuttage device were analyzed to obtain its inherent frequencies, which was used to prevent resonance, effectively reduce the impact force, and ensure the optimal operation of the device.

To solve the above-mentioned basic requirements for the automatic cuttage of arch shed pillars, the wind resistance of the arch shed was analyzed in this study and the cuttage depth of the arch shed pillar was determined. A real-time cuttage depth detection mechanism based on “current–force–depth” was constructed for the real-time monitoring of the cuttage depth. According to basic parameters, including span, height, cuttage depth, and pillar diameter, the gantry-shaped cuttage device was simulated and designed to analyze the motion trajectory, speed, and acceleration curves at the execution end, and the rationality of size parameter selection and the smoothness of the motion trajectory were verified. A modal analysis of the key components of the automatic cuttage device was performed to determine the first four order modal frequencies of the cuttage device, which prevented the occurrence of resonance, eliminated impact force, and ensured the smoother operation of the device. Finally, the prototype machine was manufactured and the cuttage experiment was performed.

2. Pillar Cuttage Depth and Wind Resistance Analysis of the Arch Shed

Wind blowing vertically against the side of the arch shed pillar has the greatest impact on the arch shed. ANSYS was used to analyze the wind resistance of the arch shed at different cuttage depths. The vertical wind on the side of the arch shed is shown in Figure 3. From the above information, it was calculated that the height of the arch shed poles should be $H = 50$ cm and the span should be $b = 60$ cm. The height of the arch shed is h and the embedded depth of the arch shed pillar is $a = H - h$ Qin et al. [4,19,20] found that the appropriate height-to-span ratio for an arch shed is $h/b = 0.5 \sim 0.67$, where $h = 35 \sim 40$ cm and $a = 10 - 15$ cm, which can be obtained from the height requirements of the arch shed.

In Yangling, Shaanxi, China, the values for altitude and air density are $z = 435 \sim 563$ m and $\rho = 0.00125e^{-0.0001z}$, respectively, and the average ground wind speed from March to April is level 2–3, with occasional strong winds of level 7–8 [21–23]. To ensure safety during operation, the pressure of a level 10 wind acting on the arch shed was considered to be the wind pressure limit; at this time, the basic wind pressure is $\omega_0 = \rho v^2/2 = 420$ N/m² [24,25]. The arch shed was a non-high-rise building with a height of less than 30 m. When the wind vibration coefficient is $\beta_z = 1$, the variation coefficient of the wind load height is $\mu_z = 1$, and the wind load shape coefficient is $\mu_s = 0.2$ [26,27], then the wind load applied to the arched shed is $\omega_k = \omega_0\beta_z\mu_z\mu_s = 84$ N/m².

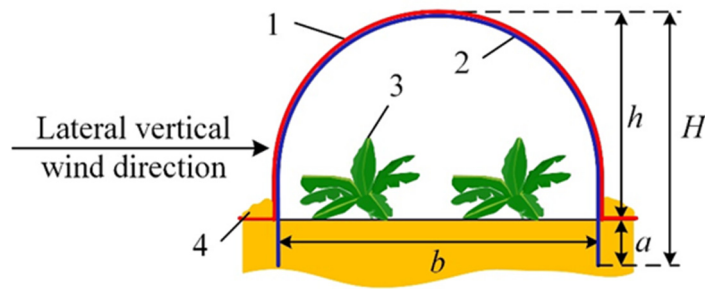


Figure 3. Schematic diagram of vertical wind on the side of arch shed. 1: plastic film; 2: arch shed pillar; 3: plant; and 4: soil. Note that b: span of arch shed pillar; H: height of arch shed pillar; h: height of arch shed and a: the embedded depth of the arch shed pillar.

Under an external temperature of 5 °C–10 °C, the compressive yield strength of the pillar material is $R_m = 2.5 \times 10^8$ Pa, the elastic modulus is $E = 1.67 \times 10^{11}$ Pa, $G = 7.69 \times 10^{10}$ Pa, $\mu = 0.3$, Young’s modulus is 2×10^{11} Pa, and the density is $\rho = 7850$ kg/m³. The arch shed pillar model was established using SOLIDWORKS and imported into ANSYS Workbench for a simulation analysis of stress, strain, and deformation to evaluate the wind resistance of the arch shed pillar under a level 10 wind. Tetrahedral elements were used to divide the grid, and the minimum grid unit size was set to 0.5 cm. Under the same wind load, fixed constraints at both ends of the arch shed pillar were added to simulate the fixation of the pillar by soil after the arch shed pillar was cut into the soil. A wind load of 84 N/m² was applied on one side of the arch shed to simulate and analyze the stress of the arch shed pillar under a level 10 wind. When the cuttage depth of the pillar ranged from 8–15 cm, the stress and strain of the arch shed pillar increased with each 1 cm-increase in the cuttage depth (Figure 4). The simulation results revealed that the stress and strain of the arch shed pillar decreased with an increase in the pillar’s embedded depth from 8 cm to 15 cm, and it was more resistant to wind and snow disasters. When the cuttage depth was greater than 10 cm, the downward trend of stress and strain became less pronounced.

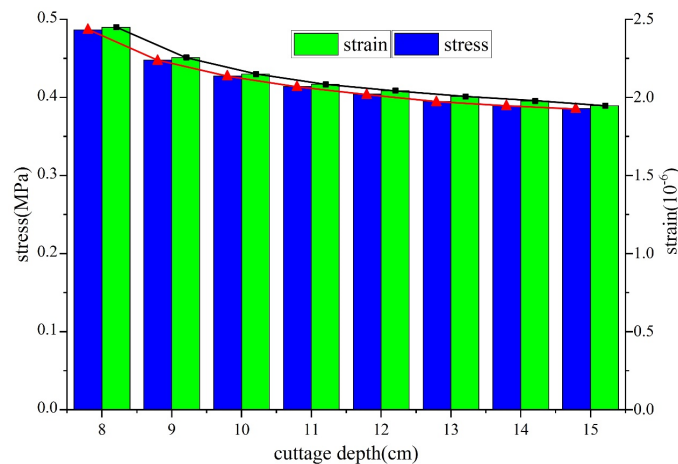


Figure 4. Pillar cuttage depth and wind resistance analysis of the arch shed.

When the height of the small arch shed increased, the living space of the plant increased as well, which was more conducive to the growth of seedlings. Therefore, within the appropriate height-to-span ratio of 0.5–0.67 cm and with $h = 40$ cm, the embedded depth of the arch shed pillar would be $a = H - h = 10$ cm. Under these parameters, the strain of the arch shed pillar was 2.15×10^{-6} , which was considerably lower than the allowable strain of the structural steel, namely $[\varepsilon] = 3.74 \times 10^{-4}$, and the equivalent stress value was 0.427 MPa, which was also considerably lower than the allowable stress of

the structural steel, namely $[\sigma] = 62.5 \text{ MPa}$. Therefore, the arch shed pillar was expected to withstand a level 10 wind.

3. Real-Time Detection Principle of Cuttage Depth Based on “Current–Force–Depth”

Assuming the use of a DC motor, the current of the motor would increase rapidly with an increasing load [28,29]. Based on this observation, an electric push rod was used to cut the arch shed pillar, and a stress analysis diagram of the pillar cuttage using an electric push rod was constructed, as shown in Figure 5. During the cuttage operation of the electric push rod, the resistance of the electric push rod would increase rapidly and the current driving the motor would correspondingly increase with an increase in the embedded depth of the pillar. In other words, as the cuttage depth of the pillar increased, the cuttage resistance increased, the resistance of the electric push rod also changed, and the current driving the motor would also increase. According to this principle, the electric push rod caused the brushless motor (1) to rotate the ball screw (4) after being decelerated by the secondary reducer (2). The rotation of the ball screw (4) caused the nut assembly (3) that is fixedly connected with the push pole (5) to move, thus converting the rotating motion of the brushless motor (1) into a linear motion of the push rod (5) and generating axial thrust. Subsequently, the relationship between the current change of the motor and the electric push rod, as well as the embedded depth of the arch shed pillar, can be calculated to detect the motor current and to infer the torque changes with the depth during cuttage.

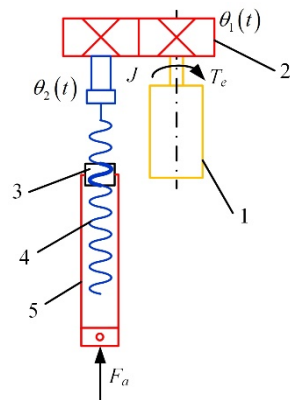


Figure 5. Stress analysis diagram of the pillar cuttage using an electric push rod. 1: brushless motor; 2: reducer; 3: nut assembly; 4: ball screw; and 5: push pole.

According to the literature, the external force on the electric push rod during operation includes the driving torque of the motor and the cuttage resistance. Let the equivalent moment of inertia on the motor spindle be J , the equivalent system damping on the motor spindle be B , the motor angular displacement be $\theta_1(t)$, the lead screw angular displacement be $\theta_2(t)$, the electromagnetic torque be T_e , and the load torque be T_L . Then, the torque balance equation on the motor shaft is:

$$T_e = J\ddot{\theta}_1(t) + B\dot{\theta}_1(t) + T_L \tag{1}$$

Let the lead screw be p_h , the transmission efficiency of the ball screw pair be η , and the cuttage resistance be F_a . Then, the relationship between cuttage resistance and the load torque is as follows:

$$T_L = \frac{F_a p_h}{2\pi\eta} \tag{2}$$

Let the current of the motor in a steady state be i , the electromagnetic torque be T_e , and the motor torque coefficient be K_t . Then, the electromagnetic torque equation is:

$$T_e = K_t i \tag{3}$$

Combining Equations (1)–(3) yields the following relationship between the motor current and the cuttage resistance:

$$i = \frac{F_a p_h}{2\pi\eta} + \frac{J\ddot{\theta}_1(t)}{K_t} + \frac{B\dot{\theta}_1(t)}{K_t} \quad (4)$$

According to Equation (4), when the cuttage device works normally, the current value flowing through the electric push rod is related to the cuttage resistance of the arch shed. Therefore, the cuttage resistance can be estimated by detecting the current value of the motor.

As mentioned above, the cuttage resistance can be obtained by monitoring the motor's current value. Therefore, the mathematical model of pillar cuttage resistance and cuttage depth needs to be established. According to the literature, when the dimensionless parameters related to the soil type, C_1, C_2, C_3 and C_4 are adopted, the area of the conical cross-section of the front end of the arch shed pillar is S , the unit of soil bulk density is D_b , the weight of the soil moisture is θ_g , and the penetrating depth of the arch shed pillar is h [30], the relationship between the cuttage resistance and the penetrating depth is as follows:

$$F_a = S \times C_1 D_b^{C_2} \theta_g^{C_3} h^{C_4} \quad (5)$$

Consequently, the relationship between the current of the electric push rod driving the motor and the penetrating depth is:

$$i = \frac{S \cdot C_1 D_b^{C_2} \theta_g^{C_3} h^{C_4} p_h}{2\pi\eta} + \frac{J\ddot{\theta}_1(t)}{K_t} + \frac{B\dot{\theta}_1(t)}{K_t} \quad (6)$$

According to Equation (6), when the electric push rod is operational, the motor current is linearly related to the penetrating depth. Therefore, the detection algorithm for the cuttage depth of the arch shed pillar can be constructed based on the current feedback by analyzing the equation for the relationship between the motor current of the electric push rod and the cuttage depth of the arch shed pillar. The cuttage depth of the arch shed pillar can be indirectly inferred through a change in the motor current of the electric push rod, to achieve real-time monitoring of the cuttage depth for an arch shed pillar.

4. Simulation Analysis of Cuttage Device

SOLIDWORKS was used to simulate and design the force feedback automatic cuttage device (Figure 6). The model included a walking chassis, a conveying platform, and an actuator of gantry structure. During operation, the arch shed pillar (4) was manually placed on the conveying platform (8) of the walking chassis, and the arch shed pillar (4) was then transported successively to the front of the machine by the conveying platform (8). On the conveying platform, two rows of hollow columns were evenly distributed with a height of 3 cm. The inner diameter of the hollow columns was 1.2 cm, which was slightly larger than the diameter of the arch shed pillars. The distance between the two rows of hollow columns was equal to the span of the arch shed pillars. The two lower end points of the arch shed pillars were placed in the hollow columns, which ensured that the pillars could be easily clamped by the execution end and transported to the tail of the fuselage while being attached on the conveying platform. Subsequently, the electric push rod (7) caused the execution end (5) to fall and clamp the arch shed pillar (4), causing it to rise. Then, the servo motor drove the lead screw sliding table (2) to transport the arch shed pillar (4) to the rear of the machine. After the transportation, the electric push rod (7) extended downward to press the arch shed (4) into the soil to achieve pillar cuttage, which performed repeatedly. In this operation, the execution end (5), the installation frame (6), and the electric push rod (7) were used to cut the arch shed pillar. Simultaneously, they were used to detect the cuttage depth of the arch shed pillar in real time.

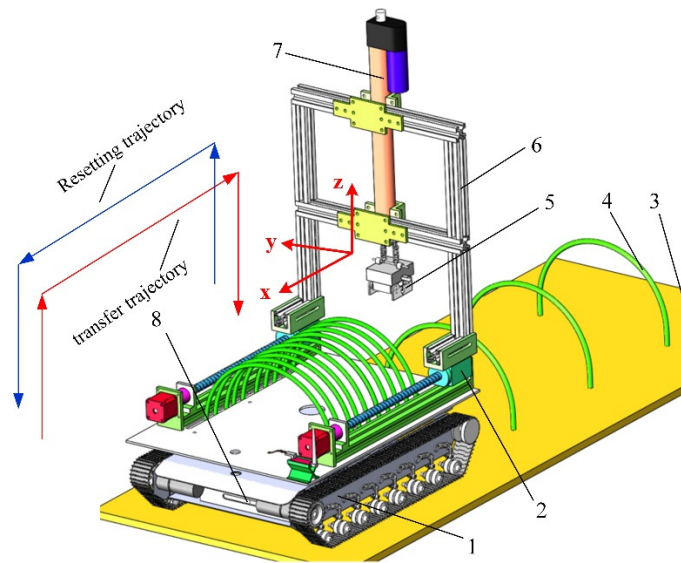


Figure 6. Simulation design diagram of the force feedback arch shed pillar cutting device. 1: walking chassis; 2: lead screw sliding table; 3: soil; 4: arch shed pillar; 5: execution end; 6: installation frame; 7: electric push rod; and 8: conveying platform.

4.1. Simulation Analysis of the Motion Trajectory of the Execution End

The execution end pulled the cuttage pillar from the front of the machine and transferred it to the rear, extending the conveying route and eliminating the vibration of the cuttage device that was generated by the short distance and the frequent starting and stopping of the motor. Therefore, the motion trajectory of the execution end was similar to the “door” shape in Figure 6, which can be further sorted into the black line through AB’C’G in Figure 7. The operation speed and the acceleration were discontinuous during the transportation of the pillar. Jumps in the displacement, speed, or acceleration caused mechanical vibration and, in severe cases, fractures in the machine material due to the right angle at the connection between the vertical and horizontal motion trajectory at the execution end. To make the motion of the execution end smooth and to eliminate the motion impact, the Láme curve [31,32] was used to optimize the operation trajectory of the execution end. The optimized trajectory is shown by the red curve through ABCDEFG in Figure 7, including the vertical rising segment AB, the horizontal moving segment CE, the vertical falling segment FG, and two transitional arcs \widehat{BC} and \widehat{EF} .

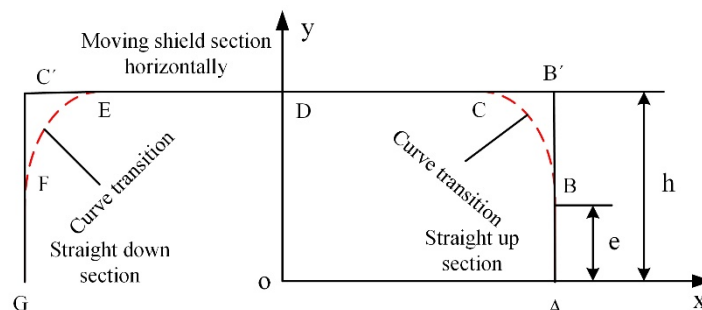


Figure 7. The motion trajectory of the execution end.

Given that the motion position point of the execution end is $P(t_i)$, and the distance traveled by the execution end is $s(t_i)$, the function for the relationship between the speed, the acceleration, and the displacement of the execution end with time t in the Cartesian coordinate system is as follows:

- (1) When $0 \leq s(t_i) \leq h$, the execution end moves along the AB segment, and the kinematic parameters of the execution end are:

$$\begin{cases} P(t_i) = (x_A & y_A & z_A + s(t_i)) ^T \\ v(t_i) = (0 & 0 & s'(t_i)) ^T \\ a(t_i) = (0 & 0 & s''(t_i)) ^T \end{cases} \quad (7)$$

- (2) When the execution end moves within the \widehat{BC} segment along the Láme curve, the kinematic parameters of the execution end are solved according to the arc differentiation method, as shown in Figure 8:

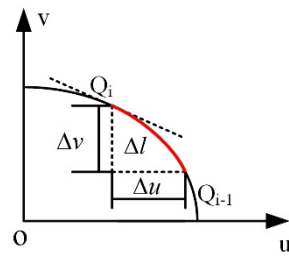


Figure 8. Schematic diagram of the Láme curve arc differential.

$$\Delta v = \frac{\Delta l}{\sqrt{1 + (u'_i)^2}} \quad (8)$$

The relationship between point Q_i and point Q_{i-1} satisfies $v_i = v_{i-1} + \Delta v$, and is substituted into Equation (8):

$$u_i = g^n \sqrt{1 - \left(\frac{v_i}{f}\right)^n} \quad (9)$$

- (3) When the execution end moves within the CD segment, the motion parameters of the execution end at time t_i are:

$$\begin{cases} \Delta s_i = \Delta u_i \\ \Delta v_i = 0 \end{cases} \quad (10)$$

- (4) The left and right sides of the motion trajectory of the execution end are symmetrical and the physical parameters of the second half of the motion are determined as described above.

From the above analysis, the curve of the distance s of the execution end versus time is shown in Figure 9. MATLAB was used to simulate and verify the motion of the execution end. The motion trajectory of the execution end required a smooth transition in all directions. According to the structure and parameters of the cuttage device, the obstacle avoidance height was $e = 5$ cm, the value of the Láme curve was $g = 12$ cm, $f = 2$ cm, $m = 2$, the horizontal transportation distance was 60 cm, and the one-way motion cycle was $T = 2$ s. The motion trajectory of the execution end and the curves of displacement s , speed v and acceleration a in the three xyz spaces versus time t in the Cartesian coordinate system are shown in Figure 10. The results in Figure 10 show that the curves of the displacement, the speed, and the acceleration of the execution end were smooth and continuous, with a zero value at the start and end points. Therefore, the trajectory optimization method can find the optimal motion law and prior dynamic performance of the execution end.

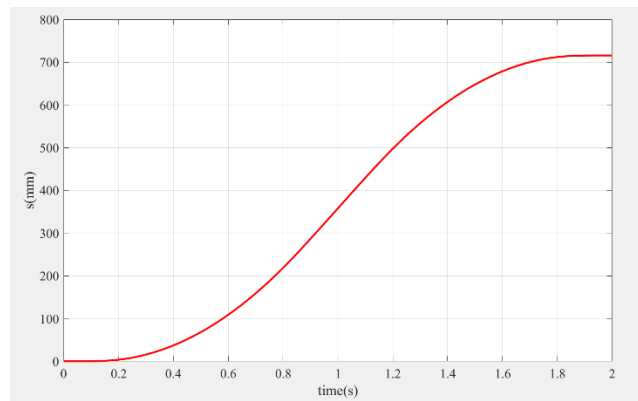


Figure 9. The distance curve of the execution end.

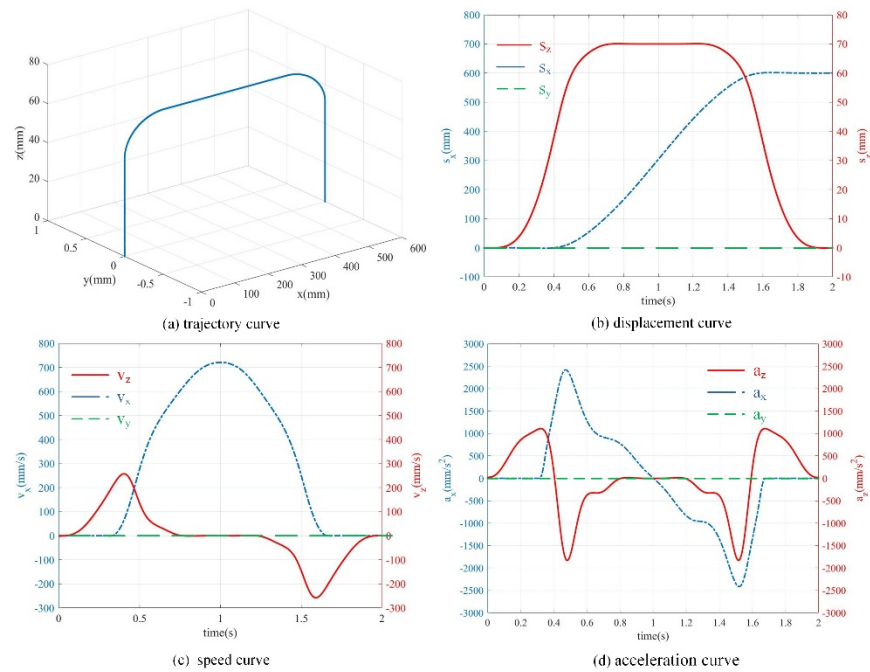


Figure 10. The motion parameter curves of the execution end.

4.2. Modal Analysis of the Installation Frame

The frequent starting and stopping of the execution end of the cuttage device caused alternating loads to act on the installation frame. When the vibration and impact frequency generated by an external force are close to the inherent frequency of the installation frame, resonance will occur, thus accelerating the failure of the installation frame and affecting its working reliability. The modal analysis method described in [33–37] must be used to obtain the modal parameters of the installation frame and study its vibration characteristics.

Let the matrices of the mass, damping, and stiffness of the system structure be M , C , and K , respectively. If x is the displacement vector of structural vibration, the external excitation of the system is $F = 0$, and the system damping is $C = 0$, then the system is underdamped without external force input, and its free vibration equation is:

$$M\ddot{x} + Kx = 0 \tag{11}$$

When the free vibration of the system is simple harmonic vibration, the vibration mode vector is ϕ , the modal frequency is ω , and the simple harmonic vibration equation is:

$$x = \phi e^{j\omega t} \tag{12}$$

Substituting Equation (12) into Equation (11) results in:

$$(K - \omega^2 M)\phi = 0 \tag{13}$$

If there is a non-zero solution to Equation (13), the expression of the inherent frequency and the vibration mode of the installation frame is:

$$|K - \omega^2 M| = 0 \tag{14}$$

Because low-order vibration has a considerable impact on the dynamic characteristics of the structure, and during the operation of the cuttage device in the field, the first four order frequencies of the installation frame were analyzed using SOLIDWORKS to obtain the inherent vibration frequency and vibration mode nephogram, as shown in Figure 11.

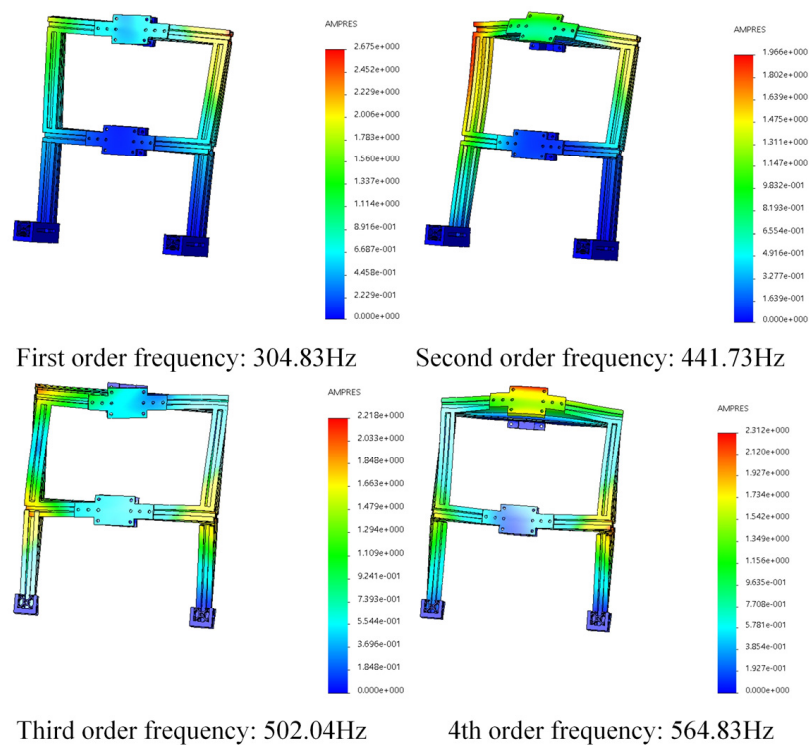


Figure 11. The vibration nephogram.

5. Experimental Results and Analysis

5.1. Construction of Entity System

An automatic cuttage device for an arch shed pillar was built based on verification using the simulation results (Figure 12). The installation frame of the cuttage device was an aluminum profile, and the servo motor (Time Chaoqun Technology Co., Ltd., Beijing, China) was used to drive the roller lead screw (800 mm, FY05, Louis Martin Flagship Store, Yancheng, China) and transport the pillar. The pillar cuttage was performed using a DC brushless electric push rod (350 mm, Hansen Motor Tools Co., Ltd., Wenzhou, China) with a 350 mm stroke, and a steering gear (DS3218, Premium Robot Co., Ltd., Shenzhen, China) was used to drive the execution end to grasp the pillar. Other non-standard components were 3D printed with PLA and photosensitive resin.



Figure 12. The automatic cuttage device for an arch shed pillar.

The control system of the cuttage device comprised a main control board (STM32F103VET6, Guangzhou Xingyi Electronic Technology Co., Ltd., Guangzhou, China), a servo motor driver (DM-055B, Time Chaoqun Technology Co., Ltd., Beijing, China), a brushless motor driver (AQMD360BLS, Love Control Electronics·Aisikong Co., Ltd., Chengdu, China) and a steering gear driver (LSC-16-V1.3, Magic Robot Official Mall, Shenzhen, China). Based on the control system, a cuttage depth sensing system for an arch shed pillar with “current–force–depth” real-time feedback was constructed, as shown in Figure 13. The main controller collected the current information of the electric push rod motor through the motor driver at a frequency of 20 Hz, detected the rotation position of the motor through the Hall encoder, and received the command sent by the main controller to drive the motor to perform the corresponding actions.

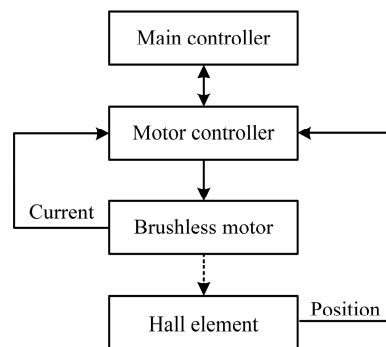


Figure 13. The cuttage depth sensing system of the arch shed pillar with “current–force–depth” real-time feedback.

The “current–force–depth” feedback control process is shown in Figure 14. During the operation, the motor controller was set to work mode in the closed-loop speed mode and operated at a constant speed to equalize the electromagnetic torque of the motor and the load torque. After data processing, the commutation pulse number and phase current information of the motor were read to obtain the phase current value and the rotation position of the electric push rod motor. After filtering, the motor phase current value I_t was obtained under different cuttage depths. A current jumping threshold was then specified as ε . When the actual current I_r and theoretical current I_t values during the operation satisfied $|I_t - I_r| > \varepsilon$, the motor braked and the electric push rod ceased to function.

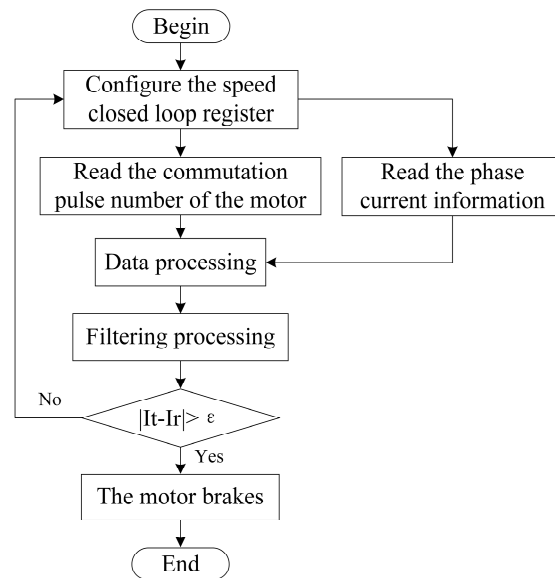


Figure 14. The “current–force–depth” feedback control process.

5.2. Verification Experiment of the Cuttage Depth

5.2.1. Verification Experiment of “Current Depth” Real-Time Feedback

The real-time current of the motor at different cuttage depths was measured under three operation conditions (Table 1) to assess the feasibility of the control system. The cuttage speed was set to 28 mm/s, and the real-time current of the motor was read at different cuttage depths. A scatter plot of the changes in the motor current is shown in Figure 15, where it is clear that when the cuttage depth was 10 cm, the current values of the motor were 230 mA, 150 mA, and 60 mA for cuttage in sandy soil, dry soil, and wet soil, respectively. At the same time, with an increase in the cuttage depth, the motor current also increased and the cuttage depth information could be obtained through the current.

Table 1. Physical parameters of the experimental soil.

Soil Type	Moisture Content (%)	Soil Firmness at Different Depths (kPa)				
		2.5 cm	5 cm	7.5 cm	10 cm	12.5 cm
Sandy soil	3.25	291.00	747.71	1604.43	1818.14	2141.29
Dry soil	19.37	162.17	544.33	720.17	1141.50	1800.17
Wet soil	37.84	159.20	427.40	606.20	622.80	725.00

5.2.2. Determination Experiment of the Cuttage Speed

The operation efficiency increases when cuttage is performed at a faster speed. Accordingly, a greater instantaneous impact force will act on the pillar, and the current value will change. To determine the most suitable cuttage speed, the real-time current was measured with a selected cuttage depth of 10 cm and a cuttage speed that varied in the range of 10–28 mm/s. The experimental data, which are presented as a scatter plot of the current in Figure 16, show that a change in cuttage speed does not cause a change in the current value in a wet soil environment. The motor current showed a rising trend with an increase in cuttage speed in the sandy soil environment, while in the dry soil environment, the motor current increased at first and then plateaued. Comprehensive consideration of the operation efficiency and safety of the motor suggests that the cuttage speed should be appropriately increased to improve the cuttage efficiency in wet and dry soil environments. When cutting in a sandy soil environment, the cuttage speed should be appropriately reduced to decrease the current and to protect the motor.

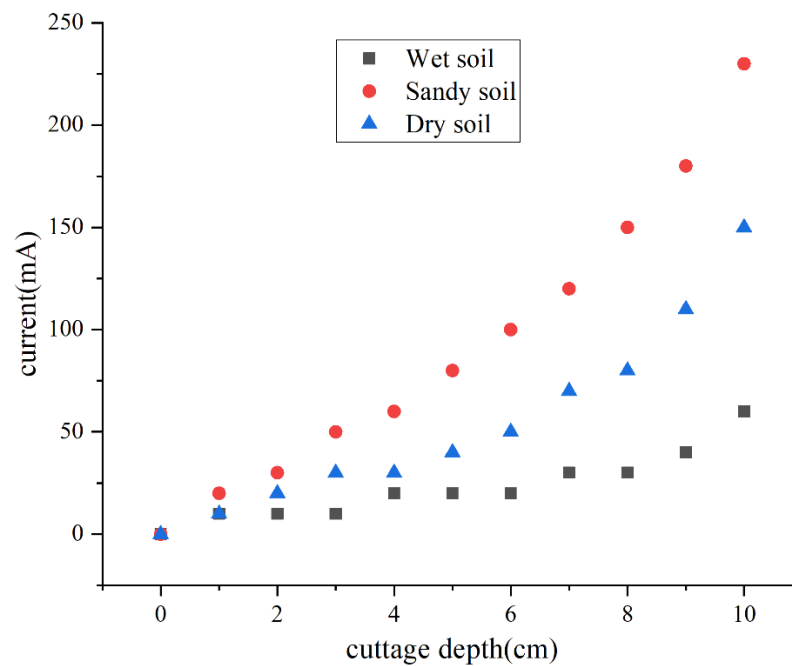


Figure 15. The verification experiment of the “current depth” real-time feedback.

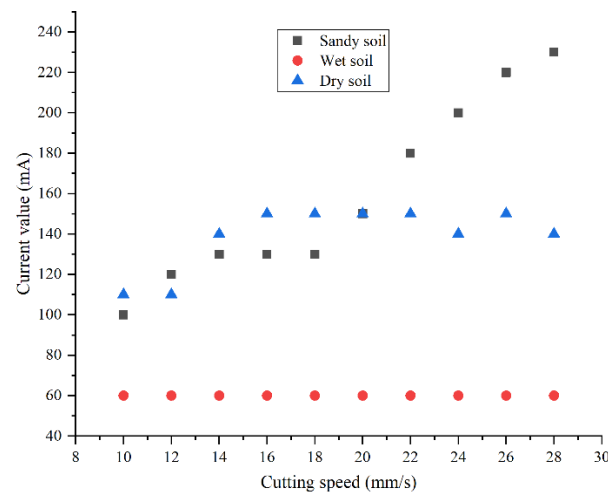


Figure 16. The determination experiment of cuttage speed.

5.2.3. Error Calibration of the Cuttage Depth

As mentioned above, the optimal stability of the arch shed was at cuttage depth of 10 cm. The motor was controlled for cuttage at different speeds, and the errors during cuttage in sandy soil (a), dry soil (b), and wet soil (c) with critical values of 230 mA, 150 mA, and 60 mA, respectively, were recorded. The experiment was repeated 40 times and an error bar for cuttage depth was drawn, as shown in Figure 17.

The results shown in Figure 17 indicate that the errors in cuttage depth were within 7 mm when cutting in dry and sandy soil environments, and within 5 mm when cutting in a wet soil environment. The error remained under 5 mm with an increase in cuttage speed. Therefore, the device was suitable for cuttage operations under wet soil conditions, which is favorable for controlling the amount of cuttage error and improving the operation efficiency.

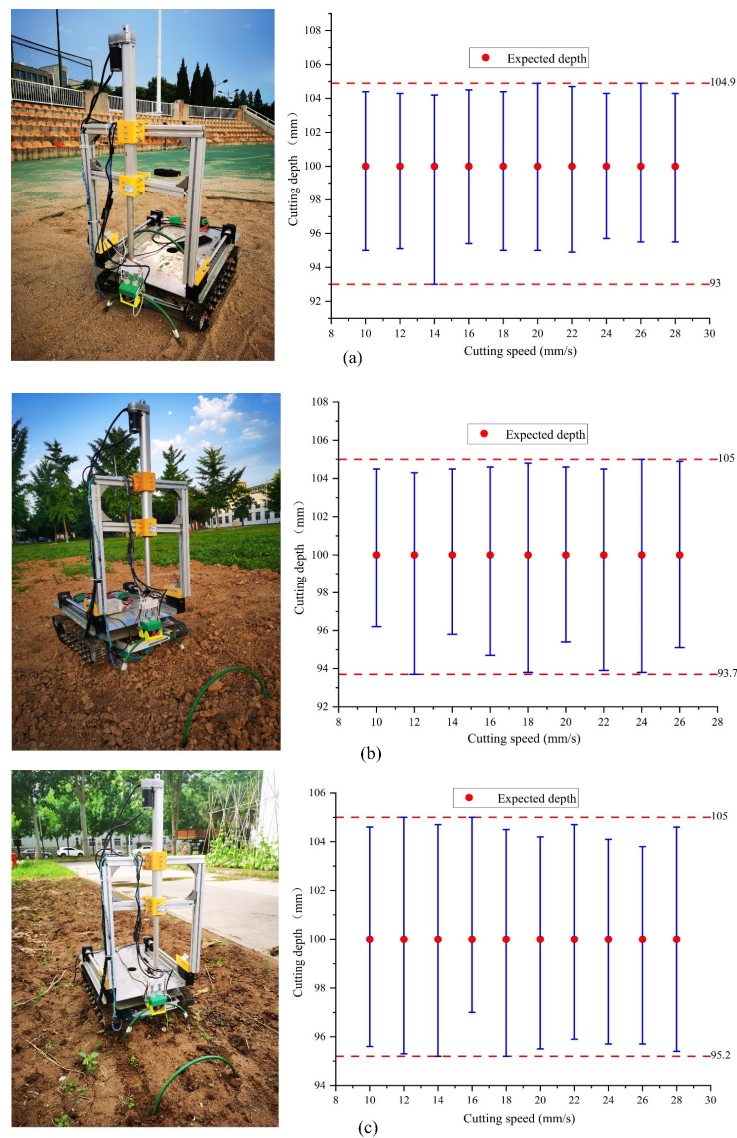


Figure 17. Error bar charts for the cuttage depth. Note that (a): Sandy soil experiments; (b): dry soil experiments; (c): wet soil experiments.

5.3. Experiment of Trajectory Planning

To assess the feasibility of trajectory planning, an experiment was performed at the execution end of the cuttage device. The specific experimental process was as follows:

- (1) According to the transportation and distance lifting of the pillar, the trajectory of the execution end was planned to obtain the theoretical data, and the theoretical curve was generated using MATLAB;
- (2) The motion trajectory of the execution end was tracked and measured, the experiment was repeated five times, and the collected data was used to generate the actual trajectory route;
- (3) The coincidence degree between the theoretical calculated trajectory and the actual trajectory was compared, as shown in Figure 18.

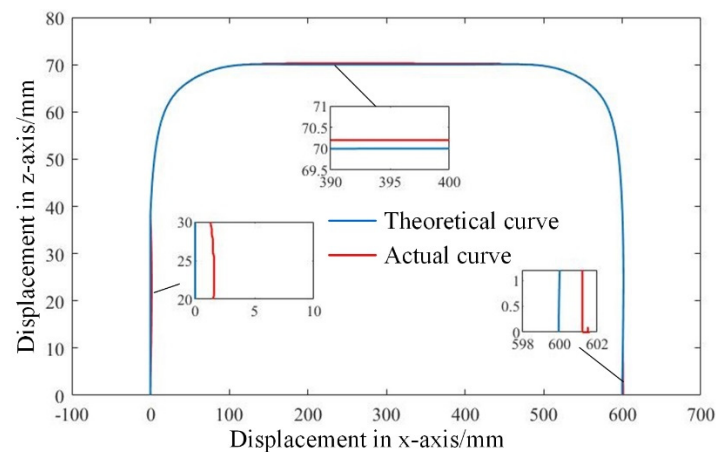


Figure 18. The verification test of the trajectory planning at the execution end.

In the experiment, the transportation and lifting actions of the pillar were achieved based on the theoretical calculated trajectory for the execution end in a continuous and relatively stable action. The comparison of the actual trajectory with the theoretical trajectory showed that they essentially coincided, with a few errors. The errors were concentrated in the initial stage and the foothold, and the maximum error was 2.1 mm, which was within the allowable error range and met the design requirements.

5.4. Modal Experiment Analysis

To verify the results of the modal simulation analysis, the modal characteristics of the installation frame were tested by using the pulse excitation method, and the experimental modal test and analysis system was built, as shown in Figure 19. The analysis system was composed of a modal force hammer (LC02, Donghua Testing Technology Co., Ltd., Taizhou, China), an acceleration sensor (DH186, Donghua Testing Technology Co., Ltd., Taizhou, China), and a data acquisition and analysis module (DH5920, Donghua Testing Technology Co., Ltd., Taizhou, China).

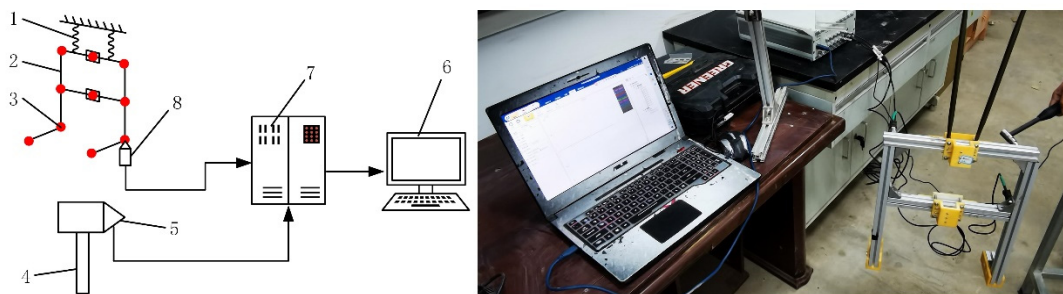


Figure 19. Experimental modal test and analysis system. 1: spring; 2: installation frame; 3: test point; 4: modal force hammer; 5: force sensor; 6: PC; 7: data acquisition and analysis module; and 8: acceleration sensor.

During the experiment, two springs were used to suspend the installation frame in a static state in the air. An acceleration sensor was arranged at the cross-linking point of the aluminum profile of the installation frame. The excitation point of the mounting frame was knocked hard along the longitudinal direction and the signal was transmitted to the data acquisition and analysis module. After being processed by the dynamic signal acquisition and analysis system, DHDAS 6.8.18, the modal parameters of the installation frame were obtained (Table 2). The results of the modal finite element analysis (shown in Table 2) were essentially consistent with those of the modal test analysis for the installation frame. The first four modal inherent frequencies of the installation frame were concentrated in the

303–565 Hz range with 2.32% of the maximum inherent frequency error, indicating the reliability of the modal finite element analysis. During the transportation of the cuttage pillar, the power was provided by the motor. The maximum speed of the motor output shaft was 3000 r/min, suggesting a frequency of 50 Hz, which was far lower than 296.58 Hz. Therefore, the random vibration with a frequency lower than 50 Hz was transmitted to the installation frame, resulting in a small possibility of resonance.

Table 2. Comparison of modal results between the finite element analysis and the test.

Order	Frequency		Vibration Shape		Frequency of Error
	Modal Finite Element Analysis (Hz)	Modal Test Analysis (Hz)	Modal Finite Element Analysis	Modal Test Analysis	
1	303.47	296.58	bending	bending	2.32%
2	441.18	443.94	bending	bending	−0.62%
3	500.69	506.72	bending + torsion	bending + torsion	−1.19%
4	564.62	554.53	bending + torsion	bending + torsion	1.82%

Note: frequency of error = (modal finite element analysis – modal test analysis)/modal test analysis.

6. Conclusions

In this study, an automatic cuttage device for an arch shed pillar based on force feedback was proposed, which provides a new idea for the automatic cutting of arch shed pillars.

- (1) The wind resistance of a small arch shed was analyzed. The simulation analysis by ANSYS software showed that the wind resistance was better when the cutting depth was 10 cm.
- (2) Three-dimensional modeling of the cuttage device was carried out through SOLIDWORKS software, the trajectory of the execution end was planned, and the relevant motion parameters were solved through MATLAB software simulation to avoid motion impact and make the motion trajectory smoother.
- (3) A modal analysis and experimental verification were carried out for the installation frame. The experiment showed that the resonance frequency was in the range of 303–565 Hz, and the device did not resonate during the operation.
- (4) A real-time feedback mechanism based on “current–force–depth” was built, which could feed back the current of the electric pusher motor in real-time. Based on this, the cutting depth was estimated in real time, allowing for the convenient building of an equal-depth pillar cuttage device. Even under the condition of the stress limit of the pillar, the automatic cutting device was able to realize “overload stop” without causing damage to the pillar, and realize the overload protection of the pillar. This could have a positive role in promoting the technical development and social application of automatic arch shed construction.

Due to the limitations of time and funds, this study did not investigate the interaction mechanisms of “arch shed pillar soil”, which have certain limitations. In the future, this further study will be carried out, as well as a study on the linear cutting of arch shed pillars, to further explore the operation efficiency in the process of automatic cutting of arch shed pillars.

Author Contributions: Conceptualization, K.C.; methodology, X.L.; software, S.J.; validation, X.H.; formal analysis, L.L.; investigation, T.W.; resources, G.M.; data curation, K.C.; writing—original draft preparation, K.C.; writing—review and editing, W.L.; visualization, Y.S.; supervision, W.L.; project administration, W.L.; funding acquisition, W.L. All authors have read and agreed to the published version of the manuscript.

Funding: This research was funded by the Wang Tongchuan Innovation and Entrepreneurship Fund Project of Northwest A&F University (4015401515010118), the Key Research and Development Program—Major (Key) Projects of the Ningxia Hui Autonomous Region (2019BFF02003) and the Key Industry Chain Innovation Project of the Shaanxi Province (2018ZDCXL-NY-03-06).

Institutional Review Board Statement: Not applicable.

Informed Consent Statement: Not applicable.

Data Availability Statement: Not applicable.

Conflicts of Interest: The authors declare no conflict of interest.

References

- Anderson, H.C.; Rogers, M.A.; Hoover, E.E. Low tunnel covering and microclimate, fruit yield, and quality in an organic strawberry production system. *HortTechnology* **2019**, *29*, 590–598. [CrossRef]
- Lewers, K.S.; Fleisher, D.H.; Daughtry, C.S.T.; Vinyard, B.T. Low-tunnel strawberry production: Comparison of cultivars and films. *Int. J. Fruit Sci.* **2020**, *20*, 705–732. [CrossRef]
- Henschel, J.M.; Resende, J.T.; Giloni-Lima, P.C.; Zeist, A.R.; Lima, R.B.; Santos, M.H. Production and quality of strawberry cultivated under different colors of low tunnel cover. *Hortic. Bras.* **2017**, *35*, 364–370. [CrossRef]
- Liu, P.; Wang, C.; Qin, H.; Hou, J.; Li, T. Design and experiment of single-row double cuttage and film covering multi-functional machine for low tunnels. *Trans. Chin. Soc. Agric. Eng.* **2021**, *37*, 1–9, (In Chinese with English Abstract).
- Liu, P.; Qin, H.; Wang, Y.; Shao, R.; Wang, Y. Design and Development of a Low Tunnel Machine. *J. Agric. Mech. Res.* **2021**, *43*, 83–89, (In Chinese with English Abstract).
- Liu, J.; Zhao, S.; Li, N.; Faheem, M.; Zhou, T.; Cai, W.; Zhao, M.; Zhu, X.; Li, P. Development and field test of an autonomous strawberry plug seeding transplanter for use in elevated cultivation. *Appl. Eng. Agric.* **2019**, *35*, 1067–1078. [CrossRef]
- Orde, K.M.; Sideman, R.G. Winter survival and second-year spring yields of day-neutral strawberry are influenced by cultivar and the presence of low tunnels. *HortTechnology* **2021**, *31*, 77–88. [CrossRef]
- Zhao, Y.; Lu, D.; Zhen, Y. Research to Enhance the Supporting Stiffness of Different U-Type Sheds. *Appl. Mech. Mater.* **2012**, *256–259*, 892–895. [CrossRef]
- Cramer, M.E.; Demchak, K.; Marini, R.; Leskey, T. UV-blocking high-tunnel plastics reduce Japanese beetle (*Popillia japonica*) in red raspberry. *Hortscience* **2019**, *54*, 903–909. [CrossRef]
- Morcous, G. Performance of Conservatories under Wind and Snow Loads. *J. Archit. Eng.* **2009**, *15*, 102–109. [CrossRef]
- Santolini, E.; Pulvirenti, B.; Torreggiani, D.; Tassinari, P. Novel methodologies for the characterization of airflow properties of shading screens by means of wind-tunnel experiments and CFD numerical modeling. *Comput. Electron. Agric.* **2019**, *163*, 104800. [CrossRef]
- Wang, C.; Jiang, Y.; Li, X.; Bai, Y.; Wang, T. Wind-induced vibration response analysis of Chinese solar greenhouses. *Comput. Electron. Agric.* **2021**, *181*, 105954. [CrossRef]
- Rack-woo, K.; Lee, I.; Kwon, K. Evaluation of wind pressure acting on multi-span greenhouses using CFD technique, Part 1: Development of the CFD model. *Biosyst. Eng.* **2017**, *164*, 257–280.
- Briassoulis, D.; Dougka, G.; Dimakogianni, D.; Vayas, I. Analysis of the collapse of a greenhouse with vaulted roof. *Biosyst. Eng.* **2016**, *151*, 495–509. [CrossRef]
- Mossadeghi-Bjorklund, M.; Jarvis, N.; Larsbo, M.; Forkman, J.; Keller, T. Effects of compaction on soil hydraulic properties, penetration resistance and water flow patterns at the soil profile scale. *Soil Use Manag.* **2019**, *35*, 367–377. [CrossRef]
- Spong, M.W. Modeling and control of elastic joint robots. *J. Dyn. Syst. Meas. Control.* **1987**, *109*, 310–319. [CrossRef]
- Chen, S.; Luo, M.; He, F. A universal algorithm for sensorless collision detection of robot actuator faults. *Adv. Mech. Eng.* **2018**, *10*, 1687814017740710. [CrossRef]
- Shi, Y.; Zhang, W.; Yang, T.; Wang, Y.; Liu, L.; Cui, Y. Flexible Joints of Picking Manipulator Based on Current Feedback. *IEEE Access* **2020**, *8*, 85329–85338. [CrossRef]
- Qin, H. Design and Experiment of Self-Propelled Variable-Pitch Arch Shed Inserting Laminator. Master's Thesis, Shandong Agricultural University, Tai'an, China, 2020.
- China Radio Network. Available online: <http://www.cnr.cn/> (accessed on 11 January 2019).
- Mistriotis, A.; Castellno, S. Airflow through net covered tunnel structures at high wind speeds. *Biosyst. Eng.* **2012**, *113*, 308–317. [CrossRef]
- Guan, Y.; Zheng, F.; Zhang, P.; Qin, C. Spatial and temporal changes of meteorological disasters in China during 1950–2013. *Nat. Hazards* **2015**, *3*, 2607–2623. [CrossRef]
- Huai, B.; Wang, Y.; Sun, W.; Wang, X.Y. The unique “Regional East Gale with Blowing Snow” natural disaster in Jeminay County, Xinjiang Uygur Autonomous Region, China. *Nat. Hazards* **2018**, *2*, 1105–1108.
- Yasushi, U.; Kazuya, T. Collapse and reinforcement of pipe-framed greenhouse under static wind loading. *J. Civ. Eng. Archit.* **2020**, *14*, 583–594. [CrossRef]
- Shaanxi Meteorological Bureau. Available online: <https://sn.cma.gov.cn/> (accessed on 2 May 2021).
- Kim, R.W.; Lee, I.B.; Yeo, U.H.; Lee, S.Y. Evaluation of various national greenhouse design standards for wind loading. *Biosyst. Eng.* **2019**, *188*, 136–154. [CrossRef]
- Xie, X.; Chen, K. Simulation test of wind load characteristics of South China type single-span plastic greenhouse. *Trans. Chin. Soc. Agric. Eng.* **2000**, *16*, 90–94, (in Chinese with English abstract).

28. Shi, J.; Li, T. New method to eliminate commutation torque ripple of brushless dc motor with minimum commutation time. *IEEE Trans. Ind. Electron.* **2013**, *60*, 2139–2146. [[CrossRef](#)]
29. Carlson, R.; Lajoie-mazenc, M.; Fagundes, J. Analysis of torque ripple due to phase commutation in brushless DC machines. *IEEE Trans. Ind. Appl.* **1992**, *28*, 632–638. [[CrossRef](#)]
30. Lin, J.; Sun, Y.; Lammers, P.S. Evaluating model-based relationship of cone index, soil water content and bulk density using dual-sensor penetrometer data. *Soil Tillage Res.* **2014**, *138*, 9–16. [[CrossRef](#)]
31. Gauthier, J.F.; Angeles, J.; Nokleby, S. *Optimization of a Test Trajectory for Scara Systems*; Springer: Berlin, Germany, 2008; pp. 225–234.
32. Barnard, C.; Briot, S.; Caro, S. 2012 Trajectory generation for high speed pick and place robots. In Proceedings of the ASME 2012 11th Biennial Conference on Engineering Systems Design and Analysis, American Society of Mechanical Engineers, Nantes, France, 2–4 July 2012; pp. 165–174.
33. Bin, Z.F.; Ong, Z.C.; Khoo, S.Y. A review of operational modal analysis techniques for in-service modal identification. *J. Braz. Soc. Mech. Sci. Eng.* **2020**, *42*, 398.
34. Jiang, X.; Jiang, F. Operational modal analysis using symbolic regression for a nonlinear vibration system. *J. Low Freq. Noise Vib. Act. Control.* **2021**, *40*, 120–134. [[CrossRef](#)]
35. Pintelon, R.; Guillaume, P.; Schoukens, J. Uncertainty calculation in (operational) modal analysis. *Mech. Syst. Signal Process.* **2007**, *21*, 2359–2373. [[CrossRef](#)]
36. Wang, Y.; Pan, J. Applications of Operational Modal Analysis to a Single-Phase Distribution Transformer. *IEEE Trans. Power Deliv.* **2015**, *30*, 2061–2063. [[CrossRef](#)]
37. Yao, Y.; Du, Y.; Zhu, Z.; Mao, E.; Song, Z. Vibration characteristics analysis and optimization of corn combine harvester frame using modal analysis method. *Trans. Chin. Soc. Agric. Eng.* **2015**, *31*, 46–53.

Article

Evaluation of Soil-Cutting and Plant-Crushing Performance of Rotary Blades with Double-Eccentric Circular-Edge Curve for Harvesting *Cyperus esculentus*

Hao Zhu, Xiaoning He, Shuqi Shang, Zhuang Zhao, Haiqing Wang, Ying Tan, Chengpeng Li and Dongwei Wang *

College of Mechanical and Electrical Engineering, Qingdao Agricultural University, Qingdao 266109, China; 20202204029@stu.qau.edu.cn (H.Z.); 201502004@qau.edu.cn (X.H.); sqshang@qau.edu.cn (S.S.); 20192204158@stu.qau.edu.cn (Z.Z.); 20202204018@stu.qau.edu.cn (H.W.); 20202204017@stu.qau.edu.cn (Y.T.); 20202204011@stu.qau.edu.cn (C.L.)

* Correspondence: 200701031@qau.edu.cn

Citation: Zhu, H.; He, X.; Shang, S.; Zhao, Z.; Wang, H.; Tan, Y.; Li, C.; Wang, D. Evaluation of Soil-Cutting and Plant-Crushing Performance of Rotary Blades with Double-Eccentric Circular-Edge Curve for Harvesting *Cyperus esculentus*. *Agriculture* **2022**, *12*, 862. <https://doi.org/10.3390/agriculture12060862>

Academic Editors: Muhammad Sultan, Redmond R. Shamshiri, Md Shamim Ahamed and Muhammad Farooq

Received: 15 May 2022

Accepted: 11 June 2022

Published: 15 June 2022

Publisher's Note: MDPI stays neutral with regard to jurisdictional claims in published maps and institutional affiliations.



Copyright: © 2022 by the authors. Licensee MDPI, Basel, Switzerland. This article is an open access article distributed under the terms and conditions of the Creative Commons Attribution (CC BY) license (<https://creativecommons.org/licenses/by/4.0/>).

Abstract: Severe plant entanglement and high power consumption are the main problems of the up-cut rotary blade during *Cyperus esculentus* harvesting. Optimization of the rotary blade edge can enhance the soil-cutting and plant-crushing performance. In this study, the double-eccentric circle method was used to design the edge curve of the IT245 rotary blade. The edge curve's dynamic sliding-cutting angle of equidistant points was analyzed to verify that the optimized rotary blade (IT245P) met the requirements of *Cyperus esculentus* harvesting. In order to accurately simulate the fragmentation of *Cyperus esculentus* plants after interaction with the rotary blade, the Hertz–Mindlin with Bonding contact model was selected to establish the flexible model of *Cyperus esculentus* plants. The plant–soil–rotary blade discrete element model was constructed to conduct simulation tests with power consumption and the plant-crushing ratio as evaluation indexes. The field experiment was carried out with tillage depth stability and power consumption as the experimental indexes. The results of the simulation test and field experiment showed that the power consumption of the IT245P rotary blade was reduced by 13.10%, and the plant-crushing rate was increased by 11.75% compared with the IT245 rotary blade. The optimal operating parameters were 1.08 m/s for forward speed, 107.11 mm for tillage depth, and 258.05 r/min for shaft speed. Under such a combination, the tillage depth stability and the power consumption were 94.63% and 42.35 kW. This study showed that a rotary blade with a double-eccentric circular curve could better realize plant-crushing and consumption reduction and meet the operation requirements of *Cyperus esculentus* and other Chinese medicinal materials' harvesting.

Keywords: up-cut rotary blade; edge curve; *Cyperus esculentus* plant; flexible model

1. Introduction

Cyperus esculentus is an excellent oilseed crop, originating in Africa and the Mediterranean region, and is known as the “underground walnut”. As a high-end healthy edible oil, it is popular among the public [1–3]. *Cyperus esculentus* is still harvested in the semi-mechanized method in most areas in China, in which the excavation job is mostly carried out using the IT245 rotary blade. However, due to the strong tillering ability and developed root system of *Cyperus esculentus*, the plant-crushing performance of the IT245 rotary blade is poor, which affects the subsequent cleaning performance [4–6]. In addition, the root of the rotary blade is particularly easily entangled by plants, which increases the power consumption and seriously hinders the development of the mechanized harvesting of *Cyperus esculentus* [7–9].

The plant-crushing performance is mainly related to the rotary blade's structural parameters, where the rotary blade edge curve is the influencing factor of the plant-crushing performance [10–13]. Similar to *Pinellia ternata* and other traditional Chinese medicine

crops, *Cyperus esculentus* has high requirements for plant-crushing. Scholars at home and abroad have conducted numerous researches on the optimal design of rotary blade edge curves. Depending on the various cutting requirements, the edge curve needs to be designed with different dynamic slip-cutting angle trends. There are two main trends of the dynamic sliding-cutting angle, one that remains constant and one that increases gradually from the tool holder to the tip. In the first one, the edge curve with an equal sliding-cutting angle is designed by a logarithmic spiral for cutting stalks of rice [14–19], corn [20–22], sunflower [23], and other crops. The edge curve with an equal sliding-cutting angle has better cutting performance and is suitable for cutting crops with coarse stalks independent of each other. Also, serrations can be added to the edge to achieve a better tearing effect [16,24–26]. In the second one, the edge curve with a gradually increasing sliding-cutting angle is designed using the Archimedean spiral and sinusoid curve, mainly used to cut objects with high cutting resistance such as clay [27–32]. The gradually increasing sliding-cutting angle can enhance the cutting performance of the cutting edge and thus reduce the working resistance. When designing the edge curve, some scholars [10,11,13] believe that the starting position of the cutting edge of the rotary blade is not the main cutting area, and the dynamic sliding-cutting angle can be reduced appropriately. However, in practical operations in areas with many plant stems, the tool holder is particularly easily entangled by plants, resulting in increased working resistance and power consumption [33,34].

In order to reduce the tillage resistance and enhance the plant-crushing performance of the rotary blade, a rotary blade edge curve was designed based on the double-eccentric circle method in this paper. Based on the discrete element method, a flexible model of the *Cyperus esculentus* plant was established. The power consumption and plant-crushing performance of IT245 and IT245P rotary blades were compared by analyzing the changes in shaft torque and broken bond numbers during the simulation test. With the evaluation indexes of tillage depth stability and power consumption, the best combination of parameters for *Cyperus esculentus* excavation was determined by field experiments to provide a reference for a reduction in power consumption for harvesting *Cyperus esculentus* and other Chinese medicinal materials as well as the optimization of the reverse rotary tiller.

2. Materials and Methods

2.1. General Structure and Working Principle

2.1.1. General Structure and Parameters

The reverse rotary tiller is composed of a frame, transmission device, shaft, rotary blade, depth limiting device, and leading flow cover; the general structure is shown in Figure 1. The rotary tiller hangs on the tractor's rear, and a one-time operation can complete the rotary tillage, throwing, and other processes. The main structural parameters are shown in Table 1.

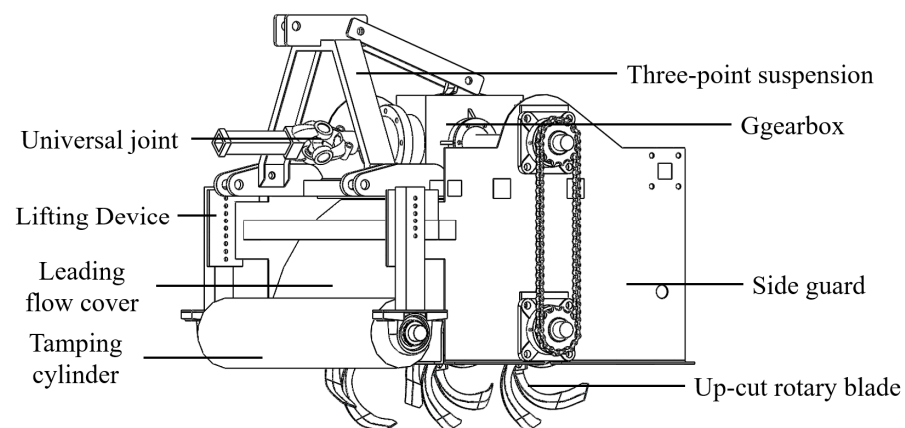


Figure 1. General structure of reverse rotary tiller.

Table 1. Main parameters of reverse rotary tiller.

Parameters	Values
Matching power/(kW)	80
Dimension (L × W × H)/(mm)	1480 × 950 × 880
Operation efficiency/(km·h ⁻¹)	0~1.5
Working width/(mm)	1200
Shaft speed/(r·min ⁻¹)	0~400
Tillage depth/(mm)	0~150

The rotary blade is an essential part of the reverse rotary tiller, and its structural parameters have a significant influence on *Cyperus esculentus* harvesting and power consumption. The rotary blade is composed of the lengthwise section, sidelong section, and holding section, as shown in Figure 2. The edge curve of the lengthwise blade has the function of cutting the soil, plant stems, and stubble; the front of the scoop surface has the function of cutting, turning, braking, and throwing the soil.

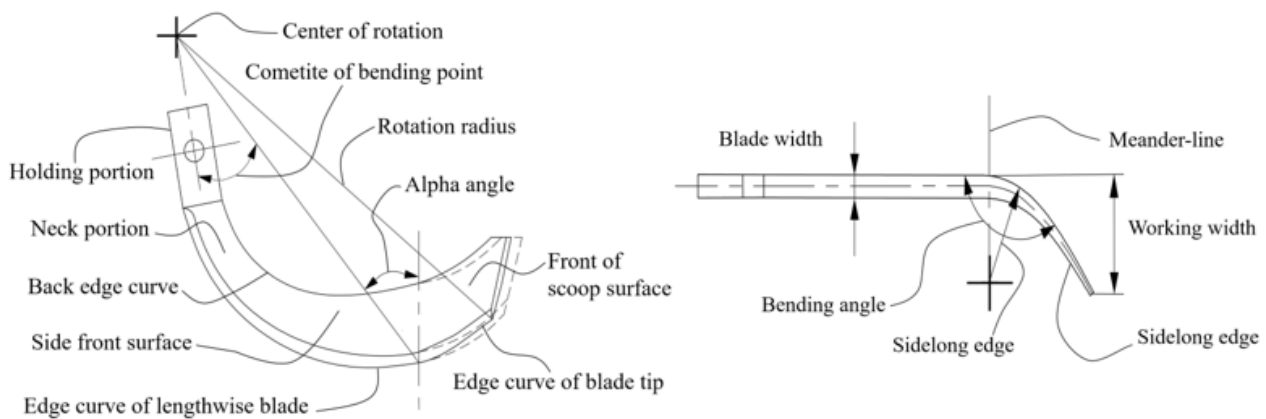


Figure 2. Structure of rotary blade.

2.1.2. Working Principle

During field operation of the reverse rotary tiller, the device is connected to the tractor by three-point suspension. The lifting device is adjusted to control the height of the tamping cylinder so that the rotary tillage depth reaches the *Cyperus esculentus* harvesting operation requirements. The tractor output shaft is connected to the transmission input shaft through the universal joint. The rotary tiller shaft is driven by the transmission output shaft to rotate and cut the soil by chain transmission. The rotation direction of the shaft is opposite to that of the tractor’s driving wheel. Under the reverse rotation, the bean–soil mixture is thrown backward along the cover to the conveying device to complete the *Cyperus esculentus* harvesting and excavation operation [35].

2.2. Design of Rotary Blade Edge Curve

The Archimedean spiral is often adopted to design the edge curve of Chinese standard rotary blades. However, the small sliding–cutting angle at the tool holder makes it easy to tangle plants and increases the excavating resistance and power consumption when working on the land with many plant stems. In this study, based on the IT245 rotary blade, two eccentric arcs with different sliding–cutting performances were used as the edge curve, which can better meet the requirements of *Cyperus esculentus* harvesting. The polar coordinate equation of the eccentric circle was calculated by

$$r = \rho \cos \varphi \pm \rho \sqrt{(R/\rho)^2 - \sin^2 \varphi} \tag{1}$$

where r is the polar radius, mm; ρ is the distance between O and O_1 , mm; φ is the angle between the polar radius of any point on the circle and the x -axis; R is the radius of the eccentric circle, mm. The derivative function of Equation (1) was

$$\frac{dr}{d\varphi} = -\rho \sin \varphi + \rho \frac{-\sin \varphi \cos \varphi}{\sqrt{e^2 - \sin^2 \varphi}} \tag{2}$$

where e is the coefficient of excentralization. The static sliding-cutting angle of the eccentric circle τ_s was calculated by

$$\tau_s = \tan^{-1}\left(\frac{\sqrt{e^2 - \sin^2 \varphi}}{\sin \varphi}\right) \tag{3}$$

As shown in Equation (3), the sliding-cutting angle of the eccentric circle edge curve is related to the coefficient of excentralization and the angle between the pole radius and x -axis. The variation law is shown in Figure 3. When the sliding-cutting angle is small, the high cutting resistance is not conducive to sliding-cutting, and it is easily entangled by plants, causing an increase in cutting load. When the sliding-cutting angle increases, the cutting resistance will be reduced, conducive to sliding-cutting, and can effectively prevent plant entanglement. However, the cutting distance increases, and the frictional resistance continues to work, resulting in increased power consumption. According to the research results [18,24], the optimal range of sliding-cutting angles is $35^\circ \sim 55^\circ$. In addition, for smooth sliding of uncut plant stems out of the blade during multi-plant stem field operations, the sliding-cutting angle of the rotary blade is required to increase gradually from the beginning to the end. Referring to the variation law of eccentric circle τ - φ , the coefficient of excentralization was taken as 1.2~1.6 to meet the sliding-cutting angle requirements for *Cyperus esculentus* harvesting.

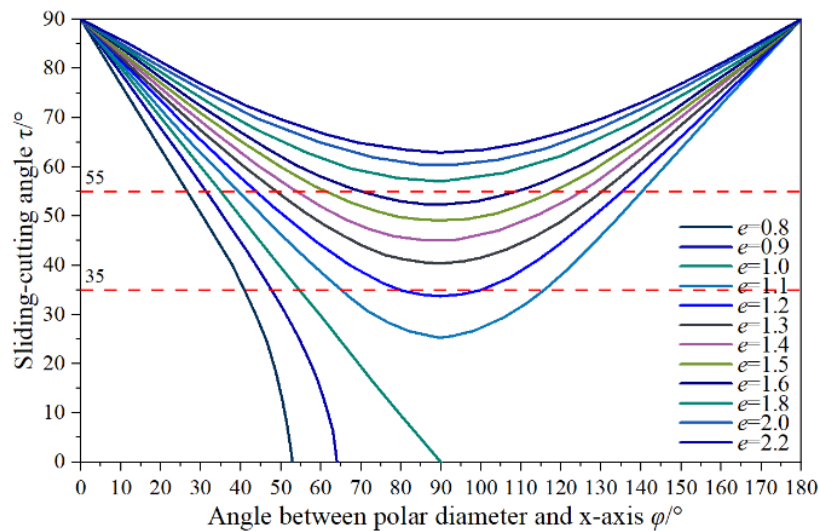


Figure 3. Variation law between sliding-cutting angle and angle between polar radius and x -axis.

In order to reduce the plant entanglement at the root of the rotary blade, the sliding-cutting angle needs to meet the conditions of uncut plant stems sliding out. Since the tool holder is the secondary working area, the blade length in this area can be reduced, and the sliding-cutting angle should be increased quickly. When the plant stems move to the middle of the cutting edge, the sliding-cutting angle should increase slowly with the increase of the pole radius. The plant stems are cut off or slide out of the rotary tillage area along the cutting edge due to the pushing action. According to the requirements of *Cyperus esculentus* harvesting and the variation law of eccentric circle τ - φ , the coefficient of excentralization of sections AB and BC was 1.2 and 1.6. In order to prevent the tool holder

from plant entanglement, the minimum working radius r_0 was reduced to 125 mm within a reasonable range. The extreme diameter r_1 at the bending line was 230 mm, consistent with the tillage depth requirements of *Cyperus esculentus* harvesting. The coordinate system was established with the rotation center as the origin, and the double-eccentric circle curves AB and BC are shown in Figure 4. The eccentric circle radius R and the polar angle φ at any point on the eccentric circle curve were calculated by:

$$R = -\frac{re}{\cos \varphi + \sqrt{e^2 - \sin^2 \varphi}} \tag{4}$$

$$\cos \varphi = \frac{r^2 - (R/e)^2(e^2 - 1)}{2rR/e} = \frac{e^2r^2 - R^2(e^2 - 1)}{2rRe} \tag{5}$$

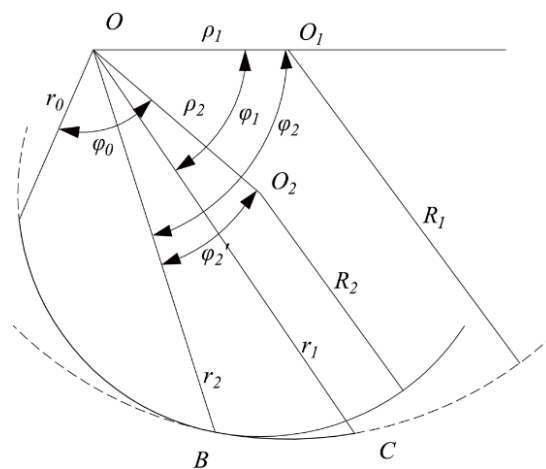


Figure 4. Double-eccentric circle curve, where O_1 and O_2 are the centers of the eccentric circle; φ_0 and φ'_2 are polar angles of points A and B on curve AB; φ_1 and φ_2 are polar angles of points C and B on curve BC; r_0 , r_1 , and r_2 are polar radii of point A, C, and B; R_1 and R_2 are the radii of the eccentric circle; ρ_1 is the distance between O and O_1 ; ρ_2 is the distance between O and O_2 .

The double-eccentric circular-edge design should ensure a smooth transition at the connection of the two arcs. Point B is the intersection point of the two arcs, in which the sliding-cutting angle of the two arcs should be equal:

$$\text{tg} \tau_s = \frac{\sqrt{e_2^2 - \sin^2 \varphi'_2}}{\sin \varphi'_2} = \frac{\sqrt{e_1^2 - \sin^2 \varphi_2}}{\sin \varphi_2} \tag{6}$$

The polar angle φ'_2 at point B on the eccentric arc AB was calculated by

$$\varphi'_2 = \sin^{-1} \frac{e_2}{\sqrt{1 + (e_1^2 - \sin^2 \varphi_2) / (\sin^2 \varphi_2)}} \tag{7}$$

The radius R_2 of the eccentric circle and the polar angle φ_0 at point A were calculated by Equations (6) and (7). In the field operation of the rotary tiller, there is an angle $\Delta\tau$ between the absolute velocity v_a and the relative velocity v_r at each point on the edge curve. $\Delta\tau$ is the difference between the dynamic sliding-cutting angle and the static sliding-cutting angle of the up-cut rotary blade, as shown in Figure 5. According to the trigonometric function relationship, $\Delta\tau$ was calculated by

$$\begin{cases} v_a^2 = r^2\omega^2 + v_e^2 + 2r\omega v_e \cos \varphi \\ v_e^2 = v_a^2 + r^2\omega^2 - 2v_a r\omega \cos \Delta\tau \end{cases} \tag{8}$$

$$\Delta\tau = \arctan(v_e/r\omega) \tag{9}$$

where v_e is the forward speed, m/s. The suitable operation parameters of the rotary tiller are 0.8~1.4 km/h for forward speed and 250~350 r/min for shaft speed [35,36]. According to Equation (9), $\Delta\tau$ is proportional to the forward speed v_e and inversely proportional to the shaft speed ω . Therefore, the operating conditions of 1.4 km/h for forward speed and 250 r/min for shaft speed were chosen as the critical conditions for the edge-curve design [37,38]. It ensured that the rotary blade met the sliding–cutting conditions under low shaft speed and high forward speed.

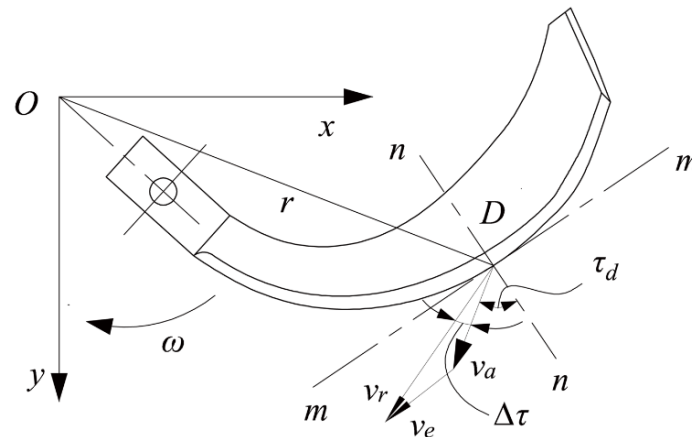


Figure 5. Speed analysis of cutting edge of rotary blade, where D is an arbitrary point on the rotary blade cutting edge; n - n is the normal line at point D ; m - m is the tangent line at point D .

After all the double-eccentric circle cutting-edge parameters were determined, four points were selected proportionally on each of the eccentric arcs AB and BC to solve the dynamic sliding–cutting angle. The results are shown in Table 2.

Table 2. Calculated values of parameters of edge curve of lengthwise blade.

Eccentric Circular Arc	NO.	Polar Radius r /mm	Polar Angle/(°)	Static Cutting Angle ϕ /(°)	Static Sliding–Cutting Angle τ_s /(°)	Dynamic Sliding–Cutting Angle τ_d /(°)	Difference between τ_s and τ_d $\Delta\tau$ /(°)
AB	1	125.00	63.26	48.07	41.93	35.15	6.78
	2	137.34	58.16	45.05	44.95	38.77	6.18
	3	149.48	53.03	41.73	48.27	42.59	5.68
	4	160.00	48.42	38.54	51.46	46.15	5.31
BC	1	174.39	80.22	38.01	51.99	47.11	4.87
	2	196.35	71.28	36.29	53.71	49.38	4.33
	3	214.73	64.04	34.18	55.82	51.86	3.96
	4	230.00	58.01	32.37	58.00	54.30	3.70

As shown in Table 2, the difference between the static sliding–cutting angle and dynamic sliding–cutting angle was inversely proportional to the pole radius. The dynamic sliding–cutting angle of the cutting edge was within 35°~55°. In the eccentric arc (AB) at the rotary blade tool holder, the dynamic sliding–cutting angle increased rapidly from 35.15° to 46.15° with the increase in the pole diameter. The eccentric arc (AB) was short as the edge curve of the secondary operation area. The dynamic sliding–cutting angle at the starting point was greater than 35° under extreme operational conditions, which can theoretically solve the problem of plant entanglement at the rotary blade tool holder and meet the preset optimization target. In the eccentric arc (BC), the dynamic sliding–cutting angle increased slowly from 46.15° to 54.30° with the increase in the pole radius. The eccentric arc (BC) was

long as the edge curve of the main operation area. The dynamic sliding–cutting angle was large, with good sliding–cutting performance for cutting soil and crushing plants.

The front of the scoop surface is an essential part of the rotary blade, which has the function of turning, braking, and throwing soil during the rotary tillage operation. In order to ensure sliding–cutting performance and smooth transition and prevent plant entanglement caused by a sudden change in the cutting-edge curve curvature, the front cutting edge was designed with the same eccentric circle curve as the end of the side cutting edge.

2.3. Discrete Element Simulation

2.3.1. Rotary Blade Model

SolidWorks 2020 (Dassault Systemes S.A) was applied to build a simplified model of the up-cut rotary blade on a 1:1 scale. The model was saved in STL format and imported into EDEM2021 (DEM Solutions Ltd., Edinburgh, Scotland, UK). The simulation model is shown in Figure 6. The material of both rotary blades was 65Mn steel [21].

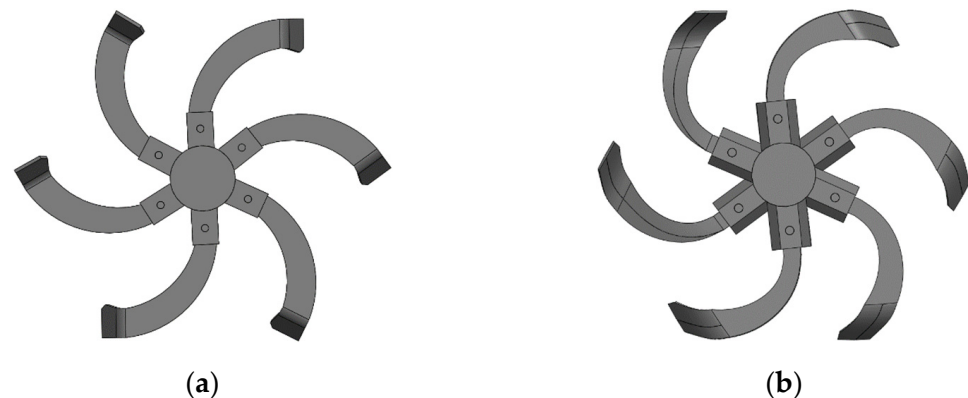


Figure 6. Simulation model of up-cut rotary blade. (a) IT245 rotary blade; (b) IT245P rotary blade.

2.3.2. Soil Model

The soils in this study were sampled by the five-point sampling method at the *Cyperus esculentus* plantation in Minquan County, Shangqiu City, Henan Province (115°18' E, 34°31' N), China, in mid-November 2020. The soil's water content, density, and firmness at different depths were measured. The experimental instruments were an RXH-14B hot-air circulation oven (Nanjing Changjiang Pharmaceutical Machinery Manufacturing Ltd., Nanjing, China), JDM-I automatic soil-density tester (Inner Mongolia Huake Jiacheng Technology Ltd., Ordos, China), TJSD-750II soil-compactness tester (Zhejiang Topunnong Technology Ltd., Hangzhou, China), soil-extraction ring knife, and shovel.

The SMJYS200 soil-testing vibrating sieve (Henan Shuangmu Machinery Manufacturing Ltd., Xinxiang, China) was used for sieving. The soil type of the *Cyperus esculentus* planting base was sandy loam, in which the clay particles (<0.002 mm) account for $10.34 \pm 1.64\%$, powder sand (0.02~0.002 mm) accounts for $22.48 \pm 1.94\%$, and sand particles (0.02~2 mm) account for $67.18 \pm 3.95\%$. Due to the minimal diameter of sandy loam particles, the number of soil particles in the simulation test reached ten million, which requires high computer performance and a long simulation time. The particle scaling method is a common and more feasible processing method to ensure test accuracy. The particles are appropriately scaled up so that the discrete element model can complete the simulation within a reasonable and adequate time [16,18]. In this study, the radius of a single soil particle was set to 2 mm according to the reference literature [17,20,21] and soil parameters of the *Cyperus esculentus* planting site. The following three models were set according to the structure of sandy loam soil particles: granular particles, columnar particles, and agglomerated particles, as shown in Figure 7.

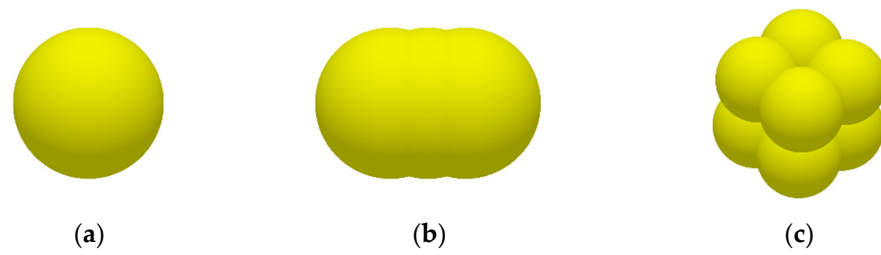


Figure 7. Sandy loam soil particle model. (a) Granular particle; (b) Columnar particle; (c) Agglomerated particle.

According to the intrinsic parameters of sandy loam soil, the soil state is loose and the cohesion between soil particles is low. The Hertz–Mindlin (no-slip) contact model does not consider the mutual attraction between particles and is suitable for studying sandy loam soil conditions, as shown in Figure 8. Therefore, the Hertz–Mindlin (no-slip) contact model was chosen as the contact mechanics model for the discrete element simulation in this study.

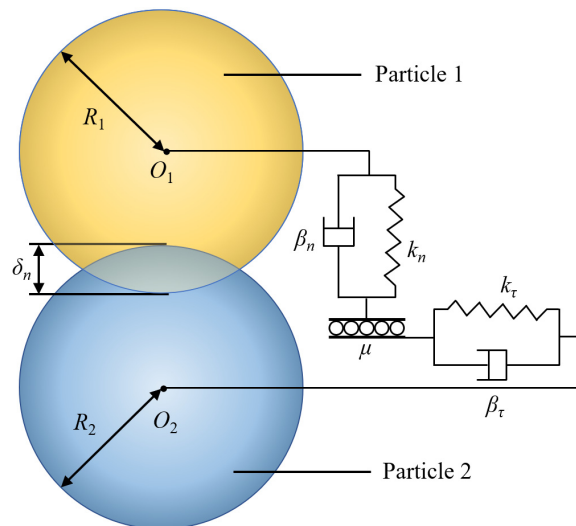


Figure 8. Hertz–Mindlin (no-slip) contact model. where O_1 and O_2 are the positions of the sphere centers of two particles, respectively; R_1 and R_2 are the radii of two particles, respectively, mm; δ_n is normal overlap after collisions, mm; k_n and k_τ are the normal and tangential Hooke coefficients of particles, respectively; β_n and β_τ are the normal and tangential damping coefficients of particles, respectively; μ is the sliding coefficient between particles.

2.3.3. *Cyperus esculentus* Plant Model

The object of this study was Henan No.1 *Cyperus esculentus*, which was sampled by a random sampling method, as shown in Figure 9. The average length, width, and thickness of plant leaves were 82.35 ± 5.74 mm, 5.12 ± 0.62 mm, and 1.52 ± 0.36 mm. The average length and diameter of the root system were 135.46 ± 9.87 mm and 0.84 ± 0.27 mm. The average moisture content of the leaves and root system of the *Cyperus esculentus* plants measured by the RXH-14B hot-air circulation oven was $24.25 \pm 4.90\%$ and $37.60 \pm 5.44\%$.

The characterization of *Cyperus esculentus* plants is complex, and the morphological changes are diverse after stress. In order to simulate the interparticle cohesion accurately, the Hertz–Mindlin with Bonding contact model was chosen to constrain the plant morphology and simulate the fragmentation of the leaves and roots of the *Cyperus esculentus* plant during rotary tillage. After the constraint was broken, bonds were no longer generated between the two particles and the contact was solved as a separate sphere model. In this soil bonding model, when the practical contact distance between soil particles was less

than the sum of the bond radius ($R_{1B} + R_{2B}$), the constraint was formed by the adhesive bond between particles [39,40], as shown in Figure 10.



Figure 9. *Cyperus esculentus* planting base. (a) Uncultivated land; (b) section of the *Cyperus esculentus* plant.

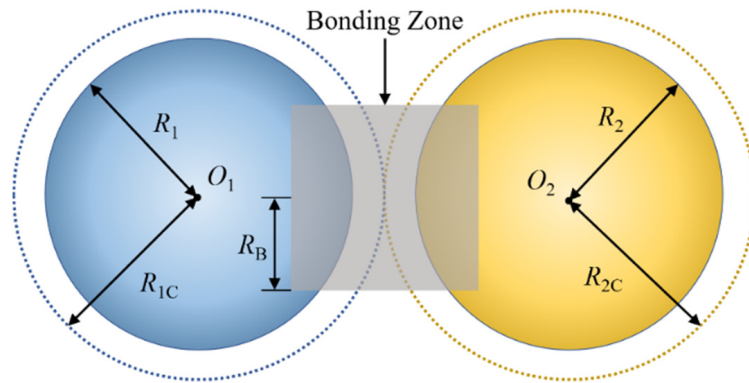


Figure 10. Hertz–Mindlin with Bonding contact model, where R_1 and R_2 are the practical radii of particles, mm; R_{1C} and R_{2C} are the contact radii between particles, mm; R_B is the bonding zone radius between particles, mm.

In a specific volume of material, the bonding zone formed between particles can be transformed into a bonding force due to the presence of water. Based on the *Cyperus esculentus* plant parameters determination results, the root particles were simplified to spheres of the same diameter and the leaf particles were simplified to two spheres connected, as shown in Figure 11. The bonding radius was calculated by

$$\omega = \frac{m_2}{m_1 + m_2} = \frac{\rho_2(\pi R_B^3 - \pi R^3)}{\rho_1\pi R^3 + \rho_2(\pi R_B^3 - \pi R^3)} \tag{10}$$

where ω is the moisture content, %; m_1 is the mass of the particle, kg; m_2 is the mass of moisture, kg; ρ_1 is the dry density of the material particle, kg/m³; ρ_2 is the density of moisture, kg/m³; R is the material particle radius, m; R_B is the bonding radius between particles, m.

The bonding radius of *Cyperus esculentus* leaf and root particles was 3.35 mm and 2.25 mm. A new meta-particle was created, and 142 leaf particles and 401 root particles were added according to the morphology and dimensions of *Cyperus esculentus* plants. The triaxial coordinates were set separately to establish a discrete metamodel of *Cyperus esculentus* plants, as shown in Figure 11 [41–44]. Contact parameters of discrete element model are shown in Table 3.

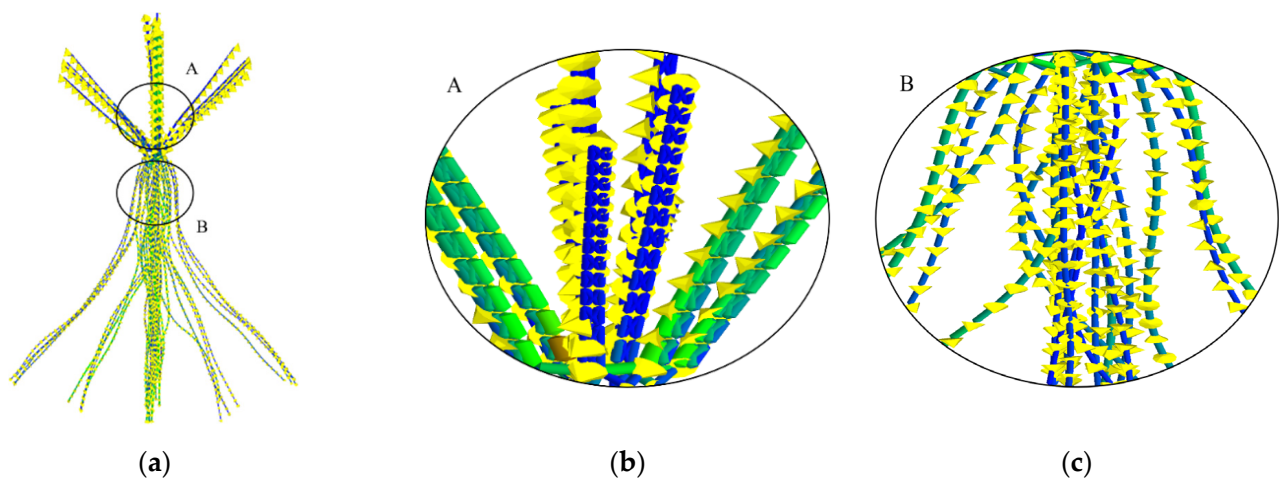


Figure 11. Flexible model of *Cyperus esculentus* plants. (a) Whole plant; (b) bonds between leaf particles; (c) bonds between root particles.

Table 3. Contact parameters of discrete element model.

Contact Model	Static Friction Coefficient	Rolling Friction Coefficient	Restitution Coefficient
Soil–Soil	0.55	0.15	0.43
Plant–Plant	0.34	0.08	0.35
Soil–Plant	0.48	0.05	0.32
Soil–65Mn	0.52	0.12	0.20
Plant–65Mn	0.33	0.10	0.30

2.3.4. Discrete Element Simulation of Soil–Plant–Rotary Blade

Based on the trial soil slot of Qingdao Agricultural University, the simulated trial soil slot was established with a length \times width \times height of 1000 mm \times 550 mm \times 360 mm and the material was 45 steel. According to the *Cyperus esculentus* planting pattern, eight plants with a length \times width \times height of 280 mm \times 200 mm \times 200 mm were established, and the plant spacing and row spacing were 200 mm and 300 mm, respectively. After the rotary blade model was imported into EDEM, the “Sinusoidal Translation Kinematic” and “Sinusoidal Rotation Kinematic” motions were added: 0.8 m/s for the forward speed and 250 r/min for the shaft speed. The simulation process of reverse rotary tillage for *Cyperus esculentus* harvesting is shown in Figure 12. At 0~0.5 s, *Cyperus esculentus* plant model was generated; 0.5~1 s, soil particle model was generated statically; 1~9 s, simulated rotary tillage operation was conducted.

2.4. Evaluation Index of Rotary Tillage Quality

2.4.1. Power Consumption

During the simulation of the rotary tillage, the difference in power consumption can be reflected by the dynamic changes in shaft torque and forward resistance. The shaft speed and forward speed of the rotary blade were 250 r/min and 0.5 m/s, respectively. The power consumption of the rotary tiller was calculated by

$$W = \frac{nM}{9550} + Fv_m \quad (11)$$

where W is the power consumption, kW; n is the shaft speed, r/min; M is the shaft torque, N·m; F is the forward resistance, N; v_m is the forward speed, m/s.

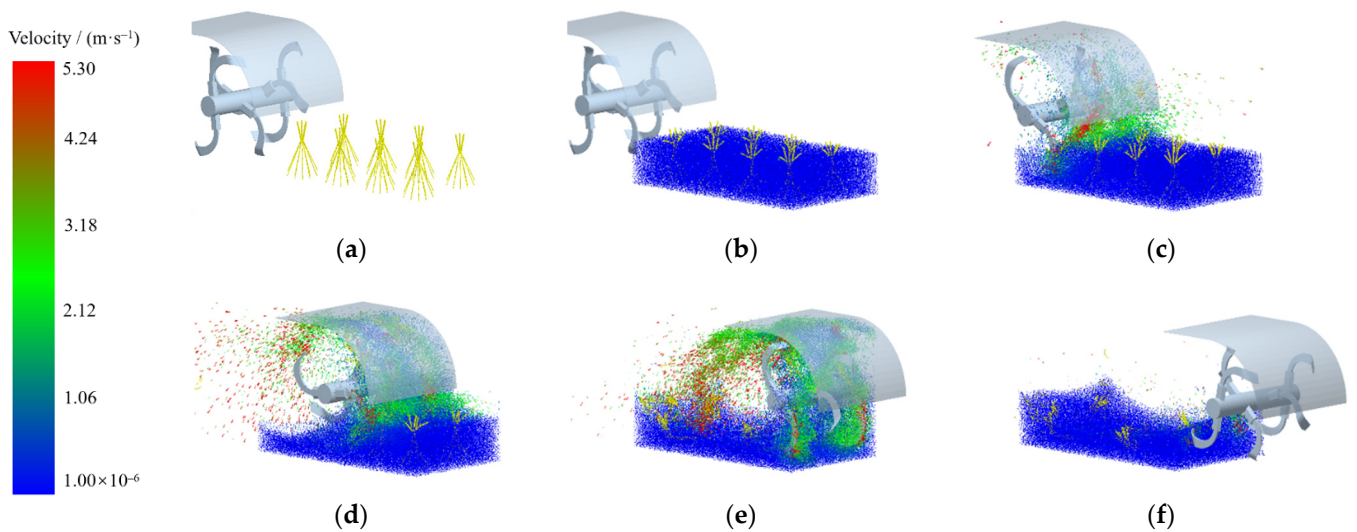


Figure 12. Simulation process of reverse rotary tillage for *Cyperus esculentus* harvesting. (a) 0.5 s; (b) 1 s; (c) 2 s; (d) 4.5 s; (e) 6.4 s; (f) 8.7 s.

2.4.2. Plant-Crushing Performance

In the initial state, the total number of intact bonds and broken bonds of the *Cyperus esculentus* plant model were 5560 and 0. The soil particles and the *Cyperus esculentus* plant particles were hidden in the reverse-rotary-tillage simulation. Only the intact bonds between the *Cyperus esculentus* plant particles were retained. With the rotary blade cutting, the *Cyperus esculentus* plant model reached the force limit, and the bonding zone was broken [45–47]. The process of breaking the bonding zone of *Cyperus esculentus* plant particles is shown in Figure 13.

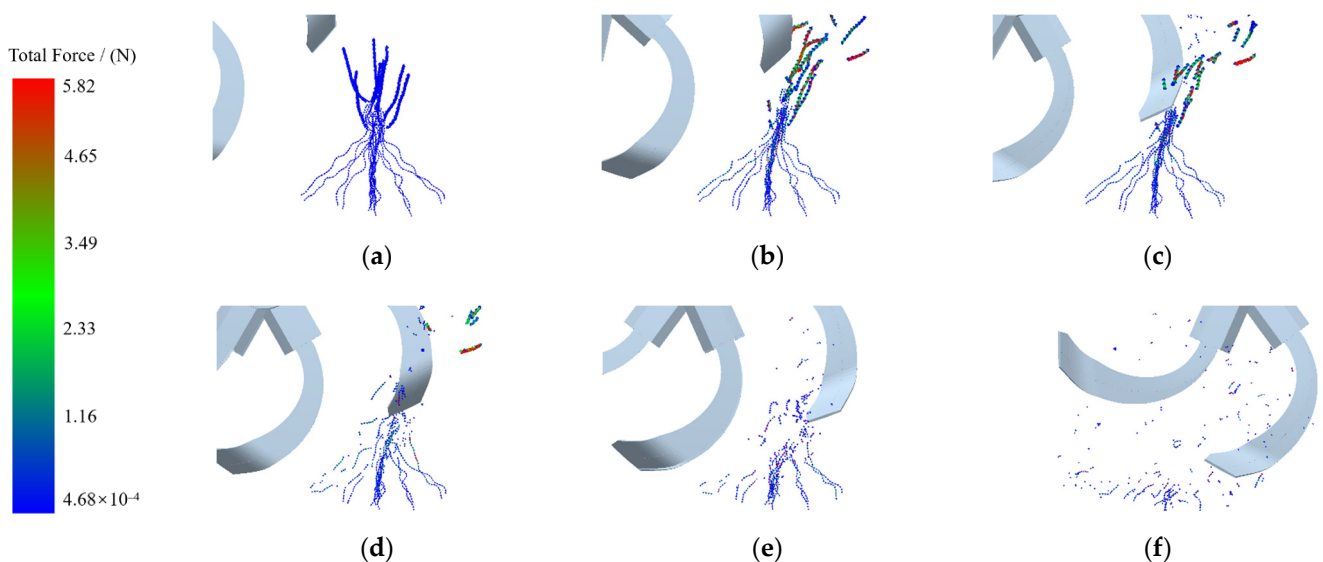


Figure 13. The crushing process of *Cyperus esculentus* plants. (a) 1.9 s; (b) 2.1 s; (c) 2.3 s; (d) 2.5 s; (e) 2.7 s; (f) 2.9 s.

2.5. Field Experiment

2.5.1. Test Conditions

To test the field operation performance of the reverse rotary tiller with an optimized edge curve, a field experiment of reverse rotary tillage excavation was conducted on 19 November 2021 at the *Cyperus esculentus* planting base in Minquan County, Shangqiu City, Henan Province (115°18' E, 34°31' N), as shown in Figure 14. Based on the GB/T

5668-2017 “Rotary Tiller”, a representative field of *Cyperus esculentus* was selected and the test conditions around the field were ensured to be the same [43,47,48]. The length of the test area was 50 m, a 10 m stabilization area was set at both sides, and the width was 32 m. Four routes were tested during the field experiment, with an 8 m interval between adjacent routes. The test devices were the Dongfeng DF604 tractor (Changzhou Dongfeng Agricultural Machinery Group Ltd., Changzhou, China, matching power: 60 hp) and the reverse-rotary-tillage device.



Figure 14. Field experiment. (a) Test device; (b) data acquisition.

The environmental parameters of the field experiment were measured in the tillage area and the results are shown in Table 4. The data collection instruments were a RXH-14-B hot-air circulation oven (Nanjing Changjiang Pharmaceutical Machinery Manufacturing Ltd.), JDM-I automatic soil-density tester (Inner Mongolia Huake Jiacheng Technology Ltd.), and TJSJ-750-II soil-compactness tachometer (Zhejiang Topunnong Technology Ltd., range: 0~7922 kPa, depth: 0~375 mm, accuracy: ±5%). Other auxiliary tools were MPL13-50 steel-frame tape measure (Hunan Maojun Baogong Electronics Ltd., Changsha, China, range: 0~150 m, accuracy: 1 mm), stainless steel straightedge (range: 0~200 mm, accuracy: 0.5 mm), XL-008-type stopwatch (Wenzhou Shengmei Instrumentation Ltd., Wenzhou, China, accuracy: 0.01 s), soil-taking ring knife, and shovel.

Table 4. Test conditions at field experiment site.

Test Site	Soil Type	Soil Moisture Content/(%)	Soil Density /(kg m^{-3})	Soil Firmness/(kPa)	Row Spacing/(mm)	Plant Spacing/(mm)	Stubble Height/(mm)	Yield Per Mu/(kg)
Minquan County	Sandy Loam	15.36 ± 1.56	2650 ± 50	425 ± 50	200 ± 15	150 ± 10	90 ± 7	1265 ± 50

2.5.2. Index and Factor of Test

According to the tillage requirements, when operating under the same working conditions, agricultural equipment should ensure the same tillage depth. The fluctuation of tillage depth will lead to problems such as increased power consumption or an increased missed digging rate. The tillage depth stability was calculated by

$$U = \left(1 - \frac{\sqrt{\sum_{i=1}^N (a_i - a)^2 / N}}{\sum_{i=1}^N a_i / N} \right) \times 100\% \tag{12}$$

where U is the tillage depth stability coefficient; a is the average tillage depth, mm; a_i is the tillage depth of point i , mm; N is the number of measurement points.

The power consumption is an important index to assess the operating quality of the rotary tiller. In the field test, the working width B_0 of each test route was measured with a

tape measure; the tillage depth h_n was measured as above; the time used for each test route was measured with a stopwatch to calculate the single-route machine forward speed v_m . Concerning the Agricultural Machinery Design Manual [46], the power consumption of the rotary tiller was calculated by

$$W = \frac{1}{\eta} B_0 \frac{h_n}{100} v_m \left(p + \frac{\rho(\pi R n)^2}{7200} \right) \quad (13)$$

where W is the power consumption, kW; η is the transmission efficiency, 0.9 in this study; B_0 is the working width, m; h_n is the tillage depth, cm; v_m is the forward speed, m/s; p is the specific resistance of cutting soil, N/m²; ρ is the soil density before tillage, kg/m³; R is the rotating radius of the rotary blade, m; n is the shaft speed, r/min.

In this experiment, the main factors affecting the harvesting quality of *Cyperus esculentus* were forward speed, shaft speed, and tillage depth. The experimental factor codes are shown in Table 5. During the experiment, the forward power was provided by the tractor and controlled by adjusting the tractor gear. The bevel gear ratio in the transmission system of the reverse-rotary-tillage device was 1.5. The chain-transmission ratio was 0.85, 1, and 1.15 from low to high, which cooperated to control the shaft speed. The tillage depth was controlled by adjusting the height of the depth-limiting device.

Table 5. Experimental factors codes.

Test Factor	Symbol	Test Level		
		−1	0	1
Forward speed/(km·h ^{−1})	A	0.8	1.1	1.4
Tillage depth/(mm)	B	100	115	130
Shaft speed/(r·min ^{−1})	C	250	300	350

3. Results and Analysis

3.1. Evaluation Index of Rotary Tillage Quality

3.1.1. Analysis of Power Consumption

The curves of the power consumption of the IT245P rotary blade and IT245 rotary blade are shown in Figure 15. During the rotary tillage excavation simulation test, the overall power consumption change trends of the IT245P rotary blade and IT245 rotary blade were similar and divided into four stages. In the first stage, the *Cyperus esculentus* plant and soil particles were generated, the rotary blade did not interact with the soil, and the power consumption of the rotary tiller was 0. In the second stage, the rotary blade rotated in the reverse direction to cut soil. At the moment of initial contact with the soil, the force on the rotary blade increased steeply, which led to a rapid increase in the power consumption of the rotary tiller. The shaft continued to rotate and the power consumption reached the first peak when the front cutting edge touched the soil. With the increase in tillage depth, the power consumption reached the maximum. In the third stage, when the rotary blade continued to rotate beyond the maximum tillage depth, the resistance of the rotary tiller gradually decreased and the power consumption had a valley value. In the fourth stage, as the rotating tiller moved forward, part of the soil collided with the deflector and fell back into the front of the rotary tiller causing congestion. The cutting resistance and the power consumption increased. The power consumption during the overall reverse-rotary-tillage operation changed periodically and coincided with the practical state of the rotary tiller cutting the soil. In the simulation test, the average power consumption of the IT245 and IT245P rotary blades were 43.90 kW and 38.82 kW, with an average power consumption reduction of 13.10%. The results showed that the optimized rotary blade could better complete the excavation of *Cyperus esculentus* with reduced resistance and consumption.

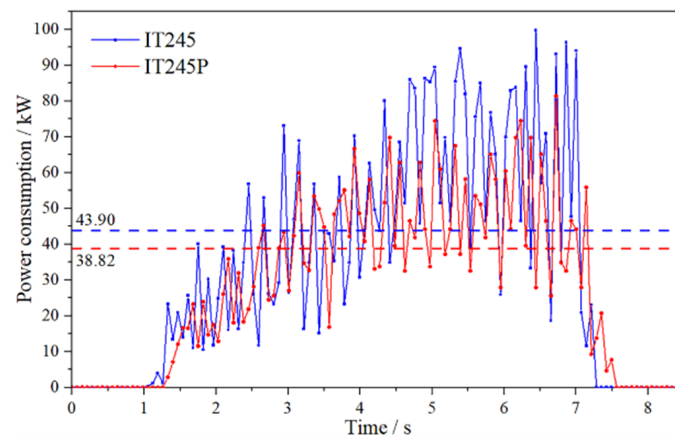


Figure 15. Power consumption curve of rotary blade.

3.1.2. Analysis of Plant-Crushing Performance

The curve of the broken bond number of *Cyperus esculentus* plant particles with time is shown in Figure 16. When the IT245 and IT245P rotary blades worked, the number of broken bonds was nonlinearly proportional to time and divided into two stages. At 0~2 s, the rotary blade cut the soil but did not touch the *Cyperus esculentus* plants. The force on the *Cyperus esculentus* plant particles did not reach the breaking limit and it remained in its original state. At 2~9 s, the rotary blade started to cut the *Cyperus esculentus* plant and the force on the plant gradually increased until it reached the limit of force. The bonds between the particles broke, which showed that the *Cyperus esculentus* plants were broken. Furthermore, as the machine moved forward, the number of broken interparticle bonds increased until the rotary tiller left the simulated operation area. The total number of broken interparticle bonds of the IT245 and IT245P rotary blades were 1575 and 1760, and the total number of broken bonds increased by 11.75%. The results showed that the optimized rotary tillage blade was more effective in breaking the *Cyperus esculentus* plants and could reduce the subsequent separation and cleaning-process burden.

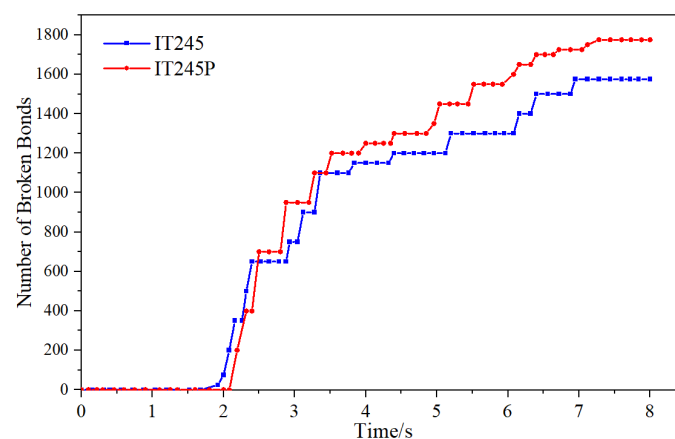


Figure 16. Comparison of broken bonds of *Cyperus esculentus* plants.

3.2. Field Experiment

According to the Box–Behnken central combination design theory of the Design-Expert software, the forward speed, shaft speed, and tillage depth of the reverse-rotary-tillage device were selected as the influencing factors for the response surface experimental research, and the response values of tillage depth stability and power consumption were used for parameter optimization by a three-factor, three-level quadratic regression orthogonal test scheme. The results of the orthogonal test are shown in Table 6.

Table 6. Experimental protocol and results.

No.	Test Factor			Evaluation Index	
	Forward Speed	Tillage Depth	Shaft Speed	Tillage Depth Stability $U/\%$	Power Consumption $W/(kW)$
1	0	−1	−1	95.99	42.51
2	−1	0	−1	95.01	42.03
3	−1	−1	0	94.63	42.20
4	1	1	0	94.78	45.90
5	−1	1	0	93.21	44.35
6	0	0	0	94.94	43.43
7	0	−1	1	95.64	43.67
8	1	−1	0	95.96	43.84
9	0	0	0	94.74	43.41
10	0	1	1	94.47	46.59
11	0	0	0	94.89	43.17
12	0	0	0	95.05	43.01
13	1	0	−1	96.04	41.84
14	0	1	−1	95.02	44.87
15	0	0	0	94.82	43.82
16	−1	0	1	94.79	42.90
17	1	0	1	95.74	44.63

3.2.1. Tillage Depth Stability of *Cyperus esculentus* Harvesting

Removing non-significant influences, the quadratic polynomial regression equation targeting the tillage depth stability of the rotary tiller was

$$U = 94.89 - 0.59A - 0.18B + 0.61C + 0.57B^2 \quad (14)$$

From the analysis of the variance of tillage depth stability, as shown in Table 7, the determination coefficient $R^2 = 0.9734$ indicated that the regression equation model applied to 97.34% of the test data. The effect of the regression model was highly significant ($p < 0.01$); the effect of shaft speed (C), forward speed (A), and the interaction term of tillage depth (B^2) on tillage depth stability was highly significant ($p < 0.01$); the effect of tillage depth (B) on tillage depth stability was significant ($p < 0.05$). The other test factors' interaction terms did not significantly affect tillage depth stability. Neglecting the non-significant factors and comparing the F values, the influence of the factors on the test mounding angle was $C > A > B$.

Table 7. Variance analysis of quadratic term model of tillage depth stability.

Source	Sum of Squares	Freedom	Mean Square	F Value	p -Value
Model	7.54	9	0.84	28.49	<0.01 **
A	2.81	1	2.81	95.53	<0.01 **
B	0.25	1	0.25	8.57	0.0221 *
C	2.98	1	2.98	101.26	<0.01 **
AB	0.010	1	0.010	0.34	0.5780
AC	0.014	1	0.014	0.49	0.5066
BC	1.6×10^{-3}	1	1.6×10^{-3}	0.054	0.8222
A^2	0.13	1	0.13	4.59	0.0694
B^2	1.37	1	1.37	46.70	<0.01 **
C^2	0.017	1	0.017	0.59	0.4687
Residual	0.21	7	0.029	—	—
Lack of Fit	0.15	3	0.050	3.61	0.1233
Pure Error	0.055	4	0.014	—	—

Note: $0.01 < p < 0.05$ (significant, *); $0.001 < p < 0.01$ (highly significant, **).

The effects of test factors *A*, *B*, and *C* on tillage depth stability *U* are shown in Figure 17. When the *A* level increased, *U* gradually decreased from 95.3% to 94.1% and the rate of the decrease gradually accelerated in the interval of $-0.25\sim-0.9$. The research of Zhang et al. [11] showed that when other factors remained unchanged, the forward speed was proportional to the cutting pitch. The greater the forward speed, the greater the protrusion height at the furrow bottom and the worse the tillage depth stability. The greater the forward speed, the greater the influence on the tillage depth stability. When the *B* level was less than 0, *U* gradually decreased in the interval of $94.9\%\sim 95.6\%$, and the decrease rate gradually tended to 0. When the *B* level was greater than 0, *U* showed an increasing trend in the interval of $94.9\%\sim 95.25\%$ and the increase rate gradually increased. The researches of Wu and Yang et al. [1,6] showed that the size and the number of *Cyperus esculentus* tubers increased with the depth, and most of the *Cyperus esculentus* tubers grew to a nearly 115 mm depth. Most of the *Cyperus esculentus* tubers grew close to a depth of 115 mm, which was the test factor tillage depth (*B*) level of 0. A large number of *Cyperus esculentus* tubers squeezed with the soil, which significantly increased the firmness of the soil layer at a 115 mm depth. When the digging depth of the rotary blade was less than 115 mm, the tillage depth stability decreased with the increase in depth. When the digging depth was around 115 mm, the top of the front surface at the maximum rotary radius of the rotary blade collided with the *Cyperus esculentus*–soil agglomeration layer forming displacement deviation, resulting in a dynamic imbalance of the rotary tiller shaft, thus affecting the tillage depth stability. When the digging depth was greater than 115 mm, the cutting edge of the lengthwise blade cut the *Cyperus esculentus*–soil agglomeration layer. Under sliding–cutting, the agglomerate layer broke up and was thrown backward under the action to in front of the scoop surface. With the increase in the *C* level, *U* showed an almost linear growth trend of $94.2\%\sim 95.4\%$. The slope of the curve changed to a small extent and slowly decreased in the interval of $0.6\sim 0.75$. The researches of Zhang and Wang et al. [11,15] showed that the shaft speed was inversely proportional to the cutting pitch under the same conditions. The distance between the neighboring trochoids gradually decreased as the cutting pitch decreased. Hence, the protrusion height at the furrow bottom decreased and the tillage depth tended to be stable.

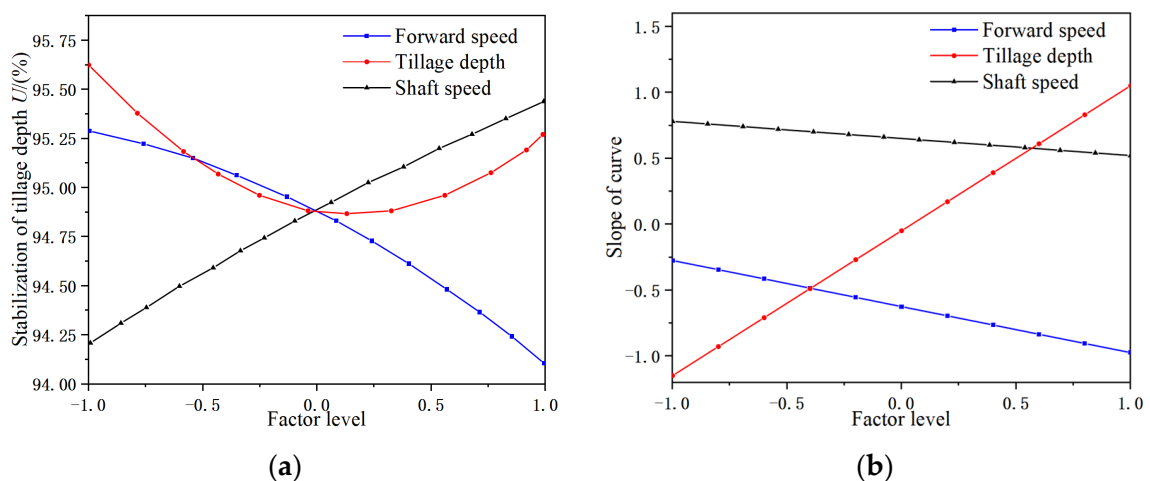


Figure 17. Single-factor effect of tillage depth stability. (a) Submodel regression curve; (b) slope of the factor curve.

The effects of the interaction factors on tillage depth stability *U* were visually analyzed by the response surface plots. As shown in Figure 18, there was no significant change in *U* when the interaction terms (*AB*, *AB*, *BC*) of forward speed, tillage depth, and shaft speed increased. This was consistent with the conclusions in the ANOVA table, that is, that the test factor interaction terms did not have a significant effect on tillage depth stability ($p > 0.05$).

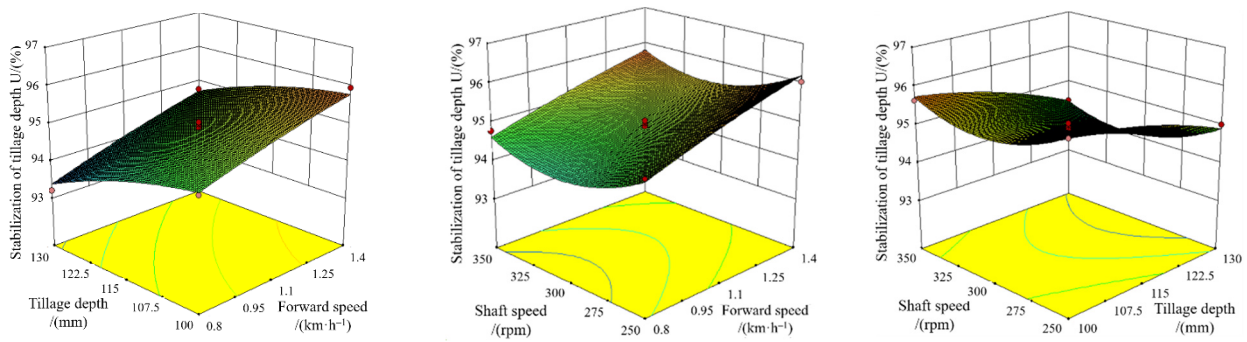


Figure 18. Response surface variation relationship influencing factors on the tillage depth stability.

3.2.2. Power Consumption of *Cyperus esculentus* Harvesting

Removing non-significant influences, the quadratic polynomial regression equation targeting the power consumption of the rotary tiller was

$$W = 43.37 + 0.59A + 1.19B + 0.82C + 0.48AC - 0.43A^2 + 1.13B^2 \quad (15)$$

In the power consumption ANOVA, as shown in Table 8, the coefficient of determination $R^2 = 0.9657$ indicated that the regression equation model applied to 96.57% of the test data. The effects of the regression model, forward speed (A), tillage depth (B), rotating shaft speed (C), and tillage depth interaction term (B^2) were highly significant ($p < 0.01$); machine forward speed and rotating shaft speed interaction term (AC) and machine forward speed interaction term (A^2) had a significant effect on power consumption ($p < 0.05$). The other test factor interaction terms had no significant effect on power consumption. Neglecting the non-significant factors and comparing the F -values, the order of the influence of each factor on the test stacking angle was $B > C > A$.

Table 8. Variance analysis of quadratic term model of power consumption.

Source	Sum of Squares	Freedom	Mean Square	F Value	p-Value
Model	26.38	9	2.93	21.91	<0.01 **
A	2.80	1	2.80	20.90	<0.01 **
B	11.26	1	11.26	84.12	<0.01 **
C	5.35	1	5.35	39.95	<0.01 **
AB	2.0×10^{-3}	1	2.0×10^{-3}	0.015	0.9056
AC	0.92	1	0.92	6.89	0.0342 *
BC	0.078	1	0.078	0.59	0.4690
A ²	0.77	1	0.77	5.76	0.0475 *
B ²	5.40	1	5.40	40.34	<0.01 **
C ²	0.034	1	0.034	0.26	0.6282
Residual	0.94	7	0.13	—	—
Lack of Fit	0.56	3	0.19	1.98	0.2596
Pure Error	0.38	4	0.094	—	—

Note: $0.01 < p < 0.05$ (significant, *); $0.001 < p < 0.01$ (highly significant, **).

The effects of test factors A , B , and C on power consumption W are shown in Figure 19. When the A level increased from -1 to 0.3 , U gradually increased from 42 to 43.3 and the growth trend gradually slowed down. When the level of A was greater than 0.3 , the slope of the U curve tended to 0 and the curve did not change significantly. The research of Zhang et al. [11] showed that the cutting pitch was proportional to the forward speed under the same conditions. When the cutting pitch was small, the cutting resistance increased with the cutting pitch. When the thickness of the soil unit exceeded the critical point, the resistance of the rotary cutter reached the peak and was only related to the rotary blade and soil parameters and was little affected by the forward speed [12,17]. U increased with the increase in B and the growth rate accelerated gradually. However, when the B

level increased from -1 to -0.4 , U varied less from 43 to 43.2 and slightly decreased. The researches of Wang and Hou et al. [5–7] showed that due to the strong tillering ability and developed root system, *Cyperus esculentus* plants were closely connected to the shallow soil. When the tillage depth was small, the cutting resistance of the rotary blade was influenced by the shallow plant leaves and root system, so there was a slight deviation in the effect of the tillage depth on power consumption. Overall, the power consumption is nonlinearly proportional to the tillage depth. The greater the tillage depth, the greater the cutting resistance of the rotary blade and the greater the power consumption [15,19,32,36]. When the C level increased, the slope of the U curve decreased slightly from 0.9 to 0.8, and overall, the U curve showed a linear growth trend. The research of Wang et al. [17] showed that the higher the shaft speed, the greater the power consumption. When the shaft speed was high, the throwing effect of the up-cut rotary blade was enhanced. The soil falling back to the front of the device was reduced and the soil-blocking situation was relieved, so the power consumption showed a slightly decreasing trend in the growth rate when the shaft speed was high.

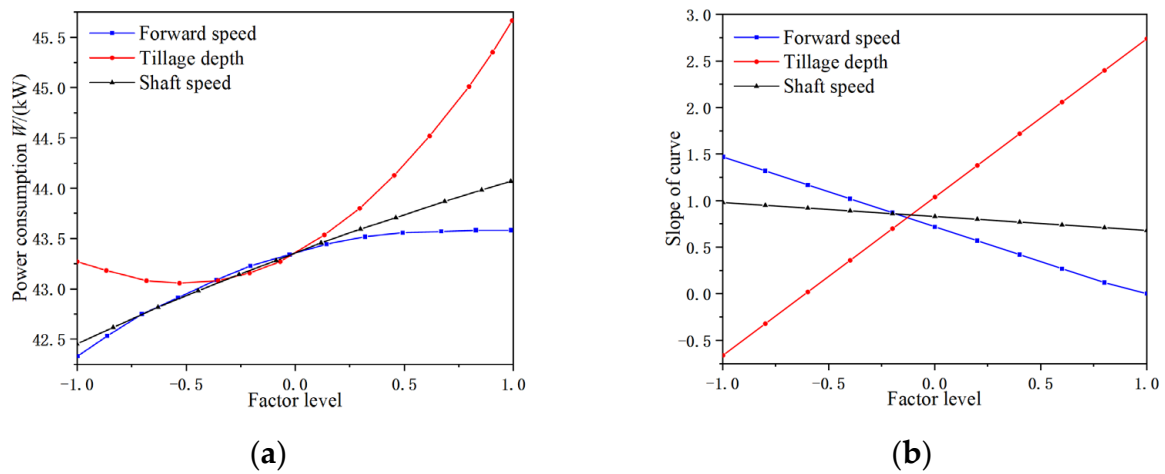


Figure 19. Single-factor effect of power consumption. (a) Submodel regression curve; (b) slope of the factor curve.

The effect of the interaction factors on power consumption W is shown in Figure 20. The power consumption of the rotary tiller gradually increased as the interaction terms of the test factors (AB , AC , BC) increased. This is consistent with the conclusion of Zhang et al. [11]. The power consumption U increased significantly when the interaction term AC increased. This was consistent with the conclusion of the ANOVA table that the effect of the interaction term AC on power consumption was significant ($p < 0.05$). Therefore, to reduce the power consumption of the reverse rotary tiller, the test factor chosen should be as small as possible to ensure the harvesting quality of *Cyperus esculentus*.

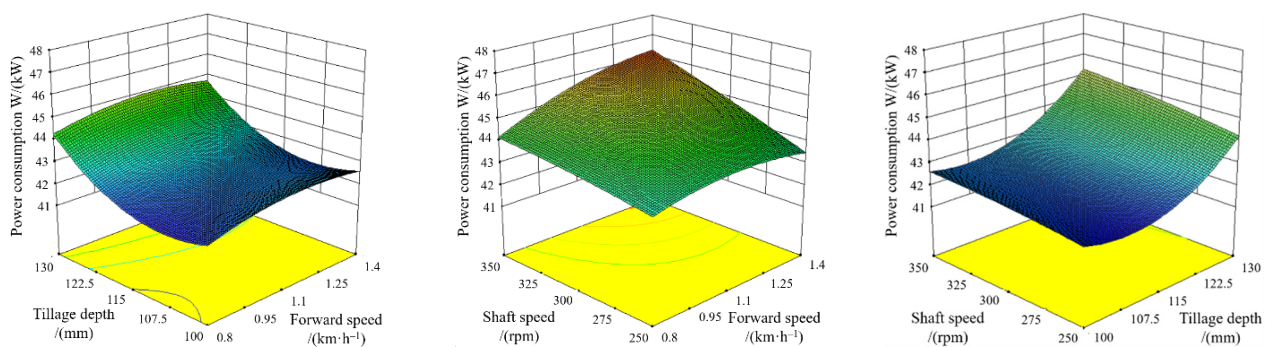


Figure 20. Response surface variation relationship of influencing factors on the power consumption.

According to the optimization function of the Design-Expert software, the optimal combination of operating parameters for the reverse rotary tiller for *Cyperus esculentus* harvesting was 1.08 m/s for forward speed, 107.11 mm for tillage depth, and 258.05 r/min for shaft speed. The tillage depth stability was 94.63% and the power consumption was 42.35 kW. Compared with the simulated value of power consumption of the rotary tiller, the practical power consumption increased by 9.10%. The reason is that in the practical operating environment, the sandy loam soil contains a small number of stones and other debris, which will increase the resistance of the rotary tiller in the process of cutting the soil, thus increasing the power consumption [15,19]. In addition, the water content of the sandy loam soil for the established soil model sample was $(14.33 \pm 1.25)\%$, whereas the soil water content increased to $(15.63 \pm 1.56)\%$ due to rainfall in the field test. In the soil's three-phase body (solid-phase skeleton, aqueous solution, and air), the percentage of water increased, the radius of adhesion between the soil particles increased, and the soil cohesion increased, which led to an increase in the soil-breaking resistance of the rotary blade and an increase in the power consumption.

4. Conclusions

- (1) In this study, two eccentric arcs with different sliding–cutting performances were used to design a rotary blade edge curve according to the requirements of *Cyperus esculentus* harvesting. By taking equidistant points of the lengthwise blade edge curve, it was calculated that the dynamic sliding–cutting angle was proportional to the pole radius. The dynamic sliding–cutting angle at the tool holder increased rapidly from 35.15° to 46.15° , which reduced plant entanglement and shortened the length of the secondary working area. The dynamic sliding–cutting angle at the tool tip increased slowly from 46.15° to 54.30° , forming a longer primary working area and good plant-crushing performance.
- (2) Based on the discrete element method, a sandy loam soil model and a flexible model of the *Cyperus esculentus* plant were established. The power consumption and plant-crushing performance of the IT245 and IT245P rotary blades were compared by simulation tests. The results showed that the average power consumption of the IT245P rotary blade was reduced by 13.10% and the crushing rate of *Cyperus esculentus* plants was increased by 11.75%.
- (3) The forward speed, tillage depth, and shaft speed were selected as the test factors, and the tillage depth stability and power consumption were selected as the evaluation indexes for the field test. The best combination of operating parameters of the reverse rotary tiller was 1.08 m/s for the forward speed, 107.11 mm for the tillage depth, and 258.05 r/min for the shaft speed. Under this optimal parameter combination, the stability of the tillage depth was 94.63% and the power consumption was 42.35 kW. This study showed that the rotary blade with a double-eccentric circular-edge curve could better complete the plant-crushing and power consumption reduction operations and meet the requirements for the harvesting of *Cyperus esculentus*.

Author Contributions: Conceptualization, H.Z. and X.H.; methodology, H.Z.; software, H.Z. and H.W.; validation, H.Z., D.W. and Z.Z.; formal analysis, H.Z. and Y.T.; investigation, H.Z.; resources, H.Z.; data curation, C.L.; writing-original draft preparation, H.Z.; writing-review and editing, S.S.; visualization, H.Z.; supervision, H.Z.; project administration, X.H.; funding acquisition, X.H. All authors have read and agreed to the published version of the manuscript.

Funding: This research was funded by the Autonomous Region Science and Technology Support Project Plan (Grant NO.2020E02112) and Major Science and Technology Projects in Henan Province (Grant NO.211100110100).

Institutional Review Board Statement: Not applicable.

Informed Consent Statement: Not applicable.

Data Availability Statement: Not applicable.

Conflicts of Interest: The authors declare no conflict of interest.

References

1. Wu, S.B.; Cui, G.F.; Wang, C.L. A new high-yield oil crop *Cyperus esculentus*. *Xinjiang Agric. Sci. Technol.* **2001**, *4*, 40.
2. Guo, T.T.; Wan, C.J.; Huang, F.H.; Wei, C.L.; Hu, Z.H. Research Progress on main nutritional components and physiological functions of *Cyperus esculentus*. *Chin. J. Oil Crop Sci.* **2021**, *43*, 1174–1180.
3. Tal, A.; Rubín, B. *Cyperus esculentus* L.—A new weed in Israel. *Phytoparasitica* **2005**, *33*, 245–246. [[CrossRef](#)]
4. Zhang, S.A.; Li, P.Z.; Wei, Z.M.; Cheng, Y.; Liu, J.Y.; Yang, Y.M.; Wang, Y.Y.; Mu, Z.S. *Cyperus* (*Cyperus esculentus* L.): A Review of Its Compositions, Medical Efficacy, Antibacterial Activity and Allelopathic Potentials. *Plants* **2022**, *11*, 1127. [[CrossRef](#)] [[PubMed](#)]
5. Hou, Z.H.; Mu, Z.J.; Zhao, J.L.; Bao, J.W.; Zhao, X.Q.; Wang, J.G.; Lu, Z.Y. Construction of evaluation index system for the windbreak and sand-fixing technology model of *Cyperus esculentus* guided by ecology, life and production integration concepts in windy and sandy areas in northern China. *J. North. Agric.* **2021**, *49*, 127–134.
6. Yang, Z.L. Characteristics and research progress of *Cyperus esculentus*. *North. Hortic.* **2017**, *17*, 192–201.
7. Ren, W.; Guo, D.Q.; Xing, G.J.; Yang, C.M.; Zhang, Y.Y.; Yang, J.; Niu, L.; Zhong, X.F.; Zhao, Q.Q.; Cui, Y.; et al. Complete Chloroplast Genome Sequence and Comparative and Phylogenetic Analyses of the Cultivated *Cyperus esculentus*. *Diversity* **2021**, *13*, 405. [[CrossRef](#)]
8. Umerie, S.C.; Uka, A.S. Brew wort from *Cyperus esculentus* tubers. *Bioresour. Technol.* **1998**, *66*, 83–85. [[CrossRef](#)]
9. Wang, Z.C.; Li, S.S.; Liang, X.; Xu, L.J.; Zou, X.J. Development status and prospect of *Cyperus esculentus* industry in China. *Sci. Technol. Indust.* **2022**, *22*, 62–67.
10. Zhu, H.B.; Qian, C.; Bai, L.Z.; Zhao, H.R.; Ma, S.W.; Zhang, X.; Li, H. Design and test of positive and negative rotating power corn stubble anti blocking device. *Trans. Chin. Soc. Agric. Eng.* **2022**, *38*, 1–11.
11. Zhang, C.L.; Xia, J.F.; Zhang, J.M.; Zhou, H.; Zhu, Y.H.; Wang, J.W. Design and test of cutter roller of six head spiral straw returning tillage machine. *Trans. Chin. Soc. Agric. Mach.* **2019**, *50*, 25–34.
12. Wang, J.Y.; Zhao, S.H.; Gao, L.L.; Yuan, Y.Y.; Yang, Y.Q. Design and test of passive disc stubble cutter with self-adjusting blade angle for corn ridge farming. *Trans. Chin. Soc. Agric. Mach.* **2021**, *52*, 59–67.
13. Pirchio, M.; Fontanelli, M.; Labanca, F.; Sportelli, M.; Frascioni, C. Energetic Aspects of Turfgrass Mowing: Comparison of Different Rotary Mowing Systems. *Agriculture* **2019**, *9*, 178. [[CrossRef](#)]
14. Zhao, T.J.; Wang, J.W. Analysis of the sliding cutting angle and installation angle of machete for returning the whole rice straw to the field and burying grass. *J. Agric. Mech. Res.* **2007**, *11*, 58–60, 63.
15. Zhao, T.J. Study on Optimal Design of Working Parameters of Rice Straw Returning Machine. Master's Thesis, Northeast Agricultural University, Harbin, China, 2007.
16. Modak, S.P.; Dogra, B.; Dogra, R.; Kumar, D. Design of rotary weeder blade. *AMA-Agr. Mech Asia Af.* **2016**, *47*, 32–40.
17. Habibi, A.J.; Surendra, S. Optimization and evaluation of rotary tiller blades: Computer solution of mathematical relations. *Soil Tillage. Res.* **2009**, *106*, 1–7.
18. Wang, Q. Design and Experimental Research of Rice Whole Stalk Deep Buried Returning Device. Master's Thesis, Northeast Agricultural University, Harbin, China, 2016.
19. He, J.; Zhen, K.; Li, H.W.; Wang, Q.J.; Chen, W.Z.; Zhang, X.C.; Wang, X.L.; Zhang, Z.Q.; You, B.X.; Zhao, H.B. Drag Reducing Rotary Tiller with Long and Short Rotary Blades. China Patent CN204948642U, 13 January 2016.
20. Lu, Z.C. Design and Experimental Research on Test Device for Cutting Corn Stubble with Discstubble Cutter. Master's Thesis, Shenyang Agricultural University, Shenyang, China, 2016.
21. Selvi, K.C. A new blade design of rotary tiller and static analysis using computer-aided tool. *Inma-Agric. Eng.* **2017**, *53*, 29–34.
22. Huang, W.Y.; Ren, D.Z.; Gong, Y.J.; Bai, X.W.; Shao, H.; Liu, C.W. Simulation and Experiment of Coupled Corn Straw Hides and Ranges Separation Based on Abaqus. *Trans. Chin. Soc. Agric. Mach.* **2021**, *52*, 124–133.
23. Lee, K.S.; Park, S.H.; Park, W.Y.; Lee, C.S. Strip tillage characteristics of rotary tiller blades for use in a dryland direct rice seeder. *Soil Tillage. Res.* **2003**, *71*, 25–32. [[CrossRef](#)]
24. Satit, K.; Was, M.S.; Panadda, N. Wear resistance of thermally sprayed rotary tiller blades. *Wear* **2007**, *263*, 604–608.
25. Guo, Q. Experimental Study on Cutting Mechanism and Performance of Cane Straw. Ph.D. Thesis, Jiangsu University, Zhenjiang, China, 2016.
26. Guo, X.; Zhang, X.L.; Xu, Y.F.; Li, P.P.; Chen, C. Mechanism and Simulation Research on efficient cutting of tomato vine straw. *J. Agric. Mech. Res.* **2017**, *39*, 17–24.
27. Tanya, N.; Sirisak, C. Development of blades for rotary tiller for use in Thai soils. *J. Food. Agric. Environ.* **2010**, *8*, 1336–1344.
28. Ding, W.M.; Wang, Y.H.; Peng, S.Z. Analysis and calculation of sliding cutting angle of reverse rotary tillage knife. *Trans. Chin. Soc. Agric. Mach.* **2001**, *6*, 26–29+21.
29. Wilmer, P.G.; Hugo, G.; Alejandro, T. Abrasive wear of rotary plow blades in a sandy loams soil. *Dyna-Colombia.* **2010**, *77*, 105–114.
30. Zhou, H.; Zhang, W.L.; Yang, Q.J.; Li, D.D.; Xia, J.F. Design and test of sliding cutting self-excited vibration drag reduction subsoiling device. *Trans. Chin. Soc. Agric. Mach.* **2019**, *50*, 71–78.
31. Zhang, Y.; Liu, J.; Yuan, W.; Zhang, R.; Xi, X. Multiple Leveling for Paddy Field Preparation with Double Axis Rotary Tillage Accelerates Rice Growth and Economic Benefits. *Agriculture* **2021**, *11*, 1223. [[CrossRef](#)]

32. Zhen, K.; Liu, G.Y.; Xia, J.F.; Chen, J.; Xu, L.; Liu, B.; Zhang, J.M.; Du, J.; Li, D.; Liu, Z.Y.; et al. Subsoiling Rotary Tillage Combined Tillage Machine for Reducing Viscosity and Resistance. China Patent CN213245577U, 25 May 2021.
33. Liu, J.Z.; Chen, H.Y.; Jin, Y.X. Straw Returning Multiple Operation Machine. China Patent CN202354047U, 1 August 2012.
34. Zhao, H.; Huang, Y.; Liu, Z.; Liu, W.; Zheng, Z. Applications of Discrete Element Method in the Research of Agricultural Machinery: A Review. *Agriculture* **2021**, *11*, 425. [[CrossRef](#)]
35. He, X.N.; Zhang, X.J.; Zhao, Z.; Shang, S.Q.; Wang, D.W.; Yuan, X.W. Design and test of resistance reducing excavation device for *Cyperus esculentus* based on discrete element method. *Trans. Chin. Soc. Agric. Mach.* **2021**, *52*, 124–133.
36. Zhao, T.J.; Wang, J.W.; Ge, Y.Y.; Zhang, M.Q.; Li, S.W.; Chen, Z.X. Improved design of cutter head of rice straw returning machine. In Proceedings of the Academic Annual Meeting of China Agricultural Engineering Society, Baoding, China, 20–22 October 2007.
37. Ji, K.Z.; Li, Y.M.; Liang, Z.W.; Liu, Y.B.; Cheng, J.H. Device and Method Suitable for Matching and Adjusting Reel Speed and Forward Speed of Multi-Crop Harvesting. *Agriculture* **2022**, *12*, 213. [[CrossRef](#)]
38. Zhou, M.K.; Xia, J.F.; Zhang, S.; Hu, M.J.; Liu, Z.Y.; Liu, G.Y.; Luo, C.M. Development of a Depth Control System Based on Variable-Gain Single-Neuron PID for Rotary Burying of Stubbles. *Agriculture* **2022**, *12*, 30. [[CrossRef](#)]
39. Mostafa, B.; Mojtaba, N.B.; Davoud, G.; Mustafa, U.; Thomas, K. Simulation of plate sinkage in soil using discrete element modelling: Calibration of model parameters and experimental validation. *Soil Tillage. Res.* **2020**, *203*, 1047–1060.
40. Subhash, C.T.; Morrissey, J.P.; Jin, S.; Chen, J.F.; Jin, Y.O. Micromechanical analysis of cohesive granular materials using the discrete element method with an adhesive elasto-plastic contact model. *Gemmina* **2014**, *16*, 383–400.
41. Hu, M.J.; Xia, J.; Zhou, Y.; Luo, C.; Zhou, M.; Liu, Z. Measurement and calibration of the discrete element parameters of coated delinted cotton seeds. *Agriculture* **2020**, *12*, 286. [[CrossRef](#)]
42. Jan, D.P.; Gemmina, D.E.; Daniel, V.F.R.; Adam, B.; Wim, M.C. Calibration of DEM material parameters to simulate stress-strain behavior of unsaturated soils during uniaxial compression. *Soil Tillage. Res.* **2019**, *194*, 104303–104312.
43. Magalhães, P.S.G.; Bianchini, A.; Braunbeck, O.A. Simulated and Experimental Analyses of a Toothed Rolling Coulter for Cutting Crop Residues. *Biosyst. Eng.* **2007**, *96*, 193–200. [[CrossRef](#)]
44. Yang, W.; Zhao, J.F.; Liu, X.Y.; Xi, L.Q.; Liao, J.A. Simulation and Test of “Separated Burying Device” of Green Manure Returning Machine Based on the EDEM Software. *Agriculture* **2022**, *12*, 569. [[CrossRef](#)]
45. Xu, G.M.; Xie, Y.X.; Matin, M.A.; He, R.Y.; Ding, Q.S. Effect of Straw Length, Stubble Height and Rotary Speed on Residue Incorporation by Rotary Tillage in Intensive Rice–Wheat Rotation System. *Agriculture* **2022**, *12*, 222. [[CrossRef](#)]
46. Chinese Academy of Agricultural Mechanization Sciences. *Agricultural Machinery Design Manual*; China Agricultural Science and Technology Press: Beijing, China, 2007; p. 854.
47. Han, L.J.; Yuan, W.; Yu, J.J.; Jin, J.J. Xie, D.S. Simulation and Experiment of Spiral Soil Separation Mechanism of Compound Planter Based on Discrete Element Method (DEM). *Agriculture* **2022**, *12*, 511. [[CrossRef](#)]
48. Shi, G.K.; Ding, L.P.; Zhang, Z.Y.; Ding, H.Z.; Kan, Z. Calibration and Tests for the Discrete Element Simulation Parameters of Fallen Jujube Fruit. *Agriculture* **2022**, *12*, 38. [[CrossRef](#)]

Article

Design and Experiment of Dry-Farming Cantaloupe Transplanter under Water

Dejiang Liu ^{1,2}, Yan Gong ^{1,*}, Xuejun Zhang ², Xiao Chen ¹, Guo Wang ¹ and Xiao Zhang ¹

¹ Nanjing Institute of Agricultural Mechanization, Ministry of Agriculture and Rural Affairs, Nanjing 210014, China; liudejiang@caas.cn (D.L.); chenxiao@caas.cn (X.C.); wangguo@caas.cn (G.W.); zhangxiao@caas.cn (X.Z.)

² College of Mechanical and Electrical Engineering, Xinjiang Agricultural University, Urumqi 830052, China; tuec@163.com

* Correspondence: gongyan@caas.cn

Abstract: To solve the problems of high temperature and drought in the Xinjiang Turpan area and the low survival rate of melon seedlings transplanted into dry soil, existing transplanters for large plant type young melon seedlings can be mechanized. For non-destructive planting for small plant types, such as Hami melon seedlings, there are still poor transplanting effects, planting point precise pile-soil, and other problems. In this study, a water transplanter for laying pipe and film for Hami melons was designed to mechanize the operation of rotating tillage, laying film and covering soil, transplanting potted seedlings on film, and water injection of the seedling root and planting hole, and soil piling and suppression. In this study, a transplanter was designed by coupling the motion of an earth-covering roller and a duck's mouth planter and realized the precise mound of soil in the planting hole, solved the difficult problem of the precise mound of soil on the membrane, and at the same time carried out water injection on the root of the melon seedlings, which effectively solved the problem of low survival rate of transplanted seedlings in the arid region of Turpan, Xinjiang, China. Field experiments showed that the survival rate of melon seedlings under drip irrigation for 8 h after transplanting into dry soil exceeded 97%. The efficiency of mechanized operation can reach 1 mu/person/hour, which is more than 8 times higher than manual operation. The operation speed of the machine is 1~1.2 m/s, and the qualified transplanting rate is 93.26%, which meets the requirements of cantaloupe transplanting agronomy. This study provides a new method for dry soil cantaloupe transplanting. This article can also provide a design reference for Hami melon transplanting mechanization in arid areas.

Keywords: cantaloupe bowl seedlings transplanting; mechanical equipment; institutional design; field test; data analysis and discussion

Citation: Liu, D.; Gong, Y.; Zhang, X.; Chen, X.; Wang, G.; Zhang, X. Design and Experiment of Dry-Farming Cantaloupe Transplanter under Water. *Agriculture* **2022**, *12*, 796. <https://doi.org/10.3390/agriculture12060796>

Academic Editors: Muhammad Sultan, Redmond R. Shamshiri, Md Shamim Ahamed, Muhammad Farooq and Francesco Marinello

Received: 6 April 2022

Accepted: 28 May 2022

Published: 31 May 2022

Publisher's Note: MDPI stays neutral with regard to jurisdictional claims in published maps and institutional affiliations.



Copyright: © 2022 by the authors. Licensee MDPI, Basel, Switzerland. This article is an open access article distributed under the terms and conditions of the Creative Commons Attribution (CC BY) license (<https://creativecommons.org/licenses/by/4.0/>).

1. Introduction

In recent years, China's agricultural supply-side structural reform and industrial layout adjustment have caused the planting area of melons and vegetables to expand and the demand for mechanization to increase. At present, there are many vegetable transplanters for pepper, tomato, cabbage, and other vegetables for open ground transplanting and membrane transplanting [1,2]. Due to the large differences in geographical and climatic conditions, soil moisture, fertility, and melon and vegetable varieties grown in different areas in China, the planting and agronomic requirements are quite different in different areas. For example, in order to prevent and control the continuous cropping obstacles and soil-borne diseases of greenhouse melons and vegetables, liquid pesticides or microbial agents should be applied to the roots while transplanting. For melons and vegetables in arid northwestern areas, agricultural film covering and integrated water and fertilizer planting modes are generally adopted. A drip irrigation belt and agricultural film are spread, and then seedlings are transplanted. In order to avoid seedling dehydration and root heat injury

caused by the high temperature of the sun at noon, it is necessary to pile soil at the planting hole. The drip irrigation system needs a unified water supply after transplanting in the whole planting area. For example, in a planting area of 50 mu, if each transplanter operates at 25 mu/day, it takes one day of work to complete the transplanting operation. After transplanting in the planting area, unified irrigation is bound to lead to a great reduction in the survival rate of transplanted seedlings. Irrigating the soil before transplanting can solve the problem of the time difference between transplanting and irrigation but, not only is it difficult for a tractor to work in the field under wet soil conditions, clay and soil accumulate on the duck's mouth type planter that is currently used for membrane transplanting, and the transplanter can not operate normally. Therefore, for the mechanized transplanting of watermelon, melon, and other non-drought-resistant varieties in the seedling stage, it is necessary for seedlings to retain water to improve the survival rate.

Research on transplanting machines for bowl seedlings started earlier in Europe and America; therefore, the level of automation there is relatively high, and its level is relatively leading. Other supporting systems and technology are also relatively perfect. Most existing studies of mechanical vegetable transplanting are about semi-automatic mechanical planters, with fewer about fully automatic planters, which can plant each row in an average of 30–60 plants/min [1–3]. Research on dry land transplantation in China began in the 1960s; it started early but did not develop quickly [4–7]. China began to develop bare seedling transplanters in the 1970s, originally used for beet transplanting, then semi-automatic vegetable transplanters began to appear. The operation efficiency of the existing chain clip and seedling guide tube semi-automatic transplanter on the market is low, with a limit speed of manual sorting and seeding of 45 plants min^{-1} and 60 plants min^{-1} . The highest transplanting rate of Ferrari Futura automatic hole plate seedling transplanting, representing the world's most advanced level, is 133 times/(min line), but it is expensive and has strict requirements for seedling bed preparation. Existing vegetable transplanters are all single function; they cannot change according to different planting areas, different melon varieties or agronomic requirements, root precision fertilization or irrigation water, nor in the planting hole, transplanted seedlings' low survival rate, and other serious problems. A transplanter must consider the soil adaptability, operation efficiency, and economy; therefore, current transplanters are not suited to Hami melon water injection transplanting [8,9].

In view of the above problems and to provide new technologies and methods that support the transplantation of cantaloupe in dry areas, in this study, a compound Hami melon transplanter is proposed. First, the front part of the machine rotates the soil, and then the pot seedlings are manually placed for transplanting. Finally, water is injected into the root of the transplanted seedlings to complete the transplanting operation. At the end of the article, the effect of the transplanting operation is verified by a field experiment, and the transplanting performance of the transplanter is evaluated.

2. Materials and Methods

2.1. Dryland Cantaloupe Watering Transplanter Whole Structure and Working Principle

2.1.1. Whole Structure

The dry land cantaloupe watering transplanter is mainly composed of rotary tillage parts, a transplanting apparatus, seedling plate, seedling feeding institutions, main transmission assembly, soil covering mechanism, film pressure mechanism, film mulching mechanism, water sitting system, and other components. The specific structure is shown in Figure 1. The whole transplanter is long, wide, and high (2300 mm \times 1500 mm \times 1700 mm). The rotary tillage parts, film and soil device, power box, and soil suppression mechanism are fixed through the beam in the front frame of the transplanter, and the length of the planting beam is 1500 mm. To stagger the space and prevent the interference of each part, the rotary tillage parts and power box are fixed and connected by vertical beams. The height of the fixed vertical beam is 650 mm, the soil covering ballast wheel is connected by

U-bolt, and the lateral distance of the fixed seat is 900 mm. The imitation laminating device is fixed by fixed bolts and planted beams with a relative distance of 1700 mm.

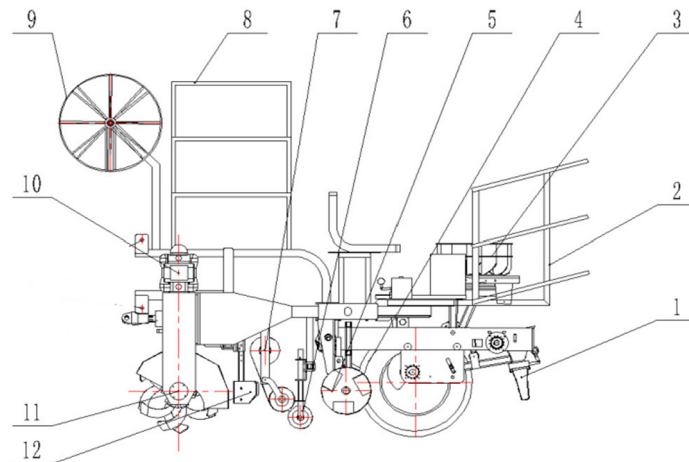


Figure 1. Dryland Cantaloupe Transplanter Under water. 1. Duck-billed transplanting apparatus; 2. The front of the seedling plate; 3. Cylinder seedling cup feeding mechanism; 4. gearset; 5. Cooling mechanism; 6. Pressure film mechanism; 7. Membrane overlying mechanism; 8. Behind the seedling plate; 9. Pipe laying parts; 10. Sitting water system; 11. Rotary tillage parts; 12. Open ditch parts.

2.1.2. Dryland Cantaloupe Watering Transplanter Whole Structure and Working Principle

Start the tractor, keep the tractor output speed of about 1000 r/min and advance at a constant speed. Before transplanting, conduct soil rotary tillage in front of the machine and then lay the film. The cantaloupe seedlings are removed from the plate when transplanting, and the bowl seedlings are placed into a circular cylinder feeding mechanism. The seedling feeding mechanism rotates slowly as the machine moves forward. The closed opening at the bottom of the cylinder opens when the cylinder feeding mechanism moves above the duck mouth planter. The bowl seedling falls by gravity from the cylinder into the cylinder mounted on the upper end of the duck beak, and the cantaloupe seedlings fall into the duckbilled transplanting apparatus through the receiver. After the duck mouth is inserted into the soil, the multibar drive mechanism turns the cam on the crank against the elbow, making the duck beak open, and the cantaloupe seedlings fall into the soil nest. At this time, open the water injection system. The root position of the transplanted seedlings is quantified at a fixed point, and water injection is not less than 50 mL so as to complete the transplanting work. The main working components of the transplanter are the rotary tillage mechanism, film laying mechanism, multi-rod drive mechanism, seedling feeding plate, duckbilled transplanting apparatus, and quantitative water injection system.

2.2. Planting Agronomic Requirements

The planting mode of cantaloupe pipe laying and sitting water transplanting is shown in Figure 2. Ridge height was 90 mm, ridge width was 700 mm, array pitch and row spacing were 400 mm, and double transplanting and adjacent ridges center distance was 900 mm. A white mulch with 900 mm width and 0.012 mm thickness was used for each ridge. Dimensions are shown in Figure 2.

Along with the characteristics of double-row transplanting on the cantaloupe film, the main technical parameters of the machines and tools are shown in Table 1.

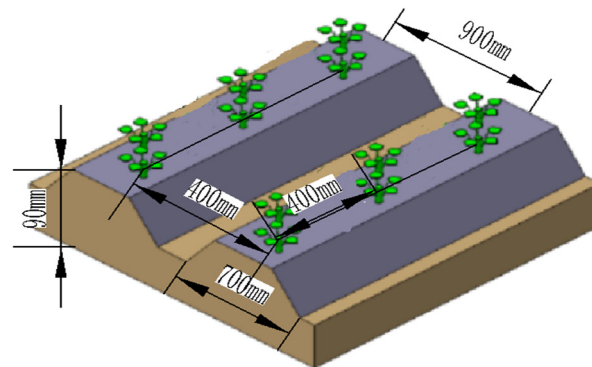


Figure 2. Ridging mode of double-row transplanting on cantaloupe film.

Table 1. Transplanting machine technical parameter table.

Project	Technical Parameters
Hang way	Tractor traction type
Supporting power (Metric horsepower)	≥50
Plant (hole) distance (tunable, mm)	300, 350, 400, 450
array pitch; row pitch (mm)	(Double row transplanting) 400
Adapt to membrane width(cm)	80–100
water injection rate (mL/hole)	50–100
Outline dimension (length × width × height: mm)	2300 × 1500 × 1700
Complete machine quality (kg)	About 760 kg
Number of operators (including tractor driver)	3
Leakage rate (%)	≤4

2.3. Design Analysis of Key Mechanisms

2.3.1. Rotary Tillage Parts

The rotary parts are mainly composed of a rotary blade shaft, blade, and knife plate. The structure is shown in Figure 3a. When working, the blade is driven by power and rotates along with the unit. The soil is cut in rotation and tossed, further hitting the retaining plate, breaking, and falling to the surface, and then is divided to both sides by the trench knife and the retaining plate. The initial design rotary radius is 220 mm; there are 14 knife plates, each with 3 rotary tiller knives, which are evenly arranged within 360 range on the knife plate, two lines of operation, 60 Mn for machine production materials [10–13].

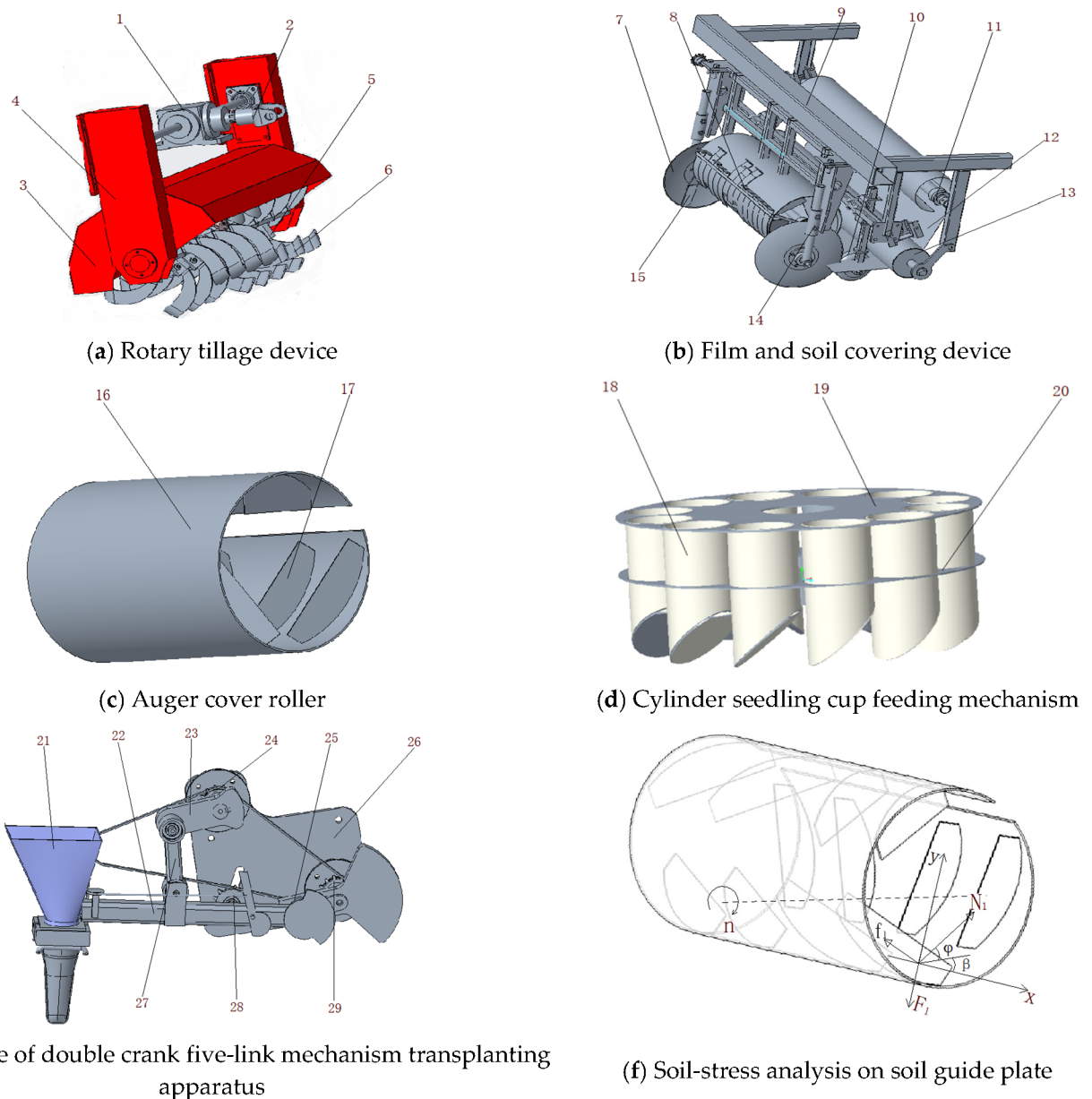


Figure 3. Key mechanisms of the transplanter. 1. Transmission case; 2. Power transmission shaft; 3. Trim shell of rotary tillage device; 4. Transmission housing; 5. Rotary blade shaft; 6. Rotary blade; 7. soil-covered plate; 8. Auger cover roller; 9. The shelf of film and soil covering device; 10. Film-pressure wheel; 11. Film roller suspension rack; 12. Film; 13. Film roller; 14. Installation support; 15. Soil-retaining plate; 16. The shell of auger cover roller; 17. Soil guide plate; 18. Seedlings cup; 19. Turntable plate; 20. Seedlings cup bracket; 21. Duckbilled transplanting apparatus; 22. Coupler-1; 23. Crank-1; 24. Gear-1; 25. Crank-2; 26. Connection plate; 27. Coupler-2; 28. Gear-2; 29. Gear-3.

2.3.2. Film Covering Soil Covering Mechanism

The design of the film-covering device takes into account the components, working environment, mechanical properties, and other factors and is designed and manufactured according to relevant standards. The coating device of dry cantaloupe water transplanting mainly consists of a soil-covered plate, auger cover roller, film roller, film-pressure wheel, installation support, guide plate, soil-retaining plate, and other components, as shown in Figure 3b above. In the device, the film rod and film roller suspension rack are cut from a 5 mm thick steel plate, and the film rod is 2 mm, respectively, seamless steel pipe of 28 mm

diameter, the film roller suspension rack is 2 mm wall thickness, 48 mm diameter, 300 mm diameter. According to the study [14], we can know the angle between the soil-covered plate and the forward direction of the transplanter is 20°, the mounting tilt angle is 18°, and the soil cutting operation effect is good. The two plates covering the soil are designed to be 1.5 m apart; it is distributed in the position of the cylinder section covered by an auger cover roller. At this time, the depth of the cutting soil is 10 mm, and the design parameters of the soil-covered plate meet the operation requirements of the melon water transplanter. The mulch is installed on the film rod during work, and the film spreading roll spreads the mulch on the ridge auger cover roller will cover the film with soil, round soil mulching plate on the film side, so as to complete the film mulching operation [10].

According to the static analysis of the auger cover roller, as shown in Figure 3c, when the transplanter is in use, the auger cover roller’s rotation speed is relatively low, and the centrifugal force is small, so the influence of the centrifugal force can be ignored in the analytical mechanics. The force of the soil on the guide plate in a critical sliding state at a certain point on the helical surface is shown in Figure 3f. The force balance equation is obtained based on the soil mechanics [10]:

$$F_N = F \sin(\varphi + \theta) \tag{1}$$

$$f_1 = F_N \tan \theta_0 \tag{2}$$

In the formula: θ_0 —Friction angle between soil and guide plate, °
 θ —Tting angle of the membrane, °;
 φ —The ical angle of the guide plate, °;
 F_N —Support force of soil guide plate to soil, N ;
 f_1 —Friction force of soil guide plate on soil, N ;
 F —The gravity of the soil itself and the circumferential tangential force under the surrounding soil extrusion pressure, N ;

When the auger cover roller rotates, the higher the rotation speed, the greater the amount of soil is transported. According to the literature study in [11–15], the differential equation of soil motion is as follows [12–14]:

$$ma = N_1 \cos(\varphi + \theta) - f_1 \sin(\varphi + \theta) \tag{3}$$

In the formula: m —soil quality, kg ;
 a —Acceleration of the axial movement of the soil along the guide plate, m/s^2 ;
 Thus, to get the soil acceleration:

$$a = \frac{1}{2} \frac{F}{m} \sin[2(\varphi + \theta)] - \frac{F}{m} \tan \theta_0 \sin^2(\varphi + \theta) \tag{4}$$

It can be seen that when the diameter and speed of the auger cover roller are certain, the function of helical angle analyzes the influence of helical angle on soil acceleration, and seeks the maximum value.

So that:

$$\frac{da}{d\varphi} = 0 \tag{5}$$

$$\cos[2(\varphi + \theta)] - \sin[2(\varphi + \theta)] \tan \theta_0 = 0 \tag{6}$$

Thus obtain the spiral angle when the acceleration of soil movement along the roller is maximum:

$$\varphi_{max} = \frac{\pi}{4} - \frac{\theta_0}{2} - \theta \tag{7}$$

Therefore, the working surface of the guide plate meets the surface axial conveying soil near the coil. The auger cover roller diameter is 350 mm, and the number of uniformly distributed circumferential soil-guide plates is 4, the 3 rows of guide plates are evenly

arranged, the spiral angle of the guide plate is 15~25 degrees, the installation distance between the retaining plate and the roller is 30 mm. When the installation angle is 30 degrees, it can meet the requirements of cantaloupe cover film transplanting.

2.3.3. Design of the Cylinder Seedling Feeding Mechanism

The seedling feeding mechanism not only carries the cantaloupe seedlings but also is the key part of determining whether the melon seedlings can be successfully put into the duck mouth of the planter. Therefore, the seedling feeding mechanism is an important part of determining the final transplanting quality. The design of the feeding mechanism, including the seedling cup, turntable plate, seedling cup bracket, reducer, and installation base, are shown in Figure 3d. When the transplanting work begins, the feeding mechanism is powered by the reducer drive rotary wheel, which drives the seedling cup rotation. The operator is responsible for placing the cantaloupe seedlings into the seedling cup. When the seedling cup turns to the designated position under the open end cover, cantaloupe seedlings fall under gravity into the duck mouth planter [16–18].

The rotation speed of the seedling cup and the planter need to match each other to make the cantaloupe seedlings fall into the duck mouth smoothly; therefore, it is necessary to determine the speed of the cup and conduct a kinematic analysis of the transmission part of the rotating cup. When the planter reaches the guide tube position, the bottom end cover of the cup is opened; therefore, the rotation speed of the cup is:

$$\omega_{\text{cup}} = \frac{\psi}{T} \quad (8)$$

In the formula: ω —Represents the angular speed of the seedlings cup, rad s^{-1} ;

ψ —It indicates the angular displacement of the seedling cup rotation, rad;

T —Time of transplanting two adjacent melon seedlings, s;

Considering the spatial layout of the planting device, the number of seedling cups designed for the seedling feeding device is 12, the angular displacement of the adjacent seedling cup is $\frac{\pi}{6}$, it takes 0.9 s and 1.5 s, respectively, to rotate the cup by $\frac{\pi}{6}$ angle according to the speed of transplanting operation. Calculated according to the above formula, the speed of the cup rotation is 0.58 rad s^{-1} , 0.35 rad s^{-1} .

2.3.4. Design of the Double Crank Five-Link Mechanism Transplanting Apparatus

The transplanting apparatus is the core component of the transplanter. The transplanting mechanism designed in this paper is the double crank five-link mechanism. The three-dimensional diagram of the transplanting apparatus is shown in Figure 3e. When the transplanter is working, all the rods of the transplanting apparatus should be coordinated, and the planting depth and standard spacing of the seedlings should be unified. To avoid the phenomenon of seedlings being injured, seedlings are clamped and seedlings taken away [19–24]. Because the duckbilled transplanting apparatus is driven by the crank of the planting mechanism, the transmission ratio of the power conveying device is:

$$i = i_{\omega} \frac{z_2}{z_1} = \frac{n_1}{n_2} \quad (9)$$

In the formula: i —Transmission box reducer reduction ratio;

z_1, z_2 —Number of teeth of the sprockets in the transplanting apparatus drive system;

n_1, n_2 —Power speed of the seedling mechanism and crank speed of the plan 1, r/min.

The crank angle speed depends on the transplanting operation speed of 4.8 rad s^{-1} , take the power speed (seedling cup speed) of the seedling delivery mechanism 0.58 rad s^{-1} , select i_{ω} generally take 10: 1 dwelling rod reducer. Transmission ratio of the transplanting apparatus chain drive according to the above data is 0.12, the number of sprocket teeth was assigned to obtain the sprocket data: $z_2 = 15, z_1 = 18$.

2.4. Field Testing

2.4.1. Test Place and Test Instrument

A field test was conducted at the Hami Cantaloupe Research Center in Turpan, Xinjiang Uygur Autonomous Region, China, in March 2021. Test instruments included steel tape ruler, angle ruler, stopwatch, etc. According to the agronomic conditions of melon transplanting, the working parameters of the transplanter were set to match the suitable planting distance and planting row distance. In this test, the plant distance of melon was 35 cm, and the planting row distance was 40 cm. The transplanter working test is shown in Figure 4a, and the transplanting effect diagram is shown in Figure 4b.



Figure 4. Field testing site. (a) Transplanter working test site. (b) The effect of transplanting cantaloupe.

2.4.2. Testing Methods

The dry-farming cantaloupe transplanter belongs to a dry land transplanting technology and method. Therefore, refer to JB/T10291 <transplanter in dry land> and manufacturer's standard Q/HY·J 0324—2019 <Melo transplanter>, and use the relevant provisions of the test method [19–22].

The experiment was conducted during the melon planting period, and the influence of transplanter operation speed on repeat transplanting rate, lodging rate, missing transplanting rate, injury seedling rate, and transplanting qualified rate were analyzed [23–26]. The corresponding index detection methods are shown as follows:

(1) Repeat transplanting rate

In theory, one cantaloupe seedling should be transplanted, and two or more seedlings should actually be planted, and the proportion of N_{CZ} and N of the repeat planting rate is:

$$D = \frac{N_{CZ}}{N} D = N_{CZ} / N$$

In the formula: D —repeat transplanting rate, %.

N_{CZ} —repeat transplanting point number, number.

N —The total number of points determined, number.

(2) Seedling lodging rate

After transplanting, the angle between the main seedling's diameter and the ground is less than 30° [27], the proportion of the total number of lodging and the total number of holes N , the lodging rate was calculated as:

$$T = \frac{N_{DF}}{N} T = N_{DF} / N$$

In the formula: T —Lodge rate, %.

N_{DF} —Lodge point number, number.

(3) Missing transplanting rate

After the transplanting work was done, near the transplanting two-hole distance (X_i) and theory hole distance (X_r), we can, on the basis of the relationship between them, determine the number of missed transplanting holes when:

Range $0 \leq X_i \leq 0.5 X_r$, plant one again;
 Range $0.5 X_r \leq X_i \leq 1.5 X_r$, within the range are qualified hole distance;
 Range $1.5 X_r \leq X_i \leq 2.5 X_r$, one missing transplant was planted;
 Range $2.5 X_r \leq X_i \leq 3.5 X_r$, two missing transplants were planted;
 Range $3.5 X_r \leq X_i \leq 4.5 X_r$, two missing transplants were planted, and so on.
 Missing planting rate calculation formula:

$$M = \frac{N_{LZ}}{N} M = N_{LZ} / N$$

In the formula: N_{LZ} —The number of missing holes, hole.

M —Missing planting rate, %.

(4) Injury seedling rate

If a transplanted melon seedling is damaged and its growth is affected, the seedling is defined as a wounded seedling. The ratio of the number of injured seedlings to the total number of measured holes in a planting row is the wound seedling rate [28]; the calculation formula is:

$$W = \frac{N_{SM}}{N} W = N_{SM} / N$$

In the formula: N_{SM} —number of injury seedlings, hole.

W —injury seeding rate, %.

(5) Transplant qualified rate

Within a test interval, seedling transplanting hole has more than one plant in line with (3) in the planting of qualified hole distance provisions, it is qualified for planting [29].

The qualified rate of planting is equal to the ratio of the number of qualified holes to the total number of holes in the test area; the calculation formula is as follows: ($N_{HG} = N - (2 N_{CZ} + N_{DF} + N_{LZ} + N_{SM})$)

$$Q = \frac{N_{HG}}{N} Q = N_{HG} / N$$

3. Results and Discussion

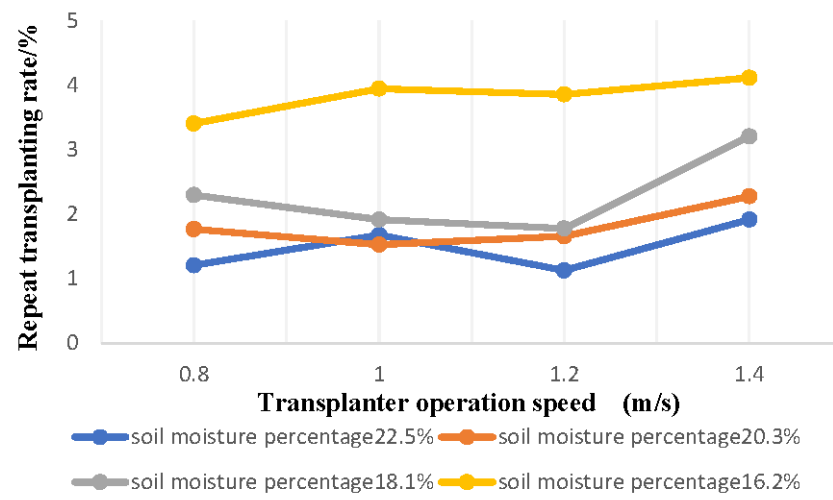
The land lots with different moisture content were selected for the test (22.5%, 20.3%, 18.1%, 16.2%). At the beginning of the transplanting test, the machines transplanted at a 0.8 m/s, 1 m/s, 1.2 m/s, 1.4 m/s operation speed, repeat transplanting rate, lodging rate, missing transplanting rate, and injury seedling rate were determined, respectively, and the transplant qualified rate was calculated. The specific test data table is shown in Figure 5a–e.

Univariate analysis was performed based on the data from the field experiments. The analysis result is shown in Figure 5a–e. In the dry land soil with a moisture content of 18.1~22.5%, the operation and machine speed increases, the rate of injured seedlings and lodging increases, the repeat planting rate and leakage planting are first smaller and larger, and the qualified rate of transplanting showed a downward trend. When the machine speed is at 1 m/s, the plant leakage rate and the seedling injury rate are the lowest. At this time, the transplanting qualified rate is the largest, 93.26%; this time is the optimal level.

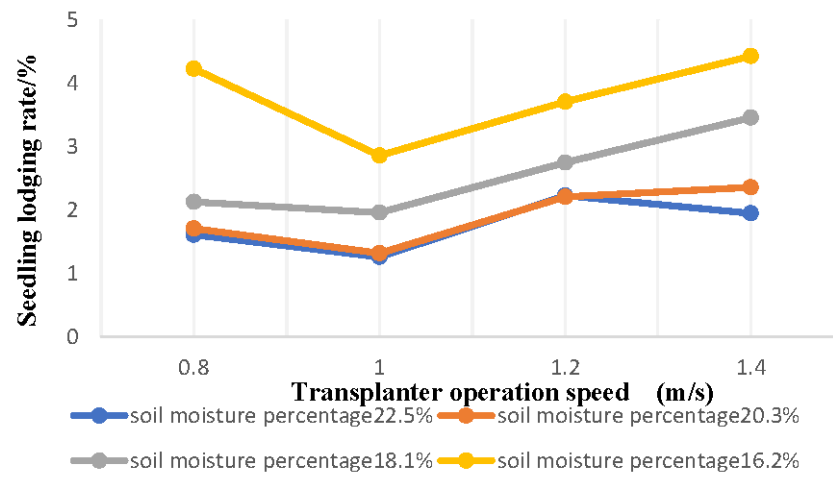
Through the experimental analysis and verification of the design of the planting mechanism, some suggestions are put forward for the key content for further research and development.

The following proposals: Although the transplanting qualification rate of planting institutions has reached the national standard, there is still much room for improvement, which should be improved in the next step. The lack of a data statistical analysis study is a deficiency of this paper. Furthermore, optimization should consider the application and improvement of institutions in field use under different terrain conditions in order to enhance the adaptability of the machine.

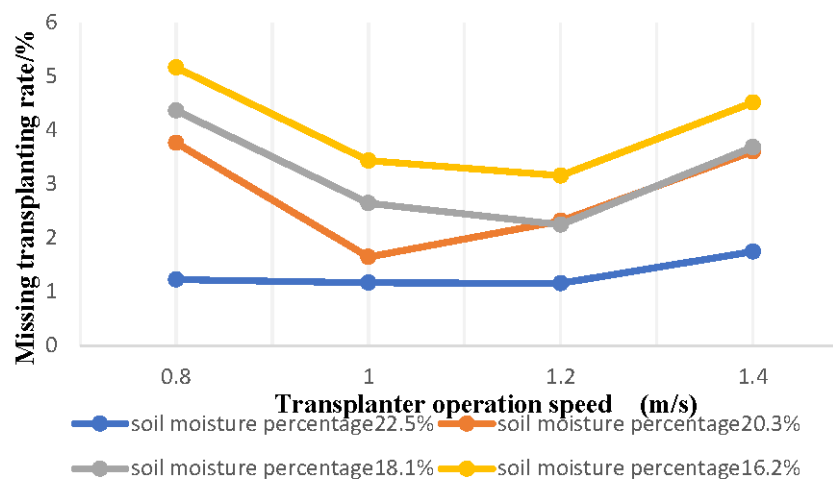
For increased adaptability and interchangeability, improve the utilization rate of the machine and realize multi-purposes of one machine. In the design, attention should also be paid to matching sets such as hole digging and water injection development.



(a)

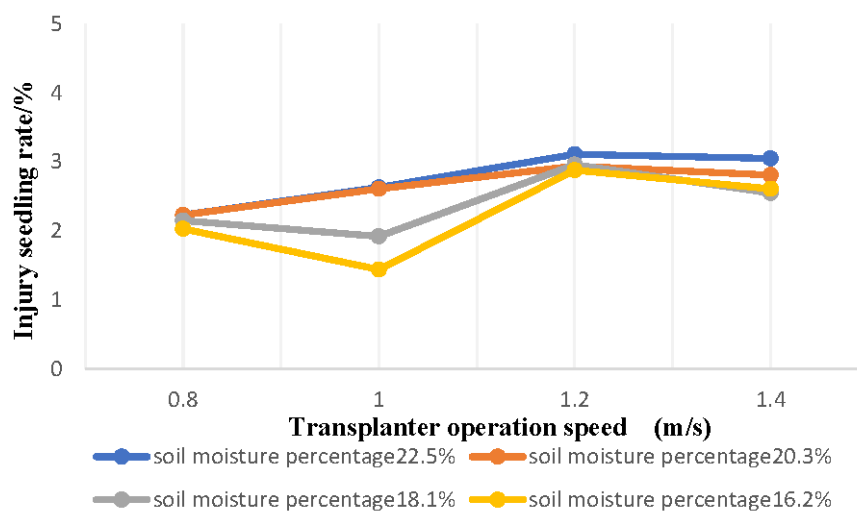


(b)

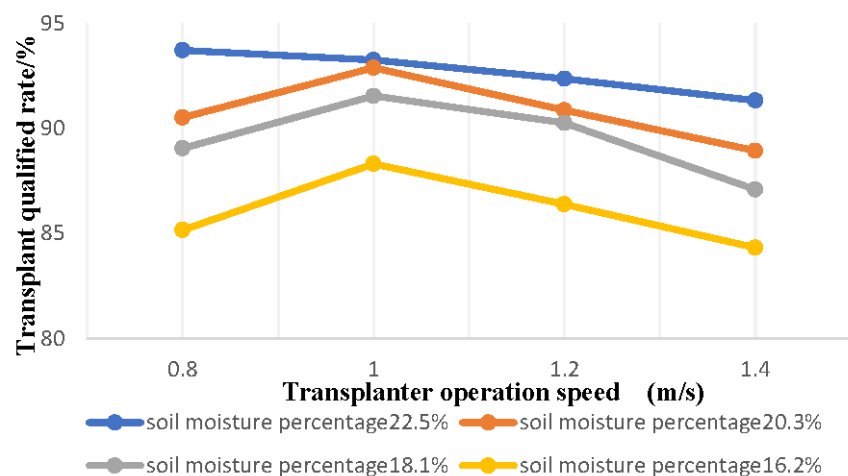


(c)

Figure 5. Cont.



(d)



(e)

Figure 5. Graph of transplanting effect at different working speeds. (a) Line chart of repeat transplanting rate changes under different operating speeds. (b) Line chart of seedling lodging rate changes under different operating speeds. (c) Line chart of the change of the missing transplanting rate under different operating speeds. (d) Line chart of the change of seedling injury seedling rate under different operating speeds. (e) Line chart of the change of transplanting qualification rate under different operating speeds.

4. Conclusions

This study proposed a non-damaging transplanting technology for cantaloupe based on a multi-step operation with a transplanter. The technology was developed for the non-destructive transplanting of cantaloupe seedlings, planting point precise pile-soil, respectively. Firstly, through the design of a double crank five-link mechanism transplanting apparatus, the nondestructive transplanting of Hami melon seedlings was guaranteed. Then, through the motion coupling design of the auger cover roller and duckbilled transplanting apparatus, precise piling of soil in the transplanting hole was realized.

In this article, the design of the transplanting technology and planting hole stacking technology of the machine effectively solve the technical problem of mechanized Hami melon transplanting in high temperature and arid climate conditions in Turpan, Xinjiang Uygur Autonomous Region, China. It could also provide guidance for the mechanization of transplanting operations in dry areas around the world. The experimental data show that the survival rate of cantaloupe seedlings treated with drip irrigation at 8 h after dry land

transplanting exceeded 97%. In dry land transplanting, water should be given to seedlings to ensure their survival rate. Mechanized operation efficiency is up to 1 mu/people/h, more than 8 times higher than the manual operation. The implement's travel speed is 1–1.2 m/s, and the transplant qualified rate is 93.26%; therefore, this technique meets the agronomic requirements of cantaloupe transplanting.

Author Contributions: Conceptualization, D.L. and Y.G.; methodology, X.C. and X.Z. (Xiao Zhang); software, G.W.; validation, D.L., X.C. and G.W.; formal analysis, Y.G.; investigation, D.L.; data curation, G.W.; writing—original draft preparation, D.L.; writing—review and editing, D.L.; supervision, X.Z. (Xuejun Zhang) and Y.G. All authors have read and agreed to the published version of the manuscript.

Funding: This research was supported by the National Key Research and Development Programme of China (2020YFD1000300), the Central Public-interest Scientific Institution Basal Research Fund (S202110-02), and the China Agriculture Research System (Grant No. CARS-25).

Institutional Review Board Statement: Not applicable.

Informed Consent Statement: Not applicable.

Data Availability Statement: The datasets used and/or analyzed during the current study are available from the corresponding author on reasonable request.

Conflicts of Interest: The authors declare no conflict to interest.

References

- Gutiérrez, C.; Serwatowski, R.; Gracia, C.; Cabrera, J.M.; Saldana, N. Design building and testing of a transplanting mechanism for strawberry plants of bare root on mulched soil. *Span. J. Agric. Res.* **2009**, *7*, 791–799. [[CrossRef](#)]
- Satpathy, S.K.; Garg, I.K. Effect of Selected Parameters on the Performance of a Semi-automatic Vegetable Transplanter. *Ama Agric. Mech. Asia Afr. Lat. Am.* **2008**, *39*, 47–51.
- Kumar, G.V.P.; Rahman, H. Automatic feeding mechanism of a vegetable transplanter. *Int. J. Agric. Biol. Eng.* **2012**, *5*, 20–27.
- Gao, Q.S.; Chen, Y.S.; Guan, C.S.; Yang, Y.T.; Guan, Z.C. Mechanized transplanting in open field. *J. China Agric. Mech.* **2021**, *42*, 193–197.
- Chen, Y.S. 2018 development report on mechanized production of vegetables in China. *J. China Agric. Mech.* **2019**, *40*, 1–6.
- Zhao, X.W.; Guo, H.; Zhang, J.; Yang, W.Z.; Han, C.J. The status quo and development trend of dryland transplanter in Xinjiang. *Xinjiang Rural. Mech.* **2014**, *4*, 25–29.
- Lu, Y.T.; Li, Y.X.; Liu, Y.; Li, B.; Wang, T. Analysis on the status quo of transplanting machines and transplanting technology at home and abroad. *Xinjiang Rural. Mech.* **2011**, *3*, 29–32.
- Yu, X.X.; Zhao, Y.; Chen, B.C.; Zhou, M.L.; Zhang, H.; Zhang, Z.C. Development status and prospects of transplanting machinery. *J. Agric. Mach.* **2014**, *45*, 44–53.
- Liu, C.X.; Li, X.H.; Yue, X.M.; Zhao, H.Y. The status quo and development trend of dryland transplanters in my country. *J. Agric. Mech. Res.* **2013**, *34*, 249–252.
- Wu, W.; Sun, S.L.; Xiao, M.T. The status quo and development trend of transplanting machinery in my country. *Agric. Technol. Equip.* **2013**, *12*, 7–8.
- Lu, Z.J.; Shan, Y.Y.; Wang, J.; Zhao, J. Research status of vegetable transplanting equipment and prospects of pot seedling transplanting equipment. *J. China Agric. Mech.* **2017**, *38*, 30–34.
- Xue, D.Q.; Hou, S.L.; Zhang, J.X. Research progress and development trend of dryland transplanting machinery in my country. *J. China Agric. Mech.* **2013**, *34*, 8–11. [[CrossRef](#)]
- Cui, Z.C.; Guan, C.S.; Yang, Y.T.; Gao, Q.S.; Chen, Y.S.; Xiao, T.Q. Research status of vegetable mechanical transplanting technology and equipment. *J. China Agric. Mech.* **2020**, *41*, 85–92.
- Xu, G.W. Research on the Key Components of the Double-Row Salvia Transplanter on a Large Ridge Film and the Design of the Whole Machine. Master's Thesis, Northeast Agricultural University, Haerbin, China, 2019.
- Li, H.; Cao, W.B.; Li, S.F.; Liu, J.D.; Chen, B.B.; Ma, X.X. Development of 2ZXM-2 fully automatic vegetable plug seedling film-laying transplanter(2ZXM-2). *Trans. Chin. Soc. Agric. Eng.* **2017**, *33*, 23–33.
- Li, G.; Li, A.; Ha, S.M.; Kang, X.S.; Yu, G.H.; Zhang, G.F. Parameter optimization of the spiral cover drum of the film planter. *Trans. Chin. Soc. Agric. Eng.* **2003**, *19*, 135–138.
- Tang, Q.; Wu, C.Y.; Yuan, W.S.; Wu, J.; Wang, S.F. Structural design of soil-covering suppression device for rape blanket seedling high-speed transplanter. *Chin. J. Agric. Mach. Chem.* **2016**, *37*, 20–22.
- Jin, L.Y. Design and Experiment of Planting Mechanism of Pepper Pot Transplanting Machine. Master's Thesis, Heilongjiang Bayi Agricultural University, Daqing, China, 2021.

19. Wu, J.; Tang, Q.; Yuan, W.S.; Wang, S.F.; Wu, C.Y. Design and parameter optimization of ditching and suppression components of rapeseed blanket seedling transplanter. *China J. Agric. Eng.* **2016**, *32*, 46–53.
20. Wu, J.; Yu, W.; Zhang, M.; Wu, C.Y.; Jiang, L.; Tang, Q. Design and test of Z Y-6. *J. Agric. Mach.* **2012**, *51*, 95–103.
21. Wang, Y.W.; He, C.L.; Wang, J.; Wu, C.Y.; Yu, G.H.; Tang, Y.H. Dryland vegetable bowl seedlings automatic transplanting machine planting Performance test. *J. Agric. Eng.* **2018**, *34*, 19–25.
22. JB/T 10291-2013; Ministry of Industry and Information Technology of the PRC Republic of China. Dryland Planting Machinery. Machinery Industry Publishing House: Beijing, China, 2014.
23. Jin, X.; Ji, J.T.; Liu, W.X.; He, Y.K.; Du, X.W. Structural optimization of duckbilled transplanter based on dynamic model of pot seedling movement. *Trans. Chin. Soc. Agric. Eng. (Trans. CSAE)* **2018**, *34*, 58–67.
24. Chen, J.N.; Xia, X.D.; Wang, Y.; Yan, J.J.; Zhang, P.H. Motion differential equations of seedling in duckbilled planting nozzle and its application experiment. *Trans. Chin. Soc. Agric. Eng. (Trans. CSAE)* **2015**, *31*, 31–39.
25. Shao, Y.Y.; Liu, Y.; Xuan, G.T.; Gao, X.M.; Han, X.; Wang, Y.X. Design and simulation analysis of multi-function duck mouth vegetable transplanting machine. *Chin. Agric. Mech.* **2019**, *40*, 9–12 and 34.
26. Xu, G.W.; Song, Y.M.; Chu, R.X.; Jian, S.C.; Qiu, X.Y.; Gao, Q. Dynamic Optimization design and experiment of five-bar salvia miltiorrhiza transplanting Mechanism with counterweight. *Chin. Agric. Mech.* **2022**, *42*, 15–21.
27. Zhang, X.L.; Wu, D.L.; Wu, C.Y. Design and experimental study of duck-mouth bowl seedling transplanting machine. *Agric. Mech. Res.* **2017**, *3*, 134–143.
28. Bao, X.; Zhao, X.; He, J.; Li, H.W.; Wang, Q.J.; Liu, W.Z. Design and performance test of plowing and rotary tillage combined machine. *INMATEH-Agric. Eng.* **2020**, *60*, 213–222.
29. Hu, M.J.; Zhang, W.Y.; Ji, Y.; Qi, B.; Xia, Q.Q.; Li, K. Effects of pepper transplanting with degradable bowls on seedling growth and development traits. *J. Chin. Agric. Mech.* **2020**, *41*, 57–62. [[CrossRef](#)]

Article

Indirect Somatic Embryogenesis: An Efficient and Genetically Reliable Clonal Propagation System for *Ananas comosus* L. Merr. Hybrid “MD2”

Argelys Kessel-Domini ¹, Daisy Pérez-Brito ², Adolfo Guzmán-Antonio ¹, Felipe A. Barredo-Pool ³, Javier O. Mijangos-Cortés ⁴, Lourdes Georgina Iglesias-Andreu ⁵, Alberto Cortés-Velázquez ², Adriana Canto-Flick ¹, Susana A. Avilés-Viñas ¹, Yaritza Rodríguez-Llanes ¹ and Nancy Santana-Buzzy ^{1,*}

Citation: Kessel-Domini, A.; Pérez-Brito, D.; Guzmán-Antonio, A.; Barredo-Pool, F.A.; Mijangos-Cortés, J.O.; Iglesias-Andreu, L.G.; Cortés-Velázquez, A.; Canto-Flick, A.; Avilés-Viñas, S.A.; Rodríguez-Llanes, Y.; et al. Indirect Somatic Embryogenesis: An Efficient and Genetically Reliable Clonal Propagation System for *Ananas comosus* L. Merr. Hybrid “MD2”. *Agriculture* **2022**, *12*, 713. <https://doi.org/10.3390/agriculture12050713>

Academic Editors: Muhammad Sultan, Redmond R. Shamshiri, Md Shamim Ahamed and Muhammad Farooq

Received: 29 March 2022

Accepted: 12 May 2022

Published: 18 May 2022

Publisher’s Note: MDPI stays neutral with regard to jurisdictional claims in published maps and institutional affiliations.



Copyright: © 2022 by the authors. Licensee MDPI, Basel, Switzerland. This article is an open access article distributed under the terms and conditions of the Creative Commons Attribution (CC BY) license (<https://creativecommons.org/licenses/by/4.0/>).

- ¹ Unidad de Bioquímica y Biología Molecular de Plantas, Centro de Investigación Científica de Yucatán (CICY), Calle 43 No. 130, Chuburná de Hidalgo, Mérida 97205, Mexico; argelys.kessel@cicy.mx (A.K.-D.); agaa@cicy.mx (A.G.-A.); nona@cicy.mx (A.C.-F.); susana@cicy.mx (S.A.A.-V.); yaritza.rodriguez@cicy.mx (Y.R.-L.)
- ² GeMBio, Grupo de Estudios Moleculares Aplicados a la Biología, Centro de Investigación Científica de Yucatán (CICY), Calle 43 No. 130, Chuburná de Hidalgo, Mérida 97205, Mexico; daisy pb@cicy.mx (D.P.-B.); betocv@cicy.mx (A.C.-V.)
- ³ Unidad de Biotecnología, Centro de Investigación Científica de Yucatán (CICY), Calle 43 No. 130, Chuburná de Hidalgo, Mérida 97205, Mexico; alonso16@cicy.mx
- ⁴ Unidad de Recursos Naturales, Centro de Investigación Científica de Yucatán (CICY), Calle 43 No. 130, Chuburná de Hidalgo, Mérida 97205, Mexico; jomijangos@cicy.mx
- ⁵ Instituto de Biotecnología y Ecología Aplicada, Campus para la Cultura, Universidad Veracruzana, las Artes y el Deporte. Av. de las Culturas Veracruzanos No. 101. Colonia Emiliano Zapata, Xalapa-Enríquez 91090, Mexico; liglesias@uv.mx
- * Correspondence: buzzy@cicy.mx; Tel.: +52-9999428369

Abstract: The objective of this study was to establish an efficient—direct or indirect—regeneration system for pineapple (*Ananas comosus* L.) plants, with a high rate of multiplication and that would preserve the genetic identity of the donor genotype (Hybrid ‘MD2’) in the regenerated plants. Ten treatments, with different concentrations of 2,4-Dichlorophenoxyacetic (2,4-D) and Picloram (P), in the absence or presence of 6-Benzylaminopurine (BAP), were used for in vitro morphogenesis induction, as well as histological and molecular techniques, in order to characterize the morphogenic responses induced. Significant differences between treatments tested, to induce callus and buds, were assessed by the Kruskal Wallis method and the Mann–Whitney U-tests. Different pineapple regeneration routes were identified, showing the high regeneration potential of this species. The medium containing 2 mg L⁻¹ 2,4-D and 2 mg L⁻¹ BAP, where indirect somatic embryogenesis occurred, was selected as the most efficient treatment, with an average of 120 somatic embryos per explant, differing significantly from the rest of the treatments. It was also demonstrated that the pineapple plants regenerated in vitro preserved the genetic identity of the donor genotype, which represents a high degree of confidence for the application of indirect somatic embryogenesis for *A. comosus* clonal propagation.

Keywords: *Ananas comosus*; somatic embryogenesis; micropropagation; organogenesis; SSR markers; ISSR markers; pineapple

1. Introduction

Pineapple (*Ananas comosus* L. Merr.) is a monocotyledonous plant native to tropical America, specifically South America, belonging to the Bromeliaceae family, and is one of the most important tropical species in the international market, due to the great acceptance of its fruit by consumers [1]. The fruit is recognized as one of the finest in tropical regions, and is considered the queen of all fruits, because it is highly appreciated for its high nutritional

value. It is rich in carbohydrates and saturated fats, free of cholesterol, low in sodium, and has high contents of vitamins A, C, and minerals. It is also a highly digestible food because it contains the enzyme bromelain [2]. It is currently the second tropical crop in terms of production volume, only surpassed by the banana (*Musa acuminata*). It is produced in many tropical regions of the world and is exported mainly to the United States of America and the European Union [3,4]. Seventy percent of its commercial production is consumed fresh, and the rest is intended for canning in syrup, so the hybrid 'MD2', known as "Extra Sweet", "Golden Sweet", or "honey pineapple", is the most demanded in the international market, since when compared with other cultivars, it stands out for: its sweetness (values from 13 to 18° Brix), its uniform golden color, and especially for its long shelf life (more than 30 days) [2,5,6].

This plant is described as a perennial herb that grows between one and one-and-a-half meters high. Prior to fruiting, this plant generates around two hundred flowers, which, when fertilized, combine to form a polyfruit, which is known as a pineapple. Each plant generates between seventy and eighty leaves, which are like pods or sheets arranged in a spiral, usually in layers. Some cultivars have thorns on the edges of their leaves. Its flowers have foliar scales that have the property of retaining water. The embryo of the plant has only one leaf, or cotyledon, and is a self-incompatible species [1], so its main form of propagation is vegetative, based on three types of tillers: crowns, cocks, and spikes [3,7]. The crowns, located in the upper part of the fruit, have a slow but uniform development, with a low percentage of natural flowering, and their cycle can be considered late. The propagules, or tillers, that grow and develop from buds located on the peduncle, and the base of the fruit are known as roosters and the number and vigor per plant vary, with the most occurring during the first harvest and being of intermediate vigor. Nails are considered scions, and grow and develop from axillary buds, located throughout the stem, and their cycle is considered the earliest, because they are more vigorous and are the most commonly used tillers for the establishment of plantations [8].

All these species characteristics imply a very low growth and multiplication rate through vegetative propagation, since the interval between planting and fruiting can be up to two years, and only two to three uniform propagules are produced per plant, which in turn drastically limits the availability of suitable planting material to establish large areas of the crop [9]. On the other hand, the incidence of pests and diseases is higher, and this condition is aggravated by the low genetic variability present in their populations, since traditional genetic improvement is delayed and inefficient [8]. Given this problem, it is necessary to use biotechnological tools that allow the rapid and massive production of uniform plants with high phytosanitary quality, in a rapid and massive way, thus producing larger fruits with higher agricultural yields. Technologies based on plant tissue culture provide us with very valuable tools for the massive and uniform propagation of this crop in very short cycles of time and at any time of the year [10,11]. However, it should be noted that the conditions required for tissue culture can result in genomic changes in plants, resulting from in vitro culture [7,12–14].

Tissue culture conditions, such as the use of growth regulators, successive transfers of explants, certain temperatures, and culture medium pH, sometimes lead to alterations at the cellular level, which result in genomic changes in plants from in vitro culture [7,12] which are not favorable in micropropagation. Authors such as Akdemir et al. [15] found that when high concentrations of cytokinins are used in long-term pineapple cultivation, somaclonal variations occur, which can be detected by molecular markers. In another study, differences in morphological and physiological characters between regenerants and mother plants were observed, when Naphthaleneacetic acid (NAA) and 6-Benzylaminopurine (BAP) were used for plant regeneration [7]. Years later, in another study using these same regulators, DNA methylation increase was found in the dedifferentiation process (callus formation) and differentiation (seedling regeneration), and it was concluded that these changes lead to somaclonal variation in pineapple [13].

Therefore, the establishment of a tissue culture technology in this valuable fruit plant requires reproducible protocols for each of the process stages, and for this, it is necessary to define the structures that originate in the different morphogenic routes; as well as to analyze if the change that originated in the genetic program of these cells leads to somaclonal variation, since a fundamental requirement in the commercial industry when working with elite genotypes is to maintain their relevant agronomic characteristics [11]. For this reason, the present research hypothesizes that with the application of somatic embryogenesis, many genetically stable plants are obtained, and the multiplication rate of this fruit species is increased in a short period of time. Therefore, the objective of this work is to present the advances achieved in the search for a highly efficient and genetically reliable mass propagation technology, in which vigorous “MD2” pineapple in vitro plants with a high survival rate are generated.

2. Materials and Methods

2.1. Explant Selection

For the induction of pineapple morphogenic structures, the leaf base from young (4–6-week-old) in vitro plants of the ‘MD2’ hybrid undergoing in vitro vegetative growth (Figure 1) was used as plant material. Leaves explants were placed horizontally with their adaxial surface on the culture medium.

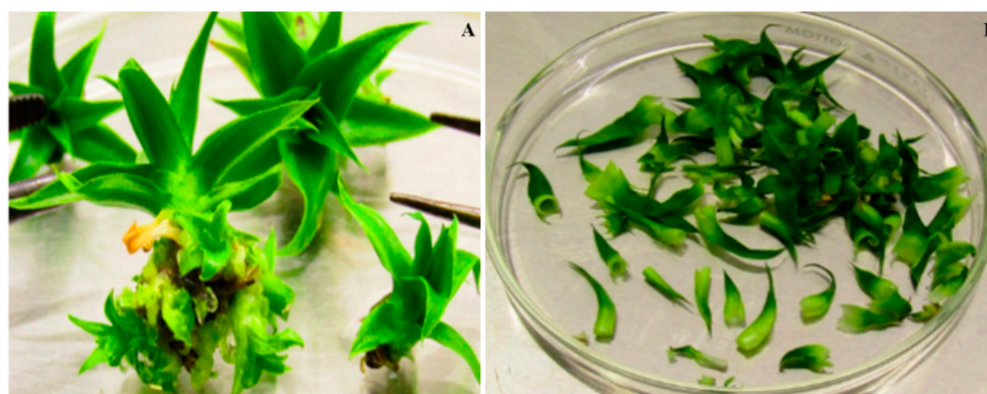


Figure 1. (A) Aseptic ‘MD2’ pineapple in vitro plants (4–6 weeks old) used as a source of explants to induce direct and/or indirect morphogenesis; (B) leaves isolated from the in vitro plants used as initial explant.

Four treatments were established and tested to induce morphogenesis, in which different concentrations of naphthaleneacetic acid (NAA) and benzylaminopurine (BAP) were used in Murashige and Skoog (MS) [14] medium, supplemented with sucrose (30 g L^{-1}), Myoinositol (100 mg L^{-1}), and Thiamine (5 mg L^{-1}). The explants remained under conditions of 16 h of light and 8 h of darkness, and a temperature of $27\text{--}30 \text{ }^{\circ}\text{C}$. The shoots obtained were subcultured on the same medium every 45 days until shoots were obtained. For callus regeneration, six treatments were established and evaluated. Where an MS medium was used, which was supplemented with sucrose (30 g L^{-1}), Myoinositol (100 mg L^{-1}), Thiamine (1 mg L^{-1}), and different concentrations of regulators: 2,4-Dichlorophenoxyacetic (2,4-D) and Picloram (P), in the absence or presence of BAP (Table 1). In this case, the explants were incubated in total darkness at $25\text{--}28 \text{ }^{\circ}\text{C}$ and subsequently, the calluses obtained were subcultured in the same medium (MS) every 45 days. From the second subculture (90 days), they were transferred to conditions of a photoperiod of 16 h of light and 8 h of darkness, and a temperature of $27\text{--}30 \text{ }^{\circ}\text{C}$, to induce the formation of morphogenic structures (embryos or shoots) in an MS medium without auxin, which contained BAP at different concentrations (0.5 , 1 , and 2 mg L^{-1}), in which they remained 145 days, with refreshing passes every 45 days. The shoots obtained were transferred to a rooting medium [MS + (NAA 1 mg L^{-1} /1 mg L^{-1} BAP)] until reaching seedlings of 6 to 8 cm in height.

Table 1. Combinations of different growth regulators that were used in the medium (MS) to induce morphogenesis in 'MD2' hybrid pineapple.

Treatments	NAA (mg L ⁻¹)	BAP (mg L ⁻¹)	2,4-D (mg L ⁻¹)	P (mg L ⁻¹)
M1		5		
M2	2	5		
M3	2	2		
M4	1	1		
M5			1	
M6		1	1	
M7		2	2	
M8				3
M9		0.05		3
M10		0.05		5

In all treatments, the media were solidified with Gelrite (3000 mg L⁻¹), and 40 mL of it were distributed in magentas and sterilized in an autoclave at 121 °C for 15 min. Five explants were planted per magenta, and a completely randomized experimental design was used, with three replications, for which a total of 45 explants were planted per treatment, and when more than 50% of the explants presented morphogenic structures, the following features were evaluated: the number of explants with morphogenic structures, the type of morphogenic response (calluses, shoots, and direct and indirect somatic embryos), number of embryos per treatment, number of shoots per treatment, and number of plants obtained.

2.2. Histological Analysis of Morphogenic Structures That Originated in In Vitro Regeneration

For histological processing, samples of the different morphogenic structures formed in the different treatments were taken. The methodology used was that described by Piven et al. [16], though slightly modified. Biological samples were taken in small portions of approximately 0.5–1.0 cm², containing callus mass, embryos, and shoots. Three samples per treatment, taken at random, were fixed for 96 h in a FAA solution containing formaldehyde (4%), glacial acetic acid (95%), ethanol (95%), and distilled water, in a ratio of 2:1:10:7, respectively. After fixation, the tissues were washed three times (30 min each) with distilled water to remove fixative residues. Subsequently, the washed samples were subjected to dehydration treatments in different concentrations of ethanol (C₂H₆O), in a gradual and ascending manner (30%, 50%, and 70%) [17]. The samples were then left to stand in the last ethanol concentration (70%) for 24 h, and the dehydration process was continued with 85%, 96%, and absolute or anhydrous ethanol. Two alcohol changes were made for each concentration, with an immersion time of one hour for each change. The tissues were then embedded in JB-4 plastic resin according to the manufacturer's instructions (Embedding Solution Poly-sciences, Los Angeles, CA, USA). The embedded tissues were immersed in solution A + catalyst (Benzoyl Peroxyde Plasticized, Polysciences, Warrington, PA, USA) and maintained for one week at room temperature (20 to 25 °C). At the end of resin infiltration, casts were made, including the tissues for transverse and tangential sectioning on an HM 325 rotary microtome (Microm, CA, USA) with a thickness of 2–4 µm. Histological sections were serially performed and spread in distilled water and collected on a 26 mm × 76 mm slide. To visualize the cellular organization, the histological sections were stained with Toluidine Blue and Paz stain, and observations were made on an Axioplan Zeiss microscope, equipped with AxioCam ICc 5 (Jena, Germany).

2.3. Acclimatization of Plants In Vitro

Seedlings with a height of 6–8 cm were extracted from the culture containers, washed with abundant running water, and placed in plastic trays for transfer to the greenhouse, where they were established in trays containing a mixture of red soil + coconut fiber + perlite (1:1:1) as substrate, following the methodology described by Guzmán-Antonio et al. (data in process of publication). After 45 days, the seedlings were transplanted into black plastic bags (22 cm × 26 cm), where they remained for about 16–20 weeks, for subsequent transfer to the field.

2.4. Analysis of the Genetic Stability of the Plants Obtained from In Vitro Regeneration

Genomic DNA extraction. For DNA extraction, leaf samples were taken from 10 plants from the different treatments. Total genomic DNA was extracted according to the method reported by Tapia et al. [18]. The quality and integrity of the DNA was determined by electrophoresis in a 0.8% (*w/v*) agarose gel, and the concentration and purity of the genomic DNA was determined by reading absorbance at 260 and 280 nm in a spectrophotometer (Nanodrop 2000, Madrid, Spain), according to the methodology described above. Once the DNA was obtained, we proceeded to the analysis to determine the genetic stability with the SSR and ISSR markers.

Amplification by SSR. To determine the appropriate alignment temperature, each SSR primer was tested at 50 °C, 55 °C, and 60 °C. Amplifications were developed in a final volume of 25 µL for a reaction, containing 40 ng of template genomic DNA, 0.3 µM of each SSR primer, 0.15 mM of dNTP mix (Invitrogen, Carlsbad, CA, USA), 1.5 mM of magnesium chloride (Invitrogen, Carlsbad, CA, USA), 1× buffer, and 1.2 U of *Taq* polymerase (recombinant) (Invitrogen, Carlsbad, CA, USA). Twenty SSR primers reported by Wang et al. [19] were evaluated. For each amplification reaction, three samples from each treatment with three replicates per primer were analyzed.

PCR reactions were performed on a Thermal cycler 2720 (Applied Biosystems, CA, USA). The amplification program began with a 2.30 min cycle at 94 °C, followed by 35 cycles at 94 °C at 45 s. The alignment temperatures were 55 °C, 60 °C (45 s), and 72 °C (1 min), with an 8-min final extension cycle at 72 °C. PCR products were separated on 2% agarose gels in a 0.1× TBE buffer (0.04 M Tris hydroxymethyl aminomethane (Tris-HCl); 1 mM ethylenediamine tetra acetic acid (EDTA); 0.04 M boric acid; pH 8) at 100 v (constant voltage). Staining was performed with ethidium bromide and gels were visualized in a U.V. light transilluminator. (BIO-RAD Gel Doc Ez Imager, Hercules, CA, USA). By comparing the size of the amplified fragments to a 1 Kb plus DNA molecular weight marker (Invitrogen, Carlsbad, CA, USA), the size of the amplified fragments was determined.

Amplification by ISSR. Amplifications were made in a final volume of 25 µL for a reaction containing 20 ng of template genomic DNA, 1 µM ISSR primer, 0.25 mM dNTP mix (Invitrogen), 2.5 mM magnesium chloride (Invitrogen, Carlsbad, USA), 1× buffer (Invitrogen, Carlsbad, CA, USA), and 1.0 U *Taq* polymerase (recombinant). Five ISSR primers (IS01, IS13, IS14, IS17, and IS19), reported by Weiguo et al. [20], were evaluated. In each amplification reaction, 10 samples per previously described treatment were analyzed, and three repetitions of the amplifications per primer were performed. PCR reactions were run on a thermal cycler 2720 (Applied Biosystems, California, USA), using the following amplification program: an initial cycle at 94 °C for 2 min, followed by 45 cycles at 94 °C (45 s), where the alignment temperature was 54 °C (45 s) and 72 °C (1 min and 30 s), and a final extension cycle at 72 °C for 7 min. PCR products were analyzed on 2% agarose gels in a 0.1X TBE buffer (0.04 M Tris hydroxymethyl aminomethane (Tris-HCl); 1 mM ethylenediamine tetra acetic acid (EDTA); 0.04 M boric acid; pH 8) at 100 v (constant voltage). The bands were visualized by ethidium bromide staining on a U.V. light transilluminator. (BIO-RAD, Gel Doc Ez Imager, Hercules, CA, USA). The size of the amplified fragments was determined by comparison with a 1 Kb plus DNA molecular weight marker (Invitrogen). The Polymorphic Information Content was calculated by the methodology cited by Anderson et al. [21].

2.5. Statistical Analysis

The SPSS program (V.17.0) was used to analyze the data. The Kruskal–Wallis method was used, and the quantitative variables that influenced the variation observed among the different treatments established were identified. Paired *t*-tests (post hoc to Mann–Whitney U) were performed to test for differences between treatments. For the molecular analysis, the percentage of monomorphism obtained by each SSR and ISSR primer was determined, considering the total number of monomorphic bands generated for each of them, over the sum of the total number of bands detected with all the primers, times 100, and this value was considered to determine the genetic stability of each treatment.

3. Results

3.1. Evaluation of the Treatments Established for In Vitro Regeneration of the Pineapple Hybrid 'MD2'

3.1.1. Direct Somatic Embryogenesis (DSE)

Results obtained in the treatments established for the in vitro regeneration of the 'MD2' hybrid showed that depending on the balance of BAP/NAA to which the explants were exposed, the morphogenic response varied (Table 2). Direct Somatic Embryogenesis occurred in some of the explants in the treatment M3 used since the formation of abundant globular structures directly from the explant was observed (Figure 2A,B). Unlike the rest of the treatments that contained these two growth regulators, the structures formed evolved rapidly at advanced stages of their development, which is shown in Figure 2B,C, as well as their conversion to plants, so M3 was identified as an adequate medium for the direct induction and proliferation of 'MD2' pineapple embryos from leaf segments. In the rest of the treatments, in which BAP and NAA were used, no embryogenic structures formation was observed, but there was formation of leaf primordia directly from the explant and multiple budding.

Table 2. Morphogenic response of leaf segments of 'MD2' hybrid pineapple seedlings grown in different treatments.

Treatments	Percentage Exp. Morph. Resp.	Morph. Resp. Type	Number of Embryos per Explant	Number of Shoots per Explant
M1	33.3	DO		20.0 ± 1.7 e
M2	66.6	IO		30.0 ± 2.22 c
M3	88.8	DSE	50.0 ± 2.63 b	50.0 ± 2.63 b
M4	88.8	DO		25.0 ± 2.63 d
M5	44.4	IO		20.0 ± 1.64 e
M6	55.5	IO		25.0 ± 2.01 d
M7	93.3	ISE	120.0 ± 8.18 a	120.0 ± 8.18 a
M8	48.8	IO		22.0 ± 2.63 e
M9	55.5	IO		25.0 ± 2.53 d
M10	44.4	IO		20.0 ± 1.37 e
Chi-square	28.821 *	-	18.778 *	38.002 *

Percentage exp. Morph. Resp.: Percentage of explants with morphogenic response; Morph. Resp. type; Morphogenic response type (DO), direct organogenesis, DSE: direct somatic embryo; IO: Indirect organogenesis (callus or shoots), ISE: indirect somatic embryo; Number of embryos and Number of shoots per explant are: mean ± SD (standard deviation), Degree's freedom (df): 9. Significance level: * 0.01 or less; same letters: not significant differences.

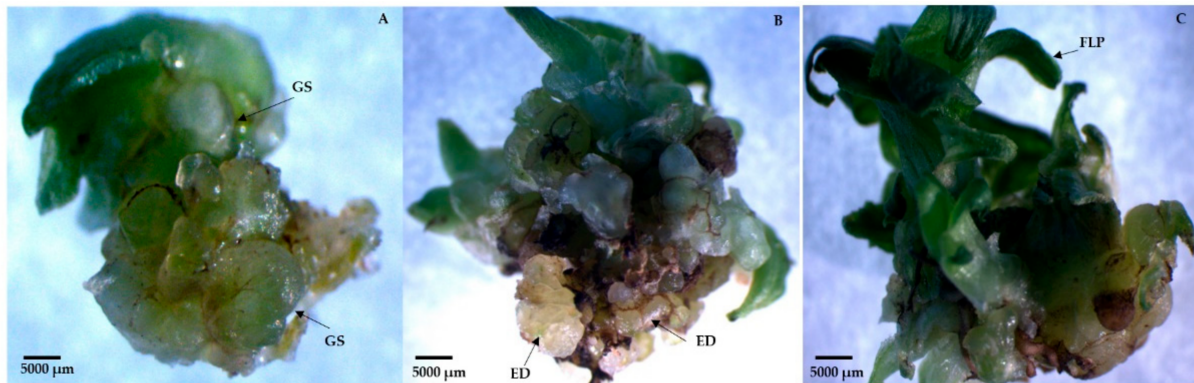


Figure 2. Somatic embryos formed directly from ‘MD2’ hybrid pineapple explants in M3 treatment. (A,B) Direct formation of globular structures (GS) from leaf explants, (ED) advance stage of embryo development. (C) Asynchronous development of formed embryos; FLP: foliar leaf primordia.

From the shoots obtained in all the treatments, the same number of plants was obtained in the rooting medium; this means that there was a 100% conversion of shoots to plants.

3.1.2. Indirect Somatic Embryogenesis (ISE)

By analyzing the response of leaf explants to the different treatments, it could be observed that in all treatments containing 2,4-D, alone or in combination with BAP, there was callus formation, although only explants exposed to the treatment with 2 mg L⁻¹ of 2,4-D and 2 mg L⁻¹ of BAP (M7) showed the formation of an embryogenic callus that rapidly evolved to form somatic embryos. At 30 days of culture, this callus was characterized by showing a creamy white coloration and a semicompact consistency (Figure 3A,B). In the treatments in which Picloram was present, the formation of a compact, slow-growing, beige-colored callus was observed, turning dark brown rapidly. After 60 days, isolated and minute outgrowths were visible on the periphery of the callus. Only in medium M7 (2 mg L⁻¹ of 2,4-D/2 mg L⁻¹ of BAP) was embryogenic callus formation observed, and 93.3% of the explants responded to the treatment (Table 2). In this treatment (M7), the callus started in the basal zone of the leaf and, six weeks later, the first embryogenic structures (globular) became visible from a primary, vitreous white, incipient, semicompact callus. These first embryos, of a faint green color, emitted a leaf primordium, typical of monocotyledonous species, which allowed for the inferring that they had a well-defined apical meristem (Figure 3A). After the first subculture (six weeks), a callus of semifriable consistency proliferated on the callus and formed 30 days after it was placed in the explant in the medium (Figure 3B), which evolved to form an abundant and granular embryogenic callus, revealing numerous embryogenic structures at early and advanced stages of their development (Figure 3C). These structures gave way to the appearance of numerous, tiny, pale green apices, which evolved into small buds located throughout the periphery of the callus, while in other areas of the callus there was an intense proliferation of embryogenic structures in early stages (globular), which shows an asynchrony typical of somatic embryogenesis (Figure 3D). The high embryogenic capacity (120 SE/Explant) of the callus induced in the M7 medium (2 mg L⁻¹ of 2,4-D and 2 mg L⁻¹ of BAP) was observed, differing significantly from the rest of the treatments evaluated. (Figure 3E). The rapid evolution of somatic embryos from globular to an advanced stage, characteristic of somatic embryogenesis in monocot species, became evident.

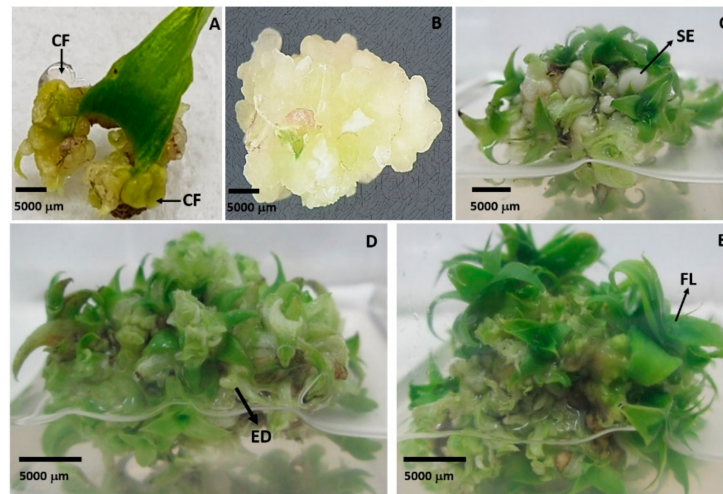


Figure 3. Indirect somatic embryogenesis (ISE) from young leaves of ‘MD2’ pineapple grown in the M7 treatment (2 mg L^{-1} of 2,4-D and 2 mg L^{-1} of BAP). (A) Incipient callus formed at the base of the leaf, CF: callus formation; (B) primary callus of vitreous white color, semicompact consistency; (C) embryogenic callus of greenish white color, with embryogenic structures (SE) visible at various stages of development; (D) appearance of globular embryos; ED: advance stage of embryo development; (E) high embryogenic capacity of the induced callus, with embryos multiplying and developing asynchronously; FL: foliar primordia.

3.1.3. Indirect Organogenesis (IO) and Shoot Development

The results obtained showed that in the treatment in which 2.0 mg L^{-1} NAA was combined with 5.0 mg L^{-1} BAP (M2), there was a high responsiveness to regeneration from the explant cells’ leaf segment, so it showed a fast and efficient response to shoot formation (Figure 4). It is worth noting that in this treatment, an average of 30 shoots per explant were formed, which was significantly higher than in the rest of the treatments in which regeneration occurred via organogenesis, both directly and indirectly (Table 2). The formed shoots were characterized by their vigor and rapid development, which preserved the vascular connection with the maternal tissue during the first generation of shoots. Figure 4 shows the evolution of this regeneration process.

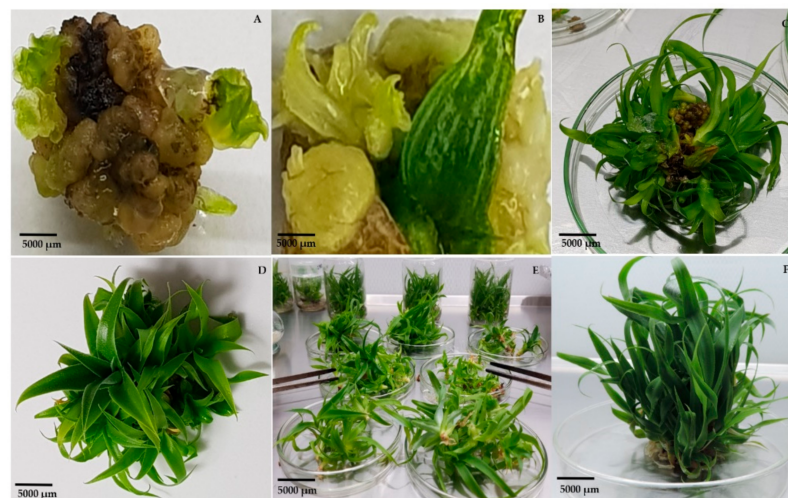


Figure 4. Efficient regeneration of pineapple shoots in the M2 treatment. (A,B) Rapid and abundant proliferation of neoformations with a globular structure; (C,D) proliferation of multiple shoots from neoformations; (E,F) efficient shoot development.

On the other hand, it was observed that the shoots formed in the M4 treatment developed and became suitable seedlings for transfer to the acclimatization phase in less time compared with the rest of the evaluated treatments. Therefore, this result allowed us to recommend this medium for the final stage of development of all the shoots obtained in the different regeneration pathways, either by direct and indirect somatic embryogenesis or by the direct organogenesis pathway. In treatments M5, M6, M8, M9, and M10—in which indirect organogenesis (IO) occurred via callus formation—the callus formed was very slow growing with a compact consistency that quickly turned dark, so none of these treatments had embryogenic structures because only tiny shoots were formed in certain areas of the callus, which subsequently evolved favorably in plants. However, it should be noted that plant regeneration was very slow in these treatments.

3.2. Histological Analysis

The histological analyses of the morphogenic structures that originated from callus in the M7 treatment showed an intense cell division activity in callus cells, clearly distinguishing the formation of abundant, well-defined meristematic centers (Figure 5A) as a prelude to somatic embryogenesis. These cells were characterized by being small and isodiametric, with a dense cytoplasm and a prominent vacuole. An intense asymmetric cell division was observed, the cells began to divide longitudinally and transversally, giving way to the histogenesis process (Figure 5A), in which asynchronously, globular somatic embryos could be observed in the same callus and in an advanced stage of their development (Figure 5B). There was not a vascular connection to maternal tissue. Through the longitudinal section of the embryo (Figure 5C), the development of the central cylinder could be seen in the innermost part of the scutelum, where later the formation of leaf primordia can be seen (Figure 5D).

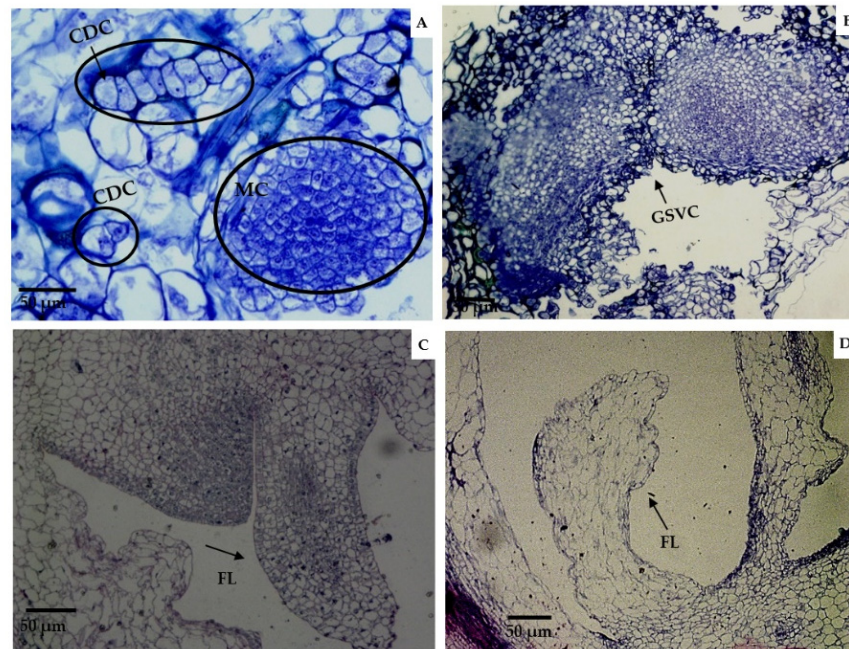


Figure 5. Histological samples that show the intense meristematic activity that occurred in the regeneration with the M7 treatment. (A) Meristematic cells (MC) in active cell division (CDC), vacuolated, isodiametric cells, and prominent nucleus are observed, as well as the successive divisions of the cells to give rise to the formation of the somatic embryo; (B) Globular embryos advanced in their development without vascular connection (GSVC) with the maternal tissue and where the suspensor rupture is appreciated; (C,D) Formation of the first leaf primordia (FL).

3.3. Acclimatization

Once the developed *in vitro* plants reached 6–8 cm in height, they were isolated (Figure 6A,B) and transferred to greenhouse conditions, where they were placed in trays containing a previously determined substrate mixture of red soil + coconut fiber + perlite (1:1:1) (data in process of publication) (Figure 6C). The *in vitro* plants, after the hardening stage in the trays (45 days), were transplanted into bags where they remained for 16–20 weeks. After this time, the *in vitro* plants showed optimal development with long, thick, dark green, shiny, and turgid leaves, and thick and vigorous stems, which demonstrated an adequate physiological state (Figure 6D). Survival of the *in vitro* plants exceeded 98% at the time of transfer to the field.



Figure 6. (A,B) Isolation of *in vitro* plantlets obtained in M3 and M7 media and developed and elongated in M4 medium. (C) Acclimatization in trays with substrate in a greenhouse. (D) Pineapple plants regenerated *in vitro* and ready to be transferred to the field after 20 weeks in polyethylene bags.

3.4. Genetic Stability of the Plants Obtained from *In Vitro* Regeneration

SSR and ISSR markers were used to assess the genetic stability of pineapple plants that were regenerated in various treatments. Of the 20 SSR primers used for molecular analysis, 15 produced amplification products with adequate resolution and reproducibility to evaluate the genetic stability of the regenerated plants. Table 3 shows a total of 21 monomorphic bands for each primer, obtaining 100% monomorphism. The number of amplified fragments for each primer was between 1 and 2 bands, for an average of 1 fragment per primer among all the treatments evaluated. The height of the fragments obtained was in the range of 100 and 300 bp, and 100% monomorphism was observed in all treatments (Figure 7). This monomorphism was also corroborated by the analysis of randomly selected individual plants from the treatment where indirect embryogenesis M7 (2 mg L^{-1} 2,4-D/ 2 mg L^{-1} BAP) occurred (Figure 7A–C) and the genetic stability of the pineapple *in vitro* plants regenerated in the 10 treatments evaluated for this marker could be appreciated.

Table 3. SSR primers [19] used in this study, alignment temperature, and the number of monomorphic bands obtained with each primer.

Primer	Sequences (5'-3')	Alignment Temperature (°C)	Monomorphic Bands (%)
DT 338176	F 5'-CTCCTCATCTACCGCACCTC-3' R 5'-CCCTAGACGACGACGAAGAG-3'	60	1
DT 336954	F 5'-CATCCATCCATCCATCCAAT-3' R 5'-GTCGTTGATCATTGCAAAA-3'	60	2
DT 3365 61	F 5'-GCAAATGAGGCCACAACTT-3' R 5'-GGGTGGTGGACTTTCTCT-3'	60	1
DT 336932	F 5'-GCATGCCAAAGGAAAGAGTT-3' R 5'-CCCTGAACAAATCACCCAAC-3'	60	2
DT 337038	F 5'-CCCTGAAGGTGGAGATTGTG-3' R 5'-AAAAACCAAACCTGGACA-3'	60	1
DT 338091	F 5'-GCTGCTCTTGCTGCCAT-3' R 5'-AAGCCATAGGACCACCAC-3'	60	2
CO 731287	F 5'-AGGGAAGCTTTGGAGGTCCAG-3' R 5'-TGCAATAGCGATGATAAACCCAG-3'	60	1
CO 731629	F 5'-AGAAGCGGAAGCGTGTG-3' R 5'-GCGGAGATCGAAGCACTC-3'	60	1
CO 73 12 35	F 5'-ATTCGAGCCCTTGGTCG-3' R 5'-TTATGGGGTCGCGTCGG-3'	60	1
CO 73 0888	F 5'-CGCATCAGCGCCAAACGC-3' R 5'-GGAAGCGAAAGGAGATCG-3'	60	2
CO 73 18 16	F 5'-CTCCTCAGCTTCGTCGCC-3' R 5'-GACGAGATTGGCGTATCCC-3'	60	1
AJ 845056	F 5'-TGCTGGCTCTGTGGGATG-3' R 5'-TTAGGTTTTCAGTGGAGAGAG-3'	60	1
AJ 845081	F 5'-ACATTCCTCAGAGTCACCAGC-3' R 5'-CACTAATCCTTGACCCAGACC-3'	55	2
AJ 845060	F 5'-TGTAGGCATATGGTGGGTCTG-3' R 5'-ATCTCTTAATCCAAGGGCCG-3'	60	2
AY 098521	F 5'-GTATATCGTGGATGCGGGAG-3' R 5'-AGCATCAAGGGTCCCGAGTT-3'	55	1

Of the five ISSR primers used for the analysis, all were appropriate to observe the monomorphism patterns with adequate resolution and reproducibility. Table 4 shows the total number of bands obtained by each primer, as well as the percentage of monomorphism. Of these 35 monomorphic bands, representing 89.74% of monomorphism, primers IS14 and IS17 were the ones that presented 100% monomorphic bands.

The number of amplified fragments for each primer ranged from 4 to 12 bands, for an average of seven fragments per primer, among all treatments evaluated. The height of the fragments obtained was in the range of 250 to 2000 bp. Figure 8 shows the band profiles obtained with primer IS19, which showed the highest number of bands.

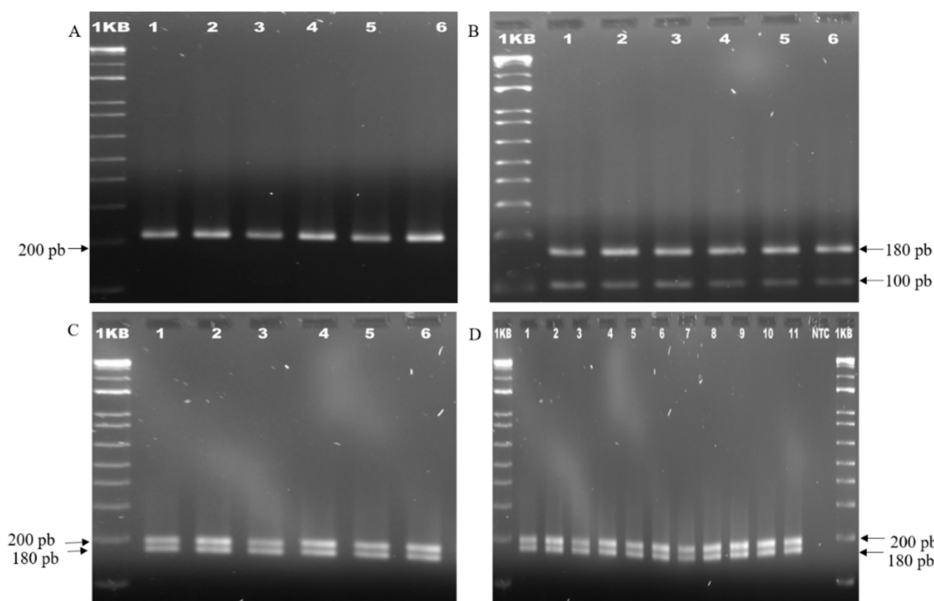


Figure 7. Banding profiles obtained. (A) AJ 805,060 SSR primer. (B) DT 338,091 SSR primer. (C) CO primer 730,888, DNA profiles show 100% monomorphic bands in individual plants from the M7 treatment (2 mg L, 2,4D, and 2 mg L BAP); Lane 1: Hybrid “MD2” donor material. Plants from M7 medium: Lanes 2, 3, 4, 5, and 6. (D) SSR CO 730,888 primer that showed 100% monomorphic bands in the analysis of regenerated plants in all treatments evaluated. 1: ‘MD2’ hybrid donor material; 2: sample of M1 regenerated plants (5 mg L BAP); 3: sample of M2 regenerated plants (2 mg L ANA/5 mg L BAP); 4: sample of M3 regenerated plants (2 mg L ANA/2 mg L BAP); 5: sample of M4 regenerated plants (1 mg L ANA/1 mg L BAP); 6: sample of regenerated plants in treatment of M5 (1 mg L 2,4D); 7: sample of regenerated plants in treatment of M6 (1 mg L 2,4D/1 mg L BAP); 8: sample of regenerated plants in treatment of M7 (2 mg L 2,4D/2 mg L BAP); 9: sample of regenerated plants in treatment of M8 (3 mg L P); 10: sample of regenerated plants of M9 (3 mg L P/0.05 mg L BAP); 11: sample of regenerated plants of M10 (5 mg L/0.05 mg L BAP); NTC: nontemplate control.

Table 4. ISSR primers [20] used in this study, alignment temperature used in the PCR, and the number of monomorphic and polymorphic bands obtained with each primer, PIC value, and percentage of monomorphism.

Primer	Sequence (3'-5')	Alignment Temperature (°C)	Total Number of Bands	Number of Polymorphic Bands	Number of Monomorphic Bands	PIC	Monomorphism (%)
IS 01	(GACA) ₄	54	4	1	3	0.25	75
IS 13	(CT) ₈ GT	54	8	1	7	0.30	87.5
IS 14	(AG) ₈ TA	54	10	0	10	0	100
IS 17	(TG) ₈ GT	54	5	0	5	0	100
IS 19	(AG) ₈ TC	54	12	1	11	0.31	91.67

With respect to the monomorphism detected (Table 5), 100% could be seen with this marker in treatments M3 (2 mg L⁻¹ BAP/2 mg L⁻¹ NAA), M4 (1 mg L⁻¹ BAP/1 mg L⁻¹ NAA), M5 (1 mg L⁻¹ 2,4-D), M6 (1 mg L⁻¹ 2,4-D/1 mg L⁻¹ BAP), and M7 (2 mg L⁻¹ 2,4-D/2 mg L⁻¹ BAP). At the same time, it was visualized that the treatment with the lowest stability, 94.26%, was the one in which the highest concentration of Picloram, M10 (5 mg L⁻¹ P/0.05 mg L⁻¹ BAP), was applied. When the PIC values were calculated, they were very low; an overall value of 0.298 was obtained, which indicates that these are genetically stable plants (Table 4).

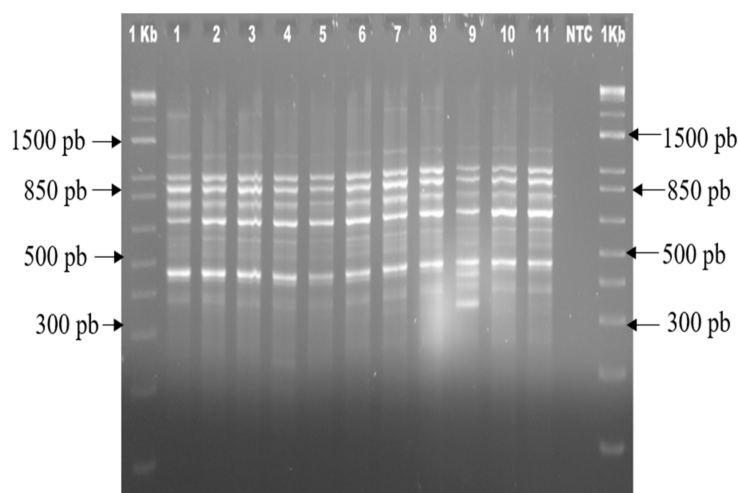


Figure 8. ISSR primer (IS 19) showed the highest number of bands. 1: Hybrid ‘MD2’ donor material; 2: sample from regenerated plants in M1 (5 mg L⁻¹ BAP); 3: sample from regenerated plants in M2 (2 mg L⁻¹ NAA/5 mg L⁻¹ BAP); 4: sample from regenerated plants in M3 (2 mg L⁻¹ NAA/2 mg L⁻¹ BAP); 5: sample from regenerated plants in M4 (1 mg L⁻¹ NAA/1 mg L BAP); 6: sample from regenerated plants in M5 (1 mg L⁻¹ 2,4-D); 7: sample from regenerated plants in M6 (1 mg L⁻¹ 2,4-D/1 mg L⁻¹ BAP); 8: sample from regenerated plants in M7 (2 mg L⁻¹ 2,4-D/2 mg L⁻¹ BAP); 9: sample from regenerated plants in M8 (3 mg L⁻¹ P); 10: sample from regenerated plants in M9 (3 mg L⁻¹ P/0.05 mg L⁻¹ BAP); 11: sample from regenerated plants in M10 (5 mg L⁻¹/0.05 mg L⁻¹ AP); NTC: nontemplate control.

Table 5. Levels of genetic stability detected by ISSR in the evaluated treatments.

Treatments	TBMT/TBM	Monomorphism (%)
M1	34/35	97.14
M2	34/35	97.14
M3	35/35	100
M4	35/35	100
M5	35/35	100
M6	35/35	100
M7	35/35	100
M8	34/35	97.14
M9	34/35	97.14
M10	33/35	94.26
Donor Plant	35/35	100

4. Discussion

Conceptually, the differences between somatic embryogenesis and organogenesis basically distinguish one from the other by the presence of both poles in the somatic embryo (caulinar and radical) and not so in organogenesis; in addition, somatic embryos have no vascular connection with the mother tissue and multiply adventitiously (secondary embryogenesis). In the present investigation, morphogenesis occurred only in the basal segments of the pineapple leaf and demonstrated a structure that was not directly connected to the callus, which subsequently emitted leaves and roots without requiring induction of the process. However, a radical pole is appreciated, apparently structurally rudimentary compared to that of the somatic embryo of other species. Figure 2F,G shows the intense multiplication of the structures, which allows maintaining the cultures at different stages

of development: callus proliferation, multiplication of morphogenic structures, and plant development. In the study, different types of tissues were observed: nodular and creamy, compact and brown, and friable and brown, and it was noted that in the treatment with 2,4-D in the presence of BAP (M7), there was a rapid formation of callus and a greater number of these, which may be related to the fact that 2,4-D is a synthetic regulator that stimulates a rapid synchronized cell division [22–24]. It was also observed that when the concentrations of 2,4-D and BAP were increased, callus texture was favored and embryogenic callus was obtained, which coincides with that reported by other researchers [25], who recommended combining cytokinin and auxin to induce embryogenesis in pineapple.

It is worth noting that several years ago, other auxin origin regulators were highlighted to induce callogenesis in pineapple, since many authors considered that in this crop, 2,4-D sometimes inhibited the induction of callus [7,26,27]. However, in the present research, the efficiency of 2,4-D in the induction of embryogenic structures that gave rise to many plants with respect to Picloram was perceived, which disagrees with what was cited by the authors. Therefore, it is not possible to generalize methodologies or work protocols, since the culture media and the selected strategies must be specific for each particular situation, and at the same time, it must be considered that not all cultivars respond in the same way to in vitro morphogenesis because there must be an interaction or synergic action between the exogenous treatments and the particular endogenous conditions of the plant in question to favor the formation of competent organogenetic meristematic centers in particular areas of the callus and, subsequently, their determination for the development of specific organs [28]. It can be inferred from in vitro regeneration of pineapple plants via somatic embryogenesis that the pattern concerning in vitro regeneration of pineapple plants, in the opinion of several authors, is not well defined [23,24]. Some consider embryogenic callus to be yellowish in color and nodular in appearance, despite the fact that no embryos can be distinguished, and use the term “shoots” for plants regenerated from embryogenic tissues [24]. Similarly, if somatic embryos are considered to develop from different structures with a closed vascular system, the term “seedlings” should be the most appropriate, according to other authors [28].

In the organogenetic system, shoot regeneration was achieved in two ways: shoots were regenerated directly from the bases of the treatment leaves (M1 and M4), or structures of nodular and globular appearance were formed (adventitious organogenesis) (M2), by which multiple sprouting was obtained. It should be appreciated that a group of authors who have worked with species of the Bromeliaceae family [29] demonstrated that the basal region of bromeliad leaves presents vascular elements as intercalary axillary meristems that attribute a high regenerative potential to the cells in dedifferentiation when activated by growth regulators and that the induction and development of monopolar structures generates adventitious shoots with high frequencies and that these structures, when isolated from a single explant, can respond and generate adventitious shoots from nodule cultures. Specifically, in the case of the *Vriesea* species, several lines of evidence suggest that the in vitro regenerative pathway follows a specific pattern associated with nodule cluster cultures [30] as competent morphogenic structures that are globular in shape, translucent to yellowish in color, and compact in texture. They also posit that, under suitable conditions, these nodule clusters develop into a series of small (0.5 cm long) buds called microhotels, which elongate to give rise to shoots. This terminology is used by them in in vitro regenerative systems in bromeliads and suggests that there are probably some species in this family that exhibit a third morphogenic route, intermediate between somatic embryogenesis and organogenesis, and that probably exceeds the morphogenic potential of the two best known routes [29,30], so that future research in culture could value a more in-depth study in this regard.

Although SSR primers have been used to assess the genetic diversity of species [19,31], their application in the analysis to detect the incidence of somaclonal variation has not been reported. In turn, ISSRs proved to be very useful in the analysis of the genetic stability of micropropagated plants by different breeding methods [32]. Hence, in the present investiga-

tion, a set of SSR and ISSR primers were used to try to analyze the entire pineapple genome, and the levels of monomorphism that were detected by both methods were evaluated, which was very useful because the application of only one type of molecular marker can underestimate the levels of monomorphism and genetic stability [33]. In the evaluation of the results obtained with each marker, ISSRs were shown to be more informative because they provided a greater number of bands than SSRs and were able to detect certain percentages of polymorphism in three of the treatments evaluated: M1 (5 mg L⁻¹ BAP), M2 (5 mg L⁻¹ BAP/2 mg L⁻¹ NAA), and M10 (5 mg L⁻¹ P/0.05 mg L⁻¹ BAP). However, when the PIC value was analyzed, the polymorphism was found to be negligible, which could be considered as monomorphism. The explanation for these differences in the resolution of the two marker systems could be related to the specificity of the species with each primer used [34] and the characteristic of ISSRs to express many bands compared to SSRs that express few, which consequently influences greater polymorphism. However, using both techniques to analyze the genetic stability in the established regeneration protocols was extremely beneficial because it allowed us to show that they are suitable for clonal propagation of this valuable fruit tree.

The present research is necessary and of great benefit since the response of *A. comosus* to growth regulators with respect to plant regeneration is considered by many researchers as variable, so that similar studies are necessary in the crop to deepen the more precise knowledge of its relationship with the different types of growth regulators, their combinations, and doses capable of stimulating a regenerative process at high frequency. From the different treatments established, it was possible to systematically characterize by optical microscopy the formation and development of morphogenic structures that gave rise to embryogenic and organogenetic tissues that can be propagated and used continuously as a source for the regeneration of new plants. In addition, when the multiplication coefficient was analyzed, a protocol of high efficiency in short-term regeneration was obtained, since an average of 120 plant shoots representing clones of the hybrid “MD2” was estimated. It was demonstrated that they are genetically homogeneous plants, so it is expected that the relevant characteristics, such as its high vitamin C and total soluble solids content, its low acidity, the striking color of its pulp, and its long shelf life, which distinguish it from the rest of the pineapple cultivars and make it the most demanded in the international market, will be maintained.

5. Conclusions

In vitro regeneration of pineapple hybrid ‘MD2’ was achieved in different ways: shoots regenerated directly from the bases of the leaves (M1 and M4), adventitious organogenesis (M2), indirect organogenesis occurred via callus formation (M5, M6, M8, M9, and M10) direct somatic embryogenesis (M3), and indirect somatic embryogenesis (M7). The most efficient treatment was M7 (2 mg L⁻¹ 2,4-D and 2 mg L⁻¹ BAP) because indirect somatic embryogenesis occurred, with an average of 120 somatic embryos per explant. The application of ISSR and SSR to analyze the genetic stability in the different established regeneration protocols demonstrated that they are suitable for the clonal propagation of this valuable fruit tree. Pineapple plants regenerated in vitro were shown to maintain the genetic identity of the donor genotype, which means that indirect somatic embryogenesis can be applied for clonal propagation of *A. comosus*.

Author Contributions: Conceptualization, N.S.-B. and A.K.-D.; methodology, A.C.-F., F.A.B.-P., A.G.-A., D.P.-B. and J.O.M.-C.; investigation, A.K.-D., S.A.A.-V., Y.R.-L. and A.C.-V.; writing—original draft preparation, A.K.-D. and N.S.-B.; writing—review and editing, L.G.I.-A., J.O.M.-C., D.P.-B. and N.S.-B.; project administration, N.S.-B. and A.C.-F.; funding acquisition, N.S.-B. All authors have read and agreed to the published version of the manuscript.

Funding: This research was funded by Consejo Nacional de Ciencia y Tecnología de México (CONACYT), grant number PN/2016/3953.

Acknowledgments: To Yasmin A. Sánchez-Rodríguez, Anuar A. Magaña-Alvarez, and Hernán Morffi-Mestre for technical support.

Conflicts of Interest: The authors declare no conflict of interest.

References

- Jaji, K.; Man, N.; Nawi, N.M. Factors affecting pineapple marker supply in Johor, Malaysia. *Int. Food Res. J.* **2018**, *25*, 365–371.
- Abdul, N.A.; Chin, B.; Razik, M.; Madon, M.; Khalid, N.; Syafawati, N. Abscisic acid and salinity stress induced somaclonal variation and increased histone deacetylase (HDAC) activity in *Ananas comosus* var. MD2. *Plant Cell Tiss. Org.* **2018**, *133*, 123–135. [[CrossRef](#)]
- Blanco, H.A.; Vargas, T.C.; García, T. Regeneración in vitro de plantas de piña (*Ananas comosus*, L. Merr.). *Rev. Colomb. Biotechnol.* **2017**, *19*, 7–20. [[CrossRef](#)]
- Hikal, W.M.; Mahmoud, A.A.; Hussein, A.H.; Ahl, S.A.; Bratovic, A.; Tkachenko, K.G.; Kakaniova, M.; Maldonado, R. Pineapple (*Ananas comosus* L. Merr.) waste streams, characterization and valorization: An overview. *Open J. Ecol.* **2021**, *11*, 610–634. [[CrossRef](#)]
- Russel, A. Piña miel: Un nuevo producto para aumentar la competitividad. 40 casos de éxitos. *SAGARPA* **2017**, 1–18. Available online: https://www.redinnovagro.in/casosexito/2017/Pi%C3%B1a_Amador_Russell.pdf (accessed on 22 November 2021).
- Mercado, J.N.; Tortoledo, O.; García, J.M.; Báez, R.; García, B.Y.; Ávila, J.; Corella, D.A.; Cruz, M.C.; Velásquez, D.; Zuñiga, B.S. Calidad comercial de piña MD2 (*Ananas comosus* L.) tratada en postcosecha con ácido 2-hidroxibenzoico. *Rev. Iberoam. Tec. Poscosecha* **2019**, *20*, 1–15. Available online: <https://www.redalyc.org/journal/813/81361553004/html/> (accessed on 22 November 2021).
- Nouri, F.; Farahani, F.; Noormohammadi, Z. Somaclonal variation in the in vitro regenerated pineapple (*Ananas comosus*): Investigation of the cellular characteristics, biochemical specificities and ISSR markers. *Phytol. Balc.* **2017**, *23*, 73–83.
- Garcidueñas, J.A. Caracterización Morfológica Y Molecular de Piña (*Ananas Comosus*, (L.) Merr.) Híbrido MD2 Y su Establecimiento in vitro. Master's Thesis, Universidad Autónoma de Chapingo, Chapingo, Mexico, 2013.
- Guzmán, N.M. Obtención de Plantas de Piña (*Ananas comosus*, (L.) Merr) por Cultivo in vitro a partir de Yemas Axilares de La Corona. Master's Thesis, Universidad Nacional Autónoma de México, Ciudad de México, Mexico, 1988.
- Souza, W.C.; Nascimento, M.; Oliveira, M.; Porcino, H.; Silva, A. Genetic diversity of *Fusarium* spp. in pineapple 'Pérola' cultivar. *Fungal Biol. UK* **2017**, *120*, 265–278. [[CrossRef](#)]
- Shamin, M.D.; Kumar, M.; Ranjan, T.; Ranjan, R.; Kumar, A.; Kumar, P.; Kumar, V.; Kumar, P. Importance of micropropagation in pineapple for disease free plantlets and rapid multiplication. *J. Pharmacogn. Phytochem.* **2016**, *5*, 359–362.
- Dhurve, L.; Kumar, K.A.; Bhaskar, J.; Sobhana, A.; Francies, R.M.; Mathew, D. Wide variability among the 'Mauritius' somaclones demonstrates somaclonal variation as a promising improvement strategy in pineapple (*Ananas comosus* L.). *Plant Cell Tiss. Org.* **2021**, *145*, 701–705. [[CrossRef](#)]
- Lin, W.; Xiao, X.; Zhang, H.; Li, Y.; Liu, S.; Sun, W.; Zhang, W.; Wu, Q. Whole-Genome Bisulfite Sequencing Reveals a Role for DNA Methylation in Variants from Callus Culture of Pineapple (*Ananas comosus* L.). *Genes* **2019**, *10*, 877. [[CrossRef](#)]
- Murashige, T.; Skoog, F. A revised medium for rapid growth and bioassays with tobacco tissue culture. *Physiol. Plant* **1962**, *15*, 473–497. [[CrossRef](#)]
- Akdemir, H.; Suzerer, V.; Tilkat, E.; Onay, A.; Ozden, Y. Detection of variation in long term micro propagated mature pistachio via DNA based molecular markers. *Appl. Biochem. Biotechnol.* **2016**, *180*, 1301–1312. [[CrossRef](#)] [[PubMed](#)]
- Piven, N.M.; Barredo, F.A.; Borges, I.A.; Herrera, M.A.; Mayo, A.; Herrera, J.L.; Robert, M.L. Reproductive Biology of Henequén (*Agave fourcroydes*) and its wild ancestor *Agave angustifolia* (*Agavaceae*). I. Gametophyte development. *Am. J. Bot.* **2001**, *88*, 1966–1976. [[CrossRef](#)] [[PubMed](#)]
- Ruzin, S.E. *Plant Microtechnique and Microscopy*; Oxford University Press: New York, NY, USA, 1999; Volume 198, p. 322.
- Tapia-Tussell, R.; Quijano-Ramayo, A.; Rojas-Herrera, R.; Larque-Saavedra, A.; Perez-Brito, D. A fast, simple and reliable high-yielding method for ADN extraction from different plant species. *Mol. Biotechnol.* **2005**, *31*, 137–139. [[CrossRef](#)]
- Wang, J.S.; He, J.H.; Chen, J.R.; Chen, Y.Y.; Qiao, F. Genetic Diversity in Various Accessions of Pineapple (*Ananas comosus* (L.) Merr.) using ISSR and SSR Markers. *Biochem. Genet.* **2017**, *55*, 347–366. [[CrossRef](#)]
- Weiguo, Z.; Zhihua, Z.; Xuexia, M.; Sibao, W.; Lin, Z.; Yile, P.; Yongping, H. Genetic relatedness among cultivated and wild mulberry (*Moraceae: Morus*) as revealed by inter-simple sequence repeat analysis in China. *Can. J. Plant Sci.* **2005**, *86*, 251–257. [[CrossRef](#)]
- Anderson, J.A.; Churcill, G.A.; Autrique, J.E.; Tanksley, S.D.; Sorrels, M.E. Optimizing parental selection for genetic linkage maps. *Genome* **1992**, *36*, 181–186. [[CrossRef](#)]
- Yancheva, S.D.; Golubowicz, S.; Fisher, E.; Lev-Yadun, S.; Flaishman, A. Auxin type and timing of application determine the activation of the developmental program during in vitro organogenesis in apple. *Plant Sci.* **2003**, *165*, 299–309. [[CrossRef](#)]
- Sripaoraya, S.; Power, B.J.; Davey, M.R. Plant regeneration by somatic embryogenesis and organogenesis in commercial pineapple (*Ananas comosus* L.). *In Vitro Cell. Dev. Biol.-Plant* **2003**, *39*, 450–454. [[CrossRef](#)]
- Firoozabady, E.; Moy, Y. Regeneration of pineapple plants via somatic embryogenesis and organogenesis. *In Vitro Cell. Dev. Biol.-Plant* **2004**, *40*, 67–74. [[CrossRef](#)]

25. Kouadio, O.; Kouadio, S.; Sopié, Y.; Kouassi, K.; Oumar, S.; Koffi, F.; Kouakou, T. Improved callogenesis and somatic embryogenesis using amino acids and plant growth regulators combination in pineapple [*Ananas comosus* (L.) Merr. (*Bromeliaceae*). *Eur. J. Biotechnol. Biosci.* **2017**, *5*, 6–16.
26. Cisnero, A.; Daquinta, M.; Rodríguez, Y.; Escalona, M.; Luna, I.; Borroto, C. Influencia de los reguladores del crecimiento clorinados en la embriogénesis somática en piña. *Rev. Bras. Frutic.* **1996**, *18*, 269–274.
27. Roostika, I.; Khumaida, N.; Wahyuning, S. RAPD analysis to detect somaclonal variation of pineapple in vitro cultures during micropropagation. *Biotropia* **2015**, *22*, 109–119. [[CrossRef](#)]
28. Bennici, A.; Mori, B.; Tani, C.; Bussi, B. Callogenesis and organogenesis in pineapple: A histological and ultrastructural study of developing callus and morphogenic processes. *Adv. Hortic. Sci.* **2007**, *21*, 19–27.
29. Paola, J.; Schmidt, C.E.; Guerra, M.P.; Bouzon, Z.; Dal Vesco, L.L.; Pescador, R. Histodifferentiation and ultrastructure of nodular cultures from seeds of *Vriesea friburgensis* Mez var. *paludosa* L.B. Smith and leaf explants of *Vriesea reitzii* Leme and A. Costa (*Bromeliaceae*). *J. Microsc. Ultra.* **2015**, *3*, 200–209.
30. Paola, J.; De Conti, D.; Guerra, M.P.; Dal Vesco, L.L.; Pescador, R. Dynamics of proteins, carbohydrates and global DNA methylation patterns during induction of nodular cluster cultures from seeds of *Vriesea reitzii*. *Acta Scientiarum. Agron.* **2020**, *42*, 442–448. [[CrossRef](#)]
31. Makaranga, A.; Songelael, M.; Ndee, A.; Mneney, E.; Mbwambo, G.; Lema, K.; Godfrey, A.; Kachiwile, M.; Mrema, M.; Theodosy, J. Diversity and genetic identity of pineapple [*Ananas comosus* (L.) Merr.] in Tanzania based on microsatellite markers. *Afr. J. Biotechnol.* **2018**, *17*, 811–817. [[CrossRef](#)]
32. Leite, R.; Fortes, C.; Da Silva, C.A.; Hilo, E.; Henrique, P.; Pereira, M.A.; Duarte, F.V. Viability and genetic stability of pineapple germplasm after 10 years of in vitro conservation. *Plant Cell Tiss. Org.* **2016**, *127*, 123–133. [[CrossRef](#)]
33. Borsai, O.; Harța, M.; Szabo, K.; Kelemen, C.D.; Andreacan, F.A.; Codrea, M.M.; Clapa, D. Evaluation of genetic fidelity of in vitro propagated blackberry plants using RAPD and SRAP molecular markers. *Hortic. Sci.* **2020**, *47*, 21–27. [[CrossRef](#)]
34. Norhayati, S.I.; Abdul, S.A.; Ab, S.F.; Zainal, R.A.; Mohd, M.F.; Zubir, N.M.; Zaynol, R. Genetic Diversity of Pineapple (*Ananas comosus*) Germplasm in Malaysia Using Simple Sequence Repeat (SSR) Markers. *Trop. Life Sci. Res.* **2020**, *31*, 15. [[CrossRef](#)]

Review

Insights into Agricultural-Waste-Based Nano-Activated Carbon Fabrication and Modifications for Wastewater Treatment Application

Syaifullah Muhammad^{1,2}, H. P. S. Abdul Khalil^{3,4,*}, Shazlina Abd Hamid³, Yonss M. Albadn³, A. B. Suriani⁴, Suraiya Kamaruzzaman^{1,2}, Azmi Mohamed⁴, Abdulmutalib A. Allaq⁵ and Esam Bashir Yahya^{6,7,*}

¹ Chemical Engineering Department, Universitas Syiah Kuala, Banda Aceh 23111, Indonesia

² ARC-PUIPT Nilam Aceh, Universitas Syiah Kuala, Banda Aceh 23111, Indonesia

³ Bioresource Technology Division, School of Industrial Technology, Universiti Sains Malaysia, Penang 11800, Malaysia

⁴ Nanotechnology Research Centre, Faculty of Science and Mathematics, Universiti Pendidikan Sultan Idris, Tanjong Malim 35900, Malaysia

⁵ Faculty of Applied Science, Universiti Teknologi MARA, Shah Alam 40450, Malaysia

⁶ Bioprocess Technology Division, School of Industrial Technology, Universiti Sains Malaysia, Penang 11800, Malaysia

⁷ Green Biopolymer, Coatings and Packaging Cluster, School of Industrial Technology, Universiti Sains Malaysia, Penang 11800, Malaysia

* Correspondence: akhalilhps@gmail.com (H.P.S.A.K.); essam912013@gmail.com (E.B.Y.)

Citation: Muhammad, S.; Abdul Khalil, H.P.S.; Abd Hamid, S.; Albadn, Y.M.; Suriani, A.B.; Kamaruzzaman, S.; Mohamed, A.; Allaq, A.A.; Yahya, E.B. Insights into Agricultural-Waste-Based Nano-Activated Carbon Fabrication and Modifications for Wastewater Treatment Application. *Agriculture* **2022**, *12*, 1737. <https://doi.org/10.3390/agriculture12101737>

Academic Editors: Muhammad Sultan, Redmond R. Shamshiri, Md Shamim Ahamed and Muhammad Farooq

Received: 7 September 2022

Accepted: 17 October 2022

Published: 20 October 2022

Publisher's Note: MDPI stays neutral with regard to jurisdictional claims in published maps and institutional affiliations.



Copyright: © 2022 by the authors. Licensee MDPI, Basel, Switzerland. This article is an open access article distributed under the terms and conditions of the Creative Commons Attribution (CC BY) license (<https://creativecommons.org/licenses/by/4.0/>).

Abstract: The past few years have witnessed extensive global industrial development that has led to massive pollution to most available water resources. There is no alternative to sustainable development, and the utilization of agricultural waste for wastewater treatment has been always a novel milestone in sustainable development goals. Agricultural-waste-based nano-activated carbon exhibits high porosity, great surface area, and unique surface functional groups that promote it to becoming a future and sustainable solution for wastewater treatment applications. Several modification approaches have been made to further enhance the adsorption capacity and reusability of such adsorbents. In this review, we presented the potential of agricultural-waste-based nano-activated carbon as a sustainable solution for wastewater treatment. We highlighted the fabrication process and properties of different nano-activated carbons in addition to different modification approaches to enhance its adsorption capacity. Finally, we critically discussed the recent advances in nano-activated carbon applications in water treatment including its role in drinking water filtration, organic dye removal, oil spill applications, heavy metals removal and the elimination of toxic compounds from wastewater.

Keywords: agricultural waste; nano-activated carbon; adsorption; wastewater treatment; modification

1. Introduction

The world's population has significantly increased from 3.75 billion in 1970 to over 7.91 billion last year (2021), and it is estimated to exceed 9 billion by 2050 [1]. Agricultural waste as well as agricultural pollution are predicted to increase as a result of the world's population increasing. The last century has witnessed a huge increase in the agricultural waste production capacities of several countries including China, India, the United States of America and several parts of Africa and Europe [2,3]. However, most of this waste is biodegradable and not significantly toxic to the environment, but their accumulation and presence in large quantities can cause adverse effect to the environment. They can be utilized to solve other accumulative issues such as water contamination [4]. Various pollutants are deposited into the environment each year, such as organic compounds, heavy metals, chemicals, toxins and other hazardous materials that can nowadays be found in most of our eco-systems [5]. Ground and surface water are mostly the end-point of

many contaminants that dissolve in water and remain for years, affecting marine life as well as plants, animals and humans [6]. Several approaches have been developed for wastewater treatment, which can be categorized into physical, chemical and biological approaches [7,8]. Physical approaches are the easiest and most used ones, which include filtration, adsorption, distillation, steam and stripping, skimming and sedimentation, etc. These approaches are used to separate the liquid (water) from different organic or inorganic pollutants. Among the physical approaches, the adsorption process is the most effective and widely used approach for wastewater treatment [9].

Several natural and synthetic adsorbents can be used to attract and accumulate water pollutants onto their surfaces and eventually to precipitate it [10]. This treatment process can be a specific or generalized step; some adsorbents are able to detect specific functional groups, while others are wide-ranging. Activated carbons are the most widely used adsorbent in water treatment applications; they have been incorporated into water filters to adsorb heavy metals and other chemicals from filtrated water [11]. Nano-activated carbon is a form of activated carbon that is characterized by its high surface area, which facilitates the adsorption of pollutants into the surface. The past few years have witnessed great advances in the fabrication and modification of nano-activated carbon for different wastewater treatment applications. Several review papers have been published on biochars [12–14], its fabrication [15], properties [16] and modifications [17]. In addition, normal activated carbon has also been covered in terms of most of its aspects. Heidarinejad et al. reviewed chemical activators used to produce activated carbon [18]. Shafeeyan et al. [19] reviewed the impact of changes in the surface chemistry and formation of specific surface groups on the adsorption properties of activated carbon. Lakshmi et al. [20] focused on the different aspects of activated carbon and covered the recent trends in the development and use of various activated carbon nanoparticles as anti-microbial agents. Limited works have addressed the use of nano-activated carbon in wastewater treatment applications. The novelty of the present work is the presentation of the utilization of agricultural waste in the production of nano-activated carbon for wastewater treatment applications. In this paper we present nano-activated carbon from agricultural waste, including its fabrication and properties, and highlight different modification approaches that have been conducted to enhance its function. We also critically discuss the recent advances in nano-activated carbon applications in terms of water treatment applications including its role in drinking water filtration, organic dye removal, oil spill applications, heavy metals removal and the elimination of toxic compounds from wastewater in addition to highlighting the challenges and prospectives that face this unique material.

2. Agricultural Waste: Types, Yield and Properties

Agricultural wastes are those which are generated as a result of different agricultural operations and processes [21]. Although most of these wastes are derived from natural sources and are not toxic to the environment, they can accumulate in large quantities and subsequently cause adverse effect to humans, animals and even plants [22]. Agricultural waste can be mainly categorized into four main categories including crop residue, livestock waste, agro-industrial waste and aqua-cultural waste (Figure 1). Crop residue and agro-industrial waste are the largest available types of waste that are produced in large quantities on a daily and sustainable basis [23,24]. However, the lack of proper management practices of these wastes, following the lack of or limited adequate information, has continuously become a great challenge, which is too great to be downplayed.

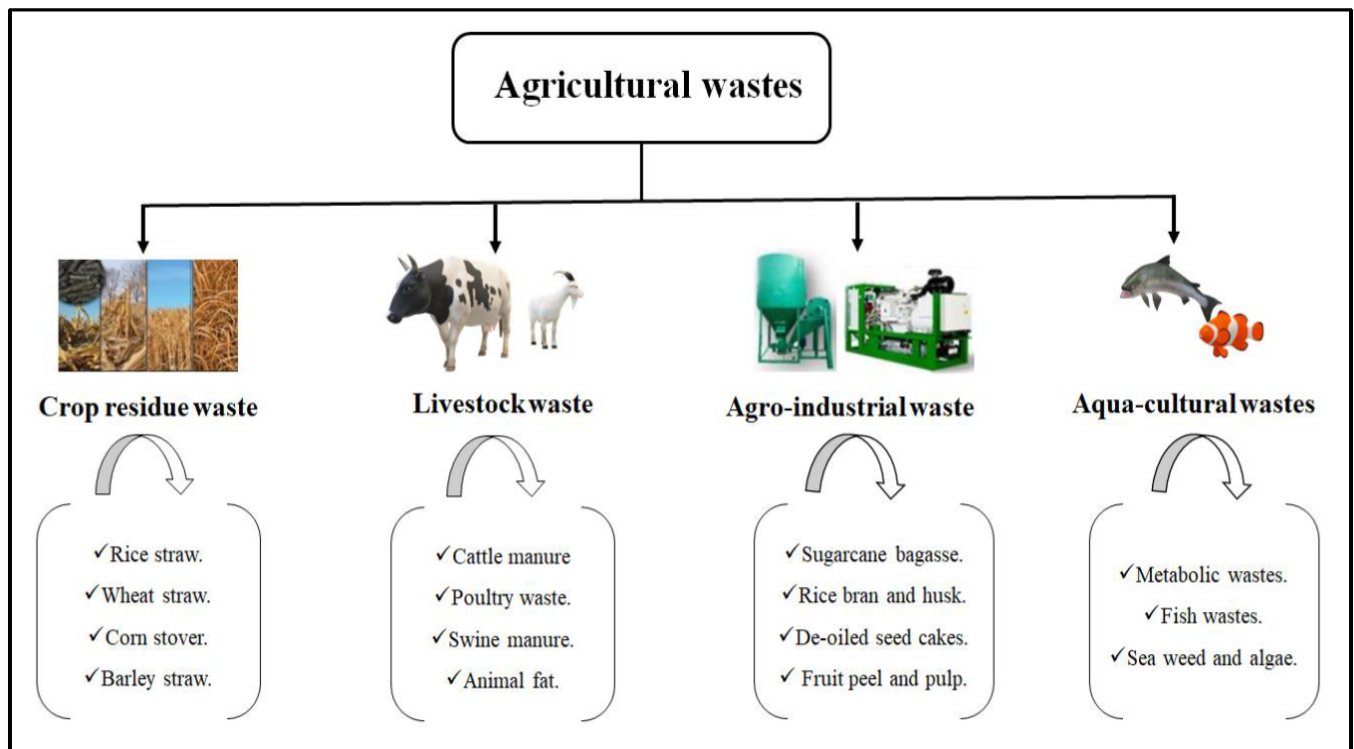


Figure 1. Illustration of different sources of agricultural waste categories.

2.1. Crop Residues Waste

Crop residues are the most common types of agricultural waste all over the world, with millions of tonnes produced every year, in which most of them are either burned or thrown into landfill. Crop residues include the straws of rice, oat, barley and wheat, corn stovers and the leaves of many fruit plants in addition to seed pods and shells. The global production of these wastes is projected to exceed 2802 million tonnes per year [25]. Corn stalks are the top produced crop waste with over 750 million tonnes produced per year, followed by wheat and rice with 600 and 360 million tonnes produced per year, respectively [26]. These organic wastes are rich in carbon, making them an attractive precursor material for nano-activated carbon production. Only a small portion of rice, corn and wheat crop residues are effectively utilized in some applications such as animal fodder and/or bioenergy production, while the rest is discarded into landfill or openly burned [27]. From a chemical aspect, crop residues contain from 40 to 45% carbon, 0.6 to 1% nitrogen and 14 to 23% potassium in addition to phosphorus and microelements that are necessary for crop growth [28].

Different types of crop residues exhibit different micro-morphological properties. In general, it has been stated that most crop residues are associated with a tubular structure, thick walls and abundant pores [29]. Thus, the resulting nano-activated carbon possesses a large specific surface area and a large pore volume and size, allowing for a great adsorption capacity. Zhang et al. [30] reported that the interior structures of rice straws have a large number of vascular bundle sheaths, intercellular canals and medullary cavities, which give these types of waste a high porosity and large surface area. In a recent work, rice-straw-based activated carbon was prepared and chemically activated by using KOH [31]. The authors stated that their activated carbon possessed a huge surface area of 1330 m²/g, which is a lot higher than that of raw rice straw (0.77 m²/g) [32]. Comparatively, wheat straw exhibits linear and multi-cavity structures that mostly bridge between the micro and nano pores that give this waste its complex network structure [33]. The properties of nano-activated carbon-based crop residues are basically dependent on the types of residues, and a good understanding of the characteristics and properties of each raw material is essential to fabricate nano-activated carbon with the desired properties.

2.2. Livestock Waste

Livestock waste consists of wastewater, solid manure from different farm animals and liquid manure. Out of these types of waste, solid manure has been used for the preparation of activated carbon as an environmentally friendly solution. Topcu et al. [34] successfully utilized poultry manure as a precursor material for activated carbon production. The production of animal manure in the European agricultural sector alone has exceeded 1500 million tonnes per year, which opens another source for activated carbon production [35]. Animal manure is a renewable resource as it basically comes from cellulosic feed and undigested residue, which is excreted by livestock animal species. Traditionally, animal manure is used as a fertilizer without any proper treatment, which can cause significant environmental problems including greenhouse gas emissions, public hazards (asphyxia poisoning and infectious pathogens), air quality deterioration and water pollution [36]. As a sustainable and eco-friendly solution, Tsai et al. [37] successfully utilized cow manure as a precursor material for activated carbon production and reported its great properties and a surface area of more than 950 m²/g. Owing to its organic source and its high carbon content, animal manure can be thermally converted (or further modified) into various forms of carbon materials and energy sources [38]. However, the low energy yield and air pollution resulting from manure processing for energy production has added additional value to it as a suitable and sustainable adsorbent for several environmental applications.

2.3. Agro-Industrial Waste

Agro-industrial waste is another type of agricultural waste that generated as a by-product from several food- and beverage-processing industries. Huge amounts of these wastes are produced every year. Sugarcane bagasse, for example, is generated from the sugar manufacturing industries, and approximately 180.73 million metric tons of it is produced every year, and it is estimated to reach 221 million metric tons in 2024 [39]. Other industries such as palm oil are also generating over 35.19 million tonnes of waste out of 85.84 million tonnes of the fresh fruit of the palm plant [40]. The huge amount of agro-industrial waste makes them highly attractive sources of activated carbon, and a significant number of studies have been conducted on the utilization of such waste in nano-activated carbon preparation [41,42].

2.4. Aquaculture Waste

The aquaculture industry is considered to be one of the fastest growing food production industries due to the fast-growing nature of fish as well as aquatic plants. Akinwale et al. [43] stated that feed has become the primary source of waste in aquaculture, followed by fish faeces. Both are harmful to fish and need to be removed as soon as possible, which means they can be utilized in nano-activated carbon fabrication [44]. In fish culture systems, the amount of released and uneaten feed varies with the system type. However, daily treatment is highly required in such systems, which generate an accumulative amount of such waste. Therefore, a general management plan and smart utilization is highly needed [45]. Limited works have been conducted on the management of aquacultural waste, and activated carbon is mostly used to treat water polluted by toxic materials in culture systems [44,46,47].

3. Agricultural-Waste-Based Nano-Activated Carbon: Fabrication and Properties

Generally, nano-activated carbon can be fabricated from different precursors including agricultural and forestry residues. These precursors are rich in carbon, leading to the production of high-yield activated carbon [48]. The production of nano-activated carbon can be achieved by grinding the clean waste into fine particles and then conducting thermal treatment of these particles (pyrolysis) followed by physical and/or chemical activation. Figure 2 presents illustration of the fabrication process starting from agricultural waste.

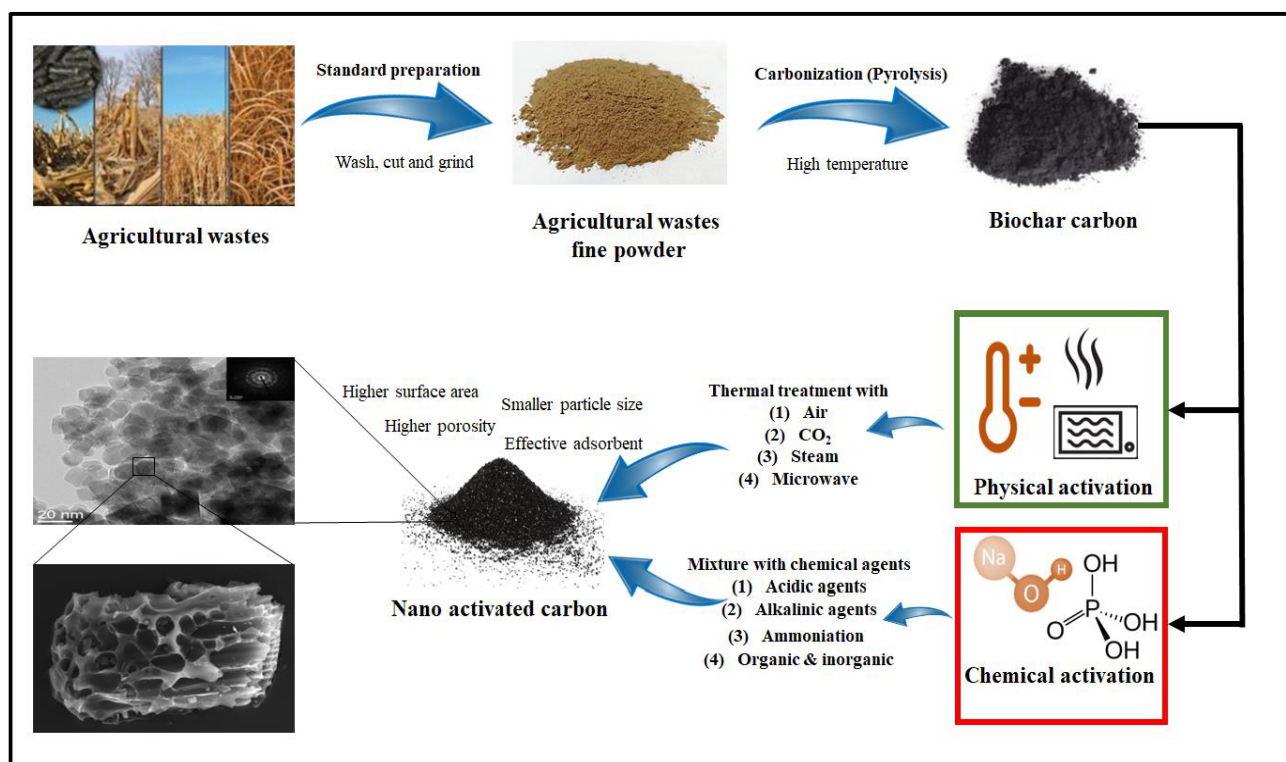


Figure 2. Schematic illustration of agricultural-waste-based nano-activated carbon fabrication.

Pyrolysis is an essential process in the fabrication process, which determines most of the nano-activated carbon's properties. Om Prakash et al. [49] recently synthesized nano-activated carbon using arhar fiber biomass and a novel technique consisting of two-stage pyrolysis followed by chemical activation. In this study, the authors used different temperatures ranging from 700 to 900 °C and reported that the one prepared at 800 °C exhibited the highest surface area (504.6 m²/g) with tiny surface micropores of a 20 Å diameter. Although a higher temperature was used, the optimum properties were not associated with the highest temperature. However, different precursor materials have different optimum temperatures for the best adsorption capacity. The optimal temperature and time depend on the type of precursor material and activation approach. It has been reported that carbon dioxide activation requires 800 °C and 1 h of holding time, compared with steam activation that requires only 700 °C and the same amount of time [50].

Physical activation can be achieved by further thermal treatment, steam exposure and microwave and/or ultrasound treatment [51]. The advantages of physical activation methods are their simplicity, the fact that they do not involve any chemical usage and the resulting production of microporous structures rather than the microporous structures achieved in the chemical activation process [52]. Carbon dioxide activation was found to produce a higher surface area and micropore volume than steam activation. In a recent study, the maximum surface area of CO₂-activated carbon was 789 m²/g compared to steam-activated carbon with a maximum surface area of 552 m²/g [50]. Owing to the decomposition of cellulosic material in plant waste, the yield of nano-activated carbon decreases with increasing the temperature [50]. Thus, reheating activated carbon could further reduce the production yield. Chemical activation is more common, using several chemical compounds such as KOH, ZnCl₂, K₂CO₃ and CaCl₂. In the work of Gan, the author discussed different chemical activation agents and their effects on the adsorption performance [53]. Although chemical activation may involve the excessive use of chemical agents, several studies have reported an adsorption capacity of up to 99% of water pollutants from water [54]. Conceptually, chemical agents with dehydration and oxidation properties are

more suitable for the activation of different plant-based carbons [55]. Refer to Table 1 for a summary of the different studies that have used different activation approaches.

Table 1. Comparison of the functional properties of using different activation approaches for activated carbon preparation.

Type of Activation	Precursor Material	Pyrolysis Conditions	Activation Agent	Removing Material	Adsorption Capacity	Reference
Physical activation	Palm kernel shells	700 W for 30 min	Steam	Herbicides	11 mg/g	[56]
	Biomass straw	600 °C for 20 min	Microwave and ultrasound	Elemental mercury	7.23 mg/g	[57]
	Cattle manure	850 °C for 60 min	CO ₂	Hydrogen sulfide	868.45 mg/g	[58]
	Corn cob residue	600 W for 20 min	Microwave and H ₃ PO ₄	Organic dyes	183.3 mg/g	[59]
	Bamboo	900 °C for 120 min	Steam and thermal	Xenon	158.49 g/g	[60]
	Prawn shells	800 °C for 180 min	KOH and HCl	Heavy metals	560 mg/g	[61]
Chemical activation	Pistachio shells	1000 °C for 240 min	CaHPO ₄	Organic dyes	-	[48]
	Lignocellulosic waste	500 °C for 120 min	H ₃ PO ₄	Pesticide	35.7 mg/g	[62]
	Cashew nut shells	500 °C for 120 min	ZnCl ₂	Dyes	476 mg/g	[63]
	Animal bone waste	600 °C for 120 min	Orthophosphoric acid	Heavy metals	27.86 mg/g	[64]
	Molasses	500 °C for 120 min	H ₃ PO ₄	Organic dyes	625 mg/g	[65]

4. Modifications of Agricultural-Waste-Based Nano-Activated Carbon

Although most nano-activated carbons exhibit a sufficient adsorption capacity for wastewater pollutants, scientists have always convinced themselves that much more can be done to enhance the adsorption performance of nano-activated carbon. Several approaches have been investigated including incorporating nano-activated carbon with metal oxides, enhancing the porosity and surface area of the particles using chemical or physical agents and the incorporation of activated carbon with specific chemical compounds for specific adsorptions.

4.1. Incorporation of Nano-Activated Carbon with Metal Oxides

To enhance the affinity of nano-activated carbon to the adsorption of heavy metals and other inorganic compounds, several elemental iron and iron (hydr)oxides have been used, especially for arsenic removal [66]. Nano-sized zero-valent iron was incorporated with activated carbon in one study, using ferrous sulfate impregnation followed by chemical reduction by NaBH₄ [67]. The authors reported the significant enhancement of arsenite and arsenate absorption at pH 6.5, and they stated that the removal markedly decreased by using phosphate and silicate. However, metal cations such as Ca²⁺ and Mg²⁺ are known for their adsorption enhancement, while ferrous iron (Fe²⁺) suppresses adsorption. In another recent investigation, nano-sized hematite-modified nano-activated carbon was prepared by coating the activated carbon particles with α-Fe₂O₃ nanoparticles [68]. Such modification enhanced the adsorption of nano-activated carbon by three times more than non-modified one, the removal process occurred in shorter duration and the authors were able to effectively regenerate their activated carbon by using HCl with a minor reduction in the adsorption efficacy after four desorption–adsorption cycles.

The use of iron-based nano particles also has the advantage of easy regeneration using a magnetic field compared with other metallic oxides. Khalil et al. [69] developed this approach by using an ethanol medium and acid thermal treatment to produce modified nano-scale zero-valent/activated carbon to enhance the removal of nitrate and phosphate from water. The authors reported that the thermal treatment of nano-activated carbon before the supporting nano-scale zero-valent modified the texture and surface of the activated carbon, leading to an enhancement of the surface chemistry properties and thus a better attraction of contaminant anions (Figure 3). The same authors reported that their optimum modification enhanced the removal efficiency of nitrate by more than 170%, while the complete removal of phosphate was achieved, which came about due to the modified surface structure of the activated carbon. Such modification can be also applied with other types of activated carbon for the removal of other pollutants. Metal oxide particles supported on activated carbon can significantly enhance the absorption and adsorption efficacy of the materials and provide effective wastewater treatment.

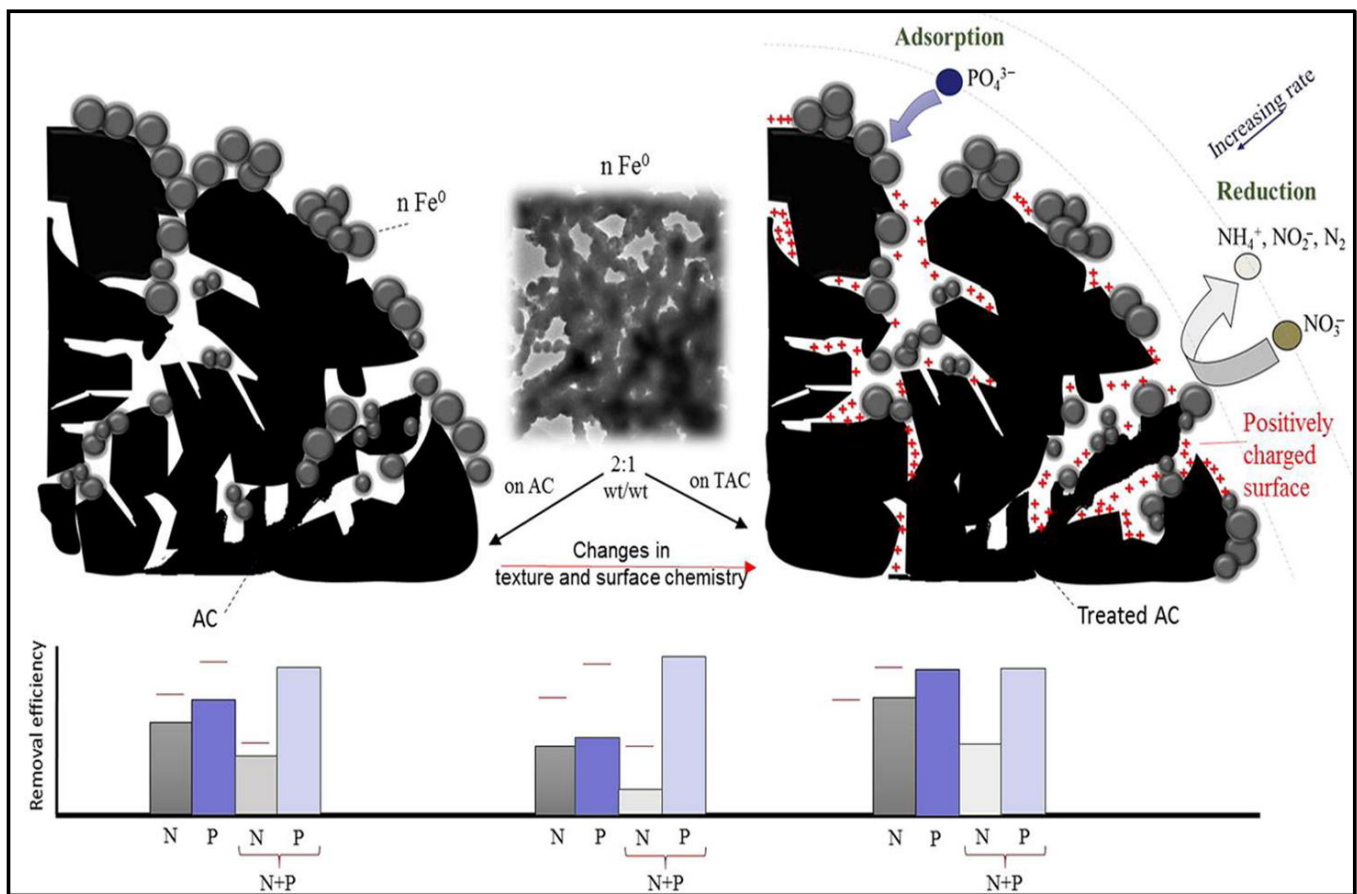


Figure 3. Schematic illustration of textile and surface chemistry modification of nano-scale zero-valent/activated carbon for the removal of nitrate and phosphate from water. The graphs show the removal efficiency of both nitrate and phosphate alone and combining together. Reprinted with permission from Ref. [69], 2017, Elsevier.

4.2. Incorporation with a Specific Chemical Compound

Several chemical compounds have been incorporated with nano-activated carbon to target the adsorption of specific heavy metals or other toxic materials from aqueous solutions. In one recent study conducted by Sabermahani & Noraldiny [70], they developed a facile and low-cost activated carbon from apricot fruit nuclei and activated it with H₃PO₄ for the removal of thallium (I). The authors modified their activated carbon by incorporated it with rhodamine B for the specific adsorption of thallium (I). The addition of rhodamine B significantly enhanced the adsorption efficiency of the activated carbon. Owing to the strong attachment between the dye and activated carbon particles, the modified particles exhibited better adsorption characteristics compared to the non-modified ones. In a different investigation, Deng et al. [71] used pristine feedstock to fabricate activated carbon and then used chitosan and pyromellitic dianhydride as chemical modifiers. The authors stated that their modified activated carbon exhibited an increased number of surface functional groups compared with the non-modified one, which led to a better adsorption of heavy metal ions. The addition of chitosan and pyromellitic dianhydride supplied the particles with nitrogen-rich functional groups in addition to the C=C and N-C=O, which were mainly responsible for the adsorption of Pb, Cd and Cu from water. Zhou et al. [72] used the same modification principal and reported a significant enhancement in the adsorption capacity in a markedly shorter time.

Several functional groups such as oxygenated groups and phosphate can be incorporated on nano particle surfaces to promote metal particle anchorage, which facilitates and speeds up the adsorption of heavy metals and other metallic-based toxic compounds. Several studies have used graphene oxide as a chemical modifier to enhance the adsorption capacity of activated carbon, which is also a carbon-rich agent [73,74]. Such modification was conducted prior to the pyrolysis process, which resulted in oxygen-rich surface-functional groups. Owing to the unique structure of graphene and its ability to integrate within the mixture after the pyrolysis, the prepared activated carbon possessed a high surface area with a significantly enhanced adsorption capacity [73,74]. The surface modification of *Pongamia-pinnata*-shells-based acid-activated carbon has been conducted in different work using a cationic surfactant (Cetyltrimethylammonium bromide) for the specific adsorption of organic dyes [75]. The authors stated that such modification significantly enhanced the uptake capacity of the activated carbon for organic dyes, which could be used as a cleaner alternative for dye adsorption from aqueous solutions. The same authors were able to regenerate their modified activated carbon and reuse it several times without any significant loss in adsorption capacity.

4.3. Enhanced Porosity and Surface Area

As an adsorption material, a large surface area is an essential character for most wastewater treatment applications. Reducing the particle size and porosity can significantly increase the surface area, leading to an enhanced adsorption efficiency. Lignocellulosic activated carbon was prepared and modified by impregnation with the precursor material in a $\text{Cu}(\text{NO}_3)_2$ solution [76]. The authors reported a higher mesoporosity in the modified particles compared with the non-modified ones, which enhanced their adsorption capacity. In different study, Huang et al. [77] investigated the effect of different activation parameters in the porosity and morphological characteristics of wood-sawdust-based activated carbon fibers. An enhanced porosity and a greater surface area were achieved with KOH activation and a temperature of above $800\text{ }^\circ\text{C}$, which generated nano pores ranging from 0.8 to 1.1 nm.

Enlarged pores can be obtained with increasing the KOH/material ratio and prolonging the activation time, and the authors were able to obtain larger pores from 2 to 5 nm [77]. The adsorption capacity of the adsorbent is directly proportional to increasing the surface area, which is also directly proportional to the porosity. Depending on the waste that needs to be absorbed, the pore size and surface functional groups of nano-activated carbon can be easily adjusted, especially with chemical activation. For this purpose, Abuzalat et al. [78] fabricated and modified nano-activated carbon from green algae *Ulva lactuca* using a novel and facile approach. The authors used zinc chloride for the activation and modification of their nano-activated carbon and reported meso–micro porous structures with a significantly higher surface area ($1486.3\text{ m}^2/\text{g}$). With such a surface area, the authors investigated the adsorption capacity of the porous nano-activated carbon in the adsorption of organic dyes and stated a maximum adsorption capacity of 149.26 mg/g , which indicated the high ability of such a modified activated carbon in the adsorption of organic dyes. In a different investigation, Jain et al. [79] enhanced the porosity of sunflower-head-waste-based nano-activated carbon and evaluated it for the removal of $\text{Cu}(\text{II})$, $\text{Cr}(\text{VI})$ and $\text{Cd}(\text{II})$ ions from polluted water. The authors used mineral acids as the activation agents to increase the porosity of their nano-activated carbon, and they stated that sulphuric acid activation produced the highest surface area pore width and volume in addition to the highest porosity (Figure 4). Having such great characteristics, the nano particles immediately adsorbed 89.4% and removed 74.5% of the $\text{Cr}(\text{VI})$ and $\text{Cd}(\text{II})$ in the first 2 min.

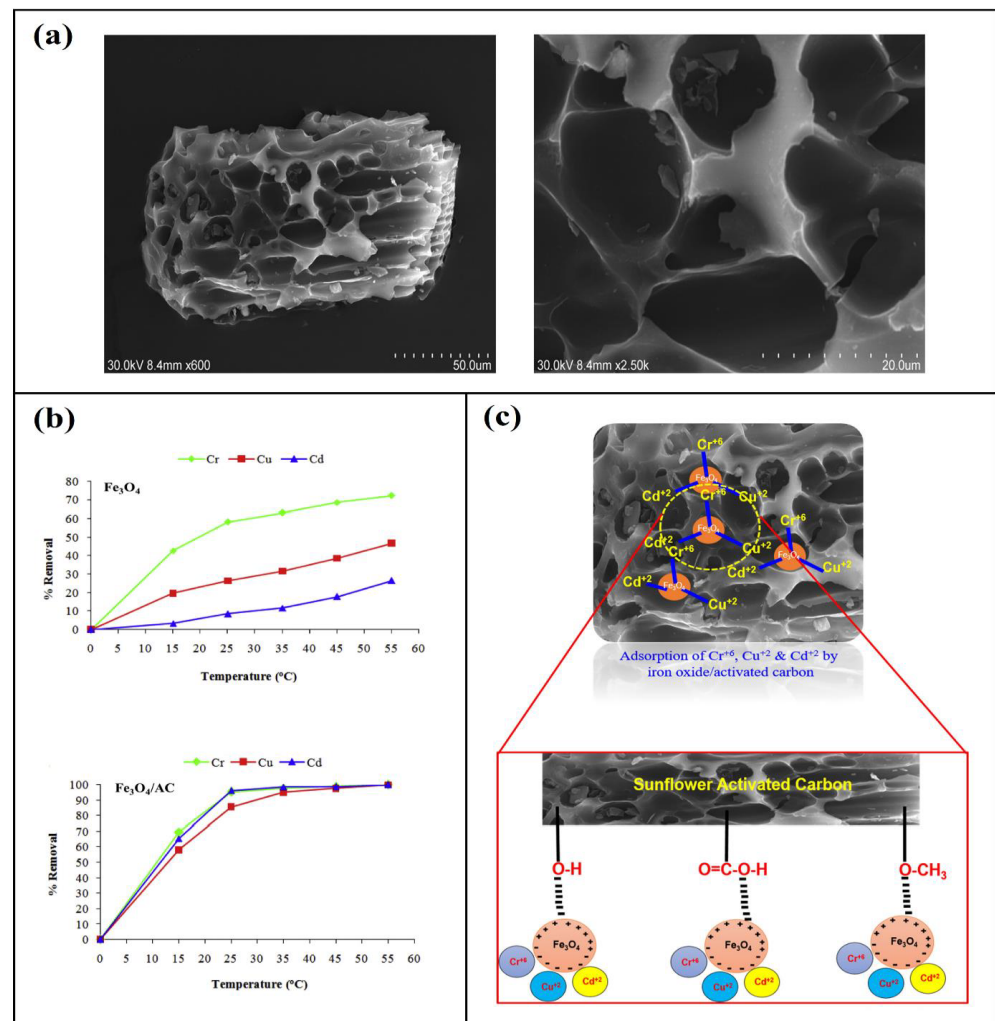


Figure 4. Illustration of sunflower-head-waste-based nano-activated carbon; (a) scanning electron microscope images at different magnifications, (b) effect of temperature on the adsorption, and (c) schematic drawing of adsorption process of heavy metals. Reprinted with permission from Ref. [79], 2018, Elsevier.

4.4. Other Modification Techniques

The facile and eco-friendly modification of agricultural-waste-based nano-activated carbon has always been a great challenge due to the need for physical and/or chemical agents to enhance the properties of the adsorbent materials [11]. However, although some modification may not be completely eco-friendly, the enhanced removal of toxins and undesired material from wastewater is worth this slight sacrifice. A bimetallic platinum-ruthenium nano adsorbent was used to modify and support nano-activated carbon using a thermal decomposition process [80]. The authors used the modified activated carbon for methylene blue dye removal from aqueous solutions and reported a great enhancement in the adsorption capacity, reaching 569.4 mg/g under the optimum conditions. In a different study, Deng et al. [81] modified their activated carbon by loading silver nano particles in its pores in order to enhance bacterial activation in drinking water. The authors used *Escherichia coli* as a standard bacterium for their investigation and reported that surface-bound silver (Ag I) was slightly converted to Ag as a result of structural reducing groups on the surface of the activated carbon (Figure 5). The attached silver nanoparticles were able to directly sterilize most of *E. coli* in the treated water by catalyzing O₂ and H₂O in the solution and generating reactive oxygen species (ROS). ROS possess great disinfection properties for most microorganisms by the oxidation sterilization process [82]. The same authors

stated that the pH strongly affected the inactivation process, and a neutral pH was the optimum compared with acidic and basic pH values. Figure 6 presents illustration of silver-nano-particles-based modified activated carbon for water disinfection and sterilization applications. Such modifications can open the door to reducing the excessive use of chlorine. Modified activated carbon may work in reducing toxic materials and disinfecting water from microorganisms at the same time without the need to further add water disinfectants. Other modification techniques have been used to modify nano-activated carbon, including ball milling and hydrothermal synthesis to further reduce the size of the particles [83,84], co-precipitation to integrate functional groups within the pores of the activated carbon [85], succinylation [86], and solvothermal treatment [87,88].

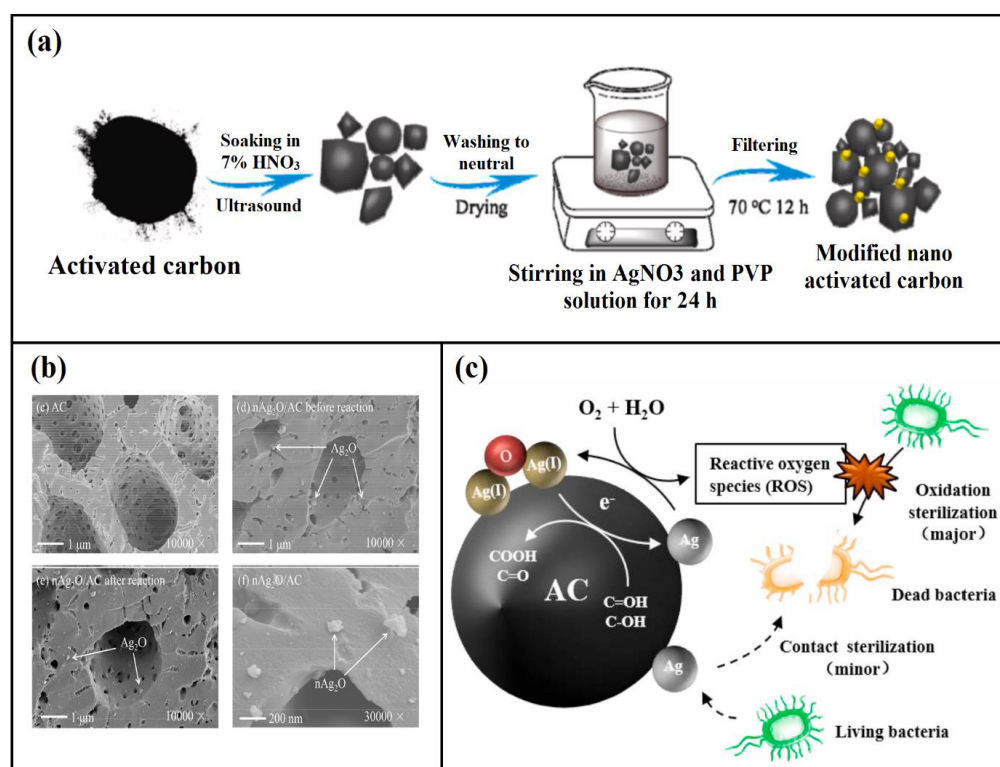


Figure 5. Modified activated carbon for water disinfection; (a) schematic illustration of the fabrication process, (b) SEM images showing the pore size and silver nanoparticles attachments and (c) the sterilization mechanism of modified activated carbon. Reprinted with permission from Ref [81], 2022, Elsevier.

5. Agricultural-Waste-Based Nano-Activated Carbon for Wastewater Treatment Applications

Massive industrial development has accelerated the accumulation of waste in the environment, which eventually ends up in water bodies. Different agricultural wastes have been extensively investigated as precursor materials to solve the issue of water pollution [89]. They are suitable raw materials for the fabrication of enhanced nano-activated carbon, which can be used for drinking water filtration, the removal of dyes and organic compounds, the removal of heavy metals and the elimination of toxins and chemical compounds in addition to solving oil spill issues and in other wastewater treatment applications.

5.1. Drinking Water Filtration

Water filtration is an essential process that removes or reduces the concentration of most of the pollutants including suspended particles and microorganisms as well as undesirable chemical compounds from contaminated water. Several approaches containing filters and membranes have been fabricated for this purpose including micro-filtration, nano-filtration, reverse osmosis, pervaporation and ultrafiltration membranes [90]. Nano-

activated carbons have gained tremendous attention recently in drinking water filtration applications due to their high surface area, nano porosity and high adsorption and removal performance in terms of organic as well as inorganic pollutants present in drinking water and wastewaters [91,92]. In a recent investigation, granular coconut-shell-based activated carbon was prepared and evaluated for the adsorption and removal of polystyrene nano plastics from drinking water [93]. Owing to the negatively charged granular coconut-shell-based activated carbon that interacted with the positively charged nano plastics, the authors were able to achieve a maximum adsorption capacity of more than 2.20 mg/g. The presence of dissolved organic matter significantly enhanced the adsorption capacity of the activated carbon, due to changing the surface charges on the nano plastics and the presence of divalent ions (Figure 6a). In a similar work, Altmann et al. [94] investigated a pilot scale of granular activated carbon integration into coagulation/filtration. The authors combined the adsorption of that activated carbon with deep-bed filtration (Figure 6b), and they were able to effectively remove both suspended solids and phosphorus from drinking water.

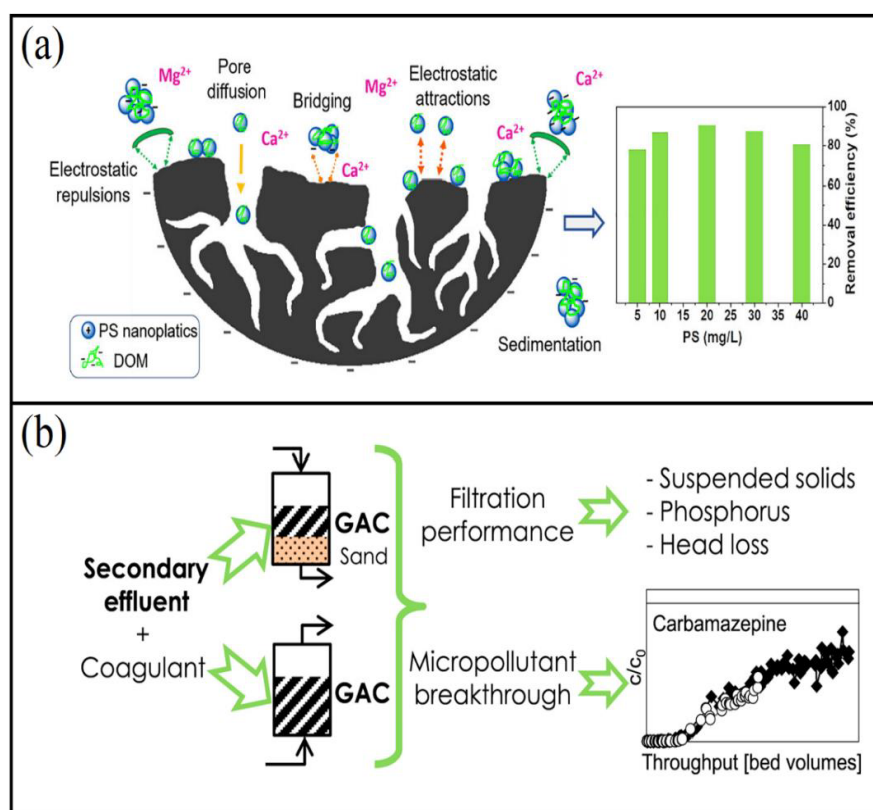


Figure 6. Granular activated carbon-based drinking water filters: (a) the adsorption and removal of polystyrene nano plastics, and (b) the removal of suspended solids and phosphorus from drinking water. Adapted with permission from ref. [93], 2021, Elsevier (a), and [94], 2016, Elsevier (b).

5.2. Removal of Dyes and Organic Compounds

Dyes are widely used in several industries such as the textile industry, paper, plastics, cosmetics, etc. Synthetic dyes are a specialized class of organic pollutants that, in most cases, are directly discharged into environmental ecosystems as wastewater from their industries [95,96]. These organic pollutants exhibit complicated structures from their aromatic assembly, making them difficult to degrade in natural conditions. Thus, it is necessary to develop an eco-friendly and cost-effective approach to treat water polluted with such pollutants. In a recent study, nano-activated carbon was prepared from Maghara raw Egyptian coal and investigated for the removal of methylene blue dye from wastewater [97]. In this study, the activated carbon particles had an average diameter of 38 nm and pore volume of over $0.183 \text{ cm}^3/\text{g}$, resulting in a high adsorption capacity of 28.09 mg/g . In different

study, Mousavi et al. [98] used corn stalks to prepare nano-activated carbon for the removal of rhodamine B dye from contaminated solutions. The authors were able to achieve a 5.6 mg/g adsorption capacity at the optimum conditions, which fitted pseudo-second-order kinetics and the Freundlich isotherm model. Owing to the porous surface and high surface area of nano-activated carbon, organic dyes can be easily adsorbed into these particles, resulting in great removal efficiency. In term of dye adsorption using of nano-activated carbon, the regeneration of the adsorbent has been always a great challenge due to activated carbon/dye bonding. Feiqiang et al. [99] developed magnetic activated carbon using a one-step approach for toxic dye removal from polluted water. The authors fabricated the adsorbent under a CO₂ atmosphere and reported that the CO₂ enhanced the surface area of the activated carbon, which enhanced the adsorption of the dyes. The authors were able to easily remove the dyes using an external magnetic field. In the same manner, Liu et al. [100] used the same principal for the fast and effective removal of organic dyes from an aqueous solution. The surface area and functional groups played a fundamental role in the dye and toxic material adsorption mechanism by attracting bonding between the chemical groups (Figure 7). The authors were able to achieve a great adsorption capacity of 182.48 mg/g and 150.35 mg/g for rhodamine B and methyl orange, respectively. Owing to the incorporation of iron oxide, the authors were able to easily regenerate and separate their adsorbent. Such effects and highly efficient adsorbents with a rapid magnetic separation have promising applications in different wastewater treatments.

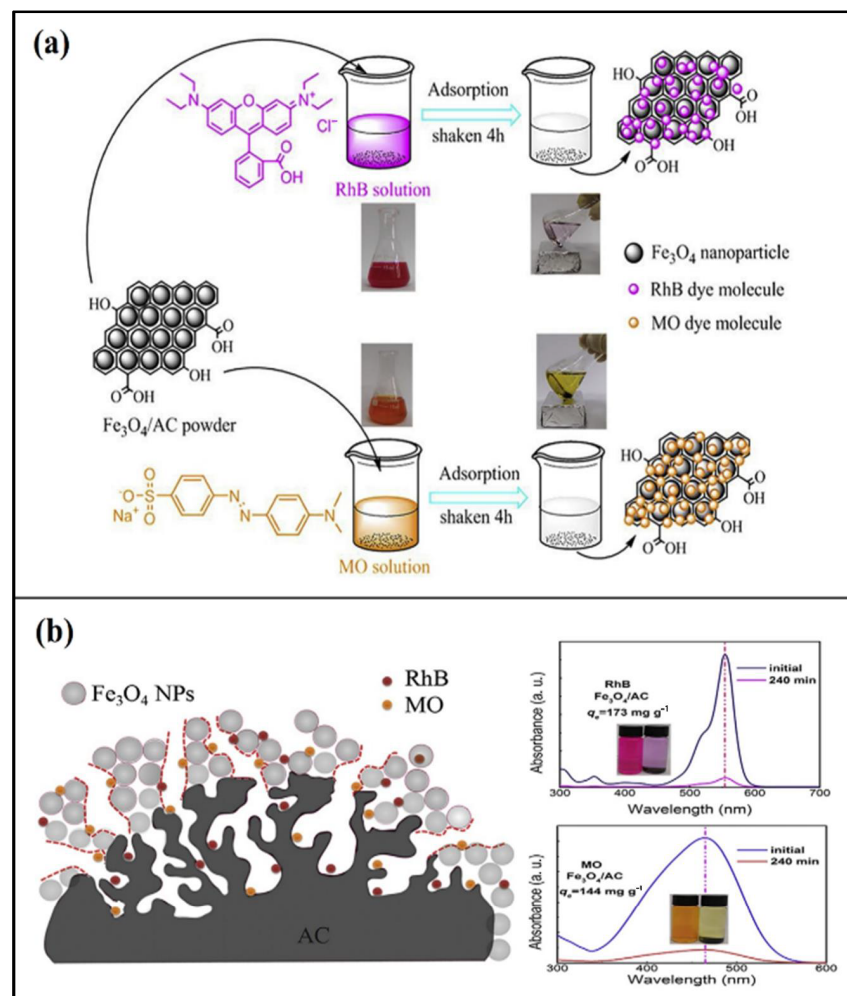


Figure 7. Schematic drawing of using magnetic activated carbon in dye removal; (a) the application of Fe₃O₄/AC sample for removing rhodamine B and methyl orange from the aqueous solution, and (b) the adsorption mechanism. Reprinted with permission from Ref. [100], 2019, Elsevier.

5.3. Removal of Heavy Metals

Heavy metals pollution has become a major concern in recent times due to massive industrial development. Some heavy metals function as micro or even macro nutrients for certain animals and plants. However, in high concentrations they are highly toxic to most living organisms [101]. Hexavalent chromium is a toxic form of the heavy metal chromium that can irritate the nose, lungs and throat and cause other adverse health effects. Li et al. [68] developed modified activated carbon that was able to significantly remove most of the hexavalent chromium from water. The authors coated their activated carbon with iron oxide nanoparticles using a facile impregnation approach, and they reported that this enhanced the adsorption capacity by three times more than the non-modified activated carbon.

Steam activation has been used to enhance the activity of carbon adsorbents in heavy metal removal applications. Lou et al. prepared activated carbon from pine sawdust using steam activation and reported an enhanced adsorption capacity [102,103]. Although the surface area was slightly reduced, the steam activation seemed to enhance the adsorption of the heavy metals. In different study, Valentin-Reyes et al. [104] investigated chemically activated carbon with a high surface area for the removal of hexavalent chromium (Cr(VI)) from water. Changing the surface chemistry during the activation process was proposed by the authors as the reason for enhancing the adsorption mechanism. A significant number of studies have been conducted on evaluating the adsorption capacity of different agricultural-waste-based nano-activated carbon on the adsorption of heavy metals (Table 2).

Table 2. Illustration of studies presenting the adsorption capacity of different agricultural-waste-based nano-activated carbon.

Agricultural Waste	Pyrolysis Condition	Type of Metal	Surface Area (m ² /g)	Maximum Adsorption (mg/g)	Reference
Coconut shell	Commercial	I–	1220	41.2	[105]
Bamboo waste	700 °C for 2 h	Cd(II)	6.79	73.45	[106]
Pig manure	700 °C for 2 h	Cd(II)	11.37	77.34	[106]
Kenaf core fiber	400 °C for 1 h	As (III)	1031	422.9	[107]
Rape straw	300 °C for 2 h	Pb(II)	699.9	253.2	[108]
Hazelnut shell	700 °C for 2 h	Hg	-	80.0	[109]
Gingko leaf	400 °C for 1.5 h	Cu(II)	310.00	59.90	[110]
Lignite and poplar leaves	600 °C for 0.5 h	Pb(II)	805.86	10.55	[111]
Pine tree residue	600 °C for 4 h	Cd(II)	N.A	85.8	[112]

5.4. Oil Spill Separation

Large oil spills are a major environmental problem that occurs as a result of accidents caused by either human error or natural calamities. These oil spills have a significantly toxic and harmful impact on different environmental eco-systems, which eventually will affect human health [113]. In recent years, activated carbon has been investigated to solve oil spill issues. Shokry et al. [114] developed nano-magnetic activated carbon from waste biomass (hyacinth roots) for facile oil spill separation by using an external magnetic field. The authors reported that the original biomass exhibited only a 2.2 g oil /g oil spill adsorption affinity compared with their modified nano-magnetic activated carbon that showed a 30.2 g oil/g adsorption affinity after one hour of placing 1 g of their activated carbon in one liter. The authors were also able to easily separate the magnetic nano-activated carbon from treatment media by using an external magnetic field.

Although great advances have been made, the commercialization of cost-effective, reusable and eco-friendly sorbents for oil separation is yet to be achieved on a large-scale level [115]. Hammouda et al. [116] developed an efficient and eco-friendly magnetic activated carbon from plant biomass for oil spill applications. The authors coated magnetic nanoparticles with activated carbon and then made a soybean oil and stearic acid surface decoration. This modification made the magnetic fabricated composite possess an excellent amphiphilicity and a great adsorption capacity to a range of oils. In a different study, coconut-shell-based nano-activated carbon was incorporated with iron oxide nanoparticles and investigated in an oil spill treatment experiment [117]. The authors reported an

excellent and fast oil retention capacity, with facile recovery by using an external magnetic field. The cost effectiveness of agricultural-waste-based nano-activated carbon and their whole fabrication and treatment processes in the required bulk quantities suggest great advances for these adsorbents in oil removal applications.

5.5. Removal of Toxins and Pharmaceutical Compounds

Several environmental toxins are highly abundant in eco-systems as a result of natural and/or anthropogenic processes [118]. Polycyclic aromatic hydrocarbons are one of these toxins that are released from the burning of coal, vehicle emissions and the burning of biofuels and biomass [119]. These toxins exhibit a highly hydrophobic nature, making them difficult to biodegrade, and thus they enter the food chain through either polluted air, sand and/or water [120]. To solve this issue, Inbaraj et al. [121] developed nano-activated carbon from green tea leaf waste. The authors evaluated their nano-activated carbon for the adsorption of four priority polycyclic aromatic hydrocarbons, and they reported that, owing to the unique spherically shaped and cubic spinel structure of the nano particles, the surface area was found to be $118.8 \text{ m}^2/\text{g}$. The adsorption capacity of these nano particles for the four priority polycyclic aromatic hydrocarbons ranged from 19.14 to 28.08 mg/g. The same authors also applied their nano-activated carbon to mineral water, tap and river water, resulting in up to an 89% removal of these toxins from mineral water and complete removal from tap and river water. In a different study, different agricultural wastes were used to prepare activated carbon fibers for the removal of cyanobacteria toxins (microcystins) from drinking water [122]. The authors were able to remove more than 98% of the toxin after only 10 min of contact time by using sugar-cane-bagasse- and pine-wood-based activated carbon fibers. Nano-activated carbon has also been used to eliminate toxic herbicides as a cost-effective, easy and effective technique. Rambabu et al. [123] developed nano-activated carbon from date-palm coir (DPC) waste via an easy and single-step carbonization and chemical activation process for the elimination of a highly toxic 2,4-dichlorophenoxyacetic acid herbicide. The nano-activated carbon exhibited a graphitic structure and a flaky morphology, with a particle size and surface area of 163 nm and $947 \text{ m}^2/\text{g}$, respectively (Figure 8). The authors were able to remove more than 98.6% of the herbicide from the contaminated water with a small dosage of nano-activated carbon. The same authors evaluated the economic value of their nano-activated carbon and stated that the economic value of the nano-activated carbon was \$3/kg, and it could be reused without any significant loss in the adsorption capacity. Such an economic analysis supports our hypothesis that agricultural-waste-based nano-activated carbon can be the future of wastewater treatment applications.

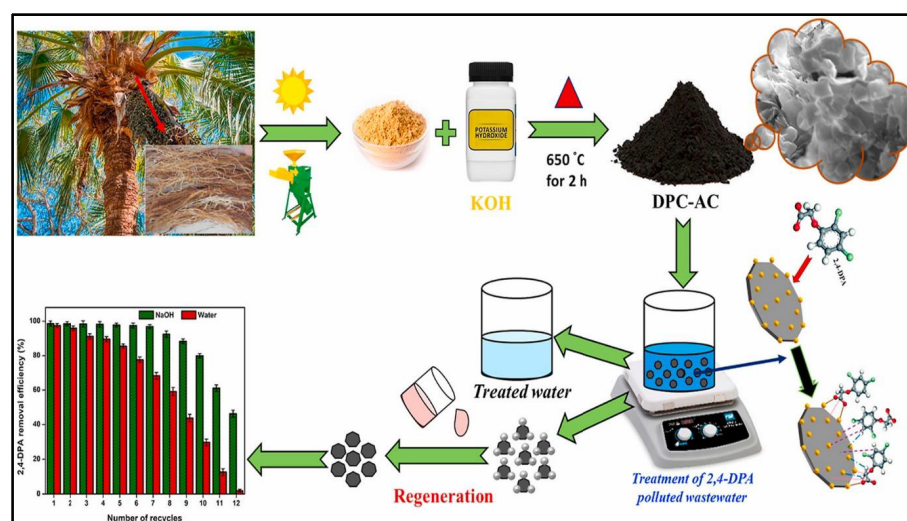


Figure 8. Schematic illustration of nano-activated carbon prepared from date-palm coir waste and its usage in toxic herbicide removal. Reprinted with permission from Ref. [123], 2021, Elsevier.

6. Conclusions and Perspectives

Different agricultural wastes can lead to serious environmental and health problems depending on their type and source. The proper management and utilization of agricultural waste can have positive impacts on the environment in terms of reducing both the waste and removing pollution from water bodies. The fabrication of nano-activated carbon from such sustainable resources has several advantages apart from their potential adverse impacts. Agricultural wastes are extremely low cost and eco-friendly, which can reduce the overall cost of the production process of wastewater treatment systems. This is meaningful, as the price of these systems and of activated carbon in particular have both increased over time. Among the two activation approaches of activated carbon, physical activation is more time consuming than chemical activation, which could slightly increase the cost in addition to the difficulties in controlling the pore size and porosity of the nano-activated carbon particles. Thus, chemical activation and modification has become more prevalent. Activated carbon, due to its current cost of manufacturing, will remain the most prominent carbon-based water filtration material for the time being, with chemical modifications being used to improve the capture capacity and efficiency, thereby maintaining its relevance. As the cost of fabricating carbon nanotubes and graphene are reduced, it is highly likely that these carbon nanomaterials will be developed into advanced filtration devices or as additional components to a broad spectrum of nano-activated carbon devices used to capture specific contaminants. Ighalo et al. [124] stated that the cost of the adsorbent material used could vary depending on the method of activation employed, with chemical activation being more expensive than physical activation. Other factors can also affect the cost, including industrial-grade precursors, the chemicals used in any stage of preparation, adsorption capacity, selectivity, operational cost and the adsorbent degradation rate [125–127]. These factors should be taken into consideration before any attempt at large-scale production of the adsorption materials. The modification of nano-activated carbon allows these advanced adsorbents to specifically target the desired pollutants even in tiny amounts, which is highly beneficial in drinking water treatment applications. The future of water treatment will witness the high utilization of nano-activated carbon-based filters and treatment systems to eliminate toxic and undesired compounds. The activation, modification and application of nano-activated carbon are increasingly being developing every day, and the near future will witness the development of high-performance nano-activated carbon that is able to generally adsorb most wastewater pollutants with a reasonable cost of production.

Author Contributions: Conceptualization, S.M., H.P.S.A.K. and E.B.Y.; validation, Y.M.A. and A.B.S.; investigation, E.B.Y.; resources, S.M. and H.P.S.A.K.; data curation, A.A.A. and S.A.H.; writing—original draft preparation, E.B.Y.; writing—review and editing, E.B.Y. and H.P.S.A.K.; visualization, A.M. and S.K.; supervision, H.P.S.A.K.; project administration, S.M. and H.P.S.A.K.; funding acquisition, Y.M.A. All authors have read and agreed to the published version of the manuscript.

Funding: This work was supported by an External Research Grant, grant number (304/PTEKIND/6501194.A158) and partially funded by LPPM-Universitas Syiah Kuala.

Institutional Review Board Statement: Not applicable.

Data Availability Statement: Not applicable.

Acknowledgments: The authors would like to thank the collaboration between Universitas Syiah Kuala, Banda Aceh 23111, Indonesia, Universiti Pendidikan Sultan Idris, 35900 Tanjong Malim, Perak, Malaysia and Universiti Sains Malaysia, Penang 11800, Malaysia that made this work possible. In addition, thanks to Lembaga Penelitian dan Pengabdian Masyarakat (LPPM) Universitas Syiah Kuala for supporting this work and providing the required resources.

Conflicts of Interest: The authors declare no conflict of interest.

References

1. Koul, B.; Yakoob, M.; Shah, M.P. Agricultural waste management strategies for environmental sustainability. *Environ. Res.* **2022**, *206*, 112285. [[CrossRef](#)] [[PubMed](#)]
2. Wang, F.; Cheng, Z.; Reisner, A.; Liu, Y. Compliance with household solid waste management in rural villages in developing countries. *J. Clean. Prod.* **2018**, *202*, 293–298. [[CrossRef](#)]
3. Raheja, S.; Obaidat, M.S.; Kumar, M.; Sadoun, B.; Bhushan, S. A hybrid MCDM framework and simulation analysis for the assessment of worst polluted cities. *Simul. Model. Pract. Theory* **2022**, *118*, 102540. [[CrossRef](#)]
4. Nasution, H.; Yahya, E.B.; Abdul Khalil, H.P.S.; Shaah, M.A.; Suriani, A.; Mohamed, A.; Alfatah, T.; Abdullah, C. Extraction and Isolation of Cellulose Nanofibers from Carpet Wastes Using Supercritical Carbon Dioxide Approach. *Polymers* **2022**, *14*, 326. [[CrossRef](#)]
5. Khounani, Z.; Hosseinzadeh-Bandbafha, H.; Moustakas, K.; Talebi, A.F.; Goli, S.A.H.; Rajaeifar, M.A.; Khoshnevisan, B.; Jouzani, G.S.; Peng, W.; Kim, K.-H. Environmental life cycle assessment of different biorefinery platforms valorizing olive wastes to biofuel, phosphate salts, natural antioxidant, and an oxygenated fuel additive (triacetin). *J. Clean. Prod.* **2021**, *278*, 123916. [[CrossRef](#)]
6. Rizal, S.; Olaiya, F.G.; Saharudin, N.; Abdullah, C.; NG, O.; Mohamad Haafiz, M.; Yahya, E.B.; Sabaruddin, F.; Abdul Khalil, H.P.S. Isolation of textile waste cellulose nanofibrillated fibre reinforced in polylactic acid-chitin biodegradable composite for green packaging application. *Polymers* **2021**, *13*, 325. [[CrossRef](#)]
7. Azamzam, A.A.; Rafatullah, M.; Yahya, E.B.; Ahmad, M.I.; Lalung, J.; Alharthi, S.; Alosaimi, A.M.; Hussein, M.A. Insights into Solar Disinfection Enhancements for Drinking Water Treatment Applications. *Sustainability* **2021**, *13*, 10570. [[CrossRef](#)]
8. Masilompane, T.M.; Tutu, H.; Etale, A. Cellulose-Based Nanomaterials for Treatment of Acid Mine Drainage-Contaminated Waters. In *Application of Nanotechnology in Mining Processes: Beneficiation and Sustainability*; Wiley-Scrivener: Hoboken, NJ, USA, 2022; pp. 33–66.
9. Kim, S.; Nam, S.-N.; Jang, A.; Jang, M.; Park, C.M.; Son, A.; Her, N.; Heo, J.; Yoon, Y. Review of adsorption–membrane hybrid systems for water and wastewater treatment. *Chemosphere* **2022**, *286*, 131916. [[CrossRef](#)]
10. Panahi, Y.; Mellatyar, H.; Farshbaf, M.; Sabet, Z.; Fattahi, T.; Akbarzadehe, A. Biotechnological applications of nanomaterials for air pollution and water/wastewater treatment. *Mater. Today Proc.* **2018**, *5*, 15550–15558. [[CrossRef](#)]
11. Mariana, M.; Abdul Khalil, H.P.S.; Mistar, E.; Yahya, E.B.; Alfatah, T.; Danish, M.; Amayreh, M. Recent advances in activated carbon modification techniques for enhanced heavy metal adsorption. *J. Water Process Eng.* **2021**, *43*, 102221. [[CrossRef](#)]
12. Elkhalfifa, S.; Al-Ansari, T.; Mackey, H.R.; McKay, G. Food waste to biochars through pyrolysis: A review. *Resour. Conserv. Recycl.* **2019**, *144*, 310–320. [[CrossRef](#)]
13. Xiao, X.; Chen, B.; Chen, Z.; Zhu, L.; Schnoor, J.L. Insight into multiple and multilevel structures of biochars and their potential environmental applications: A critical review. *Environ. Sci. Technol.* **2018**, *52*, 5027–5047. [[CrossRef](#)]
14. Dai, Z.; Zhang, X.; Tang, C.; Muhammad, N.; Wu, J.; Brookes, P.C.; Xu, J. Potential role of biochars in decreasing soil acidification—a critical review. *Sci. Total Environ.* **2017**, *581*, 601–611. [[CrossRef](#)]
15. Wan, Z.; Sun, Y.; Tsang, D.C.; Khan, E.; Yip, A.C.; Ng, Y.H.; Rinklebe, J.; Ok, Y.S. Customised fabrication of nitrogen-doped biochar for environmental and energy applications. *Chem. Eng. J.* **2020**, *401*, 126136. [[CrossRef](#)]
16. Ruan, X.; Sun, Y.; Du, W.; Tang, Y.; Liu, Q.; Zhang, Z.; Doherty, W.; Frost, R.L.; Qian, G.; Tsang, D.C. Formation, characteristics, and applications of environmentally persistent free radicals in biochars: A review. *Bioresour. Technol.* **2019**, *281*, 457–468. [[CrossRef](#)]
17. Wang, J.; Wang, S. Preparation, modification and environmental application of biochar: A review. *J. Clean. Prod.* **2019**, *227*, 1002–1022. [[CrossRef](#)]
18. Heidarinejad, Z.; Dehghani, M.H.; Heidari, M.; Javedan, G.; Ali, I.; Sillanpää, M. Methods for preparation and activation of activated carbon: A review. *Environ. Chem. Lett.* **2020**, *18*, 393–415. [[CrossRef](#)]
19. Shafeeyan, M.S.; Daud, W.M.A.W.; Houshmand, A.; Shamiri, A. A review on surface modification of activated carbon for carbon dioxide adsorption. *J. Anal. Appl. Pyrolysis* **2010**, *89*, 143–151. [[CrossRef](#)]
20. Lakshmi, S.; Avti, P.K.; Hegde, G. Activated carbon nanoparticles from biowaste as new generation antimicrobial agents: A review. *Nano-Struct. Nano-Objects* **2018**, *16*, 306–321. [[CrossRef](#)]
21. Obi, F.; Ugwuishiwu, B.; Nwakaire, J. Agricultural waste concept, generation, utilization and management. *Niger. J. Technol.* **2016**, *35*, 957–964. [[CrossRef](#)]
22. Bhardwaj, A.; Kumar, M.; Alshehri, M.; Keshta, I.; Abugabah, A.; Sharma, S.K. Smart water management framework for irrigation in agriculture. *Environ. Technol.* **2022**, *18*, 1–15. [[CrossRef](#)] [[PubMed](#)]
23. Rizal, S.; Abdul Khalil, H.P.S.; Oyekanmi, A.A.; Gideon, O.N.; Abdullah, C.K.; Yahya, E.B.; Alfatah, T.; Sabaruddin, F.A.; Rahman, A.A. Cotton Wastes Functionalized Biomaterials from Micro to Nano: A Cleaner Approach for a Sustainable Environmental Application. *Polymers* **2021**, *13*, 1006. [[CrossRef](#)] [[PubMed](#)]
24. Alsharef, A.; Aggarwal, K.; Kumar, M.; Mishra, A. Review of ML and AutoML solutions to forecast time-series data. *Arch. Comput. Methods Eng.* **2022**, 1–15. [[CrossRef](#)] [[PubMed](#)]
25. Zabed, H.; Sahu, J.; Boyce, A.N.; Faruq, G. Fuel ethanol production from lignocellulosic biomass: An overview on feedstocks and technological approaches. *Renew. Sustain. Energy Rev.* **2016**, *66*, 751–774. [[CrossRef](#)]
26. Jin, Z.; Shah, T.; Zhang, L.; Liu, H.; Peng, S.; Nie, L. Effect of straw returning on soil organic carbon in rice–wheat rotation system: A review. *Food Energy Secur.* **2020**, *9*, e200. [[CrossRef](#)]

27. Kumar, P.; Singh, R.K. Selection of sustainable solutions for crop residue burning: An environmental issue in northwestern states of India. *Environ. Dev. Sustain.* **2021**, *23*, 3696–3730. [[CrossRef](#)]
28. Wang, X.; Yang, Z.; Liu, X.; Huang, G.; Xiao, W.; Han, L. Characteristics and Non-parametric Multivariate Data Mining Analysis and Comparison of Extensively Diversified Animal Manure. *Waste Biomass Valorization* **2021**, *12*, 2343–2355. [[CrossRef](#)]
29. Huang, J.; Qiao, Y.; Liu, H.; Wang, B.; Wang, Z.; Yu, Y.; Xu, M. Effect of torrefaction on physicochemical properties and steam gasification reactivity of chars produced from the pyrolysis of typical food wastes. *Energy Fuels* **2020**, *34*, 15332–15342. [[CrossRef](#)]
30. Zhang, X.; Kong, L.; Song, G.; Chen, D. Adsorption of uranium onto modified rice straw grafted with oxygen-containing groups. *Environ. Eng. Sci.* **2016**, *33*, 942–950. [[CrossRef](#)]
31. Nam, H.; Choi, W.; Genuino, D.A.; Capareda, S.C. Development of rice straw activated carbon and its utilizations. *J. Environ. Chem. Eng.* **2018**, *6*, 5221–5229. [[CrossRef](#)]
32. Xu, J.; Zong, M.-H.; Fu, S.-Y.; Li, N. Correlation between physicochemical properties and enzymatic digestibility of rice straw pretreated with cholinium ionic liquids. *ACS Sustain. Chem. Eng.* **2016**, *4*, 4340–4345. [[CrossRef](#)]
33. Zhang, L.; Chen, K.; He, L.; Peng, L. Reinforcement of the bio-gas conversion from pyrolysis of wheat straw by hot caustic pre-extraction. *Biotechnol. Biofuels* **2018**, *11*, 1–12. [[CrossRef](#)]
34. Topcu, N.S.; Duman, G.; Olgun, H.; Yanik, J. Evaluation of Poultry Manure: Combination of Phosphorus Recovery and Activated Carbon Production. *ACS Omega* **2022**. [[CrossRef](#)]
35. Holm-Nielsen, J.B.; Al Seadi, T.; Oleskowicz-Popiel, P. The future of anaerobic digestion and biogas utilization. *Bioresour. Technol.* **2009**, *100*, 5478–5484. [[CrossRef](#)]
36. Cantrell, K.B.; Ducey, T.; Ro, K.S.; Hunt, P.G. Livestock waste-to-bioenergy generation opportunities. *Bioresour. Technol.* **2008**, *99*, 7941–7953. [[CrossRef](#)]
37. Tsai, W.-T.; Huang, P.-C.; Lin, Y.-Q. Reusing cow manure for the production of activated carbon using potassium hydroxide (KOH) activation process and its liquid-phase adsorption performance. *Processes* **2019**, *7*, 737. [[CrossRef](#)]
38. Cao, H.; Xin, Y.; Yuan, Q. Prediction of biochar yield from cattle manure pyrolysis via least squares support vector machine intelligent approach. *Bioresour. Technol.* **2016**, *202*, 158–164. [[CrossRef](#)]
39. Pattanaik, L.; Pattnaik, F.; Saxena, D.K.; Naik, S.N. Biofuels from agricultural wastes. In *Second and Third Generation of Feedstocks*; Elsevier: Amsterdam, The Netherlands, 2019; pp. 103–142.
40. Sukiran, M.A.; Abnisa, F.; Daud, W.M.A.W.; Bakar, N.A.; Loh, S.K. A review of torrefaction of oil palm solid wastes for biofuel production. *Energy Convers. Manag.* **2017**, *149*, 101–120. [[CrossRef](#)]
41. Guo, Y.; Tan, C.; Sun, J.; Li, W.; Zhang, J.; Zhao, C. Porous activated carbons derived from waste sugarcane bagasse for CO₂ adsorption. *Chem. Eng. J.* **2020**, *381*, 122736. [[CrossRef](#)]
42. Jaramillo-Martínez, D.; Buitrago-Sierra, R.; López, D. Use of Palm Oil Waste for Activated Carbons Production and Its Application in Methylene Blue Removal. *ChemistrySelect* **2022**, *7*, e202200791. [[CrossRef](#)]
43. Akinwale, A.; Dauda, A.; Ololade, O. Growth performance of african catfish (*Clarias gariepinus*) juveniles reared in wastewater treated with alum and Moringa oleifera seed. *J. Aquac. Res. Dev.* **2016**, *7*, 1000460.
44. Ferreira, C.I.; Calisto, V.; Otero, M.; Nadais, H.; Esteves, V.I. Comparative adsorption evaluation of biochars from paper mill sludge with commercial activated carbon for the removal of fish anaesthetics from water in Recirculating Aquaculture Systems. *Aquac. Eng.* **2016**, *74*, 76–83. [[CrossRef](#)]
45. Dauda, A.B.; Ajadi, A.; Tola-Fabunmi, A.S.; Akinwale, A.O. Waste production in aquaculture: Sources, components and managements in different culture systems. *Aquac. Fish.* **2019**, *4*, 81–88. [[CrossRef](#)]
46. Omoniyi, T.; Salami, H. Yield, characterization and potential application of activated carbon produced from Co-Pyrolysis of wood and plastic wastes as adsorbent for aquaculture wastewater treatment. In Proceedings of the 12th CIGR Section VI International Symposium, Ibadan, Nigeria, 22–25 October 2018; p. 25.
47. Yang, H.; Yu, X.; Liu, J.; Wang, L.; Guo, M. Preparation of magnetic Fe₃O₄/activated carbon fiber and a study of the tetracycline adsorption in aquaculture wastewater. *Mater. Technol.* **2019**, *53*, 505–510. [[CrossRef](#)]
48. Ramírez-Montoya, L.A.; Hernández-Montoya, V.; Montes-Morán, M.A.; Cervantes, F.J. Correlation between mesopore volume of carbon supports and the immobilization of laccase from *Trametes versicolor* for the decolorization of Acid Orange 7. *J. Environ. Manag.* **2015**, *162*, 206–214. [[CrossRef](#)]
49. Om Prakash, M.; Gujjala, R.; Panchal, M.; Ojha, S. Mechanical characterization of arhar biomass based porous nano activated carbon polymer composites. *Polym. Compos.* **2020**, *41*, 3113–3123. [[CrossRef](#)]
50. Zhou, J.; Luo, A.; Zhao, Y. Preparation and characterisation of activated carbon from waste tea by physical activation using steam. *J. Air Waste Manag. Assoc.* **2018**, *68*, 1269–1277. [[CrossRef](#)]
51. Mariana, M.; Abdul Khalil, H.P.S.; Yahya, E.B.; Olaiya, N.; Alfatah, T.; Suriani, A.; Mohamed, A. Recent trends and future prospects of nanostructured aerogels in water treatment applications. *J. Water Process Eng.* **2022**, *45*, 102481. [[CrossRef](#)]
52. Williams, P.T.; Reed, A.R. Development of activated carbon pore structure via physical and chemical activation of biomass fibre waste. *Biomass Bioenergy* **2006**, *30*, 144–152. [[CrossRef](#)]
53. Gan, Y.X. Activated carbon from biomass sustainable sources. *C* **2021**, *7*, 39. [[CrossRef](#)]
54. Jahanban-Esfahlan, A.; Jahanban-Esfahlan, R.; Tabibiazar, M.; Roufegarinejad, L.; Amarowicz, R. Recent advances in the use of walnut (*Juglans regia* L.) shell as a valuable plant-based bio-sorbent for the removal of hazardous materials. *RSC Adv.* **2020**, *10*, 7026–7047. [[CrossRef](#)]

55. Danish, M.; Pin, Z.; Ziyang, L.; Ahmad, T.; Majeed, S.; Yahya, A.N.A.; Khanday, W.A.; Abdul Khalil, H.P.S. Preparation and characterization of banana trunk activated carbon using H_3PO_4 activation: A rotatable central composite design approach. *Mater. Chem. Phys.* **2022**, *282*, 125989. [[CrossRef](#)]
56. Lam, S.S.; Su, M.H.; Nam, W.L.; Thoo, D.S.; Ng, C.M.; Liew, R.K.; Yuh Yek, P.N.; Ma, N.L.; Nguyen Vo, D.V. Microwave pyrolysis with steam activation in producing activated carbon for removal of herbicides in agricultural surface water. *Ind. Eng. Chem. Res.* **2018**, *58*, 695–703. [[CrossRef](#)]
57. Shan, Y.; Yang, W.; Li, Y.; Chen, H.; Liu, Y. Removal of elemental mercury from flue gas using microwave/ultrasound-activated Ce–Fe magnetic porous carbon derived from biomass straw. *Energy Fuels* **2019**, *33*, 8394–8402. [[CrossRef](#)]
58. Tuerhong, T.; Kuerban, Z. Preparation and characterization of cattle manure-based activated carbon for hydrogen sulfide removal at room temperature. *J. Environ. Chem. Eng.* **2022**, *10*, 107177. [[CrossRef](#)]
59. Jawad, A.H.; Bardhan, M.; Islam, M.A.; Islam, M.A.; Syed-Hassan, S.S.A.; Surip, S.; ALOthman, Z.A.; Khan, M.R. Insights into the modeling, characterization and adsorption performance of mesoporous activated carbon from corn cob residue via microwave-assisted H_3PO_4 activation. *Surf. Interfaces* **2020**, *21*, 100688. [[CrossRef](#)]
60. Zhao, Y.; Fang, F.; Xiao, H.-M.; Feng, Q.-P.; Xiong, L.-Y.; Fu, S.-Y. Preparation of pore-size controllable activated carbon fibers from bamboo fibers with superior performance for xenon storage. *Chem. Eng. J.* **2015**, *270*, 528–534. [[CrossRef](#)]
61. Guo, J.; Song, Y.; Ji, X.; Ji, L.; Cai, L.; Wang, Y.; Zhang, H.; Song, W. Preparation and characterization of nanoporous activated carbon derived from prawn shell and its application for removal of heavy metal ions. *Materials* **2019**, *12*, 241. [[CrossRef](#)]
62. Mohammad, S.G.; Ahmed, S.M.; Amr, A.E.-G.E.; Kamel, A.H. Porous activated carbon from lignocellulosic agricultural waste for the removal of acetamiprid pesticide from aqueous solutions. *Molecules* **2020**, *25*, 2339. [[CrossRef](#)]
63. Sharma, A.; Jindal, J.; Mittal, A.; Kumari, K.; Maken, S.; Kumar, N. Carbon materials as CO_2 adsorbents: A review. *Environ. Chem. Lett.* **2021**, *19*, 875–910. [[CrossRef](#)]
64. Prabu, D.; Kumar, P.S.; Rathi, B.S.; Sathish, S.; Anand, K.V.; Kumar, J.A.; Mohammed, O.B.; Silambarasan, P. Feasibility of magnetic nano adsorbent impregnated with activated carbon from animal bone waste: Application for the chromium (VI) removal. *Environ. Res.* **2022**, *203*, 111813. [[CrossRef](#)]
65. Legrouri, K.; Khouya, E.; Hannache, H.; El Hartti, M.; Ezzine, M.; Naslain, R. Activated carbon from molasses efficiency for Cr (VI), Pb (II) and Cu (II) adsorption: A mechanistic study. *Chem. Int* **2017**, *3*, 301.
66. Guo, X.; Chen, F. Removal of arsenic by bead cellulose loaded with iron oxyhydroxide from groundwater. *Environ. Sci. Technol.* **2005**, *39*, 6808–6818. [[CrossRef](#)]
67. Zhu, H.; Jia, Y.; Wu, X.; Wang, H. Removal of arsenic from water by supported nano zero-valent iron on activated carbon. *J. Hazard. Mater.* **2009**, *172*, 1591–1596. [[CrossRef](#)]
68. Li, B.; Yin, W.; Xu, M.; Tan, X.; Li, P.; Gu, J.; Chiang, P.; Wu, J. Facile modification of activated carbon with highly dispersed nano-sized $\alpha-Fe_2O_3$ for enhanced removal of hexavalent chromium from aqueous solutions. *Chemosphere* **2019**, *224*, 220–227. [[CrossRef](#)]
69. Khalil, A.M.; Eljamal, O.; Amen, T.W.; Sugihara, Y.; Matsunaga, N. Optimized nano-scale zero-valent iron supported on treated activated carbon for enhanced nitrate and phosphate removal from water. *Chem. Eng. J.* **2017**, *309*, 349–365. [[CrossRef](#)]
70. Sabermahani, F.; Mahani, N.M.; Noraldiny, M. Removal of thallium (I) by activated carbon prepared from apricot nucleus shell and modified with rhodamine B. *Toxin Rev.* **2017**, *36*, 154–160. [[CrossRef](#)]
71. Deng, J.; Liu, Y.; Liu, S.; Zeng, G.; Tan, X.; Huang, B.; Tang, X.; Wang, S.; Hua, Q.; Yan, Z. Competitive adsorption of Pb (II), Cd (II) and Cu (II) onto chitosan-pyromellitic dianhydride modified biochar. *J. Colloid Interface Sci.* **2017**, *506*, 355–364. [[CrossRef](#)]
72. Zhou, Y.; Gao, B.; Zimmermann, A.R.; Fang, J.; Sun, Y.; Cao, X. Sorption of heavy metals on chitosan-modified biochars and its biological effects. *Chem. Eng. J.* **2013**, *231*, 512–518. [[CrossRef](#)]
73. Tang, J.; Lv, H.; Gong, Y.; Huang, Y. Preparation and characterization of a novel graphene/biochar composite for aqueous phenanthrene and mercury removal. *Bioresour. Technol.* **2015**, *196*, 355–363. [[CrossRef](#)]
74. Shang, M.-R.; Liu, Y.-G.; Liu, S.-B.; Zeng, G.-M.; Tan, X.-F.; Jiang, L.-H.; Huang, X.-X.; Ding, Y.; Guo, Y.-M.; Wang, S.-F. A novel graphene oxide coated biochar composite: Synthesis, characterization and application for Cr (VI) removal. *Rsc Adv.* **2016**, *6*, 85202–85212. [[CrossRef](#)]
75. Patra, C.; Gupta, R.; Bedadeep, D.; Narayanasamy, S. Surface treated acid-activated carbon for adsorption of anionic azo dyes from single and binary adsorptive systems: A detail insight. *Environ. Pollut.* **2020**, *266*, 115102. [[CrossRef](#)] [[PubMed](#)]
76. Acevedo, S.; Giraldo, L.; Moreno-Piraján, J.C. Adsorption of CO_2 on activated carbons prepared by chemical activation with cupric nitrate. *ACS Omega* **2020**, *5*, 10423–10432. [[CrossRef](#)] [[PubMed](#)]
77. Huang, Y.; Peng, L.; Liu, Y.; Zhao, G.; Chen, J.Y.; Yu, G. Biobased nano porous active carbon fibers for high-performance supercapacitors. *ACS Appl. Mater. Interfaces* **2016**, *8*, 15205–15215. [[CrossRef](#)]
78. Abuzalat, O.; Wong, D.; Elsayed, M.A. Nano-porous composites of activated carbon–metal organic frameworks (Fe-BDC@ AC) for rapid removal of Cr (VI): Synthesis, adsorption, mechanism, and kinetics studies. *J. Inorg. Organomet. Polym. Mater.* **2022**, *32*, 1924–1934. [[CrossRef](#)]
79. Jain, M.; Yadav, M.; Kohout, T.; Lahtinen, M.; Garg, V.K.; Sillanpää, M. Development of iron oxide/activated carbon nanoparticle composite for the removal of Cr (VI), Cu (II) and Cd (II) ions from aqueous solution. *Water Resour. Ind.* **2018**, *20*, 54–74. [[CrossRef](#)]

80. Reçber, Z.B.; Burhan, H.; Bayat, R.; Nas, M.S.; Calimli, M.H.; Demirbas, Ö.; Şen, F.; Hassan, K.-M. Fabrication of activated carbon supported modified with bimetallic-platin ruthenium nano sorbent for removal of azo dye from aqueous media using enhanced ultrasonic wave. *Environ. Pollut.* **2022**, *302*, 119033. [[CrossRef](#)]
81. Deng, J.; Li, B.; Yin, W.; Bu, H.; Yang, B.; Li, P.; Zheng, X.; Wu, J. Enhanced bacterial inactivation by activated carbon modified with nano-sized silver oxides: Performance and mechanism. *J. Environ. Manag.* **2022**, *311*, 114884. [[CrossRef](#)]
82. Yahya, E.B.; Jummaat, F.; Amirul, A.; Adnan, A.; Olaiya, N.; Abdullah, C.; Rizal, S.; Mohamad Haafiz, M.; Abdul Khalil, H.P.S. A review on revolutionary natural biopolymer-based aerogels for antibacterial delivery. *Antibiotics* **2020**, *9*, 648. [[CrossRef](#)]
83. Cao, Y.; Xiao, W.; Shen, G.; Ji, G.; Zhang, Y.; Gao, C.; Han, L. Carbonization and ball milling on the enhancement of Pb (II) adsorption by wheat straw: Competitive effects of ion exchange and precipitation. *Bioresour. Technol.* **2019**, *273*, 70–76. [[CrossRef](#)]
84. Jia, Y.; Zhang, Y.; Fu, J.; Yuan, L.; Li, Z.; Liu, C.; Zhao, D.; Wang, X. A novel magnetic biochar/MgFe-layered double hydroxides composite removing Pb²⁺ from aqueous solution: Isotherms, kinetics and thermodynamics. *Colloids Surf. A Physicochem. Eng. Asp.* **2019**, *567*, 278–287. [[CrossRef](#)]
85. Huang, D.; Liu, C.; Zhang, C.; Deng, R.; Wang, R.; Xue, W.; Luo, H.; Zeng, G.; Zhang, Q.; Guo, X. Cr (VI) removal from aqueous solution using biochar modified with Mg/Al-layered double hydroxide intercalated with ethylenediaminetetraacetic acid. *Bioresour. Technol.* **2019**, *276*, 127–132. [[CrossRef](#)]
86. Lin, P.; Wu, J.; Ahn, J.; Lee, J. Adsorption characteristics of Cd (II) and Ni (II) from aqueous solution using succinylated hay. *Int. J. Miner. Metall. Mater.* **2019**, *26*, 1239–1246. [[CrossRef](#)]
87. Liang, S.; Shi, S.; Zhang, H.; Qiu, J.; Yu, W.; Li, M.; Gan, Q.; Yu, W.; Xiao, K.; Liu, B. One-pot solvothermal synthesis of magnetic biochar from waste biomass: Formation mechanism and efficient adsorption of Cr (VI) in an aqueous solution. *Sci. Total Environ.* **2019**, *695*, 133886. [[CrossRef](#)]
88. Gupta, S.; Sireesha, S.; Sreedhar, I.; Patel, C.M.; Anitha, K. Latest trends in heavy metal removal from wastewater by biochar based sorbents. *J. Water Process Eng.* **2020**, *38*, 101561. [[CrossRef](#)]
89. Panchal, M.; Minugu, O.P.; Gujjala, R.; Ojha, S.; Mallampati Chowdary, S.; Mohammad, A. Study of environmental behavior and its effect on solid particle erosion behavior of hierarchical porous activated carbon-epoxy composite. *Polym. Compos.* **2022**, *43*, 2276–2287. [[CrossRef](#)]
90. Xiong, B.; Zydney, A.L.; Kumar, M. Fouling of microfiltration membranes by flowback and produced waters from the Marcellus shale gas play. *Water Res.* **2016**, *99*, 162–170. [[CrossRef](#)]
91. Okonji, S.O.; Yu, L.; Dominic, J.A.; Pernitsky, D.; Achari, G. Adsorption by granular activated carbon and nano zerovalent iron from wastewater: A study on removal of selenomethionine and selenocysteine. *Water* **2020**, *13*, 23. [[CrossRef](#)]
92. Largitte, L.; Pasquier, R. A review of the kinetics adsorption models and their application to the adsorption of lead by an activated carbon. *Chem. Eng. Res. Des.* **2016**, *109*, 495–504. [[CrossRef](#)]
93. Arenas, L.R.; Gentile, S.R.; Zimmermann, S.; Stoll, S. Nanoplastics adsorption and removal efficiency by granular activated carbon used in drinking water treatment process. *Sci. Total Environ.* **2021**, *791*, 148175. [[CrossRef](#)]
94. Altmann, J.; Rehfeld, D.; Träder, K.; Sperlich, A.; Jekel, M. Combination of granular activated carbon adsorption and deep-bed filtration as a single advanced wastewater treatment step for organic micropollutant and phosphorus removal. *Water Res.* **2016**, *92*, 131–139. [[CrossRef](#)]
95. Shindhal, T.; Rakholiya, P.; Varjani, S.; Pandey, A.; Ngo, H.H.; Guo, W.; Ng, H.Y.; Taherzadeh, M.J. A critical review on advances in the practices and perspectives for the treatment of dye industry wastewater. *Bioengineered* **2021**, *12*, 70–87. [[CrossRef](#)]
96. Ambika, S.; Kumar, M.; Pisharody, L.; Malhotra, M.; Kumar, G.; Sreedharan, V.; Singh, L.; Nidheesh, P.; Bhatnagar, A. Modified biochar as a green adsorbent for removal of hexavalent chromium from various environmental matrices: Mechanisms, methods, and prospects. *Chem. Eng. J.* **2022**, *439*, 135716. [[CrossRef](#)]
97. Shokry, H.; Elkady, M.; Hamad, H. Nano activated carbon from industrial mine coal as adsorbents for removal of dye from simulated textile wastewater: Operational parameters and mechanism study. *J. Mater. Res. Technol.* **2019**, *8*, 4477–4488. [[CrossRef](#)]
98. Mousavi, S.A.; Kamarehie, B.; Almasi, A.; Darvishmotevalli, M.; Salari, M.; Moradnia, M.; Azimi, F.; Ghaderpoori, M.; Neyazi, Z.; Karami, M.A. Removal of Rhodamine B from aqueous solution by stalk corn activated carbon: Adsorption and kinetic study. *Biomass Convers. Biorefinery* **2021**, 1–10. [[CrossRef](#)]
99. Feiqiang, G.; Xiaolei, L.; Xiaochen, J.; Xingmin, Z.; Chenglong, G.; Zhonghao, R. Characteristics and toxic dye adsorption of magnetic activated carbon prepared from biomass waste by modified one-step synthesis. *Colloids Surf. A Physicochem. Eng. Asp.* **2018**, *555*, 43–54. [[CrossRef](#)]
100. Liu, X.; Tian, J.; Li, Y.; Sun, N.; Mi, S.; Xie, Y.; Chen, Z. Enhanced dyes adsorption from wastewater via Fe₃O₄ nanoparticles functionalized activated carbon. *J. Hazard. Mater.* **2019**, *373*, 397–407. [[CrossRef](#)] [[PubMed](#)]
101. Duan, C.; Ma, T.; Wang, J.; Zhou, Y. Removal of heavy metals from aqueous solution using carbon-based adsorbents: A review. *J. Water Process Eng.* **2020**, *37*, 101339. [[CrossRef](#)]
102. Lou, K.; Rajapaksha, A.U.; Ok, Y.S.; Chang, S.X. Pyrolysis temperature and steam activation effects on sorption of phosphate on pine sawdust biochars in aqueous solutions. *Chem. Speciat. Bioavailab.* **2016**, *28*, 42–50. [[CrossRef](#)]
103. Kumar, M.; Xiong, X.; Wan, Z.; Sun, Y.; Tsang, D.C.; Gupta, J.; Gao, B.; Cao, X.; Tang, J.; Ok, Y.S. Ball milling as a mechanochemical technology for fabrication of novel biochar nanomaterials. *Bioresour. Technol.* **2020**, *312*, 123613. [[CrossRef](#)]
104. Valentín-Reyes, J.; García-Reyes, R.; García-González, A.; Soto-Regalado, E.; Cerino-Córdova, F. Adsorption mechanisms of hexavalent chromium from aqueous solutions on modified activated carbons. *J. Environ. Manag.* **2019**, *236*, 815–822. [[CrossRef](#)]

105. Zhang, X.; Gu, P.; Li, X.; Zhang, G. Efficient adsorption of radioactive iodide ion from simulated wastewater by nano Cu₂O/Cu modified activated carbon. *Chem. Eng. J.* **2017**, *322*, 129–139. [[CrossRef](#)]
106. Wang, R.-Z.; Huang, D.-L.; Liu, Y.-G.; Zhang, C.; Lai, C.; Zeng, G.-M.; Cheng, M.; Gong, X.-M.; Wan, J.; Luo, H. Investigating the adsorption behavior and the relative distribution of Cd²⁺ sorption mechanisms on biochars by different feedstock. *Bioresour. Technol.* **2018**, *261*, 265–271. [[CrossRef](#)]
107. Mubarak, M.F.; Zayed, A.M.; Ahmed, H.A. Activated Carbon/Carborundum@ Microcrystalline Cellulose core shell nanocomposite: Synthesis, characterization and application for heavy metals adsorption from aqueous solutions. *Ind. Crop. Prod.* **2022**, *182*, 114896. [[CrossRef](#)]
108. Zhang, Z.; Wang, T.; Zhang, H.; Liu, Y.; Xing, B. Adsorption of Pb (II) and Cd (II) by magnetic activated carbon and its mechanism. *Sci. Total Environ.* **2021**, *757*, 143910. [[CrossRef](#)]
109. Zabihi, M.; Omidvar, M.; Motavalizadehkakhky, A.; Zhiani, R. Competitive adsorption of arsenic and mercury on nano-magnetic activated carbons derived from hazelnut shell. *Korean J. Chem. Eng.* **2022**, *39*, 367–376. [[CrossRef](#)]
110. Lee, M.-E.; Park, J.H.; Chung, J.W. Comparison of the lead and copper adsorption capacities of plant source materials and their biochars. *J. Environ. Manag.* **2019**, *236*, 118–124. [[CrossRef](#)]
111. Zhang, X.; Li, Y.; He, Y.; Kong, D.; Klein, B.; Yin, S.; Zhao, H. Preparation of Magnetic Activated Carbon by Activation and Modification of Char Derived from Co-Pyrolysis of Lignite and Biomass and Its Adsorption of Heavy-Metal-Containing Wastewater. *Minerals* **2022**, *12*, 665. [[CrossRef](#)]
112. Park, J.-H.; Wang, J.J.; Kim, S.-H.; Kang, S.-W.; Jeong, C.Y.; Jeon, J.-R.; Park, K.H.; Cho, J.-S.; Delaune, R.D.; Seo, D.-C. Cadmium adsorption characteristics of biochars derived using various pine tree residues and pyrolysis temperatures. *J. Colloid Interface Sci.* **2019**, *553*, 298–307. [[CrossRef](#)]
113. Laffon, B.; Pásaro, E.; Valdiglesias, V. Effects of exposure to oil spills on human health: Updated review. *J. Toxicol. Environ. Health* **2016**, *19*, 105–128. [[CrossRef](#)]
114. Shokry, H.; Elkady, M.; Salama, E. Eco-friendly magnetic activated carbon nano-hybrid for facile oil spills separation. *Sci. Rep.* **2020**, *10*, 10265. [[CrossRef](#)]
115. Kumar, M.; Xiong, X.; Sun, Y.; Yu, I.K.; Tsang, D.C.; Hou, D.; Gupta, J.; Bhaskar, T.; Pandey, A. Critical review on biochar-supported catalysts for pollutant degradation and sustainable biorefinery. *Adv. Sustain. Syst.* **2020**, *4*, 1900149. [[CrossRef](#)]
116. Ben Hammouda, S.; Chen, Z.; An, C.; Lee, K.; Zaker, A. Buoyant oleophilic magnetic activated carbon nanoparticles for oil spill cleanup. *Clean. Chem. Eng.* **2022**, *2*, 100028. [[CrossRef](#)]
117. Raj, K.G.; Joy, P.A. Coconut shell based activated carbon–iron oxide magnetic nanocomposite for fast and efficient removal of oil spills. *J. Environ. Chem. Eng.* **2015**, *3*, 2068–2075. [[CrossRef](#)]
118. Bolan, N.; Hoang, S.A.; Beiyuan, J.; Gupta, S.; Hou, D.; Karakoti, A.; Joseph, S.; Jung, S.; Kim, K.-H.; Kirkham, M. Multifunctional applications of biochar beyond carbon storage. *Int. Mater. Rev.* **2022**, *67*, 150–200. [[CrossRef](#)]
119. Kao, T.H.; Chen, S.; Chen, C.J.; Huang, C.W.; Chen, B.H. Evaluation of analysis of polycyclic aromatic hydrocarbons by the QuEChERS method and gas chromatography–mass spectrometry and their formation in poultry meat as affected by marinating and frying. *J. Agric. Food Chem.* **2012**, *60*, 1380–1389. [[CrossRef](#)]
120. Premnath, N.; Mohanrasu, K.; Rao, R.G.R.; Dinesh, G.; Prakash, G.S.; Ananthi, V.; Ponnuchamy, K.; Muthusamy, G.; Arun, A. A crucial review on polycyclic aromatic Hydrocarbons-Environmental occurrence and strategies for microbial degradation. *Chemosphere* **2021**, *280*, 130608. [[CrossRef](#)]
121. Inbaraj, B.S.; Sridhar, K.; Chen, B.-H. Removal of polycyclic aromatic hydrocarbons from water by magnetic activated carbon nanocomposite from green tea waste. *J. Hazard. Mater.* **2021**, *415*, 125701. [[CrossRef](#)]
122. Albuquerque Júnior, E.C.D.; Méndez, M.O.A.; Coutinho, A.D.R.; Franco, T.T. Removal of cyanobacteria toxins from drinking water by adsorption on activated carbon fibers. *Mater. Res.* **2008**, *11*, 371–380. [[CrossRef](#)]
123. Rambabu, K.; AlYammahi, J.; Bharath, G.; Thanigaivelan, A.; Sivarajasekar, N.; Banat, F. Nano-activated carbon derived from date palm coir waste for efficient sequestration of noxious 2, 4-dichlorophenoxyacetic acid herbicide. *Chemosphere* **2021**, *282*, 131103. [[CrossRef](#)]
124. Ighalo, J.O.; Omoarukhe, F.O.; Ojukwu, V.E.; Iwuozor, K.O.; Igwegbe, C.A. Cost of adsorbent preparation and usage in wastewater treatment: A review. *Clean. Chem. Eng.* **2022**, *3*, 100042. [[CrossRef](#)]
125. Luo, W.; Xiao, G.; Tian, F.; Richardson, J.J.; Wang, Y.; Zhou, J.; Guo, J.; Liao, X.; Shi, B. Engineering robust metal–phenolic network membranes for uranium extraction from seawater. *Energy Environ. Sci.* **2019**, *12*, 607–614. [[CrossRef](#)]
126. Yadav, A.K.; Yadav, H.K.; Naz, A.; Koul, M.; Chowdhury, A.; Shekhar, S. Arsenic removal technologies for middle-and low-income countries to achieve the SDG-3 and SDG-6 targets: A review. *Environ. Adv.* **2022**, *9*, 100262. [[CrossRef](#)]
127. Sawalha, H.; Bader, A.; Sarsour, J.; Al-Jabari, M.; Rene, E.R. Removal of Dye (Methylene Blue) from Wastewater Using Bio-Char Derived from Agricultural Residues in Palestine: Performance and Isotherm Analysis. *Processes* **2022**, *10*, 2039. [[CrossRef](#)]

Article

Design of Stretchable Style Pick-Up Device for Tomato Seedling Transplanters

Ling Ren *, Bindong Zhao, Weibin Cao, Wenbin Song and Ming Zhao

College of Mechanical and Electrical Engineering, Shihezi University, Shihezi 832003, China; bindong@stu.shzu.edu.cn (B.Z.); wbc828@163.com (W.C.); songwenbin@stu.shzu.edu.cn (W.S.); zhaoming@stu.shzu.edu.cn (M.Z.)

* Correspondence: rl_mac@163.com

Abstract: To solve tomato planting problems, such as high labor intensity and low efficiency, we designed a stretchable style pick-up device, which met the requirements of whole-row picking and improved the efficiency and speed of seedling picking. We designed the parts of the device according to the height of the seedlings and the size of the tray. Seedling analysis was carried out and a parametric model created. Additionally, an evaluation of seedling picking was developed, which included both parallel and vertical displacement. We manufactured the parts according to the simulation parameters, which were optimized by ADAMS. The parts were assembled and the trajectory test carried out. When whole-row seedlings were grown for 30 days, the moisture content was 65.21%, the picking success rate was 92.19%, leaf damage rate was 3.13%, and the substrate damage rate was 1.54%. The study can provide a reference for the design of automatic tomato transplanters.

Keywords: pick-up device; stretchable style; kinematical analysis; seedling picking test

Citation: Ren, L.; Zhao, B.; Cao, W.; Song, W.; Zhao, M. Design of Stretchable Style Pick-Up Device for Tomato Seedling Transplanters. *Agriculture* **2022**, *12*, 707. <https://doi.org/10.3390/agriculture12050707>

Academic Editor: Muhammad Sultan

Received: 13 April 2022

Accepted: 13 May 2022

Published: 17 May 2022

Publisher's Note: MDPI stays neutral with regard to jurisdictional claims in published maps and institutional affiliations.



Copyright: © 2022 by the authors. Licensee MDPI, Basel, Switzerland. This article is an open access article distributed under the terms and conditions of the Creative Commons Attribution (CC BY) license (<https://creativecommons.org/licenses/by/4.0/>).

1. Introduction

Tomatoes are widely grown in northwest China [1–3]; currently, people usually adopt a pattern in which seedlings growing in a plastic tray are transplanted. The single seedling transplanting method cannot meet the requirements for large-scale planting, while the whole-row seedling picking can improve the efficiency [4]. The pick-up device is one of the most important parts in the transplanters. At present, the main problems of seedling picking are low precision and high seedling damage [5].

The Pearson model in the UK and Futura in Italy [6] are the main transplanters commonly used in European countries; both adopt a clip-type pick-up device. With the ejection working, the device can pick the seedlings automatically and effectively [7,8]. In China, there are three different types of the pick-up device: the first type with a style that rotates back and forth [9–11], the second is telescopic pointer clip-type [12–14], and the third category uses other methods, such as pushing down [15], air blowing [16], vibration, or a combination of these [17]. Based on the first type, Jinxin [18] proposed a method of seedling picking that has a track similar to the Woodpecker. This kind of device can realize the picking motion applied in different vegetables. With complex structure and less picking quantity, its working efficiency is limited. Concerning the second pick-up method, Zhang [19] designed a three-finger-type device according to the TRIZ theory, relying on the cylinder pushing down to complete the picking process. Only one seedling can be picked in a working cycle, and the precision is imperfect. For the other picking device, Wang [20] proposed a pneumatic method by applying a telescopic cylinder; this procedure is conducted by air blowing. This method is quick in seedling picking, but may cause an unstable condition such as seedling damage.

In this paper, tomato seedlings are the research object, and we propose a stretchable style pick-up device. Under push-rod motion to pick the seedlings, this method can improve

efficiency. To finish the design, we optimized the device's parameters. We studied the displacement and force changes in the process of seedling picking, clamping, and releasing. All of our steps were to achieve high precision and low damage seedling work requirements. We hope our work can provide reference for the design of automatic tomato transplanters.

2. Device Structure and Working Principle

2.1. Structure of the Device

The main function of the device is to remove the seedlings from the plastic tray and transport them to the seedling belts. The stretchable slice-type seedling pick-up device is mainly composed of an upper plate, a fixed rod, a sliding rod, four stretchable slices, two seedling needles, and a withdrawal rod, as shown in Figure 1. A single seedling picking assembly completes the seedling picking. The withdrawal rod is installed on the lower side of the upper plate. When the seedling is taken by the seedling picker, there is adhesion between the root system and the substrate, so that the seedlings at the hole held by the seedling needle do not slip (as shown in Figure 1b). When releasing, it can be quickly separated from the seedling needle under the action of the seedling withdrawal rod (part 7), which is convenient for the device to push the entire seedling into the seedling belt grid.

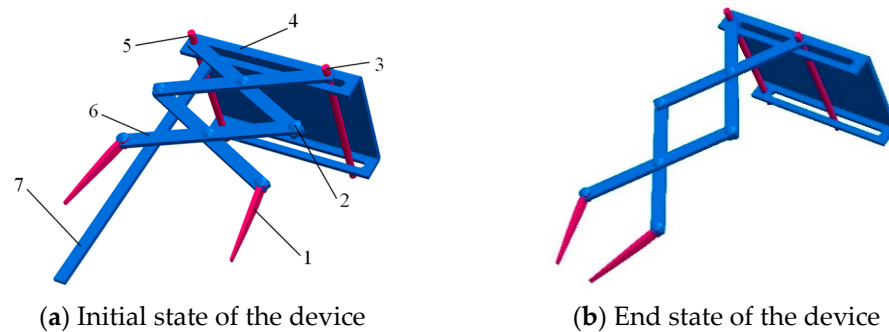


Figure 1. Structure diagram of the seedling pick-up device: 1, needle; 2, pins; 3, sliding rod; 4, upper plate; 5, fixed rod; 6, stretchable slice; 7, withdraw rod.

2.2. Working Principle

Figure 2a shows a single pick-up assembly. Eight assemblies are gathered together (Figure 2b) to achieve the whole-row seedling picking apparatus. The sliding rod moves in the upper plate chute driven by the micromotor, thus driving the assembly to complete the seedling picking and releasing.

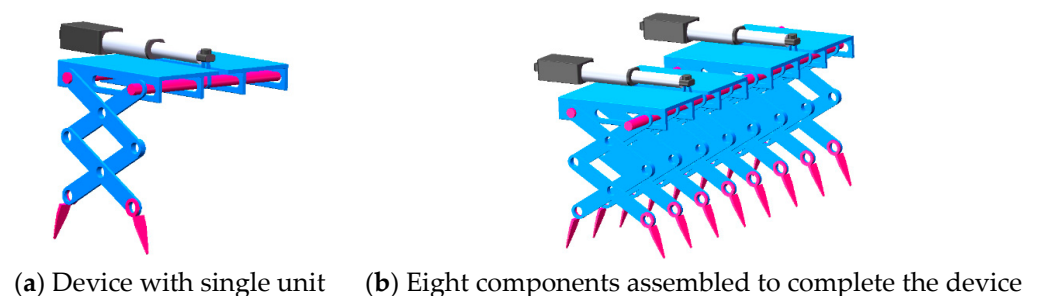


Figure 2. Stretchable unit and overall assembly.

The device is installed at the end of the longitudinal lead screw. Figure 3 is a diagram of the process, which includes the procedures of picking, transporting, and releasing. The working order of the device follows: ① The device is moved back to the preparation position, the electric push rod is pushed out, and the device picks the seedlings. ② The longitudinal lead screw moves upward first, takes the seedlings out of the tray vertically, and the seedlings that are captured move in an arc. This movement is driven by the test

bench, which is installed with the horizontal lead screw and vertical lead screw. Each is equipped with a motor and the transport routes are realized. ③ When the component of the device reaches the release position, the sliding rod shrinks back, and the device releases the seedlings under the action of the retreating rod, and falls into the grid of the seedling belt.

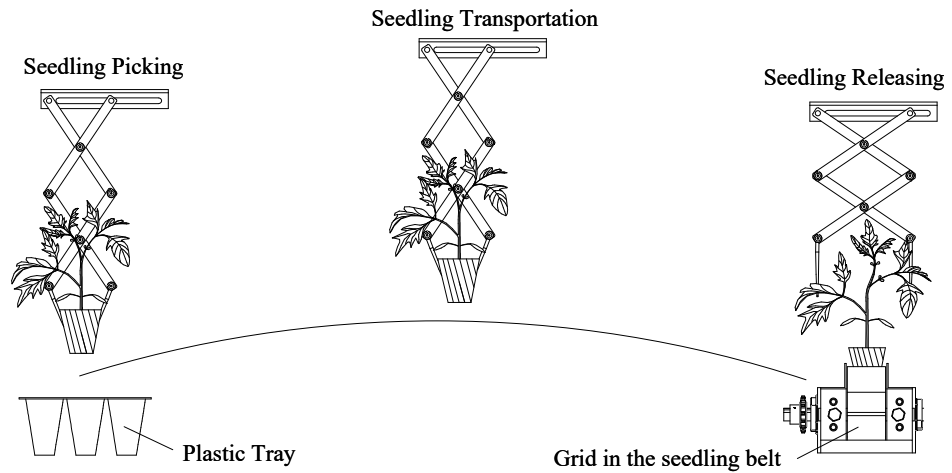


Figure 3. Procedure diagram of seedling picking.

3. Seedling Picking Model

3.1. Force Analysis of the Seedlings

A force analysis of the tomato seedlings was carried out to explore the force of the tomato seedlings when they are picked by the device and move upwards to escape from the tray. The factors affecting seedling picking were obtained, and the influence on this effect was analyzed.

When the device picks the seedlings, the substrate is picked at an angle of α . Figure 4 shows the force analysis when the seedlings are picked. We obtain Equation (1):

$$(F_{fA} \cdot \cos \alpha + F_{fB} \cdot \cos \alpha) + (F_{JA} \cdot \sin \alpha + F_{JB} \cdot \sin \alpha) - 2 \cdot \sin \alpha \cdot (F_{NB} + F_{NA}) - G = FL \tag{1}$$

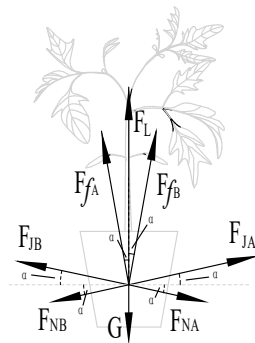


Figure 4. Force analysis of a seedling.

In Equation (1), $F_{fA(B)}$ represents static friction force of the needle A (B), $F_{JA(B)}$ is the picking force of needle A (B), $F_{NA(B)}$ signifies the adhesion of needle A (B), G is the gravity of the seedlings, and F_L indicates the seedling pulling force.

When picking seedlings, the needles A and B of the device produce a picking force on the substrate, F_{JA} and F_{JB} :

$$F_{JA} = F_{JB} = \sigma \cdot A_J \tag{2}$$

In Equation (2), σ is the anticompression characteristic of the substrate and A_J is the seedling picking area.

At the same time, when the seedlings are pulled out, static friction is generated in the direction parallel to the hole wall, F_{fA} and F_{fB} :

$$F_{fA} = F_{fB} = \mu \cdot F_{JA(B)} \tag{3}$$

In Equation (3), μ represents the static friction coefficient of the needles.

In addition, when the tomato seedling grows in the tray, the root system is entangled with the substrate and adheres to the inner wall of the hole. The adhesion is represented by F_{NA} and F_{NB} . When the device picks the seedlings and moves upward, it needs to overcome the self-weight G , adhesion $F_{NA(B)}$, picking force $F_{JA(B)}$, and static friction of the seedlings $F_{fA(B)}$, so that the seedlings can be successfully removed.

3.2. Device Motion Model

To explore various motion parameters of the device, the parametric model shown in Figure 5 was established [21], and the rotation center of the fixed rod is the coordinate origin.

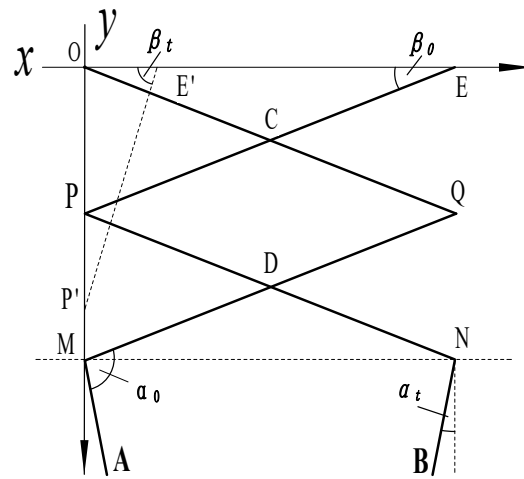


Figure 5. Structure diagram of the pick-up device. OQ, EP, PN, and QM are stretchable slices, MA and NB are needles, β is the angle between stretchable slice and horizontal plane, α_0 is the initial installation angle of seedling needles and stretchable slices, and α is the angle between the seedling needle and the horizontal plane.

Point E is one end point of the sliding rod. When the device operates, the stretchable slice EP moves forward; the angle between the stretchable sheet EP and the x-axis is represented by β . When the device moves, α is the angle between the seedling needles MA and NB and the horizontal line; α can be expressed as:

$$\alpha = \alpha_0 - \beta \tag{4}$$

In Equation (4), α_0 represents the initial angle of the needles ($\angle QMA$ and $\angle PNB$) and β shows the horizontal angle of stretchable slices ($\angle OEP$ and $\angle EOQ$).

Taking the multiple rods OQMA as the research object, the coordinates of point A can be expressed as:

$$\begin{cases} x_A = l_P \cdot \sin \alpha \\ y_A = 2 \cdot l_F \cdot \sin \beta + l_P \cdot \sin \alpha \end{cases} \tag{5}$$

In Equation (5), l_P is the length of the needles and l_F is the length of the stretchable slices. When the multiple rods EPNB is used as the research object, the coordinates of point B can be expressed as:

$$\begin{cases} x_B = l_F \cdot \sin \beta - l_P \cdot \cos \alpha \\ y_B = 2 \cdot l_F \cdot \sin \beta + l_P \sin \alpha \end{cases} \tag{6}$$

Knowing the displacement equation of the needle, the first derivative of Equation (5) with respect to time t can be calculated, and then the velocity expression at point A can be obtained:

$$\begin{cases} \dot{x}_A = l_P \cdot \cos \alpha \cdot \dot{\alpha} \\ \dot{y}_A = 2 \cdot l_F \cdot \cos \alpha \cdot \dot{\alpha} + l_P \cdot \cos \alpha \cdot \dot{\alpha} \end{cases} \quad (7)$$

Taking the first derivative of Equation (6) with respect to time t , the velocity expression at point B can be obtained:

$$\begin{cases} \dot{x}_B = l_F \cdot \cos \beta \cdot \dot{\beta} + l_P \cdot \sin \alpha \cdot \dot{\alpha} \\ \dot{y}_B = 2 \cdot l_F \cdot \cos \beta \cdot \dot{\beta} + l_P \cdot \cos \alpha \cdot \dot{\alpha} \end{cases} \quad (8)$$

Taking the derivative of Equation (4) twice, we obtain

$$\dot{\alpha} = (\alpha_0 - \beta)' = -\dot{\beta} \quad (9)$$

$$\ddot{\alpha} = -\ddot{\beta} \quad (10)$$

Differentiating Equations (7) and (8) and combining Equations (9) and (10), the accelerations of points A and B can be obtained:

$$\begin{cases} \ddot{x}_A = -l_P \cdot \dot{\beta}^2 \cdot \sin \alpha - \ddot{\beta} \cos \alpha \\ \ddot{y}_A = -(2 \cdot l_F + l_P) \cdot (\dot{\beta} \cdot \cos \alpha + \dot{\beta}^2 \cdot \sin \alpha) \end{cases} \quad (11)$$

$$\begin{cases} \ddot{x}_B = l_F \left(\ddot{\beta} \cdot \cos \beta - \dot{\beta}^2 \sin \beta \right) + l_P \left(\dot{\beta}^2 \cos \alpha - \ddot{\beta} \sin \alpha \right) \\ \ddot{y}_B = 2l_F \left(\ddot{\beta} \cdot \cos \beta - \dot{\beta}^2 \sin \beta \right) - l_P \left(\ddot{\beta} \cos \alpha + \dot{\beta}^2 \sin \alpha \right) \end{cases} \quad (12)$$

From Newton’s second law, it can be shown that the force of the seedling picker is related to its acceleration. Equations (11) and (12) are the acceleration expressions for points A and B. The influence of various factors cause the change in the needles’ acceleration, which changes the magnitude of the force. These factors include the length of the stretchable slices l_F , the length of the needles l_P , initial angle of the needles α_0 , and the horizontal angle of stretchable slices β . Therefore, the picking force can be optimized by changing these parameters.

3.3. Evaluation Indicators

To achieve precise picking of tomato seedlings, the displacement changes of points A and B at the end of the needles were analyzed. This analysis aims to avoid pinching seedlings and damaging the tray. To achieve these goals, the trajectory of the seedlings is optimized.

$$l_{AB} = \sqrt{(l_F \cdot \sin \beta - l_P \cdot \cos \alpha - l_P \cdot \sin \alpha)^2} \quad (13)$$

From Equations (5) and (6), it can be shown that the ordinates of the two points A and B are the same, and then the vertical displacement l_{DA} (l_{DB}) of the two points can be expressed as:

$$l_{DA} = l_{DB} = \sqrt{[2 \cdot l_F \cdot (\sin \beta_t - \sin \beta_0) + l_P \cdot (\sin \alpha_t - \sin \alpha_0)]^2} \quad (14)$$

In Equation (14), β_t is horizontal angle of the stretchable slices at time t , β_0 represents the horizontal angle of the stretchable slice at the initial moment, α_t is the horizontal angle

of seedling needles at time t , and α_0 shows the horizontal angle of the seedling needle at the initial moment.

From Equations (13) and (14), it can be shown that the displacement of the end of the seedling needle is related to the length of the picking needle l_p , the length of the stretchable sheet l_F , and the movement time t . These three factors can be used as optimization objects to explore the influence of parameter changes on seedling picking.

4. Component Design and Simulation

4.1. Component Design

Figure 6 is a schematic diagram showing the height of a whole seedling. When the stretchable slice is moving, the total length of them in the vertical state should be longer than the height of the seedlings. Furthermore, to ensure that the needles do not damage the plastic tray when picking the seedlings, the needle's length should be less than the depth of the tray. In addition, the length of the stretchable slice should be longer than the distance of the electric push rod. According to these requirements, the parameter range of each component can be obtained:

$$\begin{cases} 2l_F + l_P \geq H_2 + H_1 \\ l_P \leq H_1 \\ S \leq l_F \end{cases} \quad (15)$$

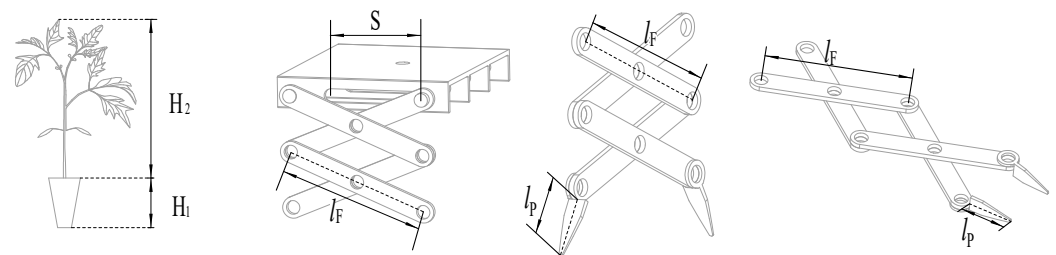


Figure 6. Schematic diagram of seedling height and the size of the part.

In Equation (15), H_1 is the depth of the tray, H_2 represents the average height of the seedlings, and S indicates the electric push rod stroke. According to Equation (15), the minimum length of the stretchable slice is calculated to be 70 mm. The maximum length of pick-up needle l_p is 36 mm. The optional maximum distance of the electric push rod S is 70 mm.

We designed the device parts using *SOLIDWORKS* software, which is a common method adopted by many designers to realize the conception of a product. Four main parts were designed: upper plate, push/fixed rod, stretchable slice, and picking needle. The following figures show the design of the parts from different viewing angles.

4.1.1. Upper Plate

As shown in Figure 7, the upper plate is a type of rectangular structure with four support slices beneath it, where the push rod can move back and forth at will. The outer dimensions of the upper plate are 90 mm × 106 mm × 16 mm, and the distance between the supporting slices is 32 mm.

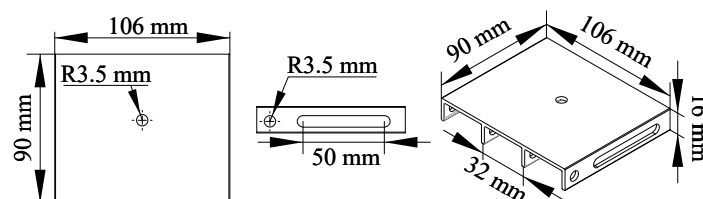


Figure 7. Drawing of the upper board structure.

4.1.2. Push/Fixed Rod

The push rod and the fixed rod are installed, respectively, in the chute and round hole of the supporting slice. The push rod can move randomly, which realizes the movement of picking and releasing. The fixed rod can connect with the stretchable slice, which can rotate around it. The two rods are 120 mm in length and 7 mm in diameter. Figure 8 shows their structure.

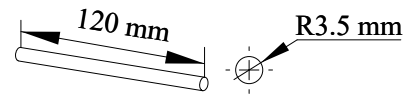


Figure 8. Drawing of pushing rod structure.

4.1.3. Stretchable Slices

The stretchable slices are the main components of the devices. As shown in Figure 9, the initial length is 70 mm and 11 mm wide. Holes with a radius of 3.5 mm facilitate connection of the device.

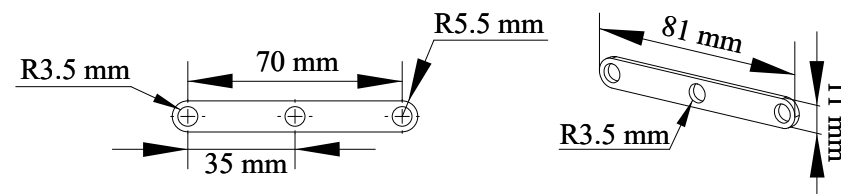


Figure 9. Drawing of stretchable slices structure.

4.1.4. Picking Needle

The picking needle is used to pick the tomato seedlings grown in the plastic tray. As shown in Figure 10, the length and width of this part are 24 and 8 mm, respectively. The spade-shaped structure is more conducive to picking of the seedlings.

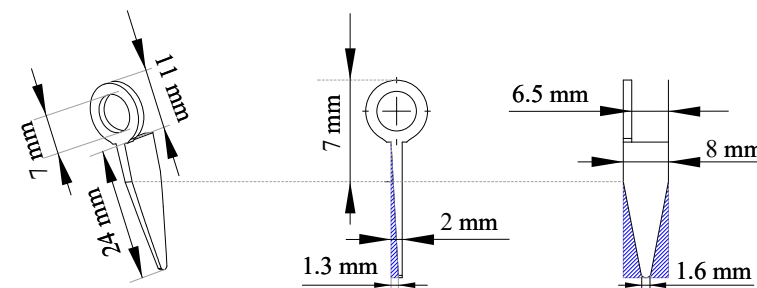


Figure 10. Drawing of picking slices structure. The blue section line in the figure is the excised part.

4.2. Simulation and Optimization

As shown in Figure 11, simulation of the device is undertaken with the procedure carried out in ADAMS [22]. As the world's most well-known and widely used Multibody Dynamics software, ADAMS improves engineering efficiency and reduces development costs. Engineers can evaluate and manage complex interactions among designs, including motion and structures, to better optimize product designs for performance.

The single factor screening method is used. The first step is to determine the reasonable length of the push rod. On this basis, the phenomenon of reverse crossover of the needles is eliminated. There are two possible options: one is to reduce the length of the pick-up needle l_p , and the other method is to increase the length of the expansion piece l_f . ADAMS simulations were carried out for the two methods and the distance between the tip of the needle at the end moment analyzed. In this way, the length of the pick-up needle l_p and the length of the stretch piece l_f are determined.

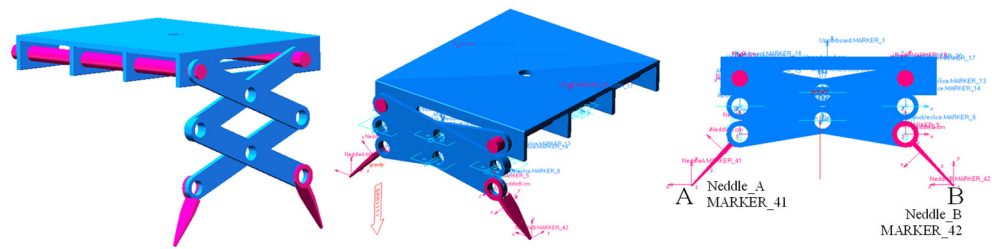


Figure 11. Simulation in ADAMS.

4.2.1. Push Rod Stroke S

The known maximum stroke of the push rod is 70 mm and its running speed is 15 mm/s; thus, the longest movement time of the putter is 4.667 s. In ADAMS, the exercise time is set at 4.667 s, and the lateral displacement of points A and B at the end of the needles is measured.

Available push-rod strokes are 10, 30, 50, and 70 mm. The corresponding movement times are 0.667, 2, 3.333, and 4.667 s. The results in Figure 12 show that when the exercise time is 0.667 and 2 s, the distance is 92.42 and 39.38 mm, respectively. Both are smaller than 32 mm (the length of the upper side of the hole in the tray), which cannot meet the requirements for taking seedlings. When the movement time is 4.667 s, its distance is -46.63 mm and the seedling needles are reversed, which easily crushes the substrate and damages the plug. Therefore, the stroke of the electric actuator needs to be between 30 and 70 mm, so an electric actuator with a stroke of 50 mm is chosen.

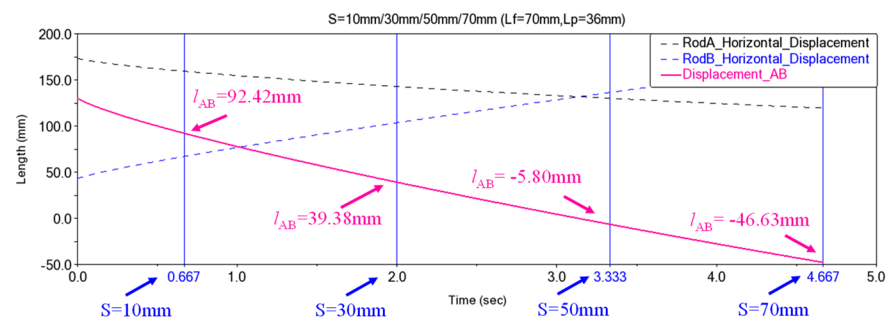


Figure 12. The change rule of the displacement AB in different push rod distance.

4.2.2. Length of the Needle l_p

When the electric push rod has a stroke of 50 mm, the distance between the needles is -5.8 mm. It indicates that the seedling needles cross in the opposite direction, which is not conducive to accurate seedling picking. It is necessary to optimize the length of the pick-up needle l_p and the length of the stretchable slices l_f to improve the accuracy of picking. Reducing the needle's length or increasing the length of the stretchable slices are possible solutions. The optimized pick-up needle lengths are 36, 24, and 12 mm. The kinematics simulation is carried out, and the statistical results are shown in Table 1.

Table 1. Motion distance of the point under different needle lengths.

Length of the Needle l_p /mm	Distance between AB at the End Time/mm	Distance of Vertical Movement of Point A or B/mm
36	-10.243	116.008
24	-0.185	117.449
12	6.305	114.085

It can be seen from the simulation results that reducing the length of the needles can avoid the reverse crossing of the needles at the end of the movement. When the length of the needle is 24 and 12 mm, the distance is -0.185 and 6.305 mm, respectively, which can

meet the requirements for picking seedlings. When the length of the needle is 24 mm, there is a larger picking area, which can ensure stable picking. Therefore, a pick-up needle with a length of 24 mm was selected.

4.2.3. Length of the Stretchable Slices l_F

When l_F is increased, the optimized stretchable sheet lengths are 75, 85, and 95 mm. The kinematics simulation is performed again, and the results are shown in Table 2.

Table 2. Motion distance of the point under different lengths of flexible slices.

Length of the Stretchable Slices l_F /mm	Distance between AB at the End Time/mm	Distance of Vertical Movement of Point A or B/mm
75	-1.700	89.437
85	-2.549	65.950
95	-4.743	53.675

From Table 2, it can be seen that increasing the length of the stretchable slices has no obvious effect on reducing the AB reverse crossing. The reverse crossing is more obvious, so the length of the stretchable slices is the same as the initial value, which is 70 mm.

4.2.4. Displacement and Trajectory of Point A and B

From the simulation described above, it is determined that the stroke S of the push rod is 50 mm, the length of the pick-up needle is 24 mm, and the length of the telescopic piece is 70 mm. The distance and vertical distance between AB can be obtained, and the ideal seedling picking time can also be known.

The displacement curve (Figure 13) shows that from 2.135 to 3.33 s the distance at the end is -0.185 mm, and the reverse crossing is not obvious. In this process, the vertical movement distance is 14.55 mm, and the picking point is taken and inserted into one-third of the substrate. This point is in a suitable picking position, which is conducive to stable picking.

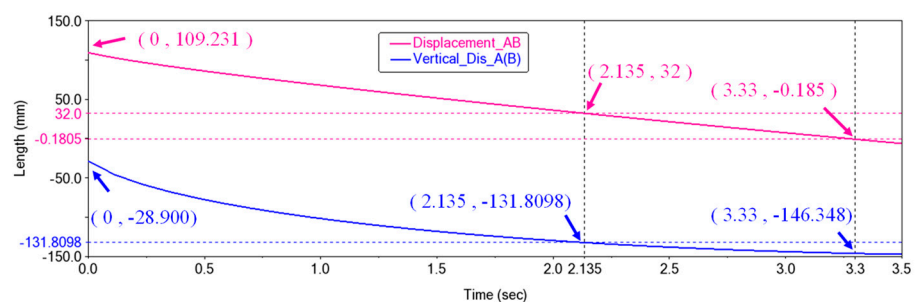


Figure 13. Displacement of AB and the distance of the vertical motion.

Figure 14 illustrates the trajectory curve of the seedling picking. The movement trajectories of points A and B are completely different. This movement characteristic ensures stable picking. This trajectory has better positioning and gripping properties.

4.2.5. Running Speed and Acceleration

As can be seen from Figure 15, the speed and acceleration show the same changing law: a rapid decrease and a stable decrease afterward. In the initial state, the speed and acceleration of taking seedlings are large, which can quickly reach the substrate plane.

Larger acceleration brings a larger force for taking seedlings, which is more conducive to successful soil breaking. After the soil is broken, the speed and acceleration are reduced to ensure stable picking. The reduction in acceleration reduces the picking force, thereby reducing substrate damage.

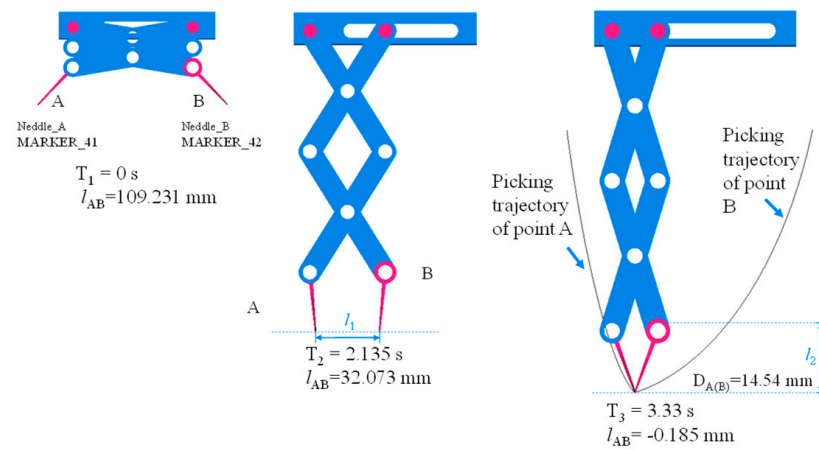


Figure 14. Trajectory diagram simulated by ADAMS.

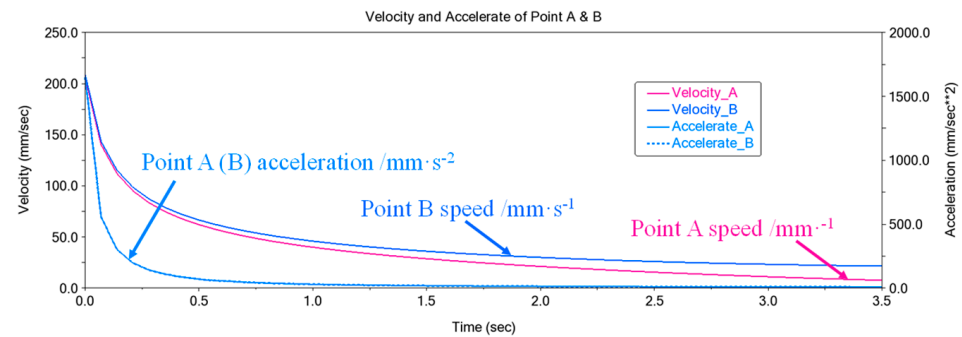


Figure 15. Velocity and acceleration at points A and B.

5. Test of the Seedling Pick-Up Device

5.1. Trajectory Test

The parts of the seedling device were manufactured (Figure 16) and assembled, and the trajectory test carried out. High-speed photography was performed on the movement process, and the seedling trajectory was obtained after processing. The actual movement trajectory of the device (Figure 17a) is consistent with the simulated trajectory (Figure 14), indicating that the actual working trajectory of the device meets the design requirements. The actual trajectories of point A and B obtained are shown in Figure 18.

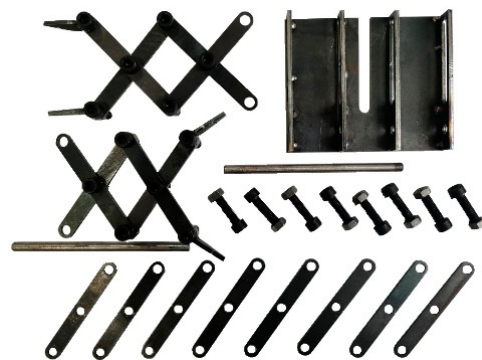


Figure 16. Components of the pick-up device.

In Figure 17b, l_1 and l_2 of the motion trajectory are measured 10 times; the results are shown in Table 3. The average distance of l_1 is 28.30 mm. When the seedling needles reach the substrate plane, the distance is smaller than the hole's top length W_1 (32 mm); this distance makes it easier for the needles to enter the substrate. The vertical movement

distance l_2 is 13.34 mm, and it is inserted into one-third of the matrix, which is in a better picking position.

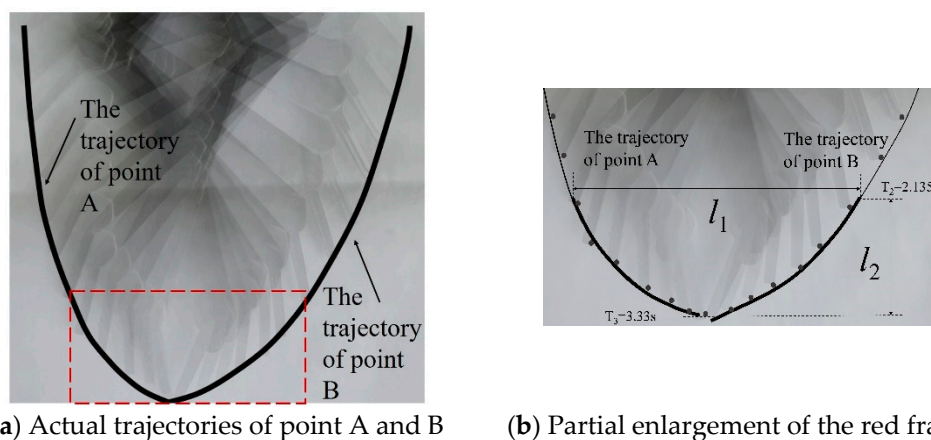


Figure 17. Movement trajectory diagram of seedling picking. At $T_2 = 2.135$ s, the device starts to take seedlings, and at $T_3 = 3.33$ s, the seedlings are picked; l_1 is the distance when the needle touches the substrate plane and l_2 is the vertical displacement of the movement.

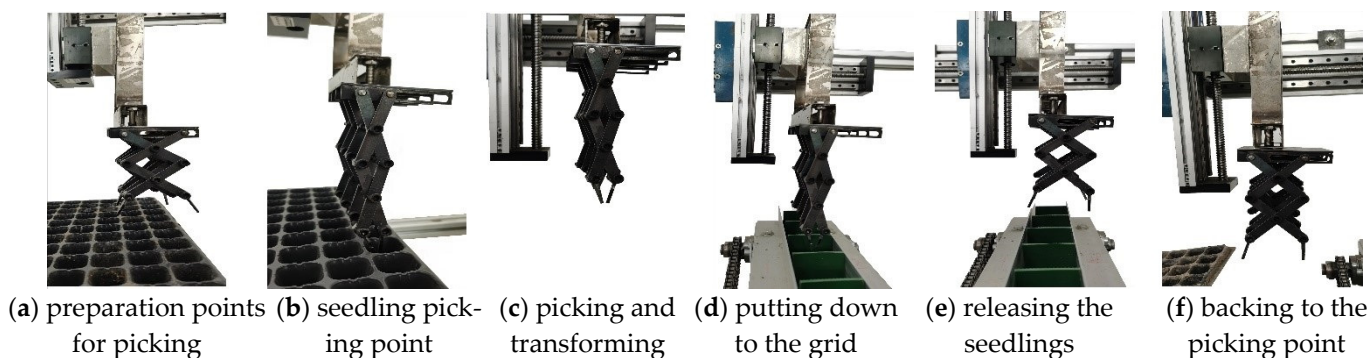


Figure 18. Process of seedling picking and releasing.

Table 3. Results of trajectory measurement.

No.	1	2	3	4	5	6	7	8	9	10	Average
l_1	28.6	28.7	27.2	26.6	29.2	29.8	28.5	28.3	28.8	27.3	28.3
l_2	12.8	13.5	14.5	12.7	12.9	12.5	13.8	12.5	13.8	14.2	13.34

5.2. Seedling Picking Test

5.2.1. Evaluation Index

Using seedling success rate Y_1 , leaf damage rate Y_2 , and substrate damage rate Y_3 as evaluation indicators, a bench test was carried out. The evaluation indicators of the test are defined as follows:

$$Y_1 = \frac{n_1}{n} \times 100\% \tag{16}$$

$$Y_2 = \frac{n_2}{n_1} \times 100\% \tag{17}$$

$$Y_3 = \frac{m - m_1}{m} \times 100\% \tag{18}$$

In Equations (16)–(18), n is the total number of tomato seedlings in the whole tray, n_1 is the number of seedlings successfully taken from the whole plate of tomato seedlings, n_2 represents the number of seedlings in which leaves are broken while successfully taken, m

is the weight of a single seedling, and m_1 indicates the weight of a single seedling after its release. When the number of damaged leaves of a single seedling exceeds three, the tomato plug seedling is determined to be damaged.

5.2.2. Test Design

The experiment was carried out in the Precision Agriculture Laboratory of Shihezi University. Seedlings with an age 30~50 d were selected and the moisture content was 35.41%~65.21%. The process of picking and releasing seedlings is shown in Figure 18. The device picks the seedlings on the left side, moves to the top of the belt on the right side, and returns to the seedling initial position. It takes 8.228 s for the device to complete the process, including soil breaking (3.33 s), upward pulling (1 s), conveying (1.831 s), release (1 s), and return (1.067 s). Eight seedlings are taken during each working cycle, and 58 seedlings are taken in one minute.

The test was carried out according to the sequence shown in Table 4; 128 seedlings were used each time. The effect of seedling picking, leaf damage, and substrate damage were counted. The calculation results are provided in Table 4.

Table 4. Results of the picking test.

No.	Factors		Evaluation Index		
	Growing Days/d	Moisture Content/%	Seedling Picking Success Rate/%	Leaf Damage Rate/%	Substrate Damage Rate/%
1	20	35.41	85.16	1.56	2.79
2	20	65.21	84.38	0.78	2.31
3	30	35.41	93.75	2.34	2.07
4	30	65.21	92.19	3.13	1.54
5	40	35.41	94.53	4.69	1.25
6	40	65.21	91.41	3.91	1.15

5.2.3. Analysis of Test Results

The effect of a different number of growing days on each evaluation index was analyzed; the data are shown in Figure 19. Figure 19a shows that the seedlings with a growth age of 30 to 40 d and moisture content of 35.41% have the highest success rate. Because the root system of the seedlings by this time is developed, the method is conducive to picking. Figure 19b shows that when the growth days increase, the leaf damage rate also increases. There is no significant relationship between leaf damage rate and moisture content. The longer the seedlings, the lush the leaves, and they are easily damaged by the pick-up device. Figure 19c shows that the substrate damage rate decreases with the increase in seedling age, and the substrate damage rate of the seedlings with a moisture content of 65.21% is lower. The seedlings with a moisture content of 65.21% have a low breakage rate. The root system developed has a stronger entanglement effect on the substrate. Increasing the moisture content increases the adhesion of the substrate, resulting in less scattering during work.

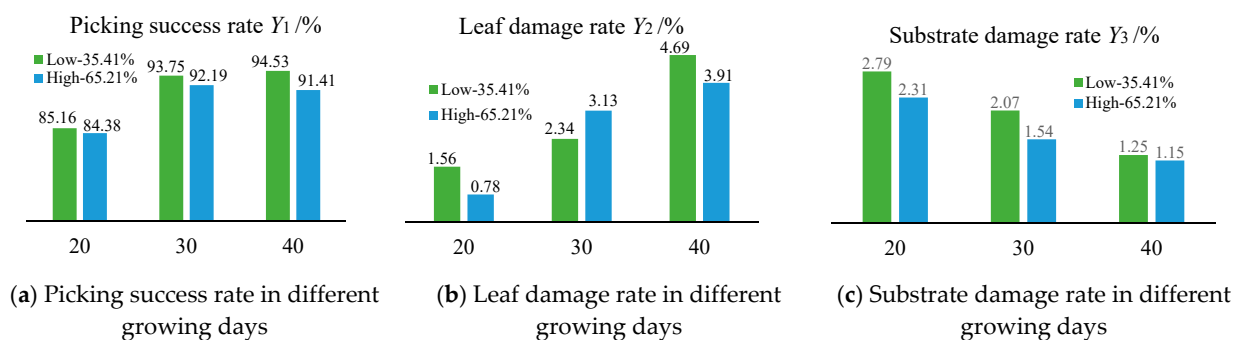


Figure 19. Results of seedling picking after 20, 30, and 40 growing days.

The pick-up device has a good effect on the seedlings that have grown for 30 days and have a moisture content 65.21%. At this time, the success rate of seedling picking was 92.19%, the leaf damage rate was 3.13%, and the substrate damage rate was 1.54%.

6. Conclusions

According to the working requirements of a transplanting machine for picking seedlings in a row, we designed a stretchable slice-type seedling picker. It is mainly composed of stretchable slices, moving rods, fixed rods, and other components. Key components were designed according to seedling height and tray size. A model of the device's movement was established and evaluation indexes proposed.

ADAMS was used to carry out kinematic simulation of the device, and we used the method of distance screening to optimize the stroke of the electric push rod, the length of the pick-up needle, and the length of the stretchable slices. We obtained better parameters for the components, and analyzed their displacement, velocity, and acceleration. The results verify that the seedling picker has the advantages of high seedling picking accuracy and minor damage to the substrate.

The parts of the device were manufactured and assembled, and a trajectory experiment completed. Our experimental results show that the actual trajectory is consistent with the simulated trajectory. The seedling picking test showed that when the seedlings were grown for 30 days and the moisture content was 65.21%, the success rate of seedling picking was 92.19%, the leaf damage rate was 3.13%, and the substrate damage rate was 1.54%.

Author Contributions: Conceptualization, L.R. and B.Z.; methodology, L.R.; software, B.Z.; validation, W.C., W.S. and M.Z.; formal analysis, investigation and resources, L.R.; data curation, B.Z.; writing—original draft preparation, L.R.; writing—review and editing, B.Z.; project administration and funding acquisition, L.R. All authors have read and agreed to the published version of the manuscript.

Funding: This research was funded by the National Natural Science Foundation of China, grant number 51765059; Shihezi University High-level Talent Project, grant number RCZK2021B17; and Shihezi University self-supported scientific research projects, grant number ZZZ202105.

Institutional Review Board Statement: Not applicable.

Informed Consent Statement: Not applicable.

Data Availability Statement: All relevant data presented in the article are stored according to institutional requirements and, as such, are not available online. However, all data used in this manuscript can be made available upon request to the authors.

Conflicts of Interest: The authors declare no conflict of interest.

References

1. Zhu, M.; Guan, Z.; Wu, F. *An Overview of the US Tomato Industry*; Florida Tomato Institute Program: Immokalee, FL, USA, 2013.
2. Costa, J.M.; Heuvelink, E. The global tomato industry. In *Tomatoes*, 2nd ed.; CABI: Boston, MA, USA, 2018; pp. 1–26.
3. Zhao, D.; Wang, Z. Improving Yield and Quality of Processing Tomato (*Lycopersicon esculentum* Miller) Using Alternate Partial Root-Zone Drip Irrigation in Arid Northwest China. *Water* **2019**, *11*, 1503. [[CrossRef](#)]
4. Kumar, G.P.; Raheman, H. Vegetable transplanters for use in developing countries—A review. *Int. J. Veg. Sci.* **2008**, *14*, 232–255. [[CrossRef](#)]
5. Choi, W.C.; Kim, D.C.; Ryu, I.H.; Kim, K.U. Development of a seedling pick-up device for vegetable transplanters. *Trans. ASAE* **2002**, *45*, 13.
6. Ji, J.; Cheng, Q.; Jin, X.; Zhang, Z.; Xie, X.; Li, M. Design and test of 2ZLX-2 transplanting machine for oil peony. *Int. J. Agric. Biol. Eng.* **2020**, *13*, 61–69. [[CrossRef](#)]
7. Han, L.; Mao, H.; Hu, J.; Tian, K. Development of a doorframe-typed swinging seedling pick-up device for automatic field transplantation. *Span. J. Agric. Res.* **2015**, *13*, 13. [[CrossRef](#)]
8. Yung, I.; Maccarana, Y.; Maroni, G.; Previdi, F. Partially structured robotic picking for automation of tomato transplantation. In Proceedings of the 2019 IEEE International Conference on Mechatronics, Ilmenau, Germany, 18–20 March 2019.
9. Yin, D.; Wang, J.; Zhou, M. Optimal Design and Experiment of Vegetable Potted Seedlings Pick-up Mechanism for Exploring and Picking-Pushing Plugs. *Trans. Chin. Soc. Agric. Mach.* **2019**, *50*, 64–71.

10. Ye, B.; Tang, T.; Yu, G. Dynamic analysis of rotary seedling pick-up mechanism of vegetable transplanting machine with counterweight. *Trans. Chin. Soc. Agric. Mach.* **2019**, *50*, 117–122.
11. Wang, L.; Sun, L.; Xu, Y. Design Method of Transplanting Mechanism of Planetary Gear Train Based on Spatial Trajectory. *Trans. Chin. Soc. Agric. Mach.* **2021**, *52*, 51–59.
12. Jiang, Z.; Jiang, H.; Tong, J. Optimal design of end-effector on automatic plug seedling transplanter. *J. Zhejiang Univ.* **2017**, *51*, 1119–1125.
13. Han, B.; Shen, D.; Guo, C. Design and Experiment of Adjustable End-effector of Cabbage Seedlings. *Trans. Chin. Soc. Agric. Mach.* **2019**, *50*, 111–120.
14. Xie, S.; Yang, S.; Liu, J. Development of the seedling taking and throwing device with oblique insertion and plug clipping for vegetable transplanters. *Trans. Chin. Soc. Agric. Eng.* **2020**, *36*, 1–10.
15. Wang, C.; Liu, C.; Li, Y. Design and Experiment of Pneumatic Punching High-speed Seedling Picking Device for Vegetable Transplanter. *Trans. Chin. Soc. Agric. Mach.* **2021**, *52*, 35–43.
16. Mao, H.; Han, L.; Zhao, H. Design of root lump loosening mechanism using air jets to eject vegetable plug seedlings. *Trans. Chin. Soc. Agric. Eng.* **2019**, *35*, 37–45.
17. Yuan, T.; Wang, D.; Wen, Y. Design and experiment of seedlings unloading mechanism based on methods of air-blowing and vibration for vegetable transplanter. *Trans. Chin. Soc. Agric. Mach.* **2019**, *50*, 80–87.
18. Jin, X. *Research on Automatic Transplanting Technology and Device for Vegetable Plug Seedling*; China Agriculture University: Beijing, China, 2014.
19. Zhang, W. *The Design and Optimization of Transplanting End-Effector on TRIZ*; Nanjing Agricultural University: Nanjing, China, 2015.
20. Wang, M. *Design and Experimental Research on Critical Components of Auto Transplanter with Combined Tray*; China Agriculture University: Beijing, China, 2017.
21. Petrescu, F.I.T. Advanced Dynamics Processes Applied to an Articulated Robot. *Processes* **2022**, *10*, 640. [[CrossRef](#)]
22. Hroncová, D.; Binda, M.; Šarga, P.; Kičák, F. Kinematical analysis of crank slider mechanism using MSC Adams/View. *Procedia Eng.* **2012**, *48*, 213–222. [[CrossRef](#)]

Article

Impact of Cropping Pattern and Climatic Parameters in Lower Chenab Canal System—Case Study from Punjab Pakistan

Ahmad Mujtaba ¹, Ghulam Nabi ^{1,*}, Muhammad Masood ¹, Mudassar Iqbal ¹, Hafiz M. Asfahan ², Muhammad Sultan ^{2,*}, Faizan Majeed ^{2,3,*}, Oliver Hensel ³ and Abozar Nasirahmadi ³

¹ Centre of Excellence in Water Resources Engineering, University of Engineering and Technology, Lahore 54890, Pakistan; ahmadm@cewre.edu.pk (A.M.); masood@cewre.edu.pk (M.M.); mudassar@cewre.edu.pk (M.I.)

² Department of Agricultural Engineering, Bahauddin Zakariya University, Bosan Road, Multan 60800, Pakistan; hmasfahan@gmail.com

³ Department of Agricultural and Biosystems Engineering, University of Kassel, 37213 Witzenhausen, Germany; ohensel@uni-kassel.de (O.H.); abozar.nasirahmadi@uni-kassel.de (A.N.)

* Correspondence: gnabi@cewre.edu.pk (G.N.); muhammadsultan@bzu.edu.pk (M.S.); faizanmajeed@bzu.edu.pk (F.M.)

Abstract: In Pakistan, groundwater resources are depleting at an alarming rate due to intensive pumping, shifting of cropping patterns, and climate change vulnerability. The present study is aimed at investigating groundwater stress in the command area of Lower Chenab Canal (LCC) and associated branch canals. Groundwater stress is determined by considering the cropping patterns, surface water availability, groundwater levels, climatic variation, and crop water requirement (CWR) in the LCC command area. The climatic data is obtained from the Pakistan Meteorological Department (PMD) from 1990 to 2020. The records of temporal variation in cropping patterns are obtained from the Crop Reporting Service (CRS), Directorate of Agriculture, Lahore for the 1995–2020 period and classified according to Rabi season (November to April) and Kharif season (May to October). The LCC surface water flows data and groundwater levels are collected from the Punjab Irrigation Department (PID) Lahore from 2003 to 2018 and from 1995 to 2016, respectively. The CWR is estimated using the Cropwat 8.0 model and groundwater levels are estimated using the Inverse Distance Weighted (IDW) tool of ArcGIS software. It has been determined that Faisalabad, Sheikhpura, and Toba Tek Singh are highly groundwater stress cities having an average drawdown rate of 0.58 m/year. The surface water availability is also decreased from 7.75 to 4.81 billion cubic meters (Bm³) for the Kharif season whilst 4.17 to 2.63 Bm³ for the Rabi season. This study concluded that due to severe conditions in highly stressed areas, policy planners, decision-makers, and stakeholders should sincerely take some steps for maintaining groundwater levels either by capacity building workshops for the farmers or limiting the number of tubewells.

Keywords: cropping pattern; water stress; LCC area; surface water availability; CROPWAT

Citation: Mujtaba, A.; Nabi, G.; Masood, M.; Iqbal, M.; Asfahan, H.M.; Sultan, M.; Majeed, F.; Hensel, O.; Nasirahmadi, A. Impact of Cropping Pattern and Climatic Parameters in Lower Chenab Canal System—Case Study from Punjab Pakistan. *Agriculture* **2022**, *12*, 708. <https://doi.org/10.3390/agriculture12050708>

Academic Editor: Aliasghar Montazar

Received: 4 April 2022

Accepted: 13 May 2022

Published: 17 May 2022

Publisher's Note: MDPI stays neutral with regard to jurisdictional claims in published maps and institutional affiliations.



Copyright: © 2022 by the authors. Licensee MDPI, Basel, Switzerland. This article is an open access article distributed under the terms and conditions of the Creative Commons Attribution (CC BY) license (<https://creativecommons.org/licenses/by/4.0/>).

1. Introduction

Water is essential for human well-being and socio-economic development. In Pakistan, surface water plays a significant role in performing agricultural activities. About 95% of the available freshwater is utilized by the agriculture sector whilst only 5% is used for domestic and industrial activities [1]. The conveyance of surface water is accomplished by the largest irrigation network, namely the Indus Basin Irrigation System (IBIS) [2]. However, the surface water supplies in IBIS are shrinking due to industrialization, urbanization, and exponential growth of population [3–5].

Groundwater is recognized as an alternative source of accessible freshwater, contributing 69% of total accessible freshwater share, and accounting for one-third of global freshwater usage [6–8]. In Pakistan, reliance on groundwater is dramatically increasing.

Approximately 62 billion cubic meters (Bm³) of groundwater is pumped out each year [9]. Figure 1 illustrates the average annual water balance of IBIS [9]. Watto et al. [10] reported exponential growth of groundwater contribution due to the massive installation of tubewells [11]. The growth rate of private tubewells was 60% only in Punjab province from 1991 to 2000 [12]. More than 70% of urban and 97% of rural populations depend upon groundwater, whilst industries fulfill their major water requirements from groundwater [13,14]. High dependency on groundwater results in a major dropdown of groundwater levels, consequently leading to the water crisis. According to Falkenmark indicator [15], Pakistan met water scarcity criteria in 2005, and there will be an absolute water scarcity in 2025 [16]. Pakistan's Water Resources Vulnerability Index (WRVI) is 77% which indicates that the country would face a serious water crisis shortly [17]. The surface water supplies are limited therefore extensive groundwater pumping is made hence placing Pakistan among the top ten countries that are dramatically affected by water pumping [18].

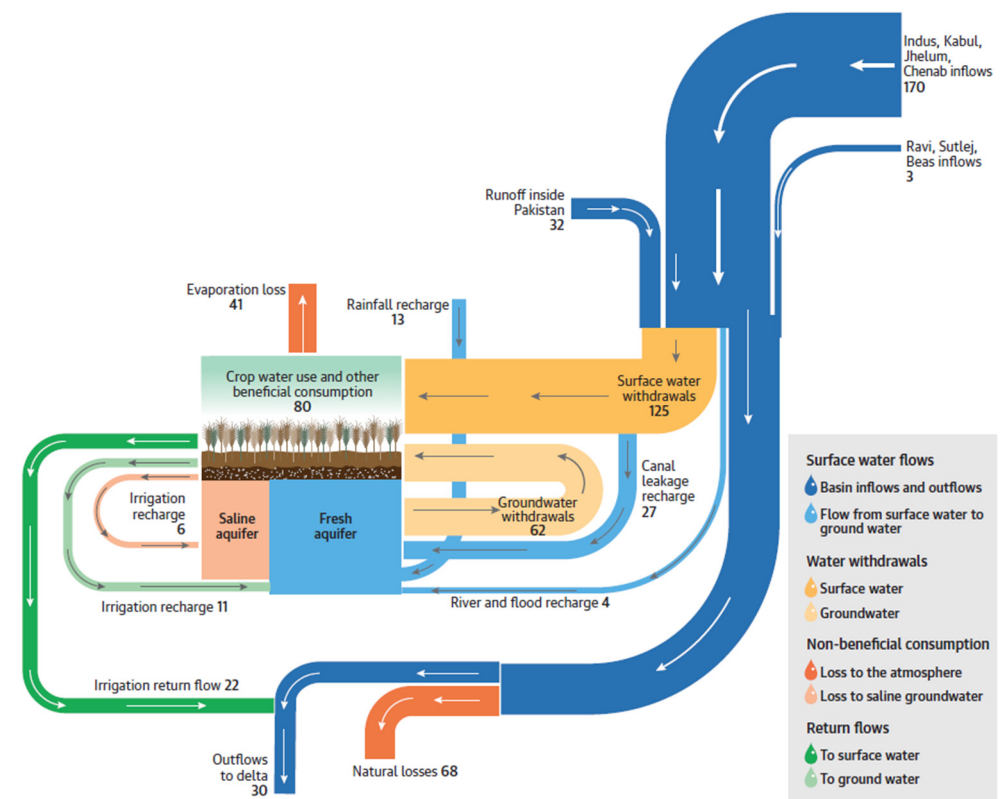


Figure 1. Average annual water balance of the Pakistan Indus Basin [9].

In Pakistan, the agriculture sector is more sensitive as compared to other sectors due to its 19.2% contribution to gross domestic product (GDP) and 38.5% employment in the labor force [19]. Human activities and climate change meaningfully affect the flow regimes of surface water and groundwater [20]. For instance, mostly in the eastern region of Pakistan, the temperature is rising, which causes an increase in agricultural water requirements [21] due to increment in evaporation rate, and transpiration rate. In addition, the shifting of rainfall patterns in northern regions of Pakistan creates a significant water shortfall during Kharif and Rabi seasons. Poor irrigation practices further lead to the water crises hence demanding strict implementation of water management strategies for socio-economic development [22,23]. In comparison to other Asian nations with low mean annual rainfall, almost 70% of the rainfall stations tended to increase rainfall during monsoon seasons [13,17]. However, during the last decade, shifting rainfall patterns and rising temperatures also influenced accessible water, resulting in a substantial decline in the countries' freshwater availability [24]. Consequently, a large amount of groundwater is being extracted from the ground to meet the crop water requirements (CWR). Farmers

are extracting groundwater to satisfy the agricultural water needs without considering the actual CWR from the perspective of getting maximum yield [1,25]. In this regard, a large number of tubewells (2700 to millions) have been installed in the country during the last 64 years [26] having no systemic trend in tubewell densities. Farmers are pumping the groundwater without any concern about groundwater depletion and its quality. In some areas of Pakistan, the quality of groundwater is degrading day by day due to the disposal of untreated industrial and domestic wastewater in nearby streams [5,9,27].

The Lower Chenab Canal (LCC) is one of the major sections of the IBIS constructed between 1892 to 1898 having a command area of 12,266 km² which includes Gujranwala, Hafizabad, Sheikhpura, Nanakana Sahib, Faisalabad, Jhang, and Toba Tek Singh [28]. Climate change, rapid urbanization, inefficient water use, and limited surface water supplies create an alarming situation in the command area of LCC for crop production. Therefore, extensive groundwater extraction is being made to meet the agricultural needs resulting in a massive drop in groundwater levels. The estimation of groundwater degradation is crucial. In this regard, several studies have been reported in the literature. For instance, Ahmed et al. [1] investigated the crop water supply-demand gap of two main distributives (Killianwala and Mungi) in the command area of LCC using CropWat 8.0 model. Land use, soil type, and topography were considered the influential aspects that impact the water deficiency. The recorded average water shortfall is 4.1 million cubic meters per year (Mm³/year) for Killianwala and 4.9 Mm³/year for the Mungi distributary. Yongguang et al. [29] quantified the groundwater pumping in Killianwala and Mungi distributaries from 2014 to 2015. It was reported that for both distributaries the groundwater pumping is compulsory due to a shortfall in canal water supplies, but lower demand as compared to canal water however, more for Mungi and less for Killianwala. Usman et al. [30] performed numerical modeling and remote sensing for estimating the inflow and outflow of groundwater in the LCC command area. It was reported that the groundwater inflow is 0.871 folds higher as compared to the pumping rate. However, a significant groundwater drawdown is expected between 2026 and 2035 due to limited canal water supplies. Awam et al. [31] utilized the Soil and Water Assessment Tool (SWAT) for determining the CWR in the command area of the LCC corresponding to varying the climatic parameters. The results shows that the CWR could be increased by 7% and 11% during 2020, under different climatic scenario.

Similarly, the area under groundwater quality associated with LCC has been degraded from 50.35% to 28.95% up to 2030 [12]. The groundwater recharge to withdrawal ratio is 0.8/1.0 resulting in the rapid drawdown of the water table in most parts of Pakistan [32]. Safe groundwater potential is about 53.04 Bm³ while abstraction is 55.51 Bm³ with an over-abstraction of 2.47 Bm³ [33]. This issue with Pakistan's water table suggests that the country's groundwater supply would be insufficient to meet future water demands. This requires continuous monitoring of groundwater and resource management [34].

For sustainable water resource planning, there should be a clear estimation of pressure on the natural water reserves. In this regard, the present study aims to estimate the water supply-demand gap in the areas under the LCC irrigation system. In addition, the groundwater fluctuation both for pre-monsoon and post-monsoon seasons was analyzed and explored using the inverse distance weighted (IDW) method. Identification of water-stressed areas and the effect of climatic parameters on the groundwater and cropping pattern are being explored. Based on the previous literature, there is no research available that identifies the effect of cropping patterns and climatic parameters for estimating groundwater stress, particularly in Punjab, Pakistan. For doing this, meteorological data, groundwater levels, streamflow records, and cropping patterns in the LCC region were collected from the Pakistan Meteorological Department (PMD), Punjab Irrigation Department (PID), and Crop Reporting Service (CRS). After performing feature engineering, the data is employed to estimate the crop water requirements using CropWat [35]. Considering the streamflow and crop water requirement, temporal water deficiency is estimated. The

present study could be supportive to employ water management practices, particularly in highly stressed cities nearby the LCC and associated branch canals.

2. Materials and Methods

The methodology and steps employed to determine the groundwater stress in the command area of LCC as shown in Figure 2. The steps comprising of: (i) collection of data from the relevant departments; (ii) data analysis; and (iii) results obtained in terms of highly stressed areas.

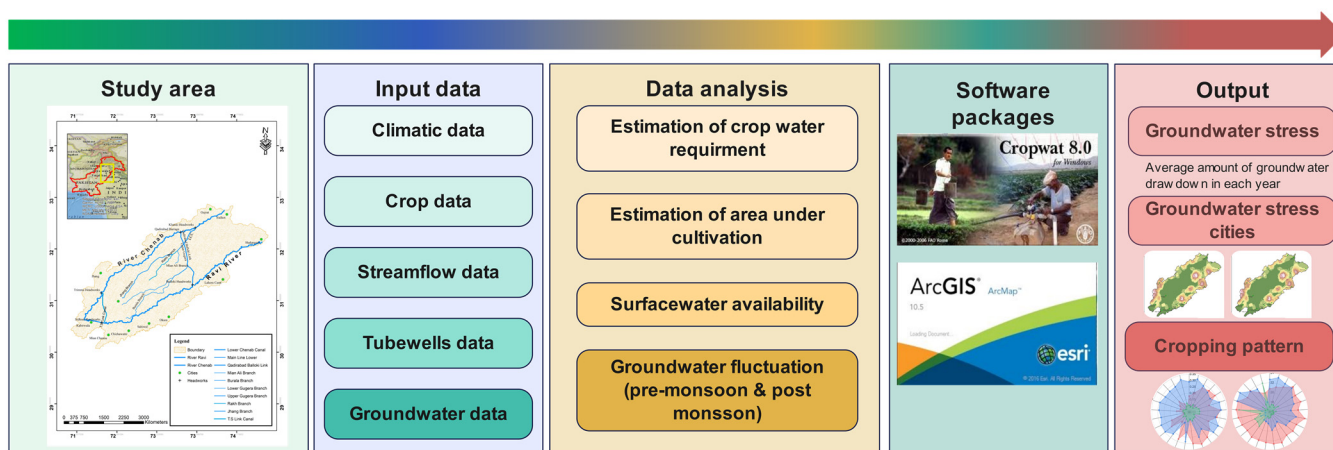


Figure 2. A detailed flow chart of the methodology adopted in the study.

2.1. Study Area

For this research, the LCC area was selected, and the canal network along with the branch canals are shown in Figure 3. The branch canals include the Upper Gugera, Lower Gugera, Burala, Mian Ali, Rakh, Jhang Upper, Jhang Lower, and Bhowana canal. Flow in this study area is Perennial. Divisions, sections, reduced distance, distances, designed head discharge, authorized tail discharge, authorized tail gauge, gross command area, and culturable command area of all of the canals are tabulated in Table 1.

Table 1. Features of main canal, branch canals in Lower Chenab Canal [36].

Description	LCC	Upper Gugera	Lower Gugera	Burala	Mian Ali	Rakh	Jhang Upper	Jhang Lower	Bhowana
Division	Khanki	Upper Gugera	Lower Gugera	Burala	Upper Gugera	Hafizabad	FSD Canal	Jhang	Jhang
Section	Chenawan	Ajniawala	Jaranwala	Farida	Salar	Main Line Lower	Bhobra	Sheikh Chur	Jaura
Distance (km ²)	64.36	90.10	123.89	156.07	32.18	88.50	98.15	59.53	27.35
Designed head discharge (m ³ /s)	230.58	210.79	74.84	58.22	20.50	38.34	88.77	42.98	14.33
Authorized tail discharge (m ³ /s)	0.00	125.87	16.21	9.00	10.76	11.27	51.93	10.96	10.87
Authorized tail gauge (m)	0.00	3.29	0.00	0.85	0.66	0.69	1.94	0.30	0.30
Gross command area (km ²)	14,973.38	4865.60	62.50	2344.6	30.46	1553.79	1616.43	38.01	12.20
Culturable command area (km ²)	13,759.32	4102.19	51.54	2064.0	25.90	1258.08	1272.17	35.15	8.89

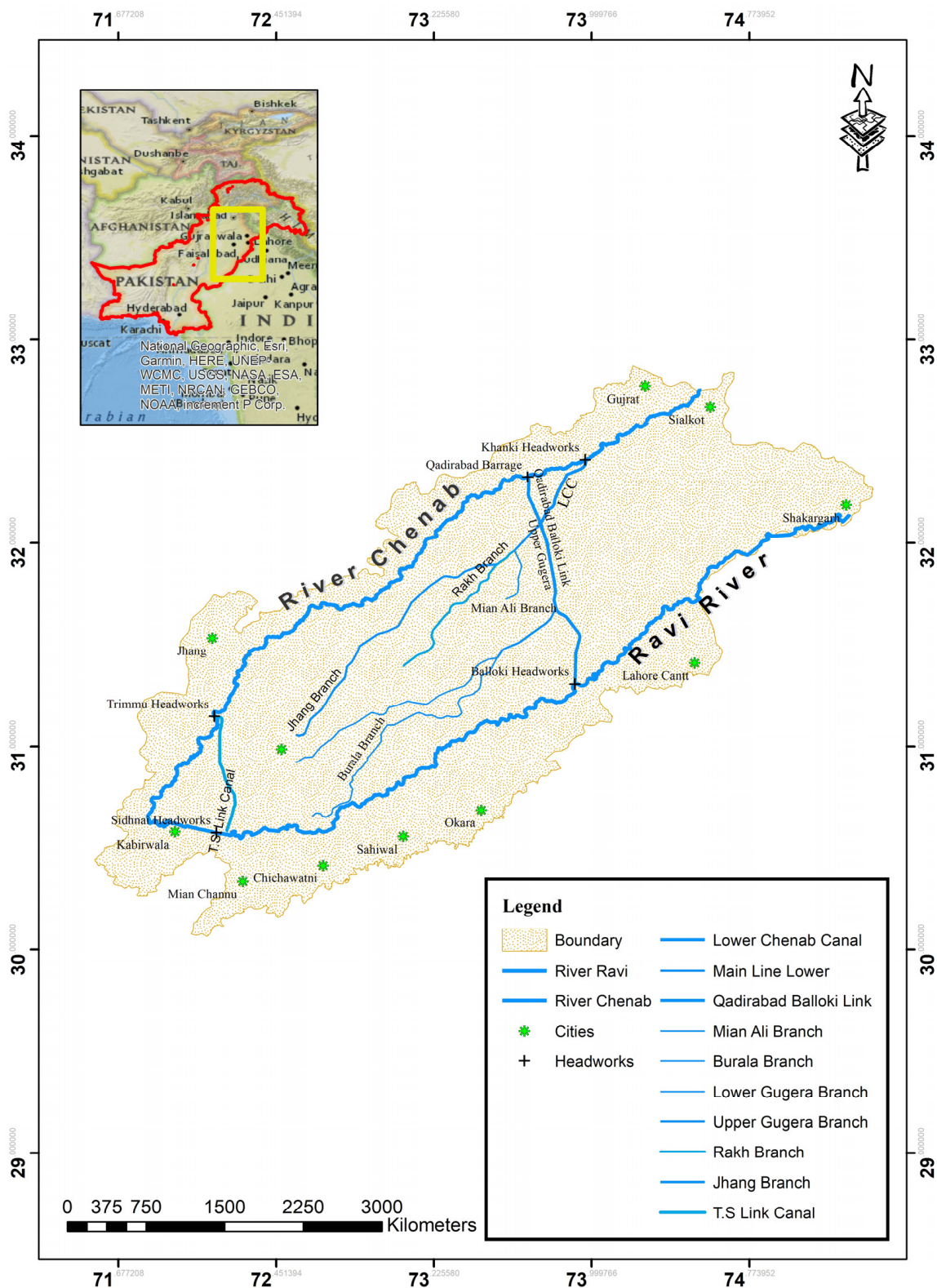


Figure 3. Location map with all rivers, canals, cities, and headworks.

Data collected from various governmental and private departments includes the number of tubewells, canal water supplies, crops grown, climatic parameters, and groundwater levels in various districts of the LCC area, which is tabulated in Table 2.

Table 2. Data collected from various organization.

Parameters	Duration	Department
Climatic Data	1990–2020 *	Pakistan Meteorological Department (PMD)
Groundwater Levels	2003–2018	Punjab Irrigation Department (PID)
Streamflow	1995–2016	Punjab Irrigation Department (PID)
Crops grown	1995–2020	Crop Reporting Service (CRS), Directorate of Agriculture, Lahore
No. of Tubewells	2008–2020	

* Limited for some stations due to not availability of climate stations.

2.2. Crop Water Requirement

Penman-Monteith method [37] is used in CropWat for the estimation of the crop water requirement (CWR). The empirical relationships used in this method is given in Equations (1)–(3).

$$CWR = ET_p \times P_e \quad (1)$$

$$ET_p = ET_o \times k_c \quad (2)$$

$$ET_o = \frac{\left(0.408\Delta(R_n - G) + \gamma\left(\frac{900}{T + 273}\right)u_2(V_s - V_a)\right)}{\Delta + \gamma(1 + 0.34u_2)} \quad (3)$$

where, in Equation (1), ET_p and P_e stand for potential evapotranspiration, and effective precipitation which excludes the losses in precipitation, respectively. Similarly, the ET_o and k_c used in Equation (2) refer to observed evapotranspiration and crop factor which are different for all of the crops, respectively. However, for determining the ET_o , Equation (3) is used, covering different meteorological and psychrometric variables. For instance, in psychrometric variables, actual vapor pressure (V_a), saturated vapor pressure (V_s), psychrometric constant (γ), and slope of saturation (Δ) of the studied areas were used. In the case of meteorological variables, net radiations (R_n), wind speed (u_2), soil heat flux (G), and temperature (T) data were deployed in CropWat 8.0, taken from the different meteorological departments as mentioned in Table 2.

For this research, the cropping pattern is analyzed to estimate the area under different crops both for the Rabi and Kharif seasons for the duration of 1995–2020. CWR is estimated for all of the crops and the whole area. Streamflow data is used for the estimation of the surface water availability within the study area for both seasons. The deficit is estimated by subtracting the surface water availability from CWR. Based on the deficit and groundwater levels, the highly stressed areas in the area were taken and analyzed to check the reasons for rapid drawdown.

3. Results and Discussions

3.1. Kharif Crops

Bajra, cotton, sorghum, maize, moong, rice, sugarcane, and fodder are commonly cultivated crops identified during the Kharif season. However, rice, sugarcane, and fodder are extensively grown crops covering more than 70% of total cultivated land in this region. In the last 25 years (1995–2020), the cumulative area for rice cultivation recorded 61,471.8 km² followed by fodder and sugarcane having 44,798 km² and 43,706.09 km², respectively as illustrated in Figure 4. Moong pulse is the least cultivated crop in this region (578.7 km²), among the mentioned Kharif crops. In comparison to 1995–1996, the overall area under cultivation has dropped around 8.2% during the 2019–2020 period. The maximum and minimum area utilized for crop production was observed in 2004–2005 and 2018–2019 having a gross production area of 8595.5 km² and 7171.0 km², respectively. In Figure 4 color gradient illustrates the shifting of the cropping pattern in consecutive years. For instance, it has been realized that the cropping pattern of the bajra is static,

between 141.6–303.5 km² from 1995 to 2020. Similarly, in the case of sorghum and moong, no significant drop or increment in the cropping pattern is observed. However, for cotton, there is a declining trend in the cultivation pattern from 1995 to 2020. In 1995–1996 the area utilized for cotton cultivation is 1205.93 km² whilst in 2015–2016 it has been reduced to 364.82 km². However, in the case of rice, and fodder the cultivated area is increasing, which indicates the shifting of the cropping pattern toward high delta crops. Consequently, the pressure on the groundwater reserve is progressively increasing.

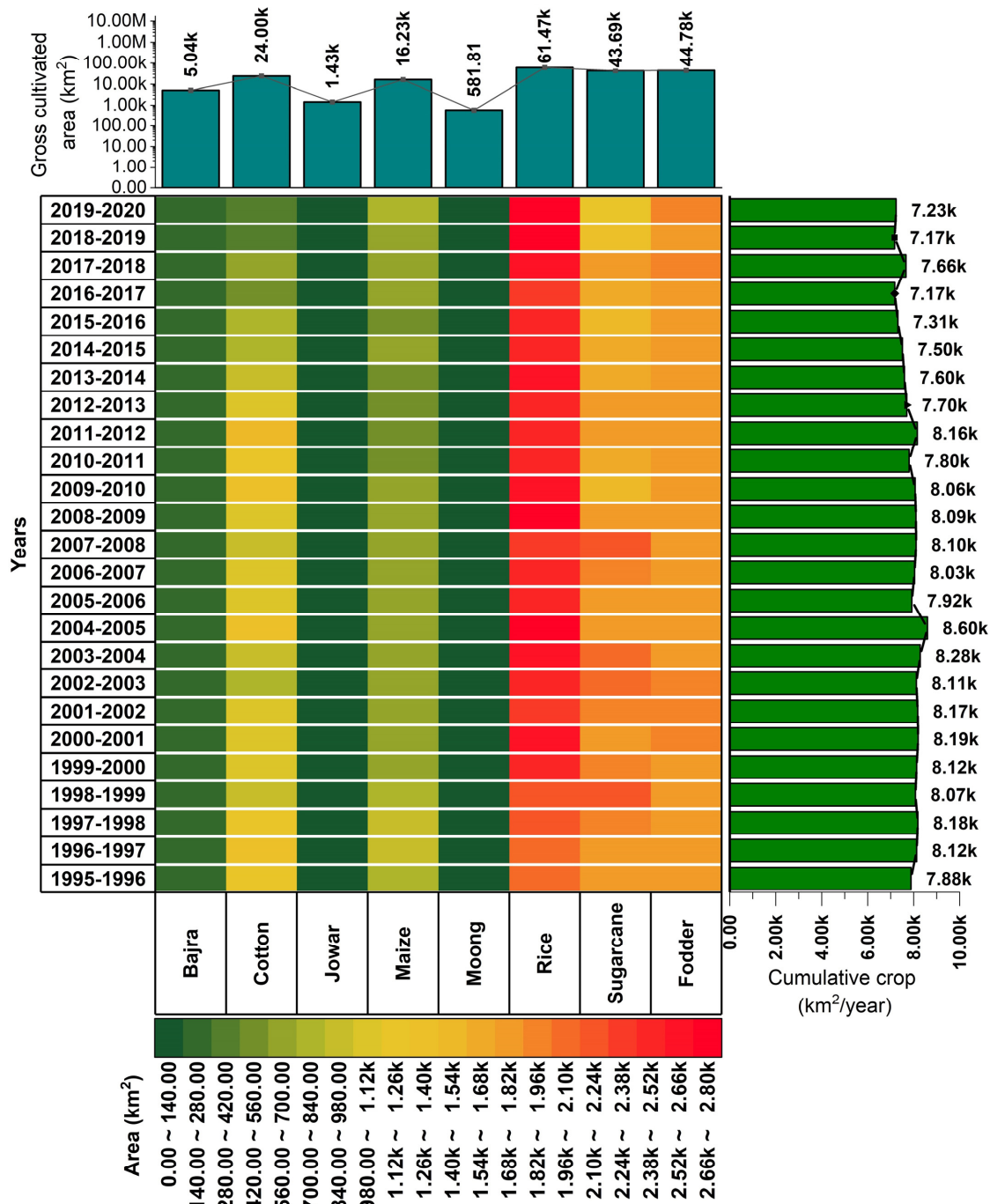


Figure 4. Shift in cropping pattern and cultivated area from 1995 to 2020 in kharif season.

3.2. Rabi Crops

During Rabi season, a total of 11 crops which includes barley, fodder, gram guava, kinnu, linseed, masoor, onion, potato, tomato, and wheat are considered normal crops are

grown in this region. However, wheat cultivation is more than the other crops, holding 70% of the land in the region associated with the LCC area. In the last 25 years, the cumulative area utilized for cultivation of the wheat was recorded at 178,547.5 km² followed by fodder (Rabi) having a cultivated area of 38,000 km². Figure 5 shows the temporal variation in the area utilized for cultivating the Rabi crops. The area employed for the cultivation of barely, guava, linseed, masoor, onion, potato, and tomato ranges between 0.57–382.8 km² from the period of 1995 to 2020. Similarly, in the case of gram and kinnu, the area employed for cultivation each year ranges between 382.0 to 764.0 km² per year. However, in the case of Fodder (Rabi), the marginal variation is observed in the area utilized for cultivation ranging between 1100 to 1900 km² per year. The area for wheat cultivation ranges within higher levels (6070.3–7284.3 km² per year). Concludingly, no shifting of cropping pattern is recorded under the studied region during the Rabi season. The cultivated area during the Rabi season in each year is greater than 8093.7 km². The reduction in the cumulative area of Rabi crops was estimated at ~5.6%. Wheat is an extensively grown crop in this region.

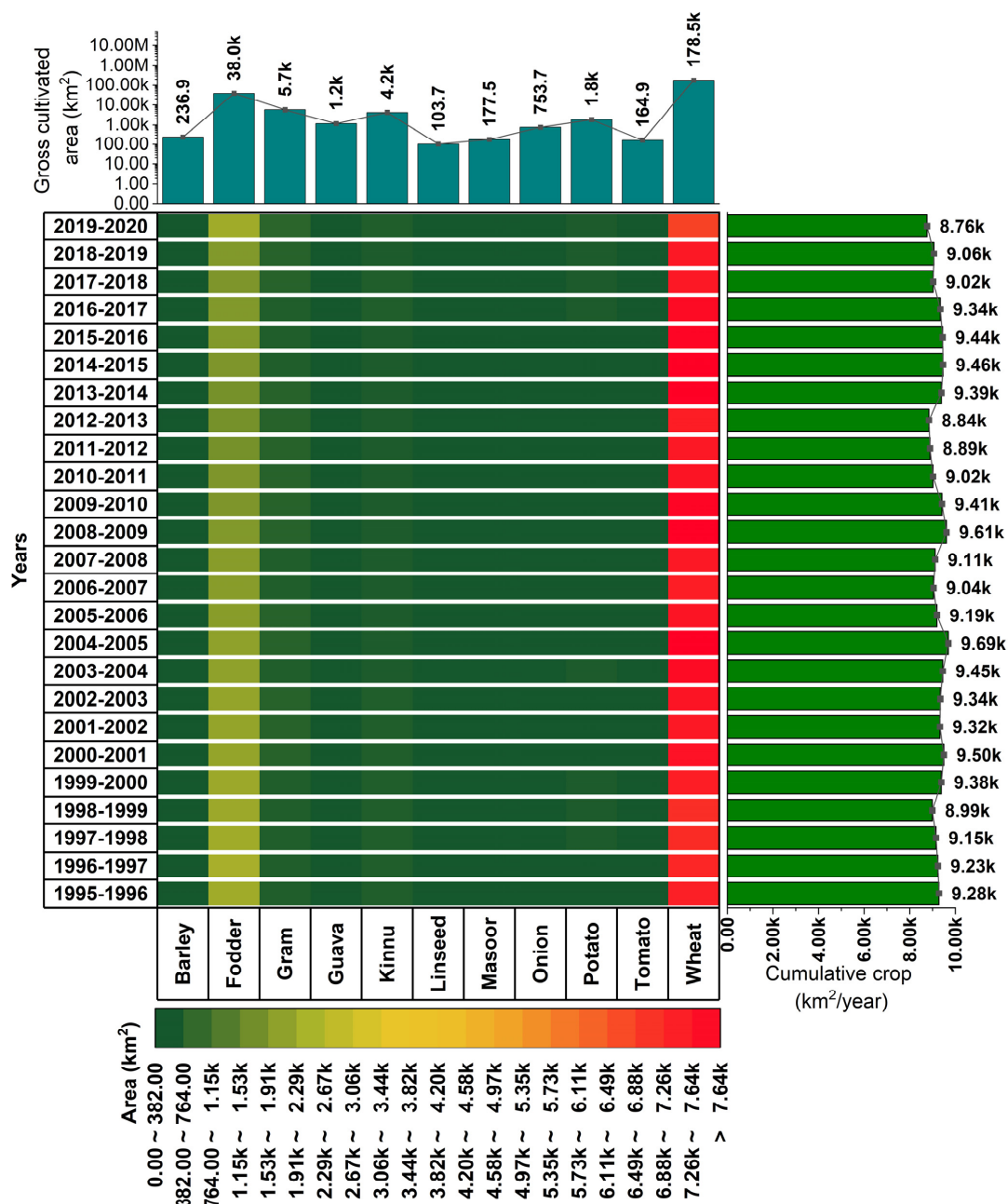


Figure 5. Shift in cropping pattern and cultivated area from 1995 to 2020 in the Rabi season.

3.3. Crop Water Requirement

By using the Cropwat 8.0 model, the crop water requirement (CWR) of the selected crops both for Kharif and Rabi is estimated and presented in Figure 6. A progressive drop is represented in the clockwise direction corresponding to the selected crops. For instance, sugarcane has the highest CWR (1577 mm) followed by rice (1182 mm), guava (1120 mm), kinnu (1067 mm), and so on. In comparison, Shakir et al. [38] reported that for Kharif and Rabi season the CWR range between 300 mm to 1450 mm and 250 mm to 400 mm, respectively. The estimated crop water requirement is in the acceptable range if compared with the study reported by Shakir et al. [38]. Since the area under cultivation is decreasing, CWR should also decrease, for both Rabi and Kharif seasons, at the same rate but due to the use of high delta crops with higher values for crop water requirements, it is decreasing at a lower rate as shown in Figure 7. In addition, Figure 7 defines the area distribution of Rabi, Kharif, and cumulative CWR.

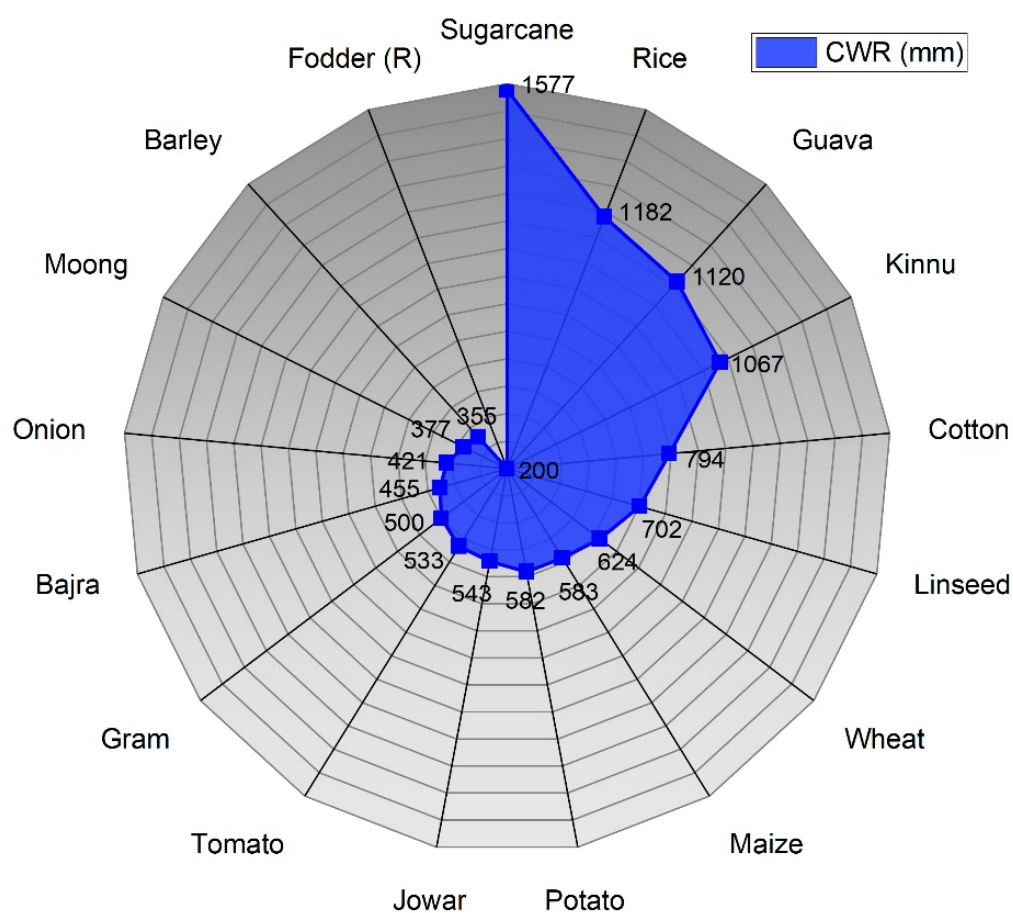


Figure 6. Crop water requirement for all crops grown in LCC area.

3.4. Surface Water Availability

Surface water availability is estimated based upon the streamflow data collected from the PID, for both Rabi and Kharif seasons as given in Figure 8a. Surface water availability in LCC decreased from 11.92 to 5.06 Bm³ from 1995 to 2002, after that an up and down trend is observed. The minimum surface water availability in LCC was recorded in 2009–2010 having a value of 3.82 Bm³. On the other hand, the water demand is estimated based on the crop water requirement and cultivated area in the region. Thereby, the water shortfall in the region is shown in Figure 8b. It has been identified that the maximum water shortfall was recorded in 2004–2005 followed by 2009–2010 with the shortfall of 8.89 Bm³ and 8.77 Bm³. In 2015–2016 the total water shortfall is 4.56 Bm³ corresponding to a water supply of 7.51 Bm³ against the demand of 12.08 Bm³. In addition, the total average deficit was recorded at

8.02 Bm³ which creates an alarming situation for the country and emphasizes the pumping of the groundwater for meeting the water shortfall. Waqas et al. [39] employed satellite remote sensing and the geographic information system (GIS) for estimating the dropdown of surface water availability in LCC. The study reported that at the Killianwala distributary the average water supply deficit is 6 Mm³ whereas in Mungi and Khurrianwala distributary water supply deficits recorded 5 and 5.5 Mm³, respectively, during the 2009–2010 period.

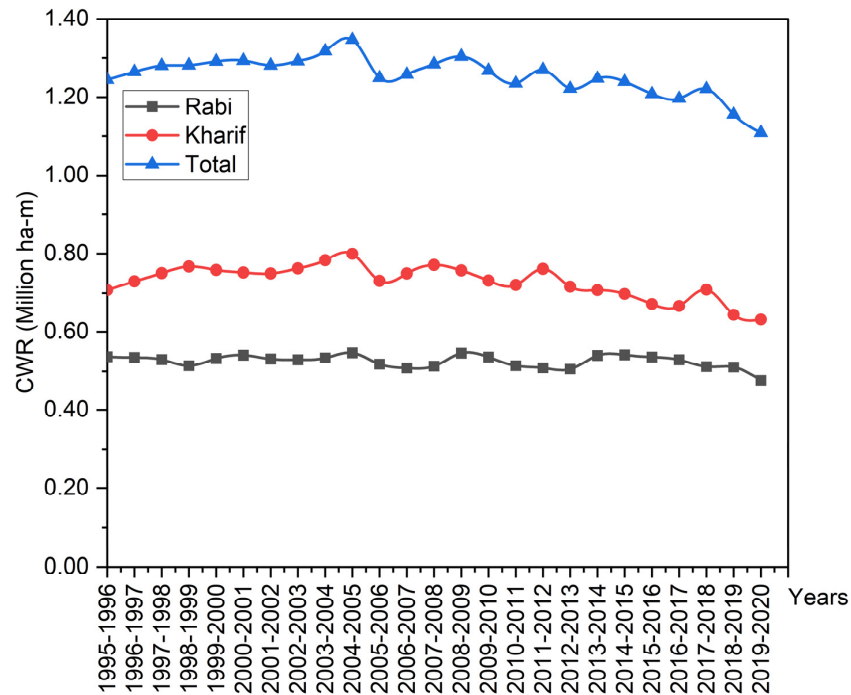


Figure 7. Temporal variation in crop water requirement during Rabi and Kharif season in LCC area.

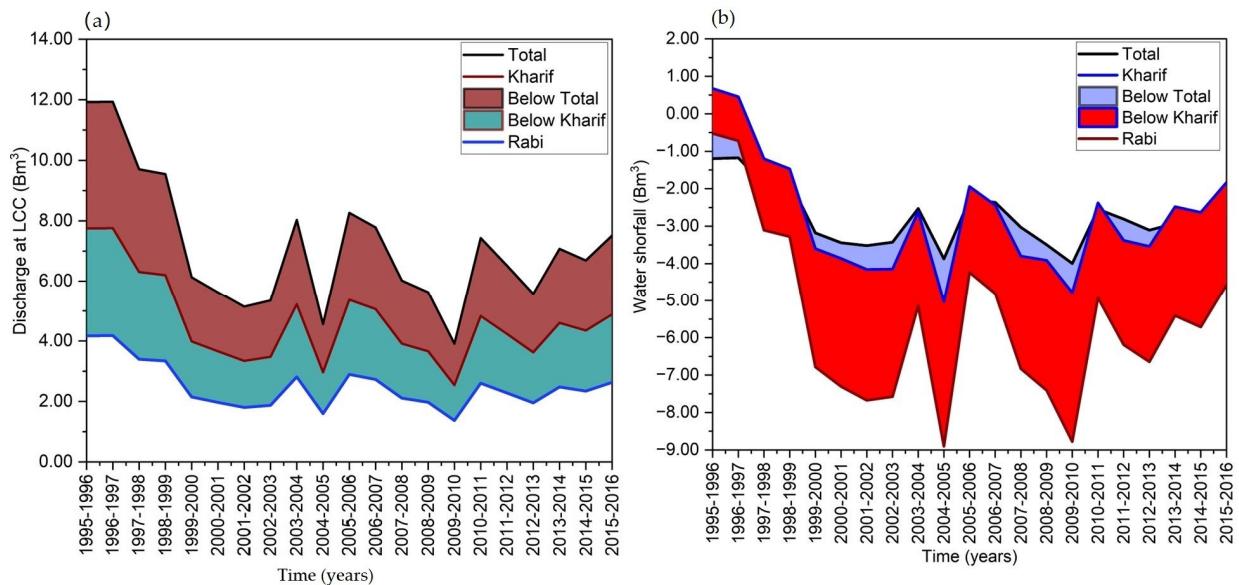


Figure 8. (a) Temporal variation in surface water availability, and (b) cumulative deficit estimated in Rabi and Kharif season.

3.5. Groundwater Fluctuations

In order to investigate the ground water fluctuations in the studied area, data of the ground water levels at specific localities were collected from the PID. After that, Inverse Distance Weighted (IDW) tool is used in ArcGIS for interpolating the groundwater levels

in the whole area from 2003 to 2018 for pre-monsoon and post-monsoon seasons as shown in Figure 9.

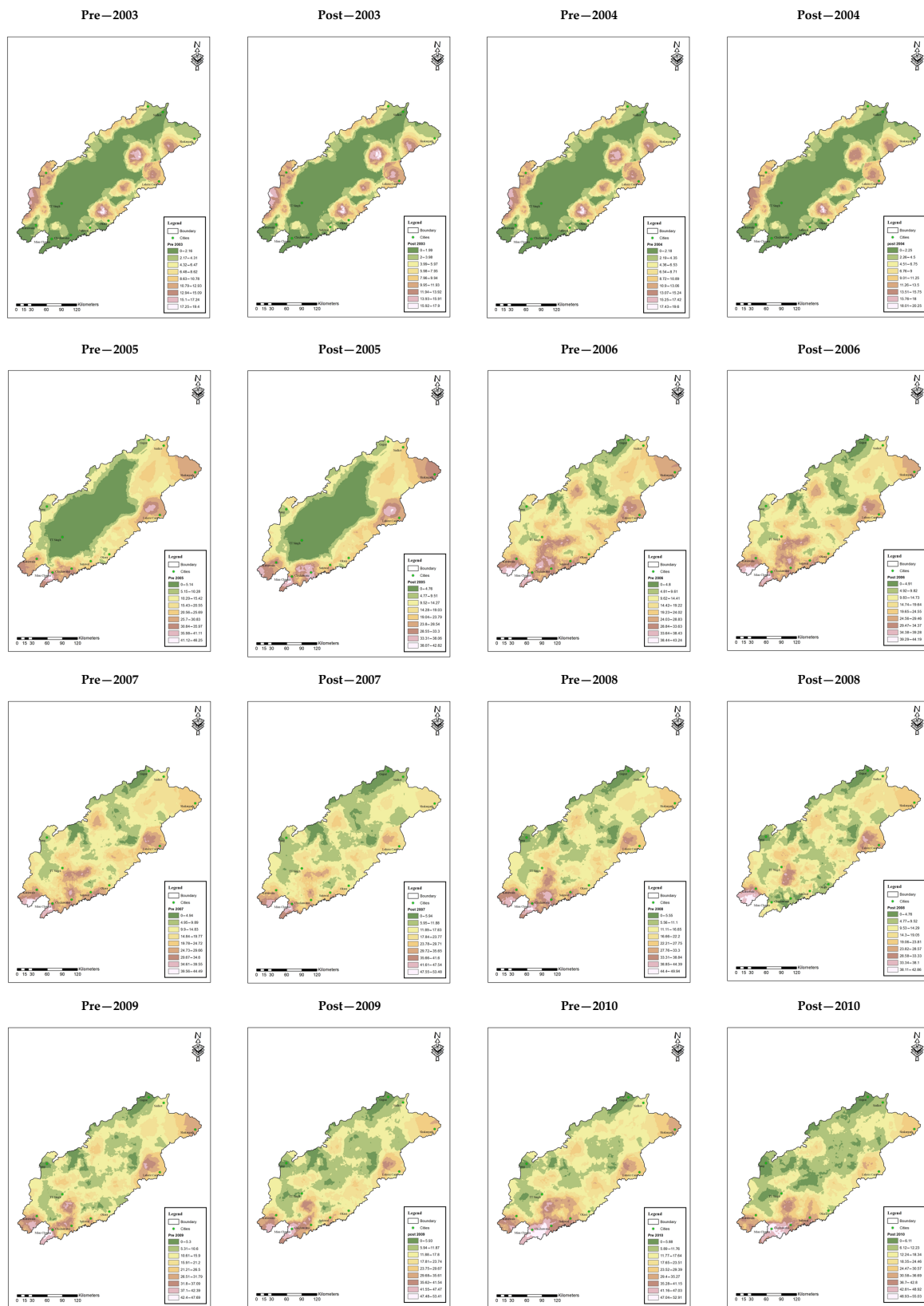


Figure 9. Cont.

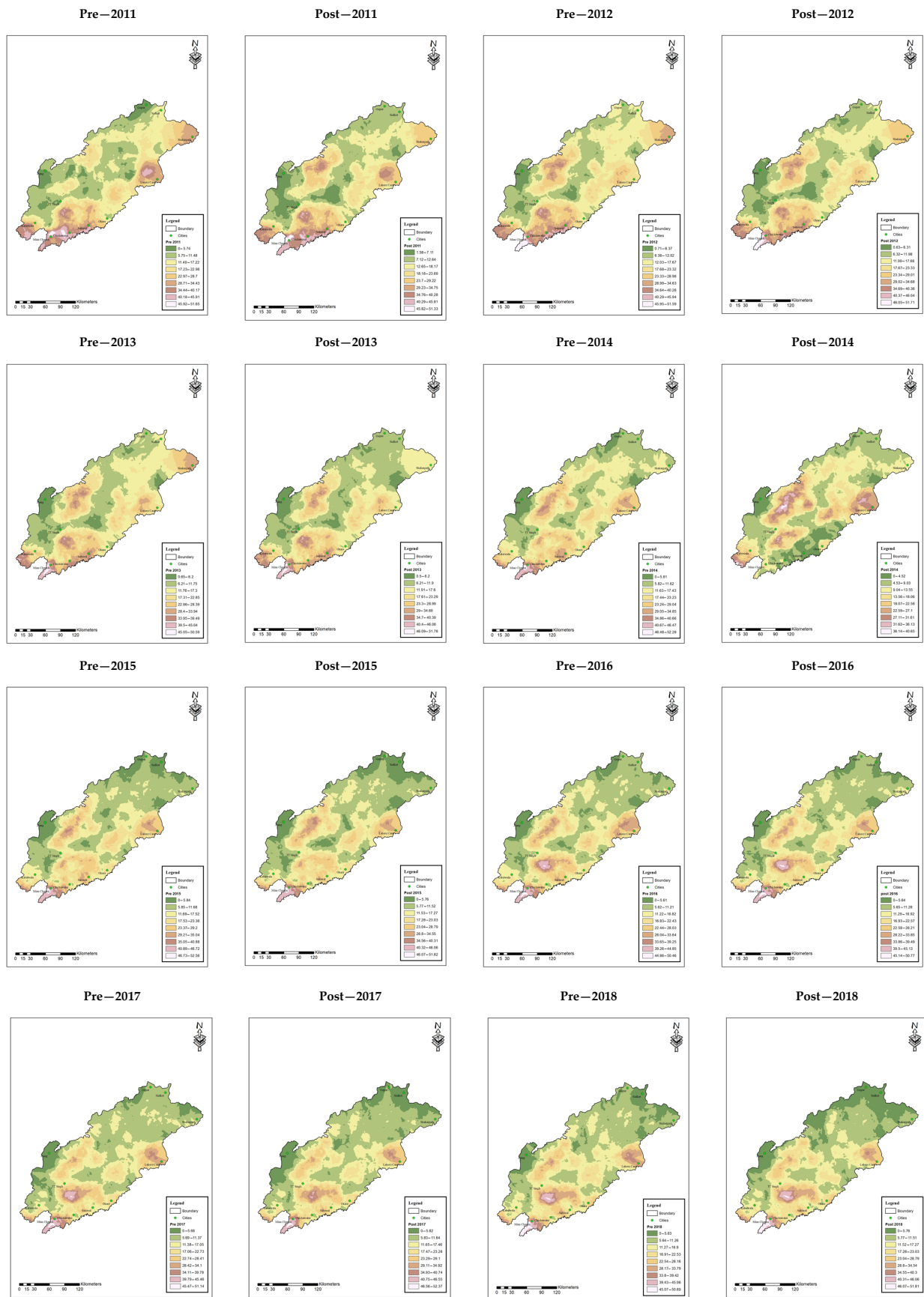


Figure 9. Interpolation of groundwater levels for pre- and post-monsoon from 2003 to 2018.

From these trends, the maximum groundwater depths from 2003 to 2018 vary from 5.91 m to 15.45 m resulting in a 9.54 m (0.61 m/year) drawdown in groundwater depth. For checking the results, a comparison is made between the net deficit and average groundwater levels for the year 2015–2016. The average groundwater depth in 2015 was 6.33 m while it is 6.18 m in 2016 which corresponds to a 0.15 m drawdown. While the net deficit in 2016 was 0.05665 m (56.65 mm), the remaining 0.09 m is used by domestic, industries, etc. In comparison to this study, Qureshi et al. [33] reported that groundwater levels in most of the irrigated parts of the study area have a drawdown up to 6 m which directly increases the pumping cost due to deep well boring.

3.6. Highly Stressed Areas

To check the possible cause of stress on groundwater, highly stressed areas in the LCC are identified from groundwater depths. The highly stressed areas are Faisalabad, Sheikhpura, and Toba Tek Singh where the groundwater is depleting abruptly. Average groundwater depletion is 9.54 m (0.58 m/year). Reasons for rapid drawdown are due to different causes such as cropping effect, climatic effect, and effect due to tubewell density.

3.7. Cropping Effect

Since, for high delta crops, crop water requirement is high, the effect of crops is analyzed based on the historical data for the highly stressed areas as shown in Figure 10. In Faisalabad, rice, sugarcane, fodder, and maize cover 6%, 31%, 30%, and 13%, respectively, in the Kharif season while wheat is covering more than 70% area in the Rabi season. Similarly, for Sheikhpura and Toba Tek Singh, the results are summarized in Table 3. Rizwan et al. [40] proposed that if the command area of the LCC crop was cultivated with a cropping pattern containing wheat, rice, and cotton, with high-efficiency irrigation practices then surface water can be saved in a range between 2.768 Bm³ and 3.699 Bm³.

Table 3. Summary of the highest growing crop in highly stressed areas in Rabi and Kharif season.

Seasons	Crops	Faisalabad	Sheikhpura	Toba Tek Singh
Kharif Season	Rice	12%	70%	11%
	Sugarcane	31%	9%	23%
	Fodder	30%	15%	21%
	Maize	13%	3%	16%
Rabi Season	Wheat	>70%	>70%	>70%

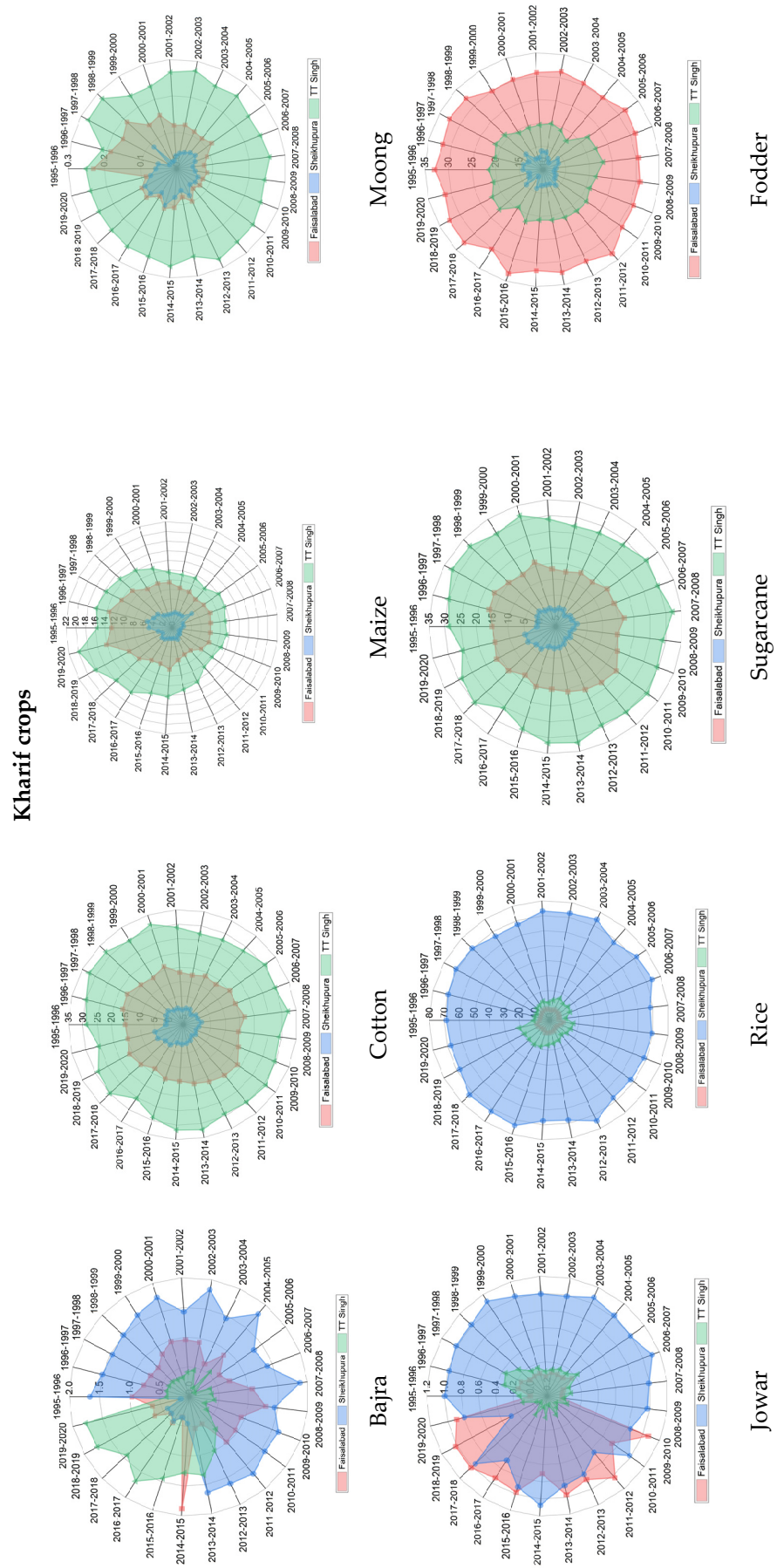
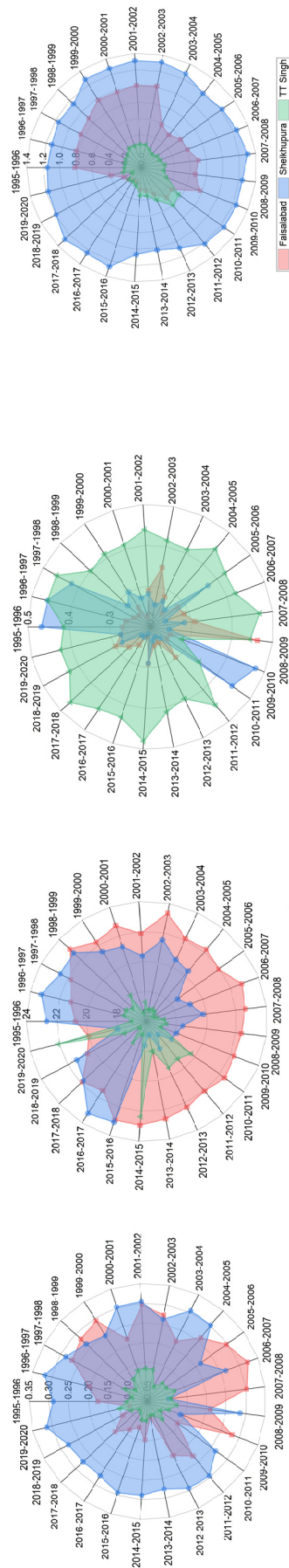


Figure 10. Cont.

Rabi crops



Guava

Gram

Fodder

Barley

Onion

Masoor

Linseed

Kinnu

Figure 10. Cont.

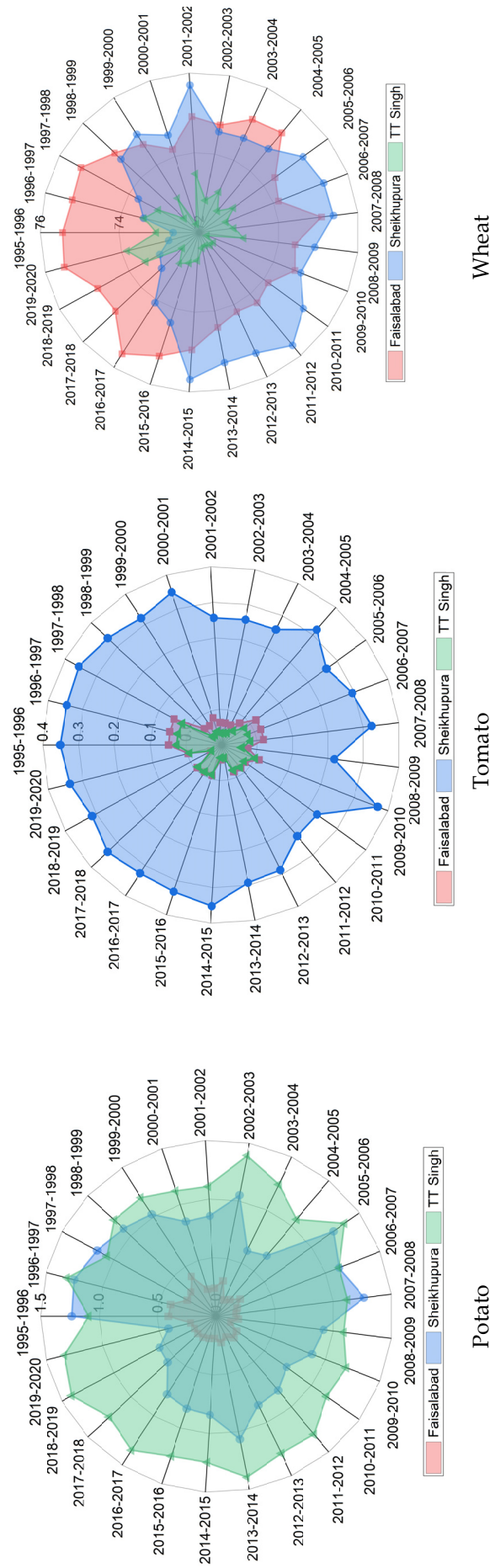


Figure 10. Change in cropping pattern percentages of both Kharif and Rabi crops in Faisalabad, Sheikhupura, and Toba Teik Singh for both Rabi and Kharif crops.

3.8. Climatic Effect and Effect of Tubewell Density

In highly stressed areas such as Faisalabad, Sheikhupura, and Toba Tek Singh, climatic factors are analyzed from the perspective of exploring their impacts on crop water requirements. Rainfall (mm), minimum temperature (°C), and maximum temperatures (°C) are selected as the meteorological parameters that significantly influence the crop water requirement. A comparison matrix of the three meteorological parameters among the highly stressed cities is presented in Figure 11. The maximum temperature recorded in Sheikhupura, Faisalabad, and Toba Tek Singh were 31 °C, 38 °C, and 34 °C, whereas the minimum temperature recorded was 18 °C, 16 °C, and 16.5 °C. The ranges of the temporal variability in the maximum and minimum temperature are summarized in Table 4. Sheikhupura’s rainfall pattern is progressively increasing with higher intensity compared to Faisalabad and Toba Tek Singh which reflects the availability of water to fulfill the crop water requirement. In Faisalabad, rainfall has an increasing trend with minimum temperature and maximum temperature of 16 °C and 38 °C, respectively. The results are summarized in Table 4. Awan et al. [31] reported that temperature and rainfall significantly impacted the use of irrigation water. The water consumption in the LCC region could increase from 7% to 11% by the end of 2020.

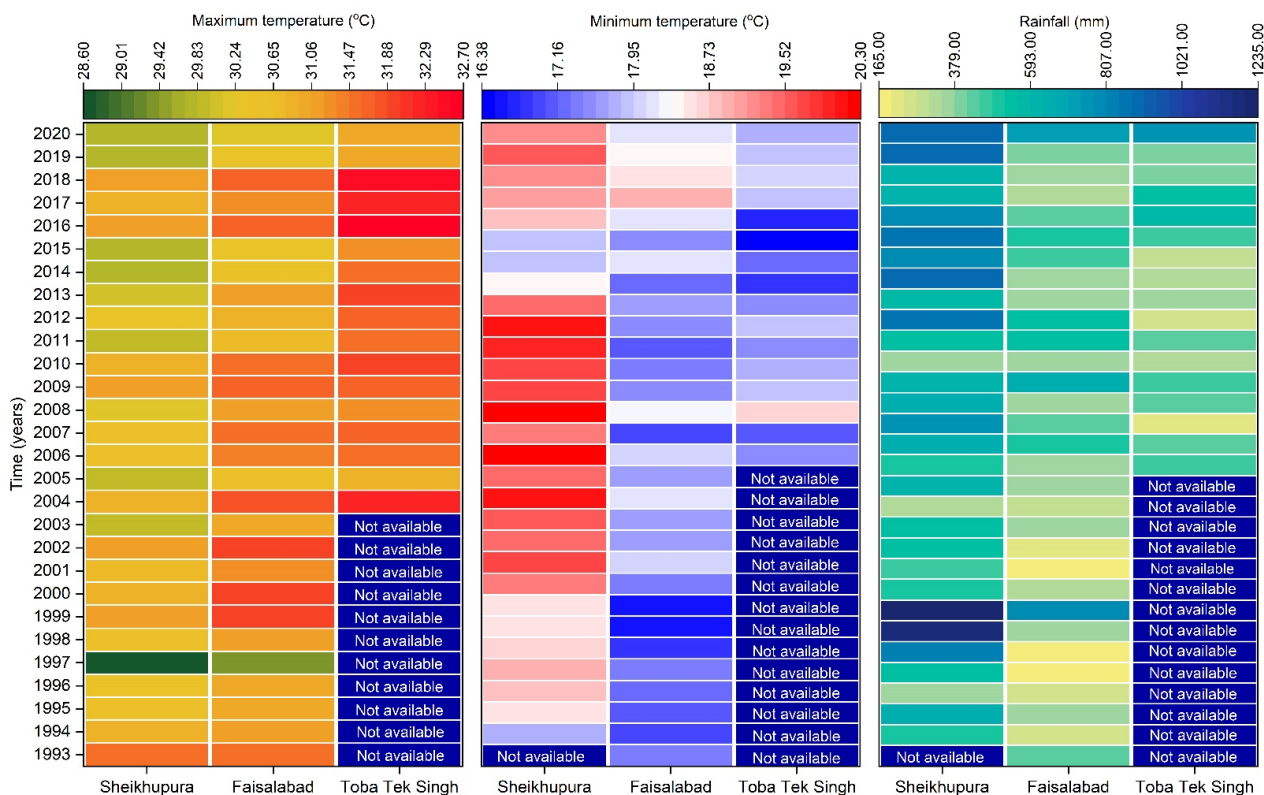


Figure 11. Historical trend of rainfall (right), minimum temperature (center), and maximum temperature (left) in highly stressed areas.

Table 4. Summary of climatic parameters in highly stressed areas.

Areas	Rainfall (mm)	Min Temperature (°C)	Max Temperature (°C)
Faisalabad	500–700	16–19	32–38
Sheikhupura	800–1200	18–20	29–31
Toba Tek Singh	400–700	16.5–18.5	30–34

Tubewells are used for various purposes such as agriculture and domestic and industrial use. Due to the rapid increase in tubewell, the extraction rate has also increased which

affected the groundwater levels. Figure 12 shows the tubewell density from 2008 to 2021. In the last decade, the number of tubewells has increased from 225,660 to 338,300 having an average growth rate of 8664.6 tubewell/year.

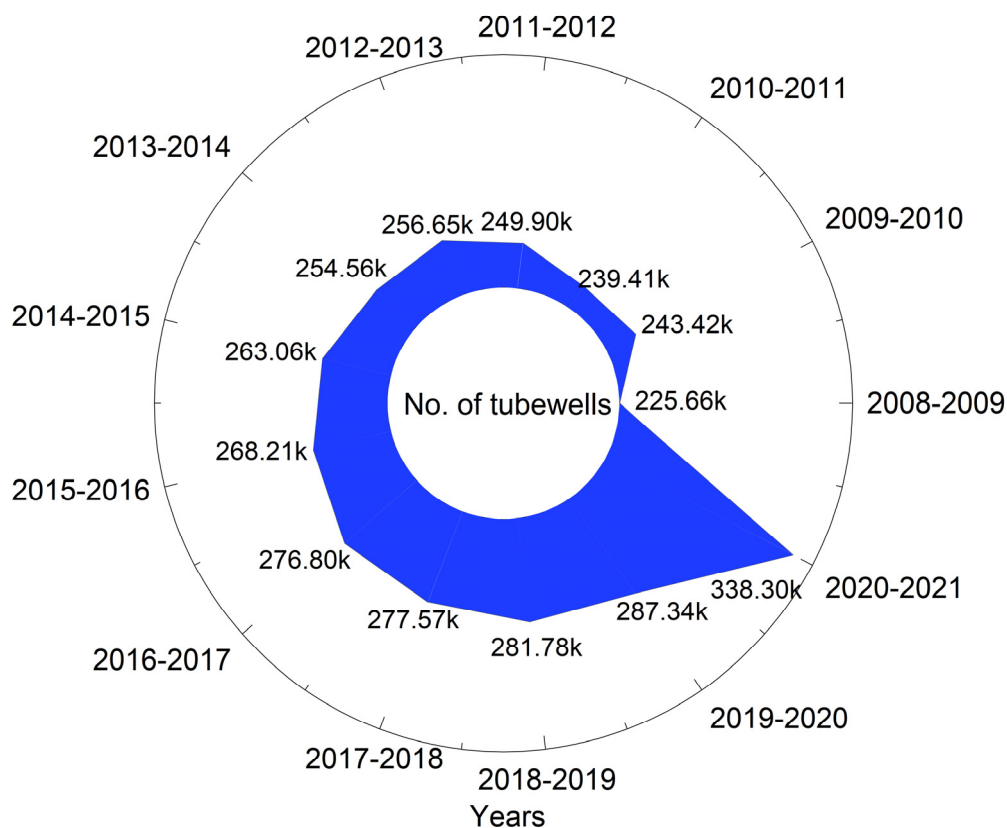


Figure 12. Change in tubewell density from 2008–2009 to 2020–2021.

4. Conclusions

Groundwater is a precious resource that has been rapidly depleting in some places of Pakistan owing to overexploitation. The present study focused on estimating the drop in groundwater levels near to Lower Chenab Canal (LCC) and its branch canals considering the temporal variation in cropping pattern, available surface water supply, and groundwater level. The results showed that rice, fodder, and sugarcane are the most frequent crops grown in the Kharif season occupying 70% of the cultivated land in the study area. Crops growing pattern is shifting towards high delta crops (i.e., rice, and sugarcane), thus increasing the crop water requirement in the region. Wheat is mostly grown in the Rabi season holding 70% of the cultivated area and ranges from 6070.3 to >7689 km² per year. On the other hand, from 1995 to 2016, surface water supplies in LCC have declined from 7.75 billion cubic meters (Bm³) to 4.88 Bm³ in the Kharif season and 4.17 Bm³ to 2.63 Bm³ in the Rabi season. An average groundwater drawdown of 0.61 m/year, is recorded in the LCC region. Faisalabad, Sheikhpura, and Toba Tek Singh are highly groundwater stressed cities due to the shifting of cropping patterns and temporal declination in groundwater levels. In Sheikhpura, cultivation of rice increased from 68% to 84% whilst in Toba Tek Singh rice, maize, and sugarcane cultivation increased from 10% to 25%, 15% to 20%, and 11% to 16%, respectively. The average annual groundwater drawdown in highly stressed cities is recorded at 0.58 m/year which creates an alarming situation. This study recommended taking some serious steps to maintain the groundwater levels by following the recharging techniques, capacity building workshops for farmers, or changing the cropping patterns.

Author Contributions: Conceptualization, A.M. and G.N.; methodology, A.M. and G.N.; software, A.M. and H.M.A.; validation, G.N., M.I. and M.S.; formal analysis, A.M., M.M. and M.I.; investigation, A.M., M.M., M.I. and M.S.; resources, G.N.; data curation, A.M., G.N., M.M. and M.I.; writing—original draft preparation, A.M. and G.N.; review and editing, H.M.A., M.S., F.M., O.H. and A.N.; visualization, A.M., H.M.A., F.M., O.H. and A.N.; supervision, G.N.; project administration, G.N.; funding acquisition, G.N., F.M., O.H. and A.N. All authors have read and agreed to the published version of the manuscript.

Funding: This research received no external funding.

Institutional Review Board Statement: Not applicable.

Informed Consent Statement: Not applicable.

Data Availability Statement: The data are contained within the article.

Acknowledgments: This work is part of thesis of first author Ahmad Mujtaba. This work is conducted at University of Engineering and Technology, Lahore under the supervision of Ghulam Nabi.

Conflicts of Interest: The authors declare no conflict of interest.

References

- Ahmed, S.; Cheema, M.J.M.; Ahmed, W.; Arshad, M. Delineation of Hydrological Response Units to Estimate Water Demand of Canal Command in Lower Chenab Canal Using Gis Modeling. *Pakistan J. Agric. Sci.* **2018**, *55*, 211–215. [CrossRef]
- Shah, M.A.A.; Anwar, A.A.; Bell, A.R.; Ul Haq, Z. Equity in a Tertiary Canal of the Indus Basin Irrigation System (IBIS). *Agric. Water Manag.* **2016**, *178*, 201–214. [CrossRef]
- Imran, M.A.; Xu, J.; Sultan, M.; Shamshiri, R.R.; Ahmed, N.; Javed, Q.; Asfahan, H.M.; Latif, Y.; Usman, M.; Ahmad, R. Free Discharge of Subsurface Drainage Effluent: An Alternate Design of the Surface Drain System in Pakistan. *Sustainability* **2021**, *13*, 4080. [CrossRef]
- Tariq, M.A.U.R.; van de Giesen, N.; Janjua, S.; Shahid, M.L.U.R.; Farooq, R. An Engineering Perspective of Water Sharing Issues in Pakistan. *Water* **2020**, *12*, 477. [CrossRef]
- Shakoor, A.; Arshad, M.; Ahmad, R.; Khan, Z.M.; Qamar, U.; Farid, H.U.; Sultan, M.; Ahmad, F. Development of Groundwater Flow Model (MODFLOW) to Simulate the Escalating Groundwater Pumping in the Punjab, Pakistan. *Pakistan J. Agric. Sci.* **2018**, *55*, 629–638.
- UNESCO World Water Assessment Programme. *The United Nations World Water Development Report 2020: Water and Climate Change*; United Nations Educational Sci.: Paris, France, 2020; ISBN 9789231003714.
- Famiglietti, J.S. The Global Groundwater Crisis. *Nat. Clim. Chang.* **2014**, *4*, 945–948. [CrossRef]
- Gorelick, S.M.; Zheng, C. Global Change and the Groundwater Management Challenge. *Water Resour. Res.* **2015**, 3031–3051. [CrossRef]
- Lytton, L.; Ali, A.; Garthwaite, B.; Punthakey, J.F.; Basharat, S. Groundwater in Pakistan’s Indus Basin: Present and Future Prospects. *Open Knowl. Repos.* **2021**, *164*, 66.
- Watto, M.A.; Muger, A.W. Groundwater Depletion in the Indus Plains of Pakistan: Imperatives, Repercussions and Management Issues. *Int. J. River Basin Manag.* **2016**, *14*, 447–458. [CrossRef]
- Programme Mondial pour L’évaluation des Ressources en eau, ONU-Eau. *The United Nations World Water Development Report 2014*; United Nations Educational, Scientific and Cultural Organization: Paris, France, 2014.
- Shakoor, A.; Mahmood Khan, Z.; Arshad, M.; Farid, H.U.; Sultan, M.; Azmat, M.; Shahid, M.A.; Hussain, Z. Regional Groundwater Quality Management through Hydrogeological Modeling in LCC, West Faisalabad, Pakistan. *J. Chem.* **2017**, *2017*, 2041648. [CrossRef]
- Muhammad, A.M.; Zhonghua, T.; Dawood, A.S.; Earl, B. Evaluation of Local Groundwater Vulnerability Based on DRASTIC Index Method in Lahore, Pakistan. *Geofis. Int.* **2015**, *54*, 67–81. [CrossRef]
- Mujtaba, A.; Nabi, G.; Masood, M.; Sultan, M.; Saleem, A.; Saleem, A.; Ali, A.; Ghaffar, M.A. Development of Water Management Strategies in Arid Region of Punjab Pakistan. *FRESENIUS Environ. Bull.* **2022**, *31*, 500–509.
- Falkenmark, M. The Massive Water Scarcity Now Threatening Africa. *Ambio* **1989**, *18*, 112–118.
- Qureshi, R.H.; Ashraf, M. *Water Security Issues of Agriculture in Pakistan*; PAS Islamabad Pak: Islamabad, Pakistan, 2019.
- Kirshen, P.H.; Strzepek, K.M. *Comprehensive Assessment of the Freshwater Resources of the World*; FAO: Rome, Italy, 1997; pp. 393–398.
- Susanne, M.S.; Treguer, O.D. *Beyond Crop per Drop*; World Bank: Washington, DC, USA, 2018; ISBN 9781464812989. [CrossRef]
- Economic Survey of Pakistan. Available online: http://finance.gov.pk/survey_0708.html (accessed on 24 March 2021).
- FAO. *The State of Food and Agriculture, 1966*; FAO: Rome, Italy, 2009; ISBN 9789251062159.
- Hussain, I.; Mudasser, M.; Hanjra, M.A.; Amrasinghe, U.; Molden, D. Improving Wheat Productivity in Pakistan: Econometric Analysis Using Panel Data from Chaj in the Upper Indus Basin. *Water Int.* **2004**, *29*, 189–200. [CrossRef]
- Li, P.; Tian, R.; Xue, C.; Wu, J. Progress, Opportunities, and Key Fields for Groundwater Quality Research under the Impacts of Human Activities in China with a Special Focus on Western China. *Environ. Sci. Pollut. Res.* **2017**, *24*, 13224–13234. [CrossRef]

23. Wu, J.; Wang, L.; Wang, S.; Tian, R.; Xue, C.; Feng, W.; Li, Y. Spatiotemporal Variation of Groundwater Quality in an Arid Area Experiencing Long-Term Paper Wastewater Irrigation, Northwest China. *Environ. Earth Sci.* **2017**, *76*, 460. [[CrossRef](#)]
24. Marengo, J.A.; Tomasella, J.; Nobre, C.A. Climate Change and Water Resources. In *Waters of Brazil*; Springer: Cham, Switzerland, 2016.
25. Ibrakhimov, M.; Awan, U.K.; George, B.; Liaqat, U.W. Understanding Surface Water–Groundwater Interactions for Managing Large Irrigation Schemes in the Multi-Country Fergana Valley, Central Asia. *Agric. Water Manag.* **2018**, *201*, 99–106. [[CrossRef](#)]
26. GoP. *Punjab Development Statistics*; Bureau of Statistics, Government of the Punjab: Lahore, Pakistan, 2014.
27. Shakoor, A.; Khan, Z.M.; Farid, H.U.; Sultan, M.; Ahmad, I.; Ahmad, N.; Mahmood, M.H.; Ali, M.U. Delineation of Regional Groundwater Vulnerability Using DRASTIC Model for Agricultural Application in Pakistan. *Arab. J. Geosci.* **2020**, *13*, 195. [[CrossRef](#)]
28. Hussain, M. Rehabilitation of Lower Chenab Canal (Lcc) System Punjab Pakistan. *Pakistan Eng. Congr.* **2020**, *33*, 449.
29. Yongguang, H.; Buttar, N.A.; Shabbir, A.; Faheem, M.; Aleem, M. Precision Management of Groundwater Abstraction on Different Spatial Scales of Lower Chenab Canal System in Punjab, Pakistan. *IFAC-PapersOnLine* **2018**, *51*, 397–401. [[CrossRef](#)]
30. Usman, M.; Qamar, M.U.; Becker, R.; Zaman, M.; Conrad, C.; Salim, S. Numerical Modelling and Remote Sensing Based Approaches for Investigating Groundwater Dynamics under Changing Land-Use and Climate in the Agricultural Region of Pakistan. *J. Hydrol.* **2020**, *581*, 124408. [[CrossRef](#)]
31. Awan, U.K.; Liaqat, U.W.; Choi, M.; Ismaeel, A. A SWAT Modeling Approach to Assess the Impact of Climate Change on Consumptive Water Use in Lower Chenab Canal Area of Indus Basin. *Hydrol. Res.* **2016**, *47*, 1025–1037. [[CrossRef](#)]
32. Qureshi, A.S.; McCornick, P.G.; Sarwar, A.; Sharma, B.R. Challenges and Prospects of Sustainable Groundwater Management in the Indus Basin, Pakistan. *Water Resour. Manag.* **2010**, *24*, 1551–1569. [[CrossRef](#)]
33. Qureshi, A.S. Groundwater Governance in Pakistan: From Colossal Development to Neglected Management. *Water* **2020**, *12*, 3017. [[CrossRef](#)]
34. Bhatti, M.T.; Anwar, A.A.; Aslam, M. Groundwater Monitoring and Management: Status and Options in Pakistan. *Comput. Electron. Agric.* **2017**, *135*, 143–153. [[CrossRef](#)]
35. Smith, M. *CROPWAT: A Computer Program for Irrigation Planning and Management*; Food & Agriculture Organization: Rome, Italy, 1992; ISBN 9251031061.
36. Programme Monitoring & Implementation Unit (Pmiu) Irrigation Department, Government of the Punjab. Available online: <https://irrigation.punjab.gov.pk> (accessed on 10 March 2022).
37. Allen, R.G.; Pereira, L.S.; Raes, D.; Smith, M. *FAO Irrigation and Drainage Paper No. 56—Crop Evapotranspiration*; Food and Agriculture Organisation of the United Nations: Rome, Italy, 1998.
38. Shakir, A.S.; Qureshi, M.M. Crop Water Requirement and Availability in the Lower Chenab Canal System in Pakistan. *WIT Trans. Ecol. Environ.* **2005**, *80*, 10.
39. Waqas, M.M.; Awan, U.K.; Cheema, M.J.M.; Ahmad, I.; Ahmad, M.; Ali, S.; Shah, S.H.H.; Bakhsh, A.; Iqbal, M. Estimation of Canal Water Deficit Using Satellite Remote Sensing and GIS: A Case Study in Lower Chenab Canal System. *J. Indian Soc. Remote Sens.* **2019**, *47*, 1153–1162. [[CrossRef](#)]
40. Rizwan, M.; Bakhsh, A.; Li, X.; Anjum, L.; Jamal, K.; Hamid, S. Evaluation of the Impact of Water Management Technologies on Water Savings in the Lower Chenab Canal Command Area, Indus River Basin. *Water* **2018**, *10*, 681. [[CrossRef](#)]

Article

Synchronization Optimization of Pipe Diameter and Operation Frequency in a Pressurized Irrigation Network Based on the Genetic Algorithm

Yiyuan Pang, Hong Li *, Pan Tang and Chao Chen

Research Centre of Fluid Machinery Engineering and Technology, Jiangsu University, Zhenjiang 212013, China; 2111911010@stmail.ujs.edu.cn (Y.P.); tangpan19@163.com (P.T.); chch3605@ujs.edu.cn (C.C.)

* Correspondence: hli@ujs.edu.cn

Abstract: The pressurized irrigation network aims to deliver water to consumption nodes at an appropriate pressure and discharge. The traditional pipe network optimization minimizes the annual operating cost or investment per unit area. The present work establishes the traditional pipe diameter and operating frequency optimization models based on flattish terrain. It proposes a new synchronization optimization method of pipe diameter and operation frequency to find the best match point for pipe diameter and operating frequency in the branched network system. The irrigation costs of the above three models, including the energy and pipe network costs, are compared with the original irrigation network system. Based on the results of optimizing the typical experimental field, the operation frequency optimization model and the pipe diameter optimization model can save about 1.4% and 10.6% in irrigation cost, respectively. Furthermore, the synchronous optimization model can significantly reduce the irrigation cost to about 19.3%, including a 26.6% reduction in the pipe network cost and a 21.9% increase in the energy cost. Compared with pipe diameter optimization, synchronous optimization can further reduce network costs while generating lower energy costs. The results of this research can be used for the design of the network system in flattish terrain to reduce the irrigation cost.

Keywords: pipe diameter; operation frequency; genetic algorithm; rotation irrigation sectoring; irrigation cost; energy cost; network cost

Citation: Pang, Y.; Li, H.; Tang, P.; Chen, C. Synchronization Optimization of Pipe Diameter and Operation Frequency in a Pressurized Irrigation Network Based on the Genetic Algorithm. *Agriculture* **2022**, *12*, 673. <https://doi.org/10.3390/agriculture12050673>

Academic Editors:

Muhammad Sultan, Redmond
R. Shamshiri, Md Shamim Ahamed
and Muhammad Farooq

Received: 29 March 2022

Accepted: 6 May 2022

Published: 9 May 2022

Publisher's Note: MDPI stays neutral with regard to jurisdictional claims in published maps and institutional affiliations.



Copyright: © 2022 by the authors. Licensee MDPI, Basel, Switzerland. This article is an open access article distributed under the terms and conditions of the Creative Commons Attribution (CC BY) license (<https://creativecommons.org/licenses/by/4.0/>).

1. Introduction

Pipeline irrigation is an important trend in the development of water-saving irrigation, while pipe network optimization is a multi-discipline issue involving global optimization, hydraulics, and intelligent algorithms [1–4]. The pressurized irrigation network (PIN), an essential system in the agricultural irrigation project, aims to deliver water to consumption nodes at an appropriate pressure and discharge [3]. The pipe network optimization minimizes the annual operating cost or investment per unit area and maximizes the system's reliability under pressure and discharge constraints [1]. With the formulation of PIN design as an optimization problem, various studies have been performed on pipe network optimization [2,5–8].

The rapidly growing world energy use has already raised concerns over supply difficulties, exhaustion of energy resources and heavy environmental impact [9]. Predictions show that energy use by nations with emerging economies will grow at an average annual rate of 3.2% and will exceed by 2020 that for the developed countries at an average growing rate of 1.1%. Energy consumption plays an important role in pipeline irrigation [10,11]. For example, energy consumption is involved in the process of water extraction, transportation, irrigation and drainage [12]. Various measures can be adopted to reduce energy consumption during the operation of pressurized irrigation systems. The irrigation network design should take into account the energy criterion for determining the optimum pipe diameter.

Conversely, more efficient management and operation of irrigation systems can be achieved using protocols and tools developed for assessing the performance using management indicators [13].

The optimization of pipe diameter combination significantly influences the investment of the whole system, leading to remarkable economic benefits [14]. Giménez et al. [15] proposed a two-level dynamic programming method to optimize networks represented by multistage graphs. Zhao et al. [16] constructed the mathematical optimization model of the pipe diameter optimization for the overall synchronized optimization of the pipeline layout and pipe diameter and achieved a total cost 27.5% lower than the empirical method. Ma et al. [14] proposed the optimization method of the mechanical pressure micro-irrigation pipe network system and established the mathematical model of the optimization design. Accordingly, the annual cost of the optimal design scheme of the irrigation pipe network has been reduced by 14%. According to various research results, optimizing the diameter of the irrigation pipe network can provide significant economic benefits [17–20]. Diameter optimization can realize the use of smaller diameter pipes to complete the system construction and to reduce the construction cost of the irrigation system.

The variable speed drive (VSD) offers many advantages in the operation of centrifugal pumps [21]. It can reduce or increase the pump head by adjusting the pump speed [22]. Lamaddalena et al. [23] and AitKadi et al. [24] indicated that about 20% and 25% of the energy for pumping could be saved by variable-speed pumps in two Italian irrigation districts and an irrigation district in Morocco, respectively. Díaz et al. [25] analyzed an irrigation district in southern Spain equipped with variable-speed pumps and simulated four alternative management scenarios for several water demand levels. In summary, by adopting the operation frequency optimization technology, adjusting the speed of the water pump, and matching the appropriate pump operating points for different irrigation groups, the energy consumption of the pumping station can be reduced, and the sustainable development of the irrigation system can be achieved [26,27].

The above research indicates that pipe diameter optimization and operating frequency optimization can significantly reduce network and energy costs, respectively. The optimization target of this paper is the irrigation cost as the sum of the annual network and energy costs. A synchronization optimization model of pipe diameter and the operation frequency is established and solved using the genetic algorithms (GA) [28–31], providing a design reference for the PIN system.

2. Materials and Methods

2.1. Problem Description and Generalization

The PIN system consists of four parts: the water source, water intake works, irrigation networks, and field irrigators. The irrigation networks are arranged according to the terrain, water source, and water consumption. Due to their low cost and convenient maintenance, branched networks have been widely utilized in agriculture [16]; this paper conducts research on the networks. Figure 1 shows the schematic diagram of the branched networks.

Irrigation costs include the investment cost (this paper only considers the cost of the pipe network, excluding equipment such as pumping stations) and the energy consumption cost [2]. There is a non-strict inverse relationship between these two costs and the pipe diameter. The network cost is positively related to the pipe diameter, and the energy consumption cost is negatively related to the pipe diameter [26].

The pipeline network investment generally accounts for 70% of the total investment in the irrigation system and determines the investment in the entire system. Plastic pipes such as PVC or PE are usually employed for the PIN. With the increase in the pipe diameter, the unit price of pipes usually increases exponentially [16]. Therefore, a reasonable reduction of the pipe diameter can significantly reduce the investment cost of irrigation projects.

Furthermore, the energy consumption cost is mainly generated by the motor that drives the pump, determined by the pump's operating point. The pump's operating point will change during the entire irrigation process according to different pipeline resistances

of different rotation irrigation sectoring [32,33]. When the pipeline resistance difference between the rotation irrigation sectoring is relatively significant, the operating point deviation of different rotation irrigation sectoring will be more obvious. This often avoids the water pump running at the optimal operating point, thus reducing the pump efficiency and increasing unnecessary irrigation energy consumption. In order to adjust the working point of the pump, the pump revolution speed can change the pump's performance curve based on VSD technology [26]. This technology can theoretically match the operating point for each rotation irrigation sectoring to realize the low energy consumption operation of all rotation irrigation sectoring.

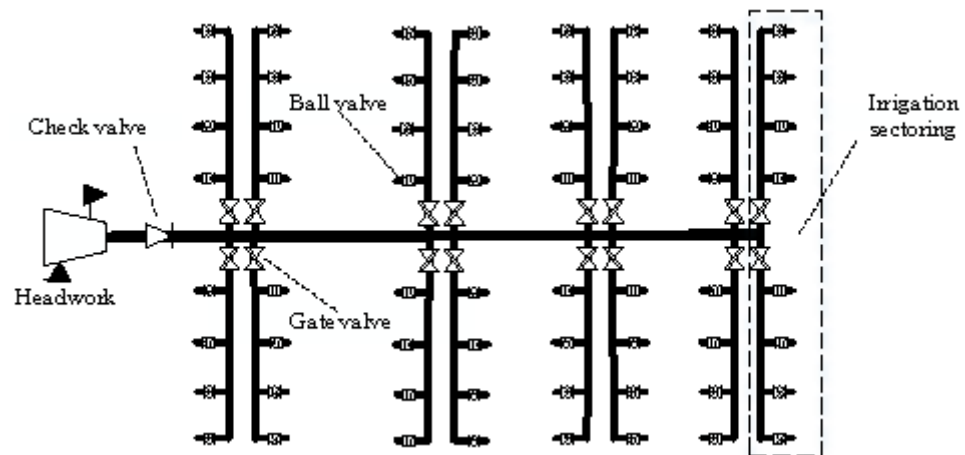


Figure 1. The schematic diagram of the branched networks and irrigation sectoring.

2.2. Mathematical Models

The PIN design is a highly complex problem. Most of the optimization methods are based on the pipe diameter optimization of the fixed speed pump [21]. Compared with the traditional optimization of branch pipe diameter and operation frequency optimization, this paper establishes a pipe diameter optimization model (PDM), an operation frequency optimization model (OFM), and a synchronization optimization model of pipe diameter and variable frequency (SOM) without changing the rotation irrigation sectoring, irrigation amount, and pipe network layout.

The synchronization optimization of pipe diameter and operation frequency process can be structured in four stages. First, mathematical models of PDM, OFM, and SOM are established. In the second stage, various irrigation constraints are established according to the engineering application requirements. In the third stage, the annual energy and network costs are evaluated. Finally, the total costs of PDM and OFM are compared with those of SOM.

Large-scale farmlands generally employ the rotation irrigation system [16]. The main pipe adopts continuous irrigation. Valves control the branch pipe for rotation irrigation; that is, the main pipe supplies water to the branch pipes according to the sequence of rotation irrigation groups. Furthermore, considering engineering applications, the pump station generally supplies water only to two branch pipes at the same node. In the proposed model, the number of main pipes is 1, the number of main pipe segments is NM , the number of branch pipes is N , and the number of branch pipe segments is NB . The number of hydrants and branch pipe segments is the same. The numbering methods of branch pipes and main pipe segments are shown in Figure 2. The division method of rotation irrigation sectoring and the number of passes through the central pipe segment are shown in Table 1. The branch pipes are numbered in sequence from the pump along the water flow direction.

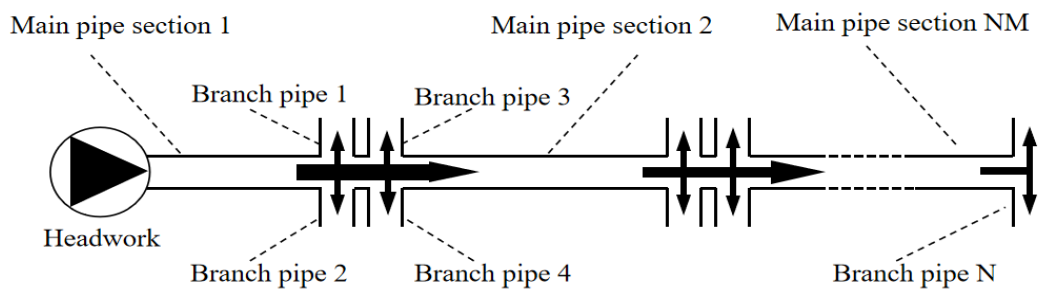


Figure 2. The schematic diagram of branch pipe number and main pipe segments number.

Table 1. Rotation irrigation sectoring and the number of main pipe segments between branch pipe and pump.

Rotation irrigation sectoring number	1	2	3	4	5	...	$N/2$
Branch pipe number	1	3	5	7	9	...	$N-1$
	2	4	6	8	10	...	N
The number of main pipe segments between branch and pump	1	1	2	2	3	...	$\lfloor \frac{N-1}{4} \rfloor + 1$

In engineering applications, the branch pipe diameter will gradually decrease along the flow direction to reduce investment. Furthermore, due to the different irrigation areas of each hydrant, the discharge of each outlet is also different during the irrigation process [34]. Therefore, to obtain a reliable hydraulic model close to reality, the pipeline resistance calculation should be performed for each pipe segment during the hydraulic calculation. For the convenience of mathematical calculation, the branch pipe segments and hydrant should be numbered. Figure 3 shows the branch pipe segments and hydrant numbers. The branch pipe segments are numbered sequentially from the furthest hydrant in the opposite direction of the water flow.

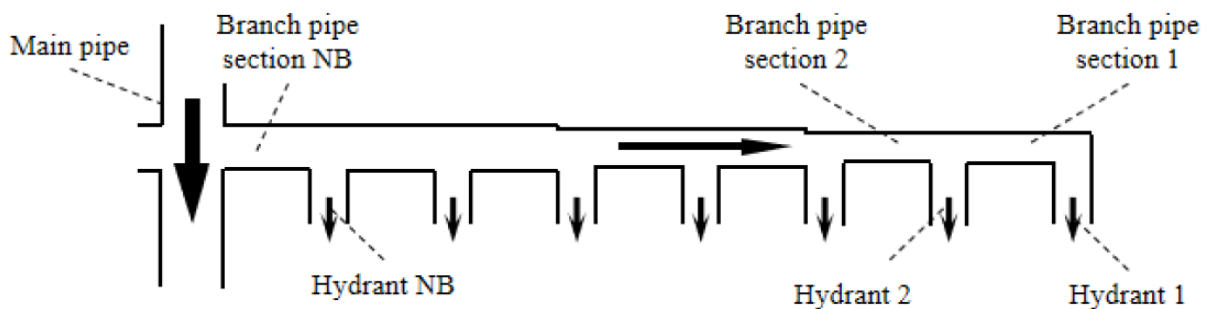


Figure 3. Schematic diagram of the branch pipe segments number and hydrant number.

2.2.1. Mathematical Model of Irrigation Cost

The PIN optimization mainly involves pipeline layout, pipe diameter selection, and pump revolution speed [16,21]. This paper optimizes pipe diameter and operating frequency (pump revolution), considering a constant pipeline layout. The pipe diameter optimization aims to determine the branch pipe diameter, considering only one standard diameter for each branch pipe segment. Operating frequency optimization mainly matches the most economical pump speed for the network characteristic curve of each irrigation sectoring.

PDM, OFM, and SOM are established in this paper. SOM can be simplified to PDM without frequency optimization, and OFM can be obtained without pipe diameter optimization. For the convenience of mathematical description, an irrigation system optimization model is established to optimize pipe diameter and operation frequency with the minimum annual cost of the rotary irrigation network as the objective function. The minimum irrigation annual cost (including the annual network and energy costs) of the irrigation system is considered the objective function, which is defined as follows:

$$\min F = \left[\frac{r(1+r)^y}{(1+r)^y - 1} + B \right] \sum_{i=1}^N \sum_{j=1}^{NB_i} C_{ij} L_{ij} + \mu \cdot \sum_{i=1}^{N/2} \frac{ET_i H_i \left(\sum_{j=1}^{NB_{2i-1}} q_{2i-1,j} + \sum_{j=1}^{NB_{2i}} q_{2i,j} \right)}{367.2 \eta_i \eta_p} \quad (1)$$

here, F is annual irrigation cost, Yuan/year; r is annual interest rate, %; y is depreciation period; B is average annual maintenance rate, %; C_{ij} is the price of branch pipe i segment j , Yuan/m; L_{ij} is the length of branch pipe i segment j , Yuan/m; μ energy consumption correction coefficient based on experimental; E is the local electricity price, Yuan/kW·h; T_i is irrigation period of rotation irrigation sectoring i , h; H_i is pump outlet pressure of rotation irrigation sectoring i , m; NB_i is the number of pipe segments of branch pipe i ; $q_{i,j}$ is the hydrant discharge of branch pipe i segment j , m³/h; η_i is pump efficiency of the rotation irrigation sectoring i , %; η_p is water utilization coefficient of pipeline system, %.

2.2.2. Constraint Conditions of the Model

- Irrigation period constraints

The irrigation period is determined according to the local irrigation test data and national standards [35]. The rotation irrigation period should not be greater than the designed irrigation period. Therefore, the following constraints are considered for the rotation irrigation period:

$$\sum_{i=1}^{N/2} T_i \leq T_s \quad (2)$$

here, T_i is the irrigation period of the rotation irrigation sectoring i , h; T_s is the longest irrigation period allowed by the project, h.

- Pipe diameter constraints

Along the direction of water discharge, the diameter of the pipe should gradually decrease [16,36]. The pipe diameter constraint established are shown below:

$$d_{i,j} \leq d_{i,j+1} \quad (3)$$

here, $d_{i,j}$ is the diameter of branch pipe i segment j , mm.

- Velocity constraints

When the network has fertilization or application tasks, the velocity in the pipe is 0.6–2.0 m s⁻¹ [36]. The flow depends on the velocity in a pipe and on the pipe diameter. The velocity constraints are given by:

$$q_{i,j} = \sum_{j=1}^j \frac{9\pi \cdot (1.4 \cdot \text{Rand} + 0.6) \cdot d_{i,j}^2}{1 \times 10^4} \quad (4)$$

- Hydrant outlet pressure constraints

Since the most basic design principle of the irrigation network is that all hydrants have a steady discharge, there should be no pressure deficit in the most remote hydrants [37]. Taking the hydrant working pressure at the end of all branch pipes in the rotation irrigation sectoring to meet the pressure conditions as constraints, the following constraints are established:

$$hye_i \geq hy_M \tag{5}$$

here, hye_i is the working pressure of the hydrant at the end of the branch pipe i , m; hy_M is the minimum working pressure of hydrant, m.

- Pump outlet pressure constraints

Each rotation irrigation sectoring in this study contains two branch pipes. Each irrigation sectoring passes through various main pipe segments, resulting in different irrigation sectoring with different main pipe dampers. Similarly, each rotation irrigation sectoring has different branch pipe dampers. In order to meet the hydrant pressure of the branch pipe with greater damping, the pressure calculation should be performed with a branch pipe with high dampers. Thus, a general mathematical model should be established to obtain the network inlet pressure of different irrigation sectoring. The network inlet pressure consists of main dampers, branch dampers, and minimum hydrant working pressure. Thus, the network inlet pressure model of different rotation irrigation sectoring can be established according to the working pressure demand of the hydrant at the end of the branch pipe.

$$h_i = \alpha \cdot \max \left(\sum_{j=1}^{NB_{2i}} \frac{f^{i-1} q_{2i,j}^m}{d_{2i,j}^b} l_{2i,j}, \sum_{j=1}^{NB_{2i-1}} \frac{f^{i-1} q_{2i-1,j}^m}{d_{2i-1,j}^b} l_{2i-1,j} \right) + \sum_{k=1}^{\lfloor \frac{2i-1}{4} \rfloor + 1} f \frac{\left(\sum_{i=1}^{NB_{2i}} q_{2n,i} + \sum_{i=1}^{NB_{2i-1}} q_{2i-1,i} \right)^m}{D_k^b} L_k + hy_M \tag{6}$$

here, h_i is network inlet pressure of rotation irrigation sectoring i , m; α is drag coefficient considering local hydraulic losses; f, m, b are friction coefficient, discharge coefficient, pipe diameter coefficient, respectively; $d_{i,j}$ is the diameter of the branch pipe i segment j , mm (OFM is consistent with the parameters of the original pipe network); $l_{i,j}$ is the length of the branch pipe i segment j , m; D_k is the diameter of the main pipe segment k , mm; L_k is the length of the main pipe k , m.

Each performance parameter of a pump is not isolated and static but interrelated and mutually restrictive. This connection and restriction have certain regularity. A polynomial curve usually represents the law of change between them [26]. A pump outlet pressure model is established based on the inlet discharge of the pipe network:

$$Hb_i = \sum_{i=1}^4 \left(B_{i,f} \left(\sum_{j=1}^{NB_{2i}} q_{2i,j} + \sum_{j=1}^{NB_{2i-1}} q_{2i-1,j} \right)^{i-1} \right) \tag{7}$$

here, Hb_i is pump outlet pressure of rotation irrigation sectoring i , m; $B_{i,f}$ is the polynomial regression coefficient of frequency f in the rotation irrigation sectoring i (The f of PDM remains unchanged and runs in 50 Hz power frequency).

This research model employs the farthest hydrant to calculate the network inlet pressure. Since the pump outlet pressure may be less than the demand of the network inlet pressure, the pump outlet pressure constraint is established as:

$$h_i \leq Hb_i \tag{8}$$

- Pump efficiency constraints

Similar to the pump outlet pressure constraint, a polynomial regression model of pump efficiency is established according to the inlet discharge of the pipe network.

$$Pb_i = \sum_{i=1}^4 \left(C_{i,f} \left(\sum_{j=1}^{NB_{2i}} q_{2i,j} + \sum_{j=1}^{NB_{2i-1}} q_{2i-1,j} \right)^{i-1} \right) \tag{9}$$

here, Pb_i is pump operating efficiency of rotation irrigation sectoring i , %; $C_{i,f}$ is the polynomial regression coefficient of frequency f in the rotation irrigation sectoring i .

2.3. Method of the Model Solving

2.3.1. Fitness Function Design of GA

GA is a computational model of the biological evolution process that simulates Darwin’s theory of biological evolution [38,39]. GA can iterate independently, allowing the individuals to perform a natural selection of survival of the fittest, retaining better individuals, and excluding inferior individuals. Since the GA is based on selecting the best individual, this paper employs the character to find the minimum irrigation cost.

The penalty function method is the most common and typical constraint processing method [40]. Numerous constraints must be managed when solving models. Usually, the penalty factor parameter setting is challenging and directly affects the search. The unreasonable function will lead to problems such as falling into the local optimum solution, too long calculation time, and instability.

The proposed model has five constraints, and the fitness function is established as follows:

$$F_{fit} = F - \lambda_1 \cdot \max \left(\sum_{n=1}^{N/2} T_i - T_s, 0 \right) - \lambda_2 \max(d_i - d_{i+1}, 0) + \lambda_3 (\min(hy_{nmin} - hy_M, 0) + \min(Hb_n - h_n, 0) + \min(pb_n, 0) + \max(pb_n - 1, 0)) \tag{10}$$

here, F_{fit} is the fitness of the irrigation cost, λ is the penalty factor.

Irrigation period and pipe diameter constraints can accept inferior solutions. Their order of magnitude is similar to irrigation cost to make the effective solution more stable. Thus, the penalty function can range from 10^2 to 10^3 . In order to meet the hydrant outlet pressure constraints, pump outlet pressure constraints, and pump efficiency constraints, the penalty factor for these constraints should be infinite.

2.3.2. Solution Process of the Model

This study employs the GA to solve PDM, OFM, and SOM. Figure 4 shows the basic calculation flow chart of the GA. Compared with PDM and OFM, the SOM is a multifactorial model. One of the optimization variables (pipe diameter or operating frequency) in the SOM is chosen the same as the original system to convert SOM to PDM or OFM.

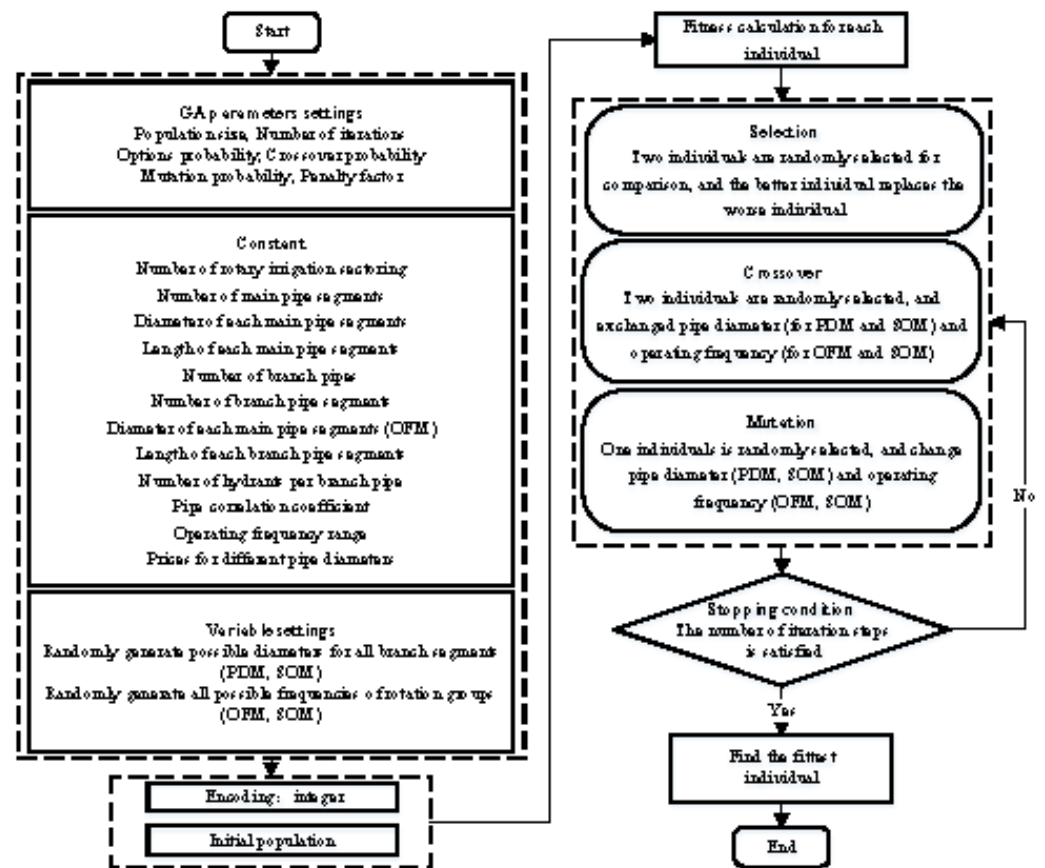


Figure 4. The basic calculation flow chart of the GA.

3. Results

3.1. Basic Information

In order to assess the performance of the proposed method, it is applied to PIN instances. The considered instances were obtained from the data from a real network in an experimental field (33°04'53.0'' N 119°52'55.8'' W) in Jiangsu Province, China. The irrigation area of the experimental field is about 30 hectares, the terrain is flat, rice and wheat are planted, and the annual irrigation amount is about 950 mm. The pipe network has many main pipe segments with a diameter of 400 mm and ten branch pipes. The pipes used in the experimental field are U-PVC, The friction coefficient, discharge coefficient, and pipe diameter coefficient are 94,800, 1.77, and 4.77, respectively. Each branch pipe is distributed with multiple hydrants, and the interval of each hydrant is 40 m. Figure 5 shows the irrigation area of each hydrant, pipe network layout, length, and diameter of the main pipe.

The irrigation network of the experimental field was designed and constructed more than ten years ago, and the original pipe network was designed by the relatively advanced economic flow method at that time [41,42]. Table 2 shows the diameters of all branch pipe segments.

Through the investigation of pipeline manufacturers near the experimental field, the latest pipe price is utilized in the model for calculation. The commercial diameters and prices listed in Table 3 are utilized for all optimization modes.

In order to determine the operational performance of the pumping station and the pipe network, the working condition confirmation was accomplished. The experimental system construction is shown in Figure 6. There is a 0.2 s high-precision electric energy meter, frequency converter, and motor in the irrigation system. The inlet pipe, pump, pressure gauge, flowmeter, main pipe, valve, and branch pipe are ordered sequentially along the water flow direction. The experimental procedure is: First, the pump's performance (50 Hz)

is evaluated by controlling the valve. Second, the output frequency of the inverter is adjusted, the previous actions are repeated, and the pump performance curve is tested at different frequencies, the polynomial regression coefficients of performance are shown in Table 4.

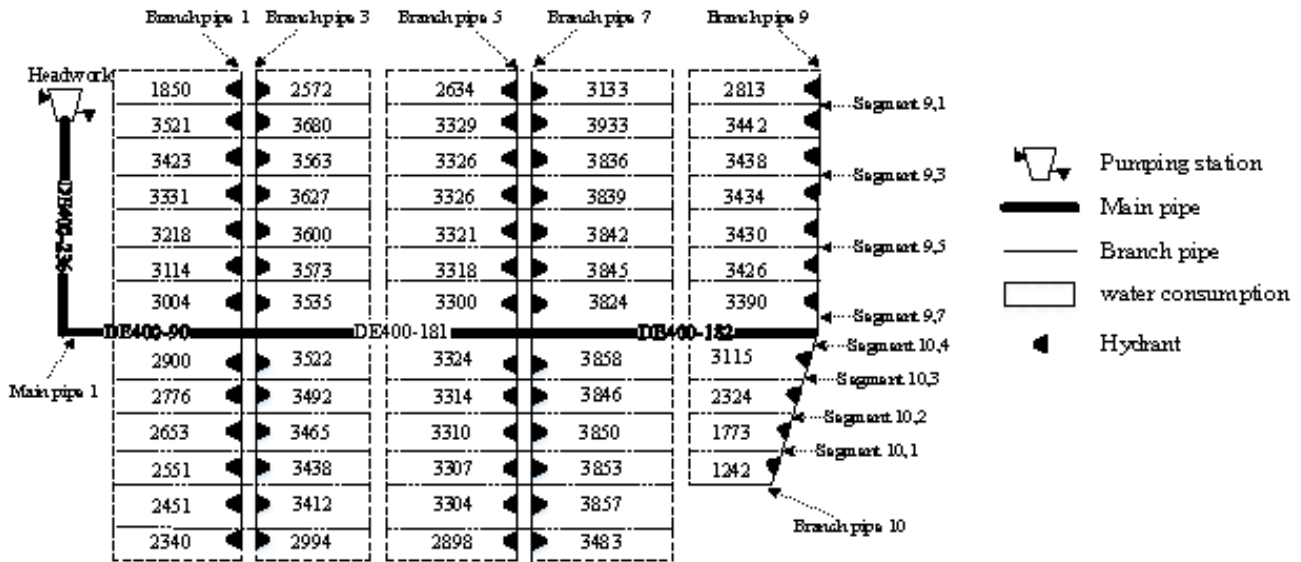


Figure 5. Diagram of the experimental field.

Table 2. The diameters of all branch pipe segments in the experimental field. Since there are too many pipe sections in the experimental field, in order to facilitate the mathematical description, this paper describes the pipe sections as two-dimensional data. Sort by branch number and assign values to all pipe segments of each branch.

Branch Pipe Number	Branch Pipe Segment Number and the Corresponding Pipe Diameter (mm)						
	1	2	3	4	5	6	7
1	160	200	250	250	315	315	315
2	160	200	250	250	315	315	-
3	160	200	250	250	315	315	315
4	160	200	250	250	315	315	-
5	160	200	250	250	315	315	315
6	160	200	250	250	315	315	-
7	160	200	250	250	315	315	315
8	160	200	250	250	315	315	-
9	160	200	250	250	315	315	315
10	160	200	250	250	-	-	-

Table 3. Unit prices of commercial different pipes.

Unplasticized Polyvinyl Chloride (U-PVC) Pipes (with a Pressure Capacity of 0.6 MPa)						
Outside diameter (mm)	140	160	200	250	315	400
Inner diameter (mm)	132.1	152.6	190.8	236.4	302.6	380.4
Unit price (Yuan/m)	28	37	56	90	142	232

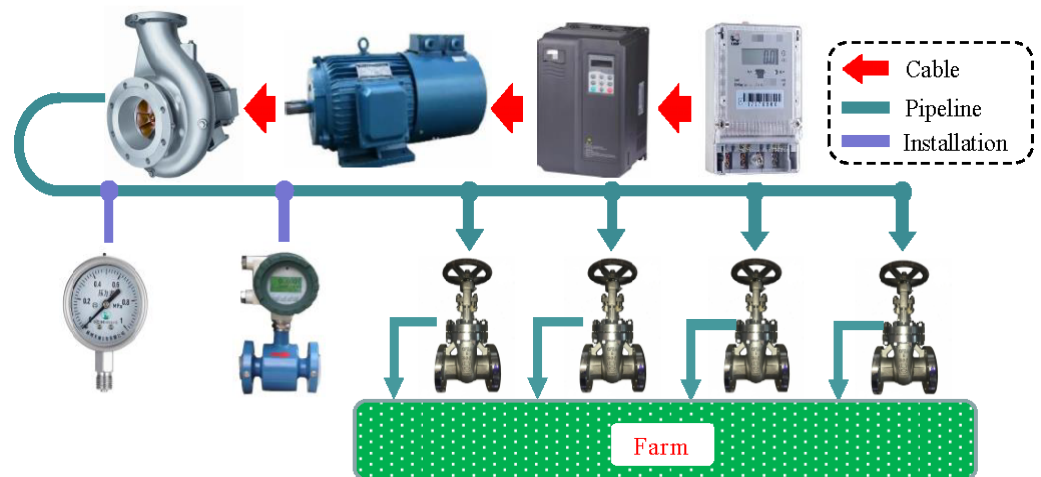


Figure 6. Schematic diagram of experimental system construction.

Table 4. The polynomial regression coefficient of the pump at the experimental site, since $B_{i,f}$ and $C_{i,f}$ have two variables, is converted into a table of different coordinates for description, irrigation sectoring (i), and operation frequency (f).

Irrigation Sectoring (i)		Operation Frequency (f)						
s	50	49	48	47	...	42	41	
B	1	21.1	20.26	19.45	18.64		14.89	14.19
	2	-0.004611	-0.004519	-0.004427	-0.004334		-0.003873	-0.003781
	3	-8.467×10^{-6}	-8.467×10^{-6}	-8.467×10^{-6}	-8.467×10^{-6}		-8.467×10^{-6}	-8.467×10^{-6}
	4	-1.329×10^{-22}	-4.025×10^{-17}	-7.911×10^{-18}	-1.066×10^{-17}		3.556×10^{-17}	7.502×10^{-17}
C	1	-0.02273	0.02265	-0.02257	0.02248	...	0.02206	0.02197
	2	0.002277	0.002316	0.002356	0.002397		0.002632	0.002685
	3	-1.919×10^{-6}	-1.919×10^{-6}	-2.068×10^{-6}	2.149×10^{-6}		-2.64×10^{-6}	2.758×10^{-6}
	4	3.97×10^{-10}	4.203×10^{-10}	4.455×10^{-10}	4.729×10^{-10}		6.493×10^{-10}	6.95×10^{-10}

The μ in the objective function (Equation (1)) should also be determined experimentally to verify its accuracy. The designed experimental process is as follows: First, the equipment in Figure 6 is employed to collect flow, pressure, running period, current, voltage, power factor, and energy consumption. Next, the above values are substituted into formula 1 for calculation, and the value of μ is determined based on the difference between theoretical and actual values of F . This paper performs the field test of the energy consumption of different pump operating points. Compared with the theoretical calculation, it is concluded that the energy consumption correction coefficient is 1.05. This work substitutes this coefficient into OFM and SOM to calculate energy consumption.

3.2. Optimization Results

3.2.1. Algorithm Results

The genetic genes of this algorithm are discharge of hydrant, branch pipe diameter, and operating frequency. Figure 7 shows an iteration diagram of the hydrant discharge at the end of branch pipe 1. It can be seen from the iteration map that the initial population distribution of hydrant discharge is wide and covers all reasonable areas. After 20 iterations, the optimal discharge range is reduced, while the optimal discharge of the hydrant value becomes stable after 40 iterations. Similarly, the convergence of branch diameter and operating frequency has a similar effect.

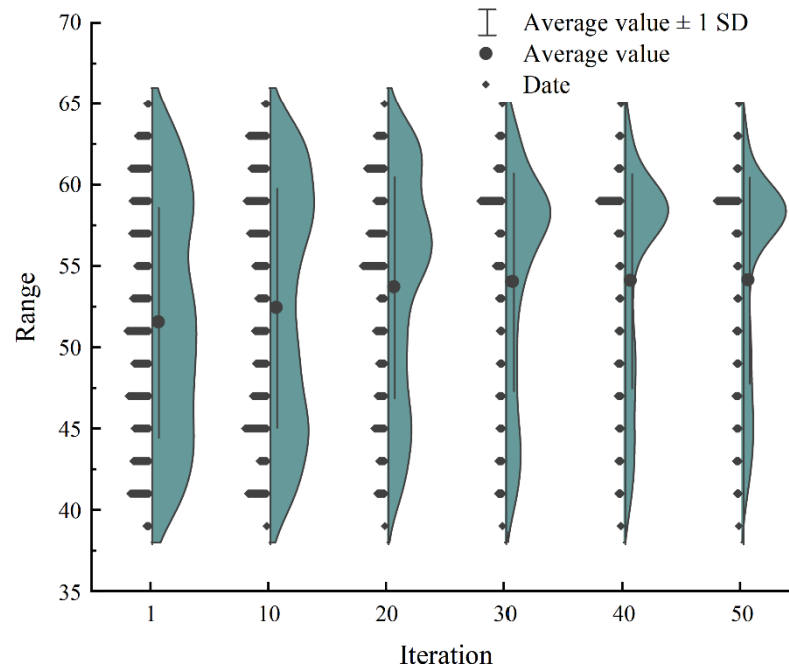


Figure 7. Population distribution of hydrant discharge during iteration.

Since the dimensions of the three models in this work are not the same, the feasible solution area is quite different. It is necessary to establish matching population sizes for different models. The orders of magnitude of OFM, PDM, and SOM are 10, 50, and 500, respectively. Therefore, to obtain better convergence, the designed population sizes are 1000, 2000, and 10,000. Figure 8 shows the model’s convergence iteration graph. Among them, the number of iterations is 30, the crossover probability is 0.4, the mutation probability is 0.2, the penalty coefficients are $\lambda_1 = 100$, $\lambda_2 = 100$, $\lambda_3 = 10,000$, the depreciation period is 50, the annual interest rate is 8%, and the average annual maintenance rate is 3%.

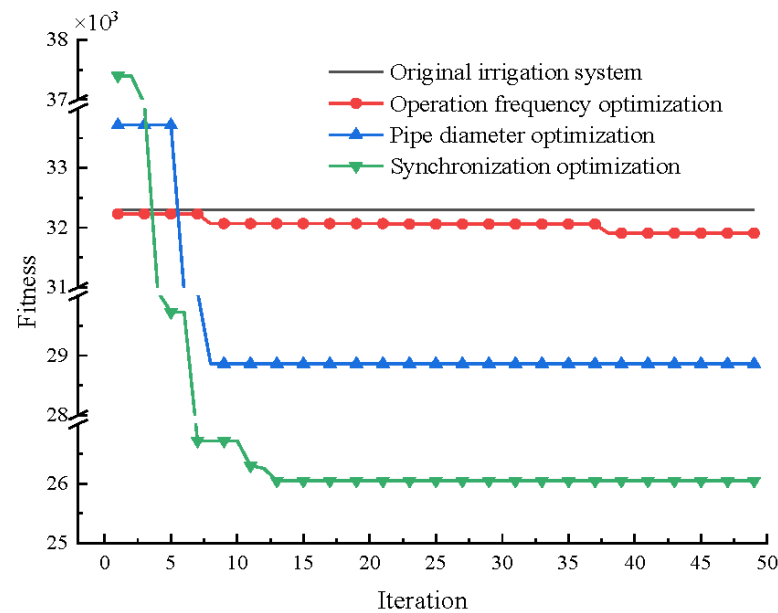


Figure 8. Iterative graph of cost for different optimization models.

3.2.2. Calculation Results

As shown in Figure 1, the branches in the irrigation sectoring have the same number of hydrants. However, asymmetry in the number of branch pipes often occurs in engineering

applications. Therefore, when solving programming, the length of the non-existent branch pipe segment should be set to 0, and its corresponding hydrant discharge should also be set to 0.

Table 5 shows the pump operating performance and irrigation period for all irrigation sectoring of different optimization models. PDM runs at power frequency (50 Hz), while OFM and SOM run at variable frequencies.

Table 5. Operating frequency, pump performance and irrigation period for all irrigation sectoring of different irrigation models.

Optimization Model	Irrigation Sectoring	Operating Frequency (Hz)	Pump Flow (m ³ /h)	Pump Head (m)	Pump Efficiency (%)	Irrigation Period (h)
PDM	1	50	844	11.2	81.6	5.1
	2	50	555	15.9	76.3	9.7
	3	50	626	14.9	79.4	8.3
	4	50	646	14.6	80	8.7
	5	50	673	14.2	80.7	6.1
OFM	1	42	593	9.6	79	8.4
	2	41	636	8.3	79.3	8.1
	3	45	727	9.6	80.4	7.1
	4	41	612	8.7	79.2	9.3
	5	44	644	10.2	75.5	7.6
SOM	1	50	579	15.6	77.5	8.6
	2	48	642	13.1	80.1	8.2
	3	43	581	10.4	78.8	8.2
	4	48	545	14.5	76.4	10.7
	5	43	593	12.3	79	6.5

Although both PDM and SOM optimize the pipe diameter, the SOM also optimizes the operation frequency. There is a clear difference in their pipe diameter optimization results, as shown in Table 6.

Table 6. The diameters of all branch pipe segments in the different irrigation models.

Optimization Model	Branch Pipe Number	Branch Pipe Segment Number						
		1	2	3	4	5	6	7
PDM	1	200	200	200	200	200	200	200
	2	250	250	250	250	250	315	-
	3	315	315	315	315	315	315	315
	4	160	200	200	200	315	315	-
	5	200	200	200	200	200	200	250
	6	200	250	250	250	315	315	-
	7	200	200	250	250	315	315	315
	8	160	200	200	200	200	200	-
	9	315	315	315	315	315	315	315
	10	160	160	160	200	-	-	-
SOM	1	200	200	200	200	250	250	315
	2	160	160	200	200	200	200	-
	3	160	160	160	200	250	250	315
	4	200	200	250	250	250	250	-
	5	200	200	200	315	315	315	315
	6	160	160	200	200	200	250	-
	7	160	160	160	160	250	250	2
	8	160	160	160	160	160	160	-
	9	160	160	200	250	315	315	315
	10	200	200	200	200	-	-	-

4. Discussion

The irrigation cost is the sum of the network and energy costs. Figure 9 shows the irrigation cost, including the network and energy costs of the original scheme and the three model schemes. As shown in Figure 9, the annual irrigation costs from high to low are the original scheme, OFM, PDM, and SOM. SOM can achieve a lower irrigation cost than OFM and PDM.

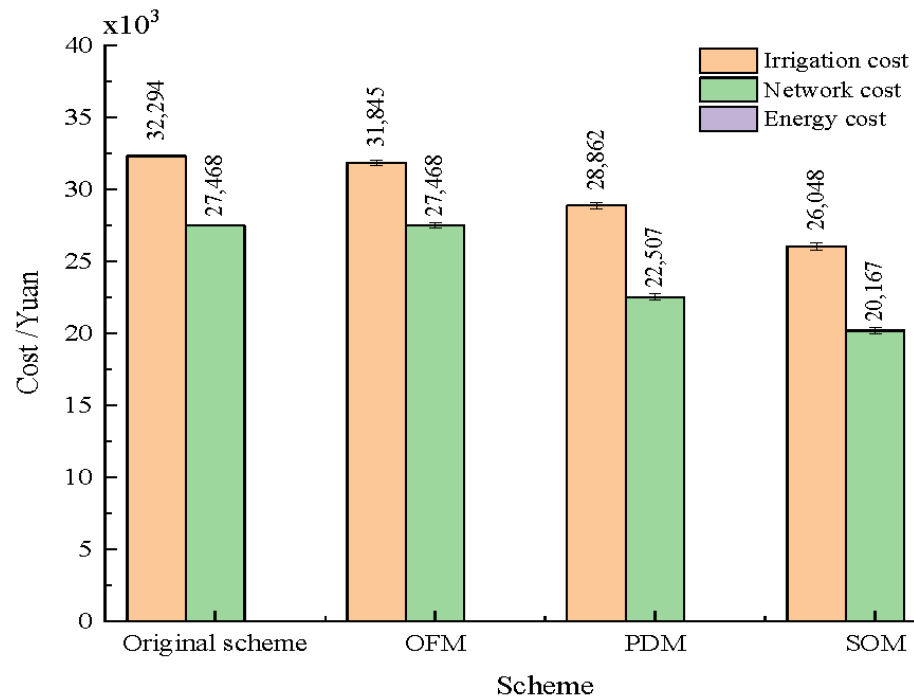


Figure 9. Irrigation cost, network cost and energy cost of the original scheme, OFM, PDM, SOM.

From the perspective of irrigation cost, the cost of a pipe network is about five times the energy consumption cost. Therefore, the pipe network optimization should reduce the pipe network cost as much as possible to complete the irrigation, rather than requiring the system to operate with lower energy consumption.

In order to compare the three optimization schemes with the original scheme, the savings rates of the irrigation cost, the network cost, and the energy cost are shown in Figure 10. A comparison between OFM and the original scheme indicates that the operation frequency optimization can achieve an energy-saving rate of 9.3%. It is verified that variable frequency drive optimization can reduce irrigation energy consumption [26,27]. However, the irrigation cost is only reduced by 1.4%, reflecting that the energy-saving effect of variable frequency drive is not apparent compared with the expensive pipe diameter cost. Furthermore, the irrigation costs of PDM and SOM are reduced by 10.6% and 19.3, the network costs are reduced by 18.1 and 19.3%, while the energy costs are increased by 31.7% and 21.9%, respectively. Therefore, although irrigation cost reduces while reducing the pipe diameter [7,16], it also has the detrimental effect of increasing energy consumption. Finally, a comparison between PDM and SOM shows that adding frequency conversion optimization can significantly reduce the irrigation cost, further reduction in the network cost and the energy consumption.

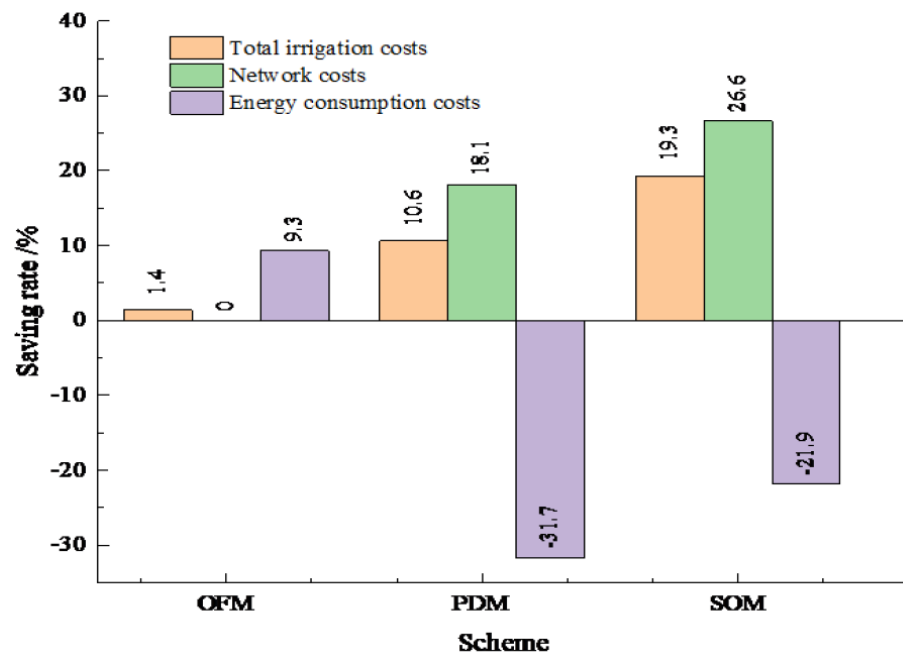


Figure 10. OFM, PDM, SOM compared with the original scheme, the saving rate of total irrigation cost, pipe network cost and energy cost.

5. Conclusions

In this study, the pipe diameter optimization model and operation frequency optimization model are established, and a synchronous optimization model for the selection of the pipe diameter and variable frequency is proposed. The premise of this research is the flattish terrain, for which the models are only applicable. If used in hilly areas, the terrain should be used as an important constraint to modify the model. Taking the irrigation cost of the sum of network costs and energy costs as the research objective and solving it using GA. The algorithm converges after 20 iterations, and the calculation results are stable after 50 iterations. It is proved that the algorithm has strong adaptability and can be used to solve symmetric and asymmetric PINs.

The market research and experimental results show that the annual network cost and annual energy costs respectively account for about 5/6 and 1/6 of the annual total cost. Therefore, the focus of piping optimization should be to reduce the cost of the pipeline network as much as possible, rather than the low-energy operation of the system.

The traditional pipe diameter optimization and operating frequency optimization aim to reduce network cost and operating energy consumption, respectively. The calculation results of these two models show that the cost-saving rates of pipe diameter optimization and frequency conversion optimization are 10.6% and 1.4%, respectively. It shows that both optimization models can reduce the irrigation cost, but the optimization of the pipe diameter can significantly reduce the cost of irrigation more than the optimization of the operating frequency. The reason is that the cost-saving effect of variable frequency drive will be weakened compared with the expensive pipe diameter cost.

Furthermore, compared with only the pipe diameter optimization and only the frequency conversion optimization, the proposed synchronization optimization model can significantly reduce the irrigation cost, while the saving rate increases from 1.4% and 10.6% to 19.3%, respectively. It shows that the synchronization optimization proposed, adding the frequency conversion optimization to the pipe diameter optimization, in this paper, has more advantages in reducing irrigation costs than the traditional optimization.

Author Contributions: Conceptualization, Y.P. and H.L.; methodology, Y.P. and P.T.; validation, Y.P.; formal analysis, Y.P. and C.C.; investigation, Y.P. and C.C.; data curation, Y.P.; writing—original draft preparation, Y.P.; writing—review and editing, P.T. and C.C.; visualization, Y.P.; supervision, P.T.; project administration, Y.P. and H.L. All authors have read and agreed to the published version of the manuscript.

Funding: This research was funded by National Natural Science Foundation of China, grant number 51939005; Key Research and Development Program of Jiangsu Province, grant number BE2021340; Jiangsu Agriculture Science and Technology Innovation Fund, grant number CX(19)2040; Graduate research and innovation plan project for the regular institution of higher learning in Jiangsu province, grant number KYCX21_3355.

Institutional Review Board Statement: Not applicable.

Informed Consent Statement: Not applicable.

Data Availability Statement: Not applicable.

Conflicts of Interest: The authors declare no conflict of interest.

References

1. Afshar, M.H. Application of a max–min ant system to joint layout and size optimization of pipe networks. *Eng. Optim.* **2006**, *38*, 299–317. [[CrossRef](#)]
2. Alandí, P.P.; Álvarez, J.F.O.; Martín-Benito, J.M.T. Optimization of irrigation water distribution networks, layout included. *Agric. Water Manag.* **2007**, *88*, 110–118. [[CrossRef](#)]
3. Caballero, J.A.; Ravagnani, M.A.S.S. Water distribution networks optimization considering unknown flow directions and pipe diameters. *Comput. Chem. Eng.* **2019**, *127*, 41–48. [[CrossRef](#)]
4. Jiménez-Bello, M.A.; Martínez, F.; Soler, V.B.; Ayala, H.J. Methodology for grouping intakes of pressurised irrigation networks into sectors to minimise energy consumption. *Biosyst. Eng.* **2010**, *105*, 429–438. [[CrossRef](#)]
5. Zhang, L.; Zhou, W.; Li, D. Research progress in irrigation mode selection of high-efficiency water-saving agriculture. *J. Drain. Irrig. Mach. Eng.* **2019**, *37*, 447–453. [[CrossRef](#)]
6. Shiono, N.; Suzuki, H.; Saruwatari, Y. A dynamic programming approach for the pipe network layout problem. *Eur. J. Oper. Res.* **2019**, *277*, 52–61. [[CrossRef](#)]
7. Afshar, M.H. Evaluation of selection algorithms for simultaneous layout and pipe size optimization of water distribution network. *Sci. Iran.* **2007**, *14*, 274–286. [[CrossRef](#)]
8. Boyne, G.G. The optimum design of fluid distribution networks with particular reference to low pressure gas distribution networks. *Int. J. Numer. Methods Eng.* **2010**, *5*, 253–270. [[CrossRef](#)]
9. Pérez, L.; Ortiz, J.; Pout, C. A review on buildings energy consumption information. *Energy Build.* **2008**, *40*, 394–398. [[CrossRef](#)]
10. Li, X.; Zhang, C.; Huo, Z. Optimizing irrigation and drainage by considering agricultural hydrological process in arid farmland with shallow groundwater. *J. Hydrol.* **2020**, *585*, 124785. [[CrossRef](#)]
11. Tsolas, S.D.; Karim, M.N.; Hasan, M.M.F. Optimization of water-energy nexus: A network representation-based graphical approach. *Appl. Energy* **2018**, *224*, 230–250. [[CrossRef](#)]
12. Ren, C.; Xie, Z.; Zhang, Y.; Wei, X.; Wang, Y.; Sun, D. An improved interval multi-objective programming model for irrigation water allocation by considering energy consumption under multiple uncertainties. *J. Hydrol.* **2021**, *602*, 126699. [[CrossRef](#)]
13. Córcoles, J.L.; de Juan, J.A.; Ortega, J.F.; Tarjuelo, J.M.; Moreno, M.A. Management evaluation of water users associations using benchmarking techniques. *Agric. Water Manag.* **2010**, *98*, 1–11. [[CrossRef](#)]
14. Ma, P.H.; Hu, Y.J.; Liu, H.S.; Li, Y.N. Simultaneous optimization of micro-irrigation subunit layout and pipe diameter and analysis of influencing factors. *J. Hydraul. Eng.* **2019**, *50*, 1350–1373. [[CrossRef](#)]
15. Giménez, J.L.; Calvet, J.L.; Alonso, A. A two-level dynamic programming method for the optimal design of sewerage networks. *IFAC Proc. Vol.* **1995**, *28*, 537–542. [[CrossRef](#)]
16. Zhao, R.H.; He, W.Q.; Lou, Z.K.; Nie, W.B.; Ma, X.Y. Synchronization optimization of pipeline layout and pipe diameter selection in a self-pressurized drip irrigation network system based on the genetic algorithm. *Water* **2019**, *11*, 489. [[CrossRef](#)]
17. Theocharis, M.E.; Tzimopoulos, C.D.; Sakellariou-Makrantonaki, M.A.; Yannopoulos, S.I.; Meletioui, I.K. Comparative calculation of irrigation networks using Labye’s method, the linear programming method and a simplified nonlinear method. *Math. Comput. Model.* **2010**, *51*, 286–299. [[CrossRef](#)]
18. Arai, Y.; Koizumi, A.; Inakazu, T.; Tamura, S. Optimized operation of water distribution system using multipurpose fuzzy LP model. *Water Sci. Technol. Water Supply* **2013**, *13*, 66–73. [[CrossRef](#)]
19. Aghdam, K.M.; Mirzaee, I.; Pourmahmood, N.; Aghababa, M.P. Adaptive Mutated Momentum Shuffled Frog Leaping Algorithm for Design of Water Distribution Networks. *Arab. J. Sci. Eng.* **2014**, *39*, 7717–7727. [[CrossRef](#)]
20. Bahoosh, S.; Bahoosh, R.; Haghighi, A. Development of a Self-Adaptive Ant Colony Optimization for Designing Pipe Networks. *Water Resour. Manag.* **2019**, *33*, 4715–4729. [[CrossRef](#)]

21. Lamaddalena, N.; Khila, S. Energy saving with variable speed pumps in on-demand irrigation systems. *Irrig. Sci.* **2012**, *30*, 157–166. [[CrossRef](#)]
22. Tolvanen, J. Saving energy with variable speed drives. *World Pumps* **2008**, *501*, 32–33. [[CrossRef](#)]
23. Lamaddalena, N.; Piccinni, A.F. Indexed characteristic curves of an irrigation network for the lifting plant design. *Riv. Ing. Agrar.* **1993**, *24*, 129–135. (In Italian)
24. AitKadi, M.; Lamaddalena, N.; Bouabe, Z.; El Yacoubi, Z. Study on the possibility of energy saving in an irrigation system equipped with pumping station. *Riv. Irrig. Dren.* **1998**, *45*, 25–30.
25. Díaz, J.A.R.; Luque, R.L.; Cobo, M.T.C.; Montesinos, P.; Poyato, E.C. Exploring energy saving scenarios for on-demand pressurised irrigation networks. *Biosyst. Eng.* **2009**, *104*, 552–561. [[CrossRef](#)]
26. Camoirano, R.; Dellepiane, G. Variable frequency drives for MSF desalination plant and associated pumping stations. *Desalination* **2005**, *182*, 53–65. [[CrossRef](#)]
27. Mahmoudi, M.; Dehghan, M.; Haghgou, H.; Keyanpour-Rad, M. Techno-economic performance of photovoltaic-powered air-Conditioning heat pumps with variable-speed and fixed-speed compression systems. *Sustain. Energy Technol. Assess.* **2021**, *45*, 101–113. [[CrossRef](#)]
28. Simpson, A.R.; Goldberg, D.E. Pipeline optimization via genetic algorithms: From theory to practice. In *Water Pipeline Systems*; Mechanical Engineering Publication: London, UK, 1994; pp. 309–320.
29. Zheng, F.; Simpson, A.R.; Zecchin, A.C. A decomposition and multistage optimization approach applied to the optimization of water distribution systems with multiple supply sources. *Water Resour. Res.* **2013**, *49*, 380–399. [[CrossRef](#)]
30. Zhan, H.; Yang, J.J.; Ding, Y.C. Improved Genetic Algorithm for Optimization of Multi-Source Pumping Tree-Type Pipe Network. *Adv. Mater. Res.* **2011**, *402*, 738–741. [[CrossRef](#)]
31. Sui, H.; Niu, W. Branch-Pipe-Routing Approach for Ships Using Improved Genetic Algorithm. *Front. Mech. Eng.* **2016**, *11*, 316–323. [[CrossRef](#)]
32. Abadia, R.; Rocamora, C.; Ruiz, A.; Puerto, H. Energy efficiency in irrigation distribution networks i: Theory. *Biosyst. Eng.* **2008**, *101*, 21–27. [[CrossRef](#)]
33. Abadia, R.; Rocamora, C.; Vera, J. Energy efficiency in irrigation distribution networks II: 1pplications. *Biosyst. Eng.* **2012**, *111*, 398–411. [[CrossRef](#)]
34. Planells, P.P.; Tarjuelo, J.M.; Ortega, J.F.; Casanova, M.I. Design of water distribution networks for on-demand irrigation. *Irrig. Sci.* **2001**, *20*, 189–201. [[CrossRef](#)]
35. GB/T 20203-2017. Technical Specification for Irrigation Projects with Pipe Conveyance (in China). 2017. AQSIQ, SAC. Available online: <http://std.samr.gov.cn/gb/search/gbDetailed?id=5DDA8BA1F40718DEE05397BE0A0A95A7> (accessed on 5 May 2022).
36. Lapo, C.M.; Pérez-García, R.; Izquierdo, J.; Ayala-Cabrera, D. Hybrid optimization proposal for the design of collective on-rotation operating irrigation networks. *Procedia Eng.* **2017**, *186*, 530–536. [[CrossRef](#)]
37. Maier, H.R.; Simpson, A.R.; Zecchin, A.C.; Foong, W.K.; Phang, K.Y.; Seah, H.Y.; Tan, C.L. Ant Colony Optimization for Design of Water Distribution Systems. *J. Water Resour. Plan. Manag.* **2003**, *129*, 200–209. [[CrossRef](#)]
38. Aguilar-Rivera, R.; Valenzuela-Rendón, M.; Rodríguez-Ortiz, J.J. Genetic Algorithms and Darwinian Approaches in Financial Applications: A Survey. *Expert Syst. Appl.* **2015**, *42*, 7684–7697. [[CrossRef](#)]
39. Slowik, A.; Kwasnicka, H. Evolutionary Algorithms and Their Applications to Engineering Problems. *Neural Comput. Appl.* **2020**, *32*, 12363–12379. [[CrossRef](#)]
40. Deb, K. An efficient constraint handling method for genetic algorithms. *Comput. Methods Appl. Mech. Eng.* **2000**, *186*, 311–338. [[CrossRef](#)]
41. Wang, X.K.; Cai, H.J. Multi-group genetic algorithms for optimization of pumping tree pipe network. *Trans. Chin. Soc. Agric. Mach.* **2004**, *6*, 20–22.
42. Wang, X.K. Optimization of pumping tree pipe network by using annealing-genetic algorithms based on infeasible degree. *Trans. Chin. Soc. Agric. Mach.* **2009**, *40*, 63–67.

Article

Study on the Hydraulic and Energy Loss Characteristics of the Agricultural Pumping Station Caused by Hydraulic Structures

Weixuan Jiao, Zhishuang Li, Li Cheng *, Yuqi Wang and Bowen Zhang

College of Hydraulic Science and Engineering, Yangzhou University, Yangzhou 214000, China

* Correspondence: chengli@yzu.edu.cn

Abstract: The pumping station is an important part of the agricultural irrigation and drainage system. The sump is one of the common water inlet types of agricultural pumping stations. In the sump, to facilitate the installation and maintenance of equipment, some hydraulic structures, such as pump beams, maintenance platforms and chest walls, are added to the sump. At present, the impact of hydraulic structures in the sump on the hydraulic performance of the pump device is not clear, so this paper focused on the impact of hydraulic structures on the hydraulic characteristics and entropy generation characteristics of the pump device by using numerical simulation methods. The results showed that the installation of hydraulic structures in the sump has the greatest impact on the efficiency of the pump device. The efficiency coefficient increased after adding a pump beam in the sump and decreased by about 2% after adding a maintenance platform and a water retaining chest wall. Results also showed that the installation of hydraulic structures in the sump will lead to uneven distribution of entropy generation in the sump, especially in the vicinity of the hydraulic structures. The installation of the maintenance platform and chest wall will lead to the increase of the total entropy generation in the sump, which also means that the hydraulic loss in the sump will increase accordingly. Hence, in addition to the pump beam, other structures should be avoided in the sump.

Keywords: agricultural engineering; irrigation and drainage system; pumping station; sump; hydraulic characteristics; entropy production

Citation: Jiao, W.; Li, Z.; Cheng, L.; Wang, Y.; Zhang, B. Study on the Hydraulic and Energy Loss Characteristics of the Agricultural Pumping Station Caused by Hydraulic Structures. *Agriculture* **2022**, *12*, 1770. <https://doi.org/10.3390/agriculture12111770>

Academic Editors: Muhammad Sultan, Redmond R. Shamshiri, Md Shamim Ahamed and Muhammad Farooq

Received: 27 September 2022

Accepted: 22 October 2022

Published: 25 October 2022

Publisher's Note: MDPI stays neutral with regard to jurisdictional claims in published maps and institutional affiliations.



Copyright: © 2022 by the authors. Licensee MDPI, Basel, Switzerland. This article is an open access article distributed under the terms and conditions of the Creative Commons Attribution (CC BY) license (<https://creativecommons.org/licenses/by/4.0/>).

1. Introduction

Irrigation and drainage system refers to the farmland water conservancy facilities that transport water from the irrigation water source to the field through irrigation channels (pipes) and buildings at all levels and drain the surplus water from the field through drainage ditches at all levels. When the water level of the irrigation water source is lower than the farmland surface, a pumping station needs to be built for water-lifting irrigation. Therefore, the pumping station is an important part of farmland irrigation and drainage systems. With the continuous acceleration of China's modernization, pumping station engineering in China has been dramatically developed. Small- and medium-sized irrigation and drainage pumping stations are widely used in agricultural irrigation and water drainage and have contributed significantly to the improvement of agricultural production conditions and China's modernization.

An open sump is a pumping station inlet building with a free water surface suction pipe to directly absorb water, which is the most common form of inlet in small and medium-sized pumping stations. The main function of the pumping station sump is to regulate the flow pattern in the sump and provide better inlet conditions for the pump inlet. Uneven flow distribution in the sump, or the emergence of a vortex sump, will not only significantly increase energy loss, affecting the device's efficiency, but also may lead to vibration of the pump device, so that it cannot work correctly. Only good inlet conditions can ensure the safe and efficient operation of the pump. Therefore, in order to improve the operation

efficiency of the agricultural irrigation pumping station and achieve the goal of energy saving and consumption reduction, it is necessary to study the hydraulic characteristics of the sump of the irrigation pumping station.

The sump in the actual project is widely used, so many experts and scholars on the open type into the sump have carried out a significant amount of experimental research, accessing many valuable results, and applied these to engineering practices. In 1998, Constantinescu et al. [1] simulated the flow field in a rectangular sump and accurately obtained the length and position of the vortex. Wang et al. [2] used the CFD method to simulate the three-dimensional turbulent flow in the coupled half-elbow sump of a large diameter axial flow pump, and found that there were increases in an obvious reflux phenomenon in the half-elbow sump and strong flow inhomogeneity at the outlet of the sump. Based on Reynolds shear stress distribution, a simplified Navier–Stokes equation, and a turbulent kinetic energy transport equation, Xi et al. [3] analyzed the formation mechanism of asymmetrically attached vortices in the side pump sump. Padmanabhan et al. [4] analyzed the scale effect of the experimental model of inflow flow. Denny et al. [5] systematically studied the vortex problem in the sump. Ansar et al. [6] analyzed in detail the flow patterns of the pump in the rectangular sump, with and without tangential reflux. With the emergence of modern flow testing technologies such as PIV and LDV, visualization of the flow field in pumps and pump devices has become the development direction of experimental research [7,8]. To sum up, experts and scholars have conducted a significant amount of research on the flow characteristics of the sump in pumping stations using numerical simulations and experimental methods, and research results have significantly guided practical projects. However, the actual engineering design often increases part of the structure in the sump to facilitate the installation and maintenance of equipment. After these structures are arranged, their influence on the flow pattern of the sump and the performance of the pump device is still unclear.

Helios et al. [9] presented an implementation of entropy generation analysis in the main flow field of a water jet pump via the CFD method. Yang et al. [10] obtained the result that the entropy production rate in the impeller is the highest among the components in the pump. With the increase in flow rate, the proportion of entropy generation of the impeller to the total value of the pump device increases continuously. Pei et al. [11] used the entropy generation method based on numerical results to assess the impact of distance on the internal flow loss distribution and overall power loss to gain a better understanding of the hydraulic loss mechanism. Fabian et al. [12] systematically analyzed the entropy generation of incompressible turbulent shear flows in Newtonian fluids and incorporated it into computational fluid dynamics programs. Zhou et al. [13] reviewed entropy generation in the pump flow, including energy loss analysis, design optimization, cavitation analysis, and fault diagnosis. Different perspectives were presented for future works and introduced to other methods such as kinetic energy dissipation theory to obtain procedures that reveal energy loss to improve the pump performance and try to understand the causes of pump failure. This review provided theoretical guidance for optimal design and assessment of the operational conditions in terms of irreversible flow losses in the pumps. Hou et al. [14] used the Reynolds stress turbulence model and energy equation model to numerically simulate 3D steady-state flow and calculate entropy generation through user-defined function codes. The range analysis was made to identify the optimal case indicating that a combination of local entropy production and orthogonal design is feasible for pump optimization. Using the results of direct numerical simulations, Donald M. McCeligot et al. [15] studied the entropy generated by friction in turbulent viscous layers with significant flow pressure gradients, including boundary layers and channels. About two-thirds or more of the entropy production per device surface area occurred there. Increasing the pressure gradient increased the direct dissipation and decreased the turbulent dissipation (in wall coordinates). Ghasemi et al. [16] studied the process of entropy generation in the by-pass transition scenario of a plate boundary layer. Here, transition occurred prematurely due to strong levels of free-stream turbulence. Reynolds-

Averaged Navier–Stokes (RANS) models and direct numerical simulations (DNS) were implemented to comprehensively study the local entropy generation and energy dissipation in pre-transitional and transitional regions. Guan et al. [17] analyzed the energy loss of double-suction centrifugal pumps by entropy generation theory. The numerical simulation results, verified by experiments, indicated that the difference in total entropy production under different flow rates is mainly affected by the entropy production in the central flow region. To explore the energy loss mechanism of PAT under different flow conditions, Lin et al. [18] used the entropy dissipation method to calculate the energy loss of each part of PAT, which could not only accurately calculate the energy loss but also diagnose the location and way of hydraulic loss. An et al. [19] applied the theory of entropy generation to the flow of a turbine and quantitatively analyzed the hydraulic loss characteristics of the turbine. Based on numerical simulation, Li et al. [20] introduced entropy generation theory to determine the flow loss of the whole passage. The variation of entropy production under different guide vane openings is presented. Zhang et al. [21] analyzed the energy dissipation mechanism of axial flow pump stations under reverse power generation using by entropy production method. In order to demonstrate the internal energy loss mechanism of the axial-flow pump, Yang et al. [22] calculated the energy loss of the total conduit of the pump device using the entropy generation method, and clarified the internal energy loss mechanism of the pump device. It can be seen that entropy generation theory has been widely used in the energy loss of hydraulic machinery. However, there are few studies on the entropy generation characteristics of the sump in the pumping station. In particular, the influence of the increase of hydraulic structures on the entropy generation characteristics of the sump is not clear.

At present, experts and scholars mainly focus on the analysis of internal flow characteristics, optimization of geometric parameters, and vortex control in the sump of the pumping station. Research on the common hydraulic structures in the sump is scarce. Because there are many different hydraulic structures in the sumps of actual pumping station projects, their influence on the flow characteristics in the sump and the hydraulic performance of the pump device cannot be ignored. Hence, this paper studied the influence of different hydraulic structures on the hydraulic characteristics and energy characteristics of the sump based on the steady control equations of incompressible fluid and the RNG k - ε turbulence model. The main contents include the following aspects: (1) The hydraulic performance curves of pump devices under different structure forms were obtained by calculation, the reasons for the formation of different curves were analyzed, and relevant suggestions are put forward; (2) Through numerical simulation of the pump device under different structure forms, the causes of the formation of different flow states were analyzed and combined with the weighted average angle and the velocity uniformity of further analysis, and a reasonable layout of the structure was proposed for engineering design reference; (3) Based on the entropy generation theory, a flow loss analysis of the sump with additional structures was carried out to obtain the structure layout plan with the minimum loss, the reason for the change of entropy generation, and the variation amplitude and proportion of different entropy generation were analyzed. This study can provide a reference for choosing different forms of hydraulic structures in practical engineering.

2. Numerical Calculation

2.1. Modeling case and Research Content

In this paper, a typical axial flow pumping station with ω -shaped back wall form was used as a model, and a sump with the pump was used as the research object. The design flow rate of the axial flow pump station is $2.6 \text{ m}^3/\text{s}$, and two 700ZLB-125 axial flow pumps are installed in the pumping station. The sump inside the pumping station is symmetrically distributed, the unilateral sump is 2.5 m wide and 2.0 m deep. The pump and suction pipe are placed in the sump, as shown in Figure 1a. This case is the prototype case. Because of the actual needs of the project, the pump beam is often added to the sump. The cross section of the pump beam is a rectangle of $0.35 \text{ m} \times 0.45 \text{ m}$, as shown in Figure 1b. To

facilitate the installation and maintenance of equipment, the pump beam will generally be widened to build a maintenance platform. The side length of the overhaul platform is 1.9 m and the height is 0.4 m, as shown in Figure 1c, as shown in Figure 1c. Some will set up a retaining parapet at the inlet of the sump, and the cross section of the chest wall is a rectangle of 0.32 m \times 0.35 m, as shown in Figure 1d.

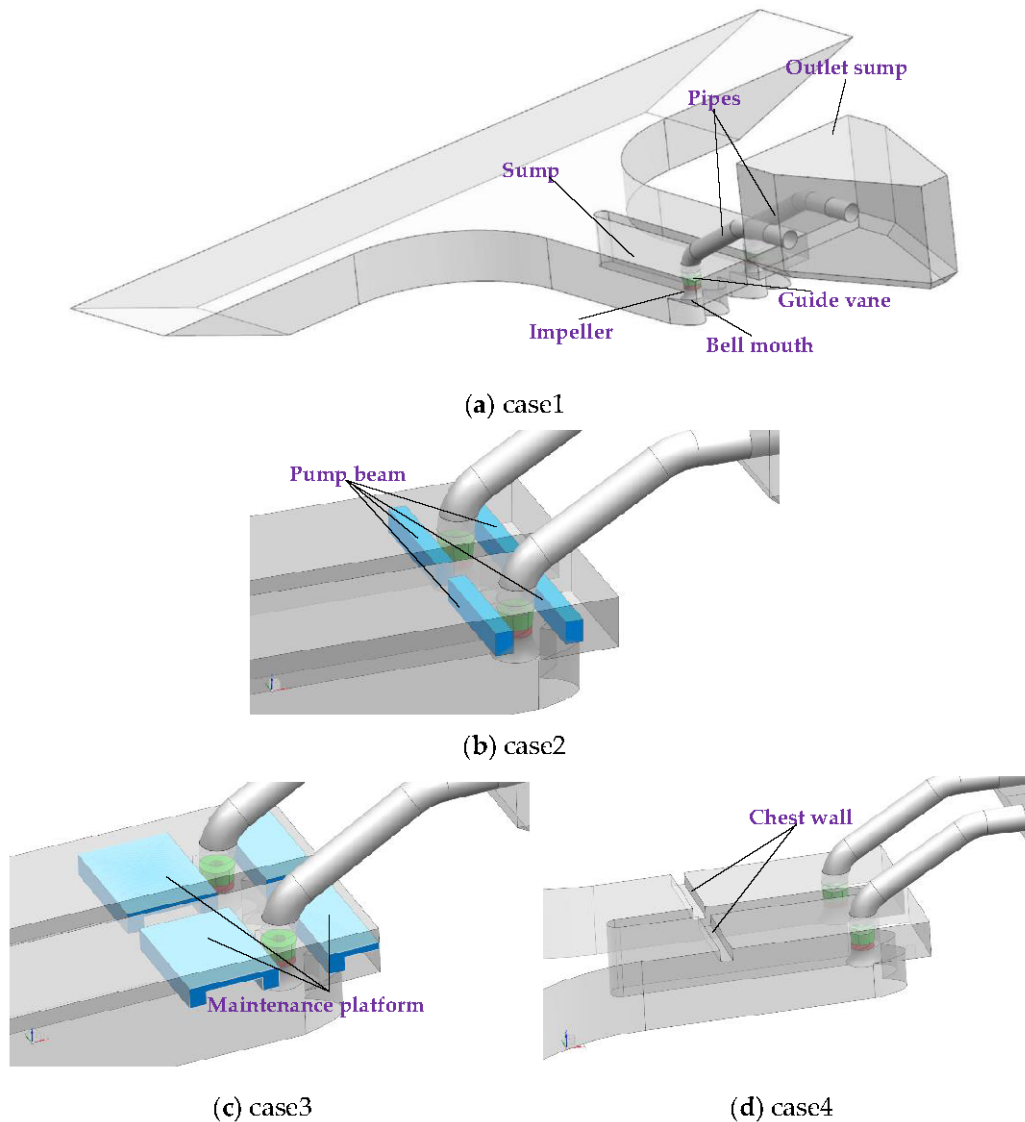


Figure 1. Design case of entering sump structure.

2.2. Governing Equation

The water flow in the open sump is in a complex three-dimensional turbulent state. This paper uses the continuity equation based on incompressible fluid and the time-averaged Reynolds equation (RANS equation), and the RNG $k-\epsilon$ model was used for the turbulence model. Several studies [23,24] have revealed that the RNG $k-\epsilon$ model can predict the swirling flow and vortex flow very well, and has good applicability in the flow field of the axial flow pump.

2.3. Generation of the Computational Grid

As shown in Figure 2, the entire computational domain was generated with hexahedral elements. The grid of the sump and impeller is presented in Figure 2. ICFM CFD software was utilized to mesh the sump, impeller, guide vanes, pipes, and outlet sump. When meshing the computational domain, the minimum angle of the grid was maintained

with a degree not less than 12° . The guide vane, the impeller, and the clearance meshed periodically. The poor-quality mesh was eliminated in this study through mesh refinement and Y-type mesh generation to ensure the grid quality of the pump device. In order to ensure the calculation accuracy, the mesh density of impeller and guide vane is encrypted. Since different turbulence models have different requirements on the grid y^+ input value, the RNG $k-\varepsilon$ model adopted in this paper requires the y^+ leaf value to be between 30 and 100. Since the calculation model includes the impeller, the mesh quality at the impeller has a great influence on the calculation results. The y^+ appreciation of the grid at the impeller was analyzed, and the y^+ value of the grid at the impeller was between 36.5 and 81.3. The y^+ value in the overall calculation domain is between 30 and 100, which meets the requirements of RNG $k-\varepsilon$ model.

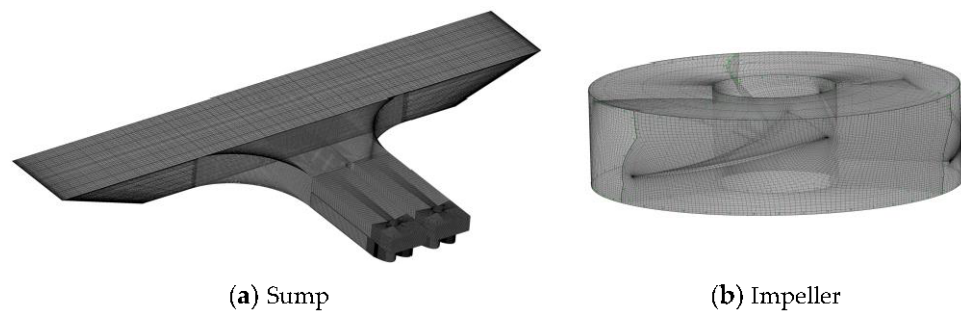


Figure 2. Grid division.

2.4. Grid Independence Analysis

The grid independence of the pump device is analyzed under the design flow condition. The numerical simulation was carried out under 9 cases of 3 million, 4 million, 5 million, 6 million, 7 million, 8 million, 9 million, 10 million, and 11 million respectively. As shown in Figure 3, the head is selected as the grid independence analysis index. It can be seen from the figure that with the increase in the number of grids, the head of the pump device shows a dynamic increasing trend, and tends to be stable after the number of grids reaches 9 million. Too many grids will consume computing resources, and too few grids cannot guarantee the accuracy of computing. Therefore, the number of grids for the pump device is finally determined to be 9 million.

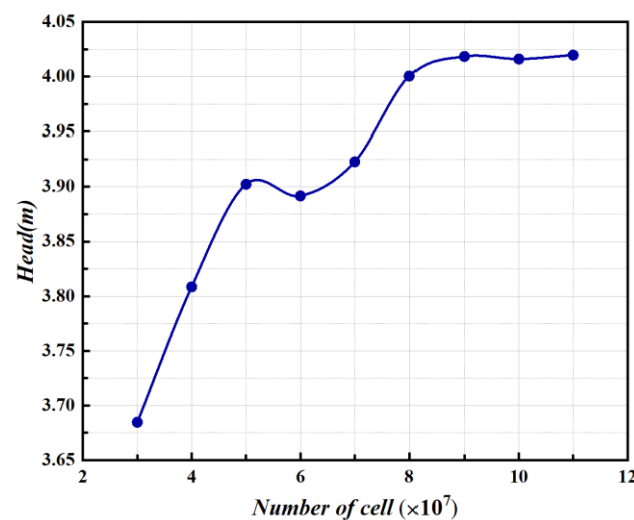


Figure 3. Grid independence analysis.

2.5. Boundary Condition Setting

The inlet is set at the upstream of the sump, and the incoming flow is considered to be uniform. The inlet of the forebay is set as the inlet boundary of the entire computational

domain, and mass flow rate is adopted as the inlet boundary condition. The nominal turbulence intensities (with a value equal to 5%) are used at the inlet boundary. The outlet of the outlet sump is set as the outlet boundary. An average static pressure outlet boundary condition is applied with 1 atm at the outlet. No-slip condition was applied at solid boundaries. The interfaces between the rotational impeller and static domain are set as the frozen stage condition. A multi-reference frame model is used to deal with the dynamic and static interface to ensure the continuity of the interface. The surface of the sump and outlet sump is a free water surface. The free surface remained almost unchanged, so the rigid-lid (RL) assumption method was used to process the free surface, and it was set as a symmetrical surface. The convergence precision is set to 10^{-5} .

3. Entropy production theory

To analyze the energy loss after the addition of structures in the sump, the entropy production calculation is performed in this paper. Entropy production is a phenomenon caused by the inevitable irreversibility of the actual fluid mechanical operation, mainly consisting of heat transfer entropy production and dissipation entropy production because the temperature remains almost constant throughout the flow process, so only the entropy production changes caused by dissipation are considered here. Zhang et al. [25] used the following entropy production theory in their study of flow loss in vertical shaft cross-flow pumps. In the general turbulent motion, dissipative entropy production mainly has three parts, the following are recorded S' , S'' , S''' , one for the turbulent direct dissipative entropy production S' , the average velocity primarily causes this part of the entropy production; two for the turbulent energy dissipation caused by the entropy production S'' , this part is mainly caused by the pulsation velocity; the first two are collectively referred to as the mainstream area entropy production S'' ; three is generated by the water flow and wall friction and wall entropy production S''' ; the sum of the three is the total dissipative entropy production S .

The entropy production \dot{S} is defined as (1):

$$\dot{S} = \frac{\dot{Q}}{t} \tag{1}$$

where \dot{Q} is the energy dissipation rate (W/m^3), t is the temperature, and its value is taken as 298.15 K, i.e., 25 °C, for the calculation.

The direct dissipation entropy production S' generated by the time-averaged velocity can be found by the following Equation (2):

$$\dot{S}' = \frac{2\mu}{t} \left[\left(\frac{\partial \bar{u}}{\partial x} \right)^2 + \left(\frac{\partial \bar{v}}{\partial y} \right)^2 + \left(\frac{\partial \bar{w}}{\partial z} \right)^2 \right] + \frac{\mu}{t} \left[\left(\frac{\partial \bar{v}}{\partial x} + \frac{\partial \bar{u}}{\partial y} \right)^2 + \left(\frac{\partial \bar{w}}{\partial x} + \frac{\partial \bar{u}}{\partial z} \right)^2 + \left(\frac{\partial \bar{v}}{\partial z} + \frac{\partial \bar{w}}{\partial y} \right)^2 \right] \tag{2}$$

where, μ is the kinematic viscosity (Pa·s); \bar{u} , \bar{v} , \bar{w} is the component of the time-averaged velocity in the x, y, and z directions (m/s).

The entropy production S' is integrated into the requested region, which leads to the direct dissipation of entropy production as (3):

$$S' = \int_V \dot{S}' dV \tag{3}$$

where, V is the volume of the calculation domain (m^3).

The entropy production resulting from turbulent dissipation S'' due to pulsating velocity is calculated as follows (4):

$$\dot{S}'' = \frac{\rho \varepsilon}{t} \tag{4}$$

where: ε is the turbulent kinetic energy dissipation rate (m^2/s^3).

Integrating the entropy production \dot{S}'' over the desired region gives the direct dissipative entropy production as (5):

$$S'' = \int_V \dot{S}'' dV \tag{5}$$

The wall entropy production \dot{S}''' generated by wall friction is calculated as follows (6):

$$\dot{S}''' = \frac{\tau \cdot v}{t} \tag{6}$$

where, τ is the wall shear stress, Pa; v is the relative velocity vector at the center of the first grid layer in the wall area (m/s).

The entropy production is integrated into the requested region. Thus the wall entropy production is obtained as (7):

$$S''' = \int_A \dot{S}''' dA \tag{7}$$

where: A is the calculated domain surface area (m^2).

4. Results and Discussion

4.1. External Characteristics

The impact of the structure in the open sump on the pump device is reflected in the influence on the efficiency and head. In different cases, the structure's influence on the pump device's performance is obtained through the comparison and analysis of the head ~ flow curve and efficiency ~ flow curve of the pump device in different cases.

In this paper, the influence of different structures on the performance of the pump device in the open sump is studied by numerical simulation. To facilitate comparison with the test results, the flow coefficient K_Q , head coefficient K_{HS} and efficiency K_η were used to analyze the calculation results with the following equations.

$$K_Q = \frac{Q}{ND^3} \tag{8}$$

where: Q is the volume flow rate in (m^3/s); N is the pump speed (rad/s); D is the impeller inlet diameter (m).

$$H_S = (P_{ins} - P_{outs})/\rho g \tag{9}$$

where: H_S is the pump head (m); P_{ins} and P_{outs} are the inlet and outlet static pressures (Pa); ρ is the density of water, taken as 10^3 kg/m^3 ; g is the acceleration of gravity, taken as 9.81 m/s^2 .

$$K_{HS} = \frac{gH_S}{(ND)^2} \tag{10}$$

$$H_T = (P_{int} - P_{out})/\rho g \tag{11}$$

where: H_T is the total head (m); P_{int} is the total pump inlet pressure (Pa); P_{out} is the total pump outlet pressure (Pa).

$$P_{shaft} = \frac{2\pi TN}{1000 \cdot 60} \tag{12}$$

$$\eta = \frac{\rho g Q H_T}{P} \tag{13}$$

$$\eta = \frac{9550 \rho g Q H_T}{TN} \tag{14}$$

$$K_{\eta} = \frac{g\eta}{N^3 D^5} \tag{15}$$

where P_{int} is the total pump inlet pressure (Pa); P_{out} is the total pump outlet pressure (Pa); η is the pump efficiency; T is the torque on the impeller in N·m; P_{shaft} is the shaft power (kW).

Figures 4 and 5 show the performance curves of pump devices with different structure cases. According to the $K_Q \sim K_{HS}$ curves of the four cases in Figure 4, the head coefficient increases with the flow rate decreases. When reduced to a certain flow rate, the head increases slowly, but beyond this area, the head rises sharply again. To further explore the influence of different structures on the performance of the pump device, the $K_Q \sim K_{HS}$ and $K_Q \sim K_{\eta}$ curves of different cases are compared.

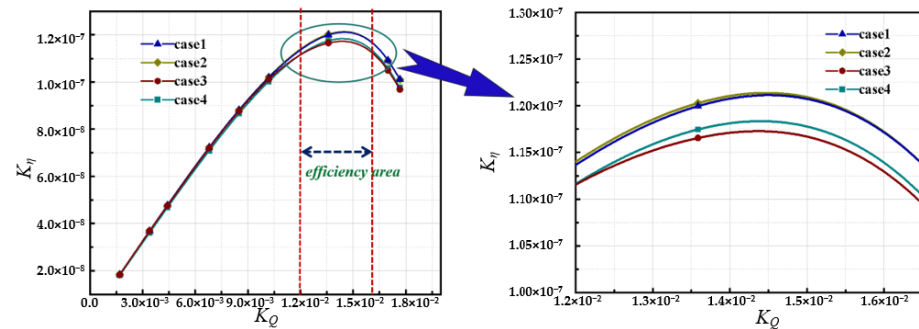


Figure 4. Efficiency ~ flow rate curves.

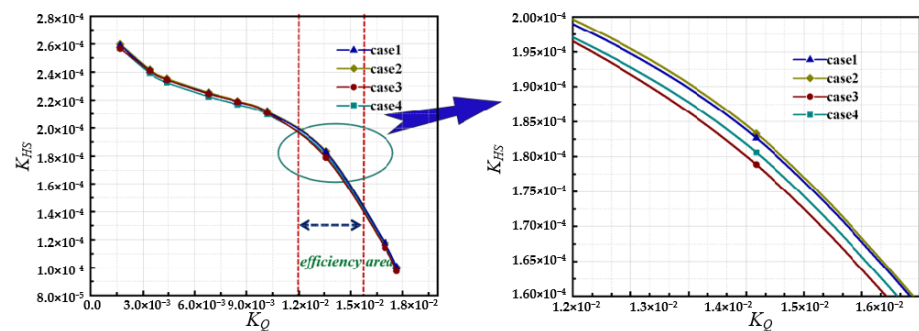


Figure 5. Head ~ flow rate curves.

It can be seen from the Figure 4, the $K_Q \sim K_{\eta}$ curves of the pump device are approximately the same under different construction conditions, and the efficiency coefficient increases and then decreases with the rise of the flow coefficient. The highest efficiency point is reached around the design flow rate. In the case of the design flow coefficient, the efficiency coefficients of case 1 and case 2 are similar. The efficiency coefficients of case 3 are slightly lower than those of the prototype. By comparing the four sets of data, it is easy to find that the installation of a maintenance platform in the sump has the greatest impact on the hydraulic performance of the pump device. The efficiency coefficient increased after adding a pump beam in the sump and decreased by about 2% after adding a maintenance platform and a water retaining chest wall.

It can be seen from Figure 5 that the $K_Q \sim K_{HS}$ curves of the pump device are roughly the same under different construction conditions. Under large flow, the head coefficient K_{HS} is small. When the flow rate is small, the head coefficient is significant. Case 1 is close to case 2, and case 3 and case 4 have slightly lower head coefficients than the prototype. To sum up, the structure of the sump affects the efficiency of the pump device, and the impact on the head is negligible.

4.2. Internal Characteristics

The sump is the installation of a water pump inlet pipe building, general requirements into the sump hydraulic design should meet two conditions: one is the sump water flow

smooth, the hydraulic loss is slight, no harmful vortex, to ensure that the pump device does not produce performance deterioration and mechanical vibration; Second, the velocity distribution of inlet section of pump impeller chamber is uniform and perpendicular to the area to ensure that the pump device reaches its best operating condition. For this reason, in this paper, the flow analysis is carried out mainly at the longitudinal section of the sump, and the axial velocity analysis at the pump inlet through numerical simulation.

4.2.1. Longitudinal Profile Flow Analysis

As seen from Figure 6a, when the sump is without the hydraulic structures, the flow pattern in the sump is stable and the streamline is smooth. However, due to the barrier effect of the wall at the back wall, it is easy to form backflow at the back wall.

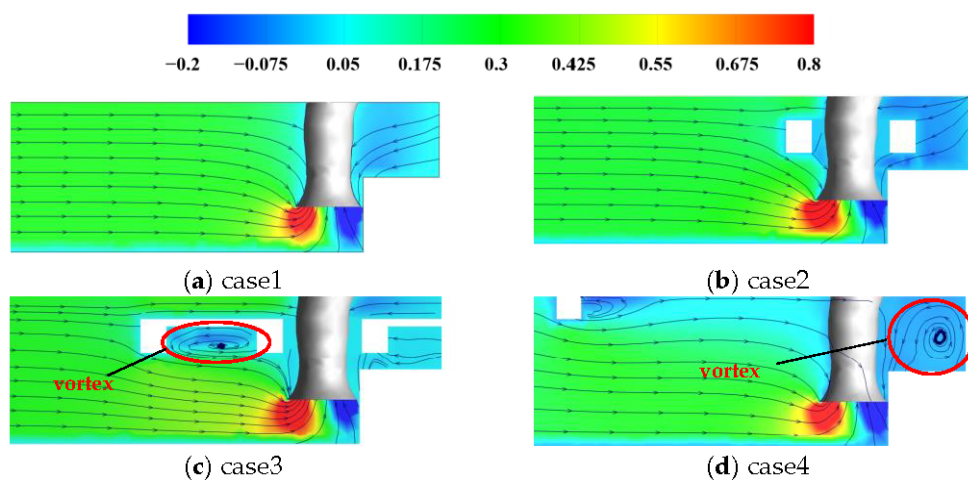


Figure 6. Contour of velocity distribution in longitudinal profile of the sump.

As seen from Figure 6b, when the pump beam is added to the sump, the influence of the pump beam on the streamline and velocity distribution in the sump can be almost ignored. Since the water space at the ω -shaped back wall is squeezed, and the original water structure is broken after the pump beam is added, the backflow at the back wall is difficult to form and the velocity distribution is more uniform.

As seen from Figure 6c, when the maintenance platform is added to the sump, the velocity distribution in the sump becomes uneven, and the transverse vortex is easy to form under the maintenance platform at the inlet side. Since the vortex occurs close to the inlet of the pump, it is very easy to be sucked in by the pump, thus aggravating the cavitation of the pump and affecting the safe operation of the pump. After the maintenance platform is installed at the ω -shaped rear wall, although the maintenance platform also breaks the original water structure, it also blocks the flow of water, leading to more chaotic flow patterns.

As seen from Figure 6d, after the additional chest wall, there is a vortex after the chest wall, affected by the vertical extrusion of the chest wall, the water flow in the middle of the sump can only enter the flapper pipe from the front half of the inlet pipe together with the lower water flow, and the water flow in the near-wall area goes around to the back of the inlet pipe and forms a backflow in the platform above the ω -shaped back wall after the inlet pipe, which affects the stable operation of the pump.

4.2.2. Flow state analysis of bell mouth

The bell mouth is the only channel for water flow into the pump in the sump, so the flow state at the bell mouth directly affects the performance of the pump. Figure 7 shows the distribution of streamline at the bottom of the sump. It can be seen from Figure 7a that the water flow at the bottom of the sump enters the bell mouth evenly from around the bell mouth. The streamline distribution is relatively uniform. The overall water flow in the

sump is stable without an adverse flow pattern. As shown in Figure 7b, when the pump beam is added to the sump, the flow pattern in the sump is almost unaffected. At this time, the water at the bell mouth is still evenly flowing into the bell mouth from around, but the streamline at the bell mouth is slightly disordered. As shown in Figure 7c, when the maintenance platform is added to the sump, the flow pattern distribution in the sump starts to become uneven, and the streamline at the inlet of the bell mouth starts to become disordered. As shown in Figure 7c, when the chest wall is added to the sump, the upper water flow in the sump will be disturbed greatly and the flow pattern will be uneven due to the water blocking of the chest wall. In particular, the water inlet state at the bell mouth changes from uniform water inlet in four directions to water inlet in three directions.

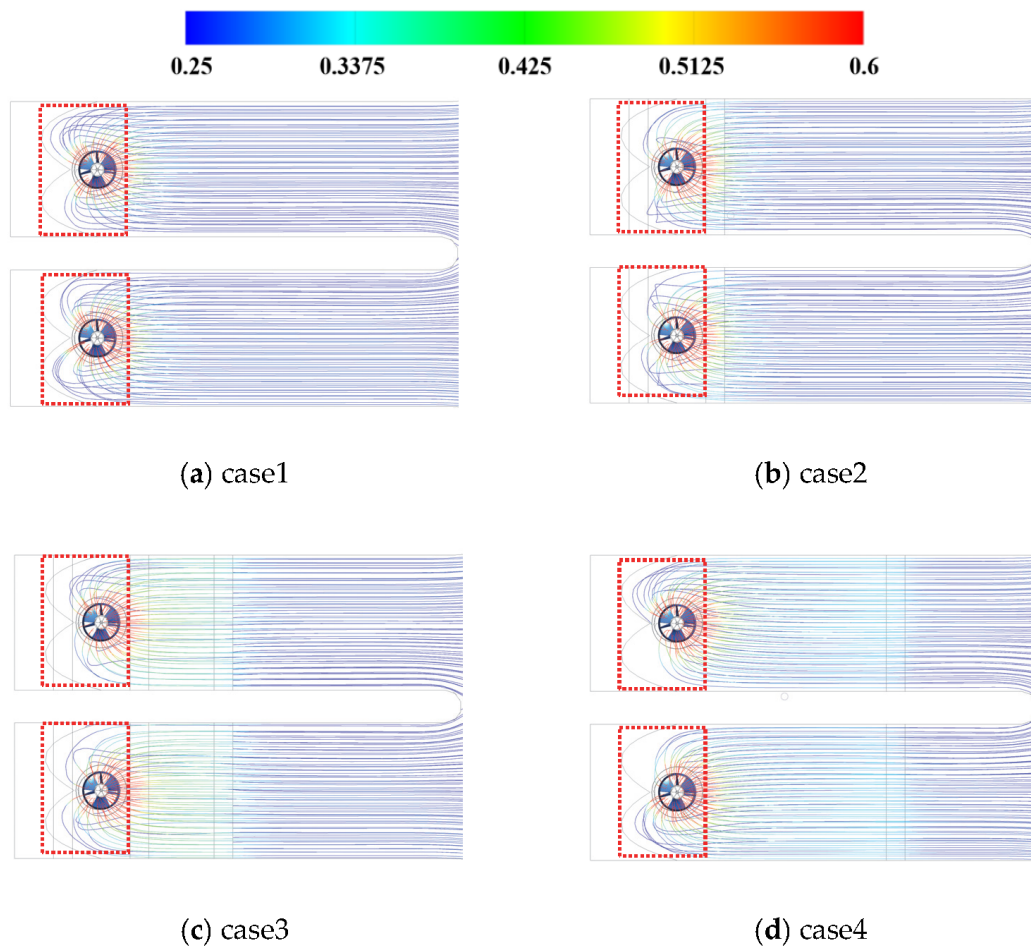


Figure 7. Streamlines distribution in the sump under different cases.

The uniformity of the velocity distribution and weighted velocity average swirl angle are important indexes to describe the flow pattern at the inlet of the bell mouth. The uniformity of the velocity distribution at the impeller inlet section is represented by the axial velocity distribution coefficient V_u . The axial velocity distribution is best when its coefficient is closer to 100%. The following formula is used to calculate V_u :

$$V_u = \left[1 - \frac{1}{\bar{v}_a} \sqrt{\frac{\sum (v_{ai} - \bar{v}_a)^2}{m}} \right] \times 100\% \tag{16}$$

where v_{ai} is the axial velocity of each element of the calculated section (m/s), \bar{v}_a is the averaged axial velocity of the calculated section (m/s), and m is the number of cells of the calculated section.

The weighted velocity average swirl angle $\bar{\theta}$ is used to measure the inflow conditions of the impeller. The flow angle perpendicular to the impeller inlet section is better when $\bar{\theta}$ is closer to 90° . The following formula is used to calculate $\bar{\theta}$:

$$\bar{\theta} = \frac{\sum_{i=1}^n \left[v_{ai} \left(90 - \arctan \frac{v_{ti}}{v_{ai}} \right) \right]}{\sum_{i=1}^n v_{ai}} \quad (17)$$

where v_{ti} is the tangential velocity of each element of the calculated section (m/s).

Figure 8 shows the uniformity of the velocity distribution and the weighted velocity average swirl angle of the bell mouth inlet for different cases at design flow rates, from which it can be seen that:

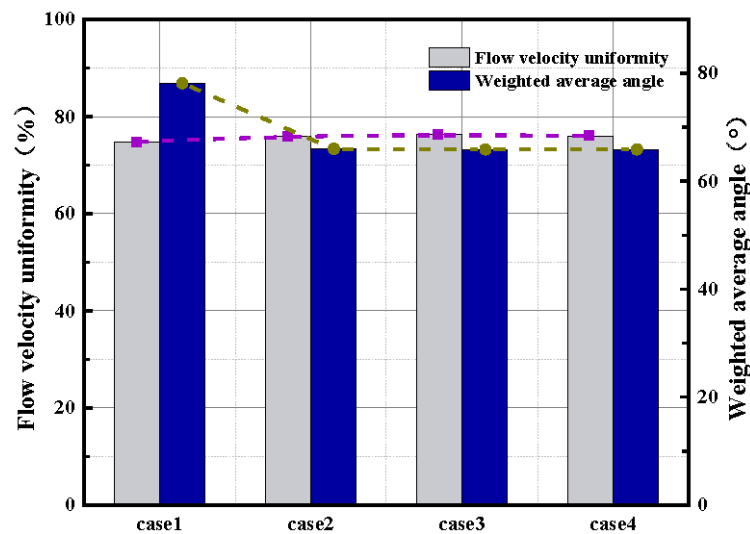


Figure 8. The uniformity of the velocity distribution and weighted velocity average swirl angle at the bell mouth inlet.

The addition of structures in the sump has an obvious influence on the weighted average angle at the inlet of the bell mouth, but has little influence on the velocity distribution at the inlet of the bell mouth. This is also consistent with the previous research results. Compared with the prototype case, the weighted average angle of the other three cases has a significant decrease, which indicates that the addition of the structure will have a certain impact on flow pattern of the sump, which may cause some hydraulic losses. Unlike flow uniformity, adding structures in the sump will affect the weighted average angle of the bell mouth inlet. The weighted average angle of 86.80° for the prototype case, 73.30° for case 2e, 73.19° for case 3, and 73.17° for case 4. The installation of structures in the sump has little impact on the velocity distribution, but has a greater impact on the angle of the pumped water flow. This is mainly because the installation of structures will break the original water structure, hinder the flow of water, and cause the angle of the pumped water flow to deflect.

4.3. Entropy Production

4.3.1. Entropy Production Distribution Characteristic

Figure 9 shows the entropy production of various cases in the sump under the designed flow rate. From Figure 9, it can be seen that the total entropy production of case 2 is slightly smaller than that of the prototype, the total entropy production of case 3 is significantly larger than that of the prototype, and the total entropy production of case 4 is slightly increased compared with that of the prototype. It indicates that adding pump beams in the sump will reduce the energy loss in the sump, while adding maintenance platforms and water retaining chest walls in the sump will increase the energy loss in the sump.

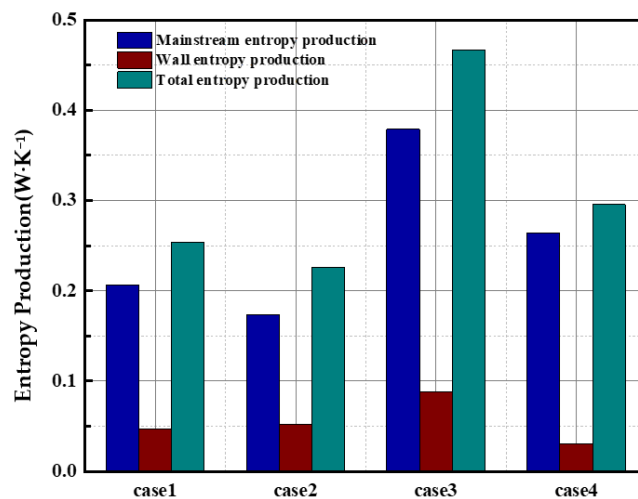


Figure 9. Dissipation entropy production value of each case.

The reasons for the change in entropy production are further analyzed according to Table 1. The total entropy production value of case 2 is $0.28 \text{ W}\cdot\text{K}^{-1}$ lower than that of the prototype case, in which the direct dissipation entropy production and turbulent energy dissipation entropy production are slightly reduced compared to the prototype case, but the wall dissipation entropy production increases compared to the prototype case. With the addition of the pump beam, the turbulent flow losses in the sump are reduced, but the entropy production from the friction between the water flow and the wall surface is increased. The entropy production of all parts of case 3 increased significantly compared to the prototype case, which indicates that the addition of an access platform in the sump has a greater impact on the energy loss in the sump. The total entropy production value of case 4 is slightly greater than the prototype case, in which the direct dissipation entropy production is smaller than the prototype case, and the turbulent motion entropy production and wall entropy production are greater than the prototype case, which indicates that the additional water retaining chest wall in the sump has a certain effect on the flow loss in the sump.

Table 1. Dissipation entropy production of each case.

Case	Entropy Production Value ($\text{W}\cdot\text{K}^{-1}$)			
	Direct Dissipation Entropy Production S'	Turbulent Energy Dissipation Entropy Production S''	Wall Dissipation Entropy Production S'''	Total Entropy Production
1	1.81×10^{-3}	0.205	0.048	0.254
2	1.54×10^{-3}	0.172	0.052	0.226
3	1.92×10^{-3}	0.377	0.088	0.467
4	1.23×10^{-3}	0.263	0.031	0.295

In order to further explore the energy loss under the design flow, the entropy production ratio of each category in the sump under the four cases of prototype cases, additional pump beam, additional maintenance platform, and additional water retaining chest wall pump were analyzed respectively. It can be seen from Figure 10 that the direct dissipation entropy production ratio of all four cases is the lowest, below 1%, and the turbulent dissipation entropy production ratio is the largest, above 75%. The direct dissipation percentage of the prototype case is 0.71%, which is larger than 0.68% of case 2, 0.41% of case 3 and 0.42% of case 4. The wall entropy production ratio varies widely, with the largest wall entropy production ratio of 23.09% for case 2, close to that of case 3 and the prototype case, and the smallest wall entropy production ratio of 10.49% for case 4. The turbulent dissipative

entropy production of case 4 is the largest, 8.52% higher than that of the prototype case, the dissipative entropy production of cases 1 and 3 are similar, and the turbulent dissipative entropy production of case 2 is 76.23%, which is 4.34% less than that of the prototype case.

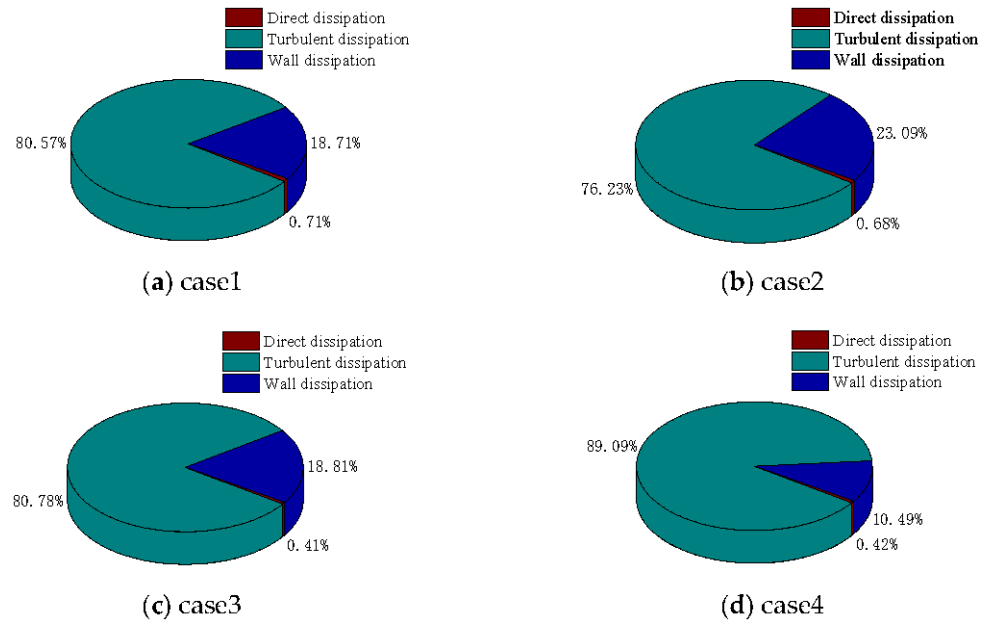


Figure 10. Percentage of entropy production by type.

4.3.2. Internal Flow Characteristics

To further investigate the entropy production distribution inside the sump, the entropy production inside the sump and impeller of the four cases were further analyzed under the design working conditions. From Figure 11a, the entropy production distribution inside the sump is more uniform when the structures inside the sump are not increased, and the location of the local high entropy production area is mainly concentrated in the bottom location of the sump. From Figure 11b, it can be seen that after adding the pump beam, a local high entropy production region appears behind the pump beam on the inlet side, in addition to a local increase in entropy production at the pump beam at the ω -shaped back wall. As can be seen in Figure 11c, after the addition of the access platform, localized high entropy production regions appear above and below the access platform on the inlet side. As shown in Figure 11d, after adding the water retaining chest wall in the sump, a more regular localized high entropy production area appears after the chest wall by the extrusion of the water retaining chest wall. As seen above, adding structures to the sump will impact the entropy production distribution in the sump, and the high entropy production area is mainly concentrated in the front and rear of the structures.

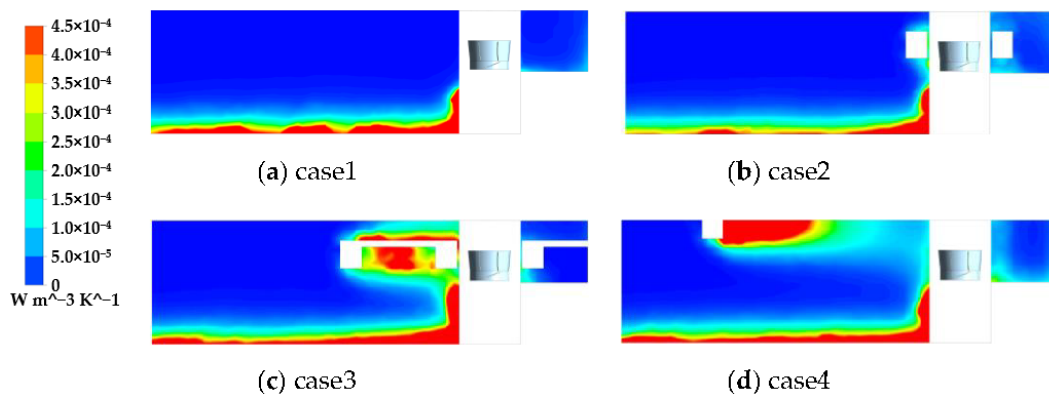


Figure 11. Contour of entropy production distribution in longitudinal section.

Figures 12 and 13 shows the entropy production at the hub and rim of the impeller under the design working condition. The figure shows that the high entropy production area at the hub is mainly concentrated in the front and middle of the suction surface, and the high entropy production area at the wheel rim is consistent with that at the hub. The distribution of entropy production at the wheel rim and the wheel hub is approximately the same for cases 1 to 4, which indicates that the addition of structures in the sump has no effect on the distribution of entropy production at the impeller, and the entropy production at the impeller is mainly related to the rotation of the impeller itself.

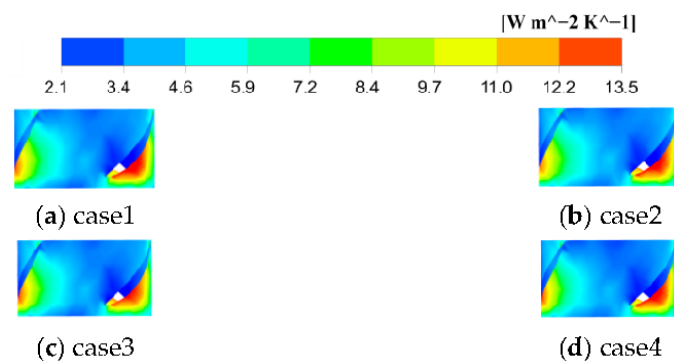


Figure 12. Entropy production contour at the hub.

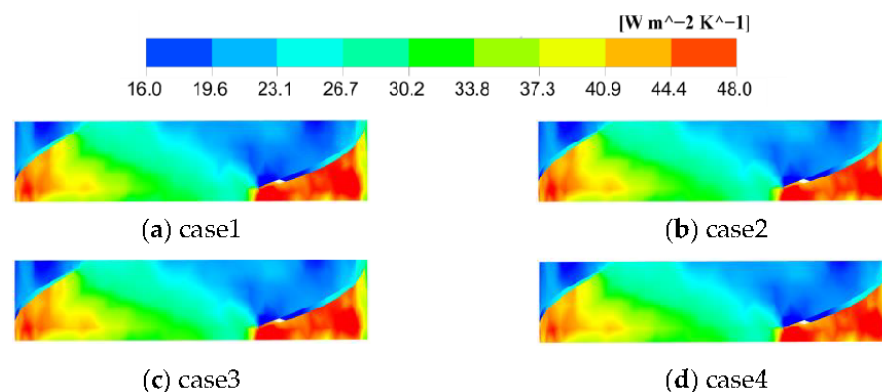


Figure 13. Entropy production contour at the rim.

5. Conclusions

The sump is one of the common types of agricultural irrigation pumping stations. In this paper, the numerical simulation method is used to study the influence of hydraulic structures on the hydraulic characteristics and entropy generation characteristics of the pump device. The conclusions are summarized as follows:

(1) The installation of hydraulic structures in the sump of the pumping station has a certain impact on the hydraulic performance of the pump device. The pump beam installed in the sump plays a role of rectification to a certain extent, and the size of the pump beam is relatively small, so its impact on the hydraulic performance of the pump device can be ignored. However, the maintenance platform and chest wall have a great impact on the flow pattern in the sump and the hydraulic performance of the pump device;

(2) The installation of hydraulic structures in the sump of the pumping station has obvious effect on the flow pattern in the sump. The installation of hydraulic structures will have adverse effects on the velocity uniformity and weighted average angle of flow at the bell mouth in the sump. Moreover, the installation of the maintenance platform and chest wall will directly affect the inlet flow pattern of the bell mouth;

(3) The installation of hydraulic structures in the sump will lead to uneven distribution of entropy generation in the sump, especially in the vicinity of hydraulic structures. The installation of the maintenance platform and chest wall will lead to the increase of the total

entropy generation in the sump, which also means that the hydraulic loss in the sump will increase accordingly.

Therefore, comprehensive consideration of the impact mentioned above, in addition to the arrangement of the necessary pump beam indicates that the set-up of a maintenance platform and chest wall in the sump should be avoided.

Author Contributions: Software, Z.L and W.J.; validation, Y.W. and W.J.; formal analysis, Z.L., B.Z. and W.J.; data curation, B.Z. and L.C.; writing—original draft preparation, Z.L. and W.J.; Funding acquisition, L.C.; writing—review and editing, L.C. and W.J. All authors have read and agreed to the published version of the manuscript.

Funding: This research was supported by the National Natural Science Foundation of China (Grant No: 52279091).

Institutional Review Board Statement: Not applicable.

Data Availability Statement: Not applicable.

Conflicts of Interest: The authors declare no conflict of interest.

References

- Constantinescu, S.G.; Patel, V.C. Numerical model for simulation of pump-intake flow and vortices. *J. Hydraul. Eng.* **1998**, *125*, 123–134. [\[CrossRef\]](#)
- Wang, F.J.; Li, Y.J.; Cong, G.H. CFD simulation of 3D flow in large-bore axial-flow pump with half-elbow suction sump. *J. Hydrodyn. Ser. B* **2006**, *18*, 243–247.
- Xi, W.; Lu, W.G. Formation mechanism of an adherent vortex in the side pump sump of a pumping station. *Int. J. Simul. Model.* **2021**, *20*, 327–338. [\[CrossRef\]](#)
- Padmanabhan, M.; Hecker, G.E. Scale effects in pump summodels. *J. Hydraul. Eng. ASCE* **1984**, *110*, 1540–1556. [\[CrossRef\]](#)
- Denny, D.F. An experimental study of air-entraining vortices in pump sumps. *IMEchE. Proc. Inst. Mech. Eng.* **1956**, *170*, 106–116. [\[CrossRef\]](#)
- Ansar, M.; Tatsuaki, N. Experimental study of 3D pump intake flows with and without cross flow. *J. Hydraul. Eng.* **2001**, *127*, 825–834. [\[CrossRef\]](#)
- Liu, C.; Li, D.; Zhou, J.; Tang, F. Application of 3D-PIV to the flow measurements in pump sump. In Proceedings of the ASME/JSME 2007 5th Joint ASME/JSME Fluids Engineering Conference, San Diego, CA, USA, 30 July–2 August 2007.
- Jiao, W.X.; Chen, H.J.; Cheng, L.; Zhang, B.W.; Yang, Y.; Luo, C. Experimental study on flow evolution and pressure fluctuation characteristics of the underwater suction vortex of water jet propulsion pump unit in shallow water. *Ocean Eng.* **2022**, *266*, 112569. [\[CrossRef\]](#)
- Helios, M.P.; Asvapoositkul, W. Numerical studies for effect of geometrical parameters on water jet pump performance via entropy generation analysis. *J. Mech. Eng. Sci.* **2021**, *15*, 8319–8331. [\[CrossRef\]](#)
- Yang, F.; Li, Z.; Hu, W.; Liu, C.; Jiang, D.; Liu, D.; Nasr, A. Analysis of flow loss characteristics of slanted axial-flow pump device based on entropy production theory. *R. Soc. Open Sci.* **2022**, *9*, 208–211. [\[CrossRef\]](#)
- Pei, J.; Meng, F.; Li, Y.J.; Yuan, S.Q.; Chen, J. Effects of distance between impeller and guide vane on losses in a low head pump by entropy production analysis. *Adv. Mech. Eng.* **2016**, *8*, 2071837044. [\[CrossRef\]](#)
- Kock, F.; Herwig, H. Local entropy production in turbulent shear flows a high-Reynolds number model with wall functions. *Int. J. Heat Mass Transf.* **2004**, *47*, 2205–2215. [\[CrossRef\]](#)
- Zhou, L.; Hang, J.; Bai, L.; Krzemianowski, Z.; El-Emam, M.A.; Yasser, E.; Agarwal, R. Application of entropy production theory for energy losses and other investigation in pumps and turbines: A review. *Appl. Energy* **2022**, *318*, 119211. [\[CrossRef\]](#)
- Hou, H.; Zhang, Y.; Zhou, X.; Zuo, Z.; Chen, H. Optimal hydraulic design of an ultra-low specific speed centrifugal pump based on the local entropy production theory. Proceedings of the Institution of Mechanical Engineers, Part A. *J. Power Energy* **2019**, *233*, 715–726. [\[CrossRef\]](#)
- McEligot, D.M.; Nolan, K.P.; Walsh, E.J.; Laurien, E. Effects of pressure gradients on entropy generation in the viscous layers of turbulent wall flows. *Int. J. Heat Mass Transf.* **2008**, *51*, 1104–1114. [\[CrossRef\]](#)
- Ghasemi, E.; McEligot, D.M.; Nolan, K.P.; Crepeau, J. Entropy generation in a transitional boundary layer region under the influence of freestream turbulence using transitional RANS models and DNS. *Int. Commun. Heat Mass Transf.* **2013**, *41*, 10–16. [\[CrossRef\]](#)
- Guan, H.; Jiang, W.; Yang, J.; Wang, Y.; Zhao, X.; Wang, J. Energy loss analysis of the double-suction centrifugal pump under different flow rates based on entropy production theory. Proceedings of the Institution of Mechanical Engineers, Part C. *J. Mech. Eng. Sci.* **2020**, *234*, 4009–4023. [\[CrossRef\]](#)
- Lin, T.; Li, X.; Zhu, Z.; Xie, J.; Li, Y.; Yang, H. Application of entropy dissipation to analyze energy loss in a centrifugal pump as turbine. *Renew. Energy* **2021**, *163*, 41–55. [\[CrossRef\]](#)

19. Yu, A.; Tang, Y.; Tang, Q.; Cai, J.; Zhao, L.; Ge, X. Energy analysis of Francis turbine for various mass flow rate conditions based on entropy production theory. *Renew. Energy* **2022**, *183*, 447–458. [[CrossRef](#)]
20. Li, D.; Gong, R.; Wang, H.; Xiang, G.; Wei, X.; Qin, D. Entropy production analysis for hump characteristics of a pump turbine model. *Chin. J. Mech. Eng.* **2016**, *29*, 803–812. [[CrossRef](#)]
21. Zhang, D.; Katayama, Y.; Watanabe, S.; Tsuda, S.I.; Furukawa, A. Numerical study on loss mechanism in rear rotor of contra-rotating axial flow pump. *Int. J. Fluid Mach. Syst.* **2020**, *13*, 241–252. [[CrossRef](#)]
22. Yang, F.; Chang, P.; Cai, Y.; Lin, Z.; Tang, F.; Lv, Y. Analysis of Energy Loss Characteristics of Vertical Axial Flow Pump Based on Entropy Production Method under Partial Conditions. *Entropy* **2022**, *24*, 1200. [[CrossRef](#)] [[PubMed](#)]
23. Cheng, X.; Wang, P.; Zhang, S. Investigation on matching characteristics of nuclear main pump guide vanes and annular casing. *J. Braz. Soc. Mech. Sci. Eng.* **2019**, *41*, 353. [[CrossRef](#)]
24. Ji, Q.; Wu, G.; Liao, W.; Fan, H. Flow Deflection between Guide Vanes in a Pump Turbine Operating in Pump Mode with a Slight Opening. *Energies* **2022**, *15*, 1548. [[CrossRef](#)]
25. Zhang, R.; Tan, S.; Ding, X.; Xu, H.; Feng, J.; Mou, T.; Fei, Z. Flow loss characteristics of vertical shaft cross-flow pump based on entropy production theory. *Adv. Sci. Technol. Water* **2022**, *3*, 9–11.

Article

Experimental Study on Fluidization Behaviors of Wet Rice Threshed Materials with Hot Airflow

Tao Zhang ^{1,2}, Yaoming Li ^{1,2,*}, Lizhang Xu ^{1,2}, Yanbin Liu ^{1,2}, Kuizhou Ji ^{1,2} and Sheng Jiang ^{1,2}

¹ Key Laboratory of Modern Agricultural Equipment and Technology, Jiangsu University, Zhenjiang 212013, China; jsdxzt@foxmail.com (T.Z.); justxlz@ujs.edu.cn (L.X.); 2111916005@stmail.ujs.edu.cn (Y.L.); jkz_jkzujs@163.com (K.J.); 2221916018@stmail.ujs.edu.cn (S.J.)

² School of Agricultural Engineering, Jiangsu University, Zhenjiang 212013, China

* Correspondence: ymli@ujs.edu.cn

Abstract: Among food crops, rice has the largest planting area, the highest yield per unit area and the largest total yield in China. However, cleaning performance is reduced by the high moisture content of rice during the harvesting process. In order to decrease the adhesion among wet rice threshed mixtures and improve the cleaning performance, the method of hot airflow cleaning was proposed. Firstly, the fluidization characteristics of wet sticky rice under the action of hot air were compared with those of dry particles. In this work, the minimum suspension velocity and the fastest suspension time were used and quantified to characterize the fluidization characteristics. It was found that the minimum suspension velocity and the fastest suspension time of the wet rice threshed mixture are both higher than those of dry particles due to the liquid bridge force. Moreover, the dispersion degree of the wet rice threshed mixture can be improved by the hot airflow due to the decrease in the surface water content of impurities. Secondly, the influence of the temperature and vibration frequency in the air-and-screen cleaning device on the dispersion characteristics of the wet rice threshed mixture were investigated. The accumulation mass was measured to quantify the dispersion degree. It was found that the increase in vibration frequency has little effect on the dispersion of the wet rice threshed mixture. The accumulation mass on the front of the sieve decreases slightly with the increase in the gas temperature range from ambient temperature to 30 °C. Then, the dispersion degree increases rapidly when the temperature exceeds 40 °C. The dispersion effect is the best when the temperature is 50 °C and the vibration frequency is 5 Hz. These results provide a basis for the cleaning of the wet rice threshed mixture in a combine harvester.

Citation: Zhang, T.; Li, Y.; Xu, L.; Liu, Y.; Ji, K.; Jiang, S. Experimental Study on Fluidization Behaviors of Wet Rice Threshed Materials with Hot Airflow. *Agriculture* **2022**, *12*, 601. <https://doi.org/10.3390/agriculture12050601>

Academic Editors:

Muhammad Sultan, Redmond R. Shamshiri, Md Shamim Ahamed and Muhammad Farooq

Received: 5 April 2022

Accepted: 21 April 2022

Published: 24 April 2022

Publisher's Note: MDPI stays neutral with regard to jurisdictional claims in published maps and institutional affiliations.



Copyright: © 2022 by the authors. Licensee MDPI, Basel, Switzerland. This article is an open access article distributed under the terms and conditions of the Creative Commons Attribution (CC BY) license (<https://creativecommons.org/licenses/by/4.0/>).

Keywords: wet rice; adhesion; hot airflow; dispersion characteristic; minimum suspension speed; surface water content

1. Introduction

Rice is the largest grain crop in China due to its high starch content [1–3]. During the rice harvest season, the climate is changeable and the weather is humid, so the moisture content of rice is too high when harvesting [4,5]. The adhesion between wet rice threshed materials occurs easily, resulting in the blockage of the cleaning screen, which seriously affects the rice quality and the working reliability of the combine harvester [6]. Hence, the air-and-screen cleaning device has been widely used in medium and large grain combine harvesters due to its high efficiency and strong adaptability [7–10]. To reduce the adhesion between the wet threshed mixture and the cleaning sieve, various methods, such as surface modification and introduction of a bionic screen, have been investigated. Ma et al. [11–14] applied the bionic non-smooth surface to the vibration screen of a rape harvester, and the test proved that the bionic non-smooth screen surface has good stability and use effect; however, the processing technology of the non-smooth screen is complex and the production cost is relatively high. Chen et al. [15] added a polytetrafluoroethylene coating to the surface of the vibrating screen to achieve the hydrophobic effect. Xu et al. [16] found

that the wettability of the rape cleaning screen surface can be reduced by a laser texture. Recently, a method to reduce the adhesion of wet sticky rice materials and the metal jitter plate by interface heating was proposed by Chen et al. [17]. The results indicated that the interface heating effectively decreased the adhesion rate between wet sticky rice materials and the jitter plate.

Before the working parameters can be determined, the influence of the working parameters on fluidization characteristics of the wet threshed mixture needs to be investigated and understood. However, only the fluidization state of the dry grain threshed mixture has been experimentally and numerically studied by a number of scholars. Chen et al. [18] studied the distribution of grain on the non-uniform air-flow cleaning unit by experiment. Li et al. [19] developed a CFD-DEM method to simulate the screening process of the air-and-screen cleaning device. The effect of the inlet airflow velocity was studied and analyzed in terms of grains and short straws' longitudinal velocity and vertical height, and cleaning loss. Bai Gali of Inner Mongolia Agricultural University [20] used a high-speed camera system to continuously collect the images of the flow field in the vertical pipe, measured the suspension velocity of several common grain particles, analyzed the influence of various factors on the suspension velocity of particle groups, and concluded that the suspension velocity of grain particles decreases with the increase in loading, and increases with the increase in the equivalent ball diameter. Hou et al. [21] studied the effect of moisture content of millet on floating speed and found that the floating speed of the grain, ear petal, stem and leaf of foxtail millet decreased with the decrease in moisture content. On the basis of the discussion of paddy cleaning mechanisms, the influence of the frequency and pulse width rate on separation was investigated by Chen et al. [22].

The capillarity of water film is an important cause of the formation of the adhesion interface, and the adhesion interface model between wet rice and the steel plate was developed by Chen et al. [17]. The fluidization characteristics of wet and dry rice threshed mixture were found to be apparently different. It was found that the understanding of fluidization characteristics of wet particles has been mainly advanced in chemical and medicine fields [23–26]. In order to reduce the agglomeration of the wet rice threshed mixture during the cleaning process, the hot airflow cleaning method was proposed. The fluidization characteristics of wet rice particles in a drying fluidized bed were first studied. Then, the dispersion characteristics of the wet rice threshed mixture were studied in the air-and-screen cleaning unit. This was helpful to reveal the dispersion mechanism of wet threshed materials and provide a theoretical basis for improving the performance of rice combine harvesters.

The objective of this study was to examine the effect of the airflow temperature on the fluidization state and dispersion characteristics in the drying fluidized bed. In addition, influences of the working parameters of cleaning device on the dispersion characteristic are also discussed in this paper.

2. Materials and Methods

2.1. Threshed Rice Mixture Samples

The test material was the indica rice planted in Miluo City, Hunan Province, China. After manual harvesting, a threshed rice mixture (see Figure 1) was obtained using the threshing device developed by Xu et al. [27].

The weight percentage of each component of rice after threshing was measured after sieving. The proportions of different components were 93.1% for rice grains, 0.7% for immature grains, 4.3% for short stems and 1.9% for light impurities. Immature grains are difficult to distinguish from grains in suspension, and their mass content is much lower than that of other materials, so they were not considered in this experiment. Each component of the threshed rice mixture was characterized by its density, equivalent diameter and moisture content. The physical properties of the rice threshed mixture were measured according to GB/T 24896-2010 and the literature [28]. The initial average values of the moisture content of rice grains, short stems and light impurities were 27.4%, 79.2% and

48.1%, respectively, and these materials were defined as wet particles, as shown in Table 1. Then, they were dried in the oven at 105 °C for 6 h and they were defined as dry particles [5]. Subsequently, these samples were kept in cold storage at 4–6 °C until further analysis.



Figure 1. Wet rice threshed mixture.

Table 1. Physical properties of rice threshed mixture.

Materials	Moist Content (%)	Length (mm)	Density (kg·m ⁻³)	Diameter (mm)
Rice grains	15.3 ^a /27.4 ^b	9.2	1085	-
Short stems	40.6 ^a /79.2 ^b	70.5	650	2.1–3.9
Light impurities	16.9 ^a /48.1 ^b	48.9	220	0.3–0.7

Note: ^a denotes dry particles; ^b denotes wet particles.

2.2. Experimental

2.2.1. Fluidized Bed Setup

A fluidized bed is commonly used to measure the suspension velocity of agricultural materials, such as wheat and cotton seed [29,30]. In this work, a drying fluidized bed was equipped to investigate the influence of hot airflow on the fluidization characteristics of the wet rice threshed mixture, as shown in Figure 2. A conical duct made of high light transmitting Plexiglas was used for observation. The height, bottom diameter and cone angle of the conical duct was 1000 mm, 140 mm and 6°, respectively. An asbestos net was located at the upper part of the steady flow cylinder to lay up rice particles and to ensure a good fluidization in the bed. Air was supplied by a centrifugal fan driven by an A.C. motor. The gas was able to reach the desired temperature by means of an electrical heater (200 kW) controlled by an A.C. contactor. Two ports were located in the side wall in the vertical direction of the column for pressure and temperature measurements. One of the ports was located at the bottom of the conical duct, and the other port was located 400 mm above the bottom port. The gas flow rate was changed gradually with a step of 18.3 m³/h. The inlet airflow velocity was measured by an intelligent anemometer (LB-FS80). Pressure readings were taken with a differential pressure transducer (LFM11, ±1.0%FS, from China). Furthermore, the airflow temperature of the fan outlet was measured by the K Type Thermometer (TES-1310, Taipei, Taiwan) with an accuracy of ±0.1 °C.

Digital images were recorded with a high-speed camera (type of i-speed 3, OLYMPUS, Tokyo, Japan) equipped with a 12.5 mm lens. The frame of the camera was 150,000 fps. The recorded images consisted of 1280 × 1024 pixels. The running time required to reach steady state conditions was determined by conducting a series of experiments over gas flow velocities ranging between 0 and 12 m/s.

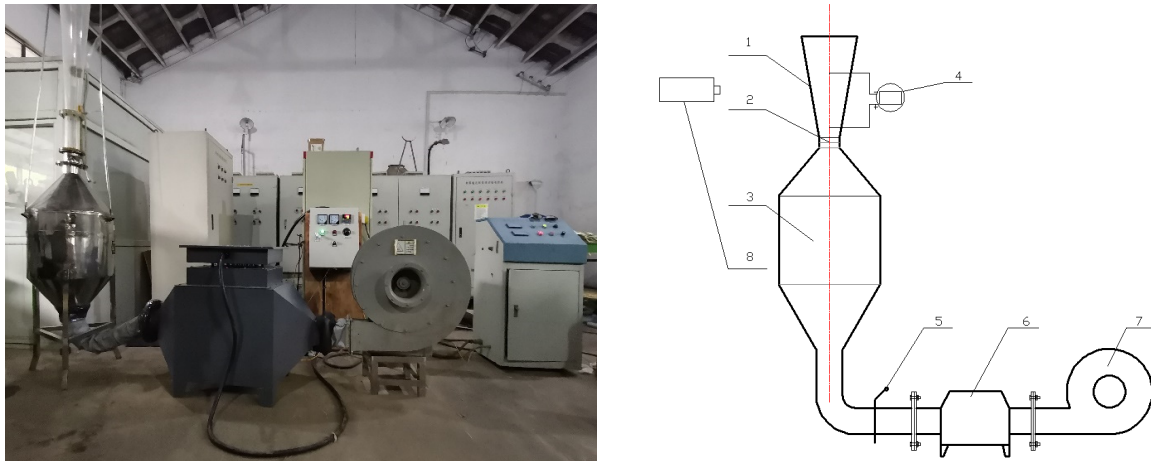


Figure 2. Scheme of the drying fluidized bed. 1. observed pipe; 2. asbestos net; 3. steady flow cylinder; 4. measuring port; 5. damper; 6. heating; 7. centrifugal fan; 8. high-speed camera.

2.2.2. Hot Airflow Cleaning Device

The cleaning unit was designed based on the previous study by Li [31], as shown in Figure 3, and the length and width of the cleaning sieve was 1200×960 mm. The outlet of heater was connected with the inlet of a cross-flow fan through a high-temperature resistant hose. The airflow temperature was adjusted by a heater (rated power 200 kW) and three thermometers (type of TM-902C, China) were used to measure the airflow temperature of the upper and lower fan outlets (test points 1, 2 and 3). The airflow temperature refers to the average value of the three test points.

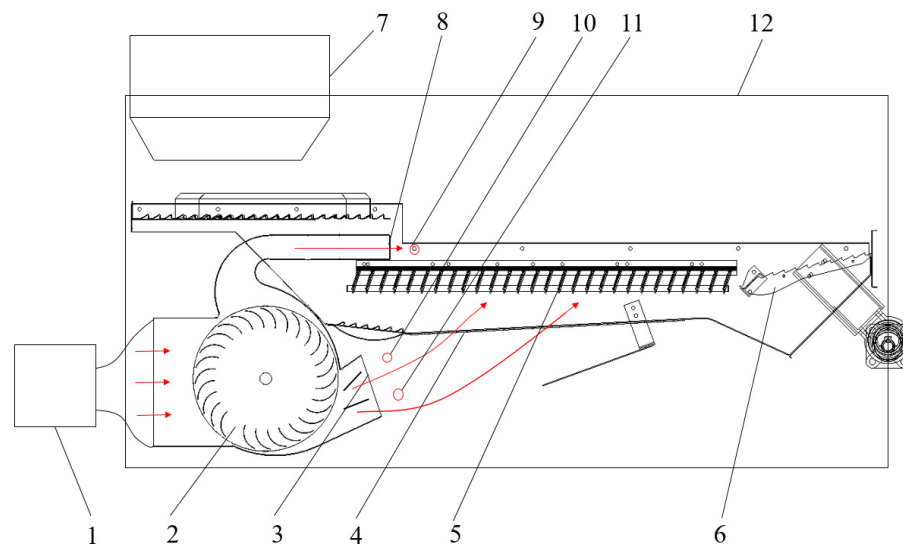


Figure 3. Sketch diagram of hot airflow. Cleaning test: 1. heater; 2. cross-flow fan; 3. lower gas outlet; 4. woven screen; 5. louvre screen; 6. tail screen; 7. hopper; 8. upper air outlet; 9. test point 1; 10. test point 2; 11. test point 3; 12. cleaning room.

2.3. Experimental Procedure

2.3.1. Fluidization Test

Two commonly used methods of measuring the terminal velocity experimentally are the drop and suspension methods [32]. The suspension method allows a particle to be suspended in a vertical duct by blowing air in a duct and measuring the air speed at the moment when the particle is suspended [33]. Study of fluidization characteristics was undertaken by investigating the effect of various airflow temperatures (12, 30, 40, 50 and 60°C) on the minimum suspension velocity and fastest suspension time with the latter

method. Wet rice mixtures with a given composition (14 g rice grains, 4 g short stems, 6 g light impurities) were first loaded into the reactors. Then, the process gas velocity was measured through the bottom test port as the fan speed increased. The gas velocity and time when the rice changed from static to completely suspended in the drying fluidized bed were determined as the minimum suspension velocity and the fastest suspension time, respectively. In order to maintain a constant mass of material in the bed, the gas was turned off abruptly after the rice grains were completely suspended. Each experiment was conducted three times under the same conditions.

The pressure drop across the bed is an important parameter, characterizing the flow behavior in a fluidized bed [34]. In order to identify the influence of flow parameters on the dispersion characteristics of the wet threshed mixture, the dispersion degree of the wet rice threshed mixture was determined by analysis of the pressure drop across the tube (see Figure 2). The pressure drop was measured at different airflow temperatures at the operation time, t , of 8 s.

The agglomerates of wet rice grains, short stems and light impurities were related to the adhesion force caused by the surface water content of the mixtures [17]; hence, the surface water content of wet rice threshed mixtures against airflow temperature for different airflow velocities was measured according to the oven method (GB/T211-2007). The surface moisture content ω_s (wet base) was calculated by:

$$\omega_s = \frac{m_2 - m_1}{m_2} \times 100\% \quad (1)$$

where m_2 is the initial mass of wet particles (g); m_1 is the mass (g) after drying at 30 °C in the oven for 8 h.

2.3.2. Hot Airflow Cleaning Test

The wet rice threshed mixture was configured as follows: The fresh rice harvested from the field was placed into a drying box and dried at a constant temperature of 110 °C for 24 h to constant weight; then, the appropriate amount of water was poured into the dry mixture using a measuring cylinder of 10 mL accuracy, and the mixture was evenly mixed. The mixture was then sealed and placed in the refrigerator (0~4 °C) for 3 days. In this work, the wet threshed rice mixture was released from the hopper above the oscillating plate, the feed mass of the threshed rice mixture was 4 kg/s and the entire cleaning process time was 30 s. Each test under different conditions was repeated three times and the average value was applied. Operation parameters are presented in Table 2.

Table 2. Experimental parameters.

Operation Parameters	Value
Heating temperature (°C)	15, 30, 40, 50
Vibration frequency (Hz)	3, 4, 5, 6
Vibration amplitude (mm)	30
Fan speed (r/min)	1000

2.4. Statistical Calculations

Statistics in this article were calculated by the data fitting function of Origin8.6 (Origin-Lab, Northampton, MA, USA).

3. Results and Discussion

3.1. Fluidization Characteristics of Wet and Dry Rice Threshed Mixture

3.1.1. Minimum Suspension Velocity and Fastest Suspension Time

The minimum suspension velocity is one of the most important hydrodynamic parameters that describes the gas–solid flow characteristics in a fluidized bed [35]. Figure 4 presents the effect of airflow temperature on the minimum suspension velocity v_{mf} of dry

and wet rice threshed mixtures within 30 s. It can be seen that the minimum suspension velocity v_{mf} of the dry threshed mixture is less than 6.5 m/s for all temperature levels, and was independent of the inlet gas temperature. For the wet rice threshed mixture, the average value of v_{mf} is higher than 7.5 m/s at ambient temperature, which indicates a larger kinetic energy is needed for suspension. This is because the high moisture content will introduce the liquid bridge force between wet granules. The drag force needed for the wet rice threshed mixture to attain suspension in gas phase would be larger than that for dry particles. Moreover, the large porosity of the wet rice threshed mixture may also cause an increase in the minimum suspension velocity v_{mf} . From Figure 4, the minimum suspension speed v_{mf} is almost constant when the temperature is less than 30 °C, and then decreases as the input airflow temperature increases. A possible reason for this is that the liquid bridge force in the packed bed decreases when the gas temperature increases from 30 to 40 °C because the liquid bridge force between wet particles decreases with the decrease in the surface tension of the liquid, which is dependent on temperature [35]. Furthermore, the liquid occupying the voids among wet particles would evaporate with the further increase in gas temperature. This would result in a smaller resistance to gas flow. When the airflow temperature exceeds 50 °C, the minimum suspension speed begins to stabilize. The minimum suspension speed of the wet threshed mixture is only 0.25 m/s larger than that of the dry mixture when the airflow temperature is 60 °C. Experimental data of the v_{mf} of the wet threshed mixture were statistically fitted to empirical curves, which were given by the following equation:

$$v_{mf} = 6.2 + \frac{1.4}{1 + (T/35)^{11.7}} \quad (2)$$

where v_{mf} is the minimum fluidized velocity (m/s); T is the airflow temperature (°C). The adjusted R-square value of the polynomial is 0.88667, which indicates the polynomial can accurately express the mathematical relation between v_{mf} and temperature T .

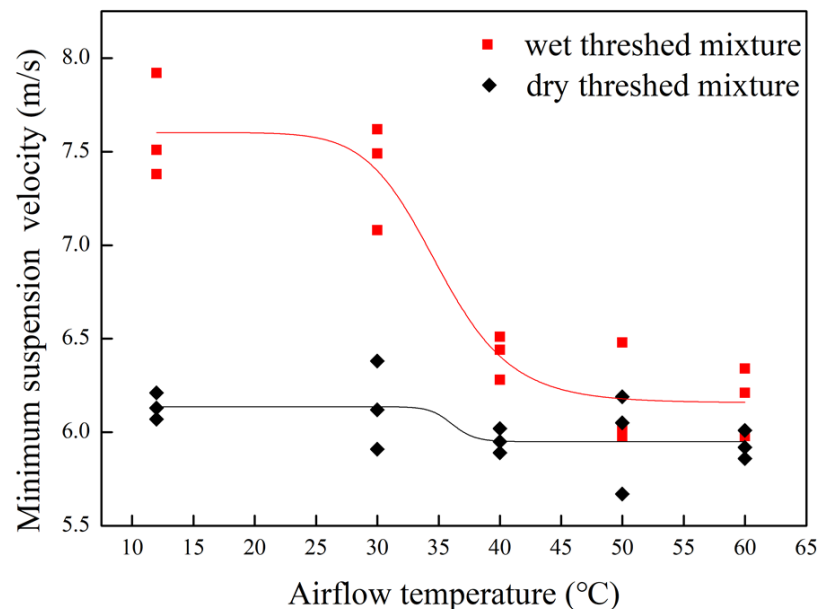


Figure 4. Minimum suspension velocity with temperature.

The time when most threshed mixture begin to be suspended in the test bed was defined as the fastest suspension time. Figure 5 shows the fastest suspension time at different airflow temperatures. A decrease in the fastest suspension time with increasing temperature was observed to occur for the wet threshed mixture. In comparison to the dry rice threshed mixture, the fastest suspension time of the wet rice threshed mixture was 27.3 s at the airflow temperature of 12 °C, which was 25 times longer than that of

dry particles. Moreover, focusing on the wet particles, the sudden decline in the fastest suspension time can be observed at the airflow temperature of 50 °C. The reason for this is that the agglomerates were broken down, thus enabling the system to fluidize. The fastest suspension time of the wet rice threshed mixture was less than 2 s when the temperature rose to 60 °C, as illustrated in Figure 5, which was close to the case of dry particles. The results show that the wet rice threshed mixture can be suspended within a very short time after heating.

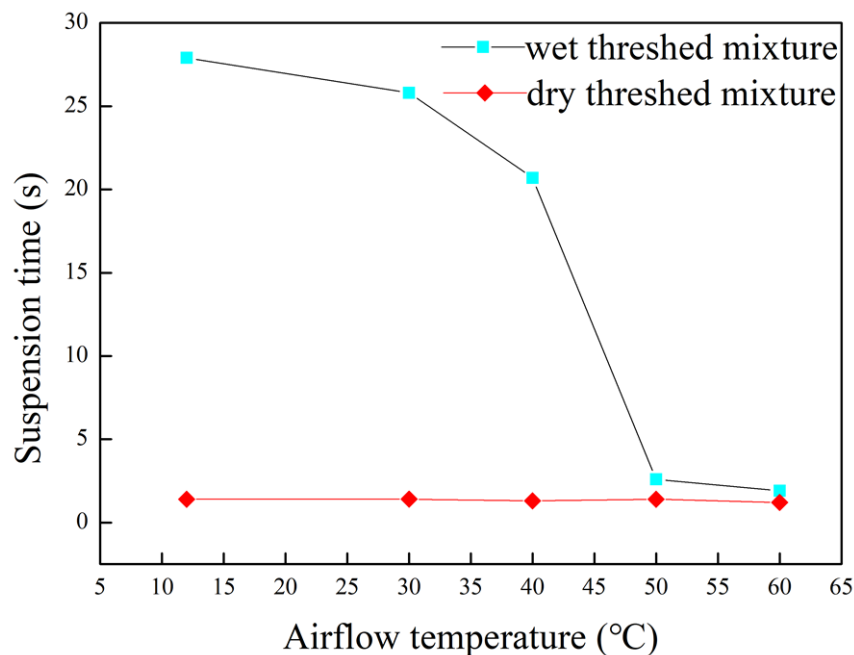


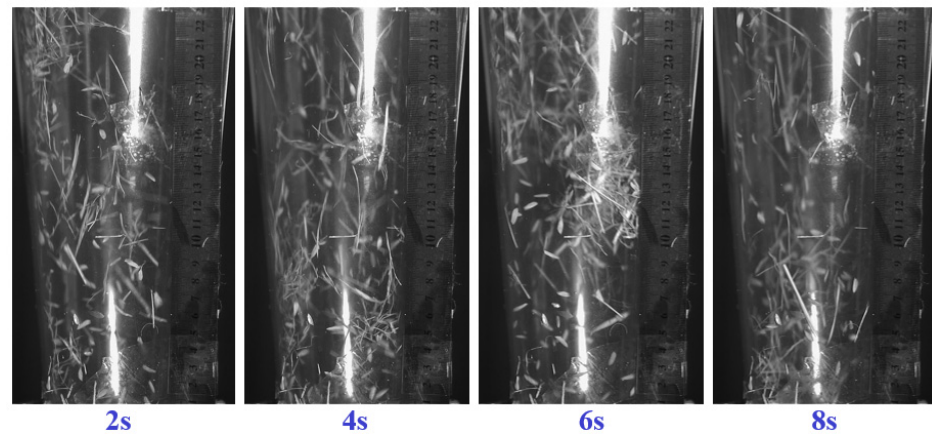
Figure 5. Suspension time with temperature.

3.1.2. Flow State

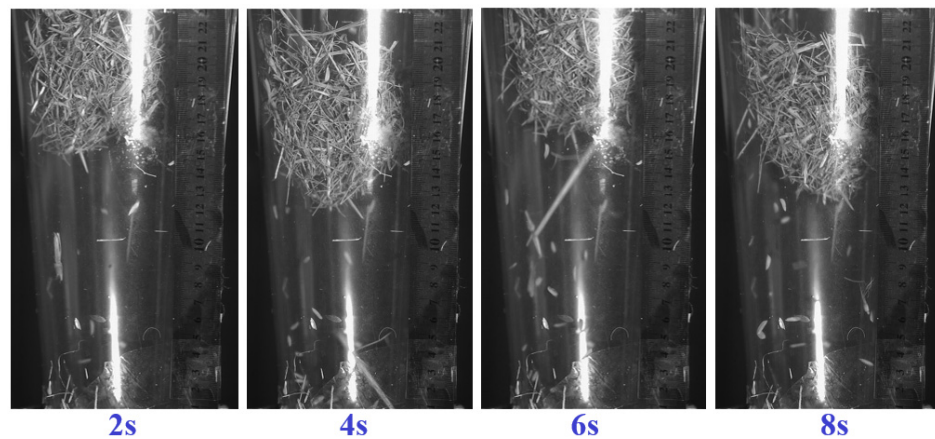
To better understand the effect of inlet gas temperature on fluidization behavior, some snapshots of the fluidization process were taken. According to the preliminary experiment of Figure 4, the minimum suspension velocities of the dry and wet threshed mixture were 6.14 and 7.60 m/s under ambient conditions, respectively. The inlet gas velocity v was 7.60 m/s and working time $t = 8$ s. The fluidization process of dry and wet rice threshed mixtures under ambient conditions is illustrated in Figure 6a,b, respectively. Fluidization does not start until the inlet gas velocity is above the minimum suspension velocity of the rice threshed mixture. Thus, once enough air is injected into the drying fluidized bed, the dry and wet particle beds can be agitated by gas bubbles, and suspension of the threshed mixtures (including rice grains, short stems and light impurities) happens. For dry particles, it can be seen that the dry threshed mixture was completely suspended and scattered in the drying fluidized bed. In addition, these dry particles rotated and tumbled in the suspension device due to their irregular shape, and large gaps among them can be observed. For wet particles, however, the agglomerate made from the wet light impurities, rice grains and short stems were suspended in the upper position of the drying fluidized bed. As suspension continued, the agglomerate hardly changed. The reason for this is that the adhesion force among the wet rice threshed mixture is far larger than the drag force. In addition, the rough surface and large length–diameter ratio of the rice threshed mixture may also cause the agglomeration.

Figure 7 shows the flow state of the wet rice threshed mixture at different gas temperatures at $v = 7.60$ m/s. Compared with 12 °C (see Figure 6b), the suspension behavior of the wet threshed mixture at 30 °C was hardly changed at $t = 5$ s, as shown in Figure 7a. A further increase in gas temperature caused the fluidization behavior to change, with the gas passing through horizontal channels. The lower half of the agglomerate was the first

to disperse and the short stems began to pass through the rice grain layer at the airflow temperature of 40 °C, as shown in Figure 7b. Then, a certain degree of dispersion occurred between rice grains and light impurities until the temperature was 50 °C (Figure 7c). At the same time, the flow pattern evolution of the wet threshed mixture in the test bed was similar to that of dry threshed mixture (see Figure 7a). According to Figure 7d, when the airflow temperature was 60 °C, all the rice grains and short stems were separated, and only a small number of light impurities were still reunited. This may be due to the intermolecular van der Waals force.



(a) Dry particles



(b) Wet particles

Figure 6. Flow state of rice threshed mixture ($v = 7.60$ m/s and $t = 8$ s).

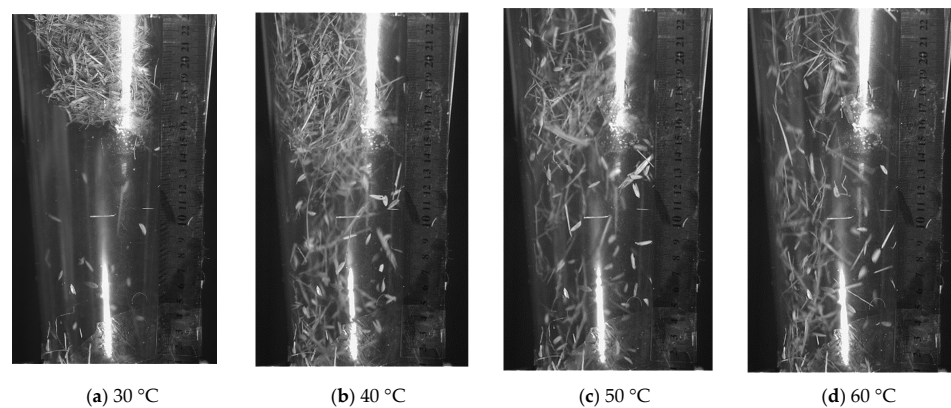


Figure 7. Flow state of wet threshed mixture at different airflow temperatures ($v = 7.60$ m/s and $t = 8$ s).

3.1.3. Dispersion Degree of Wet Rice Threshed Mixture

The results reported in this work were obtained under steady-state operating conditions at $t = 8$ s. Figure 8 shows the curve of pressure drop versus gas temperature across the bed. Room temperature ($12\text{ }^{\circ}\text{C}$) resulted in the largest pressure drop of 95.2 Pa . When the inlet gas temperature was in the range of 12 to $40\text{ }^{\circ}\text{C}$, the pressure drop decreased slowly with increasing temperature. This indicates that the dispersion degree among wet particles varied little, which confirmed the phenomenon observed in Figure 7b. When the inlet gas temperature increased from 40 to $60\text{ }^{\circ}\text{C}$, the pressure drop reduced significantly and the dropping rate exceeded 80% . At the gas temperature of $60\text{ }^{\circ}\text{C}$, the pressure drop reached the minimum, i.e., 8.3 Pa in the present condition. The results of the above analysis show that heating can improve the dispersion degree of the wet threshed mixture in the fluidized bed. Experimental data of pressure drop versus airflow temperature were statistically fitted to empirical curves, given by the following equation:

$$\Delta P = 136.5 - 5.11T + 0.18T^2 - 0.002T^3 \quad (3)$$

where ΔP is the pressure drop (Pa); T is the airflow temperature ($^{\circ}\text{C}$). The adjusted R-square value of this polynomial is 0.97695 , which indicates the polynomial can accurately express the mathematical relation between pressure drop ΔP and temperature T .

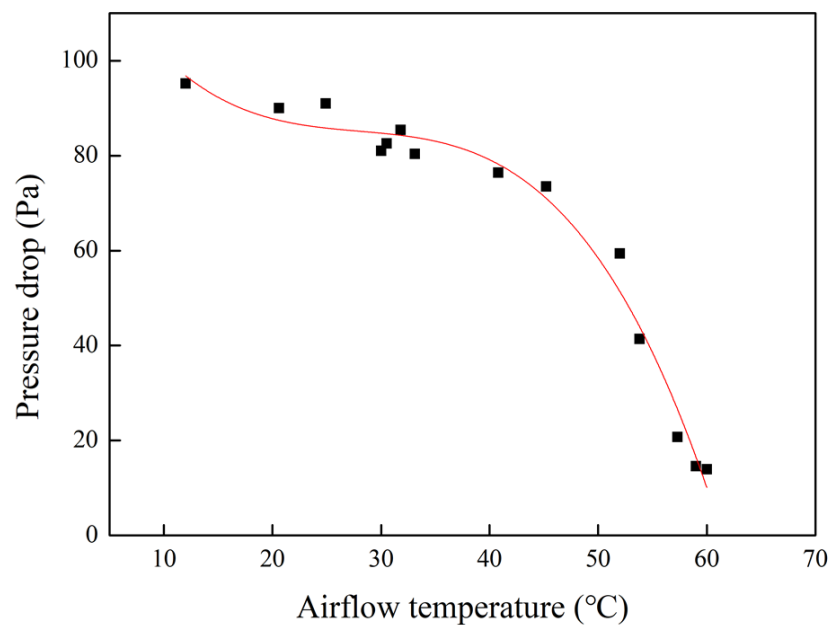


Figure 8. Pressure drop as a function of airflow temperature ($v = 7.60\text{ m/s}$ and $t = 8\text{ s}$).

3.1.4. Surface Water Content

As discussed above, the agglomerates of wet rice grains, short stems and light impurities were separated when the airflow temperature rose from ambient temperature to $60\text{ }^{\circ}\text{C}$. It was unknown whether this was related to the change in adhesion force caused by the surface water content of the mixtures. Figure 9 shows the surface moisture content of the wet threshed mixtures versus airflow temperature under steady state fluidization conditions at $t = 8$ s. A decrease in surface moisture with temperature can be observed for rice grains, short stems and light impurities. The dropping trend in the surface moisture content of light impurities is consistent with that in pressure. This indicates that the decrease in surface water content of light impurities is the main reason for the increase in dispersion degree. The moisture content of the surface of rice grains and short stems was 7.8% and 14.7% without heating, respectively, and hardly changed as the inlet gas temperature increased in the range of 12 to $40\text{ }^{\circ}\text{C}$, which also reveals the quite small dispersion degree of the wet rice threshed mixture seen from Figure 7a,b. Additionally, the surface moisture content of rice

grains and short stems was 3.4% and 7.9% when the airflow temperature was 50 °C, which clearly explains the reason for the good dispersion between wet rice grains and short stems observed in Figure 7c.

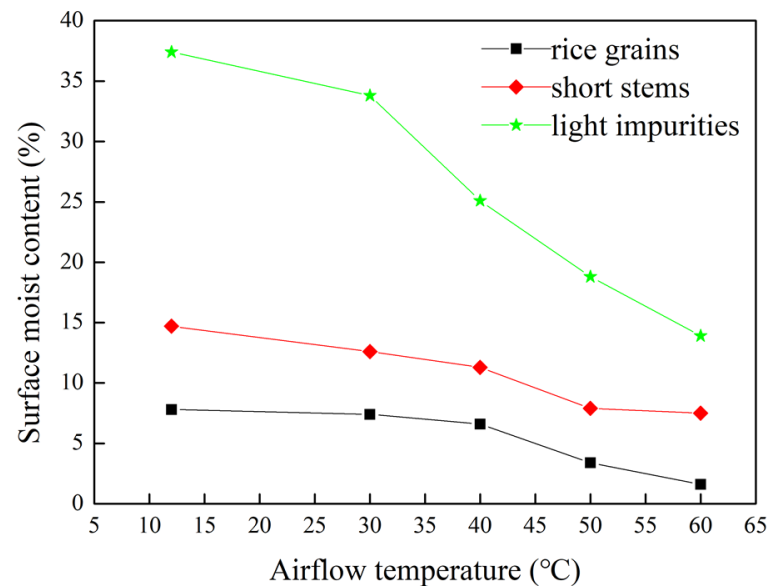


Figure 9. Curves of surface moisture content vs. temperature ($v = 7.60$ m/s and $t = 8$ s).

3.2. Hot Airflow Cleaning Test

According to the above fluidization experiment, the dispersion degree of wet rice threshed mixture in the drying fluidized bed can be improved by hot airflow. However, the adhesion phenomenon among wet rice threshed mixtures usually arises under the vibration of the cleaning sieve of the combine harvester, and the agglomerates formed by the wet rice threshed mixture block the cleaning screen. Hence, the effect of hot airflow on the dispersion characteristics of the wet rice mixture in the air-and-screen cleaning device was studied.

Figure 10 presents a snapshot of the screen surface after the screening process finished. It can be seen that the wet threshed mixture entered the front of the sieve and accumulated there. Therefore, in order to quantitatively analyze the influence of cleaning parameters on the dispersion characteristics, the accumulation mass on the front half of cleaning sieve was measured after each test was completed. At the end of each test, the surface of the cleaning sieve was cleaned by towels to reduce experimental error.



Figure 10. Snapshot of the cleaning screen surface.

The results of the accumulation mass are presented in Figure 11. It can be concluded that, for all vibration frequency levels, the accumulation mass of the wet threshed mixture on the cleaning sieve decreased with the increasing temperature. When the airflow temperature reached 50 °C, the accumulation mass was less than 250 g at 4 and 5 Hz. In addition, the accumulation mass differed little at various vibration frequencies when the airflow temperature was lower than 40 °C. When the airflow temperature and vibration frequency were 50 °C and 5 Hz, respectively, the accumulation mass on the front of the cleaning sieve was the smallest. As a result, heating can effectively reduce the accumulation on the screen surface, so as to improve the dispersion degree of the wet rice threshed mixture. However, the accumulation mass did not decrease to zero after heating; this may be due to insufficient temperature or other cleaning parameters.

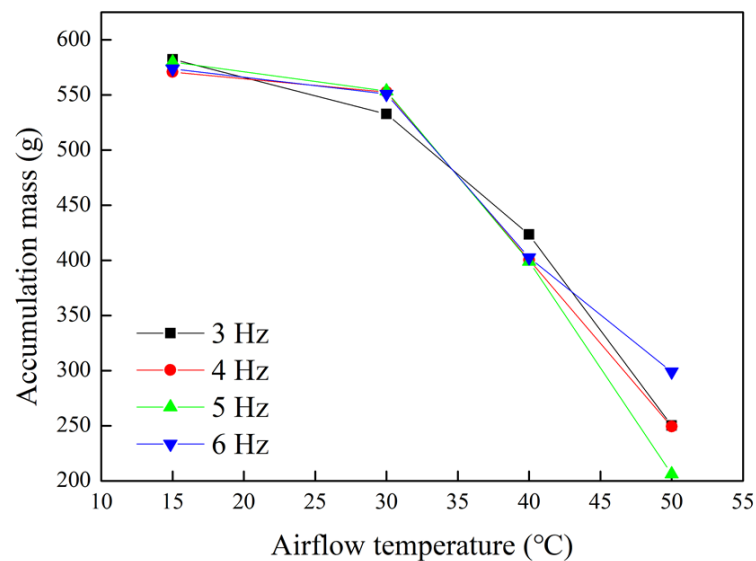


Figure 11. Effect of airflow temperature on accumulation mass.

4. Conclusions

Based on the results of the above study, the following main conclusions can be drawn:

1. With the increase in temperature, the minimum suspension velocity and the fastest suspension time decreased gradually. The minimum suspension velocity of rice grains and short stems increased slightly with inlet airflow up to the critical temperature, equal to 40 °C, and then increased markedly with temperature. The fastest suspension time of the wet rice threshed mixture was less than 2 s when the temperature increased to 60 °C. According to the observed flow state of the wet rice threshed mixture, the agglomerations formed by rice grains, short stems and light impurities are difficult to break into discrete particles under the normal temperature airflow. The lower half of the agglomerate was the first to disperse and the short stems began to pass through the rice grain layer with the increasing temperature. When the gas temperature was about 60 °C, rice grains and impurities were effectively separated.
2. The trends in the pressure drop and surface moisture content of light impurities were the same: both decreased gradually with the increase in inlet gas temperature. As the temperature increased to 60 °C, the surface moisture content of the wet particles decreased to a lesser extent, which explains the dispersion phenomenon in the fluidization process.
3. The adhesion mass on the front of the screen surface can be reduced with the increase in the inlet airflow temperature. However, it is little affected by the vibration frequency. When the airflow temperature and vibration frequency were 50 °C and 5 Hz, respectively, the accumulation mass was less than 220 g. Another beneficial effect of increasing the inlet gas temperature is that the screen sieve was heated and the adhesion was reduced.

4. In future work, more cleaning parameters, such as airflow velocity, louvre screen opening and vibration amplitude, will be considered to study the dispersion characteristics of the wet rice threshed mixture in the air-and-screen cleaning unit.

Author Contributions: In the research of this article, T.Z. mainly completed the writing and experimental part of the paper. Y.L. (Yaoming Li) and L.X. provided the guidance of scientific research funds and experimental scheme. K.J. and Y.L. (Yanbin Liu) and S.J. assisted me in completing the experimental research and helped me complete some papers. All authors have read and agreed to the published version of the manuscript.

Funding: This research was funded by National Natural Science Foundation of China under Grant grant number (51975257).

Institutional Review Board Statement: Not applicable.

Informed Consent Statement: Not applicable.

Acknowledgments: The authors gratefully acknowledge the National Natural Science Foundation of China.

Conflicts of Interest: We ensured that there was no conflict of interest.

References

1. Liu, Y.B. Study on Performance of Concentric Threshing Device with Multi-Threshing Gaps for Rice Combines. *Agriculture* **2021**, *11*, 1000. [[CrossRef](#)]
2. Bag, M.K.; Basak, N.; Bagchi, T.; Masurkar, P.; Ray, A.; Adak, T.; Jena, M.; Rath, P.C. Consequences of *Ustilaginoidea virens* infection, causal agent of false smut disease of rice, on production and grain quality of rice. *J. Cereal Sci.* **2021**, *100*, 103220. [[CrossRef](#)]
3. Bagchi, T.B.; Chattopadhyay, K.; Sivashankari, M.; Roy, S.; Kumar, A.; Biswas, T.; Pal, S. Effect of Different Processing Technologies on Phenolic Acids, Flavonoids and Other Antioxidants Content in Pigmented Rice. *J. Cereal Sci.* **2021**, *100*, 103263. [[CrossRef](#)]
4. Ni, G.; Qin, Y.; Han, K. Innovative Cleaning Technology of Rice Combine Harvester for All-weather Harvesting. *J. Agric. Equip. Veh. Eng.* **2019**, *57*, 173–174.
5. Chen, C.; Fun, J.; Chen, Z.; Ren, L.Q. Effect of vibration parameters of vibrating screen for harvester on adhesion characteristics of threshed mixtures with different moistures. *J. Trans. Chin. Soc. Agric. Eng.* **2019**, *35*, 29–36.
6. Cheng, C.; Fu, J.; Tang, X.; Chen, Z.; Ren, L.Q. Effect of vibration mode on the interface adhesion law of rice threshed mixtures. *J. Jilin Univ. (Eng. Technol. Ed.)* **2019**, *49*, 1228–1235.
7. Tang, Z.; Li, Y.; Li, H.; Xu, L.; Zhao, Z. Analysis on the eddy current of the air-and-sieve cleaning device. *Trans. Chin. Soc. Agric. Mach.* **2010**, *41*, 62–66.
8. Liang, Z.W. Development and testing of a multi-duct cleaning device for tangential-longitudinal flow rice combine harvesters. *Biosyst. Eng.* **2019**, *182*, 95–106. [[CrossRef](#)]
9. Leng, J.; Li, X.; Du, Y.; He, S.; Ding, X.; Niu, X. Analysis and optimization of internal flow field of cleaning device of single longitudinal axial flow grain combine harvester. *Trans. Chin. Soc. Agric. Eng.* **2020**, *36*, 39–48.
10. Ning, X.; Jin, C.; Yin, X. Research status and development trend of air-screen cleaning device for cereal combine harvesters. *J. Chin. Agric. Mech.* **2018**, *39*, 5–10.
11. Ma, Z.; Li, Y.-M.; Xu, L.-Z. Theoretical analysis of micro-vibration between a high moisture content rape stalk and a non-smooth surface of a reciprocating metal cleaning screen matrix. *Biosyst. Eng.* **2015**, *129*, 258–267. [[CrossRef](#)]
12. Li, Y.; Ma, Z.; Xu, L. Tribological characteristics of adhesion materials on cleaning sieve of rape combine harvester. *Trans. Chin. Soc. Agric. Mach.* **2010**, *41*, 54–57.
13. Ma, Z. *Study on Friction and Particles Motion of Bionic Anti-Clogging Screening Process in Agricultural Materials*; Jiangsu University: Zhengjiang, China, 2015.
14. Ma, Z.; Li, Y.-M.; Xu, L.-Z. Micro flow field on adjacent screen of bionic non-smooth cleaning screen. *Trans. Chin. Soc. Agric. Mach.* **2011**, *42*, 74–77.
15. Cheng, C.; Fu, J.; Chen, Z.; Ren, L. Design and Experiment on Modified Sieve with Coating of Rice Harvester. *Trans. Chin. Soc. Agric. Mach.* **2020**, *51*, 94–102.
16. Xu, L.; Ma, Z.; Li, Y. Wettability of rape cleaning screen surface by laser-texture. *Trans. Chin Soc. Agric. Mach.* **2011**, *42*, 168–171.
17. Cheng, C.; Fu, J.; Tang, X.; Chen, Z.; Ren, L. Heating Anti-adhesion Experiments of Jitter Plate of rice Harvesting Machinery. *Trans. Chin. Soc. Agric. Mach.* **2019**, *50*, 110–111.
18. Chen, N.; Huang, D.; Chen, D.; Tian, X.; Zhang, J. Theory and experiment on non-uniform air-flow cleaning of air-screen cleaning unit. *Trans. Chin. Soc. Agric. Mach.* **2009**, *40*, 73–77.
19. Li, H.; Li, Y.; Gao, F.; Zhao, Z.; Xu, L. CFD-DEM simulation of material motion in air-and-screen cleaning device. *Comput. Electron. Agric.* **2012**, *88*, 111–119. [[CrossRef](#)]

20. Bai, G.; Ta, N.; Zhu, Y. Experimental study on the grain suspension velocity by using high-speed camera system technology. *Mogolia Agric. Univ.* **2012**, *33*, 167–170.
21. Hou, H.M.; Cui, Q.L.; Guo, Y.M.; Zhang, Y.Q.; Sun, D.; Lai, S.T.; Liu, J.L. Design and test of air-sweeping suspension velocity testing device for cleaning threshed materials of grain and oil crops. *Trans. Chin. Soc. Agric. Eng.* **2018**, *34*, 43–49.
22. Chen, H.; Huang, B. Research on Technique to Clean paddy by Pulsation Fluidization. *Mod. Agric. Equip.* **2013**, *4*, 37–40.
23. Xu, H.; Zhong, W.; Yu, A.; Yuan, Z. Spouting Characteristics of Wet Particles in a Conical-Cylindrical Spouted Bed. *Ind. Eng. Chem. Res.* **2015**, *54*, 9894–9902. [[CrossRef](#)]
24. Schneider, T.; Bridgwater, J. The stability of wet spouted beds. *Dry. Technol.* **1993**, *11*, 277–301. [[CrossRef](#)]
25. Lehmann, S.E.; Hartge, E.U.; Jongsmas, A.; de Leeuw, I.M.; Innings, F.; Heinrich, S. Fluidization characteristics of cohesive powders in vibrated fluidized bed drying at low vibration frequencies. *Powder Technol.* **2019**, *357*, 54–63. [[CrossRef](#)]
26. Weber, S.; Briens, C.; Berruti, F.; Chan, E.; Gray, M. Agglomerate stability in fluidized beds of glass beads and silica sand. *Powder Technol.* **2007**, *165*, 115–127. [[CrossRef](#)]
27. Xu, L.; Li, Y.; Li, H.; Zhao, Z. Development on test-bed of longitudinal axial threshing-separating-cleaning unit. *Trans. Chin. Soc. Agric. Mach.* **2009**, *12*, 76–79.
28. Farahmandfar, R.; Farahmandfar, E.; Ramezani, A. Physical Properties of Rough Rice. *Int. J. Food Eng.* **2009**, *5*, 1–8. [[CrossRef](#)]
29. Tabak, S.; Wolf, D. Aerodynamic properties of cotton seeds. *J. Agric. Eng. Res.* **1998**, *70*, 257–265. [[CrossRef](#)]
30. Khoshtaghaza, M.H.; Mehdizadeh, R. Aerodynamic property of wheat kernel and straw materials. *Agric. Eng. Int. CIGR J.* **2006**, *8*, 1–10.
31. Li, Y.; Xu, L.; Zhou, Y.; Li, B.; Liang, Z.; Li, Y. Effects of throughput and operating parameters on cleaning performance in air-and-screen cleaning unit: A computational and experimental study. *Comput. Electron. Agric.* **2018**, *152*, 141–148. [[CrossRef](#)]
32. Carmen, K. Some physical properties of lentil seeds. *J. Agric. Eng. Res.* **1996**, *63*, 87–99. [[CrossRef](#)]
33. Neto, P.S.; Cunha, F.O.; Freire, J.T. Effect of the presence of paste in a conical spouted bed dryer with continuous feeding. *Dry. Technol.* **2002**, *20*, 789–811. [[CrossRef](#)]
34. Dong, R.; Xia, L.; Wang, H.; Jiao, D. 3-D CFD simulation of oil shale drying in fluidized bed and experimental verification. *Oil Shale* **2020**, *37*, 334–356. [[CrossRef](#)]
35. Xu, H.; Zhong, W.; Shao, Y.; Yu, A. Experimental study on mixing behaviors of wet particles in a bubbling fluidized bed. *Powder Technol.* **2018**, *340*, 26–33. [[CrossRef](#)]

MDPI
St. Alban-Anlage 66
4052 Basel
Switzerland
www.mdpi.com

Agriculture Editorial Office
E-mail: agriculture@mdpi.com
www.mdpi.com/journal/agriculture



Disclaimer/Publisher's Note: The statements, opinions and data contained in all publications are solely those of the individual author(s) and contributor(s) and not of MDPI and/or the editor(s). MDPI and/or the editor(s) disclaim responsibility for any injury to people or property resulting from any ideas, methods, instructions or products referred to in the content.



Academic Open
Access Publishing

mdpi.com

ISBN 978-3-0365-9377-7